Proceedings of:

The Twenty-fifth Annual Meeting of

The American Society for Precision Engineering

October 31 to November 4, 2010
OMNI Hotel at CNN Center
Atlanta, Georgia

The American Society for Precision Engineering (ASPE) is a multidisciplinary professional and technical society concerned with research and development, design, manufacture and measurement of high accuracy components and systems. ASPE activities encompass relevant aspects of mechanical, electronic, optical and production engineering, physics, chemistry, and computer and materials science. Membership is open to anyone interested in any aspect of precision engineering.

Founded in 1986, ASPE provides a new focus for a diverse but important community. Other professional organizations have covered aspects of precision engineering, always as a sideline to their principal goals. ASPE is based on the core of generic concepts necessary to achieve precision in any application; independent of discipline, ASPE intends to be the focus for precision technology—and to represent all facets from research to application.

ASPE – The American Society for Precision Engineering
301 Glenwood Avenue, Suite 205, Raleigh, NC 27603
P.O. Box 10826, Raleigh, NC 27605
Telephone: (919) 839-8444, Fax (919) 839-8039
http://www.aspe.net

Preface

This book comprises the proceedings of the 25th ASPE Annual Meeting. The contributions reflect the authors' opinions and are published as presented to ASPE, without change. Their inclusion in this publication does not necessarily constitute endorsement by the ASPE, or its editorial staff.

Individual readers of this book and nonprofit libraries acting for them are permitted to make fair use of the material contained in this book to be used in teaching or research; provided they copy said paper in total, as written by the author. Permission is granted to quote excerpts from the scientific or technical works in this book with proper acknowledgment of the source to include: The author's name, the book name, and the ASPE tag line. Reproduction of figures and tables is likewise permitted from the contents of this book, provided that the same acknowledgment of the same source and content is permitted.

Any other type reproduction, systematic copying or multiple reproduction of any material in this book is expressly prohibited except with the written permission of the ASPE editorial staff, addressed to the Society's headquarters.

ISBN 978-1-887706-56-8

2010

American Society for Precision Engineering
301 Glenwood Avenue, Suite 205
Raleigh, NC 27603

Printed in the United States of America

Welcome Note

Welcome to Atlanta and the Twenty-fifth Annual Meeting of The American Society for Precision Engineering. The growth and success of the Society reflects the increasing importance of precision engineering in a wide variety of fields, from manufacturing to microelectronics to basic science. The Society serves as a focus for precision engineers across all of these fields. The Annual Meeting has evolved into a premier international forum for the exchange of ideas and presentation of research results relating to precision engineering, metrology, controls, and system integration. Precision engineers and scientists from private industry, government laboratories, and universities meet to learn about the latest developments and to exchange ideas about the future directions of these technologies.

The 2010 ASPE Annual Meeting continues the tradition of offering two full days of tutorials presented by some of the foremost precision engineers and scientists in the world. The technical sessions and poster presentations offer the latest research results in the areas of ultraprecision machining, metrology, controls, precision grinding, micro-positioning, material processing, design, precision transducers, surface profilometry, and error compensation. The commercial exhibits will provide attendees with the opportunity to view and discuss the latest precision engineering equipment, products, and services.

The conference organizing committee is proud to present the program for the Twenty-fifth Annual Meeting of the ASPE. We welcome your participation and your feedback on how to make future meetings even better.

2010 Organizing & Technical Program Committee

David D. Gill
Sandia National Laboratories, Conference Chair

Luis A. Aguirre, 3M Company
Marcin B. Bauza, InsituTec, Inc.
Eric S. Buice, Delft University of Technology
Keith Carlisle, Lawrence Livermore National Laboratory
Thomas A. Dow, North Carolina State University
Jonathan D. Ellis, Delft University of Technology
Robert D. Grejda, Corning Tropel Corporation
Bradley H. Jared, Sandia National Laboratories
Byron R. Knapp, Professional Instruments Company, Inc.
Stephen J. Ludwick, Aerotech, Inc.
Brian P. O'Connor, Aerotech, Inc.
Senajith B. Rekawa, Lawrence Berkeley National Laboratory
Deming Shu, Argonne National Laboratory
Mark A. Stocker, Cranfield Precision
Pradeep K. Subrahmanyan, RAPT Industries, Inc.
Hans-Jochen Trost, MicroFab Technologies, Inc.

2010 Scholarship Recipients

Suhasa B. Kodandaramaiah, Georgia Institute of Technology
R.V. Jones Memorial Scholarship

Christopher Phaneuf, Georgia Institute of Technology

2010 Scholarship Sponsor

Aerotech, Inc.

2010 Annual Meeting

Contents

Preface ii

Welcome Note iii

Organizing Committee – 2010 Scholarship Recipients and Sponsors iv

Table of Contents v

Program vi

Keynote Address vii

Technical Exhibitors viii

Sustaining Corporate Sponsors ix

Corporate Sponsors x

Lifetime Achievement Award 1

Technical Paper Index 2-10

Technical Papers 13-458

Author Index 459-462

Program

2010 ASPE Annual Meeting

Time	Sun., Oct. 31	Mon., Nov. 1	Tues., Nov. 2	Wed., Nov. 3	Thurs., Nov. 4
8:00	Registration		Registration and Early Coffee		
9:00	Tutorials	Tutorials	Technical Session I	Technical Session III	Technical Session VI
10:00			Break	Break	Break
11:00			Technical Session II	Technical Session IV	Technical Session VII
12:00			Lunch and Committee Meetings	Awards Lunch and Business Meeting	Lunch and Open Forum
1:00					
2:00	Tutorials	Tutorials	Commercial Session	Technical Session V	Technical Session VIII
3:00			Break	Break	
4:00			Poster Session	Poster Session	
5:00			Hospitality Hr.	Hospitality Hr.	
6:00		Welcome Reception			
7:00		Keynote Address	Dinner at the High Museum of Art		
8:00					
9:00					

Exhibit Open Hours

Keynote Address

Bryan G. Dods

Executive, Manufacturing Technology Leader
Global Supply Chain Management, General Electric Energy

Monday, November 1, 7:00 p.m.

Session Chair: David D. Gill, Sandia National Laboratories

Bryan Dods serves as the Manufacturing Technology Leader for General Electric Energy. The Manufacturing Technology organization has responsibility for new product and technology introduction across GE Energy's global factory and supplier network. Before joining GE Energy in 2008, he spent 21 years in the aerospace industry. Bryan has 23 years of manufacturing experience in various quality assurance, production management, and technology development roles. He has been active in re-establishing manufacturing as a competitive advantage through participation with industry consortiums, government agencies, research institutes and universities. He was selected to the National Academy of Engineering Frontiers of Engineering program in 2004, served on the Centre of Excellence for Customised Assembly board for the United Kingdom's Advanced Manufacturing Research Center and served as the Industry Advisory Board chairman for the National Science Foundation's Industry/University Collaborative Research Center for Intelligent Maintenance Systems. Bryan is currently building GE Energy's newly created Manufacturing Technology organization using a distributed manufacturing technology center model to utilize the best of GE's internal resources and leverage partnerships with global external resources. Bryan holds a Bachelor of Science degree in Metallurgy, Mechanics, & Materials Science from Michigan State University, a Masters of Science degree in Materials Engineering from Washington University in St. Louis, and a Masters of Business Administration degree from Washington University in St. Louis.

Precision Manufacturing in a Global Supply Chain

General Electric Energy is a $60B business producing power generating & distribution, oil & gas, and water processing equipment for the global markets. Power generating & distribution products range from the traditional steam and gas turbines to today's most advanced smart meters. To produce the variety of products and to serve to global markets, GE Energy has established a large supply chain that utilizes the best available suppliers from each region in the world. The globalization of the supply chains has implications for precision engineered products.

Traditionally, precision engineered products are designed with limited comprehension of the global supply network. Product tolerancing has primarily been based on limited process capability data or on tolerance budgeting approaches. In today's globally distributed manufacturing base, the engineer may not necessarily know where the hardware they are designing will be manufactured. In order to deliver robust designs, alternative approaches may be required.

One approach could be to reverse engineer the global supply chain to develop tolerance roll-ups. For instance, understanding machine tool design and build tolerances could provide initial indications of achievable tolerances. Process tolerances could than be added to the basic machine tolerances. Process tolerances may include machine motion, cutting tool, work piece variations and measurement errors. Furthermore, at the factory level, understanding and analyzing factory capabilities such as age & usage of equipment and temperature controls. Finally, at the supply chain level, understanding variations due to location effects such as translation, conversion, and lead time.

To compare and contrast a traditional design approach and a manufacturing roll-up approach will be highlighted using a simplified flange to flange gas turbine example. The simplified gas turbine will be represented as wheels, blades, and casings.

This work performed under the auspices of the U.S. Department of Energy by Lawrence Livermore National Laboratory under Contract DE-AC52-07NA27344.

Cooperating Sponsor

Elsevier Science, Inc.

Technical Exhibitors

Aerotech, Inc.
AMETEK - Precitech, Inc.
attocube Systems AG
Bal-tec
Bruker Nano Surfaces Business
Center for Precision Metrology – University of N. C. at Charlotte
Chardon Tool
K & Y Diamond Ltd.
Krosaki Harima Corporation
Lion Precision
Makino
MicroFab Technologies, Inc.
Moore Nanotechnology Systems, LLC
New Way Air Bearings, Inc.
nPoint, Inc.
Precision Engineering Center – N.C. State University
Precision Environments, Inc.
Precision Mechatronics Laboratory – University of British Columbia
Precision MicroDynamics, Inc.
Professional Instruments Company, Inc.
Trust Automation
Western Environmental Corporation

Commercial Session

Tuesday, November 2, 1:30 - 3:00 p.m.

The Commercial Session will take place early in the week on Tuesday afternoon. This is a special session where companies and participants are free to open discussions on a less-formal basis and to promote interaction on a variety of topics. In the first part of this session, company representatives are invited to make brief presentations (five minutes) on new products associated with precision engineering. This provides participants with the opportunity to receive timely information on new technologies that have been commercialized into products and services, as well as information on advances that can be expected in the near future.

ASPE 2010 Sustaining Corporate Sponsors

3M Company
St. Paul, MN 55144
Phone: (651) 737-3790
www.mmm.com

ADCOLE Corporation
669 Forest Street
Marlborough, MA 01752
Phone: (508) 485-9100
Fax: (508) 481-6142
www.adcole.com

Aerotech, Inc.
101 Zeta Drive
Pittsburgh, PA 15238-2897
Phone: (412) 963-7470
Fax: (412) 963-7459
www.aerotech.com

AMETEK-Precitech, Inc.
44 Blackbrook Road
Keene, NH 03431
Phone: (603) 357-2511
Fax: (603) 358-6174
www.precitech.com

Bruker Nano Surfaces Business
2650 East Elvira Road
Tucson, AZ 85706-7123
Phone: (520) 741-1044
www.bruker-nano.com

Chardon Tool
115 Parker Court
Chardon, OH 44024
Phone: (440) 286-6440
Fax: (440) 286-7165
www.ChardonTool.com

Contour Fine Tooling, Inc.
143 Jaffrey Road
Marlborough, NH 03455
Phone: (603) 876-4908
www.contour-diamonds.com

Equilibria
472 Amherst Street
Unit 25
Nashua, NH 03063
Phone: (603) 880-7722
www.eqlib.com

K & Y Diamond
2645 Diab St. Laurent
Quebec H4S 1E7
CANADA
Phone: (514) 333-5606
Fax: (514) 339-5493
www.kydiamond.ca

Lion Precision
563 Shoreview Park Road
St. Paul, MN 55126-7014
Phone: (651) 484-6544
Fax: (651) 484-6824
www.lionprecision.com

Makino
7680 Innovation Way
Mason, OH 45040
Phone: (513) 573-7200
Fax: (513) 573-7360
www.makino.com

Mitutoyo America Corporation
945 Corporate Boulevard
Aurora, IL 60504-9102
Phone: (630) 723-3619
Fax: (630) 978-6471
www.mitutoyo.com

Moore Nanotechnology Systems LLC
426A Winchester Street
Keene, NH 03431-0605
Phone: (603) 352-3030
www.nanotechsys.com

PI (Physik Instrumente) L.P.
16 Albert Street
Auburn, MA 01501
Phone: (508) 832-3456
www.physikinstrumente.com

Professional Instruments Company
7800 Powell Road
Hopkins, MN 55343
Phone: (952) 933-1222
Fax: (952) 933-3315
www.airbearings.com

Specialty Components, Inc.
14 Village Lane
Wallingford, CT 06492
Phone: (203) 284-9112
Fax: (203) 672-0371
www.specialtycomponents.com

Trust Automation, Inc.
143 Suburban Road
San Luis Obispo, CA 93401
Phone: (805) 544-0761
Fax: (805) 544-4621
www.trustautomation.com

Zygo Corporation
Laurel Brook Road
Middlefield, CT 06455-0448
Phone: (860) 347-8506
Fax: (860) 347-8372
Toll-free: (800) ZYGO-NOW
www.zygo.com

ASPE 2010 Corporate Sponsors

Center for Precision Metrology
University of North Carolina at Charlotte
9201 University Blvd.
Charlotte, NC 28223
Phone: (704)-687-8499
www.cmp.uncc.edu

Corning Inc.
Science & Technology Division
HP-ME-03-055
Corning, NY 14831
Phone: (607) 974-3842
www.corning.com

Cranfield Precision
Division of Cinetic Landis Lund, Ltd.
90 Central Avenue
Wharley End
Cranfield, Bedford MK43 OJR
United Kingdom
Phone: +44-(0)1234-754023
www.cranfieldprecision.com

euspen Ltd.
Building 70
Cranfield University Campus
Bedford, MK43 OAL, United Kingdom
Phone: +44-(0)1234-754024
www.euspen.org

Moog, Inc.
30 Jamison Road
East Aurora, NY 14052-0018
Phone: (716) 687-7764
www.moog.com/industrial

nanoPrecision Products, Inc.
411-B Coral Circle
El Segundo, CA 90245
Phone: (310) 773-3550
www.nanoprecisionproducts.com

2010 ASPE Lifetime Achievement Award

Christopher J. Evans

Dr. Christopher J. Evans received his B.Sc. (with honors) in Chemical Engineering from the University of Manchester Institute of Science and Technology in 1975. He received in M.Sc. in Precision Engineering from the Cranfield Institute of Technology in 1987. He received his Ph.D. in Mechanical Engineering from the University of Birmingham in 1996.

Dr. Evans recently accepted a position as professor in the Department of Mechanical Engineering and Engineering Science at the University of North Carolina at Charlotte. Prior to this appointment and since 2001, he served as Senior Research Scientist and Chief Metrologist at the Zygo Corporation. From 1990 to 2001, he held various positions in manufacturing research at the National Institute of Standards and Technology (NIST), including Program Manager for the Advanced Optics Metrology Program. From 1984 to 1990, he was a University of Wisconsin-Madison Research Associate based at NIST. From 1975 to 1984, he was employed by IPC Science and Technology Press (later Butterworth Scientific), where he was the founding Editor of the journal Precision Engineering.

Dr. Evans' research career has included numerous activities that have explored the natural synergy between advanced metrology and advanced manufacturing processes. He has also focused on working with multi-disciplinary teams to address complex problems. Examples include: 1) design and construction of the new hermetic encasements for the Declaration of Independence, Constitution, and Bill of Rights; 2) diamond turning, where the focus on the tribo-chemical mechanisms which govern the process ultimately led to the ability to predict diamond wear based on electronic structure; 3) hard turning, including fundamental understanding of chip segmentation dynamics, white layer formation, and achievable surface quality; 4) mechanisms in polishing, including development of the rapidly renewable lap concept; and 5) self-calibration techniques for interferometry systems.

Dr. Evans is the author the book "Precision Engineering: an Evolutionary View" (with Japanese and Chinese editions), five book chapters, and over 40 refereed publications. He is also the holder of 11 U.S. patents. His honors include:

- Distinguished Service Award, American Society for Precision Engineering, 1991
- R&D-100 Award: 100 Most Technologically Significant Inventions, 1992
- Editor-in-Chief, Precision Engineering, 1991 to 1994
- U.S. Department of Commerce Gold Medal (2001) and Bronze Medals (1992 and 1999) for Superior Federal Service
- Three Best Paper Awards
- Zygo Corporation Innovation Award, 2009

Dr. Evans is a Fellow of the International Academy for Production Research (CIRP) and a Charter Member of ASPE; he also maintains memberships in the Optical Society of America, Society for Photo-Optical Instrumentation Engineers, and the European Society for Precision Engineering and Nanotechnology.

Technical and Poster Sessions Index

The technical program of the 2010 ASPE Annual Meeting contains 115 papers on precision engineering advances. Papers that lent themselves to significant verbal interaction, concise but important discoveries, or strongly visual or tactile subjects have been selected for the poster presentation. Authors will be in attendance to discuss their work during Poster Sessions I and II on Tuesday, November 2, and Wednesday, November 3 respectively, from 3:30 to 5:00 p.m.

Session I

Applications of Precision Engineering in Manufacturing

Tuesday, November 2, 2010, 8:30 AM - 10:00 AM

Session Chair: Bradley H. Jared (Sandia National Laboratories) and Pradeep K. Subrahmanyan (Data Physics Corporation)

1. **Fabrication of Periodic Metal Nanodots Arrays**
   Sun, J.; Shu, W.; Luo, X.; Ritchie, J. M.; Chang, W. (Heriot-Watt University) 13
2. **Improved Spindle Dynamics Identification Techniques for Receptance Coupling Substructure Analysis (RCSA)**
   Kumar, U. V.; Riggs, A. W.; Schmitz, T. L. (University of Florida) 17
3. **Figuring of Millimeter-thick Elliptical Mirror Substrate Using Numerically Controlled Local Wet Etching with Low-pressure Polishing**
   Nagano, M.; Yamaga, F.; Zettsu, N.; Yamamura, K. (Osaka University); and Yamazaki, D.; Maruyama, R.; Soyama, K. (J-PARC Center, Japan Atomic Energy Agency) 21
4. **Using Process Models to Optimize Modulated Tool-path Chip Breaking Operations**
   Barkman, W. E.; Babelay, Jr., E. F. (Babcock & Wilcox Technical Services, LLC); and Smith, K. S.; Assaid, T. S.; McFarland, J. T.; Tursky, D. A. (University of North Carolina at Charlotte). 25

Session II

Metrology

Tuesday, November 2, 2010, 10:30 AM - 12:00 PM

Session Chair: Brian P. O'Connor (Aerotech, Inc.) and Marcin B. Bauza (InsituTec Inc.)

1. **Self-referenced Surface Profilometry**
   Parks, R. E.; Su, P.; Oh, C. J.; Burge, J. H. (University of Arizona). 29
2. **Advanced 3D Metrology to Enhance Manufacturing of Precision Components**
   Novak , E.; Schmit, J.; Munteanu, F. (Bruker Nano Surfaces Business) 33
3. **Test Methods for Coordinated Motion of Five-axis Machining Centers**
   Moylan, S. P.; Fesperman Jr., R. R.; Donmez, M. A. (National Institute of Standards and Technology) 37
4. **Uncertainty of Angular Motion Correction Using the Extended Abbe Principle**
   Lee, V.; Ziegert, J. C. (Clemson University); and Estler, W. T.; Phillips, S. D.; Sawyer, D.; Borchardt, B. (National Institute of Standards and Technology) 42
5. **Record Resolution Absolute Length Metrology Over Large Distances**
   Roos, P. A.; Reibel, R. R.; Berg, T. J.; Kaylor, B. M.; Greenfield, N. J. (Bridger Photonics, Inc.); and Barber, Z. W. (Montana State University) 46

Session III

Precision Surface Generation

Wednesday, November 3, 2010, 8:30 AM - 10:00 AM

Session Chair: Mark A. Stocker (Cranfield Engineering) and Robert D. Grejda (Corning Tropel Corporation)

1. **Direct Diamond Turning of Aspheric Steel Molds with Ultra Precise Accuracy**
   Klocke, F.; Dambon, O.; Bulla, B. (Fraunhofer Institute for Production Technology IPT) 49
2. **Laser Generated and Structured Prototypes of Diamond Tool Tips for Microoptics Fabrication**
   Joswig, A.; Tünnermann, A. (University of Jena) and Risse, S.; Eberhardt, R. (Fraunhofer Institute for Applied Optics and Precision Engineering) 53
3. **Ultra-precision Fluid Jet and Bonnet Polishing for Next Generation Hard X-ray Telescope Application**
   Beaucamp, A. (Zeeko Research Ltd.); and Matsumoto, A.; Namba, Y. (Chubu University) 57
4. **Plasma Assisted Polishing of Reaction-sintered Silicon Carbide**
   Yamamura, K.; Ueda, M.; Takiguchi, T.; Zettsu, N. (Osaka University) 61

Session IV

Metrology with Nanometer Scale Resolution

Wednesday, November 3, 2010, 10:30 AM - 12:00 PM

Session Chair: Hans-Jochen Trost (MicroFab Technologies, Inc.) and Deming Shu (Argonne National Laboratory)

1. **Aspects of Probing on the Micro Scale**
   Bos, E. (Xpress Precision Engineering B.V.) 65
2. **Development of a System for 3-D Micro Metrology Using an Optical Fiber Probe**
   Murakami, H. (Kyushu Sangyo University); Katsuki, A.; Onikura, H.; Sajima, T. (Kyushu University); and Kawagoishi, N.; Kondo, E. (Kagoshima University) 69
3. **Dimensional Measurements of Ultra Delicate Materials Using Micrometrology Tactile Sensing**
   Bauza, M. B.; Woody, S. C. (InsituTec Inc.); Seugling, R. M.; (Lawrence Livermore National Laboratory); and Smith, S. T. (University of North Carolina at Charlotte) 73
4. **Microprobe Metrology Study: Latest Results**
   Yang, R. H.; Smith, S. T. (University of North Carolina at Charlotte); and de la Maza, B. (Asociación Innovalia) 77
5. **ISARA 400: Enabling Ultra-precision Coordinate Metrology for Large Parts**
   Donker, R. L.; Widdershoven, I.; Brouns, D. S. G.; Morel, M.; Spaan, H. A. M. (IBS Precision Engineering BV) 81

Session V

Design of Precision Machines I

Wednesday, November 3, 2010, 1:30 PM - 3:00 PM

Session Chair: Thomas A. Dow (North Carolina State University) and Craig R. Forest (Georgia Institute of Technology)

1. **Compact Manipulator Based on an Atomic Force Microscope for Multi-probe Operation**
   Iwata, F.; Kou, H.; Mizuguchi, Y.; Ito, S. (Shizuoka University); Aoyama, H. (University of Electro-Communictions); and Ushiki, T. (Niigata University) 85

2. **A Fast Scanner Design for a Scanning Multi-probe Microscope**
Lin, F.; Parker, W. C.; Smith, S. T.; Moyer, P. J. (University of North Carolina at Charlotte) 89

3. **A Three Fingered Hand for a Micro-robotic Assembly System**
Hastings, D. J.; Graham, J.; Nowakowski, B. K.; Smith, S. T.; Tomblin, Jr., J. E. (University of North Carolina at Charlotte) 93

4. **Advancements in Development of an Ultra-precision, SI-traceable Nanoindentation Platform**
Nowakowski, B. K.; Smith, S. T. (University of North Carolina at Charlotte); and Smith, D. T. (National Institute of Standards and Technology) 97

Session VI

Controls

Thursday, November 4, 2010, 8:30 AM - 10:00 AM

Session Chair: Stephen J. Ludwick (Aerotech, Inc.) and Luis A. Aguirre (3M Company, Inc.)

1. **Open Loop Inertial Cross-talk Compensation Based on Measurement Data**
Steinlin, M.; Weikert, S.; Wegener, K.; (inspire AG, ETH Zürich). 101

2. **2-D Absolute Positioning System for Real Time Control Applications**
Montes-Solano, C. A.; Ziegert, J. C.; Wong, C.; Mears, L. (Clemson University); and Tucker, T. (Tucker Innovations Inc.). 105

3. **Practical Friction Compensation for Ultra Precision Point-to-point Motion**
Bucci, B. A.; Cole, D. G.; Vipperman, J. S. (University of Pittsburgh); and Ludwick, S. J. (Aerotech, Inc.) 109

4. **A Multirate Multiprocessor Control Platform for High-speed Precision Motion Control**
Smeds, K.; Lu, X. (The University of British Columbia) 113

5. **Time-Optimal Minimum Jerk Trajectory Generation for 5-Axes Laser Drilling Applications**
Alzaydi, A. A.; Erkorkmaz, K. (University of Waterloo); Elfizy, A.; Engin, S. (Pratt & Whitney Canada) 117

Session VII

Design of Precision Machines II

Thursday, November 4, 2010, 10:30 AM - 12:00 pm

Session Chair: Keith Carlisle (Lawrence Livermore National Laboratory) and Jonathan D. Ellis (Delft University of Technology)

1. **High-accuracy Atomic Force Microscope for Dimensional Metrology**
Amin-Shahidi, D.; Ljubicic, D. M.; Trumper, D. L. (Massachusetts Institute of Technology); and Overcash, J. L.; Hocken, R. J. (University of North Carolina at Charlotte). 121

2. **Design and Testing of a Machine for Calibration of Ball Bars Up to 3 Meters in Length**
Lee, V.; Ziegert, J. C. (Clemson University); and Estler, W. T.; Phillips, S. D.; Sawyer, D. S.; Borchardt, B. R. (National Institute of Standards and Technology). 125

3. **Positioning System for Optical Disc Mastering**
Knapp, B. R.; Oss, D. D.; Arneson, D. A. (Professional Instruments Company, Inc.); and Sheridan, Tim (Lorien Consultants Group, Inc.) 129

4. **An Instrument for Controlled, Automated, Continuous Pulling of Sub-micrometer Fused Silica Pipettes**
Pak, N.; Dergance, M.; Emerick, M.; Gagnon, E.; Forest, C. R. (Georgia Institute of Technology) 133

Session VIII

Interferometry and Optics

Thursday, November 4, 2010, 1:30 AM - 3:00 PM

Session Chair: Vivek G. Badami (Zygo Corporation) and Eric S. Buice (Lawrence Livermore National Laboratory)

1. **Expanding White Light Interferometer Capabilities to be Used as a μ-CMM**
   Ramasamy, S. K.; Kasper, A. (Hutchinson Technology Inc.) 136
2. **Fourier Transform and Wavelet Algorithms for Calculating Height in White Light Interferometry**
   Medicus, K. M.; Jansen, M. J. (Mitutoyo Research Center Europe). 140
3. **Errors in Measurement and Compensation Algorithms for Periodic Nonlinearity Correction**
   Ellis, J. D.; Baas, M.; Spronck, J. W.; Munnig Schmidt, R.-H. (Delft University of Technology) 144
4. **Terahertz Time of Flight Detection for Absolute Thickness Measurements of Single Side Polished Silicon Wafers**
   Ikram, J.; Davies, A. D.; Farahi, F.; Her, T-H. (University of North Carolina at Charlotte). 148

Poster Session I

Tuesday, November 2, 2010, 3:30 PM - 5:00 PM
Wednesday, November 3, 2010, 3:30 PM - 5:00 PM

Applications of Precision Engineering in Manufacturing

1. **Precision Micro-engraving of Glass by Automatic Boundary Tracking of Complex Images**
   Chung, S.-C. (Hanyang University) 152
2. **Process Optimization in Semi-liquid Injection Molding of AZ91D Magnesium Alloy**
   Chung, S.-C. (Hanyang University) 156
3. **Analysis of Ballscrew Stiffness Owing to Contact Deformation in Leadscrew Systems**
   Chung, S.C. (Hanyang University); and Park, C.-H. (Korea Institute of Machinery & Materials (KIMM)). 160
4. **Sensor Design for On-machine Probing of Extruded Tool Joints**
   Graziano, A.; Schmitz, T. L. (University of Florida); and Joslin, A. (University of Central Florida) 164
5. **Internal Finishing of Capillary Tubes by Magnetic Abrasive Finishing Using a Metastable Austenitic Stainless Steel Tool**
   Kang, J.; Yamaguchi, H. (University of Florida) 168
6. **Combining Tool Wear and Stability in High-speed Machining Performance Prediction**
   Karandikar, J. M.; Zapata Ramos, R. E.; Schmitz, T. L. (University of Florida) 172
7. **Reduction of NC Machining Data Volume and Evaluation of Machined Surface by Circular Arc Approximation of Discrete Points**
   Kawasaki, K.; Murata, T.; Kobayashi, Y.; Shirai, K. (Nihon University); and Kondo, T. (Hakodate National College of Technology) 176
8. **Microfabrication of Circular Cross-section Microchannels for Thrombosis Assays**
   Li, M.; McKinnon, M.; Forest, C. R. (Georgia Institute of Technology); and Chase, S. (Rose-Hulman Institute) 180
9. **Friction Measurement in Precision Glass Molding**
   Mosaddegh, P.; Ziegert, J. C. (Clemson University); Tohme, Y. E. (Moore Nanotechnology Systems, LLC) 184

10. **Design, Fabrication and Testing of a High Precision Piezo-actuated Air Amplifier as an Ion Focusing Device in Mass Spectrometry**
Robichaud, G.; Dixon, R. B.; Potturi, A. S.; Edwards, J. R.; Sohn, A.; Dow, T. A.; Muddiman, D. C. (North Carolina State University) 188

11. **Design of a Monolithic Cylindrical Flexure for Precision Linear Motion Guidance**
Telleria, M. J.; Culpepper, M. L.; Weitz, D. (Massachusetts Institute of Technology) 192

Control of Precision Machines and Processes

1. **Active Reduction of a Static Deformation in a Moving Magnet Planar Actuator**
Achterberg, J.; van Lierop, C. M. M.; van den Bosch, P. P. J. (Eindhoven University of Technology). 196

2. **Microcapsule Production by Double Micro Pipette Injecters**
Aoyama, H.; Hata, N.; Terasaki, K.; Hirata, S. (University of Electro-Communications) 200

3. **High Speed Electrical Discharge Machining Using a Combination of 5-DOF Controlled Maglev Actuator and Conventional EDM Machine**
He, D.; Shinshi, T. (Tokyo Institute of Technology); Zhang, X. (Nippon Institute of Technology); and Yuzawa, T.; Sato, T. (Mitsubishi Electric Corporation) 204

4. **Performance Evaluation of a New High-precision, Quick-response Pneumatic Pressure Regulator and Its Application to an Actively Controlled Pneumatic Vibration Isolator**
Kato, T. (Fukuoka Institute of Technology); Funaki, T. (National Metrology Institute of Japan (AIST)); Shinohara, Y. (Tokkyokiki Corporation); Kawashima, K.; Kagawa, T. (Tokyo Institute of Technology) 208

5. **Precision Three Dimensional Modeling for Spatial Control of the Ion Beam Sputtering Process for Optical Thin Films**
Ness, D. C.; Wood, C. S. (Precision Photonics Corporation). 212

Design and Fabrication of Structured Surfaces

1. **Use of Ceramic Spotting Masters for Scraping**
Stussi, D. R. (Gardner Stussi Tool & Die) 216

2. **Improving Anti-adhesive Properties of Cutting Tool Surface by Nano/Micro Textures — Considering the Texture Patterns**
Sugihara, T.; Enomoto, T. (Osaka University). 219

Design of Precision Machines and Instruments

1. **Design of Flexure Hinge Mechanism for Dynamic Yaw Control of FPD Lithography Stage**
Ahn, D. H.; Kim, H.; Gweon, D.-G.; (Korea Advanced Institute of Science & Technology); and Lee, S. H.; Choi, W.; Baek, S.; Lee, S.; Park, J. (EVERTECHNO Co., Ltd.) 223

`2. **Stiffness Analysis of Parallel Leaf-spring Flexures**
Brouwer, D. M.; Meijaard, J. P.; Jonker, J. B. (University of Twente). 226

3. **6 DOF Nanopositioning Mechanism and Analysis of its Inherent Mechanical Characteristics**
Hackel, T.; Frank, T.; Lotz, M. (Technical University of Ilmenau) 230

4. **The Measurement of Meso-scale Torsion Springs**
Jared, B. H.; Yazzie, D.; Reese, I. M. (Sandia National Laboratories) 234

5. **Design and Fine Motion Test of Precision X-Theta Stage in Vacuum**
Khim, G.; Shim, J.; Park, C.-H. (Korea Institute of Machinery & Materials (KIMM)) 238

6. **Design of Novel 3-DOF Nano Precision Stage**
Kim, H.-Y.; Ahn, D. H.; Gweon, D.-G. (Korea Advanced Institute of Science and Technology (KAIST)); and Chun, B.-S. (Nanoscope System Co. Ltd.) 242

7. **Design and Performance of Telescoping Micropipette Arrays for High Throughput *in Vivo* Patch Clamping**
Kodandaramaiah, S. B.; Malik, S.; Dergance, M. J.; Forest, C. R. (Georgia Institute of Technology); and Boyden, E. S. (Massachusetts Institute of Technology) . . . 246

8. **Comparing Different Cooling Concepts for Ball Screw Systems**
Mayr, J. (IWF - ETH Zurich); Ess, M.; Weikert, S.; Wegener, K. (inspire AG, ETH Zurich) . . . 250

9. **Measurements Using the High Accuracy Atomic Force Microscope and the Sub-atomic Measuring Machine**
Overcash, J. L.; Hocken, R. J. (University of North Carolina at Charlotte); and Amin-Shahidi, D.; Trumper, D. L.; Schattenburg, M.L. (Massachusetts Institute of Technology) . . . 254

10. **Modulation of Electromagnetic Radiation Using a Dot Matrix Printer**
Pak, N.; Phaneuf, C. R.; Kodandaramaiah, S. B.; Forest, C. R. (Georgia Institute of Technology) . . . 258

11. **Parametric Modeling of Self-weighted Distortion for Plane Optical Mirrors**
Park, W. H.; Cuerden, B.; Burge, James H.; (University of Arizona); and Kim, S.-W. (Yonsei University) . . . 261

12. **Bench-top Precision Glass Molding Machine**
Wachtel, P.; Mosaddegh, P.; Gleason, B.; Musgraves, J. D.; Richardson, K. A. (Clemson University); and Dubas, B.; Painter, H. (Dyna Technologies, Inc.) . . . 265

Dimensional Metrology

1. **Interferometric Measurment of the Low Value CTE of a Ball Bar**
Miller, J. A.; Saad, M. E.-S.; Caskey, G. W. (University of North Carolina at Charlotte); and Aguilar-Martin, J. J. (Universidad de Zaragoza) . . . 269

2. **Double Sided Interferometer, Profiling Measurement Simultaneously Yields Thickness and Form**
Seugling, R. M.; Wilson, M. J.; Davis, P. J.; Peterson, S. C.; Hamilton, J. H. (Lawrence Livermore National Laboratory) . . . 273

3. **Measurements of Coating Thickness of Diamond-coated Tools by White-light Interferometry**
White, W. R.; Ogilvie, A.; Chou, Y. K. (The University of Alabama); and Novak, E. L. (Bruker Nano Surfaces Business) . . . 277

Grinding, Polishing, and Lapping

1. **A Study of Machining Strategy in Computer Controlled Ultra-precision Polishing of Structured Surfaces**
Cheung, C.-F.; Ho, L. T.; Kong, L. B. (The Hong Kong Polytechnic University) . . . 281

2. **Contact Conditions for 5-axis Grinding of Free Formed Surfaces**
Denkena, B.; Köhler, J.; Behrens, L.; Krawczyk, T. (Leibniz Universität Hannover) . . . 285

3. **Grinding of Microstructures in Brittle Materials with Multiple Microprofiled Grinding Wheels**
Denkena, B.; Köhler, J.; Kästner, J.; Hahmann, D. (Leibniz Universität Hannover) . . . 289

4. **Weakly Copper-fullerenol Layer on Chemical Mechanical Polishing Using Water Soluble Fullerenol**
Kishida, H.; Takaya, Y.; Hayashi, T.; Michihata, M.; Kokubo, K. (Osaka University) . . . 293

5. **Vibration Attenuation in Optical Pitch**
Mainuddin, M.; Mullany, B. A. (University of North Carolina at Charlotte) . . . 297

6. **Increases in Corrosion Resistance and Water Repellency of Metal Mold Surface by EB Polishing**
Okada, A.; Uno, Y. (Okayama University); and Uemura, K. (Nagata Seiki Co. Ltd.) . . . 301

Machine Tool Metrology

1. **New Method for Determination of Volumetric Positioning Error**
   Bui, C. B; Hwang, J.; Lee, C.-H.; Park, C.-H. (Korea Institute of Machinery & Materials (KIMM)) . . . 305
2. **Methods, Practices and Standards for Evaluating On-machine Touch Trigger Probing of Workpieces**
   Fesperman Jr., R. R.; Moylan, S. P.; Donmez, M. A. (National Institute of Standards and Technology) . . . 309
3. **An Estimation Method for Five Degree Freedom Error Motions of the Precision Spindle**
   Hwang, J.; Shim, J.; Park, C.-H. (Korea Institute of Machinery & Materials (KIMM)) . . . 313
4. **Positioning Repeatability Evaluation of Hydrostatic Bearing Guided Precision Machine**
   Shim, J.; Hwang, J.; Song, C. K.; Park, C.-H. (Korea Institute of Machinery & Materials (KIMM)); and Bui, C. B. (University of Science and Technology) . . . 317

Measurement Uncertainty

1. **Manufacturing Process Error Signature and CMM Uncertainty Costs**
   Ceglarek, D. (University of Warwick); and Moroni, G.; Petrò, S. (Politecnico di Milano) . . . 321
2. **Investigations of Metrological Models for the Nanomeasuring and Nanopositioning Machine with Respect to the Measurement Uncertainty by Means of a Monte Carlo Simulation**
   Kreutzer, P.; Füßl, R; Manske, E.; Dorozhovets, N. (Ilmenau University of Technology) . . . 325
3. **Short Range Displacement Sensor Using Optical Pick-up Tracking Signal**
   Lee, C.-W.; Song, J.-Y.; Ha, T.-H.; Lee, J.-H. (Korea Institute of Machinery & Materials (KIMM)) . . . 329

Micro-Electromechanical Devices

1. **Non-lithographic Fabrication of Carbon Nanotube-based Sensors for Small-scale Force and Displacement Sensing**
   Cullinan, M. A.; Panas, R. M.; Daniel, C. R.; Culpepper, M. L. (Massachusetts Institute of Technology) . . . 333
2. **Design and Characterization of a 6 Degree-of-freedom Meso-scale Nanopositioner with Integrated Strain Sensing**
   DiBiasio, C. M. (The Charles Stark Draper Laboratories); and Culpepper, M. L. (Massachusetts Institute of Technology) . . . 337
3. **Electromagnetic-force-driving Type MEMS Switch Using High Performance NdFeB/Ta Thin Film Permanent Magnet**
   Ishibashi, M.; Tanabe, R.; Shinshi, T. (Tokyo Institute of Technology); and Uehara, M. (Hitachi Metals, Ltd.) . . . 341
4. **Direct, High-speed Milling of Polymer Microchamber Arrays**
   Phaneuf, C. R.; Forest, C. R. (Georgia Institute of Technology) . . . 345

Nanotechnology

1. **Heat-controlled Injection Molding of Nanostructured Optical Elements**
   Mitsuda, T.; Nagato, K.; Hattori, S.; Hamaguchi, T.; Nakao, M. (The University of Tokyo) . . . 348
2. **Penetration of Residual Layer in Nanoimprint Lithography by Direct Oxidation of Photocatalytic Film**
   Shimoda, M.; Nagato, K.; Hamaguchi, T.; Nakao, M. (The University of Tokyo) . . . 352

Novel Equipment And Processes

1. **Measurement of Current in Electro-chemical Discharge Machining by Forced Discharge Dispersion**
   Furutani, K.; Shintani, H.; Murase, Y.; Arakawa, S. (Toyota Technological Institute) 356

2. **Optical Deflection Identification Based on Dark-field Laser Scattering for the Inspection of Crystalline Silicon Wafer in Solar Cell**
   Kim, G.-B.; Yeon, J.-S. (Chungju National University). 360

3. **Fast Detection of Micro Defects Using Magnetic Nondestructive Testing Methods**
   Nakajima, R.; Nagato, K.; Kawamoto, Y.; Kaito, H.; Nakao, M.; Hamaguchi, T. (The University of Tokyo) 364

4. **The Effect of Laser Heating on the Ductile to Brittle Transition in Silicon Carbide**
   Ravindra, D.; Poyraz, H. B.; Patten, J. A. (Western Michigan University) 368

5. **Mechanical Design of a Multi-axis Precision Flexure Stage System for Advanced X-ray Stereo Imaging Instrument for Particle Tracking Velocimetry at the Advanced Photon Source***
   Shu, D.; Lee, W.-K. (Argonne National Laboratory) 372

6. **A Novel Exposure Method Based on Dissolved Oxygen Control for Nano-stereolithography Using Evanescent Light**
   Takahashi, S.; Nagano, T.; Kajihara, Y.; Takamasu, K. (The University of Tokyo). 373

7. **Position Measurement for Miniature Robot Using Moving Line Lasers**
   Torii, A.; Yamada, T.; Ueda, A.; Doki, K. (Aichi Institute of Technology) 377

8. **Study on Multi-layering of Metal Micro-reactor Using Diffusion Bonding**
   Tsuchiya, K.; Nunokawa, T.; Kikuchi, A.; Nakao, M. (The University of Tokyo). 381

9. **Biomolecular-imaging Device Using Light-addressed Excitation on a Photocatalyst Substrate**
   Yamamoto, A.; Nagato, K.; Tsukada, T.; Tanaka, A.; Hamaguchi, T.; Nakao, M. (The University of Tokyo); and Suzurikawa, J. (Research Institute of National Rehabilitation Center for Persons with Disabilities) 385

Optics and Interferometry

1. **Evaluating the Sensitivity of Periodic Errors in Heterodyne Interferometry**
   Ganguly, V.; Kim, N. H.; Kim, H. S.; Schmitz, T. L. (University of Florida) 389

2. **Compression Molding of Refractive and Diffractive Hybrid Glass Lenses**
   He, P.; Li, L.; Yi, A. Y. (The Ohio State University); and Wang, F.; Georgiadis, K.; Klocke, F. (Fraunhofer Institute for Production Technology (IPT). 393

3. **Development of a Laser-guided Deep-hole Measurement System with Lower Production Cost**
   Katsuki, A.; Onikura, H.; Sajima, T.; Satou, T.; Nishi, H. (Kyushu University); Murakami, H. (Kagoshima University); Pietri, V. (IFMA); and Ali, Md.A. (International Islamic University Malaysia). 396

4. **Non-contact Adaptive Optic Actuator System for Wavefront Distortion Correction**
   Saathof, R.; Spronck, J. W.; Munnig Schmidt, R.-H. (Delft University of Technology). 400

5. **"NEXCERA", Zero Thermal Expansion Ceramics for Optical Applications**
   Sugawara, J.; Unno, H.; Kosugi, N.; Kuma, Y.; Abe, K. (Krosaki Harima Corporation). 404

** Extended abstract unavailable at press time*

Precision Fabrication and Assembly

1. **Mathematical Model for Sheet Glass in Air Bearing**
   Al Husseini, A. M.; Schattenburg, M. L.; Akillian, M. (Massachusetts Institute of Technology) 408
2. **Design Principles and Best Practices for Rapid Prototyping of Meso- and Micro-scale Flexures via Micromilling**
   Gafford, J. B.; Panas, R. M.; Cullinan, M. A.; Culpepper, M. L. (Massachusetts Institute of Technology) 411
3. **Integrated Prescan Optics for Laser Printers**
   Garrard, K. P.; Sohn, A. (North Carolina State University) 415
4. **Evaluation of Hydroxide Catalysis Bonding Strength**
   Kim, H. S.; Schmitz, T. L. (University of Florida) 419
5. **Eco-friendly Micro Electrochemical Machining**
   Ryu, S H.; Yu, J. (Chonbuk National University) 423

Surface Metrology

1. **Self Calibration of the Linearity Error of Angle Sensors for Differential Laser Auto-collimation**
   Uda, Y.; Shimada, S. (Osaka Electro-Communication University); and Go, Y. (Nagase Integrex Co., Ltd.) 427

Ultraprecision Machining

1. **Tool Wear in Diamond Turning of Steels**
   Furushiro, N.; Higuchi, M.; Yamaguchi, T.; (Kansai University); Terauchi, S.; Matsuda, S. (Osaka Yakin Kogyo Co., Ltd.); and Shimada, S. (Osaka Electro-Communication University) 431
2. **A Study on Ultra-fine Machining of Micro Square Type Pyramid Pattern on Large-area Roll Mold**
   Je, T.-J.; Choi, D.-S.; Yoo, Y.-E.; Jeon, E.-C.; Yoon, J.-S.; Jang, S.-H.; Whang, K. H. (Korea Institute of Machinery & Materials (KIMM)); and Park, S.-C. (National Institute of Advanced Industrial Science and Technology (AIST)) 435
3. **Diamond Tool Wear Reduction Mechanisms in Elliptical Vibration Assisted Machining**
   Lane, B. M.; Dow, T. A.; Scattergood, R. O. (North Carolina State University) 439
4. **High Speed Milling of an Alvarez Optic**
   Lineberger, J. L.; Dutterer, B. S.; Davies, M. A.; Smilie, P.; Suleski, T. J. (University of North Carolina at Charlotte) 443
5. **Creation of Microgroove with Two Flat-ends for Hard Material**
   Misawa, Y.; Nakamoto, K.; Ishida, T.; Takeuchi, Y. (Osaka University) 447
6. **Thermo-chemical Wear Study on Orthogonal Diamond Turning of Steel and Stainless Steel**
   Shi, M.; Lane, B. M.; Dow, T. A.; Scattergood, R. O. (North Carolina State University) 451
7. **Ultraprecision Shaping of Complex Prototypes With Multi Freeform Surfaces**
   Steinkopf, R.; Kolbmueller, A.; Gebhardt, A.; Risse, S.; Eberhardt, R.; Tünnermann, A. (Fraunhofer Institute for Applied Optics and Precision Engineering IOF); and Lindig, K.; Dobschal, H. J.; Rudolph, G. (Carl Zeiss AG) 455

Technical Papers

FABRICATION OF PERIODIC METAL NANODOTS ARRAYS

Jining Sun, Will Shu, Xichun Luo, James M. Ritchie and Wenlong Chang
School of Engineering and Physical Sciences
Heriot-Watt University
Edinburgh, EH14 4AS, UK

INTRODUCTION

Recently, fabrication of nanodots structure of various materials has attracted intense scientific interests because of their great potentials for wide technological applications. Metal nano-scale dots that exhibit unique properties based on their nano size effects are expected to be the building blocks of new functional nanodevices, such as catalysis, environmental remediation, DNA detection, high density data storage, and electronic and optical devices. Periodic nanodots arrays are required in some of these applications that demand low-cost nanopatterning technologies for gaining a competitive edge. Lithography tools such as electron beam lithography (EBL) and focused ion beam (FIB) allow well defined and well positioned nanodots, but they are limited by low throughput and small areas, which are not suitable for mass production when a large area of nanodots arrays is required.

In the last two decades, researchers have investigated a number of alternative and potentially low-cost nanofabrication methods, such as nanoimprint technology (NIL) and microcontact printing (μCP).

NIL was initially proposed and developed by Prof. Chou's group [1, 2] since 1990s. They used a hard structured mould to emboss into polymer material cast on the wafer substrate under controlled temperature and pressure conditions to create a thickness contrast pattern in a thin resist film carried on a substrate. Patterns were then transferred through the entire resist layer by an anisotropic etching process.

While μCP was a method to chemically pattern structured surface. Figure 1 illustrated a common practice of this method. Alkanethiols (ink) was imprinted on a gold surface where a self-assembled monolayer (SAM) was formed due to the affinity between alkanethiols or sulfhydryl (SH) groups and the gold. In this process, molecules were diffusively transported from a structured elastomeric stamp to a substrate upon conformal contact. SAM imprinted on the substrate could serve as a resist for a selective etching process. Structures down to nanometer scale could be formed in this way [3].

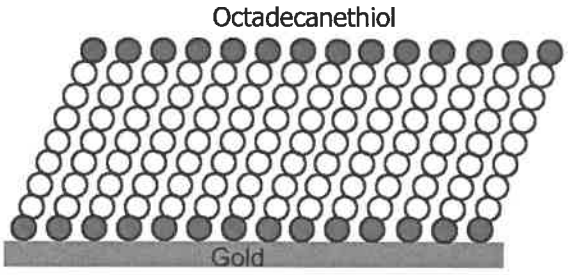

FIGURE 1. A schematic illustration of a fully assembled SAM on gold substrate

In this paper, we carried out initial proof of concept experiment with an aim to develop a fast and low cost fabrication method based on NIL and μCP for periodic gold nanodots arrays on a polymer substrate.

EXPERIMENT

In this proposed method we adopted the following procedures (as shown in Figure 2) to fabricate periodic nano gold arrays on a polymer substrate.

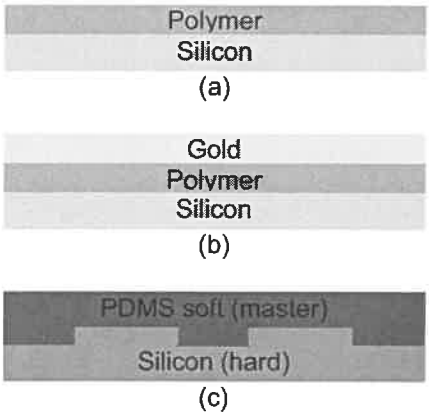

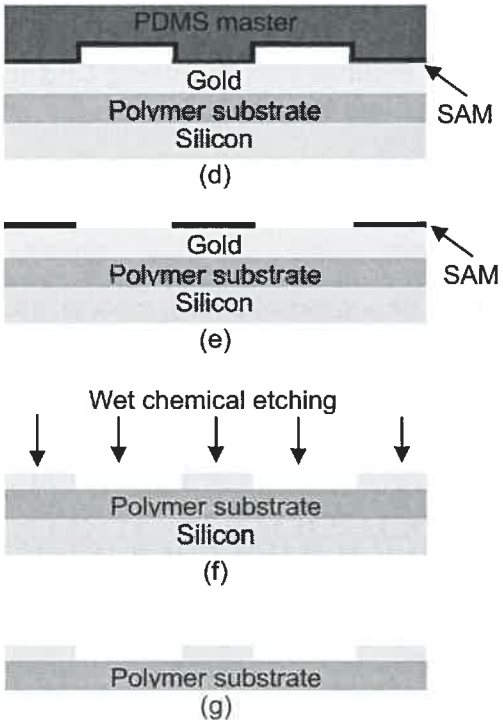

FIGURE 2. Fabrication procedure of periodic metal nanodots array (not in scale).

Formation of Gold Substrate

Firstly the substrates for the SAM fabrication were prepared by spin coating a polymer film of a thickness of 100 µm on a silicon substrate. Then a 50 nm thick gold (99% purity @ cookson gold) layer was coated on the polymer film by an electron beam evaporator at a pressure of 2E-5 Torr and a rate of 1Å/sec, primed with a 5 nm titanium adhesion layer (illustrated in Figure 2 (a), (b)).

Formation of Master

A hard silicon master with the pattern of periodic nanodots arrays was fabricated by a FIB machine (FEI Quanta 3D FEG) equipped with a liquid gallium ion source. Comparing with other beam lithography technology such as EBL and X-ray lithography, FIB was more destructive to the specimen because of higher mass of incident particles. When the high energy ions striked the specimen, they would sputter atoms from the surface with 15 nm resolution. To obtain smooth edge and vertical sidewall, the silicon hard master was fabricated under a low beam current (0.1 nA) and an acceleration voltage of 30 kV. Bitmap carrying the pattern information was created and input to the FIB controlling system. The ion beam scanning pitch along x and y directions were controlled by the ion beam view field and the bitmap resolution. Due to the large milling area, the electron beam was used to compensate the positive charging during the fabrication process. Therefore, ion beam drift was suspended by this method. As a proof of concept test, the silicon master was fabricated in an area of 200 µm by 200 µm, where each cell is 500 nm deep in an area of 1 µm by 1 µm.

The silicon master was then used for imprinting to transfer inverse pattern on a soft stamp poly dimethylsiloxane (PDMS) master. In step (c) of Figure 2 nanoimprint technique was applied to obtain PDMS masters. In this step, PDMS (10:1 mixture of Dow-Corning, Silicone Elastomer-184 and Sylgard Curing Agent 184) was used to fabricate a stamp from the master template. Before curing the mixture of PDMS, elastomer and curing agent were contained in a weighting boat and then floated in an ultrasonic cleaning bath to remove dissolved dioxygen. Therefore, the trapped bubbles from mixing of the components would eventually rise to the top of the liquid where they were broken by blowing across the surface. The PDMS was cured at room temperature for an hour followed by additional curing at 65 °C until the polymer was rigid. After cooling down to 18° C, the PDMS was carefully peeled from the silicon master.

Inking and Printing

The PDMS (soft) master was dip coated with 5mM thiol solution prepared by a dilution of octadecanethiol ($CH_3(CH_2)_6CH_2SH$ @ sigma-aldrich) in 100 ml ethanol (in step (d) of Figure 2). In wet inking process, a drop of thiol solution was dripped onto the patterned PDMS stamp. After 30 s it was blown away by continuously injecting nitrogen gas for 10 s. Inked stamps were used to print on the gold surface within 15 s after their inking. Once in contact with the gold, a monolayer of alkanethiol molecules was diffusively transported onto the surface with a well defined SMA (as shown in figure 2 (e)). The patterned SAMs could then be used as etch-resists to protect those areas of gold covered by SAMs against wet etchants.

Etching

After lift-off of the nanoimprinting master, the printed patterns were transferred into the gold substrate which then would be exposed to etching solution. Etching solution was prepared by dissolving $K_4Fe(CN)_6 \cdot 3H_2O$, $K_3Fe(CN)_6$,

$Na_2S_2O_3$ and KOH (all @ Sigma-Aldrich) in deionized water. Using a thiol pattern printed on the gold surface as a mask, chemical wet etching of gold was performed. The exposed area of gold surface would be etched away faster than the protected area of the gold patterned with SAM. The height of the nanodots on gold surface depended on the etching time. The etching time was chosen to ensure the gold outside the printed regions was dissolved completely and maintain a height of 50 nm.

In the last step (Figure 2 (g)), the silicon substrate were etched away and the periodic gold nanodots arrays on polymer film were obtained.

RESULTS AND DISCUSSIONS

On the coated gold surface, grain sizes of 20 ~ 50 nm were observed by a scanning electron microscope (SEM) (showed in Figure 3.). For fabrication of nanodots, the grain size of the coated gold should be as small as possible in order to minimize its influence on the fabricated nano structures. The fine grain size of gold coating could be achieved by decreasing the temperature of the substrate during the electron beam evaporation process. Similar results on other materials have been obtained by other researchers [4, 5] in this way.

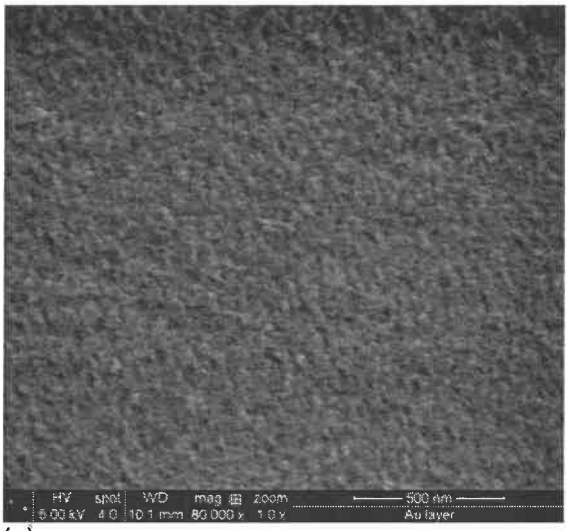

(a)

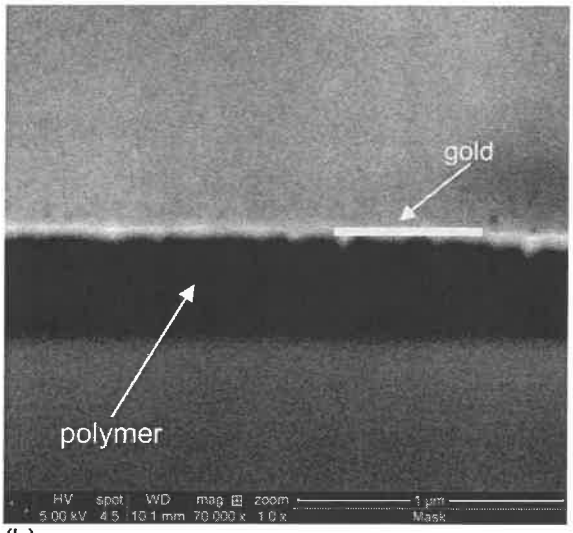

(b)

FIGURE 3. SEM micrograph of 50 nm thick gold layer coated on a polymer substrate. (a) gold surface with grain size 20 – 50 nm; (b) cross section of the coated polymer.

As illustrated in Figure 2, the area of the nanodots was printed from the hard silicon master, while the height of the gold nanodots was determined by the chemical etching process. The depth of the nanostructures on silicon master could be in a wide range gap as long as it was larger than the thickness of the SAM. Shallow structure would take less fabrication time. But it was more difficult for the forming of the PDMS stamp. The structure depth on silicon master was a compromise between the fabrication time and the imprinting quality. Although nanoimprint lithography has the capability of patterning sub 10 nm features, we chose to fabricate nanodots with heights of 500 nm in this proof of concept study in order to simplify the imprinting process.

Partial enlargement of the hard silicon master was showed in Figure 4. The square shape nanodot was strictly repeated in the whole area. The average dimensional accuracy of nanodots was 17 nm which was close to the state-of-the-art FIB fabrication accuracy. Although FIB fabrication was time consuming, once the silicon master was completed it was reusable in the fabrication of PDMS mould. Therefore, using FIB to fabricate hard silicon is inexpensive and suitable for mass production of nanodots.

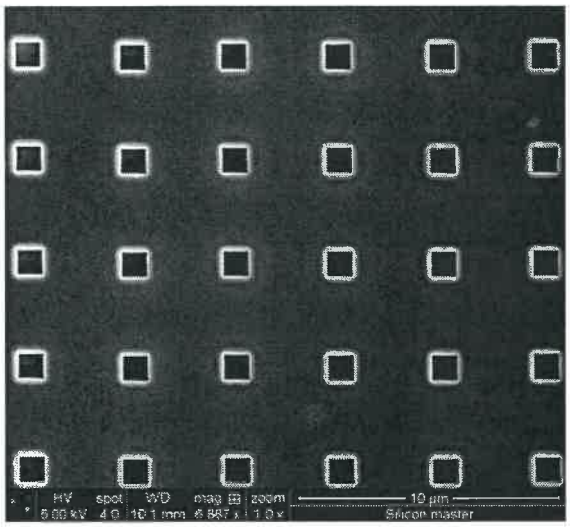

FIGURE 4. Hard silicon master fabricated by FIB

The SEM image of the fabricated nanodots array was shown in Figure 5. It can bee seen that the square shape of these nanodots were well maintained after nanoimprint lithography. Due to using silicon substrate the effect of substrate deformation on pattern fidelity was minimized. However it still need some measure to reduce the influence of PDMS deformation on pattern fidelity in the future study.

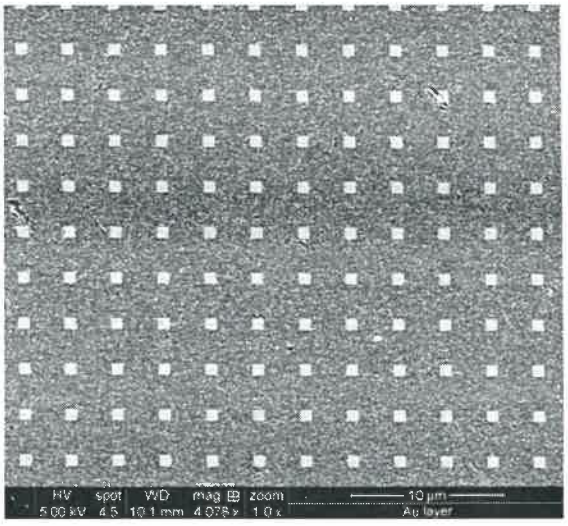

FIGURE 5. Gold nanodots array on polymer substrate

CONCLUSIONS

In this paper a fabrication method which is a combination of NIL and µCP has been used to fabricate periodic gold nanodots array on polymer substrate in an area of 200 µm by 200 µm. Good pattern fidelity was obtained. It showed that this approach was feasible and has a great potential to manufacture periodic metal nanodot arrays over large areas with low cost. Further studies were needed to further reduce the influence of mould deformation on pattern fidelity and develop sub 100 nm alignment stages in order to commercialization of this approach.

REFERENCES

[1] Chou S Y, Krauss P R and Renstrom P J. Imprint of Sub-25 nm Vias and Trenches in Polymers. Appl. Phys. Lett.1995; 67: 3114.

[2] Chou S Y, Krauss P R and Renstrom P J Nanoimprint Lithography. Science. 1996; 272: 85.

[3] Kumar A, Whitesides G M. Features of gold having micrometer to centimeter dimensions can be formed through a combination of stamping with an elastomeric stamp and an alkanethiol "ink" followed by chemical etching Appl. Phys. Lett. 1993; 63: 2002.

[4] Bentzon M D, Karlen A, and Thölén A R. Grain Boundaries between Small Gas Evaporated Particles. Supplément au Journal de Physique Colloques. 1990; 51: C1-89-C1-94.

[5] Murali K R, Sivaramamoorthy K, Asath Bahadur S, Kottaisamy M. A. Photoconductivity Behaviour of Electron Beam Evaporated CdSe Films. Chalcogenide Letters, 2008; 5:249 – 253

IMPROVED SPINDLE DYNAMICS IDENTIFICATION TECHNIQUES FOR RECEPTANCE COUPLING SUBSTRUCTURE ANALYSIS (RCSA)

Uttara V. Kumar, Andrew W. Riggs and Tony L. Schmitz
Department of Mechanical and Aerospace Engineering
University of Florida
Gainesville, FL, USA

INTRODUCTION

The tool point dynamics must be know if milling process models are to be used for parameter selection. This model-based, pre-process selection aids in avoiding chatter, improving the surface finish, and increasing part accuracy. The dynamics of the tool-holder-spindle-machine as reflected at the tool point can be obtained by modal testing, but, for the large number of tool-holder combinations in a typical production facility, the measurements become time consuming and, at times, inconvenient or impossible in the case of slender or micro-scale tools.

The Receptance Coupling Substructure Analysis (RCSA) [1-2] approach may be applied as an alternative to modal testing. In the RCSA approach, the tool-holder-spindle-machine assembly is considered as three separate components: the tool, holder, and spindle-machine and the individual frequency response of these components are analytically coupled. The archived measurement of the spindle FRF (or receptance) is analytically coupled to the free-free boundary condition receptances of the tool and the holder derived from Timoshenko beam models [1-4]. Although significant development work has been completed to improve the tool and holder modeling techniques and to better understand the connection stiffness and damping behavior, relatively less effort has been expended to improve the identification of the spindle-machine dynamics.

In this paper, three approaches to determine the spindle dynamics are compared and the subsequent tool point dynamics prediction accuracy is evaluated. Experimental results are provided for multiple spindles and tool-holder assemblies to determine the preferred spindle dynamics identification approach.

SPINDLE IDENTIFICATION

In this section the three approaches to determine the spindle dynamics are discussed.

Synthesis Approach

The individual component, or substructure, receptances, $R_{ij}(\omega)$, are defined in Eq. 1:

$$R_{ij} = \begin{bmatrix} \frac{x_i}{f_j} & \frac{x_i}{m_j} \\ \frac{\theta_i}{f_j} & \frac{\theta_i}{m_j} \end{bmatrix} = \begin{bmatrix} h_{ij} & l_{ij} \\ n_{ij} & p_{ij} \end{bmatrix} \quad (1)$$

where x_i is the substructure displacement at the coordinate location i, θ_i is the substructure rotation at the coordinate location i, f_j is the force applied to the substructure at the coordinate location j and m_j is the couple applied to the substructure at the coordinate location j. In the synthesis approach, a standard artifact with a simple cross-sectional geometry is inserted in the spindle and two receptances are measured using impact testing, where an instrumented hammer is used to excite the structure and an accelerometer is used to record the resulting response. The first measurement is a direct displacement-to-force receptance (H_{22}), where the excitation and measurement locations coincide, completed at the free end of the artifact. The second is a cross displacement-to-force receptance (H_{2a2}). In this case, the artifact is excited at its free end, but the response is recorded at a distance, s, from the free end. By differencing these measurements and dividing by s, the rotation-to-force receptance can be calculated.

$$N_{22} = \frac{\theta_2}{f_2} = \frac{\frac{x_2 - x_{2a}}{s}}{f_2} = \frac{\frac{x_2}{f_2} - \frac{x_{2a}}{f_2}}{s} = \frac{H_{22} - H_{2a2}}{s} \quad (2)$$

By reciprocity, L_{22} is set equal to N_{22}. The rotation-to-moment receptance, P_{22}, is then synthesized [1].

$$P_{22} = \frac{x_2}{m_2}\frac{\theta_2}{f_2}\frac{f_2}{x_2} = L_{22}N_{22}\frac{1}{H_{22}} = \frac{N_{22}^2}{H_{22}} \quad (3)$$

The four receptances required to populate G_{22}, the receptance matrix for the artifact-spindle-machine at its free end, are now known.

$$G_{22} = \begin{bmatrix} H_{22} & L_{22} \\ N_{22} & P_{22} \end{bmatrix} \quad (4)$$

Given this matrix, the artifact can be removed in simulation to isolate the spindle-machine response, R_{3b3b}, using Eq. 5, where the R_{22}, R_{23a}, R_{3a3a}, and R_{3a2} matrices are populated using beam models to describe the portions of the artifact beyond the flange. See Fig. 1.

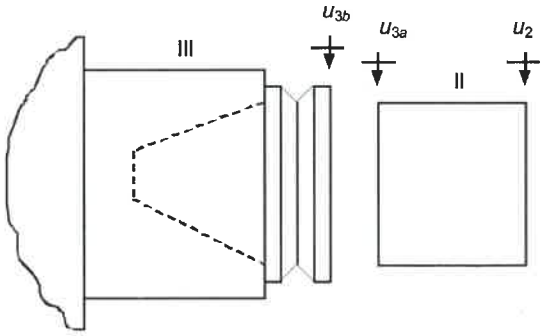

Figure 1: Artifact model for determining R_{3b3b} by inverse RCSA.

Equation 5 is rearranged in Eq. 6 to isolate R_{3b3b}. This step of decomposing the measured assembly receptances, G_{22}, into the modeled substructure receptances, R_{3a2}, R_{22}, R_{23a}, and R_{3a3a}, and spindle-machine receptances, R_{3b3b}, is referred to as "inverse RCSA".

$$G_{22} = R_{22} - R_{23a}\left(R_{3a3a} + R_{3b3b}\right)^{-1} R_{3a2} \quad (5)$$

$$R_{3b3b} = R_{3a2}\left(R_{22} - G_{22}\right)^{-1} R_{23a} - R_{3a3a} \quad (6)$$

Given R_{3b3b}, free-free models for arbitrary tool-holder combinations can be defined and coupled to the spindle-machine receptances to predict the tool point FRF, H_{11}, required for milling process simulation

Finite Difference Approach

In this approach, an additional direct displacement-to-force receptance, H_{2a2a}, is measured at the distance, s, from the free end of the artifact. With the two direct, H_{22} and H_{2a2a}, and one cross displacement-to-force receptances, H_{2a2}, a finite difference approach is implemented to identify the rotation-to-moment receptance [5] (Eq. 7). For both the first and second approaches, modal fitting via a peak picking technique is applied to reduce the effects of measurement noise on the prediction results.

$$P_{22} = \frac{H_{22} - 2H_{2a2} + H_{2a2a}}{s^2} \quad (7)$$

Euler-Bernoulli Model

As an alternative to completing multiple measurements on the standard artifact, in this approach a single direct measurement is performed at the free end of the standard artifact. It is then assumed that each mode within the measurement bandwidth can be approximated as a fixed-free beam and the individual modes are fit using the closed-form receptance (E-B) equation for fixed-free Euler-Bernoulli beams presented by Bishop and Johnson [6]. The fit is completed using Eq. 8 for the displacement-to-force receptance at the free end of a fixed-free beam, where $\lambda^4 = \omega^2 \frac{\rho A}{EI(1+i\eta)}$, $A = \frac{\pi d^2}{4}$, $I = \frac{\pi d^4}{64}$, ω is frequency (rad/s), ρ is the density, E is the elastic modulus, η is the solid damping factor (unitless), d is the beam diameter, and L is the beam length.

$$H_{22} = \frac{\sin(\lambda L)\cosh(\lambda L) - \cos(\lambda L)\sinh(\lambda L)}{\lambda^3 EI(1+i\eta)\left(\cos(\lambda L)\cosh(\lambda L) - 1\right)} \quad (8)$$

The algorithm for performing a fit is composed of five steps.

1. Determine the natural frequency, f_n (in Hz), for the mode to be fit.
2. Select a beam diameter (this is a fitting parameter). Also specify the modulus and density (steel values were used here).
3. Calculate the beam length using the closed-form expression for the natural frequency of a fixed-free beam; see Eq. 9.
4. Adjust η to obtain the proper slope for the real part of the mode in question.
5. If the predicted mode amplitude is too large, increase d to d_{new} and calculate L_{new} using Eq. 10 (to maintain the same natural frequency). If the mode amplitude is too small, decrease d and calculate L_{new}.

$$L = \left(\frac{1.87510407^2 d}{2\pi f_n} \left(\frac{E}{16\rho} \right)^{\frac{1}{2}} \right)^{\frac{1}{2}} \quad (9)$$

$$L_{new} = \frac{L}{\sqrt{d}} \sqrt{d_{new}} \quad (10)$$

Once the fit parameters d, L, and η are known (as well as the E and ρ values), the remaining receptances for the free end of the artifact are calculated as shown in Eqs. 11 and 12.

$$L_{22} = N_{22} = \frac{-\sin(\lambda L)\sinh(\lambda L)}{\lambda^2 EI(1+i\eta)\left(\cos(\lambda L)\cosh(\lambda L) - 1\right)} \quad (11)$$

$$P_{22} = \frac{\cos(\lambda L)\sinh(\lambda L) + \sin(\lambda L)\cosh(\lambda L)}{\lambda EI(1+i\eta)\left(\cos(\lambda L)\cosh(\lambda L) - 1\right)} \quad (12)$$

RESULTS

Spindle measurements and tool point predictions were made on three different machining centers: Cincinnati FTV5-2500, Olympia HT 140x60 Horizontal, and Mikron UCP-600 Vario.

Cincinnati FTV5-2500

Artifact measurements (HSK-63A holder-spindle connection) were performed to isolate the spindle-machine receptances using an artifact with s = 50 mm. Predictions and measurements are presented here using Haimer A63.140 shrink fit holders with 19.05 mm diameter endmills. Three different Data Flute three-flute solid carbide endmill models were tested at seven overhang lengths (from the holder face to the endmill free end) to compare measurements and predictions. The equivalent diameter for the fluted section was calculated using the tool mass, an assumed carbide density of 14500 kg/m^3, the shank diameter and length, the neck diameter and length, and the length of the ground flutes. For the steel sections of the Timoshenko beam models, the elastic modulus was 200 GPa, the density was 7800 kg/m^3, and Poisson's ratio was 0.29. For the carbide sections, the elastic modulus was 550 GPa, the density was 14500 kg/m^3, and Poisson's ratio was 0.22. The unitless structural (solid) damping factor was 0.0015 for all sections. Figures 2 and 3 show measurements and predictions with spindle receptances obtained by all the three approaches. In the figures, EB is the prediction made by E-B model, FD is the prediction made by finite difference approach using modal fitting, Synth is the prediction made by the synthesis approach using modal fitting, and Unfit FD and Unfit Synth are predictions made by finite difference and synthesis approach without modal fitting, respectively.

In Figs. 2 and 3, the predictions by the E-B beam model and the fitted finite difference approach are in good agreement with each other and the natural frequencies also show reasonable agreement with the measurements considering the rigid coupling assumption for predictions. In Fig. 2, the prediction by the synthesis approach (fit and unfit) shows an extra inverted mode at 2686 Hz and a much larger magnitude mode at frequency of 1881.4 Hz in Fig 3.

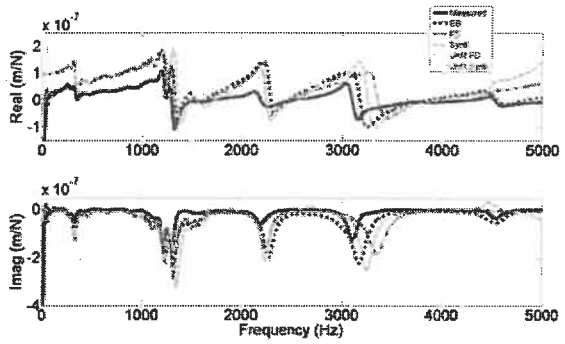

Figure 2. Comparison of measurement and tool point predictions (50.8 mm overhang length).

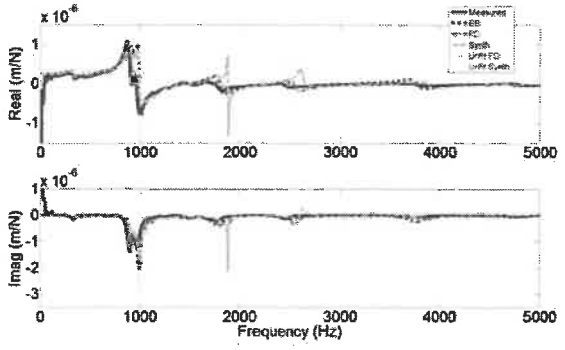

Figure 3. Comparison of measurement and tool point predictions (101.6 mm overhang length).

Olympia HT 140x60 Horizontal

Artifact measurements (HSK100A holder-spindle connection) were performed to isolate the spindle-machine receptances using an artifact with s = 40 mm. Predictions and measurements are presented here using Command H6Y3A0750 Z3.63-FSF holder for 19.05 mm diameter endmills. Figures 4 and 5 show the measurement and predictions with spindle receptances obtained by the three approaches using one artifact and two different overhang lengths of the tool.

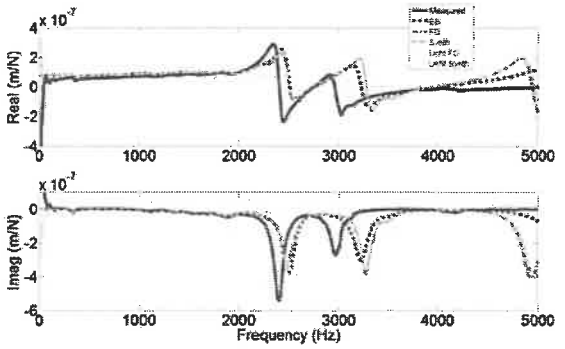

Figure 4. Comparison of measurement and tool point predictions (63.5 mm overhang length).

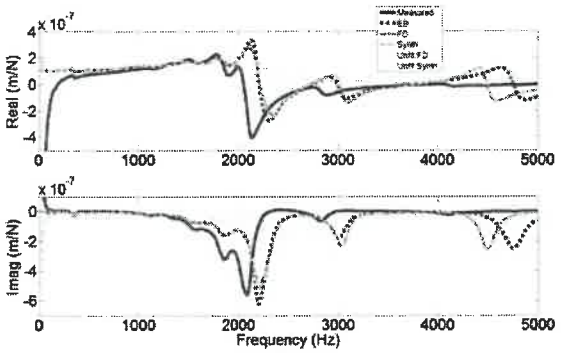

Figure 5. Comparison of measurement and tool point predictions (76.2 mm overhang length).

In Figs. 4 and 5, the E-B and fitted finite difference predictions are in good agreement with each other and also show reasonable agreement with the measurements. The unfit finite difference approach and synthesis approach show disagreement with the other predictions, as well as the measurements, both in magnitude and natural frequencies.

Mikron UCP-600 Vario

HSK-63A artifact measurements were performed to obtain spindle receptances (s = 40 mm). Predictions and measurement were completed using a shrink fit holder with 19.05 mm diameter steel blanks (overhang lengths of 88.9 mm and 101.6 mm); see Figs. 6 and 7. The measured FRFs show good agreement with the predictions by E-B model and the unfit finite difference approach. The fitted finite difference approach and fitted synthesis approach predictions show some disagreement with the E-B model prediction and the measurements in natural frequencies. The predictions using the unfit synthesis approach show large error in natural frequency and magnitude at lower frequencies.

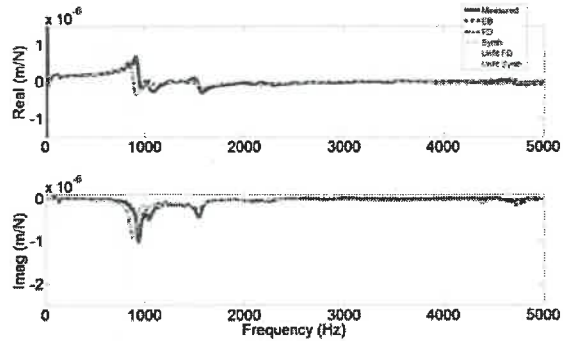

Figure 6. Comparison of measurement and tool point predictions (88.9 mm overhang length).

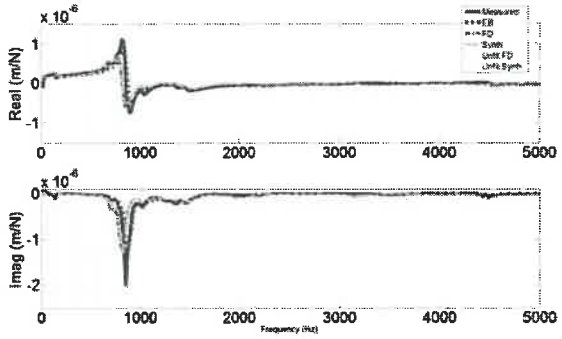

Figure 7. Comparison of measurement and tool point predictions (101.6 mm overhang length).

CONCLUSION

In this paper new techniques to identify the spindle dynamics for RCSA were discussed and the tool point frequency response predictions were compared for the three approaches using different spindles and tool-holder combinations. The tool point predictions were experimentally verified. The tool point predictions obtained using the spindle receptances determined from Euler-Bernoulli model and finite difference approach most closely matched the measured tool point receptances. Since only one direct measurement is required for the Euler-Bernoulli model, this may be the preferred option.

REFERENCES

[1] Schmitz T. and G.S. Duncan (2005). Three-Component Receptance Coupling Substructure Analysis for Tool Point Dynamics Prediction. Journal of Manufacturing Science and Engineering, Vol. 127/4, pp. 781-790.

[2] Schmitz T. and K.S. Smith (2009). Machining Dynamics: Frequency Response to Improved Productivity, Springer, NY.

[3] Weaver W. Jr., S. Timoshenko, and D. Young (1990). Vibration Problems in Engineering, 5th Edition, John Wiley and Sona, New York, NY, Section 5.12.

[4] Ertürk A., H.N. Özgüven, and E. Budak (2006). Analytical Modeling of Spindle-Tool Dynamics on Machine Tools using Timoshenko Beam Model and Receptance Coupling for the Prediction of Tool Point FRF. International Journal of Machine Tools and Manufacture, Vol. 46/15, pp. 1901-1912.

[5] Duarte M. M. Lućia, and D.J. Ewins (2000). Mechanical and Signal Processing, Vol. 14/1, pp. 205-227.

[6] Bishop R.E.D. and D.C. Johnson (1960). The Mechanics of Vibration, Cambridge University Press, Cambridge, UK.

FIGURING OF MILLIMETER-THICK ELLIPTICAL MIRROR SUBSTRATE USING NUMERICALLY CONTROLLED LOCAL WET ETCHING WITH LOW-PRESSURE POLISHING

M.Nagano[1], F.Yamaga[1], N.Zettsu[1], D.Yamazaki[2], R.Maruyama[2], K.Soyama[2] and K.Yamamura[1]

[1]Research Center for Ultra-Precision Science and Technology
Graduate School of Engineering Osaka University
Suita, Osaka, Japan
[2]J-PARC Center
Japan Atomic Energy Agency
Tokai, Ibaraki, Japan

1.Introduction

Recently, various measurements using neutron beam have attracted much attention because of the ability to identify hydrogen atoms and water molecules exactly, sensitivity to magnetism and hard penetrating power. And high-intensity proton accelerator facilities are constructed for neutron research such as J-PARC in Japan, ISIS-TS2 in UK and SNS in USA. However, neutron intensity is very weak compared with that of X-ray in the synchrotron orbital radiations, even in these latest neutron sources. Therefore, high performance optical devices for focusing of neutron beam are required to realize practical measuring. Reflective aspherical supermirror optics would offer advantage for focusing neutron beam with a wide wavelength range since it has no chromatic aberration.

We developed numerically controlled local wet etching (NC-LWE) technique to figure aspherical mirror substrates [1] and ion beam sputter deposition technique to deposit the NiC/Ti multilayer [2] for realization of usable aspherical supermirror optics. Previously, we fabricated a plano-elliptical supermirror with a clear aperture size of 90 x 40 mm^2 by applying these techniques, and obtained a focusing gain of 6 and a reflectivity of 0.64-0.7 in the near-critical-angle region for m=4 [3]. The m-value means the ratio of the effective critical angle of the supermirror to that of natural nickel.

To increase the focusing gain and the reflectivity, decreasing of the surface roughness, enlargement and multiplexing of the supermirror are essential. Previously, we have succeeded in development of fabrication process for aspherical mirror substrate with a large clear aperture size [4]. In the case of the multiplexing of supermirrors, mirror substrates must be thin to reduce the absorption loss of incident neutron beam. It is difficult to fabricate the thin mirror substrates with a form accuracy of sub-micrometric level and a surface roughness of sub-nanometric level because the conventional precision grinding deform the workpiece by its machining force and its spring back cause figure error. In addition, conventional polishing for decreasing of surface roughness causes increase of figure error. As a fabrication technique for SiC mirrors with millimeter-thickness, ELID grinding with feedback compensation method has been reported [5]. In this method, tool pass is determined from numerical calculation result of the profile deformation analyzed by FEM.

On the other hand, NC-LWE technique is very suitable for fabricating an ultraprecise millimeter-thick mirror substrate, because NC-LWE technique enables to fabricate an aspherical shape without processing pressure to the workpiece and wear of machine tools because of its noncontact removal mechanism utilizing chemical reaction. And, high reproducibility is also achieved owing to the insensitivity to the external disturbances, such as a vibration or a thermal deformation. So, NC-LWE technique is a very valid way to fabricate the ultraprecise millimeter-thick mirror substrate with high reproducibility. We developed deterministic and damage-free fabrication process for millimeter-thick elliptical neutron focusing mirror substrate. The process consists of NC-LWE figuring and low-pressure polishing with polishing pressure of less than about 7kPa (1psi). In this work, we fabricated a plano-elliptical neutron focusing mirror substrate with a thickness of 1.5 millimeter.

2. Experimental procedure

2.1. Optics design

To increase the focusing gain, it is effective to multiplex the supermirror. We designed a multiple mirror neutron focusing system be applied to reflective small angle scattering measurement in SUIREN (Apparatus for Surface and Interface Investigations with Reflection of Neutrons) in JRR-3M (Japan Research Reactor No.3 Modified of Japan Atomic Energy Agency). Fig. 1 shows the optics design of multiple mirror neutron focusing system. This focusing system consists of 4 mirrors which have the elliptical shapes represented by equation (1).

$$\frac{x^2}{a_i^2}+\frac{y^2}{b_i^2}=1 \text{ (unit:mm).} \qquad (1)$$

Each mirror's a, b values are shown in the Table 1 The thickness of each mirror substrates is 1.5 mm and clear aperture size is 100 x 50 mm^2. The magnification of these mirrors, focal length and incident angle of the outmost mirror center are 1:1, 1050 mm and 1.4°, respectively.

2.2 Figuring of elliptical mirror shape

In this report, we fabricated the mirror #4 shown in Table 1 by NC-LWE. The material and outer size are synthesized quartz glass and 150 x 150 x 1.5 mm^3, respectively. In NC-LWE technique, a figuring is performed by controlling the dwelling time of the combination nozzle which consists of a supply and a suction part of an etchant on the workpiece. Because of its non-contact chemical removal mechanism, NC-LWE enables to fabricate the millimeter-thick mirror substrate without generating subsurface damage and deformation. As the processing parameters in NC-LWE figuring, we applied the 37 wt% HF aqueous solution with a temperature of 42°C, circular nozzle with a diameter of 15 mm and a feed pith of 0.5 mm.

TABLE 1. Optical parameters of neutron focusing mirrors

Mirror #1	θ_1=1.40(dgree), a_1=1050.31, b_1=25.66 (mm)
Mirror #2	θ_2=1.19(dgree), a_2=1050.23, b_2=21.83 (mm)
Mirror #3	θ_3=1.00(dgree), a_3=1050.16, b_3=18.34 (mm)
Mirror #4	θ_4=0.83(dgree), a_4=1050.11, b4=15.17 (mm)
Focal length	f=1050 mm

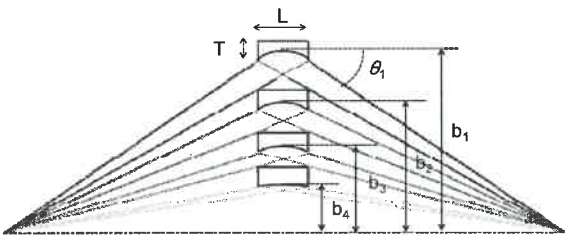

FIGURE 1. The optics design of multiple mirror neutron focusing system.

2.3 Improvement of surface roughness

In NC-LWE figuring, raster-type numerically controlled scanning is applied to correct the residual figure error. After the raster scanning, shallow periodic grooves, which are similar to the tool marks formed in conventional lathe turning, are inevitably generated on the figured surface by the overlapping of the scanned etching path. We have reported a method of lowering the height of the tool marks by a two-stage NC-LWE process [3]. However, in NC-LWE figuring with raster scanning, the tool marks cannot be completely eliminated. To remove low-spatial frequency roughness (LSFR) such as tool marks, we applied a first polishing with a hard polishing pad.

Additionally, the MSFR component of the processed surface tends to increase after NC-LWE figuring. Subsurface damage is considered as one of the causes of the increase in the MSFR because the etching rate of the damaged layer is different from that of an undamaged layer. It is essential to minimize the surface roughness to obtain higher reflectivity and thus realize the practical application of the neutron focusing mirror. Therefore a second polishing process using a soft polishing pad was applied to improve the MSFR of the figured mirror substrate.

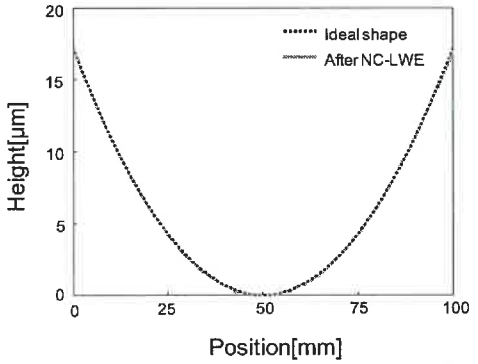

FIGURE 2. The cross-sections of the ideal shape and the fabricated elliptical mirror.

TABLE 2 Polishing parameters of first polishing.

Polishing pad	Foamed polyurethane
Load	100 [g]
Hardness of pad	58 [Shore-D]
Slurry	CeO_2 (0.19 μm)
Rotating speed	300 [rpm]
Scanning speed	100 [mm/min]
Feed pitch	0.1 [mm]
Removal depth	1 [μm]

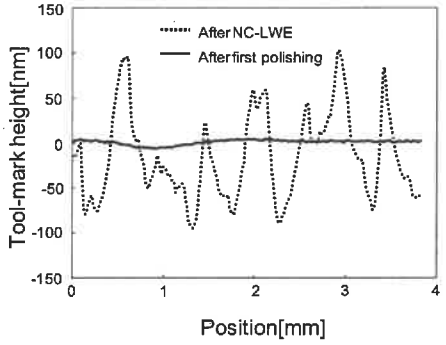

FIGURE 3. Removal of tool-mark by first polishing.

3. Results and Discussion

Fig. 2 shows the cross-sections of the ideal shape and the fabricated elliptical mirror after NC-LWE. The shapes of the mirror substrate were measured with a laser autofocus measuring machine (Mitaka Kohki NH-3SP, z resolution: 1 nm). The residual figure error was about 0.2 μm. This result indicates that the non-contact removal by controlling the dwelling time of the etchant nozzle deterministically figure the aspherical shape with sub-micrometric level form accuracy.

Fig. 3 shows the surface profiles before and after the first polishing. The spatial period and the height of the tool marks were 0.5 mm and 100-200 nm, respectively. The first polishing was performed by applying the polishing parameters shown in Table 2. A hard polishing pad was used to remove the tool marks with a long spatial wavelength, since the deformation of the polishing pad along the tool marks is small. The tool marks were perfectly removed after the second polishing with a removal depth of about 1 μm.

Figs. 4 (a) and (b) show the surface roughness of the figured mirror substrate after NC-LWE correction and after the second polishing, respectively. Table 3 shows the polishing

TABLE 3 Polishing parameters of second polishing.

Polishing pad	Foamed polyurethane
Load	100 [g]
Hardness of pad	82 [Asker-C]
Slurry	CeO_2 (0.19 μm)
Rotating speed	300 [rpm]
Scanning speed	300 [mm/min]
Feed pitch	0.1 [mm]
Removal depth	0.04 [μm]

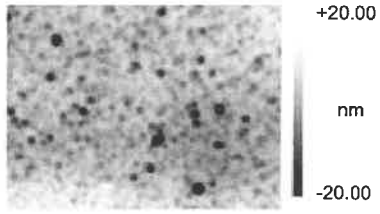

(a) After NC-LWE

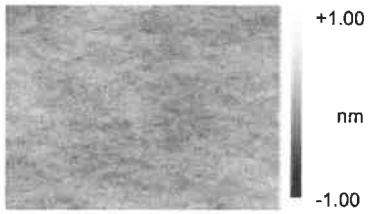

(b) After second polishing

FIGURE 4. The surface roughness of the mirror substrate. (64 x 48 μm²)

paramers used in te second polishing. The surface roughness was measured using a scanning white-light interferometer (Zygo NewView 200CHR). Many pits were seen on the surface before the third polishing, as shown in Fig. 4(a), and the rms surface roughness was 4.6 nm. To remove these undesirable surface structures, a soft polishing pad was applied in the second polishing process with a removal depth of about 40 nm. Fig. 4(b) indicates that the surface morphology was improved and an rms roughness of less than 0.15 nm was obtained by applying the second polishing. Fig. 5 shows power spectral density plots of the surface before and after the second polishing. The figure indicates that the third polishing process is very effective for improving the overall surface roughness of the mirror substrate in the MSFR region.

In general, the application of a polishing process to improve the surface roughness degrades the form accuracy because it is difficult to maintain a constant removal rate over the area of the clear

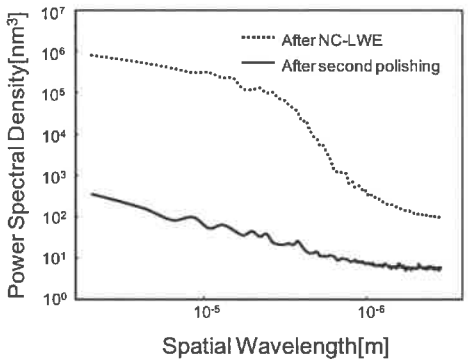

FIGURE 5. Power spectral density plots of the surface after NC-LWE and after second polishing.

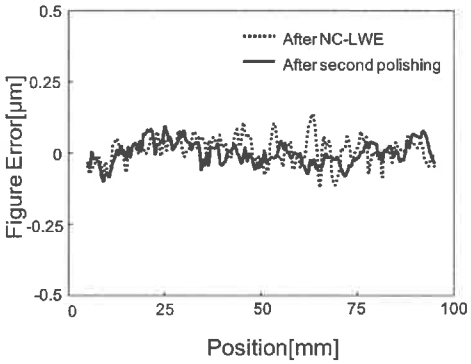

FIGURE 6. The residual figure errors after NC-LWE and after second polishing.

aperture of the mirror. Therefore, we evaluated the shape change of the figured mirror due to the low-pressure polishing. Fig. 6 shows the residual figure errors after NC-LWE and second polishing. The residual figure error after second polishing was about 0.2 μm p-v. The low-pressure polishing process has satisfactory ability to improve the surface roughness while maintaining sub-micrometer form accuracy.

These results indicate that two-step low-pressure polishing is very effective to improve the surface roughness without degrading the shape of the mirror substrate. Therefore, the application of the combined fabrication process combining NC-LWE figuring and low-pressure polishing is a highly effective method to fabricate the ultraprecision millimeter-thick aspherical mirror substrates with a sub-micrometric level form accuracy and with a sub-nanometric level surface roughness.

Summary

We developed the new fabrication process for fabricating the ultraprecise millimeter-thick elliptical mirror substrate. This process consists of NC-LWE technique for deterministic figuring with a form accuracy of sub-micrometric level and low-pressure polishing for improving the LSFR and MSFR without degrading the mirror shape. We fabricated a plano-elliptical neutron focusing mirror substrate made of synthesized quartz glass with a thickness of 1.5 millimeter, and succeeded in obtaining the figure error of 0.2 μm p-v with the surface roughness of less than 0.15 nm rms.

Acknowledgements

This work was partially supported by a grant for "Development of System and Technology for Advanced Measurement and Analysis (SENTAN)" from Japan Science and Technology Agency (JST) and the "Industrial Technology Research Grant Program in 2005" from the New Energy and Industrial Technology Development Organization (NEDO) of Japan.

REFERENCES

[1] K. Yamamura. Development of numerically controlled local wet etching. Science and Technology of Advanced Materials. 2007; 8: 158-161.

[2] R. Maruyama, D. Yamazaki, T. Ebisawa, K. Soyama. Development of high-reflectivity neutron supermirrors using an ion beam sputtering technique. Nuclear Instruments and Methods in Physics Research A.2009; 600: 68-70.

[3] K. Yamamura, M. Nagano, H. Takai, N. Zettsu, D. Yamazaki, R. Maruyama, K. Soyama, S. Shimada. Figuring of plano-elliptical neutron focusing mirror by local wet etching. Optical Express. 2009; 17: 6414-6420.

[4] M. Nagano, F. Yamaga, N. Zettsu, D. Yamazaki, R. Maruyama, K. Soyama, K. Yamamura. Development of fabrication process for aspherical neutron focusing mirror using numerically controlled local wet etching with low-pressure polishing. Nuclear Instruments and Methods in Physics Research A. 2010; in press.

[5] H. Ohmori, Y. Dai, W. Lin, T Suzuki, K. Katahira, N. Itoh, A. Makinouchi,H. Tashiro. Force characteristics and deformation behaviors of sintered SiC during annelid grinding process. ADVANCES IN ABRASIVE TECHNOLOGY V. 2003; 238-2: 65-70.

USING PROCESS MODELS TO OPTIMIZE MODULATED TOOL-PATH CHIP BREAKING OPERATIONS

William E. Barkman[1], Edwin F. Babelay, Jr.[1], K. Scott Smith[2], Thomas S. Assaid[2]
Justin T. McFarland[2], and David A. Tursky[2]
[1]Technology Development
Babcock and Wilcox Technical Services, LLC
Oak Ridge, Tennessee
[2]Department Of Mechanical Engineering
University of North Carolina at Charlotte
Charlotte, North Carolina

INTRODUCTION

This paper discusses recent results from a collaborative research project involving the Y-12 National Security Complex (Y-12) and the University of North Carolina at Charlotte (UNC Charlotte) that was first introduced at the October 2009 American Society for Precision Engineering Annual Meeting in Monterrey, California. The previous presentation, titled "Machine Performance Requirements Associated with Modulated Tool-Path Chip Breaking" described the basic process for using unique, oscillatory part programs to continuously create user-selectable chip lengths and the machine performance requirements associated with this process.

The modulated tool-path (MTP) chip breaking technique uses a part program generated oscillatory motion of the machine's axes, parallel to the machining tool path, to intermittently engage and disengage the cutting tool from the workpiece cut face, as shown in figures 1 & 2. (Figure 1 demonstrates the basic concept; figure 2 shows a more accurate representation of the chip face.)

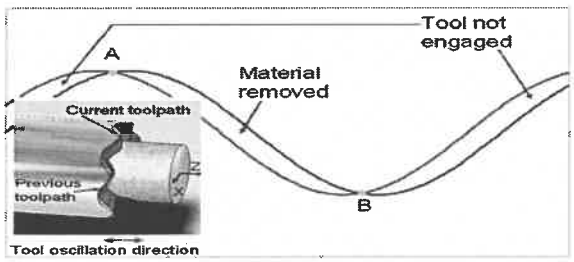

FIGURE 1. Exaggerated representation of MTP cut face and axis motion.

This approach successfully creates segmented chips by producing irregular waves in the cut face; however, it can also introduce complex

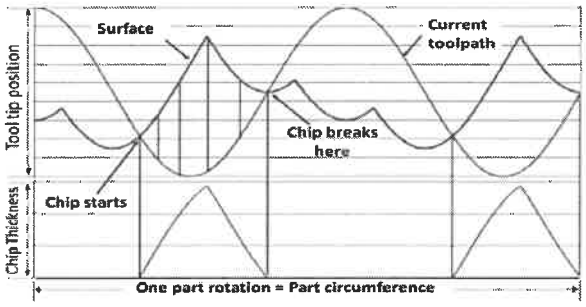

FIGURE 2. Interaction between the cutting tool and chip face that produces the segmented chips.

finish characteristics on the workpiece surface due to the varying feedrate and "recutting action" associated with the oscillatory motion. While this somewhat irregular surface finish pattern is not a concern during the roughing or semi-finish pass, it must be addressed for finishing operations, which leads to the challenge of attempting to optimize the sometimes conflicting goals of creating the desired chip length and surface texture while maintaining process throughput.

Y-12 and UNC Charlotte have developed models that predict the chip length and surface finish for various MTP process parameters and machine testing protocols have been developed that determine the ability of a particular machine to accurately execute the MTP commands. In general, shorter chip lengths are produced when using higher oscillation frequencies; however, the ability to produce the higher speed slide motion is limited by the capabilities of a particular machine tool. Reducing the spindle speed reduces the oscillation frequency needed to produce a particular chip length but this process change also impacts the machining time

and can make it difficult to achieve the desired surface feet per minute cutting conditions. Understanding the impacts of these process parameter changes on surface finish is also non-intuitive due to the changing feedrates and the "wiping motion" created by the MTP process.

This paper discusses a technique for finding the process parameter "sweet spot" that uses process models to integrate workpiece characteristics and tolerances, desired chip lengths and process "feeds and speeds," and machine performance capabilities and presents experimental results from the machining tests used to validate the process optimization predictions.

EXPERIMENTAL MODELS

Figure 3 shows the relationship between the MTP Amplitude Ratio (oscillation amplitude divided by the global feedrate) and the phase shift in the oscillation motion, between sequential spindle rotations, needed to produce broken chips.

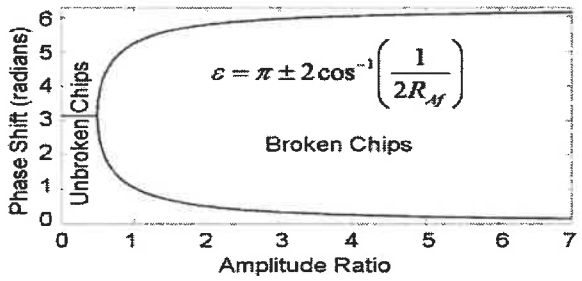

FIGURE 3. MTP parameter values that produce segmented chips. (The amplitude ratio is the MTP oscillation amplitude divided by the global feed per spindle revolution. The phase shift is the relationship between the oscillations that occur on sequential spindle revolutions.)

As might be expected, small amounts of oscillation amplitude in relation to the global feedrate (inches per spindle revolution - ipr) will not produce broken chips because there isn't enough "retract motion" to disengage the cutter from the workface. Similarly, small amounts of phase shift will produce a "wavy cut face" but the chips will be unbroken. (This region of unbroken chips is depicted as a "white area" in subsequent chip length charts in order to more easily clarify the model predictions.)

Figures 4 & 5 show two views of the results from modeling the relationship between the MTP oscillation amplitude, the number of MTP oscillations per spindle revolution (OPR), and the ratio of chip length to workpiece diameter for an axes feed of 0.003 inches per revolution (ipr). (The information is presented in terms of OPR and chip length/workpiece diameter as a means of normalizing data.)

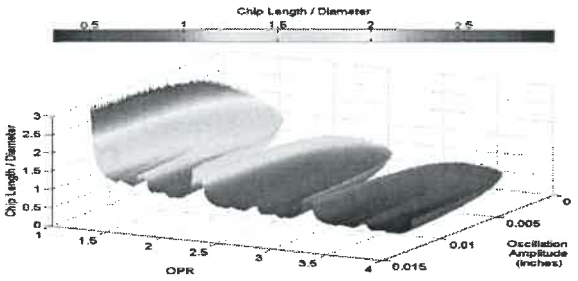

FIGURE 4. Model prediction of chip length/workpiece diameter in relation to the MTP oscillation amplitude and oscillations per spindle revolution (with a 0.003 ipr axes feed).

Two important predictions shown in these figures are that the chip length is relatively insensitive to OPR for OPR values above about 2.8 and to the oscillation amplitude. (As long as the oscillation amplitude is large enough to break the chips.) This means that if OPR values in the range of 2.2 to 2.8 can be achieved, then the chip length/diameter parameter will not change much over the oscillation amplitude range from 0.005" to 0.015". Shifting to the higher frequency range associated with OPR's around 3.5 provides little reduction in chip length and requires either a significant increase in the dynamic performance of the machine tool or an accompanying decrease in the spindle speed. The actual uncut chip length will depend on the part diameter (distance of the tool from the spindle centerline) and the degree of chip compaction and chip curling that is present. If a cylindrical part is being machined, the MTP process parameters can be selected based on the diameter of the workpiece and the desired chip size and axis feed. For a facing cut, the MTP parameter selection process is more complicated when a constant surface feet per minute (sfm) mode is desired because the spindle speed is constantly changing as the tool moves toward the spindle centerline.

The surface profile that is produced by the MTP process is also an important process characteristic and figure 6 [1] shows the model prediction of the workpiece surface finish that

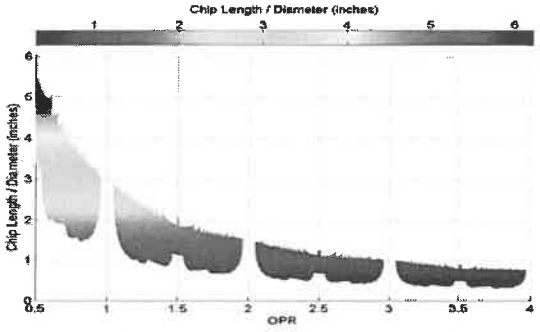

FIGURE 5. Model prediction of relationship between chip length and MTP oscillations per spindle revolution.

will be produced when using a 0.031" radius cutter, a 0.003" feed, and a speed of 300 sfm. (The dark blue regions surrounding the "oval islands" are the areas in which the chips will not break.)

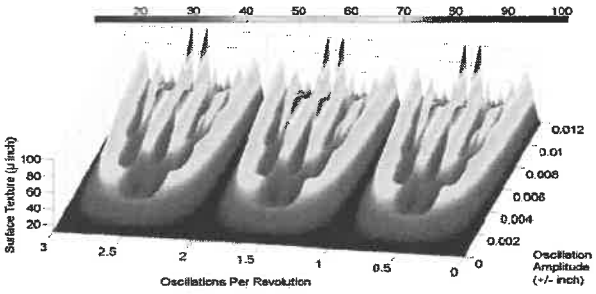

FIGURE 6. Model prediction of relationship between MTP oscillation amplitude, OPR, and workpiece surface texture.

The surface profile model results are mirror images around OPR values of 0.5, 1.5, 2.5, etc. There are also have a number of "sweet spots" that exhibit relatively low surface textures as well as areas with significantly higher surface profile values. It is also noteworthy that from a surface profile perspective, it is not necessary to use MTP parameters outside the 0 to 1 OPR range, because the "higher frequency" islands give the same results as "lower frequency" islands.

Figure 7 shows an overhead view of the lower left hand corner of figure 6. It can be seen that selecting MTP process parameters in the center of a "blue region" provides some protection against errors in the machine tool's ability to maintain the amplitude of the MTP oscillation at different oscillation frequencies. Conversely, the proximity of red and yellow regions to some of the blue regions highlights the importance of maintaining the selected OPR values. (Deviations in this parameter can be caused by the inability of the machine to deliver the desired axes dynamic response or by spindle rpm values that different from what is requested in the machining part program.)

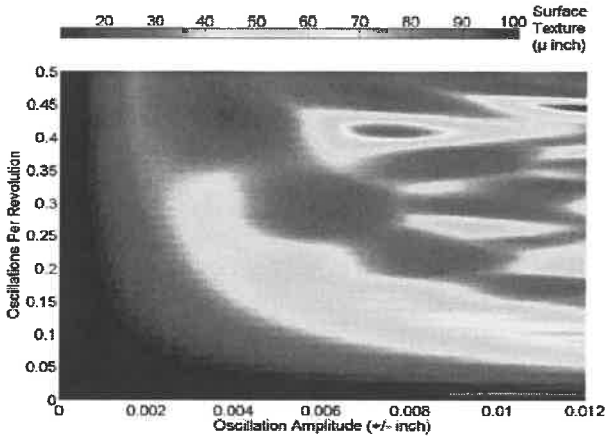

FIGURE 7. Overhead view of the lower right corner of figure 6.

An additional characteristic of the MTP surface profile is that it varies around the circumference of the workpiece as well as along the tool path, as shown the computer simulation results depicted in figure 8. In most cases, the MTP process parameters should be selected to minimize the variations in the surface profile.

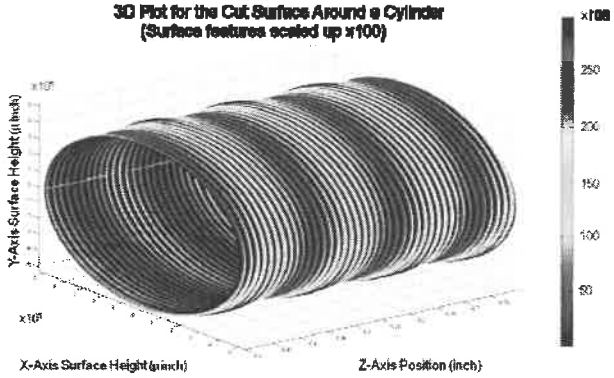

FIGURE 8. Simulation of a workpiece surface profile produced by the MTP chip breaking process that demonstrates the surface waves that occur at various locations along the cylinder as well as around the circumference of the workpiece.

EXPERIMENTAL RESULTS

Machining tests were conducted using aluminum workpieces and a diamond turning machine to

avoid machineability complications when comparing the predicted and actual surface profiles on cylindrical, facing and tapered machining operations. (The machining parameters used were 300 rpm, 0.025 ipr, and a 0.02" radius diamond tool.) Two different sets of MTP oscillation parameters were chosen to validate the model predictions. One set of parameters was chosen to produce distinctly structured surface finishes, while the other set was selected to validate the low surface texture predictions (blue regions). The surface profile was characterized using a stylus profilometer.

Figure 9 shows a summary of the results from the machining tests. The D1 – D8 data was collected from cylindrical parts, the F1 & F2 tests involved facing cuts, and the T1 – T4 experiments were performed on tapered workpieces. (The predicted surface texture value is plotted on the left for each set of test conditions.) There is generally good agreement between the predicted and measured surface profiles and the mean variation between the data sets, over the 14 test runs, is approximately 4 microinches. In addition, figure 10 shows a comparison of the predicted and actual surface profiles for the D2 test conditions.

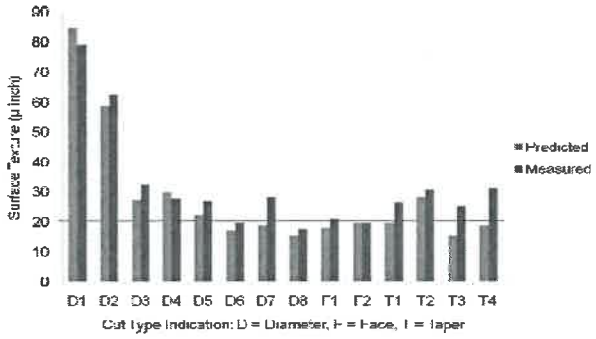

FIGURE 9. Comparison of predicted and measured surface texture values from the diamond turning tests.

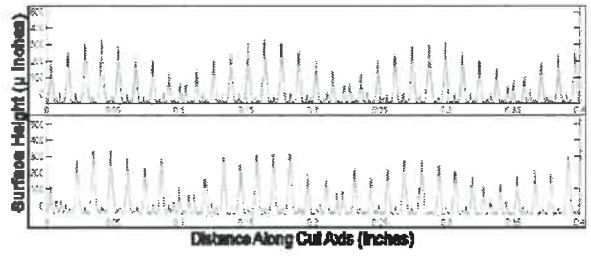

FIGURE 10. (Upper) Predicted surface profile of D2. (Lower) Measured surface profile of D2.

FUTURE WORK

The experimental tests conducted to date have demonstrated good agreement between the surface profile model predictions and the results obtained with constant rpm diamond turning operations. Future activities will extend these tests to the constant sfm machining of faces and tapers.

REFERENCES

[1] Smith K, McFarland J, Tursky D, Assaid T, Barkman W, and Babelay Jr. E. Simulating the Effect of Modulated Tool-Path Chip Breaking on Surface Texture and Chip Length. Depleted Uranium Users Conference. Oak Ridge, TN. April 19-21, 2010.

COPYRIGHT NOTICE

This document has been authored by a subcontractor of the U.S. Government under contract DE-AC05-00OR-22800. Accordingly, the U.S. Government retains a paid-up, nonexclusive, irrevocable, worldwide license to publish or reproduce the published form of this contribution, prepare derivative works, distribute copies to the public, and perform publicly and display publicly, or allow others to do so, for U. S. Government purposes.

DISCLAIMER

This work of authorship and those incorporated herein were prepared by Contractor as accounts of work sponsored by an agency of the United States Government. Neither the United States Government nor any agency thereof, nor Contractor, nor any of their employees, makes any warranty, express or implied, or assumes any legal liability or responsibility for the accuracy, completeness, use made, or usefulness of any information, apparatus, product, or process disclosed, or represents that its use would not infringe privately owned rights. Reference herein to any specific commercial product, process, or service by trade name, trademark, manufacturer, or otherwise, does not necessarily constitute or imply its endorsement, recommendation, or favoring by the United States Government or any agency or Contractor thereof. The views and opinions of authors expressed herein do not necessarily state or reflect those of the United States Government or any agency or Contractor thereof.

SELF-REFERENCED SURFACE PROFILOMETRY

R. E. Parks, Peng Su, Chang Jin Oh and J. H. Burge
College of Optical Sciences
University of Arizona
Tucson, AZ 85750

INTRODUCTION

In optical surface metrology the reference surface is usually self-calibrated against the part under test because the errors in the reference are of the same order as those in the part under test. The self-calibration, or "absolute test", is typically done by making three interferometric measurements, an initial measurement and then two more with the part under test shifted laterally slightly in orthogonal directions to obtain data sheared between reference and test part. This procedure allows one to recover the topography of both the reference and the test part.

A similar scheme can be used for profilometry with the advantage that much higher spatial resolution and comparable height resolution can be obtained while sacrificing speed of measurement. We apply the method to what we call "swing arm profilometry" but the method is more widely applicable, and some parts of the method bear resemblance to reversal methods of spindle metrology. In addition, the method is applicable to cylindrical geometries such as X-ray and synchrotron optics.

THE SWING ARM PROFILOMETER

In swing arm profilometry a sensor is attached to the end of an arm extending from a precise rotary air bearing as in Fig. 1 The sensor is aligned normal to the near spherical or cylindrical surface under test and passes through the center of the surface as the arm is swung from edge to edge. After a profile has been obtained the work piece is rotated about its center on a moderately accurate rotary table and another profile taken. This is repeated until profiles have been taken over a full revolution of the part under test as shown in Fig. 2. These profiles are then stitched together using the Maximum Likelihood method [1]. By taking a series of profiles over a full 360° we effectively have enough data to separate the errors in the part under test (the "measurand") from the odd errors in the swing arm bearing. The reversal produced by the full revolution of the part averages out all odd errors in the swing arm bearing.

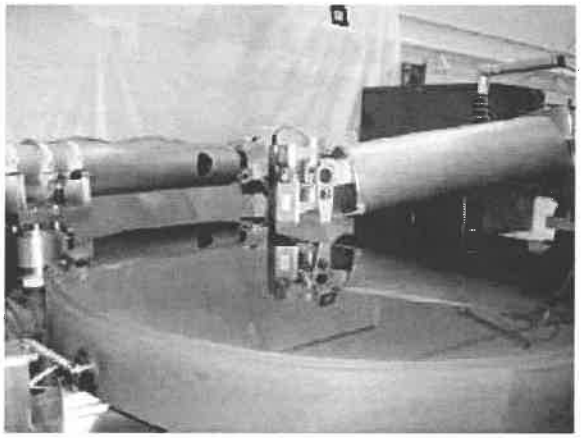

FIGURE 1. The swing arm extending in from the upper right with the sensor (blue) mounted on the end roughly over the center of the part. The air bearing is out of the picture to the right.

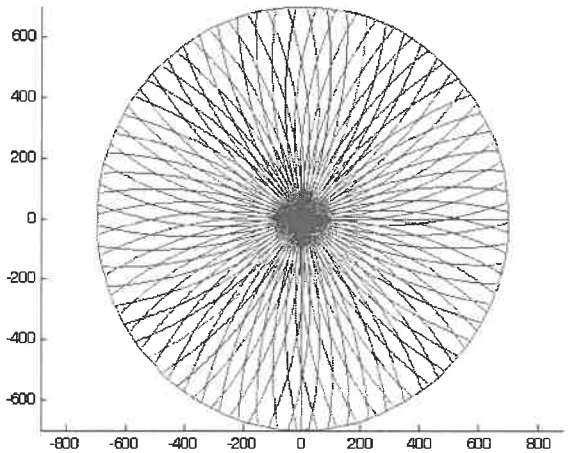

FIGURE 2. Pattern of 64 scans across the part. Scans cross each other 11 times per scan.

MAXIMUM LIKELIHOOD SOLUTION

We represent all the measured height data of a full set of scans by H_{ij} where i is the index of the scan number and j the data point index during a scan. We let H_{ij}^{a} be the part of the data that can be represented analytically. Then

$H_{ij} = H_{ij}^{a}$ + residuals = measurand + sensor + alignment terms + residuals, (1)

where the measurand = $\sum_{p=5}^{m} A_p Z_p(\rho_a, \theta_a + \varphi_{ai})$,

the sensor "surface" = $\sum_{q=5}^{n} B_q Z_q(\rho_b, \theta_b + \varphi_{bi})$,

alignment terms = $P_i Z_1 + T_{xi} Z_2 + T_{yi} Z_3 + F_i Z_4$ all with arguments $(\rho_a, \theta_a + \varphi_{ai})$ + residuals. The Z's stand for Zernike polynomials that are used to describe the heights on the circular measurand since they are orthonormal over a unit circle. The sensor describes a surface in the sense that it samples the entire circular measurand in the course of the scans where we can think of the sensor moving between scans rather than the measurand moving. The four alignment terms are piston, two tilts and power that adjust for rigid body motion between the sensor and measurand for each profile since the table under the measurand need not be very precise.

Notice that the Zernike terms describing the individual surfaces do not include rigid body terms but that one set of alignment terms is used to indicate their relative alignment. Power is included as an alignment term as this error is difficult to discern absolutely with the swing arm.
To solve for the A_p, B_q and alignment coefficients in a maximum likelihood sense we want

$$\sum_{i=1}^{u} \sum_{j=1}^{v} \left(H_{ij} - H_{ij}^{a}\right)^2 = \min \quad (2)$$

It is clear this is a large least squares problem to solve but there are ways of breaking the calculation down into manageable steps that lead to a straightforward solution. [2].

The result of this calculation is shown in Fig. 3 which is a comparison of the surface as measured with an interferometric holographic null test (top) and the swing arm profiler (lower) after removing low order Zernike terms that will be removed in final use by actuators.

REMOVAL OF EVEN BEARING ERROR

Assuming the swing arm air bearing errors are repeatable (they appear to be to the nanoradian level) it is clear that the odd errors in the bearing will cancel when the part under test is rotated 180° and scanned a second time as is the case in our scan pattern. When the two scan readings at 0 and 180° are added together the result is an even function of the bearing, or scan, angle

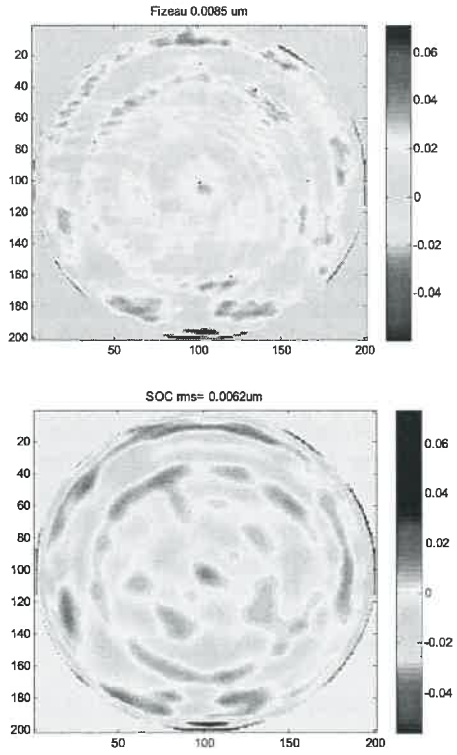

FIGURE 3. Comparison of interferometric 8.5 nm rms (top) with swing arm profilometer 6.2 nm rms results after the removal of low order Zernike terms

plus the contour of the part under test. The odd bearing errors cancel due to reversal. In our early use of the swing arm, the even bearing errors were calibrated by full aperture interferometric testing of the part. We found the even and odd bearing errors were of similar magnitude.

Recently, we added a second sensor to the swing arm that follows the same arc as the first but is displaced in angle by 3.55262° of the scan angle across the part under test. In this way, both sensors are subject to the common mode errors in the swing arm bearing but are sensing the surface at different positions along the arc. The first sensor reading, $R_1(\theta)$, is the difference between the first sensor tip, $T_1(\theta)$, and, $M(\theta)$, the mirror surface, while $R_2(\theta) = T_2(\theta+\varphi) + M(\theta)$, where φ is the angular separation of the tips. Since the two sensors are supported by the same bearing, T_2 at $(\theta+\varphi)$ is the same height as T_1 was at (θ) except for a constant and bearing errors because T_2 records the mirror surface at θ. Then the difference in sensor readings is

$\Delta R = R_2 - R_1 = T_2(\theta+\varphi) - T_1(\theta) = T(\theta+\varphi) - T(\theta)$,

where the subscript is dropped on T because the constant offset can be absorbed in ΔR.

If we describe the profile that the end of the tip traces along the arc at the end of the swing arm as the Fourier series

$$T(\theta) = \sum_j a_j \cos(j\theta) + b_j \sin(j\theta) \quad (3)$$

then it is not hard to show that

$$T(\theta + \varphi) = \sum_j a_j' \cos(j\theta) + b_j' \sin(j\theta) \quad (4)$$

where

$$a_j' = a_j \cos(j\theta) + b_j \sin(j\theta)$$

and (5)

$$b_j' = b_j \cos(j\theta) - a_j \sin(j\theta)$$

Substituting we have

$$T(\theta + \varphi) - T(\theta) = \sum_j (a_j' - a_j)\cos(j\theta) + (b_j' - b_j)\sin(j\theta) = \sum_j \Delta a_j \cos(j\theta) + \Delta b_j \sin(j\theta) \quad (6)$$

Using (5) and (6) we find

$$a_j = -0.5\left[\Delta a_j + \left(\frac{\Delta b_j \sin(j\theta)}{1-\cos(j\theta)}\right)\right]$$

$$b_j = -0.5\left[\Delta b_j - \left(\frac{\Delta a_j \sin(j\theta)}{1-\cos(j\theta)}\right)\right] \quad (7)$$

giving the even and odd Fourier coefficients describing the vertical motion of the end of the sensor tip. Then from the definition of R we can find the Fourier coefficients of the profile of the surface itself [4].

SWING ARM FOR CYLINDRICAL SHAPES

Because the swing arm profilometer worked so well for near spherical optics we decided to see if the concept would work for cylindrical shaped objects such as calendar rolls and X-ray optics that are near cylindrical shapes.

X-ray optics

There is a planned X-ray space observatory called IXO that is undergoing study for the means of manufacturing the mirror segments that to first order are sections of cones. The cones are then cut into segments subtending 15 30° angles about the cone axis [5].

One proposal for making the X-ray mirror segments is to slump thin glass sheets over convex molds or mandrels. It is the mandrels that need to be measured during their manufacture. Since cross sections of the mandrels are arcs of circles an indicator on a radius bar would be one way of profiling but the radius changes from one end of the mandrel to the other. Further, the larger problem is that profiling in a plane perpendicular to the cone axis precludes having the scan traces cross each other, an essential part of stitching the profiles together into a surface.

The swing arm geometry we suggest would use a radius rod roughly twice the radius of the mandrel cross section. This clearly will not match the mandrel sag at the edges of the mandrel. However, by rotating the swing arm bearing axis about an axis perpendicular to the cone axis, the projection of the circular arc becomes elliptical and the prolate end of the ellipse will fit the mandrel radius given the correct rotation of the swing arm bearing as shown in Fig. 4

If now the mandrel is moved into the page after each scan of the arm, and the angle the bearing axis is rotated is mirrored about the cross section of the mandrel, the scans produce a cross hatched pattern along the axis of the mandrel as shown in Fig. 5.

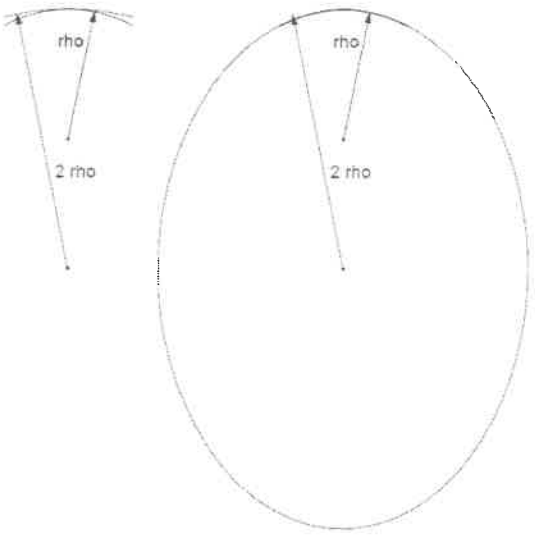

FIGURE 4. Sag difference between swing arm probe and mandrel cross section when arm is longer than mandrel radius (left), and the match between sags when the swing arm bearing axis is rotated to make the projection elliptical.

Since the IXO telescope will be made up of nests of similarly shaped mirrors, each with a slightly different radius, the scans can be matched to the different mandrels by simply rotating the bearing axis slightly. Thus one set of tooling can measure the roughly 240 mandrels in any one of the three major rings of mirrors. The maximum misfit between any of the 240 mandrels and the swing arm probe is slightly

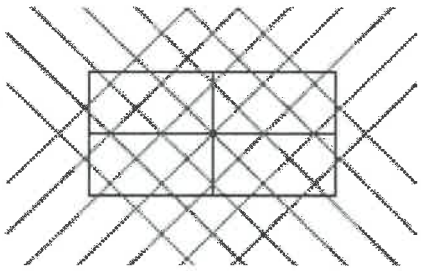

FIGURE 5. Scan pattern across an X-ray mandrel using a swing arm radius rod.

less than 1 mm. Thus the dynamic range of the sensor does not have to be more than 1 mm and the scan can be made with only a single precise rotary bearing motion. As in the case of the use of the swing arm for near spherical optics, the table on which the part under test sits does not have to be very precise.

Error Sources for Cylindrical Surfaces

With near spherical optics the sensor remains nearly normal to the surface being measured (the "measurand"). We use a single mode fiber interferometer as a sensor where the interference is between the fiber tip and the measurand. The only light reflected back into the fiber tip is that striking the surface at normal incidence and thus the distance measured is tip to surface along the normal to the surface.

In the swing arm geometry for the X-ray optics the probe tip is mounted parallel to the swing arm pointing through the swing arm bearing. There will only be one point in the scan where the normal to the measurand is parallel to the probe. At the corners of the mandrels the difference between the normal to the measurand and the probe can be as much as 11°. This means that the point on the surface being measured will shift laterally by as much as 200 μm over the 1 mm range and depends linearly on the separation between the probe tip and the surface. This correction will have to be applied to each point measured when the precision in the measurement must be at the nm level. The correction is analogous to correcting for a touch probe tip ball radius but in this case the radius of the ball is a function of the distance being measured.

CONCLUSION

We have shown how a profilometer that has only a single, rotary scanning axis coupled with two sensors with modest dynamic ranges but high resolution can be used to measure surfaces that are near spheres or cylinders in a self referenced manner to nm rms levels of precision. The method uses a pair of sensors to remove even order swing arm bearing errors as common mode errors and reversal to remove the odd order errors. The fiber interferometric sensor probe has high spatial resolution so that surface roughness can be measured along with overall figure error. The practical aspect of this work in addition to the precision is that the swing arm can be integrated into the polishing machine so that testing is performed *in situ*, avoiding the time and risk of moving the part being polished to a separate test apparatus.

REFERENCES

[1] Frieden, R., Probability, Statistical Optics and Data Testing, (Springer Verlag, 1983).

[2] Su, P., Burge, J. H. and Parks, R. E., "Appli cation of maximum likelihood reconstruction of subaperture data for measurement of large flat mirrors", **Appl. Optics, 49**, 21-31 (2010.

[3] Su, P., Oh, C, J., Parks, R. E. and Burge, J. H. "Swing Arm Optical CMM" Proc. ASPE Spring Topical Meeting, 2009.

[4] The derivation follows R. E. Parks, "Removal of test optics errors", **Proc. SPIE, 153**, 56-63 (1978).

[5] Zhang, W. W., Content, D. A., Lehan, J. P., Petre, R. and Saha, T. T., **Proc. SPIE 5900,** 59000V (2005).

ADVANCED 3D METROLOGY TO ENHANCE MANUFACTURING OF PRECISION COMPONENTS

Erik Novak, Joanna Schmit, Florin Munteanu
Veeco Instruments
Tucson, AZ, USA

INTRODUCTION

The past several years have seen a dramatic increase in the role of three-dimensional metrology in arenas traditionally served by other metrology techniques. 3D ISO standards are being finalized describing both the various metrology techniques that provide such information as well as key analyses enabled by the increased information content of a 3D surface map. New hardware and software capabilities are being introduced to further facilitate a transition to 3D techniques in a variety of precision manufacturing situations.

White-light interferometric (WLI) optical profilers provide rapid, accurate, and reproducible three-dimensional metrology for a wide variety of research and industrial applications. While hardware has steadily advanced, allowing greater automation capabilities, lower noise, and faster measurement times, the greatest advancements in system capability are coming from advanced software and processing techniques. Extracting more information, combining different types of information, and simultaneously working with large numbers of measurements in an iterative fashion are enabling WLI systems to serve applications which were impossible to consider a few years ago. This paper will explore some of the combinations of hardware and software used to solve different industrial problems through customization of the system for those types of applications.

ADVANCED SIGNAL PROCESSING FOR HIGH-ASPECT RATIO METROLOGY

White-light interferometry is a mature, powerful technology for three-dimensional surface measurements. The technique is area-based, so that a large field of view can be measured at once and does not lose any vertical resolution as magnification or field of view are changed. Vertical resolution of 0.01nm and lateral resolution of 0.4µm can be achieved with measurement times of less than five seconds. Systems come in a variety of configurations, and production units even self-calibrate so that vertical accuracy is assured. With those advantages, there is a continual desire to extend the capabilities of the instruments into areas currently poorly served by three-dimensional measurement techniques.

One such area is the measurement of very high-aspect ratio structures, particularly through silicon vias (TSVs). As TSV implementation moves from CCD arrays with structures 50 µm wide or larger, to logic chips with structures between 1 and 5 µm wide, accurate measurement of the width and depth of the features has become problematic. Aspect ratios of these structures range from 1:1 to 15:1.

A standard white-light interferometric optical profiler, does an excellent job of measuring features greater than 5 µm width with capability of aspect ratios of 4:1 for the narrowest features and up to 100:1 for features of 50 µm or wider. However, for narrower features multiple issues arise, including shadowing from off-axis optical elements and illumination and inability to penetrate to the bottom of narrow, deep structures. These issues may be solved with laser-alignment of components and design of custom microscope objectives with structured illumination to penetrate the vias.

However, a more difficult problem arises from diffraction effects at the boundaries of narrow structures. Figure 1 below shows the signal through focus for a single line of the CCD image. The solid line denotes the location of the actual surface with respect to the scan. The ellipses show that even where there is no substrate, diffraction causes the interference signal to extend into the void, creating a false signal. With standard analyses, these 'ghost fringes' would create measurement errors. Similarly, at the bottom of the trench, signal extends to the left and right of the actual structure.

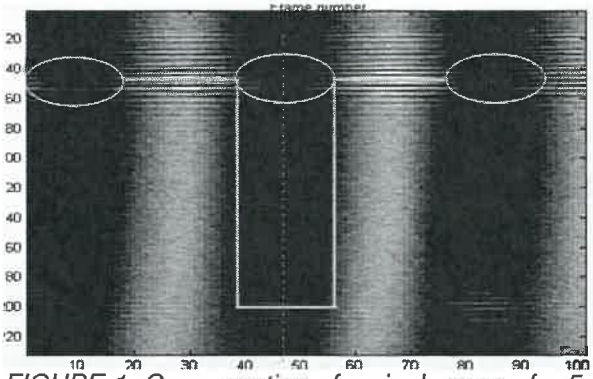

FIGURE 1. Cross section of a single scan of a 5 µm wide, 55 µm deep via. The solid line denotes the approximate surface location and the circles the spurious fringes from diffraction from the substrate.

To avoid adverse effects from this spurious signal, advance processing techniques must be used. One must consider the phase of the signal, its gradient, the localization of best contrast fringes, the modulation strength, and the effective wavelength as perceived by the instrument to precisely determine the true boundary. By combining all of this information in an intelligent manner, system capability can be extended to features below 1.5um in width and aspect ratios of 15:1 even on narrow features. Figure 2 below shows measurement of a 5 µm wide, 55 µm deep via. Results were verified by looking at a cross-section and were accurate to within 0.1 µm. You can see the edges are sharp, despite the presence of the erroneous fringes at the top in the scan.

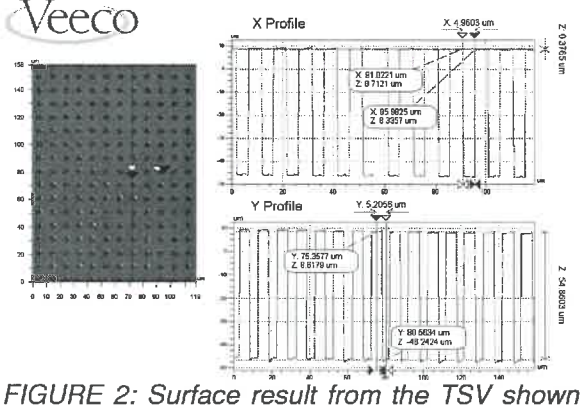

FIGURE 2: Surface result from the TSV shown in Figure 1 after proper signal processing. Features are sharp, as expected, and the height measures properly to within 100nm.

COMBINATORIAL DATA PROCESSING FOR QUANTIFYING SMALL STEEP FEATURES

Another area where advanced signal processing enables new capabilities is in the measurement of small features for light emitting diodes (LED's). Patterned sapphire substrates (PSS) are used by LED manufacturers to enhance efficiency. The features, however, are very small and steep on an optical scale, typically only 1-2 microns wide and 1-2 microns tall, with pitch between 3 and 5 microns. Small deviations in height can lead to a wavelength shift or drop in efficiency, while deviations of just a few tens of nm can lead to actual shorts in the final LED. Manufacturers of course wish to find such defects before depositing the epitaxial layer, which ties up expensive equipment and takes many hours of processing. The most critical parameters are width, height, and pitch of the regions.

Again, standard signal processing such as is used by most white light interferometers does not produce acceptable results. The signal from the features is quite noisy, distorted by diffraction and other optical effects. Figure 3 (top) shows a standard measurement of a substrate, where the features appear highly irregular and the tops of the bumps are not smooth.

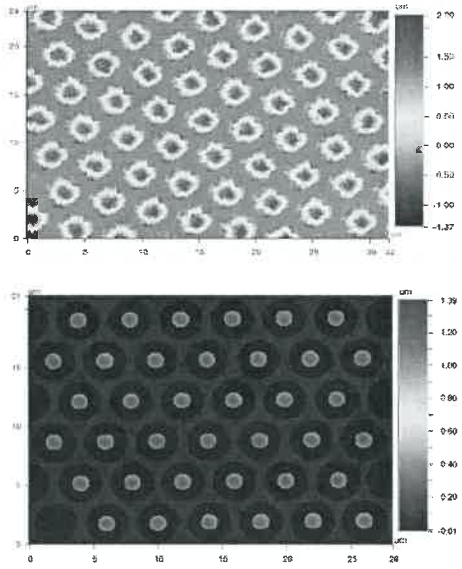

FIGURE 3. Top: PSS substrate result using standard signal processing. Bottom: result after combining multiple signals. Features are the proper height, shape, and results are repeatable to 5nm 3 sigma.

By combining contrast, phase, and coherence envelope information, however, these features may be accurately measured. The lowest signal regions are removed from consideration, the signal is corrected for the local slopes, and

phase information, which is the most accurate, is used to determine the final surface. These enhancements, combined with continuous system calibration, provide 3 sigma standard deviations of height, width, and pitch of less than 5nm even over a 5 day measurement run.

ENHANCED LATERAL RESOLUTION BY COMBINING MULTIPLE MEASUREMENTS

Signal processing of single images provides a powerful extension of white light interferometric capabilities. However, even greater flexibility can be achieved by using the ever increasing processing power of today's computers to combine multiple images. With new 64 bit processors and software, programs can access far more system memory, allowing highly advanced calculations combining hundreds or even thousands of measurements to produce data unachievable just a few years ago.

One area where this is readily apparent is in extending the lateral resolution of such systems beyond the conventional limits. Like all optical systems, white light interferometric microscopes are typically limited in lateral resolution by the diffraction limit of light. This roughly limits the minimum resolvable feature size to about 0.6 times the average wavelength, or about 400nm in a typical visible system.

However, by combining many measurements, along with employing sophisticated hardware and algorithms which account for the focus properties of the optics, resolution of such systems may be extended beyond the conventional limits.

Figure 4 shows a 150nm linewidth standard measured using conventional white light interferometry (left) and a combination of multiple measurements with the appropriate hardware and software processing (right). Expected features height is 15nm. Initially the features measure less than 7nm in height and can barely be distinguished. With the enhanced resolution measurement mode, however, feature height is greater than 12nm and the two lines are clearly resolved. For these measurements the Rayleigh diffraction limit of the system was 450nm. Thus, this measurement technique enhances lateral resolution by approximately a factor of three. Total measurement time remains under one minute.

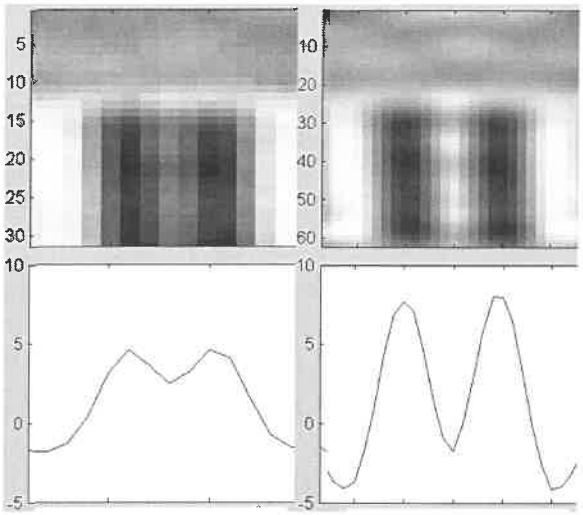

FIGURE 4. Contour map (top) and cross section (bottom) of two, 150nm linewidth structures. Left image is the conventional measurement using white light interferometry. The right image is using an enhanced measurement mode which uses additional processing as well as multiple measurements to achieve much higher fidelity.

LARGE-AREA STITCHING FOR PRECISE MEASUREMENT OF LEAD ANGLE

Combining many separate measurements are not just useful for measuring the very small, however, but also for characterizing very large surfaces. A key need in precision manufacturing currently is a precision measurement of the angle of machining marks on cylindrical sealing shafts. Increasing emissions requirements, reliability expectations, and efficiency expectations are causing rapidly tightening tolerances on sealing surfaces.

The traditional method of measuring lead angle employs a weighted string, which walks right or left on a rotating shaft depending on the angle of the turning marks [1]. This method has insufficient repeatability and resolution for many modern processes, and in some cases is entirely unusable on smoother shafts currently in production. Three-dimensional metrology offers a solution, employing the Std surface parameter currently under standards voting by ISO.

However, in order to get the desired 0.005 degree or better angular resolution, many thousands of points must be obtained on a surface. In addition, to create a method which does not rely on precise mounting of the shaft with respect to the measuring instrument, one must be able to precisely determine the angle

the cylinder makes with respect to the system axis. Both simulations and practical measurements have shown that measurements of at least 4000x4000 points are needed. High enough lateral resolution must be maintained to perform calculations on individual grooves, and enough area must be measured to adequately represent the overall part.

Figure 5 below shows a single measurement region, where slight cylindricity is apparent as well as the features along the cylinder. For sufficient lead angle resolution on this surface, more than 100 measurements had to be combined, resulting in over 80 megabytes of information. The combined dataset from so many fields of view also had to undergo sophisticated processing to be generated due to artifacts created by real-world limitations: the cylinder is not perfectly shaped; the center axis of the cylinder not perfectly aligned with the rotation center; the cylinder is tilted and decentered with respect to the system. Iterative techniques which operate on individual measurements and then globally are employed.

Thus far capability has been proven on cylinders from 1.5 to 8 inches in diameter, with a variety of surface finishes and lead angles. Each measurement is optimized based on the surface under test, but all employ large amounts of data which could not be readily handled for production-line systems prior to the past several years.

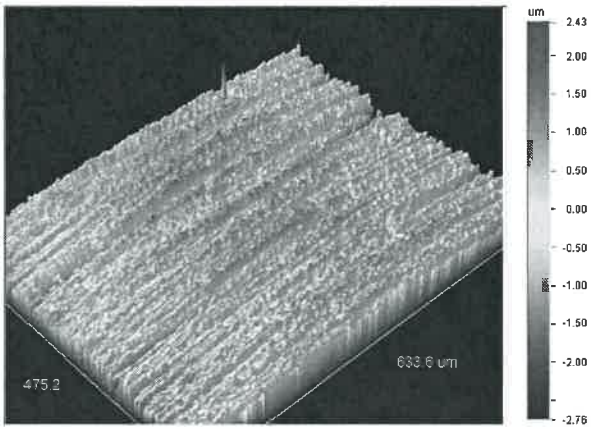

FIGURE 5. Three-dimensional image of a single field of view from a sealing shaft for which lead angle must be measured. Approximately 100 images are typically combined for accurate characterization.

CONCLUSIONS

Three-dimensional metrology employing white light interferometry has been around for more than 25 years. While the basic optical system and mechanics have advanced significantly over that time frame, the biggest advances currently are coming from enhanced signal processing. In some cases, additional information is being derived from the basic signal and a single measurement to extend capability for highly challenging applications. In other regimes, data from multiple measurements is intelligently combined to provide capability which is unachievable with the information content in a single scan. Such customization of results for advanced applications is increasingly common, and it is expected that further extensions of the technology into new applications spaces will be forthcoming.

REFERENCES

[1] Ray-Ming Lin et al, Enhanced Extraction and Efficiency of Blue Light Emitting Diodes Prepared Using Two-Step Etched Patterned Sapphire Substrates, Journal of The Electrochemical Society, 156 _11_ H874-H876 _2009_

[2] Rubber Manufacturers Association (1985), "Shaft finishing Techniques," RMA Handbook, OS

TEST METHODS FOR COORDINATED MOTION OF FIVE-AXIS MACHINING CENTERS

Shawn P. Moylan, Ronnie R. Fesperman, and M. Alkan Donmez
Manufacturing Engineering Laboratories
National Institute of Standards and Technology[1]
Gaithersburg, Maryland, USA

INTRODUCTION

Despite the increase in demand and usage of five-axis machine tools and considerable research in the area (*e.g.*, [1-3]) users and builders are not getting optimum performance from their machine tools because a robust set of measurements assessing the accuracy of coordinated complex motion involving multiple linear and rotary axes does not yet exist. Currently, a standard specifying certain kinematic tests for machining centers, concerning the accuracy of paths described by the simultaneous movement of three or more numerically controlled linear and/or rotary axes is in draft status [4].

This draft standard proposes four tests. Two tests are intended to check the accuracy of the circular trajectories when the motion of two linear axes is synchronized with the rotation of one rotary axis. The other two tests check the accuracy of the trajectories when three linear axes and two rotary axes are controlled simultaneously. Of these four tests, three offer alternative methods of performing the tests. This paper presents the results of the tests we carried out to compare these alternative methods applied on a five-axis machine tool in our shops.

DESCRIPTION OF THE MACHINE

The machine used for this study is configured with a tilting rotary table. The machine has a non-orthogonal tilting B'-axis, inclined from the Y-axis by 45° (see Fig. 1).

THE EXPERIMENTS

The draft standard proposes tests for various structural configurations of five-axis machines. These tests involve creating a tool path to keep a constant positional relationship between the tool point and the workpiece, either at the same nominal position or at a constant radius from a nominal workpiece position. Therefore a fixed set of linear displacement sensors or alternatively a telescoping ballbar can measure the deviations from an ideal tool path in three orthogonal directions in the workpiece coordinate system (WCS). To maintain the constant positional relationship, the rotary axis motion is commanded and the motions of the linear axes are automatically coordinated using the machine's tool center point (TCP) control function. The difference between the maximum and minimum deviations recorded for each measurement is reported to represent the accuracy of the coordinated motion.

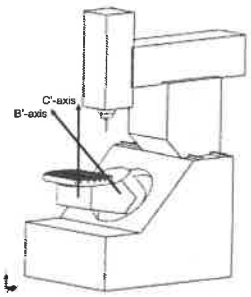

FIGURE 1. Schematic of the machine used in the current study with rotary axes' directions.

Descriptions of the measurements

Test 1 checks coordinated motion of the tilting (B') axis with the three linear axes (45° orientation of B'-axis requires the coordination of three linear axes). A test sphere mounted in the spindle should be positioned a distance *R* away from the rotary axis average line. The rotary axis is rotated at 360 degrees/minute and the full travel of the axis is tested (or the maximum stroke allowed by possible interferences). Path deviations resulting from the coordinated motion are measured in three orthogonal directions in the WCS.

[1]Official contribution of the National Institute of Standards and Technology (NIST); not subject to copyright in the United States. The full descriptions of the procedures used in the paper require the identification of certain commercial products. The inclusion of such information should in no way be construed as indicating that such products are endorsed by NIST or are recommended by NIST or that they are necessarily the best materials, instruments, software or suppliers for the purposes described.

Instead of measuring in the WCS X-, Y-, and Z-directions as prescribed by the standard, we measured in the directions tangential, radial, and parallel to the motion generated by the rotary axis. This change allows a more direct comparison between alternatives and eases diagnosis of machine errors. For the current study, the three measurements were performed simultaneously using an R-test device [1] consisting of a three-sensor nest calibrated against a reference sphere.

An alternative method for this test is to generate a tool path that keeps a constant distance between the tool point and the workpiece point allowing measurement with a telescoping ballbar. With this alternative, the three measurements are carried out with the ballbar oriented in: a) the direction tangential to the rotation of the rotary axis under test, b) the direction radial to the rotary axis under test, and c) the direction parallel to the rotary axis under test. The table mounted sphere should be located a distance R from the rotary axis under test. The radius, r, of the path of the spindle mounted sphere should be a) $r = \sqrt{L_B^2 + R^2}$, b) $r = L_B + R$, and c) $r = R$ where L_B is the nominal length of the telescoping ballbar (100 mm in the current case). All other test parameters are the same as those previously mentioned.

The other tests are designed similarly to those already described above. Test 2 checks coordinated motion with the rotary table (C'-axis). This test also has an alternative using the telescoping ballbar. The only notable difference for this test is that because our rotary table has infinite travel, the test was performed over 360° with an additional 10° at the beginning and end of each move for lead in and lead out. Test 3 checks coordinated motion of all five axes. Again there are three measurements. They are taken as a) tangential, b) radial, and c) parallel to the rotation of the rotary table (C'-axis). For this test the rotary table is directed to move from 0° to 360° while the tilting axis is directed to move from 0° to 90° and from 90° to 0°. This five-axis test also has a ballbar alternative.

Analyzing and reporting data

It is important to note that a best-fit circle is not removed from the recorded data. This differs from circular contouring tests (tests that examine coordinated motion of two linear axes) where a best-fit circle is removed in order to remove effects of setup error. When coordinated motion involves at least one rotary axis removing a best-fit circle is inappropriate because, while effects of setup error will be removed, it will also mask errors associated with the rotary axes (location errors of the axis average line with respect to the linear axes in the machine coordinate system).

Setup

Since a best-fit circle will not be removed from the data, the operator must take special care to minimize any error in the measurement setups. Specifically, the operator should ensure the test sphere is properly mounted in the spindle. Firstly, the sphere center must be aligned to the spindle axis average line. Secondly, the distance from the spindle gage line to the center of the sphere must be accurately determined (likely with a tool setting station) and input into the controller as the "tool height." These two aspects of the setup are of primary importance because the TCP function of the controller positions the center of the tool of a known length.

A simple example can illustrate the sensitivity of these tests to an improper setup. Measurement a) of test 2 is the most easily visualized. For the sake of example, the test is setup with the test sphere misaligned to the spindle average line by 10 μm in the Y-direction. As the axes move throughout the test the WCS rotates with the rotary axis, but the tool coordinate system does not. The effect of this is a perceived deviation in motion that is double the initial setup error (see Fig. 2). This sensitivity can be compounded in the case of the ballbar test if the common procedure of using the tool mount to set the table-mounted sphere is followed.

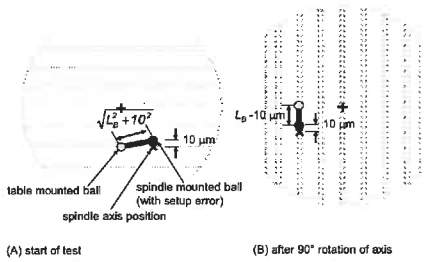

FIGURE 2. Schematic demonstrating the effect of setup error on Test 2 measurement a).

RESULTS

Results of all of the tests and measurements performed are shown in Table 1. Plots of the data for several of the measurements are shown

in Figs. 3 through 5. These plots demonstrate that the data from the two alternatives do resemble each other. The standard uncertainty in the measurements—a function of the linear displacement sensor and error in the setup—is approximately 0.9 μm for the R-test measurements and 0.8 μm for the ballbar measurements. As such, the expanded uncertainty for the results shown in Table 1 is 3.7 μm for the R-test measurements and 3.2 μm for the ballbar measurements.

In addition to the experimental results, the tests were evaluated using a computer model. The model incorporates the nominal kinematics of the machine tool as well as simulated kinematic errors. The trajectories of the spindle-mounted sphere and the table-mounted component were input into the model and their actual paths were output. The model was run with only one error present at a time, allowing the measurements' sensitivities to individual errors to be evaluated. Magnitudes of 50 μrad for axis orientation errors (squareness of Y rotated about the Z-axis, COY; squareness of Z rotated about the X- and Y-axes, AOZ and BOZ; mis-orientation of the B' around the X-axis, AOB; mis-orientation of the B' around the modified Z-axis, COB; and squareness of the C' around the X- and Y-axes, AOC and BOC) and 10 μm for axis location errors of the rotary axes (offset of the B' in the X- and modified Z-directions, XOB and ZOB; and offset of the C' from the B'-axis in the X- and Y-directions, XOC and YOC) were used. The results are shown in Table 2.

TABLE 1. Range in deviations (in μm) observed in each measurement. "Int." indicates that the measurement could not be completed because of interference problems.

	Measurement	R-test	Ballbar
Test 1	a) Tangential	26.1	21.2
	b) Radial	42.2	Int.
	c) Parallel	14.9	13.7
Test 2	a) Tangential	30.4	36.8
	b) Radial	35.1	43.0
	c) Parallel	3.4	4.4
Test 3	a) Tangential	46.2	Int.
	b) Radial	40.0	Int.
	c) Parallel	17.3	21.1

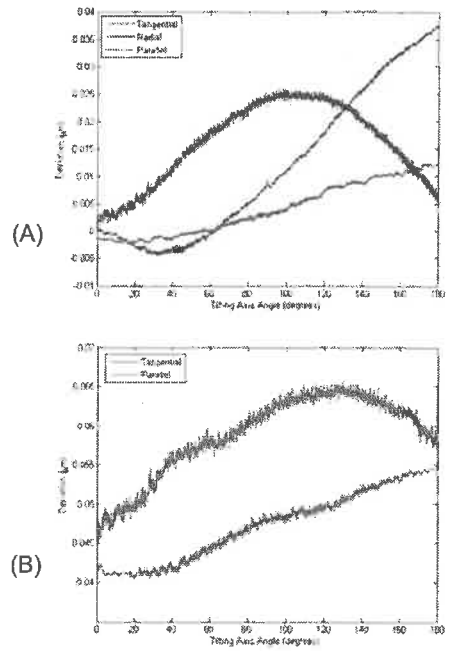

FIGURE 3. Deviations recorded during Test 1 using (A) the R-test and (B) the ballbar. R-test measurements were recorded simultaneously while ballbar measurements in series.

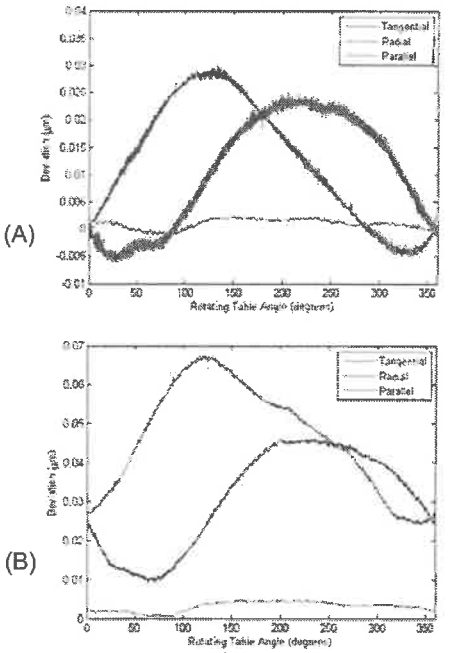

FIGURE 4. Deviations recorded during Test 2 using (A) the R-test and (B) the ballbar. R-test measurements were recorded simultaneously while ballbar measurements in series.

TABLE 2. Results of computer model evaluations of tests. Ranges in deviation are reported in μm. Error magnitudes are in μrad for the orientation errors and in μm for the location errors. R = 125 mm

Error	Magnitude	Test 1						Test 2						Test 3					
		Meas. a)		Meas. b)		Meas. c)		Meas. a)		Meas. B)		Meas. c)		Meas. a)		Meas. b)		Meas. c)	
		R-test	ballbar	R-test	ballbar	R-test	ballbar	R-test	ballbar	R-test	ballbar	R-test	ballbar	R-test	ballbar	R-test	ballbar	R-test	ballbar
COY	50	7	6.3	4	3.2	0	0	6.3	8	6.3	11	0	0	6.5	7.8	5.8	10.4	5.7	4.9
AOZ	50	2.9	5	5	4.4	4.4	4.4	0	0	0	0	0	0	4.2	5.8	4.0	7.2	2.5	2.2
BOZ	50	7	9.3	4.1	3.2	0	0	0	0	0	0	0	0	2.8	3.5	3.4	6.2	4.7	4.9
AOB	50	4.4	4.4	8.8	8.8	8.8	8.8	0	0	0	0	12.5	12.5	4.4	4.4	0	0	11.1	11.1
COB	50	8.8	8.8	4.4	4.4	4.4	4.4	0	0	0	0	8.8	8.8	4.4	4.4	0	0	11.1	11.1
XOB	10	20	20	10	10	0	0	0	0	0	0	0	0	17.7	17.7	16.5	16.5	7.1	7.1
ZOB	10	10	10	20	20	0	0	0	0	0	0	0	0	17.7	17.7	16.5	16.5	7.1	7.1
AOC	50	0	0	0	0	0	0	0	0	0	0	12.5	12.5	0	0	0	0	12.5	12.5
BOC	50	0	0	0	0	0	0	0	0	0	0	12.5	12.5	0	0	0	0	12.5	12.5
XOC	10	0	0	0	0	0	0	20	20	20	20	0	0	20	20	20	20	0	0
YOC	10	0	0	0	0	0	0	20	20	20	20	0	0	20	20	20	20	0	0

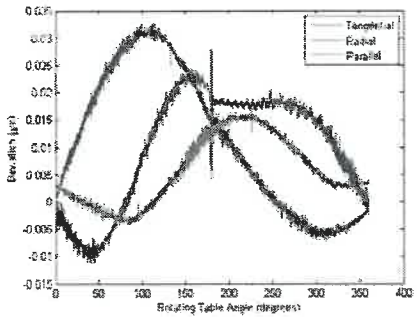

FIGURE 5. Deviations recorded during Test 3 using the R-test. Measurements were recorded simultaneously.

CONCLUSIONS

The data presented in the previous section lead to two conclusions. The majority of the deviation observed while testing our machine (see Table 1 and Figs. 3 – 5) is the result of location errors of the axes of rotation (i.e. XOB, ZOB, XOC, and YOC) with a small amount of deviation resulting from mis-orientation of the B-axis (AOB) and possibly squareness of the Y-axis (COY). More importantly, the R-tests and the ballbar tests, as currently described in the draft standard and as carried out in this study, will lead to differing results when there are orientation errors present in the linear axes (i.e. COY, AOZ, and BOZ).

In order for the ballbar measurements to be a true alternative to the R-test measurements and for the tests to better accommodate inclined tilting axes, we recommend users follow certain practices. In the R-test measurements, the three orthogonal directions in which the deviations are measured/reported should be specified with respect to the rotary axis under test (radial, tangential, and axial). This allows mis-orientations of the rotary axis to be better observed and diagnosed. With the five-axis test, the three orthogonal directions should be with respect to the rotary table. For the ballbar alternative to provide similar results to the R-test regarding errors in the linear axes, those axes must travel the same distances in both alternatives. To accomplish this, the spindle mounted sphere of the ballbar should be positioned a distance R from the rotary axis. This will result in an offset distance r between the axis average line of the rotary axis and the center of the table-mounted sphere of $r = R - L_B$ when the ballbar is radial to the rotary axis, $r = R$ when the ballbar is parallel to the rotary axis, and $r = \sqrt{R^2 + L_B^2}$ when the ballbar is tangential to the motion created by the rotary axis.

REFERENCES

[1] Weikert S, R-Test, a New Device for Accuracy Measurements on Five Axis Machine Tools. CIRP Annals. 2004; 53: 429-432.

[2] Tsutsumi M, Yumiza D, Utsumi K, and Sato R, Evaluation of Synchronous Motion in Five-Axis Machining Centers With a Tilting Rotary Table. Journal of Advanced Mechanical Design Systems and Manufacturing. 2007, 1, 24-35.

[3] Zargarbashi S, and Mayer J, Assessment of Machine Tool Trunnion Axis Motion Error, Using Magnetic Double Ball Bar. International Journal of Machine Tools and Manufacture. 2006, 46, 1823-1834.
[4] ISO/CD 10791-6;2009, Machine Tools— Test Conditions For Machining Centres— Part 6: Accuracy of Speeds and Interpolations.

UNCERTAINTY OF ANGULAR MOTION CORRECTION USING THE EXTENDED ABBE PRINCIPLE

Vincent Lee[1], John Ziegert[1], W. Tyler Estler[2], Steven D. Phillips[2], Daniel Sawyer[2], and Bruce Borchardt[2]

[1]Mechanical Engineering Dept.
Clemson University
Clemson, SC, USA

[2]Large Scale Metrology Division
National Institute of Standards and Technology
Gaithersburg, MD, USA

INTRODUCTION

Ernst Abbe states in his Abbe Principle that "*If errors in parallax are to be avoided, the measuring system must be placed coaxially with the axis along which the displacement is to be measured on the workpiece.*" In situations where this principle cannot be adhered to, the Extended Abbe principle may be used to correct for "Abbe" errors that occur due to angular motions of the moving body [1-2]. The Extended Abbe method utilizes multiple, parallel displacement measurements a known distance apart, at known distances from the target point of interest to correct for the effects of the angular motion. During the design of a particular machine used for measuring ball bars, dubbed the one dimensional measuring machine (1-DMM), the Extended Abbe principle was applied [3]. This machine uses a single moving sled, which nominally moves linearly in one axis, and carries a point of interest (POI) that needs to be tracked with great precision. As the sled travels along the guide ways of the machine, the sled undergoes some yaw due to imperfections in the guide ways. As a result of this yaw displacement, coupled with the offset distance between the measurement line, and the measurement axis, measurement errors will occur. Adding an additional measurement axis that is parallel to the first axis, and arranging the POI to be co-planar with the measurement axes allows for the correction of these Abbe errors (FIGURE 1). [4]

While application of the extended Abbe Principal is straightforward and relatively widespread, for precision metrology instruments it is necessary to characterize the added measurement uncertainty that results. In applying this principle to the design of the 1-DMM, it was found that the uncertainty due to the Abbe correction is a strong function of the geometric arrangement of the point of interest (POI) and measurement axes. Also, under certain conditions there exists a unique arrangement which will minimize the uncertainty of the Abbe correction.

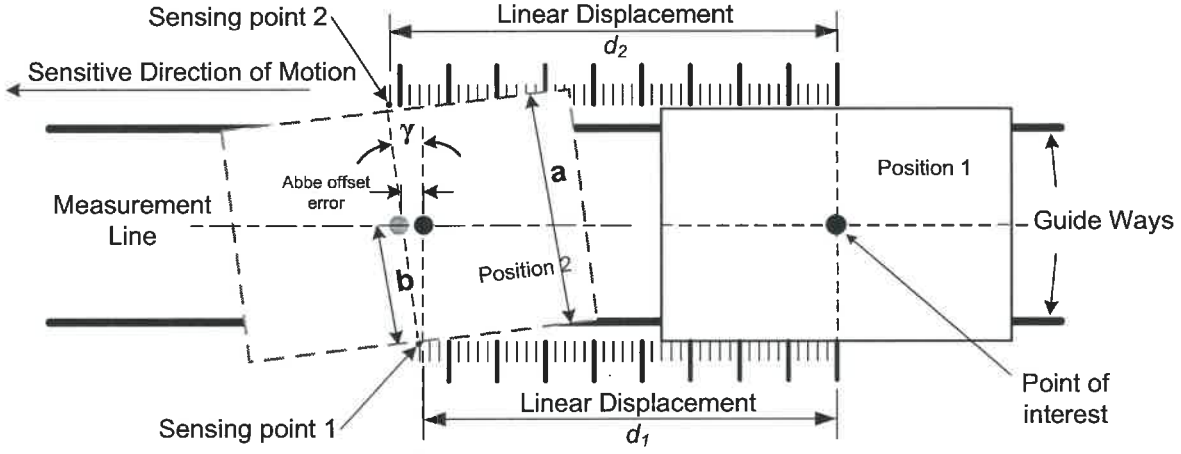

FIGURE 1. Angular displacement of sled induces error motions to the point of interest

APPLYING THE EXTENDED ABBE PRINCIPLE

The 1-DMM uses two parallel laser interferometers aligned in one plane, and located symmetrically either side of the measurement POI. Knowing the position of the POI, in relation to the two measurement scales allows for the estimation of the Abbe offset error, and a more accurate estimation of the actual displacement of the POI in the direction of motion. To perform this estimation, the amount of angular displacement γ is calculated using the following equation (Eq. 1.1)

$$\gamma = \sin^{-1}\left(\frac{d_2 - d_1}{a}\right) \approx \left(\frac{d_2 - d_1}{a}\right) \quad (1.1)$$

where: d_1 = displacement; sensor 1

d_2 = displacement; sensor 2

a =separation between sensor 1 & 2

Next the amount of Abbe offset error is given by the following equation (Eq. 1.2).

$$\Delta d \approx b\gamma \approx b\frac{(d_2 - d_1)}{a} \quad (1.2)$$

where: b location of POI

Now the total displacement of the POI in the sensitive direction of motion is given adding the error motion calculated using equations 1.1 and 1.2, to the displacement d_1.

$$D = d_1 + \Delta d \quad (1.3)$$

However, the correction, Δd, is only an estimate. At the highest levels it is necessary to know the uncertainty of that estimate. Referring to the preceding figure, the uncertainty of measuring the displacement of the sled, while using the extended Abbe principle, will depend on influences, such as:

- Uncertainty of the distance between the two measurement axes
- Uncertainty of the location of the measurement line/POI relative to the measurement axes
- Arrangement of the measurement axes relative to the POI
- Uncertainty of the displacement measurement system

MEASUREMENT UNCERTAINTIES

Determination of measurement uncertainties is well covered in the literature [5]. Considering planar motion in one dimension, as shown in FIGURE 1, the mathematical model for estimating the displacement of the POI, utilizing the extended Abbe offset principle, is given by equations 1.1 to 1.3. Pitch and roll motions of the axis are not corrected, and assumed to be an insignificant contribution to the measurement error in this case since they cause displacements of the POI orthogonal to the measurement axis. The measurement equation for estimating the displacement of the POI is given by:

$$D = d_1 + b\frac{(d_2 - d_1)}{a} \quad (1.4)$$

Sensitivity coefficients are calculated as follows:

$$\frac{\partial D}{\partial d_1} = 1 - \frac{b}{a} \quad (1.5)$$

$$\frac{\partial D}{\partial d_2} = \frac{b}{a} \quad (1.6)$$

$$\frac{\partial D}{\partial a} = -b\frac{(d_2 - d_1)}{a^2} \quad (1.7)$$

$$\frac{\partial D}{\partial b} = \frac{(d_2 - d_1)}{a} \quad (1.8)$$

Since two measurement systems are being used to estimate the motion of a single POI, the amount of correlation between the two displacement measurement sensors needs to be taken into account. An additional sensitivity coefficient for correlations between these two uncertainty contributors is needed.

$$2r\frac{\partial D}{\partial d_1}\frac{\partial D}{\partial d_2} = 2r\frac{b}{a}\left(1 - \frac{b}{a}\right) \quad (1.9)$$

where: r is the correlation coefficient

The combined standard measurement uncertainty for determining the displacement of the POI in FIGURE 1 is as follows:

$$u = \sqrt{\left(\frac{\partial D}{\partial d_1}\right)^2 u_{d_1}^2 + \left(\frac{\partial D}{\partial d_2}\right)^2 u_{d_2}^2 + \left(\frac{\partial D}{\partial a}\right)^2 u_a^2 + \left(\frac{\partial D}{\partial b}\right)^2 u_b^2 + \left(2r\frac{\partial D}{\partial d_1}\frac{\partial D}{\partial d_2}\right)^2 u_{d_1} u_{d_2}}$$
$$= \sqrt{\left(1-\frac{b}{a}\right)^2 u_{d_1}^2 + \frac{b^2}{a^2}u_{d_2}^2 + \frac{b^2(d_2-d_1)^2}{a^4}u_a^2 + \frac{(d_2-d_1)^2}{a^2}u_b^2 + \left(2r\frac{b}{a}\left(1-\frac{b}{a}\right)\right)^2 u_{d_1} u_{d_2}} \quad (1.10)$$

Equation 1.10 may be simplified by applying the following:

- Express ratio $\frac{b}{a}$ as α;
- Since $(d_1 \approx d_2)$, let $u_{d_1}^2 = u_{d_2}^2 = u_d^2$;
- Also, since $(d_1 \approx d_2)$, $(d_2 - d_1)^2 u_a^2 \approx (d_2 - d_1)^2 u_b^2 \approx 0$

The resulting combined standard uncertainty after these simplifications is:

$$u^2 = \left[(1-\alpha)^2 + \alpha^2 + 2r\alpha(1-\alpha)\right] u_{d_1}^2 \quad (1.11)$$

What remains is a function that is dependent on "α" and "*r*". For various correlation coefficients the normalized uncertainty for estimating the displacement of the POI is plotted in the following figure (FIGURE 2).

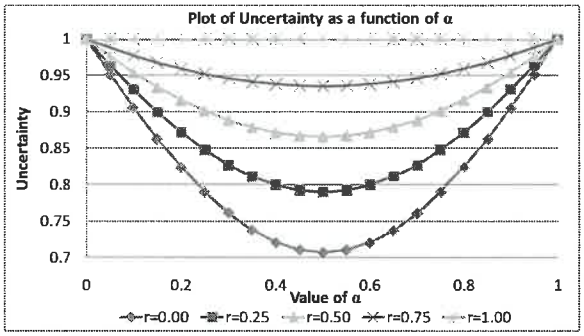

FIGURE 2.Variation of uncertainty due to Abbe offset as a function of α and r

As FIGURE 2 shows, the measurement uncertainty for displacement of the POI (shown in FIGURE 1) varies depending on its lateral location, "b"; relative to the measurement axis 1. However this is only true if the correlation coefficient between the two measurement axes is less than 1. In situations where the correlation coefficient is equal to 1, the uncertainty for estimating the displacement of the POI is constant. To obtain a better understanding of the characteristics of the displacement measurement system used on the 1-DMM, a few experiments were performed.

EXPERIMENTATION

The experiments performed consist of measuring the yaw of the sled of the 1DMM and calculating the correlation coefficient between the two measurement axes, and comparing the displacement estimate of the 1-DMM using the extended Abbe method with direct measurement of the POI displacement using a third laser interferometer.

Yaw measurements

Yaw measurements were performed by incrementally moving the sled along the length of the 1-DMM and recording the displacement of each measurement axis (FIGURE 3).

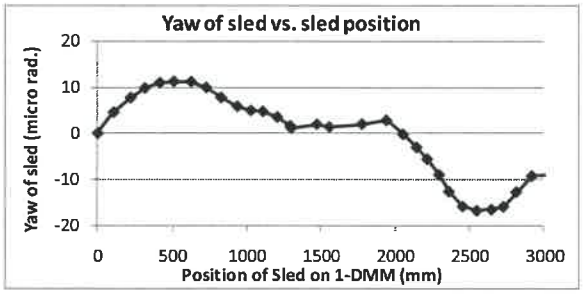

FIGURE 3. Yaw of sled versus position on 1-DMM.

Correlation Coefficients

During the yaw measurements, data for each axis was sampled at the rate of 20Hz for 20s at each measurement position to evaluate apparent signal noise in each of the measurement axes. Changes in the operating environment will induce changes to the refractive index of air and causes spurious readings from the interferometer. If both interferometers experience the same perturbations and display the same response/noise, they would be fully correlated with each other. Recording the amount of noise at various sections of the 1-DMM, and comparing the two interferometers against each other, allows us to estimate the correlation coefficient between the two displacement sensors (Figure 4).

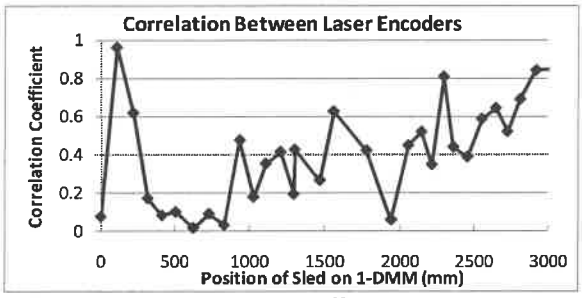

FIGURE 4. Correlation coefficient between laser interferometers.

Displacement errors of measurement line

To gauge the accuracy of the 1-DMM's displacement measurements system using the extended Abbe principle, a separate laser interferometer was used to directly measure the displacement of the sled at the POI. The difference between the displacement of the POI, as estimated by the 1DMM, and that measured by the secondary laser interferometer is shown in the following figure (FIGURE 5).

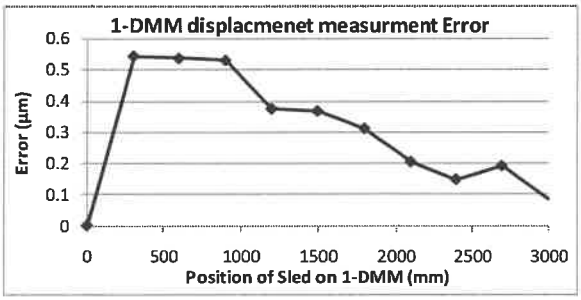

FIGURE 5. Displacement error, measured at the POI on 1-DMM

DISCUSSION OF RESULTS

From the data gathered, the correlation coefficient could be estimated, which is necessary to obtain an accurate estimate of the instrument's measurement uncertainty. Under the operating conditions at the time, it was found that the correlation coefficient ranged from 0.01 to 0.96; with an average of 0.4. For the purposes of estimating the displacement measurement uncertainty of the 1-DMM, a correlation coefficient of 0.4 will be assigned.

From the yaw measurements, the maximum yaw which the sled experiences was 16.8 µrad; a difference of 3.6 µm between the two measurement axes. Using this value and the following measurement conditions (TABLE 1), the estimated expanded measurement uncertainty (k=2) for yaw and displacement is 6.86 µrad and 0.146 µm respectively. Multiple experiments showed that the yaw at each location of the 1-DMM was repeatable.

TABLE 1. Displacement measurement conditions for 1-DMM

Property	Value
Room temperature	20±0.05°C
Room Relative Humidity	50%±1%
Room Air Pressure	101.3±0.5 kPa
Maximum Displacement	3.0 m
Component misalignment	± 0.25 mm
Correlation Coefficient	0.4

And lastly, a maximum difference of 0.55 µm was observed comparing the 1-DMM with a separate independently calibrated laser interferometer over a 3 m range.

CONCLUSION

By utilizing the extended Abbe principle, displacement measurement errors from an Abbe offset can be compensated to provide accurate displacement measurements. In situations where the primary and secondary measurement axes (measurement scales) are uncorrelated, the ideal placement of the measurement line is at the centerline between the two measurement axes, where b=a/2, referring to FIGURE 1. In multi-axis machines where the position of the POI relative to the measurement lines for each axis may change, the measurement uncertainty will also change significantly, unless the correlation coefficient between the two measurement axes used to perform the Abbe correction is quite high.

REFERENCES

[1] Bryan, J. B., 1979, "The Abbé Principle Revisited: An Updated Interpretation," Precision Engineering, Vol. 1(3) pp. 129-132.

[2] Slocum, A.H., 1992, "Precision Machine Design," Prentice-Hall, New Jersey

[3] Lee, V., Ziegert, J. C., Estler, T. W., 2010, "Design and Testing of a Machine for Calibration of Ball Bars Up to 3 Meters in Length," American Society of Precision Engineers, .

[4] Koning, R., Flugge, J., and Bosse, H., 2007, "A Method for the in Situ Determination of Abbé Errors and their Correction," Measurement Science and Technology, 2(18) pp. 476-481.

[5] International Organization for Standardization, 2008, "Guide to the Expression of Uncertainty in Measurement,"

RECORD RESOLUTION ABSOLUTE LENGTH METROLOGY OVER LARGE DISTANCES

Peter A. Roos[1], Randy R. Reibel[1], Trenton J. Berg[1], Brant M. Kaylor[1], Nathan J. Greenfield[1], Zeb W. Barber[2]
[1]Bridger Photonics, Inc.
Bozeman, MT, 59715, USA
[2]Spectrum Lab at Montana State University
Bozeman, MT, 59715, USA

INTRODUCTION

Two metrology technologies, frequency-domain optical coherence tomography (OCT) [1,2] and frequency-modulated continuous-wave (FMCW) laser detection and ranging (LADAR) [3], are very similar in operation, but exhibit different strengths. OCT is capable of performing metrology with very fine resolution, but only over very small measurement windows or depths of focus. It has found application primarily in the biomedical imaging industry, but is now beginning to find broader metrology applications. On the other hand FMCW LADAR can perform metrology over extremely large windows, but exhibits poorer resolution (though still very good by LADAR standards). It is typically used in military and space applications that require resolution better than 10 cm over kilometer-level range baselines.

At Bridger Photonics, Inc., we have developed a technology that combines the benefits of both OCT and FMCW LADAR. Our metrology system exhibits very fine resolution and precision (better than 20 nanometers precision demonstrated) over very large measurement windows (from <1 millimeter to >100 meters) for absolute length and thickness measurements.

The potential applications for this combination of capabilities range from precision dimensional metrology including gauge block and coordinate measuring machine calibration, surface topology and thickness measurements including precision optical component inspection, machine vision and 3D imaging, and even precision surveying, 3D mapping, and multi-kilometer target identification.

BACKGROUND AND THEORY

Our technology, as well as both frequency domain OCT and FMCW LADAR operate on the same fundamental principle, which is depicted schematically in Figure 1. The optical frequency of a laser swept or chirped linearly in time. One copy of the chirped laser light is transmitted to the target, as shown in the figure. The light returning from the target (called the "return" beam) is collected and interferometrically combined with a local reference copy of the chirped light (called the "reference" beam), which has not traveled to the target. The combined beam is directed onto a photodetector and an RF beat note results from the time delay between the two combined copies of the chirp at frequency $f_{beat} = \kappa\tau$, where κ is the chirp rate (often in MHz/μs), and τ is the time delay between the two chirps. With accurate knowledge of the chirp rate and the beat note frequency, f_{beat}, the time delay can be determined. From the time delay, the range to target is given simply by $R = \tau c / 2$, where c is the speed of light.

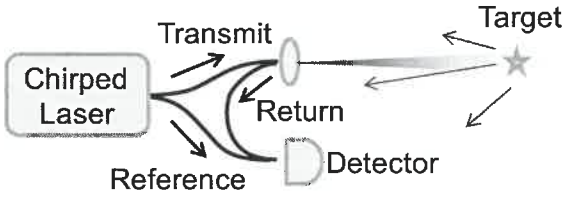

FIGURE 1. Simplified schematic of both frequency domain OCT and FMCW LADAR. The reference and return light are combined to generate an RF beat note measured by the detector. The frequency of the beat note indicates the target range.

The predicted resolution for such a length metrology system can be calculated. We use NIST's definition of resolution as "the smallest distance separation (along the scan axis) between two distinct objects that can be detected in a single return"[4]. For Fourier-transform-limited waveforms, the range

resolution can be expressed mathematically simply by $\Delta R = c/2B$, where B is the total information bandwidth of the chirp, which is the optical bandwidth covered for this case.[5] This equation makes clear the desire for larger optical bandwidths in order to achieve better resolutions. The range resolution is a useful parameter for comparing different metrology systems on equal footing because it does not depend on any details of the transceiver or target, such as transmitted power, target reflectivity, light collection aperture, or detector noise, etc.

The range precision (taken to be synonymous with repeatability here) is typically the parameter that is most interesting when determining the usefulness of a device in practice. Unfortunately, the precision depends on the signal-to-noise (SNR) ratio and, expressed as the standard deviation of a statistically significant number of range measurements of the same target. Mathematically, a lower limit for the range precision, expressed as the standard deviation, is given by the Cramér-Rao relation $\sigma \approx \Delta R/\sqrt{SNR}$.[4] The precision that a system can achieve can therefore be far better than its resolution. By averaging over multiple measurements the precision can be further improved as $1/\sqrt{N}$ for incoherent averaging and as $1/N$ for coherent averaging, where N is the number of measurements, and where the noise processes have been assumed stochastic.

In addition to the chirp bandwidth and SNR, the other parameter that critically affects performance for these systems is the chirp linearity, which is related to the laser coherence. The laser coherence (relative to linearity) determines the range window (or depth of focus) over which high-resolution measurements can be performed. This is where OCT differs from FMCW LADAR. OCT can offer very large bandwidths, which result in very fine resolutions (~10 microns) and precisions. However, the coherence of OCT sources is relatively poor, which results in millimeter-level measurement windows. On the other hand, FMCW LADAR can offer extremely high coherence, which results in very large measurement windows (>1 km). However, traditional FMCW LADAR bandwidths are limited, which results in very poor resolution (>1 cm) by OCT standards.

At Bridger Photonics, we have demonstrated linearization of extremely broadband frequency chirps to enable both fine resolution comparable to OCT and large measurement windows comparable to FMCW LADAR. The results of our linearization can be observed in Figure 2. The figure shows range profiles for the same target in optical fiber at a range of 51.3 meters. However, the red trace is the range profile when our linearization technique is not used, while the blue trace is the profile when our linearization is engaged. When our linearization is engaged the resolution of our system improves by more than four orders of magnitude from about 0.5 meters to a Fourier-transform-limited range peak of <50 microns full-width at half-maximum (Hanning filtered).

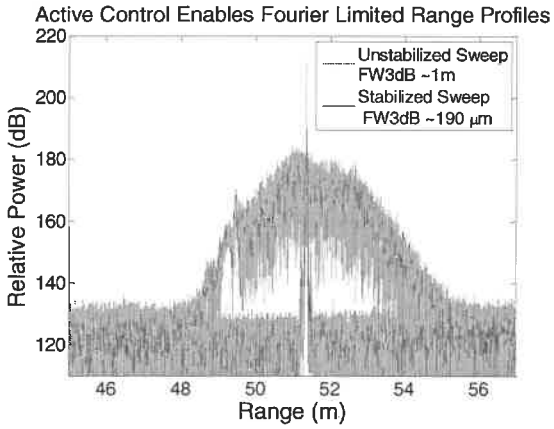

FIGURE 2. Setup used for measuring thickness of cover slip. λ/4 is a quarter-wave plate and PBS is a polarizing beam splitter. The combination of these two elements allows the reflections from the target to be separated from the transmitted beam to the target.

Many industrial metrology applications are interested in the precisions that we can achieve over stand-off distances far less than 50 meters. We therefore conducted several experiments to demonstrate the performance of this system at shorter stand-off distances.

EXPERIMENT AND RESULTS

For these demonstrations, we focused the transmit beam from our system onto the surface of a U.S. penny from a stand-off distance of 1 meter. We mechanically scanned the penny in both cross-range (lateral) dimensions and recorded the range peak center for each scan position. The range peak centers were found by Gaussian fits to the peaks. The resulting 3D image that we created is shown in Figure 3. The

topology of Lincoln's face is clearly evident in the image

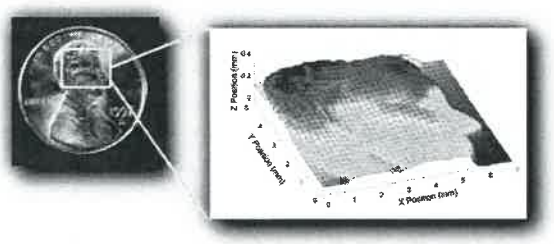

FIGURE 3. 3D image of Lincoln's face on a U.S. penny from a 1 meter stand-off distance.

For more quantitative measurements, we scanned across a thin (<1 mm), optically transparent sample from 17 cm stand-off. This sample allowed us to highlight our abilities to measure two surfaces simultaneously and to measure thickness. Figure 4 shows the scans across the front and back surfaces, with the mean positions of the surfaces subtracted out to emphasize the departures from flatness. We achieved measurement precision (repeatability) of 52 and 51 nanometers for the front and back surfaces, respectively, for repeated scans over 40 mm of the sample. From the figure, our system is easily capable of measuring the bow of the front surface and the bow and wedge on the back surface of the sample.

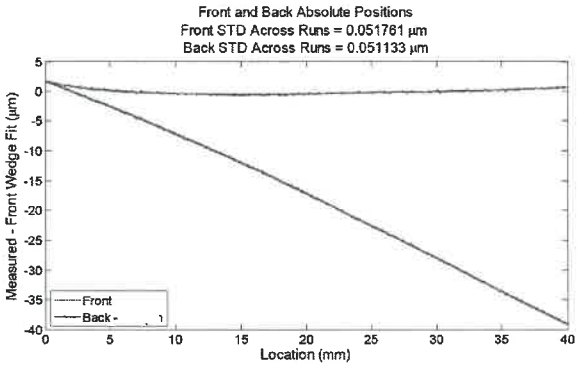

FIGURE 4. Position of the front and back surfaces across a 40 mm portion of the sample.

However, much of the measurement fluctuations were common mode to both the front and back surfaces. We were therefore able to measure the thickness more precisely by subtracting the front from the back position and doing this, we obtained 13 nm measurement precision on the thickness. Figure 5 shows a full 3D image generated for the thickness of the sample across a 30 mm x 30 mm sample area. Both the mean thickness and a linear wedge have been removed from the plot to enable observation of the nonlinear components of the sample thickness variation.

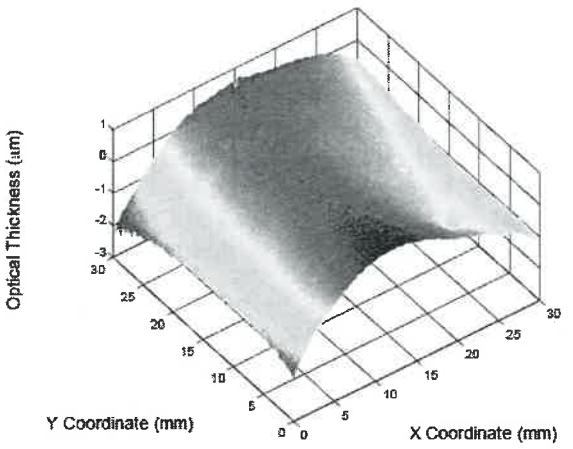

FIGURE 5. Surface plot of thickness measured across transparent sample. The precision across repeated lateral slices was 13 nm.

Although we did not stabilize the reference for our chirp rate for this work, we have done so for other measurements and demonstrated stability of better than 1 part in 10^6.

We are unaware of other techniques that can measure with such fine resolution and precision over such large measurement windows.

REFERENCES

[1] Bouma B, Tearney J, eds. Handbook of Optical Coherence Tomography (Marcel Dekker, New York, 2002).

[2] Leitgeb R, Hitzenberger C K, and Fercher A F, "Performance of fourier domain vs. time domain optical coherence tomography," Optics Express 11, 889-894 (2003).

[3] Stone W, Juberts M, Dagalakis N, Stone J, Gorman J. Performance Analysis of Next Generation LADAR for Manufacturing, Construction and Mobility. National Institute of Standards and Technology, NISTIR *7117*, 2004.

[4] Cheok G S (ed.), "Proceedings of the 2nd NIST LADAR Performance Evaluation Workshop," National Institute of Standards and Technology, NISTIR 7266, March 2005.

[5] Krause B, Gatt P, Embry C, and Buck J, in Laser Radar Technology and Applications XI, Kamerman G W and Turner M D, eds. (SPIE, 2006).

DIRECT DIAMOND TURNING OF ASPHERIC STEEL MOLDS WITH ULTRA PRECISE ACCURACY

Fritz Klocke, Olaf Dambon, Benjamin Bulla
Department of Process Technology
Fraunhofer Institute for Production Technology IPT
Aachen, Germany

INTRODUCTION

Ultra precise steel parts with optical surface qualities and complex shaped geometries are required for modern optics fabrication e.g. in injection molding of precision plastic optics.

Nowadays optical molds for injection molding are coated with a nickel-phosphor layer, in order to be able to machine the surface with single crystal diamond tools. Directly machining the steel parts would significantly decrease the total production time and costs of the mold, making the coating step unnecessary. Additionally, the life time of the mold is increased and therefore the single optic price is reduced. Steel tools have a higher scratch resistance and no risk of delamination. Therefore the potential and benefit of directly machining steel with monocrystalline diamond is exceptionally high.

Though diamond machining is conventionally limited to non ferrous, a few crystalline and plastic materials. The affinity between the carbon (diamond) and the iron (workpiece) leads to excessive tool wear in conventional machining of steel even at very small cutting distances.

The ultrasonic assisted technology enables the direct manufacturing of steel components with monocrystalline diamond tools. This technology has been investigated over years within the Fraunhofer IPT and has proven its potential. Surface roughness in the range of Ra = 5 nm are reached and the diamond wear is reduced by a factor 100 or higher for a single contact point [1].

In this publication the most recent investigations in ultrasonic assisted diamond machining of hardened steel at the Fraunhofer IPT will be presented. The results of aspherical steel molds (material: Stavax ESU, 53 HRC) directly cut with diamond tools will be introduced. Two representative aspherical geometries were chosen in order to prove the process potential for the production of industrially relevant parts. Special focus will lie on surface quality, form accuracy and tool wear. The goal is to reach optical surface roughness and a shape accuracy below 300 nm.

TECHNOLOGY INTRODUCTION

The basics of ultrasonic assisted diamond turning have been introduced several times in different paper. Therefore the focus of this publication will be the results of the manufacturing of the aspherical geometries. Though a brief summary of the most important fundamental fact regarding this technology will be given.

The ultrasonic assisted turning system works with a fixed transducer. On top of the mounted sonotrode a monocrystalline diamond tool tip is clamped. In literature two different types of oscillation movements appear, uniaxial and elliptical. In this paper the tool movement occurs exclusively in the cutting direction with a unique frequency of 80 kHz. This unique ultrasonic system is shown in Figure 1.

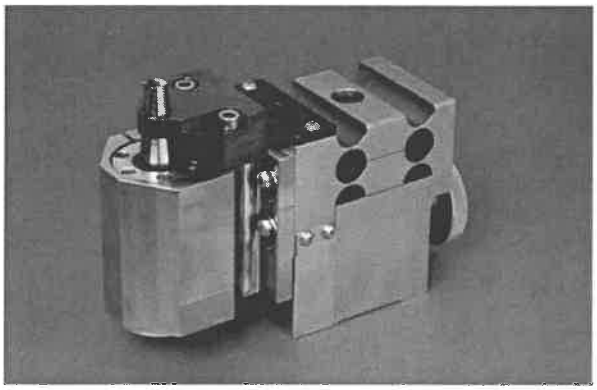

Figure 1: Unique ultrasonic system for diamond turning with 80 kHz

It is essential for the transition from the conventional to the vibration assisted process, that the maximum oscillation speed reached in the zero-crossing, is bigger than the constant

workpiece speed. Only when this condition is met the tool does detach itself from the chip during the oscillation. The contact occurs again during the upward motion after the vibration direction changes at the bottom oscillation point.

Accordingly, the effective contact time between the part and the cutting edge is reduced significantly by the high frequency excitation of the tool. In comparison to the conventional process, the contact time is decreased down to 20% of the total machining time. As previously demonstrated, this modification in the kinematics of the turning process has a considerable impact on the efficiency of ultra-precision operations conducted on critical materials such as steel or glass [2,3]. The cooling conditions of the tool are improved, even a small lubricant layer can be formed between tool and material causing hydrodynamic friction.

From a theoretical point of view the process with a higher frequency works with a shorter contact time per cycle. Each chemical reaction needs a starting time. Therefore the time, in which the chemical reactions, oxidations and diffusion reactions causing the wear can start and take place is significantly reduced. Hence from this point of view the frequency increase to 80 kHz should improve the overall process quality.

ASPHERE MANUFACTURING

Derived from an optical component in two mold geometries, one concave and one convex, were specified in cooperation with Jenoptik in order to prove the industrial potential of the applied process. The aspheres will only be machined in the hardest steel with 53 HRC, where, based on the fundamental experiments, optimal results were achieved with a feed rate of 5 µm. Therefore this parameters will be applied for the asphere finishing. In the following the results are presented.

Manufacturing of Concave Asphere

The concave asphere that was manufactured by ultrasonic assisted diamond machining in hardened steel (53HRC) had an aperture of 8 mm with a depth (sag) of approximately 1 mm and a maximum slope of 25 degree. The desired form accuracy is P-V < 300 nm and a surface roughness of Ra < 5 nm.

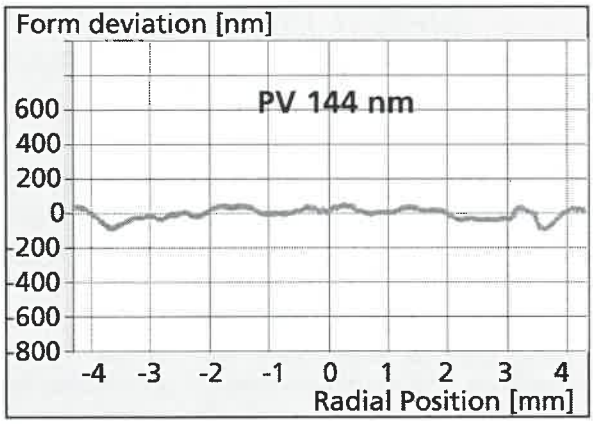

Figure 2: Achieved shape accuracy of concave aspheric steel mold

Figure 2 shows the impressive form accuracy that could be achieved applying the ultrasonic assisted process. The shape accuracy that was reached in this first experiments was under P-V < 150 nm, which was beyond the initial goal. This was possible through an iterative process applying an on machine measurement and correction system (Moore Nanotech 350 FG with WEC).

Not only the shape accuracy was reached, also an optical surface roughness could be achieved (Figure 3). The part was pre machined with four overruns a respective cutting depth of 10 µm and a feed rate of 30 µm for the pre machining and 5 µm for the additional finish machining. The iteration steps are required in order to reach the high accuracies demanded in this application. The achieved surface roughness after fine machining is shown in Figure 3. The roughness value is clearly under 10 nm which was the goal.

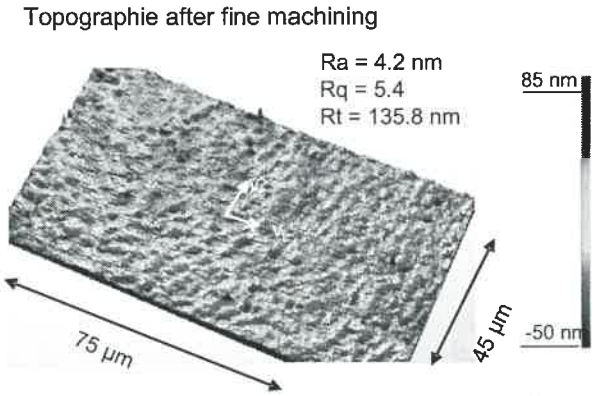

Figure 3: Surface topography of the asphere after fine machining

Besides the form accuracy and the surface quality, the diamond tool wear is of interest. The tool that was used for the pre machining and for the fine machining operation is shown in Figure 4. There cannot be detected any tool wear under the SEM after this five overruns.

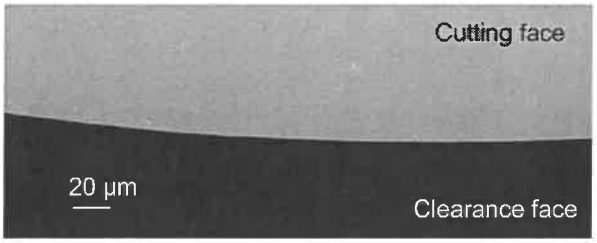

Figure 4: Monocrystalline diamond tool that was used for the pre and finish machining of concave steel asphere applying ultrasonic vibration

In conclusion, the concave asphere could be machined within the desired geometrical specification without any detectable tool wear.

Manufacturing of Convex Asphere

The aspherical shape of the convex steel mold was also derived from an optical component by Jenoptik. The geometry has an aperture of 10 mm and a height of approximately 4 mm. The maximum slope of the curve is approximately 41 degree. This asphere shall also be machined into a hardened steel part (53HRC) within the same tolerances (P-V < 300 nm; Ra < 10 nm).

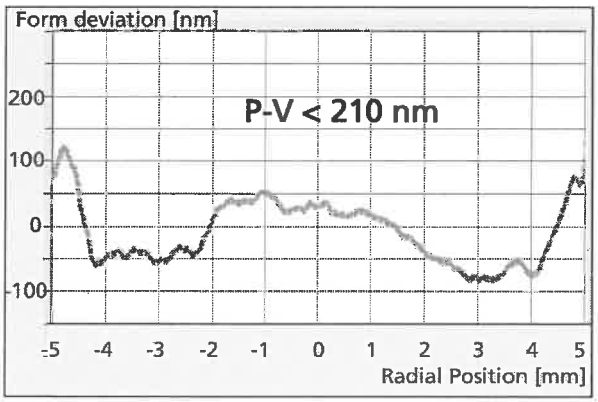

Figure 5: Achieved shape accuracy of concave aspheric steel mold

Figure 5 shows the absolute shape of the convex asphere (left) and the form deviation of the manufactured part (right). This part even reaches a form accuracy below P-V < 210 nm on a total aperture of 10 mm. For the manufacturing of the aspherical part five overruns were necessary in order to, iteratively, achieve the high shape accuracy. Two overruns were accomplished with a cutting depth of 10 µm, the last three overruns with a cutting depth of 5 µm. The employed feed rate was 5 µm per revolution.

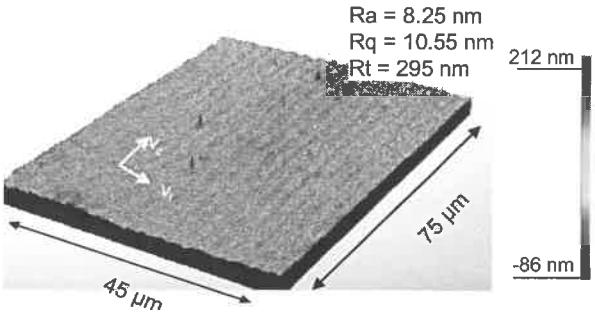

Figure 6: Surface topography of the asphere after the ultrasonic assisted machining operation

The achieved surface roughness is shown in Figure 6. The Ra roughness value is below 10 nm which demonstrates that also on a convex shapes optical surfaces can be realized in combination with highest form accuracies.

The convex part as well as the concave part was manufactured with one monocrystalline diamond tool respectively. Therefore the tool was applied for the pre and fine machining operations applying the parameters described before. After the machining of the convex steel part, there could not be detected any tool wear (Figure 7). At high resolution (10 000x) small material build up welding can be identified on the edge of the tool. Though the sharpness of the tool does not seem to be deteriorated.

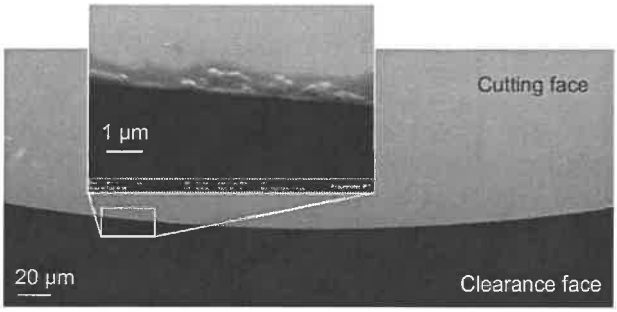

Figure 7: Diamond tool that was used for the pre and finish machining of convex steel asphere applying ultrasonic vibration

During all manufacturing processes a continuous chip was generated which verifies a ductile cutting process similar to the conventional cutting of non ferrous metals such as aluminum.

Summary and Conclusion

Fundamental investigations on ultrasonic assisted diamond machining of hardened steel applying a highly innovative ultrasonic vibration of 80 kHz were the basis for this publication.

The overall goal of the investigations was to transfer the lab scale research into industrial application. Therefore two different aspherical shapes were defined by Jenoptik, which were derived from actual plastic optics. The shapes were concave (D = 8 mm) and convex (D = 10 mm) respectively in order to get representative results.

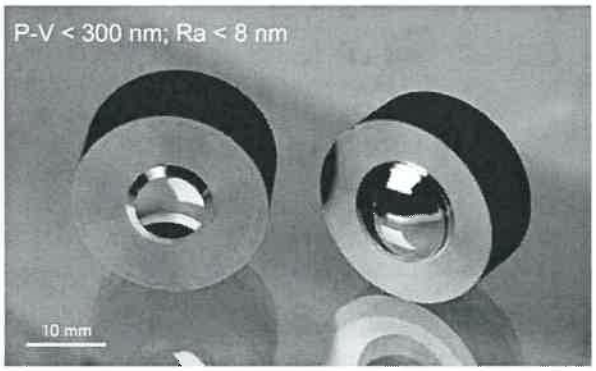

Figure 8: Aspheres manufactured in hardened steel applying ultrasonic assisted diamond turning

The machining operations for both aspheres required several pre machining and a fine machining steps. For the machining of each part one monocrystalline diamond tool was employed. In contrast to the conventional machining of steel, there could not be detected any tool wear after the processes.

The desired shape accuracies and surface roughness values (P-V < 300 nm; Ra < 10 nm) were reached by far on both aspherical geometries. The aspherical parts are shown in Figure 8 . This demonstrates the capabilities of this new technology and opens the door for this technique to compete with established manufacturing processes, such as the manufacturing of nickel plated mold inserts. The ultrasonic diamond machining with 80kHz enhances several advantages, high flexibility, faster production time, stronger mold inserts, etc. and will therefore strongly improve and establish its future position on the market as a manufacturing technology.

In conclusion the results of the presented investigations demonstrate that the ultrasonic process is suitable for the production of industrial relevant components within the actual state of the art accuracies.

REFERENCES

[1] Moriwaki, T.; Shamoto, E.: Ultraprecision Diamond Turning of Stainless Steel by Applying Ultrasonic Vibration, Annals of the CIRP Volume 40/1/1991, Page 559-562

[2] Rübenach, R.: Schwingungsunterstützte Ultrapräzisionsbearbeitung optischer Gläser mit monokristallinen Diamant-werkzeugen, PhD Thesis, RWTH Aachen, 2001, Page 42-54

[3] Olaf Dambon, Fritz Klocke, Michael Heselhaus, Benjamin Bulla, Andreas Weber, Ralf Schug, Bernd Bresseler, Vibration-Assisted Machining Research at Fraunhofer IPT – Diamond Turning and Precision Grinding, Proceedings of the 23rd Annual Meeting of the American Society for Precision Engineering, 2006

LASER GENERATED AND STRUCTURED PROTOTYPES OF DIAMOND TOOL TIPS FOR MICROOPTICS FABRICATION

Andreas Joswig[1,2], Stefan Risse[2], Ramona Eberhardt[2] and Andreas Tünnermann[1,2]
[1]Institute of Applied Physics, University of Jena, Thuringia, Germany
[2]Fraunhofer Institute of Applied Optics and Precision Engineering, Jena, Thuringia, Germany

INTRODUCTION

Excellent mechanical and thermal properties, such as high thermal conductivity and extreme hardness and therefore high wear resistance, make diamond the number one material for tools for ultra precision turning, milling and grinding applications. However, in the same way these properties also make it hard to generate diamond tools, especially those for turning and milling applications where only single crystal tools can be used. Due to thermal and mechanical stress while machining tool tips with common techniques like grinding or lapping, only tools with dimensions of tens to hundreds of microns and with small aspect ratios can be produced,[1-3]. Furthermore, due to its hardness being dependent on crystal orientation, diamond can only be machined in certain crystal directions, which limits the variety of possible tip shapes to simple geometries, e.g. spheres, planes and cylinders.

Using the fs-laser pulse technique for structuring diamonds can overcome the above mentioned limitations. First, laser processing of diamond is independent of the crystal orientation. Second, within the very short interaction time (fs to ps) between laser and diamond, no significant amount of heat can dissipate from the laser ablation area into the diamond. Therefore thermal as well as mechanical stress within the unaffected areas of the diamond material is almost negligible. As a result, the achievable feature size is only limited by the spot size of the laser focus, which can be in the range of several hundred nanometers up to several microns. Furthermore, the laser focus as a machining tool, in comparison to the commonly used grinding tools, stays in shape at all process times because it depends only on the energy constancy and stability of the beam profile of the laser itself, neither of which are altered due to material tool interaction.

EXPERIMENTAL SETUP

The cutting experiments were carried out with amplified femtosecond Ti:Sa lasers, a Tsunami-Spitfire combination from Spectra-Physics or a Mira-RegA system from Coherent, respectively, with pulse durations of 150 to 250 fs within a pulse energy range of 40 nJ to 10 µJ at a center wavelength of about 800 nm. The pulse repetition rate is 1 kHz for the Tsunami-Spitfire and 100 kHz for the Mira-RegA system. Without any additional beam shaping element the femtosecond laser beam is focused directly onto the diamond surface with an NA 0.25 microscope objective. Using this technique, focus diameters of about 4 µm can be achieved.

The samples are mounted onto a high precision 4-axes air bearing positioning system (Aerotech) with a total positioning error below 200 nm for x,y,z-movement at a resolution of 2 nm. The system consists of two perpendicularly stacked axes (ABL1500 and ABL1000) for sample movement in the xy-plane and an additional ABRS150-axis mounted on top for 360 degrees of continuous sample rotation. A mechanically decoupled z-axis (ABL1000) moves the microscope objective perpendicular to the xy-plane for focusing.

Sample materials are artificial polycrystalline CVD diamonds (Diamond Materials) and natural single crystal diamonds (Contour).

Experimental results were obtained by using SEM, AFM and white light interferometry.

RESULTS AND DISCUSSION

Cutting

Quasi arbitrary structures and cutting edges can be generated by directing the focused laser beam with synchronized xyz-movement over the diamond surface. The material is ablated within a volume predetermined by the size of the laser focus size and the ablation depth.

However, deep cuts (accumulated ablation depth of several µm) shade the incident laser beam in the boundary areas at the height of the primary surface, so that a) a significant amount of energy is lost and b) the energy density in the boundary areas may be sufficiently high to ablate material as well, which leads to a decrease of cutting edge sharpness. To minimize shading of the laser beam due to sample surface geometries, like steps or grooves, the laser focus is directed meander-like in an appropriate way, e.g. in straight or curved lines, over the diamond surface ablating the material line by line with a depth of only about 2 to 100 nm, depending on the laser pulse energy. Afterwards, the laser focus is again positioned at the starting xy-position and the new z-position. The whole process is reiterated to ablate the diamond plane by plane until a desired depth is reached and the designed tool shape is complete.

For simplicity in the first experiments the laser focus is moved in straight lines meander-like over the diamond surface layer by layer to produce plane cuts, shown in *FIGURE 1*.

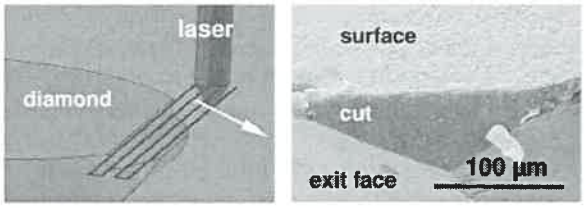

FIGURE 1. Left: Depiction of the meander-like laser focus pathway over the sample surface. The working direction is indicated by the arrow. Right: Resulting simple plane cut in a discharged single crystal diamond tool.

Surface quality

Usually the surfaces that are generated parallel to the laser beam show ripples in the nm-regime, shown in *FIGURE 4*. They have a height of about 120 nm and a lateral period of 400 nm which is exactly half the laser wavelength. These ripples always appear with constant size and period perpendicular to the polarization direction of the laser light, which implies that these ripples are formed due to a correlated interaction between the material itself and the linearly polarized photons by superposition of the incident and reflected beam, [4,5].

Using a fluence of 1.57 J/cm^2 (single pulse threshold fluence $F_{th}(1)$ for diamond is around 1.5 J/cm^2, [6]) within the laser focus and a writing speed of 80 µm/s, a roughness as low as 30 nm rms can be obtained and almost no nano-ripples are visible, *FIGURE 2*. Both an increase in cutting speed and, even more so, an increase in the laser fluence (energy per area) lead to an increase in surface roughness. Slight distortions in the flatness of the laser generated planes, which can be seen in *FIGURE 3*, are due to imperfections in the tuning and therefore yawing of the positioning stage.

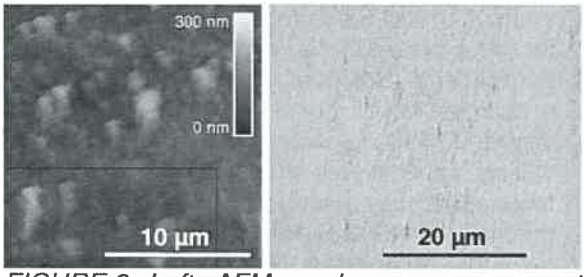

FIGURE 2. Left: AFM roughness measurement of a plane cut, roughness of about 30 nm rms can be obtained with appropriate laser and cutting parameters. Right: Large area SEM-image of the cut, containing the area of the AFM-image on the left, the sample tilt is 60 °.

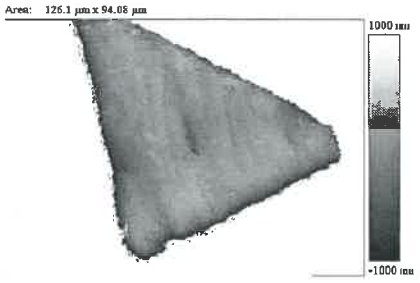

FIGURE 3. White light measurement of the surface geometry of a laser cut plane. Slight distortions in flatness of the surface are due to yawing of the positioning system.

Beam entry and exit

The difference between the edge radii at the beam entry and exit is distinctive. While the edge of the beam entry is radiused to 9 µm, the edge at the beam exit is very sharp with a radius of 400 nm, *FIGURE 4*. This can be explained by the above mentioned shading, which occurs at cutting depths greater than the rayleigh length of the laser focus. At these depths up to half of the laser energy is absorbed at the sample surface, resulting in a significant decrease in edge quality.

If the laser focus is moved towards the future edge while cutting, almost no shading effect is visible and the edge radius at the beam entry can be minimized to far below 1 µm as can be seen in *FIGURE 6.*

Tool tips

Using the femtosecond laser technique, generation of stress-free cutting edges in diamond independent of its crystal orientation is possible. Therefore high aspect ratio tool tips in almost any arbitrary shape are achievable.

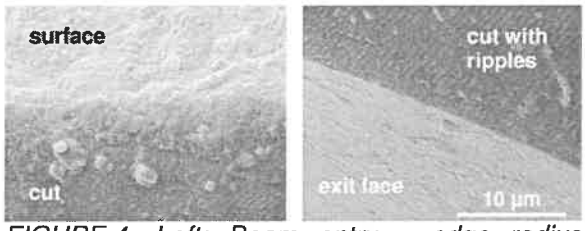

FIGURE 4. Left: Beam entry – edge radius 9 µm, Right: Beam exit – edge radius 0.4 µm.

Laser generated tool tips

In FIGURE 5 a top view of the first prototype of a needle-like tool tip machined into a discharged single crystal diamond tool is shown. The needle has a width at the backside of 20 µm and a total length of 200 µm, which leads to a lateral aspect ratio of 1:10 at a structure depth of about 100 µm. No cracks or disruptions are visible in the walls of the laser generated structure, which indicates that very little thermal or mechanical stress is applied due to the laser ablation process.

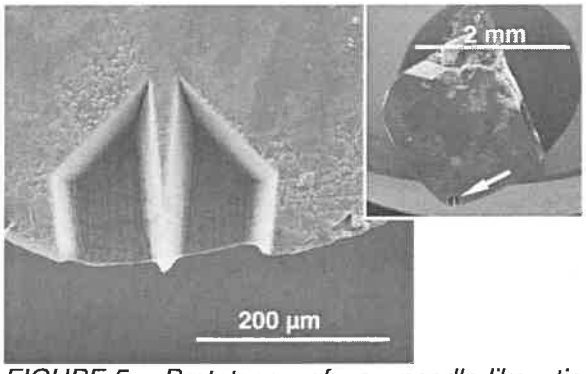

FIGURE 5. Prototype of a needle-like tip (100 µm deep) in a discharged single crystal diamond. Aspect ratio is greater 1:10. The inset shows the whole diamond tool with the structure marked with an arrow.

In addition, in some turning experiments where similar produced "tools" with plane cuts are used to turn aluminum, the tips showed no wear or raptures afterwards which also indicates that the femtosecond laser cutting of diamond is stress-free as far as possible.

FIGURE 6 shows a saw-tooth-like structure in polycrystalline CVD-diamond plate. The dimensions of a single tooth are about 130 µm in length and 30 µm in width. The cutting depth is about 25 µm.

Compared to the best cuts in single crystal diamond (roughness of 30 nm rms on a plane) the walls of this structure are slightly imperfect due to imperfections of the polycrystalline diamond itself and a non optimized cutting process at high process speed. At this time tools with this surface quality could already be used for milling (which is a highly statistical process), where the surface quality of the tool isn't as important for obtaining a (very) good quality within the workpiece as in diamond turning.

The saw-tooth-like geometry can be easily projected onto an axially symmetric shape like a circle for generating a cylindrical milling tool, for example.

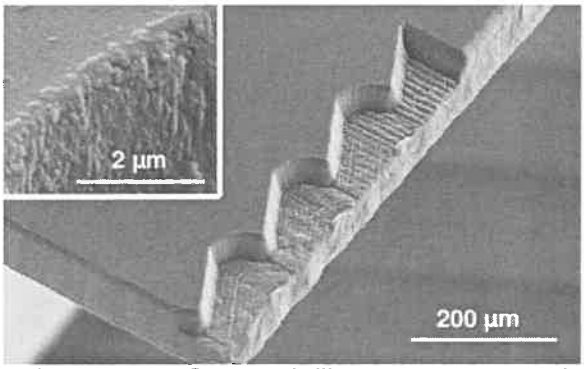

FIGURE 6. Saw-tooth-like structure in polycrystalline CVD diamond. Structure depth is 25 µm. The inset shows a magnified section of the beam entry at the diamond surface. The edge radius is about 0.5 µm.

Laser modified tips

Femtosecond laser structuring can not only be used for cutting arbitrary shapes into diamond but to modify tool tips as well. FIGURE 7 shows the modified surface of a polycrystalline CVD-diamond platelet. The larger linear structures are directly carved into the diamond by moving the laser focus over the surface line by line with a lateral period of 5 µm. Within these structures even smaller, highly periodically and seamlessly

connected ripples with a period of 400 nm can be observed.
The orientation of the nano-ripples only depends on the polarization direction of the laser beam and is absolutely independent of the laser pathway. Hence, the direction of the nano-ripples and the laser pathway along the surface can be adjusted arbitrarily and separately by changing the orientation of polarization of the laser light or the laser pathway, respectively. Furthermore, with a change in the laser wavelength even the period of the nano-ripples is adjustable.

Such surface structures can be used to a) guide chips in a desired way or direction to minimize cutting forces while turning and/or b) adhere cooling lubricant while providing an enlarged interaction interface between cooling lubricant and the diamond tool for maximum heat transport away from the tool tip into the coolant.

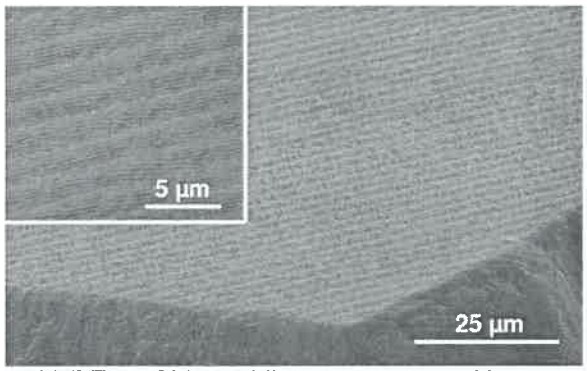

FIGURE 7. Chip guiding structures with nano-ripples in the surface of a polycrystalline CVD diamond, tilt 60°. The period of the structure is 5 µm, the period of the nano-ripples is 400 nm. The inset shows a magnification of a representable part of the whole structured area.

It should be mentioned that femtosecond laser machining of diamond is at this point in time a relatively time consuming process. With an optimized cutting speed of about 80 µm s^{-1} (NA 0.25) at 1 kHz pulse repetition rate it takes about two to three hours to generate tool tips, like these shown above, with dimensions of about 200x100 $µm^2$ and a structure depth of about 25 to 100 µm. The pulse energy at the highest available repetition rates of the research lasers systems which were used is the limiting factor. However, newly developed (fiber based) high power femtosecond and picosecond laser sources, with repetition rates in the MHz range and sufficient pulse energies are commercially available meaning that the technique of laser machining of diamond can easily be upscaled in process speed by a factor greater than 100 without decreasing the structure quality.

SUMMARY AND OUTLOOK

We have successfully generated or modified diamond tool tips for cutting, turning and milling applications by using femtosecond laser ablation. The quality of the surface and form of the structures is quite good but not yet sufficient for direct diamond turning and cutting for optical applications. Therefore further investigations have to address an increase of surface contour quality and cutting speed as well as to decrease the cutting edge radii.

ACKNOWLEDGEMENT

The work presented in this paper was part of the research and development project "nanoreplica" that is funded by the German Federal Ministry of Education and Research (BMBF), fund number 03IP609, and is managed by the Project Management Agency Projektträger Jülich (PtJ).

REFERENCES

[1] W.J. Zong, et al. - The basic issues in design and fabrication of diamond-cutting tools for ultra-precision and nano metric machining, International, Journal of Machine Tools & Manufacture. 550 (2010), 411-419
[2] W.J. Zong, et al. - Contact accuracy and orientations affecting tool sharpness of diamond cutting tools by mechanical lapping, Diamond and Related Materials 15, (9), (2006), 1424–1433
[3] W.J. Zong et al. - Analysis for the wear resistance anisotropy of diamond cutting tools in theory and experiment, Journal of Materials Processing Technology 210 (2010) 858–867
[4] R. Wagner, J. Gottmann - Sub-wavelength ripple formation on various materials induced by tightly focused femtosecond laser radiation, Journal of Physics: Conference Series 59 (2007) 333–337
[5] B. Tan, K. Venkatakrishnan - A femtosecond laser-induced periodical surface structure on crystalline silicon, Journal of Micromechanics and Microengineering. 16 (2006) 1080–1085
[6] P. Bartholomé, Diploma Thesis 2007, University of Applied Sciences, Jena.

ULTRA-PRECISION FLUID JET AND BONNET POLISHING FOR NEXT GENERATION HARD X-RAY TELESCOPE APPLICATION

Anthony TH. Beaucamp[1,2], Akihiro Matsumoto[1,2] and Yoshiharu Namba[1]
[1]Department of Mechanical Engineering
Chubu University
Kasugai, Japan
[2] Research and Development
Zeeko LTD
Coalville, United Kingdom

1 INTRODUCTION

Single-point diamond-turning is a well-established method to create precise axially-symmetric forms on ductile materials, including flats, spheres, aspheres and cylindrical shapes. A typical example is the production of large off-axis aspheric mirrors for the three-mirror astigmatic configuration [1]. Other applications include various infrared mirrors, and mandrels for producing the cylindrical forms of Wolter-type X-ray mirrors. The main limitation of this method has been the resulting micro-structure which is cyclic in nature ('turning marks') and which produces diffraction and stray light effects. For this reason, molding dies for X-ray mandrels in particular are post-polished to achieve both the form and texture required.

Namba et.al have previously described their work on replication-mandrels for Wolter Type 1 mirrors used in soft X-ray microscopy [2] and hard X-ray telescopes [3]. The mandrels were produced by single-point diamond turning, but required post-polishing by hand to remove the high spatial frequencies on the surface. As they pointed out, this is extremely difficult on aspheres, and leads to an inevitable trade-off between quality of the surface texture achieved and destruction of the aspheric figure. Clearly an automated method to remove the diamond-turning signature without destroying form could be an important step forward.

Fluid-jet polishing (FJP) is a method in which slurry of polishing particles is pressurized and projected through a nozzle towards the surface to be polished. The jet impacts the surface of the part directly, i.e. with no physical tool contact. Booij et.al [4] have shown the linear dependence of removal rate with slurry concentration. They have also shown the non-linear dependence with impact-velocity, due to the combined effects of i) a minimum velocity-threshold below which no removal occurs, ii) the increased rate of particle-delivery with increased velocity and iii) the square relation between particle kinetic energy and velocity. They conclude that, using appropriate abrasive and particle size with the right flow velocity, FJP can achieve ductile-regime removal with stable volumetric removal-rate. L. Yang et.al have also investigated fluid jet polishing and concluded [5] that the removal process is a mixture of shear and collision mechanisms.

Bonnet polishing (BP) is a method based on a more traditional approach. A reinforced rubber tool is kept under constant back pressure, and pressed into a workpiece to generate a contact area [6]. A polishing cloth is stuck on the bonnet, and slurry sprayed onto the surface. The abrasion rate can be controlled by changing various parameters such as pressure, bonnet spindle rotation speed, precess angle, and tool offset.

Both of these processes can produce stable sub-aperture footprints, and can be controlled by the Precessions corrective polishing software to improve form-error on freeform surfaces [7].In the work reported in this paper, the FJP process has been used to attenuate diamond-turning marks on plano electroless nickel coated samples. This process was complemented by subsequent smoothing of the surface roughness with the BP process, using slurry of nano-sized particles. The BP process has also been used to correctively polish sections of a borosilicate mandrel, which is being investigated as an alternative to electroless nickel for making X-Ray molding dies. The method described potentially opens up new applications for diamond-turned surfaces, as well as improving the performance of glass optics.

2 EXPERIMENTAL PROCEDURE

2.1 Nickel and Borosilicate Samples

A7075 aluminum alloy was cut into 100mm diameter and 30 mm thick plano samples and turned by a single-point diamond turning machine. A layer of nickel-phosphorus alloy 0.1 mm thick was deposited on the diamond-turned aluminum alloy samples by electroless nickel plating in industry. The hardness of the electroless nickel and aluminum alloy were 568 Hv and 183 Hv respectively. All samples were single-point diamond turned (SPDT) again in order to obtain consistent surface conditions.

A hollow borosilicate glass cylinder was obtained directly from industry, with dimensions 200mm diameter and 200mm length. The process used to make the mandrels ensures uniform surface texture across the sample, around 0.5nm rms, but poor straightness in the range 3-5um. The cylinder was cut into rectangular sections 50mm by 100mm.

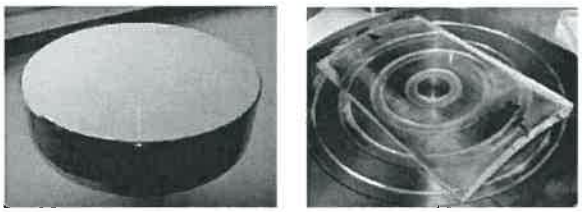

FIGURE 1. Nickel and Borosilicate samples.

2.2 Fluid Jet and Bonnet Polishing

The diamond-turned plano samples were polished by FJP on a Zeeko IRP200 CNC polishing machine. CeO2 slurry was used, with particles ranging between 0.6-1.0um, and a concentration of 80g/L. The samples were subsequently polished by BP on the same machine. Slurry of nano-sized SiO2 particles (7-30nm diameter) was drip fed onto the surface directly above the bonnet, while the rest of the surface was regularly fine sprayed with pure water to prevent crystallization of the slurry over the sample.

The borosilicate samples were polished by FJP and BP using the CeO2 slurry described above. The objective of FJP was to assess the effect of pressure on surface texture, while that of BP was to assess corrective polishing capability.

2.2 Surface Texture Measurement

Surface micro-topography of the samples was measured with three-dimensional NewView and ADE optical profilers. Form error on the borosilicate samples was measured with a Form Talysurf profilometer.

3 RESULTS AND ANALYSIS

3.1 Fluid Jet Polishing of SPDT Nickel

The fluid was pressurized at 18bar, and expelled in laminar flow through a small nozzle (1mm diameter). The CNC machine was programmed to raster the workpiece with a track spacing of 0.1mm and feed rate of 500mm/min. The resulting surface texture showed no residual marks from the prior diamond tool machining, and improvement in the surface roughness from 3.05nm rms down to 1.47nm rms (see Figure 3a and 3b). Figure 2 shows power spectral density analysis performed on the surface texture before and after FJP. The two high powered frequencies associated with the SPDT processing step were completely eliminated.

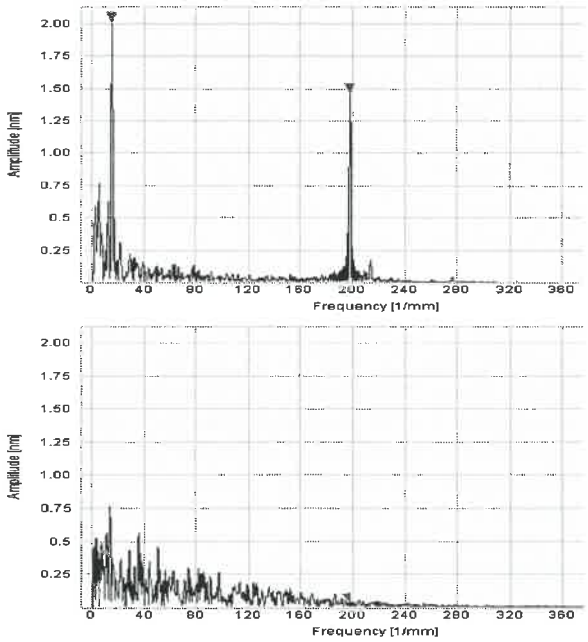

FIGURE 2. PSD analysis of electroless nickel surface before and after FJP.

The edge of the zone polished by FJP was imaged with a stitching optical profiler. Figure 4 shows very clearly the progressive overriding of directional tool marks from prior diamond turning (left hand side) with a random FJP texture (right hand side). This effect is very desirable since it produces a surface with no strong frequency that could lead to diffraction or stray light effects on the final replicated mirror.

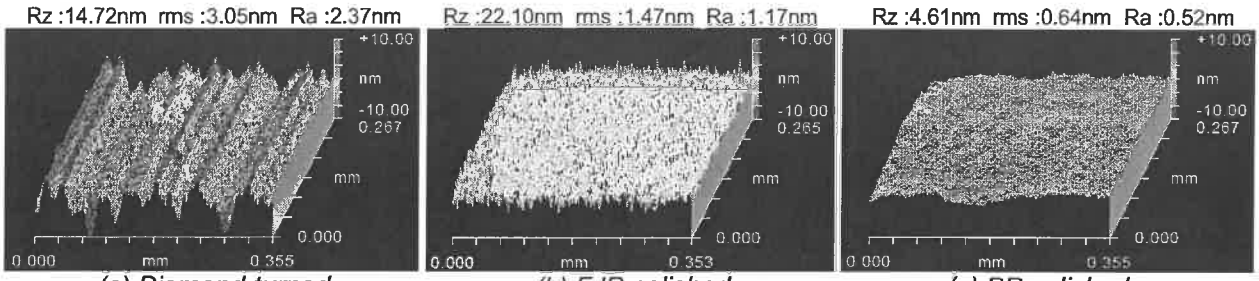

(a) Diamond-turned (b) FJP polished (c) BP polished

FIGURE 3. Surface texture of electroless nickel surface at various machining stages (optical profiler).

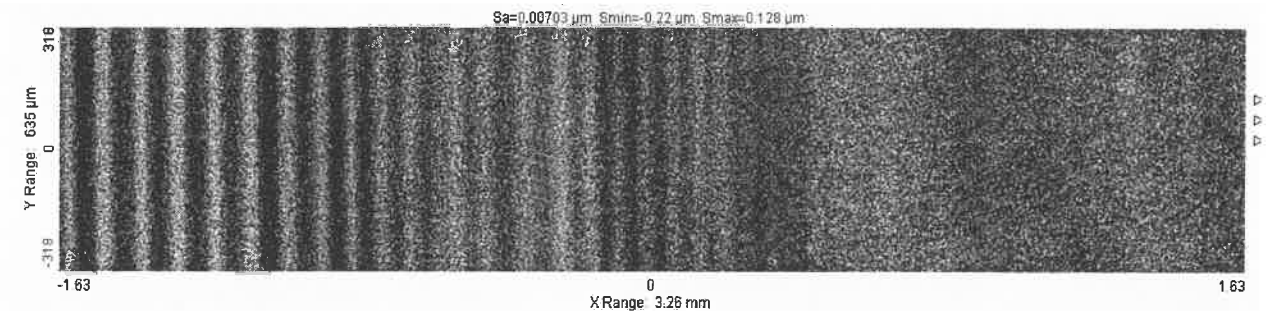

FIGURE 4. Surface texture of electroless nickel surface at edge of FJP zone (stitching optical profiler).

3.2 Bonnet Polishing of SPDT Nickel

The surface texture obtained from FJP was not sufficiently smooth for hard X-Ray application. Subsequent smoothing by BP was thus investigated. A powder of ultra fine SiO2 nano-particles with average size 7nm was mixed with pure water at a concentration of 20g/L. The slurry was delivered above the bonnet at a rate of 12L/H. To prevent drying of the slurry on the surface, which can cause crystallization, the surface was sprayed with a fine mist of pure water every few seconds. The slurry and water were thus delivered in total loss mode.

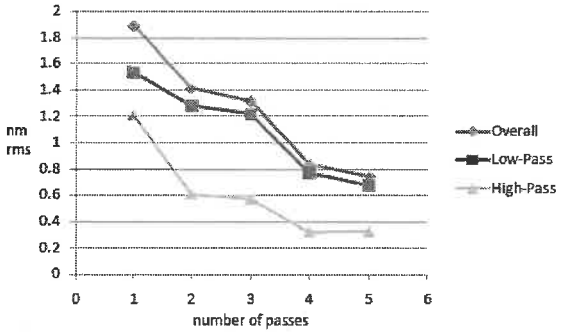

FIGURE 5. Surface texture variation on electroless nickel sample.

Bonnet pressures in the range 0.2 to 3.0bar and spot sizes in the range 5mm to 15mm were experimented with. The best pressure was found to be 1Bar, and the best spot size 15mm. The surface texture was evaluated after each raster pass of the tool on the surface. Using FFT Auto filtering, the evolution of waviness (low-pass) and roughness (high-pass) could be assessed. The result is shown on Figure 5. The roughness was very effectively reduced by the polishing to circa 0.3nm rms. The waviness was slower to remove, and reached a lower limit of 0.65nm rms.

The best surface texture obtained on a sample was 0.64nm rms (see Figure 3c). The main issue was identified as residual waviness from the bonnet polishing tool, in the region of 0.6-0.7nm rms. This value is not yet sufficiently low for Hard X-Ray applications, so future research will concentrate on reducing the waviness induced by the bonnet polisher. The effect of hardness of the tool in particular will be investigated. In the meantime, it is possible to use this automated process to reduce the final hand polishing time by as much as 75% [3].

3.3 Fluid Jet Polishing of Borosilicate

The Borosilicate samples were polished at different FJP pressures and the effect on surface texture assessed with the same method as described in the previous section. Figure 6 shows that the effect of pressure on roughness was almost linear, while waviness was degraded only

slightly at lower pressures. The removal rates were very low because of the small size of the nozzle (only 1mm diameter). Removal rates were in the range 0.0004-0.008mm^3/min.

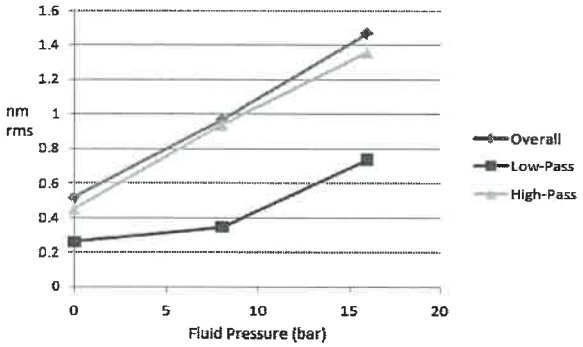

FIGURE 6. Surface texture on borosilicate sample as a function of FJP polishing pressure.

A new slurry management system capable of higher flow rate was recently delivered that will enable the use of larger diameter nozzles in future experiments. It is hoped that with sufficient removal rates (circa 0.04mm^3/min) FJP will be used in the future at pressures of 8-10Bar to correct form error on the surface while leaving waviness in the range 0.3-0.4nm rms and roughness in the range 0.9-1.0nm rms. Subsequent polishing by BP with nano-particles may then reduce the roughness back to circa 0.3nm rms (see 3.2).

3.4 Bonnet Polishing of Borosilicate

Form correction was carried out on a borosilicate sample with BP using the 0.6-1.0um CeO2 slurry. The precessions software was used for this purpose [7]. After 3 corrective iterations, the form error was reduced from PV 3.2um down to 0.18um (see Figure 7).

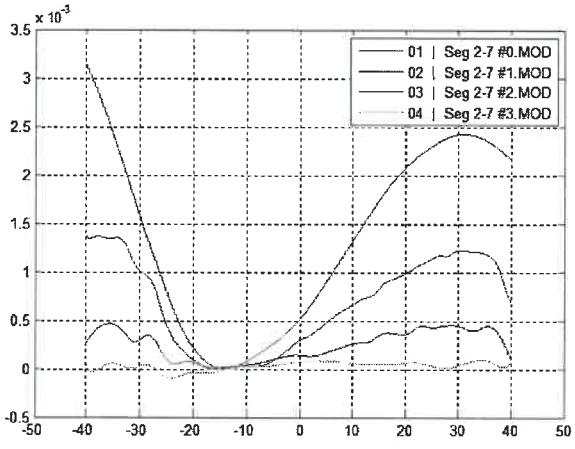

FIGURE 7. Improvement of form-error on borosilicate cylindrical sample.

4 SUMMARY

A study of automation of hard X-Ray molding dies polishing by FJP and BP was carried out. The following conclusions were drawn:

1. Surface roughness in the range 0.6-0.8nm rms can be obtained on electroless nickel samples by a combination of Fluid Jet polishing with micro-particles followed by Bonnet polishing with nano-particles.
2. Automated corrective polishing was demonstrated on a borosilicate cylindrical sample, with form error improvement from PV 3.2um down to 0.18um.
3. By using the automated process to get surface texture down to circa 0.6-0.8nm rms, it is possible to reduce the time of final hand polishing to 0.3nm by as much as 75% [3].

5 REFERENCES

[1] H.S. Kim, E.J. Kim, B-S. Song, Diamond turning of large off-axis aspheric mirrors using a fast tool servo with on-machine measurement, Journal of Materials Processing Technology. 2004; Vol. 146, Issue 3, pp 349-355.

[2] Chon, K. S., Namba, Y. and Yoon, K. H., Precision Machining Electroless Nickel Mandrel and Fabrication of Replicated Mirrors for a Soft X-Ray Microscope, JSME Int'l Journal Series C. 2006; 49/1:56-62.

[3] Y. Namba, T. Shimomura, A. Fushiki, A. Beaucamp, I. Inasaki, Ultra-Precision Polishing of Electroless Nickel Molding Dies for Shorter Wavelength Applications, Annals of the CIRP. 2008; 57/1:337-340.

[4] S.M Booij, H. van Brug, J.J.M. Braat, O.H. Fahnle, Nanometer Deep Shaping with Fluid Jet Polishing, Opt Eng. 2002; Vol. 41 (8), pp 1926-1931

[5] P. Guo, H. Fang, J. Yu, Computer Controlled Fluid Jet Polishing, Proc. SPIE. 2007; Vol. 6722

[6] D.D. Walker, D. Brooks, A. King, R. Freeman, R. Morton, G. McCavana, K. Sug-Whan, The 'Precessions' tooling for polishing and figuring flat, spherical and aspheric surfaces, Optics Express. 2003 ; Vol. 11, issue 8, pp. 958-964

[7] D.D. Walker, R. Freeman, R. Morton, G. McCavana, A. Beaucamp, Use of the 'Precessions' process for pre-polishing and correcting 2D & 2½D form, Optics Express. 2006; Vol. 14, issue 24, pp. 11787-11795

PLASMA ASSISTED POLIHING OF REACTION-SINTERED SILICON CARBIDE

Kazuya Yamamura, Masaki Ueda, Tatsuya Takiguchi, and Nobuyuki Zettsu
Research Center for Ultra-precision Science and Technology
Graduate School of Engineering, Osaka University
Suita, Osaka, Japan

INTRODUCTION

Reaction-sintered silicon carbide (RS-SiC) is a promising material for mirror of next-generation space telescope, components of semiconductor manufacturing equipment, heat exchanger parts of hydrogen production systems, and so on [1, 2]. SiC is a difficult-to-machine material because of its hardness and chemical inertness, and is generally polished by applying micro diamond abrasives. Therefore, micro-scratches and subsurface damages, which deteriorate surface integrity, are inevitably generated on the workpiece surface. In contrast, chemical mechanical polishing (CMP) techniques are being developed for finishing the surface of single-crystal SiC and/or GaN substrate, which are promising materials as the next-generation semiconductor power device. However, polishing rate of single-crystal SiC is very low (less than 0.5μm/h), and it is very difficult to obtain an adequate level of surface integrity for epitaxial growth because SiC and GaN are hard and chemically-inert materials [3, 4].

To resolve these issues, we propose a new machining technique, which utilizes an assist of atmospheric pressure plasma irradiation, to realize high-efficient and high-integrity finishing of difficult-to-machine materials. The irradiation of plasma modifies the mechanical and/or chemical properties of the surface of the hard material to remove easily. In our previous study, X-ray photoelectron spectroscopy (XPS) analysis revealed that the surface of single-crystal 4H-SiC (0001) irradiated by helium-based water vapor plasma and oxygen plasma was oxidized in both cases [5]. Furthermore, it was found that the water vapor plasma is superior to the oxygen plasma with regard to the oxidation rate of the SiC. The results of ball-on-disc test using alumina ceramic ball, which performed in ambient air condition, shows that the wear rate of SiC surface irradiated by the water vapor plasma is 20 times higher than that of the surface without plasma irradiation. Similar effects were also observed in the case of tungsten carbide (WC) material. Therefore, surface oxidation of those hard materials is very effective to increase the removal rate in the mechanical removal process, such as lapping and polishing.

In this paper, we describe the machining properties of the RS-SiC in plasma-assisted lapping technique. RS-SiC substrate used in this research has no pores and has 2-3 times larger bending strength than conventional RS-SiC [1].

EXPERIMENTAL SETUP

Fig. 1 shows the schematic of the experimental apparatus used. This apparatus consists of plasma generation and mechanical removal parts, which are separately installed to investigate the basic removal mechanism, such as chemical structure of modified surface and dependency of combination between abrasive and base material in removal rate. Atmospheric pressure plasma is generated by applying a RF (f =13.56 MHz) electric power, and helium containing water vapor (1.7-2.6%) is supplied as a process gas with a flow rate of 1.5 L/min. Water vapor is introduced into the process gas by the helium bubbling of ultrapure water (UPW), and its concentration is measured using a dew-point meter (DPM). The copper electrode used is covered with a quartz glass to prevent arc discharge by generating dielectric barrier discharge. In the mechanical removal part, a

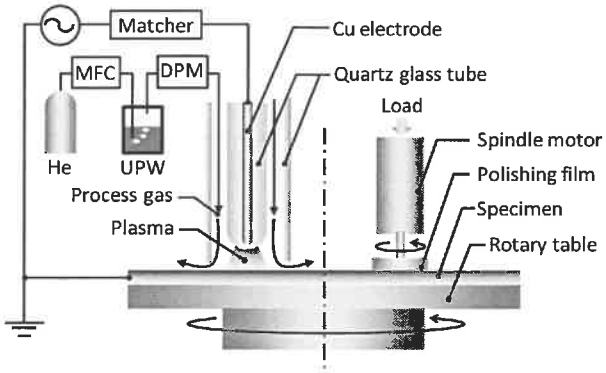

FIGURE 1. Schematic of experimental apparatus.

lapping/polishing test with a polishing film (φ8 mm) can be conducted. The test sample is installed on the rotary table, and the surface modification by plasma irradiation and mechanical removal using a polishing film are sequentially conducted.

RESULTS AND DISCUSSION

Fig. 2 shows the optical emission spectrum of the atmospheric pressure water vapor plasma. The emission spectrum from the plasma was measured using a multichannel spectrometer. Strong emissions from hydroxyl radical (λ=309 nm) and Hα (λ=656.3 nm), which were generated by dissociation of H_2O molecule, were observed.

Figs. 3(a), (b) and (c) show the XPS spectra of the RS-SiC surface. Processed surface was prepared by only irradiation of the water vapor plasma without mechanical removal. Dashed line and solid line show the unprocessed and plasma irradiated surface, respectively. Strong peak due to the Si-O bond (103.6eV, 533.0eV) is observed from the surface irradiated by water vapor plasma, while the peak due to the C-Si bond (282.7eV) drastically decreases. These results indicate that irradiation of the water vapor plasma strongly oxidizes the surface of the RS-SiC, and it is considered that dominant oxidizing species is hydroxyl radical from the result of optical emission spectroscopy. These results lead to expectation that softening caused by oxidation facilitates the removal of hard SiC surface.

Fig. 4(a) shows the load-displacement curves of the SiC surface measured by the nanoindentation method. The Berkovich-type indenter made of diamond was used, and the maximum load was 0.5 mN. The hardness of the surface was calculated by the Oliver-Pharr method [6]. The following two types of specimen were evaluated: an unprocessed substrate and a substrate modified by the irradiation of the water vapor plasma to form an oxidized film. The obtained results shown in Fig. 4(b) indicate that the hardnesses of the unprocessed and modified surfaces are 15.6 GPa and 1.4 GPa, respectively. The hardness of RS-SiC is about half compare with that of 4H-SiC, and it decreased in one order of magnitude by irradiation of water vapor plasma. Similar decreasing tendency was observed in the case of 4H-SiC [5]. Hence, the irradiation of the water vapor plasma is very effective for softening the RS-SiC surface.

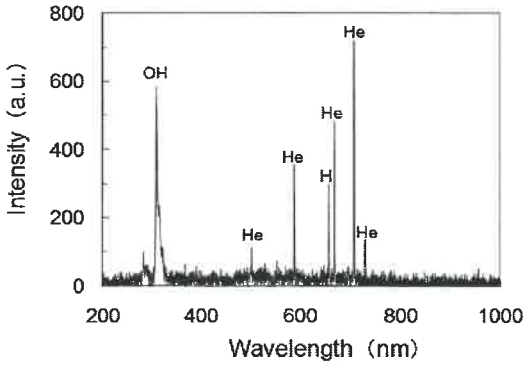

FIGURE 2. Optical emission spectrum of the atmospheric pressure water vapor plasma.

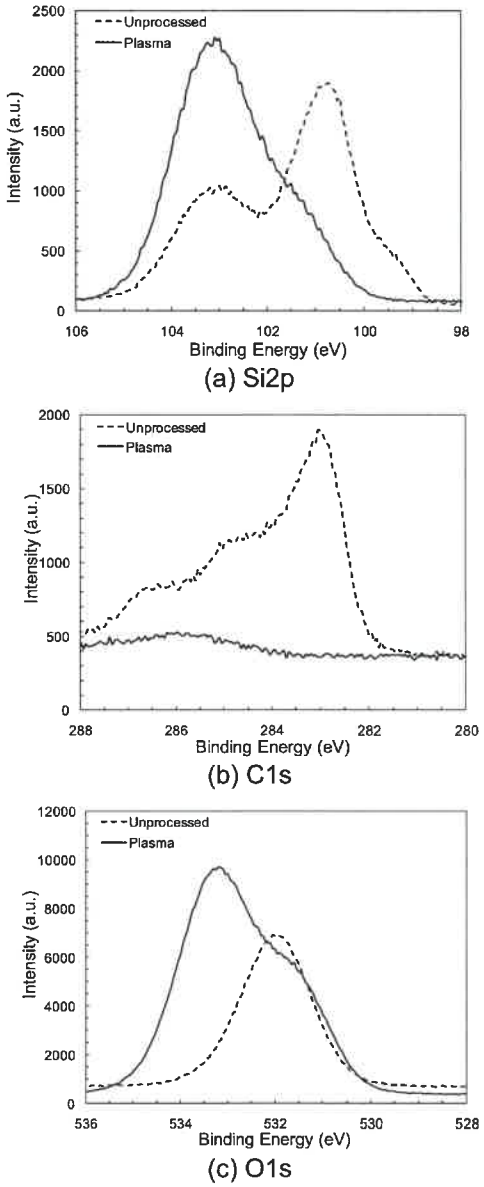

FIGURE 3. XPS spectra of RS-SiC.

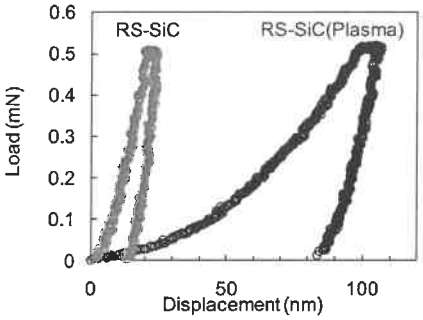

(a) Load-displacement curve.

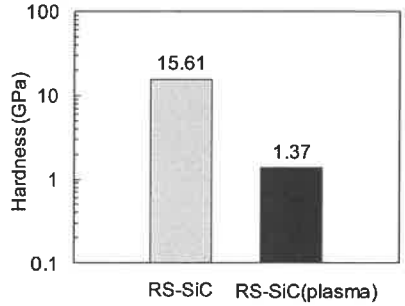

(b) Hardness calculated from measured data (a).
FIGURE 4. XPS spectra of RS-SiC.

TABLE 1. Experimental parameters.

Abrasive	Diamond, CeO_2
Grit size	0.5 μm
Load	30 g
Process gas	He + H_2O (2.04%), 1.5 L/min
RF power	9 W
Rotation speed	120 rpm (substrate) 3700 rpm (polishing pad)
Specimen	RS-SiC (#600 finish) (Japan Fine Ceramics Co., LTD.)

We conducted some preliminary experiments using polishing film to evaluate an effect of water vapor plasma irradiation in finishing of RS-SiC. Diamond or CeO_2 abrasives are fixed on the polyethylene terephthalate (PET) film using adhesive. Experimental parameters are shown in Table 1.

Figs. 5 (a), (b) and (c) show the surface morphologies measured with a microscopic interferometer, and Fig. 6 indicates cross-section of processed surface showed in Fig. 5. Diamond abrasive polishing caused formation of deep pits on the surface as shown in Fig. 5(a) and Fig. 6, while many protrusions were observed on the surface processed by plasma-assisted polishing using ceria abrasives. Results of skewness evaluation shown in Fig. 7 indicate that the surfaces applied diamond abrasive polishing and plasma-assisted ceria polishing have negative and positive skewness value, respectively. These results imply that removal mechanism is different in both polishing processes. In the case of diamond abrasive polishing, detachment of SiC grain or preferential removal of Si phase existing between SiC grains are considered as the causes of pit formation. On the other hand, it is considered that softened layer, which is formed by plasma irradiation, is easily removed by ceria abrasive, while the region of which is inadequate oxidation remains because ceria abrasive is softer than SiC. We have confirmed that removal of RS-SiC was hardly observed by applying ceria abrasive polishing without plasma irradiation. In the case of monocrystalline 4H-SiC, we obtained rms surface roughness of less than 0.3 nm [5,7]. These results lead to the conclusion that inhomogeneous structures of RS-SiC cause formation of the protrusion on the processed surface because plasma-assisted polishing is mainly based on the chemical reaction.

Combined polishing process, which is consist of plasma-assisted ceria abrasive polishing followed diamond abrasive polishing, enabled us to obtain rms surface roughness of 1.8 nm as shown in Fig. 5(c) and Fig. 6. Fig. 7. shows that the skewness changed from positive to small negative value after combined polishing due to the removal of protrusion. Therefore, combined polishing process proposed is effective to decrease the surface roughness of the material that has inhomogeneous structure like the RS-SiC.

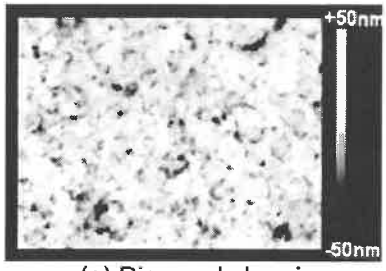

(a) Diamond abrasive
(Processing time: 240 min, 418 nm p-v, 10.2 nm rms)

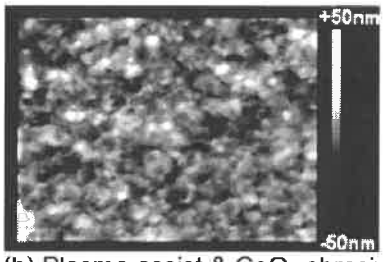

(b) Plasma assist & CeO_2 abrasive
(Processing time: 240 min, 108 nm p-v, 9.7 nm rms)

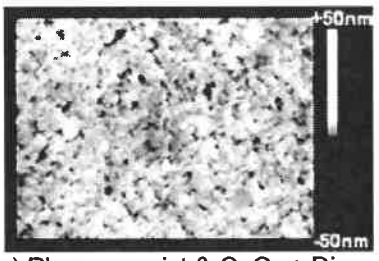

(c) Plasma assist & CeO_2 + Diamond
(Processing time: 240+240 min, 20.9 nm p-v, 1.8 nm rms)

FIGURE 5. Microscopic interferometer images of processed RS-SiC surface.(Evaluated area: 64x48μm)

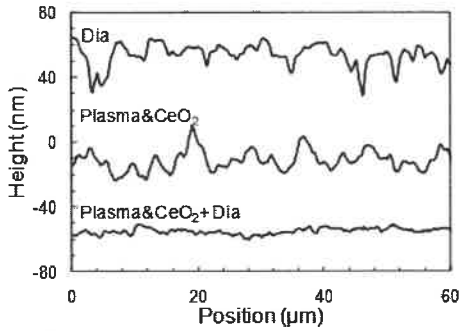

FIGURE 6. Cross-section of processed RS-SiC surface.

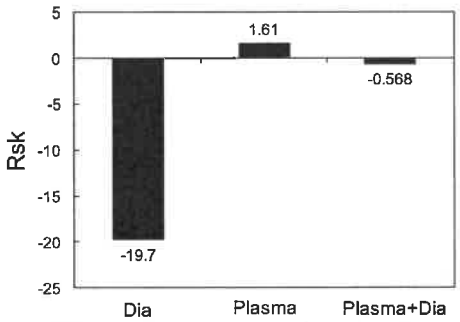

FIGURE 7. Skewness of processed RS-SiC surface.

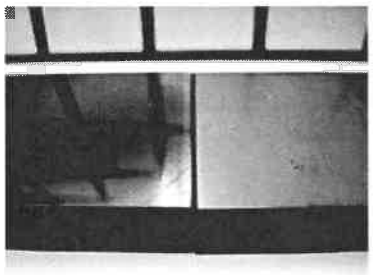

FIGURE 8. Photograph of RS-SiC surface before and after combined polishing.

Fig. 8. shows photograph of RS-SiC substrate. It is found that combined polishing improved the roughness of #600 ground surface (right side) to the mirror surface (left side).

CONCLUSIONS

A novel polishing technique combined with the irradiation of atmospheric pressure plasma was proposed for smoothing the roughness of RS-SiC. Irradiation of the water vapor plasma oxidized the surface, and it enables us to obtain the smooth surface without introducing scratch on the surface.

ACKNOWLEDGEMENTS

This work was partially supported by a Grant-in-Aid for Scientific Research (B) (20360068) from the MEXT, Japan, a research grant from the Die and Mold Technology Promotion Foundation and a Mazak Foundation.

REFERENCES

[1] Suyama S, Kameda T, Itoh Y. Development of high-srength reaction-sintered silicon carbide, Diamond and Related Materials. 2003; 12: 1201-1204.

[2] Suyama S, Itoh Y. Evaluation of microstructure of high-strength reaction-sintered silicon carbide of optical mirror, Proc. of SPIE. 2007; 6666: 66660K-1-11.

[3] Zhou L, Audurier V, Pirouz P. J. Chemomechanical polishing of silicon carbide, Electrochem. Soc. 1997; 144: L161-L163.

[4] Heydemann V. D, Everson W. J, Gamble R. D, Snyder D. W, Skowronski M. Chemomechanical polishing of silicon carbide, Mater. Sci. Forum. 2004; 457-460: 805-808.

[5] Yamamura K, Takiguchi T, Zettsu N. Development of Atmospheric-Pressure-Plasma-Assisted High-efficient and High-integrity Machining Process of Difficult-to-Machine Materials, 10th International Conference of the European Society for Precision Engineering and Nanotechnology. 2010: 299-302.

[6] Oliver W. C, Pharr G. M. An improved technique for determining hardness and elastic modulus using load and displacement sensing indentation experiments, J. Mater. Res. 1992; 7: 1564-1583.

[7] Yamamura K, Takiguchi T, Ueda M, Hattori A. N, Zettsu N. High-integrity finishing of 4H-SiC (0001) by plasma-assisted polishing, Adv. Mater. Res. 2010: in press.

ASPECTS OF PROBING ON THE MICRO SCALE

Edwin J.C. Bos[1]
[1]**Research and Development**
Xpress Precision Engineering B.V.
Eindhoven, The Netherlands

INTRODUCTION

There is a need for 3-dimensional characterization of components with micrometer sized features. Applications include medical implants, aspheric lenses, inkjet and diesel engine injector nozzles and micro-fluidic chips.

Coordinate measuring machines (CMMs) have long been commonly used for 3-dimensional characterization of mechanical parts. By positioning the tip of a tactile probing system in contact with the surface of a work piece the position of a measurement point in space can be obtained. By repeating this point-to-point measurement operation or by dragging the tip of the probe over the surface of the work piece, i.e. scanning, a point cloud of measured points is obtained and the dimensional characteristics of the work piece can be calculated from them.

Currently, the applicability and uncertainty of tactile measurements are limited as a result of the effects that influence the interaction between the probe tip and work piece on the micro scale.

CONTACT FORCES DURING PROBING

Contact forces consist of two parts, over travel forces and impact forces, as shown in figure 1. Impact forces F_{imp} are the result of the collision between probe tip and work piece during single point probing. During this collision the kinetic energy of the probing system changes, resulting in an impact force F_{imp}.

When contact is detected a signal is provided to the CMM to stop its motion. Over travel x_{ovt} is the distance the CMM travels between the point of initial contact and the point where its movement ends. A precision CMM typically has an over travel distance x_{ovt} of 7 µm for a 1 mm/s approach speed [1]. The over travel force F_{ovt} results from the stiffness c_t of the loop between probe tip and work piece and x_{ovt}: $F_{ovt} = x_{ovt}\, c_t$.

To prevent plastic deformation due to the impact force F_{imp} and over travel force F_{ovt}, the colliding mass and stiffness at the probe tip should be minimized. Plastic deformation of a work piece can also be prevented by reducing the approach speed [1], see table 1. The maximum admissible speed is calculated for the contact between a ruby sphere with a 0.15 mm radius and a planar aluminum work piece. Of course, a lower admissible speed increases measurement time.

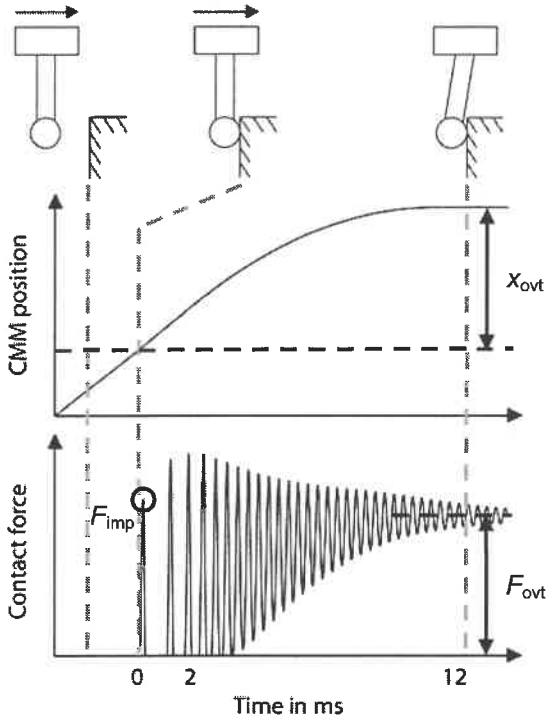

FIGURE 1. Schematic of the contact forces between probe tip and work piece during single point probing.

When probing on the micro scale, the size of the contact region approaches the grain size of the work piece material. As a result, the effective Young's modulus increases [2]. Mechanical properties at the surface of a bulk material may also be influenced by surface segregation and oxide layers. This will increase the admissible approach speed for all probes shown in table 1.

Figure 2 shows the results of a simulation of the contact force between probe tip and work piece during single point probing. It can be seen that the maximum contact force results from both the impact F_{imp} and over travel F_{ovt} forces.

Probing system	Dynamic mass	Stiffness at tip	Max. speed of collision	Max. speed for over travel	First natural frequency	Inertia noise at 0,1 m/s^2
Gannen XP	50 mg	450 N/m	0.73 mm/s	0.8 mm/s	480 Hz	11 nm
Gannen XM*	50 mg	50 N/m	0.73 mm/s	2.8 mm/s	160 Hz	0.1 µm
Zeiss F25*	500 mg	160 N/m	0.23 mm/s	1.5 mm/s	90 Hz	0.3 µm
NPL capacitive	370 mg	10 N/m	0.27 mm/s	6.4 mm/s	26 Hz	3.7 µm
Mecartex**	7000 mg	26 N/m	0.14 mm/s	3.9 mm/s	11 Hz	27 µm

TABLE 1. Some characteristics of tactile probes for measuring micro components.
* Stiffness is non-isotropic, value for xy-direction is used (z-stiffness is higher)
** An additional flexure is added between tip and suspension to reduce impact forces

From these results also a bouncing effect of the probe tip on the surface of the work piece can be observed for probes with a first natural frequency above 100 Hz. After the initial collision, the probe tip bounces of the work piece. As a result, the relative speed between tip and work piece will increase in subsequent bounces.

Without sufficient damping the maximum contact force can be a factor of 1-2 higher than the initial impact force F_{imp}.

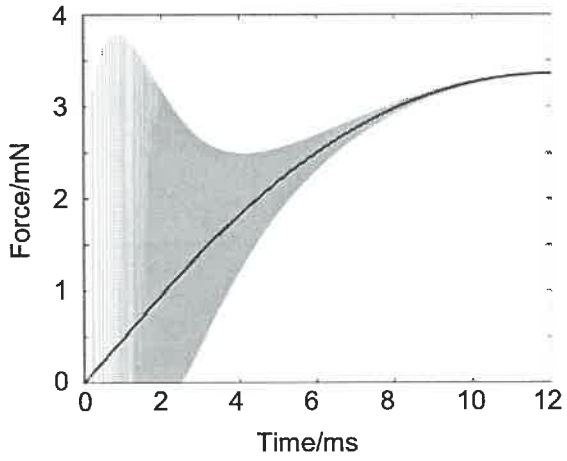

FIGURE 2. Simulation of the contact force between a Gannen XP probe tip and work piece in x-direction at an approach speed of 1 mm/s.

BUILDUP OF SURFACE FORCES

As discussed in the previous section, contact forces should be small to minimize the risk of product damage when probing micro products. When contact forces are minimized the relative importance of surface forces increases [3]. The effects of surface forces can therefore not be neglected when measuring micro components.

The effect of surface forces during a single point probing operation is measured using a plane mirror differential laser setup. In this setup, a work piece is displaced using a piezo actuator. This displacement is measured by both the probing system and the laser interferometer simultaneously.

When the object approaches the probe tip a 'snap in' effect of approximately 15 nm can be observed, as shown in figure 3. The effect is caused by forces between the tip of the probe and the object prior to contact.

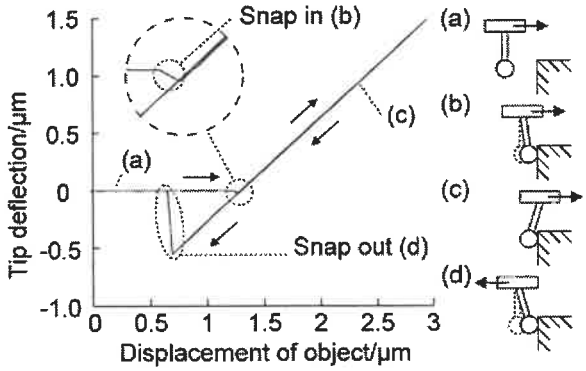

FIGURE 3. Measurement of the effects of surface forces during a single point probing operation using a Gannen XP probing system.

After contact, the movement of the object continues until the probe tip is deflected by 1.5 µm. Similar to a single point probing operation, the object is then retracted. Due to surface forces the object will stick to the work piece, as shown in figure 3. After a certain displacement, the forces due to the deformation of the probe suspension will prevail over the sum of the surface forces between the probe tip and object and a 'snap out' effect can be observed.

Figure 4 shows the results of repeated probing on a fresh work piece. It can be seen that the magnitude of the 'snap in' and 'snap out' effect increases during subsequent measurements. This is most likely caused by film mobility and an increase in localized condensation of water, which increases the thickness of the water layer at the contact position.

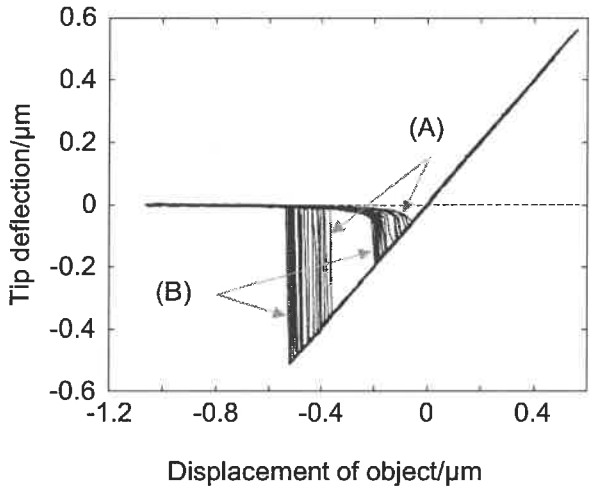

FIGURE 4. Tip deflection as a result of surface forces during 20 consecutive single point probing operations; A: first, B: last.

STICK SLIP WHEN SCANNING

The effects of static and dynamic friction between probe tip and work piece are of interest for scanning applications. The static friction coefficient, in combination with the force component F_N orthogonal to the plane, limits the smallest measuring step that can be performed.

The dynamic friction coefficient influences stick-slip during scanning. This is illustrated by equation 1, where the stick-slip distance Δy is given as a function of the coefficient of friction μ.

$$\Delta y = \mu\left(\frac{F_N}{c_t}\right) = \mu\left(\frac{\Delta x c_t + F_S}{c_t}\right) = \mu\left(\Delta x + \frac{F_S}{c_t}\right) \quad (1)$$

Here, Δx is the probe deflection during scanning, c_t is the stiffness of the probe in its tip and F_s are the surface forces between tip and work piece. It can be seen that the influence of surface forces during scanning is increased for a decreasing stiffness at the probe tip.

The release distance and stick-slip during scanning is given in table 2 for different probes and taking into account the stiffness of the stylus. Using ionized air, stylus vibrations, surface coatings, etc. [3] the magnitude of the surface force and its effect on the measurement can be reduced. As these are applicable to all systems, their effect is not taken into account in this table and the nominal value is used.

	Release distance	Stick-slip when scanning
Gannen XP	0,2 µm	0,2 µm
Gannen XM	1,7 µm	0,5 µm
Zeiss F25	0,6 µm	0,3 µm
Mecartex	3,9 µm	1,0 µm
NPL capacitive	10,0 µm	2,2 µm

TABLE 2. Release distance and stick-slip during scanning for different probes using a probe tip with a diameter of 120 µm on a 100 µm stylus.

FINITE STIFFNESS OF PROBE STYLUS

The effects of a finite stiffness of the stylus is of interest for probing systems where the stylus is a part of the metrology loop, e.g. in the Gannen probes. Here, the stiffness of the stylus is used to deform the suspension of the probing system.

By decreasing the stiffness of the stylus, a result from using thinner styli, the deformation of the suspension for a given tip displacement decreases which reduces the sensitivity of the probe.

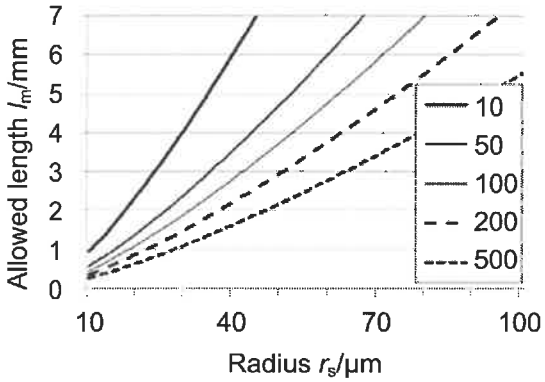

FIGURE 5. Allowed length l_m vs radius r_s of the stylus measurement part for different values of the suspension stiffness in N/m.

When the probe is calibrated after assembly, the direct effect of stylus stiffness on measurement uncertainty can be neglected as the effect is repeatable. The effect on the signal-to-noise ratio becomes apparent when the stiffness of the stylus is in the same order of magnitude as that of the probe suspension. Figure 5 shows the

admissible length as a function of the radius of the stylus, for different stiffness values. In this case, the influence on measurement uncertainty is still limited and can often be neglected.

PROBE REPEATABILITY

Probe repeatability is determined by comparing the displacement of a work piece as simultaneously measured by a laser interferometer setup, as discussed before, and the probe. From this, a graph is calculated that gives the residual between the measured displacement of probe and laser interferometer at different positions of a work piece.

Figures 6 and 7 show the residuals when probing in z- and x-direction, respectively. The probe residuals in x-, y- and z-direction, r_x, r_y and r_z, respectively, are shown as a function of work piece displacement, i.e. the graph shows the measurement behavior of the probe over its measurement range.

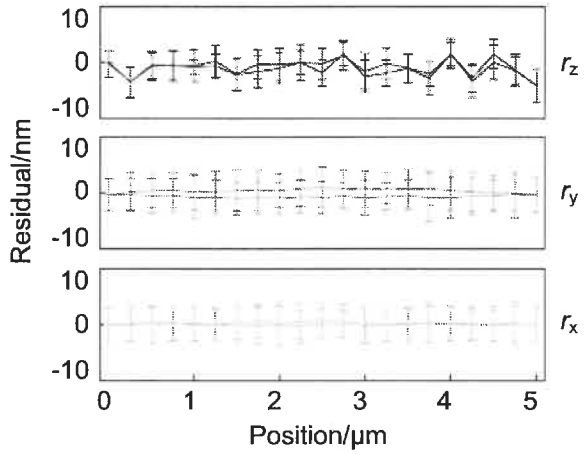

FIGURE 6. Residual with respect to the nominal displacement of a work piece in z-direction.

Over a 6 hour time frame the work piece is repeatedly translated over 5.5 µm and a total of 2050 measurements are taken at each position.

The maximum top-top variation and the standard deviation in any measurement point and for all directions are 11 nm and 2 nm, respectively. The average value and the 95% confidence interval at each measurement point are indicated in figures 6 and 7.

Finally, the residual in z-direction, r_z, when probing in x-direction, figure 7, shows a linear relation with displacement. This is the result of the suspension of the probe, based on three slender rods. When probing in x-direction the suspension rotates around the y-axis. As the stylus and probe tip are rigidly connected to the suspension, the tip rotates with the same angle.

The result is a displacement of the probe tip over the surface of the work piece, the rolling effect. As can be seen in figure 7, the displacement of the probe tip over the work piece surface due to this rolling effect is measured by the probe and does not contribute to measurement uncertainty.

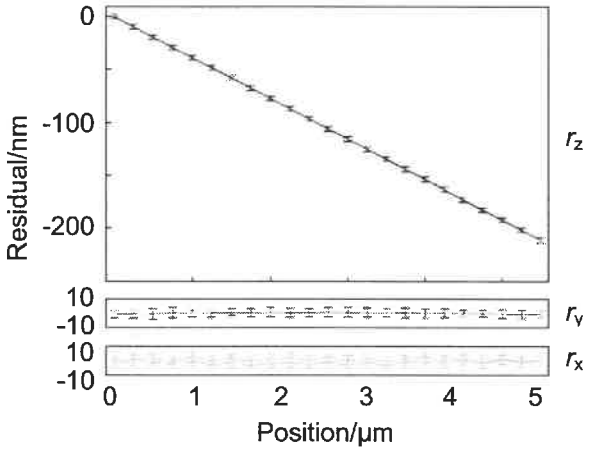

FIGURE 7. Residual with respect to the nominal displacement of a work piece in x-direction.

ACKNOWLEDGEMENT

The author gratefully acknowledges the support of prof. Piet Schellekens, the section Micro- and NanoScale Engineering (Eindhoven University of Technology) and SenterNovem (Dutch Ministry of Economic Affairs) in the framework of the program "IOP Precision Technology".

CONCLUSION

Several aspects of tactile probing on the micro scale have been discussed. To prevent plastic deformation of a work piece, probing forces should be minimized. Probing forces become so small that the influence of surface forces can no longer be neglected. Finally, finite stiffness effects of the stylus are a main limitation for tactile probes using ever smaller tips.

REFERENCES

[1] W.O. Pril, Development of High Precision Mchanical Probes for Coordinate Measuring Machines, ISBN 90-386-2654-1, PhD. Thesis, TU/e (2002).

[2] F. Meli, A. Küng, AFM investigation of surface damage caused by mechanical probing with small ruby spheres, Meas. Sc. and Techn., 18, pp. 496-502 (2007).

[3] H. van Brussel, et al., Assembly of Microsystems, Annals of the CIRP, 49/2, p.451-472 (2000).

DEVELOPMENT OF A SYSTEM FOR 3-D MICRO METROLOGY USING AN OPTICAL FIBER PROBE

Hiroshi Murakami[1], Akio Katsuki[2], Hiromichi Onikura[2], Takao Sajima[2], Norio Kawagoishi[3], and Eiji Kondo[3]
[1]Department of Mechanical Engineering, Faculty of Engineering Kyushu Sangyo University Higashi-ku, Fukuoka, Japan
[2]Department of Mechanical Engineering, Faculty of Engineering, Kyushu University
[3]Department of Mechanical Engineering, Graduate School of Science and Engineering, Kagoshima University

INTRODUCTION

In recent years, demand has increased for a method to measure the precision of micro structures of mechanical micro parts, MEMS, micro molds, optical devices, and micro holes, and the like. It is very difficult, however, to precisely measure the shape of microstructures with a large increase of length/diameter (L/D) ratio because of the difficulty of probe fabrication and sensing method with very small measuring force. Many studies have reported micro structure measurement techniques that employ a variety of probes, such as optical probes, vibroscanning probes, vibrating probes, tunneling effect probes, opto-tactile probes, fiber deflection probes, optical trapping probes, diaphragm probes [1–6], among others.

This paper presents a system for 3-D micro structure measurement using an optical fiber probe that is available as a kind of displacement measuring probe with low contact force and that has a wide measuring range. It is also easy to fabricate the probe whose stylus tip diameter is smaller than 5 μm with an aspect ratio larger than 200. The stylus of the optical fiber probe was fabricated using an acid etching technique [7]. The shaft of the stylus is not necessarily rigid in order to detect measuring force because its deflection is measured by a non-contact method. In this research, the design parameters of the optical system are determined by using a ray tracing method, and a prototype of the probing system is fabricated on trial to verify the simulation results of the ray tracing method. Also, the utility of this system is confirmed by measuring the shape of a 10 μm diameter micro hole and a 600 μm diameter ruby sphere.

MEASUREMENT PRINCIPLE

Figure 1 shows an illustration of the probing system and a photograph of the stylus shaft and the stylus tip. The fiber probe consists of a stylus shaft (optical fiber) and a stylus tip with diameters of 3 and 5 μm, respectively (Fig. 1(b)). The probing system consists of the fiber stylus, two laser diodes (LDX, LDY), and two dual-element photodiodes (PX, PY) in the X and Y directions. The fiber probe is installed perpendicular to the XY plane between the laser diodes and the dual-element photodiodes (Fig. 1(a)). The stylus shaft is irradiated by two focused laser beams emitted by two laser diodes through condenser lens in the X and Y directions. The dual-element photodiodes, PX and PY, are opposite to the laser diodes, LDX and LDY, with respect to the stylus shaft respectively. Each laser beam, that penetrates the stylus shaft, impinges upon the corresponding dual-element photodiode. The intensities detected by PX and PY are converted into voltage signals and are represented as I_{PX1}, I_{PX2}, I_{PY1}, and I_{PY2} (V).

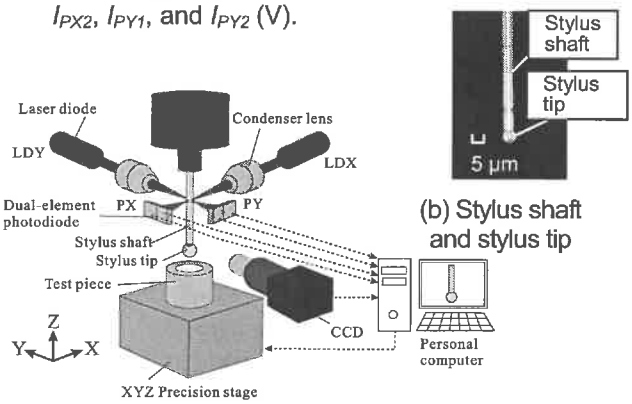

(b) Stylus shaft and stylus tip

(a) Schematic diagram of the probing system

FIGURE 1. Optical measurement system.

Figure 2 shows the principles governing the measurement process. Before the stylus tip contacts the measured plane, the light intensity measured by each element of the dual-element photodiode is equal ($I_{PX1} = I_{PX2}$, $I_{PY1} = I_{PY2}$), as shown in Figure 2(a). When the stylus tip contacts the measured plane in the X direction, the stylus shaft is displaced, and the light intensity of each element of the dual-element photodiode becomes unequal ($I_{PX1} = I_{PX2}$, $I_{PY1} > I_{PY2}$), as shown in Figure 2(b). Additionally, when the stylus tip contacts a measured plane in the Y direction, the stylus shaft is displaced, and the light intensity of each element of the dual-element photodiode becomes unequal ($I_{PX2} > I_{PX1}$, $I_{PY1} = I_{PY2}$), as shown in Figure 2(c). As a result, the contact direction and magnitude of the stylus tip can be ascertained.

The displacement of the fiber stylus is magnified by the probe shaft, which works as a rod lens. The surface of the micro structure is scanned in the XYZ direction using a precision stage, and the accuracy of the micro structure is measured by recording the coordinates of contact points and the displacement of the fiber stylus.

Output signal I_X in the X direction using I_{PY1} and I_{PY2} and output signal I_Y in the Y direction using I_{PX1} and I_{PX2} are defined by Equations (1) and (2), respectively.

$$I_X = I_{PY1} - I_{PY2} \quad (1)$$

$$I_Y = I_{PX1} - I_{PX2} \quad (2)$$

OPTICAL ANALYSIS AND EVALUATIVE EXPERIMENT

When the displacement of the fiber stylus is detected, the resolution of the system changes by the distance L_0 between the focal position of the condenser lens and the fiber stylus, the distance L_1 between the fiber stylus and the dual-element photodiode, and the diameter D of the stylus shaft. In this study, we determine the design parameters of the optical system using a ray tracing method.

First, random numbers with a Gaussian distribution are generated using the Box–Muller method, and rays based on this distribution are radiated from the condenser lens. The radiation intensity distribution of this laser beams is assumed to be the Gaussian distribution. For this simulation of ray tracing method, the intensities detected by each photodiode are defined as relative intensities for all radiation rays and are expressed as I_X (%) and I_Y (%). The rays are then traced through the optical system, and the intensity expected at each

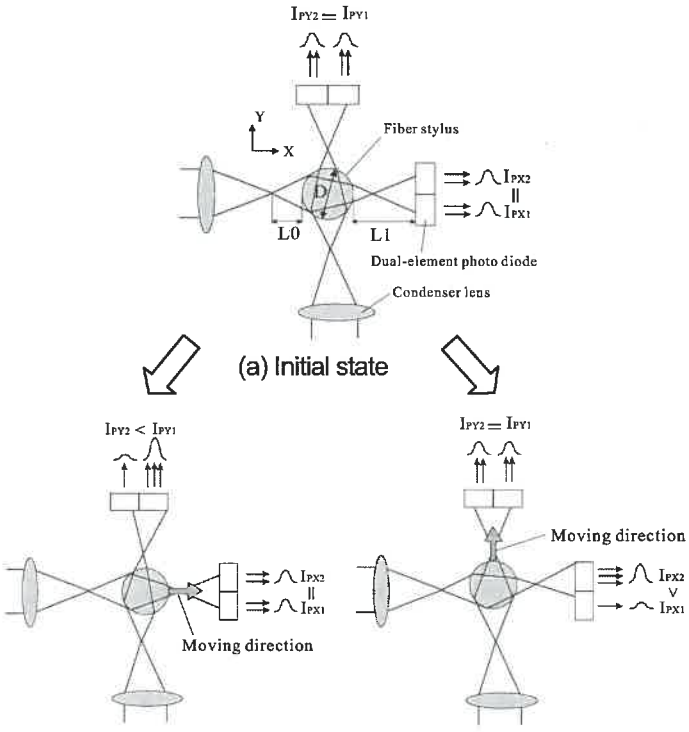

FIGURE 2. Measurement principle.

TABLE 1. Simulation conditions.

Laser source	Wavelength: 650 nm
Stylus shaft diameter D	3 μm
Distance between planes 0 and 1 L_0	10 μm
Distance between planes 2 and 3 L_1	40 mm
Numerical aperture of the condenser lens	0.13
Displacement X	−7.0 ~ 7.0 μm
Laser beam diameter D_S	10 μm

photodiode is calculated. Table 1 lists the simulation conditions.

Figure 3 shows a graphic display of the ray tracing result when the stylus shaft is displaced toward Y =−0.5 μm.

Also, Figures 4 and 5 show the overlapping display of ray-tracing simulation and

experimental results in case that the stylus tip displacement from -7 to +7 μm in the X direction. In this graph, the theoretical value is converted into the displacement of the stylus tip. The stylus length is 1 mm and the distance between the stylus tip and the cross section of the stylus shaft irradiated by the laser beam is 0.5 mm. Therefore, the displacement of the stylus tip is magnified to about 3 times that of a diameter of the stylus shaft irradiated by the laser beam when the stylus shaft is regarded as the cantilever beam of rigid support.
The theoretical value agrees with the experimental value. Therefore, the utility of this simulation is confirmed.

EVALUATION OF THE MEASUREMENT RESOLUTION

An experiment is carried out to evaluate the measurement resolution of the fiber stylus in the X and Y directions. The changes of an output signal I_X in the X direction are examined when the stylus tip is displaced by 10-nm step in the X direction. Figure 6 shows the output voltage I_X which is induced by the displacement of 10 nm step feeding of the stage toward +X direction. The horizontal axis shows the measurement time, and the vertical axis shows the changes in an output signal I_X in the X direction. The voltage change I_D ($V_{P\text{-}P}$) is caused by various noises. However, it is possible to distinguish the 10 nm step, which shows that the measurement resolution of this system is 10 nm. In order to improve the measurement resolution, it is necessary to reduce the noise, develop the signal processing method, and use a high-power laser diode.

MEASUREMENT EXAMPLES OF MICRO HOLE (ϕ 10 μm) AND RUBY SPHERE (ϕ 600 μm)

Measuring experiments on a micro hole and a ruby sphere were performed to demonstrate the applicability of the optical fiber probe.
Figure 7 shows a photograph of the ϕ 10 μm micro hole while it is measured by a ϕ 5 μm diameter stylus tip. The hole shape was ascertained by scanning the hole wall at contact angle intervals of 10°. The hole wall was displaced in the X and Y directions by the XYZ precision piezoelectric stage to maintain a state in which output signal $I = \sqrt{I_X^2 + I_Y^2}$ was equal to the threshold value; the coordinates of the stage were then recorded, and the hole wall was displaced by 5 μm in the –Z direction. This

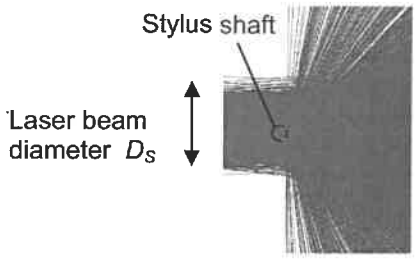

FIGURE 3. Graphic display of ray tracing (Movement of the stylus shaft toward Y=-0.5 μm).

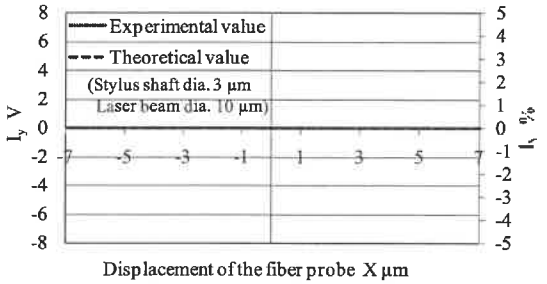

FIGURE 4. Variation of output voltage I_Y with X displacement of the stylus tip (L_1: 40 mm).

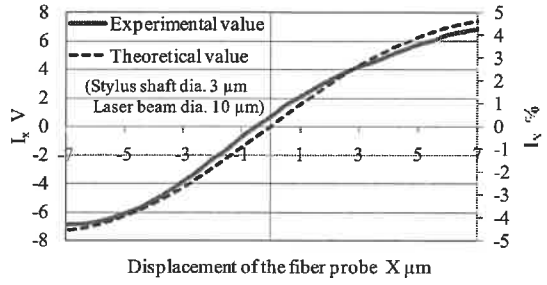

FIGURE 5. Variation of output voltage I_X with X displacement of the stylus tip (L_1: 40 mm).

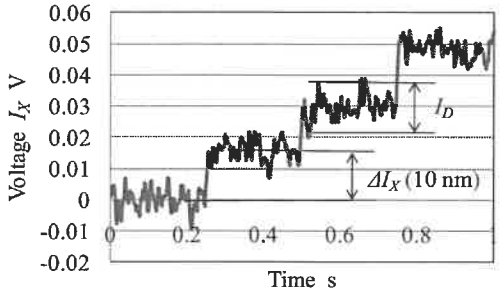

FIGURE 6. Variation of output voltage I_X induced by displacement of step feeding by 10 nm.

operation was repeatedly carried out, to ascertain the shape of the micro hole. The resolution of the stage in X and Y directions is 1 nm. The hole wall fixed by the stage was fed at a rate of 1 μm/s. The measured length was 40 μm. Figure 8 shows the results of form measurement of the micro hole. The maximum value of the hole diameter in the measuring range is 10.45 μm.

Figure 9 shows a photograph of the ϕ 600 μm ruby sphere while it is measured by a S ϕ 5 μm diameter stylus tip. The measuring area was 300 × 300 × 100 μm for the X, Y and Z directions. When the stylus tip comes into contact with a measured plane in Z direction, the stylus shaft is buckled and then deflected. This deflection is measured. The ruby sphere was displaced in the +Z direction by the XYZ precision stage to maintain a state in which output signal $I = \sqrt{I_X^2 + I_Y^2}$ was equal to the threshold value, the coordinates of the stage were then recorded, and the ruby sphere was moved to the initial position. The resolution of the stage in Z direction is 10 nm. The ruby sphere fixed by the stage was fed at a rate of 1 μm/s in the Z direction. Then, the ruby sphere was displaced by 30 μm in the X or Y direction. This operation was carried out repeatedly, to ascertain the shape of the ruby sphere. The total number of probing points was 100. Figure 10 shows the measurement result. The diameter of the best-fit sphere using the least square method is 598.28 μm.

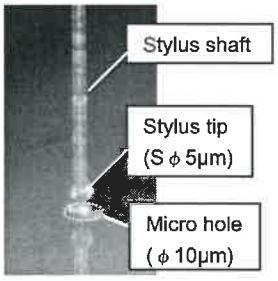

FIGURE 7. Photograph of a ϕ 10 μm micro hole and a S ϕ 5 μm diameter stylus tip.

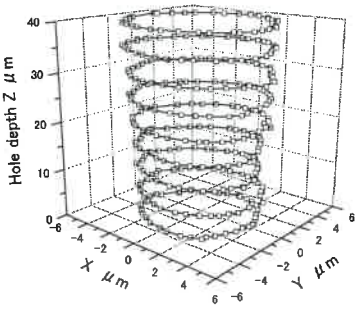

FIGURE 8. Shape of the ϕ 10 μm micro hole measured by the measurement system.

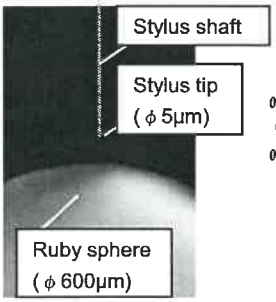

FIGURE 9. Photograph of a ϕ 600 μm ruby sphere and a S ϕ 5 μm diameter stylus tip.

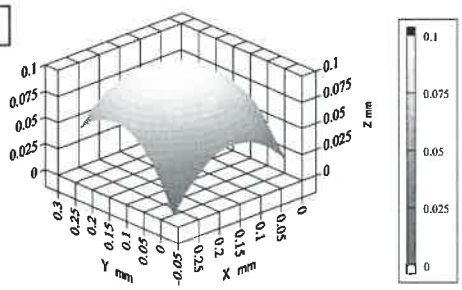

FIGURE 10. Shape of the ϕ 600 μm ruby sphere measured by the measurement system.

ACKNOWLEDGMENT

The authors would like to thank Dr. Osamu Ohnishi from the Kyushu University for his technical support in the experiments.

This work was supported in part by a Industrial Technology Research Grant Program in 2009 from New Energy and Industrial Technology Development Organization (NEDO) of Japan.

CONCLUSIONS

The system for measuring a 3-D micro structure using an optical fiber probe is developed. The design parameters of this system are determined by ray tracing method. Then, after a trial measurement system was fabricated, the measurement accuracy was examined by using basic experimental apparatus. As a result, the following are our result.

1. The design parameters of the optical system are determined by ray tracing method.
2. The resolution of the measurement system is approximately 10 nm.
3. The utility of this system is confirmed by measuring the shape of a 10 μm diameter micro hole and a 600 μm diameter ruby sphere.

REFERENCES

[1] Hidaka K. et al., CIRP Annals, Vol.59, (2010) 517-520.

[2] Liebrich T. et al., CIRP Annals, Vol.59, (2010) 513-516.

[3] Michihata M. et al., CIRP Annals, Vol.57, (2008) 493-496.

[4] Muralikrishnan B. et al., Precision Engineering, Vol.30, (2006)154-164.

[5] Bauza M. B. et al., Review of Scientific Instruments, Vol.76, (2005) 095112-1-095112-8.

[6] Schwenke H. et al., CIRP Annals, Vol.50, No.1, (2001)361-364.

[7] Murakami H. et al., Journal of Advanced Mechanical Design, Systems, and Manufacturing, in press.

DIMENSIONAL MEASUREMENTS OF ULTRA DELICATE MATERIALS USING MICROMETROLOGY TACTILE SENSING

Marcin B. Bauza[1], Shane C. Woody[1], Richard M. Seugling[2], Stuart T. Smith[3]
[1]InsituTec Inc.
Charlotte, NC, USA
[2]Engineering Technologies Division - Precision Systems & Manufacturing
Lawrence Livermore National Laboratory
Livermore, CA, USA
[3]Center for Precision Metrology
University of North Carolina at Charlotte
Charlotte, NC, USA

INTRODUCTION

Quality inspection of microscale parts is very challenging. The need to measure smaller feature sizes, higher aspect ratio features such as side walls, and more complex shapes such as free-form engineered surfaces is becoming prevalent. Inspection tools for microscale parts typically fall into two categories, non-contact and contact based metrology. Non-contact tools are generally optical based technologies such as white light interferometry or confocal microscopy. A distinct advantage with optical metrology is the ability to rapidly measure parts with high throughput as well as avoiding touching the part. However, optical methods have many drawbacks including sensitivity to ambient conditions such as lighting, and detailed understanding of the refractive index of the specific material. Additionally, steep curvatures, narrow microscale features, and transparent or highly reflective parts are difficult to measure optically.

Contact based sensing, generally refers to tactile sensors. A survey of the microscale probing industry reveals that probes are designed in a wide variety of tip sizes ranging from 20-250 µm diameter, contact forces are typically quoted as 1-500 µN and probe stiffnesses specified from 10-500 N/m [1]. Most microscale probing systems in this scale produce contact forces that have high Hertzian contact stresses that elastically or plastically deform the measured surface [2]. As a consequence, the characterization of both 3D surface topography and dimensional features of components made of delicate materials and shapes remains a significant challenge.

METROLOGY SENSOR

The aim of this presentation is to discuss dimensional metrology of ultra delicate, thin and complex form components using standing wave microscale probes [3,4,5]. The sensor technology comprises a small microscale fiber which is 7 µm in diameter and up to 3.5 mm in length providing an aspect ratio of 500:1. The fiber is vibrated at 32 kHz using a quartz crystal oscillator which produces a pronounced mechanical standing wave in the fiber. The contact force calculated based on beam bending theory is <50 nN. During scanning, the probe has two scanning modes of operation referred to as near-field scanning (out of contact) and contact scanning, FIGURE 1.

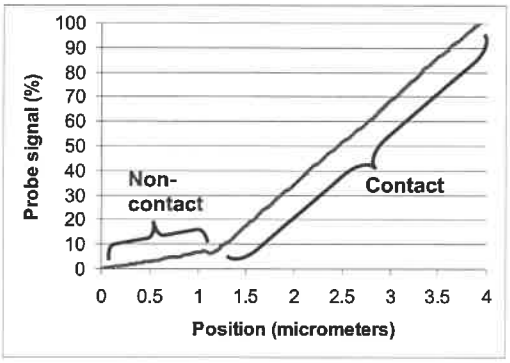

FIGURE 1. Example of probe output signal as a metallic surface approaches and contact the standing wave fiber tip.

EXPERIMENTAL APPARATUS

The instrument used during the experiments presented in this work comprises an engineered gauge head that is rigidly attached to a Moore 1.5 machine frame as shown in FIGURE 2. The gauge head is composed of a precision spindle and scanning head which are used to position

the microscale standing wave probes. The measured components are positioned with an Aerotech™ FiberMax 5 axis positioning platform. The *X, Y* and *Z axes* are located on the Moore 1.5 and subsequently used only for coarse alignment. Once the fiber probe and workpiece are positioned within the correct working volume of the FiberMax, the stages on the Moore 1.5 are locked and are not used during the measurement process.

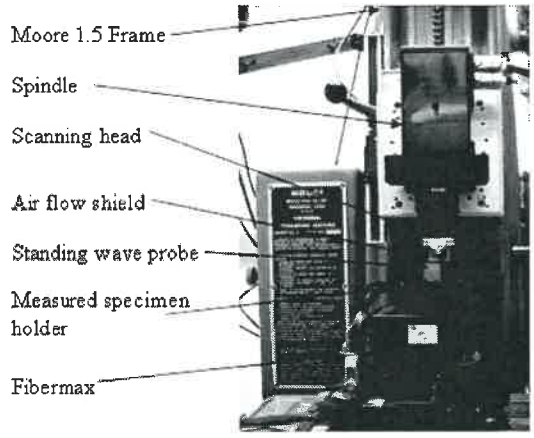

FIGURE 2. Test bed used during experiments.

EXPERIMENTAL MEASUREMENTS

The case studies that will be discussed in detail include thin foils, aerogel foams and miniature optic lenses.

Delicate foam - aerogel

Aerogels represent one of the most challenging and delicate materials to measure. Optical methods cannot measure the material because the reflectivity at normal incidence is very low. While other techniques such as grazing incidence interferometry for surface measurements and transmission based techniques maybe realized for some portion of the overall required part metrology, they are limited to specific geometries and require a detailed understanding of the refractive index of the specific material. The combination of density variation throughout the bulk coupled with complex geometries inhibits the use of most optical techniques.

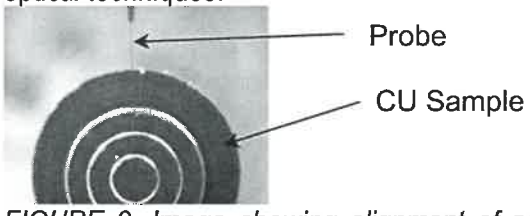

FIGURE 3. Image showing alignment of probe and Cu sample during measurement.

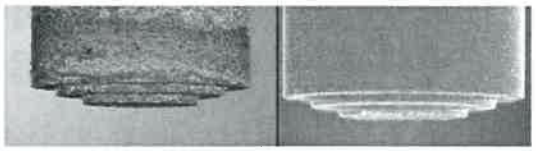

FIGURE 4. Image of the copper foam 5% full density (left) and SiO_2 55 mg/cc foam (right).

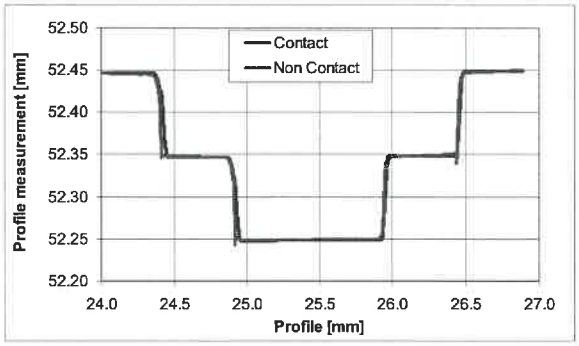

FIGURE 5. Measurement of the copper sample using contact and non contact method.

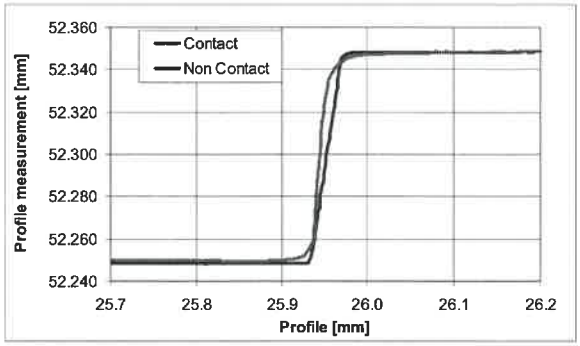

FIGURE 6. Zoom in on the step measured using contact and non-contact method.

A study was undertaken to assess the capability of employing standing wave probes for scanning profiles of these materials. Three cylindrical materials that included copper, 5% copper foam and SiO_2 55 mg/cc foam were diamond turned with 100 micrometer steps, (FIGURE 3, 4). The solid copper material was scanned in both non-contact and contact mode (FIGURE 5, 6). Steps were calculated from this data using a least square method to determine the heights. The results reveal an approximately 1 µm discrepancy between those two methods with 56 nm standard deviation for contact and 229 nm standard deviation for non-contact measurement as shown in TABLE 1. Next, the two aerogel samples were both measured in contact and non-contact modes. The contact mode damaged the aerogel surfaces of the sample but the non-contact mode demonstrated sub micron repeatability (FIGURE 7, 8) and TABLE 1. It is important to mention the contact mode has not

been shown to damage other soft materials such as gold deposition and plastics. Aerogel foams are the only known instance in which damage appears to occur when contacting the part.

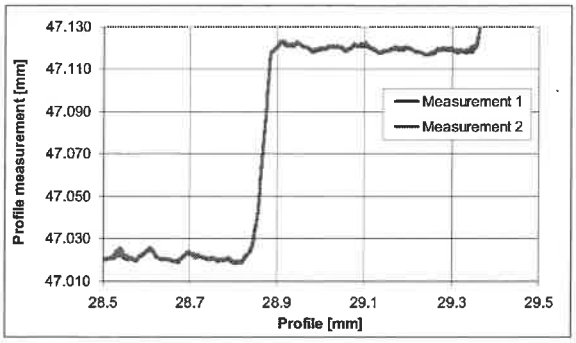

FIGURE 7. A Step measured twice for the CU foam using the non-contact method.

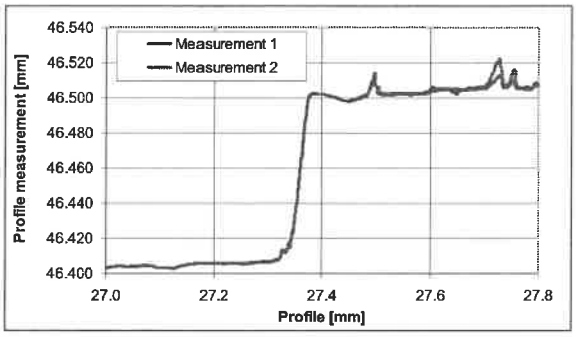

FIGURE 8. A step measured twice for the SiO_2 foam using the non-contact method.

TABLE 1. Calculated step heights based on least squares curve fit

	SiO_2	CU foam	CU - contact mode	CU - non contact mode
Average step (micrometers)	97.872	98.740	99.561	98.599
Standard Deviation based on 3 measurements (micrometers)	0.416	0.110	0.056	0.229

Thin foil

Dimensional metrology of thin foils of less than 100 µm thickness is another challenge in tactile sensing due to the ability to elastically deflect during the measurement process. A case study was undertaken to measure a 60 µm nominal thick foil with a manufactured sinusoidal pattern of 2 µm amplitude and 50 µm wavelength (FIGURE 9, 10). Additionally, the profile was scanned above the impression on both sides of the foil part by rotating the probe 180 degrees for each scan. The probe tip offset was calibrated by scanning on either side of a XXX 450 micrometer gauge block. FIGURE 11 shows the thickness variation as measured across one height of the foil is. The results indicate the outer edges are thinner compared to the center. This could be due to the manufacturing process because the part was polished. In general, despite the thin structure there was no noticeable bending of the part during the measurement.

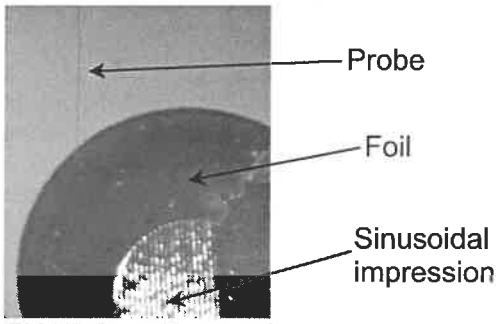

FIGURE 9. Image of thin foil 63 µm nominal thickness and sinusoidal impression.

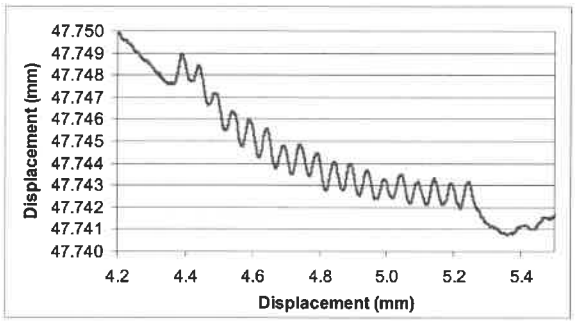

FIGURE 10. Measurement of the sinusoidal impression with 2 µm nominal amplitude.

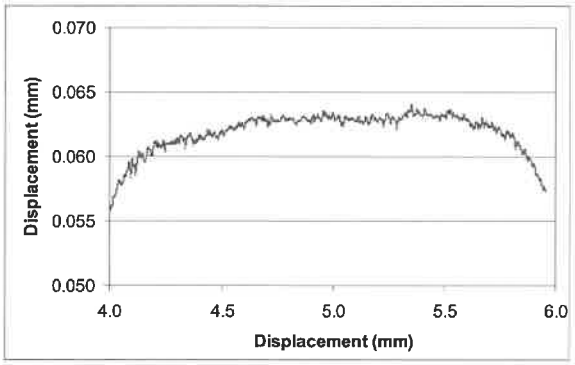

FIGURE 11. Measurement of thickness variation across the polished thin foil.

Miniature optics

The metrology of optics and free form surfaces is dominated by white light interferometry. General interferometry methods are very

accurate when measuring deviations from a curved surface. However, these instruments have difficulty measuring the radius of curvature better than 1-5 micrometer. A low contact force profilometer could offer the ability to measure highly accurate radius of curvatures assuming the stylus forces are low enough to not damage the surface while the interferometry tool could still yield accurate measurements of the deviations from a curved surface. A short study is currently underway to measure miniature optics using the standing wave probes. A plano-convex optic with specified radius of curvature of 3.4 mm and a diameter of 2 mm was used for this study. The probe was scanned across the center of the optic and two scans are overlaid, (FIGURE 12, 13). The calculated radius of curvature was determined to be 3.411 µm. Further studies will compare results with optical methods as well as perform measurements on smaller scale optics.

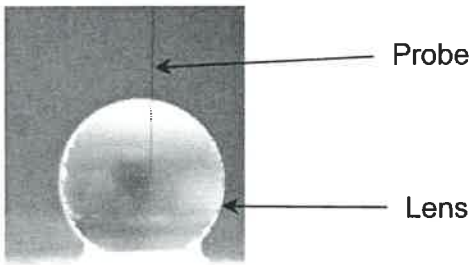

FIGURE 12. Image of miniature lens during measurement.

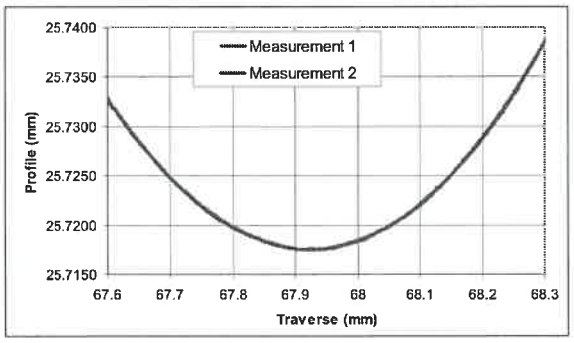

FIGURE 13. Two consecutive measurements of miniature lens with 3.4 mm nominal radius.

CURENT WORK

Most of the work to date has been performed with a 5 axis motion platform that was not designed for metrology applications and introduces measurement uncertainties that are difficult to predict. Current work is now ongoing to interface the AccuSurf gauge head and standing wave probing system with a Zeiss scanning CMM, FIGURE 14, to provide a unique metrology platform capable of measuring delicate materials and thin foils as well as high aspect ratio features such as holes channels and microscale features of complex parts. As a result higher repeatability of dimensional measurements along with surface texture and form measurements will be achievable.

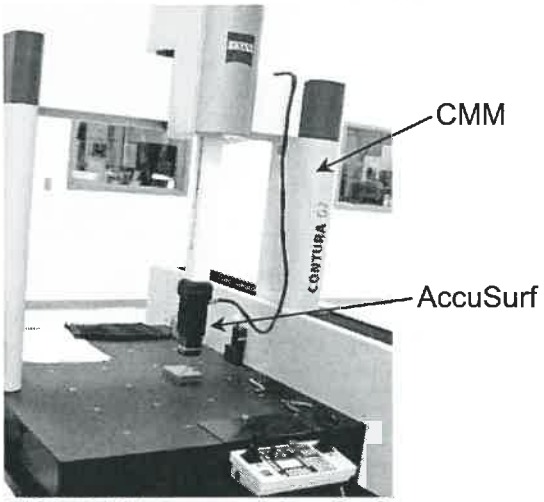

FIGURE 14. Image of AccuSurf being integrated to Zeiss scanning CMM.

ACKNOWLEDGMENTS

This work was performed in part under the auspices of the U.S. Department of Energy by Lawrence Livermore National Laboratory (LLNL-PROC-439393) under Contract DE-AC52-07NA27344 and in part supported by National Science Foundation under Grant No. 0924000.

REFERENCES

[1] Weckenmann A., Estler T., Peggs G., McMurtry D. Probing Systems in Dimensional Metrology. Annals of the CIRP

[2] Bhushan B. Nanoscale tribophysics and tribomechanics Wear 225-229 (1999) 465-492.

[3] Bauza M.B., Hocken R.J., Smith S.T., Woody S.C., Development of a virtual probe tip with an application to high aspect ratio microscale features. Rev. Sci. Instrum. 76, 095112 (2005)

[4] Bauza M.B., Woody S.C., Woody B.A., Smith S.T. Surface profilometry of high aspect ratio features. WEAR, 2010.03.028.

[5] Bauza M.B., Woody S. C., Smith S. T., Seugling R. M., Darnell I. M., Florando J. N., Microscale metrology using standing wave probes, Proc. of 23rd ASPE, 2008.

MICROPROBE METROLOGY STUDY: LATEST RESULTS

Raymond H. Yang[1], Stuart T. Smith[1], Borja de la Maza[2]
[1]Center for Precision Metrology
University of North Carolina at Charlotte
Charlotte, NC, USA
[2]Asociacion Innovalia, Spain

OVERVIEW

This abstract presents continuing work on an evaluation study of recently developed microprobe systems integrated into an ultra-precision, eight-axis motion control stage. As of writing, mechanical mounts and hardware interfacing for four different probes is complete. As a first step in this study, measured contact point deviations in one direction are used as a measure of repeatability. A gage block artifact has been produced and multiple measurements of surface separation are used to determine deviations of dimensional measurement for the simplest possible case. The next step is to extend this to dimensional measurement of the artifact geometry with probes used in 1D mode. A scan algorithm has been developed and first results will be shown. Probes to be studied include; 1D UNCC, Triskelion IBS, PTB ACP and Insitutec MicroTouch.

STAGE SYSTEM

A dynamic ultra-precision positioning machine for nanoscale engineering has been developed.

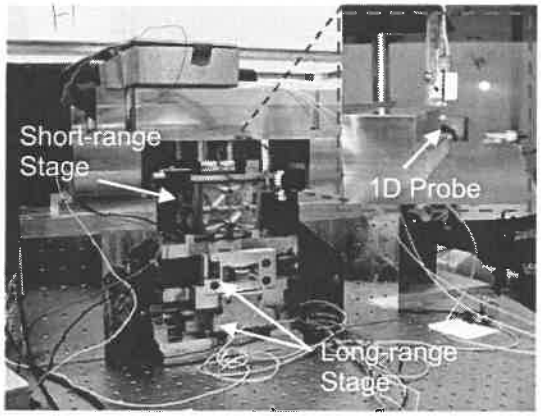

FIGURE 1: Stage system comprising of a 2 DOF long range stage carrying a 6 DOF short range flexure-based actuator stage and 1D probe system.Inset shows probe in-situ.

The complete system comprises of two orthogonal long range translation stage carrying a 6 DOF short range stage. Each of the long

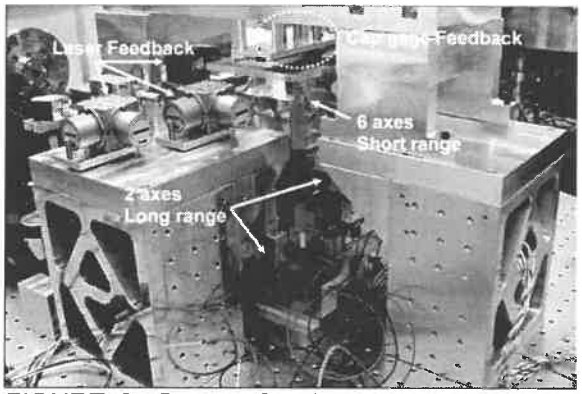

FIGURE 2: Current feedbacks include 3 laser positioning signals and a nest of 3 capacitance gages measuring in the vertical plane.

range stage can traverse 50 mm while the short range stage can provide up to 17 micrometers of linear positioning and 160 x 10^{-6} radians of angular motion [1]. The main operation of the short range stage is to compensate errors generated by the long range stage during traverses. FIGURE 1 shows the positioning stage and a blow-up view of the one dimensional probe. Currently, positioning of the *x*- and *y*-axis along with angular motion about the *z*-axis is monitored by laser interferometers, while positioning of the *z*-axis and angular motion of *x*- and *y-axis* are monitored by 3 capacitance gages. FIGURE 2 shows the back view of the stage system with the two different measurement systems. The probe system is mounted on the metrology frame and drops vertically down to the working platform. Note that in this configuration, the work piece is moving and the probe is stationary. A full eight axis control of the measuring machine was achieved by combining previous work on controlling a single axis system with recent studies on

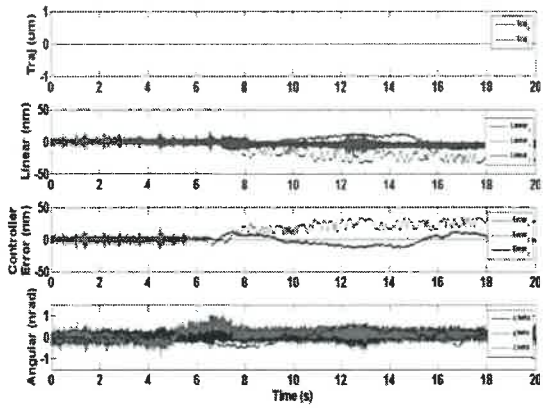

FIGURE 3: Graphs show demand (top), displacement readings, linear controller error and angular measurement (bottom).

cascaded controller strategies [2]. As a measure of full 8-axis capability, a 'hold' demand over an extended period was monitored. FIGURE 3 shows a time period of 20 seconds where the controller was switched 'off' after 6 seconds.

1D PROBE

As a first step to integrate a probe system with the ultra-precision positioning stage, a 1D capacitance base probe has been developed and has been used to measure a common reference artifact. FIGURE 4 shows a solid model and a photograph of the 1D cap probe. This comprises a cantilever beam that is etched ¾ along its length. Two glass plates with patterned electrodes are clamped either side of this beam so that the ¾ etched length can move freely in the gaps determined by etching depth. The two electrodes on the glass plates form a differential capacitor with the beam as the moving electrode. A sphere attached to the free end of the beam forms the contact probe tip.

The reference artifact used for these measurements is constructed from three steel commercial gage blocks wrung together with the

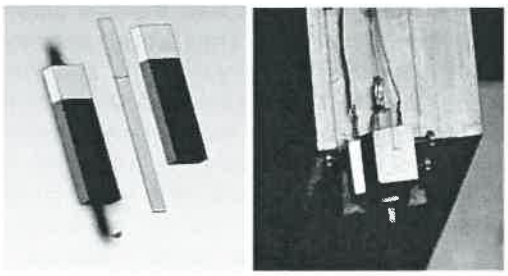

FIGURE 4. (left) Exploded solid model of 1D probe (right) Photo of 1D probe mount.

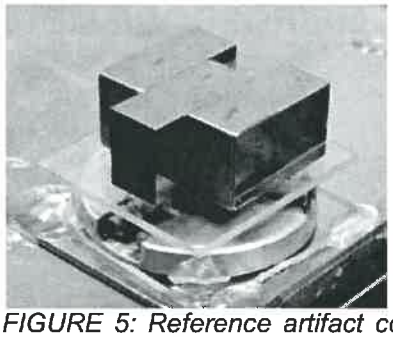

FIGURE 5: Reference artifact constructed from three Mitutoyo gage blocks ASME Grade 0.

central block offset as shown in FIGURE 5.

A first test measurement of the 1D probe was carried out to determined system measurement repeatability. This test was performed by touching the probe to the inner surface of the two outer gage blocks in the gap created by the offset block. In FIGURE 6, a sinusoidal translation of the artifact is applied so that the probe cyclically comes in contact with gage blocks 1 and 3. The red oval in FIGURE 6 highlights data at one of the contact regions. A closer analysis reveals what is happening as the probe comes in contact with the gage block surface. FIGURE 7 shows a close up view of what is happening in the contact region. For this system, the probe is stationary and the artifact is moving. A number of regions can be identify in this plot, these are; a) Artifact approaching probe, b) Artifact contacts with probe, c) Artifact continues moving in probe direction, probe is being deflected, d) Artifact stops moving, probe has reach maximum deflection point, e) Artifact

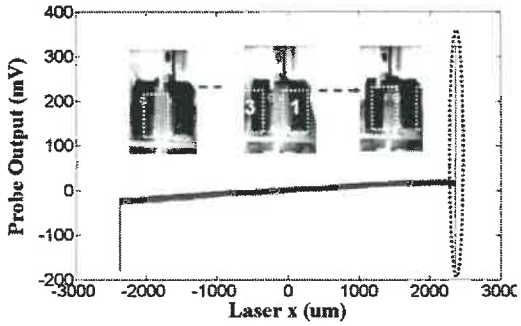

FIGURE 6: A sinusoidal input signal is applied at position (0,0) in the x direction until probe is in contact with Gageblock 1 and 3. The left and right probe voltages represents contact of GB1 and GB3. A total of 23 cycles is collected over 70 minutes.

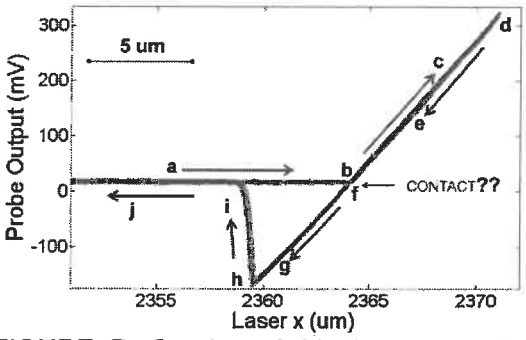

FIGURE 7: Overlay of 23 data sets where gage block artifact moves to contact with probe for one side.

moving in opposite direction(retracting), but still in contact f) Position where surface first contacts probe, surface adhesion forces keep the probe in contact, g) Adhesion forces keep probe in contact, deflecting probe in opposite direction, h) Adhesion forces at its maximum, i) Adhesion forces broken, probe returns to null position, j) Artifact continues moving away from probe.

A major issue at this time is defining a contact point based on a continuous stream of data during contact. From FIGURE 7, during the approach of the probe towards the specimen, there are two clear sets of data; one region being the horizontal data set from a to b (probe prior to contact), the second region being b to c (probe in contact). It seems reasonable as one definition of contact to use the point of intersection between two straight line fits of the data in these two regions. Other definition of probe contact point can be considered. FIGURE 8 shows the deviation of these contact measurements for contacts on one of the

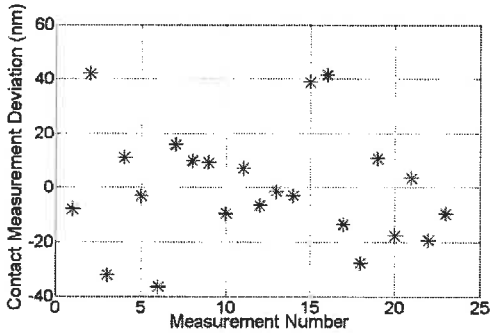

FIGURE 8: Deviation of 23 contact measurements at 0.005 Hz on the same surface from the same direction about X position of 2364212 nm, with a standard deviation of 23 nm.

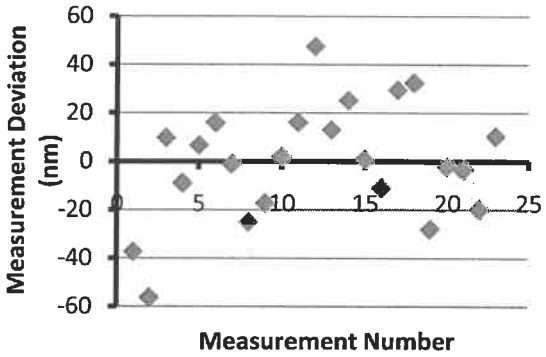

FIGURE 9: Deviation of measurements between the two inside gage block surfaces with a standard deviation of 24 nm.

surfaces. FIGURE 9 shows the deviation of measurements of successive separations between the two inside gage block surfaces from which a standard deviation of 24 nm was found.

TRISKELION PROBE

A second probe that is under evaluation is the Triskelion Probe produced by the combined efforts of IBS Precision Engineering and Lion Precision. FIGURE 10 shows a picture of the Triskelion probe mounted into the measuring machine. This probe has a ruby spherical probe tip of diameter 500 micrometers attached to a tungsten carbide shank of length 8.5 mm. It should be noted that, in contrast to the previous probe, this is a 3D isotropic probe. While the mounting and hardware interfacing has been completed. Repeatability studies and full artifact scan algorithms have been implemented for this and the 1D probe mention in the previous

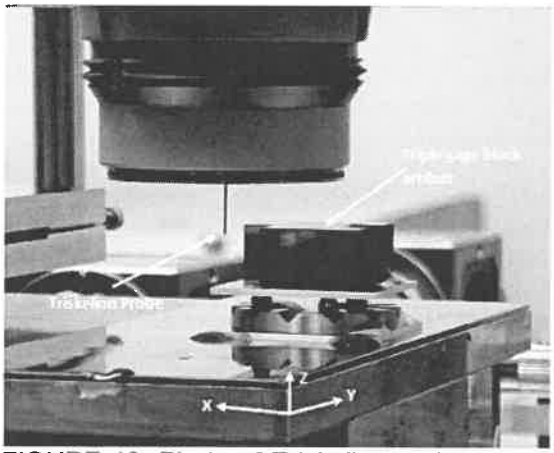

FIGURE 10: Photo of Triskelion probe mounted in operation.

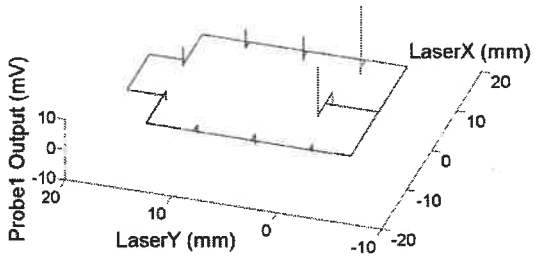

FIGURE 11: Raw data cloud of laser reading of X, Y and probe1 data during three complete cycles around the artifact. The positive and negative probe output represents different contact direction.

section. This study is still ongoing, as an example of the data set corresponding to a full scan of the artifact FIGURE 11 shows a measured data set obtained from x and y laser interferometer displacement of the stage and the correspond output of one of the capacitance sensors of the Triskelion probe.

CONCLUSIONS

A full 8 axis control of the displacement platform has been demonstrated. Mechanical mounting and hardware interfacing for different probes to be used as part of a probe performance evaluation study is complete. Early measurements using our in-house developed 1D probe have shown repeatability values both of around 20 nanometers for repeated contacts at the same point on a surface as well as measurement deviations of dimension between two surfaces on a gage block artifact. These deviations have many contributing factors and it is not easy to separate individual effects at this level. Significant sources of error are considered to be thermal variations that disturb components of the measurement loop, ambient variations effecting interferometer measurement and contact interactions, ground borne and airborne vibrations, particulate and environmental surface contamination, algorithms for the extraction of contact point location from complex contact interaction signals and contact interaction force variations both from point to point as well as at the same location over time. Efforts to reduce these effects through compensation, reduction and environmental control are ongoing.

In addition to implementation of the machine controls, we have implemented an algorithm to scan multiple points around the artifact obtained measurements using the 1D and Triskelion probe. Currently, we are post processing data and developing algorithms to extract contact point data from signals provided by these different probes.

ACKNOWLEDGEMENTS

The authors would like to thank the center for precision metrology, CPM affiliates for funding the study and IBS precision engineering for loaning the probe and equipments.

REFERENCES

[1] Eric S. Buice, Implementation of a dynamic positioning machine for nano-scale engineering, PH.D thesis dissertation, University of North Carolina at Charlotte

[2] Teo C.S., Yang H., Smith S.T., Hocken R.J., Buice E.S. and Otten D., 2009, Controller strategies for an Ultra-high Precision Stage, Proc. EUSPEN, P2.13-220 Vol[1].

ISARA 400: ENABLING ULTRA-PRECISION COORDINATE METROLOGY FOR LARGE PARTS

Rilpho Donker, Ivo Widdershoven, Derk Brouns, Michel Morel and Henny Spaan
IBS Precision Engineering
Eindhoven, The Netherlands

INTRODUCTION

IBS Precision Engineering has designed and realized a new ultra-precision coordinate measuring machine (CMM) with an unprecedented ratio of measurement volume vs. measurement accuracy. The aim of this CMM, the "Isara 400" is to enable ultra-precison 3D coordinate metrology for large products. The design details and the realization of this machine were presented at the ASPE annual meeting 2009 [1]. The current work presents the fully realized machine. Test results will be presented, such as the performance of the metrology frame sub-assembly, as well as the integration of the probe system and the first measurement results obtained with the fully functional system.

ISARA 400 DESIGN AND REALIZATION

Isara 400 concept

The metrology concept of the Isara 400 CMM fulfills the "Abbe principle" [2] for all three translation axes. Three plane-mirror laser interferometers measure the axes positions; the interferometers each measure against the sides of a Zerodur mirror table, on which the work piece is mounted. The interferometers are mounted in a single body metrology frame, which also holds the probe system (see figure 1).

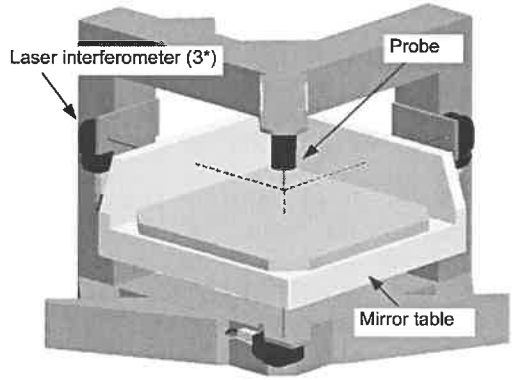

FIGURE 1. 3D Abbe principle as applied in the Isara 400 CMM

The laser beams are aligned to the probe tip and their mutual alignment does not change with axes movements, thus fulfilling the Abbe principle in 3D within the measuring volume of 400 x 400 x 100 mm. The expected measuring uncertainty is 45 nm per axis and 100 nm in 3D, within the complete measuring volume.
In the configuration of the translation axes, a machine concept was chosen in which the variable product mass does not need to be moved vertically. The product is mounted on the mirror table, which moves only in X- and Y-direction over a granite plate, guided by air bearings. The complete metrology frame moves in Z-direction, with guiding provided by air bearings against a vertical granite surface.
Figure 2 shows a complete overview of the Isara 400 CMM. A short overview of the design of several key components is given in the next sections.

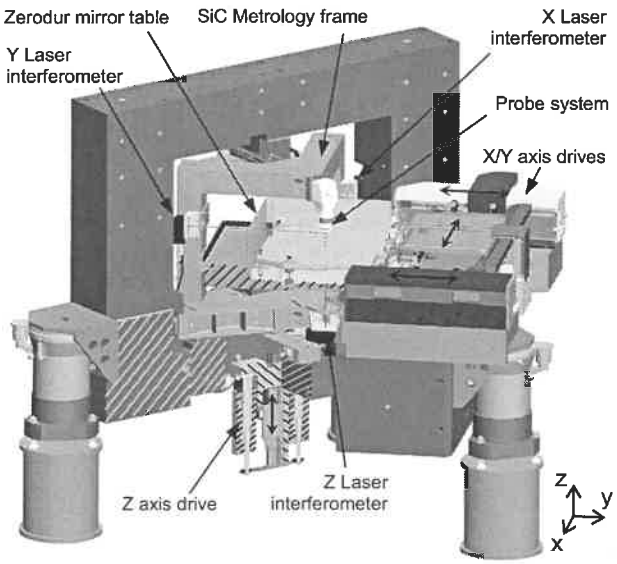

FIGURE 2. Design overview of the Isara 400.

Mirror table

The mirror table of the Isara 400 is a monolithic Zerodur part with three reflective sides. An additional Silicon Carbide (SiC) product table is used as an interface between product and mirror table (figure 3).

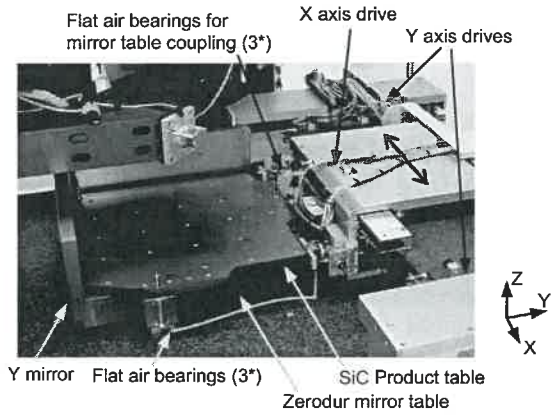

FIGURE 3. Realized assembly of floating table and X/Y-axis drives with Zerodur mirror table.

The mirror table is supported by three flat air bearings, whose preload is provided by the weight of the mirror table assembly with product. The coupling between the floating mirror table and the X-carriage must define three degrees of freedom (X, Y and Rz) and allow for differences in thermal expansion. This coupling is also realized with three flat air bearings [1].

Metrology frame

The function of the metrology frame, shown in figure 4, must maintain the mutual position and alignment of the probe and the three laser interferometers with high stability. The metrology frame was designed as an assembly of hollow beams of Silicon Carbide (SiC), resulting in a structure which is both stiff and lightweight, while also providing good thermal stability.

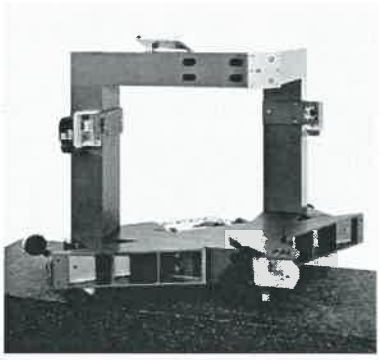

FIGURE 4. Realized SiC metrology frame.

The metrology frame is statically determined in six degrees of freedom by means of five flat air bearings to the granite base and a strut joint to the Z-drive. All bearings are preloaded with flat air bearings on the opposite side. As the machine is a multi- probe machine, it contains a kinematic probe mount for a quick and reproducible exchange of probes.

The Z-drive moves the metrology frame in vertical direction. It is placed below the metrology frame and connects with a strut directly through the centre of mass (see figure 2).

The Z-drive contains an air bearing guide for the linear motor, with an integrated weight compensation system. The heat generation of this drive is thus very low, as the linear motor does not need to counteract the weight of the metrology frame. The realized Z-drive has been separately tested and has been mounted in the machine.

TRISKELION ULTRA PRECISION PROBE

The Triskelion probe system (figure 5) features an elastically suspended stylus, thus allowing deflection of the tip during probing measurements. The stylus consists of a stiff tungsten carbide shaft with a small ruby sphere (Ø 0.5 mm) at the end. The flexure part is a monolithic metal foil. Three targets for the capacitive probes are integrated in the leaf spring design. The displacements of these targets are measured with capacitive sensors and can be used to determine the X, Y and Z deflections of the probe tip. Except for the sensors, the stylus and the probe tip, the complete probe is made from invar to ensure good thermal stability.

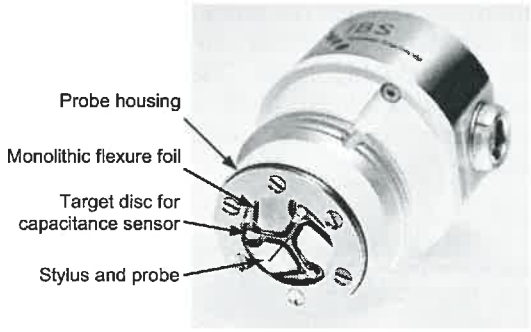

FIGURE 5. Triskelion ultra-precision probe

The sensitivity calibration of this probe system is performed on the Isara 400 CMM. For all measurements up to 5 µm tip deflection, the absolute measurement errors are <10 nm per axis of the coordinate system and <15 nm in 3D.

A miniaturized version of the Triskelion probe, featuring a stylus with a probe tip diameter of only 70 µm, has been realized. The small tip will enable measurements of very small features,

such as the inside diameters of very small holes, up to 1 mm depth. The suspension foil was redesigned to further reduce the probing forces, so that the contact stress between the small tip and the work piece does not cause surface damage. Figure 6 shows a photograph of the miniaturized stylus, as well as a comparison photograph of the two Triskelion probes.

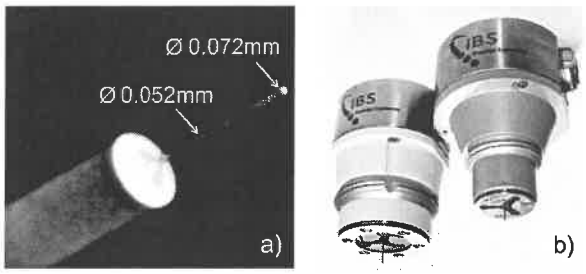

FIGURE 6. a) Photograph of miniaturized stylus. b) Photograph of the two Triskelion probes.

EXPERIMENTS AND SIMULATIONS

The design of the metrology frame was optimized to be both stiff and lightweight. Figure 7 shows results of both a theoretical modal analysis and a first measurement, where the frame was excited in the machine while the frequency spectra of the three laser interferometric displacement measurements against a fixed target were measured.

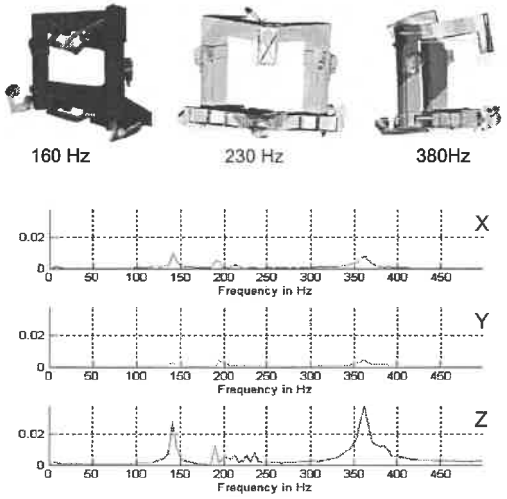

FIGURE 7. FEM modal analysis of SiC metrology frame with frequency spectrum of displacement measurements against fixed target during excitation of frame.

To fulfill the Abbe principle, all probes must be aligned to the Abbe point in 3D; this is done with a special alignment tool. The maximum offset that is allowed is 0.1 mm for X, Y and Z. Consequently, all parasitic rotary error motions must be within 100 µrad, so that remaining Abbe errors are less than 10 nm. The rotations of the X and Y axes are checked with external laser interferometer measurements. Measurements of the parasitic Rz movements of both the X and Y axes show, that these rotations are well within the specification of 100 µrad.

In addition, the dynamic behavior of the mirror table coupling to the X-axis is being investigated. Figure 8a shows the first calculated eigenfrequency of this coupling. This resonance mode is a Rz rotation at 161 Hz. The dynamic Rz rotation of the mirror table coupling was measured with a laser interferometer system to validate this calculation. For this measurement, the mechanical brakes of the X-axis and the Y-axis were activated. Figure 9b shows the frequency spectrum of the rotation measurement. The largest resonance peak is observed at 190 Hz.

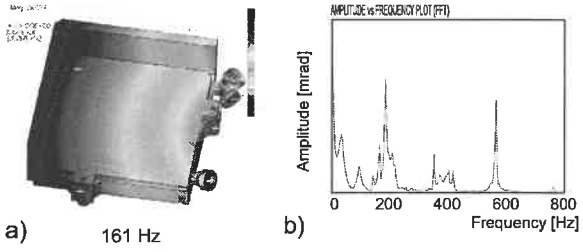

FIGURE 8. a) First resonance mode from FEM modal analysis. b) Dynamic measurement of mirror table Rz rotation.

FIRST MEASUREMENT RESULTS

Using the fully functional Isara 400, some preliminary measurements were performed. The measurement setup is shown in figure 9. A Zerodur straightedge was mounted on the product table. The Triskelion probe (Ø 0.5 mm tip) was mounted in the metrology frame and touches the straightedge from the top. A complete surface flatness measurement on the top surface of the straightedge was performed.

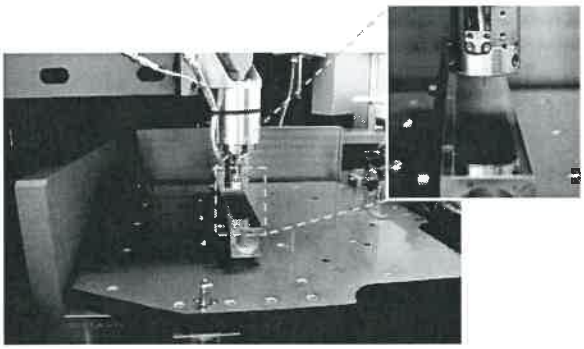

FIGURE 9. Measurement setup for straightedge measurements.

A flatness measurement is performed by measuring a grid of 25 x 10 points on the straightedge surface of 240 x 20 mm. Figure 10 shows the resulting flatness plot, which is obtained after subtracting the best-fitting plane.

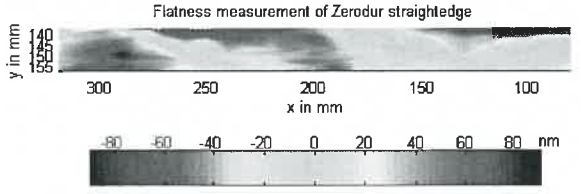

FIGURE 10. Result of flatness measurement.

The measured peak-to-peak flatness is approximately 180 nm. It can be observed that most of this is caused by deformation of the straightedge due to the way it is mounted. Additionally, the flatness of the mirror table of the Isara 400 has not yet been calibrated; flatness deviations from these mirrors are thus part of the measurement result. In the future, this contribution will be mapped and compensated.

CONCLUSIONS AND OUTLOOK

The new Isara 400 CMM has been fully realized (see figure 11) and is currently operational. Extensive analyses and test measurements have been performed on various critical subassemblies and first product measurements have been performed with promising results. Tactile probes, such as the presented Triskelion ultra precision touch probe, as well as other possible (optical) probe systems can be used to perform scanning or point measurements.
Extensive testing will continue in the following months, as well as the complete calibration of the machine. The most important remaining calibration is the flatness and out-of-squareness of the mirror table, which will be performed on the machine itself, using a Zerodur reference artifact.

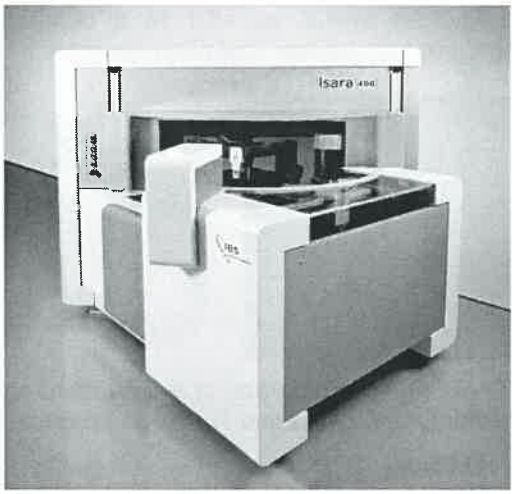

FIGURE 11. Overview of the complete Isara 400 CMM with covers.

ACKNOWLEDGEMENTS

The work presented in this document is part of the European sixth framework program projects NanoCMM, FP6-026717-2 and Production4µ, FP6-2004-NI-4.

REFERENCES

[1] Donker R, Widdershoven I, Brouns D, Spaan H. Realization of Isara 400: a large measurement volume ultra-precision CMM. Proceedings of the ASPE annual meeting, 2009.

[2] Abbe E. Meßapparate für Physiker. Zeitschrift Für Instrumentenkunde. 1890; 10: 446-448.

COMPACT MANIPULATOR BASED ON AN ATOMIC FORCE MICROSCOPE FOR MULTI-PROBE OPERATION

Futoshi Iwata[1], Hideyuki Kou[1], Yuya Mizuguchi[1], So Ito[1], Hisayuki Aoyama[2] and Tatsuo Ushiki[3]
[1]Department of Mechanical Engineering, Faculty of Engineering, Shizuoka University, Hamamatsu, Shizuoka, Japan
[2]Department of Mechanical Engineering and Intelligent Systems, University of Electro-Communications, Chofu, Tokyo, Japan
[3]Division of Microscopic Anatomy, Graduate School of Medical and Dental Scinences, Niigata University, Niigata, Japan

INTRODUCTION

Scanning probe microscopes (SPMs) are well known as surface imaging tools with nanometer scale resolution. SPMs can be used not only for surface observation but also for local surface manipulation. Using the SPM probes, micro and nanometer-scale objects can be manipulated. Several studies concerning manipulations have been performed [1,2]. However, as for such nanometer-scale manipulation based on a conventional SPM, the manipulated scenes can not be monitored during the operation, which leads to damage of the sample or probe. Therefore, real-time monitoring systems have been desired during the SPM manipulations. One solution to the problem is to combine SPMs with other types of microscopes. As another solution, a haptic device can be coupled with SPMs. In the realm of force feedback control, haptic technology refers to technology that supplies an interface between the operator and a machine via the operator's sense of touch while applying forces. This emerging technology has been widely used in various fields such as games, computer-aided design, medical simulations, and remote control robotics. Recently, haptic technologies have been introduced in nanometer-scale manipulations using AFMs [3,4]. Using a haptic device, an operator can directly move an AFM probe on a surface and feel the response from the surface being manipulated by the AFM. The haptic technique should be very useful for nanometer-scale manipulations and fabrications, particularly in the fields of biology and anatomy.

In this paper, we describe a nanometer-scale manipulator based on an atomic force microscope (AFM) which can be operated under observation using a scanning electron microscope (SEM). The design of the AFM unit was sufficiently compact, that a few units could be put on the sample stage for multi-probe operation. Nano manipulations of biological samples using the haptic control system of the AFM are demonstrated.

EXPERIMENTAL PROCEDURE

Compact AFM Manipulator

Figures 1 show a photograph of the AFM manipulator we constructed. The AFM body was compact enough to be installed into a sample chamber of a scanning electron microscope (HITACH S-3700). The gap between the objective lens and the sample holder was less than 10 mm; thus, there was no space to place an optical lever system to detect the deflection of the AFM cantilever. In our apparatus, a commercial self-sensitive type cantilever (NPX1CTP003, SII Nanotechnology) was employed. The self-sensitive cantilever includes piezo-electric resistive elements; thus, the deflection of the cantilever can be directly detected as an electric signal without optical lever systems. The self-detective cantilever can be inserted just under the objective lens of the SEM, which allowed us to design a compact AFM body for operation under SEM observation. The AFM head is a stand-alone type, which has a *z*-axial coarse positioning stage and *x*-, *y*-, *z*-axial fine-positioning mechanisms. As for *z* axial coarse positioning, a small *z*-axial stage was assembled with a miniature piezoelectric motor (30 nm / step, 4 mm displacement). In order to achieve a large scanning range for biological cell manipulation, flexure guide stages consisting of a parallel spring structure and a piezoelectric actuator were constructed for both the *x* and *y* axes; these stages mechanically amplify by three times the stroke of the piezoelectric actuator.

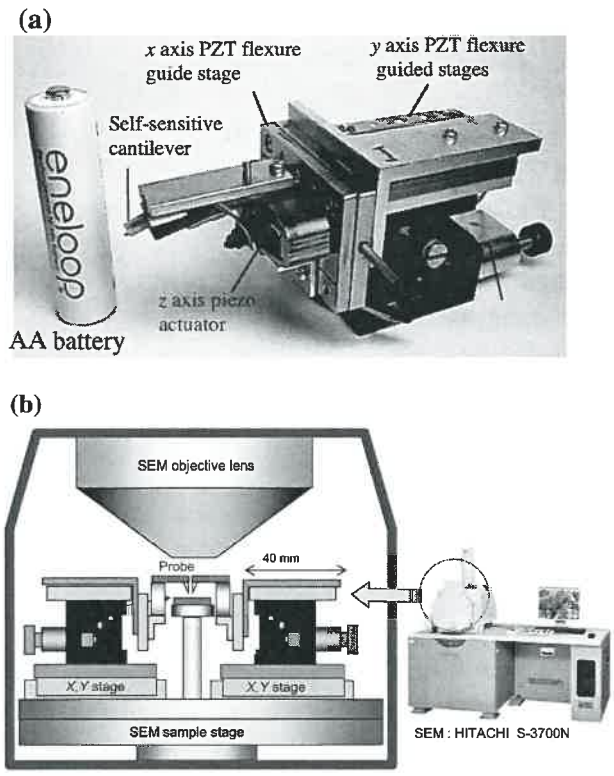

FIGURE 1 Compact and stand alone AFM manipulator. The manipulators are put on the sample stage in the SEM chamber (S-3700N, Hitachi)..

As for z-axis, an external elliptical shell including a piezoelectric actuator was employed. The mechanism uses the elastic deformation of a rigid shell to increase the displacement of the PZT actuator. The maximum strokes of the x-, y- and z-axis scanners are 50, 50 and 60 um, respectively, which is within the range to be able to manipulate a biological cell. A couple of AFM manipulators can be put on the sample stage of the chamber for multi-probe manipulation as shown in Fig. 1 (b).

Coupling with a Haptic Device

Figure 2 shows the schematic diagram of the manipulation system. The total system consists of the AFM head, a controller, a PZT driver, a haptic device and a personal computer (PC). The compact and stand-alone AFM head was put on the sample stage in the SEM chamber (S-3700N, Hitachi). We employed a commercial haptic device that has a pen-like handle with a

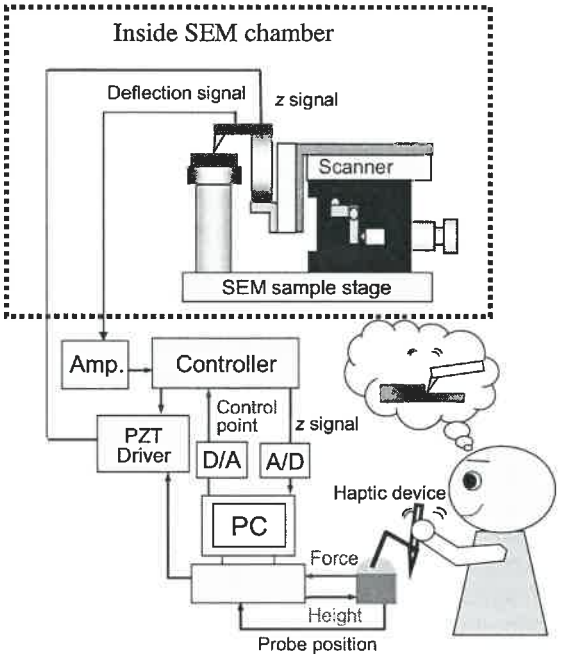

FIGURE 2. Schematic diagram of the experimental setup of the AFM manipulator. The AFM is coupled with a haptic device, so the operator feels the response from the sample during scratching.

serial link mechanism (PHANTOM Desktop; SensAble Technologies). The operator can move the AFM cantilever directly on the sample and feel the response from the surface. A homemade controller and software were modified to couple the haptic device for the manipulation. With respect to lateral movements in the *x* and *y* directions, a signal from the haptic device was sent to a personal computer, and then the signal was sent to the piezo drive circuit passing through a digital-to-analog converter. The topographical signal detected in the AFM controller was fed to the personal computer, and then the signal was converted to the displacement in the *z*-direction of the pen handle of the haptic device. Using this process, nanometer-scale topographical information detected by the AFM can be scaled up to millimeter movements of the pen handle of the haptic device, and the nanometer-scale topography on the surface could be felt in the operator's fingers holding the pen handle. Thus, the operator could move the AFM cantilever at any position on the sample surface and feel the response from the surface according to the cantilever deflection. During the manipulation, if

the operator pushes the pen handle haptic device against the response, a signal is sent to the personal computer to calculate and convert the force feedback signal; then the converted signal is sent to the feedback controller to change the set point of the feedback control. The system changes the force between the probe and the surface in response to pushing by the operator. By this sequential process, the operator can change the applied force for manipulation or fabrication of the surface by feeling the response from the surface via the haptic device.

EXPERIMENTAL RESULTS

AFM Imaging under SEM Observation

As a system demonstration, AFM topographical imaging was carried out under SEM observation. Figure 3(a) shows an SEM image of a HeLa cell, which is a cell line of human cervical cancer cells widely used in medical research. As shown in the image, it is easy to recognize the probe edge. The square area of the SEM image was scanned for AFM imaging. In this operation, the probe was easily positioned at a certain area for AFM imaging; then scanning could be carried out in contact mode under SEM observation. Figure 3(b) shows the AFM image obtained under SEM observation. The AFM image of the HeLa cell is exactly corresponding to the square region of the SEM image shown in Fig. 3(a). The topographical detail information of the cell can be seen in the AFM image. In general, SEM imaging with secondary electrons provides high contrast; however, it does not correspond to the exact surface topography. For instance, the edge line of the HeLa cell is brighter in the SEM image even though this part is topographically lower. On the other hand, the middle of the cell is darker even though that part is topographically higher. Therefore, by coupling SEM imaging with AFM measurement, it becomes possible to analyze the topographical information.

Scratching Fabrication

As a demonstration of the manipulator, nano dissection of a HeLa cell was performed. Using the haptic device, the HeLa cell was scratched with the AFM probe. The spring constant of the cantilever was 4 N/m. In general, biological samples exhibit complicated scratched behavior due to the sliding interaction between the AFM probe and the viscoelastic surface, making it difficult to cut soft material surfaces smoothly

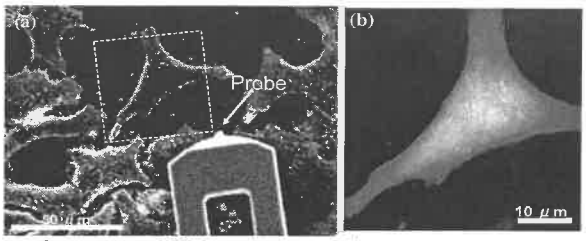

FIGURE 3. AFM imaging of the HeLa cell under SEM observation. (a) SEM image of the AFM scanning area. The square area was obtained by the AFM. (b) AFM topographical image. The AFM topographical image was successfully obtained.

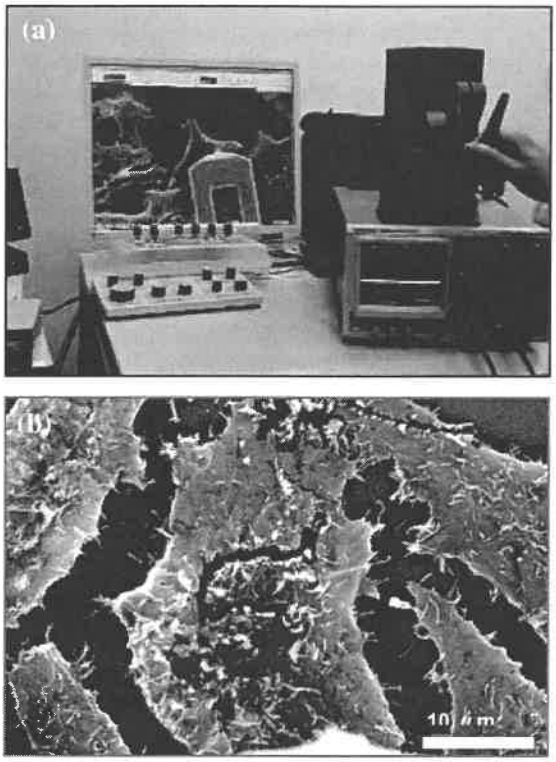

FIGURE 4. Scratching fabrication on surface of the HeLa cell. (a) Operation system by using the haptic device. (b) SEM image of scratching fabrication on the HeLa cell surface. Letter "S" was drawn on the surface by the probe with a strong loading force.

for micro or nanometer-scale fabrication. For modification of viscoelastic surfaces, it is known that vibration cutting,i.e., scratching with an oscillating probe, is effective at cutting such soft material surfaces without distortion [5]. To cut the HeLa cell surface smoothly and effectively, we carried out vibration cutting with probe oscillation. A modulation signal of 9 kHz with an

amplitude of 50 nm was added to the y-axis scanner. The average loading force was 2 μN. Figure 4(b) shows the cell surface fabricated by vibration cutting the letter "S", which is the first letter of "Shizuoka University". As shown in the image, the curved line is relatively smooth. During the process, we could cut the surface while sensing a smooth response in the haptic device.

Performance of Multi-probe Manipulation

As a demonstration of multi-probe AFM manipulators, biological samples were dissected using the two probes. Figures 5 shows the dissection scenes of a crystalline lens taken from a rat eye. Because the crystalline lens consists of a fibrous texture, if the sample is scratched by only one AFM probe applying a strong loading force, it was easily moved without dissection. Therefore, in order to dissect the sample without moving the surface, two AFM manipulators were employed. Figure 5(a) shows an SEM picture of the rat crystalline lens before the dissection. The spring constant of the employed cantilevers was 40 N/m. The right cantilever was used to dissect the sample by scratching the probe toward the right side of the image. The left cantilever was used to hold on the sample to avoid moving against the scratching force. Figure 5(b) shows the crystalline lens after the dissection. The crystalline lens was successfully dissected. Thus, using a multi-probe system, even such complicated and sophisticated manipulations could be achieved. Therefore, the manipulator system will be a very convenient technique, especially in the fields of micro and nanometer-scale anatomy and engineering.

CONCLUSION

We developed a compact nano manipulator based on an AFM system for multi-probe operation under SEM observation. The probe of the manipulator was operated using a haptic device. The manipulator could be put on the SEM sample stage. Thus, it was possible to operate the manipulator while observing the manipulation scene using SEM. As demonstrations, a HeLa cell was successfully scratched, and the crystalline lens of a rat eye was manipulated and observed by a multi-probe system. These results show the ready availability of this technology for application to various fields, such as micro or nano engineering and anatomical fields.

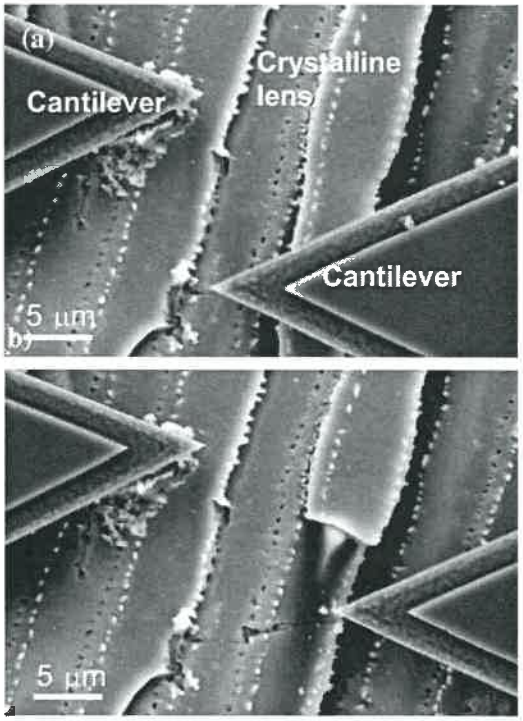

FIGURE 5. Nano dissection of rat eye crystalline lens. (a) SEM image of sample before dissection. (b) After the dissection of sample.

REFERENCES

[1] Decossas S, Patrone L, Bonnot A M, Comim F, Decossas M, Baraski A, and Chevrier J, ``Nanomanipulation by atomic force microscopy of carbon nanotubes on a nanostructured surface, " Surf. Sci. 2003; 543: 57-62.

[2] Yan Y, Sun T, Liang Y, and Dong S, `` Investigation on AFM-based micro/ nano-CNC Machining System, " Int. J. Machine Tool Manuf. 2007; 47: 1654-1659.

[3] Li G, Xi N, Wang D H, ``In situ Sensing and Manipulation of Molecules in Biological Samples using a Nanorobotic System, " Nanomedicine 2005; 1: 31-40.

[4] Iwata F, Ohara K, Ishizu Y, Sasaki A, Aoyama H, and Ushiki T `` Nanometer-Scale Manipulation and Ultrasonic Cutting using an Atomic Force Microscope Controlled by a Haptic Device as a Human Interface, " Jpn. J. Appl. Phys 2008; 47: 6181-6185.

[5] Iwata F, Yamaguchi M, Sasaki A, Nanometer-scale layer modification of polycarbonate surfaceby scratching with tip oscillation using an atomic force microscope Wear 2003; 254: 1050-1055.

A FAST SCANNER DESIGN FOR A SCANNING MULTI-PROBE MICROSCOPE

Feilong Lin[1] Wes Parker[2] Stuart T. Smith[1] Patrick J. Moyer[2]
[1]Center for Precision Metrology, UNC Charlotte, NC 28223
[2]Department of Physics and Optical Science, UNC Charlotte, NC 28223

OVERVIEW

This abstract presents the design, performance evaluation and applications of a fast xy translation stage to create area scans of the optical spot in a metrological confocal microscope system. Scanning is achieved by moving the output of the fiber light source over an area of 60 x 60 µm that corresponds to a scan of around 5.2 µm of the spot size. The fiber scanner has a first mode resonance of 1.4 kHz and scans at rates of up to 80 lines per second are presented.

INTRODUCTION

We have developed a novel three-dimensional metrology stage for biomedical imaging systems that will enable the spatial co-registration of diagnostic information using optical and mechanical probes [1]. This Scanning Multi-Probe Microscope (SMPM) utilizes the mechanical and optical probes which are stationary relative to the instrument frame while

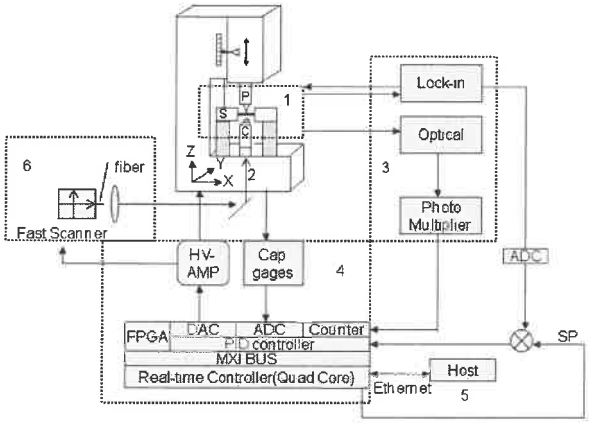

FIGURE 1. schematic diagram of the Scanning Multi-Probe Microscope (SMPM).

the specimen can be navigated in a three-dimensional space in the probing field, translating over an XYZ range of 50 µm by 50 µm by 30 µm in each axis, respectively, at closed loop speeds of greater than 10 line scans a second. FIGURE 1 shows the main components of the system.

Block 1 contains the XYZ scanner and sample holder S, mechanical probe P that can be adjusted in three axes for alignment with the focal spot of the confocal lens C that illuminates the specimen from the underside.

Block 2 is the instrument base that also includes a manually adjustable coarse motion stage to adjust the specimen position and orientation with respect to the confocal probe.

Block 3 is the electrical part of signal conditioner for the mechanical probe and intensity and photon counters for optical measurement.

Block 4 is the hardware control systems for dynamic positioning of the probes relative to the specimen. It comprises several newly integrated hardware controls. Software implementation is achieved using LabVIEW 8.6 Real-Time™ with program code running on 2.6 GHz quad processor computer as a high speed real time controller. The controller connects to a PXI-7852RA through MXI bus. An FPGA based 40 MHz counter is used to count photons to produce the fluorescence image. Digital to analogue convertors (DACs) and ADCs are used to read the signals from the sensors and provide the command voltage to the piezoelectric actuators via a high voltage amplifier. Multi-channel proportional-integral-differential (PID) controllers are used for the closed loop control of the fine stage scanning and probe surface tracking. Three capacitance sensors built into the sample holder measure the displacements of three axes of the fine stage and therefore provide the measured displacement to the controller.

Block 5 is the host computer running under Windows XP. A flexible and user-friendly GUI was designed and built using LabVIEW in the host computer. It realizes the function of sending controls and scanning parameters to the real time controller, receiving, post-processing and displaying the measurement results.

FAST SCANNER DESIGN AND OPERATION

Recently, we proposed a novel scanning method for the fluorescence probes microscopy of SMPM in which the fiber is mounted to an *XY* piezoelectric actuated fast scanner shown in block 6 in FIGURE 1. By scanning the fiber in an *XY* plane, the focused beam is able to scan the sample object plane. Initial experiment and results show that the scan range of the positioner was around 60 µm in each axis for the corresponding scan of 5 µm range of the spot. Such an attenuation of around 12:1 for this optical system may be of particular benefit for ultra-high resolution, metrological confocal microscopy. The low mass of the optical fiber enables high speed imaging of samples without having to move the more massive sample stage with specimens also sometimes comprising liquid specimen environments.

To achieve smooth, frictionless, fast response a flexure constrained, *XY* piezoelectrically actuated, scanner has been designed to have a range of 60 µm by 60 µm and more than 1 kHz bandwidth in open loop operation, FIGURE 2. Because of the optical attenuation of approximately 12:1, it is desired that the scanner maintain controller errors within 10 nm over the 60 µm scan range corresponding to a signal to noise target of around 10,000:1.

Because the piezoelectric actuators employed have a maximum displacement of 16 µm, a tip-tilt design is used to obtain a displacement amplification factor of four, see FIGURE 2. To maximize stiffness (and therefore dynamics) and match dynamic performance in the two axes, it is based on a parallel-kinematic design with two orthogonal pairs of differentially-driven piezoelectric actuators. FIGURE 2c) illustrates the amplification mechanism in one axis. The scanning range can be calculated from

$$2\delta = 2\frac{L}{l}\varepsilon \qquad \text{Equation 1}$$

where ε is half of the extension of each PZT and the ratio of lengths is the mechanical lever ratio. Ignoring lost motion, the stroke is calculated to be around 60 µm for the design used in these experiments. Four, orthogonally symmetric, leaf spring flexures on the upper face of the mechanism provide the preload.

Theoretical modeling and finite element analysis was conducted to estimate the system's static and dynamic performance. The platform with the fiber holder located underneath has a stiffness of about 0.95 $N \cdot \mu m^{-1}$ and an angular resonant frequency at around 1.8 kHz predicted using FEA. The fiber holder's first mode of resonant frequency is about 3.4 kHz. Direct knife-edge displacement sensors for closed loop control feedback sensing[2]. Again scanning and imaging is achieved using the PXI-7852R smart Daq card in LabVIEW Real-time with an FPGA based controller. With the integrated fast scanner and the FPGA-based dual stage controller, the SMPM is able to obtain confocal images of a smaller area of interest within the longer range *XYZ* fine stage scanning volume. Currently this optical detection is capable of measurement of fluorescent resonance energy transfer, fluorescence anisotropy and single molecule imaging.

DYNAMIC RESPONSE

Open loop frequency response of the fast scanner has been measured using an HP 35693A dynamic signal analyzer. The displacement responses of each axis as a function of frequency are measured by the optical displacement sensor. Table 1 lists the measured resonant frequency of each axis for three different damping conditions. Damping has been added by applying Kopr-Kote (a colloidal grease with fine copper particulates) into the gap between the center hole of the base and the tube/cylinder. It decreases the Q by 15-20 while the resonant frequency is maintained at 1445.6Hz. FIGURE 3a) shows the result that the natural frequency of the PZT2 with Kopr-Kote. FIGURE 3b) is the step response of the PZT2 with a setting time of 5 ms. As an alternative damping treatment a 1:40 ratio Sylgard, a type of silica gel, was used to fill the gap. It gives a damping ratio two times larger than the copper oil, as well as adding substantial stiffness which increased the resonant frequency to 6,884 Hz.

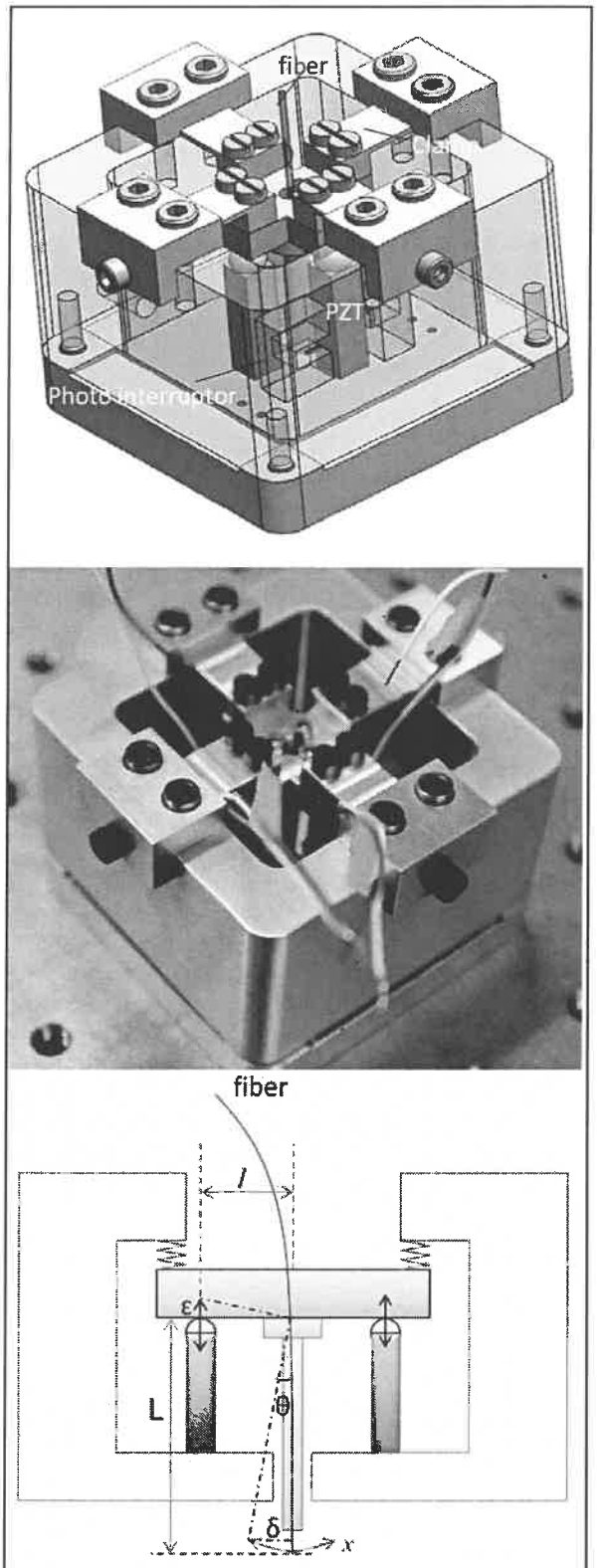

FIGURE 2. (a) CAD model of the fast scanner (b) photograph of the fast scanner (c) principle of operation L = 46mm, l = 10mm

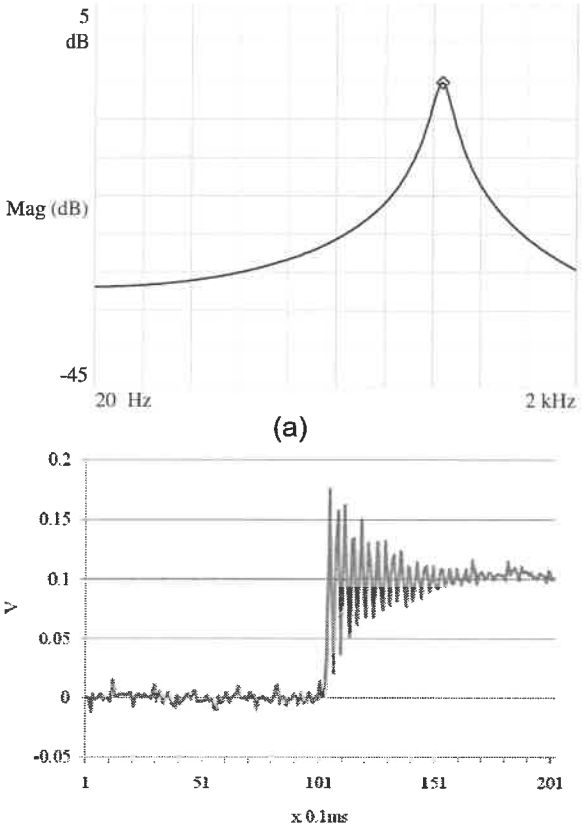

FIGURE 3. a) Frequency response fiber scanner using copper oil as a damper b) Step response

TABLE 1. Resonant frequencies of each axis with different damping treatments

Wn/Hz	AxisX1	Axis Y1	Axis X2	Axis Y2
Air	1475.3	1470.4	1475.3	1470.4
CopperOil	N/A	1445.6	N/A	1445.6
Sylgard	N/A	6884	N/A	6884

RESULTS

FIGURE 4. a) shows a 23.2 µm x 22.8 µm fluorescence images of a calibration grid using the longer range scanner. The grid is fabricated using electron beam lithography. It consists of a thin gold film (30 nm thick) patterned with 400 nm round holes, with a periodicity of 800 nm. The sample is then spin-coated with a PMMA film that contains rhodamine 6G fluorescent molecules. The image is acquired by illuminating in the epi-fluorescence mode from the bottom of the sample with the PMMA film on top of the gold film. The light is then collected also from

the same bottom objective so that bright fluorescence spots are present where the holes of the film exist. FIGURE 4b) is a 5 µm x 5 µm scan range of the grid at a speed of 4 lines per second. FIGURE 4c) shows a zoom section of 5 µm x 5 µm from the image in 4a). The resolution is only a 5.5 pixels per micrometer.

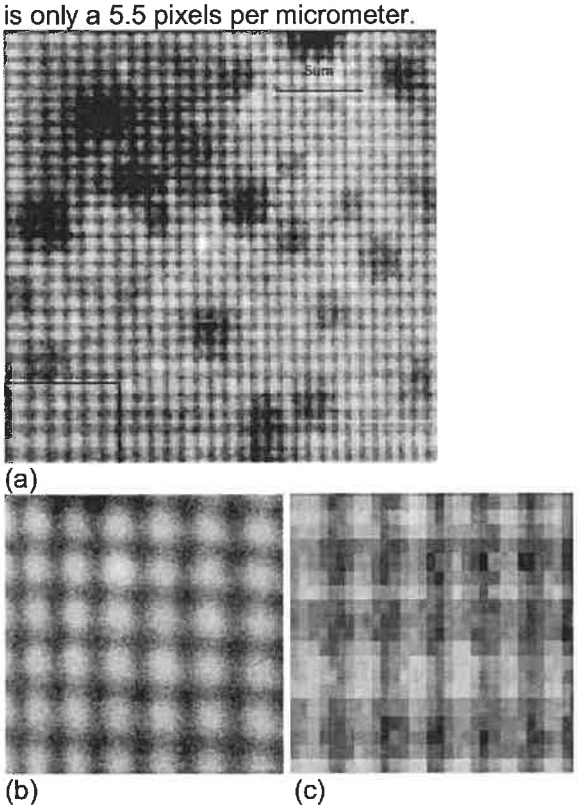

(a)

(b) (c)

*FIGURE 4. Images obtained using large scanner. a) Range: 23.2 µm x22.8 µm, 128*128 pixels at 4 lines per second; b) Range: 5 µm x 5 µm 128*128 pixels at 4 lines per second; c) section magnifying lower left image in FIGURE 4.a);*

FIGURE 5. shows two scanning results using the fiber fast scanner. Both images are obtained at a full scan range. With an optical attenuation of about 12, the laser spot navigates over a range of 5 µm x 5 µm in the sample plane. FIGURE 5a) is captured with a line scanning speed of 4 Hz while in FIGURE 5b) this speed goes up to 78 Hz. The contrast drops in higher speed because the sampling time (therefore photon counting statistics) for each pixel is reduced .The stretch in dimension along the y axis (fast axis) comes from a dynamic amplitude decrease at the scan frequency. Compared with the result in FIGURE 4c), both show a same area of 5 µm x 5 µm on the grating, while FIGURE 5b) has much higher resolution and contrast of 25.6 pixels per micrometer at 1.6 second for a frame. With the fast fiber scanner and original scanner, a five times better pixel resolution than FIGURE 4a).

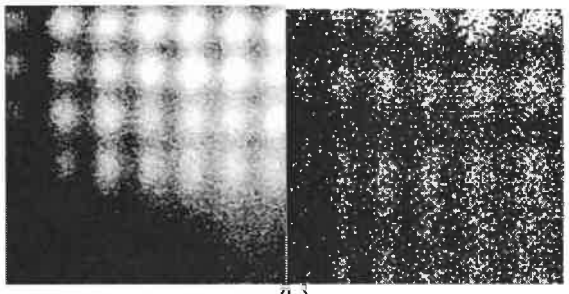

(b)

*FIGURE 5. Fast scanner imaging. a) Range: [10V*10V] 128*128 pixels at 4 lines per second; b) Range: [10V*10V] 128*128 pixels at 78 lines per second*

CONCLUSION

The current fast scanner is working in open loop operation. While the fast dynamic response and high resolution has significantly increased productivity as a biological research tool. There remain many challenges; validation of this methodology for metrological measurement, optimizing damping, filtering for smoothing digitized drive signals, working in resonant mode, a high stiffness mount for the fast scanner, utilizing displacement sensors to remove image distortions, and developing scan algorithms capable of recording and storing large data files. Further data incorporating these enhancements as well as interesting confocal measurement case studies will be presented.

REFERENCES

[1] F. Lin, K.E. Elliott, W. Parker, N. Chakraborty, C.S. Teo, S.T. Smith, G.D. Elliott, and P.J. Moyer. Confocal and Force Probe Imaging System for Simultaneous Three-Dimensional Optical and Mechanical Spectroscopic Evaluation of Biological Samples. Rev. Sci. Instrum., 2009: 80: 55110.

[2] F. Lin, S.T. Smith, H. Ghazanfar. Direct knife edge sensors for precision displacement measurement, Meas. Sci. Technol., 2010, (submitted)

A THREE FINGERED HAND FOR A MICRO-ROBOTIC ASSEMBLY SYSTEM

Hastings D. J., Graham J., Nowakowski B. N., Smith S.T. and Tomblin J.
Center for Precision Metrology
University of North Carolina at Charlotte
Charlotte, NC 28223

OVERVIEW

This abstract presents the design and operation of a micro-scale robotic system which is used to manipulate and measure micrometer size components for the purpose of positioning and assembly. Components are gripped using a 3 fingered 'hand' with pick-and-place being provided by a three axis moving 'factory floor'. Finger displacement sensors and fingertip force sensing provides grip and dimensional feedback while cameras and a multi-function 'joystick' enable an operator to remotely control the assembly process. Examples of stacked spheres on a razor blade edge and an assembled proximity probe are presented to demonstrate the system capability.

INTRODUCTION

Additive and reductive manufacturing processes with micro and nanometer capability are continuously developing. Initially emerging as a spin-off from the microelectronics industries, many of these could be classified as planar processes predominantly capable of forming or shaping uniform thin layers. Today there is a growing range of manufacturing processes that have emerged to satisfy the demand for more complex shapes for components having functional features spanning dimensional scales from millimeters to nanometers, sometimes on the same part. Examples include; freeform growth from solids liquids and vapors, rapid prototyping, micro-EDM, water jets, electroforming and imprint lithography to name a few. The goal of this present work is to produce tools and evaluate issues for assembly of micro-scale systems from components manufactured from multiple manufacturing processes.

PRINCIPLE OF OPERATION

A block diagram of the complete micro-robotic assembly system is shown in FIGURE 1. This described system is an extension of collaborative efforts with InSituTec in standing wave based pick and place tools and comprises a three fingered 'gripper hand' with self-sensing 'finger tips' and optical displacement sensing to measure finger movement. As previously reported, these finger tips comprise carbon

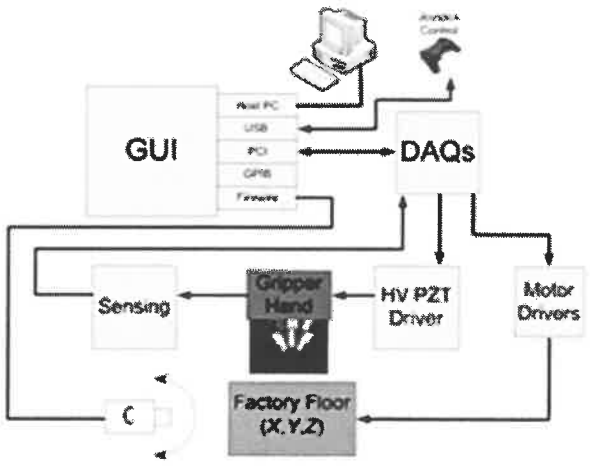

FIGURE 1. Block diagram representation of micro-robot system.

fibers of diameter 7 μm and length 3 mm attached to quartz tuning fork resonators that, if energized, can be used to detect contact interactions upon contact with the component surface [1, 2, 3]. Pick and place operation for assembly is achieved with the hand being stationary while the factory floor is translated about a three dimensional cubic volume of length 20 mm using motor driven feedscrews to translate in three orthogonal axes. Assembly is controlled by an operator using a multi-function joystick. This joystick can be toggled to enable motor controls, individually move the fingers in and out and activate oscillation of the finger tips. Two cameras (only one is shown labeled "C' in FIGURE 1) provide visual feedback to the operator. All hardware interfacing (DAQ, camera's, joystick, function generators), controls and process measurements are implemented using Labview™ software.

The attributes of this new design include:

- Independent displacement and force measurement of each finger.
- Three point measurement of object being manipulated by fingers.

- Independent alignment of each finger for collocating of finger tips.
- Open design to enable real-time imaging using cameras at the top, front, and side of assembly area.
- Automated characterization for replacement of finger tips and the ability to utilize different size fingers.
- Using force sensing, it is possible to provide haptic type feedback for tactile response of gripping action or finger collision.
- It is possible to grip the object with all three probe fingers being excited to minimize finger tip to specimen adhesion.

GRIPPER HAND DESIGN

A photograph of the gripper hand and factory floor is shown in FIGURE 2. This can be considered to comprise four major components. At the top of the hand three horizontal metal plates can be seen each of which are rotationally symmetric about the central vertical axis with 120 degree pitch. Because the hand hangs downwards, the upper plate of this assembly is the base which supports all components and also provides channels for routing wiring harnesses to two DB9 connectors. Below this base plate is a flexure that supports the three fingers and provides adjustments in four degrees of freedom to enable manual alignment of each finger tip. The lower of these three horizontal plates houses the three vertical alignment screws for adjustment of the fingers as well as serving as the mount for the optical knife edge sensors with another horizontal set of screws for zeroing these sensors. In total, this hand mechanism provides 21 independent alignments.

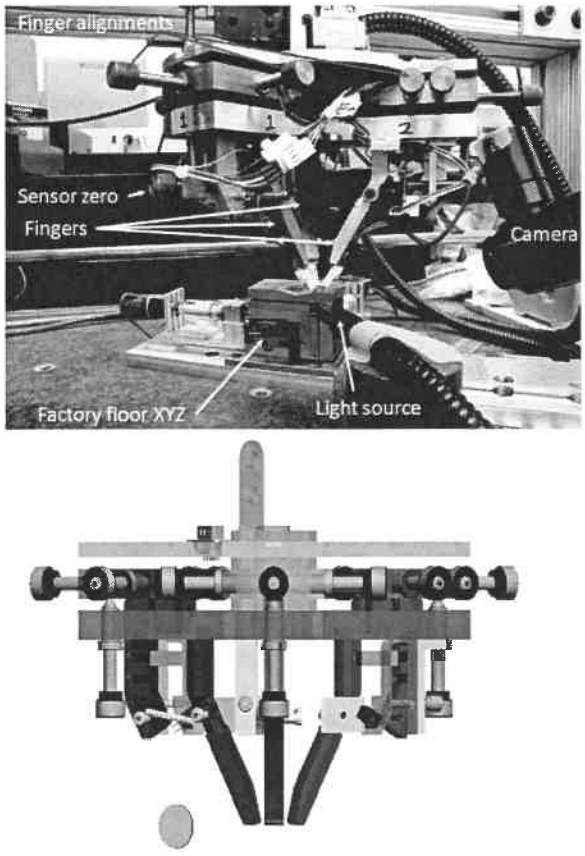

FIGURE 2. Micro-robotic assembly system, photograph showing hand above the moving factory floor (above) plus a solid model of the three fingered hand (below). For scale, the grey disk at the bottom of this lower figure is the size of a US quarter.

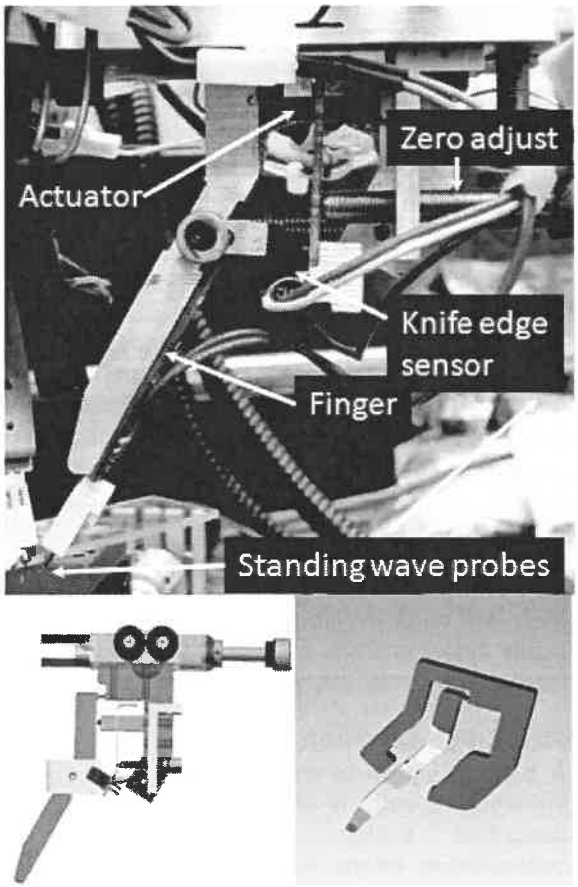

FIGURE 3. Close up photograph of an individual finger with solid model of finger assembly (below left) and color contour showing displacement of finger about notch hinge (below right)

A photograph of an individual finger is shown in FIGURE 3. Each finger is machined from a monolithic plate of aluminum which comprises a long bar with the standing wave probe mounted at the lower (free) end. The other end of this bar connects to the finger base through a notch type flexure hinge. A horizontally acting piezoelectric actuator is attached to the base plate and contacts the finger a short distance from the flexure hinge. By pushing near to the hinge, the 16 µm range of the actuator results in an amplified motion of around 80 µm at the finger tip (i.e. a lever ratio of ≈ 5:1). Further down the finger from the notch hinge, a knife edge is attached to the finger and this is positioned to bisect the optical path of a photo-interrupter-based, knife edge displacement sensor [4]. This sensor is, in turn, mounted on a slender circuit board that serves as a cantilever flexure to enable manual offset of the sensor.

The probes comprising the finger tips of the hand consist of resonant fiber sensors with a 7 µm diameter carbon fiber attached to one tine of a quartz tuning fork oscillator and have a mechanical resonance of around 32 kHz. These probes have been extensively studied over the last decade and have demonstrated an ability to attenuate problems associated with adhesion forces and provide a sensitive measure of contact between the fiber tip and specimen surface, see [1,2,5]. In this finger design, the modular probes can be easily replaced after which the software is used to run a frequency sweep to determine operating frequencies and amplitudes, see results section.

SENSOR CALIBRATIONS

During operation, in addition to camera visualization of the process, there are two voltage based measurement signals to provide feedback to the operator, the sensing signal from the standing wave probe and displacement for the optical sensor. In general, a frequency response curve can be obtained for each fiber using a sine swept function from a function generator to the tuning fork and measuring the amplitude output response. In our software, the frequency response curve can be obtained and algorithms used to obtain the peak amplitude and resonance frequency peak, see [2].

For probe displacement metrology it is necessary to convert the knife edge displacement sensor voltage to a displacement. Calibration of each sensor was carried out by translating the knife edge of each sensor on a linear translation stage monitored using an Optodyne™ laser interferometer. From the measurements it is possible to plot the laser measurement against knife edge sensor output to derive a polynomial expression for this relationship, see FIGURE 4. In practice this displacement occurs at a point on the lever with a considerable offset to the probe tip. Currently, displacement is estimated from this calibration and the lever ratio calculated from the geometry of the finger.

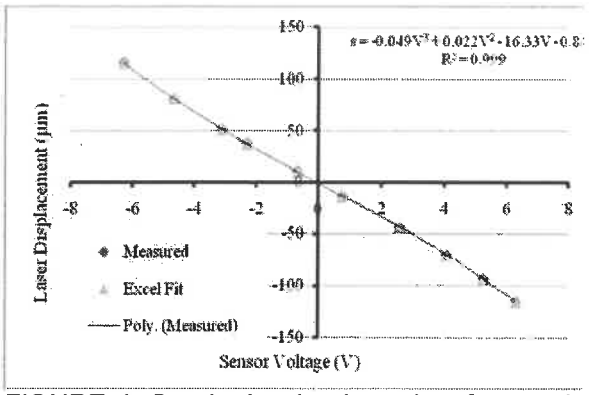

FIGURE 4. Graph showing laser interferometric displacment measurement as a function of output voltage from knife edge sensor

ILLUSTRATIVE ASSEMBLIES

As an example of the pick and place capabilities of this system, FIGURE 5 shows a photograph of an assembly comprising two spheres of approximately 30 µm diameter stacked on top of each other on the edge of a razor blade. Also shown in this figure is the sequence of 6 steps for this assembly. Components are held in place by the naturally occurring adhesion forces between the glass sphere and steel blade in an air environment.

As part of an indentation instrumentation initiative, it is desired to use a surface proximity sensor with nanometer level sensitivity and stability. We are currently exploring the use of a quartz tuning fork oscillator with spheres attached at the free end of the tines to create an interacting surface, for more details see [6]. For symmetry spheres of nominally the same size are glued near to the end of each tine.

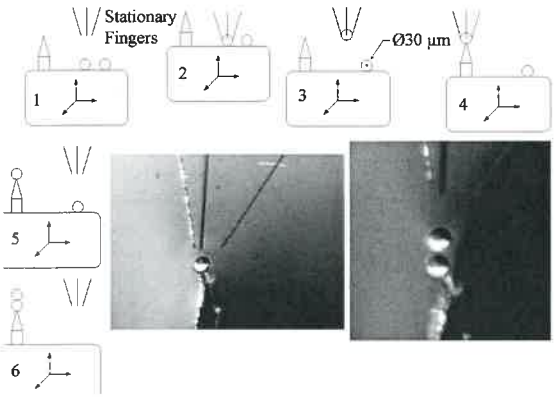

FIGURE 5. Assembly of two stacked spheres on the edge of a razor blade. Cartoons indicate the sequence of steps for assembly. Photographs represent steps 4 and 6.

FIGURE 6 shows two steps in the assembly process. The tuning fork tines can be seen to the left of these two photographs with a sphere of diameter ≈80 µm being assembled on the upper surface of the top tine. On the right is a horizontal tungsten fiber of 75 µm diameter with a globule of glue at its free end. Prior to attaching the sphere, a small amount of glue is deposited onto the tine with volume being controlled by droplet size and contact time with the tine surface. The sphere that was previously selected from the factory floor is then contacted with the glue adhesion forces of which dominate making it easy to release. In some cases the probe fingers are used to apply pressure to the sphere as the glue cures.

CONCLUSIONS

A system that can be adjusted to meet the demands of different scales of assembly, ranging from millimeter to micrometer size objects. The open architecture enables the system to expand to meet the changing needs of the assembly process. This expansion ranges from using different size tips (and the ability to collocate each tip) to the addition of multiple cameras in different locations to the use of metrology for artifact verification or determination. Performance of the system is shown by the ability to stack micro-sized objects onto the thin tip of a razor blade and the assembly of high resolution proximity probes.

Future work will include the addition of haptic feedback to the user, evaluation of the metrology capability against known artifacts, and addition of a rotary stage to the hand assembly to enable a 4th axis to the process. Because of

FIGURE 6. Assembly of symmetric tuning-fork based proximity sensor. Probe just before sphere attachment (left) and after making contact with bonded tuning fork (right)

the scale of the probes it is relatively difficult to align them properly, which becomes more important as the size of handled object decreases. As probe size reduces, visualization will become more difficult and it is speculated that alternative methods involving sensing of known artifacts to determine relative finger tip location will be necessary. There is also ongoing work to determine performance of fingers as a function of excitation frequency and amplitude. As of writing, it is not clear how this can be optimized to enhance control of gripping and releasing objects of different scales.

REFERENCES

[1] Bauza M., Woody S.C., Hocken R.J, and Smith S.T., 2005, Development of a virtual probe tip with an application to high aspect ratio microscale features, *Rev. Sci. Instrum.*, 2005: **76**(9): 095112.

[2] Woody S.C., Nowakowski B., Bauza M.B., Smith S.T., Standing Wave Probes for Microassembly, Rev. Sci Instrum, 2008: 79: 085107.

[3] Bauza M.B., Woody S.C., Smith S.T., Self sensing tweezers for micro-assembly and manipulation, US Patent 7,735,358; June 15, 2010.

[4] F. Lin, S.T. Smith, H. Ghazanfar. Direct knife edge sensors for precision displacement measurement, *Meas. Sci. Technol.*, submitted, 2010.

[5] Bauza M.B., Woody B.A., Woody S.C. and Smith S.T., Surface profilometry of high aspect ratio features, *Wear*, permanent URL dx.doi.org/10.1016/j.wear.2010.03.028

[6] Nowakowski B.K., Smith S.T. and Smith D.T., Advancements in development of an ultra-precision, SI-traceable nanoindentation platform, *Proc. ASPE*, Atlanta, GA, 2010.

ADVANCEMENTS IN DEVELOPMENT OF AN ULTRA-PRECISION, SI-TRACEABLE NANOINDENTATION PLATFORM

Bartosz K. Nowakowski[1] , Stuart T. Smith[1] , Douglas T. Smith[2]
[1]Center for Precision Metrology, UNC Charlotte, NC 28223
[2] Ceramics Division, NIST, MD 20899

ABSTRACT
This paper presents a discussion of the design features of a precision indentation platform for measuring indents with traceable uncertainties at the nanometer scale. In particular, the goal of the instrument is to simultaneously measure penetration distance of an indenter tip into a surface as a function of the applied load. Components of design that will be discussed include; capacitance gauges for measurement of indenter penetration and load, AC bridge balancing for high sensitivity, a proximity probe for surface location sensing, a null control to create a constant force measurement datum from the specimen surface, alignment of the proximity probe relative to the indenter tip and preliminary results from proximity probe sensitivity testing.

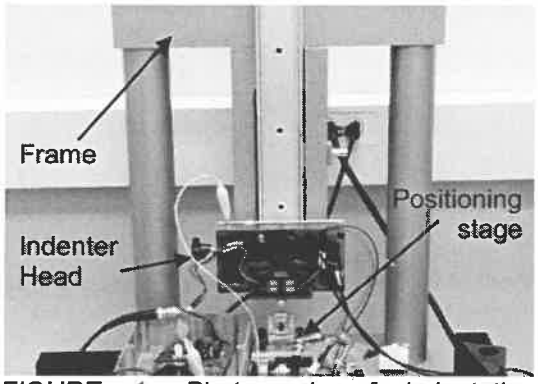

FIGURE 1. Photograph of indentation platform indicating major system components.

OVERVIEW
The indenter system comprises three major components. These are the specimen positioning stage, a bridge-type instrument frame and the indenter flexure, see FIGURE 1. This complete system will be assembled on a portable base that can be loaded into a vacuum system for advanced surface indentation studies.

To discuss design features of the indenter flexure assembly a close up view is shown in FIGURE 2 with a cross section through the

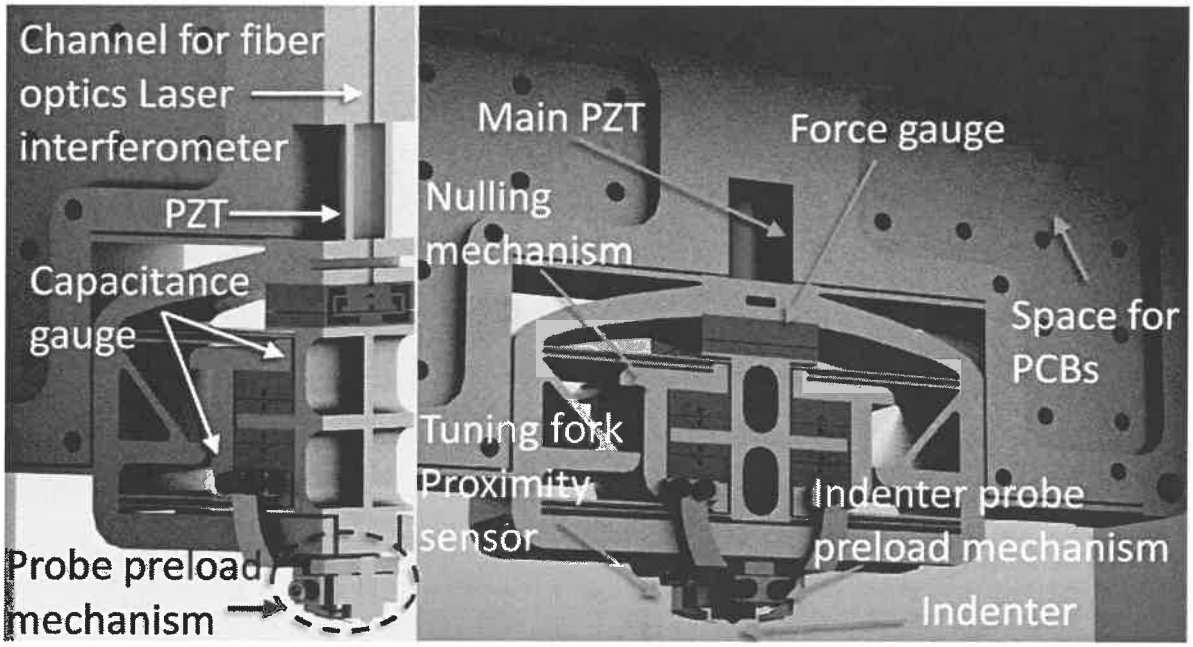

FIGURE 2. Solid model of assembled indenter flexure.

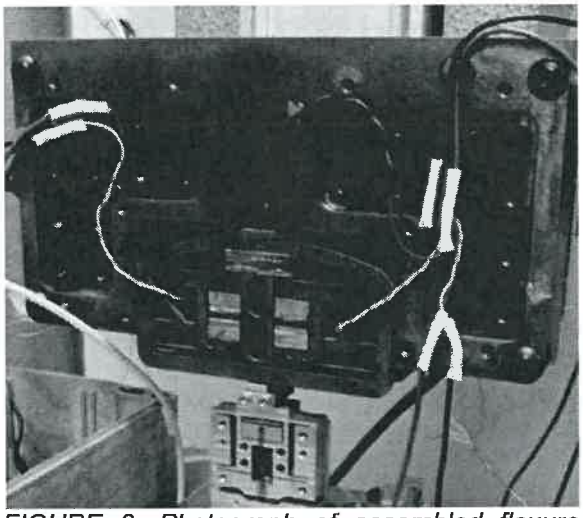

FIGURE 3. Photograph of assembled flexure with load cell in contact with a piezoelectric translation stage.

central symmetric plane being shown on the left-hand side. A photograph of the assembled indenter during performance characterization of the load cell capacitance gauge is shown in FIGURE 3. Referring to FIGURE 3, all components of the indenter system are assembled on a monolithic flexure having a vertical axis of symmetry that is maintained after all components of the assembly are installed. The indenter mounts to the underside of the flexure with the tip being coincident with the axis of symmetry. The base into which the indenter is mounted corresponds to the load cell platform and also has two horizontal members to mount four capacitance gauge electrodes. Two 'C' frames house an additional four electrodes resulting in a, differential-mode, capacitance displacement gauge on either side of the load cell platform. A surface proximity sensor is attached to each of the 'C' frames via a bracket that enables these sensors to be positioned near the indenter tip. Each of these proximity sensors must be positioned to be lower than the indenter tip prior to contacting the surface of the specimen to be tested. This positioning mechanism will be discussed shortly. Both the load cell platform and the two 'C' frames are attached to an indenter frame via leaf-type flexures. To create a reference to the specimen surface, these 'C' frames can also be displaced relative to the load cell platform using piezoelectric actuators mounted on the indenter frame. This indenter frame is attached to a solid base block via a final set of four leaf type flexures.

Operation of the indenter is probably most easily understood by considering a typical indent sequence. Motion the indenter frame using the main PZT actuator displaces the indenter towards the specimen until the proximity sensor, which is lower than the indenter tip, detects contact with the surface. As motion of the indenter frame continues the "C' frame actuators will contract to keep a constant signal, and, therefore, force, from the proximity sensors. To within the uncertainties of the proximity measurement, each 'C' frame will form a reference to the top surface of the specimen at the region of the contact interaction. Continued motion of the instrument will bring the indenter into contact with specimen surface with contact forces being detected by the load cell. Subsequently, during indentation, the

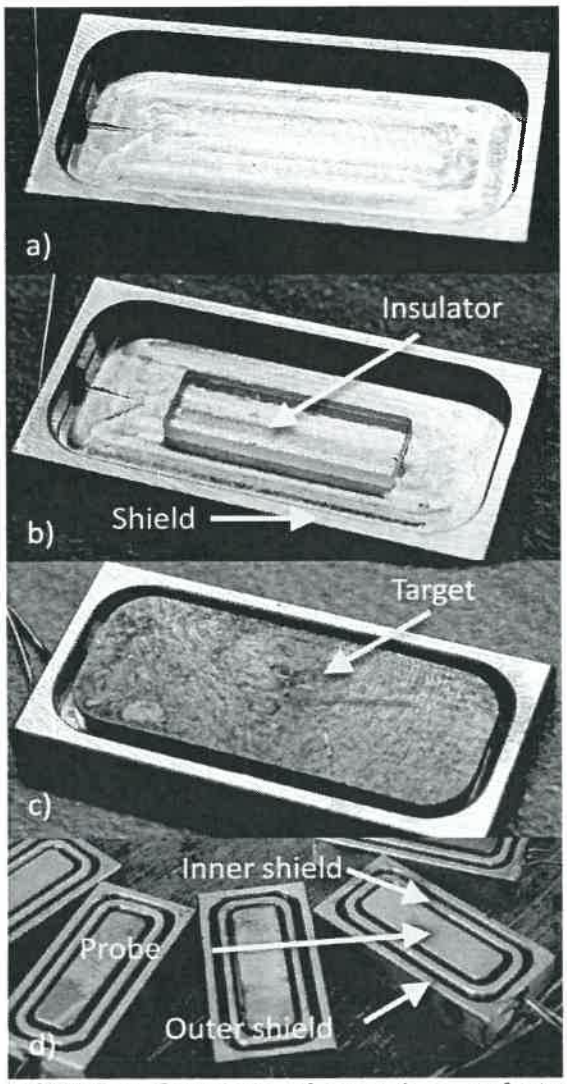

FIGURE 4. Sequence of steps in manufacture and assembly of capacitance gauge electrodes.

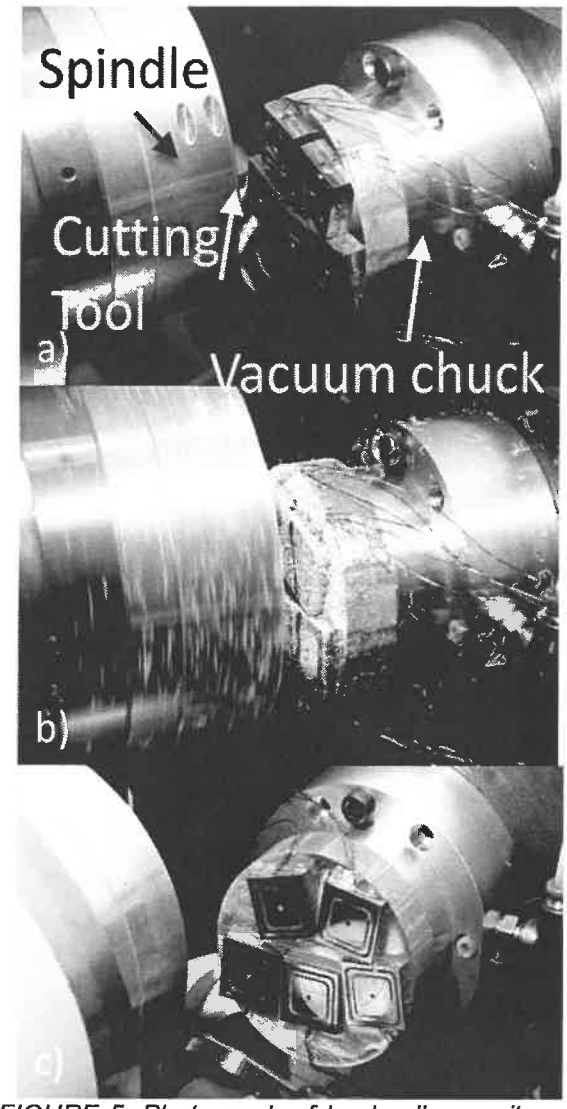

FIGURE 5. Photograph of load cell capacitance gauge probe electrodes during diamond turning.

displacement of the indenter into the surface is measured from the two differential capacitance gauges either side of the load cell.

CAPACITANCE GAUGE MANUFACTURE

The capacitance gauges used for displacement measurements in both the load cell and indenter tip displacement comprise a target electrode to which an AC carrier signal is applied and a probe electrode that is monitored using an instrumentation amplifier. Both target and probe sensors are shielded by a surrounding box. A further inner shield is used to minimize fringing effects at the probe electrode. All electrode components are made from oxygen-free copper. FIGURE 4 shows the assembly of the electrodes by bonding the nested parts with high purity silica separating plates. To create flat, parallel and specularly reflecting surfaces, the assembled electrodes are then bonded to aluminum housing and attached to a vacuum chuck in a diamond turning machine. The electrodes are fly cut on both front and back surfaces, using a diamond tool in the spindle of the machine as shown in FIGURE 5. The requirement that the electrodes be specularly reflecting is to enable additional displacement measurement using a fiber interferometer with picometer resolution [1] that will be fed through the center of the probe electrode and reflect from the target surface.

SYNCHRONOUS DETECTION

Both the capacitance gauges and proximity probes sensors are measured using an AC differential circuit with synchronous demodulation to convert the carrier signal to a DC amplitude, as shown in FIGURE 6. To balance these reactive circuits, a dual output oscillator is used with one output being the carrier and the other acting as a reference. By using a dual oscillator with both outputs at exactly the same frequency it is relatively easy to adjust both the amplitude and phase of the reference channel to achieve a null prior to amplification.

PROXIMITY PROBE

The proximity probe adopted for this indenter is a modification of the tuning fork based AFM probe. To better define the contact geometry

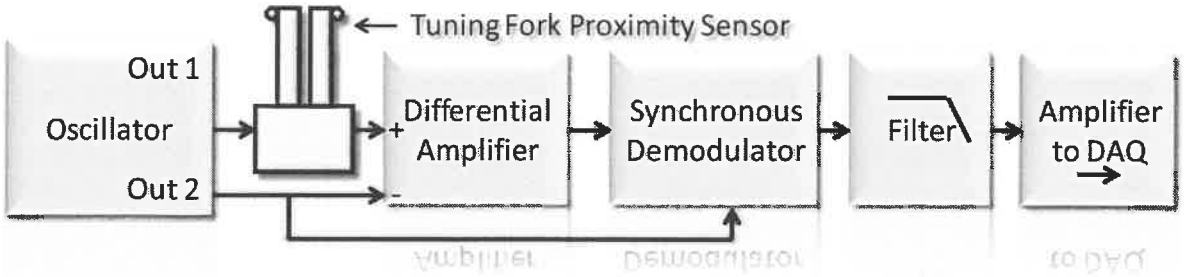

FIGURE 6. Differential bridge for high sensitivity proximity probe detection.

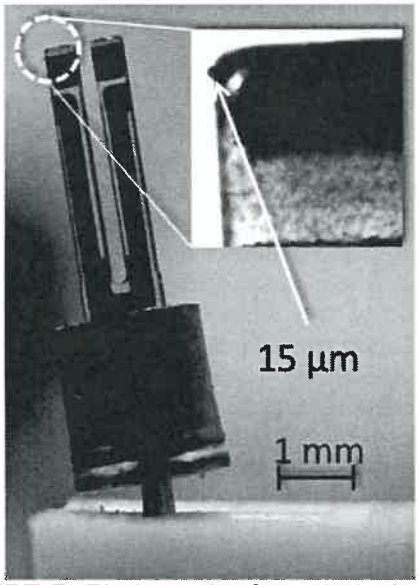

FIGURE 7. Photograph of quartz tuning fork proximity sensor with a 15 µm sphere attached at the free end of each tine.

and location small spheres of ≈15 µm diameter have been attached to the outer surface of each tine near to the free end, FIGURE 7 [2]. In turn this tine is mounted using a vee groove clamp in the housing of an adjuster, FIGURE 8. To bring

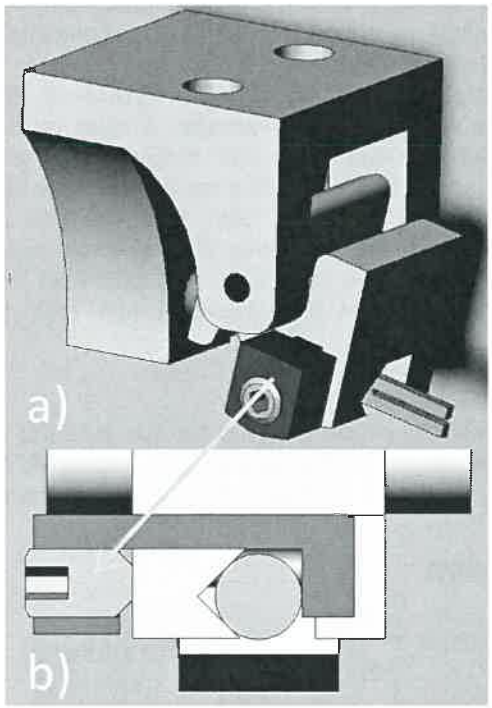

FIGURE 8. Solid model of coarse/fine adjustment mechanism for the proximity sensor, a) isometric view, b) cross section through the probe clamp mechanism.

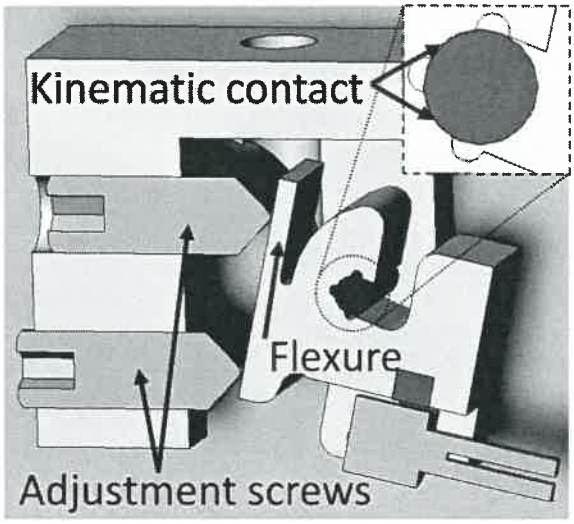

FIGURE 9. Cross section through solid model of coarse/fine adjustment mechanism for the proximity sensor.

the outer surface of the sphere below that of the indenter tip, the housing pivots on a rod that can be rotated using two adjustment screws, FIGURE 9. The lower screw represents coarse positioning, while the upper screw pushes

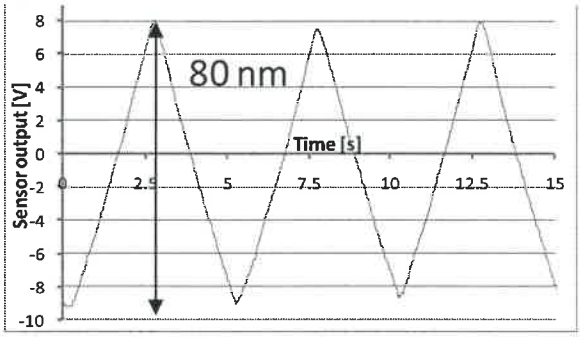

FIGURE 10. Output voltage from proximity sensor interacting with a gauge block surface cyclically displacing a distance of 80 nm.

against a more compliant part of the housing for fine adjustment. The output from this sensor, shown in FIGURE 10, has demonstrated a sensitivity of approximately 5 nm V^{-1}.

REFERENCES

[1] D. T. Smith, J. R. Pratt, and L. P. Howard, A fiber-optic interferometer with subpicometer resolution for dc and low-frequency displacement measurement, Rev. Sci. Instrum., 80: 035105: 2009.

[2] Hastings D.J., Graham J., Nowakowski B., Smith S.T. and Tomblin J., A three fingered hand for a micro-assembly system, *Proc. ASPE*, Atlanta, Ga, 2010.

OPEN LOOP INERTIAL CROSS-TALK COMPENSATION BASED ON MEASUREMENT DATA

Markus Steinlin[2], Sascha Weikert[2], and Konrad Wegener[1,2]
[1]Institute of Machine Tools and Manufacturing (IWF)
[2]inspire AG
Swiss Federal Institute of Technology (ETH)
Zurich, Switzerland

ABSTRACT
Inertial cross-talk consists of displacements perpendicular to the intended direction of motion owing to a lateral offset between the driving force and the centre of mass, which causes a tilting motion during acceleration and deceleration. The amount of cross-talk can be determined with a small number of measurements. With the derived proportional factors between acceleration and lateral cross-talk an efficient model can be built and used for offline compensation on an industrial numerical control (NC).

INTRODUCTION
Dynamic deviations become more and more relevant for machine tool applications as the dynamic loads get increased due to an always ever increasing demand for productivity. One of these systematic dynamic deviations is the so-called inertial cross-talk as mentioned in ISO/CD 230-8.23 which consists of displacements perpendicular to the intended direction of motion owing to a lateral offset between the driving force and the centre of mass (CM), which causes a tilting motion during acceleration and deceleration. The tilting causes an orthogonal deviation of the tool center point (TCP) depending on the axial TCP offset from the centre of mass (see Figure 1). Ordinarily in the development of machine tools structures inertial cross talk should be minimized as far as possible [1].
Caused by the application, work-space accessibility and restraints concerning cost, for a large number of cases inertial cross-talk can not be fully eliminated by conceptual means only [2]. For these numerous cases the procedure described in this paper shall be applied.
This procedure consists of measuring the systematic cross-talk values and then using the derived proportional factors for the displacement compensation. Due to the linear nature of the inertial cross-talk phenomena a position and movement dependent generation of additional superposed axes movements can be applied.

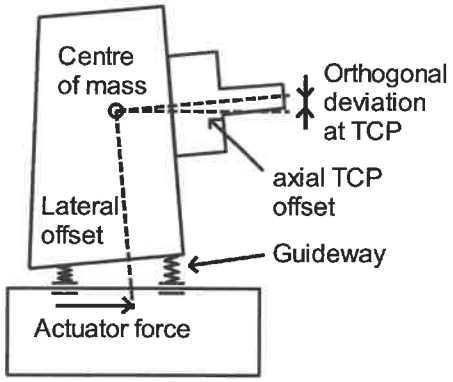

FIGURE 1. The figure shows the principle of cross-talk.

METHODOLOGY
This chapter explains the single steps required to build a cross-talk model for cross-talk compensation on an industrial numerical control.

Measurement
Firstly the perpendicular displacements caused by acceleration (or deceleration) have to be measured. An appropriate measurement system is the grid encoder from the Heidenhain Company [3]. Here the axial and the lateral components of motion can be captured simultaneously with moderate practical effort. For a complete compensation of cross-talk on a machine tool every axis has to be accelerated and every orthogonal direction has to be measured individually. In this chapter the movement and measurement process is shown for one specific acceleration direction only. The measurement is done for one specific orthogonal direction only. To be able to find a proportional factor for a specific deviation (example EYX for X-axis acceleration) and machine configuration in the working volume, several different set-point accelerations have to

be defined. Exemplarily the acceleration in Figure 2 is changed to 50, 100 and 200% of the suggested maximum acceleration for displacement over 100mm.

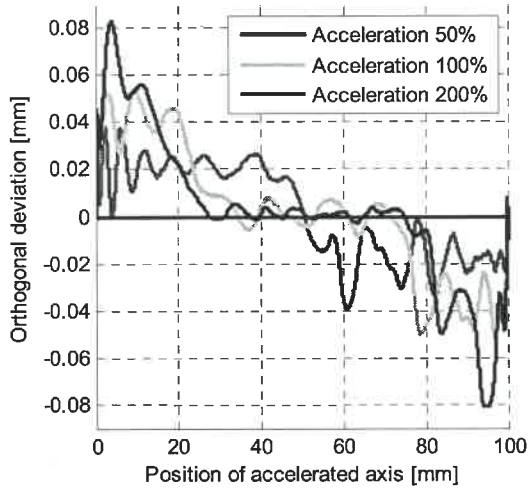

FIGURE 2. Grid encoder measurement with different maximal accelerations defined in the NC. The abscissa shows the positioning movement over 100mm. The ordinate shows the orthogonal deviation mainly caused by cross-talk.

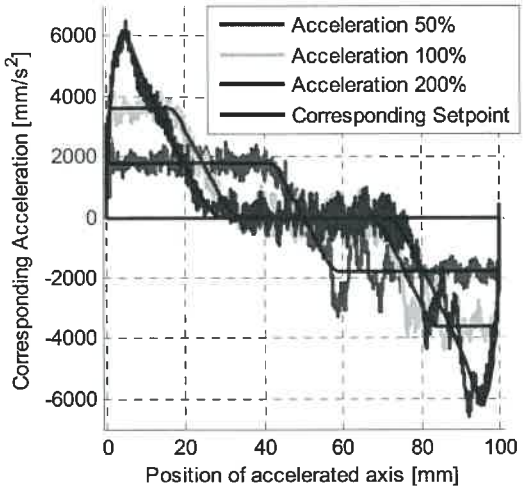

FIGURE 3. Different measured accelerations over the position of the movement. The solid black lines indicate the set-point accelerations.

Proportional Factors

Figure 3 shows the grid encoder measurements and the corresponding set-point accelerations over the positioning movement. Comparing the acceleration profiles with the orthogonal deviation profile in Figure 2 some correlation becomes obvious [4]. Cross-talk is proportional to the acceleration as is explained in Figure 1. This proportional factor can be determined through a linear fit (trend) in acceleration to cross-talk plot as shown in Figure 4. By plotting the acceleration versus the orthogonal deviation the linear correlation becomes obvious.

For the linear fit, all the measurements of different accelerations are put together; thereby some measurement filtering is needed. A measured acceleration never goes to zero, thus measurement points with low accelerations do not represent the cross-talk effect and therefore should not affect the linear fitting process. Therefore these points are neglected as described in Figure 4 by defining a lower boundary for acceleration. A lower boundary for the orthogonal deviation is defined to ignore non-cross-talk effects in the fitting process. Additionally all the measurement points from 25 to 75mm are neglected too (Figure 2 and 3).

This proportional factor has to be determined for every measured axis configuration of the machine tool.

Figure 4 contains additional information about the possibilities of the cross-talk modeling. The span of the orthogonal deviation on the ordinate-direction describes the amount of orthogonal errors that can't be modeled. Taking a short look at Figure 2 it becomes obvious that excited free oscillations can't be compensated. In contrast to them, the cross-talk which appears to be a forced oscillation (proportional to the acceleration in Figure 3) can be compensated.

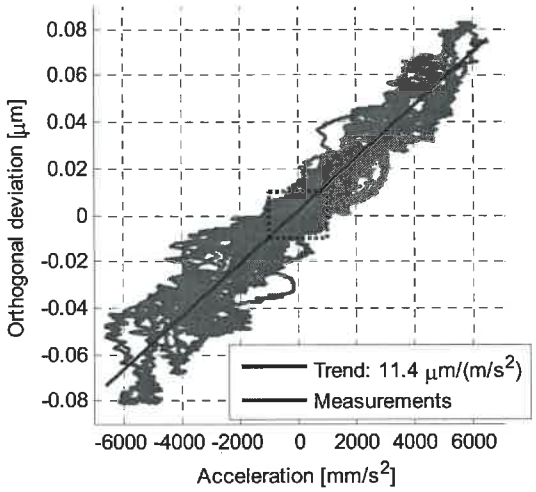

FIGURE 4. 2D representation of measurements; orthogonal deviation versus axial acceleration. The trend-line (black) shows a linear fit of the data. The dotted area shows points which were neglected for the trend line.

Model Fit

According to the effects described in [1] an axis-position (machine configuration) dependant model can be created and parameterized by the measurements. The offset of the tool center point from the center of mass (axial TCP offset) as well as the distance of the driving force to the center of mass (lateral CM offset) do influence the cross-talk behavior.

TABLE 1. The proportional factor (PF) determined by a set of measurements and calculated from a machine configuration dependant model are shown. (indicates a double weighted machine configuration)*

Offset		Cross-talk PF [µm] / [m/s²]		
CM lateral	*TCP axial*	*Measurement*	*Model*	*delta*
Back	Small	0	-0.3	-0.3
Back	Medium	3.2	3.5*	+0.3
Back	Large	7.6	7.3	-0.3
Front	Small	3.4	3.1	-0.3
Front	Medium	6.5	6.8*	+0.3
Front	Large	10.8	10.5	-0.3

In the current example the measurement was mainly position dependant but not influenced by the moved mass. The observed influence was taken in account using a linear dependence of the orthogonal position.

Cross-talk Compensation

The compensation of the cross-talk effect is based on feed-forward control. For a given acceleration set-point curve the cross-talk model is applied and the position deviation calculated. These values are then superposed to the original set-points. Using multiple models at a simultaneous axis movement, the compensation values can be accumulated axis-wise. The cross-talk effects inserted onto the system by the set-point compensation is neglected because of the low acceleration that is required. For successful set-point compensation the demanded acceleration and jerk have to correspond to the dynamic capabilities of the compensating axes.

The basic plant model [5] is used to investigate the transfer function behavior from the set-point to the internal measurement system. As shown in Figure 5, the plant model applied on the compensating movement inhibits the compensation due to its limited dynamics. To resolve this loss a scaling factor is applied to the set-point compensation. Applying the plant model, the loss of compensation can be recovered. To determine the scaling factor the simulation is compared with the compensation of the cross-talk model.

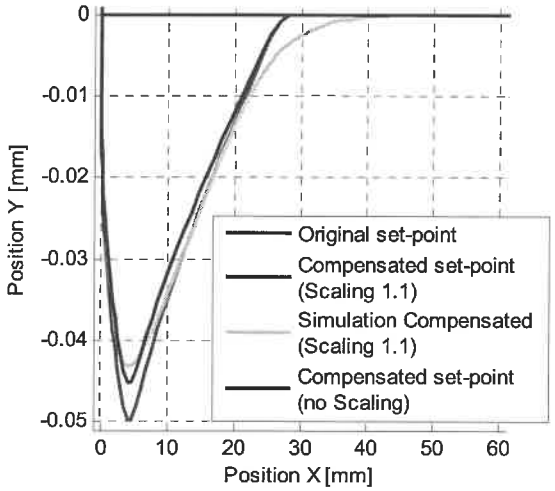

FIGURE 5. Set-point profiles using a cross-talk model for compensation (first part of positioning motion). Calculated compen-sation in dark gray, scaled compensation in light gray.

RESULTS

The cross-talk compensation described above can be implemented in an actual NC.

Using Industrial Numerical Control

The simple model described above does allow a machine configuration dependant implementation on an industrial numerical control. For the measurements shown below firstly the original set-point values for the 100mm positioning movement were captured on the Siemens numerical control (Sinumerik 840D). The modified compensated set-point values were then fed back directly as input for the position feed-back controller. The compensation can't be implemented through ISO-NC code due to geometry and feed-rate optimization inside the numerical control.

Measurement Results

For a corresponding machine configuration, a compensated set-point trajectory was applied on the machine tool. All the settings for the positioning movement, including jerk, acceleration and velocity stayed the same beside the small lateral compensational movements. In Figure 6 the original measurement is compared with the resulting compensated measurement. The results show a reduction of the maximal cross-talk deviation by

about 50% without influencing the dynamics of the machine tool.

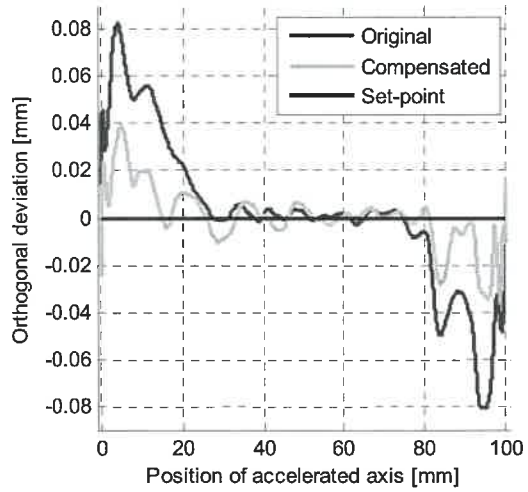

FIGURE 6. Measured cross-talk deviation for the non-compensated system (dark gray), for the compensated system (light gray). The programmed set-point is indicated black.

CONCLUSION AND RECOMMENDATIONS

Summary

This paper gives a step by step description for a compensation of inertial cross-talk on an industrial machine tool. The first step is a dynamic machine configuration dependent measurement in representative positioning and measurement directions. These measurements are performed with different maximum accelerations. Based on these measurements a proportional factor describing the ratio of the orthogonal deviation depending on the acceleration and the machine configuration can be determined. The given drive dynamic can be taken into account by using a scaling factor. For a given set-point trajectory (including acceleration profile) the compensation can be calculated and feed back in the industrial numerical control.

The step by step procedure is applied in an example for a single positioning direction and an over 50% reduction of the maximal cross-talk effect was achieved.

Discussion

The result shown in Figure 6 clearly leaves potential for improvement. The compensated trajectory still has cross-talk characteristics, meaning acceleration and deceleration lead to a definable orthogonal derivation direction.

The proportional factor (see Figure 4) is sensitive to the selection of points for the trend calculation. The observed sensitivity in the example is 0.5 µm per m/s^2.

Recommendations

In the chapter of compensation the additional scaling of the compensation is suggested because some of the compensation is lost due to actuator dynamics and non-linearity. An alternative approach could be the use of an inverted model of the plant.

ACKNOWLEDGMENT

This project was supported by the Swiss Commission for the Promotion of Applied Research (KTI) and by Swiss industrial partners.

REFERENCES

[1] Rehsteiner F, Weikert S, Rak Z Accuracy Optimization of Machine Tools under Acceleration Loads for the Demands of High-Speed-Machining, ASPE-Proceedings of the ASPE Annual Meeting, St. Louis. 1998; Oct, 25-30: 602-605

[2] Maglie P, Carbini R, Weikert S, Wegener K Efficient mechatronic evaluation of machine tool designs using model reduction, Proceedings of the 12th Mechatronics Forum, Biennial International Conference. 2010; 1: 285-292.

[3] http://www.heidenhain.de/en_US/products_and_applications/setup_and_measurement/machine_measurement/kgm/ 2010-6-30

[4] Bringmann B, Maglie P A method for direct evaluation of the dynamic 3D path accuracy of NC machine tools, CIRP Annals – Manufacturing Technology. 2009; 58: 343-346.

[5] Zirn O, Weikert S Modellbidung und Simulation hochdynamischer Fertigungssysteme, Springer 2006.

2-D ABSOLUTE POSITIONING SYSTEM FOR REAL TIME CONTROL APPLICATIONS

Carlos A. Montes[1], John C. Ziegert[1], Chan Wong[1], Laine Mears[1] and Tommy Tucker[2]
[1]Department of Mechanical Engineering
Clemson University,
Clemson, SC 29634, USA
[2]Tucker Innovations Inc.

INTRODUCTION

The present research introduces a 2-D absolute position feedback method with application to real time position control for manufacturing equipment, such as machine tools. The desired planar displacement command of the tool is produced by an active element or active target on a liquid-crystal display (LCD). A fixed vision sensor is located so that camera plane is parallel to the LCD, which moves freely in the XY plane based upon control action. The sensor observes the motions of the active target and also provides a 2-D coordinate frame based on which in-plane position errors are determined. The machine axes move to reduce these errors causing the planar positioning stage to follow the motions of the target image on the display. Due to the direct-sensing nature of the position transducer no geometric error compensation is required. An image processing algorithm has been developed to retrieve high resolution position and orientation information of a cross-hairs target, displayed on the LCD. This algorithm allows positioning resolution of less than 1/100th of the pixel size on the display. The time delay in the feedback signal to the control system associated with slow hardware frame acquisition rate and long image processing times is addressed through a Smith predictor control scheme. Experimental results are presented.

TESTBED

The current research is implemented on an XY stage that allows two dimensional motion. An LCD screen is placed upside-down on top of the stage and moves with the stage (Figure 1). The position of the stage is determined through a stationary CCD digital camera that is fixed to the support structure of the stage and aimed at the LCD. A displacement command is displayed on an LCD screen as a moving target image (or active target); then, the position of this target with respect to a reference point in the image plane (CCD) is estimated. The present work is focused on achieving the desired resolution levels for the proposed platform and fully defining a robust control system structure.

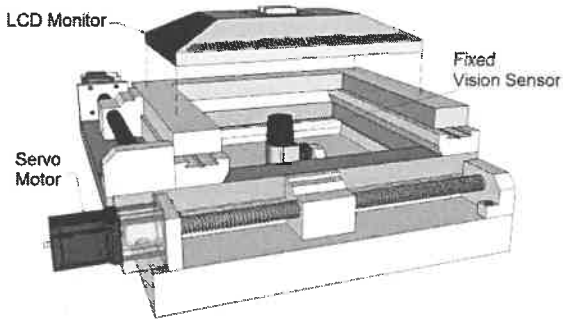

FIGURE 1. 2-axis stage with LCD monitor and fixed CCD camera.

Cross-Hair Dynamic Target

The target is represented by the intersection of two perpendicular lines displayed on the LCD, i.e. a cross-hairs target. Previous tests have shown that for an 8-bit display, with pixel intensities varying from 0 (lowest, black) to 255 (highest: R, G or B), the optimal configuration is achieved by displaying a high-intensity target over black background (Figure 2 (a)). Aside from the cross-hairs target, four Reference Elements are displayed close to the intersection. These Reference Elements are spaced by known distances on the LCD and are used to estimate the magnification, f/Z, of a thin-lens perspective projection model, where f is the focal length and Z is the out-of-plane distance between the lens and the LCD. If the principal point PP on the CCD (Figure 2 (b)) is regarded as the reference, then an in-plane position error vector can be defined at any time t, with respect to this reference. As such, a target point **C** on the LCD would have an error vector $\mathbf{e}(t)=\mathbf{c}$ on the CCD. This vector can be used as the control loop

position error, where the controller's goal is to bring the target to the reference position, i.e. PP.

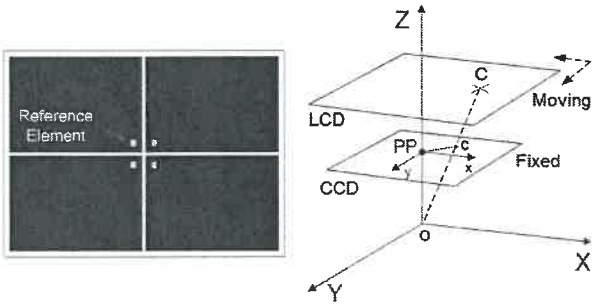

(a) (b)

FIGURE 2. (a) Pixelated dynamic target on LCD with four Reference Elements, and (b) pinhole camera model.

2-D ABSOLUTE POSITIONING THROUGH NEWTON-RAPHSON ITERATIVE APPROACH

The procedure for locating the target, once captured as a digital image though a CCD monochrome camera, is described in three steps: 1. Fine point location and definition of the line sets; 2. Constrained curve fitting through Newton-Raphson method; and 3. Estimation of pixel magnification using Reference Elements.

Fine Point Location and Definition of Sets

A fine point location on the CCD is achieved by calculating the intensity weighted center of mass or centroid around an intensity transition. An intensity transition of interest is defined as a vertical or horizontal transition that starts in a black region, goes through a saturation point at 255 and finally goes back to a black region. For a discrete-valued function such as an image, $I(x,y)$, where x varies in a discrete manner over a horizontal array of pixels e.g. $x \in [0, m-1]$, and y is fixed to the current row under analysis e.g. $y=j$, the center of mass is

$$X_{c,j} = \frac{\sum_{i=0}^{m-1} x_i I(x_i, j)}{\sum_{i=0}^{m-1} I(x_i, j)} \tag{1}$$

The vertical centroid can be easily calculated by fixing x to a given column and letting y vary within a vertical neighborhood of interest. The target orientation, governed by θ, is measured with respect to the CCD X-axis and is used to determine the type of transitions present in the target image (Figure 3). If $|\theta| \le 15°$ then the image processing algorithm searches for both horizontal and vertical intensity transitions. Only horizontal transitions are analyzed, otherwise. The threshold value of 15° is selected based on trial and error tests using experimental data. Once the centroids are calculated they are separated in two sets later associated to two different lines.

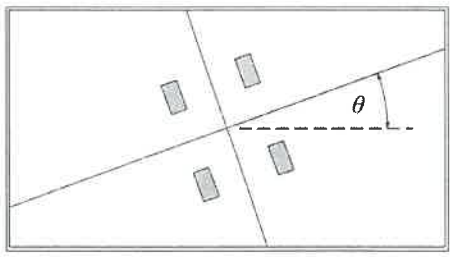

FIGURE 3. Target orientation θ.

Constrained Curve Fitting

The location of the target is obtained by calculating the two lines that best fit the data collected in the previous step, and then analytically computing the intersection of these lines. The two data sets obtained from the previous step are denoted as *DS*1 and *DS*2 and are known to contain n_1 and n_2 data points, respectively. The best fit lines are constrained to be perpendicular with respect to each other. The previous statement is equivalent to finding $\mathbf{y}^{\text{model}}$, where

$$\mathbf{y}^{\text{model}} = \begin{cases} a_0 + a_1 x, & a_0, a_1 \in \mathbb{R} \text{ and } x \in DS1 \\ a_2 - \frac{1}{a_1} x, & a_2 \in \mathbb{R} \text{ and } x \in DS2 \end{cases} \tag{2}$$

such that

$$S(a_0, a_1, a_2) = \sum_{data} \left(\mathbf{y}_i - \mathbf{y}^{\text{model}} \right)^2$$

$$= \sum_{DS1} \left(y_i - a_0 - a_1 x_i \right)^2 + \sum_{DS2} \left(y_i - a_2 + \frac{1}{a_1} x_i \right)^2 \tag{3}$$

is minimized. The minimum is obtained by finding a_0, a_1, and a_2 such that $\partial S / \partial a_0 = 0$, $\partial S / \partial a_1 = 0$ and $\partial S / \partial a_2 = 0$. From $\partial S / \partial a_0 = 0$, $\partial S / \partial a_2 = 0$, respectively, the following two equations result

$$a_0 = \frac{1}{n_1} \left(v_2 - a_1 v_1 \right) \tag{4}$$

$$a_2 = \frac{1}{n_2}\left(w_2 + \frac{1}{a_1}w_1\right) \quad (5)$$

where $v_1 = \sum_{DS1} x_i, v_2 = \sum_{DS1} y_i, v_3 = \sum_{DS1} x_i y_i, v_4 = \sum_{DS1} x_i^2$ and w_i, i=1,..,4, is equivalent to v_i but using *DS2*. The calculation of $\partial S/\partial a_1 = 0$, knowing the results from (4) and (5), yields a nonlinear equation of the form $f(a_1)$=0, where f is assumed to have a continuous first derivative f'. This is

$$f(a_1) = \frac{v_1 v_2}{n_1} - v_3 + a_1\left(v_4 - \frac{v_1^2}{n_1}\right) + \frac{1}{a_1^2}\left(\frac{w_1 w_2}{n_2} - w_3\right) + \frac{1}{a_1^3}\left(\frac{w_1^2}{n_2} - w_4\right) = 0 \quad (6)$$

Equation (6) is solved using Newton-Raphson's iterative method, which implies calculating

$$a_1(n+1) = a_1(n) - \frac{f(a_1(n))}{f'(a_1(n))}, \quad n = 1,2,...,k \quad (7)$$

until

$$|a_1(n+1) - a_1(n)| \le \varepsilon |a_1(n)| \quad (8)$$

where $a_1(n)$ represents a constant value given to the variable a_1, k is the total number of iterations, ε is an arbitrary threshold and the factor $|a_1(n)|$ in (8) is required in case of roots of very large or very small absolute value. Once a value for a_1, satisfying (8), is found (4) and (5) can be calculated and (2) is fully defined. An initial value for a_1 in (7) is determined by applying unconstrained curve fitting to *DS1*; the slope of the unconstrained best fit line is regarded as $a_1(0)$. If the criterion diverges for a given target image, unconstrained curve fitting is applied to *DS2* as well, and the target is defined as the intersection of the unconstrained curves.

Magnification

The magnification between the LCD- and CCD-pixels is obtained by determining the distance between the four Reference Elements on the CCD and comparing it with the real LCD spacing between these points. The locations of the Reference Elements on the target image are calculated with subpixel resolution using (1) over the areas containing these elements.

COMMAND ISSUING

One LCD pixel consists of three individual stripes (RGB). The intensity of a single LCD-pixel stripe is usually defined in an 8-bit scale. Color intensities on the LCD map to grayscale intensities on the CCD (also in the in an 8-bit scale for an 8-bit camera). Displacement commands are given by changing the intensity weighted centroid on the LCD target pixels, and thereby moving the target by increments in the order of microns. In practice, the camera cannot reliably distinguish between all possibly intensity states of the LCD display. Therefore, a three-tone intensity basis, used to generate horizontal displacement commands, is selected and applies only to those pixels on the target vertical line: $I_B^X = \{0,127,255\}$. Hence, a displacement basis can be defined: $D(I_B^X) = \{0.00, \pm 32.58, \pm 49.00\}$ µm (Table 1). From Figure 4 (a) it should be clear that the horizontal displacement basis only needs to cover a 0- to ±49µm range, starting from a reference stripe X_0. For displacement bigger than |49|, a different reference stripe is selected.

TABLE 1. Horizontal centroid change as a function of intensities I(0) and I(1), corresponding to two adjacent stripes and for an LCD pixel size of 294x292µm.

I(0)	I(1)	ΔX_C (µm)
255	0	0.00
255	127	32.58
255	255	49.00

In order to command horizontal displacements of a fraction of the displacements provided by the basis, some of the LCD pixels on the target vertical line that lie within the camera FOV are set to exhibit a centroid in one location and the rest are set to exhibit a displaced centroid (Figure 4 (b)). For example, if a horizontal displacement command of 34µm was to be issued, 88% of the pixels in the vertical line would present a centroid at 32.58µm and 12% would present a displaced centroid at 49.00µm. Notice that, 34≈0.88*32.58+0.12*49, with an error of less than one micron. For the case of vertical displacement commands a five-tone intensity basis is selected: $I_B^Y = \{0,80,130,180,255\}$. A corresponding vertical displacement basis is defined: $D(I_B^Y) = \{0.00, \pm 58.26, \pm 82.40, \pm 101.00 \pm 122.00\}$ µm

. In general a 2-D displacement command, ΔX_{LCD}, must consider the target orientation θ. Therefore, a displacement command ΔX_{LCD}, displayed on the LCD but referenced to the camera plane, requires a displacement $\Delta \hat{X}_{LCD}$ of the target image referenced to the LCD plane. These two quantities are related through a rotation matrix R_θ, i.e. $\Delta X_{LCD} = R_\theta \Delta \hat{X}_{LCD}$.

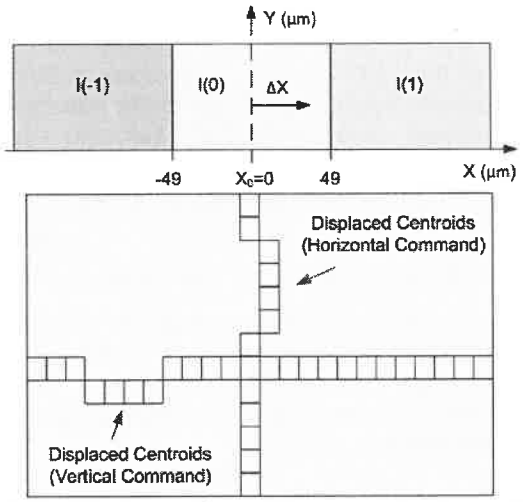

FIGURE 4. (a) One LCD pixel consisting of three stripes: R, G and B. (b) Target on LCD showing a horizontal and a vertical command through displaced centroids.

CONTROL SYSTEM TIME DELAY

Low camera frame rates and time for image processing cause delays in the acquisition of the computed position of the target image. The delay in the vision-based control system is addressed through a modified version of the well known Smith predictor scheme.

TEST RESULTS

Experimental data is collected using BMP images. A 100-image sample of the same static target presented a standard deviation of 0.253μm.

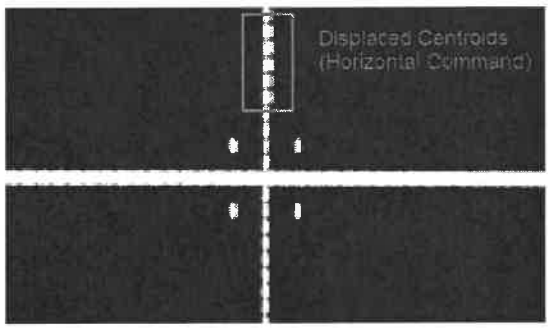

FIGURE 5. Zoom-in experimental target image.

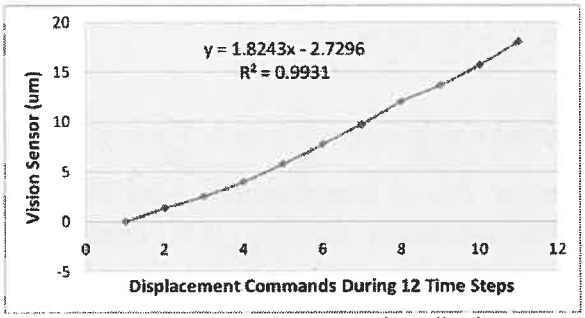

FIGURE 6. 11 horizontal displacement commands of 2μm are represented on the target image. The resulting best fit line has a slope of 1.8243μm/command and a correlation coefficient of 0.9931.

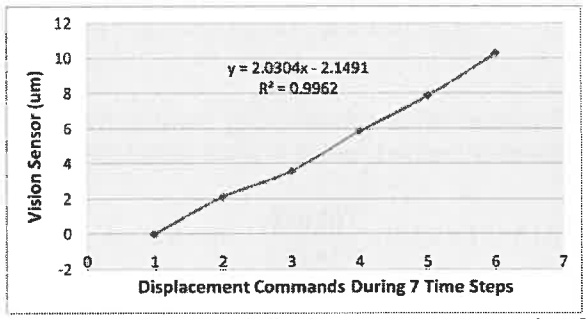

FIGURE 7. 6 vertical displacement commands of 2μm are represented on the target. The resulting best fit line has a slope of 2.0304μm/command and a correlation coefficient of 0.9962.

CONCLUSIONS

A 2-D position feedback method for real time control applications was presented. Experimental results demonstrate that resolutions on the order of 2μm can be reliably sensed, and displacement commands of the same size can be issued through intensity variations.

ACKNOLEDGEMENTES

This material is based upon work supported by the National Science Foundation under Grant No. 0800507. Any opinions, findings, and conclusions or recommendations expressed in this material are those of the author(s) and do not necessarily reflect the views of the National Science Foundation.

REFERENCES

[1] Chu, D., Trujillo, H., Whitney, E. and Young, J. 2006. "Rapid High Resolution Absolute 2-D Encoding by Low Resolution Digital Imaging of a Mathematically Generated 3-Tone Target". ASPE Proceedings - Annual 2006.

PRACTICAL FRICTION COMPENSATION FOR ULTRA PRECISION POINT-TO-POINT MOTION

Brian A. Bucci[1], Daniel G. Cole[1], Jeffrey S. Vipperman[1], Stephen J. Ludwick[2]
[1]Department of Mechanical Engineering
University of Pittsburgh
Pittsburgh, PA, United States
[2]Aerotech Inc.
Pittsburgh, PA, United States

INTRODUCTION

The force of friction is known to cause detrimental effects to precision servomechanisms with rolling contacts. With regard to ultra precision, rapid point-to-point motion frictional effects are manifest in extended and inconsistent settling times. Over sub-micrometer displacements, the force of friction is best characterized as a hysteretic stiffness. Since simple friction models such as the viscous model and Coulomb model do not make a sufficient description of the force of friction over this regime, more advanced friction models, such the Dahl model[1], LuGre model[2], and generalized Maxwell-slip model[3] are often used[4].

However, the effects of friction on servomechanisms appear to be subject to some measure of uncertainty. Thus, a single parameterization of even the most advanced friction model is not guaranteed to capture all frictional effects, all of the time. Considering the factors that cause changes in frictional characteristics also becomes exceedingly complex. Inevitably, some changes in frictional characteristics must be attributed to unknown factors. For a friction compensation method to be practical, it must be able to deal with changes in the frictional process while still maintaining a measurable increase in system performance and without posing a risk of system instability. The aim of this effort is too compare the friction observer[5] to a friction model-based gain scheduling (FMBGS) method at the task of settling after a stepping motion.

CONTROL PROBLEM

A servo subject to friction can be modeled as

$$m\ddot{x} + F_r = u(t), \tag{1}$$

where m is the mass, F_r is a generic term representing the force of friction, and $u(t)$ is the control signal. When the servo is very near velocity reversals, as is likely to occur when settling after a step motion, pre-rolling friction can often dominate the other system dynamics[6]. This leads to an approximation of the servo during final settling as

$$F_r = u(t). \tag{2}$$

If the force of friction is represented by the simple Dahl model, Bliman [7] shows that the force of friction can be expressed as a function of displacement. For positive motion

$$F_r^+(x) = F_C - (F_C - F_0)\exp\left(-\frac{\sigma}{F_C}(x - x_0)\right), \tag{3}$$

and for negative motion

$$F_r^-(x) = -F_C + (F_C + F_0)\exp\left(\frac{\sigma}{F_C}(x - x_0)\right), \tag{4}$$

where F_C is the level of Coulomb friction, σ is the initial contact stiffness, F_0 is the value of the force of friction at the previous velocity reversal, and x_0 is the location of the previous velocity reversal. For now, assume that motion only occurs in the positive direction also, set $F_0 = 0$ and $x_0 = 0$. Let a error signal be defined as $e = r - x$, where r is a position reference signal. In the settling problem let r be constrained to a constant value, as it is common to hold a position reference signal constant during settling. Further, since positive motion is to be studied, let $r > 0$. Thus, for these conditions, the system in equation 2, under PI control could be expressed as

$$F_C\left(1 - \exp\left(-\frac{\sigma}{F_C}(r - e)\right)\right) = \int_0^t k_I e(t)dt + k_P e(t), \tag{5}$$

where k_I is an integral gain and k_P is a proportional gain. Some further manipulation leads to an expression of the error dynamics as

$$\dot{e} = -\frac{k_I}{\sigma\exp\left(-\frac{\sigma}{F_C}(-e + e_0)\right) + k_P}e, \tag{6}$$

where e_0 is the initial condition on e or the value of e at the previous velocity reversal. Now introduce multiplicative uncertainty of the initial contact stiffness parameter as $\sigma^+ = \sigma(1+\delta)$, where σ^+ is the true parameter value and δ is the perturbation away from the nominal value. This leads to error dynamics of

$$\dot{e} = -\frac{k_I}{\sigma(1+\delta)\exp\left(-\frac{\sigma(1+\delta)}{F_C}(-e+e_0)\right)+k_P}e. \tag{7}$$

FRICTION OBSERVER

Let $F = \sigma(1+\delta)\exp\left(-\frac{\sigma(1+\delta)}{F_C}(-e+e_0)\right)$, which is the true frictional behavior and let $\hat{F} = \sigma\exp\left(-\frac{\sigma}{F_C}(-e+e_0)\right)$, which is the nominal friction model. If a friction observer was designed to cancel the nonlinearity due to the pre-rolling phenomenon the resulting error dynamics are

$$\dot{e} = -\frac{k_I}{F-\hat{F}+k_P}e, \tag{8}$$

where the integral action drives the system to zero position error. Assuming that $F = \hat{F}$, the integral action could be designed to give the desired system response by setting $k_I = \frac{1}{\tau_d}k_P$, where τ_d is the desired time constant for the system.

FRICTION MODEL-BASED GAIN SCHEDULING (FMBGS)

Again assuming that $F = \hat{F}$, another way the achieve the error dynamics of $\dot{e} = \frac{1}{\tau_d}e$ is by setting

$$k_I = \frac{1}{\tau_d}\left(\hat{F}+k_P\right). \tag{9}$$

Thus, the controller integral action is scheduled by a friction model. This results in higher integral gains when the system is near a velocity reversal and lower integral gains when the system is further from a velocity reversal. In the case where $F = \hat{F}$ the resulting system will have identical behavior to the friction observer when $F = \hat{F}$.

REALISTIC TESTING SCENARIO

Two methods of friction compensation for servo settling have been introduced and shown to be equivalent in the case of perfect modeling. To explore their utility in a practical application, it is desired to compare their performance in the presence of modeling error. In interest the of making a fair comparison a test case is constructed based on real data and real control settings for an actual precision servo. These parameters are shown in table 1.

TABLE 1. This table lists the simulation parameters estimated from an actual precision servo.

Simulation Parameters
m=1.5 kg
Cross-over frequency= 100 Hz
Phase Margin = 45 °
k_P = 900,000 N/m
k_D = 850 Ns/m
σ mean = 8×10^6 N/m
σ min = 4×10^6 N/m
σ max = 16×10^6 N/m
-0.5$\leq \delta \leq$1
F_C= 1 N
$\tau_d = \frac{1}{250}$ s

MASSLESS SIMULATION

In this section a numerical simulation of the concepts presented in equations 8 and 9 are discussed. First, introduce a normalization called characteristic length of pre-rolling friction defined as $\overline{X} = \frac{F_C}{\sigma}$. For the nominal test scenario $\overline{X}$=125 nm. This value appears reasonable as previous experience has shown pre-rolling effects to be very significant at distances of $\leq$100 nm. In this study, the time it takes the perturbed system to settle to 2% of the initial reference value will be compared to the settling time of the system with the nominal plant. Figure 1 shows the results of this study. In figure 1 each level

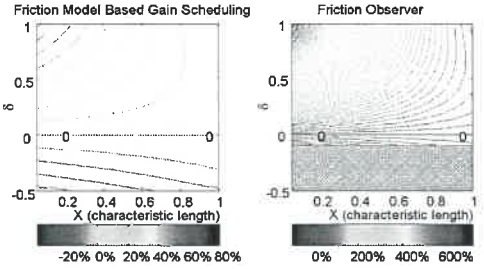

FIGURE 1. A contour plot shows the percentage change in settling time for the FMBGS (left) and the friction observer (right) for a range of uncertainty of the initial contact stiffness.

curve is equivalent to a 10% change in settling time. The crosshatch areas indicated regions of instability. Since the simulation of the friction observer contains far more level curves (-100% to 600%) than the FMBGS (-20% to 80%) and the friction observer also has predicted instability, the FMBGS should be more robust than the friction observer.

SIMULATION INCLUDING MASS

While the assumption of negligible inertial response lead to very nice results, it is obvious that this assumption cannot be valid under every possible condition. Thus, it is necessary to show that there are cases when this assumption is valid, or at least this assumption provides a reasonable approximation in spite of higher order behavior. One of the main differences between simulation with mass and massless simulations is that numerous velocity reversals are expected in the higher order simulations. The previous simulations were nonlinear but, only first order and velocity reversals did not occur during the settling process. Thus, when solving the higher order equations care must be taken to look for a velocity reversal, stop the simulation, collect the appropriate initial conditions, switch to the equation of the opposite direction, and then resume solving.

The higher order equations for the friction observer can be summarized as

$$m\dddot{e} + k_D\ddot{e} + \left(F - \hat{F} + k_P\right)\dot{e} + \frac{1}{\tau_d}k_P e = 0. \quad (10)$$

Similarly, the higher order equations for the FMBGS are summarized as

$$m\dddot{e} + k_D\ddot{e} + (F + k_P)\,\dot{e} + \frac{1}{\tau_d}\left(\hat{F} + k_P\right)e = 0. \quad (11)$$

The simulations including mass are conducted with an initial error condition of 62.5 nm, well within the pre-rolling regime. A few interesting cases are presented. In the first simulation, figure 2, δ = 0, thus, it is assumed that the friction model exactly captures the real system behavior. In this case the massless observer and FMBGS series are not visible because they are directly beneath the ideal case. The effect of adding mass to the system is clearly seen in the slight oscillations shown in these respective simulations.
In figure 3, δ=1, the upper bound on uncertainty. Once again the massless, approximations are difficult to see because they lie almost directly under their respective mass included simulations. In this case the FMBGS clearly converges much faster than the friction observer. The case where δ = -0.05, shown in figure 4, is interesting because the massless observer simulation (figure 1) suggests that the system should actually converge faster than the nominal case but, it is near the boundary of stability. When mass is included, the observer does not converge faster but, instead,

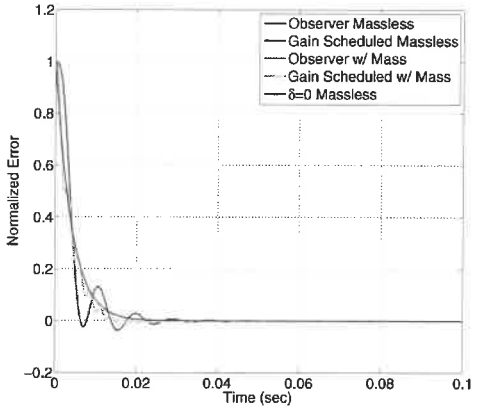

FIGURE 2. The systems' behaviors are shown for the case of δ=0.

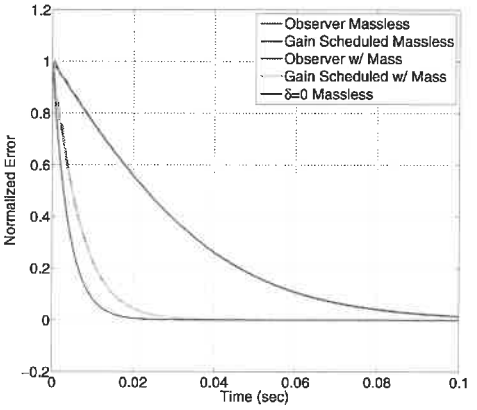

FIGURE 3. The systems' behaviors are shown for the case of δ=1.

rings, more like a system close to instability. Although there is some ringing in the higher order FMBGS simulation, the general behavior is still captured rather well by the massless approximation. Finally, case where δ=-0.5 is shown in figure 5. At this point, both simulations of the friction observer have gone unstable and are not plotted. The FMBGS with mass included tends to take considerably longer to settle than the massless simulation would suggest but, the system is still stable for the entire range of the parametric uncertainty.

EXPERIMENTAL RESULTS AND CONCLUSIONS

To further investigate the proposed control algorithm, an experiment consisting of 100 instances

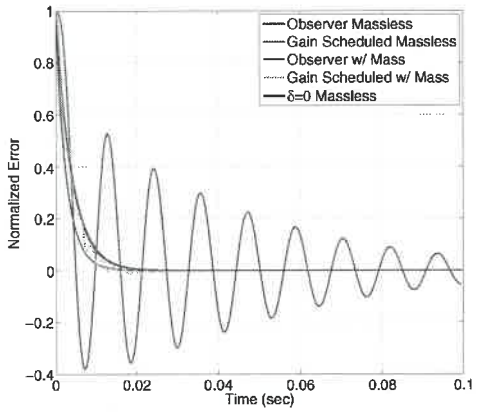

FIGURE 4. The systems' behaviors are shown for the case of δ=-0.05.

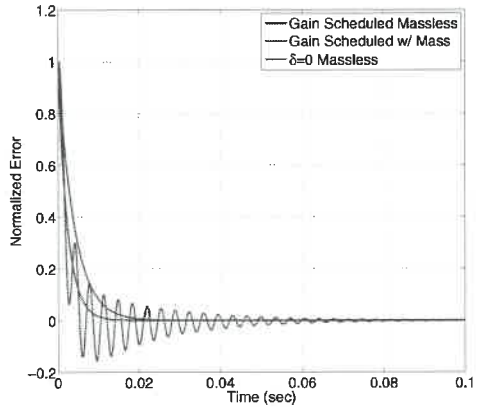

FIGURE 5. The systems' behaviors are shown for the case of δ=-0.5.

of 5 mm steps, for each control algorithm, were conducted along the length of travel of the linear servo. As a point of reference, the friction observer and the FMBGS are compared to the performance of the factory tuned PID control. Across the experiments, all proportional gains, derivative gains, and friction models are identical. The only difference between the simulation and the experiment is that $\sigma = 4 \times 10^6$ N/m was used in to avoid instability of the observer. Figure 6 shows the distribution of +/- 10 nm settling times. From figure 6, it seen that the FMBGS was able to reduce settling time by 65%, compared to the PID controller. The friction observer actually increased settling time by 8%, compared to the PID controller. It is also interesting to note that the FMBGS produced a tighter grouping of settling times, compared to

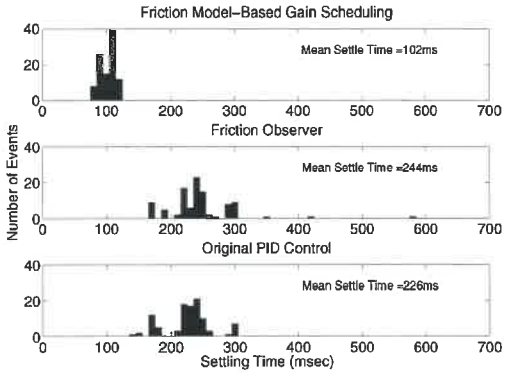

FIGURE 6. The histograms compare the time it takes each method to settle to +/-10 nm of the position reference.

the other methods. Thus, the FMBGS appears to be an easy to implement, and practical method of increasing settling performance of servo mechanisms.

REFERENCES

[1] Dahl P. A Solid Friction Model. Space and Missile Systems Organization Air Force Systems Command; 1968.

[2] de Wit CC, Olsson H, Åstrom K, Lischisnsky P. A new model for control of systems with friction. IEEE Transactions on Automatic Control. 1995 March;40(3):419–426.

[3] Swevers J, Al-Bender F, Ganseman C, Prajogo T. An Integrated Friction Model Structure with Improved Presliding Behavior for Accurate Friction Compensation. IEEE Transactions on Automatic Control. 2000;45:675–689.

[4] Bucci B, Cole D, Vipperman J, Ludwick S. Friction modeling of linear rolling element bearings in high precision linear stages. In: Proceeding of the American Society for Precision Engineering; 2009. .

[5] Olsson H. Control of Systems with Friction. Lund Institute of Technology; 1996.

[6] Futami S, Furutani A, Yoshida S. Nanometer positioning and its micro-dynamics. Nanotechnology. 1990;1:31–37.

[7] Bliman PJ. Mathematical study of the Dahl's friction model. European Journal of Mechanics. 1992;11:835–848.

A MULTIRATE MULTIPROCESSOR CONTROL PLATFORM FOR HIGH-SPEED PRECISION MOTION CONTROL

Kristofer Smeds, Xiaodong Lu
The University of British Columbia
Vancouver, British Columbia, Canada

INTRODUCTION

Many high-speed precision applications, such as fast-tool servos (FTS) and atomic force microscopes, can greatly benefit from digital controllers with both MHz range sampling and precision data acquisition. For example, a FTS with a bandwidth above 20 kHz is highly desired in the production of microstructures, such as micro-lens arrays for light enhancing films. To achieve such high bandwidth motion with high precision, a sampling rate of at least 500 kHz is required for the digital motion controller. A typical commercial real-time control platform can offer sampling rates of 10-20 kHz. Some high-end controller hardware, such as dSpace, can achieve 100 kHz sampling rates; however, this is still far less than what is desired for many high-speed high precision motion control applications.

This paper presents a new control platform, Tsunami, intended to greatly increase the performance of a digital controller in high-speed precision applications through the use of a triple-body architecture and multirate multiprocessor controller implementation. The triple-body architecture introduced in [1] is used to maximize the sampling rate and minimize the input-output latency while still maintaining very high motion precision. The multiprocessor environment is ideal for multirate control, which (due to its parallel nature) is well suited to take advantage of the additional resources. A wide range of interchangeable application specific I/O resources are made available to interface with sensors and actuators for motion control. Further, this high performance hardware is easy to use, offering Simulink® integration for digital controller design and LabVIEW® integration for graphical user interface development.

CONTROL PLATFORM ARCHITECTURE AND FEATURES

The developed control platform consists of an application independent motherboard that interfaces to application specific expansion IO cards. A functional diagram of the motherboard is shown in Figure 1. It includes four 500 MHz TigerSHARC TS-201 processors for controller computation, 256MB SDRAM for handling large amounts of application data, a Virtex-5 FPGA for interfacing to the application specific IO, a gigabit Ethernet link for communicating with the host computer, and two expansion IO card slots.

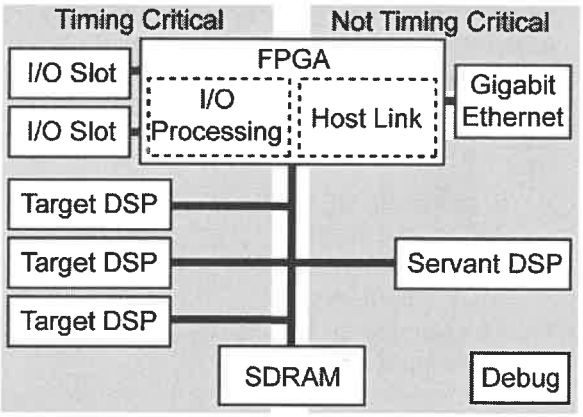

FIGURE 1. Function diagram of the control platform motherboard.

The triple-body architecture is realized by dedicating one of the processors as a servant to handle all host interactions. This processor is then tightly coupled through a 64-bit 125 MHz multiprocessing bus to the remaining three target processors, which are responsible purely for controller execution. This allows the servant to access information on the targets with minimal impact on controller execution. Thus, timing critical control tasks are separated from non-timing critical host interactions such as parameter tuning, signal monitoring, and data logging. Additionally, this allows the target processors to run in polling mode, eliminating interrupt latency from the timing critical loop while still maintaining a flexible user interface via the servant. The control platform motherboard connected to two expansion IO cards is pictured in Figure 2.

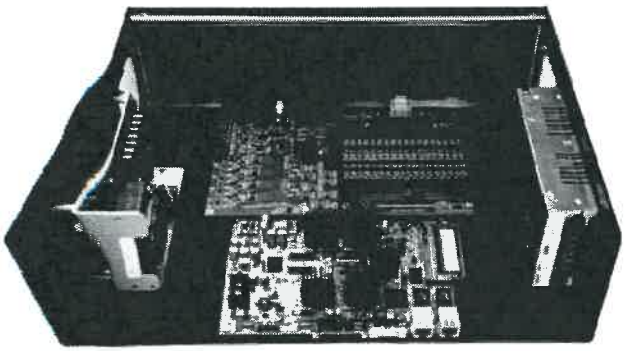

FIGURE 2. Picture of the Tsunami control platform motherboard connected to two expansion IO cards.

Each expansion slot connects to the FPGA allowing for application specific expansion I/O cards. Currently two cards have been created that interface to a wide range of sensors and actuators. The available I/O resources on these cards are:

- 4 channels of 4 MSPS 16-bit ADCs with ±10V input range
- 4 channels of 50 MSPS 16-bit DACs with ±10V output range
- 16 channels of 500 kSPS 16-bit ADCs with ±10V input range
- 32 channels of 500 kSPS 16-bit DACs with ±10V output range
- 6 channels of quadrature encoder inputs with 0.6 ns timestamp resolution and 32-bit position counter.
- 2 channels of Camera Link inputs with base configurations (2 Gbps data rate) with trigger outputs.
- 48 channels of PWM outputs capable of a 200 kHz modulation frequency with 2.6 ns resolution.
- 20 channels of general purpose digital I/O

The four high-speed (4 MSPS) ADCs and four high-speed (50 MSPS) DACs are ideal for high-speed precision systems. The other DACs and ADCs allow the control platform to also handle larger multi-input-multi-output systems. The Camera Link inputs enable multi-degree of freedom optical position sensing at up to 80 kHz sampling. All these I/O resources are made accessible via an easily-accessible external interface panel.

BENEFITS TO CONTROL PERFORMANCE

The block diagram of a typical digital control system is shown in Figure 3.

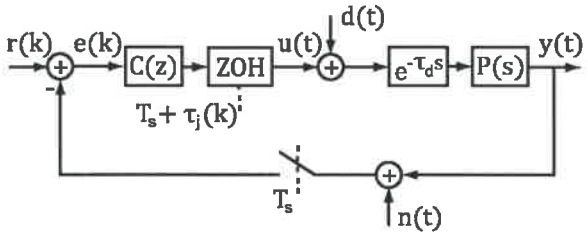

FIGURE 3. Block diagram of a typical digital control system

The diagram includes sensor noise, $n(t)$, input-output latency, τ_d, control output disturbance, $d(t)$, control output jitter, τ_j(k), and the system ideal sampling period T_s. The input-output latency is the sum of the analog-to-digital conversion time, the controller computation time, and the digital-to-analog conversion time. From a controls standpoint this can be viewed as a pure delay in the system. In addition, the zero-order hold adds another delay that is dependent on the sampling period. For the frequency region of $\omega < \omega_s/4$ this can be approximated as

$$ZOH = \frac{1 - e^{j\omega T_s}}{j\omega} \approx T_s e^{-\frac{j\omega T_s}{2}} \qquad (1)$$

The total delay resulting from digital control is $\tau_d + T_s/2$ and the whole plant in the discrete domain can be represented as

$$G_z(e^{-j\omega T_s}) \approx e^{-j\omega\left(\tau_d + \frac{T_s}{2}\right)} G(j\omega) \qquad (2)$$

Assuming that the entire sampling period is utilized to complete the control action, $\tau_d \approx T_s$, then the phase loss contributed by the total delay can be estimated for given sampling rates. This is shown in Figure 4 for various ratios of sampling rate, f_s, to system crossover frequency, f_c. For example, if a system requires a bandwidth (loop transmission crossover frequency) of 20 kHz, then a sampling frequency of 100 kHz will result in a phase loss contribution of 108 degrees from the control hardware alone. When the sampling frequency is increased to 1 MHz the resulting phase loss contribution decreases to only 11 degrees.

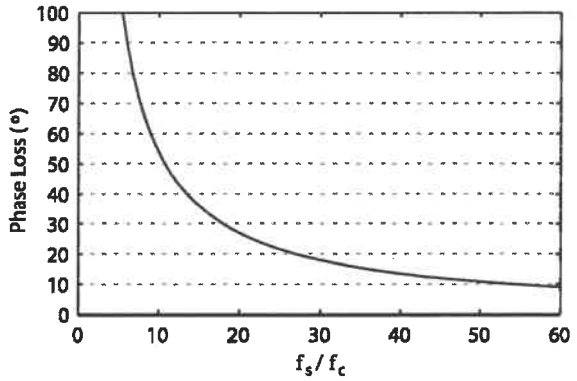

FIGURE 4. Phase loss associated with digital control total delay plotted for various ratios of sampling rate over system crossover frequency.

The Tsunami platform enables the use of faster sampling rates, which increases the system phase margin, and potentially the system bandwidth through the use of a more aggressive controller. Another benefit of operating at faster sampling rates is that it provides an oversampling effect that will improve the signal-to-noise ratio in data acquisition. In addition to being useful for multirate control, the extra computational resources available from having multiple processors also enable more complex control algorithms to be implemented without having to reduce the sampling rate. As there are no interrupts or user requests handled by the target processors, a very consistent controller computation time is achieved with the control platform. This results in very low control output jitter, $\tau_j(k)$, which is defined as the deviation between the ideal time and the actual time that the control output becomes available. In [2] it was shown how this is important in reducing positioning error in high-speed precision systems.

PERFORMANCE BENCHMARKS

The key performance benchmarks for the control platform that can affect the control performance are the input-to-output latency, the achievable sampling rate, the control output jitter and the data acquisition noise levels.

The control timing performance is measured using a sample control algorithm that consists of an ADC conversion, several addition, subtraction, and multiplication computations, a 20th order filter computation, a sine computation, a cosine computation, a square-root computation and a DAC conversion. The results for the Tsunami control platform are summarized in Table 1.

Table 1: Timing performance benchmark results for the Tsunami control platform using a sample control algorithm.

Benchmark	Tsunami
Input-output latency	1.1 μs
Achievable sampling rate	1 MHz
Total delay	1.6 μs
Control output jitter	6.0 ns RMS

The data acquisition performance is characterized in terms of the ADC noise floor. The measured noise floors of the 4 MSPS ADCs and 500 kSPS ADCs are 0.45 least-significant-bits (LSB) and 0.76 LSB, respectively. A sample measurement for one of the 4 MSPS ADCs is shown in Figure 5.

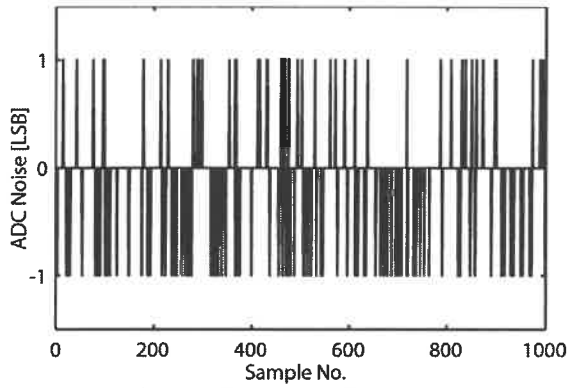

FIGURE 5. Measured noise floor for one of the 4 MSPS ADCs.

TOOLS FOR CONTROLLER DEVELOPMENT AND GRAPHICAL USER INTERFACE DESIGN

Controller design for the platform is done with Simulink®. A separate model is created for each target processor to be used. Any tunable parameters are specified as inputs to the model, any monitored signals are specified as outputs, and any connections to I/O resources are made using the library of custom blocks shown in Figure 6. MATLAB® Real-time Workshop with Embedded Coder is used to convert Simulink® models into C code that can be compiled, loaded, and executed on the control platform automatically from within MATLAB®.

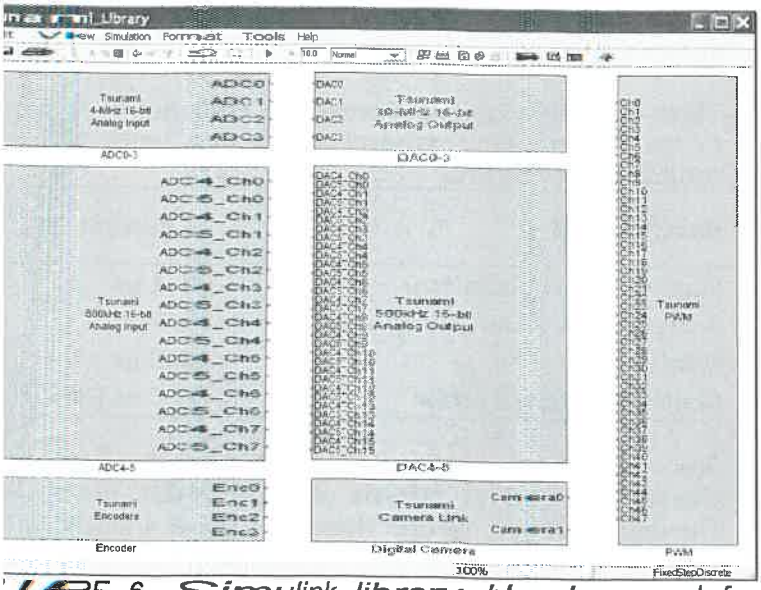

URE 6. Simulink library blocks used for ecting to the platform I/O resources.

e the controller design is complete the ified signals and parameters are passed LabVIEW® for development of the graphical interface used to communicate with the rol platform. An instrument driver has been ted that handles all low level communication provides the user with access to functions signal monitoring, parameter tuning, data g, and system identification. The available ment blocks are shown in Figure 7.

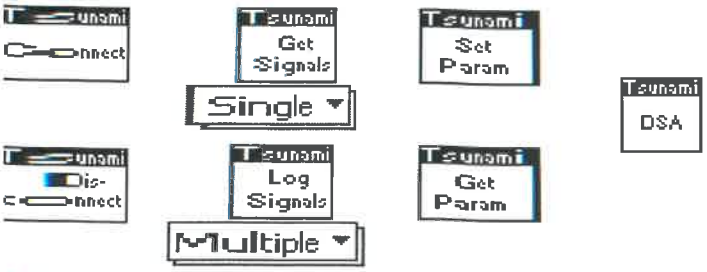

URE 7. LabVIEW instrument driver blocks for communicating with the Tsunami l platform.

pproach allows the user to easily develop cation specific graphical user interfaces and ge the many powerful signal processing ions available in LabVIEW. An example ce for the Fast-Tool Servo discussed in [1] wn in Figure 8.

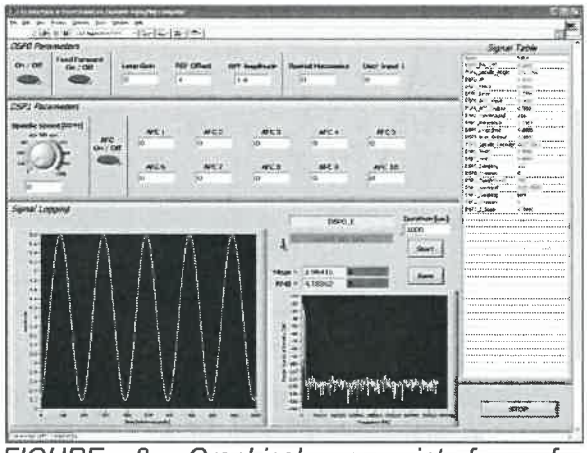

FIGURE 8. Graphical user interface for communicating with a fast-tool servo controlled by the Tsunami control platform.

CONCLUSION

A high performance multiprocessor control platform has been developed that has demonstrated 1 MHz sampling with only 1.6 µs total control loop delay. High-speed precision applications can experience both increased closed-loop bandwidth and lower positioning error by utilizing the faster sampling rate, lower latency and precision data acquisition made possible by this platform. By using a triple-body architecture the platform is able to obtain this high performance while still maintaining a flexible interface for tuning and monitoring the system in real-time. The custom Simulink® and LabVIEW libraries allow for easy controller and interface design, respectively. The existing high performance I/O resources including ADCs, DACs, encoder inputs, Camera Link inputs, PWM outputs and digital I/O make for quick integration with a variety of sensors and actuators. Further research is being done to investigate ways that multirate control can best take advantage of the multiprocessor platform to further increase the system performance.

REFERENCES

[1] X.-D. Lu. Electromagnetically-Driven Ultra-Fast Tool Servos for Diamond Turning. 2005; 197-224.

[2] K. Smeds, I. Usman, X.-D. Lu. Effect of Control Output Jitter on Precision Positioning. Proceedings of the ASPE Spring Topical Meeting on Control of Precision Systems. 2010; 23-28.

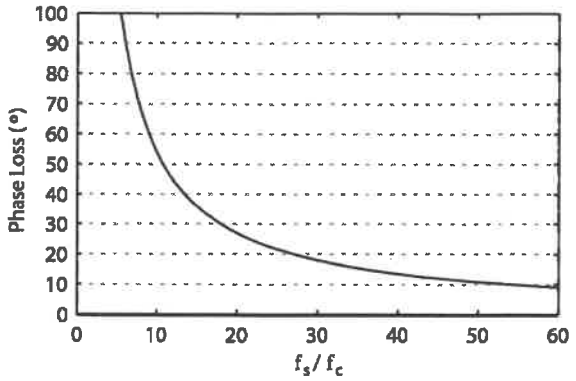

FIGURE 4. Phase loss associated with digital control total delay plotted for various ratios of sampling rate over system crossover frequency.

The Tsunami platform enables the use of faster sampling rates, which increases the system phase margin, and potentially the system bandwidth through the use of a more aggressive controller. Another benefit of operating at faster sampling rates is that it provides an oversampling effect that will improve the signal-to-noise ratio in data acquisition. In addition to being useful for multirate control, the extra computational resources available from having multiple processors also enable more complex control algorithms to be implemented without having to reduce the sampling rate. As there are no interrupts or user requests handled by the target processors, a very consistent controller computation time is achieved with the control platform. This results in very low control output jitter, $\tau_j(k)$, which is defined as the deviation between the ideal time and the actual time that the control output becomes available. In [2] it was shown how this is important in reducing positioning error in high-speed precision systems.

PERFORMANCE BENCHMARKS

The key performance benchmarks for the control platform that can affect the control performance are the input-to-output latency, the achievable sampling rate, the control output jitter and the data acquisition noise levels.

The control timing performance is measured using a sample control algorithm that consists of an ADC conversion, several addition, subtraction, and multiplication computations, a 20th order filter computation, a sine computation, a cosine computation, a square-root computation and a DAC conversion. The results for the Tsunami control platform are summarized in Table 1.

Table 1: Timing performance benchmark results for the Tsunami control platform using a sample control algorithm.

Benchmark	Tsunami
Input-output latency	1.1 μs
Achievable sampling rate	1 MHz
Total delay	1.6 μs
Control output jitter	6.0 ns RMS

The data acquisition performance is characterized in terms of the ADC noise floor. The measured noise floors of the 4 MSPS ADCs and 500 kSPS ADCs are 0.45 least-significant-bits (LSB) and 0.76 LSB, respectively. A sample measurement for one of the 4 MSPS ADCs is shown in Figure 5.

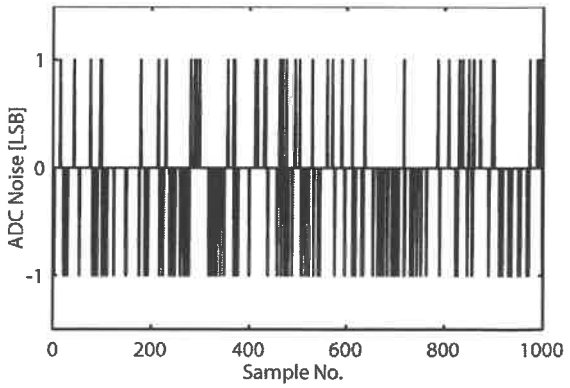

FIGURE 5. Measured noise floor for one of the 4 MSPS ADCs.

TOOLS FOR CONTROLLER DEVELOPMENT AND GRAPHICAL USER INTERFACE DESIGN

Controller design for the platform is done with Simulink®. A separate model is created for each target processor to be used. Any tunable parameters are specified as inputs to the model, any monitored signals are specified as outputs, and any connections to I/O resources are made using the library of custom blocks shown in Figure 6. MATLAB® Real-time Workshop with Embedded Coder is used to convert Simulink® models into C code that can be compiled, loaded, and executed on the control platform automatically from within MATLAB®.

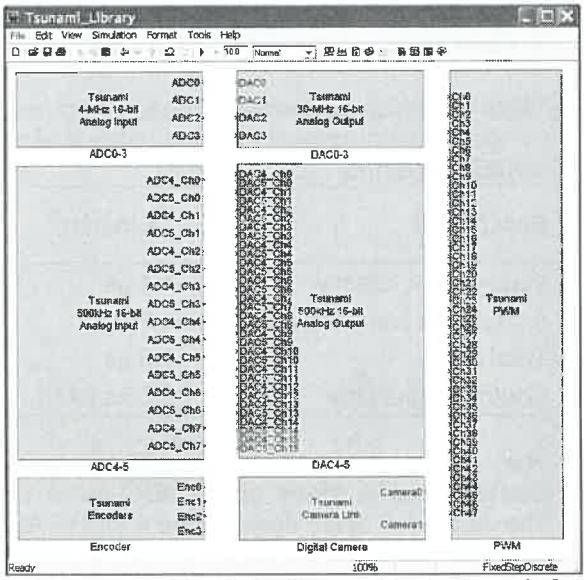

FIGURE 6. Simulink library blocks used for connecting to the platform I/O resources.

Once the controller design is complete the specified signals and parameters are passed into LabVIEW® for development of the graphical user interface used to communicate with the control platform. An instrument driver has been created that handles all low level communication and provides the user with access to functions for signal monitoring, parameter tuning, data logging, and system identification. The available instrument blocks are shown in Figure 7.

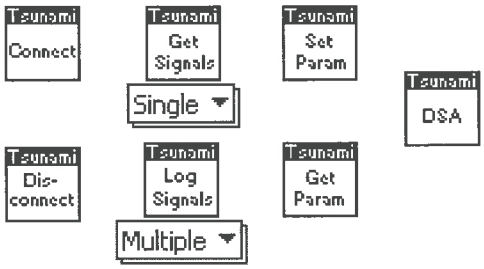

FIGURE 7. LabVIEW instrument driver blocks used for communicating with the Tsunami control platform.

This approach allows the user to easily develop application specific graphical user interfaces and leverage the many powerful signal processing functions available in LabVIEW. An example interface for the Fast-Tool Servo discussed in [1] is shown in Figure 8.

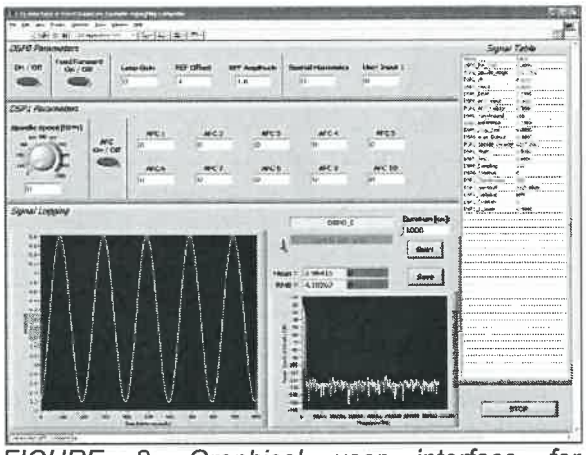

FIGURE 8. Graphical user interface for communicating with a fast-tool servo controlled by the Tsunami control platform.

CONCLUSION

A high performance multiprocessor control platform has been developed that has demonstrated 1 MHz sampling with only 1.6 μs total control loop delay. High-speed precision applications can experience both increased closed-loop bandwidth and lower positioning error by utilizing the faster sampling rate, lower latency and precision data acquisition made possible by this platform. By using a triple-body architecture the platform is able to obtain this high performance while still maintaining a flexible interface for tuning and monitoring the system in real-time. The custom Simulink® and LabVIEW libraries allow for easy controller and interface design, respectively. The existing high performance I/O resources including ADCs, DACs, encoder inputs, Camera Link inputs, PWM outputs and digital I/O make for quick integration with a variety of sensors and actuators. Further research is being done to investigate ways that multirate control can best take advantage of the multiprocessor platform to further increase the system performance.

REFERENCES

[1] X.-D. Lu. Electromagnetically-Driven Ultra-Fast Tool Servos for Diamond Turning. 2005; 197-224.

[2] K. Smeds, I. Usman, X.-D. Lu. Effect of Control Output Jitter on Precision Positioning. Proceedings of the ASPE Spring Topical Meeting on Control of Precision Systems. 2010; 23-28.

TIME-OPTIMAL MINIMUM JERK TRAJECTORY GENERATION FOR 5-AXES LASER DRILLING APPLICATIONS

Ammar A. Alzaydi[1], Kaan Erkorkmaz[1], Amr Elfizy[2], and Serafettin Engin[2]
[1]Mechanical and Mechatronics Engineering
University of Waterloo
Waterloo, Ontario, Canada
[2]Pratt & Whitney Canada
Longueuil, Quebec, Canada

INTRODUCTION

Laser drilling provides a highly productive method for producing hole clusters on freeform surfaced aerospace parts, such as gas turbine combustion chambers [1]. Although the process is capable of achieving a high throughput, current machine tool controllers do not provide the appropriate trajectory generation functions that can take full advantage of the processing speed. This paper presents a new time-optimized trajectory generation algorithm to addresses this problem.

TRAJECTORY OPTIMIZATION ALGORITHM

The hole clusters on the parts need to be 5-axis drilled, preferably at a fixed laser pulsing frequency [2]. The machine kinematics is similar to the one shown in Figure 1. Sample representation of hole cluster data is shown in Figure 2. While it is desirable to keep the laser pulsing frequency constant within one cluster, different clusters on the same part can be drilled at different firing frequencies. The machine constraints are the position envelope, velocity, acceleration, and jerk limits. To limit hole elongation a cap is imposed on the projection of the workpiece velocity vector (at the hole location) on the x-y plane orthogonal to the laser beam. The objective is to maximize the laser pulsing frequency for each cluster, and also to minimize the duration required to re-position the beam between clusters.

Objective: Minimize the total cycle time.
Constraints:

- Keep velocity, acceleration, & jerk profiles for the x,y,z,a,c axes within their limits;
- Bound the magnitude of the part velocity x-y component at hole locations;

First, a trajectory for each cluster is optimized individually. Then, the optimized cluster trajectories are stitched together, also time-minimized segments. Due to its flexibility and ease of parameterization, quintic polynomials have been used as the basis curve:

$$[x(t)]_k = A_{xk}t^5 + B_{xk}t^4 + \ldots + F_{xk}, 0 \le t \le T_k \quad (1)$$

Eq. (1) represents a single (kth) segment in the x-axis. T_k is the segment duration.

1. Optimization of Each Cluster

Optimization within each cluster is realized using a two-step procedure:

1.1. Minimum-jerk spline fitting

First, the initial trajectory is planned as a jerk-minimized quintic spline passing through the hole locations as way-points. This is obtained by minimizing the objective function:

$$J = \sum_{k=1}^{N} \int_0^{T_k} \dddot{x}^2(t)dt \quad (2)$$

subject to position, velocity, acceleration, and jerk continuity conditions at the connection points. These trajectories are fitted assuming free velocity, and zero acceleration and jerk boundary conditions at the start and end points of each cluster. This leaves the consideration of accelerating into and decelerating out of the clusters to the later step of stitching the individual optimized trajectories together. It also allows a higher laser pulsing frequency, since

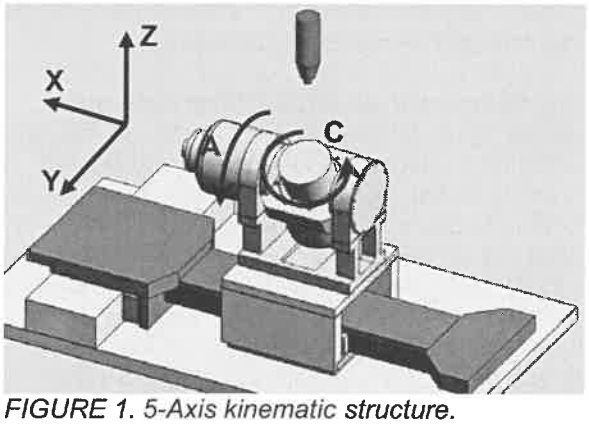

FIGURE 1. 5-Axis kinematic structure.

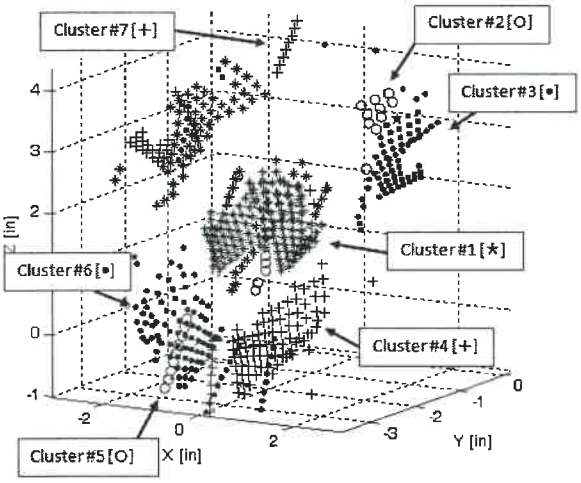

FIGURE 2. Hole cluster data.

the cluster entry and exit are at nonzero velocity. It was shown in [3] that solving the minimum jerk trajectory results in a quadratic minimization problem subject to linear constraints. The solution essentially takes the form of a set of linear equations.

Due to the fixed laser period, durations of consecutive segments will be identical throughout the same cluster ($T_1 = T_2 = ... = T_N$). Timing of the overall trajectory is then scaled to ensure that none of the velocity, acceleration, and jerk profiles, and x-y plane velocities at hole locations violate their limits. Considering:

$$\alpha_x = \max\{\frac{\| \dot{x} \|_\infty}{v_{x\max}}, \sqrt{\frac{\| \ddot{x} \|_\infty}{a_{x\max}}}, \sqrt[3]{\frac{\| \dddot{x} \|_\infty}{j_{x\max}}}\} \quad (3)$$

which represents the time scaling that needs to be applied in the x-axis to ensure that the peak velocity, acceleration, and jerk magnitudes are within their limits. Hence, the overall time scaling that needs to be used for all axes is obtained as,

$$\alpha = \max(\alpha_x, \alpha_y, ..., \alpha_c, \alpha_{xy}) \quad (4)$$

The x-y velocity component is calculated by considering the Jacobian matrix, defined by the machine and workpiece kinematics [4].

1.2. Sequential Quadratic Programming

Following initial fitting and adjustment of the jerk-minimized quintic spline, which guarantees a feasible initial guess in the vicinity of a local optimum, the second step refines the solution by invoking a Sequential Quadratic Programming (SQP) step. Due to the close initial guess, this algorithm converges quickly within a few iterations, thereby further compressing the cycle time by pushing the trajectory profiles closer to their limits where applicable, as in Figure 3.

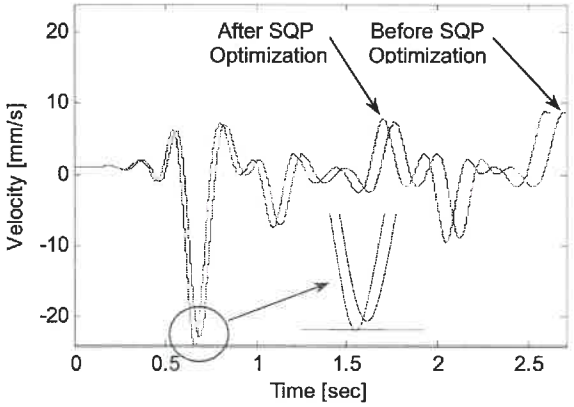

FIGURE 3: Y-axis velocity before & after SQP cluster trajectory optimization

The optimization variables are the velocity and acceleration boundary conditions at the knots ($\dot{X}_k, \dot{Y}_k$, ..., $\dot{C}_k$ and $\ddot{X}_k, \ddot{Y}_k$, ..., $\ddot{C}_k$ as illustrated in Figure 4), and the segment duration (T_k, which is uniform throughout the cluster). From this information, every quintic segment can be uniquely constructed, e.g. in the x-axis,

$$\left.\begin{aligned} A_{xk} &= [6(X_{k+1} - X_k) - 3(\dot{X}_{k+1} + \dot{X}_k)T_k + ... \\ &\quad \frac{1}{2}(\ddot{X}_{k+1} - \ddot{X}_k)T_k^2]/T_k^5 \\ B_{xk} &= [15(X_k - X_{k+1}) + (7\dot{X}_{k+1} + 8\dot{X}_k)T_k + ... \\ &\quad (\frac{3}{2}\ddot{X}_{k+1} - \ddot{X}_k)T_k^2]/T_k^4 \\ C_{xk} &= [10(X_{k+1} - X_k) - (4\dot{X}_{k+1} + 6\dot{X}_k)T_k - ... \\ &\quad (\frac{3}{2}\ddot{X}_{k+1} - \frac{1}{2}\ddot{X}_k)T_k^2]/T_k^3 \\ D_{xk} &= \frac{1}{2}\ddot{X}_k, \quad E_{xk} = \dot{X}_k, \quad F_{xk} = X_k \end{aligned}\right\} \quad (5)$$

The objective is to further minimize the value of T_k, subject to the constraints outlined at the beginning of Section 2. The constraints are checked at equal time intervals along 5 points in each segment. Although for large clusters, the SQP step can take as much as 10 minutes on a Pentium IV Matlab implementation, analytical expressions for the constraint gradients can also be derived and used, as was done in [3], to further speed up the convergence.

2. Stitching Between Clusters

The pre-optimized cluster trajectories are stitched together using the position, velocity, and acceleration boundary conditions inherited from the cluster exit and entry points on consecutive clusters. Each stitching trajectory is parameterized to consist of 6 segments, of

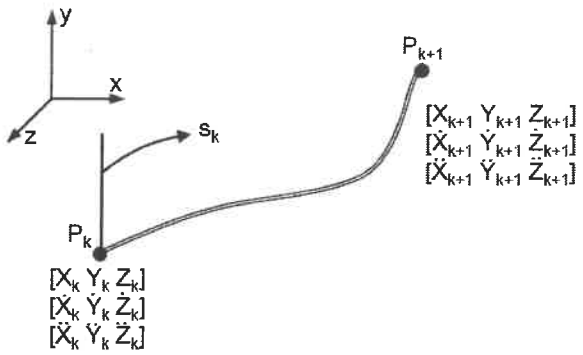

FIGURE 4. Single spline segment (in x-y-z).

which the durations T_1, T_2, ..., T_6 need to be optimized. Once again, the minimum-jerk quintic spline is used. However, this time the positions of the intermediate knots are not fixed. The only requirement is that the profiles connect seamlessly at the knots at the position, velocity, acceleration, and jerk levels, and that they respect the initial and final boundary conditions when exiting from, and connecting into consecutive clusters.

The stitching trajectories are solved by initially setting the sub-segment durations to be equal to each other and determining the minimum-time minimum-jerk quintic spline which yields no constraint violation, similar to the approach in Eq. (3) and (4). Afterwards, SQP is invoked, which modulates the segment durations in search of a faster stitching trajectory subject to the constraints stated at the beginning of Section 2. Should a feasible stitching be unobtainable at the initial guess stage, which so far has not been encountered, the nonzero velocity and zero acceleration and jerk boundary conditions allow for connecting clusters to be stitched together using at most three linear segments with full stops in between: 1) Decelerating to rest from the exit velocity of the previous cluster; 2) Re-positioning the axes; 3) Accelerating to the entry position and velocity for the next cluster. Although this solution can lead to a longer cycle time over the optimized quintic stitching, it guarantees a fall-back feasible solution every time.

SIMULATION RESULTS

The developed trajectory generation algorithm has been tested using the hole pattern in Figure 1. The final 3-axis trajectory comprising of clusters and stitching sections is shown in Figure 5. The resulting position, velocity, acceleration, and jerk kinematic profiles in the X,Y,Z,A.C axes are shown in Figure 6, for the limits also designated in the same figure. As can

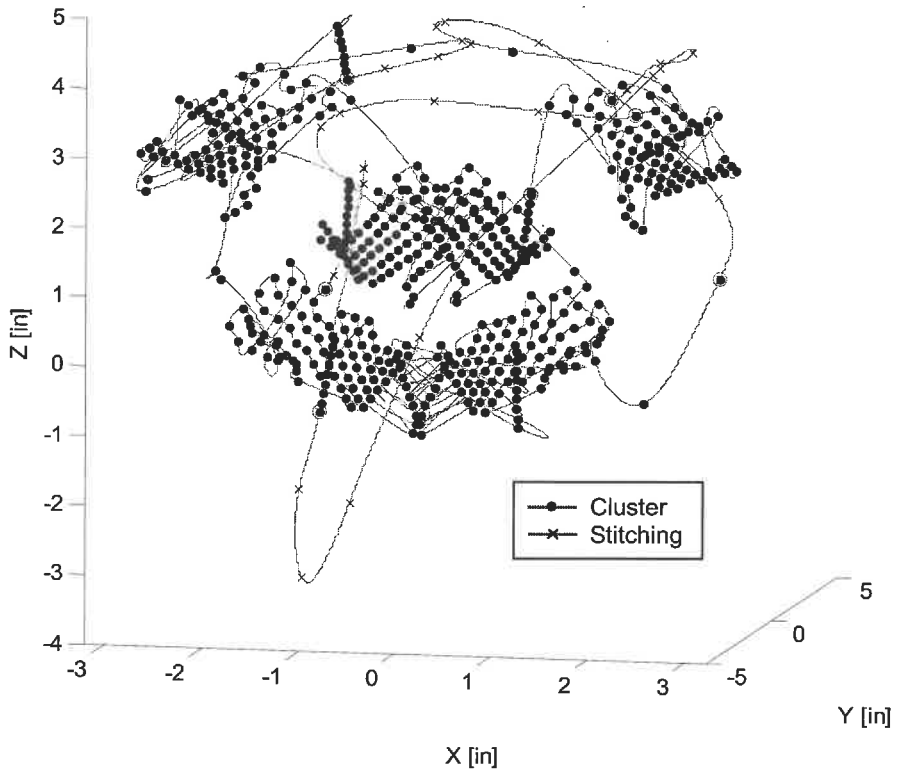

FIGURE 5. Optimized trajectory including clusters and stitching sections.

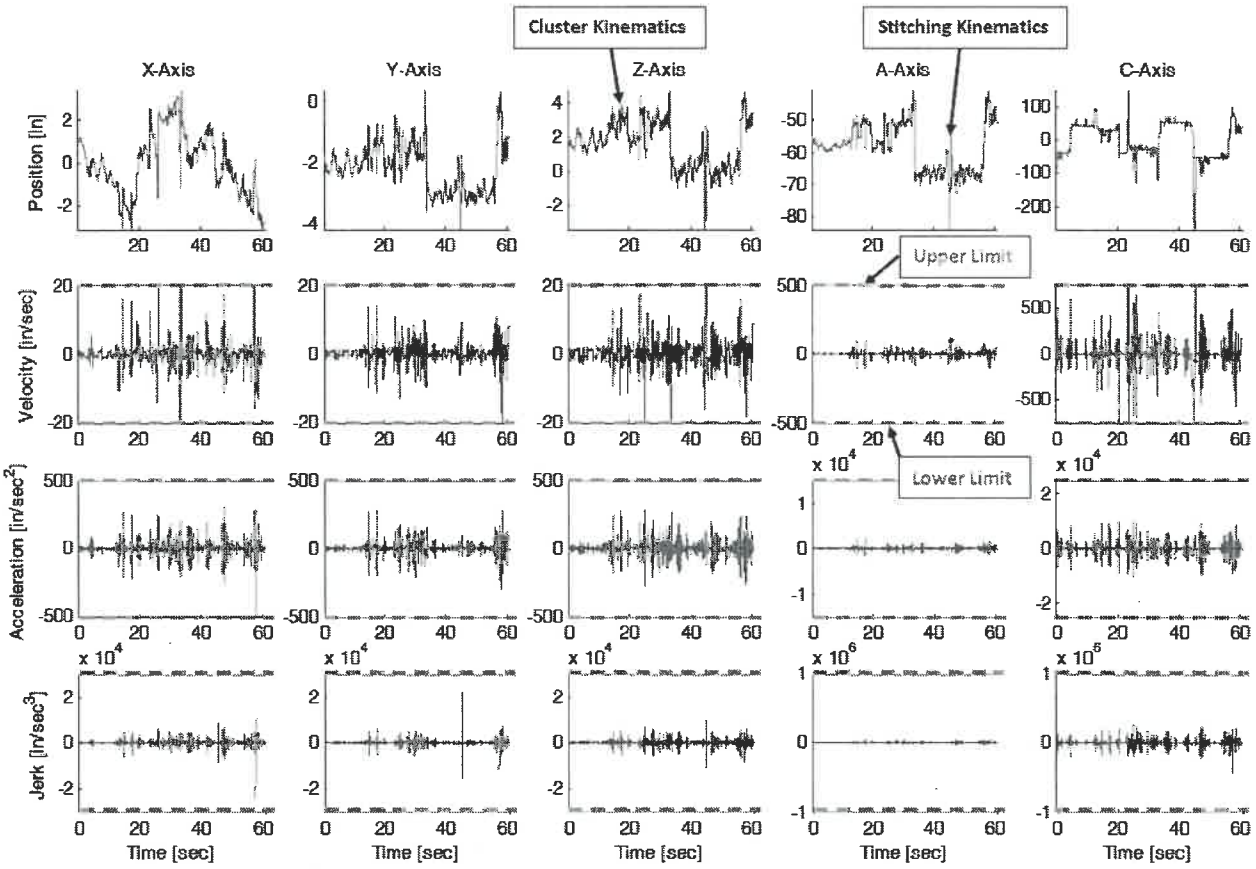

FIGURE 6. Kinematic profiles of optimized trajectory.

be seen, all of the profiles remain within their limits. Overall, the cycle time of the laser drilling operation can be reduced noticeably, using the optimal trajectory generation algorithm presented here. Currently, preparations are underway to implement similar optimized trajectories in part production trials.

CONCLUSION

The proposed algorithm allows for feed drive trajectories to be generated to yield minimum cycle time in laser drilling operations while respecting the velocity, acceleration, and jerk limits pertaining to the machine tool and laser drilling process. Currently, preparations are under way to experimentally validate the developed trajectory algorithm in production trials.

REFERENCES

[1] Elfizy A., High Speed Laser Drilling Machine andMethod, US Patent No US7,538,296 B2, May 26, 2009.

[2] Elfizy A., Method for Drilling Holes According to an Optimized Sequence, US Patent Application Pub. No US 2009/0196699A1, Aug 6, 2009.

[3] Altintas Y., Erkorkmaz K., Feedrate Optimization for Spline Interpolation in High Speed Machine Tools. 2003; CIRP Annals. 52/1:297–302.

[4] Yoshikawa T., Foundations of Robotics, MIT Press, Cambridge, MA: 1990.

HIGH-ACCURACY ATOMIC FORCE MICROSCOPE FOR DIMENSIONAL METROLOGY

Darya Amin-Shahidi[1], Dean M. Ljubicic[1], Jerald L. Overcash[2], Robert J. Hocken[2], David L. Trumper[1]
[1]Mechanical Engineering Department
Massachusetts Institute of Technology
Cambridge, MA, USA
[2]Mechanical Engineering Department
University of North Carolina at Charlotte
Charlotte, NC, USA

INTRODUCTION

In this paper, we present the design, control, and experimental results of a high-accuracy AFM head (HAFM) with sub-nanometer resolution. The HAFM's mechanical design was completed in the master's thesis of Ljubicic [1]. The HAFM is designed to be utilized as a high-accuracy single-axis metrology probe. In order to be used for metrology, HAFM will be integrated with the Sub-Atomic Measuring Machine (SAMM) [2], originally designed in the doctoral thesis of Michael Holmes. The SAMM can scan a sample in-plane over a range of 25-mm by 25-mm with 30-nm accuracy and 1-nm repeatability. The HAFM tracks and measures the sample normal to the plane with 0.12-nm RMS resolution at 100-Hz bandwidth.

The HAFM uses a commercially available self-sensing Akiyama AFM probe to detect the surface. The self-sensing probe eliminates the need for an optical sensing mechanism and can achieve a more compact design for better integration with SAMM. For higher detection bandwidth, we use the probe in a frequency-measuring mode, in which the probe moves perpendicular to the sample to maintain a constant self-resonance frequency that corresponds to a fixed tip-sample gap. A piezoelectric-stack moves the probe and three capacitive displacement sensors measure its surface-tracking motion.

SYSTEM DESIGN

The HAFM system configuration is shown in *FIGURE 1*. The HAFM sits on the SAMM's metrology frame using three ball and groove kinematic mounts. The Akiyama probe is fixed to the end of the moving stage and faces the sample surface. The HAFM guide flexure constrains the moving stage to only axial motion. A piezoelectric-stack actuator, with a range of 20 µm, drives the moving stage. A coupling flexure is used to transfer the actuator's axial motion and to attenuate any non-axial error motion of the piezoelectric actuator.

The probe's output current signal, which is less

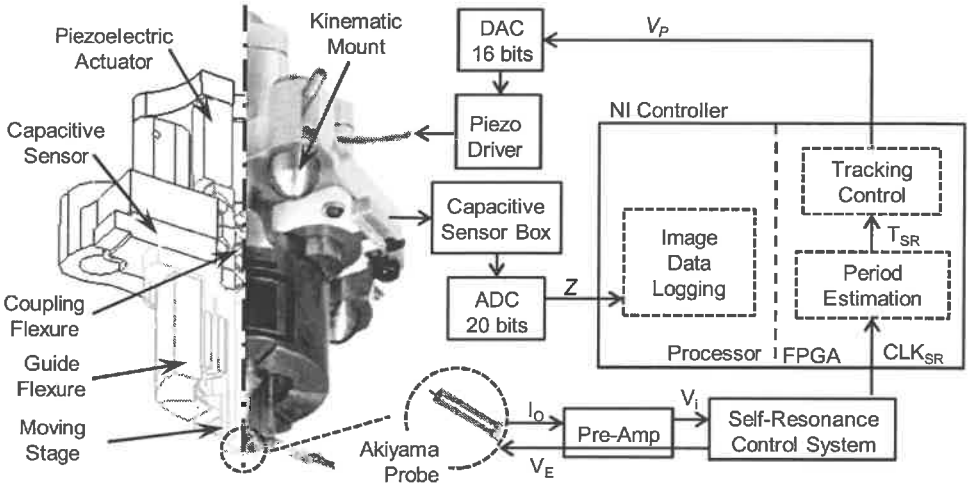

FIGURE 1. HAFM system design showing the cross-sectioned AFM head and the control electronics.

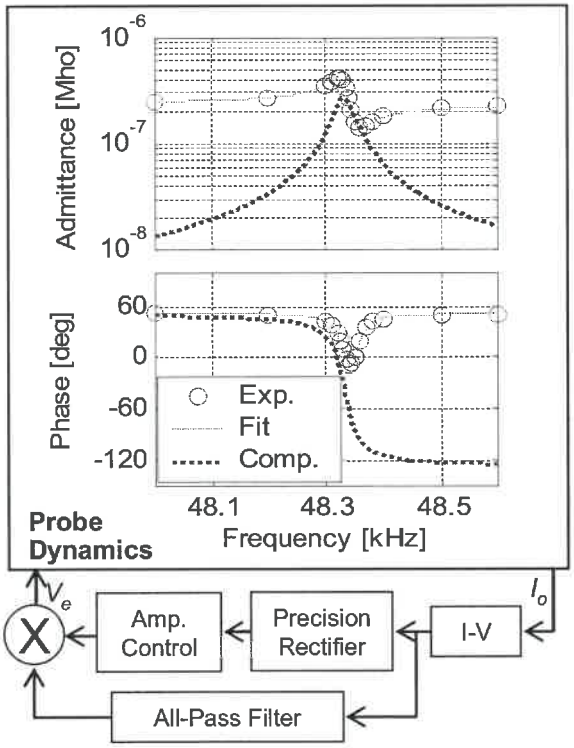

FIGURE 2. Self-resonance loop including the probe dynamics and the control blocks.

than 100 nA, is amplified and converted to a voltage signal on a board close to the probe. A self-resonance control system sets the probe in controlled amplitude self-resonance. The sinusoidal self-resonance signal is converted to a square wave with a comparator (CLK_{SR}) and is passed to the National Instruments real-time controller's FPGA board. The period (T_{SR}) of CLK_{SR} is measured and used as feedback. The tracking controller commands the piezo driver to move the probe and maintain a constant self-resonance period (T_{SR}), which corresponds to a constant tip-sample gap.

Three ADE8810 capacitive displacement sensors, with 50 µm range, are symmetrically spaced around the moving stage to measure its motion as it tracks the sample surface. The average of the three sensors provides a resolution of 0.18 nm RMS at 1-kHz bandwidth.

SELF-SENSING AFM PROBE

Two advantages of using an AMF probe for metrology are sub nanometer resolution and localized sensing (less than 15-nm tip radius for the Akiyama probe). To achieve a more compact design, the HAFM uses a commercially

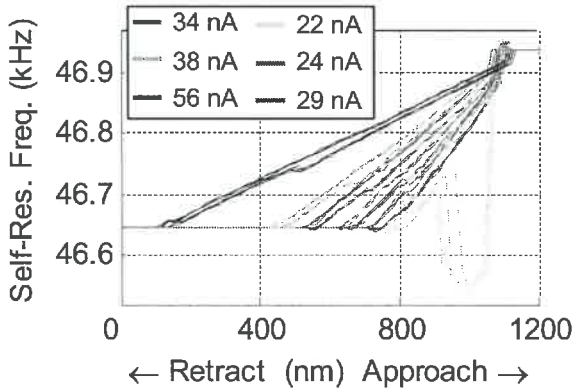

FIGURE 3. Sensing curves for an Akiyama probe at different oscillation amplitudes.

available[1] self-sensing Akiyama AFM probe, which does not require an optical-lever sensing mechanism. The Akiyama probe consists of a quartz tuning fork and a cantilever symmetrically attached to the ends of the tuning fork's prongs. The probe's tip is located at the free end of the cantilever. The application of a harmonic voltage (V_e) to the tuning fork terminals sets the tip in a tapping motion. The tip-sample interaction forces reflect back on the tuning fork's dynamics, and can be sensed as shifts in the tuning fork's electrical admittance. Reference [3] describes the probe's design in more detail.

FIGURE 2 shows the probe's admittance and a diagram of the self-resonance control blocks that we have incorporated around it. The experimentally obtained probe admittance matches the fit based on our lumped parameter model, which includes the admittance of the quartz tuning fork in parallel with its parasitic capacitance. We cancel the parasitic capacitance current by injecting its opposite to the probe's current signal. The resulting compensated response's resonance corresponds to the mechanical resonance of the probe, where dynamic stiffness is minimized, and hence the probe's sensitivity to interactions with the sample is maximized.

With a tuning fork, the Akiyama probe has a high quality-factor of about 1200 in air. A high quality-factor improves the probe's sensitivity but reduces the decay rate of any transient. Long lasting transients reduce the probe's bandwidth for amplitude-measuring (AM) AFM mode. Albrecht [4] presented a frequency-measuring (FM) AFM mode with a bandwidth independent

[1] Akiyama probe is a product of NanoSensors™. Probe image in *FIGURE 1* is from Nanosensors, with permission.

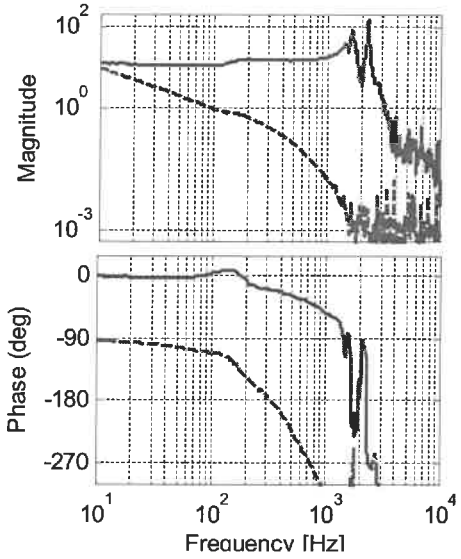

FIGURE 4. Bode plot of the open-loop (solid) and the compensated (dashed) tracking loop.

of the probe's quality-factor. In FM-AFM, the probe's resonance frequency, which shifts with the tip-sample gap, is directly measured. The AFM moves the probe to maintain a reference resonance frequency, corresponding to a fixed tip-sample gap. A review of FM and AM AFM methods is provided in reference [5].

We use the Akiyama probe for FM AFM in a manner similar to the design in [6]. To measure the probe's resonance frequency, we condition the probe's input such that it self-resonates at its shifting natural resonance frequency within the control bandwidth. *FIGURE 2* shows a diagram of the self-resonance control system. To achieve sustained self-resonance, the loop phase must be zero (phase condition) and the loop gain must be one (amplitude condition) at the self-resonance frequency. We use an all-pass filter with a varying break frequency to empirically adjust the loop phase at the resonance frequency once for each probe. The loop gain is multiplicatively scaled by the amplitude controller to actively satisfy the amplitude condition and maintain the reference oscillation amplitude. We use a precision rectifier to measure the amplitude of oscillations. The amplitude controller, which is implemented using op-amps, consists of an integrator in series with a lead-lag compensator.

In this configuration, the probe's self-resonance frequency shifts with the tip-sample gap. *FIGURE 3* shows the probe's sensing curves, which we captured at different probe oscillation

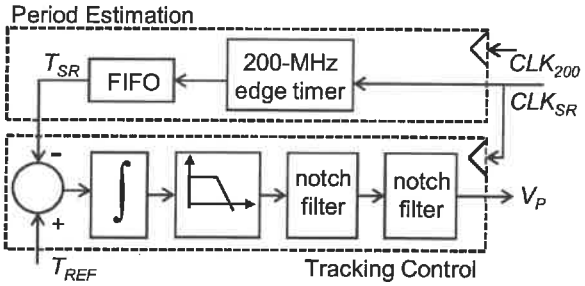

FIGURE 5. Diagram of the period estimation and controller blocks.

current amplitudes. We recorded the probe's self-resonance frequency over several approach-retract cycles. The retract curve is located below the approach curve and contains a discontinuity that is likely due to probe-sample adhesion. The probe's sensitivity is inversely proportional to the oscillation amplitude. However, there is an oscillation amplitude limit below which we cannot sustain steady oscillations. This limit is 24nA for the probe under test that corresponds to a maximum sensitivity of 0.78 Hz/nm.

SURFACE TRACKING CONTROL

The surface tracking resolution depends on the resolution of self-resonance period estimation. We use a pre-amplification board, shielding on all signals, and signal conditioning buffers to obtain a high quality self-resonance signal. The sinusoidal self-resonance signal is digitized by a precision comparator. A 200-MHz digital timer implemented on an FPGA measures the interval (T_{SR}) between the falling/rising edges of the digitized self-resonance signal (CLK_{SR}) with a resolution of 5 ns. A timing error of 5 ns results in an edge rate estimation error of 50 Hz for a probe resonating at 50 kHz. A common way to enhance the resolution is to average the period of multiple cycles, but this would create phase lag. Instead, we use the tracking controller and the AFM plant's low-pass dynamics to filter the period measurements.

Converting the self-resonance period to a frequency value requires a non-linear division operation, which would mix the frequency content and prevent effective filtering of the noise. To avoid this, we use the self-resonance period as feedback. Furthermore, the measurement and the controller update rates must have an exact integer multiplicative relation to prevent creation of low frequency aliased components. The measurement updates at the

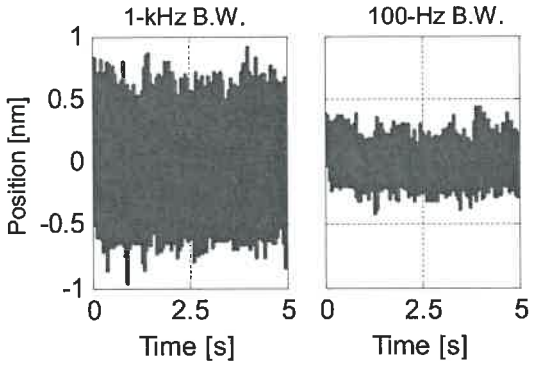

FIGURE 6. Tracking a stationary sample, noise is 0.24 and 0.12 nm RMS at 1000 and 100 Hz measurement bandwidths respectively.

changing CLK_{SR} edge rate, which is not exactly known. To guarantee a perfect integer multiplicative relation between the controller sampling and the CLK_{SR}, we sample the controller at the edges of CLK_{SR} as well.

FIGURE 4 shows the Bode plot of the open-loop and the compensated loop transfer functions from the piezo-driver command (V_P) to the probe's self-resonance period (T_{SR}). The two open-loop resonances are structural modes of the HAFM and set the limit on the attainable closed-loop bandwidth. *FIGURE 5* shows the period estimation and controller blocks. The controller uses an integrator to establish a -1 slope at cross-over, a low-pass filter to attenuate high frequency noise, and two notch filters to mask the structural resonances. The unity gain loop cross-over frequency is 100 Hz with 65 degrees of phase margin.

EXPERIMENTAL RESULTS

For the tracking controller's unity cross-over frequency of 100 Hz, we tested HAFM's noise and dynamic performance at a stationary sample point. *FIGURE 6* shows the position noise when tracking a stationary sample. *FIGURE 7* shows the step response of the

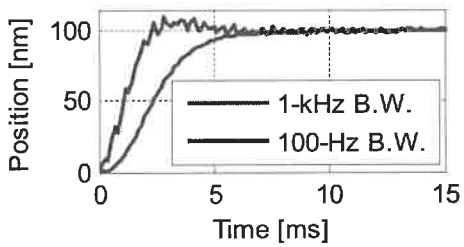

FIGURE 7. Tracking response to a step disturbance at piezo-driver's input (V_P).

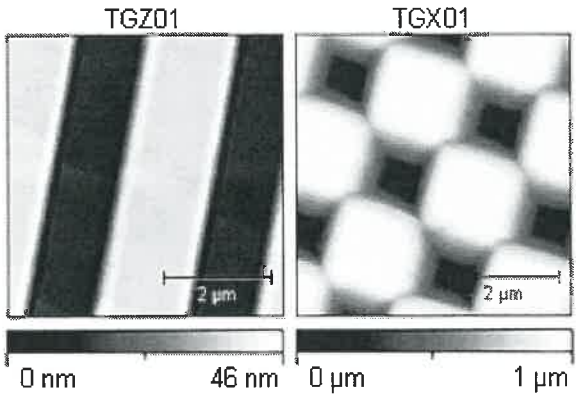

FIGURE 8. TGZ01 and TGX01 gratings imaged at 5 and 10 µm/s scan speeds respectively.

closed-loop system to a step disturbance added at the piezo driver input (V_P). We also successfully tested the HAFM for imaging by integrating it with a Veeco MultiMode E scanner. *FIGURE 8* shows the images of the TGZ01 and TGX01 gratings captured at 5 and 10 µm/s scan speeds respectively. The gratings are a product of MikroMasch. The TGZ01 is specified to have a channel height of 25.5±1 nm, which we measured as 25.6 nm on average. The TGX01 is designed for in-plane calibration and is not precise out of the plane. It is shown here as a sample with larger features.

ACKNOWLEDGEMENT

We thank Dr. Georg Fantner and Mr. Dan Burns for giving us access to their AFM scanner system and helping us with the imaging tests. This work was supported by the National Science Foundation (contract DMI-0506898).

REFERENCES

[1] D. L. Ljubicic, "Flexural Based High Accuracy Atomic Force Microscope," 2008.

[2] R. J. Hocken, D. L. Trumper and C. Wang, "Dynamics and Control of the UNCC/MIT Sub-Atomic Measuring Machine," *CIRP Ann. Manuf. Technol.*, vol. 50, pp. 373-376, 2001.

[3] T. Akiyama, U. Staufer and N. F. de Rooji, "Symmetrically Arranged Quartz Tuning Fork with Soft Cantilever for Intermittent Contact Mode Atomic Force Microscopy," *Rev. Sci. Isnstrum.*, vol. 74, pp. 112, January 2003. 2003.

[4] T. R. Albrecht, P. Grutter, D. Horne and D. Rugar, "Frequency Modulation Detection Using High-Q Cantilevers for Enhanced Force Microscope Sensitivity," *J. Appl. Phys. ; J. Appl. Phys.*, vol. 69, pp. 668-673, January 15, 1991. 1991.

[5] R. Garcia and R. Perez, "Dynamic atomic force microscopy methods," *Surf. Sci. Rep.*, vol. 47, pp. 197-301, September. 2002.

[6] Nanosensors. (2009, 03-23). Akiyama-probe (A-probe) technical guide. pp. 1.

DESIGN AND TESTING OF A MACHINE FOR CALIBRATION OF BALL BARS UP TO 3 METERS IN LENGTH

Vincent Lee[1], John Ziegert[1], W. Tyler Estler[2], Steven D. Phillips[2], Daniel Sawyer[2], and Bruce Borchardt[2]

[1]Mechanical Engineering Dept.
Clemson University
Clemson, SC, USA

[2]Large Scale Metrology Division
National Institute of Standards and Technology
Gaithersburg, MD, USA

INTRODUCTION

Ball bars are typically used to evaluate the volumetric performance of coordinate measuring machines (CMM). With the ever increasing sizes of CMMs and with wide spread application of larger articulated arm CMMs, larger ball bars are needed. In addition, laser tracking systems also require long reference length artifacts (a.k.a. optical ball bars) for evaluating their performance in accordance with standards similar to ASME's B89.4.19. As these ball bars grow in size and evolve, new capabilities and techniques are necessary to calibrate them. During the 2001 ASPE Annual conference a machine called the one dimensional measuring machine (1-DMM), specifically designed to calibrate ball bars up to one meter in length, was introduced [1]. While this design concept was fine for short ball bars (≤1m), it was impractical for longer ball bars. To overcome this difficulty an alternate design and self-initialization method have been created. The new 1-DMM discussed in this paper has the capability of measuring ball bars up to 3 meters in length, incorporates interferometer displacement measurement, and utilizes a dedicated un-calibrated artifact to initialize the instrument's displacement measurement system.

MACHINE DESIGN CONCEPT

The new version of the 1-DMM uses a precision granite straight edge beam, with a steel sled supported by air bearings straddling it. The ball bar being measured is supported at one end by a kinematic seat rigidly affixed to the granite beam, and at the other end by a kinematic seat affixed to the sled. The kinematic seats are nominally centered along the longitudinal centerline of the granite beam. A pair of laser interferometers is symmetrically arranged on the machine such that the measurement axes are parallel to the sensitive direction of motion, and co-planar to the axis of a ball bar when it is supported by the kinematic seats. (FIGURE 1).

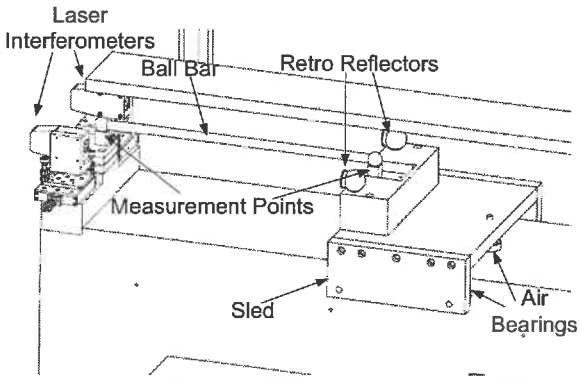

FIGURE 1 Component layout of new 1-DMM

The laser interferometers are used to track the linear displacement of the two sides of the sled. Since the measurement line is between the measurement axes, this allows for correction of any Abbe errors due to yaw motions of the sled.

Direct measurement of a ball bar is performed by placing the ball bar onto the kinematic seats. However, before the 1-DMM can perform measurements it needs to be initialized to provide absolute distance between the kinematic seats rather than displacements of the sled.

Self Initialization

One unique feature of this machine is its ability to initialize the displacement measurement sensors using an un-calibrated artifact. For this, the 1-DMM relies on a ball bar with three

nominally collinear balls, and placed in three different positions on the machine. This procedure is outlined in the following figure (FIGURE 2).

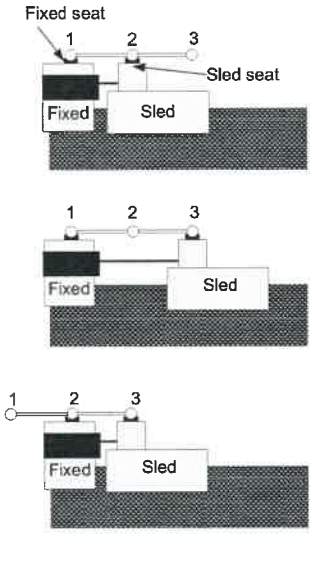

STEP 1
Set calibration artifact with ball 1 in fixed seat and ball 2 onto sled seat. Reset laser interferometers to read "zero"

STEP 2
Unseat ball 2 from sled seat and seat ball 3 onto sled seat. Record the distance displaced during movement; this measured distance between ball 2 &3 will be used to initialize the laser interferometer.

STEP 3
Unseat ball 1 from fixed seat and seat ball 2 onto fixed seat. Enter the value recorded from STEP 3 to initialize 1-DMM's laser interferometer.

FIGURE 2. Procedure for initializing measurement sensors on 1-DMM

By placing the 3-ball ball bar in these positions, the length of one section of the bar is measured by the machine, and is then used to initialize the measurement sensors on the 1-DMM to provide absolute distance between the kinematic seats.

Measuring a Ball Bar

After initialization of the machine, the length of any other ball bar is determined by supporting it in the two kinematic seats (FIGURE 3). From the measurement sensor outputs, the length of the ball bar (L) is calculated from the following equation:

$$L = L_0 + D_1 + \frac{b(D_2 - D_1)}{a} \quad (1.1)$$

L_0 is the initialization length

D_1 is the displacement of encoder 1

D_2 is the displacement of encoder 2

a is distance between retroreflectors

b is destance from ecoder 1 to ball bar axis

Since this new design does not allow for strict adherence to the Abbe principle, the extended Abbe principle is employed to correct for yaw motions of the moving stage by using two parallel displacement sensors. By knowing the values of "a" and "b", and the two readings fo the laser interferometers, D_1 and D_2, the length of the ball bar can be precisely estimated using equation 1.1. The yaw of the sled is implicit in equation 1.1 and its value can be calculated.

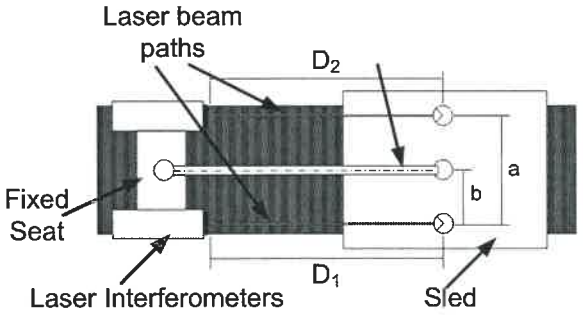

FIGURE 3. Top schematic view of 1-DMM

MEASUREMENT UNCERTAINTY OF 1-DMM

The new 1-DMM can have measurement uncertainty introduced at two stages, the initialization stage (setting the instrument to L_0), and the ball bar measurement stage (measuring D_1 and D_2). Uncertainty contributors include environmental effects, alignment errors in the components of the machine, gravitational effects, and positioning repeatability of the ball bars in the kinematic seats.

A Type B uncertainty analysis was performed on this design prior to construction, assuming the following measurement conditions (TABLE 1). The correlation coefficient defines the extent to which the two interferometers react independently to localized environmental fluctuations [2].

TABLE 1. Assumed conditions for Type B uncertainty analysis

Property	Value
Room temperature	(20±0.05) °C
Room Relative Humidity	50 %±1 %
Room Air Pressure	(101.3±0.5) kPa.
Nominal Initialization Length (L_0)	0.3 m
Ball Bar length	1.0 m
Ball Bar Temperature	(20±0.05)°C
Component misalignment	± 0.25 mm
Correlation Coefficient	0.4

Under these conditions, the estimated standard uncertainty to initialize the 1-DMM and measuring a nominal 1 meter ball bar are outlined in the following table (TABLE 2)

TABLE 2. Estimated standard uncertainty of measuring a 1 meter ball bar (μm)

Uncertainty Analysis	Value
Measuring a 1 m ball bar	Std.Uncr.
Uncertainty in Initializing to L_0(250mm)	**0.1880**
Uncertainty of measuring distance "D"	
Absolute wavelength	0.0115
Wavelength Stability	0.0577
Resolution	0.0200
Environmental error	0.1386
Deadpath error	0.0866
Laser alignment (cosine)	0.0083
Laser alignment (Abbe)	0.0361
Glass path thermal	0.0173
Combined Uncertainty of D	**0.1796**
Other Error Sources	
Ball bar misalignment - u(BBM)	0.0722
Kinematic seat repeatability - u(KSR)	0.0577
Thermal errors - ball bar - u(BBT)	0.3060
Combined Std. Uncertainty (*k=1*) u (L)	**0.3920**
Expanded Uncertainty (*k=2*)	**0.7840**
Target Expanded Uncertainty (k=2)	***0.3800***

All values in μm

The targeted expanded measurement uncertainty (k=2) for ball bar measurements is:

$$U_L = (0.2 + 0.2L)\ [\mu m] \qquad (1.2)$$

L is ball bar length, given in meters

From this preliminary uncertainty analysis, this instrument doesn't meet the target measurement uncertainty. However, it is anticipated that the actual operating environment for the new 1-DMM may be better than what was assumed for this analysis. Therefore it was decided to proceed with construction.

BALL BAR MEASUREMENT RESULTS

The 1-DMM is able to measure ball bars directly after it has been initialized, and there are two methods that may be used to initialize the 1-DMM. One method uses a *master ball bar*, whose length is pre-calibrated on an independent measuring machine, to set the initial separation between the two kinematic seats; we'll call this "mastered gauging". In this method the 1-DMM serves as a comparator type instrument, where each subsequent ball bar measured is compared to the length of the initial ball bar. The second method uses the method described in FIGURE 2. We'll refer to this as "*masterless gauging*", since a pre-calibrated master artifact isn't used to set the initial distance between the kinematic seats. A series of experiments was performed to evaluate the accuracy and repeatability of ball bar measurements using each method. Prior to the start of the experiments, two precision ball bars were calibrated by the Moore M-48 CMM at NIST, the machine traditionally used to calibrate ball bars [3].

Environmental compensations are applied to the laser interferometer system, as well as correction for thermal deformations of the ball bar.

Mastered Gauging

Using mastered gauging, one of the pre-calibrated ball bars was used to initialize the machine, following which the other was measured as an unknown. This measurement procedure was performed ten times for each ball bar to obtain an estimate of the 1-DMM's repeatability. The reported length is the mean of these measurements. The results of the measurements are outlined in the following table (TABLE 3).

TABLE 3. Measurements obtained using mastered gauging method.

Mastered Gauging			
1-DMM	2*Std. Dev	M48 Length	Diff.
499.723358	0.000123	499.723344	0.000014
898.766634	0.000148	898.766586	0.000048

All units in mm

Masterless Gauging

In the second set of experiments the masterless method was used to initialize the 1-DMM. Each initialization was followed by a measurement of the 500mm and 900mm ball bars. This again was performed ten times to estimate the repeatability and bias of the machine. Three different 3-ball calibration artifacts are used to initialize the 1-DMM; short, medium and long. The following figure and table describes these 3-ball ball bars (3-BBB) (FIGURE 4 & TABLE 4).

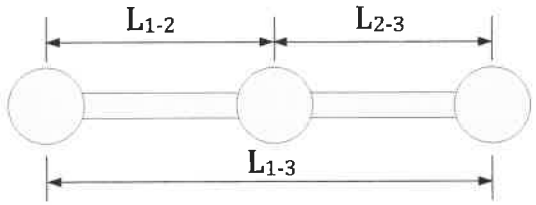

FIGURE 4. 3-ball ball bar used for initializing 1-DMM

TABLE 4.Nominal dimensions of 3-BBBs used for initializing 1-DMM

Nominal Dimensions of 3-BBBs			
Size	L_{1-2}	L_{2-3}	L_{1-3}
Short	100	100	200
Medium	250	250	500
Long	500	500	1000

All values in mm

Ball bar measurement results acquired using the masterless method are outlined in the following table (TABLE 5).

TABLE 5. Measurements obtained using masterless gauging.

Masterless Gauging Using Short 3-BBB			
1-DMM	2*Std. Dev	M48 Length	Diff.
499.723711	0.000255	499.723344	0.000367
898.766809	0.000862	898.766586	0.000223
Masterless Gauging Using Medium 3-BBB			
1-DMM	2*Std. Dev	M48 Length	Diff.
499.723673	0.000133	499.723344	0.000329
898.766745	0.000166	898.766586	0.000159
Masterless Gauging Using Long 3-BBB			
1-DMM	2*Std. Dev	M48 Length	Diff.
499.722227	0.000172	499.723344	-0.001117
898.765458	0.000185	898.766586	-0.001128

All units in mm

DISCUSSION OF RESULTS

Utilizing equation 1.2, the target expanded uncertainties for the 400mm and 900mm ball bar are 0.30µm and 0.38 µm respectively. The mastered method, where a ball bar of known length was used to initialize the machine, provided the best measurement results.

However, utilizing the masterless method to initialize the 1-DMM yielded mixed results in measurement repeatability and bias. To investigate the effects of initialization artifacts of varying lengths, 3-ball ball bars of varying sizes were tested. Of the 3-ball ball bars, the medium length ball bar, with a nominal initialization length of 250mm, provided the best results and was able to meet the target measurement uncertainty.

The relatively large measurement error observed when the long 3-ball ball bar is used is likely due to its flexibility. Gravitationally induced sagging of the ball bar may have caused an error in the measurement of the initialization length.

CONCLUSION

Initial measurements of ball bars less than one meter long demonstrate that the 1-DMM can achieve measurement uncertainty similar to the original 1-DMM when using the mastered method. The masterless method was highly repeatable, but didn't yield results as accurate as the mastered method. When the 3-ball ball bars are on the kinematic seats, they are supported below their neutral axis. Under this condition, because of their flexibility, any bending of these initialization artifacts under gravity will cause the 1-DMM to measure them longer than the true values of their center to center distances. Future experiments will involve investigating optimal geometry and construction techniques for a 3-ball ball bar, and evaluating the measurement performance of this machine when ball bars up to 3 meters in length are measured.

REFERENCES

[1] Ziegert, J., Rea, L. D., Phillips, S. D., 2001, "Design and Testing of a One Dimensional Measuring Machine for Determining the Length of Ball Bars," Proceedings of the 2001 Annual American Society of Precision Engineers Conference, .

[2] Guide to The Expression of Uncertainty in Measurement. 2008, International Organization for Standardization

[3] Stoup, J., 2009, "A Few Case Studies in Uncertainty Using the NIST M48 CMM," ASPE 2009 Spring Topical Meeting.

POSITIONING SYSTEM FOR OPTICAL DISC MASTERING

Byron Knapp[1], Dan Oss[1], Dave Arneson[1]and Tim Sheridan[2]
[1]Professional Instruments Company
Hopkins, Minnesota, USA
[2]Lorien Consultants
Eagan, Minnesota, USA

ABSTRACT

The evolution of optical disc formats from Compact Disc (CD) to Digital Versatile Disc (DVD) and now Blu-ray Disc (BD) requires increasing recording capacities and precision manufacturing. The most advanced format, the BD, is a leap forward in recording capacity that was driven consumer demand of high definition media and displays. The increased information density of BD is enabled by improvements to the optical stylus components and reduction of the size and tolerance of the physical disc features. In this work, the precision engineering aspects of two key components of an optical disc mastering system are discussed—a linear air bearing slide and a rotary air bearing spindle. Details of the design are given and the system is tested to demonstrate suitability for BD mastering.

BACKGROUND

The CD format was established in 1982 to provide 74 minutes of two-channel audio signal with a recording capacity of approximately 670 MB on a Ø120 mm disc. The DVD format was established in 1996 to provide over 2 hours of standard definition video with a recording capacity of 4.7 GB. In order to record over two hours of high definition video, the BD format was established in 2002 with a capacity of 25 GB (single layer). This capacity of a single layer BD is equivalent to 37 CDs or 5 DVDs.[1]

Illustrated in Figure 1, the capacity of BD is enabled by the reduced wavelength blue laser, increased numerical aperture, reduced cover layer thickness and switch to phase transition mastering.[2] This increased capacity requires increased precision in the manufacturing process with pit tolerances less than one nanometer. Some characteristics of the three generations of optical discs are summarized in Table 1.

TABLE 1. Comparison of three generations of optical disc formats.[1,3,4]

	CD	DVD	BD
Capacity (GB)	0.64	4.7	25
λ (nm)	780	650	405
NA	0.45	0.6	0.85
Beam Ø (µm)	2.11	1.32	0.58
Track pitch (µm)	1.6	0.74	0.32
Pitch tolerance (nm)	±100	±30	±3
Linear velocity (m/s)	1.3	3.49	4.92
1R speed (Hz)	3-8	10-28	12-40
Shortest pit (nm)	833	400	149
Data bit length (nm)	300	133.3	74.5
Length tolerance (nm)	±30	±1.4	±0.7
Radial noise (nm RMS)	30	22	6.4

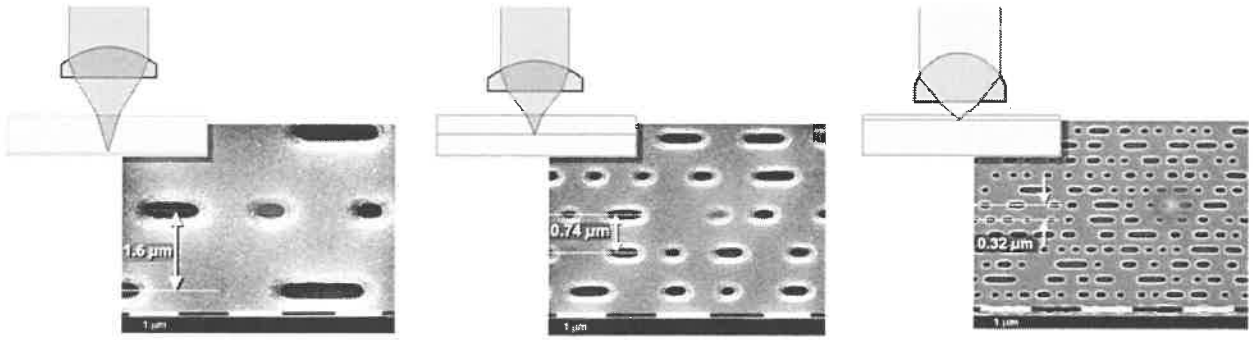

a) CD b) DVD c) BD

FIGURE 1. Three generations of optical disc: a) CD, b) DVD, and c) BD.[5] *Increased data density of BD requires improved precision in disc mastering. Photo credit: Philips.*

The data follows a spiral track consisting of a succession of pits variable in length and spacing. For replication, a master disc is mounted to a rotary axis while the laser that encodes the data in the disc is mounted to a linear axis.

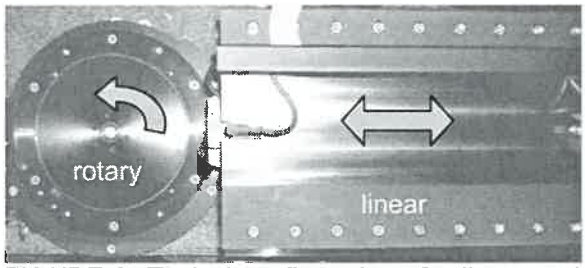

FIGURE 2. Typical configuration of a linear and rotary axis for optical mastering.

Radial noise, or radial asynchronous error, is a critical variable for the manufacture of the master. The rotary axis provides rotation of the disc with nanometer-level asynchronous error while the linear axis must position the laser with nanometer-level accuracy. Magnetic bearing prototypes have been built for mastering with some success.[6-8] However, air bearings with tight clearances are commonly used due to reduced cost and complexity.

LINEAR AXIS

The 140 mm travel linear axis for BD mastering needs to have a natural frequency above 1 kHz. This requirement led to the use of a hollow square shuttle with compound compensation. This square shuttle uses a combination of orifice and groove restriction. The pad design is shown in Figure 3. Properly implemented, the combination of these two restrictor types with tight clearances (6-8 μm air films) yields high load capacity and stiffness.

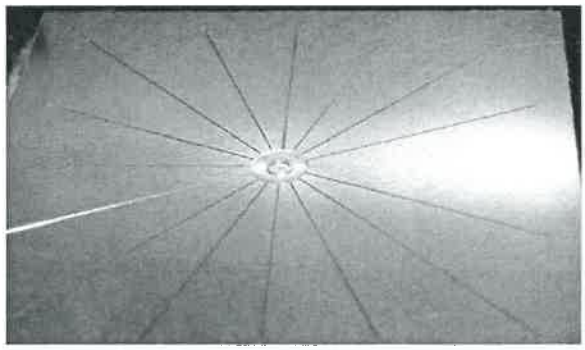

FIGURE 3: Compound compensation using orifice and groove restriction.

Several precision engineering principles are considered in the design. The air is supplied to the translating shuttle, rather than the stationary box structure. This eliminates pitch errors caused by mass centerline changes. A slight disadvantage to this technique is air lines must be included in the slide umbilical connection. The linear motor (not shown) is mounted so that the actuation force passes through the center of gravity of the shuttle. This reduces moment loads on the shuttle over the travel. Finally, the Abbé offset is minimized by locating the linear scale (not shown) at the same height as the substrate. This slide assembly uses a Zeodur™ glass ceramic encoder (Heidenhain LIP-382) with a signal period of 128 nm. Flexures are used to mount the scale to allow for structural bi-material expansion rate differentials from a single epoxy point located near the center of the scale.

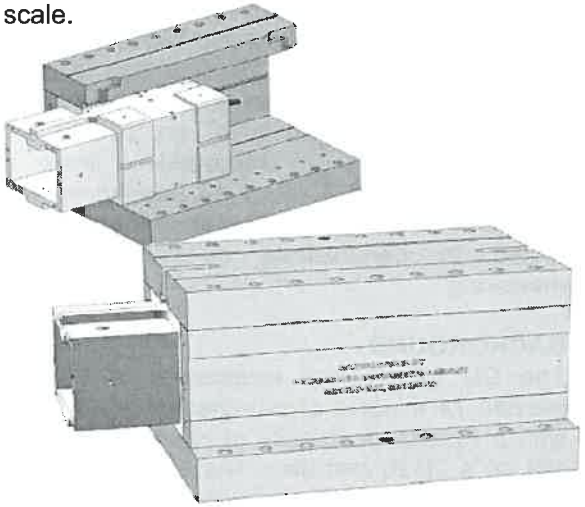

FIGURE 4. Schematic view of the linear axis. The partial section view shows the pad configuration.

Static test results estimate the normal load capacity of the slide to be 1,500 N at 0.6 MPa inlet air pressure. The estimated normal static stiffness is 200 N/μm and the tilt stiffness is 1.2 Nm/μrad at 0.6 MPa inlet air pressure. These values are approximately linear with inlet air pressure.

A modal analysis was performed to determine the dynamic response of the slide. An impact hammer (Kistler 2 mV/N) was used to excite the structure and an accelerometer (Kistler 100 mV/g) is used to measure the response (Hewlett-Packard Dynamic Signal Analyzer 35670A). With an inlet pressure of 0.55 MPa (80 PSI), the first mode in the horizontal direction

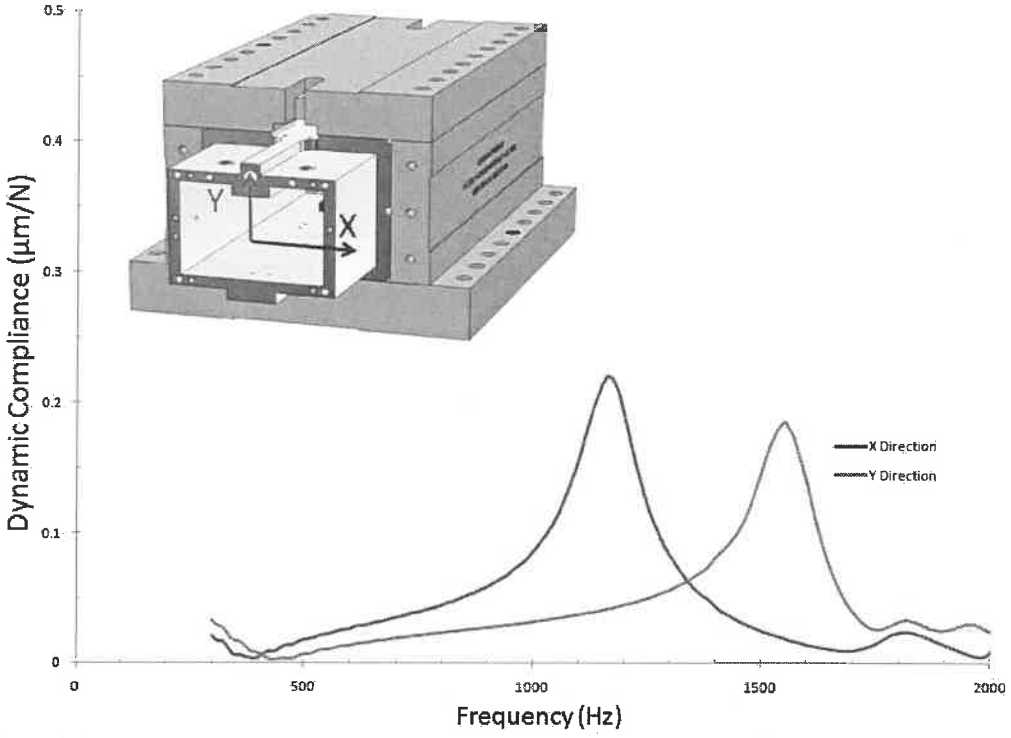

FIGURE 5. Dynamic response of the linear slide is used to determine the first natural frequency. The inlet air pressure was 0.55 MPa (80 PSI) for this test.

occurs at 1,170 Hz and the first mode in the vertical direction is 1,550 Hz.

ROTARY AXIS

The rotary axis for BD mastering requires radial asynchronous error motions less than 2 nm and radial synchronous less than 25 nm. Originally designed to meet the strict requirements of servo track writing, the ISO 3R is ideally suited for BD mastering. ISO spindles use long radial journal bearings separated by a central thrust, captured on both sides by air bearing surfaces.

As with the linear slide, a combination of compensation schemes and tight clearance (6-8 µm air films) is used to achieve the asynchronous error requirement. In this case, porous media restriction is combined with groove compensation. The porous media is used for the radial air bearings and the grooved compensation is used for the axial bearings as shown in Figure 7.

The radial error motions of the spindle are measured using precision spindle metrology techniques.[9] A capacitive displacement sensor (Lion Precision) targets a Ø25 mm lapped sphere. The spindle incorporates a 4096-count rotary encoder (MicroE Systems) and brushless, frameless motor and amplifier (MCS custom wound motor and LA-2000 amplifier). The radial error motion result at 250 Hz rotational speed (15,000 RPM) is shown in Figure 7. The synchronous error includes the ball out-of-roundness but is still less than 25 nm. The asynchronous error is less than 2 nm.

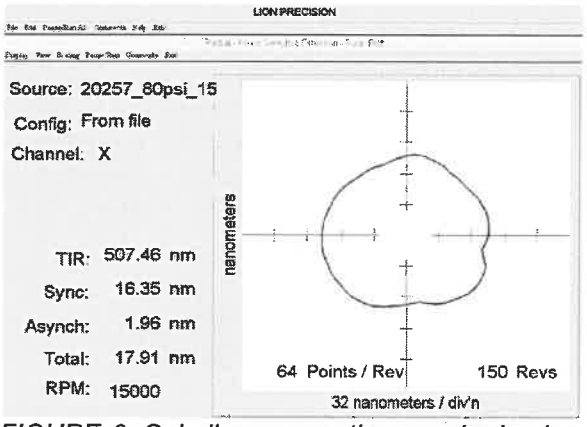

FIGURE 6. Spindle error motion acquired using Lion Precision SEA software. Air inlet pressure is 80 PSI and speed is 15,000 RPM.

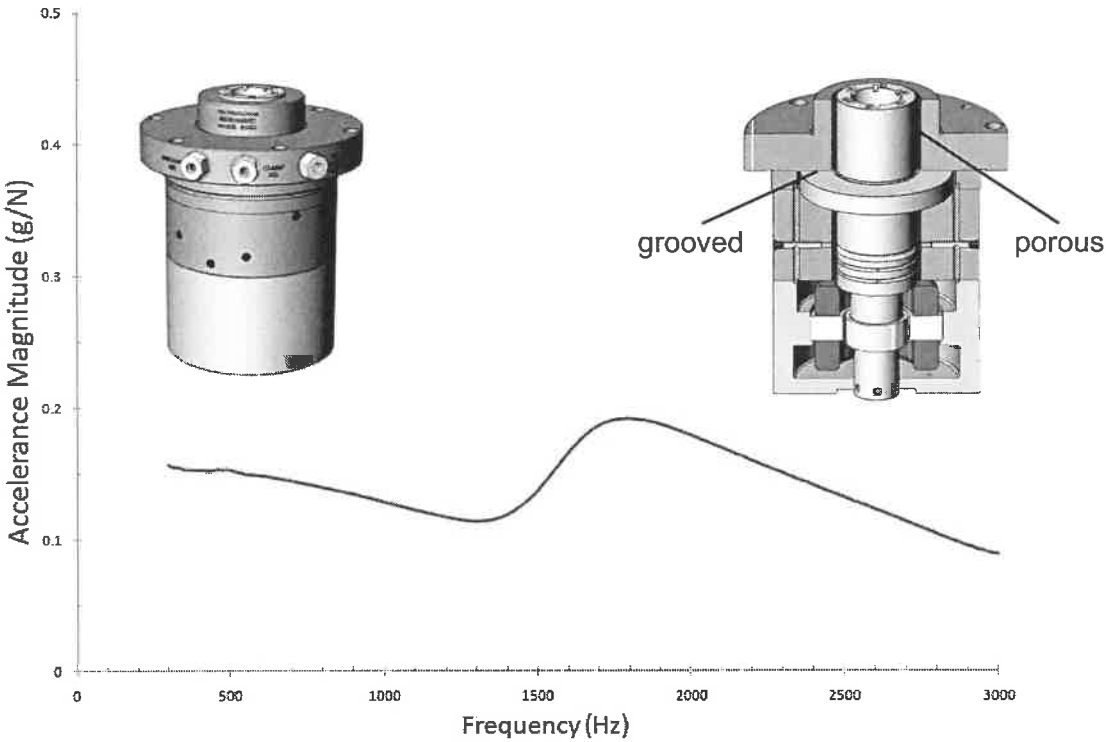

FIGURE 7. Dynamic response of the ISO 3R is used to determine the first natural frequency. The inlet air pressure was 0.55 MPa (80 PSI) for this test.

BD mastering also requires a high first natural frequency for the spindle (greater than 1 kHz). With an inlet pressure of 0.55 MPa (80 psi), the first mode is in the tilt direction and it occurs at 1,630 Hz.

CONCLUSION

The nanometer-accuracy demanded by Blu-ray mastering is achieved with hybrid-compensated air bearing spindles and slides. Dynamic errors are minimized by maximizing the stiffness and natural frequency of the air films and their support structures. Other errors are minimized by precision manufacturing and adherence to precision engineering design principles. The result is a positioning system meeting Blu-ray requirements.

REFERENCES

[1] Taylor, J, Crawford, CG, Armbrust, CM and M Zink. Blu-ray Disc Demystified. McGraw Hill. Chicago: 2009.

[2] Peek, H, Bergmans, J, van Haaren, J, Toolenaar, F and S Stan. Origins and Successors of the Compact Disc. Springer. Netherlands: 2009.

[3] ECMA International. Data Interchange on Read-only 120 mm Optical Data Disc. ECMA-130, 1996.

[4] ECMA International. 120 mm DVD – Read-only Disc. ECMA-267, 2001.

[5] Philips Research © 2004-2010 Koninklijke Philips Electronics N.V. [cited June 2010] Available from: www.research.philips.com.

[6] Spronck, JW, El-Husseini, MH, Jabben, L, Overschie, PM, Hobbelen, DGE, du Pau, P, Polinder, H and J van Eijk. "Mastering High-Density Optical Disks: a New Concept Design." Assembly Automation. vol 24, no 4, 2004, pp 406-415.

[7] Jabben, L. Mechatronic Design of a Magnetically Suspended Rotating Platform. Delft University of Technology. Netherlands: 2007.

[8] Laro, D. Mechantronic Design of an Electromagnetically Levitated Linear Positioning System Using Novel Multi-DOF Actuators. Delft University of Technology. Netherlands: 2009.

[9] Marsh, ER. Precision Spindle Metrology. 2nd Edition. DEStech Publications. Lancaster, PA: 2010.

AN INSTRUMENT FOR CONTROLLED, AUTOMATED, CONTINUOUS PULLING OF SUB-MICROMETER FUSED SILICA PIPETTES

Nikita Pak, Michael Dergance, Matthew Emerick, Eric Gagnon, and Craig R. Forest
George W. Woodruff School of Mechanical Engineering
Georgia Institute of Technology
Atlanta, Georgia, United States

ABSTRACT

Glass micropipettes are drawn glass needles with tip openings of 1 μm or less, useful for a wide range of biological and electrophysiological applications. In the state-of-the-art of fabrication of micropipettes, a skilled individual is able to produce about 2-4 micropipettes per minute. Many labs, which utilize hundreds of pipettes on a weekly basis, would benefit by the increased speed, accuracy, and repeatability of an automated fabrication apparatus. Therefore we have designed, built, and tested a working prototype of a fully automated fused silica micropipette puller. We report on the design and operation of this device along with measurements on the size and deviation of the micropipette tips. A trend has been determined between pulling velocity and tip geometry. This relationship allows for the ability to pull micropipettes with a specified geometry. Such control and automation has previously never been available and saves many hours of skilled labor.

INTRODUCTION

Current manufacturing of micropipettes consists of manually loading previously prepared lengths of capillary glass into a fabrication device and clamping them into place. A program is entered, and the two ends are pulled in opposite directions after a section of the glass is raised to the glass transition temperature [1]. The axial force necessary to pull the capillary apart is usually achieved via a hanging weight, solenoid [2], pneumatic actuator [3], or combination thereof. While this design has proven simple and robust enough to dominate the commercial offering, it is not the most flexible or readily adaptable for continuous automation.

Fused silica, while offering superior mechanical and electrical properties to the traditionally used borosilicate or aluminosilicate glass, is not often utilized for pipettes due to the high melting point compared to other glasses. However, devices do exist which are capable of reaching the greater than 1600°C needed to pull fused silica glass.

Our design relies on automated feeding of a continuous spool of fused silica capillaries via a set of pinch rollers. The capillary is then fixed in place with pneumatic clamps and heated with a gas torch. A stepper motor driven lead screw then pulls one end of the capillary. Our prototype utilizes a gas torch to achieve the necessary temperatures to pull fused silica glass, but subsequent prototypes could easily replace this with other means of heating, such as a CO_2 laser.

For a micropipette puller to be useful it must be able to manufacture tips of 1 μm and have high repeatability. Therefore, we have measured the tips created through runs of different parameters to calculate their average size and standard deviation. Also, this has led to a characterization of the relationship between pull velocity and tip geometry.

METHODS

Heating of the fused silica capillaries is done by a propylene gas jet which burns at about 1980°C; a higher temperature than propane. Based on this temperature, the dimensions of a typical capillary, fused silica properties, and propylene properties a heating model was created. The model consisted of first calculating the Grashof and Reynolds numbers. Since it was found that the Grashof number was much smaller than the Reynolds number, it was seen that forced convection dominates the heating, as was expected. Next, the Nusselt number was calculated using the Churchill and Bernstein correlation. From this the convective heat transfer coefficient was found. This model was used to get an estimate of the heating time required to reach the necessary temperature of about 1680°C to melt fused silica glass.

Pulling of the pipettes required two separate force calculations. It is known that a pull force of

about 45 N is necessary to pull the pipettes. The clamping force and pulling force must be great enough to achieve this requirement. The clamps [Festo, EV-20/75-5] are rated to provide a force of 600 N at the maximum stroke length and 600 kPa. These clamping modules are covered in silicon to provide a higher coefficient of friction. Empirically, we determined from four bench tests that the coefficient of friction for this setup is at least 0.22. This results in a clamping force of approximately 132 N.

A lead screw and stepper motor assembly is used to pull the pipettes. Given the torque of the motor, the coefficient of friction between the screw and nut, and the lead of the screw, the axial force was determined to be about 199 N. These calculations have shown that the pull force is much higher than that required to produce pipettes. Also, since the torque is a function of the driving frequency, the pull force was reduced so as to not pull the capillary out of the clamp.

MATERIALS

The machine is fabricated from a rigid aluminum base and an acrylic exterior, as shown in Fig.1. The aluminum base provides a rigid yet lightweight structure to allow very repeatable pulls and still maintain a bench top scale. The prototype is controlled via an Arduino micro controller; this allows a vast range of input and output capabilities. Parameters are entered via a 3.5" touch screen panel that is both efficient and user-friendly. As we develop better controls for the machine the Arduino can be quickly updated to provide end users with the most up-to-date system.

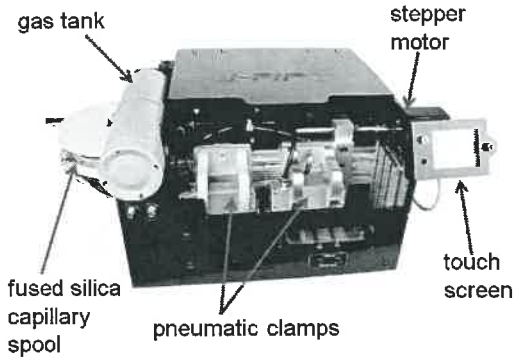

FIGURE 1. Photograph of a fully automated fused silica micropipette puller.

Our machine works off the principle of controlling pull velocity rather than specifying a fixed pull force. This is a much better control scheme because it allows direct control over what causes the capillary to break. The heated glass is a viscoelastic material that will yield when a certain strain rate is reached. By controlling the velocity of the pull the strain rate can be controlled.

EXPERIMENTAL RESULTS

Our device allows for many micropipettes to be created using the same parameters with no human interaction. Using this capability, we pulled seven sets of ten micropipettes each with varying pull velocity between each set. The length and diameter were then measured for each micropipette. The results for length and diameter can be seen in Fig. 2a and 2b respectively.

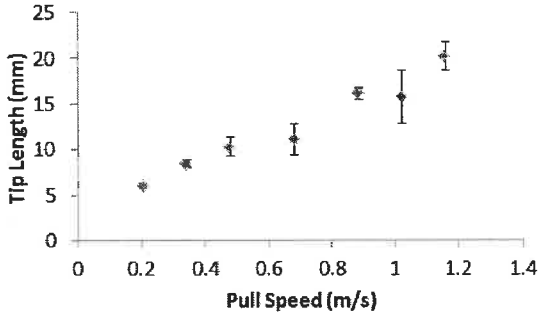

FIGURE 2a. Relationship between pull speed and tip length, with standard deviation.

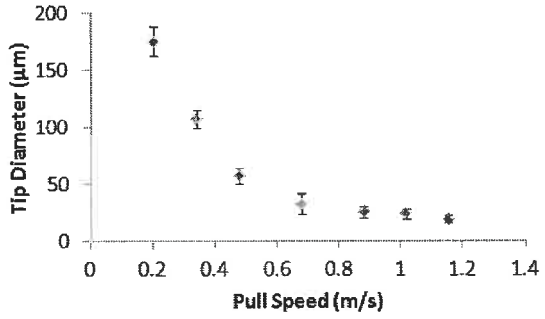

FIGURE 2b. Relationship between pull speed and tip diameter, with standard deviation.

As can be seen, the repeatability varies from 0.24 mm to 2.9 mm for the length measurement, and 12 µm to 3.5 µm for the diameter measurement. These plots show that a relationship can be established between both heating time and length, and heating time and diameter.

Another set of pulls was performed to try to obtain the necessary geometry of a useful pipette. The heating time was increased, and the result can bee seen in Fig. 3.

FIGURE 3. Microscope image of a micropipette pulled on our machine with a desirable tip geometry of less than 1 µm.

CONCLUSION

A device has been built to automate the manufacture of fused silica micropipette tips. It has been shown to be able to make the specified geometry required for electrophysiological experiments with relatively little deviation. A relationship between heating time and tip geometry has been determined. These results show that a device like this can be programmed to produce a specific geometry of micropipette tip, something that has never previously been accomplished. A user is able to input the capillary material, inner, and outer diameter. The machine is able to produce as many tips as necessary of a specified geometry based on this relationship. Such a device saves many hours of skilled labor.

REFERENCES

[1] Flaming D, inventor. Method and apparatus for forming a micropipette with uniform application of heat. United States patent US 4,921,522. 1990 May 1.

[2] Sutter Instrument Company [Internet]. updated 2009 August 4; cited 2010 July 1] P-2000 | Quartz Micropipette Puller. Available from: http://www.sutter.com/products/product_sheets/p2000.html

[3] MicroData Instruments, Inc. [Internet]. [updated 2009 February 9, cited 2010 July 1] PMP-102Q Quartz Glass Micropipette Puller. Available from: http://www.microdatamdi.com/pmp-102q.htm

EXPANDING WHITE LIGHT INTERFEROMETER CAPABILITIES TO BE USED AS A μ-CMM

Suresh Ramasamy[1], Ann Kasper[2]
[1]Advanced Vision and Measurement Group
[2]Metrology Laboratory
Hutchinson Technology Inc.
Hutchinson, MN, USA

ABSTRACT

White Light Interferometers (WLI) have been traditionally been used for single field-of-view (FOV) surface measurements with emphasis on Z-axis resolution. Previous generation WLIs could accommodate panel level skew and rotation errors, and correct for those errors to locate individual single FOV measurements. But those systems didn't allow for component level translation and rotation correction. Further, the panel level corrections were more operator based visual alignments. The new generation machines have the capability of using vision analysis tools to make simple dimensional measurements like diameters and widths. But most of the applications are limited to only single FOV measurements and do not allow two-way communication between 2D and 3D datasets. This paper explains the efforts being conducted at Hutchinson Technology Inc (HTI) to explore the possibility of utilizing WLI as a versatile coordinate measuring machine (CMM) with a 10x10x0.35mm measuring range and at least 100nm resolution in at least one axis, which can handle z-data analysis on specified locations determined by datums that are established using vision processing on image data.

BACKGROUND

HTI has traditionally relied on WLIs for precise z axis measurements for surface roughness and thick film thickness. The systems in place on our previous generation product line are offline systems. The parts are presented in a panel form and overall panel rotation errors could be calculated and used for positioning the sensor to the selected region of interest in a part, for making single FOV measurements. Even the panel level rotation errors were calculated based on operator manually positioning a fiducial mask on the selected panel level datum features. The next generation of instruments had software upgrade options that could utilize the 3d data of datum features to convert into binary images for image processing, but lacked the flexibility to correct for panel and part level errors. Current generation of systems have tremendous flexibility to be integrated to inline systems with respect to sensor orientation, speed and light requirements.

HTI implemented in its new product lines, an inline WLI measurement system that is capable of making vision measurements for panel level alignment and precise positioning on individual part locations. Old measurement process flow is shown in figure 1. The current measurement process flow is shown in figure 2. An offline WLI system has also been established, which does individual part based error compensation enabling precise positioning of masks.

FIGURE 1. Old measurement process flow

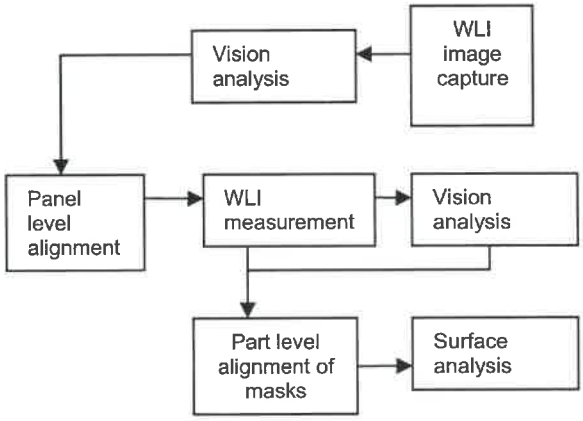

FIGURE 2. Current measurement process flow

Initial vision analysis of border alignment coupon is used for panel level alignment and then part datum hole is used for part level alignment. A histogram based z-ht data separation and

centroid calculation algorithm for repositioning masks on trace widths and gimbal pads (internally called as "Flexible Masks") is also being used.

CAPABILITY EXPANSION EFFORTS

Peter de Groot et al [1] describe a WLI capable of measuring surface flatness, parallelism and thickness of planar parts. This setup inspired HTI's efforts to explore the flexibility of existing WLI systems in-house. WLI capability expansion efforts were split into three phases. The first phase involved separating 3D datasets into sub images for further vision based dimensional analysis. The second phase involved datum establishment on 3D data converted to 2D image and then using that information to reposition masks back on 3D dataset. Stitching 10mm x 5mm area is time consuming, so ability to stitch data with only specific regions of interest would result in tremendous time saving. The potential disadvantage is that the cross correlation based stitching of data cannot be utilized and instead rely on the stage positioning accuracy.

Phase 1

As a first phase, dimensional measurement from stitched datasets was examined. The dataset was split into individual layers by height based layer separation, 3D data was converted to 2D image format and further processed for trace widths, dielectric widths, as shown in figure 3. Initial studies have shown that the system is repeatable to within 30nm.

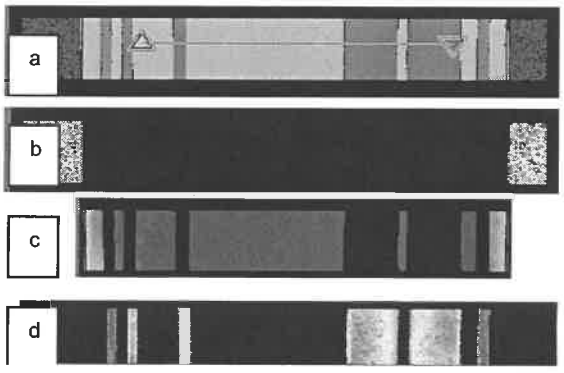

FIGURE 3. (a) Entire stitched dataset
(b) Stainless Steel Reference surface
(c) Dielectric surface
(d) Copper surface

Phase 2

As the second phase, stitched 3D data files were utilized to generate 2D image to find datum features, calculate translation and rotation parameters for repositioning the masks on to 3D data, to find separate regions of interest for further surface analysis, as shown in figure 4. The stitched 3D data of entire part is shown in figure 5. Measurements were taken at 20x magnification on a CP7300 system by Zygo Corporation [1-3]. This data is converted to 2D data and analyzed using VisionPro® software by Cognex Corporation, as shown in figure 6. The datum features are then used to position a mask onto the 3D data at specific locations as shown in figure 7, for calculating or obtaining required results from 3D data within those mask locations.

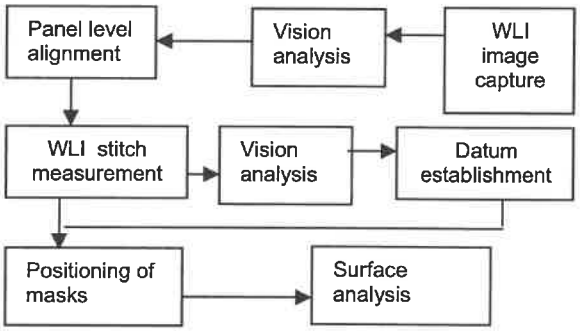

FIGURE 4. Process flow for phase 2

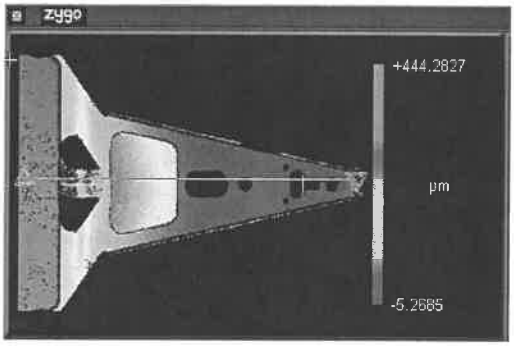

FIGURE 5. Stitched 3D data

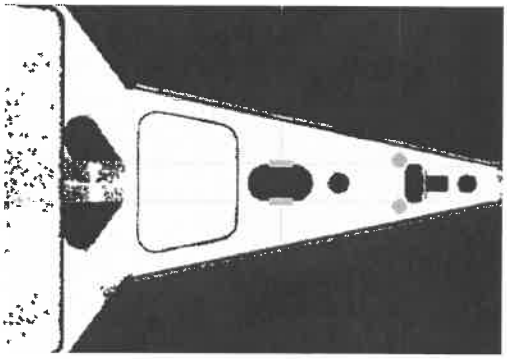

FIGURE 6. Image after datum analysis

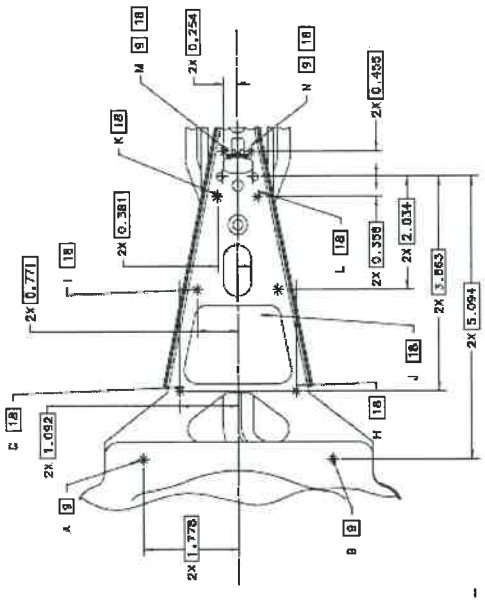

FIGURE 7. Drawing showing locations of interest on the part – A,B, G-N

Phase 3

For the third phase, attempts are being made to explore the possibility of stitching datasets relying on only the stage position instead of the conventional stitching based on overlap [4] and cross-correlation or iterative closest point [5] methods among the many options. To test the capability, a 10x10mm gauge block surface with four hole pattern as shown in figure 8 was chosen. The entire surface was stitched for the first 15 runs and only the areas 'a' and 'b' shown in figure 9 was stitched for the second 15 runs, using the 'zip stitch' option provided in CP7300, with the parameter settings shown in figure 10.

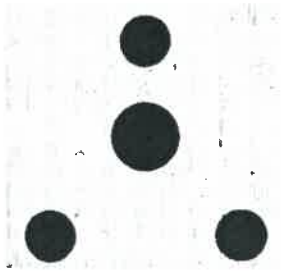

FIGURE 8. 10x10mm stitched area, z data converted to binary image

The 30 data sets were tested first for XY plane accuracy by converting the datasets into binary images and processing those in VisionPro® software. The center of bigger diameter hole in patch 'a' shown in figure 9 was considered as origin and center of the upper hole in patch 'a' was used for alignment and the coordinates of centers of holes in patch 'b' were calculated. Normal stitching method resulted in an average standard deviation of 0.77µm and the zip stitching method resulted in a 32% increase to 1.02µm. A stage with 1µm positioning error was used, hence this increase was within expectation.

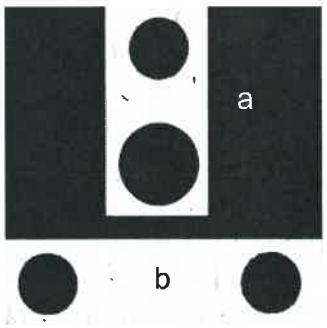

FIGURE 9. Zip stitched areas 'a' and 'b', z data converted to binary image

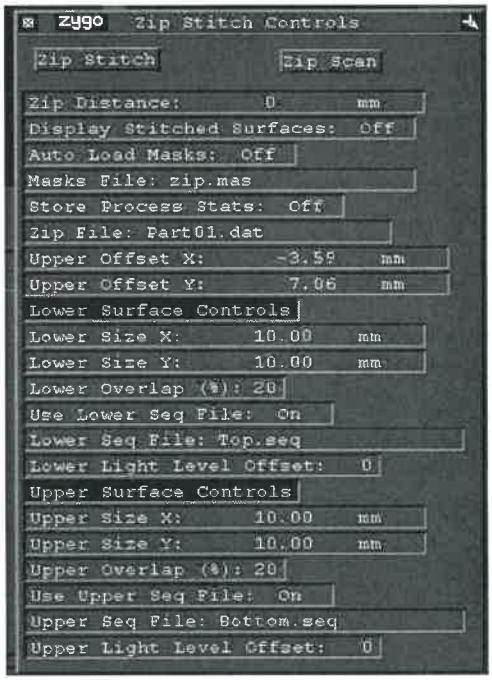

FIGURE 10. Zip stitch settings

The 30 data sets were then tested for Z and angular repeatability. Rectangular mask covering patch 'a' shown in figure 9 was used to obtain the reference surface and another rectangular mask covering patch 'b' was used to obtain the test surface on all 30 datasets. The average height, tip and tilt angles were calculated for the test surface with respect to the reference surface and shown in table 1.

		Stitch Method	
		Normal	Zip
Average	Height (µm)	1.5616	5.2246
	Tip (°)	0.0052	-0.0082
	Tilt (°)	-0.0271	0.0033
Std. Dev	Height (µm)	0.0511	0.2167
	Tip (°)	0.0003	0.0017
	Tilt (°)	0.0015	0.0020

TABLE 1. Stitch analysis results

Test results show that the repeatability worsens by a factor of 5 with the zip stitch method, apart from having 3.7µm shift in height.

CONCLUSION

Bonnet [6] illustrated the trends in microscope image processing, where multimodal image processing, localized signal processing and image fusion and segmentation were key issues. At the current stage of capability expansion, we feel that we have taken the same trend - first phase accomplished the multimodal data processing capability, phase two accomplished two-way communication between data in two different modes, image segmentation and localized signal processing. These phased capability expansion efforts have enabled HTI to measure as per print rather than just visual alignment of fixtures on the table, critical product features after establishing datums based on hole and slot locations and specific locations as per print for surface analysis like surface roughness, apex point, apex line etc.

Phase three tested fusion of data sets offset larger than FOV and no overlap, but showed unacceptable levels of errors in height shift and repeatability.

FUTURE WORK

Proposed future work would be to accomplish fusion of data obtained from different magnifications. The major issues associated with this phase would be the following:

- *Turret repositioning error* – when using different magnifications, either the objective turret or the zoom tube turret has to be used, resulting in a repositioning error.
- *Optical errors* – error maps need to be generated that would be subtracted from individual data sets. Measurement strategy needs to be established in such a way to measure using an optical mirror and compensate for it.
- *Data fusion* – Different variants of wavelet transform [7-9] have been proposed to be viable options for image fusion. Initially, those need to be tested for datasets with minimal z offset (within 30µm) and then fusion schemes need to be validated for large offsets. Further, methods for fusion on data sets with no overlap also need to be established.

ACKNOWLEDGEMENTS

The authors would like to thank Manas Lakshmipathy from Zygo Corporation and Joanna Schmit from Veeco Corporation for their discussions and suggestions regarding this initiative.

REFERENCES

[1] Peter de Groot, Jim Biegen, Jack Clark, Xavier Colonna de Lega and David Grigg. Optical interferometry for measurements of the geometric dimensions of industrial parts. Applied Optics. 2002; Vol. 41, No.19: 3853-3860.

[2] http://www.zygo.com/met/markets/semicon/cp7300/cp7300br.pdf

[3] Leslie Deck, Peter de Groot. High-speed non contact profiler based on scanning white-light interferometry. Applied Optics. 1994; Vol. 33, No. 31: 7334 – 7338.

[4] http://www.veeco.com/pdfs/appnotes/an504_20large_20field_20of_20view.pdf

[5] Szymon Rusinkiewicz, Marc Levoy. Efficient variants of the ICP algorithm. Proceedings of the Third International Conference on #D Digital Imaging and Modeling. 2001; 145-152.

[6] Noël Bonnet. Some trends in microscope image processing. Micron 35. 2004; 635-653.

[7] Nikolov S.G., Bull D.R, Canagarajah C.N., Halliwell M., Wells P.N.T. Image fusion using a 3D wavelet transform. Image Processing and its applications, IEE Conference Publication No. 465. 1999; 235-239.

[8] Li Jun, Li Deren. Data fusion for multisensor images based on edge features. SPIE Vol 3504; 376-382.

[9] Hui Xie, Weibin Rong, Lining Sun, Wei Chen. Image fusion and 3D surface reconstructions of microparts using complex values wavelet transforms. ICIP 2006, IEEE 2137-2140.

FOURIER TRANSFORM AND WAVELET ALGORITHMS FOR CALCULATING HEIGHT IN WHITE LIGHT INTERFEROMETRY

Kate M. Medicus and Maarten J. Jansen*
Mitutoyo Research Center Europe
Best, The Netherlands

INTRODUCTION

White light interferometry (WLI) has many names including coherence scanning interferometry and vertical scanning interferometry [1]. Generally WLI takes a 2.5D microscopic measurement of a surface using an interference objective. During the measurement, the part (or objective) is scanned so that all the pixels on the part move through focus. During the scan, the camera records an interference signal for each pixel on the part. This signal is called the correlogram. By analyzing this correlogram, we can determine the location (along the scan) where the pixel is located. By analyzing all of the pixels, we can obtain a surface height map.

In this paper we show two methods for converting the correlogram to a surface height map. In addition we also show a method for correcting errors that are possible in the height map. This paper uses the terms height map and profile interchangeably.

OBTAINING PROFILES

There are many known methods to calculate a profile from the set of white light correlograms [1]. The methods described here result in a coherence profile and multiple phase profiles. The coherence profile is a coarse, but quick method for finding the surface height map. Coherence profiles are subject to noise, diffraction (especially at edges [2]), dispersion, and other slope dependent effects.

The phase profile is more sensitive and thus has a higher resolution. But, the phase profile is subject to fringe order identification errors. Fringe order identification errors come from the errors in the coherence profile. Our correction method will combine the coherence and phase profiles to arrive at a high resolution profile without fringe order identification errors.

The calculation methods are described here are for a single camera pixel. To determine the entire surface map, the same methods are applied to each camera pixel.

Inverse Fourier Method

In this method for determining the profile, the Fourier Domain is used. The irradiance of the WLI correlogram is trimmed to isolate the correlogram from the full signal as shown by the center portion of the signal in the top graph of Figure 1. The signal is leveled and the mean removed so the Fourier transform is properly applied. The Fourier transform of the signal, shown by the line in the bottom of Figure 1 is taken. Then we apply a filter in the Fourier domain. This filter zeros all non-relevant frequencies and applies a Hamming window over the relevant frequencies. The filtered Fourier signal is shown by the dotted signal in the bottom graph of Figure 1.

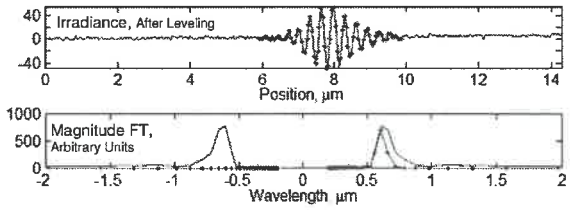

FIGURE 1. Top: An example correlogram and Bottom: Its raw and filtered Fourier transform.

Then we inverse Fourier transform the filtered signal as shown in Figure 2. The top graph shows the magnitude and the bottom the phase of the inversed signal. The coherence profile can be found from the peak location of the magnitude of this signal. The peak location can be found using a fit to a Gaussian curve or parabola, or it can be found using the center of mass of the signal, as is done here (shown by the vertical line in the top graph). This location is the coherence profile, *CP*. The phase profile is

* Now at ASML, Veldhoven, The Netherlands

then the location of the zero-crossing nearest to the coherence profile location. This shown by the vertical line labeled 0 in the bottom graph of Figure 2. This location of the zero-crossing is the phase profile 0, PP_0. Also shown are vertical lines labeled 2π and -2π, which are next nearest zero-crossings. These values are recorded because the coherence profile location may have misidentified the fringe order. These other locations form the phase profiles $PP_{2\pi}$ and $PP_{-2\pi}$. These profiles will be used in the correction algorithm shown below.

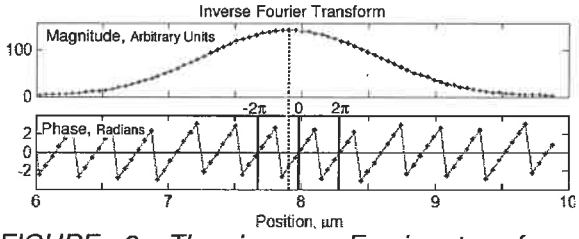

FIGURE 2. The inverse Fourier transform, magnitude (top) and phase (bottom). The profile locations are marked with the vertical lines.

Figure 3 shows PP_0, the phase profile at the zero crossing. This measurement should show a smooth tilted flat with a smooth pattern deposited on top. The height of the deposited pattern is about 60 nm. The profile shown here has many fringe order identification errors. This sample was shown as an example to illustrate these errors and the correction of them. Not all measurements have this many fringe order identification errors. For example, a typical measurement of a nearly flat, highly reflective mirror has no fringe order identification errors.

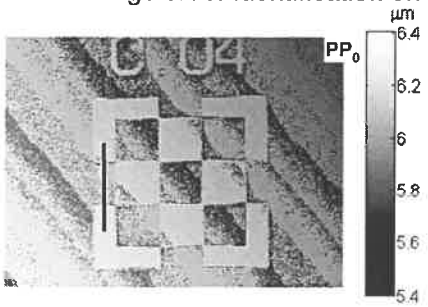

FIGURE 3. Phase profile at the zero crossing.

Wavelet Method

For the wavelet method, we use the Morlet complex wavelet [3] shown in Figure 4. We apply the wavelet transform to the correlogram in the convolution manner. This convolution results in the magnitude and phase signals shown in Figure 5. As before, the coarse coherence profile is found from the center of mass of the magnitude signal. The phase profiles are the locations at the 0, 2π, and -2π phase crossings as shown in Figure 5. As before, there is a possibility for fringe order identification errors in the phase profiles, and thus correction is then still required.

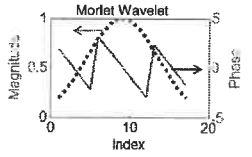

FIGURE 4. The Phase and Magnitude of the Morlet Wavelet.

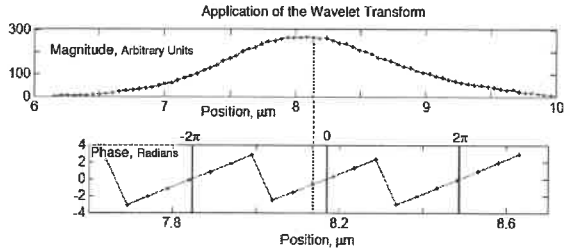

FIGURE 5. The signal, after applying the wavelet using convolution, magnitude (top) and phase (bottom). The profile locations are marked with the vertical lines.

CORRECTION OF THE PHASE PROFILES

The phase profile has better resolution than the coherence profile, thus generally it is the more desirable result. But, it can be subject to fringe order identification errors that look like jumps. Correction of these errors is required to obtain the best profile. Correcting the fringe order identification errors to obtain a high resolution profile has been done in the past [2,4]. Here though, we approach the problem differently. We combine multiple phase profiles that are separated by 2π into one, final phase profile. The requirements for this method are three (at minimum) phase profiles that are separated by 2π and one coherence profile. All profiles must be known relative to the measuring axis absolute scale.

Figure 3 shows PP_0, the phase profile at the zero crossing with many fringe order identification errors. These errors can also be seen in Figure 6, which shows the four profiles: PP_0, $PP_{2\pi}$, $PP_{-2\pi}$, and CP.

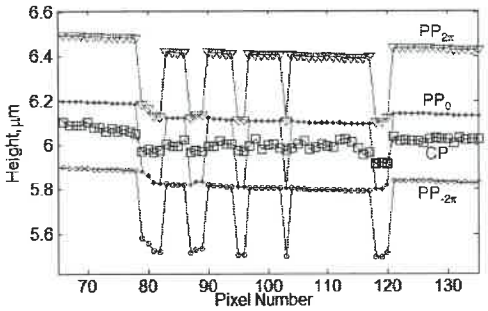

FIGURE 6. The four profiles of the line shown in Figure 3, in order: $PP_{2\pi}$, PP_0, CP, and $PP_{-2\pi}$.

As we see, there are two continuous phase profiles: the combination of PP_0 and $PP_{2\pi}$ and the combination of PP_0 and $PP_{-2\pi}$. To make these combined profiles, we must replace the areas of PP_0 where there are errors with the same areas of $PP_{2\pi}$ (or $PP_{-2\pi}$). These areas are found analytically using the difference between the *CP* and PP_0, shown in Figure 7. This height map (which has a distorted color scale for ease of viewing) clearly shows the areas that need replacing. The value the divides the two areas (into keep and replace) is called the separation value. Here, the separation value is about 0 µm.

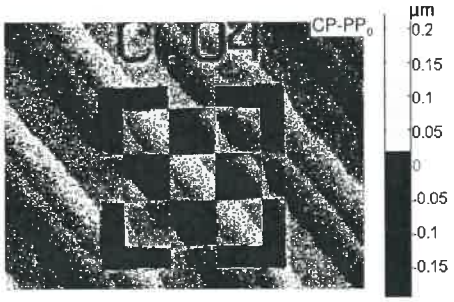

FIGURE 7. The difference between the coherence profile and the zero phase profile ($CP\text{-}PP_0$) clearly shows the separation between the areas the need to be kept and those than need to be replaced. Note the binary color scale.

Another view of the separation between the keep/replace areas is shown in Figure 8, the partial measurement of a 500 µm diameter sphere. Only part of this measurement is shown for ease of viewing. The top graph shows the three phase profiles, which clearly shows which areas need replacing. The middle graph shows the difference between the coherence profile and PP_0, and there is a clear binary difference between the areas that need replacing and those that do not. Here, again the separation value is about 0 µm.

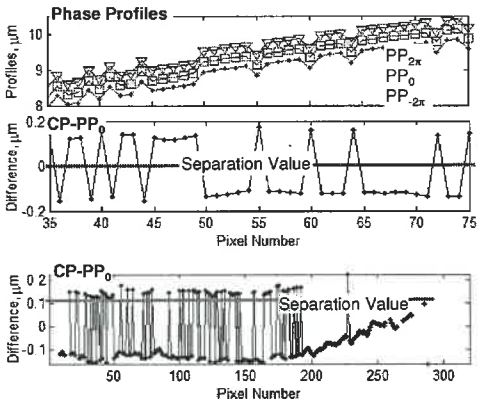

FIGURE 8. The measurement of a 500 µm diameter sphere. Top: Part of the three phase profiles showing where correction is required. Middle: Part of $CP\text{-}PP_0$ showing a 0 µm separation value. Bottom: The full $CP\text{-}PP_0$ shows that a separation value of 0.1 is required.

After finding the pixels than need to be replaced, we make the two combined profiles by starting with the PP_0 profile, and then replacing the found pixels with the pixel values from the $PP_{2\pi}$ profile (and $PP_{-2\pi}$ profile).

Generally, the separation value is 0 µm, but in some cases, the difference between the coherence profile and phase profile is not constant across the field of view. This is due to uneven illumination and sample effects, such a slope and roughness. Figure 8, bottom graph shows the non-constant profile across the whole field of view for the sphere measurement. Here, we see that the separation value should be about 0.1 µm, not 0 µm.

To make certain that the proper separation value is found, we make a set of the combined profiles with varying separation values. Then we apply a merit function to these profiles to find the best one. The merit function is the number of discontinuities between adjacent pixels in the profile. When this merit function is at a minimum, the proper separation value is found. A set of combined profiles is shown in Figure 9, where the number of discontinuities is plotted relative the separation value. Here, we see that any separation value between 0.05 µm and 0.05 µm could be used. For other measurements, the selection of the separation value is more precise.

After the proper separation value is used, two combined height profiles result: the combination of PP_0 and $PP_{2\pi}$ and the combination of PP_0 and

$PP_{-2\pi}$. The final corrected profile is then the one that is closest in mean value to the coherence profile. Figure 10 shows the final corrected profile for the sample with the deposited pattern.

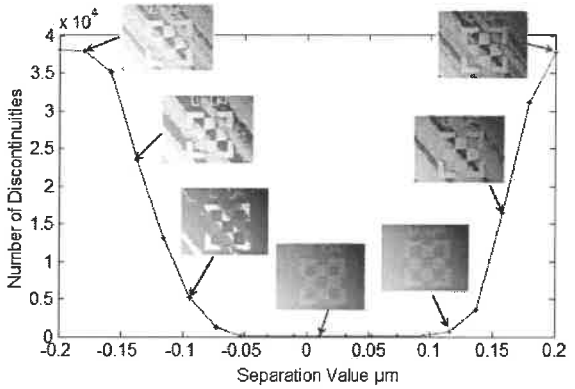

FIGURE 9. The number of discontinuities is the combined profile versus the separation value. Also shown are the combined profiles at selected separation values. As is clearly shown, the profiles at the 0 µm value have few discontinuities.

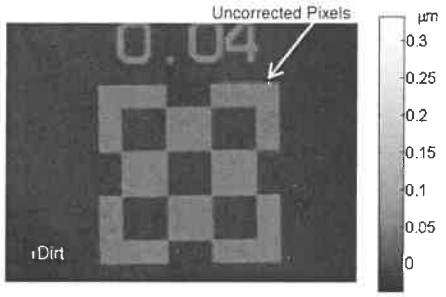

FIGURE 10. Final corrected profile of Figure 3 (plane removed). The few pixels of dirt in the lower left can be ignored. The few white pixels along the step edge are uncorrected pixels and show the limitation of the correction method. .

The key advantages of this correction method are that is does not require any foreknowledge about the sample, nor are continuous surfaces required. Because the merit function looks for the minimum of discontinuities, the measured sample is permitted to have any number of discontinuities. In addition, missing areas in the measurement are not a problem in this method, unlike unwrapping type methods. For example, WLI does not measure at high slopes. If the measurement area contained an island of high slope (i.e. no data), this correction method still works, because the coherence profile is used to determine which phase profile is the correct one. Also, this method keeps the absolute measured scale, which allows for measurement between multiple fields of view.

Figure 10 shows the limitation of this correction method. There are a few pixels along the step edge in the upper right of the measurement that were uncorrected. The fringe order identification error here was actually two orders, not one. This correction method only fixes one fringe order error. To fix two fringe order errors, we would either need to combine the two combined profiles (PP_0 & $PP_{2\pi}$ and PP_0 & $PP_{-2\pi}$) or use more phase profiles ($\pm 4\pi$) to achieve the corrected result. The method would be the same though, only the calculation time would increase.

CONCLUSIONS

We have shown here two methods for determining the coherence and phase profiles of a white light interferometric measurement. One method uses filtering in the Fourier domain to produce a magnitude and phase signal. The second method uses a Morlet wavelet to produce these signals. The coherence profile is then the center of mass of the magnitude. The phase profiles are the zero and $\pm 2\pi$ crossings nearest to the coherence profile. The profiles are then found using the same method.

After the phase profiles are found, a correction is applied to fix any fringe error identification errors. This correction uses the best applicable phase profile. The advantages of this correction method are that is does not require any foreknowledge about the sample, nor are continuous surfaces required.

Another advantage of these methods is that the absolute position is kept throughout the process.

REFERENCES

[1] Schmit J, Creath K, Wyant J. Surface Profilers, Multiple Wavelength, and White Light Interferometery. In: Malacara D, editor. Optical Shop Testing. Hoboken, NJ: Jon Wiley & Sones, Inc; 2007. p. 667-755.

[2] Harasaki A, Schmit J, Wyant, J. Improved Vertical-Scanning Interferometery. Applied Optics. 2000; 39: 2107-2115

[3] Morlet J, Arens G, Fourgeau E, Glard D. Wave Propagation and Sampling Theory—Part I, Geophysics. 1982; 47: 203-221

[4] De Groot P, Colonna de Lega X, Kramer J, Turzhitsky M. Determination of Fringe Order in White Light Interference Microscopy. Applied Optics. 2002; 41; 4571-4578.

ERRORS IN MEASUREMENT AND COMPENSATION ALGORITHMS FOR PERIODIC NONLINEARITY CORRECTION

Jonathan D. Ellis, Michiel Baas, Jo W. Spronck, and Robert H. Munnig Schmidt
PME: Mechatronic System Design
Delft University of Technology, Delft, The Netherlands

INTRODUCTION

In lithography systems, the image overlay error between the mask and the wafer is a critical parameter to reduce. Reducing the overlay error between subsequent layers in a chip means smaller linewidths can be achieved and more functions can be placed with a higher density. In this research, we investigate and estimate the effect of periodic nonlinearity in interferometers and the overall optical design on the overlay error used for feedback on the wafer stages. We simulate and compare two different measure-and-correct algorithms for characterizing and compensating the periodic nonlinearity under estimated operating conditions. Also, interferometer design parameters such as heterodyne split frequency and sampling frequency are considered.

SIMULATION PARAMETERS

The simulation parameters were estimated from a lithography tool projecting a 26 mm wide slit and scanning a distance of 33 mm at a constant speed of 600 mm/s and a maximum stage acceleration of 35 m/s^2. At this velocity and acceleration, the wafer stage has a position and velocity profile similar to the profile shown in Figure 1, where two consecutive dies scans are shown.

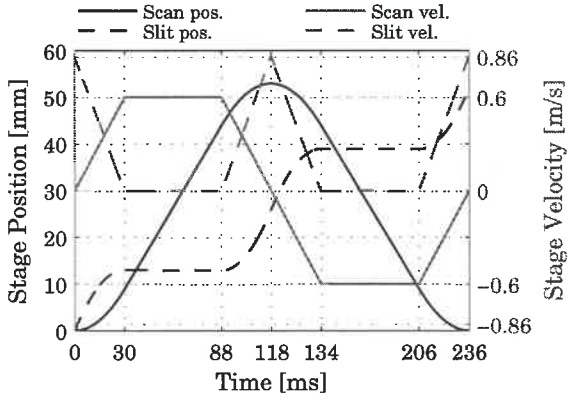

FIGURE 1. Profiles for the stage position (black) and velocity (grey) in the scanning and slit directions while scanning two consecutive dies. The slit direction is held at a constant position while the wafer is scanned.

PHASE MEASUREMENT PARAMETERS

In these simulations, a four pass Michelson plane mirror interferometer is used to measure the displacement. A schematic of the interferometer and electronics is shown in Figure 2. The measurement and reference signals are sent to a digital lock-in amplifier to measure the phase. Both signals are band-pass filtered (BPF) to remove aliasing and DC intensity fluctuations. Matching sine and cosine signals are generated from the reference signal using a phase locked loop (PLL). Two multipliers are used, mixing a sine and a cosine reference signal with the measured signal. Low pass filters (LPF) remove the high frequency components, generating quadrature signals (X,Y) for the continuous elliptical fit [2]. The quadrature signals are also sent to an arctangent function, which computes the phase (ϕ) after unwrapping. This is then used for the Chu-Ray compensation algorithm [3].

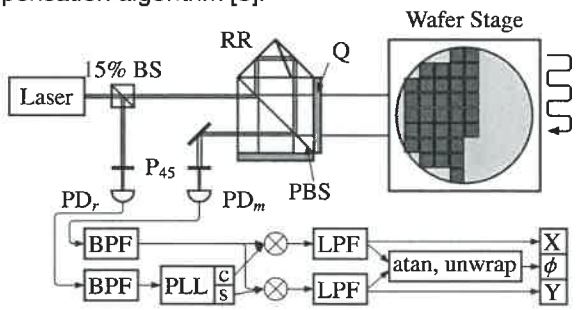

FIGURE 2. Schematic of a plane mirror interferometer measuring the wafer stage scanning motion axis (not to scale). An individual die is illuminated and then the stage shifts in the orthogonal direction, while reversing the scan direction. The signals are then sent to a digital lock-in amplifier and controller.

From Figure 3, it is clear there are several unwanted signals in the measurement bandwidth as a function of stage velocity. If the split frequency is too low, the doppler shift induced frequency change will pass through zero frequency, causing a direction ambiguity. Additionally, when a negative doppler shift occurs, there can be multiple harmonics in the measurement bandwidth. Also, there is first and second order periodic nonlinear where the former occurs at

the split frequency (f_s) and the latter is mirrored from the main frequency shift with respect to the split frequency.

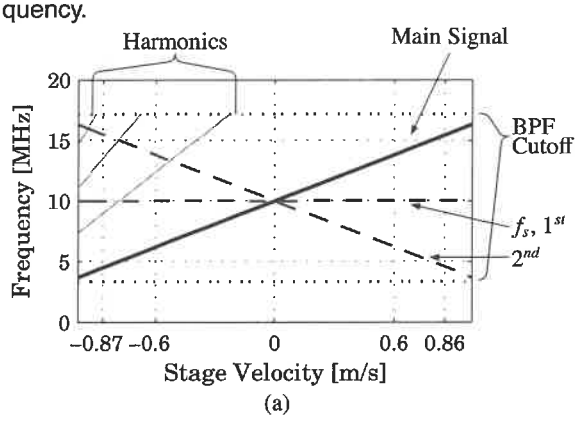

FIGURE 3. Signals in the measurement bandwidth as a function of velocity for a 10 MHz heterodyne frequency. The main measurement signal sweeps from approximately 4 MHz to 16 MHz with several harmonics and 1st and 2nd order periodic components in the measurement bandwidth.

When determining the optical system specifications, there are several user controlled variables. The laser split frequency (f_s) can be chosen to shift the overall measurement bandwidth. The BPF should be selected to limit aliasing and slow amplitude fluctuations while also accommodating the measurement frequency range. A higher sampling frequency (F_s) can be chosen with the tradeoff of less resolution (typically). The laser power can be increased to reduce noise at the detector. The periodic nonlinearity from frequency mixing should be reduced to also limit errors.

The source of periodic nonlinearity has been widely investigate and alignment techniques have been proposed for limiting periodic nonlinearity. In these simulations, we model the periodic errors as described by Wu [1]. Additionally, there are several algorithms for either measurement or measurement-and-correction of periodic nonlinearity. Assessing periodic nonlinearity and the interplay between other error sources and optical design parameters is important in displacement interferometry. Additionally, this investigation is simulated situations which mimic the practical application. This is particular to the controller design because the phasemeter updates at a much higher rate than the controller. A typical phasemeter must update at MHz rates while a controller will typically run at 20 kHz with a mechanical bandwidth limit of 300 Hz. Thus, it is important to see how this downsampling will affect the measurement for the controller.

ALGORITHMS

There are three main algorithms used in this investigation[1]. The first algorithm is only used for characterizing the nonlinearity amplitude when the motion is linear. After detrending the main displacement, a Fourier analysis is performed on the residuals. If the frequency axis is appropriately scaled for displacement (or fringes), the single sided amplitude spectrum can be used to detect the amplitude of periodic errors, either those fundamental to the interferometer or those due to stage motions.

The second algorithm used is a continuous elliptical compensation algorithm by Eom, *et. al.* [2], which is based on their Lissajous fitting algorithm [4]. The parameters for the Lissajous ellipse are determined using a least squares fit of a conical ellipse with the in-phase (X) and quadrature (Y) signals from the lock-in amplifier. Those signals are then converted to the amplitudes and phase for the Lissajous fit and then sent to a multiplier and adder as described in their paper.

The last algorithm used in this work is the Chu-Ray algorithm for first and second order periodic non-linearity correction [3]. Essentially, this algorithm takes a segment of data (320 points), performs a second order polynominal detrending, and a sinusoidal fit and compensation is performed on the residuals. This removes the first order periodic nonlinearity. The second order error is removed by multiplying the phase by two and repeating the first order algorithm.

SIMULATION RESULTS

Simulations were performed assuming different heterodyne frequencies, different sampling rates, and varying levels of periodic nonlinearity. The complete profile from the start of the acceleration in the scan direction to half way through the scan. This was chosen because the rapid acceleration in the scan direction and deceleration in the slit direction combined with the periodic errors may affect the overall alignment. The alignment error is this paper is deviation from the ideal path assuming no periodic errors. The alignment error was determined by simulating a nominal displacement profile and also the simulated values after correcting with the two algorithms. The simulated measurements were

[1]The algorithms used in this work were all implemented in Matlab. For more information on their specific implementation or copies of the algorithms, please contact the authors.

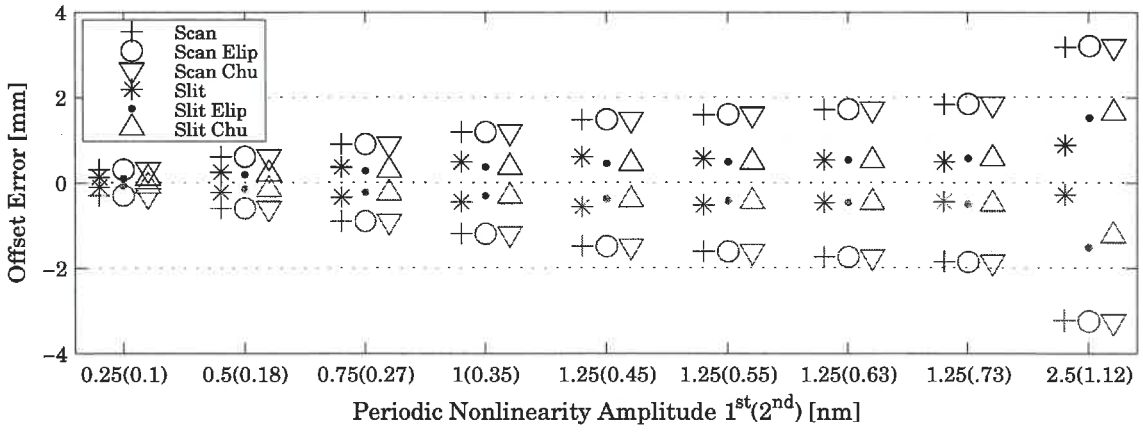

FIGURE 4. Offset error from the ideal path during illumination for the scan and slit directions assuming a 20 MHz heterodyne frequency with a 130 MHz sampling frequency. The simulations were nominally the same between positive doppler shifting (black) and negative doppler shifting (grey). In each case, the two periodic error algorithms did not compensate this offset and made the error worse for higher periodic error amplitudes.

then downsampled to 20 kHz where the offset, noise level (standard deviation), and error range was calculated.

20 MHz Split Frequency

Displacement interferometers often have a heterodyne frequency of 20 MHz because it is a high enough frequency to account for, a high stage velocity in both directions. The sampling frequency was 130 MHz, which was 5× the highest doppler frequency shift. Because the stage speed is high and the controller bandwidth is low in comparison, the direct periodic errors in the scan direction are not seen. However, there was a consistently increasing offset as a function of periodic error amplitude, as shown in Figure 4. The uncorrected measurements also showed significant noise and a high range of errors, although these were at frequencies much higher than the mechanical bandwidth of 300 Hz and can be reduced with proper filtering. The results are similar for the slit direction where there was little noise added from the algorithms but an increasing offset as a function of periodic error amplitude. The offset error in the slit direction was approximately half the offset error in the scan direction. In both directions, the periodic error correction algorithms reduced the noise and range of the error but did not reduce offset error. In the high periodic nonlinearity case, the correction algorithms increased this error in the slit direction.

10 MHz Split Frequency

Since the doppler frequency shift is at most 7 MHz, it is possible to use a 10 MHz heterodyne frequency without passing through zero frequency. Also, because the highest measured frequency is around 17 MHz, the requirements for the sampling frequency can be reduce 85 MHz while still having 5 points per cycle at the highest frequencies.

The same simulations for a 20 MHz heterodyne frequency were performed assuming a 10 MHz heterodyne frequency and an 85 MHz sampling rate. These results, shown in Figure 5a, had a similar trend for the scan direction compared to the 20 MHz results. However, in the slit direction, the results has a different trend where the periodic error correction algorithms increased the offset error.

The slower split frequency also allowed for a higher sampling frequency than in the 20 MHz case. The same simulations were repeated, but this time with a sampling frequency of 119 MHz, as shown in Figure 5b. The effect of the higher sampling frequency is quite clear in the slit direction. The uncorrected results showed a significant offset, while the corrected results show a similar trend to the previous 10 MHz case. Also, the magnitude of the offset error is slightly more with a higher sampling frequency.

PRELIMINARY CONCLUSIONS

These simulations show there is a coupled effect between the offset error and the amount of periodic nonlinearity in the measurement system. This offset error increase with increased periodic nonlinearity and will ultimately contribute uncertainty to the overlay error in the lithography tool. The difference

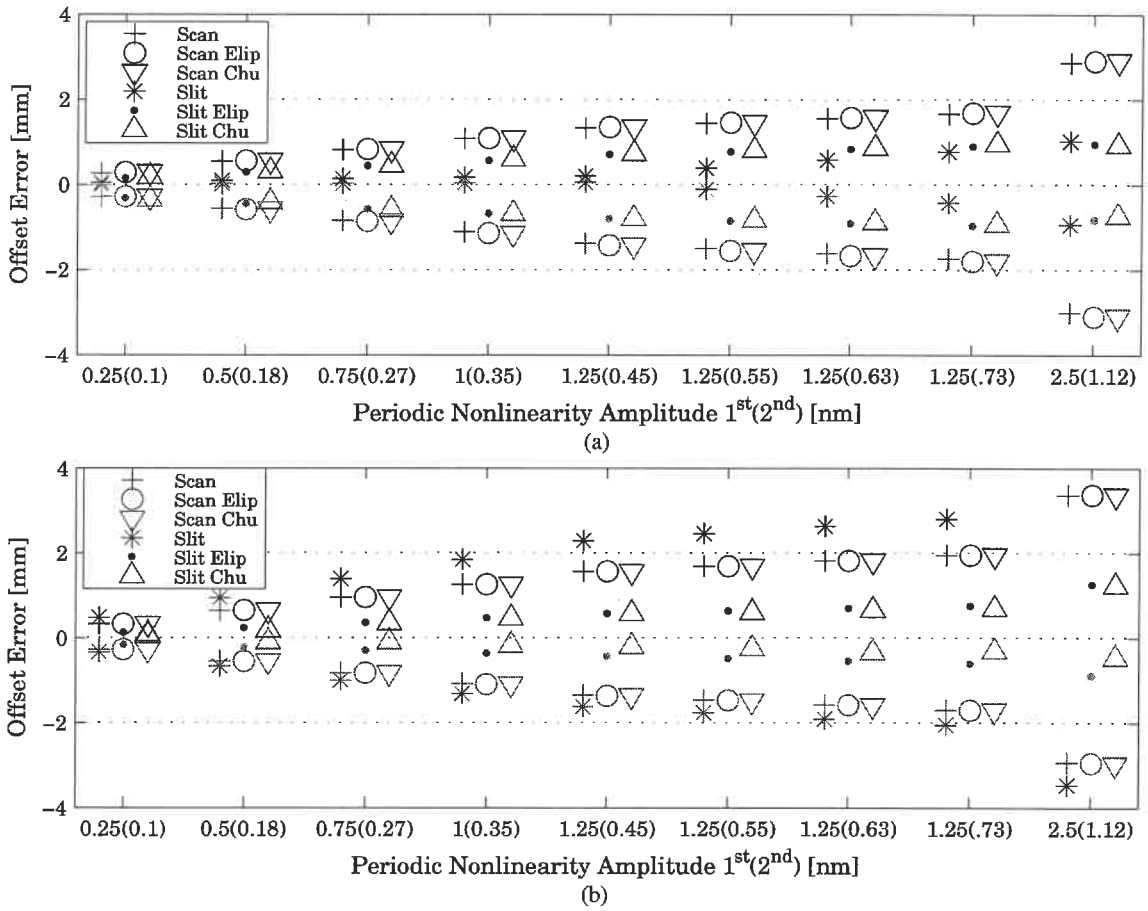

FIGURE 5. (a) Offset error from the ideal path during illumination for the scan and slit directions assuming a 10 MHz heterodyne frequency and an 80 MHz sampling rate. In the slit direction, the periodic error correction algorithms increase the offset error. (b) Offset error from the ideal path during illumination for the scan and slit directions assuming a 10 MHz heterodyne frequency and an 112 MHz sampling rate. The increased sampling frequency increased the offset error, although the periodic nonlinearity correction algorithms reduce this effect. [positive doppler shifting (black); negative doppler shifting (grey)]

in heterodyne frequency in the system had little effect on this offset error but the sensitivity to sampling frequency effects suggest this could an aliased or spurious signal in the desired measurement band. In these simulations, this was accounted for, thus we are currently unsure about what causes this effect. In each of the simulations, both periodic nonlinearity algorithms reduced the pk-pk error and the noise level when compared to uncorrected measurements. The Chu-Ray algorithm had pk-pk errors and noise levels that were approximately twice the values obtained after correcting using the continuous elliptical fit. In most cases, the pk-pk error was less than 0.5 nm and the noise level was approximately 0.1 nm, typically the resolution of a commercial phasemeter.

This research has been supported by the Dutch IOP under project IPT06104. The authors thank Dr. Ki-Nam Joo and Dr. Eric Buice for fruitful discussions.

REFERENCES

[1] Wu, C, Opt. Comm, 2003, **215**(1); 17–23

[2] Eom TB, *et. al.*, Meas. Sci. & Technol, 2008, **19**; 075302 (6pp)

[3] Schmitz TL, *et. al.*, Precis. Eng., 2008, **33**(4); 353–361

[4] Eom TB, *et. al.*, Meas. Sci. & Technol, 2002, **13**; 222–225

TERAHERTZ TIME OF FLIGHT DETECTION FOR ABSOLUTE THICKNESS MEASUREMENTS OF SINGLE SIDE POLISHED SILICON WAFERS

Javaid Ikram[1,2], Angela D. Davies[1,2], Faramarz Farahi[1,2], Tsing-Hua Her[1]
[1]CENTER FOR OPTOELECTRONICS AND OPTICAL COMMUNICATION
[2]CENTER FOR PRECISION METROLOGY
University of North Carolina at Charlotte
Charlotte, NC, USA

ABSTRACT

We present a solution for a challenge in semiconductor manufacturing, which is the measurement of the absolute thickness of single side polished silicon wafers. Our thesis is that terahertz time of flight detection can be used in non-destructive measurement applications in precision engineering such as the example discussed here. Here we discuss the application of the method to measure the thickness of single-sided silicon wafers. A transmission mode terahertz time of flight system was designed, constructed and used to demonstrate this technique. This is a challenging measurement in a manufacturing environment and a terahertz approach offers many advantages. Furthermore, the absolute thickness measurement was performed. The results show that the terahertz time of flight metrology system is repeatable and has a measurement speed of less than 2 minutes making it suitable for high volume process control.

INRODUCTION

Terahertz radiation refers to far infrared or sub millimeter radiation and its frequency lies between the microwave and infra red region of the electromagnetic spectrum. In terms of wavelength, terahertz radiation corresponds to 10^{12} Hz and hence 0.3 mm in free space. The advent of ultrafast lasers heralded the start of the terahertz era. Technological advances and applied research in terahertz radiation has increased exponentially ever since.

The terahertz spectral region lies between the electronic part and the optics part of the electromagnetic spectrum and is referred to as the terahertz "gap". Photon energies in the terahertz region are below the electronic state transition energies in material that are necessary for optical sources. Moreover, terahertz photons cannot excite electrons above the band gap energy in a photodiode. On the other hand of the gap, terahertz frequencies are too high to be directly generated and detected by microwave technology. These technological challenges in generating and detecting terahertz radiation are overcome using ultrafast optics [1,2].

As a result of the growing interest in terahertz radiation, a multitude of system configurations have emerged for various applications in terahertz research and development. The first demonstration of a terahertz imaging system for non destructive testing was done by Hu and Nuss [3] at AT&T and Bell labs. They used photoconductive antennas as a source and detector of terahertz radiation. A mode locked Ti: Sapphire laser at a wavelength of 800 nm was used to excite the photoconductive antenna. Other research groups independently demonstrated the applications of terahertz radiation using different configurations. A commonly used design was the use a photoconductive antenna to generate terahertz radiation and a non linear electro-optic crystal for terahertz detection [4]. Photoconductive antennas are the most widely used sources for generating terahertz radiation. They are used in most terahertz systems because of the high power and signal to noise ratio.

Free space electro-optic sampling measures the amplitude and phase of the terahertz electric field in the time domain. In this method, the change in polarization of an ultrafast probe beam is measured. The measured polarization change can draw an exact picture of the terahertz field.

NON DESTRUCTIVE TESTING USING TERAHERTZ RADIATION

Applications in precision engineering and precision metrology are relatively unexplored. Terahertz radiation has potential for

precision metrology of internal structures or defects in insulating materials such as coatings, ceramics, insulation and many composite materials that are difficult or impossible to characterize otherwise. Examples include paint film thickness, voids, crack, and internal geometries [5].Terahertz radiation provides unique advantages over other non destructive techniques. The property of terahertz radiation to penetrate insulating material opaque at other wavelengths enables various applications.

Terahertz metrology has great potential in in-process monitoring of some aspects of the semiconductor manufacturing process. The concept of production line inspection using terahertz radiation has been demonstrated by *Yasui et al* [5]. They successfully designed and implemented a terahertz paintmeter system that was employed to measure the thickness of paint films. They also studied different non destructive testing methods and demonstrated the use of terahertz radiation to measure the thickness of paint films. In their technique, the temporal delay between reflected pulses is measured and converted into thickness information.

Other technologies such as ultrasonic thickness meters are currently used for this purpose and offer a great degree of portability and reliability. However, such devices perform contact measurements and can be impractical in in-process inspection. Given these advantages, we decided to design and construct a terahertz time of flight system that could be used for non-destructive measurement applications.

OPERATIONAL PRINCIPLE

The fundamental components of the terahertz system are, femtosecond laser, terahertz source, terahertz beam optics and the terahertz detector.

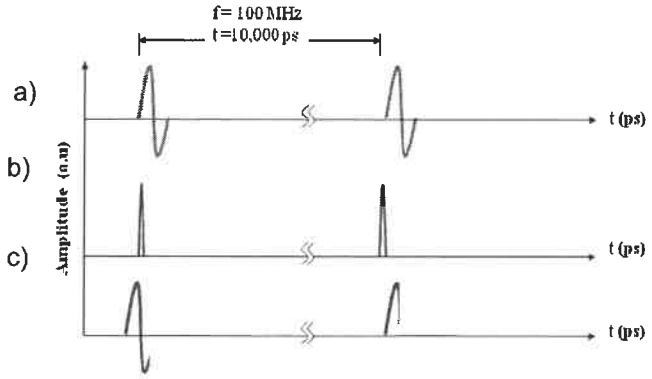

FIGURE 1. Sampling of terahertz waveform by femtosecond laser pulse. (a) Terahertz waveform. (b) corresponding femtosecond optical pulse. (c) measured terahertz waveform obtained by sampling (a) and (b).

Figure 1 illustrates the sampling of the terahertz signal by a femtosecond optical pulse. A single femtosecond pulse generates one terahertz pulse. Identical copies of the femtosecond pulse, and hence the terahertz pulse, are produced at the repetition rate of the laser. Making the two optical path lengths equal ensures that each terahertz pulse interacts with the corresponding femtosecond pulse. By translating the delay line we look at a different set of identical pulses. Hence we are not looking at a single pulse but the average shape of many terahertz pulses

METROLOGY OF SINGLE SIDE POLISHED/ETCHED WAFERS

Infrared transmission has been used in the semiconductor industry for measuring silicon crystals. Such systems are generally limited to measuring only double side polished silicon wafers. A rough back surface destroys the spatial coherence of the light enough to eliminate interferometric fringes. *Schmitz et al.* describe the use of infrared interferometer developed at the National Institute of Standards and Technology (NIST) to measure the thickness variation in silicon wafers. The interferometer makes use of interferometric fringes and as a result can only measure double-side polished silicon wafers [6]. A similar interferometer was implemented at UNC Charlotte. The interferometer is setup in the Twyman Green configuration utilizing infrared radiation. A tunable laser is used for this setup [7].

In both of these configurations, the reflection from the back surface needs to be sufficiently specular, as the measurement is based on the spatially coherent interference condition over the area of the wafer. If the surface is rough the interference fringes will not be observed and the measurement will not be possible. Our terahertz metrology instrument demonstrates a fast measurement of single side polished or etched silicon wafer.

EXPERIMENTAL SETUP

A transmission mode time domain terahertz instrument was developed. The terahertz time

domain metrology system was used to measure the thickness of single side silicon wafer.

Figure 2 shows the schematic of our terahertz metrology system.

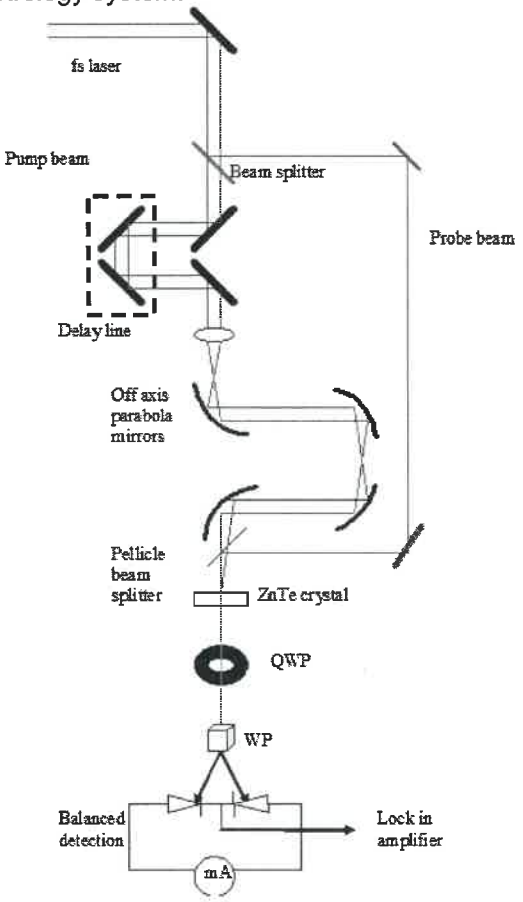

FIGURE 2. Terahertz metrology system.

The terahertz system is powered by a Spectra Physics Tsunami Ti:Sapphire laser. The laser is pumped by a Spectra Physics Millenia V Nd-YAG laser. Femtosecond laser pulses are split by a 90:10 beam splitter. The stronger portion of the beam called the pump beam is focused on the terahertz photoconductive antenna by an achromatic lens. The antenna was purchased from Zomega Terahertz Corp. The configuration is a strip-line antenna. It consists of two metallic leads with a 150 μm gap deposited on a GaAs substrate. The terahertz radiation generated is used to probe the sample in the desired configuration (e.g transmission), then the terahertz beam is collimated and focused using off axis parabolic mirrors on the terahertz detector crystal. The weaker femtosecond laser pulse is incident at the terahertz detector crystal after passing through a computer controlled mechanical optical delay line. The process is very sensitive and can extract the true waveform of the terahertz electric field. The terahertz pulse is sampled using the weaker femtosecond pulses through a balanced detection setup. Free space electro optic sampling is used to detect terahertz radiation in our system. The reference signal from the function generator (that drives the antenna) is also input to the lockin amplifier. The terahertz signal extraction is illustrated in figure 3.

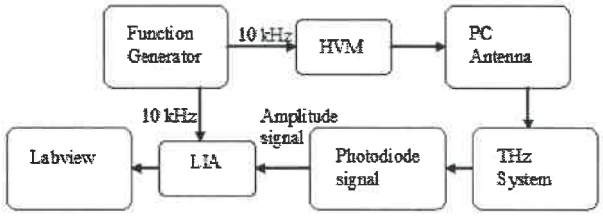

FIGURE 3. The function generator input to the high voltage modulator (HVM) causes the THz repetition rate to be 10 kHz. The terahertz signal is extracted by referencing the lock in amplifier (LIA) with the same 10 kHz signal.

RESULTS AND DATA ANALYSIS

The terahertz signal measured in free space is shown in figure 4. The FWHM of the measured signal is calculated using MATLAB and found to be 0.32 ps. The time for one scan is less than 2 minutes. The data is graphed in real time and also sent to a file for post processing. In order to extract information about a material using terahertz radiation, a transmission measurement can be done where the terahertz pulse is propagates through the material. A comparison between the resultant pulse and a reference free space pulse in the time domain enables us to derive various quantitative conclusions about the material.

The wafer is placed at the focus of the terahertz beam and the thickness is measured with 8 scans. The thickness can be calculated by knowing the refractive index and temporal displacement of the terahertz pulses using the following formula [8].

$$D = \frac{c_o \Delta T}{n_{THz} - 1}$$

Static repeatability is defined as the measure of inherent variability of the measurement tool itself. It signifies the repeated measurements in which the part is not removed from the tool

between measurements. A static repeatability analysis is performed for the reference silicon wafer. Table 1 shows the static repeatability data of the reference terahertz wafer.

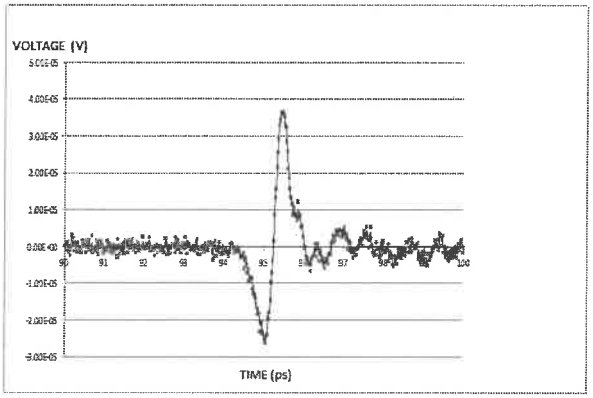

FIGURE 4. Free space terahertz waveform

Figure 5 shows the time delay for a propagating terahertz beam through a single side polished silicon wafer.

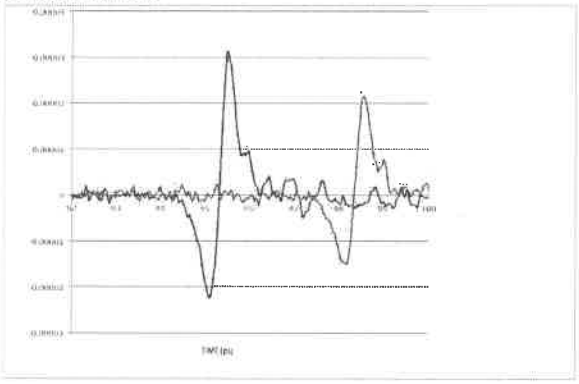

FIGURE 5. Transmission through single side polished silicon wafer.

TABLE 1. Time delay and the corresponding absolute thickness measurements.

ΔT (ps)	D (μm)
3.06	383.0
3.06	383.6
3.06	383.1
3.06	382.8
3.03	379.0
2.9	374.9
3.03	379.1
3.06	383.2

CONCLUSION

This research focuses on applications of terahertz radiation in metrology. A reliable transmission mode time domain terahertz instrument was implemented which enables the measurements of a wide variety of specimens. The terahertz time domain metrology system was used to measure the thickness of single side polished/etched silicon wafers. This is a challenging measurement in a manufacturing environment and a terahertz approach represents a significant advance.

REFERENCES

[1] X-C Zhang. Terahertz wave imaging: horizons and hurdles. Phys. Med. Biol. 2002; 47: 3667-3677

[2] Kawase K, Terahertz imaging – new steps towards real life applications. 12th Interaritional conference on terahertz electronics. 2004; 29: 553-554

[3] B.B. Hu, M.C. Nuss, "Imaging with terahertz waves", Optics letters. Vol. 20, No. 16, August 1995

[4] J. Cunningham, C. Wood, A. Burnett, P.C. Upadhya, W.H. Fan, E.H. Linfield, A.G. Davies, "Terahertz time domain spectroscopy – present and future modalities", Microwave symposium, 2007, IEEE/MTT-S International

[5] Yasui T, Yasuda T, Sawanaka K, Araki T. Terahertz paintmeter for non contact monitoring of thickness and drying progress in paint film. Applied Optics 2005; 44: 6849-6856

[6] Schmitz T, Davies A, Evans C.J. Silicon wafer thickness variation measurements using the National Institute of Standards and Technology infrared interferometer. Optical Engineering. 2003; 42(8): 2281-2290

[7] Suratkar A. Absolute thickness metrology using wavelength scanning interferometry. 2009; PhD Dissertation. UNC Charlotte.

[8] Ellrich F, Theuer M, Torosyan G, Jonuscheit J, Beigang R. Thin film measurements with terahertz radiation. 2008; 978-1-4244-2120-6

PRECISION MICRO-ENGRAVING OF GLASS BY AUTOMATIC BOUNDARY TRACKING OF COMPLEX IMAGES

Sung-Chong Chung
Hybrid System Design & Control LABoratory
School of Mechanical Engineering, Hanyang University
Seoul 133-791, KOREA

ABSTRACT

Design is important in the IT, digital appliance, and auto industries. Aesthetic and artistic images have been applied for better quality of products. 2.5D engraving of glass products is important to fabricate aesthetic patterns in the jewelry industry. Grinding, laser and chemical methods have been used to fabricate jewelry. However, to improve productivity and quality of 2.5D machining on the glass, micro engraving through micro end-milling is required. In this paper, to improve productivity and quality of 2.5D machining on the glass, 2.5D engraving method has been developed through the ABT (Automatic Boundary Tracking) algorithm and glass machining technique. In addition, to obtain optimum cutting conditions in glass machining for jewelry, micro ball end-milling processes with crack free conditions are studied through Taguchi method. Performance of the developed system is verified through case studies.

KEYWORDS: 2.5D engraving, ABT, Aesthetic pattern, Glass machining, Micro end-milling.

INTRODUCTION

Recently, design is important for upgrading quality of products and manufacturing high value-added goods. Using the aesthetic and artistic design patterns, design quality of commercial products is significantly upgraded. This generates TechArt technology in the IT, digital appliance, and auto industries. TechArt means a design technology to transform engineering items to products with aesthetic design features. Using the artistic design patterns, design quality of commercial products is significantly upgraded. Valuation of jewelry, IT, digital appliance and auto products is improved as well [1,2].

2.5D engraving of glass products is important to fabricate aesthetic patterns in the jewelry industry. Grinding, laser and chemical machining methods have been used to fabricate jewelry. However, heat affection, chemical damage and lack of the 2.5D engraving system have limited the engraving application so far. To fabricate a small and complex aesthetic pattern on the jewelry, precision glass engraving technique through crack-free machining is required. As the glass is brittle material, cracks are generated due to impact load of milling. To increase machining performance, high-speed micro end-milling with critical depth of cut is required for the development of crack-free micro engraving process. In this paper, to obtain optimum cutting conditions in the high-speed glass machining, Taguchi method is applied. Using the previously developed ABT algorithm and NURBS modeling [1], construction of embossed CAD data from any kinds of artistic pictures or images has been achieved. Combining the previously developed CAD/CAM technique based on the ABT algorithm with the high-speed crack-free end-milling technique, precision micro-engraving of glass has been performed. Performance of the developed system is verified through case studies.

2.5D ENGRAVING METHOD

Images are contaminated by noise. It deteriorates quality of reconstructed 2.5D CAD models. To reduce the noise, color images are transformed to gray images first. To remove impulse and salt-and-paper noises without blurring of the image, an adaptive median filter [1,2] is applied to the image. Then binary image is obtained through multiple threshold according to designer's intention. In the application of the adaptive median filter, selection of the proper window size is important to enhance clearness of the image [2].

To get 2.5D solid CAD models from an image, edge information should be extracted from the image first. The ABT is used to get boundary curves from point loops, as well as real loops composed of closed curves or closed twist curves in a 2D image [1]. Fig. 1(a) shows a 2D image. Fig. 1(b) shows extracted boundary curves through the ABT algorithm. It is

confirmed that the devised ABT algorithm works well to extract closed boundary curves of aesthetic images.

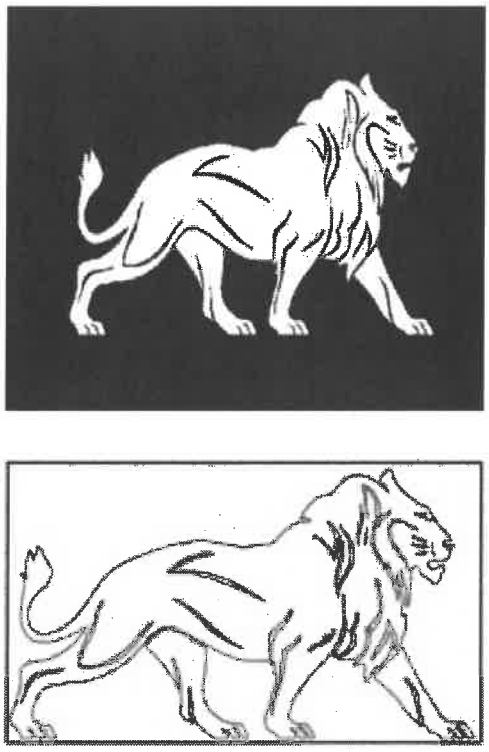

FIGURE 1. (A) 2D IMAGE, (B) EXTRACTED BOUNDARY CURVES BY ABT ALGORITHM.

Secondly, to make 2.5D CAD models from pixels of the boundary curves, NURBS curve fitting of them is required. Using the chord length and average knot value methods, control points matrix for the fitting is obtained. Then, the NURBS curve of the boundary curve is obtained as

$$P(u) = \frac{\sum_{i=0}^{n} w_i P_i N_{i,k}(u)}{\sum_{i=0}^{n} w_i N_{i,k}(u)} \quad (1)$$

where P_i is the i *th* control points, w_i is the weight of P_i, and $N_{i,k}(u)$ are blending functions given by

$$N_{i,1}(u) = \begin{cases} 1 & t_i \le u < t_{i+1} \\ 0 & otherwise \end{cases}$$
$$N_{i,k}(u) = \frac{u - t_i}{t_{i+k-1} - t_i} N_{i,k-1}(u) + \frac{t_{i+k} - u}{t_{i+k} - t_{i+1}} N_{i+1,k-1}(u) \quad (2)$$

where t_i is the i th knot value. To secure continuity of the NURBS curve, order k is selected 3 in this paper.

To visualize and manipulate the CAD model on the commercial CAD/CAM system. IGES file conversion is used [3,4] and then endmill simulation has been performed through the solid model as shown in Fig. 2.

FIGURE 2. MACHINING SIMULATION ON POWERMILL.

TABLE 1. PROPERTIES OF GLASS.

Material	Soda-lime Glass
Size	21x25x1 (mm)
Density	2490 (kg/m³)
Young's modulus	69 (Gpa)
Poisson's ratio	0.22

FIGURE 3. EXPERIMENTAL SETUP.

EXPERIMENTS

Soda-lime glass with property shown in Table 1 is applied for glass machining. Brittle fracture occurs during ball end-milling on the glass. Vertical and horizontal cracks are generated due to thrust and axial loads. To remove cracks in cutting, chip thickness should be controlled less than the critical thickness [5,6]. And to reduce thermal damage during cutting, machining speed achievable by the spindle speed is selected as high as possible. Fig. 3 shows the overall experimental set up installed on the high-precision CNC milling machine. TiAlN coated 2 flutes Φ0.3mm ball end-mill attached to the air-spindle with 150,000rpm spindle speed is used for experiments. This is actuated by 0.5 Mpa air pressure (HTS-1501; Nakashini Inc.).

Preliminary experiments were conducted to derive proper range of feed, axial depth of cut and rotational speed. Table 2 shows $L_9(3^4)$ orthogonal array for crack- free ball end-milling of glass in Taguchi experiments.

TABLE 2. $L_9(3^4)$ ORTHOGONAL ARRAY.

	Spindle speed (rpm), S_i	Feed rate (mm/min), F_i	Axial depth of cut(mm), A_i
1	120,000	3	0.06
2	120,000	4.5	0.08
3	120,000	6	0.1
4	135,000	3	0.08
5	135,000	4.5	0.1
6	135,000	6	0.06
7	150,000	3	0.1
8	150,000	4.5	0.06
9	150,000	6	0.08

TABLE 3. CRACKSIZE (mm^2) AND S/N RATIOS.

	1st	2nd	3rd	Average	S/N
1	0.0592	0.1771	0.2604	0.165567	14.6565
2	0.1155	0.1045	0.0937	0.104567	19.5808
3	0.1316	0.0989	0.078	0.102833	19.562
4	0.1637	0.1383	0.0982	0.1334	17.323
5	0.0788	0.1363	0.1277	0.114267	18.6334
6	0.0709	0.1712	0.1264	0.122833	17.7544
7	0.2397	0.181	0.127	0.182567	14.504
8	0.0737	0.1423	0.1292	0.115067	18.5003
9	0.1696	0.0681	0.1281	0.121933	17.7979

The objective of process optimization is to determine optimal process parameters and to reduce variation of product quality. Taguchi methods use signal-to-noise (*S/N*) ratio to quantify experimental variation [5,6]. In this paper, 'smaller-the-better' (SB) *S/N* ratio given by Eq. (1) is applied for reducing crack size.

$$S/N = -10\log\left[\frac{1}{n}\sum_{i=1}^{n} y_i^2\right] \quad (1)$$

where n represents number of repetition of a test, and y_i is measured crack size.

Table 3 shows experimental results according to Table 2. Crack size, averaged crack size and *S/N* ratio are obtained. Averaged *S/N* ratios according to each process parameter are shown in Fig. 4. Spindle speed 150,000rpm, feed rate 3mm/min and axial depth of cut 0.06 mm has been selected for optimal parameters.

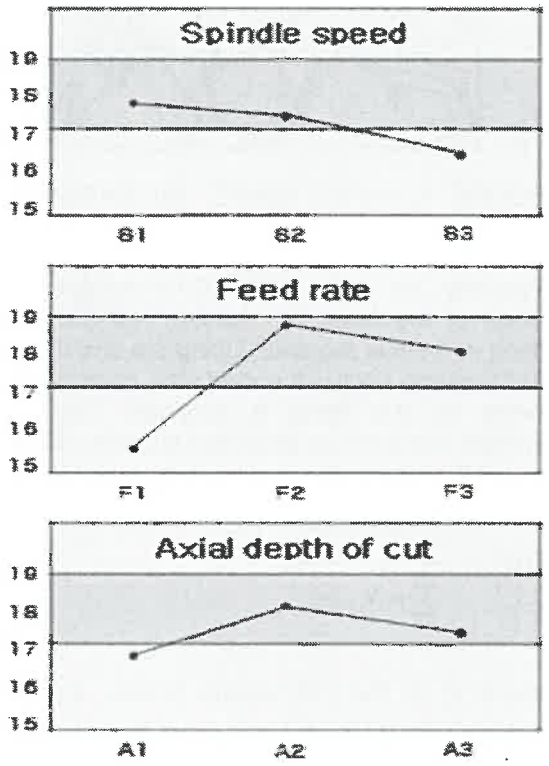

FIGURE 4. MEAN S/N RATIOS VS. LEVELS.

To verify performance of the developed 2.5D glass embossing system, reconstruction of CAD models, tool-path generation and micro end-miiing of glass have been conducted as follows. Applying the devised ABT algorithm and the NURBS interpolation method to the image of Fig.

1, a CAD model has been obtained. To visualize and manipulate the CAD model on commercial CAD/CAM systems, it is converted to IGES files [3,4]. After constructing the 2.5D solid CAD model with 0.2mm embossment on CATIA, micro ball end-milling simulation on PowerMill is performed as shown in Fig. 2. Through G-codes obtained from PowerMill and optimal micro end-milling conditions obtained from Taguchi experiment, glass machining is conducted as shown in Fig. 5. 2.5D micro-engraving result shown in Fig. 6 is obtained from the machine vision measurement [6]. There is no crack. This confirms 2.5D micro-engraving through the developed ABT algorithm and Taguchi method on the glass is conducted well.

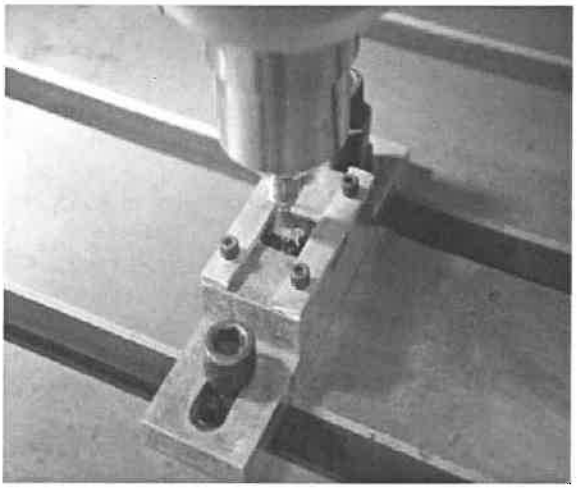

FIGURE 5. MICRO BALL END-MILLING OF GLASS.

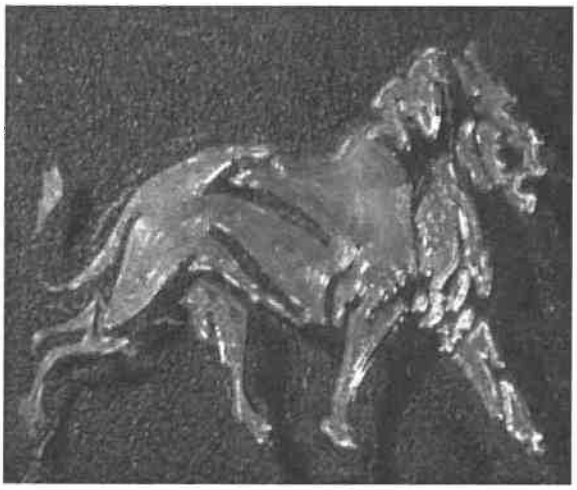

FIGURE 6. 2.5D ENGRAVING RESULT ON GLASS.

CONCLUSIONS

A precise 2.5D micro-engraving of glass by automatic boundary tracking (ABT) for product design has been devised. Following conclusions have been obtained:

1. Developed ABT technique including median filtering, multiple threshold and binary conversion of images extract boundary curves from any pictures well.
2. Solid models of the obtained boundary curves are obtained well through the NURBS interpolation with the chord length and average knot value methods.
3. IGES interface enables generation of G-codes on the commercial CAD/CAM system. Two flutes Φ0.3mm ball end-mill with 150,000rpm spindle speed, feed rate 3mm/min and axial depth of cut 0.06 mm has been selected for crack free micro-end milling of soda-lime glass.
4. Quality and performance of the developed system is confirmed through experiments.

REFERENCES

[1] Chung, S-C. Precision Embossing of Molds and Dies by Automatic Boundary Tracking of Complex Images. *Proceedings of the American Society for Precision Engineering.* 2009; 47: 427-430.

[2] Lee, W. S. and Chung, S. C. Development of the 3D Engraving System from 2D Images. *Transaction of NAMRI/SME. 2008;* 37: 89-96.

[3] Lee, S-B., Kim K-D. and Chung, S-C. Machined Surface Inspection Based on Surface Fairing on the Machined Tool. *Trans. of the KSME(A).* 2000; 24: 937-945.

[4] Lee, S-B. and Chung, S-C. On-the-Machine Measuring and Inspection System for Freeform Surfaces based on IGES Format. *Trans. of the KSME(A).* 1999; 23: 590-607.

[5] Lee, K. J., and Chung, S. C. Modeling of Cutting Parameters and Optimal Process Design in Micro End-milling Processes. *Journal of the KSMTE. 2009;* 18: 261-269.

[6] Kim H H, Chung S, Kim S C, Jee W H, Chung S C. Condition Monitoring of Micro-Drilling Processes on Glass by using Machine Vision. Proceedings of the ASPE. 2006; 21: 535-538.

PROCESS OPTIMIZATION IN SEMI-LIQUID INJECTION MOLDING OF AZ91D MAGNESIUM ALLOY

Sung-Chong Chung
Hybrid System Design & Control Laboratory
School of Mechanical Engineering, Hanyang University
Seoul 133-791,KOREA

ABSTRACT
Semi-liquid injection (SLI) is called thixomolding process using thixotropic property. To design optimal thixomolding processes to fabricate magnesium (Mg) alloy parts, molding conditions such as slurry temperature, mold temperature and injection time should be determined properly. Selection of these factors has been dependent upon engineers' experience and intuitiveness. In this paper, to improve mechanical properties of the thixomolded product, optimal selection of process variables such as injection velocity, barrel temperature and die temperature in the process has been studied through the microstructural analysis and the Taguchi method. Performance of the process has been verified through experiments.

KEYWORDS: Mg, Micro structure, Semi-liquid Injection, SF_6, Thixotropy

INTRODUCTION
Mg parts have been produced through the die casting process. However, Mg alloys in liquid state oxidize rapidly and has explosive reaction when exposed to air at high temperature. This rapid oxidative burning has been controlled by inert gas argon, SO_2, CO_2 and/or SF_6. For several decades the Mg industry has used cost-effective sulfur hexafluoride (SF_6) to shield the Mg alloy from the air during casting processes. Unfortunately, SF_6 is a critical greenhouse effect gas with a 100-year global warming potential estimated at 23,900 times that of CO_2 [1].

Contrary to the die casting, the thixomolding process secures semi-liquid Mg alloy, slurry, against the air within the barrel of the thixomolding machine shown in Fig. 1. This prevents the slurry from any contact with air, and then pollution free casting is achieved without using SF_6 gas [2-3]. In addition, microstructure of the thixomolded part consists of spheroidal particles, which is compared with dendrites of conventional casting products. As the injected material into the die has laminar flow and the injection pressure is much greater than the die casting, SLI molding gives high-integrity and low-porosity products. Better mechanical property (strength, ductility, *etc.*) is achievable comparing with the die casting process [2-5]. However, there is difficulty for maintaining coexistence of liquid and solid in the thixomolding process. An inadequate set of process parameters causes high porosity and unequal cooling in the SLI process. It causes warpage of products and nonhomogeneity as well [2,4]. Therefore optimal molding parameters of the SLI process should be studied thoroughly to meet the required characteristics of products.

In this paper, to produce precision SLI parts with better mechanical properties, optimal selection of process variables such as injection velocity, barrel temperature and die temperature in the process has been studied through the microstructural analysis of thixomolded products. Performance of the process has been verified and confirmed through experiments on JSW thixomolding machine, JLM220-MG shown in Fig. 1.

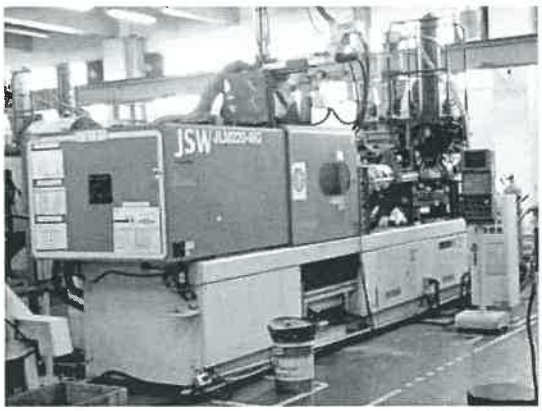

FIGURE 1. THIXOMOLDING MACHINE (JSW INC., JLM220-MG)

THIXOMOLDING PROCESS
Thixomolding of Mg alloy is a hybrid process of the injection molding and die casting processes. It uses thixotropic phenomenon, which refers to the reversible changes from solid to flowable

solid-liquid gel. The injection units are similar to those of plastic injection molding machines. The hydraulic drive unit for the shot composed of the screw and barrel is more like that of the die casting machine. The screw entrains Mg chips and conveys them by rotation to the screw tip. During this process the metal passes through the external heating zone of the barrel. On the way to the screw tip, the Mg alloy is continually mixed and undergoes uniform heating to achieve the required solid to liquid ratio in the two-phase region. The barrel temperature is selected according to the liquidus and solidus values of the phase diagram in the slurry. In addition, the material viscosity decreases and it has the consistency of butter before injection. It retains flow characteristics of liquid metal but flows more smoothly, in a laminar mode, to fill the die cavity. At the temperature range between solidus and liquidus, this shearing due to the vigorous stirring causes reshaping of the initial dendritic structure into spherical solid particles as well. When the temperature is reached at the prescribed point, the injection is progressed as the SLI process. This thixomolding process generates the uniform material structure and the stabilized casting product without internal defect and porosity. In this paper, AZ91D Mg alloy with chemical composition of Table 1 is selected to fabricate a cell-phone battery cover.

PROCESS OPTIMIZATION

The objective of the parameter design is to determine optimal process parameters and to reduce variation of product quality. Taguchi methods use signal-to-noise (*S/N*) ratio to quantify experimental variation [4]. In this paper, 'larger-the-better' (LB) *S/N* ratio given by Eq. (1) is applied for improvement of mechanical property such as tensile strength, ductility and hardness.

$$S/N = -10\log\left[\frac{1}{n_s}\sum_{i=1}^{n_s}\frac{1}{y_i^2}\right] \qquad (1)$$

Aanalysis of variance (ANOVA) is a statistical method to analyze influence of factors in the process design. Fundamental technique is a partitioning of the total sum of squares into components related to the effects used in experiments. Variances of each factor are applied to analyze contribution of factors in the process. In Taguchi method, a factor is considered to be significant if its influence is large compared with experimental errors through the ANOVA statistical equations given in [4].

EXPERIMENTS

Fig. 2 shows the core and cavity to produce the battery cover. Table 2 shows experimental conditions with three factors and three levels determined through prior experiments [4].

Microstructure

To observe microstructure of the product, resin mounted specimens were prepared through grinding with #500, #1200 and #2400 sandpapers, and polished with 1~3μm diamond powder. Then they are chemically etched in a 3% solution of nitric acid in ethanol. Using Nikon's EPIPHOT 300U inverted metallurgical microscope and image analysis software, quantitative graphic analysis of microstructure image including edge detection, volume fraction, size and morphology of solid phase has been performed. Fig. 3 shows 200 times magnified morphology of primary solid particles from different $L_9(3^4)$ SLI conditions. They depend upon formation of solid particles α-Mg dispersed in a liquid matrix. The amount of primary solid, α-Mg, depends upon the barrel temperature. It reveals that volume fractions of the primary solid (average diameter between 25 and 55μm) distributes from 4% to 52%.

TABLE 1. CHEMICAL COMPOSITION OF AZ91D.

Elements	Al	Zn	Mn	Fe and Ni	Mg
Composition (%)	8.5	0.75	0.3	below 0.001	Balance

TABLE 2. EXPERIMENTAL CONDITIONS.

Level	A (m/s)	B (℃)	C (℃)
1	48	600	200
2	55	590	220
3	62	580	240

A: Injection velocity, B: Barrel temperature, C: Mold temperature

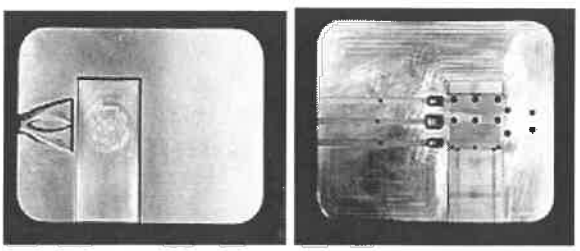

FIGURE 2. CORE AND CAVITY FOR THIXOMOLDING.

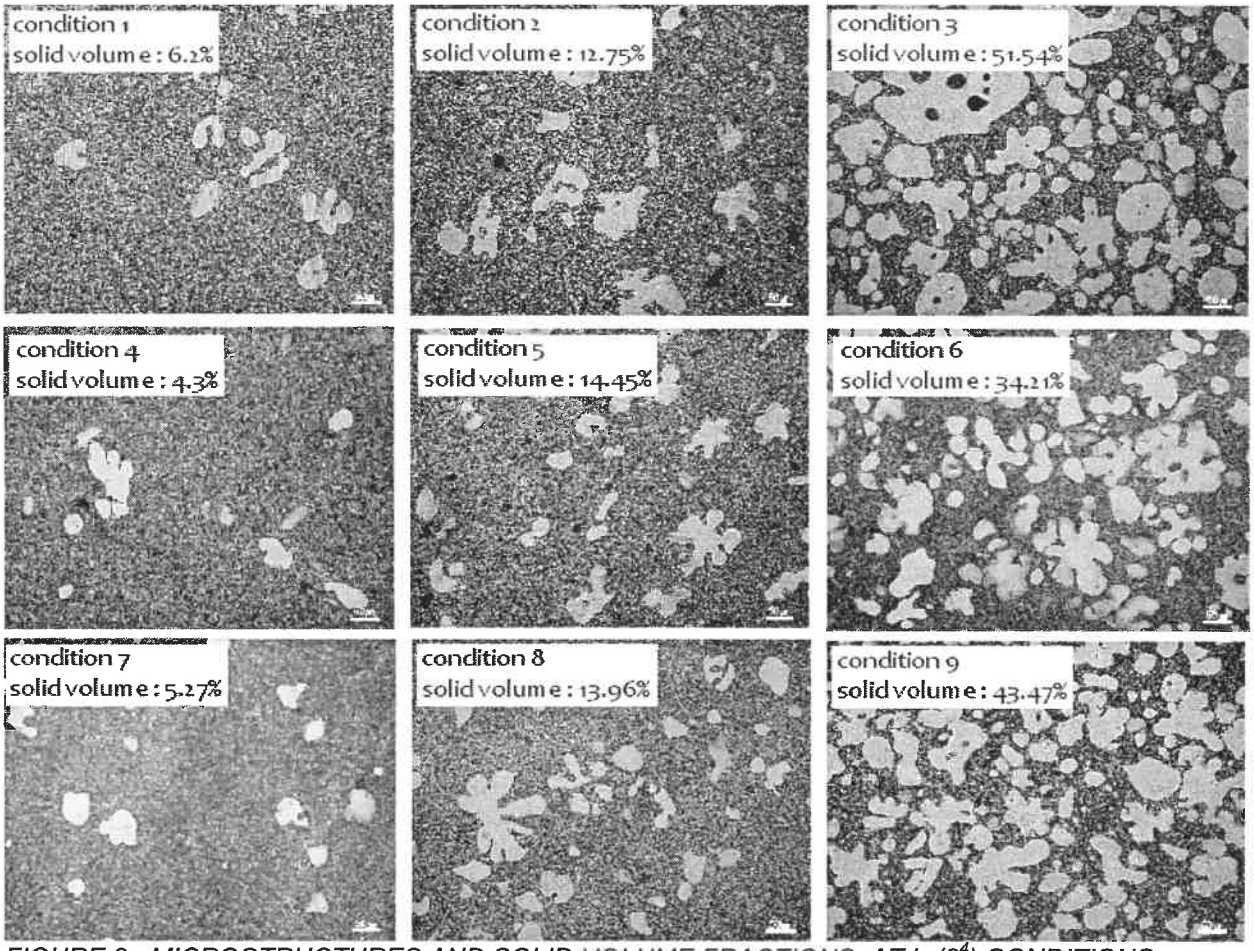

FIGURE 3. MICROSTRUCTURES AND SOLID VOLUME FRACTIONS AT $L_9(3^4)$ CONDITIONS.

Mechanical Properties

Table 3 shows mechanical properties and *S/N* ratios obtained from experiments. TS, YS, and EL have been measured through flat tension specimens and universal testing machine. Better TS is obtained when the *S/N* ratio has maximum value such as 62m/s injection speed, 600℃ barrel temperature, and 200℃ mold temperature. Fig. 4 shows TS according to the volume fraction of α-Mg. It is between 280 and 230 Mpa. Reduction of TS with improvement of primary solid is similar to other results [2,3,5]. Fig. 5 shows EL according to the volume fraction of α-Mg. Reduction of EL with improvement of primary solid is similar to others [2,3,5]. As the injection pressure of the current SLI thixomolding is around 30 Mpa and the product has no porosity, this research generates slightly better results comparing with others. Hardness is measured by the Vickers hardness tester (Akashi Inc., HM122). Similar optimal process conditions are obtained as in other mechanical properties.

ANOVA analysis has been performed using the corresponding *S/N* ratios of TS, EL and hardness. Tables 4~6 show ANOVA results. Barrel temperature, factor B, has contribution of over 96% about TS. YS, EL and hardness show similar tendency as well. Taguchi experiments confirm that barrel temperature should be carefully selected to obtain better mechanical properties in the SLI thixomolding process.

TABLE 3. MECHANICAL PROPERTIES AND S/N RATIOS OF AZ91D ACCORDING TO THIXOMOLDING CONDITIONS.

No	TS (MPa)	YS (MPa)	Elongation (%)	Hardness (Hv)	S/N_{TS}	S/N_{EL}	S/N_{Hv}
1	274.32	177	5.55	100.2	24.383	7.444	40.016
2	262.03	170	4.67	96.9	24.183	6.693	39.730
3	232.73	153	3.89	95.4	23.668	5.903	39.590
4	267.56	174	5.42	100.1	24.274	7.337	40.011
5	246.68	165	4.73	98.0	23.921	6.747	39.825
6	240.40	163	4.10	96.6	23.809	6.128	39.702
7	281.58	181	6.17	101.3	24.496	7.899	40.108
8	254.04	168	5.05	97.5	24.049	7.034	39.782
9	235.36	157	4.06	96.1	23.717	6.082	39.660

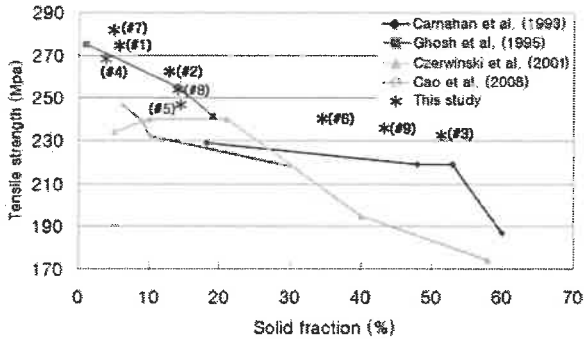

FIGURE 4. TENSILE STRENGTH VS. RIMARY SOLID VOLUME FRACTION.

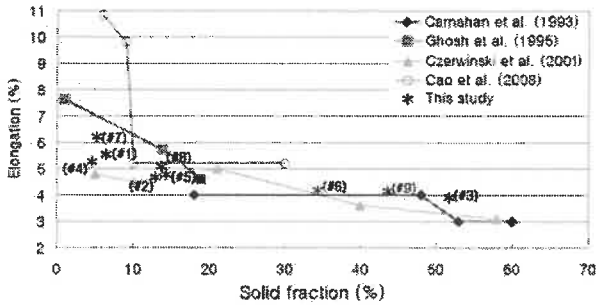

FIGURE 5. ELONGATION VS. PRIMARY SOLID VOLUME FRACTION.

TABLE 4. POOLED ANOVA RESULTS OF TS.

Factor	SS	DOF	V	F_0	P(%)
B	0.639	2	0.319	27.691	96.51
A+C +Error	0.069	6	0.012		3.49
Total	0.708	8	0.331		100

TABLE 5. POOLED ANOVA RESULTS OF EL.

Factor	SS	DOF	V	F_0	P(%)
A	0.181	2	0.090	3.880	4.87
B	3.479	2	1.740	74.789	93.87
C+Error	0.093	4	0.023		1.26
Total	3.753	8	1.853		100

TABLE 6. ANOVA RESULTS OF HARDNESS.

Factor	SS	DOF	V	F_0	P(%)
A	0.010	2	0.005	3.440	3.71
B	0.243	2	0.121	86.639	93.49
C	0.004	2	0.002	1.590	1.72
Error	0.003	2	0.001		1.08
Total	0.260	8	0.130		100

CONCLUSIONS

A thin-walled cell-phone battery cover made of AZ91D has been fabricated to understand the thixomolding process along with microstructures. Taguchi method has been applied to determine optimal process conditions for obtaining better mechanical properties. ANOVA has been also applied to quantize the contribution of process variables. Following conclusions have been obtained:

1. Mechanical properties such as TS and EL are dependent upon volume fraction of primary solid α-Mg. TS and EL remain over 250 Mpa and 4.5% respectively, under 20% of the primary solid. Further increase of the primary solid by controlling the barrel temperature has caused a gradual reduction of both to the level of 215 Mpa and 3.7%, respectively for the solid fraction of 50%. These confirms that the volume fraction of the primary solid depends upon barrel temperature significantly.

2. ANOVA results show that strength is significantly governed by barrel temperature (96.51%). It should be selected carefully in the thixomolding process.

3. 62m/s injection speed, 600℃ barrel temperature, and 200℃ mold temperature are optimal values to obtain tensile strength over 250 Mpa.

REFERENCES

[1] Bartos S., C. Laush, J. Scharfenberg, and R. Kantamaneni. Reducing Greenhouse Gas Emissions from Magnesium Die Casting. Journal of Cleaner Production. 2007; 15: 979-987.

[2] Friedrich, H.E. and B.L. Mordike. Magnesium Technology: Metallurgy, Design Data, Applications. Springer-Verlag, Berlin: 2006.

[3] Kainer K.U. Magnesium Alloys and Technology. WILEYVCH GmbH & Co. Berlin: 2003.

[4] Chung S.C. Robust Gate System Design for Precision Semi-Solid Casting Processes. Proceedings of the ASPE 2009 Annual Meeting. 2009; 47: 423-426.

[5] Czerwinski, F. *et al.* Correlating the Microstructure and Tensile Properties of a Thixomolded AZ91D Magnesium Alloy. Acta MATERIALIA. 2001; 49: 1225-1235.

[6] Yoon K.W. and Chung S.C. Selection of Optimal Machining Parameters in Diamond Core Drilling Processes. Proceedings of the ASPE 2007 Annual Meeting. 2007;42: 398-401.

ANALYSIS OF BALLSCREW STIFFNESS OWING TO CONTACT DEFORMATION IN LEADSCREW SYSTEMS

Sung-Chong Chung[1] and Chun-Hong Park[2]

[1]School of Mechanical Engineering, Hanyang University, Seoul 133-791, KOREA
[2]Intelligent Manufacturing System Division, KIMM, Daejeon 305-343, KOREA

ABSTRACT

Positioning error of ballscrew driven feeddrives depends upon stiffness of leadscrew systems. Total axial stiffness of the leadscrew system consists of stiffnesses of the nut, the screw shaft, the support bearings, and the nut bracket. The nut stiffness depends upon screw characteristics, preload and operating conditions. This should be thoroughly studied according to the contact deformation between balls and grooves. In this paper, ballscrew nut stiffness due to contact deformation between balls and grooves according to the preload and operating conditions is studied. Positioning accuracy estimation method is also proposed.

KEYWORDS: Ballscrew, Contact deformation, Hertzian constant, Positioning error, Stiffness

INTRODUCTION

Ballscrews utilize rolling contact with low friction. They are widely used as precision feeddrive units of machine tools, flat-panel fabrication devices and semiconductor manufacturing equipment. Positioning error of the ballscrew driven unit depends upon geometric error and stiffness of the leadscrew system. Stiffness estimation of the ball screw is critical for accurate positioning and design of precision machinery.

The nut stiffness depends upon screw characteristics, preload and operating conditions. Recalling that the contact deformation of the nut assembly governed by Hertzian contact is affected by the groove shape, preload and thrust force, the nut stiffness of ballscrews should be thoroughly studied according to the contact deformation between the ball and groove. For stiffness calculation, a rigid model assuming the nut and screw shaft are rigid except for contact points with balls had been used. However, it has been pointed out that the measured stiffnesses are considerably lower than the calculated values obtained from the rigid models [1,2]. They claimed that the calculated stiffness incorporating the flexibility of the screw shaft and nut matched the measured stiffness. However, they did not present explicit theoretical expressions for the stiffnesses of ballscrews. In this paper, calculation of nut stiffness due to the contact deformation between balls and raceway grooves incorporating flexibility of the ballscrew shaft and nut is studied. The estimation of the stiffness and positioning error due to the contact deformation is conducted as well.

HERTZIAN CONSTANT

Fig. 1(a) shows a cross section of a ballscrew composed of balls, shaft, nut and circular arcs in TC (Tension in the shaft and Compression in the nut: forward motion case) loading condition. Contact state of a ball and grooves is shown in Fig. 1(b). D means the ball diameter, α is the contact angle of the ball and grooves, γ represents the lead angle of the screw shaft, P and P_i stands for contact loads, F_a is the thrust force applied, and f_s and f_n denote conformity factors of the screw and nut grooves, respectively.

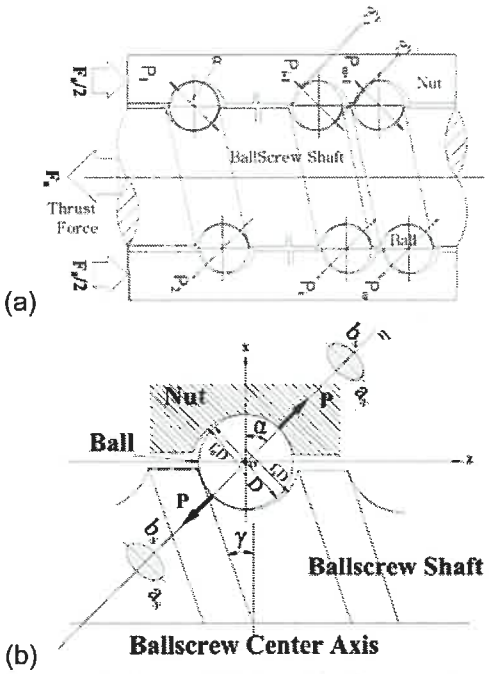

FIGURE 1. BALLSCREW GEOMETRY AND CONTACT MECHANISM.

Considering geometry at contact points shown in Fig. 1(b), curvatures on the elliptic contact surfaces in normal axes x and y are obtained [4]. Solving the first and second kinds of elliptic integrals through the Landen transformation and approximation when the contact load P is applied as shown in Fig. 1(b), contact deformations δ^H_{bn} between the ball and nut groove, and δ^H_{bs} between the ball and shaft groove are given by

$$\delta^H_{bn,bs} = \delta^{H^*}_{bn,bs} \frac{\sum \rho_{bn,bs}}{2} \cdot \left[\frac{3P}{2\sum \rho_{bn,bs}} \left(\frac{(1-\zeta_b^2)}{E_b} + \frac{(1-\zeta_{n,s}^2)}{E_{n,s}} \right) \right]^{\frac{2}{3}} \quad (1)$$

where $\delta^H_{bn,bs}$ means δ^H_{bn} and δ^H_{bs} . δ^H_{bn} is computed from $\delta^{H^*}_{bn}$, $\Sigma\rho_{bn}$, Young's modulus of nut E_n and Poisson ratio of nut ζ_n. According to Hertz contact theory [4], contact deformations due to load P between the ball and raceway groove are given by

$$\delta^H_{bn,bs} = C_{bn,bs} P^{\frac{2}{3}} \quad (2)$$

Comparing Eqs. (1) and (2), Hertzian constants are given by

$$C_{bn,bs} = \frac{\delta^*_{bn,bs} \sum \rho_{bn,bs}}{2} \cdot \left[\frac{3}{2\sum \rho_{bn,bs}} \left(\frac{(1-\zeta_b^2)}{E_b} + \frac{(1-\zeta_{n,s}^2)}{E_{n,s}} \right) \right]^{\frac{2}{3}} \quad (3)$$

These constants are determined according to curvatures of the contact points, conformity factors of the groove arch, ballscrew geometry, material property, *etc.*

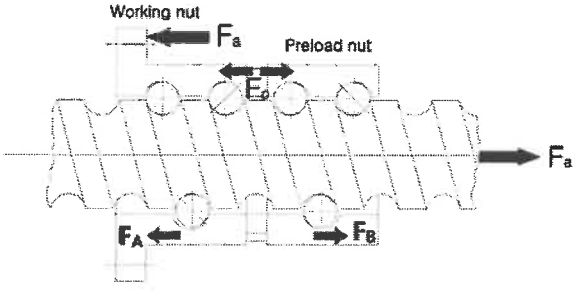

FIGURE 2. PRELOADED DOUBLE-NUT BALL SCREW.

Figure 2 shows a preloaded double-nut ballscrew subjected to axial load F_a and tension preload F_p. Assuming the preload F_p is applied by a spacer and the ball load P_i is equally distributed in the ballscrew, ball load P is given by

$$P = \frac{F_p}{Z \sin\alpha \cos\gamma} \quad (4)$$

where Z is total number of loaded balls, and α and γ are the contact and helix angles of the ballscrew, respectively. Total axial contact deformation due to the preload is

$$\delta^H_p = \frac{(C_{bn} + C_{bs})}{\sin\alpha \cos\gamma} P^{\frac{2}{3}} = C_B F_p^{\frac{2}{3}} \quad (5)$$

where Hertzian constant of the ballscrew C_B is given by

$$C_B = (C_{bn} + C_{bs}) Z^{-\frac{2}{3}} [\sin\alpha \cos\gamma]^{-\frac{5}{3}} \quad (6)$$

Figure 3 and 4 show Hertzian constant according to the conformity factor and contact angle of the ballscrew assembly given in Table 1. As the conformity factor expresses the ratio of the curvature radius of the screw groove and the radius of the ball, groove type varies the conformity factor and contact angle. These values affect the variation of Hertzian constant significantly. For the constant conformity, Fig. 4 shows the axial stiffness degraded seriously when the contact angle is less than 30°. It is confirmed that ballscrew stiffness is severely influenced by the groove shape of the ballscrew.

TABLE 1. BALLSCREW SPECIFICATIONS.

d_m [mm]	25.8	$\zeta_{n,s}$	0.3
D [mm]	3.175	$f_{n,s}$	0.567
Lead [mm]	6	Z	62
γ	4.234°	$E_{n,s}$[Kgf/mm^2]	21x10^3
α	45°	E_b [Kgf/mm^2]	20x10^3

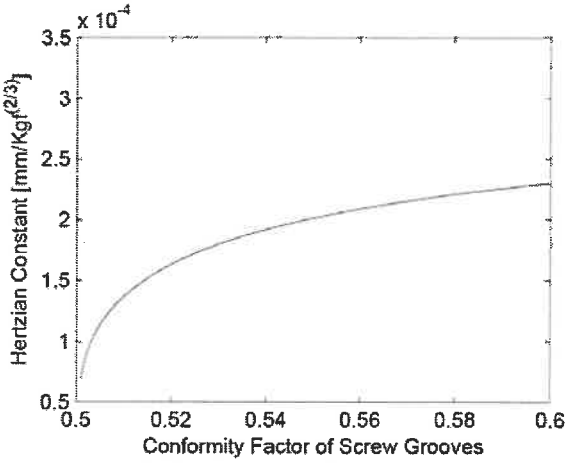

FIGURE 3. HERTZIAN CONSTANT VS. CONFORMITY FACTOR.

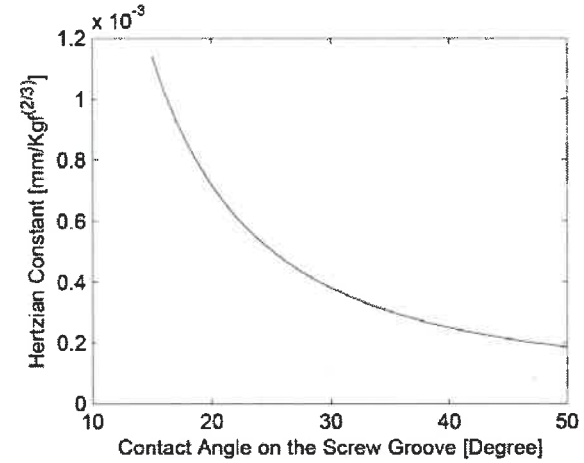

FIGURE 4. HERTZIAN CONSTANT VS. CONTACT ANGLE.

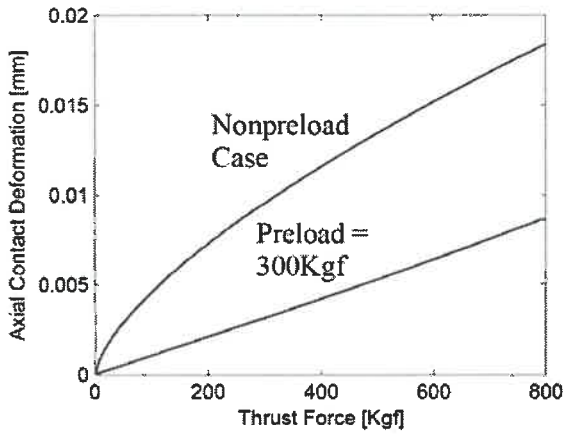

FIGURE 5. AXIAL HERTZIAN CONTACT DEFORMATION.

AXIAL DEFORMATION

Ballscrews are usually used as a preloaded double nut to eliminate backlash and to improve the axial stiffness. Eq. (5) gives axial deformations of preloaded nuts shown in Fig. 2 in opposite direction (TT mode: Tension in shaft and Tension in nut; backward motion case). Since the preloaded deformations are canceled each other, positioning error due to the contact and elastic deformation does not generate when the thrust force is not applied to the screw assembly. As the thrust force F_a is applied to the preloaded ballscrew as shown in Fig. 2, ball load increases in the working nut and decreases in the preloaded nut. Since the increment of the axial deformation in the working nut equals to the decrement of it in the preloaded nut, following nonlinear equations are obtained for $0 \le F_a \le 2.82F_p$:

$$P_A^{\frac{2}{3}} + P_B^{\frac{2}{3}} = 2\left[\frac{F_p}{Z\sin\alpha\,\cos\gamma_s}\right]^{\frac{2}{3}} \tag{7}$$

$$(P_A - P_B)Z\sin\alpha\,\cos\gamma_s = F_a \tag{8}$$

where P_A and P_B are uniformly distributed ball load due to nut load F_A and F_B developed by the thrust force F_a and preload F_p. After solving P_A from Eqs. (7) and (8), net axial deformation due to the contact load is obtained as

$$\delta^H{}_a = \delta^H{}_A - \delta^H{}_p = \frac{C}{\sin\alpha\cos\gamma_s}\left[P_A\right]^{\frac{2}{3}} - C[\sin\alpha\cos\gamma_s]^{-\frac{5}{3}}\left[\frac{F_p}{Z}\right]^{\frac{2}{3}} \tag{9}$$

where $C = (C_{bn} + C_{bs})$. Fig. 5 shows elongation errors due to the axial contact deformation according to the thrust force F_a when F_p = 0 (nonpreload) case and F_p = 300 Kgf, respectively. It is confirmed that the stiffness is improved significantly by incorporating the preload to the ballscrew.

In addition to the Hertzian contact deformation, the axial deformation error of the ballscrew is generated from elastic deformation of the screw shaft and the nut body as well. On the i th and $(i-1)$th ball locations, ball loads P_i , P_{i-1}, and shaft deformation $\tilde{\delta}^s_i$, $\tilde{\delta}^s_{i-1}$ and nut deformation $\tilde{\delta}^n_i$, $\tilde{\delta}^n_{i-1}$ are defined in the ball contact direction. Using the compatibility and force equilibrium conditions, following body deformations between the two balls have been obtained:

$$\delta^s_{i-1,i} = (\tilde{\delta}^s_{i-1}\sin\alpha_{i-1} - \tilde{\delta}^s_i\sin\alpha_i)\cdot\cos\gamma = \frac{L/2}{E_s\cdot A_s}\left[(P_{i\text{-}1}\sin\alpha_{i-1} - P_i\sin\alpha_i)\cdot\cos\gamma\right] \tag{10}$$

$$\delta^n_{i-1,i} = (\tilde{\delta}^n_{i-1}\sin\alpha_{i-1} - \tilde{\delta}^n_i\sin\alpha_i)\cdot\cos\gamma = \frac{L/2}{E_n\cdot A_n}\left[(P_{i\text{-}1}\sin\alpha_{i-1} - P_i\sin\alpha_i)\cdot\cos\gamma\right] \tag{11}$$

$$\delta^B_{i-1} = \delta^s_{i-1,i} \pm \delta^n_{i-1,i} \quad \text{for} \quad [\text{TC}(+);\text{TT}(-)] \tag{12}$$

where A_n, A_s are effective cross sectional areas of the screw shaft and nut, respectively. L is the distance between uniformly selected two balls. For the loading condition TT shown in Fig. 2, total body deformation is

$$\delta^B_{total} = \sum_{i=2}^{p}\delta^s_{i-1,i} - \sum_{i=2}^{p}\delta^n_{i-1,i} \tag{13}$$

From Eqs. (9) and (13), total axial deformation of the ballscrew is given by

$$\delta_{total} = \delta^H_a + \delta^B_{total} \tag{14}$$

For a longer nut length (Z=84 comparing with 62) ballscrew similar to Table 1, Fig. 6 shows axial

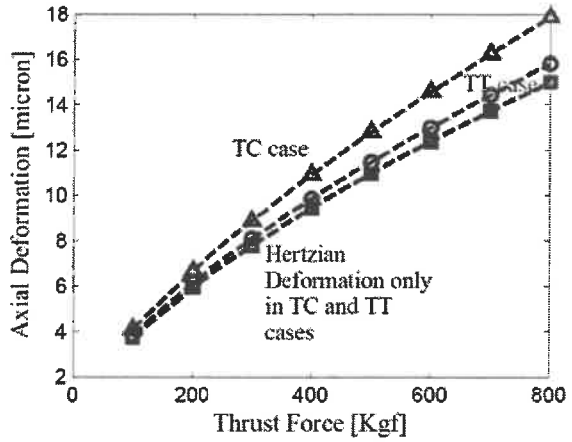

FIGURE 6. AXIAL DEFORMATION VS. THRUST FORCE.

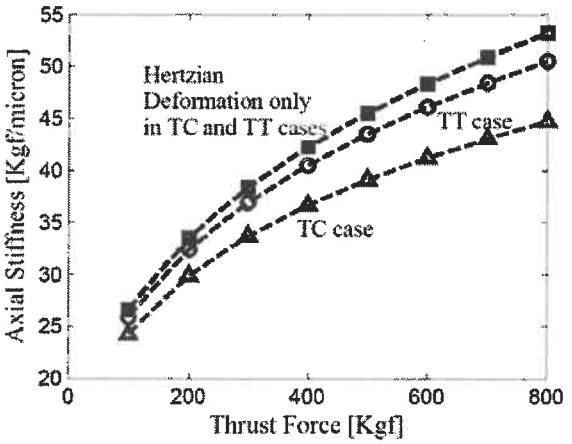

FIGURE 7. AXIAL STIFFNESS VS. THRUST FORCE.

deformations according to the thrust force. Axial deformation due to Hertzian contact deformation in TC and TT loading conditions are much the same. Adding the body deformation to the axial deformation, total axial deformations of TC case is larger than those of TT case. It is confirmed that both cases have larger deformation errors than those of Hertzian deformation case. Fig. 7 shows axial stiffnesses according to thrust forces. TT case has larger stiffness than TC case. Both stiffnesses are less than those of the Hertzian deformation case. As the ball screw moves in forward (TT case) and backward (TC case) directions during operation, stiffness variation generates positioning errors of the precision machinery. To improve stiffness and reduce stiffness variation during motion, preload should be applied to the ballscrew, as well as groove shape for manipulation of conformity factor and contact angle, ball size, and nut length and dimensions should be designed and selected properly.

POSITIONING ERROR ESTIMATION

To fabricate precision machinery, estimation of positioning errors of ballscrew driven feeddrives are available and amendable in the design process accurately. As the positioning accuracy depends upon geometric errors and stiffness of the leadscrew system, the estimated axial positioning error is modeled as

$$\delta_a^{est} = \delta_{total} + \delta_{grade} \tag{15}$$

where δ_{grade} is the accumulated reference lead deviation of the ballscrew, and δ_{total} is given by Eq. (14) according to the preload F_p, axial load F_a , and the ballscrew assembly conditions described in previous sections. δ_{grade} is selected from the performance certificate given by the ballscrew manufacturer. Using Eq. (15), designers are able to predict the positioning accuracy of their precision machinery in the design process. They can select effective ballscrews from the market confidently.

CONCLUSIONS

Mathematical modeling of ballscrew stiffness has been conducted through the contact and body deformation analysis in various loading and assembly conditions. It is confirmed that the stiffness depends upon ballscrew groove geometry, as well as ball, nut and shaft dimensions, and loading conditions. During operation of the precision machinery, the stiffness varies according to the geometric error and the moving direction. This degrades the positioning accuracy. To predict the positioning accuracy and feedback it to the design process of the feeddrive unit, the mathematical estimation method of positioning errors has been conducted.

REFERENCES

[1] H. Shimoda. Stiffness analysis of ball screws, Int. J. Japan Soc. Prec. Eng. 1999; 33: 168-172.

[2] K. Takafuji and K. Nakashima. Stiffness of a ball screw with consideration of deformation of the screw, nut and screw thread (preloaded double nut). JSME International Journal, Series III. 1990; 33: 620-626.

[3] X. Mei, et al. Study on the load distribution of ball srews with error. Mechanism and Machine Theory. 2003; 38: 1257-1269.

[4] T. A. Harris. Rolling Bearing Analysis, 3rd. ed. John Wiley & Sons Inc.: 1991.

SENSOR DESIGN FOR ON-MACHINE PROBING OF EXTRUDED TOOL JOINTS

Arthur A. Graziano[1], Andrew Joslin[2], and Tony L. Schmitz[1]
[1]Department of Mechanical and Aerospace Engineering
University of Florida
Gainesville, FL, USA
[2]Department of Mechanical, Materials, and Aerospace Engineering
University of Central Florida
Orlando, FL, USA

INTRODUCTION

This paper describes the design and evaluation of two contact probes used to measure the length and bore concentricity of cylindrical, extruded tool joints while clamped in a production lathe spindle. The axisymmetric tool joints, which provide connections between individual drill pipes in the oil industry, are produced using two primary manufacturing processes: the joints are initially extruded and then finish machined. One typical obstacle to optimizing the turning performance is deviations from the nominal dimensions for the extrusions, including length variations and non-concentricity of the inner and outer diameters. This causes more or less material to be removed than commanded during the ensuing turning, boring, and facing operations. If the part is larger than nominal, a conservative machining approach is required to avoid larger depths of cut than commanded and the subsequent potential for tool/part damage and/or accelerated tool wear. A natural alternative to conservative part paths is pre-machining measurement while the parts are chucked or clamped in the machine. Yandayan and Burdekin [1] provide a review of the different methods used to accomplish this task (up to 1996) and Vacharanukul and Mekid [2] continue the survey through 2003. In this study, two LVDT-based contact probes were developed to measure the length and bore concentricity of tool joints while clamped in a lathe spindle in order to provide pre-machining extrusion dimensions. These results can be used to modify the part program in real time.

PROCESS BACKGROUND

Variations in the indirect extrusion process lead to geometric imperfections that affect the turning process; see Fig. 1. First, as the material flows up and around the pin during extrusion, a bulge can be created at the end; the bulge peak is not necessarily located at the midpoint between the inner and outer diameters. Second, length variations occur due to fluctuations in the part temperature (a high-temperature shearing operation precedes the extrusion process). Third, after many extrusion cycles, the pin may both: 1) begin the extrusion off-center with respect to the container centerline; and 2) lose its parallelism to the container axis during extrusion. The combination of these issues generates parts with length variation, non-flat ends, and non-concentric bores (with non-constant concentricity along the bore length). The extruded parts are machined on Okuma LC-40 lathes, which include two independent turrets. The upper turret (A) is used to perform boring and drilling operations on the extrusions, while the lower turret (B) is used for facing and turning cuts. The turrets enable relative motion between the part and tool in both the *z* (parallel to the spindle centerline) and *x* (diametral) directions.

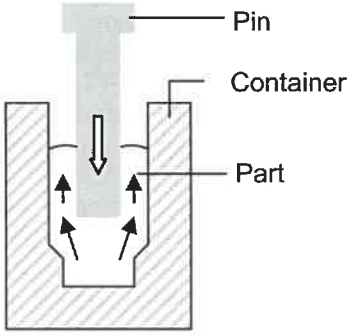

FIGURE 1. Indirect extrusion process.

SENSOR DESIGN

An LVDT-based design was chosen for the contact probes. Three measurements were required to define the part geometry: length, inside diameter, and bore concentricity (the outer diameter was considered to be sufficiently accurate based on prior experience). The length measurement could be completed by contacting

the extrusion face in the *z* direction. However, the latter two measurements required contact with the (inner) bore diameter. Because it was inconvenient to align the LVDT axis in the *x* direction within the bore (based on LVDT sizes and the bore diameter), a design was required that would transfer motion along the surface normal of the inside diameter to the *z* direction, where it was convenient to orient the LVDT axis. A parallelogram leaf-type flexure and 45 deg surface were chosen to accomplish this task. Figure 2 demonstrates the design concept where *x* displacement of the platform caused by variation in the surface location is transferred to the *z* direction via the 45 deg surface.

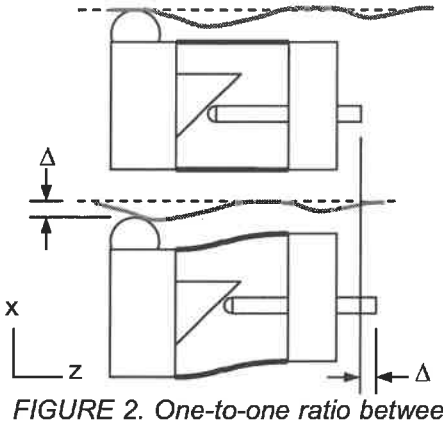

FIGURE 2. One-to-one ratio between x direction surface location and z direction shaft motion.

The depths of cut for roughing passes are up to 5.1 mm. A 1% error in the commanded depth of cut is therefore 51 μm. Assuming that this 1% error is an acceptable variation in the actual depth of cut, the target uncertainty for the two probes was set to 50 μm.

Length Probe

It was determined that side (lateral) loading of the LVDT resulted in poor transducer performance. Therefore, a shaft supported by linear ball bearings was incorporated to resist the inherent side loading from the rough extrusion surface and transfer only axial motion to the LVDT. Figure 3 shows the design, where the 12.7 mm diameter shaft is constrained using two linear ball bearings (to increase lateral stiffness) and the LVDT is supported by two collars inside a 2024 aluminum tube (310.4 mm length). This ensures that both the shaft and LVDT share (nominally) the same motion axis. A 440C hardened stainless steel 9.5 mm diameter sphere is fixed to the end of the shaft; this sphere serves as the contact surface during measurements. The shaft is spring-preloaded against the part during measurements (see the collar and 720 N/m spring at the left end of the assembly). The LVDT is preloaded against the shaft using its own internal spring. The probe is mounted in turret A using a boring bar holder. This ensures that the probe axis is (nominally) coincident with the *z* axis with a zero offset in the *x* direction.

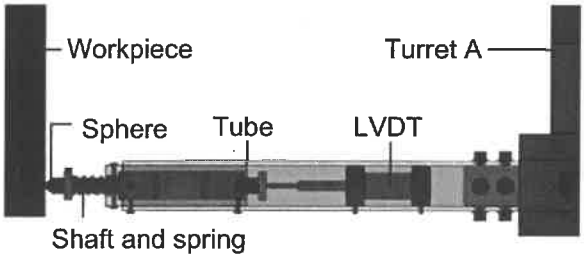

FIGURE 3. Length probe solid model.

Concentricity Probe

Figure 4 shows the concentricity probe design. As noted previously, this design includes a flexure and 45 deg surface to transfer the *x* direction bore surface location to the *z* direction (and the LVDT axis). The flexure platform carries a 12.7 mm diameter 440C hardened stainless steel sphere to provide contact with the bore surface. As the part rotates, the radial variation in the surface location causes the platform to be deflected in the *x* direction. This motion is transferred to the *z* axis through the 45 deg machined surface on the platform (the flexure was designed such that parasitic motion is negligible [3]). A shaft supported by linear bearings is again used to isolate the LVDT from side loads. A second sphere (9.5 mm diameter, grade 24, Rockwell C58-C65) is attached to the shaft which maintains contact with the 45 deg surface; preload is supplied by a spring/collar. To reduce friction and abrasion at the 45 deg surface, a thin glass sheet was epoxied to the 45 deg surface.

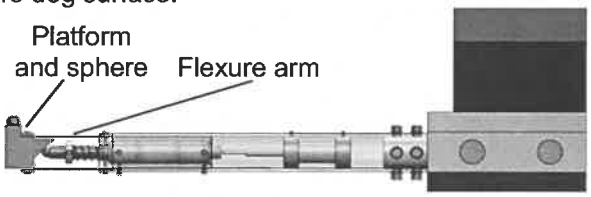

FIGURE 4. Concentricity probe solid model.

MEASUREMENT PROCEDURES

Length Probe

Once the probe was mounted in the boring bar holder on turret A, an initial calibration constant,

K_L, was determined to compensate for any misalignment during assembly. Turret A was then used to position the probe against the part backstop located inside the chuck; the backstop provides a hard stop for inserting extrusions in the spindle collet chuck. The turret's z coordinate was then recorded as z_{ref} and the corresponding LVDT mean voltage was recorded as V_{ref}.

The presence of the part backstop provided a convenient reference surface for transforming the LVDT displacements into part dimensions with values larger than the LVDT range. The approach was to use the machine position (as reported by the controller) for macro-scale motion between the backstop and the unclamped end of the part. By combining the change in the z axis value with the difference in LVDT voltages when touching the backstop and part face, the length could be determined.

Once the reference location was identified, a part was chucked in the lathe and the probe was placed in contact with the part face near the part's outer diameter. This turret z location was recorded as z_{meas}. Ten measurements were completed at equally spaced x locations from the outer to inner diameter. Since the voltage decreased as the LVDT pin was depressed, the machine x value associated with the lowest voltage identified the location where the bulge was largest (for this radial location). The turret x value was recorded as x_{peak} for this position.

The next step was a continuous measurement around the face of the part at the x_{peak} radial location. The part was rotated at 18 rpm while the voltage was recorded at 5 kHz for 15 seconds (to capture multiple revolutions). After applying a Butterworth low pass filter with a 5 Hz cutoff frequency and isolating a single revolution of data, the lowest voltage, V_{meas}, was used to calculate the part's maximum length. See Eq. 1.

$$L = \left(z_{meas} - z_{ref}\right) - \left(\frac{V_{meas} - V_{ref}}{K_L}\right) \qquad (1)$$

Concentricity probe

A similar process was used for the concentricity probe. However, because a diametric reference surface was not available on the lathe, an artifact, with known diameter, D, was used to determine the probe's calibration constant, K_C, and reference values, V_{ref} and x_{ref}. Part measurements were completed by placing the probe in contact with the inner bore diameter at the desired depth. The x_{meas} axis location was recorded and then data was collected during rotation of the part, filtered, and one revolution was isolated. For subsequent measurement at other depths, the spindle was returned to (ideally) the same orientation before beginning data collection.

The LVDT voltage recorded during part rotation provided information about both the hole radius and the offset of its center from the spindle axis, which was assumed to coincide with the part's axis of rotation defined by its outer diameter. Figure 5 shows an exaggerated representation of the measurement as the part rotates counterclockwise. The outer circle represents the part's outer diameter, while the smaller solid circle represents the off-center bore. As the part rotates, the bore center traces the smaller dashed circle. The center offset, o, is the distance from the spindle axis to the bore center. The bore radius, r, is the perpendicular distance from the bore center to the surface of the inner diameter. Note, however, that the probe measures x displacement only, not part radius.

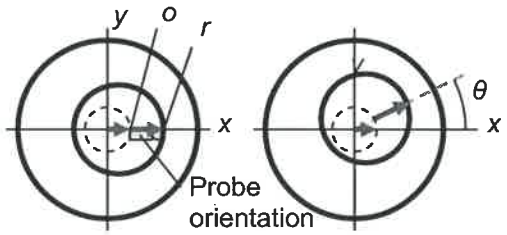

FIGURE 5. Concentricity measurement geometry.

To determine x, the location of the bore surface as a function of the spindle rotation angle, from the sinusoidal measured voltage, Eq. 2 is applied. This equation is similar to Eq. 1, except that the artifact diameter is required because the reference voltage was not taken at a zero part reference location, but rather at a distance $D/2$ from the spindle axis of rotation. Additionally, the sign change was necessary because an increase in diameter caused an increase in voltage, while an increase in part length corresponded to a decrease in voltage. Finally, the difference between x_{meas} and x_{ref} must be divided by two because the controller gives x values in diametral coordinates.

$$x = \frac{x_{meas} - x_{ref}}{2} + \frac{V_{meas} - V_{ref}}{K_C} + \frac{D}{2} \qquad (2)$$

Given the sinusoidal filtered output, x, of the sensor as a function of angle of rotation, θ, both the radius and bore center offset from the spindle axis at the selected z location along the bore can be calculated. The radius is the mean value and the offset is the difference between the maximum and minimum values divided by two. The variation in the bore center location is determined by comparing the results from different z locations. The phase shift for the maximum x was used in conjunction with Eqs. 3 and 4 to determine the coordinates of the bore center location, x_c and y_c, for the selected z depth inside the bore.

$$x_c = o\cos(\Delta\theta) \quad (3)$$

$$y_c = o\sin(\Delta\theta) \quad (4)$$

RESULTS

In order to verify the probe's performance, measurements of the artifact using the length and concentricity probes were compared to dimensions obtained using a coordinate measuring machine (CMM) in Table 1. The probe values show reasonable agreement with CMM results. Although the disagreement is larger than the two-standard deviation uncertainty in the CMM measurements (2·0.012 = 0.024 mm) for the radius measurement, the results are acceptable for this application. Note that the length probe algorithm identifies the maximum length of the part. For any chucking error (i.e., if the part axis is not parallel to spindle axis after clamping), the length probe measurement will therefore give a result which is larger than the actual part length.

TABLE 1. Artifact measurement results.

	CMM result (mm)	Probe result (mm)	Difference (mm)
L	316.662	316.684	-0.022
r	77.222	77.262	-0.040
o	0.014	0.006	0.008

Repeated length measurements were performed on a single part (without removing it from the spindle) in order to establish the length probe measurement repeatability. Five length measurements were completed. The resulting lengths were {521.272, 521.269, 521.266, 521.266, and 521.264} mm. The range is 0.008 mm with a standard deviation of 0.003 mm.

Similarly, repeated measurements were completed using the concentricity probe. A single part was measured five times each at four axial locations without unclamping the spindle chuck. The range of variation for the center offset and radius was 0.005 mm or less for all five locations. The center location was less repeatable, but this is to be expected since the spindle angular orientation could not be reset to the same starting point between measurements (no spindle encoder access was available).

To evaluate the influence of chucking repeatability, the same part used for the length measurements was removed from the spindle and then reclamped. The difference in measured length for multiple parts was approximately 0.200 mm. Using the radial error motion at the part surface taken with a dial indicator (±0.61 mm to ±2.2 mm) and the part geometry, each time a part is chucked there is a potential for a ΔL change in length of 0.182 mm to 0.653 mm. This range encompasses the variation in the on-machine length measurements and verifies that clamping non-repeatability is a significant contributor to part length deviation.

CONCLUSIONS

In this study, two contact probes were designed, fabricated, and implemented to measure the length and bore concentricity of cylindrical, extruded tool joints while clamped in a production lathe spindle. Given the pre-machining part dimensions, a selection could be made from a pre-defined matrix of part programs that are defined using the anticipated range of part dimensions. The part program would be selected such that depths of cut that are significantly larger than expected (based on nominal part dimensions) would be avoided. In this way, the time-consuming approach of defining the part program based on the largest possible part would be replaced and the cycle time and machining cost would be reduced while increasing the tool life.

REFERENCES

[1] Yandayan T, Burdekin M. In-process dimensional measurement and control of workpiece accuracy, International Journal of Machine Tools and Manufacture. 1997; 37: 1423-1439.

[2] Vacharanukul K, Mekid S. In-process dimensional inspection sensors, Measurement. 2005; 38(3): 204-218.

[3] Smith ST. Flexures: Elements of Elastic Mechanisms. CRC Press LLC, Florida: 2000.

INTERNAL FINISHING OF CAPILLARY TUBES BY MAGNETIC ABRASIVE FINISHING USING A METASTABLE AUSTENITIC STAINLESS STEEL TOOL

Junmo Kang[1] and Hitomi Yamaguchi[1]
[1]Department of Mechanical and Aerospace Engineering
University of Florida
Gainesville, FL, USA

INTRODUCTION

In magnetic abrasive finishing (MAF), as the tube inner diameter (ID) becomes less than 1 mm, critical control of the magnetic field at the finishing area inside the tube is required to generate the force acting on the magnetic abrasive needed for finishing. That control can be achieved by modifying the pole-tip geometry or the position of the pole tips relative to the tube [1]. For capillary tubes (ID < 1 mm), the typical pole-tip width is 4 mm (in the axial direction), which is therefore the default finished length [1, 2]. Feeding the pole tip in the axial direction allows the entire surface of a long tube to be finished. However, due to difficulties in lubricant control at the finishing area, the finished length is limited in practice to just a few times the pole tip width [2]. The accumulation of multiple short finishing passes is needed for long tube finishing, and the longer finishing time is a critical drawback for practical applications.

In the case of large tube finishing, neither lubricant control nor pole tip feed length is an issue. Moreover, multiplication of the pole tips and the insertion of either a permanent magnet tool (or a ferrous tool with magnetic abrasive) have been applied to extend the default finishing length and improve the finishing efficiency [3-5].

The aim of this paper is to propose a method to extend the default finished length using a heat-treated metastable austenitic tool in combination with multiple pole tips, which enables (1) the simultaneous finishing of multiple regions, and (2) the efficient long-length finishing with a short pole-tip feed stroke. This paper discusses the relationships between the magnetic properties of the tool, behaviors of the tool and magnetic abrasive, and the finishing characteristics. Moreover, a mechanism to extend the finished length is clarified.

A NEW METHOD USING HEAT-TREATED METASTABLE AUSTENITIC STAINLESS STEEL TOOL IN COMBINATION WITH MULTIPLE POLE TIPS

Figure 1 shows a schematic of a typical magnetic abrasive finishing setup with a single pair of pole tips, hereafter called a *single pole tip system*. The desired magnetic field at the finishing area is generated by two permanent magnets are attached to a steel yoke. A mixed-type magnetic abrasive introduced into the tube is pushed by magnetic force against the tube surface and finishes the tube when the tube is rotated at high speed. The pole tip width is the default finished length, and the accumulation of multiple short-length finishing passes is needed for long tube finishing.

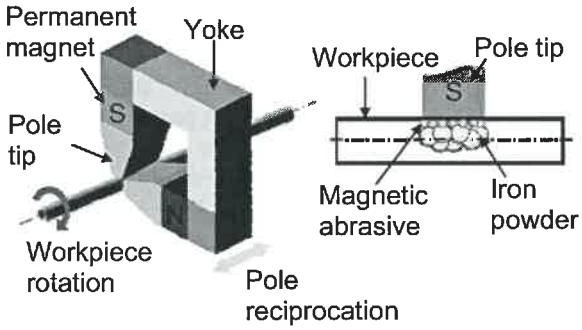

FIGURE 1. Schematics of magnetic abrasive finishing process.

Figure 2 conceptually shows the proposed method to extend the default finished length. An additional pair of pole tips is added (and yoked together as shown Fig. 2) and a long magnetic tool is placed inside the tube. The mixed-type magnetic abrasive is introduced into two sections inside the tube; this doubles the finishing area and, thus, doubles the finishing efficiency. Hereafter, it is referred to as a *multiple pole tip system*. In the case of large diameter tube finishing, introducing the mixed-type magnetic abrasive into the two separated

sections is not difficult. In contrast, the small diameter of a capillary tube makes it difficult to insert the mixed-type magnetic abrasive into the tube and to further manipulate it into the area corresponding to the pole tip. Instead, the mixed-type magnetic abrasive tends to build up in the area corresponding to the entry side of the pole tip.

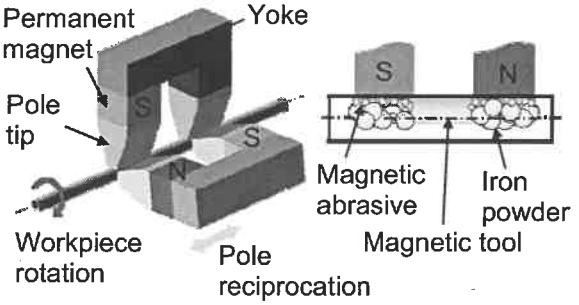

FIGURE 2. Schematics of magnetic abrasive finishing process using multiple pole tip system.

During this research, it was found that the mixed-type magnetic abrasive can be introduced into the capillary tube using a magnetic tool as a guide. The magnetic properties of the tool play an important role in realizing this concept. Figure 3 is a photograph of 54 mm magnetized (a) carbon steel and (b) 304 stainless steel tools with iron particles. Because of the remanent magnetization, the iron particles are mostly attracted by the tool ends. Due to its magnetic anisotropy, this trend is more visible with the stainless steel tool than the carbon steel tool. However, when they were inserted into the tube (using the experimental setup shown in Fig. 4), the tool and iron particles were not able to follow the pole tip feed in either case.

In the case of Fig. 3(a), the iron particles were attracted by magnetic force to the entire surface of the carbon steel tool when placed inside the tube; this did not lead to the conditions shown in Fig. 2. Instead, the carbon steel tool generated

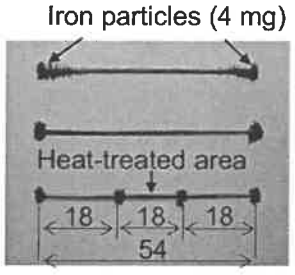

(a) Carbon steel tool (∅0.5×54 mm)
(b) 304 stainless steel tool (∅0.51×54 mm)
(c) Heat-treated 304 stainless steel tool (∅0.51×54 mm)

FIGURE 3. Magnetized tools with iron particles.

strong magnetic force and pushed against the tube inner surface. This increased the friction force against the tube surface and prevented the tool from following the pole tip feed. In the case of Fig. 3(b), the iron particles were attracted by the pole tips and separated into two sections. When the pole tips were moved, the iron particles followed the pole tip motion, but the stainless steel tool stayed at the same position. The magnetic field distribution generated by the combination of magnetic pole tips and tool failed to cause the tool to follow the pole tip feed.

To materialize the concept shown in Fig. 2, the magnetic field generated by the pole tips and tool should exhibit a large gradient in the magnetic field intensity between the pole tips. This separates the iron particles into two sections and generates the magnetic force to drive the tool covered with the iron particles to follow the pole tip feed. In doing this, the tool must exhibit alternating magnetic properties corresponding to the pole tips. This study proposes the use of a partially heat-treated metastable (304 stainless steel) tool.

Once the metastable austenitic stainless steel tool has undergone cold working, it experiences a martensitic transformation and exhibits ferromagnetism. However, the austenitic phase can be retrieved (and thus exhibit nonmagnetic

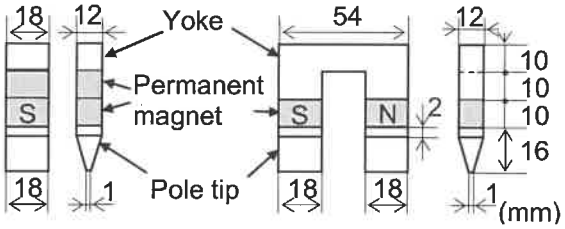

(a) Single pole tip (b) Multiple pole tips

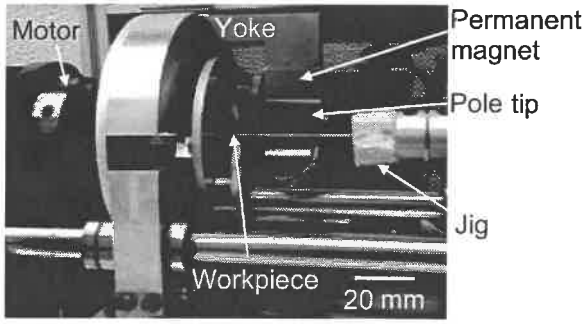

(c) Photograph of experimental setup

FIGURE 4. Pole set geometry and experimental setup.

properties) by heat treatment beyond the Curie temperature (at least 600 °C) [6, 7]. This treatment can make multiple alternations in the magnetic property of a single tool. Figure 3(c) shows the partially heat-treated 304 stainless steel tool (hereafter referred to simply as the *stainless steel tool*) with iron particles. The middle section of the tool exhibits paramagnetism, thus the iron particles are attracted to the ends of ferromagnetic sections.

The conditions in Fig. 3(c) led to the conditions shown in Fig. 2. Once the pole tips were moved along the tube axis, the iron particles and tool both followed the pole tip reciprocation. Without any pole tip feed, the default finished length was the sum of two sections of 18 mm. If the pole tip stroke in the axial direction is sufficient to cover the gap between two pole tips, the finished length is 72 mm. In the case of the single pole tip system (see Figs. 1 and 4(a)), the 18 mm pole tip stroke covers only a length of 36 mm, and it requires two finishing steps, which requires twice the time, to finish the 72 mm length.

The next chapter will discuss the characteristics of the 72 mm length finished using the multiple pole tip system with a 54 mm stainless steel tool. The finishing characteristics of the two-step process using the single pole tip system will be also discussed for comparison.

FINISHING CHARACTERISTICS

Table 1 shows the experimental conditions. As workpieces, stainless steel tubes (1.27 mm OD, 1.06 mm ID, 100 mm long, initial surface roughness: 2~3 μm *Rz*) were prepared for this study. Ten millimeters at one end of the tube is chucked and the other end is supported by a flexible jig that reduces the run-out during rotation. The finished length began 5 mm from the free tube end. The tube rotational speed was set at 2500 min^{-1}, and the pole feed rate was set at 0.59 mm/s. In the case with the single pole tip system, 15 mg of mixed-type magnetic abrasive was applied, which took up 45.3 % of the enclosed volume of the finishing area. In the multiple pole tip system, 47.3 % (mixed-type magnetic abrasive: 24.2 %, stainless steel tool: 23.1 %) was taken up at each finishing area. In both cases, 90 μL of lubricant was initially supplied into the tube, and 50 μL was added after every 20 strokes. For each finishing experiment, the total number of strokes was 180. After each experiment, the tube was cleaned in

Table 1. Experimental conditions.

System	Single pole tip	Multiple pole tips
Workpiece	304 stainless steel tube (∅1.27×∅1.06×100 mm)	
Workpiece revolution	2500 min^{-1}	
Mixed type of magnetic abrasive	Iron particles (-50/+100 mesh, 150-300 μm diameter): 80 wt% + Aluminum oxide (WA) particles (Mean dia. 80 μm) in magnetic abrasive (< 10 μm): 20 wt%	
	15 mg	8 mg / finishing area
Magnetic tool		Heat-treated 304 stainless steel rod: ∅0.51×54 mm
Lubricant	Soluble-type barrel finishing compound (pH 9.5, 755 mPa·s at 30°C), 490 μL	
Pole feed	Length: 18 mm Speed: 0.59 mm/s Total number of strokes: 180	
Processing time	6 hr (3 hr / step)	3 hr

an ultrasonic cleaner using ethanol, sectioned along the tube axis, and the inner surface was evaluated using an optical profiler and a microscope. The material removal was calculated by comparing the weight (measured using a micro-balance with 10 μg resolution) before and after finishing.

Figure 5 shows the surface roughness as a function of the distance from the tube end. The roughness values are the averages of ten measurements. The roughnesses at *X*=85 mm are the values of unfinished surfaces.

In the MAF process, the finishing operation is performed by a mass of magnetic abrasive aligned with the line of magnetic force. Generally, the finishing capability diminishes at the borders corresponding to the pole tip edges due to the unstable magnetic abrasive motion. As a result, the areas around *X*=5, 41, and 77 mm were less finished, which is more clearly shown in results from the single pole tip system. However, the higher roughness conditions that resulted in those areas could be eliminated by slightly

extending (by 1~2 mm, for example) the pole feed stroke.

The material removal realized by the single pole tip system was 12.98 mg (after the first step) and 11.05 mg (second step). These values are about 1.5 times higher, per finishing step, than the 7.85 mg of material removed by the multiple pole tip system. As mentioned before, the number of cutting edges active in the multiple pole system is estimated to be about half of the number with the single pole tip system. Regardless of the greater magnetic force acting on the magnetic abrasive in the multiple pole tip system, the lower number of active cutting edges resulted in less material removal and a rougher surface than the case of the single pole tip system. It should be noted that the single pole tip system took twice the time, however, to completely finish the target 72 mm length.

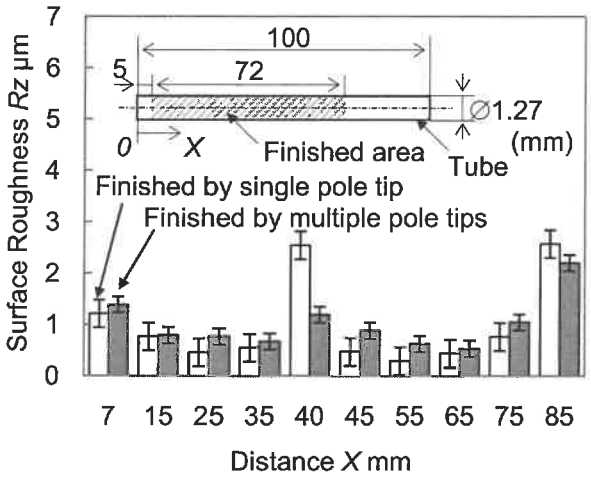

FIGURE 5. Changes in surface roughness with distance X.

CONCLUSIONS

This study proposed a new method using a heat-treated metastable austenitic stainless steel tool in combination with a multiple pole tip system to improve the finishing efficiency by performing simultaneous finishing of multiple regions. The results of this study can be summarized as follows:

1) A condition required to realize the proposed method is the use of a magnetic tool consisting of alternating magnetic and nonmagnetic regions. This can be fabricated by the partial heat treatment of a metastable austenitic stainless steel tool.
2) The combination of the heat-treated stainless steel and multiple pole tip system enables the magnetic abrasive to be inserted into multiple regions inside the capillary tube and to follow the pole tip reciprocation. This led to the long-tube finishing with a short pole stroke length, improving the finishing efficiency.

With multiple pole tip sets, the finished length of the system is extended. The ratio between the volume of the magnetic tool and the magnetic abrasive, finishing speed, pole stroke length are other important parameters that influence the finished surface quality. This will be continuously studied.

REFERENCES

[1] Yamaguchi H, Shinmura T, Ikeda R. Study of Internal Finishing of Austenitic Stainless Steel Capillary Tubes by Magnetic Abrasive Finishing. ASME Transactions, J. Manuf. Sci. Eng. 2007; 129(5): 885–892.

[2] Yamaguchi H, Kang J. Study of Ferrous Tools in Internal Surface and Edge Finishing of Flexible Capillary Tubes by Magnetic Abrasive Finishing. Transactions of the North American Manufacturing Research Institution of SME. 2010; 38: 177–184.

[3] Shinmura T, Yamaguchi H, Aizawa T. A New Internal Finishing Process of Non-ferromagnetic Tubing by the Application of a Magnetic Field. Int. J. Japan Soc. Prec. Eng. 1993; 27(2): 132–137.

[4] Shinmura T, Yamaguchi H. Study on a New Internal Finishing Process by the Application of Magnetic Abrasive Machining –Internal Finishing of Stainless Steel Tube and Clean Gas Bomb, JSME International Journal, Series C. 1995; 38(4): 798–804.

[5] Zou Y, Shinmura T. A New Internal Magnetic Field Assisted Machining Process using a Magnetic Machining Jig –Machining Characteristics of Inside Finishing of a SUS304 Stainless Steel Tube, Advanced Material Research. 2009; 69-70: 143–147.

[6] Mumtaz K, Takahashi S, Echigoya J, Kamada Y, Zhang F. L, Kikuchi H, Ara K, Sato M, Magnetic Measurements of Martensitic Transformation in Austenitic Stainless Steel after Room Temperature Rolling. J Mater Sci. 2004; 39: 85–97

[7] Childress J, Liou S. H, Chien C. L. Magnetic Properties of Metastable 304 Stainless Steel with BCC Structure. J. Phys. Colloques. 1988; 49(C8): 113–114.

COMBINING TOOL WEAR AND STABILITY IN HIGH-SPEED MACHINING PERFORMANCE PREDICTION

Jaydeep M. Karandikar, Raúl E. Zapata, and Tony L. Schmitz
Department of Mechanical and Aerospace Engineering
University of Florida
Gainesville, FL, USA

INTRODUCTION

Tool wear imposes an important process limitation in milling, along with chatter (self-excited vibrations) and surface location error (due to forced vibrations). Prior research has shown an increase in the cutting forces and, subsequently the force model coefficients, as a result of tool wear [1]. Therefore, tool wear effects can be incorporated through the force model coefficients used to calculate stability lobe diagrams, which graphically represent the boundary between stable and unstable combinations of spindle speed and axial depth of cut. This research explores tool wear as a process limitation through its effect on milling stability lobes.

This is achieved using the milling "super diagram" that incorporates limitations to milling productivity and part quality imposed by stability, surface location error, and tool wear [2]. Combinations of axial depth of cut and spindle speed that offer stable cutting conditions with an acceptable, user-defined surface location error (SLE) level are identified using a gray-scale color coding scheme. The effect of tool wear is incorporated by determining the variations in force model coefficients used for process dynamics prediction with tool wear. The force model coefficients tend to increase as a function of the flank wear width (used as a measure of tool wear). The increase in force model coefficients is determined as a function of the volume of material removed. Using these coefficients, a unique super diagram is constructed for any user-defined volume of material removed using the selected cutter. Additionally, user beliefs about data and model accuracy are applied to identify safety margins relative to the deterministic boundaries in the diagrams.

In this paper, experimental results are provided for an inserted (carbide) cutter used to machine 1018 steel. The wear behavior is incorporated as changes in the force model coefficients as a function of the volume of material removed at different operating parameters. The flank wear is also measured using an on-machine microscope (to avoid tool removal from the spindle) and correlated to the force model coefficients. Super diagrams are developed that correspond to the new and worn tool performance and experimental results are provided to verify changes in the process stability with tool wear.

TOOL WEAR TESTS

In this section, the experimental steps required to collect the tool wear data for the new super diagram are described for a 19 mm diameter inserted endmill (one square uncoated Kennametal 107888126 C9 JC carbide insert; zero rake and helix angles, 15 deg relief angle, 9.53 mm square x 3.18 mm) that was used to machine 1018 steel.

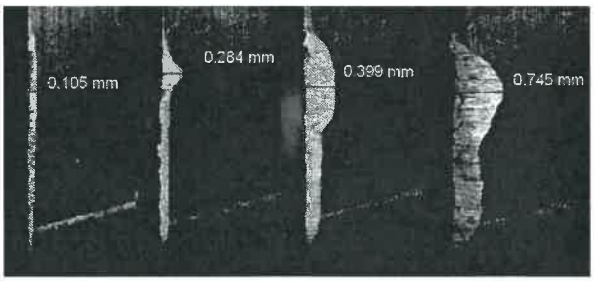

FIGURE 1. Images of FWW at 60x magnification (from left to right, V = {50, 125, 200, and 275} cm^3).

$$F_t = K_t bh + K_{te} b$$
$$F_n = K_n bh + K_{ne} b \quad (1)$$

The cutting forces were monitored using a table-mounted force dynamometer (Kistler 9257B) and the four cutting force coefficients in Eq. 1 were identified intermittently while wearing the tool by performing a linear regression to the mean x (feed) and y direction forces over a range of feed per tooth values: {0.03, 0.04, 0.05, 0.06, and 0.07} mm/tooth [3,4]. The feed per tooth while wearing the tool was kept constant at 0.06 mm/tooth. The radial and axial depths of

cut were 4.7 mm (25% radial immersion) and 3 mm.

In addition to monitoring the cutting force, the insert wear status was also measured at intervals of volume of material removed, V. To avoid removing the insert/tool from the spindle, a handheld microscope (60x magnification) was used to record the rake and flank surfaces. The calibrated digital images were used to identify the FWW (no crater wear was observed). Example results for a spindle speed, Ω, of 2500 rpm are provided in Fig. 1.

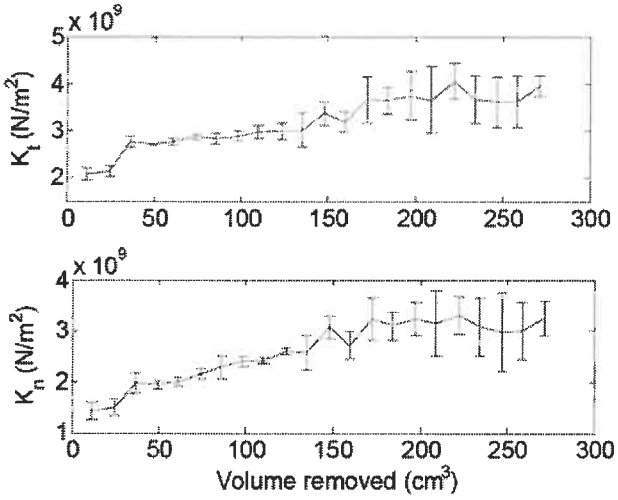

FIGURE 2. Variation in K_t and K_n with volume removed (Ω = 2500 rpm).

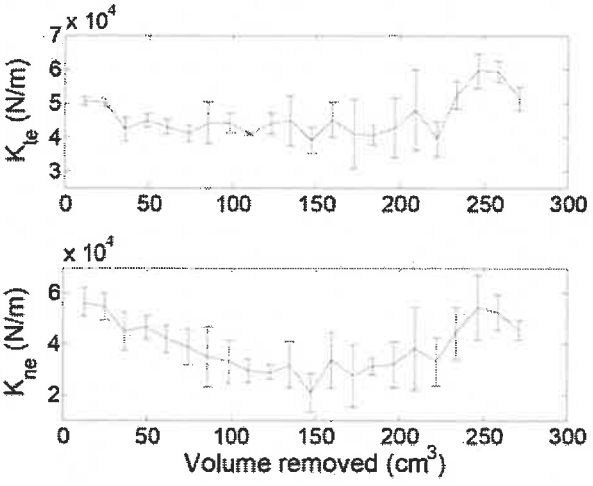

FIGURE 3. Variation in K_{te} and K_{ne} with volume removed (Ω = 2500 rpm).

At V intervals of 12 cm^3, the four cutting force coefficients were determined. These results are given in Figs. 2 and 3. For the tool/material pair tested here, there was an approximately linear growth in K_t and K_n, while the K_{te} and K_{ne} values showed no clear trend.

To evaluate the change in coefficient behavior with spindle speed, additional tests were completed at {3750, 5000, 6250, and 7500} rpm. The results are displayed in Fig. 4, as well as the linear least squares fits. As expected, the rates of K_t and K_n growth (i.e., the slopes) increase with spindle speed. While the results are not shown, the K_{te} and K_{ne} values again did not exhibit any significant trend at the additional spindle speeds.

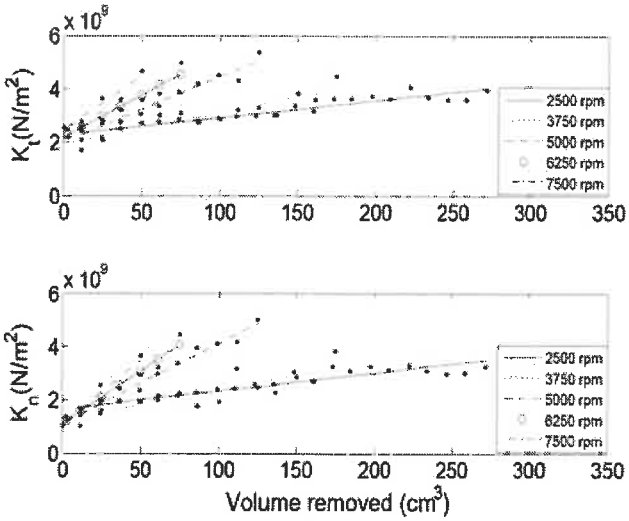

FIGURE 4. Variation in K_t and K_n with volume removed for various spindle speeds.

The slopes of the individual (K_t and K_n versus volume removed) lines in Fig. 4 are plotted against spindle speed in Fig. 5. It is seen that these slopes grow linearly with increasing speed. Therefore, a model which linearly relates the K_t and K_n values to Ω and V can be applied for this tool-material pair; see Eq. 3. The slopes of the lines in Fig. 5 are 7.1×10^3 $(N/m^2/cm^3)$/rpm for the K_t data and 9.1×10^3 $(N/m^2/cm^3)$/rpm for the K_n data. The intercepts for the linear relationships in Eq. 3 are determined from the mean V = 0 (new tool) values from Fig. 2. Because a significant trend in K_{te} and K_{ne} was not observed, these values can be set equal to the mean values from Fig. 3, i.e., $K_{te} = 4.6\times10^4$ N/m and $K_{ne} = 3.9\times10^4$ N/m. Given this relationship, the super diagram that incorporates tool wear can then be developed by applying the

user-selected volume and calculating K_t and K_n for each spindle speed in the {Ω, b} domain.

$$K_t(\Omega,V) = 2.2\times10^9 + (7.1\times10^3\cdot\Omega)V$$
$$K_n(\Omega,V) = 1.2\times10^9 + (9.1\times10^3\cdot\Omega)V \quad (2)$$

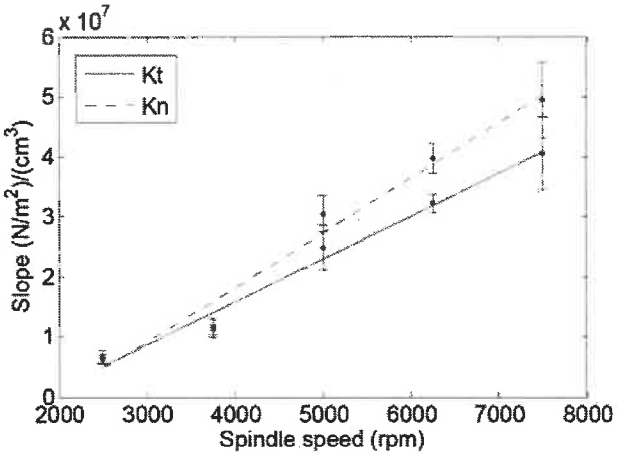

FIGURE 5. Variation in slope of K_t and K_n versus volume removed lines (from Fig. 4) with spindle speed.

STABILITY TESTS

The tool wear experimental results showed a linear increase in cutting force coefficients K_t and K_n with volume removed due to progressive flank wear. The rate of increase of force coefficients increased linearly with speed. This increase in force coefficients causes the limiting axial depth of cut to decrease. To explore this wear effect, the tool point frequency response function was measured by impact testing and the stability limit was calculated using force coefficients based on a new and worn insert. An insert was worn by removing 275 cm^3 at Ω = 2500 rpm. The force coefficients were determined for both a new insert and the worn insert using a linear regression of the average x and y direction forces at varying feed per tooth values as described previously. These force coefficients are provided in Table 1. For stability testing at 5100 rpm, the equivalent volume removed which would yield the K_t and K_n values for the worn insert was calculated to be 121 cm^3 using Eq. 2. The stability limit for the new insert was calculated using the new insert values (V = 0). For the worn insert, the K_t and K_n values at each spindle speed were calculated using Eq. 2 and the stability limit was generated [5]. However, as shown by the error bars in Fig. 5, there is uncertainty in the K_t and K_n values for both the new and worn inserts. A Monte Carlo simulation was completed where random K_t and K_n values were selected from the experimental distributions and a new stability limit was calculated for each set. See Fig. 6, where the radial depth of cut is equal to the tool diameter (slotting). The band of stability limits indicates the uncertainty. This information could be used, for example, to aid a user in selecting his/her safety limits for the super diagram. The mean limiting depth of cut at 5100 rpm is 2.15 mm for the new insert and 0.85 mm for the worn insert.

Table 1: Force coefficient values for new and worn inserts.

	K_t (N/m^2)	K_n (N/m^2)	K_{te} (N/m)	K_{ne} (N/m)
New	1.90×10^9	0.78×10^9	45500	46650
Worn	4.98×10^9	4.51×10^9	45500	25500

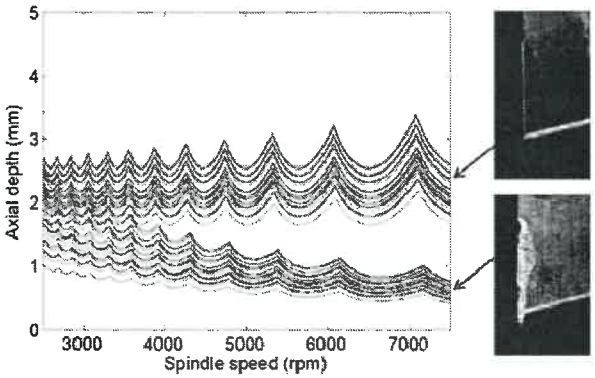

FIGURE 6. Stability lobe diagram for new (V = 0) and worn inserts (V = 121 cm^3).

Cutting tests were completed at b = {0.8, 1.6, 2.2, and 3} mm with the new and worn inserts. A once-per-revolution force sampling strategy for the x (F_x) and y (F_y) directions was used to identify chatter. The once-per-revolution samples were obtained by sampling the force data at the commanded spindle rotating frequency. For stable cutting conditions, the once-per-revolution samples (due to forced vibration only) are synchronous with spindle rotation and produce a small cluster of points [6] in the F_x vs. F_y plot. Unstable behavior, on the other hand, produces a more distributed set of points due to its asynchronous nature. A statistical variance ratio, R, is used as an indicator of chatter [7]; see Eq. 3, where $\sigma^2_{opr,x}$ and $\sigma^2_{opr,y}$ are the variances in the once-per-revolution sampled forces in the x and y directions and σ^2_x and σ^2_y are the variances in the x and y direction forces. Figure 7 shows

once-per-revolution samples for tests at b = 1.6 mm and Ω = 5100 rpm for the new and worn inserts.

$$R = \frac{\sigma_{opr,x}^2 + \sigma_{opr,y}^2}{\sigma_x^2 + \sigma_y^2} \quad (3)$$

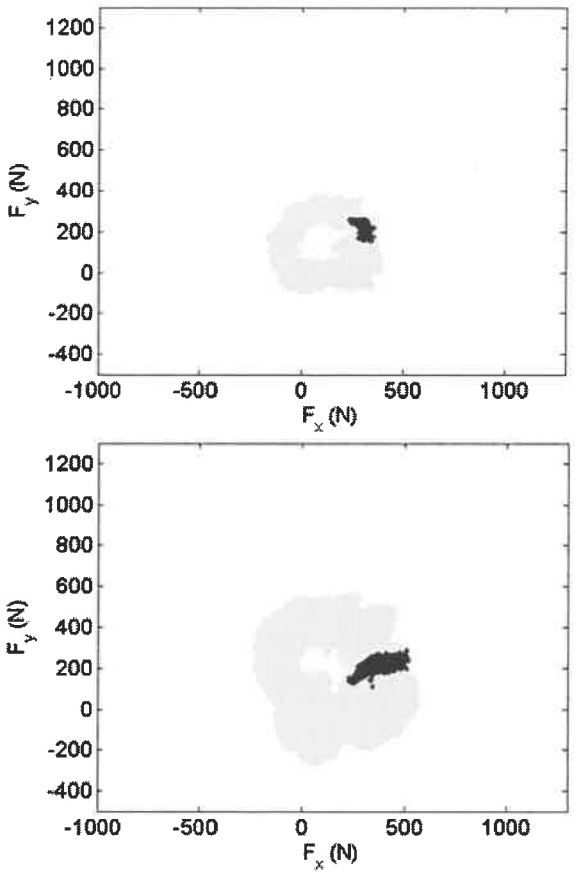

FIGURE 7. Once-per-revolution samples for 1.6 mm axial depth of cut and 5100 rpm spindle speed (top: new insert, bottom, worn insert).

As seen in Fig. 7, the distribution of once-per-revolution samples increases for the unstable cut using the worn insert. Similar results were obtained b = 0.8 mm (which is within the stability limit distribution for the worn tool in Fig. 6), 2.2 mm, and 3 mm. Figure 8 shows the R values for different axial depths of cut, where the R value is larger for all cuts with the worn insert and increases substantially for both the new and worn insert at b = 3 mm (violent chatter occurred in both cases for this depth).

CONCLUSIONS

In this work, the effect of tool wear on milling stability was evaluated experimentally. By modifying the force model coefficients according to the wear status (as a function of volume removed), tool wear effects were incorporated into the milling super diagram. Cutting tests were completed to verify the change in process stability with tool wear status.

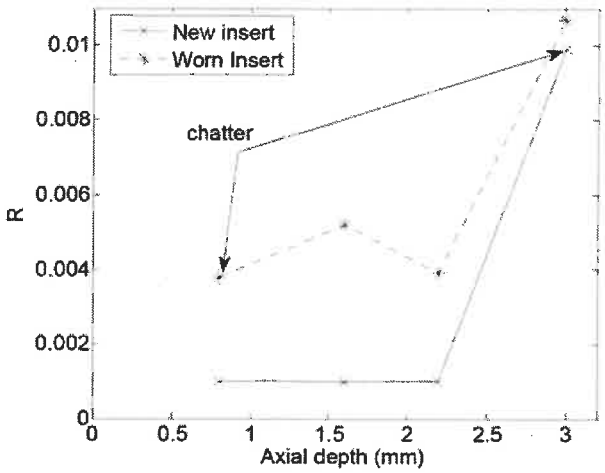

FIGURE 8. Variance ratio, R, for new and worn inserts at different axial depths of cut.

REFERENCES

[1] Cui, Y., B. Fussell, R., Jerard, and D. Esterling (2009). Tool Wear Monitoring for Milling by Tracking Cutting Force Model Coefficients. Transactions of the NAMRI/SME, Vol. 37, pp. 613-620.

[2] Zapata, R., J. Karandikar, and T. Schmitz, (2009). A New 'Super Diagram' for Describing Milling Dynamics. Transactions of NAMRI/SME, Vol. 37, pp. 245-252.

[3] Altintas, Y. (2000). Manufacturing Automation. Cambridge University Press, Cambridge, UK.

[4] Schmitz, T. and K.S. Smith (2009). Machining Dynamics: Frequency Response to Improved Productivity, Springer, NY.

[5] Altintas, Y. and E. Budak (1995). Analytical Prediction of Stability Lobes in Milling. Annals of the CIRP, Vol. 44/1, pp. 357-362.

[6] Davies M., B. Dutterer, J. Pratt, A. Schaut, and J. Bryan (1998). On the Dynamics of High-Speed Milling with Long, Slender Endmills, Annals of the CIRP, Vol. 47/1, pp. 55-60.

[7] Cheng C., T. Schmitz T., and G.S. Duncan (2007). Rotating Tool Point Frequency Response Prediction using RCSA, Machining Science and Technology, 11, pp. 433-446.

REDUCTION OF NC MACHINING DATA VOLUME AND EVALUATION OF MACHINED SURFACE BY CIRCULAR ARC APPROXIMATION OF DISCRETE POINTS

Kiyotaka KAWASAKI, Tetsuya MURATA,
Yoshikazu KOBAYASHI, and Kenji SHIRAI
Department of Computer Science, College of Engineering, Nihon University
Koriyama 963-8642, Japan
Tsukasa KONDO
Hakodate National College of Technology, Hakodate 042-8501, Japan

1. INTRODUCTION

Recently, machined shapes are increasingly diversifying with changes in user values and preferences towards products, leading to the increase in NC(Numerical Control) data volume in machining processes. As NC data is composed of point groups, the number of point groups and machining time increase in the machining of free-form surfaces. Efficient use of NC data requires high speed NC machine tools, but because these are generally costly, existing NC machine tools are often employed. Such NC machine tools take extremely long machining time to process large data volume due to their slow transfer speed. In this study, the authors thus aimed to reduce NC data volume and shorten the machining time of machine tools by applying circular arc approximation to point groups composing free-form curves within the required range of accuracy.

2. PROPOSED APPROXIMATION METHOD

2.1 Circular Arc Approximation for Free-Form Curves

Figure 1 shows the algorithm of the processing method used to apply point groups to circular arc. The circular arc approximation method is generally proposed as a technique for applying the NC data used for the machine tools. With this method, the circular arc is applied to the point groups composing free-form curves using the least squares method within the required accuracy[1][2]. The procedure is as follows; The data of the point groups used for the tool path is called from a file. Next, the tolerance and maximum point groups to be applied are specified. The smaller the tolerance, the nearer is the arc to a point. One method of circular arc approximation is by connecting by C1 continuity or C0 continuity according to the point group data. Figure 2 shows the connection methods by circular arc of C1 continuity and by C0 continuity. As shown in Figure 2(a), C1 continuity connects the previous and next arcs and realizes smooth joints, while with C0 continuity, the joint between arcs is not smooth and a hollow is formed as shown in Figure 2(b).

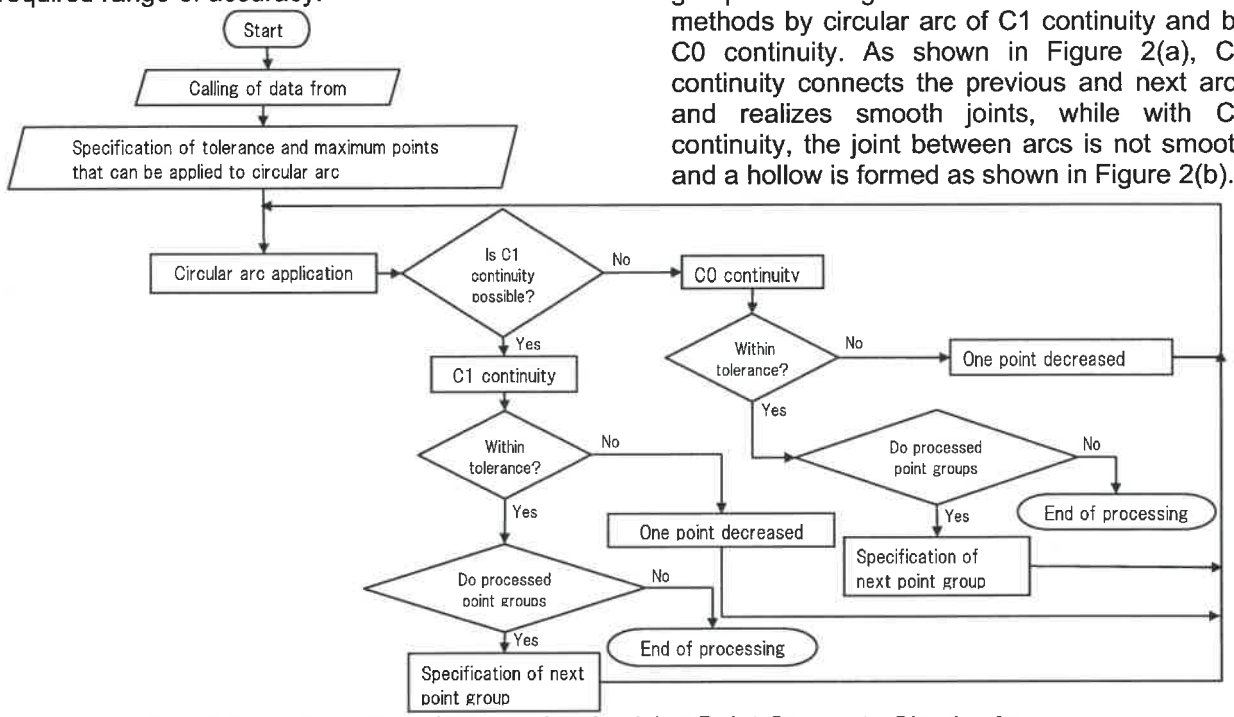

FIGURE 1 : Algorithm of Processing Applying Point Groups to Circular Arc

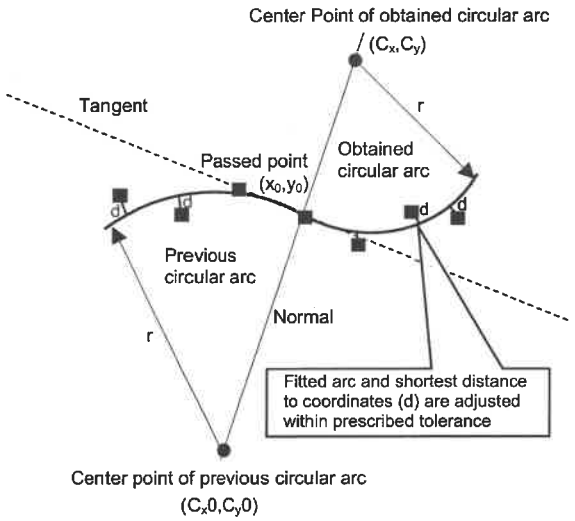

(a) Connection of Circular Arc by C1 Continuity

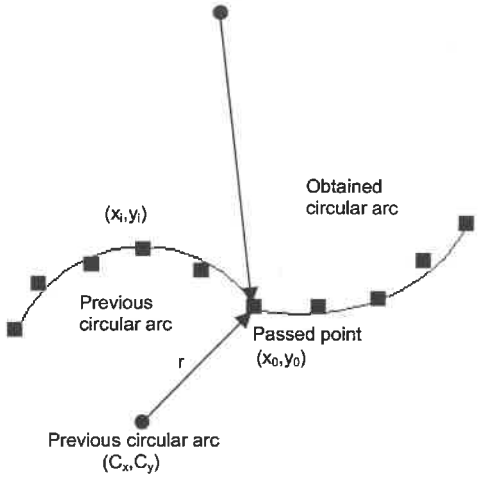

(b) Connection of Circular Arc by C1 Continuity

FIGURE 2 : Connecting of Circular Arc by C1 Continuity and C0 Continuity

As a precondition, C0 continuity requires agreement between the end point of a circular arc and the starting point of the next circular arc applied. This condition is expressed in the following equation (1);

$$(x_0-C_x)^2+(y_0-C_y)^2=r^2 \qquad (1)$$

where (x_0,y_0) is the coordinate value of the passed point of the previous circular arc and the obtained circular arc, (C_x,C_y) is the coordinate value of the center point of the obtained circular arc, and r is the radius. Another condition of C1 continuity is that the center points of the two circular arcs lie in the normal direction. This condition is expressed by the following equations (2) and (3);

$$C_x=a(x_0-C_x0)+C_x0 \qquad (2)$$

$$C_y=a(y_0-C_y0)+C_y0 \qquad (3)$$

where a is the multiple of the distance to the center coordinates of the next circular obtained from those of the previous circular, and (C_x0,C_y0) is the center coordinates of the previous circular arc. The point group data divided into C1 continuity and C0 continuity during circular arc approximation is then processed respectively. At this step, it is determined if the shortest distance (d) from the given points to the arc applied by the circular arc approximation method is within the prescribed tolerance for both C1 continuity and C0 continuity. If within the tolerance, it is concluded that the circular arc can be applied, and the following point group is specified. If outside the tolerance, one applied point is decreased, and the circular arc is applied again. This process is repeated until the last point is reached.

2.2 Acquisition of Coordinate Value

In this study, we also verified the effects of reducing NC data volume in the above process through experiments. The point groups used in the experiments consist of BMP(Bitmap) image data. First, the original image is binarized to clarify the outline of the image. The resultant image is a monochrome image without gray scale. Next, the outline of the monochrome image is extracted by eight-point continuous extraction method to obtain the coordinates of the image[3]. In this study, the alphabet C, numeral 3, image of a hand and image of a reindeer were chosen as subjects, and the coordinates of their shapes were acquired.

3. OUTLINE OF CIRCULAR ARC APPROXIMATION PROGRAM

Figure 3 shows the processing method of the proposed circular arc approximation program. The circular arc of $\overset{\frown}{PaPb}$ shows C1 continuity in this figure, while the circular arc of $\overset{\frown}{PbPc}$ shows C0 continuity. Pc1 and Pc0 in the figure are the center points of C1 and C0 circular arcs respectively. The tolerance and applied number of points are assigned the tolerance and applied

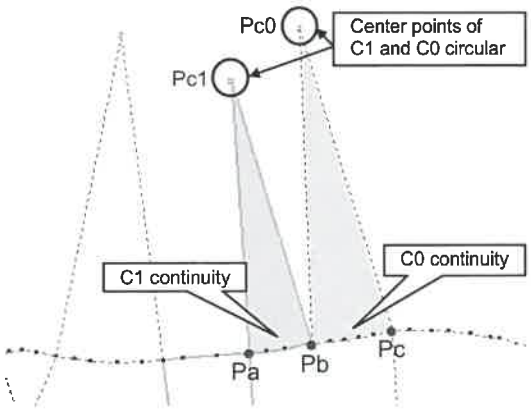

FIGURE 3 : Processing by Circular Arc Approximation Program

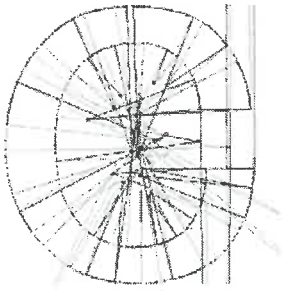

(a) Circular Arc Approximation

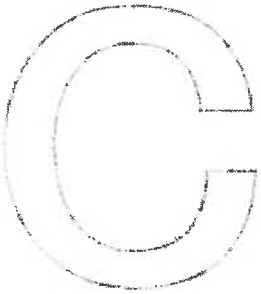

(b) Result of Circular Arc Approximation Process

FIGURE 4 : Flow from Circular Arc Approximation to Real Processing

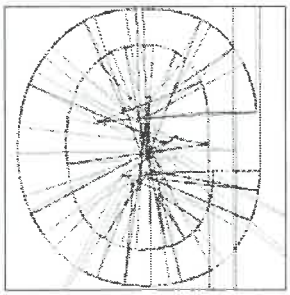

(a)Alphabet C
Tolerance 0.29mm
Maximum points applied:22

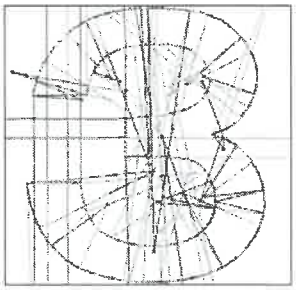

(b)Numeral 3
Tolerance 0.49mm
Maximum points applied:20

(c) Tool Path

(d) Processing

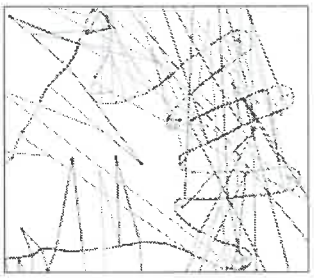

(c)Image of Hand
Tolerance 0.78mm
Maximum points applied:20

(d)Image of Reindeer
Tolerance 0.70mm
Maximum points applied:22

FIGURE 5 : Results of Circular Arc Approximation Program

number of points are changed to assign the point groups making up the circular arc. The smaller the tolerance, the nearer is the point to the circular arc. However, C0 continuity increases in the connection with the following circular arc, while C1 continuity increases when the tolerance is increased. However, the circular arc approximation in this case is not smooth and accuracy is poor, indicating that C1 continuity cannot be applied for all point groups data.

Figure 4 (a) to (d) show the flow from circular arc approximation to the actual grinding process. Figure 4 (a) shows the circular arc approximation process, Figure 4 (b) shows the results of applying the point groups data to the circular arc, Figure 4 (c) shows the tool path, and Figure 4(d) shows the processing results. Figure 5 (a) to (d) shows the results by circular arc approximation for the alphabet C, numeral 3, image of hand, and image of reindeer. The results of these four cases demonstrate that the corresponding circular arc could not be applied outside the tolerance prescribed. The tolerance shown in figure is the minimum value possible for the circular arc in the application. The tolerance is particularly large for the hand and reindeer, because their shape is considerably rugged.

TABLE 1 : Comparative Result of Processing Experiment

	Interpolation Method	Maximum Point Groups Applied	Number of C0/C1 Points	Data Volume
Alphabet C	Straight Line Interpolation	339		9.83KB
	Circular Arc Interpolation	53	24 points /29 points	2.38KB
Numeral 3	Straight Line Interpolation	428		12.4KB
	Circular Arc Interpolation	62	26 points /36 points	2.66KB
Image of Hand	Straight Line Interpolation	402		11.6KB
	Circular Arc Interpolation	74	25 points /49 points	2.58KB
Image of Reindeer	Straight Line Interpolation	560		16.5KB
	Circular Arc Interpolation	100	45 points /55 points	3.03KB

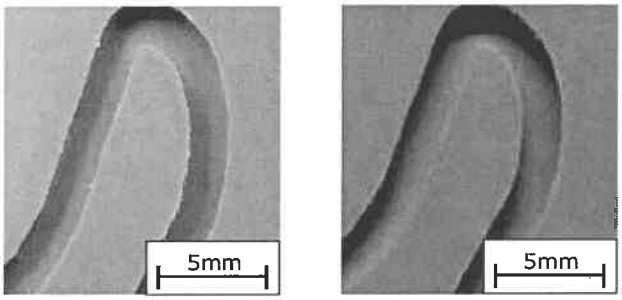

(a) No Circular Arc Approximation Processing

(b) Circular Arc Approximation Processing

FIGURE6 : Comparison of Processing Results

4. COMPARISON OF APPROXIMATION FOR LINEAR AND CIRCULAR ARC

In these experiments, NC data created by circular arc approximation and that created by collinear approximation were compared for the maximum point groups that can be applied, NC data capacity, and processing time according to the above conditions. The work material used was chemical wood, the tool used was a square end mill of 2mm in radius, and the feed rate of the tool was set at 300mm/min. Table 1 shows the comparative results of the circular arc approximation experiments. The grinding time is the same for all four cases. But the total number of point groups could be reduced by about 1/6, and the data volume by about 1/5. Figure 5 shows the comparison of the approximation results. There are no differences between the two shapes, and smooth surface is realized by circular arc approximation as shown in Figure 6(b).

5. CONCLUSION

The present study aimed to reduce NC data volume and shorten the machining time of machine tools by applying circular arc approximation to point groups composing free-form curves within the required range of accuracy. Approximation experiments were conducted using a circular arc approximation program, and the following results were obtained.

(1)The total number of point groups of a free-form curve could be reduced by about 1/6 and the data volume by about 1/5 by circular arc approximation.

(2)No difference was seen when the workpieces ground by circular arc approximation were compared by circular arc approximation and collinear approximation.

In future studies, investigations will be carried out to compare the NC data volume and machining accuracy when the tolerance is set at 0.1mm and 1.0mm in these four cases.

REFERENCES

[1]S.Sakai, T.Kondo : Effective Use of Conventional NC Machine Tool Using Circular Approximation of Surface Machining CL Data, Proceeding of 2004 Annual Meeting of JSPE Hokkaido Branch, 2004

[2]T.Kumagaya, T.Kondo : A Study on Circular Fitting with C1 Continuity Based on a Series of 2D Data Points, Proceeding of 2009 Annual Meeting of JSPE Hokkaido Branch, 2009

[3]K.Hori : Techniques of Similar Handwritten Characters Recognition by Using Different Feature Vectors, Research annals of Akashi National College of Technology,2006

MICROFABRICATION OF CIRCULAR CROSS-SECTION MICROCHANNELS FOR THROMBOSIS ASSAYS

Melissa Li[1], Steven Chase[3], Michael McKinnon[1], Craig R. Forest[1,2]
[1]Wallace H Coulter Department of Biomedical Engineering
[2]George W. Woodruff School of Mechanical Engineering
Georgia Institute of Technology
Atlanta, GA, USA
[3]Department of Applied Biology and Biomedical Engineering
Rose-Hulman Institute
Terre Haute, IN, USA

INTRODUCTION

The ability to accurately, inexpensively, quickly and repeatably fabricate sub-millimeter scale features has made soft-lithography based microfluidics a vital tool for the biomedical research and lab-on-a-chip assays. However, traditional methods used in this field, such as photolithography, deposition, and etching are generally limited to creating features with rectangular cross-sections, low aspect ratios, and feature heights below 200 μm [1]. These limitations cause several problems in the application of microfluidics to biological assays. Specifically, rectangular cross sections induce non-physiological gradients in fluid shear rate, velocity, and pressure in contrast with the rounded cross-sections found in most natural physiological systems, such as blood vessels and airways. Further, fabrication of features with multiple heights is complex and costly. Finally, casting and releasing around complex features can be problematic. Thus the development of methods for fabricating a wide range of heights and cross-sections within the same device would provide a valuable complement or replacement to standard microfabrication techniques.

Although previous groups have formulated methods for obtaining rounded channels such as reflow of photoresist during photolithography of the device mold, molding through the use of small wires, or by using additional coating hexanes within square channels, all of these methods have shown poor control over the resultant geometries and are unable to vary shapes and aspect ratios [1,2]. In contrast, micromilling channel molds is an option which can address a wide range of features and dimensions.

In this work we present a technique for the fabrication of an array of micro-scale channels of varying cross-sectional shape and areas with dimensions from 100 – 750 μm. In addition, we demonstrate the utility of these channels for investigating effects of varying local flow conditions on assessing

MATERIALS AND METHODS

Device Design and Modeling

Heart attacks occur when the coronary arteries fill with clots which prevent the flow of blood—a process known as thrombosis. Presence of local constrictions within these vessels can induce high shear rates and accelerate formation of occlusive clots. Assessment of heart attack susceptibility is often clinically characterized by the percentage of reduction in cross-sectional area as well as by the eccentricity of the vessel [3,4]. Recent intravascular angiographic clinical studies of human coronary arteries affected by atherosclerosis have shown that affected vessels exhibit localized constricted cross sections with predominantly eccentric elliptical or circular cross sections. Overall area reductions in cases of patients characterized as extremely high risk for thrombosis were reported in the range from 50-84% [3,4]. Thus there is great interest in designing instruments to better understand how and why these conditions of altered artery shapes impact patients' risk for thrombosis.

To study the effects of vessel shape, we designed an array of microchannels to study clot formation within four constricted regions with distinct cross-sectional areas: circular, square, semicircular, and eccentric (elliptical). Square and semicircular cross sections were chosen to

represent the dynamics of traditionally fabricated microchannels, while the circular and eccentric channels were chosen to represent the clinical conditions described previously. Square and circular cross sections had equal hydraulic diameters, while eccentric and circular cross sections had the same area constrictions were reduced in area by 84% relative to the rest of the channel to correspond to patients at very high risk for thrombotic stroke [3,4].

Device dimensions and added downstream resistance elements were chosen such that each channel would experience identical average shear rates of 7000 s^{-1}, an amount representative of conditions in patients at high risk for thrombosis and one which we have verified to cause clot formation in previous experiments [5,6]. In order to address such high shear rates for small volumes (less than 5 mL) of blood per trial, we required a wide range of feature heights and widths from 100 – 750 µm. These dimensions were modeled and verified using both an analytical Poiseuillar flow analysis in conjunction with finite volume characterizations using Navier-Stokes equations (Ansys Fluent).

Fabrication

We first used micromilling to construct a mold from which we cast parts which were subsequently aligned, and bonded to create enclosed channels with the desired cross sectional areas.

The mold was cut from brass alloy 385 on a vertical milling machine (Haas OM-1) using square endmills from 1.57mm to 254 µm in diameter and a 508 µm ball endmill at spindle speeds from 5,000 - 30,000 rpm. For all tools, feed rates were 50.8 mm/minute with depth of cuts set to 1/3 the tool diameter. Surface milled toolpaths were generated using MasterCAM X3 software. After machining, the mold was treated for eight hours with a silanizing agent (UCS Chemicals) to facilitate polymer release during the casting step.

Next the mold was cast in the high fidelity, transparent polymer polydimethylsiloxane (PDMS) (Sylgard 184, Dow Chemical). After thermal curing, the polymer was peeled away from the mold and plasma bonded using high frequency corona bonding (Electrotechnic). Alignment of the layers before bonding was achieved manually under a stereomicroscope. All channels except the semicircular channel were bonded to a mirror image. The complete process of milling and alignment is shown in *FIGURE 1(b).*

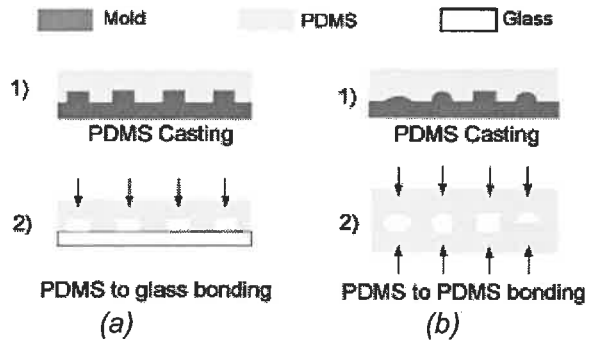

FIGURE 1. A comparison between (a) conventional microfluidic channel fabrication, and (b) our method for forming microfluidic round channels using micromilling and manual alignment.

Finally, blood was flowed through the final assembled device at a controlled pressure and shear rate while platelet based occlusion was monitored both by flow rate measurements and video microscopy.

RESULTS

Metrology

Verification of the mold's dimensions was performed using high-resolution digital microscopy (Keyence VHX-600). Special attention was given to the four constricted regions, where the modeled shear rate peaks at the desired 7000 s^{-1}. Results of metrology on these areas were characterized by figure error on curved surfaces as well as by absolute channel heights and widths. Figure error was calculated as the mean of the absolute value of the difference between the measured profile and the desired profile, results are shown in *TABLE 1.* Surface roughness along the flat face of the channel was sub-micrometer, and provided a sufficiently smooth surface for bonding castings of PDMS to PDMS along these regions.

Alignment and bonding of cast parts was performed manually under a stereomicroscope through which accuracy of 31 to 46 µm was achieved.

TABLE 1. Comparison between designed and fabricated mold dimensions within the constricted area of interest measured using digital microscopy.

	Eccentric	Circular	Square	Semi-circular
Designed Height(μm)	106	150	150	150
Measured Height(μm)	106.05	152.4	159.9	150.9
Designed Width(μm)	424	300	300	300
Measured Width(μm)	468	328	302.8	341.9
Figure Error (μm)	6.6	3.6	10.18	3.2

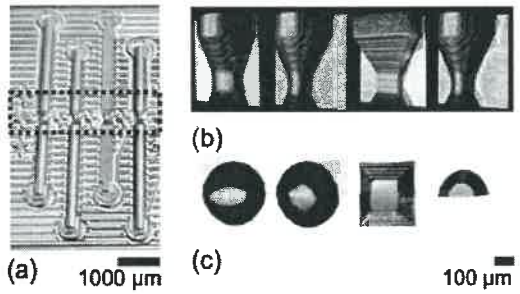

FIGURE 2. Images of the milled microchip mold (a) with enlarged images of the constricted regions of interest of varying cross sectional areas within the mold (b): eccentric, circular, square, and semicircular. Devices were cast from the mold in PDMS,bonded and aligned as shown in FIGURE 1. (c) Final stenotic cross sections.

Thrombosis Assays

The devices were used to assess the effects of variations in cross-sectional area on the formation of clots. Tests were run by flowing blood under specific shear rate conditions and monitoring the time it takes for clots to form and stop flow within each microchannel, simulating a heart attack.This quantity is defined as the time to occlusion[5,6]. Flow was monitored through the use of video microscopy and mass flow measurements with 10 μL resolution *(TABLE 2)*. Clot formation for each channel was also monitored through the use of video microscopy *(FIGURE 3)*.

TABLE 2. Experimental measurements of times for blood flow to occlude microchannels for varying cross-sectional shapes under conditions of identical shear rates (n=3 for all cross-sections).

	Eccentric	Circular	Square	Semi-circular
Time to Occlusion μ+σ(s)	78 +/- 47.5	313 +/- 55.2	170 +/- 41.7	66 +/- 48.1

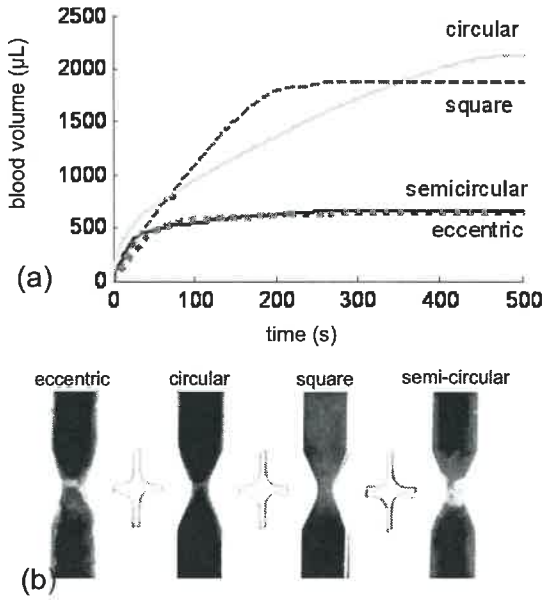

FIGURE 3. (a) Channel occlusion was measured by mass flow of blood through the microchannels of different cross-sectional areas at equal shear rates. (b) Images of blood clots in channels at 500 seconds.

DISCUSSION

We have developed a method for achieving a variety of three-dimensional features unachievable by traditional soft-lithography semiconductor fabrication processes. Employing this method, we demonstrated the creation of a single device mold containing four different cross sectional areas, with smoothly transitioning feature sizes ranging from 100 to 750 μm and aspect ratios ranging from 2:1 to 1:1. Variations in clotting time reveal the differential behavior of clot formation and nucleation over a range of cross-sectional areas.

The device fabricated in this work demonstrates the ability of micromilling to address hereto-unattainable feature dimensions. Analysis of the

milled mold showed a wide range of heights and a surface shapes with figure error within10 μm and absolute dimensions within 44 μm. Width dimensions showed the largest feature errors due to artefacts of the metrology method. The limiting factor for the entire fabrication method occurs in the manual alignment of the two molded parts, which could be improved through inclusion of specialized techniques such as temporary methanol bonding and the use of a mechanical stage. [7].

Our results showed that the time to occlusion for the circular channel was higher than within the square channel by almost three standard deviations. Since both channels had identical hydraulic diameters and shear rates, we conclude that this effect is largely due to differences in shear effects between square and circular cross-sectional shapes. Thus the estimation of hydraulic diameter for square cross-sections, a common practice in microfluidics, does not accurately predict fluid behavior for shear-dependent applications. Additional evidence for the importance of hydraulic diameter is provided by comparing the circular channel's time to that of the eccentric channel with the same percentage constriction and cross-sectional area. These variations in clotting time for channels of similar shear rates demonstrate the importance of both cross-sectional channel shape as well as hydraulic diameter and may provide substantial differences in thrombosis assays. These initial findings underscore the importance of developing a method for improved manufacturing techniques in microfluidic assays. Finally, it also suggests that the common clinical assessment of arterial constriction by area is insufficient to assess patient risk for thrombosis.

CONCLUSIONS

This work presents a simple method for creating three dimensionalfeatures, using a novel combination of micromilling and soft lithography. Future work on this method will include improvements in the alignment step of fabrication. Blood assay devices will continue to be developed towards pharmaceutical assays as well as biomedical research.

REFERENCES

[1] Xia Y, Whitesides G. Soft Lithography. AngewandteChemie International Edition. 1998; 37: 550-575.

[2] Fiddes L, Raz N, Srigunapalan S, Tumarkan E, Simmons C, Wheeler, A, Kumacheva E. A circular cross-section PDMS microfluidics system for replication of cardiovascular flow conditions. Biomaterials. 2010; 31: 3459-3464.

[3] Nissen S, Gurley J, Grines C, Booth D, McClure R, Berk M, Fischer C, DeMaria A. Intravascular ultrasound assessment of lumen size and wall morphology in normal subjects and patients with coronary artery disease. Circulation. 1991; 84: 1087-1099.

[4] Enrico B, Suranyi P, Thilo C, Bonomo L, Costello P, Schoepf U. Coronary artery plaque formation at CT angiography: morphological analysis and relation to hemodynamics. 2009; Eur Radiology. 19: 837-844.

[5] Wootton D, Markou C, Hanson S, Ku D. A mechanistic model of acute platelet accumulation in thrombogenic stenoses. Annals of Biomedical Engineering, 2001; 29(4): p. 321-329.

[6] Sodeman A, Li M, Mayor R, Forest C. Micromilling of molds for microfluidic blood diagnostic devices. Proceedings of the Annual Meeting of the American Society for Precision Engineering. 2009; Monterey, CA, October 4-9, 2009.

[7] Kim J, Baek J, Lee K, Lee S. Automatic aligning and bonding system of PDMS fabrication of 3D microfluidic channels. Sensors and Actuators. 2005; 119: 593-598.

FRICTION MEASUREMENT IN PRECISION GLASS MOLDING

Peiman Mosaddegh[1], John C. Ziegert[1], and Yazid Tohme[2]
[1]Department of Mechanical Engineering
Clemson University
Clemson, SC, USA
[2]Moore Nanotechnology Systems LLC
Swanzey, NH, USA

INTRODUCTION

Extensive growth of opto-electronic technologies has created a demand for high quality lenses and has driven the industry toward an inexpensive process for manufacturing of aspheric glass lenses called Precision Glass Molding (PGM). This method offers a cost-effective alternative for the mass production of these lenses in comparison to conventional methods involving grinding and polishing. PGM offers the possibility of rapidly creating finished lenses that require no additional processing or finishing, and also is a green technology requiring no environmentally damaging coolant.

One problem with the current PGM process is the cost of creating molds, since the lenses created by PGM do not typically possess the same geometry of the molds used to create them [1,2]. The reason for this is the visco-elastic behavior of glass at temperatures near the glass transition temperature, Tg, and differential thermal expansion of the glass and mold material. For these reasons, the mold geometry required to create a desired lens geometry is typically found by trial and error, and can involve the manufacture of numerous expensive molds before the correct geometry is discovered. To improve the mold design procedure and avoid these multiple iterations, Finite Element Analysis (FEA) has been used to predict the lens geometry resulting from a given mold geometry and set of process parameters; and if sufficiently accurate could enable the correct mold geometry to be discovered by simulation instead of experiment.

Having a realistic simulation to predict mold geometry depends on the right model of material behavior at an elevated temperature, the appropriate value of heat flux between the surfaces of the glass and the molds at a high temperature and pressure, the appropriate value of friction coefficient between surfaces at an elevated temperature, and the viscoelastic stress and structural relaxation during the cooling step. Of these issues, friction behavior at elevated temperatures has been the focus of this study. The ultimate aim of this research is to experimentally study and characterize the frictional behavior between glass and a mold surface at elevated temperatures typical of the PGM process and under conditions similar to those for this process.

Our study [3] on friction measurement in glass molding reveals that the friction coefficient between mold and glass in the vicinity of its transition temperature and in conditions similar to glass molding depends on temperature, feed rate, normal force, and surface roughness. Among them, temperature has the most significant effect since the glass viscosity is very sensitive to temperature.

In this study, friction force data for a WC-BK7 pair under process parameters similar to those used in glass molding are measured, and the values are reported that can be used for simulation of the PGM process.

MACHINE DESIGN

The machine used here, originally designed and manufactured by Moore Nanotechnology Systems LLC [4] for use in the PGM process, enables accurate control of the position, force, and temperature of the process. As the schematic side view in Figure 1 shows, this PGM machine is comprised of three main elements:

1- The lower base which includes the lower mold chamber, the push rod attached to a leadscrew driven by a servomotor, and a cylindrical glass tube outside the lower mold chamber. The cylindrical glass tube is raised and lowered outside the lower mold chamber using the two air cylinders installed on the bottom of this glass tube. When the glass tube is raised, the molding environment is isolated from the room

conditions as the chamber is closed, and the interior can be filled with an inert gas or other gas such as nitrogen to prevent oxidation of the mold surfaces.

2- The upper base which includes the upper mold chamber, the force transducer, and the copper tubing connecting the mold chamber to the induction heating system unit.
3- The induction heating system (IHS) which is used to heat the mold and glass sample under test.

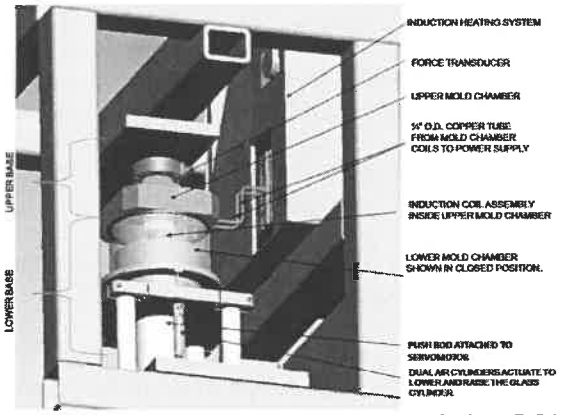

FIGURE 1. Schematic side view of the PGM machine (Moore Nanotechnology LLC [4]).

FRICTION TEST EXPERIMENTAL SETUP

To measure the friction forces versus displacement, the PGM machine was modified to collect data and determine the friction coefficient at elevated temperatures.

To conduct friction measurements at elevated temperatures required the mold setup to be modified and then manufactured. The design again has two parts: the top and bottom section. The top section was installed in the upper mold chamber and the bottom section in the lower mold chamber.

However, unlike conventional molding, the new upper and lower portions were designed so that the contact surface between the samples under test are in the vertical plane and parallel to the actuation direction of the machine's actuator, which will be used to cause relative sliding motion between them. Separate systems are provided to create a constant normal force between the sliding surfaces. To insure balanced loading, the apparatus was designed to always simultaneously test two samples arranged 180° apart on the upper section.

Based on these requirements and constraints and using SOLIDWORK and ABAQUS, the components of the friction test apparatus were designed as shown in Figure 2 and Figure 3 for the top and bottom sections respectively. As Figure 2 shows, the top section includes a fixture holding the metal mold sample. An induction coil surrounds the upper cylindrical part of the mold that is attached to the top platen by six Inconel screws.

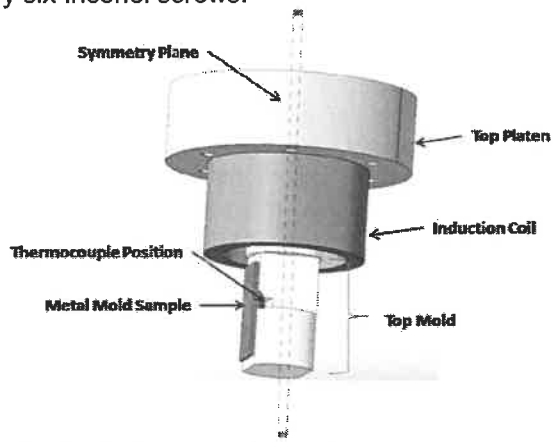

FIGURE 2. Top section assembly.

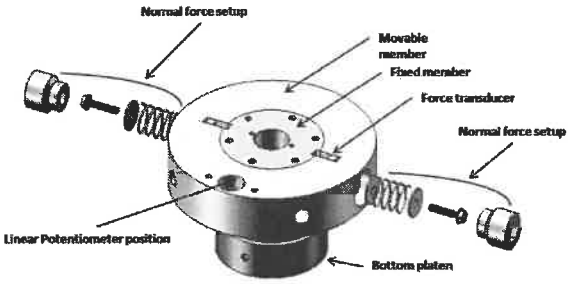

FIGURE 3. Bottom section assembly.

The bottom section consists of a fixed and a movable part to guarantee easy attachment and alignment of the sample and measurement equipment, i.e. the glass piece, thermal insulator, and force transducer, inside the assembly. The former is attached to the bottom platen with the movable member encircling it. The movable member is seated after inserting the friction measurement equipment. Finally, a washer, spring and set screw are attached to the movable fixture to guarantee the perpendicular alignment of the entire system. Normal forces between the samples under test are measured by two miniature load cells that are loaded through a spring and adjusting screw assembly. A linear potentiometer (not shown in the figure) is attached to the movable fixture to measure

the displacement between the bottom mold and the top mold which is fixed.

PROCESS PARAMETERS AND MOLD CONDITIONS USED IN THIS STUDY FOR FRICTION MEASUREMENT BETWEEN A PAIR OF POLISHED AND COATED WC AND BK7 GLASS

After validating the machine functionality, a set of trials using a polished and coated WC-BK7 glass pairs were conducted at different elevated temperature. The WC molds were EMT 100NG grade which has the grain size of less than 0.8 µm from Extramet Inc. For all these tests, the normal force was adjusted to 100N and the feed rate to 1 mm/min. The room temperature was 22 ±1°C and the molding chamber was purged with UHP Nitrogen to avoid mold surface oxidation. The mold surfaces were polished (with the surface roughness less than 50 nm) and coated (TiAlN-CrN-S4) while the BK7 had a surface finish of 2nm. Before each test, both surfaces of glass and mold were cleaned with acetone, ethanol, and isopropanol to be sure there was no contamination between glass and mold. The typical temperature and position vs. time profiles used for these tests are shown in Figure 4. In this figure, the actual measured temperature on the back of molds is shown by a red line while the commanded temperature (green line) was set to 577°C. The position vs. time is shown by the solid black line.

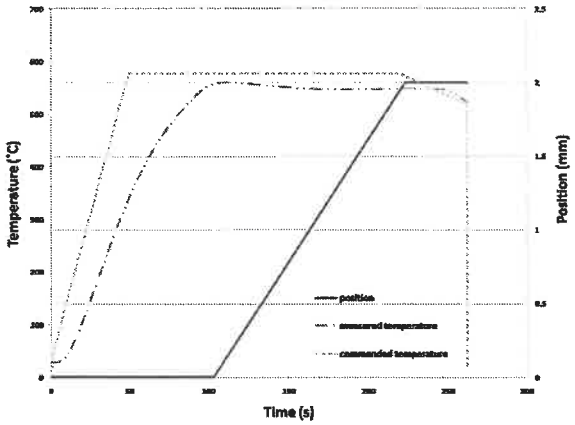

FIGURE 4. Typical temperature and position profile for friction test.

THE FRICTION FORCE BETWEEN POLISHED AND COATED WC-BK7 PAIR AT CONDITIONS SIMILAR TO GLASS MOLDING PROCESS

A set of tests at different elevated temperature were conducted and the results are shown in Figure 5. These curves clearly show that the friction force is increasing with increasing temperature. This may be related to the visco-elastic behavior of BK7 at elevated temperatures. Friction is related to the mechanical interlock between two bodies and glass properties vary substantially with temperature, as described in reference [5]; the friction force is strongly dependent on temperature.

Also, at temperatures close to the glass transition temperature, Tg, which is 557°C for BK7, the glass exhibits a viscoelastic response to applied loads while WC is in the elastic regime. This glass viscoelasticity introduces time dependent response to the dynamic friction data; meaning that the feed rate of the test can affect the measured frictional load.

Stick-slip was not observed on any of these tests since the molds used for them have high surface finish and are coated to prevent chemical interaction between the glass and mold surface, and are conducted in an atmosphere of UHP Nitrogen.

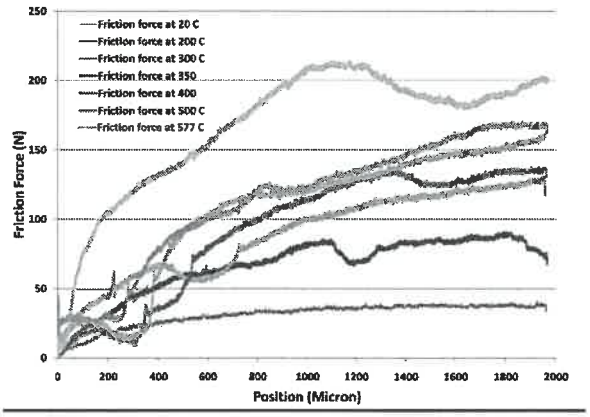

FIGURE 5. Frictional force generated between a pair of polished and coated WC-BK7 at 20, 200, 300, 350, 400, 500, and 577°C.

To evaluate the repeatability of the friction test at temperatures close to Tg, multiple tests for coated and polished WC-BK7 pairs were conducted at 560°C and the results are shown in Figure 6. The repeatability results show that the change in friction force is less than 30 N which is 20% of maximum friction force.

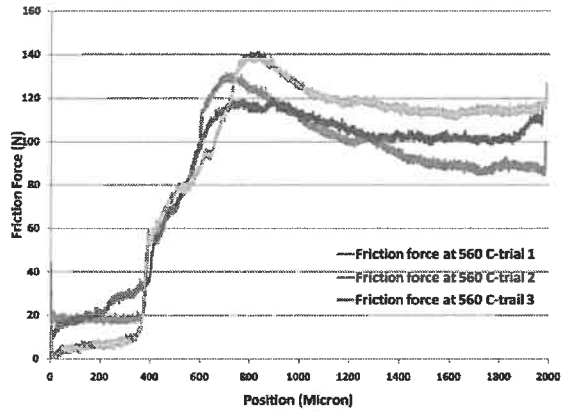

FIGURE 6. Frictional force generated between a pair of polished and coated WC-BK7 at 560°C for three trials with same process parameters at the same conditions.

Dividing the friction force by the normal force, which is 100 N on each side, gives the instantaneous normalized friction coefficient data. These data are plotted in Figure 7 and they show that in the worst-case scenario, the normalized friction coefficient ramps up to 0.7 and then levels off at around 0.6. There is a smooth transition between static and dynamic friction.

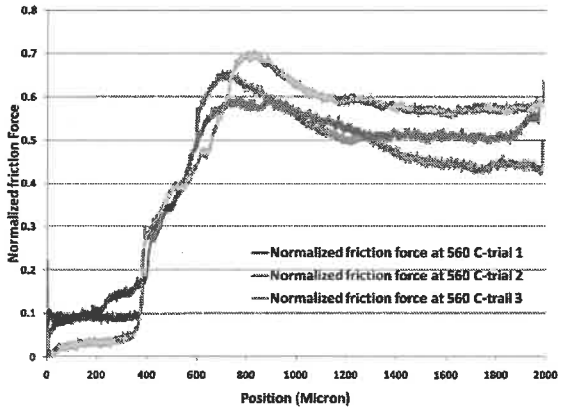

FIGURE 7. Friction Coefficient from FIGURE 6.

CONCLUSIONS

In the PGM process, which takes place at temperatures close to Tg, sliding frictional forces are generated at the interface between the glass/mold surfaces, and these forces affect the final shape and internal stress distribution of the molded lens. Accurate simulations of the PGM process require good models of the frictional behavior at elevated temperature. The lack of such data in the literature motivated the development of the apparatus described here for experimental measurement of the friction behavior between glasses and mold materials under conditions similar to those for the PGM process.

Increasing the temperature in the mold/glass interface causes the friction force to increase. Any other process parameter that indirectly results in temperature change between glass and mold at the interface also can change the local viscosity of the glass and subsequently the frictional data.

The friction coefficient between a polished and coated WC mold and BK-7, which is a typical material for glass molding, and in conditions similar to those used in the PGM process ramps up to 0.7 and then levels off around 0.6.

ACKNOWLEDGMENTS

The authors would like to thank Moore Nanotechnology LLC for providing the PGM machine used for this study. Special thanks to Dr. Kathleen Richardson for providing laboratory equipment for glass characterization and space for the molding machine in the Advanced Materials Research Lab.

REFERENCES

[1] Sellier, M., et al., An iterative algorithm for optimal mould design in high-precision compression moulding. Proceedings of the Institution of Mechanical Engineers, Part B: Journal of Engineering Manufacture, 2007. 221(1): p. 25-33.

[2] Klocke, F., et al., Finite element analysis of glass moulding. Proceedings of the Institution of Mechanical Engineers, Part B: Journal of Engineering Manufacture, 2008. 222(1): p. 101-106.

[3] Mosaddegh P., Friction Measurement in Precision Glass Molding, PhD dissertation, 2010.

[4] Http://www.nanotechsys.com/

[5] Shelby, J.E., Introduction to Glass Science and Technology. 2nd ed. 1997: The Royal Society of Chemistry.

DESIGN, FABRICATION AND TESTING OF A HIGH PRECISION PIEZO-ACTUATED AIR AMPLIFIER AS AN ION FOCUSING DEVICE IN MASS SPECTROMETRY

Guillaume Robichaud[3], R. Brent Dixon[1], Amarnatha S. Potturi[2], Jack R. Edwards[2], Alex Sohn[3], Thomas A. Dow[3], David C. Muddiman[1]
[1]Chemistry, W.M. Keck FT-ICR Mass Spectrometry Laboratory
[2]Mechanical and Aerospace Engineering,
[3]Precision Engineering Center
North Carolina State University,
Raleigh, North Carolina 27695

INSTRUCTIONS

Mass spectrometry is an analytical method widely used by chemists and biologists to determine the presence or the abundance of specific molecules and proteins in a sample. Capability to detect very low concentrations of a molecule is often critical in applications such as finding cancer biomarkers in blood samples. To identify molecules in a mass spectrometer, they must be ionized and put into a gas phase. Electrospray ionization [1] has gained prominence over the last decade and it the method of choice to produce multiply charged analyte ions. Although the electrohydrodynamic process responsible for producing individual gas phase ionized molecule from a charged droplet is not fully understood, it is estimated that less than 1% of the gas phase ions that have been created will be successfully captured by the mass spectrometer.

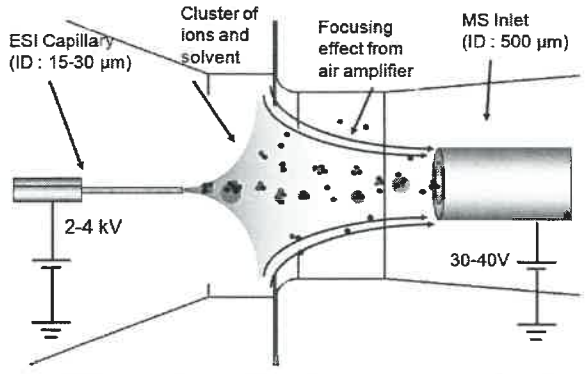

FIGURE 1. Clusters of ions and charged droplets are ejected from the ESI capillary, mainly due to the applied electrical field. Solvent evaporates and gas phase ions are desorbed from the clusters. Scattering ions are then focused by air amplifier toward the inlet of the mass spectrometer (on the right).

This inefficiency is due to the coulombic repulsive force scattering the ions of same polarity away from each other. The air amplifier shown on Figure 1 can refocus the scattered ions and increase the abundance of the captured ions [3-6]. However, very little is known about the effect of the geometry of the amplifier on its performance. A multidisciplinary effort to design, fabricate and test a precision engineered, diamond turned air amplifier with a piezo-actuator to control the annular gap.

DESIGN

Proof of concept showing signal improvement using an air amplifier has been made using a crude commercial device. It was found that imprecise gap control and misalignment were impacting the performance and repeatability of the results. With the collaboration of NCSU's Aerospace Engineering CFD Laboratory, a suitable aerodynamic profile has been established. The air amplifier relies on the Venturi and the Coanda effects to focus the scattering ions. The Coanda effect describes the formation of a thin boundary layer of fluid along a curved surface. The Venturi effect is based on Bernoulli's Principle where a reduced pressure region is created from the conversion of a high pressure gas (in this case) to a high velocity jet. The velocity profile plot presented in Figure 2 illustrates this phenomenon and provides more details on the geometry of the proposed device. According to the CFD model, the ideal annular gap was in the range of 50-70 µm and to ensure a uniform and radially symmetrical flow, the annular gap faces had to be parallel to < 1 µm. The finish of the Coanda surfaces had to be smooth and radially symmetric. Because the optimal annular gap was to be set experimentally, the gap is controlled with three D1CM20 piezoelectric

actuators from Kinetic Ceramics. Preload of the actuators is done using Belleville washers. Preload is sufficient to keep the piezo-stacks in compression plenum is pressurized at 45 psi (max operating pressure).

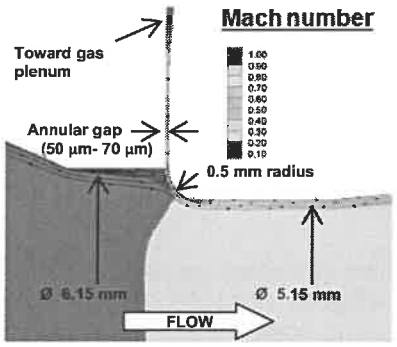

FIGURE 2. Enlarged section view of the Coanda profile and the annular gap region of the air amplifier. Coanda effect is the tendency of a fluid to stay attached to a smooth surface. Velocity profile plot from CFD models shows the pressurized (N_2) from the plenum accelerate as it decompresses and remains attached to the Coanda profile.

The top and bottom inserts were designed to be interchangeable items so that other profiles can be tested without fabricating an completely new device. The air amplifier was fabricated in aluminum 6061-T6, selected for its machinability and resistance to chemical corrosion (ESI involves organic solvent solutions). A section view of the device is presented on figure 3.

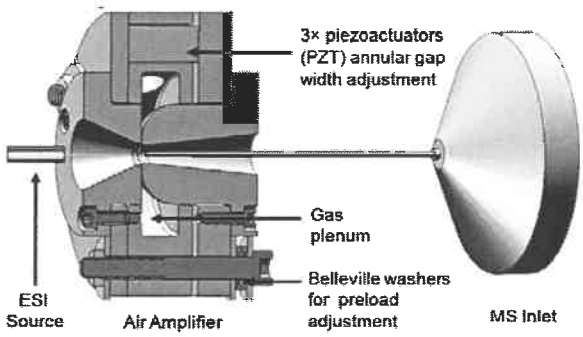

FIGURE 3. Section view of the air amplifier. Annular gap can be changed from 50 µm to 70 µm using three piezo-actuators.

FABRICATION

The components for the air amplifier were rough machined at a local CNC shop. The geometric and dimensional tolerances for the rough part machining were designed to ensure that enough material would remain to perform final diamond turning for dimensional accuracy and surface finish. This final machining was performed at the PEC using a precision lathe (ASG 2500 from Rank Pneumo) and a single crystal diamond tool. The in-house controller of the diamond turning machine has a resolution of the tool position on the order of 0.01µm

To create uniform flow around the air amplifier, the mating surfaces have to be parallel and concentric and the variation in the assembled gap has to be small compared to the desired 50-70 µm value. To machine a specific diameter, the location of the tool edge must be known with respect to the rotational center of the spindle. To get a specific length, the tool edge must be known with respect to some fiducial surface. Efforts were made to determine the tool location using tool centering techniques developed at the PEC [2] and in conjunction with the slide encoder, the OD and ID of parts could be produced to high fidelity. To ensure the desired gap, the OD was machined first and 1 µm steps were removed on the ID until parts could be assembled, guaranteeing a maximum misalignment of 1 µm for both the top and bottom insert.

The annular gap between the top and bottom of the plenum cannot be measured directly because it is not accessible once the parts are assembled. Indirect measurements were performed to set the nominal gap to 50 µm. For the axial machining, all parts were machined to their nominal dimension except for the top insert mating face. Parallelism between faces and flatness of each part were measured with a Gage 2000 Coordinate Measurement Machine (CMM) from Brown & Sharpe and maintained below 3 µm.

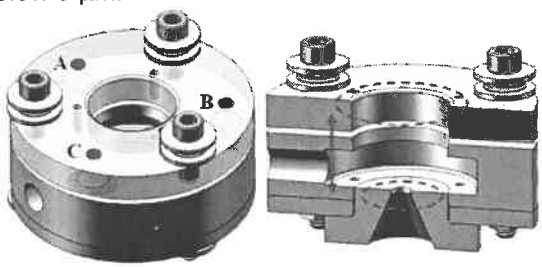

FIGURE 4. Indirect measurements performed with CMM to adjust parallelism. Left : distance between plane and point above pzt (see Table 1). Right : Plane-Plane parallelism and distance.

TABLE 1. Perpendicular distance between plane and point above pzt as shown on Figure 4.

PZT	Before Correction	Shim Used	After Correction
A	26.333	1	26.352
B	26.332	2	26.350
C	26.348	0	26.351

All parts were assembled except for the top insert. Parallelism between mating face of the top insert and the annular gap bottom face was then adjusted. Because height of the PZT stacks are part of the measurement chain defining the annular width and that this dimension can vary by more than 10 µm, 13 µm (0.0005 in) SS shims are used on top of PZT to correct the resulting parallelism error between the two faces. These critical measurements are presented in Figure 4 and results before and after shimming are presented inTable 1. In Figure 5 is presented the relation between the voltage applied to the PZT stacks and the plane-plane distance. After level correction, an out of parallelism of 2 µm at top insert bolting radius will result in an out of parallelism of 0.5 µm between the two annular gap faces, which satisfies the design criteria of 1 µm established earlier.

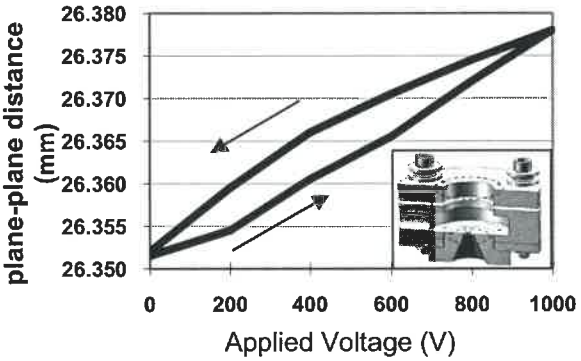

FIGURE 5. Plane-plane distance between bottom face of annular gap and mating flange of top insert vs voltage applied to PZT. These results were used to determine nominal height of top insert (50 µm at 0 V) and to calculate indirectly the annular gap as a function of applied voltage.

Crititical surfaces of Coanda profile has finally been inspected to make sure that there was no abrupt transition.

RESULTS

When pressurized, the air amplifier successfully created a Venturi effect and static pressure has been measured along the flow axis for different pressure and annular gap position using a pitot tube. From Bernouilli's relation for an adiabatic gas, the the pressure drops as the velocity of the fluid is increased. The maximum vacuum pressure was measured 1 mm downstream of the annular gap, revealing the existence and location of a focal point. Moreover, increasing the annular gap width had the same effect on the flow profile as increasing the plenum pressure.

Stagnation pressure measured at the outlet of the air amplifier using an open ended pitot tube was used to compare the flow profile along the radial line and evaluate its symmetry. A clear improvement in the symmetry of the radial has been obtained with the precision engineered air amplifier when compared to the commercial device in Figure 6.

A second iteration of the air amplifier has been designed and fabricated. Although the outlet cone of the device is shorter to allow a more compact design, the Coanda geometry and the aerodynamic profiles are exactly the same. This iteration does not have piezoelectric actuators and has a fixed gap of 50 µm. Analysis of static pressure profiles demonstrated that reproducible results could be obtained and therefore fabrication procedure allow the production of identical devices (result not included).

Several mass spectrometry experiments were performed to evaluate the effect of the air amplifier on the signal abundance. The mass spectrometer signal obtained without any air amplifier was compared to the signal obtained with the air amplifier. To systematically explore the experimental space defined by the many variables that can affect the performance of the air amplifier (position, plenum pressure, annular gap width, solvent composition, ESI voltage, etc), fractional factorial design was used to find the significance of each. The results showed that signal improvement could not be obtained under all condition but were significant at higher solvent flow rates and larger ESI capillary tips (up to 34 folds of improvement in this case [7]). Mass spectrometry tests to be performed with 2nd iteration of the device will serve to better explore this specific zone of the experimental space.

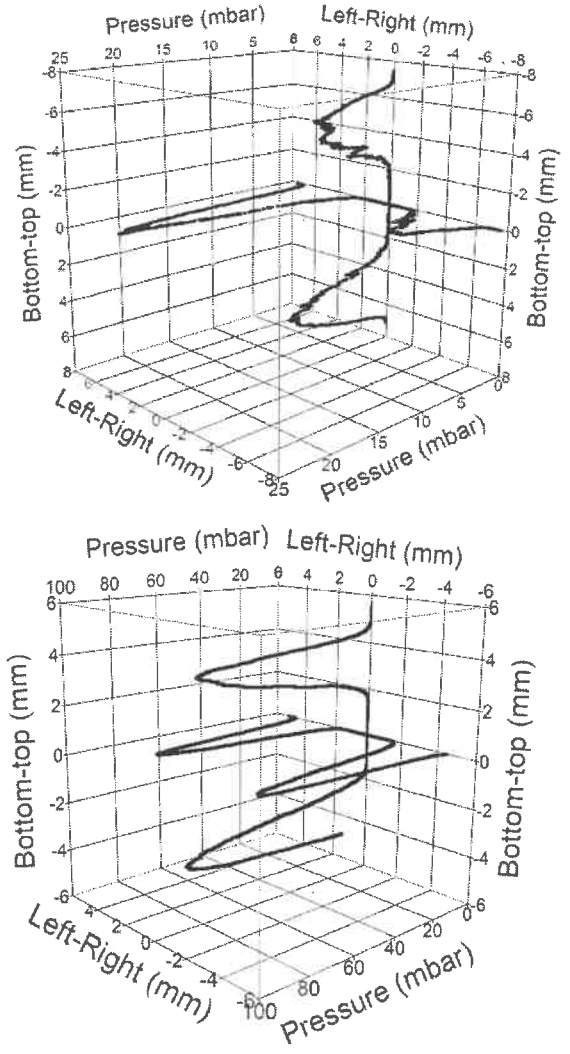

FIGURE 6. Comparison of stagnation pressure along the radial line at the exit of the air amplifier (top: old device, bottom: new air amplifier). Radial symmetry, hence the capability of obtaining a precise aerodynamic focal point is improved with the precision engineered device when compared to the threaded commercial version.

CONCLUSION

Tests performed on the air amplifiers showed that the design and fabrication of a high precision air amplifier with adjustable annular gap has been successfully achieved. Air flow measurements correlated with the CFD model and it was demonstrated that radial symmetry had been improved significantly leading to more precise focusing capability. Although experiments on mass spectrometry instrument have shown improvements under specific operating conditions, a better understanding of the effect of air amplifier on the mass spectrometer is now possible since a improved control on the device quality has been achieved.

REFERENCES

[1] Fenn, J. B.; Mann, M.; Meng, C. K.; Wong, S. F.; Whitehouse, C. M., Science 1989, 246, (4926), 64-71.

[2] Sohn A., Diamond Tool Centering for Cylindrical Turning, Proceedings of Annual Meeting of the ASPE, Vol 47, 2009, pg 435-437.

[3] Hawkridge, A. M., Zhou, L., Lee, M. L., Muddiman, Analytical performance of a venturi device integrated into an electrospray Ionization Fourier transform ion cyclotron resonance mass spectrometer for analysis of nucleic acids D. C., Anal. Chem. 2004; 76: 14, 4118-4122.

[4] Yang, P. X.; Cooks, R. G.; Ouyang, Z., Hawkridge, A. M.; Muddiman, D. C., Gentle Protein Ionization Assisted by High-Velocity Gas, Flow Anal. Chem. 2005; 77, (19), 6174-6183.

[5] Dixon, R.B., Muddiman, D.C., Quantitative comparison of a flared and a standard heated metal capillary inlet with a voltage-assisted air amplifier on an electrospray ionization linear ion trap mass spectrometer Rapid Commun. Mass Spectrom. 2007; 21: 19, 3207-3212.

[6] Dixon, R.B., Hawkridge, A.M., Muddiman, D.C., Probing the Mechanisms of an Air Amplifier Using a LTQ-FT-ICR-MS and Fluorescence Spectroscopy, J. Am. Soc. Mass Spectrom. 2007; 18: 11, 1909-1913

[7] Robichaud G. et al., Design, Modeling, Fabrication, and Evaluation of the Air Amplifier for Improved Detection of Biomolecules by Electrospray Ionization Mass Spectrometry, Int. J. Mass Spectrom. 2010; in press.

DESIGN OF A MONOLITHIC CYLINDRICAL FLEXUREFOR PRECISION LINEAR MOTION GUIDANCE

Maria J. Telleria[1], Martin L. Culpepper[1] and David Weitz[2]
[1]Department. of Mechanical Engineering
[2]Lincoln Laboratory
Massachusetts Institute of Technology
Cambridge, MA

ABSTRACT

We present design rules for a cylindrical flexure (CF) that is based upon the double four bar flexure concept. These rules enable understanding of how to best achieve functional requirements with few tradeoffs. The CF concept is useful as it is (1) symmetric and therefore thermally insensitive, (2) adjustable which enables error correction, (3) easily assembled with other cylinder-shaped elements (dampers, actuators, etc...), which is useful for co-axial assemblies that are common to optics, and (4) easily made in volume with low-cost tube stock via conventional machining processes.

We have fabricated a prototype CF for a Fourier Transform Spectrometer (FTS) application. The CF guides the motion of a scanning mirror with constant velocity along a line with low tip/tilt error. Understanding general design rules and tradeoffs is important as a larger linear range increases FTS resolution, while reducing tip/tilt error yields lower errors in the collected data.

INTRODUCTION

Overview of Fourier Transform Spectrometry

A FTS measures spectral components of incident radiation. Applications of long-wave infrared FTS include hyperspectral imaging of chemical plumes for early warning of accidental or deliberate releases. Lincoln's latest design consists of a Michelson interferometer. The moving mirror's translational motion, in one arm of the two-arm interferometer, modulates the incident IR radiation. Demodulation via a Fourier transform provides the spectral information content of the incident radiation. The mirror must translate at a constant velocity in forward and reverse linear-motion sweeps when data is collected. The optic reverses course at each end of the sweep (when no data is collected). The linear motion is required over several centimeters and this must occur with tip and tilt errors of a few tens μradians or less [1].

Flexure concept

Our concept is an adaptation of the double four bar that is shown in Figure 1A. The arcuate motions of the four bars elements cancel other out, thereby yielding nominal linear motion [2].

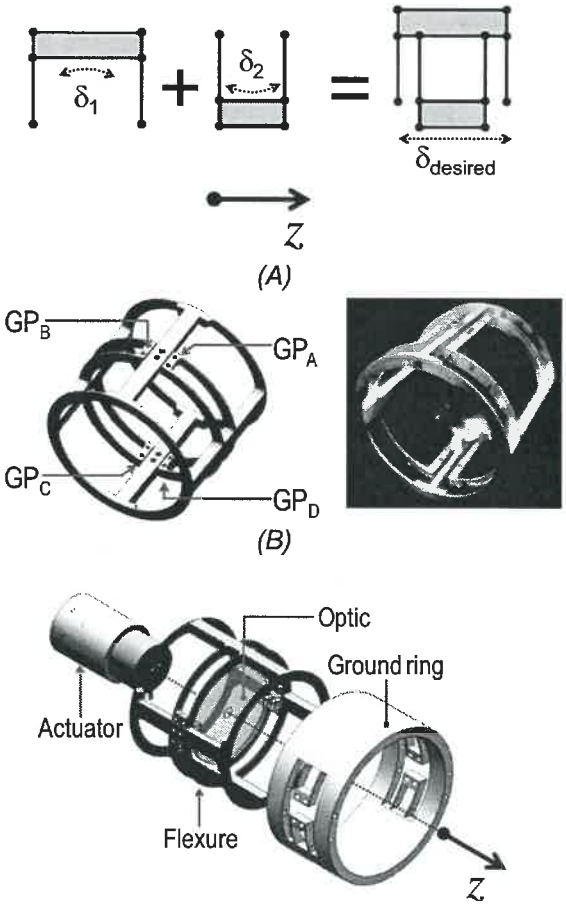

FIGURE 1. Planar four bar linear motion flexure (A) and cylindrical adaptation (B) and FTS system which uses cylindrical flexure (C)

A cylindrical embodiment is shown in Figure 1B. In the figure, GP denotes the locations at which the flexure is grounded. The non-grounded

components of the flexure are able to move parallel to the axis of the cylindrical geometry. The flexure will be integrated with the main FTS system components as shown in Figure 1C. The requirements for the FTS mechanism are listed in Table 1.

TABLE 1. Functional/Application Requirements.

Requirement	***Value***
Minimum range (cm)	1.00
Maximum tip error (μradian)	± 10.0
Maximum tilt error (μradian)	± 10.0
Volume (cm^3)	12x10x7

Error correction

Tip and tilt misalignment will occur due to fabrication and assembly errors. These errors may be corrected by adjusting the ground points of the flexure. As shown in Figure 1C, the design includes a ground ring to which the flexure ground points are attached. The ground points may be adjusted by screws along the axis of the tube. This adds a corrective angular displacement that removes tip and tilt errors.

The need for general design rules

Prior art are deals with specific uses, for example (i) torsion couplings, (ii) linear guidance flexures [Trumper et. al] and (iii) rotary flexure bearings [3-4]. These examples illustrate the utility of CFs in specific application. Our purpose is to uncover the general design rules that enable rapid engineering of the flexures for a broad range of applications. We first recognize that there is a variety of CFs that must first be categorized. In those whose flexures lie perpendicular to the cylindrical axis, such as the CF presented here, the curvature of the CF fundamentally changes the interaction between the flexing members.

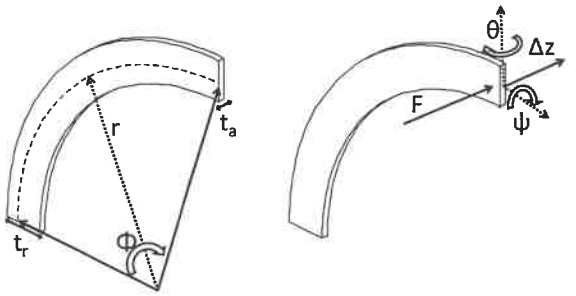

FIGURE 2. Curved beam labels, loading conditions, and resulting displacements.

The curvature impacts the (i) number of relevant design/geometry parameters, (ii) effective constraint direction therefore some constraint-based rules for planar/strain flexures do not apply and (iii) stress distribution in the beam which causes behavior to differ from that of the simpler straight beam. The moments generated in a flexure cause deformation and therefore motions that are not expected when designing planar flexures. For example, as shown in Figure 2, when the flexure is loaded normal to the plane of curvature the beam translates along the cylindrical axis, Δz, twists, θ, and rolls, ψ.

Figure 3a shows that for a given length (or rΦ) the range of a curved flexure decreases with increasing sweep angle, Φ. The graph plots a ratio of range of the curved beam to the range of a straight beam of the same length and other dimensions. In applications the CF's volume will often be limited and therefore it is not feasible to use small sweep angles. Figure 3b shows that the range of a curved beam increases with increasing sweep angle given a fixed radius.

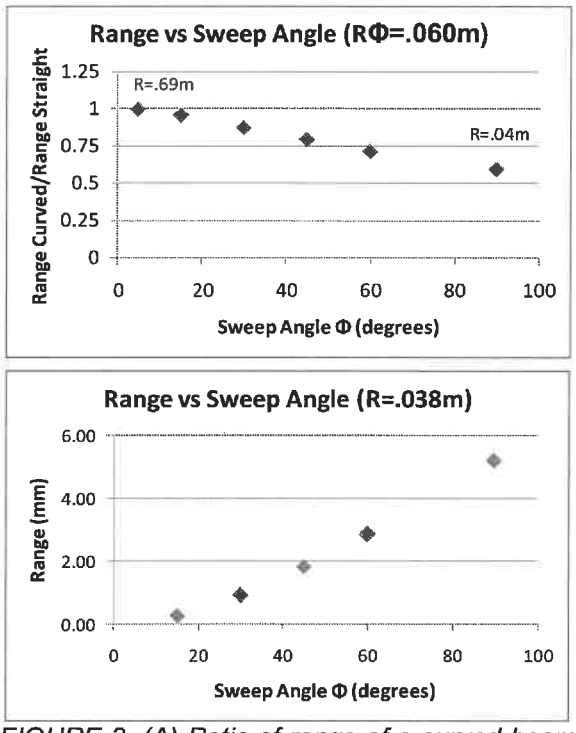

FIGURE 3. (A) Ratio of range of a curved beam to the range of a straight beam vs. sweep angle for a given beam length, (B) Range of a curved beam vs. sweep angle for a given radius.

The effects of curvature result in new issues/parameters that (i) must be addressed in

the design and (ii) require different perspective and modeling approaches to deal with them. A full, general understanding will require several years. In our work so far, we report on rules and insights that we found for the parallel four bar CF.

PROTOTYPE FABRICATION

The prototype CF for the FTS application was fabricated out of 7075 Aluminum using a 4th axis Mazak lathe. The actuated tool holders were used to mill pockets out of a tube of aluminum stock. A holder secured the stock ends between two flat plates. A .25mm thick web was left at the bottom of the pockets to keep the flexures from vibrating.

Other possible fabrication methods include a waterjet with a rotary axis, a 5-axis wire EDM, and a laser cutter with a rotary axis. In laser cutting the parts may have to be heat treated post processing.

FINAL PROTOTYPE DESIGN

To demonstrate the feasibility of fabrication of the double four bar CF a prototype was machined. Table I lists the dimensions of the prototype, these were dictated by volume and range constraints.

TABLE I. Nominal flexure geometry.

L [cm]	ID [cm]	OD [cm]	tr [mm]	Φ [deg]	Range (mm)
76.2	7.6	8.9	0.64	70	20

TESTING AND RESULTS

The tip and tilt of the prototype CF was tested using the experimental setup shown in Figure 4. A stainless steel shim disk representing the future optic was attached to the flexure's translating stages using a piece of aluminum stock. Three capacitance probes were used to measure the tip and tilt of the disk. Capacitance probes were used because of their resolution which allowed us to measure down to 5 μradians. The tip and tilt of the flexure was measured at different points of the full range. Each tip/tilt measurement corresponds to the error over a 0.051 mm step. Figure 5 shows the averaged measured tip/tilt of the flexure over three trials. The error bars correspond to the resolution limits of the capacitance probes.

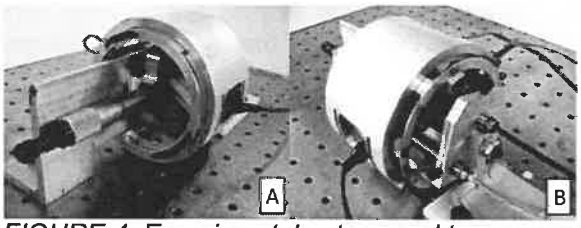

FIGURE 4. Experimental setup used to measure the tip/tilt of a stainless steel shim driven by the CF. (A) Loading using depth micrometer, (B) capacitance probes to record displacement.

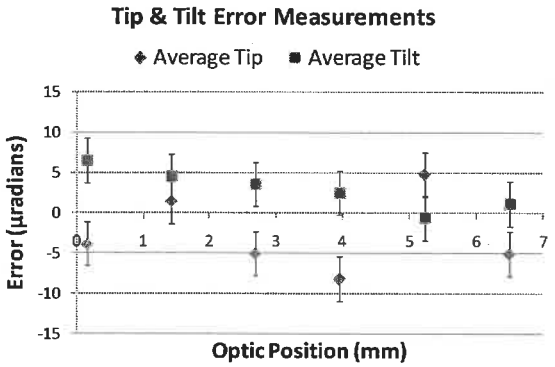

FIGURE 5. Averaged measured tip & tilt error for three trials. Each measurement corresponds to a .051mm step. Error bars indicate sensor resolution.

Future work will constitute of collecting more data on the tip and tilt errors over the entire range of the flexure. The error correction capabilities of the flexure will be used to center the error at zero. The measured tip and tilt are due to manufacturing and assembling errors.

FROM SIMULATION TO DESIGN RULES

The main requirements for our CF were range, volume, and tip/tilt error. Given a set volume we have shown that larger sweep angles yield larger ranges. This is simply because the length of the beam increases with sweep angle for a given radius. The range is also constrained by the spacing of the flexures. The distance between the inner and outer flexure of the four bar should be set to act as a mechanical stop to prevent yield. FEA was used to explore the effect of the flexure spacing on the CF's error correction capability as well as its frequency response.

Figure 6 shows that the 3rd through 5th frequency modes of the CF increase when the spacing ratio (SR) increases. The SR compares the

distance between the inner flexures to the distance between the inner and outer flexures. The 1st and 2nd frequency mode shapes result from the side stages translating along the cylindrical axis. These frequency modes can be mitigated using a damping material between the CF and the grounding ring.

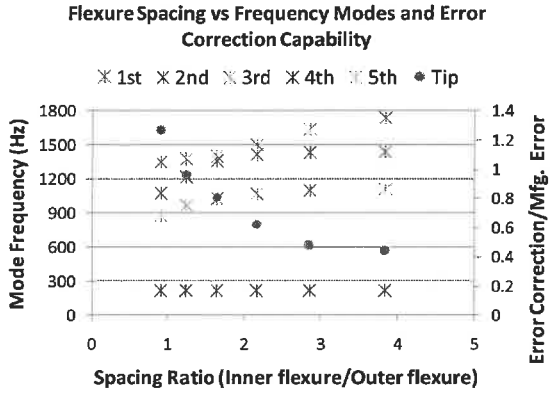

FIGURE 6. FEA calculated effect of the flexure spacing ratio on the frequency response of the CF and on its tip error correction capability.

Figure 6 also shows that the tip error correction capability of the CF decreases with increasing SR. The error correction is graphed at the ratio of the error correction to the manufacturing error. The tip manufacturing error is the result of a worst case scenario in which all the top half flexures of the CF were machined to be .25mm thinner in the axial direction.

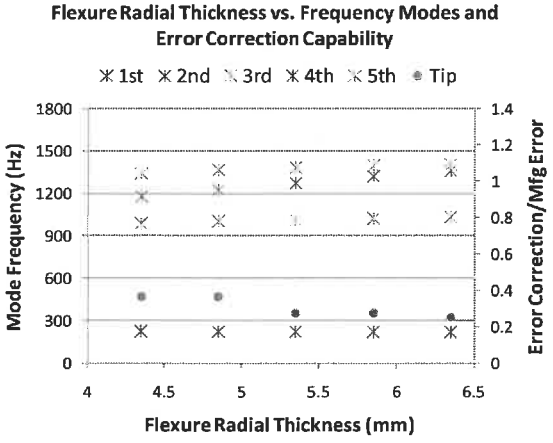

FIGURE 7. FEA calculated effect of the flexure radial thickness on the frequency response of the CF and on its tip error correction capability.

The effect of the flexures' radial thickness, t_r, was analyzed to provide another parameter with which to tune the CF's performance. Figure 7 shows that increasing the t_r increases the 3rd through 5th frequency modes, but decreases the error correction capability.

The radial thickness is limited given minimum beam dimensions as well as volume constraints. It can be used in conjunction with the spacing ratio to tune the performance of the CF.

FUTURE WORK

For the FTS project our next steps will involve more data collection and demonstration of the error correction capability of the flexure. The design rules we have developed have highlighted the importance of the spacing between the flexures. The next prototype will be designed using these rules to improve the error correction capability. The frequency response of the flexure will become important as we begin to consider the deployment of these CFs into field and space FTS.

Our future work will continue our goal of developing design rules for the rapid engineering of CFs. These rules will exploit the advantages of cylinder based geometry and mitigate the disadvantages. First is to develop a classification for CFs so that then we can determine which rules apply. We are currently working on a mathematical model for the double four bar CF. Our focus will be to devise an easy way for the designer to determine the stiffness matrix of the CF and thus how it will behave.

REFERENCES

[1] Griffiths P. R., De Haseth J. A., 2007, *Fourier transform infrared spectrometry, 2ed*, Wiley-Interscience, Hoboken, N.J., pp. 108-109.

[2] Alexander H. Slocum, Precision Machine Design, Prentice-Hall, 1992.

[3] Ljubicic, D.M., "Design and Analysis of a Monolithic Flexure Atomic Force Microscope", Master's Thesis, MIT, 2008.

[4] Luo, H.P., Zhang, B., and Zhou, Z.X., "A rotary flexural bearing for micromanufacturing," CIRP Annals-Manufacturing Technology, Vol. 57, 2008, 179-182.

ACTIVE REDUCTION OF STATIC DEFORMATION IN A MOVING MAGNET PLANAR ACTUATOR

J. Achterberg, C.M.M. van Lierop, P.P.J. van den Bosch
Department of Electrical Engineering
Eindhoven University of Technology
Eindhoven, The Netherlands

INTRODUCTION

In the semiconductor lithographic industry planar actuators are used to replace xy-drives in waferstages. The ironless permanent magnet planar actuators considered in this paper combine longstroke motion in both the x and y direction into a single stage, with the mover electromagnetically levitated. Although the moving coils topology is being applied nowadays, the obtainable accuracy is limited due to the errors caused by power supply cables and cooling hoses. Since the moving magnet topology is completely wireless, it does not suffer from this problem. However, this commutation uses the applicability of a dual stage concept. Therefore, the total accuracy should be obtained for a single stage moving magnet planar actuator.

Many moving magnet type actuators [1][2][3] consist of a permanent magnet array with quasi Halbach magnetisation, to focus the magnetic field on one side. This Halbach array experiences large repelling forces among the individual magnets, which deform the translator[4]. To limit the deformation a stiff structure is connected to the magnet array. For higher acceleration profiles it is desired to lower the mass of the translator and, consequently, decrease its stiffness.

A less stiff structure will experience larger deformations by both static Halbach forces and dynamic excitation forces. This paper will focus on the static forces, and how to actively reduce them by making further use of the redundancy in the coils. This redundancy is necessary in moving magnet actuators in order to enable longstroke motion.

ACTUATOR CONFIGURATION

Various topologies exist for moving magnet actuators but most of them use permanent magnet arrays with quasi Halbach magnetisation for the mover and a coil array structure with a dedicated pattern for the stator. Existing coil structures are among rectangular coils in a herringbone pattern[2], a three coil basketweave pattern[1] and circular coils in a square grid[3].

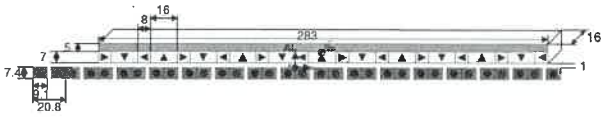

FIGURE 1. 3 DoF Topology (dimensions in mm).

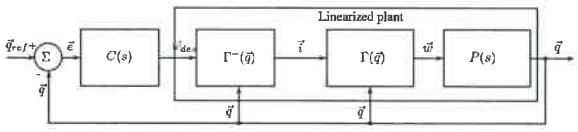

FIGURE 2. Planar actuator control structure with $\Gamma(\vec{q})$ the position dependent coupling matrix and $P(s)$ the rigidbody dynamics, $\vec{w}$ the wrench vector and $\vec{q}$ the position and rotation vector

For ease of presentation and verification of the method, this paper will focus on a three Degree of Freedom (DoF) simplification, the actuator comprises only one strip of magnets in a Halbach configuration and a row of rectangular coils that are assumed infinitely large. Furthermore, the forces orthogonal to the directions of actuation are also neglected, only forces in the x and z direction and one torque around y are considered (see Figure 1).

Let it be noted, however, that the method presented in this paper is not limited to three DoF and can easily be extended to six DoF.

DIRECT WRENCH DECOUPLING

Moving magnet planar actuators have an intrinsic redundancy in the coupling of coil currents to wrench (force and torque) components due to the need for longstroke motion. This coupling depends nonlinearly on the position. Therefore, to apply linear control this electromagnetic position dependency has to be decoupled from the mechanical Linear Time Invariant (LTI) dynamics.

The decoupling, i.e. commutation, is achieved by using a model of the coupling of coil currents with the wrench (forces and torques) vector. For a

given position this coupling can be inverted, resulting in the required decoupling. Notice, however, that because of the redundancy in the coupling a lot more coils than the number of considered wrench components are used. Consequently, the inverse of the coupling has to be a generalised inverse. Which results in a weighed minimisation of the coil currents. This is illustrated in Figure. 2, which shows the control scheme, where the position dependent coupling is denoted by $\Gamma(\vec{q}_p)$ and the corresponding decoupling by $\Gamma^{-}(\vec{q}_p)$.

$$\Gamma(\vec{q}_p) = \left[\vec{\gamma}_{c_1}(\vec{q}_p)\ \vec{\gamma}_{c_2}(\vec{q}_p) \cdots \vec{\gamma}_{c_N}(\vec{q}_p) \right]$$

where the $\vec{\gamma}_{c_i}(\vec{q}_p)$ is the contribution of a current i_{c_i} through coil i to the wrench components depending on the position $\vec{q}_p$,

$$\begin{bmatrix} F_{xc_i}(\vec{q}_p) \\ F_{zc_i}(\vec{q}_p) \\ T_{yc_i}(\vec{q}_p) \end{bmatrix} = \vec{\gamma_{c_i}}(\vec{q}_p) i_{c_i} = \begin{bmatrix} \gamma_{F_x c_i}(\vec{q}_p) \\ \gamma_{F_z c_i}(\vec{q}_p) \\ \gamma_{T_y c_i}(\vec{q}_p) \end{bmatrix} i_{c_i}.$$

The weighed minimisation of the 2-norm of the coil currents, $\sqrt{\vec{i}^{\top}\Delta\vec{i}}$, is given by,

$$\arg\min_{\vec{i}} \|\vec{i}\|_{\Delta}$$
$$\text{s.t. } :\vec{w}_{des} = \Gamma(\vec{q}_p)\vec{i}$$

Which is solved by the generalised inverse[5], $\vec{i} = \Gamma^{-}(\vec{q}_p)\vec{w}_{des}$, where

$$\Gamma^{-}(\vec{q}_p) = \Delta(\vec{q}_p)\Gamma^{\top}(\vec{q}_p)\left(\Gamma(\vec{q}_p)\Delta(\vec{q}_p)\Gamma^{\top}(\vec{q}_p)\right)^{-1}$$

This property of those planar actuator topologies to have many more coils that have coupling with the translator than the degrees of freedom of the translator can be exploited to influence other features of the actuator. However, this will be at the expense of the efficiency, since the minimisation will have less freedom to minimise the coil currents.

DISTRIBUTED FORCE MODEL

Since the force distribution is needed to determine the deformation, another model needs to be used. It has to calculate the forces and torques acting at a single permanent magnet ($B_r = 1.24$ T) due to coil currents. This model was obtained by modeling the magnetic field of a single magnet by surface charges and calculating the Lorenz force at the conductors of the coil[4][6]. Figure 3 illustrates the x and z force components and the torque around y of an in z magnetised permanent magnet with a single coil as function of their relative x-displacement.

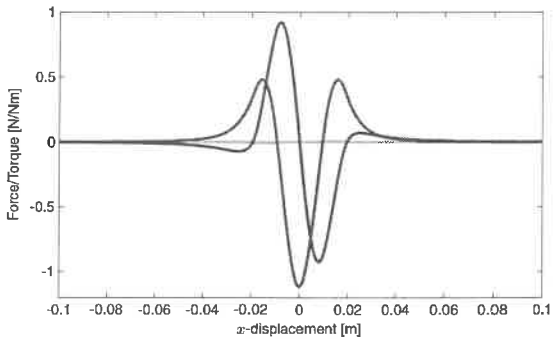

FIGURE 3. 3DOF Wrench at a in z magnetised permanent magnet due to a one Ampère coil current as a function of their relative displacement in x. F_x (blue) F_z (red) T_y (green)

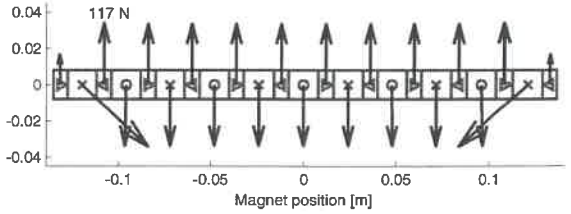

FIGURE 4. Static forces among the permanent magnets due to their Halbach configuration. The largest z-force is depicted above the vector.

The static Halbach forces obtained by the method of [4] are shown in Figure 4. The resulting deformation, obtained with the model which will be presented in the next section, for a strip of permanent magnets is shown in Figure 5.

DEFORMATION MODEL

The model used for calculating the deformation is based upon the Euler-Bernoulli beam equation[7], which yields the relation between the deflection $u(x)$ and the distributed load $q(x)$,

$$\frac{\mathrm{d}^4 u(x)}{\mathrm{d}x^4} = \frac{q(x)}{EI} = f(x),$$

where E is the elastic modulus and I the second moment of area. Only deflection in the z-direction is considered due to forces in the z direction.

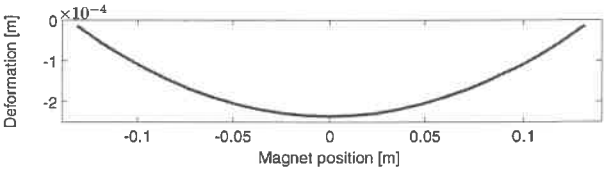

FIGURE 5. Deformation due to the magnet forces

ending of the stiffness structure, i.e. the um strip in Figure 1, is considered. The assumed to be piecewise constant due to ger stiffness of the NdFeB magnets. The that cause rigid body movement are sub- from the magnet forces, thus the resulting will only cause bending. To solve the Ordi- ifferential Equation (ODE), boundary con- corresponding to simply supported ends plied:

$$\left.\frac{u}{2}\right|_{x=\pm\frac{L}{2}} = 0, \quad \text{and} \quad u(x=\pm\frac{L}{2}) = 0.$$

a piecewise constant loading vector $f = {}_N\,]^\top$ is assumed, the solution to the ODE in rval of constant loading is known to be a order polynomial, $u_i = \frac{f_i}{24}x_i^4 + a_i x_i^3 + b_i x_i^2 + d_i$. For easy solving, the stiffness struc- divided in intervals of equal length, with mm magnets covering two intervals. The ients of the polynomials can be solved by ng suitable boundary conditions:

$$_{j=0} = u_i|_{x_i=1}, \quad \left.\frac{\mathrm{d}^2u_j}{\mathrm{d}x_j^2}\right|_{x_j=0} = \left.\frac{\mathrm{d}^2u_i}{\mathrm{d}x_i^2}\right|_{x_i=1},$$

$$= \left.\frac{\mathrm{d}u_i}{\mathrm{d}x_i}\right|_{x_i=1}, \quad \left.\frac{\mathrm{d}^3u_j}{\mathrm{d}x_j^3}\right|_{x_j=0} = \left.\frac{\mathrm{d}^3u_i}{\mathrm{d}x_i^3}\right|_{x_i=1},$$

$_{j=0}$

$j-1$ with $i \in [1,\ldots,N-1], j \in [2,\ldots,N]$ $\in [0,1]$ the local normalised coordinates rval i, which connect the polynomials in nterval through their boundaries. These ons can be expressed as a matrix equation $[\,f_i\ f_i\ f_i\ f_i\,]^\top$ with $\xi_i = [\,a_i\ b_i\ c_i\ d_i\,]^\top$ and C

$$C = \begin{bmatrix} 24 & 24 & 24 & 24 & 0 & 0 & 0 & -24 \\ 18 & 12 & 6 & 0 & 0 & 0 & -6 & 0 \\ 12 & 4 & 0 & 0 & 0 & -4 & 0 & 0 \\ 6 & 0 & 0 & 0 & -6 & 0 & 0 & 0 \end{bmatrix}.$$

er with the two boundary conditions at the all coefficients can be calculated. The equations on the coefficients can be ex- d as a matrix equation, $A\xi = b$, where the A is constructed as,

$$A = \begin{bmatrix} 0 & 2 & 0 & 0 & \cdots & & & \\ 0 & 0 & 0 & 24 & \cdots & & & \\ & & & & C & & & \\ & & & & & \ddots & & \\ & & & & & & C & \\ & & & & \cdots & 12 & 4 & 0 & 0 \\ & & & & \cdots & 24 & 24 & 24 & 24 \end{bmatrix}.$$

$[\,0\ 0\ f_1\ f_1\ f_1\ f_1 \cdots f_{N-1}\ f_{N-1}\ f_{N-1}\ f_{N-1}\ f_N\ f_N\,]^\top$.

lution x follows from $x = A^{-1}b$. The de- value for the magnet is chosen at half the interval, $u_i(\frac{1}{2}) = \frac{1}{16}\frac{f_i}{24} + \frac{1}{8}a_i + \frac{1}{4}b_i + \frac{1}{2}c_i + d_i$. Which can also be described by the linear relation $u = Mf$, with,

$$M = \tfrac{1}{16\cdot 24} I - \begin{bmatrix} \frac{1}{8} & \frac{1}{4} & \frac{1}{2} & 1 & 0 & \cdots & 0 & 0 & 0 & 0 \\ & & & & & \ddots & & & & \\ 0 & 0 & 0 & 0 & 0 & \cdots & 0 & \frac{1}{8} & \frac{1}{4} & \frac{1}{2} & 1 \end{bmatrix} A^{-1} \begin{bmatrix} 0 & 0 & \cdots & 0 \\ 0 & 0 & \cdots & 0 \\ 1 & 0 & \cdots & 0 \\ 1 & 0 & \cdots & 0 \\ 1 & 0 & \cdots & 0 \\ 1 & 0 & \cdots & 0 \\ & \ddots & & \\ 0 & \cdots & 0 & 1 \\ 0 & \cdots & 0 & 1 \end{bmatrix}.$$

This linear relation between magnet forces and deformations, can be obtained via other methods too, such as from FEM software.

COMMUTATION OF STATIC DEFORMATION

Combining the force distribution model together with the deformation model gives the mapping between coil currents and deformation. The coupling of a coil current to forces per magnet is stored in the vector $\vec{\gamma}_{fc_i}(\vec{q}_p) \in \mathbb{R}^N$ where N is the number of permanent magnets on the strip. The resulting deformation is given by, $\vec{\gamma}_{uc_i}(\vec{q}_p) = M\vec{\gamma}_{fc_i}(\vec{q}_p)$.

The vector containing the static Halbach deformation $\vec{u}_H = M\vec{f}_H$, where $\vec{f}_H$ is the vector of static Halbach forces acting on the permanent magnets. The contribution of a coil current to this deformation is given by projecting $\vec{\gamma}_{uc_i}$ on the normalised static Halbach deformation $\vec{u}_{nH} = \frac{\vec{u}_H}{\|\vec{u}_H\|}$,

$$\gamma_{Hc_i}(\vec{q}_p) = \vec{u}_{nH}^\top \vec{\gamma}_{uc_i}(\vec{q}_p).$$

This coupling between coil current and contribution to the static deformation can be used to extend the coupling matrix Γ which is used in the commutation.

This amounts to extending the coupling matrix $\Gamma(\vec{q}_p)$ with the coupling between coil currents and deforming the magnet array in the shape of the static Halbach deformation.

$$\Gamma_E(\vec{q}_p) = [\,\vec{\gamma}_{Ec_1}(\vec{q}_p)\ \vec{\gamma}_{Ec_2}(\vec{q}_p) \cdots \vec{\gamma}_{Ec_N}(\vec{q}_p)\,]$$

with the extended coupling per coil given by,

$$\vec{\gamma}_{Ec_i}(\vec{q}_p) = \begin{bmatrix} \gamma_{F_x c_i}(\vec{q}_p) \\ \gamma_{F_z c_i}(\vec{q}_p) \\ \gamma_{T_y c_i}(\vec{q}_p) \\ \gamma_{Hc_i}(\vec{q}_p) \end{bmatrix}$$

It should be noted that the control output should be $\begin{bmatrix} \vec{w}_{des} \\ -\|\vec{u}_H\| \end{bmatrix}$ to constrain the commutation to compensate for the static deformation.

Only bending of the stiffness structure, i.e. the aluminum strip in Figure 1, is considered. The load is assumed to be piecewise constant due to the larger stiffness of the NdFeB magnets. The forces that cause rigid body movement are subtracted from the magnet forces, thus the resulting forces will only cause bending. To solve the Ordinary Differential Equation (ODE), boundary conditions corresponding to simply supported ends are applied:

$$\left.\frac{\mathrm{d}^2u}{\mathrm{d}x^2}\right|_{x=\pm\frac{L}{2}} = 0, \quad \text{and} \quad u(x=\pm\frac{L}{2}) = 0.$$

Since a piecewise constant loading vector $f = [\, f_1 \ldots f_N \,]^\top$ is assumed, the solution to the ODE in an interval of constant loading is known to be a fourth order polynomial, $u_i = \frac{f_i}{24}x_i^4 + a_i x_i^3 + b_i x_i^2 + c_i x_i + d_i$. For easy solving, the stiffness structure is divided in intervals of equal length, with the 16 mm magnets covering two intervals. The coefficients of the polynomials can be solved by imposing suitable boundary conditions:

$$u_j|_{x_j=0} = u_i|_{x_i=1}, \qquad \left.\frac{\mathrm{d}^2u_j}{\mathrm{d}x_j^2}\right|_{x_j=0} = \left.\frac{\mathrm{d}^2u_i}{\mathrm{d}x_i^2}\right|_{x_i=1},$$

$$\left.\frac{\mathrm{d}u_j}{\mathrm{d}x_j}\right|_{x_j=0} = \left.\frac{\mathrm{d}u_i}{\mathrm{d}x_i}\right|_{x_i=1}, \qquad \left.\frac{\mathrm{d}^3u_j}{\mathrm{d}x_j^3}\right|_{x_j=0} = \left.\frac{\mathrm{d}^3u_i}{\mathrm{d}x_i^3}\right|_{x_i=1},$$

for $i = j-1$ with $i \in [1, \ldots, N-1], j \in [2, \ldots, N]$ and $x_i \in [0,1]$ the local normalised coordinates of interval i, which connect the polynomials in each interval through their boundaries. These equations can be expressed as a matrix equation $C\xi_i = [\, f_i \; f_i \; f_i \; f_i \,]^\top$ with $\xi_i = [\, a_i \; b_i \; c_i \; d_i \,]^\top$ and C as:

$$C = \begin{bmatrix} 24 & 24 & 24 & 24 & 0 & 0 & 0 & -24 \\ 18 & 12 & 6 & 0 & 0 & 0 & -6 & 0 \\ 12 & 4 & 0 & 0 & 0 & -4 & 0 & 0 \\ 6 & 0 & 0 & 0 & -6 & 0 & 0 & 0 \end{bmatrix}.$$

Together with the two boundary conditions at the ends, all coefficients can be calculated. The linear equations on the coefficients can be expressed as a matrix equation, $A\xi = b$, where the matrix A is constructed as,

$$A = \begin{bmatrix} 0 & 2 & 0 & 0 & \cdots & & & & \\ 0 & 0 & 0 & 24 & \cdots & & & & \\ & & & & C & & & & \\ & & & & & \ddots & & & \\ & & & & & & C & & \\ & & & & \cdots & & 12 & 4 & 0 & 0 \\ & & & & \cdots & & 24 & 24 & 24 & 24 \end{bmatrix}.$$

And $b = [\, 0 \; 0 \; f_1 \; f_1 \; f_1 \; f_1 \cdots f_{N-1} \; f_{N-1} \; f_{N-1} \; f_{N-1} \; f_N \; f_N \,]^\top$. The solution x follows from $x = A^{-1}b$. The deflection value for the magnet is chosen at half the interval, $u_i(\frac{1}{2}) = \frac{1}{16}\frac{f_i}{24} + \frac{1}{8}a_i + \frac{1}{4}b_i + \frac{1}{2}c_i + d_i$. Which can also be described by the linear relation $u = Mf$, with,

$$M = \tfrac{1}{16\cdot 24} I - \begin{bmatrix} \frac{1}{8} & \frac{1}{4} & \frac{1}{2} & 1 & 0 & \cdots & 0 & 0 & 0 & 0 \\ & & & & & \ddots & & & & \\ 0 & 0 & 0 & 0 & 0 & \cdots & 0 & \frac{1}{8} & \frac{1}{4} & \frac{1}{2} & 1 \end{bmatrix} A^{-1} \begin{bmatrix} 0 & 0 & \cdots & 0 \\ 0 & 0 & \cdots & 0 \\ 1 & 0 & \cdots & 0 \\ 1 & 0 & \cdots & 0 \\ 1 & 0 & \cdots & 0 \\ 1 & 0 & \cdots & 0 \\ & \ddots & & \\ 0 & \cdots & 0 & 1 \\ 0 & \cdots & 0 & 1 \end{bmatrix}.$$

This linear relation between magnet forces and deformations, can be obtained via other methods too, such as from FEM software.

COMMUTATION OF STATIC DEFORMATION

Combining the force distribution model together with the deformation model gives the mapping between coil currents and deformation. The coupling of a coil current to forces per magnet is stored in the vector $\vec{\gamma}_{fc_i}(\vec{q}_p) \in \mathbb{R}^N$ where N is the number of permanent magnets on the strip. The resulting deformation is given by, $\vec{\gamma}_{uc_i}(\vec{q}_p) = M\vec{\gamma}_{fc_i}(\vec{q}_p)$.

The vector containing the static Halbach deformation $\vec{u}_H = M\vec{f}_H$, where $\vec{f}_H$ is the vector of static Halbach forces acting on the permanent magnets. The contribution of a coil current to this deformation is given by projecting $\vec{\gamma}_{uc_i}$ on the normalised static Halbach deformation $\vec{u}_{nH} = \frac{\vec{u}_H}{\|\vec{u}_H\|}$,

$$\gamma_{Hc_i}(\vec{q}_p) = \vec{u}_{nH}^\top \vec{\gamma}_{uc_i}(\vec{q}_p).$$

This coupling between coil current and contribution to the static deformation can be used to extend the coupling matrix Γ which is used in the commutation.

This amounts to extending the coupling matrix $\Gamma(\vec{q}_p)$ with the coupling between coil currents and deforming the magnet array in the shape of the static Halbach deformation.

$$\Gamma_E(\vec{q}_p) = [\, \vec{\gamma}_{Ec_1}(\vec{q}_p) \; \vec{\gamma}_{Ec_2}(\vec{q}_p) \cdots \vec{\gamma}_{Ec_N}(\vec{q}_p) \,]$$

with the extended coupling per coil given by,

$$\vec{\gamma}_{Ec_i}(\vec{q}_p) = \begin{bmatrix} \gamma_{F_x c_i}(\vec{q}_p) \\ \gamma_{F_z c_i}(\vec{q}_p) \\ \gamma_{T_y c_i}(\vec{q}_p) \\ \gamma_{Hc_i}(\vec{q}_p) \end{bmatrix}$$

It should be noted that the control output should be $\begin{bmatrix} \vec{w}_{des} \\ -\|\vec{u}_H\| \end{bmatrix}$ to constrain the commutation to compensate for the static deformation.

given position this coupling can be inverted, resulting in the required decoupling. Notice, however, that because of the redundancy in the coupling a lot more coils than the number of considered wrench components are used. Consequently, the inverse of the coupling has to be a generalised inverse. Which results in a weighed minimisation of the coil currents. This is illustrated in Figure. 2, which shows the control scheme, where the position dependent coupling is denoted by $\Gamma(\vec{q}_p)$ and the corresponding decoupling by $\Gamma^{-}(\vec{q}_p)$.

$$\Gamma(\vec{q}_p) = \left[\, \vec{\gamma}_{c_1}(\vec{q}_p)\ \vec{\gamma}_{c_2}(\vec{q}_p)\ \cdots\ \vec{\gamma}_{c_N}(\vec{q}_p) \,\right]$$

where the $\vec{\gamma}_{c_i}(\vec{q}_p)$ is the contribution of a current i_{c_i} through coil i to the wrench components depending on the position $\vec{q}_p$,

$$\begin{bmatrix} F_{xc_i}(\vec{q}_p) \\ F_{zc_i}(\vec{q}_p) \\ T_{yc_i}(\vec{q}_p) \end{bmatrix} = \vec{\gamma_{c_i}}(\vec{q}_p) i_{c_i} = \begin{bmatrix} \gamma_{F_{xc_i}}(\vec{q}_p) \\ \gamma_{F_{zc_i}}(\vec{q}_p) \\ \gamma_{T_{yc_i}}(\vec{q}_p) \end{bmatrix} i_{c_i}$$

The weighed minimisation of the 2-norm of the coil currents, $\sqrt{\vec{i}^{\top}\Delta\vec{i}}$, is given by,

$$\arg\min_{\vec{i}} \|\vec{i}\|_{\Delta}$$
$$\text{s.t. } :\vec{w}_{des} = \Gamma(\vec{q}_p)\vec{i}$$

Which is solved by the generalised inverse[5], $\vec{i} = \Gamma^{-}(\vec{q}_p)\vec{w}_{des}$, where

$$\Gamma^{-}(\vec{q}_p) = \Delta(\vec{q}_p)\Gamma^{\top}(\vec{q}_p)\left(\Gamma(\vec{q}_p)\Delta(\vec{q}_p)\Gamma^{\top}(\vec{q}_p)\right)^{-1}$$

This property of those planar actuator topologies to have many more coils that have coupling with the translator than the degrees of freedom of the translator can be exploited to influence other features of the actuator. However, this will be at the expense of the efficiency, since the minimisation will have less freedom to minimise the coil currents.

DISTRIBUTED FORCE MODEL

Since the force distribution is needed to determine the deformation, another model needs to be used. It has to calculate the forces and torques acting at a single permanent magnet ($B_r = 1.24$ T) due to coil currents. This model was obtained by modeling the magnetic field of a single magnet by surface charges and calculating the Lorenz force at the conductors of the coil[4][6]. Figure 3 illustrates the x and z force components and the torque around y of an in z magnetised permanent magnet with a single coil as function of their relative x-displacement.

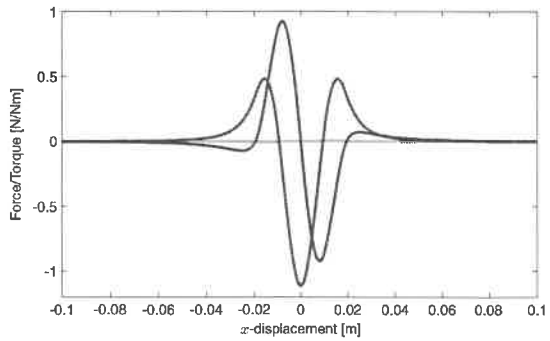

FIGURE 3. 3DOF Wrench at a in z magnetised permanent magnet due to a one Ampère coil current as a function of their relative displacement in x. F_x (blue) F_z (red) T_y (green)

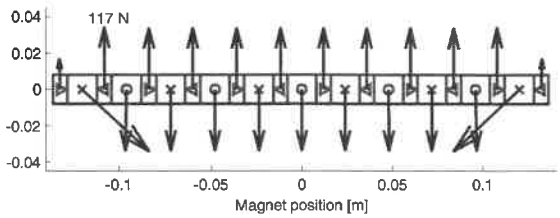

FIGURE 4. Static forces among the permanent magnets due to their Halbach configuration. The largest z-force is depicted above the vector.

The static Halbach forces obtained by the method of [4] are shown in Figure 4. The resulting deformation, obtained with the model which will be presented in the next section, for a strip of permanent magnets is shown in Figure 5.

DEFORMATION MODEL

The model used for calculating the deformation is based upon the Euler-Bernoulli beam equation[7], which yields the relation between the deflection $u(x)$ and the distributed load $q(x)$,

$$\frac{\mathrm{d}^4 u(x)}{\mathrm{d}x^4} = \frac{q(x)}{EI} = f(x),$$

where E is the elastic modulus and I the second moment of area. Only deflection in the z-direction is considered due to forces in the z direction.

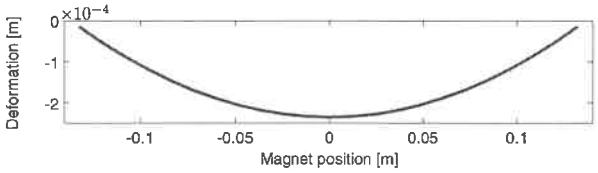

FIGURE 5. Deformation due to the magnet forces

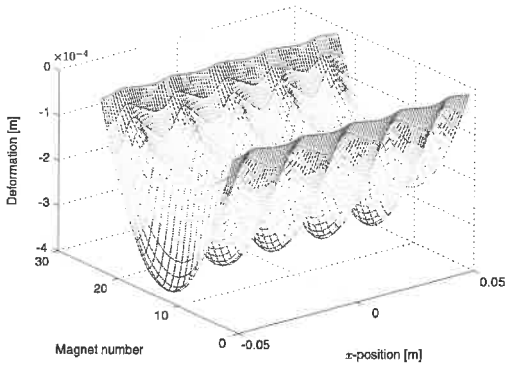

FIGURE 6. Deformation without compensation

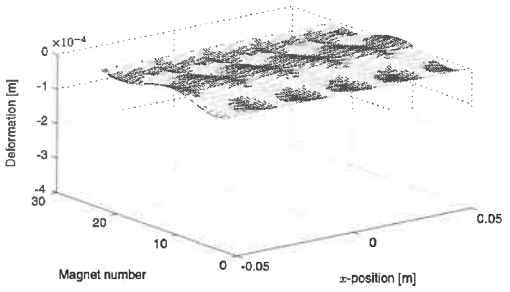

FIGURE 7. Deformation with the compensation

In Figure 6 the resulting deformation of the original commutation of a desired wrench vector of $\vec{w}_{des} = [5\ 10\ 0]^\top$ is shown for different magnet array positions. One can observe that this commutation increases the static deformation at the majority of the simulated positions. In Figure 7 the deformation is shown when applying the extended commutation with the static deformation reduction, again a desired wrench vector of $\vec{w}_{des} = [5\ 10\ 0]^\top$ is applied. A significant decrease in the static deformation, of at least a factor ten compared to the original commutation, is obtained.

Figure 8 shows the power consumption for both commutation methods, the power usage of the deformation compensating commutation is on average three times higher.

CONCLUSION

In this paper a method has been presented which can actively reduce static deformations in a strip of magnets, when applied as a magnetically levitated mover of a 3 DoF moving magnet actuator. The method uses a model that gives the contribution of coil currents to the static deformation, which is used in the commutation to minimise the

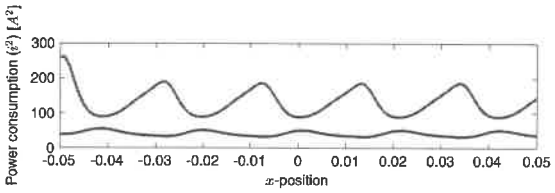

FIGURE 8. Power usage at various positions

deformation. A factor ten reduction of the deformation was observed which was at the expense of an over position averaged increase of three times the original power consumption. By extending the model of the deformation of a beam to a plate, the same techniques can be used to influence the deformation of a magnet array, used in various planar actuator topologies.

In future work this method should be applied on plates, also one could optimise the topology so that the deformation reduction will have a lower increase in power consumption. It should be noted that the deformation model assumes simply supported ends at the boundaries of the beam, which is not valid for a levitated beam, this should also be solved before applying the method on a real setup.

REFERENCES

[1] Compter JC, Frissen PCM, van Eijk J, inventors; Displacement device. WO 2006/075291 A2; 2006.

[2] Jansen JW, van Lierop CMM, Lomonova EA, Vandenput AJA. Ironless magnetically levitated planar actuator. vol. 103. AIP; 2008. p. 07E905.

[3] de Boeij J, Lomonova E, Duarte J. Contactless Planar Actuator With Manipulator: A Motion System Without Cables and Physical Contact Between the Mover and the Fixed World. IEEE Trans Ind Applicat. 2009 nov-dec;45(6):1930 –1938.

[4] Rovers JMM, Jansen JW, Lomonova EA, Ronde MJC. Calculation of the static forces among the permanent magnets in a halbach array. IEEE Trans Magn. 2009 Oct;45:43724375.

[5] Rao CR, Mitra SK. Generalized inverse of matrices and its applications. Wiley; 1971.

[6] Jansen JW, van Lierop CMM, Lomonova EA, Vandenput AJA. Modeling of Magnetically Levitated Planar Actuators With Moving Magnets. IEEE Trans Magn. 2007 Jan;43(1):15–25.

[7] Timoshenko S. History of strength of materials. McGraw-Hill New York; 1953.

MICROCAPSULE PRODUCTION BY DOUBLE MICRO PIPETTE INJECTERS

Hisayuki Aoyama, Naoya Hata, Kiyoshi Terasaki and Shinnosuke Hirata
Department of Mechanical Engineering and Intelligent Systems
University of Electro-Communications
1-5-1, Chofu Tokyo, Japan

INTRODUCTION

Recently it becomes more important to produce the microcapsule for such drug derivery system in medical application. For these years, many styles based on chemical reaction and micro flud dynamics have been developed, although the accuracy of the microcapsule size is not good enough to control the activate time. In this report, a pair of the micro pipette injecters is developed and the liquid in the tube can be pushed out by the thin rod travering in the tube. The contained liquid with higher viscosity in the tube can be pushed out in the solvent and then the small capsule can be generated when the thin rod is retracted quickly.

In the experiments, several layouts of the micro pipette injecters were designed and set up in order to check the performances. With the double tube pipette with the diameter of 50um, the small amount of two different liquids are preset in the pipette with the help of the surface tention force at first and then the thin rod can push out them into the solvent. Under the careful speed control of the thin rod, the single emulsion with the core and the shell can be genetrated in the solvent. This simple mechanical sequence can be repeated precisely and the the accurate capsules with the size of 160um are able to be produced with the deviation of 10%. Another layout that two micro pipette dispensers are aligned with appropriate angle can allow to produce the capsule with the different core and shell materials. At first, the liquid for shell is pushed out from the right pipette injecter and then the second injecter can insert into the capsule from the left hand side and the core material can be injected. This unique and precise sequence can allow to produce such micro capsule with any kinds of materials although materials are limited with the chemical procedures. In the primary experiment, it is shown that the control system of the developed linear motor driven micro glass pipette injecter, and several single or double layer capsules with different materials succesfully have been demonstrated with the high speed video motion pictures. Here the shell diameter of 500um with that of 200um core material of oil was succesfully made in the solvent by this unique micromechatronics technique.

SINGLE PIPETTE INJECTION

Principle of single pipette injection

The sequencial view of the single pipette injection in the liquid is shown in Fig. 1. It is composed of a glass pipette and a thin needle. Here the glass pipette is filled with an inner liquid and the thin needle passes through the glass pipette. The glass pipette and the thin needle can be inserted into the base liquid. The inner liquid can be pushed out into the base liquid by the thin needle. The inner liquid becomes a sphere by the surface tensity. The inner liquid gathers around the top of glass-pipette tip. When the thin needle and the glass pipette are pulled up from the base liquid, the inner liquid is parted from the thin-needle tip. When the thin needle is retracted from the glass-pipette tip, the inner liquid is replenished. Single emulsion can be generated in the base liquid.

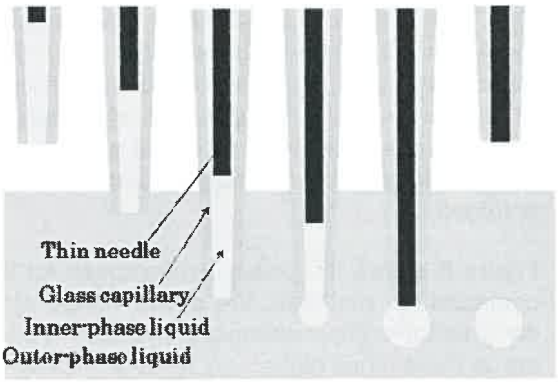

FIGURE.1 Sequential view of the single pipette injection in the liquid.

Experiment of single pipette injection

Optimized diameters of the glass pipette and the thin needle were investigated from the primary experiment of single injection. In the experiments, the aqua purificata was used as

the inner liquid. Vegetable oil was used as the base liquid. The thin needle was made of tungsten. When single emulsion was generated by pushing out the aqua purificata to the vegetable oil, it was monitored by a highspeed microscope. At first the glass pipette tip was set at 1.5 mm above the vegetable oil. The thin-needle tip was kept on 0.4 mm above the glass-capillary tip. Fig. 2 shows an appearance of single emulsion generation. When the gap between the glass pipette tip inner diameter and the thin needle tip diameter was small, then the single emulsion could be generated. Several single emulsions were iteratively generated for checking the repeatability. The glass pipette tip inside diameter was 85 μ m. The thin-needle-tip diameter was 70 μ m. The aqua purificata was filled in the glass pipette. The aqua purificata was pushed out into the vegetable oil by the thin needle once three second. Single emulsions iterative generation can be monitored by a microscope instrument.

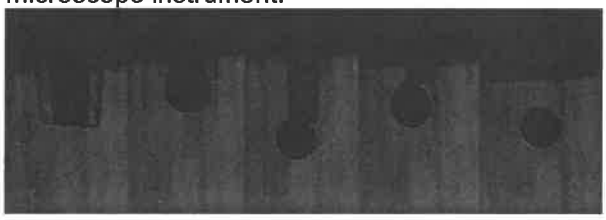

FIGURE.2 Experiment of signle emulsions generation pushed out the pipette.

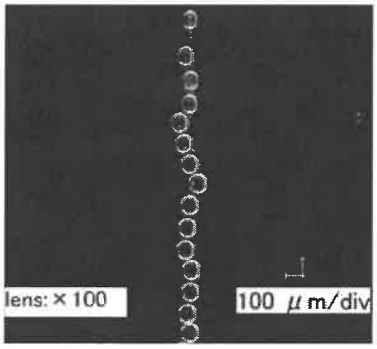

FIGURE.3 Continuous signle emulsions in the base liquid.

Fig. 3 shows the single emulsion iterative generation. The diameters of single-phase emulsions were measured by the images processing. Fig.4 shows the distribution of the diameters of 50 single emulsions. The average diameter was 163 μ m, and the deviation of the diameters was within ±15 %.

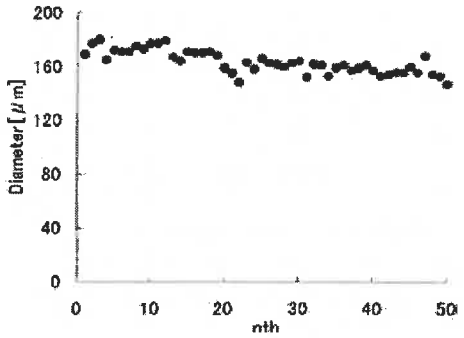

FIGURE.4 Distribution of diameter with 50 emulsions by single pipette generation.

DOUBLE LAYER INJECTION BY SINGLE PIPETTE AND COAXIAL DOUBLE PIPETTE

Principle of double layer injection

The double layer injection by single pipette and by coaxial double pipettes are shown in proposed in Fig. 5 . A mechanism of the coaxial arranged pipettes method is composed of two glass capillaries, which are arranged coaxially, and a thin needle. The proposed method consists of an emulsion generation process and a liquids replenishment process. The emulsion generation process is shown.

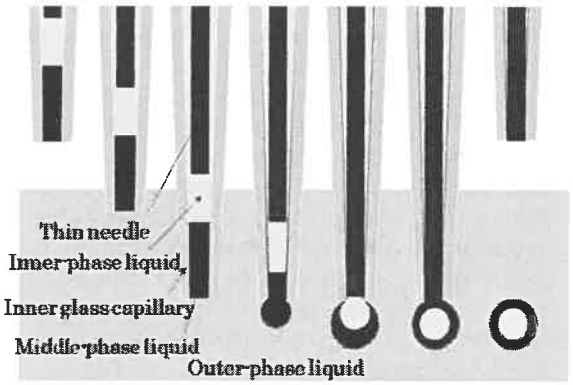

FIGURE.5 Double layer emulsion by single pipette and coaxial double pipettes.

The first liquid and the second one are filled in the inner glass pipette. The inner glass pipette and the thin needle are gone down into the base liquid. At first, the first liquid is pushed out into the base liquid by the thin needle. The first liquid becomes a sphere by the surface tensity. The first liquid is adhered the glass pipette tip. Then the second liquid is pushed out into the first liquid by the thin needle. The second liquid becomes also spherical by the surface tensity. Then the second liquid is put in the first liquid. When the thin needle and the inner glass pipette

are gone up from the base liquid, the first liquid and the second liquid are parted from the thin-needle tip. Thus the double layer emulsion is generated in the base liquid. The first liquid in the pipette are consumed in the emulsion generation process. Therefore the liquid replenishment process is required as shown in Fig. 5. The inner pipette and the thin needle are gone up into the outer glass pipette. When the thin needle is gone up, the second liquid is raised into the inner glass pipette. Furthermore, the first liquid is gone down under the thin-needle tip. The inner glass pipette is gone down outside the outer glass pipette.

Experiment of double layer pipette injection

The coaxial arranged pipette method was checked by the experiment of double layer emulsion generation. In the experiments, chili oil was used as the first liquid. Aqua purificata was used as the second liquid. Vegetable oil was used as the base liquid. The inner glass pipette tip inside diameter was 100 μ m. The outer glass pipette tip inside diameter was 150 μ m. The thin needle tip diameter was 70 μ m. The chili oil was filled in the inner glass pipette. The aqua purificata was filled in the outer glass pipette. The chili oil and the aqua purificata were filled in the inner glass pipette by the liquids replenishment process. The aqua purificata was sucked from the inner glass pipette tip to 1 mm above. The glass-pipette tip was set at 1 mm upper from the vegetable oil. The thin needle was put the inner glass pipette tip to 2 mm above. The inner glass pipette and the thin needle were gone down into the vegetable oil in the emulsion generation process. When double layer emulsion was generated, it was monitored by a digital microscope. Double layer emulsion could be generated as shown in Fig. 6. The aqua purificata sphere diameter was 500 um. The chili-oil-sphere diameter was 300 um. Double-phase emulsion generation was succeeded by the coaxial arranged pipette method.

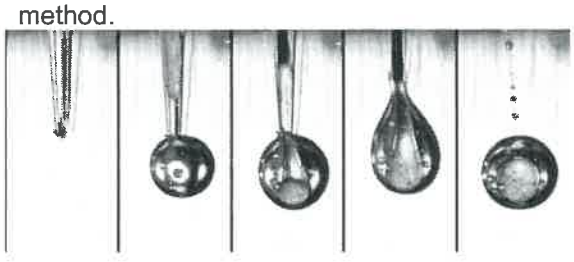

FIGURE.6 Experiment of capsule generation by double layer single pipette.

V-SHAPE LAYOUT TWIN PIPETTES INJECTION

Principle of V-shape twin pipettes injection

A V-shape arranged pipettes method is shown in Fig. 7. The V-shape arranged pipettes method is composed of two single emulsion generation methods, which are aligned with V-shape. The first liquid is filled in a left-side glass pipette and the second liquid is filled in a right-side glass pipette. At first, the left-side glass pipette is gone down into the base liquid. The second liquid is pushed out into the first liquid by a left-side thin needle. The first liquid becomes a sphere by the surface tensity. The first liquid is adhered the left-side glass-capillary tip. Then the right-side glass pipette is inserted into the first liquid. The second liquid is pushed into the first liquid by a

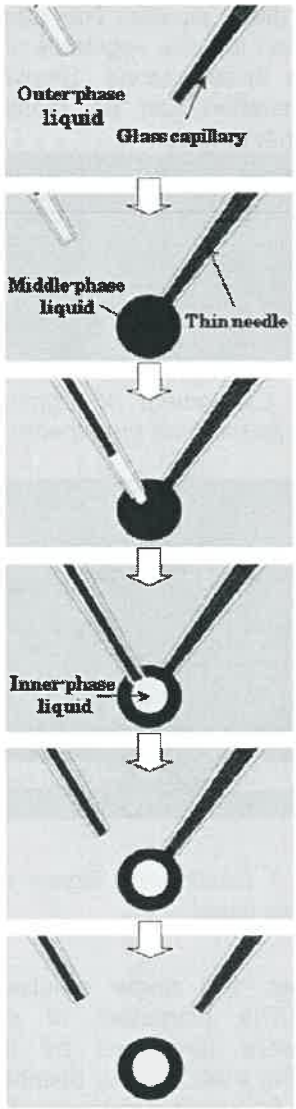

FIGURE.7 Sequence of V arranged twin pipettes injection for capsule generation.

right-side thin needle. When the thin needles and the glass pipettes are gone up from the base liquid, the doulbe layer emulsion are parted from the thin needle tips. When the thin needles are gone up from the glass pipette tips,the double layer emulsion, the capsule can be generated in the base liquid.

Experiment of V-shape twin pipettes injection

In Fig.8, the experimental set up is shown. The thin rods and glass pipettes are aligned with V layout and they can driven by the linear stages. The positions and the speeds of them are controlled precisely by FPGA control unit. In the experiments, chili oil was used as the first liquid. Aqua purificata was used as the middle phase liquid. Vegetable oil was used as the outer-phase liquid. The thin needle was made of tungsten. The glass pipette tip inside diameter was 90 μ m. The thin-needle-tip diameter was 70 μ m. The aqua purificata was filled in the right side glass pipette, and chill oil was filled in the left side glass pipette. The glass pipette tips were set at 1.5 mm above from the vegetable oil. The thin needle tips were kept on 1.5 mm above from the glass pipette tips. The right side glass pipette and the thin needle were gone down into the vegetable oil. The left side glass pipette and the thin needle were gone down into the vegetable oil. Whether double-phase emulsion was generated was observed by a digital microscope. Double layerd emulsion, capsule could be generated as shown in Fig. 9. The aqua purificata sphere diameter was 500 um and the chili oil diameter was 200 um. Double layer emulsion generation succeeded in producing by the V-shape aligned pipettes method.

CONCLUSION & FUTURE WORKS

In this paper, micro encapsulation methods using glass pipette and thin needles for wide variety and small quantity production is proposed. Single layer emulsion generation and double layer emulsion iterative generation were succeeded. Double layer emulsion also succeeded in generating by the coaxial aligned pipettes method and the V-shape arranged pipettes method in the experiments. In the future, such chemical reactive and optical reactive materials can be used to produce the functional capsule.

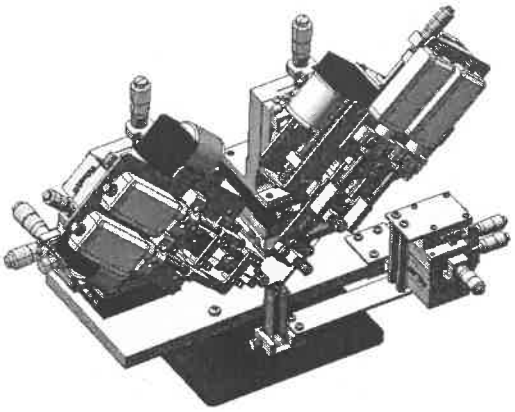

FIGURE.8 Experimental setup of V arranged twin pipettes injection controlled by FPGA servo unit.

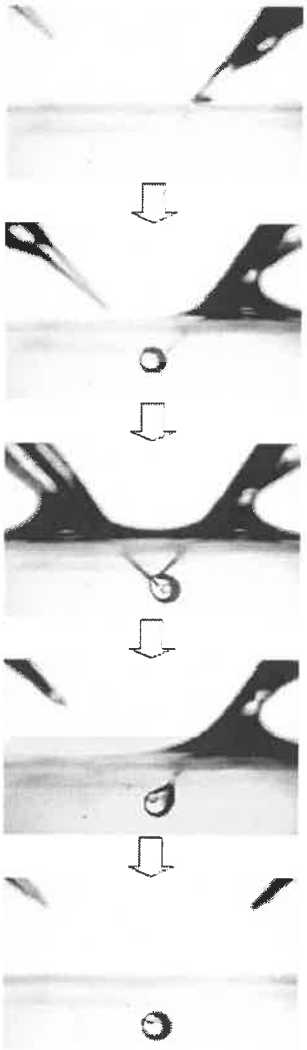

FIGURE.9 Experimental result with V arranged twin pipettes injection.

HIGH SPEED ELECTRICAL DISCHARGE MACHINING USING A COMBINATION OF 5-DOF CONTROLLED MAGLEV ACTUATOR AND CONVENTIONAL EDM MACHINE

Dongjue He[1], Tadahiko Shinshi[1], Xiaoyou Zhang[2], Takashi Yuzawa[3] and Tatsushi Sato[3]

[1]Precision and Intelligence Laboratory
Tokyo Institute of Technology
Yokohama, Kanagawa, Japan
[2]Department of Mechanical Engineering
Nippon Institute of Technology
Saitama, Japan
[3]Advanced Technology R&D Center
Mitsubishi Electric Corporation
Amagasaki, Japan

INTRODUCTION

Electrical discharge machining (EDM) is a non-contact material removal process, which is widely used for machining complex shapes or hard material parts [1, 2]. During the process of EDM, the distance between the work-piece and the electrode changes as material is being removed from the work-piece and the electrode.

In conventional EDM machines, stacked one-degree-of-freedom (1-DOF) lead-screw mechanisms or linear positioning tables are normally used to position the electrode or the work-piece, the positioning response of such mechanisms being somewhat slow, due to the rotary inertia of the lead-screws and the mass of stacked tables, such that the electrode or the work-piece cannot be re-positioned sufficiently quickly to maintain the suitable distance from the work-piece [3,4]. Furthermore, machining debris accumulating around the electrode cannot be removed efficiently and prevents abnormal electrical discharge.

In order to improve machining speed and accuracy, combinations of conventional EDM machines, having a long positioning range together with local actuators possessing wide-bandwidth and high positioning accuracy, have been proposed [5-8]. The local actuators can realize high-speed positioning of the electrode to maintain a suitable distance between the work-piece and the electrode. Furthermore, the debris can be removed more efficiently by rotation, high frequency vibration or rapid retraction of the electrode. These motions are generated by local, multi-DOF controlled actuators [9, 10].

This paper reports the adoption of a combination of a prototype 5-DOF controlled maglev local actuator (MLA) and a conventional EDM machine (MEMH8N, Mitsubishi Electric Corporation) for deep-small-hole machining, as shown in Fig. 1. During machining of the small-deep-holes, the electrode was co-operatively positioned by the MLA and the EDM machine, known as co-operative EDM. The machining speeds using the EDM machine, alone, and using the combination of the EDM machine with the MLA rotating the electrode are discussed.

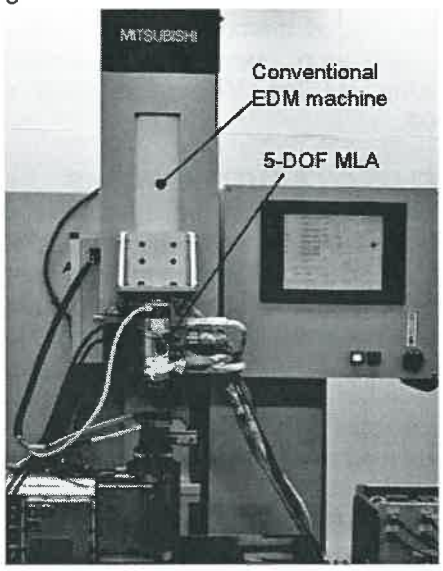

FIGURE 1. Co-operative EDM System

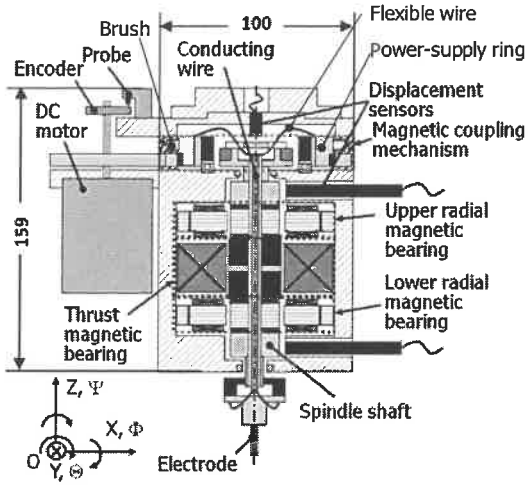

FIGURE 2. Configuration of 5-DOF MLA

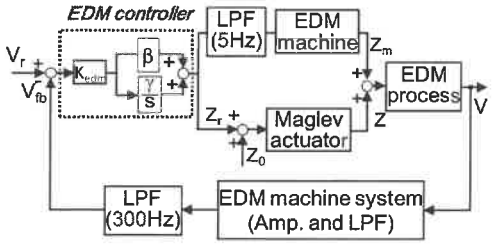

FIGURE 3. Co-operative Control System

5-DOF CONTROLLED MLA

Fig. 2 shows the configuration of the prototype MLA mainly consisting of a 5-DOF controlled magnetic bearing (MB) system and a magnetic coupling mechanism for supplying a discharge current to the electrode, as well as transmitting torque to the spindle shaft. The 5-DOF controlled MB system is used to levitate and position the spindle shaft, precisely and speedily, in three orthogonal (X, Y and Z) and two tilt (Θ and Φ) directions.

The height of the fabricated MLA, without an electrode and its attachment, is 159mm and the width, without the DC motor, is 100mm. The weight of the MLA with all the attachments is approximately 10kg.

Experimental results show that the spindle shaft possesses a sub-micron positioning resolution and an angular resolution of several micro-radians, with bandwidths greater than 200Hz in all the 5-DOF directions, and full positioning strokes of 2mm in the thrust direction, 180μm in the radial direction and 3.6mrad in tilt direction [11].

CO-OPERATIVE EDM

In order to realize not only high positioning response of the electrode, but also a positioning stroke greater than that of the MLA, a cooperative control system has been adopted for EDM. In the co-operative EDM, the MLA is mounted on a positioning stage of a conventional EDM machine, which has a large stroke with high positioning accuracy but low positioning response.

Fig. 3 shows the co-operative control system for machining small-deep holes in the Z direction. During the EDM, the discharge voltage, V, between the electrode and work-piece was monitored through a LPF with a cut-off frequency of 300Hz and was used as a feedback signal. The EDM controller generated the reference position of the electrode in the thrust direction according to the feedback voltage, V_{fb}, and a reference EDM voltage, V_r.

The reference position was entered into the maglev actuator system, directly, and into the conventional EDM machine through a LPF with a cut-off frequency of 5Hz. Following the reference position, the MLA adjusted the electrode, speedily and precisely, to maintain a suitable distance from the work-piece, and the conventional EDM machine fed the mounted MLA with the electrode, slowly and continuously in the machining feed direction, to avoid the saturation of the positioning stroke of the MLA.

EXPERIMENTAL MACHINING

To evaluate the effectiveness of high-speed and high-accuracy re-positioning, together with the rotation of the electrode by the MLA, small holes were machined using the co-operative EDM, both with and without electrode rotation and also with the conventional EDM machine only, without electrode rotation.

Cylindrical shaped copper electrodes with diameters of ϕ0.5mm and ϕ 1mm were used and the machining was continued to a thickness of 4mm until the electrode penetrated a pre-hardened steel work-piece with a hardness of 40 HRc (NAK 80, Daido Steel Corp., Ltd.). The machining fluid was pure water. The capacitor in the EDM power-supply was charged and discharged using a controllable high-frequency switching circuit. The polarity of the electrode was changed every 17μsec in order to avoid the electrical erosion of the EDM machine. The absolute open-circuit voltage value was 237V.

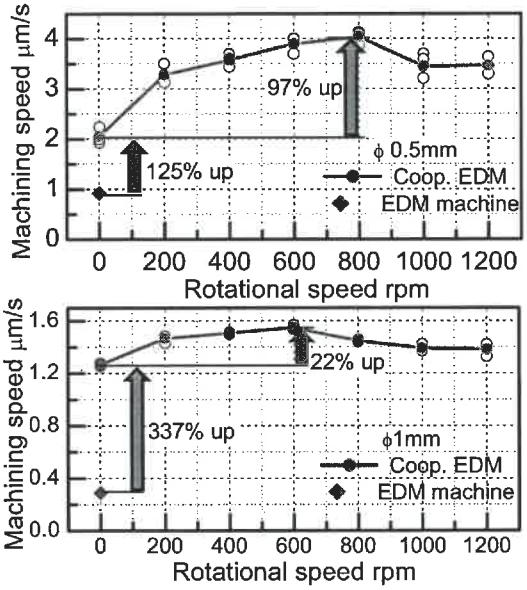

FIGURE 4. Machining Speeds of 4-mm Through Holes

Machining Speeds

The machining speed was defined as the ratio of the machining time to the depth of the machined hole. Fig. 4 shows the machining speeds of ϕ0.5mm and ϕ1mm through holes machined by using the conventional EDM machine only without electrode rotation and by the co-operative EDM at various rotational speeds of the electrode.

According to the results, compared to the machining using the EDM machine only without the electrode rotation, the co-operative EDM increased the machining speeds by 125% in the case of ϕ0.5mm and 337% in the case of ϕ1mm. The increase in the machining speed resulted from the high response speed of the MLA.

Additionally, in the co-operative EDM, holes were machined utilizing the electrode with rotational speeds varying from 200rpm to 1,200rpm. As shown in Fig. 4, electrode rotation increased the averaged machining speeds by 97% at 800rpm in the case of ϕ0.5mm and 22% at 600rpm in the case of ϕ1mm.

In the experiment, debris accumulating around the electrode may cause abnormal electrical discharge sparks between the electrode side surface and the inner surface of the machined hole. When the electrode was not rotating, the abnormal discharge continued for a relatively

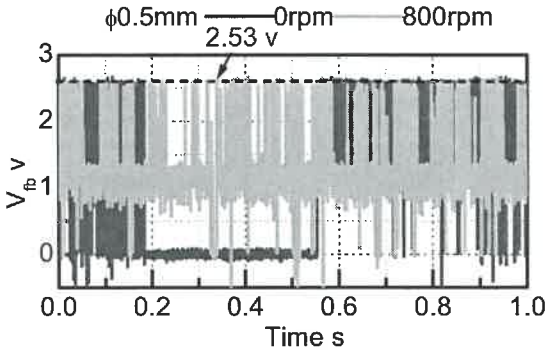

FIGURE 5. Feedback Voltage of Co-operative EDM

long time, lowering the machining efficiency. However, when the electrode was rotating, the abnormal discharge seldom happened. The rotation might help the efficient removal of the debris the increased flushing.

Since the machined holes had the same depth but different diameters. The smaller the diameter, i.e. the larger aspect ratio, the more difficult the ejection of the debris accumulating around the electrode become. Thus, a more noticeable effect on the machining speed occurred in ϕ0.5mm through-holes machining with electrode rotation.

Feedback Voltage

During the EDM, the filtered feedback voltage, V_{fb}, was measured with a data recorder (EZ7501, NF Corp., at a sampling frequency of 5 KHz), Fig. 5 shows the V_{fb} during ϕ0.5mm co-operative EDM at 0rpm and 800rpm.

Although the signals do not show the open and short circuit conditions in the strict sense, a V_{fb} of 0v implies a short circuit condition and a V_{fb} of 2.53v implies an open circuit. The voltage between the electrode and the work-piece was equal to the power-supply voltage (237V).

At 800rpm, the rate of incidence of short and open circuits was decrease relative to that at 0rpm.

Electrical Discharge Probability

Assuming that stable electrical discharge takes place when the V_{fb} is between 20% and 80% of the open-circuit voltage, the total electrical discharge time may be calculated using the measured feedback voltage.

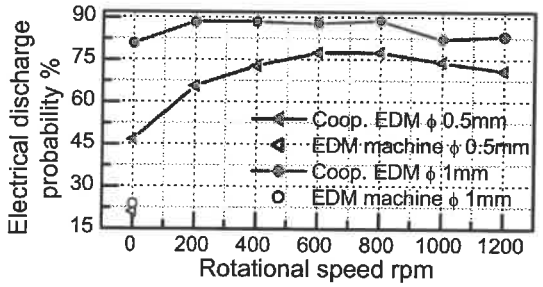

FIGURE 6. Electrical Discharge Probability

In this study, the electrical discharge probability (EDP) is defined as the ratio of the total electrical discharge time to the machining time. Fig. 6 shows the EDP of ϕ0.5mm and ϕ1mm through holes machined by using the conventional EDM machine only without electrode rotation and using the co-operative EDM at various electrode rotational speeds.

The co-operative EDM exhibited a much higher EDP than that of EDM machine alone due to the improved response speed. Furthermore, the co-operative EDM with the electrode rotation at 600-800rpm had a higher EDP than the value at the other rotational speeds due to the more efficient debris removal

CONCLUSION

In this research, small-deep-through holes having a depth of 4mm and a diameter of ϕ0.5mm and ϕ1mm were machined using the conventional EDM machine, alone, and a system using the combination of the EDM machine with a high-speed, high-accuracy and 5-DOF controlled MLA. Experimental results show that the co-operative EDM increased the machining speed. resulting from the high response speed of the MLA. Electrode rotation in the co-operative EDM increased the machining speed by increasing the flushing of dielectric machining fluid to remove debris. Furthermore, the electrode rotation has a significant improvement in machining higher aspect ratio and small holes.

REFERENCES

[1] Kunieda M, Lauwers B, Rajurkar K, Schumacher B. Advancing EDM through Fundamental Insight into the Process. CIRP Annals. 2005; 54(2): 64-87

[2] Ho H K, Newman T S. State of the Art Electrical Discharge Machining (EDM). International Journal of Machine Tools and Manufacture. 2003; 43(13): 1287-1300

[3] Varanasi K, Nayfeh S. The Dynamics of Lead-screw Drives: Low-Order Modeling and Experiments. Trans ASME J Dyn Syst Meas Control. 2004; 126: 388-396

[4] Zhao Y, Zhang X, Liu, Yamazaki K. Geometric Modeling of the Linear Motor Driven Electrical Discharge Machining (EDM) Die-sinking Process. International Journal of Machine Tools & Manufacture. 2004; 44: 1-9

[5] Imai Y, Satake A, Taneda A. Improvement of EDM Machining Speed by Using High Frequency Response Actuator. International Journal Electrical Machining. 1996; 1: 21–26

[6] Masuzawa T, Tanaka K, Fujino M. Study on the High Speed Machining by EDM Using a Moving Coil Head Type Feed Control. Proc. of the 19th International MTDR Conference. 1978: 543-549.

[7] Imai T, Nakagawa T, Miyake H, Hidai H, Tokura H. Local Actuator Module for Highly Accurate Micro-EDM. Journal of Materials Processing Technology. 2004; 149(3): 328-333

[8] Ghoreishi M, Atkinson J. A comparative experimental study of machining characteristic in vibratory, rotary and vibro-rotary electro-discharge machining. Journal of Material processing Technology. 2001; 120: 374-384

[9] Zhang X, Shinshi T, Kajiwara G, Shimokohbe A, Imai Y, Miyake H, Nakagawa T. 5-DOF Controlled Maglev Local Actuator and its Application to Electrical Discharge Machining. Precision Engineering. 2008; 32: 289-300

[10] Zhang X, Shinshi T, Shimokohbe A, Sato T, Miyake H, Nakagawa T. High-speed Electrical Discharge Machining By Using a 5-DOF Controlled Maglev Local Actuator. Journal of Advanced Mechanical Design, Systems, and Manufacturing. 2008; 2(4): 493-503

[11] He D, Morita H, Zhang X, Shinshi T, Nakagawa T, Sato T, Miyake H. Development of a Novel 5-DOF Controlled Maglev Local Actuator for High Speed Electrical Discharge Machining. Precision Engineering. 2010; 34(3): 453-460

[12] Zhang X, Shinshi T, Li L, Shimokohbe A. A combined Repetitive Control for Precision Rotation of Magnetic Bearing. Precision Engineering. 2003; 27: 273-282

PERFORMANCE EVALUATON OF A NEW HIGH-PRECISION, QUICK-RESPONSE PNEUMATIC PRESSURE REGULATOR AND ITS APPLICATION TO AN ACTIVELY CONTROLLED PNEUMATIC VIBRATION ISOLATOR

Tomonori Kato[1], Tatsuya Funaki[2], Yuichiro Shinohara[3], Kenji Kawashima[4], and Toshiharu Kagawa[4]

[1]Fukuoka Institute of Technology, 3-30-1 Wajiro-higashi, Higashi-ku, Fukuoka, Fukuoka, Japan

[2]National Metrology Institute of Japan, AIST, Tsukuba Central 3, 1-1-1 Umezono, Tsukuba, Ibaraki, Japan

[3]Tokkyokiki Corporation, 2-5-15, Higashi-kanda, Chiyoda-ku, Tokyo, Japan

[4]Tokyo Institute of Technology, R2-45 4259 Nagatsuta-cho, Midori-ku, Yokohama, Kanagawa, Japan

INTRODUCTION

The aim of this research is stabilization of the pressure of air supplied to ultraprecision pneumatic systems. In the field of precision measurement and positioning, air-spring vibration isolators are commonly used. Fluctuations in the pressure of the supplied air to these isolators may cause variations in the position of an isolated table. An attempt is usually made to suppress such fluctuations by using a multi-connection air regulator. However, even this method often cannot completely eliminate pressure fluctuations. To solve this problem, we developed a novel high-precision, quick-response pressure-regulating device named an HPQR (High-Precision, Quick-response pressure Regulator) and used it to control the pressure of air supplied to an actively controlled pneumatic vibration isolator [1].

In this research, we propose a method of evaluating the performance of pressure regulators. The evaluation device consists of an absolute pressure sensor, an isothermal chamber, and a differential pressure gauge. The performance of the HPQR was examined using the fabricated device. The HPQR was used to regulate the supply pressure for an actively controlled pneumatic vibration isolator. The isolator consists of 3 air springs having a volume of 1.5 L each, with a mass of about 200 kg. In experiments, we positioned the HPQR between an air-supply system (compressor) and an isolator. To evaluate the performance of the HPQR, a step-shaped disturbance is introduced upstream of the HPQR. For comparison, we conducted the same experiments using commercially available regulators instead of the HPQR.

DEVELOPMENT OF HPQR

Structure of HPQR

A photograph and schematic of the pressure regulator are shown in Figs. 1 and 2, respectively. It consists of a spool-type servo valve (SP valve) (FESTO MPYE-5-M5-SA), a quick-response laminar flow sensor (QFS), an isothermal chamber, a pressure differentiator (PD sensor), a pressure sensor (TOYODA PD-64S500K), and a controller. Although the SP valve has 5 ports, it was used as a 3-port servo valve, i.e., supply, control and exhaust ports. The unused ports were plugged. The Isothermal Chamber is the result of previous research [2]. It is filled with metal wool, which creates a nearly isothermal state change within the chamber. The isothermal chamber used has a volume V of 0.026 m^3. The PD Sensor measures the pneumatic pressure differential with high precision and with a quick response [3]. The resolution of the PD sensor used in this research is about 200 Pa/s, and the break-point frequency of the sensor is about 190 Hz.

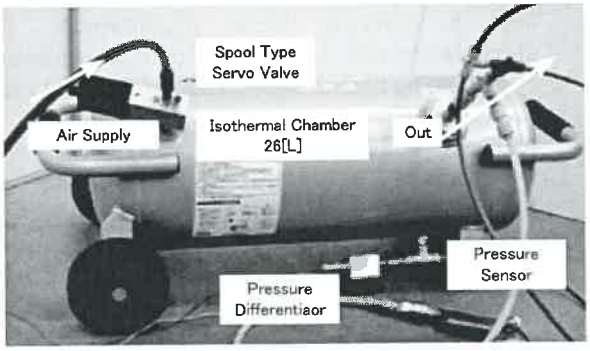

Fig. 1: Photograph of developed HPQR

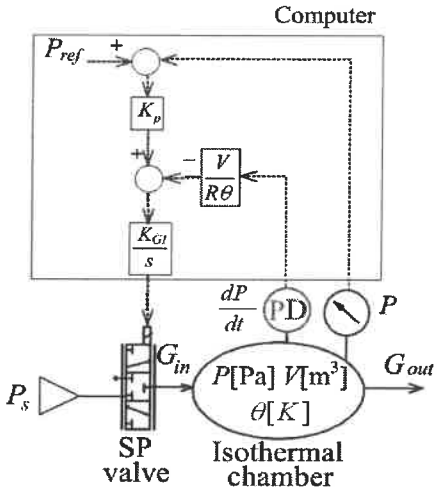

Fig. 2: Schematic of developed HPQR

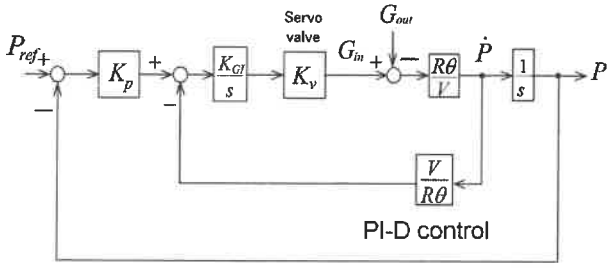

Fig. 3: Block diagram of pressure regulator

Minute pressure changes within the chamber are detected by the PD sensor, and fed back to the servo valve to maintain the pressure at a desired value.

Controller Design

The purpose of the HPQR is to maintain the pressure within the isothermal chamber at a set value. The important point is that, irrespective of upstream or downstream disturbances, the pressure within the isothermal chamber should be maintained at a constant value. A block diagram of the developed HPQR is shown in Fig. 3. The symbols are: P_{ref} : reference value of pressure [Pa], K_p: proportional gain [(kg/s)/Pa], K_{GI}: integral gain [V/kg], K_v: flow rate gain of SP valve [(kg/s)/V], G_{in}: input flow rate [kg/s], G_{out}: output flow rate [kg/s], R : gas constant [J/(kg K)], θ : temperature in chamber [K], V : volume of chamber [m^3] , P : pressure in chamber [Pa].

The SP valve characteristics are approximated to the linear constant Kv. The main loop is a pressure-feedback loop. In the minor loop, the differentiated value of pressure is a feedback quantity. Therefore, a PI-D control system is constituted to maintain the pressure within the isothermal chamber at a set value, irrespective of upstream or downstream disturbances. The affects of the nonlinear characteristics of the SP valve and the affects of supply-pressure fluctuations can also be reduced by the minor loop. Assuming that the time constants of the minor loops are much shorter than those of the main loop, the transfer function of the main loop can be expressed as:

$$\frac{P}{P_{ref}} = \frac{1}{1+T_p s} = \frac{1}{1+\frac{V}{K_p R\theta}s} \qquad (1)$$

In this research, K_p is set as 1.545×10^{-6} (kg/s)/Pa, so T_p is calculated as 0.2055 s.

PROPOSED PERFORMANCE EVALUATION METHOD

Structure of Proposed Device

To evaluate the performance of the HPQR, the device shown in Fig. 4 was fabricated. The evaluation device consists of an absolute pressure sensor (YOKOGAWA MT210, resolution: 1.0 Pa), an isothermal chamber (0.2 L), a differential pressure gauge (Nagano-keiki KL-17 + -1.0 kPa), a hand valve (ball valve), a gas duster, a quick-response laminar flow sensor (QFS) [4], and a computer for measurement. The device evaluates the stability of the downstream pressure of the HPQR (shown as P_2). The measurement procedures are as follows. First, after the pressure P_2 settles at the set value, the hand valve is closed (now, P_2=P_3). Then, a disturbance (for example a change in the flow rate) is applied to the HPQR. Although the bias pressure value is measured by the absolute pressure sensor at high resolution, the measurement dynamic characteristics of the absolute pressure sensor is not high enough (the response time is indicated as 2.5 s in the manufacturer's catalog).

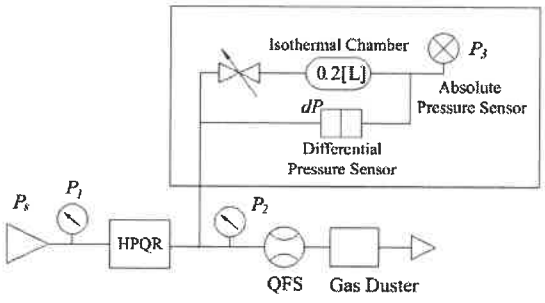

Fig. 4: Schema of HPQR testing device

Therefore, quick fluctuations in disturbance are measured by the differential pressure gauge (dP), which has a resolution of 0.1 Pa and dynamic characteristics of several hundred Hz. By adding the signals of the absolute pressure sensor and the differential pressure gauge, P_2 can be measured as Eq. (2).

$$P_2 = P_3 + dP \tag{2}$$

Experimental Procedure and Result

A performance evaluation was carried out using the setup shown in Fig. 4. Air from a compressor, P_s is supplied at a pressure of around 0.8-0.9 MPa (abs). Downstream of the HPQR, are a gas duster and a QFS. The QFS is used to generate a more precise disturbance, and measures the output flow rate through the gas duster. In the experiments, the reference pressure value of the HPQR, P_{ref}, is set to 371.3 kPa (abs), which is the designated value of supply pressure to an actively controlled pneumatic isolator, which is used in the next section. After the pressure P_2 settles at 371.3 kPa (abs), the hand valve is closed. Then, at the 65 s, the gas duster is opened, and at 85 s, the gas duster valve is closed to generate a downstream flow rate disturbance as indicated in Fig. 5.

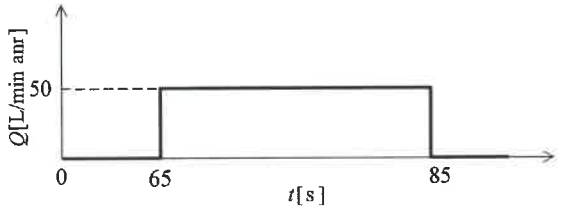

Fig. 5: Time chart of step disturbance

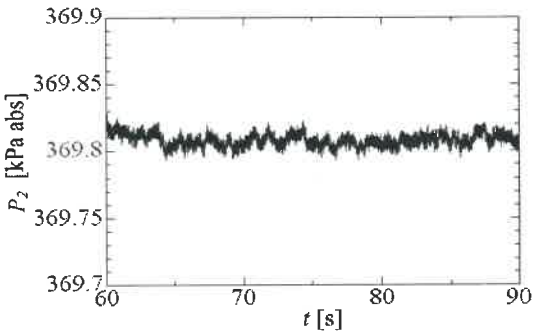

Fig. 6: Experimental result

The experimental result, P_2 (calculated by Eq. (2)) is shown in Fig. 6. The result shows the pressure value differs by about 1.5 kPa from 371.3 kPa (abs). The reason for this is thought to be a difference in calibration between the pressure sensor of the HPQR and the absolute pressure sensor. Irrespective of the disturbance, the result value stabilizes itself within 10 Pa.

APPLICATION OF DEVELOPED REGULATOR TO PNEUMATIC VIBRATION ISOLATOR

Experimental Setup

Figure 7 shows an HPQR fitted upstream of an actively controlled pneumatic vibration isolator. The control diagram of the isolator is also shown in Fig. 7. The relative displacement (x-x_0) and the acceleration on the isolation table are fed back to the controller and control signals, as constituting skyhook damping. The control signal is sent to a nozzle-flapper type servo valve. A photograph of the isolator used in this research is shown in Fig. 8. A weight of about 200 kg is supported by 3 air springs, having a volume of

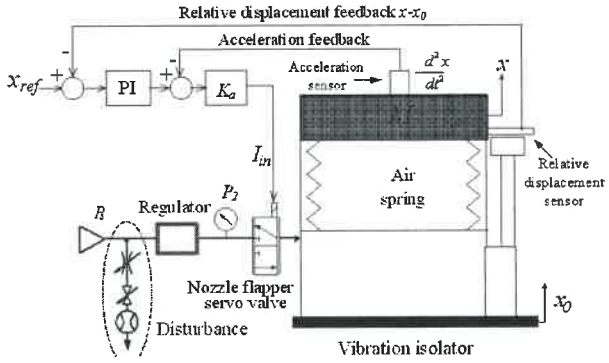

Fig. 7: Experimental setup

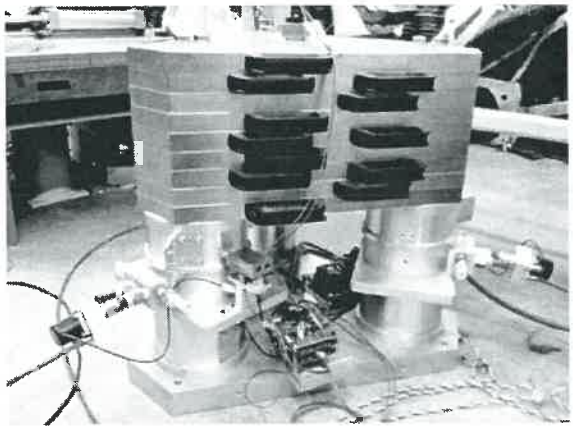

Fig. 8: Photograph of the pneumatic vibration isolator used in this research

1.5 L each. Each air spring is equipped with an eddy current-type noncontact relative displacement sensor (3.0 μm in resolution). An acceleration sensor of 1.0×10^{-6} m/s^2 in resolution is positioned on the weight.

Experimental Procedure and Result

In the experiments, the supply pressure from the compressor, P_s is 0.8-0.9 MPa (abs). First, the displacement of the table was set to a reference value of x_{sv}=2.5 mm. At t=15 s, the hand valve was opened and a disturbance created. The disturbance flow rate was about 100 L/min (anr). At t=18 s, the hand valve was closed. This type of disturbance imitates the usage of other machines in a factory, which causes a reduction in the supply pressure and flow pulsation. For comparison, the experiment was repeated with three types of commercially available precision regulators (DH : Diaphragm-type regulator, NF : Nozzle-flapper type regulator, and an ER : Electronic regulator) installed in place of the developed HPQR. The relative displacement

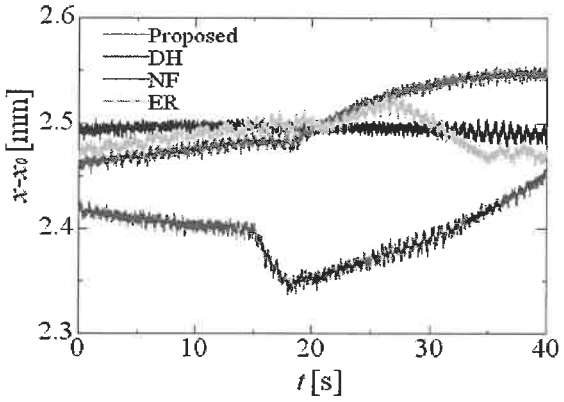

Fig. 9 Experimental results (displacement)

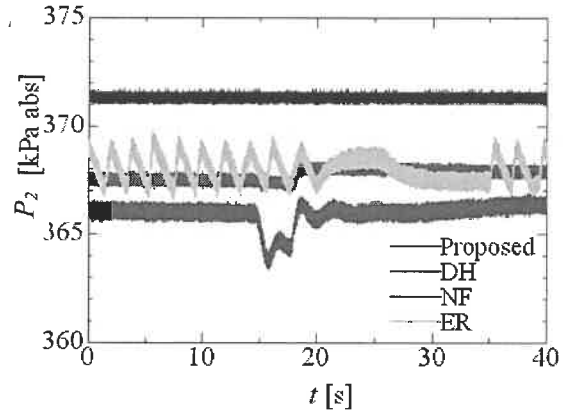

Fig. 10 Experimental results (pressure)

(x-x_0) and the pressure P_2 were recorded during the experiments. The experimental results are shown in Figs. 9 and 10. In the cases of DH, NF and ER regulators, as the disturbance begins, the relative displacement and the pressure visibly fluctuate by about 0.01-0.1 mm and 1-5 kPa, respectively. Whereas, when the HPQR is employed, both the displacement and the pressure are constant.

CONCLUSION

In this research, a performance-evaluation method for a newly developed high-precision, quick-response pressure regulator (HPQR) was proposed and an evaluation device was fabricated. The evaluation device consisted of an absolute pressure sensor, an isothermal chamber, a differential pressure gauge, a quick response laminar flow sensor (QFS), an air duster, and a computer. The performance of HPQR was examined using the performance-evaluation device. Then, the HPQR was used to stabilize the supply pressure for an actively controlled pneumatic vibration isolator. Compared with the performance of three types of commercially available precision pressure regulators, the superiority of the developed HPQR was clearly visible, especially in terms of avoiding affects from disturbances that occur upstream of the pressure-regulating device.

ACKNOWLEDGEMENT

This work was supported by KAKENHI (21760176).

REFERENCES

[1] Kato T., Kawashima K., Funaki T., Tadano K., and Kagawa T., "A New, High-Precision, Quick-Response Pressure Regulator for Active Control of Pneumatic Vibration Isolation Tables," Precision Engineering, 2010, 34,1, pp.43-48.

[2] Kawashima K., Kagawa T., and Fujita T., "Instantaneous flow rate measurement of ideal gases," Trans. ASME, J. Dyn. Syst. Meas. Control, 2000, 122, pp. 174-178.

[3] Kawashima K., Kato T., Yamazaki Y., Yanagisawa M., and Kagawa T., "Development of slit type pressure differentiator using an isothermal chamber," Meas. Science and Technology, 2005, 16, pp. 1150-1156.

[4] Funaki T., Sengoku K., Kawashima K., and Kagawa T., "Dynamic calibration of laminar flow sensor for gases," Proc. of SICE Annual Conference 2004, CD-ROM (2004).

PRECISION THREE DIMENSIONAL MODELING FOR SPATIAL CONTROL OF THE ION BEAM SPUTTERING PROCESS FOR OPTICAL THIN FILMS

Dale C Ness, Chris S. Wood
Precision Photonics Corporation
Boulder Colorado USA

OVERVIEW

The Ion Beam Sputtering (IBS) process is known to produce the lowest scatter and lowest loss optical thin films. IBS films have numerous, significant advantages including: Near bulk density, highly repeatable and fully automated process control, very low absorption and scatter, and high laser damage thresholds. Additionally, IBS is an energetic deposition process, which leads to dense film morphology and improved film adhesion[1, 2].

Because of these advantages, Ion Beam Sputtering is the coating technology of choice for precise, robust optical thin film coatings, such as very high-reflectors (T < 20ppm), steep filters, polarizers, and dichroic beam splitters. With suitable process controls and modeling tools, the inherent stability and repeatability of the IBS process lends itself to applications with difficult coating thickness control requirements, such as large optics with stringent uniformity requirements.

Because IBS process pressures (~ 10E-4 Torr) are lower than those of other coating technologies, such as electron beam evaporation and magnetron sputtering, we are able to develop deterministic mathematical models based on the (largely) ballistic trajectories of coating material as it forms the film on the substrate. Such models allow us to leverage the inherent precision of the IBS process and achieve coating thickness control on the order of a monolayer of material in certain circumstances.

In this paper we discuss the development and application of PPC's VirtualChamber™ which is a sophisticated three dimensional mathematical model of the IBS deposition process. When coupled with shadow masking techniques, we utilize VirtualChamber™ to achieve precision spatial control of the IBS deposition process. We discuss the underlying assumptions of the model, which utilizes computational geometry algorithms to calculate the effects of the shadow masks, analogous to calculating highlights and shadows in a computer graphics animation. The shadow masks, developed using VirtualChamber™, are fabricated using CNC machining, a process facilitated in a production setting by synchronizing the coordinate systems of VirtualChamber™ with those of the CAD software being employed.

Finally, we outline three applications of VirtualChamber to precision manufacturing challenges drawn from PPC's production and R&D work.

THE ION BEAM SPUTTERING PROCESS AND THE THREE DIMENSIONAL MODEL

FIGURE 1 shows a simplified sketch of the IBS process, which takes place within a high vacuum chamber. A beam of ions (typically Argon) is produced by the Ion Source and is accelerated towards a sputtering target. Material (e.g. Ta) is sputtered off of the target and combines with the reactive gas (e.g. O2) to form a stoichiometric film (e.g. Ta2O5) at the substrate. In general the net deposition plume in the region of the substrate is highly non-uniform. In practice, one achieves coating uniformity by a combination of substrate rotation and shadow masking techniques.

PPC's VirtualChamber™ (shown in *FIGURE 2*) has excellent agreement with experiment because it is a semi-empirical model which utilizes calibration data and captures essential real-world coating chamber attributes:

- The sputtering target is an extended emitter, and our film deposition occurs in the near field regime of this emitter. Each point on the substrate "sees" deposition over an extended range of angles θ.
- The sputter yield depends on ejection angle θ'
- The intensity from a given dA' (surface area element in the target plane) along a given

vector R from target point to substrate point falls off by the inverse square law

- The deposition angle θ (from a given dA') depends on the specific substrate and target locations
- The mask is positioned in 3-d space between the target and the substrate and is parameterized by its transmission as a function of the vector R.

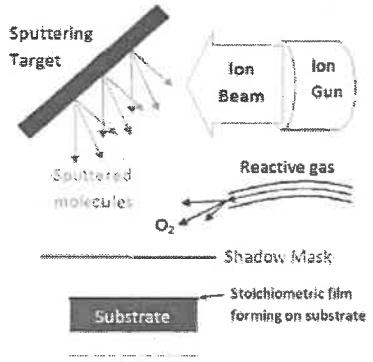

FIGURE 1. A simplified sketch of the IBS process

The instantaneous deposition rate can be calculated for an arbitrary position within the coating chamber. The coating thickness is then calculated as the path integral substrate of the deposition rate equation.

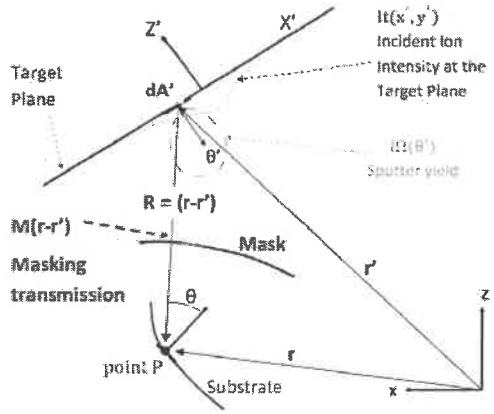

FIGURE 2. The mathematical quantities in VirtualChamber describe the physical IBS process in detail.

In *FIGURE 3* is an example of a planar ratefield, calculated using VirtualChamber™, which is useful for modeling traditional planar orbit configurations. We define the ratefield as the instantaneous deposition rate as a function of position, calculated over an extended surface. The substrates typically orbit in the ratefield surface during coating deposition.

A common planar substrate fixturing system is a planetary (dual) rotation system. The required coating thickness is achieved in this case with the use of a shadow mask which selectively blocks the coating material for a fraction of the substrates' orbits.

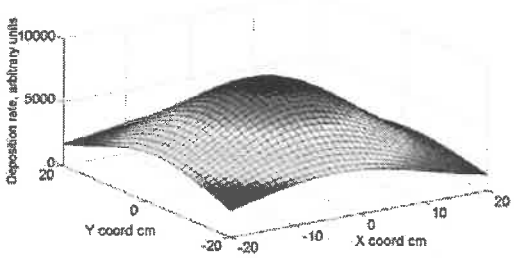

FIGURE 3. The planar ratefield is the predicted coating deposition rate as a function of position in a 2-d plane within the coating chamber.

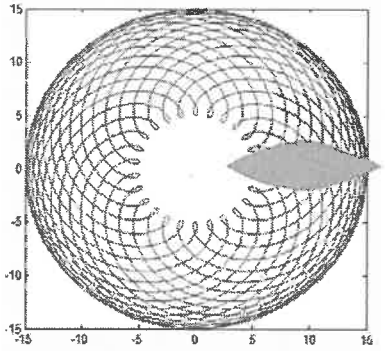

FIGURE 4. The orbit of a given point on a substrate in a planar planetary rotation fixture. This orbit occurs in the plane of the ratefield in the previous Figure. An example shadow mask for this configuration is indicated by the 'willow leaf' shape.

In this case, the uniformity mask is often shaped like a willow tree leaf, as shown in *FIGURE 4*. We note that the three dimensional model is helpful, but not essential to solve this problem. The uniformity mask contour can also be determined by iterative empirical techniques and 2-d approximations well known to coating manufacturers.

When solving more challenging problems, such as coating uniformity inside steeply curved surfaces, the three dimensional VirtualChamber™ model becomes an enabling tool. In *FIGURE 5* we show a deep concave lens where the radius of curvature is on the order of the diameter of the lens. In this configuration, and in the absence of any corrective mask, the coating is thicker in the center of the lens than it is at the edge of the lens, which is due to two competing effects: The center of the lens is further from the sputter source than the edge of the lens, which makes the coating at the *center* of the lens comparatively thinner, however the average incident angle of the coating material at the edge of the lens is relatively greater, which makes the coating at the *edge* of the lens relatively thinner.

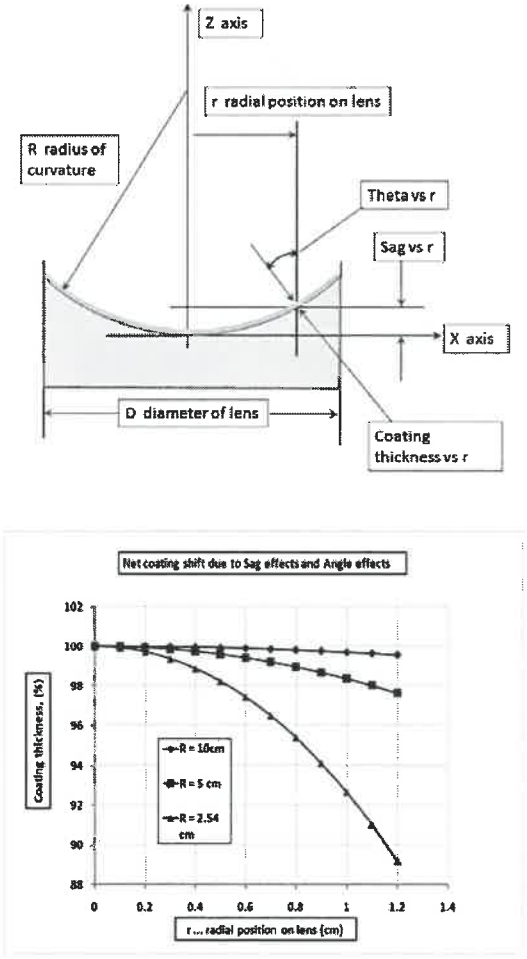

FIGURE 5. Net coating shift due to sag and angle effects for a 1 inch diameter concave lens, for radii of curvature of 2.54cm, 5cm, and 10cm.

The net effect is calculated in VirtualChamber™ and is shown in *FIGURE 5* (bottom). In the case of a 2.54cm diameter lens, with a 10cm radius of curvature, the net coating shift is on the order of 0.5%. Depending on application and customer specifications, even this relatively small level of coating non-uniformity may require correction with the use of precision shadow masks, developed in VirtualChamber™. For an example optical coating such as an anti-reflective coating at 633nm, the total coating thickness is on the order of 200nm. Therefore our model is giving predictions on the order of 0.5nm, which is at the level of a monolayer in average coating thickness.

In *FIGURE 6* we show a more extreme case of a deep concave surface, which is a tangent ogive missile nose cone, positioned within a coating chamber and is configured for coating the interior dome surface. In this case there are more significant challenges, such as the presence of glancing incidence coating trajectories relative to the steeply curved surface, as well as the fact that the dome shape 'self- shadows' some of the coating trajectories.

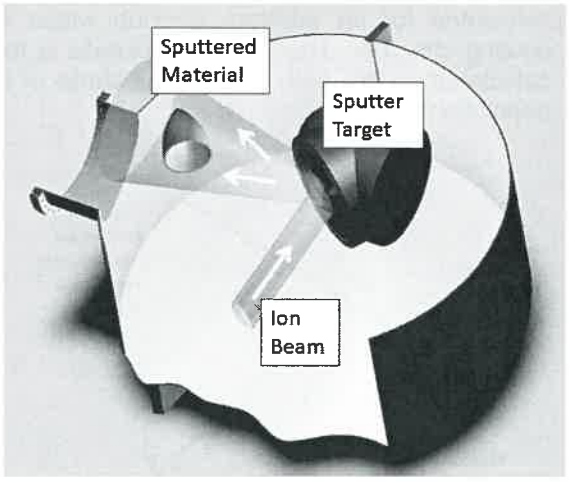

FIGURE 6. A tangent ogive dome in an IBS coating chamber

To address these challenges, we utilize PPC's VirtualChamber to calculate the 3-d effects of the shadow masks, and of dome self shadowing by incorporating computer graphics algorithms analogous to those used for calculating highlights in a computer generated animation, as illustrated in *FIGURE 7*.

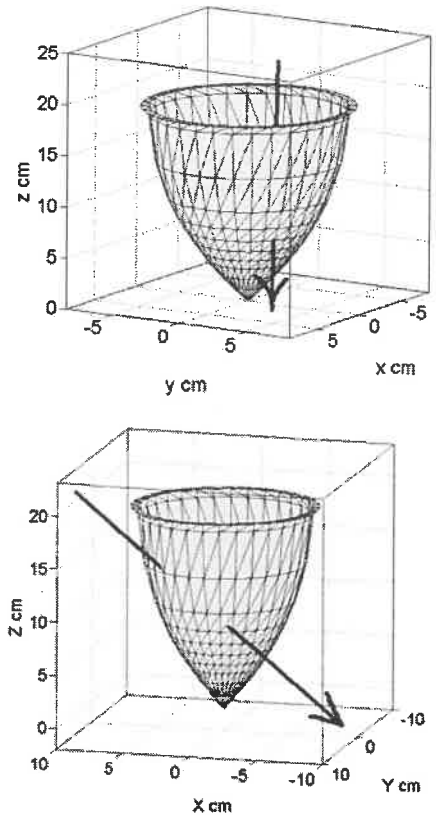

FIGURE 7. (top) An example coating ray being deposited on the interior dome surface. (bottom) An example of dome self-shadowing: The coating ray is blocked by the dome's exterior. This ray is 'self-shadowed' and does not contribute to the interior coating thickness.

In the case of the tangent ogive dome we calculate the ratefield at the interior surface of a 3-d ogive curve as shown in *FIGURE 8.* The resultant ratefield can be specified conveniently by the Z/Phi coordinates (i.e. cylindrical coordinates) along the interior dome surface.

VirtualChamber™ allows us to optimize the configuration of the dome within the coating chamber, and provides a tool for developing the shadow masking required to achieve the customer's thickness profile specifications. The contours of the shadow masks are conveniently exported to CAD software, such as SolidWorks[3] for detailing and subsequent machining, a process greatly facilitated by synchronization of the coordinate systems of VirtualChamber™ with those of the CAD model.

ACKNOWLEDGEMENTS

This work is supported by the Naval Air Warfare Center Weapons Division, China Lake, under contract N68936-10-C-0020.

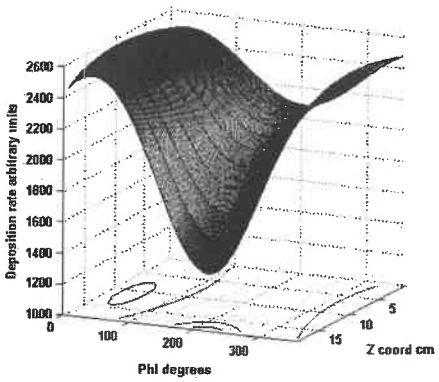

FIGURE 8. An example dome interior ratefield calculated using VirtualChamber™, plotted in z/phi coordinates.

REFERENCES

[1] P.W. Baumeister, "Optical Coating Technology," SPIE Press, Bellingham Washington, 2004.

[2] D.L. Smith, "Thin Film Deposition, Principles and Practices", McGraw – Hill, Inc, 1995.

[3] www.solidworks.com

USE OF CERAMIC SPOTTING MASTERS FOR SCRAPING

David R. Stussi
Gardner-Stussi Tool and Die

The fundamental techniques of scraping have been around for a long time. However, the specifics are often subject to variations due to circumstances, personal preferences, skill sets and tools at hand. The following paper is based on the techniques I have used over the years following a fortuitous tool substitution.

Standard cast iron masters with bluing and lead pigment are used through the roughing process and continue until the surface is within .0002 (.005mm) of the desired shape. At that time the master is inspected and corrected and the spotting process is used. The spotting process involves the rubbing of the master and the part but no bluing is used. The high spots are then visible as shining spots with the proper lighting.

Some years ago during the re-scraping of the v-ways of a Moore #5, the cast iron box square I used as a master was in need of correction. A ceramic straight edge was in process and had just been inspected. I decided to use the ceramic as a spotting master and the results were a marked improvement in all respects.

Due to the cutting action of the ceramic, the spotting marks showed much brighter than the results of the burnish action of a cast iron master. The metal removed transferred to the ceramic master after a short time. The removed metal loaded the master preventing the masters from cutting too aggressively. The geometry of the surface to be scraped was improved prior to a scraping cut being taken as a result of the cutting action of the ceramic master.

The ceramic straight edge was then inspected after several days of being used as a spotting master and had no significant wear. A standard cast iron master would have developed enough wear over this period to require some attention.

During the following years several ceramic masters have been acquired to be used in this spotting process and the following information details the results of scraping a Moore #3 table top.

Moore table 11 x 24 (280mm x 610mm) after rough scraping flat within .0003 (.008mm)

8in x 20in (200mm x 510mm) 99.5 Alumina ceramic master flat within .0001 (.0025mm)

The process used was to inspect the table, rub the ceramic master, inspect the table, and scrape (spot) the table and inspect. This process was repeated 4 times with a resulting table flatness of .00004 (.001mm). Each rub of the ceramic master improves the flatness generally about .00002 (.0005mm). Upon completion the ceramic master was inspected and no wear was detected. I have noted that any wear on the master shows as a localized improvement of the surface finish. To keep a uniform and effective cutting action the ceramic master has the surface finish roughed up with a small diamond charged hand lap to yield approximately a 20 to 32rms finish. It is important that this reconditioning be done 2 directions (or more) 90 degrees to each other to create 'peaks' rather than a 'ridge line' effect. During this process it is also possible to improve the flatness of the master through selective lapping.

The inspection was carried out with a .00001(.00025mm) mikrokator mounted to the spindle and a standard scraper block

1st) Machine Table (numbers in μ of inch)

0	40	40	-40
-40	20	20	-40
-80	-20	-40	-80
-120	-40	-60	-120

160 deviation

Table after ceramic master rub

0	40	40	0
-20	30	30	-20
-40	0	10	-40
-100	-40	-40	-80

140 deviation

2nd) Machine Table after spotting

0	40	40	20
-20	20	30	-20
-40	-20	0	-20
-80	-20	-20	-80

120 deviation

Table after ceramic master rub

0	20	40	20
0	30	20	-10
-40	-20	20	0
-60	-20	-20	-60

100 deviation

3rd) Machine table after spotting

0	30	40	20
10	20	30	0
-10	10	20	0
-60	-10	-10	-40

80 deviation

Table after ceramic master rub

0	20	40	20
0	20	20	0
-20	0	20	20
-30	-10	0	-30

70 deviation

4th) Machine table after spotting

0	20	40	20
0	20	20	-10
-10	20	10	-10
-40	0	-10	-40

80 deviation

Table after ceramic master rub

0	20	30	20
0	30	20	20
0	0	20	20
-30	-20	-10	-30

60 deviation

5th) Machine table after final spotting

0	20	20	10
20	20	20	0
10	20	20	20
-20	0	0	-20

40 deviation

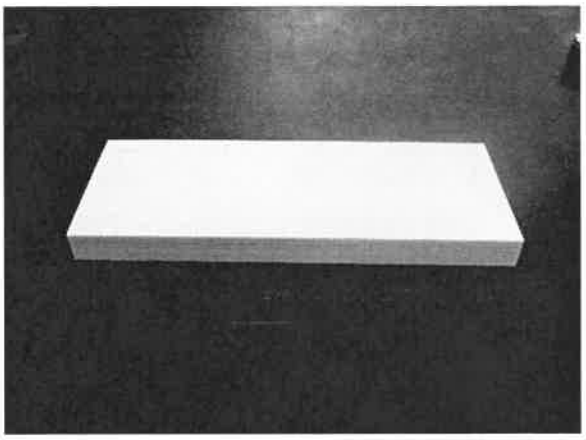

Ceramic Master

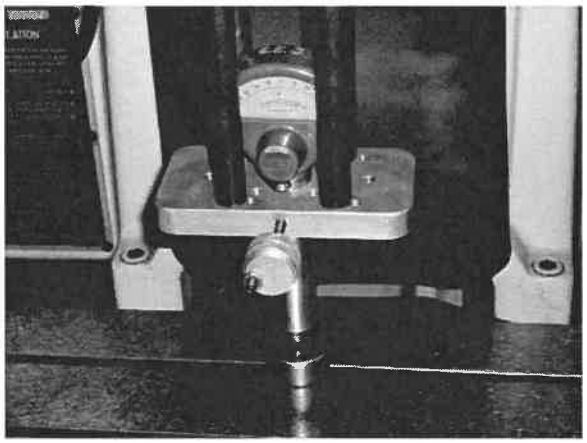

Inspection of table flatness

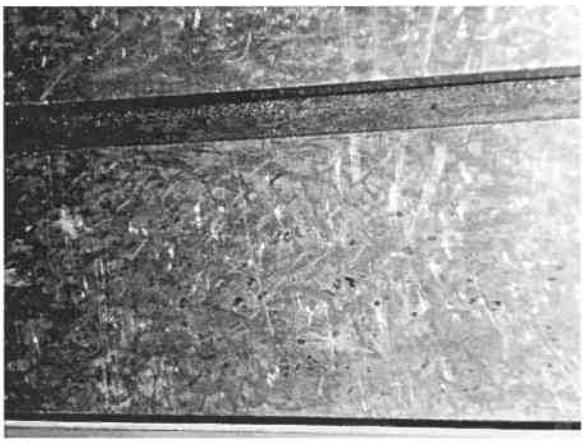

Examples of spotting

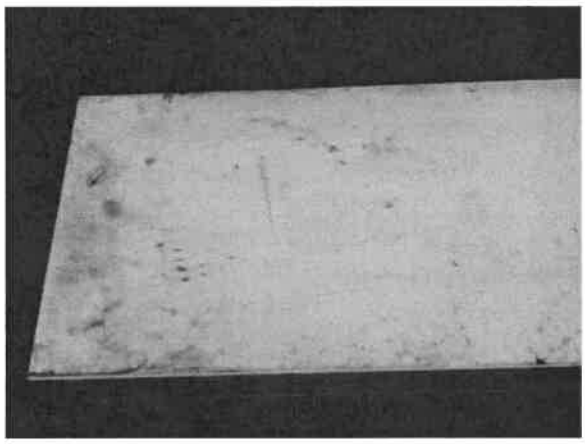

Loaded master after use

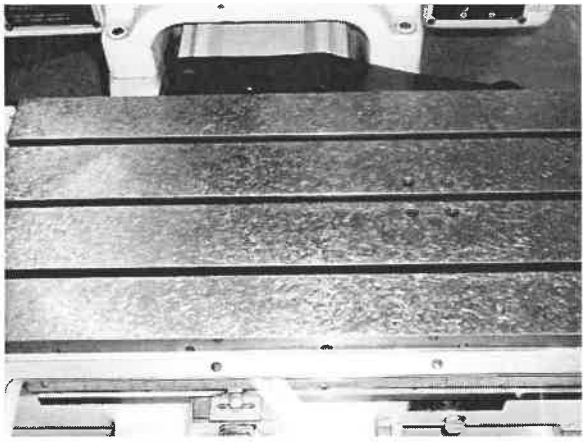

Table after final spotting

IMPROVING ANTI-ADHESIVE PROPERTIES OF CUTTING TOOL SURFACE BY NANO/MICRO TEXTURES -CONSIDERING THE TEXTURE PATTERNS-

Tatsuya SUGIHARA[1], Toshiyuki ENOMOTO[1]
[1]Department of Mechanical Engineering,
Graduate School of Engineering, Osaka University
Suita, Osaka, Japan

INTRODUCTION

Such advantages as a high ratio of strength to mass and good corrosion resistance have rapidly raised for lightweight aluminum alloy composites, especially in the transport industry. Their low hardness compared to steel makes aluminum alloys easy to cut, but this can be outweighed in certain applications by their low melting point and high ductility, witch make aluminum chips adhere strongly to the cutting edges of tools, leading to tool breakage. Then many cutting tool technologies such as cutting tool geometry, and cutting tool surface coating and finishing have been developed. In particular, diamond-like carbon (DLC) coated tools with extremely low friction are being applied in the dry or near dry cutting of aluminum alloys, but adherence of aluminum chips to DLC coated tools still requires a flooded cutting fluid in practical use [1]. Furthermore, tool breakage occurs frequently in cutting processes such as deep hole drilling, milling and tapping, in which it is difficult to directly supply cutting fluid to the cutting point.

To solve these problems, we used a surface engineering approach, namely, a highly functionalization of tool surfaces by textures to determine the role of textured surfaces in: (i) retaining cutting fluid and (ii) reducing actual contact area between the tool and chips. Effective application is expected to increase lubricity and promote anti-adhesive properties at tool chip interface. As shown in Fig. 1, a DLC-coated cutting tool with nano/micro-textured surface using femto-second laser technology was developed. A series of aluminum alloy face-milling experiments showed that the nano/micro-textured surface promoted anti-adhesiveness at the tool chip interface [2] and, however, the adhesion problem still remained

In this paper, the ways to improve the anti-adhesive properties using nano/micro-textures were studied in order to overcome the above-mentioned problem. Based on this, a cutting tool with a banded nano/micro-textured surface was newly proposed to ensure excellent anti-adhesive properties.

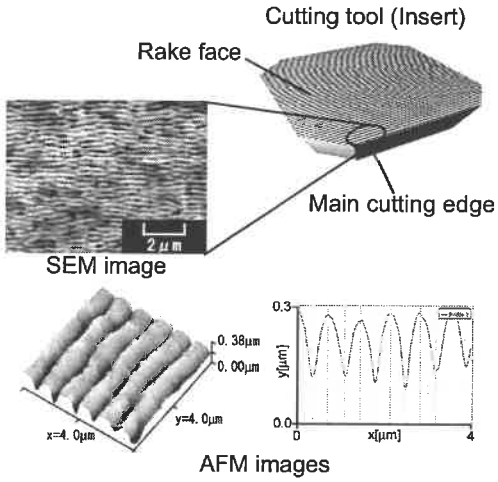

FIGURE 1. Previously Developed cutting tool with nano/micro-textured surface [2].

PROBLEMS ASSOCIATED WITH CUTTING TOOL WITH NANO/MICRO-TEXTURED SURFACE

Cutting Tool with Nano/Micro-Textured Surface

Femto-second laser technology was adopted to generate nano/micro-grooves [3] on the rake face of cemented carbide cutting tool. Precise regular grooves are produced using liner polarized femto-second laser energy near the ablation threshold, and spacing of regular structures about the same as the laser wavelength. Applying this technology, the regular nano/micro-grooves 100-150 nm deep and spaced at 700 nm were produced on the rake face of the cemented carbide cutting tool using a laser (Canon Machinery Inc., Model Surfbeat R; peak wavelength 800 nm, pulse duration 150 fs, cyclic frequency 1 kHz, pulse energy 300 μJ). Before laser irradiation, the tool surface was polished with diamond slurry to a surface roughness of P-V 40 nm. After grooving, the plasma-CVD DLC film was coated on the textured surface to improve anti-

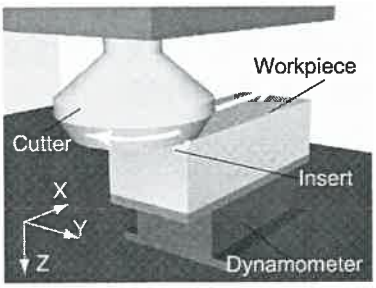

FIGURE 2. Experimental setup of face milling test.

TABLE 1. Cutting conditions.

Workpiece	A5052 W 75 mm - L 210 mm	
Tool (Insert)	Cemented carbide K10 SEKN42M, Sumitomo Electric Hardmetal	
Tool geometries	Axial rake angle θ_A	20°
	Radial rake angle θ_R	-3°
	True rake angle α	12.4°
	Corner angle γ	45°
	Cutter diameter D	80 mm
Cutting speed	380 m/min (1500 rpm)	
Depth of cut	3 mm	
Feed rate	0.12 mm/rev.	
Cutting fluid	Emulsion type (JIS A1) Finecut CFS-100, NEOS	
Supply rate	12.6 L/min	

adhesiveness. The coating decreased grooves depth 10-20 nm.

Cutting Experiment Procedures and Performance

Cutting experiments were conducted on aluminum alloys A5052 using a vertical machining center (Yamazaki Mazak Corp., AJV-18), as illustrated in Fig. 2. The center of the cutter was set on the center line of the workpiece. Table 1 lists the cutting conditions. Emulsion type cutting fluid (NEOS Co., Ltd., Finecut CFS-100) was supplied at a flow rate of 12.6 L/min.

In cutting performance, the rake face of the cutting tool was observed after 1800 m cutting to evaluate tool surface adhesion. Scanning electron microscope (SEM) (Hitachi High-Technologies Corp., S-3400NX) and energy dispersive X-ray spectrometry (EDX) analysis of the rake face aluminum (Fig. 3) confirmed large adhesion to the rake face of a conventional DLC-coated, namely polished tool. In contrast to this, it was found that the nano/micro-textured, particularly, nano/micro-grooves parallel to the main cutting edge, improved anti-adhesion, but not sufficiently on the cutting tool surface (Fig. 3(b)).

Then the enlarged SEM observation was done to

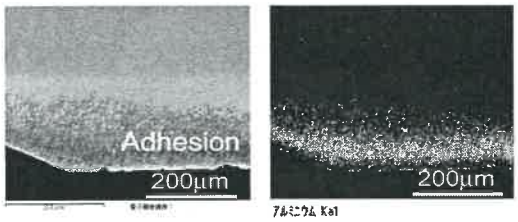

(a) Polished tool

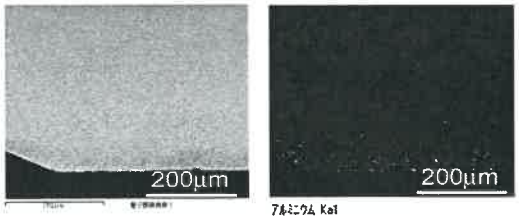

(b) Developed tool with grooves parallel to edge

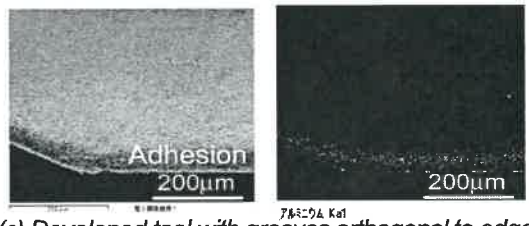

(c) Developed tool with grooves orthogonal to edge

FIGURE 3. Rake face of DLC coated tool with nano/micro-texture after cutting. (Left: SEM image, Right: EDX-Al image)

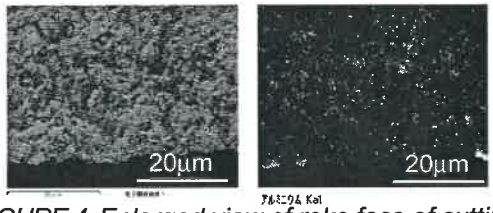

FIGURE 4. Enlarged view of rake face of cutting tool with grooves parallel to edge. (Left: SEM image, Right: EDX-Al image)

determine adhesion to the tool surface in detail (Fig. 4). Although it was confirmed that nano/micro-grooves were not buried by adhesion after cutting for 1800 m, as SEM image showed, aluminum adhered slightly as EDX-Al imaging showed. Concern arose that adhesion could become worse with increasing cutting distance, eventually leading to tool breakage, making it vital to increase anti-adhesive properties.

Anti-Adhesive Properties with Nano/Micro-Texture in Dry Cutting

As stated, the nano/micro-textured surface plays two roles, namely: (i) retaining cutting fluid and (ii) reducing actual contact between the tool and chip. To evaluate these two roles individually, dry cutting experiments were conducted using basically the

same cutting conditions as in Table 1.
In addition to SEM and EDX analysis of the aluminum on the rake face after dry cutting for 1800 m (Fig. 5), the aluminum atom concentration on the tool rake face in EDX-Al imaging was measured to quantitatively evaluate aluminum adhesion (Fig. 6). Compared to wet cutting, aluminum adhesion in dry cutting increased in the tool with a nano/micro-texture and, in contrast, aluminum decreased in the tool with a polished surface.
This is thought to be due to the tool surface making strongly solid contact with chips in dry cutting. The tool with a polished surface had such a large contact area between tool and chips that high cutting heat was generated, decreasing adhesion and suppressing the build-up edge. On the other hand, in the tool with a nano/micro-texture, cutting temperature did not become high due to the small contact area, making adhesion greater than that in the tool with a polished surface. Moreover, chip material also entered easily into nano/micro-grooves under solid contact, i.e., nonlubrication.
It was found that wet cutting with the tool having a nano/micro-texture was superior - the aluminum atom concentration was 3.9 % - in decreasing tool surface adhesion in all types of cutting tool and cutting conditions.
From the above-mentioned consideration, it was found that the retention of cutting fluid on the tool surface was essential for achieving good anti-adhesive properties. Nano/micro-texture ensured that cutting fluid was well retained and that, as a result, anti-adhesion was high under wet cutting conditions.

PROPOSED CUTTING TOOL WITH BANDED NANO/MICRO-TEXTURE

Cutting Tool Development

Two types of texture pattern on the cutting tool surface thought to be effective in retaining cutting fluid are patterns that (1) prevent retained fluid leaking from grooves and (2) increase the amount of retained fluid. Then the DLC-coated cutting tool with a banded nano/micro-textured surface was newly developed, as shown in Fig. 7. Nano/micro-grooves in a direction parallel to the main cutting edge were generated in bands 50 μm wide on the polished tool surface.
The nano/micro-texture is sandwiched between polished surfaces, preventing fluid retained in the textured area from leaking. The banded nano/micro-texture surface is 100-200 nm deep, increasing the amount of fluid retained.

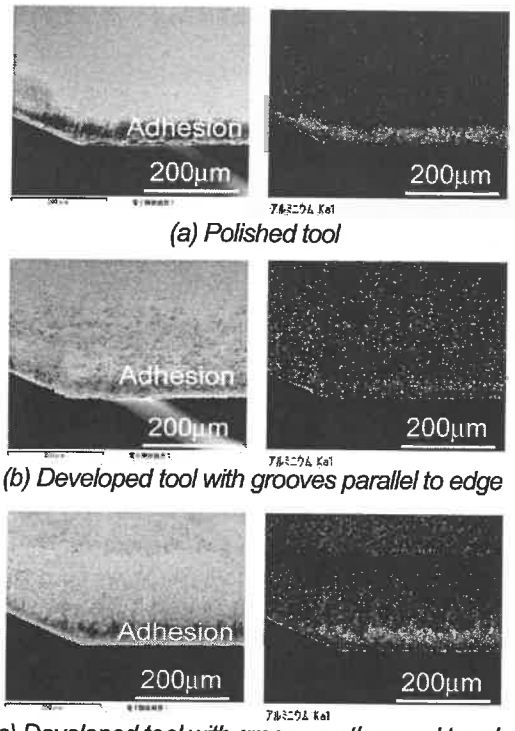

FIGURE 5. Rake face of cutting tool after dry cutting. (Left: SEM image, Right: EDX-Al image)

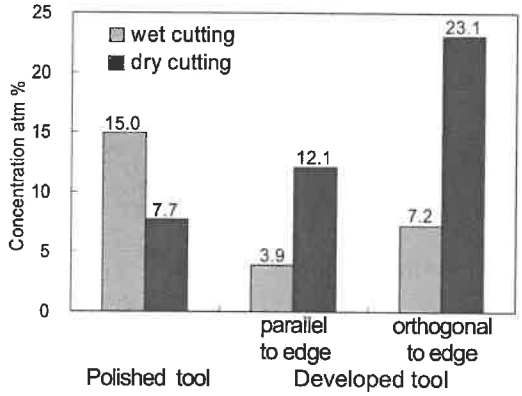

FIGURE 6 Concentration of aluminum atom on the rake face of cutting tool.

Evaluation of Anti-Adhesive Properties

The result of cutting experiments with the newly developed tool (Table 1) were analyzed using SEM and EDX analysis of the aluminum on the rake face after wet cutting for 1800 m (Fig. 8) and the aluminum atom concentration on rake faces of several tools was measured, including the newly developed one (Fig. 9). From these results, it was found that the banded nano/micro-textured surface provided excellent anti-adhesive properties reducing adhesion less than half compared to the tool having nano/micro-grooves overall.

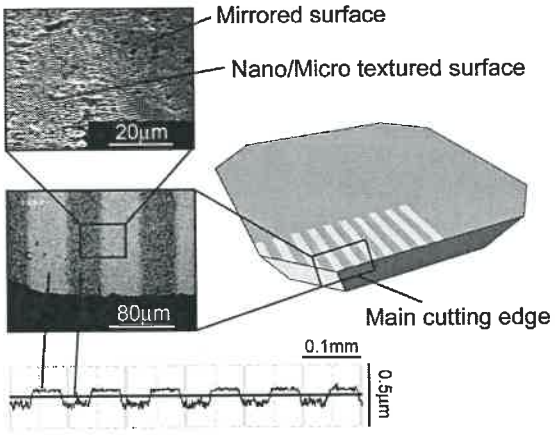

FIGURE 7. Newly developed cutting tool with banded nano/micro-textured surface.

The observation of the tool surface with optical scope (Keyence Corp., VF-7500) was carried out each 180 m in cutting distance to evaluate changes adhesion as cutting progressed. Fig. 10 shows the changes of the aluminum adhesion area, which was calculated with the image analysis from the microphotograph. Increased adhesion areas were very few in the newly developed tool – 1/15 compared to that of the polished tool and 1/2 compared to that of the tool with grooves overall.

CONCLUSIONS

A cutting tool with a nano/micro-textured surface was developed to improve anti-adhesive properties in aluminum alloy cutting, with the following findings:

- Nano/micro-textured surface increased adhesion of aluminum chips to the surface in dry cutting, but decreased adhesion in wet cutting.
- Improve cutting fluid retention on the tool surface is essential for achieving a good anti-adhesive properties in aluminum alloy cutting.
- The banded nano/micro-textured cutting tool surface significantly improves anti-adhesive properties.

ACKNOWLEDGEMENTS

We thank everyone at Canon Machinery Inc., Nippon ITF Inc., and Neos Co., Ltd., for their assistance and advice. This work was supported by Grant-in Aid for JSPS Fellow.

REFERENCES

[1] Yoshimura H, Moriwaki T, Shibasaka T, Okita J, Toda Y, Omae S, Nakai T, Kinoshita H. Study of generation and growth of adhesion mechanism in near-dry cutting of aluminum alloys. Journal of the Japan Society for Abrasive Technology 2007; 51 (7); 416-421.

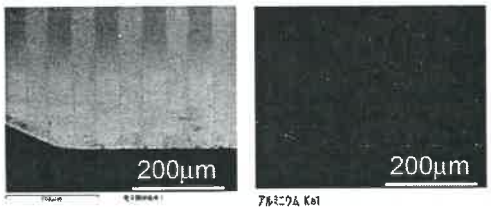

FIGURE 8. Rake face of the newly developed cutting tool after wet cutting. (Left: SEM image, Right: EDX-Al image)

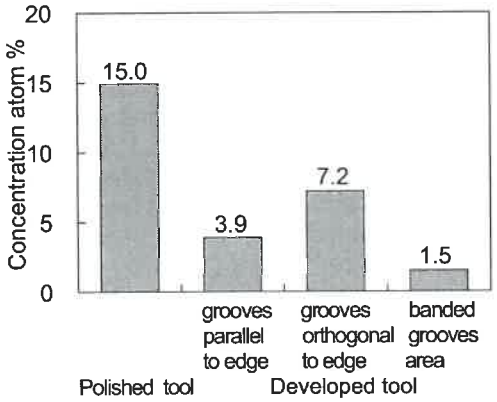

FIGURE 9. Concentration of aluminum atom on the rake face of cutting tool after wet cutting.

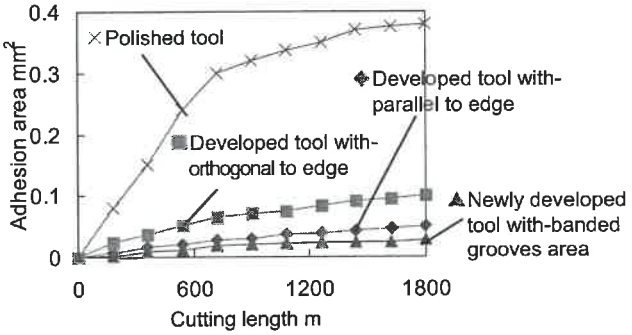

FIGURE 10. Changes of adhesion area on rake face with cutting length.

[2] Enomoto T, Sugihara T. Development of a cutting tool with nano/micro-textured surface. Improvement of anti-adhesive effect. Transactions of the Japan Society of Mechanical Engineers Series C 2008; 74 (745): 2315-2320.

[3] Sawada H, Kawahara K, Ninomiya T, Kurosawa H, Yokotani A. Precise periodic structuring with femtosecond-laser. Journal of the Japan Society for Precision Engineering 2003; 69 (4); 554-558.

DESIGN OF FLEXURE HINGE MECHANISM FOR DYNAMIC YAW CONTROL OF FPD LITHOGRAPHY STAGE

Dahoon Ahn[1], Hyunchang Kim[1], Daegab Gweon[1]
Sunho Lee[2], Woohyuck Choi[2], Sungtaek Baek[2] Sanghoon Lee[2] Junkyu Park[2]
[1]Department of Mechanical Engineering
Korea Advanced Institute of Science and Technology
Daejeon, Republic of Korea
[2]Stage Business Team
EVERTECHNO Co., Ltd
Cheonan, Republic of Korea

INTRODUCTION

In the lithography process of the flat panel display (FPD) manufacturing, a highly precision device such as XY H-type planar motion stage is used for positioning of a glass panel. This type of stage usually employs linear motors and air bearings, both are frictionless and laser interferometers as position sensors for high precision. Yaw(θ_z) motion error caused by inevitable parasitic motion of a stage, is defined as the amount of the stage rotation in the XY plane which means the change of orientation of the glass panel. So, dynamic compensation of the yaw motion error is extremely important for precision and accurate performance of the stage.

'Gantry control', a method to compensate the yaw motion has been commonly used, but it has weakness for the stage employing an air bearing guide. Motion of the stage by 'gantry control' may cause failure of the air bearing.

This letter introduces a flexure hinge mechanism for the dynamic yaw control of the precision stage. Analytic modeling and optimal design are achieved. Dynamic and static performance of the designed flexure hinge mechanism is verified in FEM simulation, finally.

GNATRY CONTROL OF THE AIR BEARING STAGE

The yaw motion error of the highly precision lithography stage is undesirable and should be eliminated. The yaw motion error can be measured using a pair of laser interferometers in real-time and global sense and compensated by the many control methods known as 'gantry control' already introduced in the before research [1-2]. However those methods have disadvantage of latent risk that may lead to failure of the air bearing. Correction of the yaw motion error by control of the two motors in parallel causes variation of the gap between air bearing and reference surface, even scratch on the surface of the air bearing as shown in the figure 1.

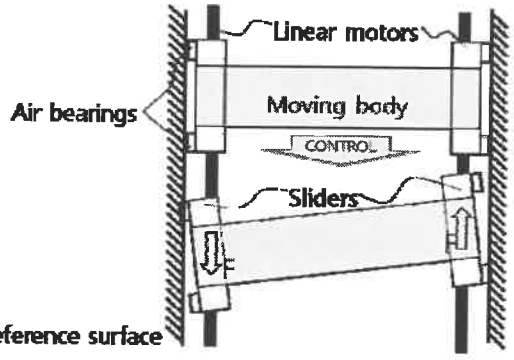

FIGURE 1. Gantry control of the air bearing guided stage

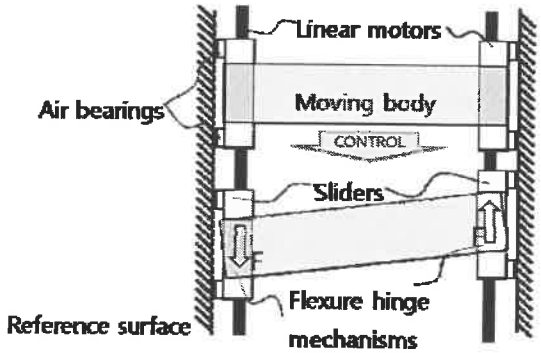

FIGURE 2. Gantry control of the air bearing guided stage with the flexure hinge mechanisms

In order to compensate the yaw motion error without any risk on the air bearing, a flexure hinge mechanism is introduced. Design process

of the flexure hinge is as following; Concept of kethe flexure hinge mechanism, The analytic modeling and the optimal design of the flexure hinge mechanism, Verification of the optimal design through the FEM analysis and Conclusion are given.

CONCEPT OF THE FLEXURE HINGE MECHANISM

The flexure hinge mechanism gives to the moving body one degree of freedom(d.o.f), rotation(θ_z) relative to the each sliders which carry the air bearing pads so that gap between the air bearing and the reference surface is always maintained to a few micro-meters, as shown in the figure 2. The rotational freedom is realized by the flexure hinge which has ideally continuous elastic deformation, because inherent friction of rotary bearing, for example, makes destructive effect on high precision although it has relatively simple structure.

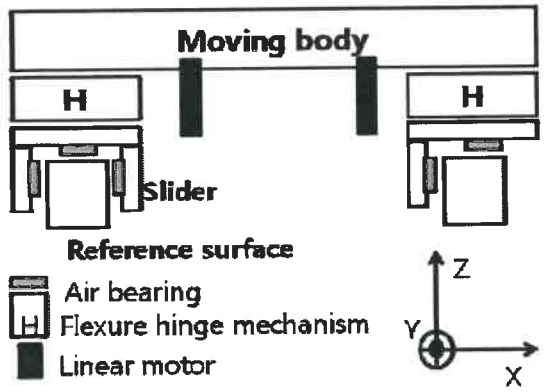

FIGURE 3. Structure of the stage system with the flexure hinge mechanisms

The flexure hinge mechanism has stiffness in all 6 directions, 3 translation and 3 rotation, and the stiffness in each direction should have proper value so that many requirements on the rotating mechanism are satisfied.

First, the rotational stiffness in θ_z direction of the flexure hinge mechanism, should be minimized because the driving moment to make the moving body rotate about z axis is limited by the pre-determined capability of the two linear motors and minimization of the power consumption at the motors is also required. However zero stiffness of the flexure hinge mechanism is impossible and low stiffness in θ_z direction causes also low stiffness in the other directions. The stiffness of the flexure hinge mechanism in all directions except one, rotation about z axis, is related to the structural mode of the stage and all modes are uncontrollable with linear motors. Therefore stage system is weak to external and direct disturbances and the gravity force due to the massive own weight if the flexure hinge mechanism has low stiffness.

Here the flexure hinge mechanism, which can have low stiffness in θ_z direction and high stiffness in the other 5 directions is proposed.(figure 4.) The requirements on the mechanism show trade-off one another, so the analytic modeling of the stiffness is carried out for the optimal design.

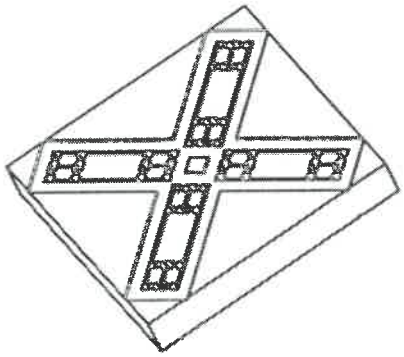

FIGURE 4. Concept of the proposed flexure hinge mechanism

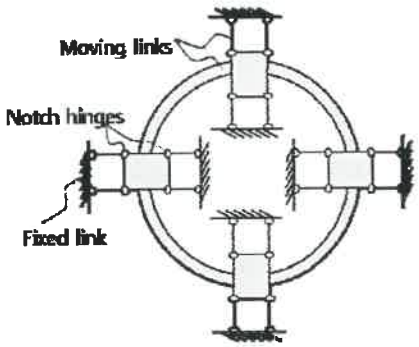

FIGURE 5. Skeleton diagram of the proposed flexure hinge mechanism

THE ANALYTIC MODELING AND THE OPTIMAL DESIGN OF THE FLEXURE HINGE MECHANISM

The flexure hinge mechanism inserted into each space between the moving body and the sliders has structure of the 1 fixed link, the 17 moving links and the 32 notch hinges as shown in the figure 5, the skeleton diagram of the flexure hinge mechanism. In order to obtain stiffness of 6 d.o.f, Ryu's method[3] is used. All the notch hinges are modeled as springs which can store

potential energy by their own elastic deformation and all the moving links are modeled as inertias which can have kinetic energy. Using the geometry of the flexure hinge mechanism and Lagrangian method, governing equation of the mechanism dynamics is derived. Final stiffness matrix of the whole flexure hinge mechanism obtained from the equation is used for the optimal design.

The stiffness in θ_z direction and reciprocals of the stiffness in the other directions are the cost function of the optimal design. The amount of deflection due to gravitation and the direct disturbances are constraints. Variables are the dimension of the notch hinges and the moving links. The optimization process was realized using the MATLAB® optimization toolbox based on a sequential quadratic programming method. Results of the optimal design are shown in table 1. The low stiffness in θz direction relative to those in the other directions makes the stage available to gantry control and still robust to external and direct disturbance.

TABLE 1. Results of optimal design

Optimal design result				
direction	Stiffness	Item	Target	Result
x & y	9.76E+08 N/m	Reaction to motor force in x direction	200 nm	81.9 nm
z	4.92E+08 N/m	Deflection under gravity	3 um	1.99 um
θx & θy	1.36E+06 Nm/rad	Reaction to motor force in y direction	3 arcsec	1.96 arcsec
θz	8.63E+04 Nm/rad	Max. yaw motion	90 arcsec	113 arcsec

TABLE 2. Verification of optimal design

Item	Target	Design result	FEM	Margin
Reaction to motor force in x direction	200 nm	81.9 nm	88.3 nm	56%
Deflection under gravity	3 um	1.99 um	2.19 um	27%
Reaction to motor force in y direction	3 arcsec	1.96 arcsec	2.15 arcsec	28%
Max. yaw motion	90 arcsec	113 arcsec	105.5 arcsec	17%

VERIFICATION OF THE OPTIMAL DESIGN THROUGH THE FEM ANALYSIS

The results from the optimal design are reviewed by FEM analysis. The Static stiffness is verified and the structural resonant frequencies and the stress under maximum load are examined. The material used is Al 7075 T6 and the control frequency is in the range of 50~100 Hz. The static results show the margins are enough to satisfy the requirements and the maximum stress is 219 MPa which is smaller than the yield strength of 508MPa. The first uncontrollable structural resonant frequency is 155 Hz which is higher than the control frequency.

CONCLUSION

The flexure hinge mechanism to compensate the dynamic yaw motion error of the XY stage without any harmful effect to the air bearing guide was proposed. The anlaytic modeling and the optimal design of the flexure hinge mechanism were accomplished and the final results were verified through the FEM analysis.

ACKNOWLEDGEMENT

This research was supported by Ministry of Knowledge Economy within the project "Development of Digital Maskless Lithography System Technology".

REFERENCES

[1] K. K. Tan, T. H. Lee, and S. Huang, Precision Motion Control – Design and Implementation, Springer-Verlag, London: 2008.

[2] C.S. Teo, K.K. Tan, S.Y. Lim, S. Huang, and E.B. Tay, Dynamic modeling and adaptive control of a H-type gantry stage, Mechatronics, 2007; Vol. 17: 361-367

[3] J. W. Ryu, S.-Q. Lee, D.-G. Gweon and K. S. Moon, Inverse kinematic modeling of a coupled flexure hinge mechanism, Mechatronics, 1999; Vol. 9: 657-674

STIFFNESS ANALYSIS OF PARALLEL LEAF-SPRING FLEXURES

D.M. Brouwer[1,2], J.P. Meijaard[1] and J.B. Jonker[1]
[1]Department of Mechanical Automation and Mechatronics
University of Twente
Enschede, the Netherlands
[2]DEMCON advanced mechatronics
Oldenzaal, the Netherlands

ABSTRACT

Approximate straight displacements are often made using a parallel leaf-spring flexure. This flexure serves as a typical case for studying the influence of shear and the compliance of the reinforced mid sections of the leaf-springs in the support stiffnesses c_z and c_y. The conclusions drawn, however, hold true for the rotational stiffness c_{rx} also, while the stiffness in the *ry* and *rz* direction can be approximated based on c_z and c_y. It turns out that shear plays an important role for short relatively wide leaf-springs at small deflections. The compliance of a reinforcement needs to be taken into account for determining the support stiffness at small deflections.

INTRODUCTION

A design principle that plays an important role in precision manipulation is determinism [1]. This rule promotes the use of flexure mechanisms because these mechanisms do not suffer from friction or backlash and therefore result in highly repeatable behavior. Approximate straight displacements are often made with two parallel leaf-springs in a parallel leaf-spring flexure as is shown in Figure. 1.

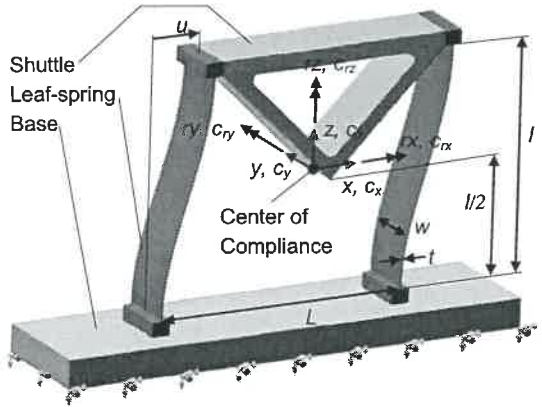

FIGURE 1. Parallel leaf-spring guidance.

Applications for flexure-based parallel or straight guidances can be found in precision motion or alignment of various sensors, optical components and slits. In MEMS for example comb-drive electrostatic actuators make use of flexure-based straight guidances to yield a relatively high axial stiffness to prevent actuator pull-in. Many types of elastic straight guidances exist, such as folded flexures, compound leaf-spring flexures, crab leg flexures and double parallel leaf-spring flexures in its basic form the parallel leaf-spring flexure serves as a typical case which will be evaluated in the paper.

A drawback of a parallel guidance with prismatic leaf-springs is the limited capacity of managing compressive loads. The danger of buckling is very real. By reinforcing the mid-sections (Figure 2) of the leaf-springs the maximum allowable compressive force and the support stiffness (c_y, c_z, c_{rx}, c_{ry} and c_{rz}) increase significantly [1][2] if the displacement u is externally constrained. However, also the bending stresses increase. A trade-off needs to be made.

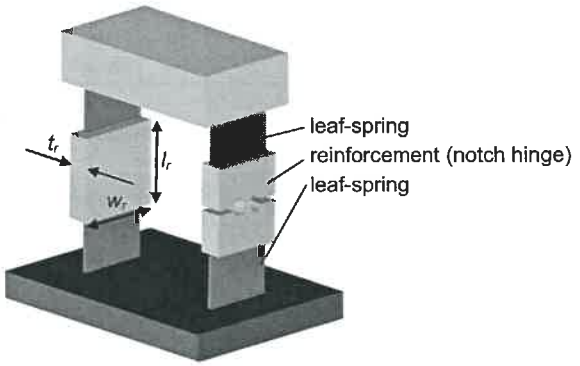

FIGURE 2. Exactly constrained parallel leaf-spring mechanism with reinforcements.

Although extensive analysis of the parallel leaf-spring flexure has been reported in the past [2] and so-called rules of thumb exist [1], they are generally restricted by the assumption that the length over width ratio of the leaf-springs is large so shearing effects do not need to be taken into

account, reinforcements are thick enough to be taken rigid, the shuttle has a prescribed position u by a rigid external support in x- or drive direction, and anticlastic curving effects are small. We present the dominating support stiffnesses c_z and c_y taking into account flexibility of the reinforcement and shearing effects. The support stiffness c_{rx} has been calculated as well but is not presented in this paper. The conclusions drawn, however, hold true also for c_{rx}. The stiffness in the ry and rz direction can be approximated for $L >> t$, if the distance L between the leaf-springs is known:

$$c_{ry} = \tfrac{1}{2} c_z L^2 \quad ; \; c_{rz} = \tfrac{1}{2} c_y L^2 \quad (1)$$

The stiffness change in the driving direction is generally small. However for leaf-springs with aspect ratio $w^2 / l{\cdot}t > 4$ the transverse stress due to Poisson contraction can be significant for deflections u/l larger than 0.1 [2].

Ideally the shuttle has a stiff external support in the drive or x-direction. However, in general the external support has a limited stiffness c_d, the 'drive-stiffness'. The strong influence of ratio c_d/c_x on c_z has been shown [4], and is in particularly important for MEMS applications.

SUPPORT STIFFNESS

By reinforcing the mid-sections of flexures, as shown in Figure 2, the maximum allowable compressive force increases significantly [1] if c_d / c_x is large. At the same time the reinforcement is advantageous for the support stiffness. The bending stress however increases unfavorable. As a fair compromise often the reinforcement factor p = 5/7 is applied as a rule of thumb [1], in which $l_r = p{\cdot}l$ is the reinforcement length. Van Eijk [2] provide rules of thumb for the stiffness in z-direction in case the reinforcements are thick enough to be taken rigid, the drive stiffness can be approximated at infinity, the l/w ratio is large so shearing effects do not need to be taken into account. We present the stiffnesses c_y and c_z taking into account limited reinforcement thickness and shearing.

The stiffnesses c_y and c_z of the shuttle at the center of compliance (shown in Figure 1) as a function of the relative displacement u/t are calculated using the flexible multibody software package SPACAR which uses beam theory including shear. The drive stiffness has been taken infinite. Figures 3a and 3b show a comparison of the relative stiffnesses c_y / c_{y0} and c_z / c_{z0} between a rigidly reinforced, p = 5/7, parallel leaf-spring guidance and a prismatic leaf-spring guidance. The stiffnesses are scaled by the respective stiffnesses at zero deflection c_{y0} and c_{z0}. The stiffnesses of the prismatic leaf-spring parallel guidance at zero deflection c_{y0} can be calculated by:

$$c_{z0} = \frac{2Ewt}{l(1-p)} \quad (2)$$

$$c_{y0} = \left(\frac{12+11\nu}{10(1+\nu)} \frac{b}{Gtw} + \frac{4b^3 + 12ab^2 + 12a^2 b}{Etw^3} \right)^{-1} \quad (3)$$

$$a = \frac{pl}{2} \quad ; \quad b = \frac{l(1-p)}{2} \quad (4)$$

The c_z/c_{z0} stiffness is independent of the ratio length over width (l/w). The c_{z0}-stiffness is increased by a factor of 3.5 due to reinforcing. Loading the shuttle in z-direction causes a 1st order bending-mode in the leaf-spring at deflection when loaded in the z-direction. Reinforcement stiffens this 1st order bending-mode effectively, as the bending length is shortened.

Leaf-springs with a small l/w ratio show a greater decrease in c_y-stiffness during deflection in the x-direction than leaf-springs with a large l/w. This can be explained as follows: during deflection the c_y-stiffness becomes a series stiffness of bending and torsion stiffness. The torsional component is caused by a combination of u-deflection and a force in y-direction of a moment in rx-direction. A small l/w results in a relatively large c_{y0}-stiffness in relation to torsion stiffness of the leaf-springs, as the bending stiffness is proportional to tw^3 and the torsion stiffness is more or less proportional to $t^3 w$ for these types of cross-sections. The large c_{y0}-stiffness for small w/l due to large w/t ratios is compromised more by the torsion stiffness at u-deflection than that of leaf-springs with a large w/l. The c_{rx}-stiffness shows comparable behavior.

The ratio c_y / c_{y0} becomes worse by reinforcing leaf-springs for $l/w < 2$. A reinforced parallel leaf-spring flexure is much stiffer than a comparable prismatic version at zero deflection. Both are deformed predominately by shear, but the reinforced version is deformed much less due to shorter flexure parts. At deflection however the y-stiffness becomes a series stiffness of bending, shear and torsion stiffness. The torque due to deflection and a force in y-direction is at its maximum near the shuttle and base in the flexures. Therefore the resulting twist of a

reinforced leaf-spring is not that much smaller than the twist in a prismatic leaf-spring. In a series stiffness the most compliant link predominantly determines the overall stiffness, which in this case becomes the torsional compliance at large *u*-deflections.

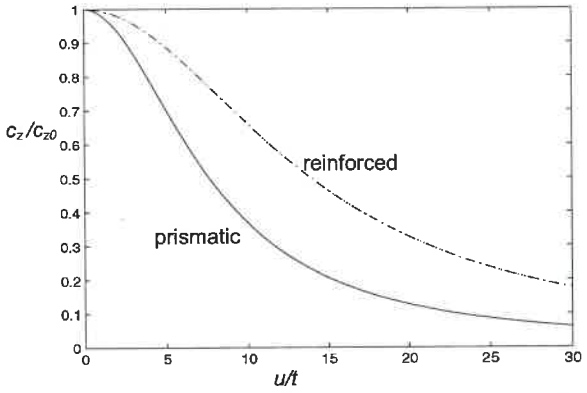

FIGURE 3a. The c_z/c_{z0} stiffness comparison between a reinforced and a prismatic parallel leaf-spring guidance.

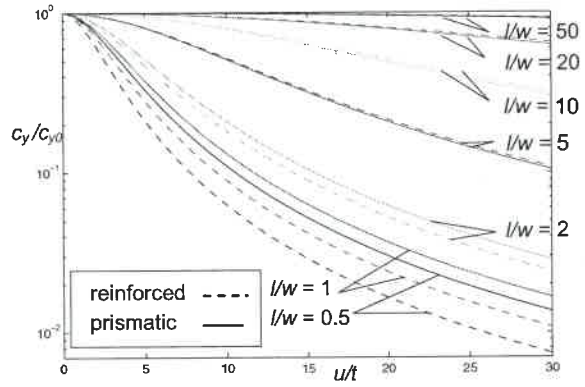

FIGURE 3b. The c_y/c_{y0} stiffness comparison between a reinforced and a prismatic parallel leaf-spring guidance for various l/w ratios.

SHEARING DECREASES THE SUPPORT STIFFNESS

Shearing effects decrease the c_y-stiffness especially for small *l/w* at small deflections. To show the influence of shearing effects on the c_y/c_{y0} stiffness a comparison between a parallel prismatic leaf-spring guidance with and without shearing effects taken into account is given in Figure 4. The c_y/c_{y0} stiffness needs to be calculated taking shearing effects into account for $l/w \leq 2$ and $u/t \leq 5$. The larger the deflection the less the shearing plays a significant role in the c_y-stiffness.

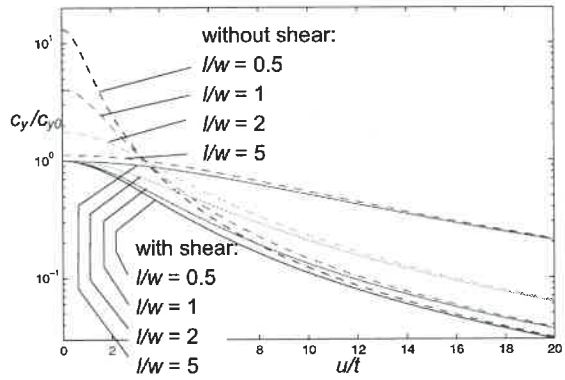

FIGURE 4. The c_y/c_{y0} stiffness comparison between the parallel leaf-spring guidance with and without shearing effects taken into account.

REINFORCEMENT LENGTH

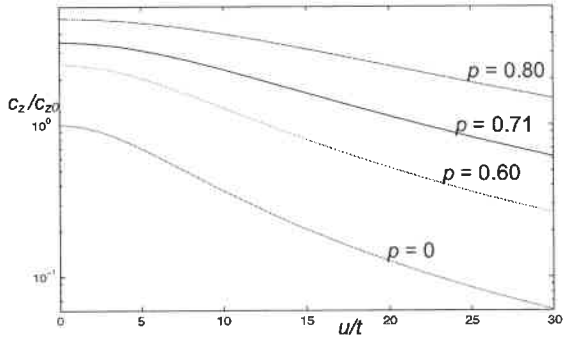

FIGURE 5a. The c_z/c_{z0} stiffness of a reinforced parallel leaf-spring guidance for various reinforcement factors p.

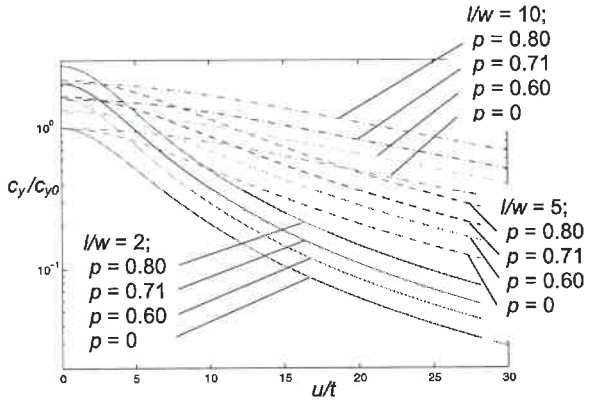

FIGURE 5b. The c_y/c_{y0} stiffness of a reinforced parallel leaf-spring guidance for various reinforcement factors p.

Figures 5a and 5b show the effect of the reinforcement factor *p* on the c_z- and c_y-stiffness for *l/w* = 0.5, 2 and 5, for a rigidly reinforced

parallel leaf-spring guidance. The stiffnesses are scaled by the respective stiffnesses at zero deflection of a prismatic leaf-spring guidance. The larger p the higher the y- and z-stiffness, however also the higher the x-stiffness [1]:

$$c_x = \frac{Ewt^3}{l^3}\frac{1}{1-p^3} \qquad (5)$$

and the bending stress [1].

$$\sigma = \frac{3Ehu}{l^2}\frac{1}{1-p^3} \qquad (6)$$

As a compromise p = 5/7 is often used, but for specific requirements p can be tuned.

COMPLIANCE OF THE REINFORCEMENT

To find the influence of the reinforcement thickness t_r on the stiffness the compliance of the reinforcements is taken into account. Figures 6a and 6b show the effects for various t_r/t on the c_z- and c_y-stiffness for p = 5/7. The stiffnesses are scaled by the respective stiffnesses at zero deflection of a prismatic leaf-spring guidance.

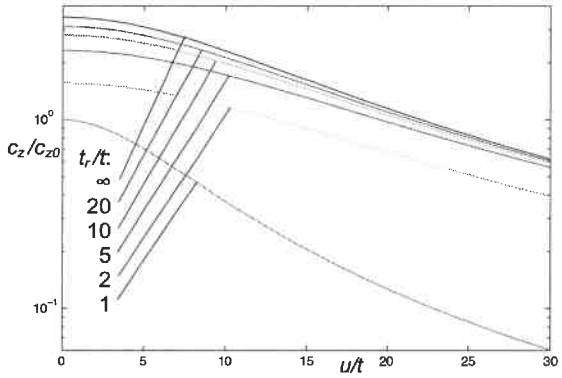

FIGURE 6a. The c_z/c_{z0} stiffness of a reinforced parallel leaf-spring guidance for various relative reinforcement thicknesses t_r/t (p = 5/7).

Even with a reinforcement thickness of t_r = 20t the reinforcement cannot be taken as a rigid body for small deflections. The support stiffness increases only slightly at large deflections when reinforcing more than 5 to 10 times the leaf-spring thickness. For $l/w \geq 5$ and at limited deformations $u/t < 10$ it could make sense to take the reinforcement thickness $t_r \geq 10t$. Furthermore, with respect to dynamic properties the effects of increased mass of the reinforcement which cause lowered vibration mode frequencies should be considered. For relatively large deformations $u/t > 10$, as a compromise between increased support stiffness and dynamic properties the reinforcement thickness can be taken $t_r \leq 5t$.

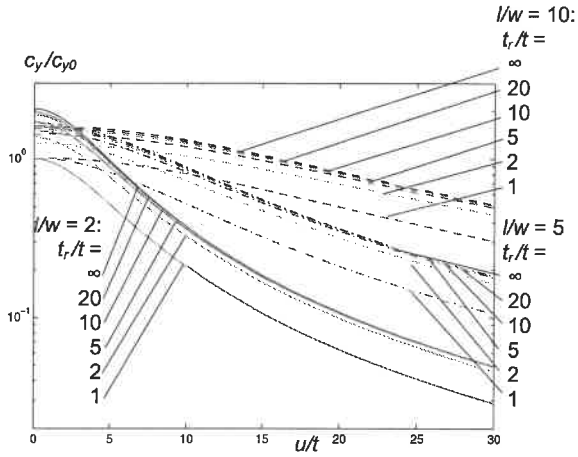

FIGURE 6b. The c_y/c_{y0} stiffness of a reinforced parallel leaf-spring guidance for various relative reinforcement thicknesses t_r/t (p = 5/7).

CONCLUSION

It can be concluded that for the c_y/c_{y0} stiffness of a parallel leaf-spring flexure shear plays an important role for $l/w \leq 2$ and $u/t \leq 5$. But shear can be neglected for deflections $u/t > 12$. The compliance of a reinforcement even for t_r = 20t needs to be taken into account for determining the support stiffness at small deformations. For $u/l > 10$ the optimal z-stiffness is approached for $t_r/t > 5$, and the optimal y-stiffness is approached for $t_r/t > 2$. A trade-off is required between the support stiffnesses due to a large reinforcement factor p and the stress in the leaf-springs.

REFERENCES

[1] Soemers HMJR, Design Principles for Precision Mechanisms, Lecture notes of the University of Twente, 930, 2010.

[2] van Eijk J, On the design of plate-spring mechanisms, Ph.D. Thesis, Delft, The Netherlands, 1985.

[3] Jonker JB and Meijaard JP, SPACAR – Computer program for dynamic analysis of flexible special mechanisms and manipulators, Multibody Systems Handbook, Springer-Verlag, Berlin, pp.123-143, ISBN 0-387-51946-7.

[4] Brouwer DM, *et al.*, Design and modeling of a precision 6 degrees-of-freedom MEMS-based parallel kinematic TEM sample manipulator, Proc. ASPE, pp. 115-118.

6 DOF NANOPOSITIONING MECHANISM AND ANALYSIS OF ITS INHERENT MECHANICAL CHARACTERISTICS

Tobias Hackel[1], Thomas Frank, Markus Lotz
[1]Department of Precision Engineering,
Ilmenau University of Technology, Germany

INTRODUCTION

The requirements of nanopositioning machines are to provide nanometer accuracy in a macroscopic spatial working volume. It should have traveling ranges of several decimeters in all directions, including the direction of gravity. That means to move macroscopic parts (e.g. measuring mirrors) and permanently actively support heavy weights in static and high dynamic modes. In order to prevent disturbances on the implemented measuring systems the dissipation loss of the actuators must be minimized.

A methodical approach to the solution of this task must emanate from the design principles of precision engineering known from micrometer range. For reaching nanometer accuracy these principles must be applied, validated and refined. Therefore a nanopositioning stage with a long stroke in the vertical direction has been developed and tested to find out some basic experiences about nanometer positioning.

BASIC COARSE/ FINE CONFIGURATION

The basic idea to decrease dissipation loss coming from the active parts into the measuring system is to use actuators like self-locking spindle drives and piezotranslators that are able to oppose static loads like gravity in a nearly passive mode. Neither kind of actuator is able to fulfill the entire positioning task (both long stroke and nanometer accuracy). The same problem exists while selecting passive functional elements like guidings and bearings for the nanopositioning system. Thus the design principle of *functional separation* is used to combine the advantageous characteristics of dissimilar components e.g. to create fine/ coarse driven structures. One possible variant of a basic technical principle working in one direction is shown in *Figure 1*. Different combinations of the number of actuators and passive DOF of the mechanism are possible. The shown technical principle describes a structure of actuators each with a associated guiding. Thus a precision actuator with a precision guiding e.g. elastic guiding and a coarse drive with a long travel guiding of reduced accuracy create cooperating substructures with dissimilar properties. As result the kinematic DOF of the structure is higher than the functional DOF of the object. Basically the static and dynamic positioning error of the coarse subsystem must be smaller than the traveling ability of the fine drive part.

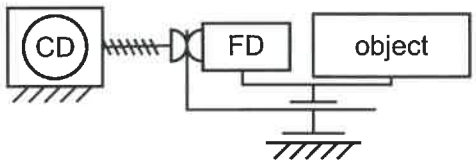

FIGURE 1. basic principle of a linear coarse/ fine drive system (CD..coarse drive (e.g. spindle drive), FD..fine drive (e.g. piezo translator))

KINEMATICS WITH HIGHER DOF

To create structures with higher maneuverability of the object the necessary number of the coarse/ fine drive systems shown in *Figure 1* could be combined kinematically in a series or a parallel (e.g. as hexapod) overall structure. Alternatively a fine drive substructure with the necessary DOF consisting of precision actuators and guidings can be set on top of a coarse drive substructure. This second variant has the following advantages. The fine drive components with little stroke allow the design of a lightweight optimized substructure for adjusting the positioning error in a dynamic mode. Thus the dynamic disturbance caused by the inertia while fine positioning can be minimized. Coarse drive components are more heavyweight but belong to the coarse substructure, whose primary task it is to provide a stable support for the fine drive subsystem and move it quasi-statically over relatively long ranges. Thereby a lightweight optimization is irrelevant. This is advantageous for designing a structure with high stiffness to minimize deviations. Additionally the concentrated inertia decreases the nominal frequency whereby the deviating effect of mechanical disturbances, e.g. coming from the fine drive substructure, is minimized.

EXPERIMENTAL SETUP

The experimental setup is designed as a simplified version of a nanopositioning machine that includes all necessary functional elements and allows a determined examination of the functional influence of the mechanical components in the nanometer range. The coarse/ fine configuration is implemented. The fine drive subsystem is included as a discrete functional module, that can operate as a stand-alone device with 6 DOF, to allow the examination of transmission characteristics, which describes how the actuator stroke affects the object over macroscopic passive elements. A macroscopic measuring mirror for laser-interferometry is used as the object. *Figure 2* shows the kinematic structure. The end effector

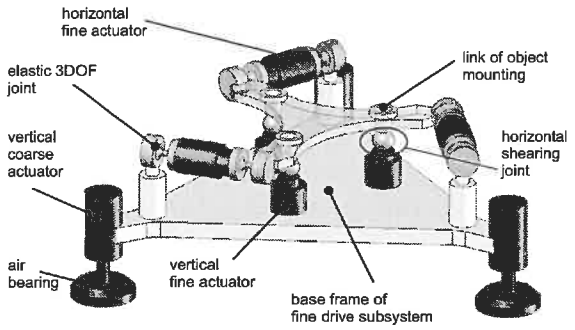

FIGURE 2. kinematic principle of the experimental setup

of the coarse drive subsystem is the fine drive's base frame. This is connected to 3 vertical working spindle drives and horizontal actuators (not shown). The guidings are air bearings in horizontal direction and ball bearings that are included in the spindle drives. The maximal stroke is $\pm 20mm$ and the accuracy ca. $\pm 1\mu m$ in each direction. The fine drive subsystem is located between the coarse drive and the object whereby it is possible to adjust the actual positioning error. *Figure 3* shows the realized setup and *Figure 4* a typical measuring plot while moving in the vertical direction. The measuring results appear very positive because no filter and climatisation were applied while testing the setup.

DYNAMICS OF FINE DRIVE

The fine drive subsystem must permanently adjust the existing positioning error resulting from mechanical deviations. That ability is given and limited by the transmission behavior of the subsystem which depends on several soft- and hardware solutions of the system e.g. controller, DAQ, delay of actuators etc. An analysis was required

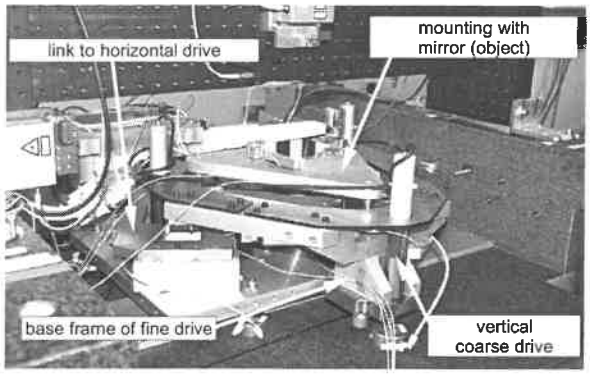

FIGURE 3. realized experimental setup

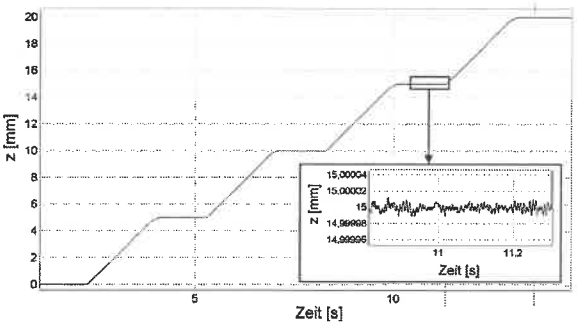

FIGURE 4. steps and accuracy in working range

to quantify the contribution of mechanical design parameters to the overall transfer function.

The design of the fine drive substructure (*Figure 2*) was optimized according to the design principles of precision engineering for reaching high possible dynamics. The basic kinematic structure has a sufficiently passive DOF to avoid over-determination and deformating constraints, which is reached by a necessary number of links. The links are designed as elastic or multipart rolling elements to minimize stick-slip-effects, clear mounting tolerances, reach small construction height and high stiffness in the working directions of the actuators. A very small number of passive transmission components avoid sources of error resulting from elasticity. The actuators are located as near as possible to the object to get lightweight moving parts and to create stiff connections. Especially in direction of gravity the length of the force flow is minimized and minimal bending stress is generated. The lateral dimension around the center of gravity is demanded in order to create available space for the laser beam of the measuring system to touch the measuring mirror in the vertical direction . The mechanical components are designed in very ele-

mentary shapes to allow a specific and most accurate analysis of its influence on the mechanic characteristics of the overall system.
Quasi-static positioning is satisfactorily possible, but the nominal frequency of the passive fine drive substructure of ca. $250Hz$ is hard limiting the ability of adjusting dynamic deviations in the nanometer range, although the design is according to the precision engineering principles. The reason for that is the insufficient stiffness of the structure caused by the bending transmission elements and multipart links under Hertzian stress which are represented in the model in *Figure 5*. Compression/ tension loads appear to be irrelevant. To evaluate a design element and its parameters, their specific contribution to the overall elasticity must be quantified. Thus theoretical modeling of the mechanical parameters is applied. This eliminates the influence of non mechanical parameters that are necessary to operate the realized experimental setup on the analysis.

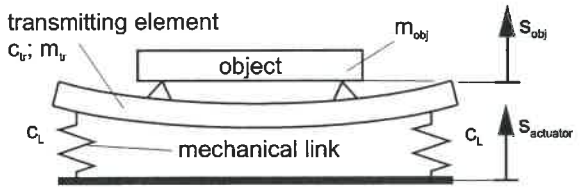

FIGURE 5. steps and accuracy in working range

For the multi-part links the stiffness can be analytically calculated using a simple model like *Figure 6* and common empirical equations to describe the approach of surfaces under loads in the case of Hertzian stress. The resulting elasticity depends on the geometry, curvature, material and preload. In the considered design the stiffness of point contact is about $20kN/mm$ and of line contact (e.g. ball against champfering) about $300kN/mm$ which are relatively very high single values. For expanded and complex transmission elements FE-method for the calculation of a stiffness is advantageous. The only relevant element of the experimental setup is the mirror mounting whose stiffness has been calculated to about $16KN/mm$ (*Figure 7*). The damping ratio of the entire system was measured with about 10^{-2}.

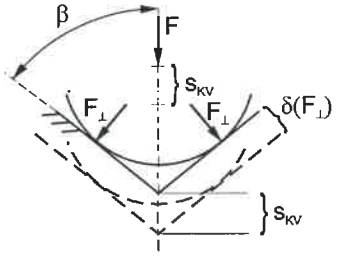

FIGURE 6. model of ball–v-groove link

FIGURE 7. Identifying stiffness with FEM

INTERPRETATION OF THE PARAMETERS

A important result is the knowledge that links and bending transmission elements have a stiffness of the same magnitude. That means that neither kind of design element is insignificant in a dynamic analysis. The mistake is probably using a FEM or MBS for an examination while considering the system either as a homogenic elastic structure or as a combination of solid parts with connections of specific behavior.
To model the entire system the single elasticities must be connected. The number of elasticities of bending transmission elements is minimized because of the usage of the design principle of *shortening the force flow*. In contrast the design principle of *avoiding over-determinations* produces a multitude of links in series which decreases the overall stiffness. This design principle appears adaptive to reach high accuracy in precision engineering of μm-ranges. In the nm-range the demands on stability to disturbing forces are higher by a factor of 1000. To get demonstrative information about the possible performance of the designed mechanical structure the model can be simulated in a time domain neglecting all disturbances of peripheral devices existing in a real structure. Thus the designer learns about the behavior of the passive mechanical structure. *Figure 8* shows how the model follows testing scenarios according to a scanning task of a surface with different scanning velocities. The limitation of the ability to follow the vertical steps by the mechanical part of the system is identifiable.

POTENTIAL DESIGN IMPROVEMENT

Because the coherence of single geometrical parameters and elasticity is known and the mechanical ability can be simulated, the theoretical effect of varying the design can be calculated. The

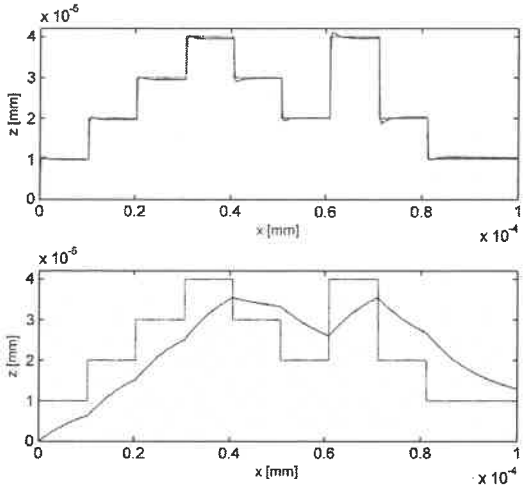

FIGURE 8. Scanning surface with $v_x = 3.5\mu m/s$ and $v_x = 350\mu m/s$

goal is to maximize the dynamic ability by increasing the nominal frequency. The first variation assumes that the material is changed from steel to AL_2O_3. The results of further variations are shown in *Figure 9. Figure 9;above* shows that it is easier for design to increase the stiffness of a bending transmission element than that of a link (by increasing diameters of included balls), even for different aspired stiffness ratios. In *Figure 9;below* the expected nominal frequency at different parameter values is plotted. The diminishing dependency shows a practical limitation of the dynamic ability at a suboptimal level for nanopositioning tasks as long as just parameters are varied. The functional insuffiency seems to be caused by the structural design solution. That means that either the design principles of precision engineering of the μm- range or the demands on dynamics are not reasonable for the nanopositioning range.

SUMMARY

A design for nanopositioning tasks basing on coarse/ fine drive configuration was developed and successfully tested as a prototype sample in an experimental setup. The principle is optimized for low dissipation losses and high dynamics and accuracy in nm-precision around the working point. The realization of the structure is according to the design principles of precision engineering. The mechanical setup was analyzed to quantify the influence of mechanical design elements and their parameters on the nanopositioning ability. In particular, the elasticities were examined. The results show that the passive me-

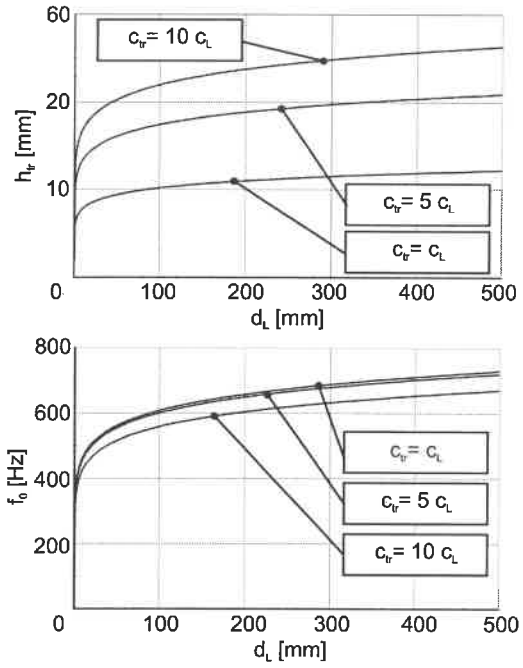

FIGURE 9. Effect of varying design parameters(above: varying stiffness by sphere diameter (d_L) in links and transmission elements by bending height(h_{tr}) and creating different stiffness ratios of design elements; below: increasing nominal frequency by design parameters)

chanical structure and its components do not appear to be irrelevant in reaching necessary dynamics in order to fulfill the nanopositioning task. The design principles of precision engineering must be evaluated differently to apply them in the nanopositioning range. The elasticity of links as well as bending transmission elements must be considered in mechanical simulations.

REFERENCES

[1] Hackel, Tobias: Grundlegende Untersuchungen zu vertikalen Positioniersystemen fuer Nanopraezisionsmaschinen. Technical University of Ilmenau, Germany; MV-Verlag 2010.

[2] Lotz, Markus: Konstruktion von Messspiegeln hochgenauer Mess- und Positioniermaschinen. Ilmenau, Germany; ISLE Verlag 2009.

[3] Frank, Thomas: Konzeption und konstruktive Gestaltung der Messkreise von Nanomessmaschinen. Ilmenau, Germany; 2010.

THE MEASUREMENT OF MESO-SCALE TORSION SPRINGS

Bradley H. Jared[1], Dennis Yazzie[1] and Isaac M. Reese[2]
[1]Advanced Prototyping S&T
[2]Satellite Test Systems
Sandia National Laboratories
Albuquerque, NM

INTRODUCTION

The characterization of meso-scale torsion springs is an important activity for applications relying on the miniaturization of mechanical mechanisms. Designers continue to push the design limits for springs, and are faced with significant uncertainty in the quantification of the static, dynamic and fatigue behavior of small torsion springs. While static stiffness is the primary parameter specified in designs, providing in-situ measurements of dynamic stiffness, fatigue life and operational torque loads would give designers information necessary for further optimization and improved reliability. Because commercial systems do not exist that meet the requirements for range, accuracy or dynamic response, this paper will describe work to develop a measurement system for the characterization of meso-scale torsion springs.

MESO-SCALE TORSION SPRINGS

Figure 1 shows an example of a spring targeted by the new measurement system. They are produced through traditional coil winding processes and typically consist of drawn Elgiloy, Hastelloy, Inconel or stainless steel wire. Coil diameters and lengths are typically 4mm or less with wire diameters spanning from 50 to 500µm. Mounting methods vary with the design application, so end geometries may have curved or straight tangs with radii of curvature and bend angles in any orientation. Operational torque loads are typically 0.5 to 2.0mN·m, with initial preloads in the range of 0.5 to 1.5mN·m. Normal mechanism motions rely on 20 to 30° of spring rotation beyond their initial preloads at cycle rates up to 100Hz.

MEASUREMENT SYSTEM REQUIREMENTS

While systems for measuring torsion springs exist[1], no commercial equipment meets the requirements for meso-scale torsion springs. Fundamental shortcomings of commercial systems are their inability to measure dynamic spring motions or to quantify torque below

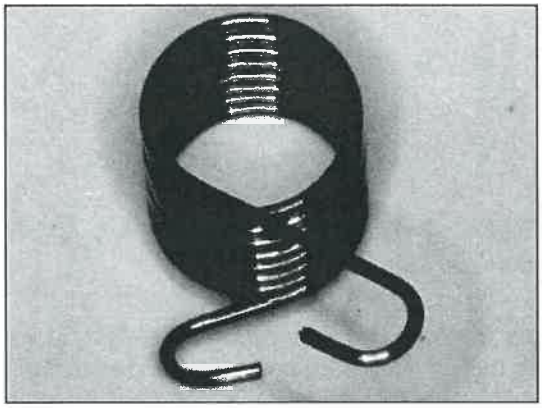

FIGURE 1. A representative meso-scale torsion spring. The wire diameter is 0.175mm, the spring length is 3.8mm, the coil diameter is 2.5mm, and the wire material is Elgiloy.

10mN·m[2,3,4]. Additional problems with measurement accuracy, with traceability and with system reliability have been observed with customized equipment delivered to SNL. The presented work details a system developed to address each of these weaknesses. The proposed system has been designed to measure in-situ torque ranging from 0.1 to 10mN·m, at frequencies up to 100Hz and with dynamic rotations of ±15°. Such requirements enable the measurement of both static and dynamic spring rates. As a result, the effects of resonance, cyclic loading, fatigue, end effecter geometry and even defects on operational performance should be quantifiable.

SYSTEM DESIGN

The prototype measurement system, Figure 2, was designed to be simple, and yet to provide the functionality necessary to meet the design requirements[5]. Critical elements of the design are its torque sensor, actuation mechanism and controller.

Torque Sensor

A Kistler 9329A torque cell and 5015A charge meter were selected for torque measurements. While several techniques exist for measuring

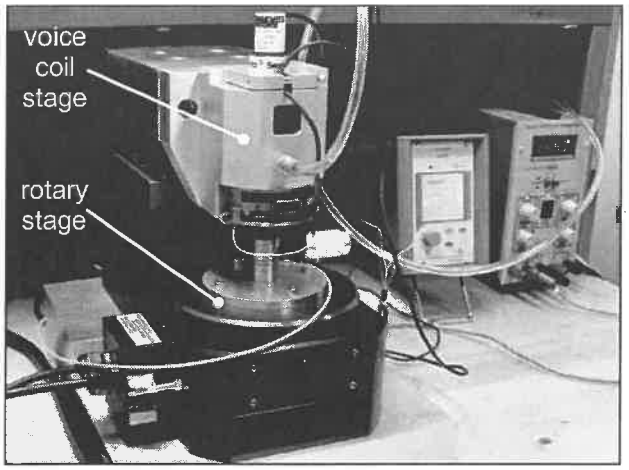

FIGURE 2. The prototype system for the measurement of meso-scale torsion springs.

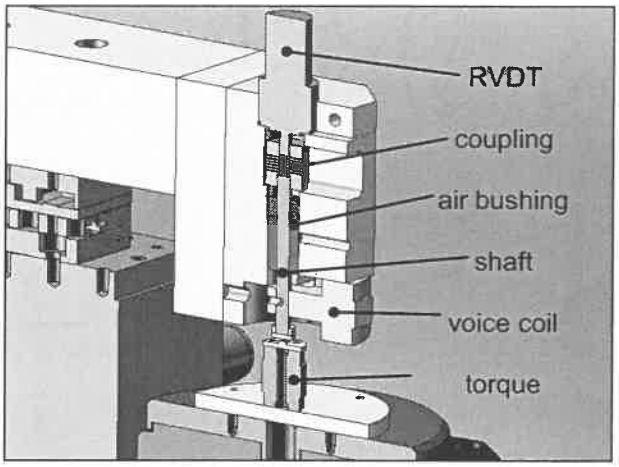

FIGURE 3. A cross-sectional view of the prototype system.

torque[6], the PZT based sensor was chosen due to its desired range, resolution and bandwidth. While the 9329A provides a maximum measurement range over ±1N·m with a natural frequency greater than 50kHz, the 5015A charge meter provides ranges adjustable down to ±1mN·m and a threshold of 0.03mN·m. The ±0.03mV/sec drift rate of the charge amplifier does restrict measurements, however, to the "quasi-static" regime.

Actuation

A cross-sectional view of the system actuation elements is shown in Figure 3. Each component in the actuation sub-assembly was selected or designed to maximize the bandwidth of the voice coil moving mass. Large spring rotations, and hence static preloads, are created by an Aerotech ADRS-150 rotary stage. The Kistler torque sensor is mounted to the rotary stage, allowing direct measurement of spring torques without contributing to the dynamic mass. Higher frequency rotations are created using a BEI-Kimco RA29-11-002A rotary voice coil. The RA29-11-002A provides ±16° of travel, a peak operating torque of 226mN·m and a mechanical time constant of 23msec. A 0.25in New Way air bushing and shaft provide the support bearing necessary for proper alignment and motion of the voice coil rotor. Due to the small torques and moments required in testing meso-scale torsion springs, a single bushing was incorporated directly into the housing sub-assembly, simplifying the assembly and maintaining a compact, low mass design. Shaft position is measured directly using a Schaevitz R30D rotary variable differential transformer (RVDT). It has a linear measurement range of ±30°, a bandwidth of 500Hz and produces approximately 0.32mN·m of resistance torque. Extension springs were added to the voice coil stage after initial testing to improve the dynamic response of the system. While the design of a flexure mechanism is required to match the performance of the RA29-11-002A rotary actuator, schedule and cost considerations forced reliance on a non-optimized solution.

Controls

Real time control of the measurement system is performed using a single PC. The rotary stage is operated by Aerotech's standalone NViewMMI software, while data collection from the torque cell and control of the voice coil actuator are simultaneously achieved using LabView. The control signals generated by the LabView application are output from a NI BNC-2100 data acquisition block as voltage commands. A Newtons 4th Ltd LPA05A wideband amplifier with a 10X gain is then used to convert the voltage signal into the current signal used to drive the rotary voice coil. Closed loop feedback is achieved using a simple PID algorithm based on angular position data from the R30D RVDT, Figure 4.

SYSTEM TESTING

Several tests were performed to examine the performance of the measurement system. One simple test was to determine the electrical noise from the RVDT signal. Data was collected with the RVDT in a stationary position under a variety of environmental conditions. An rms signal on the order of 1.5mV was measured across the various test conditions, including that of the fully operational system, demonstrating satisfactory

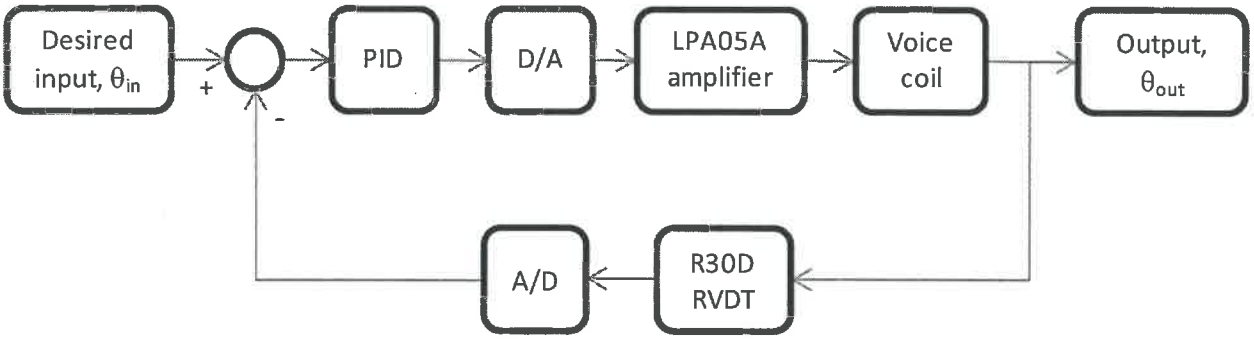

FIGURE 4. Voice coil controller block diagram.

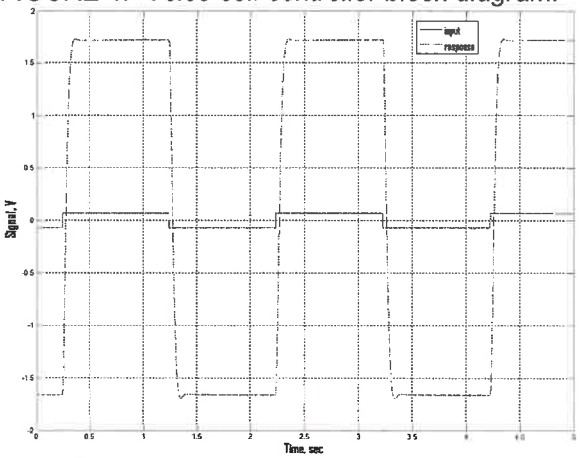

FIGURE 5. Voice coil actuator step response to a 0.5Hz, ±70mV square wave input.

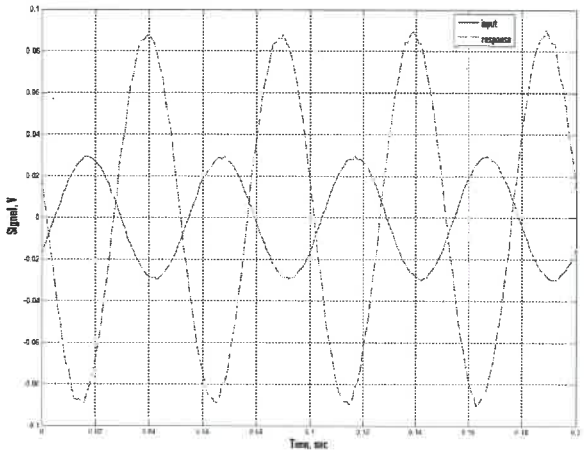

FIGURE 6. Voice coil actuator response to a 20Hz, ±30mV sine wave input.

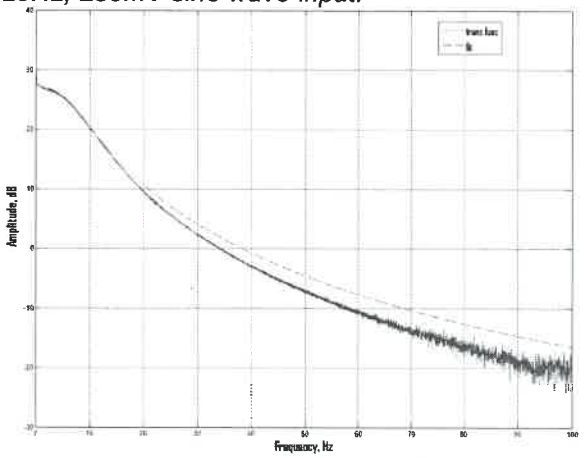

FIGURE 7. Voice coil actuator open loop transfer function.

stability of the feedback signal. This signal level corresponds to a resolution limit of 0.01°, which is courser than expected, but adequate for spring testing.

Dynamic performance of the open loop voice coil was examined using a variety of input waveforms. Figure 5 shows the step response to a 0.5Hz, ±70mV square wave input produced by an HP 8116A function generator. The voice coil demonstrates better than expected damping characteristics as it exhibits only 1.0% of overshoot. Unfortunately, the settling time is roughly 150msec, and is much longer than the 10msec response desired from initial specifications. Further confirmation of the slow response of the system is observed in Figure 6 where a 165.6° phase lag is observed for a ±30mV sine wave at only 20Hz.

Figure 7 provides the open loop transfer function of the voice coil stage based on a ±200mW swept sine wave input with a frequency range from 0.5 to 100Hz. A model of the transfer function was fit to the experimental data using a single degree-of-freedom, damped, spring-mass system in the form

$$G(s) = \frac{K}{s^2 + 2\zeta\omega_n s + \omega_n{}^2}$$

where K is the open loop gain, ζ is the damping ratio and ω_n is the resonance frequency. Figure 7 shows a good model fit where K is $59.6e10^3$, ζ is 0.88 and ω_n is 8Hz. While the original design

intent was to achieve a 100Hz bandwidth and initial design calculations predicted a voice coil limit approaching 40Hz[5], the open loop response is significantly poorer. Some improvements are expected thru the implementation of closed-loop feedback, however, as on-going work continues.

CONCLUSIONS AND CONTINUED WORK

The design of a prototype system for the dynamic torque testing of meso-scale torsion springs has been summarized. Initial performance tests have been discussed that provide the foundation for closed loop system control. Continued work focuses on the control system and will continue toward the testing of meso-scaled torsion springs.

ACKNOWLEDGEMENTS

The authors wish to thank Ernie Wilson from the Sandia National Laboratories, Engineering Design and Integration center, for his guidance and direction in understanding requirements for mechanism springs. Sandia is a multi-program laboratory operated by Sandia Corporation, a Lockheed Martin Company, for the United States Department of Energy's National Nuclear Security Administration under contract DE-AC04-94AL85000. This document has been reviewed and approved for unclassified, unlimited release under SAND2010-5194C.

REFERENCES

[1] Larson DA, Dixon WR, inventors; Larson Systems Inc., assignee. Torsion spring tester. United States patent US006094980. 2000 Aug 1.

[2] AG Measurematics Model TSTM100M, www.agmpl.com/stm_tor.htm.

[3] Andilog Technologies Springtwist Manual Torque Tester, www.springtest.info.

[4] MTS Bionix EM Torsion Test System, www.mts.com/en/Material/Univ/index.asp.

[5] Jared BH, Gill, DD, The Measurement of Meso-Scale Torsion Springs. Proceedings 24th Annual Meeting of ASPE; 2009 October, Monterey, CA.

[6] Brenner W, Suemecz F, Vujanic A. Principles of micro torque measurement - an overview. Proceedings XVII IMEKO World Congress; 2003 June 22-27; Dubrovnik, Croatia.

DESIGN AND FINE MOTION TEST OF A PRECISION X-THETA STAGE IN VACUUM

Gyungho Khim[1], Jongyoup Shim[1], and Chun-Hong Park[1]
[1]Department of Ultra Precision Machines and Systems
Korea Institute of Machinery and Materials
Daejeon, South Korea

INSTRUCTIONS

Recently, precision stages in vacuum are required in many applications such as mastering processes for high density optical disc [1-2], and lithography equipments for wafer or mask. These processes rely on electron beams, which are operable in only high vacuum. In this paper, a precision X-Theta stage aimed at being used for vacuum applications, representatively electron beam mastering equipments, is developed. A brief design method and experiment result focused on fine motion using commercialized controller are introduced.

DESIGN OF A X-THETA STAGE

In the mastering processes of optical disc, two degree of freedom motions, linear(X) and rotary(Theta) motions, are mainly required. The linear stage is designed using linear motion ball bearings(THK, HR2555M) while rotary stage used air bearings because rotational accuracy is more important. The HR model used for linear stage has characteristics of very low height and compact size, and easy adjustment of clearance. Coreless linear motor(Trilogy, 210-4N) and linear scale(Heidenhain, LIP481R) were also used in the linear stage. These are chosen to be vacuum-compatible. Maximum stroke is 250 mm and a scale resolution is set to 5 nm. FIGURE 1 shows a structure of the linear stage.

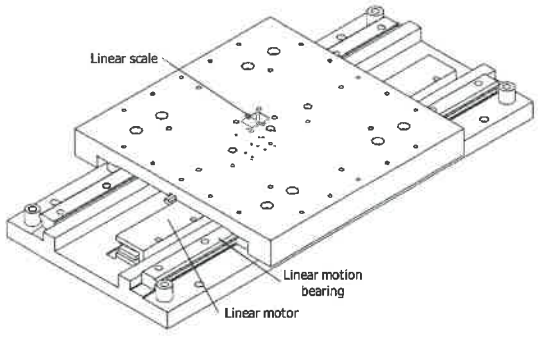

FIGURE 1. Structure of a linear stage

The rotary stage used a vacuum-compatible air bearings(carbon porous) for extremely high accuracy, and a slotless direct drive motor (Aerotech, S130-39-B) to suppress unwanted motion errors caused by cogging force, and a thin type of rotary encoder(Sony, BH20) to shorten the overall height of the stage. The Turbo PMAC2 controller (Delta Tau) and linear amplifier (Varedan, LA400) are used for both stages. The commutation for motor driving is carried out using not a hall sensor but encoder signal for a better smoothing motion. The rotary encoder has a resolution of 0.162 μrad (0.03 arcsec) by means of dividing the analog sine signal using interpolator board (Delta Tau, ACC-51P)

The air leakage problem from the air bearings has been solved using differential exhaust method [2-3]. Sufficient vacuum level for electron beams can be obtained using three steps of exhaust system. The first exhaust line is open to the atmosphere, and the second, third exhausts are connected outside vacuum pumps. The first exhaust line is also used as feedthroughs for a motor, encoder cables, and compressed air line as well as exhaust of air. This region is connected to outside atmosphere using bellows, and always maintains atmospheric condition. Therefore non-vacuum-compatible components can be used. This is one of the big merits. FIGURE 2 shows a structure of rotary stage.

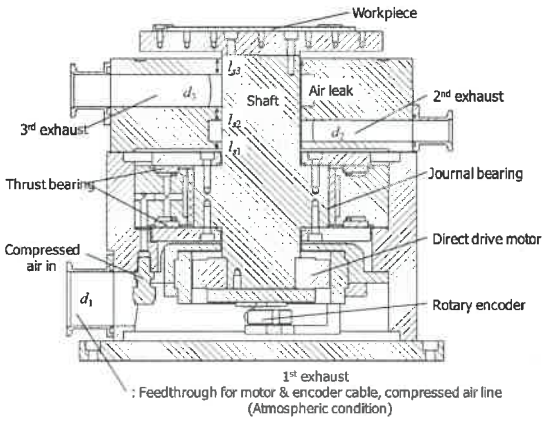

FIGURE 2. Structure of a rotary stage

The gap between the inside of housing and the outside of shaft in differential exhaust system is very small (5~10 μm). This small gap prevents air from leaking into the vacuum chamber. The design parameters such as diameter of exhaust lines (d_i), seal lengths(l_{si}), and pumping speeds of vacuum pumps(S_i) are optimally decided using optimized method with genetic algorithm [3]. Table 1 shows design results. We can also know which type of pumps should be used for the second and third exhaust lines by means of the inlet pressures(P_{pi}) calculated in Table 1.

VACUUM LEVEL TEST

FIGURE 3 shows the X-Theta stage installed inside the vacuum chamber. The stages were fabricated with anodized aluminum 7075. It was used because of high hardness characteristic in spite of a disadvantage in outgassing. FIGURE 4 represents a vacuum chamber and various feedthroughs for signals and flows. The vacuum chamber was installed on the anti-vibration table. FIGURE 5 demonstrates a pressure variation of a vacuum chamber obtained while the air bearing is working. Turbo molecular pump(TMP) of a 550 l/s was used for exhausting the vacuum chamber. The chamber pressure was measured with a full-range vacuum gauge (PFEIFFER Vacuum, TPG 261). The chamber pressure reached 5.1×10^{-4} Pa within 29 hours of operation without activating the air bearing. Then, the second and third exhaust pumps were operated for preparation of activating the air bearing. After 1 hour, the chamber pressure was reduced to 4.7×10^{-4} Pa. Compressed air of 0.4 MPa was supplied to the air bearing. The chamber pressure suddenly increased to 5.2×10^{-4} Pa, but then began to decrease slowly to 4.3×10^{-4} Pa after 5 hours later. This level of vacuum pressure is sufficient for using electron beams. Moreover, it is expected that high vacuum level less than 10^{-4} Pa could be achieved with increasing time, as shown in FIGURE 5.

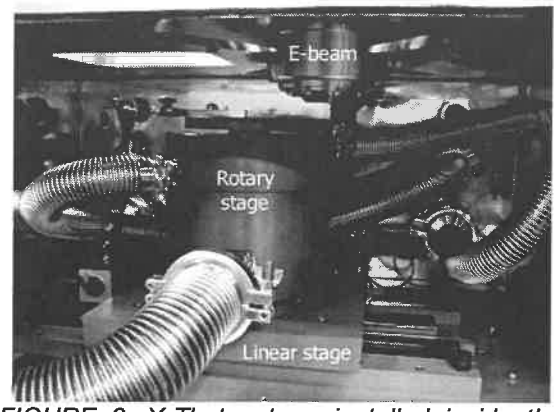

FIGURE 3. X-Theta stage installed inside the vacuum chamber

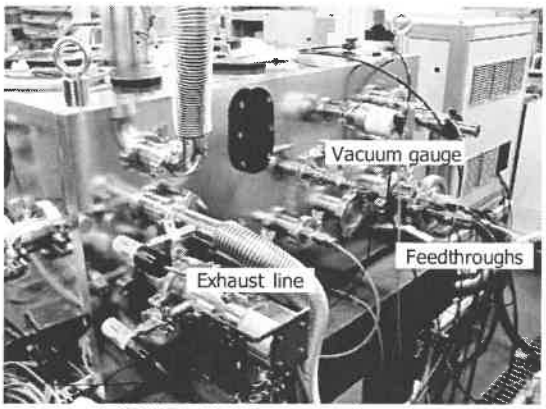

FIGURE 4. Vacuum chamber

FIGURE 6 shows a pressure variation of a vacuum chamber obtained while the air bearing(rotary stage) is moving. The stage is rotated with velocities of 100, 200, and 300 rpm, and the pressures are continuously measured. The pressure rise is evaluated by means of "100 log (P/P_0)," where P_0 is a pressure just before moving, and P is a pressure measured during moving. The pressure increased with velocity, however, it showed only increase of 0.5 % for a velocity of 300 rpm. This amount of increase is negligible.

TABLE 1. Optimal design of exhaust system

	Chamber pressure (Pa)	Seal lengths of i-th exhaust lines, l_{si} (mm)			Diameters of i-th exhaust lines, d_i (mm)		Pumping speeds of i-th vacuum pump, S_i (liter/s)			Inlet pressures of i-th vacuum pump, P_{pi} (Pa)		
		l_{s1}	l_{s2}	l_{s3}	d_2	d_3	S_1	S_2	S_3	P_{p1}	P_{p2}	P_{p3}
Optimal design	2.3×10^{-5}	4.8	10.2	11.6	16.2	24.2	Atm.	24.5	61.9	Atm	40.7	3.8×10^{-3}

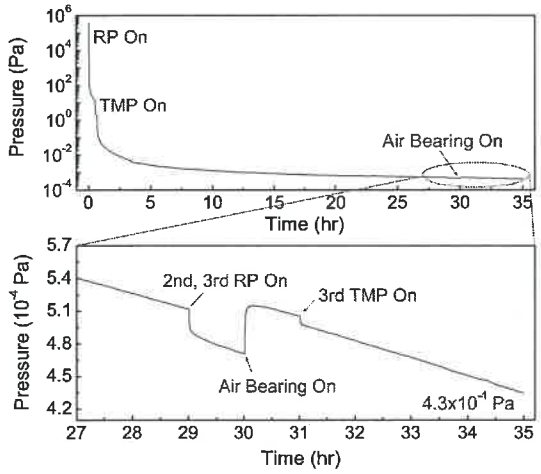

FIGURE 5. Pressure variation while air bearing is working

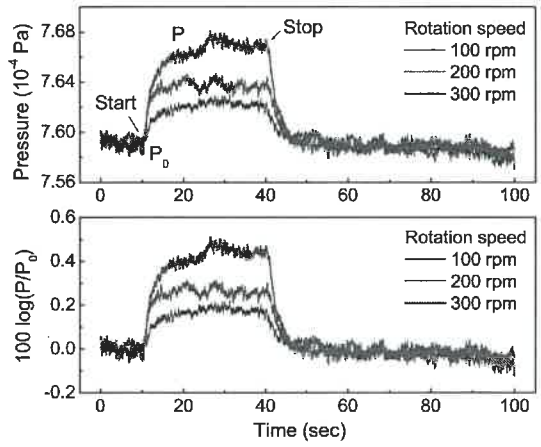

FIGURE 6. Pressure variation during air bearing movement

FINE MOTION TEST

Vacuum-compatible grease was firstly used as a lubricant in the linear motion bearing, however, its friction was considerably high due to a high viscosity characteristic. Instead of grease lubrication, solid lubrication was adopted. DLC (Diamond Like Carbon) coating on the linear motion bearing was carried out by sputtering deposition because the DLC coating exhibits super-low friction and high hardness, and high atomic structural stability in vacuum [4].

Capacitance sensor(ADE, 2803V, 0.5 nm resolution) and acquisition board(Dewetron, Dewe-43, 24bit resolution) were used to evaluate a fine motion and the repeatability. The displacements were measured after low pass filtering for eliminating environmental noise and electrical noise. FIGURE 7 shows a fine motion step response of 5 nm, which is the same as scale resolution, in the linear stage. The result showed the stage exactly moved 5 nm, and better fine motion would be obtained if the higher scale resolution were used. FIGURE 8 shows the bi-directional repeatability at a point. The displacements were measured for stopping at a zero position while the stage reciprocally moved 1000 counts within the measurement range of the capacitance sensor. The result showed 2σ (σ:standard deviation) of 0.005 μm.

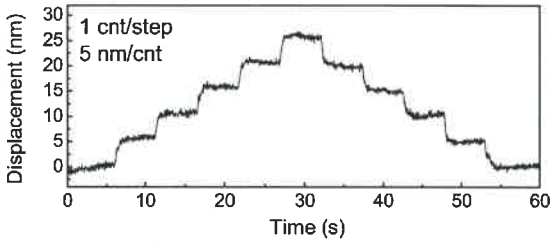

FIGURE 7. Fine motion step response in the linear stage

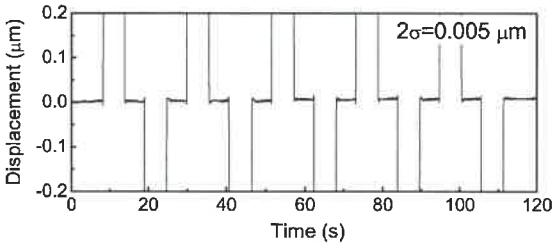

FIGURE 8. Bi-directional repeatability in the linear stage

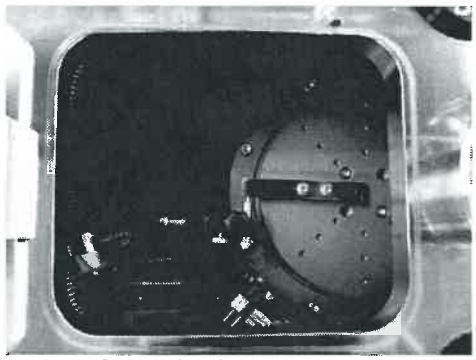

FIGURE 9. Setup for fine motion step response in the rotary stage

The fine motion step response in the rotary stage was measured using a bar installed upper table of the rotary stage, and converted to angular position, as shown in FIGURE 9. The result showed the stage exactly moved a resolution of 0.162 μrad, which is the same as encoder resolution, as shown in FIGURE 10. The bi-directional repeatability was also

evaluated like the method done in the linear stage. The result showed 2σ of 0.054 μrad, as shown in FIGURE 11.

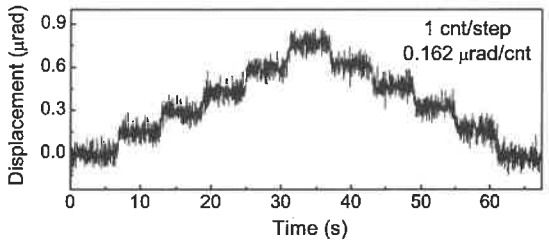

FIGURE 10. Fine motion step response in the rotary stage

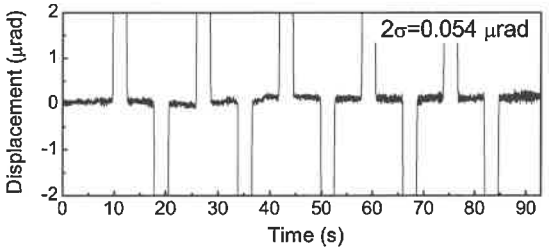

FIGURE 11. Bi-directional repeatability in the rotary stage

SIMULTANEOUS MOTION TEST OF X-THETA STAGE

Simultaneous motion between a linear and rotary stage was evaluated. When machining optical disc, the constant linear velocity control is required. So the velocity of the rotary stage must decrease with increasing radius (that is, position of the linear stage). The simultaneous motion performance was carried out using only PMAC controller without a DSP board and advanced control scheme. The linear stage must move 320 nm while the rotary stage is moving one revolution for a 25 GB Blu-ray disk. FIGURE 12 shows the experimental result that following error is lower than ±10 nm. FIGURE 13 demonstrates the comparison between command and actual velocity. Actual velocity was calculated from position of the linear stage and velocity of the rotary stage at the moment. The result showed that actual velocity is well coincided with command velocity.

CONCLUSIONS

This paper describes a design and fine motion performance of a precision X-Theta stage for vacuum applications. The linear stage(X) which is designed with solid-lubricated linear motion ball bearings showed the same step response as scale resolution(5 nm). The rotary stage (Theta) which is equipped with vacuum-compatible porous air bearings showed a vacuum level of 10^{-4} Pa, and the same step response as encoder resolution(0.162 μrad). The following error caused by simultaneous motion of X-Theta stage showed ±10 nm.

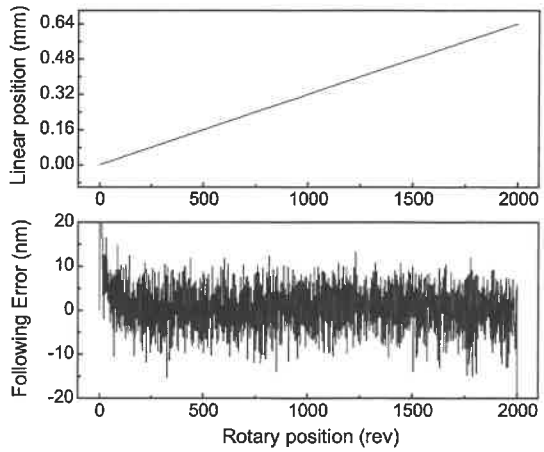

FIGURE 12. Simultaneous motion test of X-Theta stage

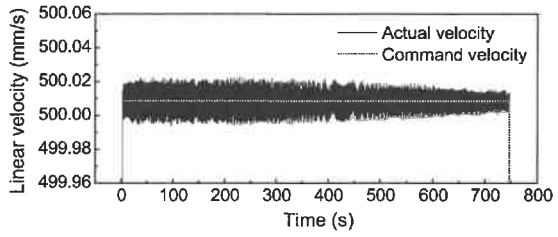

FIGURE 13. Comparison between command and actual velocity

REFERENCES

[1] Kojima Y, et al., High Density Mastering Using Electron Beam. Japanese Journal of Applied Physics. 1998; 37: 2137-2143.

[2] Furuki M, et al., Electron Beam Recording with a Novel Differential Pumping Head Realizing more than 50 GB/Layer Capacity Disc. Japanese Journal of Applied Physics. 2003; 43: 759-763

[3] Khim G, et al., A Vacuum-Compatible Air Bearing: Design Analysis and Optimization. Key Engineering Material. 2007; 339: 37-44.

[4] Andersson J, et al., Friction of Diamond-Like Carbon Films in Different Atmospheres. Wear. 2003; 254: 1070-1075.

DESIGN OF NOVEL 3-DOF NANO PRECISION STAGE

Hyo-Young Kim[1], D.H. Ahn[1], B.S. Chun[2], D.G. Gweon[1]
[1]Department of Mechanical Engineering KAIST Daejeon Korea
[2]Nanoscope System Co. Ltd Daejeon Korea

INSTRUCTIONS

Precision nano-positioning techniques have become very important for biomedical science, optics and microscopy. PZT and flexure compliant mechanisms are widely used in these various fields and applications within these fields. Compliant mechanisms are flexible structures, which can generate the desired motions by undergoing elastic deformation instead of through rigid linkage/joints as in rigid body mechanisms [1]. The advantages of flexure mechanisms include the lack of backlash, the lack of non-linearity, a simply monolithic structure, and ease of manufacturing. These advantages would have enabled ultra-high-precision positioning. Therefore, it is suitable to be used in the fields of biomedical nano-stage. The stage in the field of biomedical is required to design as a hollow type and compact size for the measurement of biological specimens. Several in-plane motion (3-DOF) flexure stages were designed for precision stage. Hua designed a 3-DOF ($XY\theta_z$) compliant micro positioning stage with amplification mechanism and performed optimal design and input coupling analysis [1]. Tian presented the mechanical design and dynamics of a 3-DOF flexure stage with amplification mechanism [2]. And aside from these, similar parallel mechanism stages were designed for many applications. In particular, several stages have double amplification mechanism for longer working range [3, 4]. However, although above all 3-DOF stages have sufficient working range, ultra-precision accuracy and compact size, these stages are not designed as a hollow type. It is easy to design 2-DOF stage of hollow type, relatively. But, in 3-DOF parallel type stage, it is not easy to design due to triangular structure. Moreover, if the stage should have designed a hollow type maintaining a compact size, it is more difficult to arrange the PZT actuators and the flexure amplification mechanisms. Especially, design of a compact amplification mechanism was great difficulty in proposed stage. Design and modeling a various hinge lever mechanism of amplification device is presented for increasing small PZT actuator out range [5]. As before, many developed stage has an amplification mechanism basically [6, 7]. In those studies, various design conditions to achieve higher magnification ratio were considered. However, it is not suited for stage of hollow type. This paper discusses the mechanical design of a 3-DOF flexure based parallel compliant mechanism for hollow type biomedical specimen stage. Even though the proposed stage is applied both parallel compliant mechanism and hollow type, the stage have a large working range, nanometer resolution with compact size.

DESIGN

The main purpose of this novel stage is the measurement equipment stage. For biological specimens in particular, the stage should be designed as a hollow type with a compact size. The type of hollow stage has many space restrictions. Both the PZT actuator and the amplification hinge mechanism must be inside the small stage. At the same time, the stage should be designed to attain ±100 μm in the X and Y directions, and ±0.1 ° in the yaw direction. The number of PZT actuators is an important consideration in the stage. To actuate the three axis drives, the stage requires three or more PZT actuators; however, it is more efficient to use fewer actuators. Therefore, only three PZT actuators are used. The three actuators were arranged at intervals of 120 degrees with an offset from which the rotational moment was obtained and two circular flexures were placed at the center of each side.

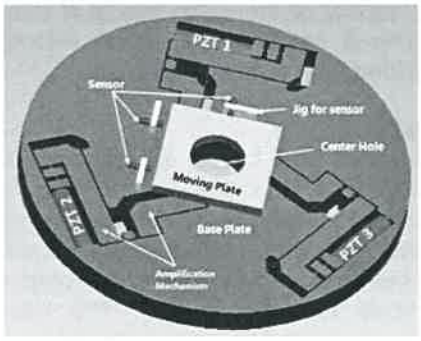

FIGURE 1. Proposed Flexure Stage

The symmetric design reduces the effects of the temperature gradient on the structure. The diameter of the center hole should be greater than 55 mm. Therefore, except for this center hole, the three actuators and amplification mechanism were placed on the circle base plate, where a rectangular moving plate with a hole was added. A biological specimen is placed on the moving plate. Fig. 1 presents a schematic illustration of proposed concept design that includes three capacitive sensors for sensing displacement of moving plate, three PZT actuators for providing driving forces, PZT displacement amplification mechanism and the moving plate for specimens. In order to meet the stage specifications, a PZT actuator with a 60 μm stroke should be amplified to provide a maximum range of 400 μm. Figure 2 presents a schematic illustration of the designed flexure hinge amplification device. The amplification device consists of four circular hinges and four cartwheel hinges. A displacement of PZT actuator is amplified by the first L-shape lever mechanism which is expressed as a rigid body '3'. The rigid body '4' which has amplified displacement by first L-shape lever mechanism applies the force at the second L-shape lever mechanism which is expressed as a rigid body '5'. Therefore, a displacement of the rigid body '4' is amplified by the second L-shape lever mechanism like a displacement of a PZT actuator which is amplified by the first L-shape lever mechanism. If the motion amplification ratio of the first lever is **b/a** and the motion amplification ratio of the second lever is **d/c** , the rigid body '19' which is joined the moving plate is amplified by amplification ratio '$(\mathbf{b/a})\times(\mathbf{d/c})$'. The most important point in the novel stage is that the three amplification mechanisms should not block the space of the center hole, whose diameter is greater than 55 mm.

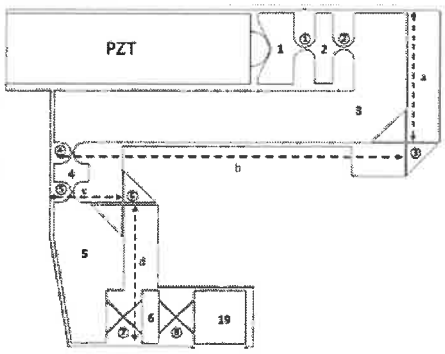

FIGURE 2. Proposed Amplification Device

Table 1 Stiffness Verification of the 3-DOF stage

	Analytic model	FEM simulation	Error
K_x	0.102 N/μm	0.111 N/μm	8.1 %
K_y	0.106 N/μm	0.112 N/μm	5.3 %
K_z	5.026 N/μm	5.263 N/μm	4.5 %
$K_{\theta x}$	5625.4 Nm/rad	5837.1 Nm/rad	3.6 %
$K_{\theta y}$	5845.2 Nm/rad	6164.4 Nm/rad	5.2%
$K_{\theta z}$	173.1 Nm/rad	189.4 Nm/rad	8.6 %

At the same time, the total stage should be less than 280 mm x 280 mm in size including the three PZTs and the amplification mechanisms. In addition, it should be considered that the flexure mechanism is easily manufactured. The amplification mechanism proposed above satisfied all these conditions.

MODELING AND OPTIMAL DESIGN

To optimize the flexure mechanism, static and dynamic modeling of the stage must be performed. The proposed $XY\theta_z$ stage can be modelled by a spring-mass system. The flexure hinge is regarded as spring and the rigid body is regarded as mass. The stage consists of 24 flexure hinges and 19 rigid bodies. The spring-mass system is modeled by Ryu's method [3]. This method requires the 6×6 stiffness matrix of all springs. As mentioned earlier, the cartwheel hinge and circular hinge, two kinds of hinges are in use in the developed stage. Both flexure hinges have been widely used in precision PZT stage. There have been many methods adopted to derive satisfactory compliance equations of these hinges. Koseki made a stiffness matrix of circular hinge easily [8]. And Kang calculated the stiffness of the cartwheel hinge using four general leaf springs and an imaginary body [9].

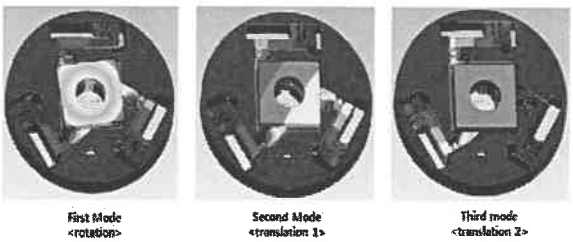

FIGURE 3. FEM Simulation

Table 2 Verification of Dynamic Model

	Analytic model	FEM simulation	Error
Mode 1 (rotation)	221 Hz	221 Hz	6.7 %
Mode 2 (translation 1)	251 Hz	226 Hz	11 %
Mode 3 (translation 2)	252 Hz	230 Hz	9 %

Using the stiffness matrices from these two references, the total flexure mechanism is modeled as rigid bodies connected through hinge spring. There are twelve cartwheel hinges and twelve circular hinges and nineteen rigid bodies.

$$Kx = F \quad (1)$$

Since there are nineteen rigid bodies and each body has six degree of freedom, the size of K matrix is (114×114) and the size of x and F vectors is (114×1). The stiffness values of analytic model are compared with FEM simulation results. The dynamic model verification result via FEM is presented in Table 2 and Fig. 3 shows the mode shapes of the lower three modes. After completing the total system analytic modeling, the optimal design was performed. The design variables were the circular hinge radius, thickness, width, and the cartwheel hinge length, thickness, width and lever ratio. Other parameters do not greatly affect the system performance; therefore, the other parameters' values are defined as constants. The objective of the optimization is to maximize the system bandwidth to improve the dynamic characteristics. It guarantees a fast response and robustness against several dynamic disturbances. Therefore, the first natural frequency was maximized. The performance of the optimization is given in Table 3, with the first natural frequency being 89 Hz and the maximum range of translation motion being 228 μm.

EXPERIMENT AND RESULT

The proposed stage can be manufactured from a single monolithic piece via wire electro discharge machining (WEDM), therefore, reducing the problems associated with assembly. The material is used Al7076 T6 which yield strength is 506MPa. After manufacturing, the stage is integrated with PZT actuators (Pst 1000/25/60) produced by Piezomechanik. The

Table 3 Performance of Stage with Optimal Design

	Analytic model	FEM Simulation
Max Displacement (X- direction)	238 μm	228 μm
Max Displacement (Y- direction)	229 μm	225 μm
Max Displacement (θ_z - direction)	0.23 °	0.23 °
Mode 1 (rotation)	88.24 Hz	89.91 Hz
Mode 2 (translation 1)	98.34 Hz	94.53 Hz
Mode 3 (translation 2)	99.21 Hz	95.12 Hz

controller is a DS1103 (dSPACE corp.), the amplifier to drive PZT actuators is SVR 1000-3 (Piezomechanik. Corp.) and the capacitor sensors are three CPL190 (Lion Precision). These sensors were attached by three sensor jigs and measured X, Y, θ_Z directional displacements of moving plate. Using these three displacement sensor and PID control algorithm, the stage was controlled in 3-Axis. Fig. 4 shows the hardware components of the system and Fig. 5 shows the final system with case.

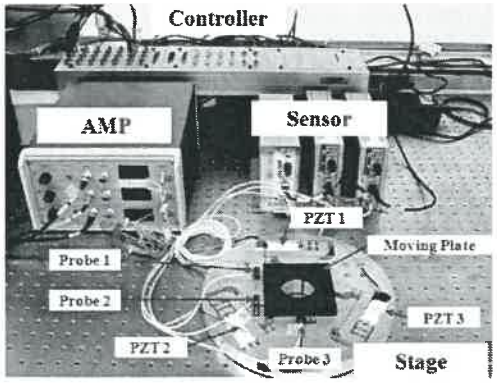

FIGURE 4. Hardware Components

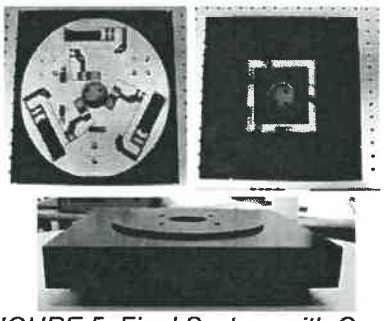

FIGURE 5. Final System with Case

The stroke of the translational movement is 220 μm, and the stroke of the rotational movement is 0.22°, whereas their in-position stability is ±2 nm and ±30 nrad, respectively, and their resolution is 5 nm and 0.25 μrad, respectively. The settling time is below 50 msec.

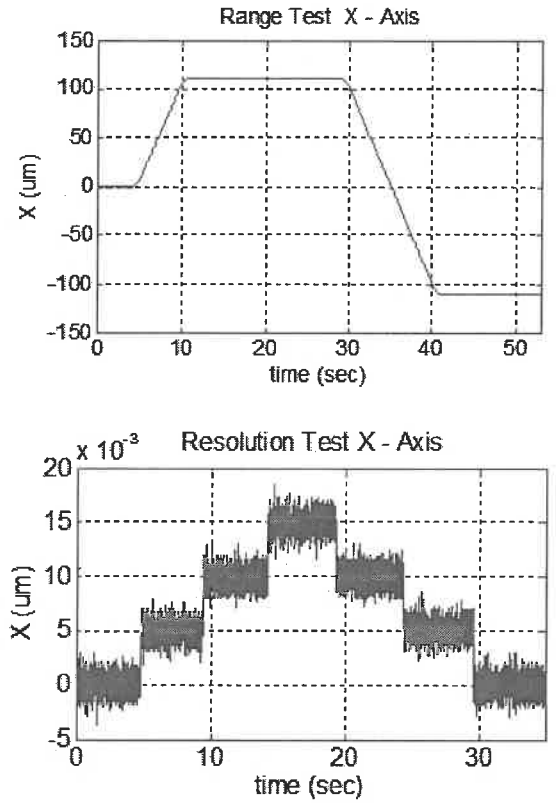

FIGURE 6. Experiment Result

CONCLUSIONS

A novel $XY\theta_z$ - stage designed to have the center hole as well as long working range is proposed. To achieve a long working range, a novel double amplification mechanism with cartwheel hinge is developed. The optimization procedure to select the parameters that would optimize the design of the stage is performed. Based on the optimal design parameters, the system is manufactured and tested for verification of the system. Experiment results demonstrate the performance of the ultra-precision stage. The stroke of the translational movement is ±110 μm and the stroke of the rotational movement is ±0.11 °. The resolution is 5nm and 0.25 μrad, respectively.

ACKNOWLEDGEMENTS

This work was supported by the Small Business Administration within the project "$XY\theta_z$ Nano-Stage driven by PZT Actuators"

REFERENCE

[1] Wang H, Zhang X. Input coupling analysis and optimal design of a 3-DOF compliant micro-positioning stage. Mechanism and Machine Theory. 2008;43:400-10.

[2] Tian Y, Shirinzadeh B, Zhang D. Design and dynamics of a 3-DOF flexure-based parallel mechanism for micro/nano manipulation. Microelectronic Engineering. 2010;87:230-41.

[3] Ryu JW, Gweon D-G, Moon KS. Optimal design of a flexure hinge based XY[phi] wafer stage. Precision Engineering. 1997;21:18-28.

[4] Hu K, Kim JH, Schmiedeler J, Menq C-H. Design, implementation, and control of a six-axis compliant stage. Review of Scientific Instruments. 2008;79:025105.

[5] Choi K-B, Lee JJ, Hata S. A piezo-driven compliant stage with double mechanical amplification mechanisms arranged in parallel. Sensors and Actuators A: Physical. 2010;161:173-81.

[6] Yao Q, Dong J, Ferreira PM. A novel parallel-kinematics mechanisms for integrated, multi-axis nanopositioning: Part 1. Kinematics and design for fabrication. Precision Engineering. 2008;32:7-19.

[7] Byung-Ju Y, Goo Bong C, Heung Yeol N, Whee Kuk K, Il Hong S. Design and experiment of a 3-DOF parallel micromechanism utilizing flexure hinges. Robotics and Automation, IEEE Transactions on. 2003;19:604-12.

[8] Koseki Y, Tanikawa T, Koyachi N, Arai T. Kinematic analysis of a translational 3-d.o.f. micro-parallel mechanism using the matrix method. Advanced Robotics. 2002;16:251-64.

[9] Kang D. Development of six-axis parallel nano-positioning system based on flexure joints and piezoelectric stepping positioners. KAIST. 2007;Ph.D. Thesis:100-5.

DESIGN AND PERFORMANCE OF TELESCOPING MICROPIPETTE ARRAYS FOR HIGH THROUGHPUT *IN VIVO* PATCH CLAMPING

Suhasa B. Kodandaramaiah[1], Saifullah Malik[1], Mike J. Dergance[1], Edward S. Boyden[2] and Craig R. Forest[1]
[1]George W. Woodruff School of Mechanical Engineering
Georgia Institute of Technology
Atlanta, Georgia, United States
[2]Department of Brain and Cognitive Sciences
Massachusetts Institute of Technology
Cambridge, Massachusetts, United States

ABSTRACT

Precise positioning (e.g., 1-100 μm) of an electrode or arrays of electrodes is a critical requirement for many *in vivo* electrophysiology studies. We are developing an instrument to manipulate arrays of micropipette electrodes utilizing a novel actuation strategy wherein flexible fused silica micropipettes telescope within teflon conduits configured in non-rectilinear configurations. This strategy circumvents the steric hindrances that limit the number micropipettes to just one in conventional setups. To prove this concept, we have designed a device that allows the simultaneous actuation of an array of four micropipettes. We have experimentally characterized the linear translation of micropipettes in this device and have achieved a minimum step resolution of 1 μm. Further *in vivo* electrophysiology experiments validate the efficacy of this device for in vivo patch clamping.

INTRODUCTION

In vivo patch clamping (IVPC) is an electrophysiology technique used to measure sub-threshold synaptic events, as well as intrinsic channel activities, with extremely high signal-to noise and fine temporal precision, during defined behavioral or pathological states [1,2]. Using IVPC to record from multiple neurons simultaneously in behaving animals would allow us to understand how neural dynamics emerge from the synaptic and electrical processes within neuronal networks. Despite the advantages, it has proven to be a very difficult technique to use and to date, no system has been proposed for recording arbitrarily large numbers of cells, in the fashion of tetrodes or multi-electrode arrays. The stereotaxic hindrance in a conventional IVPC setup limits the number of micropipettes that can be simultaneously controlled in the confined experimental space to just one.

We are working to develop instrumentation for precise positioning of the tips of densely packed array of micropipettes to be used for patch clamping *in vivo*. It is based on a novel actuation strategy that allows micrometer resolution positioning of flexible fused silica micropipettes that telescope within sheaths in non-rectilinear configurations (Figure 1).

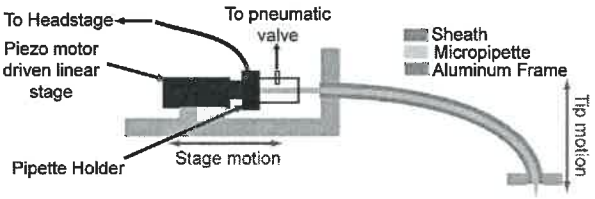

FIGURE 1. Schematic of the micropipette actuation strategy. The teflon sheath forms a curved, rigid and low friction conduit for the translation of a flexible fused silica micropipette.

The micropipette tips used for IVPC can be closely spaced in a 2-dimensional array (e.g., 1 mm apart), while the distal ends (e.g., the ends away from the brain, which connect to amplifiers and manipulators) can be spaced far apart, so that inexpensive motors and stages can be used to perform the actuation. The fused silica micropipettes are flexible laterally yet stiff axially for accurate translation and force feedback. Since fused silica is not typically used for IVPC, we have characterized its ability to subserve precision movement and electrophysiology.

MATERIALS AND METHODS

In order for IVPC to be scalable to multiple micropipettes, several key design criteria must be satisfied. First, the micropipettes must have a very consistent tip size and access resistance

[3]. Second, the micropipettes must be packable in close proximity (e.g., within a millimeter of each other) so that they can record neurons in the same brain, and ideally the same microcircuit, without steric hindrance from the amplifiers and translation stages that are typically attached to the micropipettes. Third, the system must allow for positive and negative pressure to be delivered to each micropipette, in an automated fashion, as traditional single-electrode patching methods will not scale easily to many electrodes.

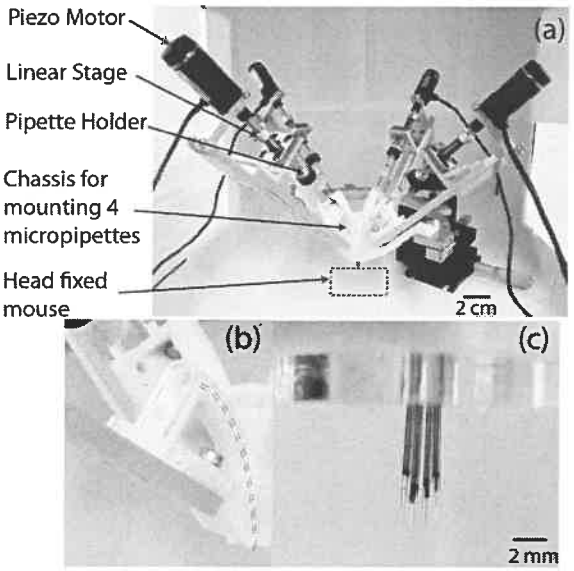

FIGURE 2: (a) Photograph of the prototype fourmicropipette array, (b) the configuration of the curved Teflon sheaths within it, and (c) headstage containing 4 parallel translating fused silica micropipettes.

Accordingly, we set out to design the micropipette array that allows independent control of an array of 4 micropipettes spaced 1 mm apart with a travel range of 10 mm and minimum step resolution of 1 μm (Figure 2). The micropipettes were formed by pulling polyimide coated fused silica capillaries (300 μm ID, 650 μm OD, Polymicro Technologies Inc) using the P2000 pipette puller (Sutter Instrument Company). They were routed between the control hardware and dense, parallel packing of the tips in a 1 mm x 1 mm square area via Teflon sheaths (AWG 21, Zeus Inc) that act as conduits (See Figure 2b,c). This packing density is advantageous for introducing multiple micropipettes into a 3 mm x 3 mm craniotomy on a head-fixed mouse. The sheaths are routed in a curved configuration through a 3D printed ABS chassis. The curvature of the sheaths was empirically determined (see the following section) to be the most effective for telescoping fused silica capillaries within them. They are fixed in place by filling the chassis with epoxy adhesive and letting it cure, thus forming rigid and low-friction conduits for the micropipette translation. A spring loaded shaft translating in a linear-roller ball bearing acts as an inexpensive interface between a pipette holder (Axon instruments Inc) and a piezo-motor (Newport Corporation) for linear actuation.

EXPERIMENTAL RESULTS

Linear Translation Characterization

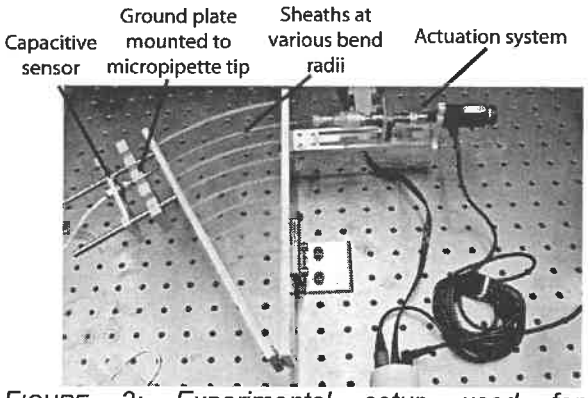

FIGURE 3: Experimental setup used for screening geometrical parameters affecting micropipette translation.

Using the setup shown in Figure 3, we tested the feasibility of actuating micropipettes telescoping in sheaths fixed in various configurations. We systematically varied two main geometric parameters: the bend radius (8-22 cm), and micropipette length (5-20 cm) as shown. We observed stick slip phenomenon in the lower bend radii configurations (8 and 10 cm). Further, the maximum length of the micropipettes in the device had to be limited to 10 cm to facilitate easy back filling. Using these criterions, we designed the micropipette array to telescope within 6cm long sheaths bent at 12cm radius.

We characterized the displacement of successive components of the actuation system as a function of the piezo-motor micro-steps (Figure 3). Shown in figure 4 is the displacement of the micropipette tip with respect to piezo-motor actuated at 1-μm steps.

We have been successful in achieving the aimed minimum step resolution of 1+/-0.287 μm and the actuator exhibits good linearity (r^2=0.997) for a range of up to 10 millimeters.

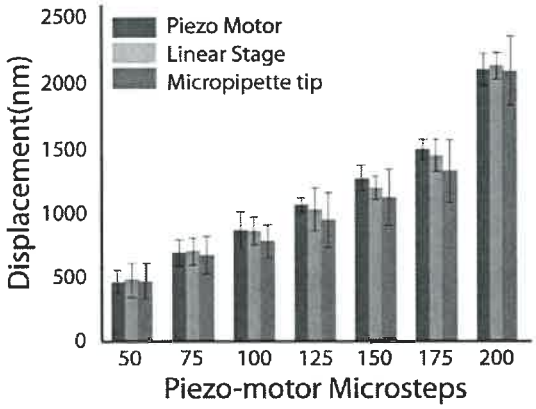

FIGURE 3: Displacements of various components of the actuation system as function of piezo-motor microsteps. Accuracy of displacement increases with successive steps in the system.

We conducted the metrology experiments using both contact (dial gauge, Mahr Inc) and non-contact (capacitive sensor, Capacitec Inc) methods. Thus, the actual penetrative motion of the micropipette in the brain tissue is an interpolation of the motion characteristic observed in these two methods.

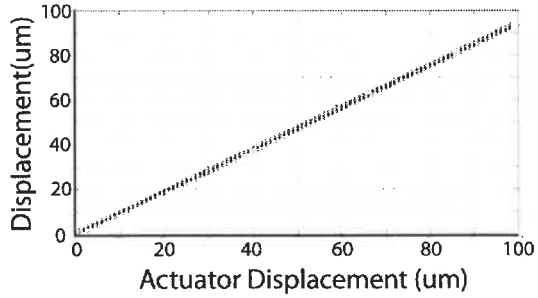

FIGURE 4: Displacement of the micropipette tip with respect to actuator input. Measured accuracy is +/- 0.287 μm, r^2=0.997 (n=5).

The principle difference observed was the introduction of a settling time of 1.6 seconds for the micropipette to reached the desired displacement when the measurements were taken using the dial gauge. This is because of the force exerted on the micropipette tip by the dial gauge head. However, no dynamic effects were observed in the electrophysiology experiments described in the following section.

In rare instances, it is advantageous in an IVPC experiment to be able to retract the micropipette to de-clogging the tip. We have measured the micropipette translation backlash error to be 12 μm.

In Vivo Electrophysiology

To test the efficacy of the device, *in vivo* electrophysiology experiments were conducted on anesthetized mice using the micropipette array. We have successfully recorded dendritic spikelet activity *in vivo* (Figure 5a). Further, we compared the electrical impedance changes in the fused silica micropipette in the proximity of a neuron to a conventional IVPC experimental setup where a borosilicate micropipette was actuated by the commercially available MPC 200 (Sutter Instruments Inc) micromanipulator (Figure 5b).

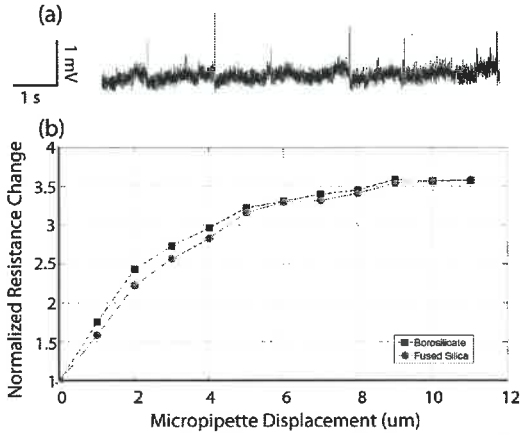

FIGURE 5: (a) Dentritic spikelet recordings from a neuron in vivo using the designed micropipette array, (b) comparison of the micropipette resistance to the change observed in a borosilicate micropipette in a standard IVPC setup as a neuron is approached (zero displacement is taken as the point at which resistance change is first observed).

In both methods, the micropipettes could be advanced 10-15 μm from the time an increase in resistance was observed before impaling/brushing past the neuron (indicated by a drop in resistance). Thus we can conclude that the micropipette actuation strategy can be used with the predicted accuracy even as it penetrates the brain tissue.

CONCLUSION

Independent micrometer resolution manipulation of densely packed micropipette arrays enables

the measurement of sub-threshold synaptic activity *in vivo* from multiple neurons simultaneously. We have characterized the linear translation telescoping actuation strategy can be used to actuate the micropipettes with micrometer step resolution. *In vivo* electrophysiology experiments show that micropipette can be successfully used for patch clamping and are comparable to commercially available micromanipulators. This device will allow us to target up to four neurons simultaneously *in vivo*. Further scaling of the device and developing an algorithm to automate the patch clamping protocol could allow the control of up to 25 such micropipettes. This will represent a paradigm shift in the scalability of patch clamping technology and will, in future years, potentially enable recordings from arbitrarily large numbers of cells, in the fashion of tetrodes and multi-electrode arrays.

REFERENCES

[1] Harvey C D, Collman F, Dombeck D A, Tank D W, Intracellular dynamics of hippocampal place cells during virtual navigation. Nature 2009. 461(7266): p. 941-U196.

[2] Dombeck D A, Khabbaz A N, Collman F, Adelmann T A, Tank D W, Imaging large-scale neural activity with cellular resolution in awake, mobile mice. Neuron, 2007. **56**(1): p. 43-57.

[3] Margrie T W, Brecht M, and Sakmann B, In vivo, low-resistance, whole-cell recordings from neurons inthe anaesthetized and awake mammalian brain. Pflugers Arch, 2002. 444(4): p. 491-8.

COMPARING DIFFERENT COOLING CONCEPTS FOR BALL SCREW SYSTEMS

Josef Mayr[1], Markus Ess[2], Sascha Weikert[2], and Konrad Wegener[1,2]
[1]Institute of Machine Tools and Manufacturing (IWF)
[2]inspire AG
Swiss Federal Institute of Technology (ETH)
Zurich, Switzerland

ABSTRACT

Different design modifications to reduce the thermo-elastic deviations on a prototype lathe caused by moving linear axis are discussed. The machine tool has no linear encoders for the controlled axis whereby the TCP-displacements particularly at long-term machining can be enormous.

A simulation study was used to find out what design modifications can help to reduce the thermally induced deviations between the work-piece and tool and to what extent the deviations can be reduced. The example illustrates that the thermally induced TCP-displacements of the prototype can be reduced to about 15% of the original deviations by design modifications without using linear encoders.

Short-term variations in the boundary conditions cause unwanted long computation time. If possible, boundary conditions with short-term variations should be simplified. In an example the interpolation of the temperature range of the coolant temperature control reduces computation time by a ratio of almost five. With such simplifications the whole simulations study with more than 25 simulations can be realized in less than three days computation time including model modification.

INTRODUCTION

Internal and external heat sources and sinks initiate thermo-elastic deformations on machine tools as well as on the work-piece. In the end the thermo-elastic deformations lead to geometrical inaccuracies on the work-piece. Thermal influences are typically the major source of reduced machining accuracy on machine tools and prominently contribute to the overall geometrical inaccuracy of the work-piece [1,2].

The basic effects of thermal inaccuracies of machine tools have thoroughly been investigated for decades. Based on this, design rules have been derived, which thoroughly are applied in ultra precision machine design [4].

To improve thermal stability of linear axes typically linear encoders are used. The benefits of using linear encoders have frequently been demonstrated. Other methods like cooling the ball screw spindle with a temperature controlled coolant may have disadvantages. For example a shaft feedthrough may be required. An other disadvantage of cooling the ball screw spindle is that if no linear encoders are used the spindle is used as reference frame and therefore the control range of the coolant temperature swayed the axis position [5,6].

For precision machine tools ball screw manufacturers developed cooled nuts [7]. The cooled nut should inhibit the heat flux from the ball screw system into the machine tool structure.

BALL SCREW MODEL

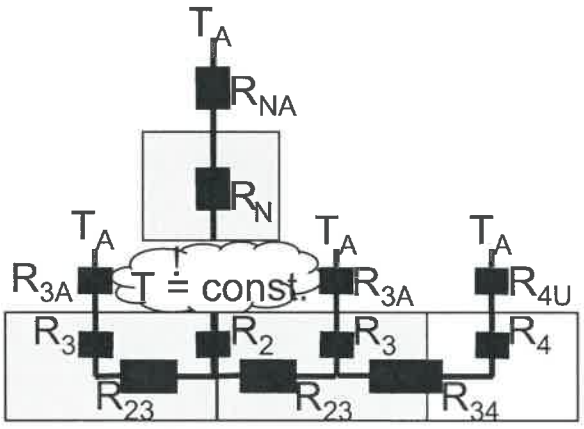

FIGURE 1. Thermal equivalent circuit diagram of the ball screw system, R: thermal resistance, T_A: ambient temperature, T: rolling body temperature.

In Figure 1 the thermal equivalent circuit diagram of the ball screw system is shown. The equivalent circuit diagram has three main elements: the rolling bodies, the spindle and the nut.

The model is used to determine the heat flux in the ball screw system. One part of the heat

generated during operation flows into the spindle which leads to a temperature increase in this element. The temperature increase leads to a part of the heat being led down to the ambient air via convection. The other part of the heat generated in the ball screw system flows into the nut and from the nut to the ambient air.
The spindle is subdivided into 2 areas. On the one hand the area which is passed by the nut during operating (shown in Figure 1 highlighted in gray) and on the other hand the area which is just in contact with the ambient air (shown in Figure 1 highlighted in white).
The rolling body temperature is unknown. It is assumed that through the rotation of the rolling bodies the temperature on all contact points is equal.
Thermal effects on machine tools usually are long-term effects. Therefore having the same temperature at all contact points the ratio of the heat flux into the spindle and into the nut can be assumed as being the same as in steady state.
With these assumptions the thermal equivalent circuit diagram can be simplified to the equivalent resistance diagram shown in Figure 2 using Kirchhoff's laws.

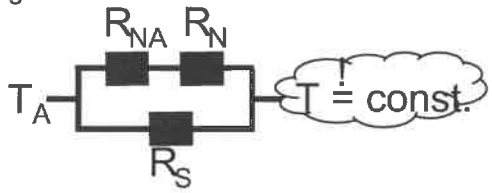

FIGURE 2. Simplified thermal equivalent circuit diagram of the ball screw system, R_S: thermal resistance spindle side, R_N: thermal resistance of the nut, R_{NA}: convective thermal resistance of the nut to the ambient air.

MACHINE TOOL MODEL

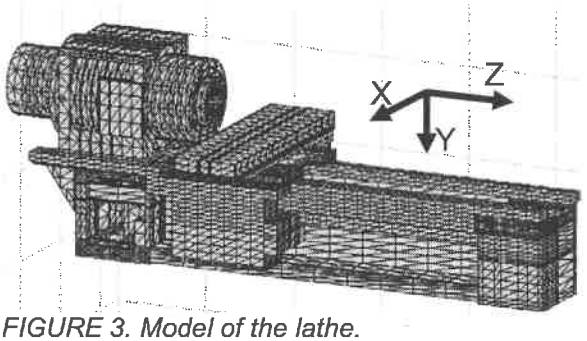

FIGURE 3. Model of the lathe.

The model of the lathe under investigation is shown in Figure 3. The model includes all necessary structural components of the machine tool like the spindle, the spindle cooling system, the bed and the linear axes. The motors e.g. are not included into the model. The motor temperature is included as thermal boundary condition based on measurements.

LOADING CONDITIONS

The simulation study was done for a load case consisting of a moving Z-axis: The Z-axis oscillates between the measurement position (the axis position shown in Figure 3) and the end of the axis travel at a distance of 318mm. The considered heat sources and sinks are the friction in the ball screw system and hydrodynamic linear guides, the coolant, the ambient temperature profile and the linear axes motor temperatures.
In the first 1.8 hours the Z-axis oscillates with 3m/min feed rate. Afterwards the Z-axis is 3.8 hours oscillating with 5m/min feed rate. At the end of the simulation cycle the z-axis is positioned at the measurement position for cooling down for another 14 hours. To ensure that the simulations can be compared with measurements the simulation cycle was chosen based on measurements previously done. From this measurement all boundary conditions like the ambient temperature profile are known. As examples the measured boundary conditions ambient temperature profile and the temperature of the Z-axis motor are shown in Figure 4. The measurement profiles have typically to be smoothed before they can be used as boundary conditions for simulation in order to reduce simulation time. As shown in Figure 4 different interpolation methods are used: E.g. the ambient temperature profile and the motor temperature interpolated based on linearly or on exponentially fitted curves.

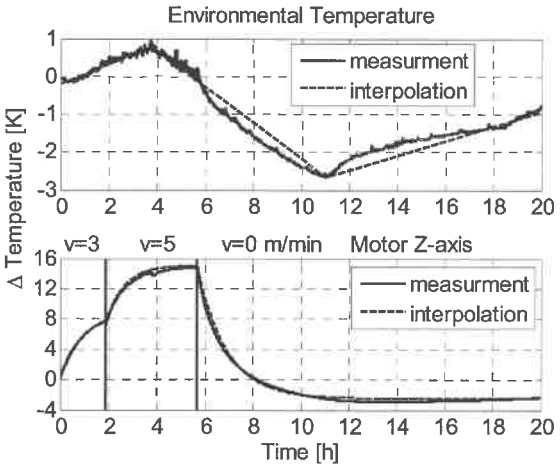

FIGURE 4. Measured and interpolated temperature profiles, top: environmental temp., bottom: temp. of the z-axis motor.

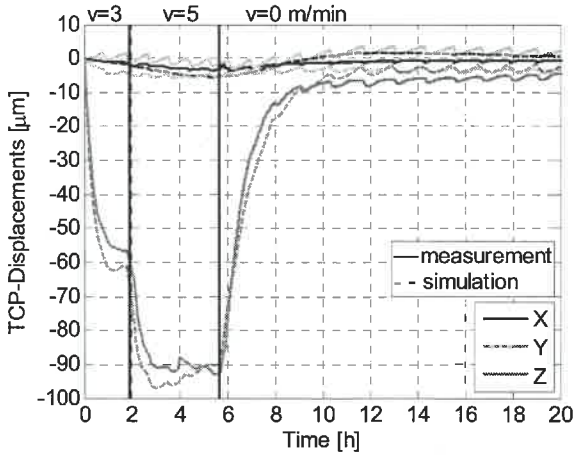

FIGURE 5. Measured and simulated TCP-displacements in X-, Y- and Z-direction.

As can be seen in Figure 5 the measured and computed TCP-displacements show a good correlation within a difference in maximum of about 10µm in Z-direction. In the other directions the TCP-displacements and also the difference between simulation and measurement are even smaller.

COOLANT TEMPERATURE

The coolant of the spindle is controlled to 21.5 ± 1.7°C. If the maximum temperature of 23.2°C is reached the cooling process starts while the temperature is higher than 19.8°C. The consequence of this control is a saw tooth profile in spindle coolant temperature. Applying this saw tooth profile in the simulation leads to abrupt changes in the boundary conditions. Such changes in boundary conditions usually cause an increase of computation time due to reduced step size. Therefore it is advisable to simplify those boundary conditions as shown in Figure 6.

The control range of the temperature of the coolant can be reproduced as sinusoidal profile or as being constant. The cycle period with the saw tooth profile is not constant. Here, the measured profile was used which is swayed by the ambient temperature and the heat input.

In Figure 7 the step sizes chosen by the solver (Matlab/Simulink, ODE 15s) are shown. As it can be seen every change in boundary conditions enormously reduces the step size. Therefore with the saw tooth profile the computation of the temperature distribution over a simulation time of 20 hours takes about 850 s using the FDEM simulation approach [3,4]. With a sinusoidal profile the same simulation just takes 181 s and with constant flow temperature of the coolant just 167 s are required. As it can been seen in Figure 7 with a sinusoidal flow temperature of the coolant the maximum step size of 1'000 s (chosen by the operator) cannot be reached by the step size control but the influence to the total cost of computation time is secondary.

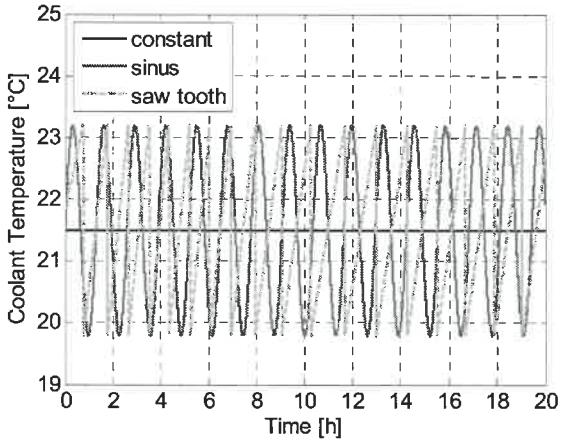

FIGURE 6. Flow temperature of the coolant used as boundary conditions in the simulation.

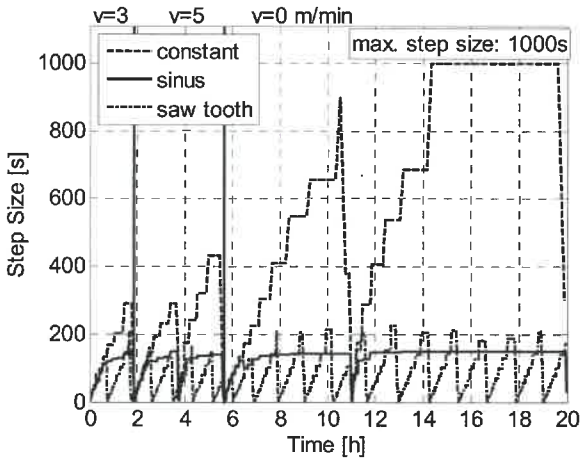

FIGURE 7. Step size with different interpolated coolant temperature profiles.

SIMULATION STUDY

With a simulation study it should be investigated whether the TCP-displacements can be reduced without applying linear encoders. For this, several design modifications are discussed. The ball screw manufacturer for example offers two types of cooled nuts. Another modification is changing the location between the ball screws thrust and floating bearing. At the end of the bed, at the opposite side to the main spindle, the Z-axis motor and the thrust bearing of the ball screws are located. On the prototype ball screws are all used in fixed-free configuration. With the modified assembly the thrust bearing is located

at the main spindle side and at the motor side an additional floating bearing is mounted to support the forces from the transmission.
Other ideas discussed are using cooling fins or cooling plates to isolate the thermal influence of the motor from the bed. The two assemblies discussed are shown in Figure 8.

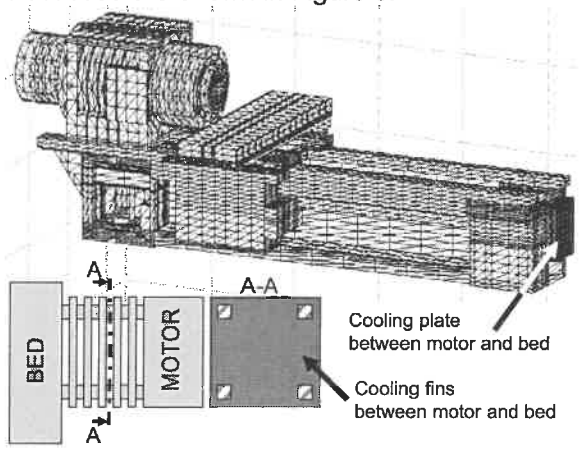

FIGURE 8. Cooling plates and cooling fins for isolating the motor temperature from the bed.

Cooling fins like the shown assembly in Figure 8 help to keep off the motor heat from the bed. The simulations have shown that through the isolation the temperature of the motor is rising. Therefore it is not unconditionally advisable to use such an assembly.
Cooling plates reducing the motor and bed temperature can always be used for isolating heat sources from machine tool structures.

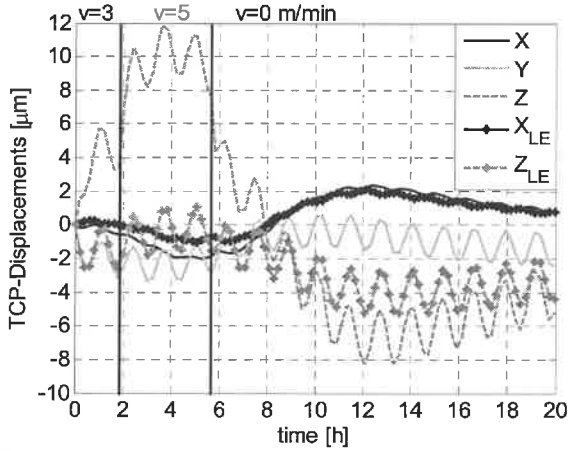

FIGURE 9. Simulation results, translatory TCP-displacements after implementing design modifications into the model, LE linear encoders are additionally considered, original curves see Figure 5.

Based on the ball screw model shown in Figure 2 the heat flow into the nut can be swayed when changing the boundary conditions. With a fluid cooled nut the convective resistance R_{NA} can be reduced. In such a case more heat flows into the nut while the thermo-elastic deformation of the spindle is reduced. The ball screw model has shown that over 97% of the friction heat generated in the ball screw can be conducted through the nut into the coolant. Nevertheless a limit in reducing thermo-elastic deformations of the spindle will be reached earlier because other heat sources like the friction heat of the bearings become more prominent.
In Figure 9 the minimum reachable translatory TCP-displacements after implementing the design modifications are shown. The greatest influence has the change of thrust bearing position and the cooled nut. Other changes like isolating the motor heat from the bed have secondary influence to the translatory TCP-displacements but help reducing rotatory TCP-displacements. The simulations study has also shown that the TCP- displacements can be reduced more when linear encoders for the X- and Z-axis are used additionally.

ACKNOWLEDGEMENT
The authors like to thank the Swiss Federal Office for Professional Education and Technology (OPET/CTI) for financial support.

REFERENCES

[1] J.Bryan. International Status of Thermal Error Research. Annals on the CIRP. 1990; 39/2: 645-656
[2] M.Weck, P.McKeown, R.Bonse, U.Herbst. Reduction and Compensation of Thermal Errors on Machine Tools. Annals on the CIRP. 1995; 44/2: 589-598
[3] J. Mayr, M.Ess, S.Weikert, K.Wegener. Simulation and prediction of thermally induced deformations on machine tools caused by moving linear axis using the FDEM simulation approach. Proceedings ASPE 2008 Annual Meeting. 2008
[4] J. Mayr, M.Ess, S.Weikert, K.Wegener. Thermal Compensation uning Three-Dimensional Physical Machine Tool Models. Proceedings of the 12th Mecha-tronics Conference. 2010; 1/2: 279-284
[5] J.Braasch. Genauigkeit von Vorschub-antrieben. Heidenhain Technische Information. 2004; 5
[6] J.Braasch. Optimizing feed axis precision. Motion System Design. 2002; 23-25
[7] HIWIN. Lineartechnologie. www.hiwin.de. 2009: 60-64

MEASUREMENTS USING THE HIGH ACCURACY ATOMIC FORCE MICROSCOPE AND THE SUB-ATOMIC MEASURING MACHINE

Jerald L. Overcash[1,2], Robert J. Hocken[2], Darya Amin-Shahidi[3], David L. Trumper[3], and Mark L. Schattenburg[4]

[1]Opto-Alignment Technology, Inc.
Charlotte, North Carolina, USA
[2]Center for Precision Metrology
University of North Carolina at Charlotte
Charlotte, North Carolina, USA
[3]Mechanical Engineering Department
Massachusetts Institute of Technology
Cambridge, Massachusetts, USA
[4]Space Nanotechnology Laboratory
Massachusetts Institute of Technology
Cambridge, Massachusetts, USA

ABSTRACT

The preliminary results of mating the MIT developed High Accuracy Atomic Force Microscope (HAFM) with the Sub-Atomic Measuring Machine (SAMM) at UNC Charlotte is discussed. The SAMM positions the sample with respect to the probe tip with independent control in 6 degrees of freedom via a magnetic levitation/neutrally buoyant stage assembly. The SAMM has a travel volume of 25 mm x 25 mm in the plane of the sample and 100 µm of travel normal to the plane surface. The HAFM provides an additional single degree of freedom motion in the vertical direction, normal to the sample surface with 20 µm of travel. All of the control loops run independently to allow the AFM tip to track the sample surface. Through this research effort we have enabled high accuracy measurements with sub-nanometer resolution over a sample area of 25 x 25 millimeters.

BACKGROUND

The Sub-Atomic Measuring Machine (SAMM) was designed to enable accurate measurements with high resolution over long ranges using a magnetic levitation stage. The instrument design was carefully considered and therefore the instrument remains at the state-of-the-art even after nearly a decade. The recent, last 4 years of upgrades have been primarily with regard to the control and laser delivery systems to take advantage of advances in computing technology to bring the instrument up-to-date in this area while at the same time increasing the positioning performance of the machine and integrate a newly developed AFM probe head [1, 2, 3, 4].

Sub-Atomic Measuring Machine

The SAMM uses 4 planar type linear motors fixed to the base of the instrument with 4 opposing Halbach magnet arrays affixed to the moving platen to provide actuation forces in 6 degrees of freedom. The platen is neutrally buoyant and is floated in high viscosity fluid to reduce the actuation effort for levitation and provide damping in all 6 degrees of freedom. The Zerodur sample holder/mirror monolith is attached to the platen and is held above the fluid by a flexure based Kelvin clamp. Laser interferometers provide feedback for x, y, and theta z degrees of freedom and capacitance probes provide feedback for z, theta x, and theta y. The feedback sensors reside on the Zerodur metrology frame, also a monolith. The custom interferometer optics allow for 4 passes between the optics and the mirror (where a pass refers to a path to and from the mirror). The capacitance probes are deposited directly onto the metrology frame. The detection scheme for the lasers is time based and allows for increased resolution by mixing the heterodyne frequency down and time stamping the zero crossings to a high frequency clock. This configuration allows 10 pm position resolution [5, 6]. The source has been upgraded to an offset frequency locked HeNe laser referenced to an iodine stabilized

HeNe increasing the accuracy of the measurements.

A sealed chamber allows for a stable environment for the measurements and provides for purging the chamber with helium, also increasing the measurement accuracy. To further address the accuracy concerns, a wavelength tracking interferometer was added to monitor and correct the position measurements for changes in the refractive index.

Atomic Force Microscope

The AFM probe head assembly was designed, assembled, and tested at MIT and delivered to UNC Charlotte for integration with the SAMM [1]. The major components are the PZT actuator, capacitance probes, probe tip, and flexure. The AFM has 1 degree of freedom that is actuated by the PZT, guided by the flexure and monitored by the capacitance probes. The PZT has 20 µm of vertical travel such that the probe tip can follow the features on the sample and prevent contact between the tip and sample. The probe tip is tuning fork based and therefore is of the self-actuating/self-sensing type. These are commercially available Akiyama probes where the tip is attached to both tines of the tuning fork and provides out of plane motion with respect to the tuning fork motion. The resonance of these probes is at approximately 50 kHz.

SAMM, Microscope Integration

The mated systems are shown in figure 1. The AFM module rests on the SAMM metrology frame in kinematic mounts with elastic bands providing preload.

The primary aspects of integrating the two systems included physical mating, aligning, wiring and controlling. Of these the aspects, the wiring seems to be the most difficult when designing, building and assembling precision mechatronic systems. The probe electronics consists of two boards since it was not known in the design stage whether the preamplifier for the return signal from the probe needed to be inside the chamber or could be located outside the chamber. In the end all of the electronics were placed outside the chamber and all of the connections pass through floating type vacuum feed through connections. The only heat source inside the chamber is the PZT actuator. A borescope allows visual operator feedback for macro-scale sample features when the chamber is sealed and operating.

From the controls side, the AFM self resonance control board handles driving the Akiyama probe at fixed amplitude at resonance. The height is controlled via a digital controller running on a National Instruments FPGA board inside the PXI control chassis. The control loop is closed using the probe resonance as feedback to drive the PZT to maintain a fixed oscillation frequency of the Akiyama probe. The capacitance probes on the AFM probe head read the position of the head and are not in the control loop. The AFM capacitance probes are read in the SAMM control loop on the real-time side of the National Instruments PXI controller. A host PC communicates to the real-time controller and provides the user interface.

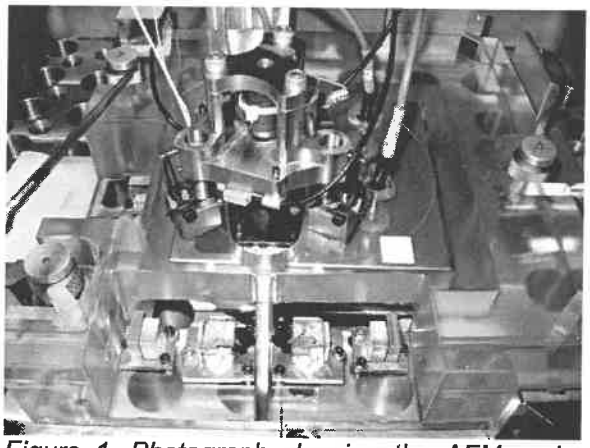

Figure 1. Photograph showing the AFM probe head mated to the SAMM metrology frame.

MEASUREMENT LIMITATIONS

There are several factors that limit the speed at which a scan can take place. Since the laser interferometer signals are frequency mixed down to 8 kHz to increase resolution this becomes the first limit on the scan speed since the frequency shift depends on stage velocity and the limit is somewhere above zero frequency. Limiting the velocity induced frequency shift to 4 kHz gives a velocity limit of 0.3 mm/s for the SAMM. Another limit is the bandwidth of the closed loop control of the atomic force microscope which is the second limit on the scan speed. The sample geometry factors complicates the speed limit further and must be considered in conjunction with the closed loop bandwidth of the atomic force microscope. Assuming a periodic sample geometry one can easily convert this to the frequency at which the microscope must oscillate to follow this geometry. Consider a

sample with a sinusoidal grating with a period of 200 nm. With a 0 dB closed loop crossover of 50 Hz the stage velocity should be limited to below 0.01 mm/s. The control system and sampling speed are the final limiting factors that limit how fast a scan can take place. The entire control loop for the stage is currently closed at 1 kHz, including sampling the feedback sensors, calculating the control effort, converting the control effort into the current output for the motors and outputting a voltage command to the power amplifiers for the motors. This limits the sampling to 1 ms per sample point. With little effort this could be pushed to 2 kHz and with more efficient programming could likely be pushed closer to 5 kHz. In the end, for the sample considered, the limit is the closed loop bandwidth of the AFM probe head.

MEASUREMENT RESULTS

Preliminary measurements utilizing the High Accuracy Atomic Force Microscope and the Sub-Atomic Measuring Machine show promising results, see figure 2. The image shows one of the first scans utilizing the integrated systems. The sample is a sinusoidal grating manufactured on the MIT Nanoruler and has features with a period of 200 nm and height of 40 nm [7]. This image shows a 500 nm by 500 nm surface scan sampled at 256 points by 256 points. The data are presented in raw format with no filtering on the x, y or z data or removals including slope. Also the data are presented in true x, y, z format, not pixel, pixel, z. The sample was aligned on the sample holder using a surface profilometer and adjusting the sample holder to minimize the tilts when inserted in the SAMM for subsequent scanning. In this case the sample was scanned beneath the AFM using the SAMM for scanning in the x, y plane and holding position in z, theta x, theta y, and theta z. The HAFM was responsible for following the sample surface. Therefore the height information displayed in the data is gathered from the capacitance probes in the HAFM and the x, y positions are gathered from the laser interferometers on the SAMM.

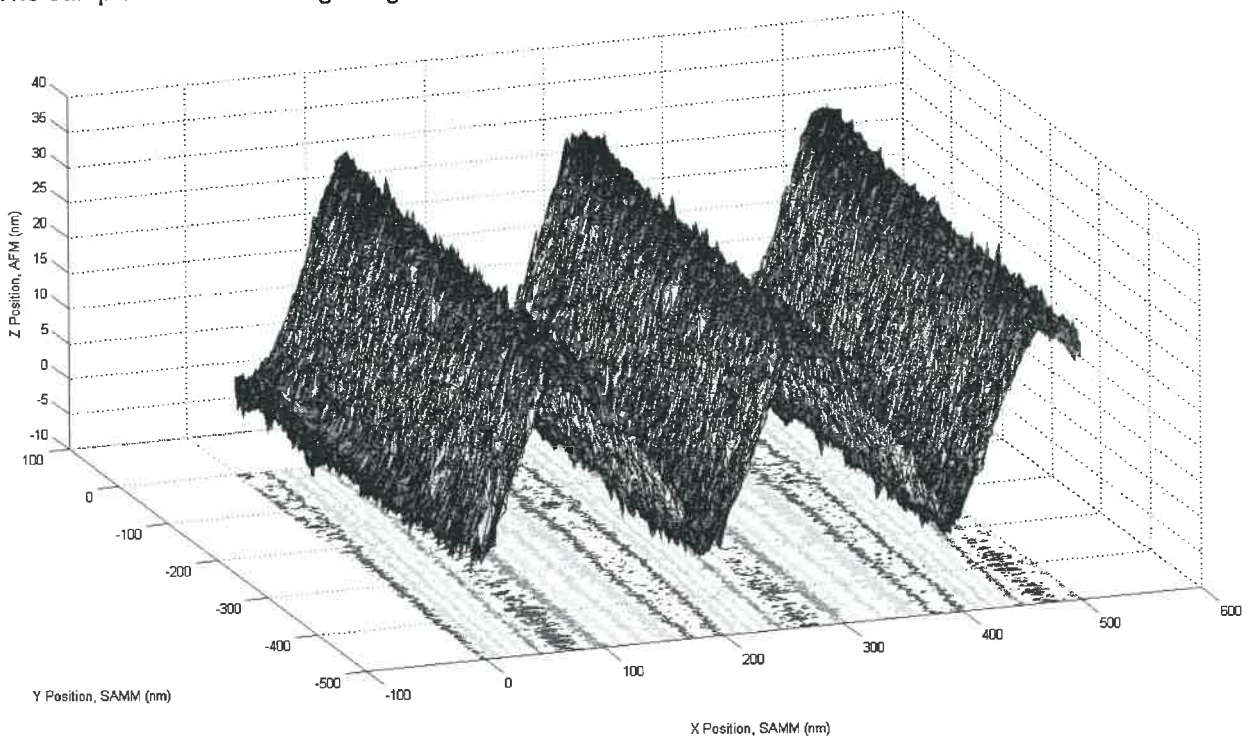

FIGURE 2. Measurement data of sinusoidal grating. Image size 500 nm x 500 nm, 256 points x 256 points. Scanned at 10 ms per point.

CONCLUSIONS

The successful integration of the AFM probe head with the SAMM has been demonstrated with initial measurements completed. The next steps in this project will aim to quantify the accuracy and stability of the newly assembled instrument. We continue to develop a calibration artifact that will be used to complete the error mapping of the SAMM errors [8]. We are also researching and developing the error mapping algorithm to be implemented. Comparisons with other instruments will ultimately be necessary to further quantify the accuracy of the instrument.

ACKNOWLEDGEMENTS

This research is funded by the National Science Foundation under award number 0506898 and carried out in the Center for Precision Metrology. Any opinions, findings, and conclusions or recommendations expressed in this material are those of the author(s) and do not necessarily reflect the views of the National Science Foundation.

REFERENCES

[1] Darya Amin-Shahidi, Dean L. Ljubicic, Jerald L. Overcash, Robert J. Hocken, David L. Trumper, High-Accuracy Atomic Force Microscope for Dimensional Metrology (II), ASPE 2009 Annual Meeting.

[2] Jerald L. Overcash, Charles Stroup, and Robert J. Hocken. Recent Developments And Upgrades In-Progress Of A Precision Six Degree-Of-Freedom Magnetically Suspended Measuring Instrument. ASPE 2007 Annual Meeting.

[3] Charles Stroup, Jerald L. Overcash, and Robert J. Hocken. The Development of an Offset-Locked Frequency Stabilized Heterodyne Laser Source for Precision Metrology. ASPE 2008 Annual Meeting.

[4] Jerald L. Overcash, Charles Stroup, and Robert J. Hocken. Updating the Sub-Atomic Measuring Machine. ASPE 2008 Annual Meeting.

[5] Jerald L. Overcash, Robert J. Hocken, and Charles G. Stroup, Jr., Noise Reduction and Disturbance Rejection at the Sub-Nanometer Level, ASPE 2009 Annual Meeting.

[6] Jerald L. Overcash, Charles Stroup, and Robert J. Hocken. Resolution Considerations in Interferometer Based Ultra-Precision Machines. 10th Euspen Conference, 2008.

[7] C.H Chang, Y. Zhao, R.K. Heilmann, and M.L. Schattenburg, Spatial-frequency multiplication with multilayer interference lithography, J. Vac. Sci. Technol. B 26, 2135-2138 (2008).

[8] T.D. Lemmons, R.J. Hocken, J.L. Overcash, Macroscopic Transfer Artifact for Nano-positioning. ASPE 2009 Annual Meeting.

MODULATION OF ELECTROMAGNETIC RADIATION USING A DOT MATRIX PRINTER

Nikita Pak, Christopher R. Phaneuf, Suhasa B. Kodandaramaiah, and Craig R. Forest
George W. Woodruff School of Mechanical Engineering
Georgia Institute of Technology
Atlanta, Georgia, United States

ABSTRACT

Spatial modulation of electromagnetic radiation is crucial for many optical systems. We are focused on the design of a biological instrument that relies on spatially varying infrared laser radiation for heating of aqueous solutions within an array of 1.5 μL microchambers. Such a radiative heating method is preferable to conductive and convective heating because it allows for fast heating rates at absorption wavelengths, there are no risks of incompatible materials coming into contact with the reaction, and it allows for the possibility of a disposable reaction environment. A single radiation source directed to multiple reaction chambers can reduce complexity of the overall device and also cost. We have developed an optical shutter designed to partially block radiation to a select chamber. This allows for two adjacent chambers to achieve different temperatures. Testing of the device has resulted in a direct, linear relationship between the shutter's duty cycle and the amount of radiation passing through. This device will allow us to control the temperature in two chambers heated by one source of radiation.

INTRODUCTION

Many microfluidic applications require the ability to control the temperature of tiny liquid volumes (e.g. 1-10 μL). An example of such an application is the polymerase chain reaction (PCR) in which a DNA template is amplified via a heat-stable polymerase enzyme and thermal cycling [1]-[3]. A major limitation on current PCR cyclers is the inability to run multiple thermally independent reactions simultaneously, which would require the ability to locally control the temperature in each reaction chamber during thermal cycling [4]. Critical temperatures for this reaction are in the range of 50-60°C, and adjacent chambers require temperature differences as large as 5°C.

A source of electromagnetic radiation can be blocked to locally decrease the temperature on a microfluidic chip. Therefore, we have developed an optical shutter utilizing the solenoids of a dot matrix printer. By opening and closing the shutter at a varying duty cycle, different amounts of radiation are allowed to pass through to the reaction chamber. This allows one source of radiation to control multiple temperature profiles in adjacent chambers. Our current setup is shown in Fig. 1.

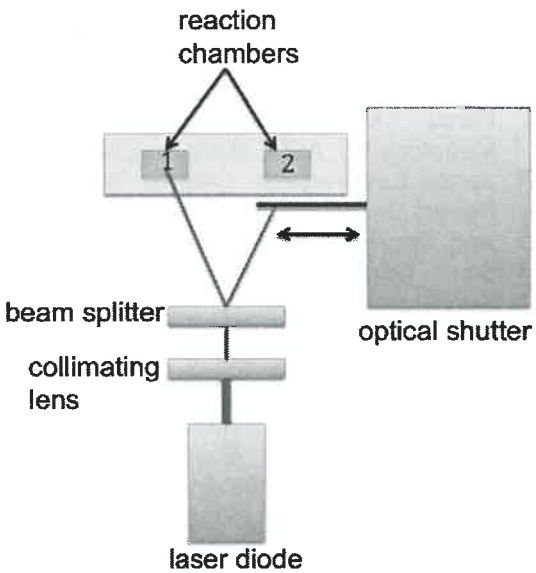

FIGURE 1. Schematic of dot matrix printer based optical shutter. Chamber 2 will have a lower temperature depending on the duty cycle at which the shutter operates. The two chambers are heated by a single source of radiation; a laser diode.

A 1450 nm laser diode is collimated and split into two beams focused on two identical 1.5 μL reaction chambers. The optical shutter is mounted directly below one of the chambers. When it is activated, the temperature of that chamber decreases based on the duty cycle at which the shutter operates.

MATERIALS AND METHODS

The challenges associated with utilizing an optical shutter on a microfluidic device are the space constraint and speed. The shutter must fit on or around the small area of the microfluidic chip but still operate at a high enough frequency to effectively control temperature. Traditional solenoids are far too large to fit into the device architecture so a dot matrix printer head is used, which has 24 individually activated miniature solenoids.

Thermocouples are inserted into both reaction chambers to monitor temperature. The temperature in each chamber is controlled with a Labview program, which has different set points for each chamber. To decrease the temperature of the blocked chamber, the program increases the duty cycle of the shutter. In this way, the temperature of the blocked chamber is less than or equal to that of the unblocked chamber.

The maximum displacement of the shutter, from a dot matrix printer [NEC, Pinwriter P2200XE] is 0.58 mm, and the minimum duty cycle that produces full displacement is 0.05 at 10 Hz. High speed video [Phantom, v9.0, Wayne, NJ] analysis has revealed the time to close the shutter as 1.841 ms, and the time to retract as 1.315 ms. The chamber width of 0.50 mm is fully blocked by this displacement, and the sufficiently low displacement time effectively makes this a digital shutter.

EXPERIMENTAL RESULTS

The shutter was characterized by measuring the amount of radiation passing through at a given duty cycle. This was done using a photodiode, which recorded intensity data through Labview. The results can be seen in Fig. 2.

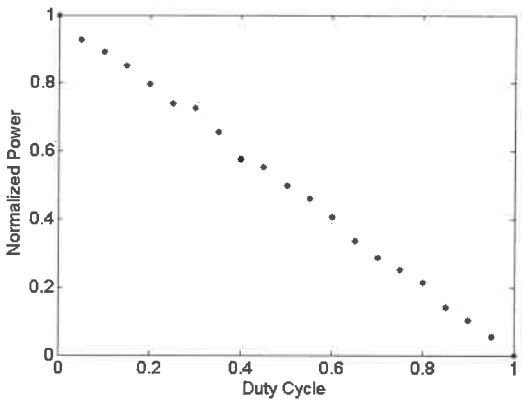

FIGURE 2. Plot of normalized power as a function of duty cycle. Data was obtained by changing the shutter duty cycle while measuring transmitted power with a photodiode.

The power was normalized based on full irradiation and no irradiation. This plot shows the linear relationship between duty cycle and power.

Decreasing the temperature in chamber 2 will lead to some temperature drop in the other chamber because of conduction. Therefore, it was important to understand what the maximum temperature difference between the chambers was at a given temperature. To achieve this, the two chambers were brought up to the same temperature, Tss. The shutter was then run at a duty cycle of 1, or fully closed. This was done for several temperatures and plotted in Fig. 3.

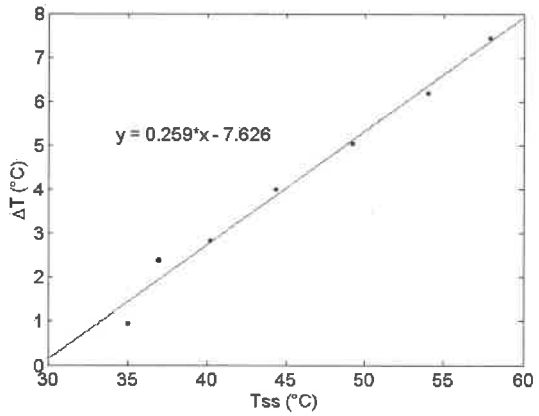

FIGURE 3. Plot of temperature difference between the chambers as a function of steady state temperature in chamber 1. The duty cycle was set to a value of 1.

The temperature in the first chamber was maintained through feedback control. As can be seen, the trend is fairly linear. These

temperature differences exceed the required 5°C at Tss > 49°C.

To show that varying the duty cycle has an effect on temperature, different duty cycles were used at the same set point. This can be seen in Fig. 4.

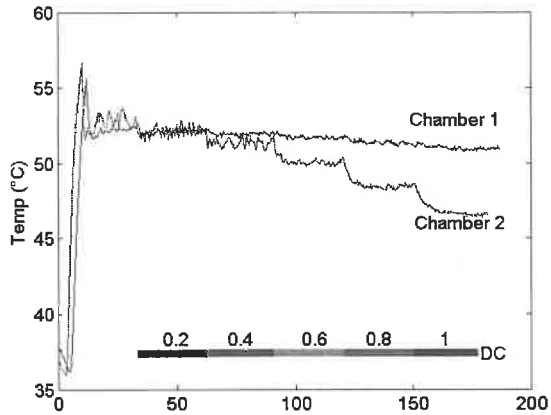

FIGURE 4. Plot of temperature in both chambers vs. time. The temperature of chamber 2 is varied by changing the shutter duty cycle.

The line on the bottom of the graph marks the duty cycle at which the shutter was operating at for that period of time. It can be seen that there are clear and distinct regions of decreased temperature at each of the different duty cycle values.

CONCLUSION

Independent temperature control in microfluidics is a useful feature in many biological applications. Achieving this with a single source of electromagnetic radiation has the added benefits of simplicity, lower cost, and a heat source that is isolated from the reaction environment. We have developed an optical shutter that is small enough to fit into a microfluidics environment yet has the speed to effectively control temperature. The power output as a function of duty cycle was plotted, and the temperature isolation between adjacent chambers was obtained. It was also shown that by varying the duty cycle, distinct temperatures could be achieved. This device will allow us to run two independent PCR reactions on the same microchip. Further scaling of our shutter could allow for up to 25 microchambers to be independently controlled from the 24 solenoids in the dot matrix printer.

REFERENCES

[1] Liu CN, Toriello NM, Mathies RA, Multichannel pcr-ce microdevice for genetic analysis. Analytical Chemistry. 2006 Jun 7;78(6):5474–5479.

[2] Huhmer AFR, Landers JP, Noncontact infrared-mediated thermocycling for effective polymerase chain reaction amplification of dna in nanoliter volumes. Analytical Chemistry. 2000 Sep 23;72(6):5507–5512.

[3] Hou CSJ, Godin M, Payer K, Chakrabarti R, Manalis SR, Integrated microelectronic device for label-free nucleic acid amplification and detection. Lab on a Chip. 2007;7(8):347–354.

[4] Slyadnev M, Lavrova M, Erkin M, Kazakov V, Ganeev A, Development of a multireactor microfluidic system for the determination of dna using real-time polymerase chain reaction. Journal of Analytical Chemistry. 2008 Feb 8;63(7):192–198.

PARAMETRIC MODELING OF SELF-WEIGHTED DISTORTION FOR PLANE OPTICAL MIRRORS

Won Hyun Park[1], Brian Cuerden[2], Sug-Whan Kim[3], and James H. Burge[1]
[1]College of Optical Sciences,
University of Arizona,
1630 E. University Blvd, Tucson, Arizona 85721, USA
[2]College of Optical Sciences,
University of Arizona,
1630 E. University Blvd, Tucson, Arizona 85721, USA
[3]Space Optics Laboratory, Dept. of Astronomy,
Yonsei University,
134 Sinchon-dong, Seodaemun-gu, Seoul 120-749, Republic of Korea

INTRODUCTION

Most optical surfaces are influenced by mount induced distortions which arise from the effects of gravity, thermal stresses, and moments induced by overconstraints. The support designs and the mirror geometry are typically optimized to limit these effects. While any particular design can be modeled to high fidelity using finite element methods, the design choices must be driven by simpler models. Only after choosing the simple design can the detailed model be created. This paper is the first in a series that uses the parametric modeling capabilities in the finite element design programs to create design rules for distortions. This paper specifically treats the self-weighted deflection of a plane circular mirror and provides simple parametric relationships that allow the designer to efficiently estimate performance as a function of design choices.

For this paper we treat plane circular mirrors of varying thickness with common configurations of 3-point, 6-point, and continuous ring support. The performance of the mirror is quantified in terms of the P-V and rms self-weight deflection. In addition, the power (or low order shapes that can be corrected elsewhere) is quantified, as well as the residual surface deflection after power is removed. This is very important for optical applications, which may typically have quite different requirements for curvature and residuals because the curvature induces a focus change, which is accommodated elsewhere. These performance metrics are evaluated for the different configurations and material properties. The results are provided in the form of tables and parametric functions.

THEORETICAL BACKGROUND FOR THE PARAMETRIC MODEL

Based on thin plate bending theory[1] and the well-known scaling law by Nelson[2], we have the following equation to estimate the rms self-weight deflection (δ_{rms}) of any circular plates with multipoint supports:

$$\delta_{rms} = \gamma_N \frac{q}{D}\left(\frac{A}{N}\right)^2\left[1+2\left(\frac{h}{u}\right)^2\right],\quad D=\frac{Eh^3}{12(1-\nu^2)}$$

where γ_N is the support efficiency, q is the applied force per unit area, A is the plate area, N is the number of support points, h is the plate thickness, u is the effective length between support points, and D is the flexural rigidity. In the flexural rigidity, E and ν are the Young's modulus and Poisson's ratio, respectively.

While Nelson's equation provides acceptable rms deflection including shear effects for thin plates, it produces over 30% relative difference between the calculation and finite element analysis results when the plate has a small aspect ratio (i.e. large thickness relative to diameter).

Nelson also provided the relationship to estimate surface slopes, but it also has large difference. We developed the simple parametric relationship with γ and f for plane mirrors mounted by 3-point, 6-point and continuous ring support as shown below.

$$\frac{\delta_{P-V} \text{ or } \delta_{rms} \text{ or } \tilde{\delta}_{P-V} \text{ or } \tilde{\delta}_{rms}}{(\Delta_{P-V}d) \text{ or } (\Delta_{rms}d) \text{ or } (\tilde{\Delta}_{P-V}d) \text{ or } (\tilde{\Delta}_{rms}d)} = \gamma\frac{q}{D}A^2(1+f)$$

γ is similar to Nelson's support efficiency after accounting for N and f replaces the shear term in Nelson's equations. We introduce eight optical surface performance indicators. δ is the

deflection, Δ is the slope, and $\widetilde{\delta}$ (tilde) means the residual values after removing low order curvature. The slopes are obtained first in the forms of $\Delta \cdot d$ for a unit diameter and then calculated by dividing by the diameter of the mirror. Also four indicators has both P-V and rms values.

In the earlier study [3], significant amounts of FE calculations were performed for a 3-point supported circular flat mirror which has uniform thickness where Poisson's ratio, Young's modulus, aspect ratio (diameter/thickness), density, and diameter were all varied. The study implied that the 3D FE model acts differently than the traditional thin plate models. The aspect ratio and Poisson's ratio especially had additional deforming effects on the mirror surfaces. Therefore we expect that f is a function in terms of aspect ratio and Poisson's ratio. An f that contains basis functions and scalars of them is determined by parametric study using a FE design program in the following chapters.

FINITE ELEMENT MODEL

Using FE design programs, a series of FE models covering the reasonable ranges of aspect ratios (5~32) and Poisson's ratios (0.1~0.35) were generated. We took 11 samples and 6 samples, respectively. With three different support configurations, a total of 198 cases were simulated in the program. Young's modulus, density and diameter were fixed and normalized. The standard shear modulus $E/(2\cdot(1+\nu))$ was set in the model.

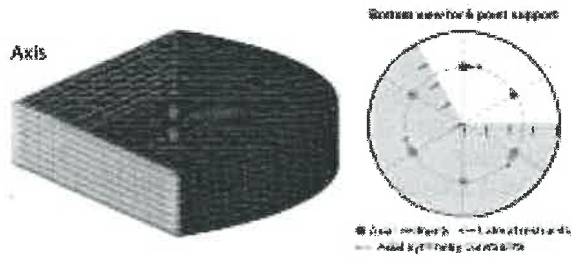

FIGURE 1. Finite element slice model of a solid plate (left). Axial symmetry constraints and restraints at support points were defined (right).

A one-third slice model instead of whole circular plate was utilized and axial symmetric constraints were defined on both side faces (see Fig. 1). The model consists of 8 layers for reasonable bending behavior. Likewise, there are 12 tetrahedral elements (equivalent to around 24 nodes) along the radius.

THE PARAMETRIC MODEL OF SELF-WEIGHTED DISTORTION

For the mathematical form of f, we define the normalized difference(f_i) as shown below.

$$f_i = \frac{\delta_i - (\gamma \frac{qA^2}{D})_i}{(\gamma \frac{qA^2}{D})_i},$$

δ_i can be replaced to $(\delta_{\text{rms}})_i, (\delta_{\text{PV}})_i, (\Delta_{\text{rms}}d)_i,$
$(\Delta_{\text{PV}}d)_i, (\widetilde{\delta}_{\text{rms}})_i, (\widetilde{\delta}_{\text{rms}})_i, (\widetilde{\Delta}_{\text{rms}}d)_i,$ and $(\widetilde{\Delta}_{\text{PV}}d)_i$

where i means a single FE simulation.

γ is varied by only support location when the mirror has the highest aspect ratio in our range (i.e. 32) and the Poisson's ratio was zero. In other words, when the normalized difference (f_i) is close to zero, then the coefficient γ as a function of support location is readily obtained from above equation.

A series of FE simulations of the particular mirror were performed to investigate the optimized positions of supports when δ_{rms} , $\widetilde{\delta}_{rms}$, $\Delta_{rms}\cdot d$ and $\widetilde{\Delta}_{rms}\cdot d$ were minimized, respectively. The optimized support positions as a percentage of the diameter and γ are summarized in table 2~4.

Finally, we developed the mathematical expression for f which contains three free parameters to fit to all sets of the normalized difference.

$$f = A\cdot\alpha^{-1}\cdot e^{-\nu} + B\cdot\alpha^{-1/2}\cdot\nu + C$$

where A , B and C are parameters we will control, α is aspect ratio and ν is Poisson's ratio.

The figure of merit (FOM) is defined as shown below. It will be minimized to obtain the values of the three parameters (i.e. A , B and C).

$$FOM = \sqrt{\frac{\sum_m \{\delta_i - \gamma \frac{qA^2}{D}(1 + A\cdot\alpha_i^{-1}\cdot e^{-\nu_i} + B\cdot\alpha_i^{-1/2}\cdot\nu_i + C)\}}{m}}$$

The parameters were obtained using the steepest decent (or gradient decent) method [4] with specific constraint. This well-known optimization method is suitable for non-linear functions space. The method may consume a lot of time to find a local minimum or may never converge to the minimum when function spaces have very different curvatures in different direction. However, our functions are smooth in the chosen aspect ratio and Poisson's ratio

ranges, so optimization runs are finished in a few minutes.

The specific constraint as shown below,

$$\frac{\left|\gamma \frac{qA^2}{D}(1+A\cdot\alpha_i^{-1}\cdot e^{-\nu_i}+B\cdot\alpha_i^{-1/2}\cdot\nu_i+C)-\delta_i\right|}{\delta_i}<10\%$$

controls performance of the parametric model. Even though the FOM is minimized, the algorithm perturbs the three parameters again to find global minimum if the relative difference is larger than 10%. Consequently, the parametric model, which includes the resulting A, B and C values, can calculate all optical performance variables presented above within 10% relative difference in our coverage due to the constraint.

RESULTS AND SAMPLE CALCULATIONS

All values of γ, A, B, and C are presented in the tables of appendix section.

With the tables, we can calculate any optical performances among eight indicators. For example, if one wants to see the rms slope of a ring support system, the mirror support should minimize the surface rms after removing optical power. We look up the table 4 for ring support and find the optimal support location is 57.5%. We take then the γ, A, B, and C are 356.8×10^{-5}, 1.09, -1.65, and -11.8×10^{-2}, respectively. Substituting mirror material properties and geometries into the parametric formula, we can get rms slope for a unit diameter. Finally, the rms slope is divided by the diameter of the mirror to get the actual rms slope.

As a demonstration, two different types of circular plane mirrors generally used in optical systems were dealt with to verify the design rule for optical distortion. Zerodur was used for a glass mirror. A 6061 aluminum alloy mirror was chosen for the second type. The aspect ratio was set to 5 and 32, respectively. The Poisson's ratio was 0.24 and 0.33 for each case. Substituting the three parameters in table 1~3 to the design rule, the expected eight distortions were calculated for the two cases. A normalized fit residual is defined to quantify the performance of the parametric model as the following

$$normalized\ fit\ residual=\frac{model-FEA}{FEA}\cdot100\,(\%)$$

Table 1 shows the normalized fit residuals of eight self-weight distortions calculated by the parametric model. Also they are compared to the rms surface deflection calculated by the Nelson's traditional formula. It is obvious that the parametric model gives self-weight distortions very close to finite element simulation result over all cases (normalized fit residual < 5%). The improvement over Nelson's model was especially significant when estimating the rms surface deflections for mirrors with small aspect ratio (i.e. Zerodur glass mirror).

TABLE 1. Normalized fit residual

Sample	Optical performance	3-point support	6-point support	ring support	Nelson's formula
Zerodur α = 5 ν = 0.24 *E* = 91 GPa ρ = 2530 kg/m^3 Optimized for δ_{rms}	δ_{P-V}	2.50%	0.57%	1.94%	-
	δ_{rms}	1.99%	1.60%	0.96%	34.0%
	$\tilde{\delta}_{P-V}$	2.50%	0.64%	2.41%	-
	$\tilde{\delta}_{rms}$	2.20%	0.00%	0.53%	-
	$\Delta_{P-V}\cdot d$	3.46%	0.10%	3.86%	-
	$\Delta_{rms}\cdot d$	1.67%	1.34%	1.21%	-
	$\tilde{\Delta}_{P-V}\cdot d$	1.38%	2.29%	0.72%	-
	$\tilde{\Delta}_{rms}\cdot d$	2.01%	1.12%	0.10%	-
6061 Aluminum α = 32 ν = 0.33 *E* = 69 GPa ρ = 2700 kg/m^3 Optimized for $\tilde{\delta}_{rms}$	δ_{P-V}	1.72%	2.71%	2.58%	-
	δ_{rms}	1.75%	2.64%	2.60%	2.68%
	$\tilde{\delta}_{P-V}$	3.38%	7.60%	4.30%	-
	$\tilde{\delta}_{rms}$	2.61%	1.07%	1.00%	-
	$\Delta_{P-V}\cdot d$	2.39%	4.78%	3.08%	-
	$\Delta_{rms}\cdot d$	2.25%	2.77%	2.64%	-
	$\tilde{\Delta}_{P-V}\cdot d$	2.50%	2.99%	2.01%	-
	$\tilde{\Delta}_{rms}\cdot d$	2.60%	3.36%	0.17%	-

CONCLUDING REMARKS

We used the parametric modeling capabilities in the finite element design programs to create design rules for distortions with a parametric relationship and tables of γ, A, B, and C. The optical performance indicators we calculated above were estimated efficiently within a 10% relative difference level without detailed FE design.

This parametric method will be applied in a follow up paper that will present parametric relations for induced deflections from lateral supports.

REFERENCES

[1] S. Timoshenko and S. Woinowsky-Krieger, Theory of Plates and Shells , McGraw-Hill, New York: 1959.

[2] J. E. Nelson, J. Lubliner, and T. S. Mast, Telescope Mirror Supports: Plate Deflection on Point Supports, Proc. Soc. Photo-Opt. Instrum. Eng. 1982; 332: 212.

[3] W. Park, D. Kim, J. Burge, and S. Kim, Parametric Model for Mirror Deflection with Axial Support, in Optical Fabrication and Testing, OSA Technical Digest. 2008; paper OWD7.

[4] Jan A. Snyman, Practical Mathematical Optimization: An Introduction to Basic Optimization Theory and Classical and New Gradient-Based Algorithms. Springer Publishing: 2005.

APPENDIX

TABLE 2. 3-point support

Optimal Target & Support	Optical performance	γ ($\times 10^5$)	A	B	C ($\times 10^2$)
δ_{rms} 66.3%	δ_{P-V}	246.7	0.50	4.10	-2.79
	δ_{rms}	58.58	1.27	2.93	-6.56
	$\tilde{\delta}_{P-V}$	240.2	0.51	4.21	-0.17
	$\tilde{\delta}_{rms}$	56.42	1.31	3.21	-5.12
	$\Delta_{P-V} \cdot d$	396.7	0.78	3.91	-6.39
	$\Delta_{rms} \cdot d$	264.3	1.20	2.70	-5.38
	$\tilde{\Delta}_{P-V} \cdot d$	391.2	1.31	3.55	-1.36
	$\tilde{\Delta}_{rms} \cdot d$	246.4	1.34	3.26	-4.84
$\tilde{\delta}_{rms}$ 40.9%	δ_{P-V}	632.5	1.16	-1.00	-10.6
	δ_{rms}	176.6	1.39	-1.17	-11.7
	$\tilde{\delta}_{P-V}$	110.2	1.86	1.86	-8.67
	$\tilde{\delta}_{rms}$	23.99	2.13	1.60	-9.31
	$\Delta_{P-V} \cdot d$	1087	1.32	-1.06	-11.8
	$\Delta_{rms} \cdot d$	778.1	1.20	-1.14	-12.5
	$\tilde{\Delta}_{P-V} \cdot d$	395.8	2.17	1.31	-11.7
	$\tilde{\Delta}_{rms} \cdot d$	182.6	2.74	1.00	-12.3
$\Delta_{rms} \cdot d$ 67.1%	δ_{P-V}	248.2	0.52	4.23	-0.19
	δ_{rms}	58.88	1.26	3.15	-5.85
	$\tilde{\delta}_{P-V}$	248.2	0.52	4.23	-0.19
	$\tilde{\delta}_{rms}$	58.00	1.29	3.24	-4.99
	$\Delta_{P-V} \cdot d$	397.8	1.15	4.24	-6.20
	$\Delta_{rms} \cdot d$	262.9	1.13	2.91	-3.78
	$\tilde{\Delta}_{P-V} \cdot d$	400.1	1.30	3.63	-1.29
	$\tilde{\Delta}_{rms} \cdot d$	253.6	1.31	3.30	-4.69
$\tilde{\Delta}_{rms} \cdot d$ 49.7%	δ_{P-V}	473.6	0.88	-0.81	-9.81
	δ_{rms}	128.2	1.29	-1.14	-11.1
	$\tilde{\delta}_{P-V}$	125.3	1.12	2.74	-4.73
	$\tilde{\delta}_{rms}$	29.18	1.68	2.56	-6.85
	$\Delta_{P-V} \cdot d$	847.7	1.01	-1.02	-9.52
	$\Delta_{rms} \cdot d$	578.7	1.28	-1.25	-11.5
	$\tilde{\Delta}_{P-V} \cdot d$	314.4	0.56	1.94	-5.03
	$\tilde{\Delta}_{rms} \cdot d$	154.9	2.23	1.99	-8.86

TABLE 3. 6-point support

δ_{rms} 68.5%	δ_{P-V}	36.59	6.12	3.57	-24.4
	δ_{rms}	8.380	6.04	4.37	-36.7
	$\tilde{\delta}_{P-V}$	37.12	3.83	1.18	-14.7
	$\tilde{\delta}_{rms}$	8.374	4.41	1.34	-18.1
	$\Delta_{P-V} \cdot d$	116.5	4.74	2.30	-27.9
	$\Delta_{rms} \cdot d$	67.17	3.68	1.14	-21.0
	$\tilde{\Delta}_{P-V} \cdot d$	114.2	2.16	1.91	-7.62
	$\tilde{\Delta}_{rms} \cdot d$	66.47	4.17	1.39	-17.2
$\tilde{\delta}_{rms}$ 57.2%	δ_{P-V}	257.5	0.77	-1.77	-10.5
	δ_{rms}	77.62	1.05	-1.71	-10.8
	$\tilde{\delta}_{P-V}$	16.50	7.46	2.35	-26.0
	$\tilde{\delta}_{rms}$	3.585	6.47	2.06	-26.1
	$\Delta_{P-V} \cdot d$	523.7	1.08	-1.53	-11.3
	$\Delta_{rms} \cdot d$	365.8	1.11	-1.62	-11.9
	$\tilde{\Delta}_{P-V} \cdot d$	105.3	1.62	1.02	-11.8
	$\tilde{\Delta}_{rms} \cdot d$	42.59	4.34	1.38	-15.1
$\Delta_{rms} \cdot d$ 69.2%	δ_{P-V}	45.93	4.99	3.56	-25.9
	δ_{rms}	9.855	5.82	4.53	-31.4
	$\tilde{\delta}_{P-V}$	38.10	3.72	1.13	-14.2
	$\tilde{\delta}_{rms}$	8.695	4.28	1.33	-17.8
	$\Delta_{P-V} \cdot d$	119.0	4.68	2.79	-19.4
	$\Delta_{rms} \cdot d$	63.27	4.47	1.84	-21.4
	$\tilde{\Delta}_{P-V} \cdot d$	128.1	1.68	1.35	-3.50
	$\tilde{\Delta}_{rms} \cdot d$	69.75	4.04	1.35	-16.8
$\tilde{\Delta}_{rms} \cdot d$ 59.9%	δ_{P-V}	196.5	0.65	-1.97	-10.6
	δ_{rms}	59.77	0.94	-1.86	-10.9
	$\tilde{\delta}_{P-V}$	22.06	5.94	1.71	-20.8
	$\tilde{\delta}_{rms}$	4.190	6.86	1.84	-26.1
	$\Delta_{P-V} \cdot d$	411.5	1.30	-1.55	-11.5
	$\Delta_{rms} \cdot d$	289.9	1.13	-1.76	-11.7
	$\tilde{\Delta}_{P-V} \cdot d$	78.40	4.87	1.32	-21.0
	$\tilde{\Delta}_{rms} \cdot d$	37.57	5.45	1.59	-17.4

TABLE 4. Continuous ring support

δ_{rms} 68.5%	δ_{P-V}	29.33	6.55	4.09	-29.2
	δ_{rms}	7.574	6.54	4.36	-39.0
	$\tilde{\delta}_{P-V}$	29.83	4.08	0.95	-16.5
	$\tilde{\delta}_{rms}$	7.568	4.12	1.02	-16.7
	$\Delta_{P-V} \cdot d$	91.94	5.12	2.53	-31.9
	$\Delta_{rms} \cdot d$	59.98	3.31	0.74	-21.2
	$\tilde{\Delta}_{P-V} \cdot d$	91.34	4.61	1.08	-19.2
	$\tilde{\Delta}_{rms} \cdot d$	59.18	3.88	1.06	-16.2
$\tilde{\delta}_{rms}$ 57.5%	δ_{P-V}	248.6	0.76	-1.84	-10.6
	δ_{rms}	75.62	1.03	-1.73	-10.7
	$\tilde{\delta}_{P-V}$	13.51	8.21	1.70	-33.5
	$\tilde{\delta}_{rms}$	2.950	7.44	1.58	-28.2
	$\Delta_{P-V} \cdot d$	510.5	1.18	-1.60	-11.8
	$\Delta_{rms} \cdot d$	356.8	1.09	-1.65	-11.8
	$\tilde{\Delta}_{P-V} \cdot d$	101.1	1.37	0.65	-6.2
	$\tilde{\Delta}_{rms} \cdot d$	36.12	4.59	1.22	-18.6
$\Delta_{rms} \cdot d$ 69.3%	δ_{P-V}	39.33	5.46	3.23	-27.1
	δ_{rms}	9.544	5.59	4.75	-31.9
	$\tilde{\delta}_{P-V}$	30.74	3.92	0.96	-16.1
	$\tilde{\delta}_{rms}$	7.907	3.94	1.00	-16.2
	$\Delta_{P-V} \cdot d$	99.66	5.01	2.64	-24.3
	$\Delta_{rms} \cdot d$	55.07	4.35	1.95	-23.2
	$\tilde{\Delta}_{P-V} \cdot d$	96.90	4.26	1.04	-18.2
	$\tilde{\Delta}_{rms} \cdot d$	62.94	3.69	1.02	-15.6
$\tilde{\Delta}_{rms} \cdot d$ 60.3%	δ_{P-V}	184.5	0.59	-2.12	-10.5
	δ_{rms}	57.05	0.91	-1.92	-10.7
	$\tilde{\delta}_{P-V}$	17.58	6.99	1.56	-26.9
	$\tilde{\delta}_{rms}$	3.629	7.33	1.69	-28.2
	$\Delta_{P-V} \cdot d$	401.2	1.24	-1.74	-11.8
	$\Delta_{rms} \cdot d$	277.6	1.09	-1.83	-11.5
	$\tilde{\Delta}_{P-V} \cdot d$	57.75	6.88	1.61	-26.7
	$\tilde{\Delta}_{rms} \cdot d$	30.06	6.19	1.53	-23.7

BENCH-TOP PRECISION GLASS MOLDING MACHINE

Peter Wachtel[1], Peiman Mosaddegh[2], Benn Gleason[1], J. David Musgraves[1], Kathleen Richardson[1], Brandon Dubas[3], and Howard Painter[3]
[1]Material Science & Engineering
Clemson University
Clemson, SC, U.S.A.
[2]Mechanical Engineering
Clemson University
Clemson, SC, U.S.A.
[3]Dyna Technologies, Inc.
Sanford, FL, U.S.A.

INTRODUCTION

Extensive growth of opto-electronic technologies has created a demand for high quality lenses and has driven the industry toward a less expensive process for manufacturing of aspheric glass lenses called Precision Glass Molding (PGM). Based on the current understanding of thermal and mechanical response of glass at elevated temperatures, there is a need for a new type of machine which will allow the user to control specific process parameters. This paper discusses the use of such a tool, in support of material optimization for the PGM process.

Moore Nanotechnology Systems LLC. [1] and Toshiba Machine CO. [2] are two suppliers for glass molding machines in the US and both have designed their machines to be compatible with medium to large volume production of optics. Scientific research has a need for a smaller, bench-top sized version of these machines with flexibility in machine design optical component geometries and process parameters. The GP-5000HT precision glass molding machine from Dyna Technologies Incorporated (DTI) [3] was designed for this purpose. The machine has functionality comparable to commercially available products and also the flexibility for laboratory testing, research and prototyping of lens design.

The main objective of this study is to define the machine's functionality and measure the accuracy of the new design's control over thickness of pressed or molded lenses, an attribute (commonly described at center thickness, CT) which is critical in lens manufacturing. To this end, repeatability tests were conducted using two polished planar Tungsten Carbide (WC) molds and Ohara L-BAL35 as the glass sample.

MACHINE FUNCTIONALITY

The GP-5000HT has a frame to house the heating system, mechanical system, and instrumentation. The frame is composed of two rectangular plates and four posts. The four posts close the structural loop of the machine by passing through the corners of the lower plate and connecting to the corners of the upper plate. The components of the frame and other mechanical parts of the machine can be found in Figure 1. Of all the machine systems described in this study, the only system attached to the frame of the machine is the mechanical system.

Mechanical Systems

The mechanical system is composed of an electric actuator and two pneumatic cylinders attached to the upper frame plate. The pneumatic cylinders are used to raise and lower the upper molding chamber. The upper portion of the molding chamber is connected to the ends of the pneumatic cylinders and the lower portion attached to the lower frame plate. This allows the lower portion to slide in and out from under the upper molding chamber. This sliding movement allows the user to easily insert or remove a molding sample. When the lower molding chamber is under the upper molding chamber, and when the chamber is closed the electric actuator can be operated.

The electric actuator provides the movement along the axis of the molds and the force needed for molding the glass. The actuator is attached to the upper frame plate and is connected in series with the load cell, post, and upper mold, respectively. The lower mold

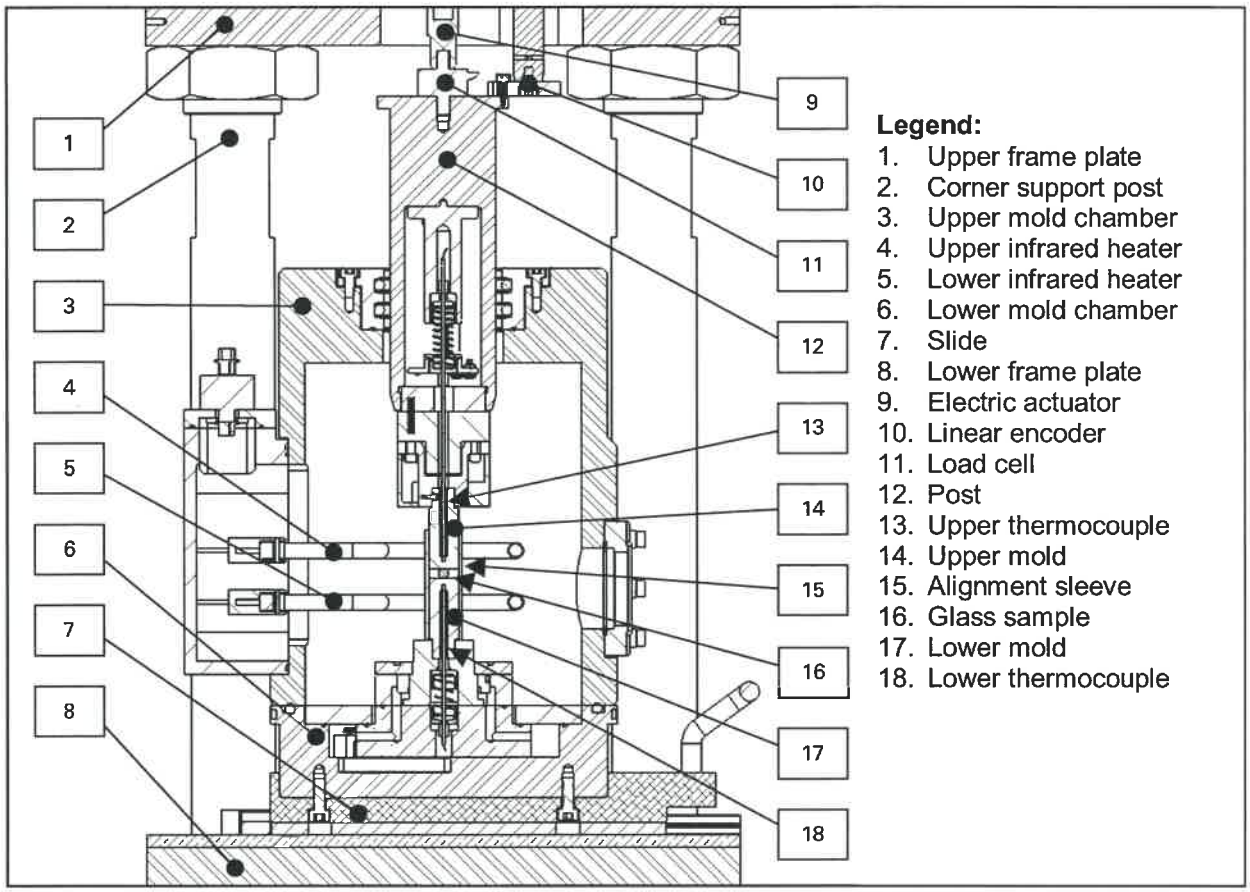

FIGURE 1. Above is a cross-section of the GP-5000HT revealing its critical components. The pneumatic air cylinders that lift the upper mold chamber along with the control boxes, which contain the electrical equipment for operating the GP-5000HT, have been excluded.

remains stationary throughout the molding process, and it is connected to the lower molding chamber. A sleeve around the lower mold is utilized to align the upper and lower molds which are made of WC. The WC is used because of its robust mechanical and thermal properties at higher temperatures[5].

Heating System

The heating system uses two omega-shaped infrared (IR) lamps. These allow the press to achieve temperatures up to 800 °C. The IR heaters are attached to the upper bell housing and are positioned so that each heats the molding sleeve equally. Power to the heaters is controlled by a proportional, integral and derivative (PID) heater controller. Heat from the sleeve is transferred to the molds through conduction. The glass sample is heated by conduction from the molds. The heating system also has the capability to heat and cool at specific rates within the limitations of the maximum heating rate and the maximum cooling rate. Inert gas, typically nitrogen, is used for cooling cycles.

Instrumentation

The instruments used for assessing the press' performance are composed of sensors and other measurement devices. The sensors act as safety features, preventing any damage to the heating system, mechanical system, or the user of the press.

The measurement devices include the thermocouples, pressure transducer, load cell, and linear encoder used to govern the molding process. There is a hole aligned axially with the molds that are used for inserting a thermocouple to measure temperature, located up to 1/4" away from the molding surfaces. The readings obtained from these thermocouples are used to represent the temperature of the glass sample. The pressure transducer measures the static pressure of one of the pneumatic lines coming into the molding chamber. The load cell is

aligned axially with the molds and it is connected in series to the actuator to instantaneously measure the force applied to the glass sample during molding.

Molding Cycle

The molding cycle is comprised of several stages: purging, heating, soaking, molding and cooling. The molding process is driven by the measurement devices. Before a cycle starts, the user programs the setpoints for a molding program. The setpoints are the triggers that cause the press to move to the next stage in the cycle. The user has two options for running a pressing cycle: Auto Mode runs through a full cycle when the start button is pressed; Manual Mode gives the user control over when the different stages begin.

The user first inserts a glass sample onto the bottom mold. The press is then evacuated using a vacuum pump and then backfilled with inert gas three times in order to prevent oxidation of the molds and other components in the molding chamber. Once purged, the actuator moves into the sleeve and makes contact with the glass sample with a specified force. The heating stage begins, and the heaters heat at the user or controller defined ramp rate. After reaching temperature above the glass transition temperature of the sample, the press begins to soak for a specific amount of time. The soak allows the glass sample to equilibrate at a uniform temperature to be sure the glass has a uniform viscosity. The actuator then begins to press the glass into the shape of the molds. Once the specified position has been reached, cooling gas actively flows into the chamber. The press can be cooled at the maximum cooling rate or using up to three different cooling stages with control over the cooling rate and applied force. This cooling ramp control gives more control over the relaxation behavior of the glass. When the press reaches a safe user defined temperature, the mold chamber is raised and the molded glass sample is removed.

REPEATABILITY RESULTS

The goal of the repeatability measurements is to determine the ability of the press to produce similar results on a day to day basis, and also on a per cycle basis. Two data sets were collected to analyze the performance of the press. The target function for both of the data sets is thickness of the sample after it has been pressed.

Methodology

The samples used during the pressing cycles are square-cut plane parallel plate (PPP) windows of L-BAL35 glass. The glass used in the current study was L-BAL35 from Ohara, as there is sufficient published data on its optical and thermal properties. The glass's physical properties needed for PGM such as viscosity, glass transition temperature, viscoelastic response, and structural relaxation parameters are well known for L-BAL35 [4]. Dimensionally each PPP window square measures approximately 5 mm on a side, with a thickness of approximately 2 mm. While in AUTO mode, the press heats the sample to 587 °C and molds the sample with a force of 100 lbs. The sample is cooled in two stages, with a different rates of cooling.

The first data set includes only the data from the first cycle of the day. This data set is representative of the day to day variations. The second set of tests include data from all cycles, including the first-cycle-of-the-day data presented in the first data set. The second data set mimics a typical production cycle used in industry. Three sets of pressing cycles were taken on different days, with each day consisting of 10 consecutive cycles. The sample thickness was measured in 10 places to determine a mean value and standard deviation.

In the 10 consecutive cycles there are two distinct phases in the press' repeatability. The first phase, or the 'warm up' phase, includes the first 2-4 runs, where the press experiences thermal expansion between pressing cycles. The second phase, referred to as the 'steady state', includes all cycles after the warm up phase. The boundary line between the two phases is somewhat arbitrary, but is distinguished by a significant drop in the standard deviation of the thickness of the sample.

Results

The individual measurements of each sample show that they have a highly uniform thickness, varying only a few microns with a maximum standard deviation of 2 microns as listed in Table 1.

The change in thickness from one sample to the next can be attributed to the small scale thermal expansion and thermal conductivity of the system that continues even after the pressing

TABLE 1: lists the standard deviation and the total range of the thickness of an individual sample, the first molding cycle of the day, and the steady state.

	Individual Samples	First Cycle	Steady State
Standard Deviation (μm)	2	113	9
Total Range (μm)	6	246	19

cycle has finished. Table 1 also shows the total range and the standard deviation of the first cycle and of the steady state. There is a big difference in repeatability capabilities from the first cycle to the steady state; there is an order of magnitude drop of the standard deviation and the total range from the first cycle to the steady state cycles.

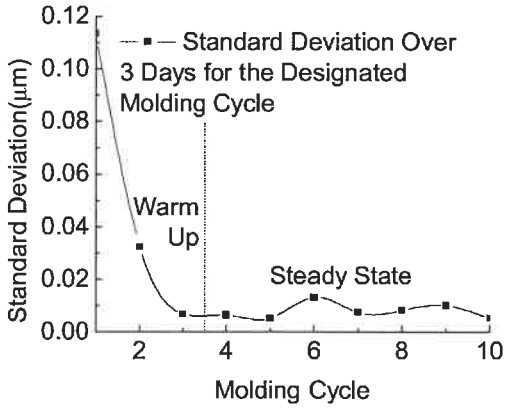

FIGURE 2: The standard deviations of the number cycle over multiple days in 10 consecutive pressing cycles.

Within the whole data set, the effect of thermal expansion on the target function can be analyzed. These results show several machine tool attributes that would be important to a manufacturer: the uniformity of the pressed part thicknesses, and how quickly (how many pressing cycles) before this uniformity can be obtained. As the press transitions from room temperature through the warm up phase, the average thickness of the resulting samples continually changes. However, once the press has reached its "steady state phase", the thicknesses remain fairly constant. Comparing the standard deviation of each numbered cycle, from 1 to 10, over 3 consecutive days of cycles, a definite trend is evident, and is shown in Figure 2. As the number of cycles increases, the standard deviation of the sample thickness decreases.

CONCLUSIONS

A bench-top precision glass molding machine is a valuable tool for research in the demanding and growing opto-electronic industry and scientific field. It is a tool that can help bridge the difficult and important gap between scientific research and industrial manufacturing. The GP-5000HT is a glass molding machine with functionality similar to a full-production molding machine but is also versatile enough to be used for scientific research purposes.

Preliminary repeatability results utilizing pressed part thickness of plano-plano samples has shown an increase in thickness consistency from day to day as the number of molding cycles increases. There is still a large uncertainty to the first cycle results and that there is a definite "warm up" period, though industrial practioners routinely run dry cycles over some defined period. The tolerances of the final thickness become much tighter after the system reaches thermal equilibrium, typically after 3 molding cycles. During the steady state cycles done over multiple days, the total range of thicknesses is 19 μm with a standard deviation of 9 μm.

Routine future tests (daily, weekly, etc.) with target boundaries and final piece tolerances can also be developed from this set to ensure the press is performing within acceptable limits of operation.

REFERENCES

[1] Nanotechsys.com [Internet]. New Hampshire: Moore Nanotechnologies LLC.; [cited 2010 Jul 20]. Available from: http://www.nanotechsys.com/machines/nanotech-gpm-glass-press-molding/.

[2] Toshiba-machine.co.jp [Internet]. Japan: Toshiba Machine Co. LTD.;[cited 2010 Jul 20]. Available from: http://www.toshiba-machine.co.jp/english/product/high/contents/molding.html.

[3] Dti-fla.com [Internet]. Florida: Dyna Technologies, Inc.; [cited 2010 Jan 15]. Available from: http://dti-fla.com/glassmolding.html.

[4] Gaylord S. Thermal and Structural Properties of Candidate Moldable Glass Types [dissertation]. Clemson (MI): Clemson University; 2008.

[5] Mosaddegh P. Friction Measurement in Precision Glass Molding [dissertation]. Clemson (MI): Clemson University; 2010.

INTERFEROMETRIC MEASUREMENT OF THE LOW VALUE CTE OF A BALL BAR

Jimmie A. Miller[1], Juan J Aguilar[2], Mohamed Saad[1], and Greg W. Caskey[1]
[1]Center for Precision Metrology
William States Lee College of Engineering
University of North Carolina at Charlotte
Charlotte, NC USA
[2]Dpto. Ingeniería de Diseño y Fabricación
Instituto de Investigación en Ingeniería de Aragón
Universidad de Zaragoza
Zaragoza, Spain

INTRODUCTION

Fixed length ball bar[1]-[3] reference standards have traditionally been used for performance verification of rectilinear based coordinate measuring machines (CMMs). These CMMs are often operated in a controlled environment which limits the change in length of the ball bars to acceptable levels. Recently these ball bars have also been standardized for use in the performance evaluation of articulated arm coordinate measuring machines (AACMM)[4][5] for which the working environment is typically not controlled. The AACMMs are commonly made out of thermally stable materials having low coefficient of thermal expansion (CTE) values or are "thermally compensated." Since the working environment for the AACMM is thermally changing it is desirable to calibrate the AACMMs with ball bars that have insignificant CTE [6]. Additionally, rectilinear CMM's used in controlled environments have also been tested with low CTE ball bars [7]. In order to properly to correct or estimate the contribution of the ball bar's CTE to the performance evaluation uncertainty it is necessary to know the ball bar's CTE. The purpose of this paper is to describe a method used for determining the CTE of these ball bars in the sub-parts-per-million per °C range.

MEASUREMENT SETUP

Ball bars are composed of two balls attached to each other via a connecting bar. In general usage the ball center to ball center distance is measured to verify CMM performance. Because low CTE ball bars often have differing materials for the connecting bar and balls the effective CTE of the ball bar must be measured in a way that mimics the CMM measurement. The particular ball bar in this paper consists of two 440 SS 1.5" balls connected magnetically to a carbon fiber composite bar. The balls were modified using electro-discharge machining (EDM) to produce a step near the center of each ball to use as reference surfaces to mount the components of an interferometer. The modified balls attached to the bar and interferometer components are shown in *FIGURE 1*.

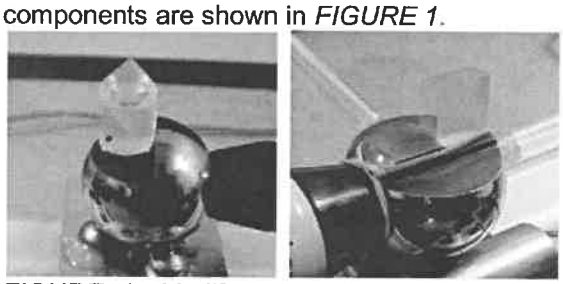

FIGURE 1. Modified balls and interferometric components.

The plane mirror interferometer schematic is shown in *FIGURE 2*. The double-reflection configuration doubles the effective path change and allows for slight non perpendicularity of the mirror.

The ball bar was placed in a thermal chamber and the temperature varied from 20 °C to 25 °C and back to 20 °C while measuring the interferometric displacement. The ball surface temperatures along with several points in the air between the balls were recorded along with the air humidity and pressure.

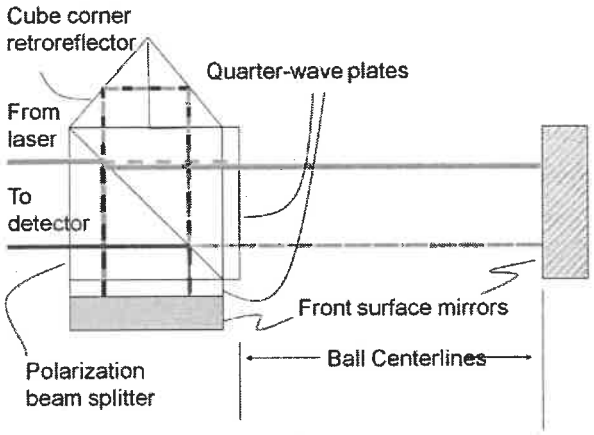

FIGURE 2. Internally-balanced double-reflection plane mirror interferometer schematic.

MATHEMATICAL MODEL

The interferometer measurement data, I_M, has components:

E_{BB}, expansion of the ball bar

E_{IW}, error due to the changing wavelength of the laser light due to the temperature, pressure, and humidity changes in the air path and

E_O, optics expansion due to temperature where

$$I_M = E_{BB} - E_{IW} + E_O$$

or

$$E_{BB} = I_M + E_{IW} - E_O$$

The detailed components of these are:

$$E_{IW} = 2L_{BB}(k_T \Delta T_{\text{Air}} - k_P \Delta P_{\text{Air}} + k_V \Delta V_{\text{Air}})$$

$$E_{BB} = 2L_{BB}\alpha_{BB}\Delta T_{\text{BB}} = \text{E}_{\text{Bar}} + \text{E}_{\text{Ball}}$$
$$= 2L_{Bar}\alpha_{Bar}\Delta T_{\text{Bar}} + 2L_{Ball}\alpha_{Ball}\Delta T_{\text{Ball}}$$

$$E_O = S_O \Delta T_{\text{O}}$$

The parameters are:

L_{BB}, 597 mm, nominal length of the ballbar from ball centers

L_{Ball}, 35 mm, length of the ball bar due to the ball material which is shorter than the diameter due to the way the bar connects the ball.

L_{Bar}, 562 mm, length of the connecting bar

k_T, 0.93 ppm/°C, air temperature coefficient

k_P, 0.36 ppm/mmHg, air pressure coefficient

k_V, 0.05 ppm/mmHg, air cooeficient for the partial pressure of water (related to humidity)

ΔT_{Air}, change in air temperature

ΔP_{Air}, change in air pressure

ΔV_{Air}, change in partial pressure of water in air

ΔT_{BB}, change in the temperature of ball bar

ΔT_{Bar}, change in temperature of connecting bar

ΔT_{Ball}, change in temperature of the balls

S_O, optics expansion sensitivity to temperature

ΔT_O, change in temperature of the optics

α_{BB}, CTE of the ballbar

α_{Bar}, CTE of the connecting bar

α_{Ball}, CTE of the balls

From these equations the effective CTE of the ballbar is determined by

$$\alpha_{BB} = \frac{E_{BB}}{2L_{BB}\Delta T_{\text{BB}}} = \frac{I_M + E_{IW} - E_O}{2L_{BB}\Delta T_{\text{BB}}}$$

MEASUREMENT RESULTS

The interferometric data plot is shown in *FIGURE 3*. The effective path length is about 1.2 meters and was corrected for the influence of air temperature, humidity (minimal effect), and pressure which is also shown in *FIGURE 3* along with the individual corrections for temperature and pressure.

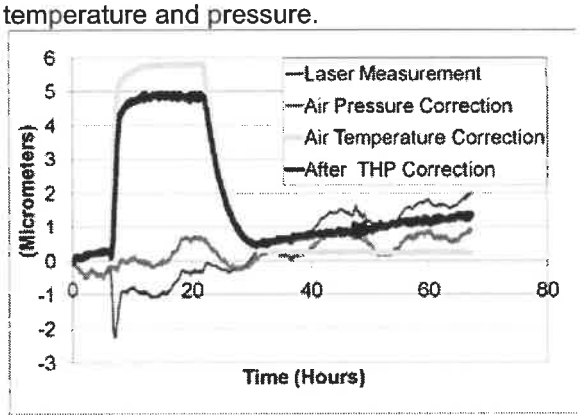

FIGURE 3. Interferometric data as measured and corrected for temperature humidity and pressure.

A very obvious feature of the corrected data is a linear slope equivalent to about 15 nm/hr. Attempts to pinpoint the source of this drift were unsuccessful. Given the repeatability of this drift rate over long periods of time it was subtracted from the data to obtain the CTE. The resultant CTE over the range where the temperature was stable was calculated as the calculated change in expansion of the balls divided by the average temperature of the balls. The resultant value was 0.7 µm/m/°C with a variation of 0.03 µm/m/°C. For the calculations ΔT_{BB} was taken as the average temperature of the balls because the CTE of the balls is more than an order of magnitude greater than the bar.

Optics Expansion Measurement

The optics' thermal sensitivity was tested by moving the opposing ball mirror to make a single interferometric unit as shown in *FIGURE 4*. The setup was held together by a elastic band. The temperature was stepped up by 5°C for 24 hours

and back down while measuring the output of the interferometer system. The results are plotted in *FIGURE 4* . The optics responded with a time constant on the order of 1-2 days. S_O was not calculated due to the long time required for equilibrium to be reached. From the graph E_O was estimated as 0.1 µm for a 5°C step.

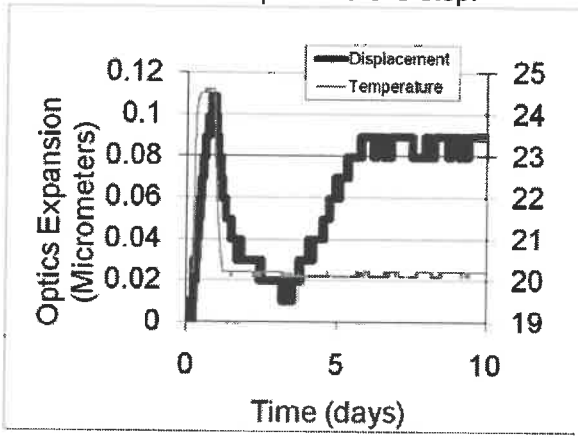

FIGURE 4. Optics expansion test showing data and setup

Ball Expansion Measurement

In order to obtain the CTE of the connecting bar the ball CTE was first determined. To accomplish this a ball was cut using EDM to produce parallel faces removing 2.5 mm from each side. Additionally, a rectangular hole was made in the center so that the laser could pass through the ball. The optics were them placed on either face and held in place by a rubber band as shown in *FIGURE 5*. The temperature was varied from 20 to 25 and back to 20°C The data as taken and corrected are shown in *FIGURE 6* and the calculated CTE of the ball is shown in *FIGURE 7*. Comparing *FIGURE 3* to *FIGURE 6* shows that the majority of the ball bar expansion is due to the balls and not to the connecting bar between them.

Bar CTE Calculation

The CTE of the connecting bar was calculated using the equation

$$\alpha_{Bar} = \frac{L_{BB}\alpha_{BB}\Delta T_{\mathrm{BB}} - L_{Ball}\alpha_{Ball}\Delta T_{\mathrm{Ball}}}{L_{Bar}\Delta T_{\mathrm{Bar}}}$$

where L_{BB}=597mm; L_{Bar}=562 mm; L_{Ball}=35.2mm; α_{BB}=0.7 µm/m/°C α_{Ball}=11.2 µm/m/°C ΔT_{BB}=5.2 °C ΔT_{Ball}=5.2 and ΔT_{Bar}=4.9°C.

This yielded an effective CTE of the bar α_{Bar}=0.05 µm/m/°C.

FIGURE 5. Ball CTE measurement setup.

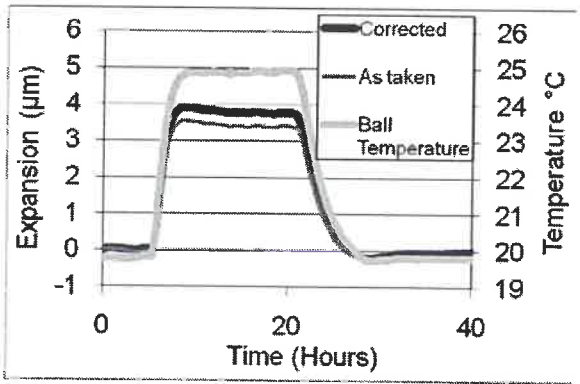

FIGURE 6. Expansion of ball as taken and after corrections for temperature, humidity and pressure .

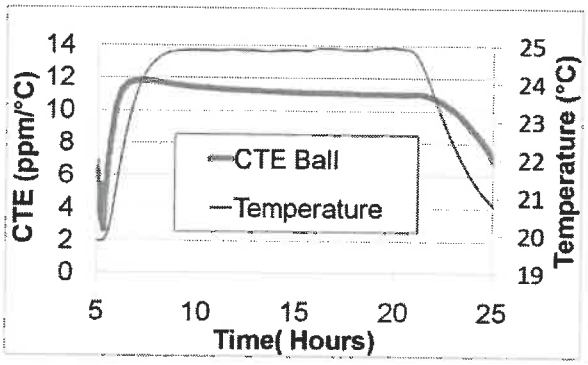

FIGURE 7. Ball temperature and calculated CTE.

UNCERTAINTY ESTIMATIONS

TABLE 1 summarizes the estimations of the uncertainty influences on calculated values for each numbered (N) factor. A square root of the sum of the squares (Σ) is shown (not including the terms in italics which are included via other contributions).

TABLE 1. Uncertainty contribution estimations. All unspecified values are µm/m/°C.

N	*Factor*	U_N	$U\alpha_{BB}$	$U\alpha_{Ball}$	$U\alpha_{Bar}$
1	L_{BB}	0.5mm	0.0006		0.001
2	L_{Bar}	0.5mm	*0.0006*		0.001
3	L_{Ball}	0.5mm	*0.001*	0.16	0.01
4	ΔT_{BB}	0.1°C	0.014		0.015
5	ΔT_{Ball}	0.1°C	*0.013*	0.23	0.014
6	ΔT_{Bar}	0.2°C	*0.004*		0.004
7	E_O	100nm	*0.027*	*0.28*	*0.02*
8	I_M	200nm	0.04	0.57	0.07
9	E_{IW}	100nm	*0.02*	*0.28*	*0.02*
10	α_{BBC}		0.03		0.03
11	α_{BallC}			0.3	0.018
Σ			**0.05**	**0.7**	**0.08**

α_{BBC} and α_{BallC} are the variations in the calculations using the measured data.

BALL BAR LENGTH CHANGES DUE TO PRESSURE

The ball bar was maintained at near 20 °C for over 80 hours while recording the interferometric measurement changes. The temperature was stable at six different locations to within 0.05°C. During this period the pressure changed by about 10 mmHg (0.4" Hg) as shown in *Figure 8*.

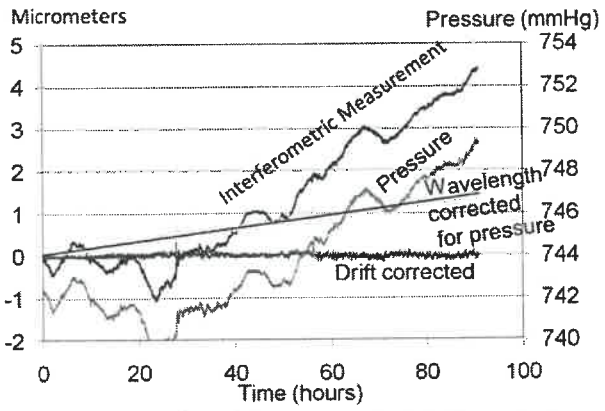

Figure 8. Extended-time constant-temperature measurements.

The measurement signal tracked the changes in pressure. After the wavelength correction was made for the pressure the data was very nearly a straight line indicating that pressure variations on the order of 0.4 inches of mercury do not visibly affect the length of the ball bar. Note that the 15 nm/hr drift is still apparent in the data.

REFERENCES

[1] Bryan J.B., A simple method for testing measuring machines and machine tools Part1: principles and applications, Precision Engineering 1982; 4(2); 61-9 http://dx.doi.org/10.1016/0141-6359(82)90018-6

[2] Bryan J.B., A simple method for testing measuring machines and machine tools, Part2: Construction details, Precision Engineering 1982; 4(3); 125-38 http://dx.doi.org/10.1016/0141-6359(82)90075-7

[3] Phillips S.D., Borchardt B., Doiron T., and Henry J, Properties of free-standing ball bar systems, Precision Engineering 1993; 15(1); 16-24 http://dx.doi.org/10.1016/0141-6359(93)90274-E

[4] B89.4.22 - 2004 Methods for Performance Evaluation of Articulated Arm Coordinate Measuring Machines (CMM) www.asme.org

[5] Jorge Santolaria, Juan-Jose Aguilar, Jose-Antonio Yague, Jorge Pastor, Kinematic parameter estimation technique for calibration and repeatability improvement of articulated arm coordinate measuring machines, Precision Engineering, 2008: 32(4); 251-8, http://dx.doi.org/10.1016/j.precisioneng.2007.09.002

[6] Santolaria, J., Yagüe J.A,. Jiménez, R., Aguilar J.J., Calibration-based thermal error model for articulated arm coordinate measuring machines, Precision Engineering 2009; 33(4); 476-85 http://dx.doi.org/10.1016/j.precisioneng.2009.01.002

[7] P.S. Lingard, M.E. Purss, C.M. Sona, E.G. Thwaite, G.H. Mariasson, Temperature perturbation effects in a high precision CMM, Precision Engineering 1991; 13(1); 41-51 http://dx.doi.org/10.1016/0141-6359(91)90220-D

DOUBLE SIDED INTERFEROMETER, PROFILING MEASUREMENT SIMULTANEOUSLY YIELDS THICKNESS AND FORM

Richard M. Seugling, Michael J. Wilson, Pete J. Davis, Shawn C. Peterson and James Hamilton
Lawrence Livermore National Laboratory
Livermore, CA 94551

INTRODUCTION

Thickness measurements have been a basis for metrology since its inception and represent a fundamental technique for calibration of reference artifacts used world-wide, such as gage blocks. However, as materials and their applications have become more exotic, traditional contact based measurement techniques have become less applicable. In addition, quantification of from deviation between two surfaces has become more critical and usually requires a large point density to describe in detail. Optical probing or imaging techniques offer an alternative where there is little or no interaction with the part and can provide fast, accurate data for a large number of materials, but can be limited by reflectivity, acceptance angle seen by sensor and optical depth. A modular optical system adaptable to commercially available white light profilometers and optical coordinate measuring machines (CMMs) has been developed to measure absolute thickness and form.

For the purposes of this work "thickness" is defined as the distance between two points along a vector, such that the vector is normal to at least one surface of the sample under investigation.

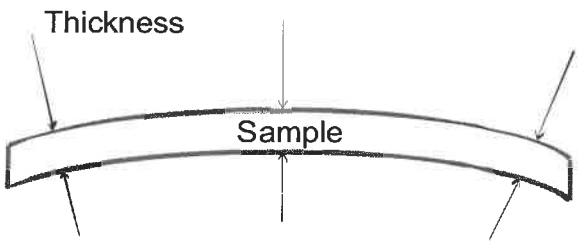

FIGURE 1. Absolute thickness of a foil or stacked sample is a combined measurement relating the upper and lower surface topography.

Samples of interest are nominally 2 mm - 8 mm in diameter and vary in thickness from 10 μm to 5 mm. Materials of interest include transparent and opaque solids such as polished metals and ceramics, but may also include low density metal and ceramic foams often combined as a laminate stack as illustrated in Figure 2. Surface finish requirements span from specular to having several micrometers of roughness. In addition, the quantification of engineered features formed into the surface, such as sine waves, have to be characterized. These features can represent upwards of 5.0% of the overall thickness of the free standing sample. Characterization of engineered surfaces and their relationship to the complete assembly is important to the overall understanding of these materials during dynamic deformation. The relationship between finish, form and thickness has to be quantified to 0.5% to 1.0% level.

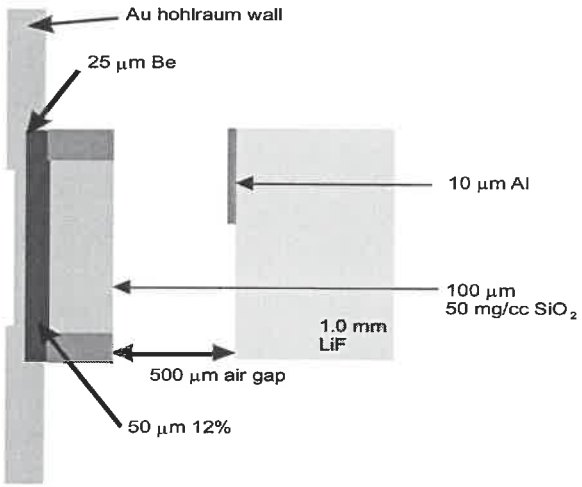

FIGURE 2. Typical assembly consisting of five stacked subassemblies. This assembly includes low density foam, metal and plastic foils and a partially coated tamper material with an ideal assembled thickness of 1.675 mm.

Because of the wide array of materials being studied at Lawrence Livermore National Laboratory (LLNL), no one measurement technique can be utilized exclusively. National

Laboratories [1,2], academia and industry [3] have spent a lot of effort trying to minimize measurement uncertainty utilizing a number of different techniques. For the most part these include some type of opposing probe technique where either a contact or optical probe pair oriented in opposing directions scan or image a sample and relate the two surfaces to a calibrated reference. Other measurement options include transmission based techniques [4] where some form of radiation is used in conjunction with material properties to determine thickness. The goal of the work is to adapt commercially available optical measurement systems to allow absolute thickness and form measurements.

DESIGN

The optical system was designed to be integrated into commercially available optical profilometer and/or CMM to optimize its value without limiting the instruments capability. The designed optical system consists of coated plane mirrors oriented such that the optical path lengths as seen by the optical probe are equal for both sides of the sample being investigated as shown in Figure 3. The turning mirrors are flat to 1/20th wave and have better than 1 nm S_a surface roughness.

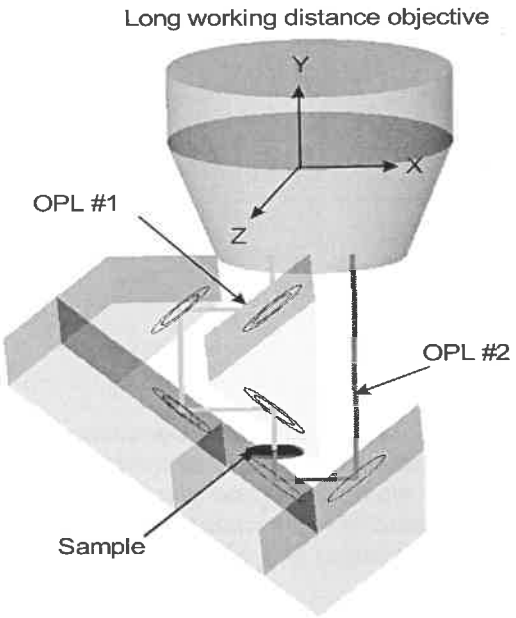

FIGURE 3. Modular optical system design showing top and bottom optical path length and long working distance objective.

In addition to matching the optical path lengths, the parallelism between the two paths is an important part of the measurement as it will introduce an apparent wedge into measurement data. In theory this error can be removed because it is stable and repeatable, but in practice the combined angular errors limit operation depending on the instruments optical probes numerical aperture and/or acceptance angle. It can also introduce lateral shifting between the front and rear surfaces causing a cosine error in absolute thickness.

To quantify the error attributed to the manufacture of the modular optical system a set of homogenous transformation matrices (HTMs) [5] were derived using small angle approximations. In this case, the reference coordinate system is defined by the objective of the optical probe. Each mirror is represented by the combination of three rotations and one translation matrix in the form of,

$$\mathbf{T_m} = \begin{bmatrix} \mathbf{R_m} & \mathbf{V_m} \\ 0 & 1 \end{bmatrix}. \quad (1)$$

Assuming small angles and removing second order terms the rotation matrix ($\mathbf{R_m}$) for each mirror can be expressed as,

$$\mathbf{R_M} = \begin{bmatrix} C(\alpha_m) - \varepsilon_z S(\alpha_m) & \varepsilon_z C(\alpha_m) - S(\alpha_m) & \varepsilon_y \\ S(\alpha_m) + \varepsilon_z C(\alpha_m) & C(\alpha_m) - \varepsilon_z S(\alpha_m) & -\varepsilon_x \\ \varepsilon_x S(\alpha_m) - \varepsilon_y C(\alpha_m) & \varepsilon_y S(\alpha_m) + \varepsilon_x C(\alpha_m) & 1 \end{bmatrix}, \quad (2)$$

where α_m is the reflected beam angle (2 times the angle of incidence on the mirror), ε_x, ε_y and ε_z are the angular alignment errors about the x-, y- and z-axes respectively.
The vector $\mathbf{V_m}$ is the translation vector between each mirror coordinate system given by,

$$\mathbf{V_m} = \begin{Bmatrix} a_m \\ b_m \\ c_m \end{Bmatrix}. \quad (3)$$

Transforming the optical paths back to the reference coordinate system is given by,

$$\{\mathrm{I}\}_{\mathrm{ref}}^{\mathrm{OPL1}} = {}^{\mathrm{ref}}\mathbf{T}_1 \; {}^{1}\mathbf{T}_2 \; {}^{2}\mathbf{T}_3 \; {}^{3}\mathbf{T}_4 \; \{\mathrm{I}\}, \quad (4)$$

$$\{\mathrm{I}\}_{\mathrm{ref}}^{\mathrm{OPL2}} = {}^{\mathrm{ref}}\mathbf{T}_5 \; {}^{5}\mathbf{T}_6 \; \{\mathrm{I}\}, \quad (5)$$

where {I} represents the vector normal to the image plane from each reflective surface. By transforming the image plane location back through the front (OPL #1) and rear optical paths (OPL #2) and comparing to the ideal path, the errors between paths can be represented. The difference between equations (4) and (5) show that the angular errors multiplied by the offset distances of each path length when summed individually relative to the sample image plane must be minimized to maintain parallelism. The detailed analysis is left as an exercise for the reader. Based on the analysis described above, a design specification of 70 μrad about the x- and z-axes was used to define the parallelism between the upper and lower beam paths.

RESULTS

To calibrate and determine performance of the apparatus a 100 μm gage block with a thickness uncertainty of ± 0.25 μm was used a reference artifact. The front and rear surface of the sample were scanned using the double sided optical system highlighted above (see Figure 3).

Two commercial based systems were used to evaluate thickness. The first was a Nikon NEXIV VMR 3020 optical measuring machine. The front and rear surfaces of the gage were scanned in two orthogonal directions using a laser confocal probe. The manufacturer stated uncertainty in the z-direction is 1.5 μm for the scan lengths used in this experiment. Results of a sample measurement are shown in Figure 4. In this case we measured an average thickness of 103.4 μm with a standard deviation of 2.6 μm.

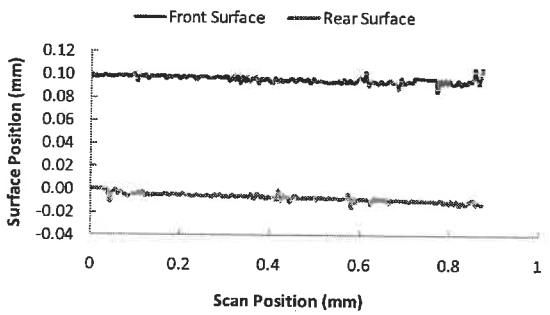

FIGURE 4. Thickness measurement of 100 μm gage block using a Nikon NEXIV VMR 3020 optical measuring machine.

The second measurement system evaluated was a Veeco NT8000 white light surface profilometer. Analogous to the Nikon instrument, both the front and rear surface of the gage were scanned using the double-sided optical system. Manufacturer stated uncertainty for long-range scanning in the z-direction for the optical profilometer is 0.05% of the scan range (50 nm). 2D images representing the front and rear surfaces of the gage are shown in Figure 5a. Figure 5b shows a line trace across both the front and rear surface of the gage block. The calculated average thickness was found to be 104.5 μm a standard deviation of 0.5 μm.

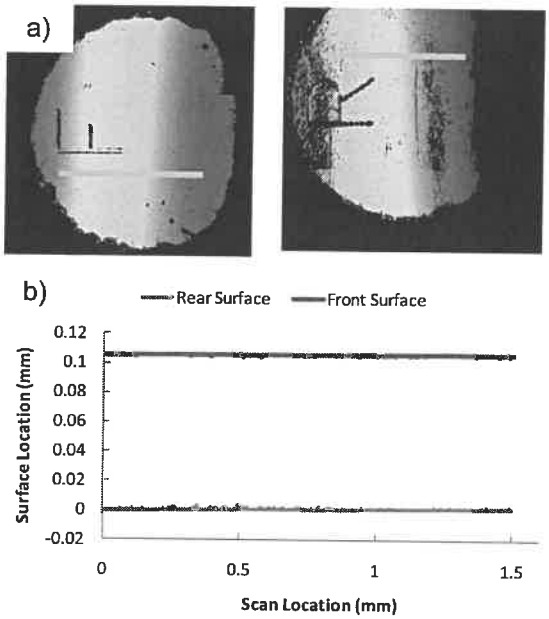

FIGURE 5. a) Profiles of front and rear surfaces of the gage block as measure by the profilometer. b) Line trace data from the optical profile showing the thickness of the gage block at 104.5 μm.

There are two predominant sources of uncertainty with the white-light profilometer and optical CMM. The first is the parallelism of the optical paths, which can be calibrated and removed in software as discussed earlier. Optical path angular deviation of the prototype system was measured to be ~110 μrad and accounts for the slope variation between front and rear surface measurements.

The second is the location of the "zero" plane where OPL #1 and OPL #2 are equal. Because the location of the part mid-plane is independent

of the "zero" plane location, the absolute thickness can appear to be thick or thin depending on where the sample lies within the optical path. Ideally, the mid-plane of the sample would be aligned with the "zero" plane of the optic resulting in a "true" measured value. For the optical CMM, this is part of the calibration process and is removed mathematically. In the case of the profilometer, the z-location can also be derived from the calibration artifact and included in the thickness analysis. However, the absolute z-location for each scan is reset between scans, which add to the overall uncertainty of the measurement. Again, in theory this can be removed mathematically, but relies on stage, optical package and sample holder stability. At present these uncertainty sources are under investigation.

SUMMARY

A modular optical system has been designed and prototyped for measuring the absolute thickness of samples ranging in thickness from 10 μm to 5 mm with a diameter of upwards of 8 mm. This optical package was evaluated on two commercial measuring systems using a 100 ± 0.25 μm calibrated gage block as a reference. A Nikon NEXIV optical CMM measured a thickness of 103.4 μm with a 2.5 μm standard deviation; while the Veeco NT8000 white-light profilometer measured a thickness of 104.5 μm with a standard deviation of 0.5 μm. Although the white-light profilometer is potentially more accurate, due to the displacement laser interferometer positional feedback in the z-axis, the combination of optical package, sample mount and machine stability coupled with the z-location of each scan being reset between front and rear scans, adds significantly to overall measurement uncertainty.

Work continues on evaluating the stability limit of the optical system and sample mount. Also, modification to the commercial software to allow tracking of the z-axes during multiple scans is being addressed with the manufacturer.

ACKNOWLEDGMENTS

- HEDS Manufacturing team – Dave Swift, Alex Hamza, Don Bennett, Pete DuPuy, Craig Akaba, Mike McClure, Steve Stodbecht, Rick Vargas, Gino Mercado, Kerry Bettencourt, Paul Mirkarimi, Kerri Blobaum, John Sain and Marcia Kellam from LLNL
- Erik Novak (Veeco), Greg Maksinchuk (Veeco), Phil Castle (Nikon)

REFERENCES

[1] Kelly, D. (2004) Design and Qualification of an Absolute Thickness Measuring Machine. Master's thesis. Massachusetts Institute of Technology in Mechanical Engineering.

[2] Nederbragt, W., et al (2005), Design And Use Of A High-Accuracy Non-Contact Absolute Thickness Measurement Machine *ASPE 20th Annual Meeting.*

[3] Drabarek, P, *et. al.* (2009) Interferometrical System For High Precision Measurements of Flatness, Thickness and Parallelism of Mechanical Parts *ASPE 24th Annual Meeting (2009)*

[4] Ghim, Y-S., Suratkar, A., and Davies, A., (2010) Reflectometry-based wavelength scanning interferometry for thickness measurements of very thin wafers, *Optics Express*, 18 (7).

[5] Slocum, A.H., (1992), *Precision Machine Design*, Society of Manufacturing Engineers.

MEASUREMENTS OF COATING THICKNESS OF DIAMOND-COATED TOOLS BY WHITE-LIGHT INTERFEROMETRY

William R. White[1], Andrew Ogilvie[1], Kevin Chou[1] and Erik Novak[2]
[1]Mechanical Engineering Department
The University of Alabama
Tuscaloosa, Alabama, USA
[2]Veeco Metrology Inc.
Tucson, Arizona, USA

ABSTRACT

In this study, the coating thickness of diamond-coated tools was evaluated and investigated by non-contact measurements. Commercial cobalt-cemented tungsten carbide (WC-Co) cutting inserts (edge radii from 5 to 80 microns) were used as substrates for varying CVD-diamond depositions. A white-light interferometer (WLI) was used to acquire the surface profile data around cutting edges. MATLAB algorithms were generated to further analyze the tool geometry using the data cloud obtained from the WLI.

The characteristics of a cutting edge (the edge radius, the rake/flank surfaces, and the wedge angle) were then obtained by curve fitting. This methodology was applied to both uncoated and coated tools for the geometry characterizations. To evaluate the coating thickness, the fitted uncoated and coated profiles (from the same tool) were overlapped with the edge rounding centers kept at the same location. The coated profile was then rotated to have the rake face parallel to the uncoated one (as a reference). The normal distance between the two tool profiles (uncoated vs. coated) was used for coating thickness estimates. The combination of WLI and the developed algorithm is capable of efficient coating thickness measurements. Tools with large edge radii had high uncertainties in coating thickness.

INTRODUCTION

Chemical vapor deposition (CVD)-grown diamond films have been increasingly explored for cutting tool applications as an alternative to costly polycrystalline diamond (PCD) tools [7]. Coating attributes such as the coating thickness significantly affect the coating-substrate interface stresses resulted from the deposition process. Therefore, accurate estimates of coating thicknesses, especially around the tool tip is important for quality control and process modeling.

Presently, multiple options exist for coating thickness measurements. Many accurate methods, such as differential interferometry [5], stylus profilometry [10], scanning electron microscopy [11], involve scratching/cratering [1] or other destructive methods. Acoustic thickness measurements are non-destructive; however, the resolution may not be sufficient for the thicknesses used for diamond-coated tools [13]. Raman spectroscopy is a promising prospect, but presently, it is only used for ultra-thin coatings on the order of nanometers [14]. Optical pyrometry has also shown favorable results, but it can only offer an average coating thickness over a large surface [2].

WLI has been applied to coating thicknesses measurements before; however, most cases have only employed a single measurement after the deposition process. This approach is limited by the need to precisely know the refractive index of the tool materials (both coating and substrate) in order to calculate the difference in distances traveled by light reflected from the coating and substrate surfaces [3]. Also, the method has only been applied to ultra-thin coatings [8] and has proven largely ineffective on opaque coatings [6].

The objective of this study was to investigate the coating thickness of diamond-coated cutting tools by WLI. WLI data was processed using generated algorithms which objectively evaluate the tool geometry. These algorithms were applied to individual tools before and after the diamond coating process. The results from each tool were compared and used to calculate diamond coating thickness.

METHODOLOGY

Experimental Setup

A white light interferometer, NT1100 from Veeco Metrology, was used to collect surface data around cutting edges using the vertical scanning interferometry mode. An objective lens of 50X and a 0.5X field of view lens were used. Commercial WC-Co cutting inserts of square shape were used (SPG422): 12.7 mm width and 3.1 mm thickness. The nominal corner radius was 0.8 mm and the wedge angle was 79°. Four separate tool sets (coded A through D) of various edge radii (A: 18 µm, B: 39 µm, C: 80 µm and D: 4 µm), each including five individual samples was tested. Straight cutting edges were measured, 4 edges for each tool sample. A single scan mode was used. In addition, the tools were subsequently diamond coated with 3 different thicknesses, and then further measured by the WLI.

Edge Measurements

An example of a cutting edge surface acquired by the WLI is shown in Figure 1. The instrument software (Vision) was also used for initial data processing including a low pass filter and data restoration to interpolate and replace any missing data. Once finished, the data file can be processed using MATLAB.

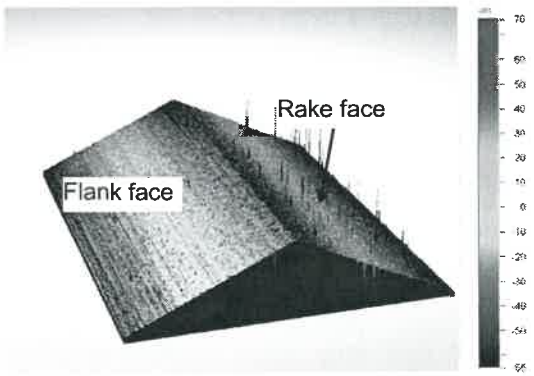

FIGURE 1. A cutting edge image from measurement.

An algorithm to characterize the straight cutting edge was developed in order to allow coating thickness measurements later. After importing the data matrix into MATLAB, an algorithm developed was applied to approximate the edge profile and returns the edge radius and the wedge angle [12]. Figure 2 conceptually shows an example of the results described above.

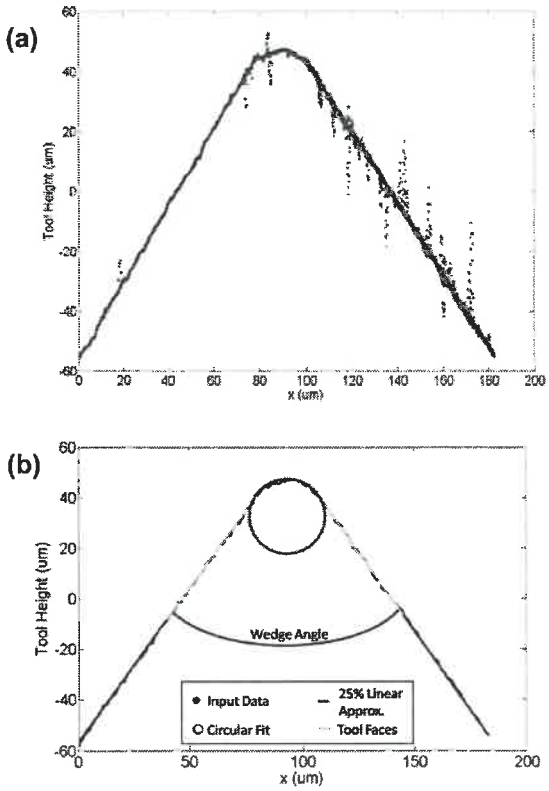

FIGURE 2. (a) 2D projection of raw data, (b) linear and circular fits of the edge profile.

Coating Thickness Algorithm

After performing the above algorithm for the uncoated and coated datasets for each tool, the 2D profile results were then used to calculate each tool's coating thickness. To begin, the uncoated and coated datasets were plotted, directly using the results of the previous algorithm. Next, the coated data was translated such that its approximated tool edge center point lied concentric with that of the uncoated dataset. Because of the positioning of the tools during diamond coating and the coating process's "line-of-sight" method, it was known that the uncoated and coated rake faces should be referenced as parallel. Thus, the coated tool data needed to be rotated in order to accurately represent the associated coated tool. This was accomplished by rotating the coated tool data about its edge center point until the rake face lied parallel with the uncoated rake face.

After the translation and rotation, the varying sizes of the coated and uncoated tool matrices necessitated the removal of overlying edges of each dataset. In particular, the data edges

needed to be cut on a line perpendicular to the tool face in order to simplify the coating thickness calculation process. This was obtained by using the previously calculated tool face slopes and a simple point-slope calculation. Once the data edges were removed, the thickness calculation process began. The uncoated and coated data matrices were input into a separate inter-point distance matrix (IPDM) algorithm [4]. This allowed quick calculations of the distances between all points of the two datasets.

Due to the large number of data points, the minimum values were used as approximates of the perpendicular distance between the coated and uncoated tool faces at each data point. Finally, the diamond coating thickness along the tool edge was calculated using the difference of the coated and uncoated edge radii measurements.

RESULTS AND DISCUSSION

Result Example

Specimens with different edge radii and coating thicknesses were thoroughly tested using the developed methodology. Even with these large deviations in tool geometry, the developed algorithm proved effective on most cases. Figure 3 and Table 1 show a typical result output from an uncoated and a coated tool samples.

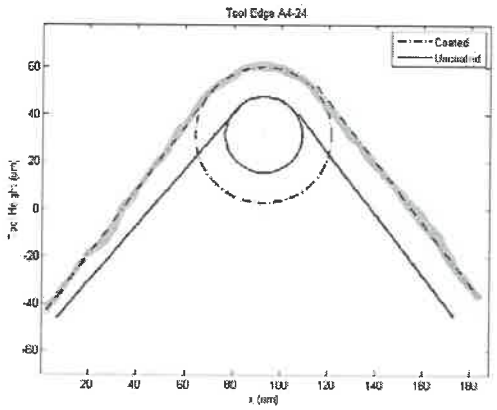

FIGURE 3. Final plot of coated and uncoated fits prior to measurement.

It should also be noted that the methodology employed displays some limitations when viewing extremely large radii tools (~70 µm or larger such as C case). A single WLI scan did not have enough data to provide a robust fit. Thus, multiple scans with the stitching function are needed to acquire more data.

TABLE 1. Sample results from Figure 3.

Uncoated Tool Data			
Radius [µm]	Std. Dev [µm]	Angle [°]	Std. Dev. [°]
16.1230	0.7676	78.1334	0.1992

Coated Tool Data			
Radius [µm]	Std. Dev [µm]	Angle [°]	Std. Dev. [°]
29.8457	1.5192	75.2752	0.4270

Coating Thickness Data				
Rake Face Thickness [µm]	Flank Face Min. Thickness [µm]	Flank Face Avg. Thickness [µm]	Flank Face Max. Thickness [µm]	Tool Edge Thickness [µm]
13.6816	6.9283	9.7147	12.5117	13.7227

Tool samples with varying edge radii and coating thicknesses were analyzed using the algorithms described above. The results showed that the rake face coating thickness was typically thicker than the flank coating thickness. Further, it was observed that thin coating tools resulted in more uniform thickness over the measured regions. Conversely, thick coatings resulted in a tapered coating thickness on the flank tool face. This was expected, due to the "line-of-sight" diamond coating process and the inward tilt of the flank face during that process. Example plots of thin and thick tool coatings are demonstrated in Figure 4: (a) a medium edge radius with a thin coating and (b) a sharp edge with a thick coating. Coating thicknesses were analyzed for tools which underwent the CVD coating process for varying amounts of time. Tools with three different edge radii (A, B, and D) were tested for each coating time type. Table 2 below shows the averaged results from the three cases for each of the coating processes.

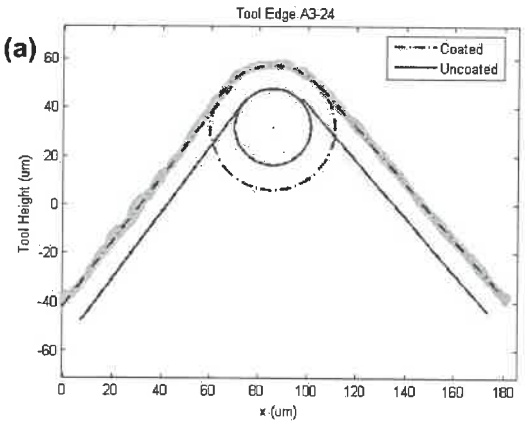

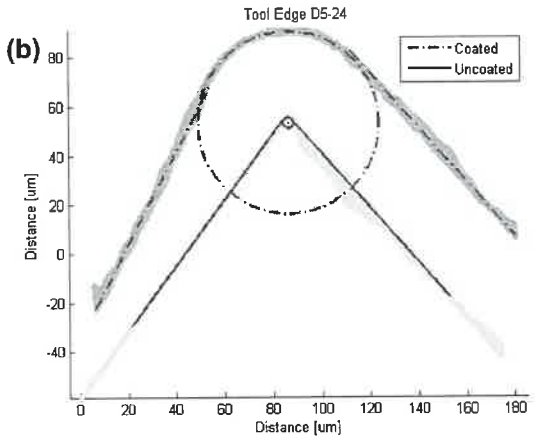

FIGURE 4. (a) Plot of thin coating edge, (b) plot of thick coating edge.

TABLE 2. Coating thickness results.

Case No.	Average Coating Thickness (um)		
	Short<-------Coating Time-------->Long		
A	5.93	16.71	32.58
B	5.11	10.98	22.13
D	11.12	16.27	33.95

CONCLUSIONS

This study investigated and analyzed the coating thicknesses of diamond coated cutting tools using WLI. Algorithms were developed to filter and process the WLI data before estimating tool geometry and coating thickness. The major findings are summarized as follows:

(1) The combination of WLI and the developed algorithm is capable of efficient coating thickness measurements. Tools with large edge radii had high uncertainties in coating thickness.

(2) Coating thickness can be slightly thicker at the tool edge than at the rake/flank faces.

(3) Coating thickness is uniform at the rake face, but shows a linearly decreasing trend along the flank face. This feature became more prevalent with increased coating thicknesses.

ACKNOWLEDGEMENTS

This research is supported by the National Science Foundation, Grant No. CMMI 0728228.

REFERENCES

[1] Bouzakis K. Application in Milling of Coated Tools with Rounded Cutting Edges after the Film Deposition. CIRP Annals – Manufacturing Technology. 2009, 28: 61-64.

[2] Catledge S. In Situ Diagnostics of Film Thickness and Surface Roughness of Diamond Films on a Ti-6Al-4V Alloy by Optical Pyrometry. Applied Physics Letters. 1998, 73(2): 181-183.

[3] Constantino S. Wide Band Interferometry for Thickness Measurement. Optics Express. 2003, 11(8): 952-957.

[4] D'Errico J. IPDM: Inter-Point Distance Matrix. 2008 Apr 21 [cited 2009 Oct 1]. In: MATLAB Central File Exchange. Available from: http://www.mathworks.com/matlab central/fileexchange/18937.

[5] Du Y. New Data-Processing Technique for Measurement of Metallic Foil Thickness with Differential White-Light Interferometry. Optics and Lasers in Engineering 2007, 45:240-244.

[6] Flournoy P. White-Light Interferometric Thickness Gauge. Applied Optics. 1972, 11(9): 1907-1915.

[7] Kanda K. Application of Diamond-Coated Cutting Cools. Surface and Coatings Technology. 1995, 73: 115-120.

[8] Kim N. Real Time Thickness Measurement of Thin Film for End-Point Detector (EPD) of 12-Inch Spin Etcher Using the White Light Interferometry. Microsystems Technology. 2005, 11: 958-964.

[9] Kitamura T. Effect of Residual Stress on Delamination from Interface Edge Between Nano-Film. Engineering Fracture Mechanics. 2003, 70(15): 2089-2101.

[10] Matsumoto S. Phase-Shift Interference Microscope Employing a Simple Method to Depress Speckle Noises for the Thickness Measurement of Thin Films. American Vacuum Society Journal of Technology. 1998, 16(5): 3145-3147.

[11] Miyoshi K. Measurements and Diagnostics of Diamond Films and Coatings. Measurement. 2001, 29: 113-126.

[12] Ogilvie A. An Investigation into Cutting Edge Geometry of Uncoated and Coated Tools by Optical Profilometry, Transactions of NAMRI/SME, 2010, 38: 197-204.

[13] Pant B. Paint Thickness Measurement Using Acoustic Interference. IEEE Transactions on Instrumentation and Measurement. 2006, 55(5): 1720-1724.

[14] Scharf T. Thickness of Diamond-Like Carbon Coatings Quantified with Raman Spectroscopy. Thin Sold Films. 2003, 440: 138-144.

A STUDY OF MACHINING STRATEGY IN COMPUTER CONTROLLED ULTRA-PRECISION POLISHING OF STRUCTURED SURFACES

Chi-fai Cheung[1], Lai-ting Ho[1], Ling-bao Kong[1] and Suet To[1]
[1]State Key Laboratory in Ultra-precision Machining Technology
The Hong Kong Polytechnic University
Hung Hom, Kowloon, Hong Kong

ABSTRACT

This paper presents a pilot study of the machining strategy in ultra-precision polishing of structured surfaces. Preliminary polishing experiment has been conducted. The results show that preferred structure surface texture can be generated by appropriate selection of polishing strategy. The results of the study provide an important means for better understanding of the surface generation as well as the optimization of the surface quality in ultra-precision polishing of structured surface.

INTRODUCTION

Structured surfaces are surfaces possessing specially designed functional textures which are widely used in the development of a wide range of products. Over the past decades, surfaces possessing specially-designed structures in optical science have been found to perform desirable optical functions while unstructured surfaces are incapable of doing this [1].

Those structures may be periodic and random. For example, a film with a periodic structure successfully maintains a high transmissivity of p-polarized light instead of having holes pierced on the film [2]. Some research work [3, 4] shows that a surface with a longitudinal rib structure has a lower shear stress than a smooth surface. This technology can be used in commercial aircraft [5].

In nature, compound eyes and shark skin are typical examples of structured surfaces. Compound eyes of insects provide the advantage of a wide field-of-vision (FOV) and they are very sensitive to the surroundings. Although there has been extensive research on different types of structured surfaces, the research work on fabrication and machining of structured surfaces is far from complete.

Currently, structured surfaces are manufactured by different methods such as electroforming [6] and laser machining [7], which are expensive and time-consuming. There is a need for the development of more economic and controllable methods to construct both periodic and random structured surfaces. Computer Controlled Ultra-precision Polishing (CCUP) is an emerging technology for machining freeform surfaces with high form accuracy and good surface roughness. The surface generation in CCUP relies heavily on the planning of the process steps in terms of the use of polishing conditions and polishing fluid on the specific materials being cut. However, the research of the generation of functional surface textures by CCUP has received relatively little attention. As a result, this paper presents a pilot study of CCUP of structured surfaces.

EXPERIMENTAL SETUP

In the present study, polishing experiment is conducted to study the effect of machining strategy on surface generation in mechanical polishing of optical surfaces. The computer controlled polishing is undertaken by an ultra-precision multi-axis freeform polishing machine named the IRP200 from Zeeko™ Ltd., UK as shown in Figure 1. The machine has 7-axis of motion of which four axes control the workpiece motion and the other three axes control the polishing head as shown in Figure 2.

FIGURE 1. Ultra-precision freeform polishing machine

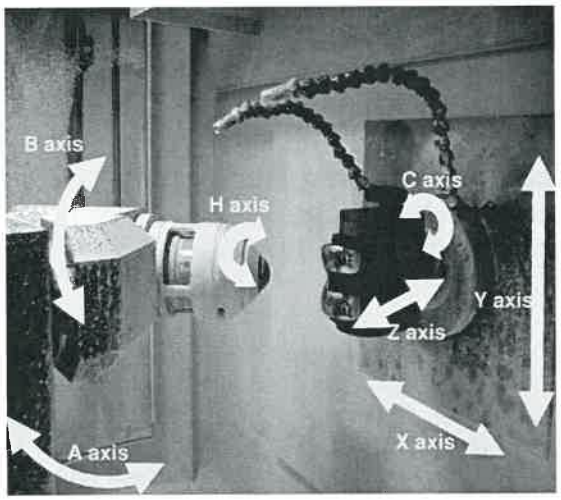

FIGURE 2. 7-axis motion of the machine (Zeeko IRP200 from Zeeko Co. UK)

The workpiece material is Nickel Copper which is rough cut by single point diamond turning with spindle speed 1200rpm and feed rate 4mm/min using a Nanoform 200 ultra-precision machine from Precitech Inc, USA. Then, a series of mechanical polishing is undertaken on the surface.

Two machining strategies were used to produce the similar patterns of structure surfaces on the workpiece, i.e. Machining Strategy A and Machining Strategy B, respectively. The polishing parameters are shown in Table 1. Three trajectories of the polishing tool paths are used include horizontal, spiral and vertical polishing. The trajectories of the tool path of various stages of polishing for machining strategy A and machining strategy B are shown in Table 2 and Table 3, respectively.

TABLE 1. Polishing conditions used

Precess angle (deg)	15
Head speed (rpm)	1200
Tool offset (mm)	0.3
Tool pressure (bar)	1
XY spacing (mm)	1
Surface feed (mm/min)	50
Tool size	20mm radius bonnet
Polishing cloth	Cerium oxide D'16
Polishing slurry	Al2O3 (1.5μm)

TABLE 2. Trajectories of the tool path for machining strategy A

1st polishing step	2nd polishing step	3rd polishing step
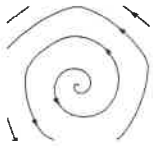		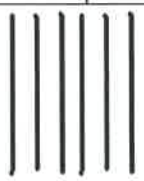
Spiral	Vertical raster	Horizontal raster

TABLE 3. Trajectories of the tool path for maching strategy B

1st polishing step	2nd polishing step	3rd polishing step
	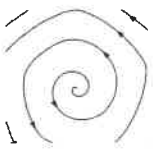	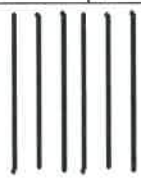
Vertical raster	Spiral	Horizontal raster

RESULTS AND DISCUSSION

Figure 3 shows the 3D surface topographies generated after each polishing stage for machining strategy A. It is interesting to note that the texture of the surfaces is modified from spiral texture to a horizontal raster texture and hence a grid texture according to the 3 stages of polishing. This infers that patterns of surface textures can be produced and synthesized by appropriate use of machining strategy with predefined tool path trajectories.

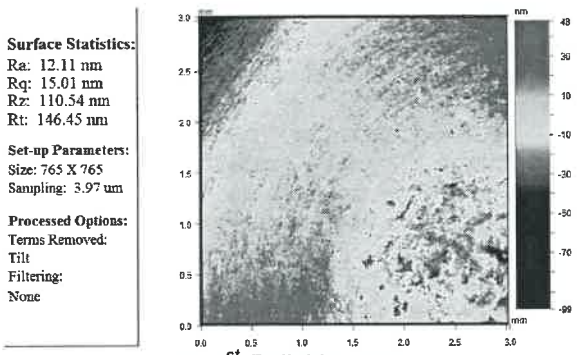

(a) 1st Polishing step

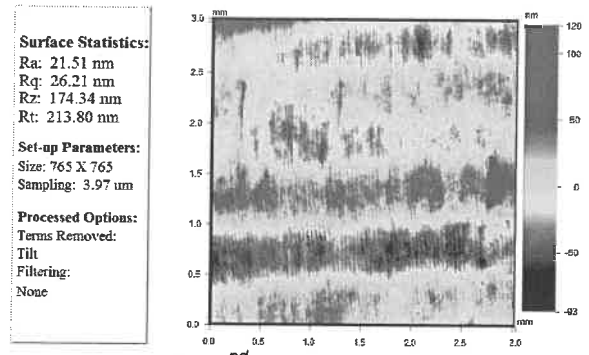

(b) 2nd Polishing step

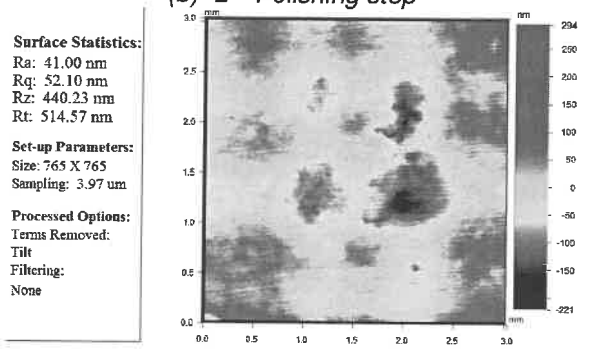

(c) 3rd Polishing step

FIGURE 3. Surface topology for the workpiece after each stage of the polishing process for machining strategy A

It is interesting to note that similar grid pattern of structure surface was generated by polishing strategy B according to the vertical raster, spiral and horizontal raster trajectories of the polishing sequence. Although the generated patterns of structure surfaces appear to be similar, it is found that the polishing strategy A appears to generate grid pattern with high surface roughness as compared to that from polishing strategy B. The results throw some light for the use of ultra-precision polishing technology for the generation of preferred patterns of structure surfaces with proper polishing strategies.

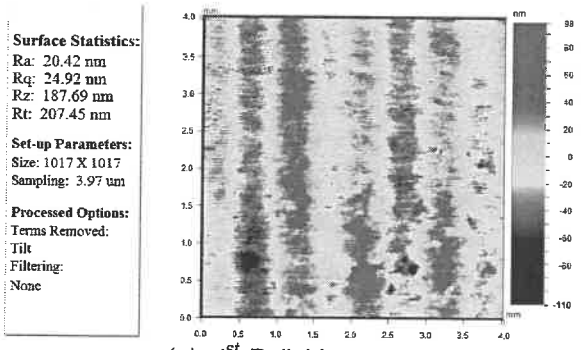

(a) 1st Polishing step

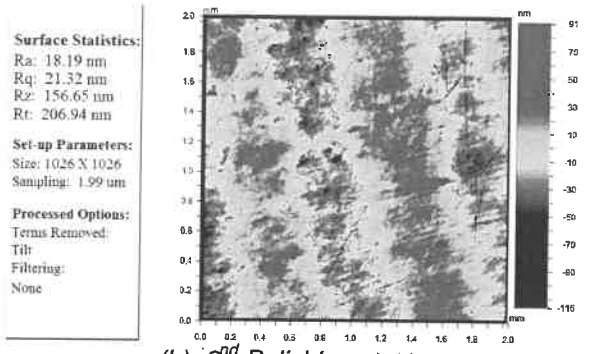

(b) 2nd Polishing step

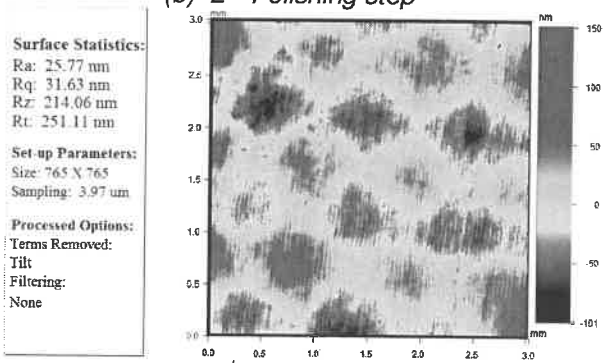

(c) 3rd Polishing step

FIGURE 4. Surface topology for the workpiece after each stage of the polishing process for machining strategy B

CONCLUSION

The fabrication of the advanced optical components requires ultra-precision machining technology which is capable of machining the surfaces with sub-micrometer form accuracy and surface roughness at nanometric levels. Computer Controlled Ultra-precision Polishing (CCUP) is an emerging technology which is capable of addressing the shortcoming limitations of other ultra-precision machining process such as diamond turning, raster milling, etc. In this paper, a pilot study of the effect of machining strategy in CCUP of structured surfaces has been conducted. The results show that preferred surface texture and surface topography can be generated and synthesized with appropriate planning and use of predefined tool path trajectories. The results provide an important means for the design and fabrication of structured surfaces for various functional applications such as diffusers and grating used in the optical applications.

ACKNOWLEDGEMENTS

The authors would like to express their sincere thanks to the Research Committee of The Hong Kong Polytechnic University for the financial

support of the research work under the projects nos.G-YF55 and RGYW, respectively. Many thanks are also due to Zeeko Ltd. for the technical support.

REFERENCES

[1] Leskova TA, Maradudin AA.Structured surfaces as optical metamaterials, Metamaterials. 2007: 1(1): 19-39.

[2] Avrutsky I, Zhao Y. ochergin V, Surfaceplasmon-assisted tunneling of light through periodically corrugated thin metal films. Optics Letter. 2000: 25: 595-597.

[3] Walsh MJ. Drag reduction of V-groove and transverse curvatureriblets. In: Hough GR (ed) Viscous flow drag reduction. Progress in astronautics and aeronautics, AIAA, New York, 1980: 72: 168-184.

[4] Walsh MJ. Riblets. In: Bushnell DM, Hefner JN (eds) Viscous drag reduction in boundary layers. Progress in astronautics and aeronautics. AIAA, Washington 1990: 123: 203-262.

[5] Bechert DW, Bruse M, Hage, W, Meyer R. Fluid Mechanics of Biological Surfaces and their Technological Application. Naturwissenschaften. 2000: 87: 157-171.

[6] Johansen LS, Ginnerup M, Ravnkilde JT, Tang PT, Löchel B. Electroforming of 3D microstructures on highly structured surfaces. Sensors and Actuators. 2000: 83: 156-160.

[7] Dumitru G, Romano V, Weber HP, Haefke H, Gerbig Y, Pflüger E. Laser microstructuring of steel surfaces for tribological applications. Applied Physics A. 2000: 70: 485-487.

CONTACT CONDITIONS FOR 5-AXIS GRINDING OF FREE FORMED SURFACES

Berend Denkena[1], Jens Köhler[1], Leif Behrens[1], Thomas Krawczyk[1]
[1]Institute of Production Engineering and Machine Tools, Germany
Leibniz Universität Hannover

INTRODUCTION

Nowadays free formed surfaces are machined by grinding for increasing number of industrial applications. Those are for example friction-reduced surfaces of compressor blades and wear-resistant steel-ceramic forging dies [1, 2].
So far, multi-curved surfaces are commonly machined by 3+2-axis processes using an axially parallel strategy [3]. However, this strategy often causes undesirable contour deviations due to tool deflection resulting from the unsteady contact conditions between tool and workpiece surface [4].
An advanced strategy is the surface normal machining. Here the peripheral surface of the grinding tool is set permanently normal to the workpiece surface normal vector. Consequently, constant contact conditions over the whole workpiece surface can be ensured [5, 6]. Considering the tool macro geometry also constant material removal and surface properties can be achieved. FIGURE 1 summarizes the relevant advantages of this strategy.

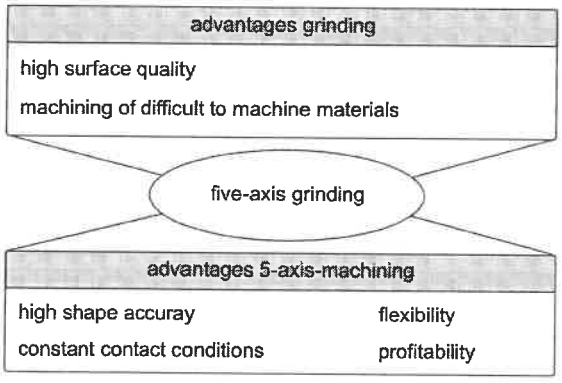

FIGURE 1. Advantages of five-axis surface normal grinding strategy

In this paper the fundamental contact conditions and tool-workpiece-interpenetrations in five-axis orthogonal machining are discussed analytically. Especially, the relevant characterizing factors for the tool workpiece interaction are identified in and orthogonal to the feed direction.
To ensure constant contact conditions between the grinding tool and the workpiece surface the geometric contact length (l_g) and the non-congruence defects (S_F) are identified as the predominant characterizing values.

CONTACT CONDITIONS

The analysis of a free formed surface, e.g. compressor blades, shows that the surface can be locally described by a curve in feed direction (1st curve) and a curve orthogonal to the feed direction (2nd curve).

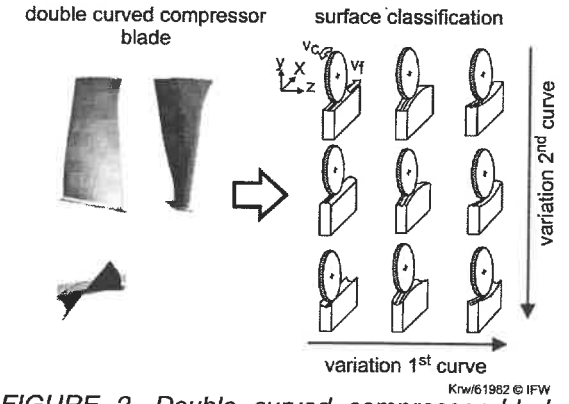

FIGURE 2. Double curved compressor blade and the various grinding cases

Both curves can be planar, concave or convex. Hence, nine different grinding cases can be defined as shown in FIGURE 2. However, the first and the second curve radius of free formed surfaces change continuously during the grinding process resulting in varying contact conditions. A concave curved surface in feed direction for example limits the applicable grinding wheel radius, which always has to be smaller than the curve radius. In the following the impact of the two workpiece curves on the geometric contact length l_g and the non-congruence defects S_F is discussed for different contact conditions.

GEOMETRIC CONTACT LENGTH

The geometric contact length is one of the relevant characterizing factors for the determination of mechanical and thermal loads on the grinding tool and the workpiece subsurface. Here generally large contact lengths result in higher process forces and temperatures. When grinding free formed surfaces three different contact cases can be distinguished in feed direction (FIGURE 3). Beside the first curve of the workpiece the geometric contact length l_g is influenced by the depth of cut a_e and the major radius of the grinding tool R_{WZ}.

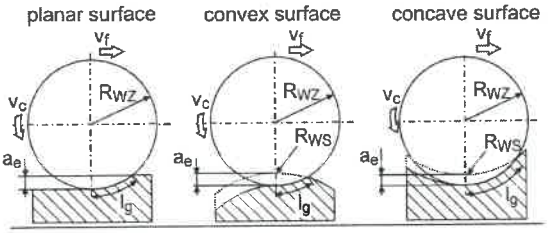

FIGURE 3. Geometric contact length

The contact length of a planar surface can be calculated as:

$$l_g = \frac{R_{WZ} \cdot \pi}{180°} \arccos\left(1 - \frac{a_e}{R_{WZ}}\right) \qquad (1)$$

In the case of convex and concave surfaces the workpiece radius (R_{WS}) the contact length l_g can be calculated as [7]:

$$l_g = \frac{R_{WZ} \cdot \pi}{180°} \arccos\left(1 - \frac{\frac{a_e^2}{R_{WZ}} \pm 2 \cdot a_e \cdot \frac{R_{WS}}{R_{WZ}}}{2 \cdot (R_{WZ} \pm R_{WS})}\right)$$

$$\text{with } \frac{(-)\text{ concave surface}}{(+)\text{convex surface}} \qquad (2)$$

FIGURE 4 (right hand side) displays the impact of the depth of cut on contact length at a constant tool- (R_{WZ} = 40 mm) and workpiece-radius (R_{WS} = 100 mm). The contact length increases digressively with the depth of cut. Hereby, the contact length of the concave case is always longer than in the convex case. On the left hand side of FIGURE 4 the contact length is shown as a function of the workpiece radius in feed direction with a grinding wheel radius of 40 mm and a depth of cut of 0.030 mm. For a convex surface there is an exponential increase of the geometric contact length with the curve radius. In contrast, at concave formed surface the contact length decreases exponentially with increasing curve radius. Both contact lengths converge to 1.5 mm, which is the contact length at planar surfaces. The difference between the contact length of a concave and convex surface with the same workpiece radius exceeds for small workpiece radii.

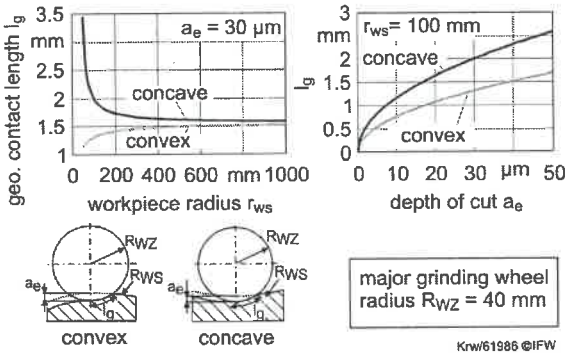

FIGURE 4. Geometric contact length as a function of the depth of cut

Equations (1) and (2) suppose a constant workpiece radius. However, the analysis of free formed surfaces show that the curves in feed direction change steadily. To predict the geometric contact length in this case a geometrical simulation has been accomplished. This simulation determines the point where the grinding tool exits the workpiece. So the contact length is calculated by the tool radius and the contact angle. FIGURE 5 displays an unsteady concave surface section. The radii of the surface decrease progressively in feed direction (from position 1 to 5).

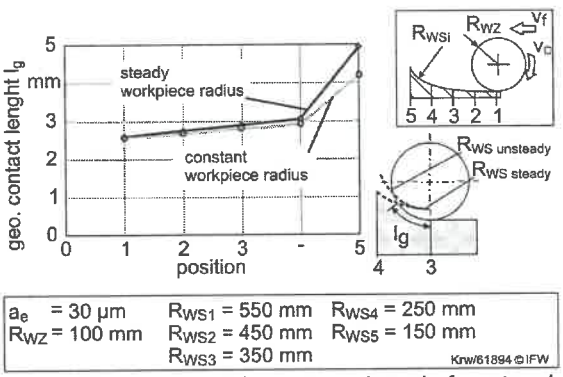

FIGURE 5. geometric contact length for steady and unsteady workpiece radii

For the calculation of the geometric contact length two cases are derived. In the first case it

is assumed that the curve radius is constant for the section between two consecutive positions whereby the curve radius decreases from one section to another. In the second case the workpiece radius changes continuously. On the left hand side of FIGURE 5 the contact length is plotted for both described cases. The calculated contact length for steady and unsteady workpiece radii is nearly similar between position 1 and 4. For smaller workpiece radii the contact length is larger in case of an unsteady workpiece radius (position 5). This can be explained by the exponential growth of the contact length for decreased workpiece radii.

NON-CONGRUENCE DEFECT

The non-congruence defect S_F is the characterizing value for the shape deviation between the grinding tool profile and the second workpiece curve. The non-congruence defect is generally influenced by the grinding-tool-profile - radius and -width. While the first workpiece curve affects the geometric contact length, the material removal is also influenced by the second curve orthogonal to the feed direction.
Assuming a planar grinding wheel for a concave workpiece surface the grinding tool removes material with its edges, which results in surface damages. In the case of a convex workpiece surface the grinding wheel does not remove material with its edges which consequently results in shape deviations (FIGURE 6).

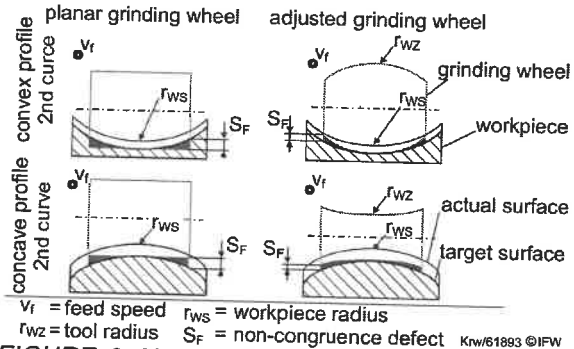

FIGURE 6. Non-congruence defect for different workpiece shapes and grinding tool profiles

In both cases the targeted surface of the workpiece is not achieved. In order to decrease the non-congruence defects, the profile of the grinding tool has to be adjusted to the workpiece surface contour. Nevertheless, it is not possible to eliminate these described defects completely, due to the continuously changing second workpiece curve.

FIGURE 7 outlines an iterative procedure to define an applicable grinding tool profile, which results in a non-congruence defect within the tolerance of about 10 µm. In a first step, the second workpiece curve is analyzed with the aim to identify the workpiece radii and the shape of curve (convex or concave) orthogonal to the feed direction. In the second step the profile of the grinding tool is calculated. To machine a constant concave surface section the grinding tool has to be dressed with a constant convex radius. For a constant convex surface section the grinding tool profile must have a constant concave radius. For unsteady curve shapes a grinding wheel profile has to be chosen, which results in a non-congruence defect within the pretended tolerance. When this requirement is fulfilled, the NC-Code is generated.

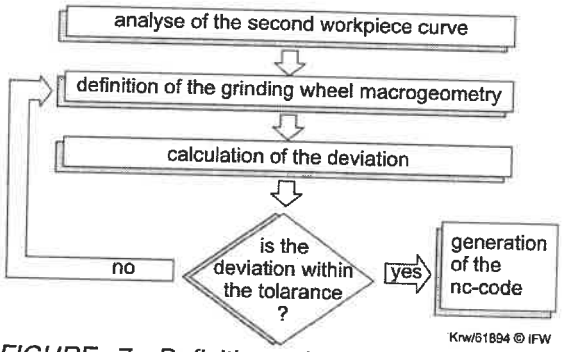

FIGURE 7. Definition of the grinding wheel macro geometry

To demonstrate this procedure the non-congruence defect has been calculated for a free formed compressor blade of a gas turbine. This component has to be micro structured in stream wise direction by grinding with a constant depth of cut over the whole grinding width (FIGURE 8). These structures are used for the friction reduction and have to be manufactured with an angel of 30° concerning the blade root. Thus, it is necessary to tilt the grinding wheel 30°, too. Seven second workpiece curves are calculated along the grinding path as shown in FIGURE 8. Due to the convex shape of the second workpiece curves, the profile of the grinding tool ideally is to be dresses with a concave shape.
However, a planar grinding wheel profile is assumed first. This is a compromise between the ideal grinding tool macro profile and the ability of an economically micro profiling of the grinding tool. Thus, the non-congruence defect can be influenced by the grinding tool width only. In the first step a grinding tool width of 20 mm is

assumed. The maximum non-congruence defect for this grinding tool width is pictured for the seven workpiece second curves in FIGURE 8. The largest non-congruence defect of about 120 µm occurs at the smallest concave radius of the second workpiece curve at profile 1. The non-congruence defect is between 50 µm and 80 µm for the other profiles due to the larger concave radii. However, the non-congruence defects clearly exceed the target tolerance of 10 µm. As a consequence, the width of the grinding wheel was reduced from 20 mm to 7 mm in the next step. The calculation of the non-congruence defects with this tool width shows that it can be decreased significantly and matches the requirements. Nevertheless, the largest non-congruence defects also occur at the smallest concave second workpiece curves.

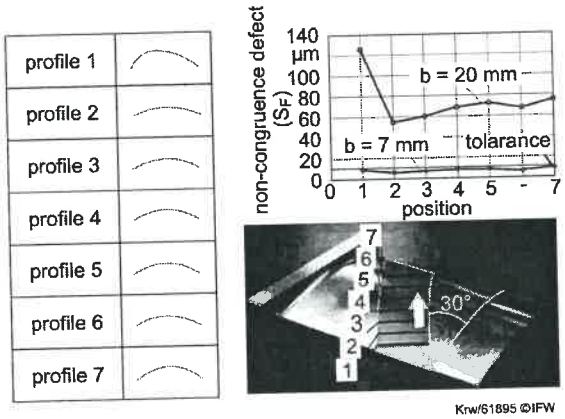

FIGURE 8. Non-congruence defects for different grinding wheel widths

CONCLUSIONS

In this paper the fundamental contact conditions and tool-workpiece-interpenetrations in five-axis orthogonal machining are discussed analytically. The aim is to ensure constant contact conditions between the grinding tool and the workpiece surface. Here, the geometric contact length (l_g) and the non-congruence defects (S_F) have been identified as the predominant characterizing values.

The geometric contact length has been analytically modeled for plain as well as for constant and steady changing concave and convex surfaces. This model can be applied for the calculation of critical geometric contact length resulting in high mechanical or thermal loads.

Furthermore, the non-congruence defect between plain, concave and convex shaped tool and workpiece geometries have been calculated. Applying adapted grinding tool profiles and widths a relatively constant depth of cut can be archived over the tool engagement width within the predefined tolerances. This procedure has been exemplarily applied to design the machining process of compressor blades.

ACKNOWLEDGEMENTS

The investigations described in this paper were undertaken with the support of the German Research Foundation (DFG) within the collaborative research center SFB 489 "Process chain for manufacturing precision forged high performance components" and within the project "Riblets on Compressor Blades".

REFERENCES

[1] Denkena, B.; Kästner, J.; Wang, B.: Advanced microstructures and its production through cutting and grinding, CIRP Annals - Manufacturing Technology, Vol. 59 (1), pp. 67-72, (2010)

[2] Weule, H.; Timmermann, S.; Eversheim, W.: Automation of the Surface Finishing in the Manufacturing of Dies and Molds, CIRP Annals – Manufacturing Technology Vol. 39, pp. 299-326, (1990)

[3] Bambach, M.; Taleb Araghi, B.; Hirt, G.: Strategies to improve the geometric accuracy in asymmetric single point incremental forming, Production Engineering Research and Development 3(2), pp. 145-156, (2009)

[4] Bang, Y.B.; Lee, K.M.; Oh, S.: 5-axis micro milling machine for machining micro parts, The International Journal of Advanced Manufacturing Technology 25, pp 888–894, (2005)

[5] Weinert K.; Blum H.; Kuhlenkötter B.; Schröder A.; Zhang X.; Scheele C.; Surmann T.: New methods for calculating the forces distribution within belt grinding process. Production Engineering Research and Development 1(3), pp 285-289, (2007)

[6] Cho, H. D.; Jun, Y. T.; Yang, M. Y.: Five-axis CNC milling for effective machining of sculptured surfaces, International Journal of Production Research 31(11), pp 2559-2573, (1993)

[7] Gehring, V.: Numerisch gesteuertes Formschleifen von gekrümmten Werkstückoberflächen, Dr.-Ing. Dissertation, Universität Hannover (1993)

GRINDING OF MICROSTRUCTURES IN BRITTLE MATERIALS WITH MULTIPLE MICROPROFILED GRINDING WHEELS

Denkena, B.[1]; Köhler, J.[1]; Kästner, J.[1]; Hahmann, D.[1]
[1]Institute of Production Engineering and Machine Tools
Leibniz Universität Hannover
Garbsen, Germany

INTRODUCTION

The manufacturing of complex shaped microstructures on microsystem parts in brittle materials provides a high geometrical accuracy [1]. This requirement can only be met by using microgrinding processes. There, metal bonded diamond grinding tools offer a remarkable potential due to their favorable wear behavior [2]. However, the dressing of complex microprofiles on these tools is not possible using mechanical dressing methods because of a high dresser wear and high dressing forces. Thus, Electro contact discharge dressing (ECDD) is used for the microprofiling of the grinding wheels. ECDD is a numerically controlled dressing process offering the possibility to create the geometry and topography of the grinding wheel simultaneously at negligible dressing forces [3]. The power of an electric circuit thermally removes the metal bond of the grinding wheel in ECDD [4,5].

This paper presents investigations about the influence of the workpiece material and the grinding process parameters on the chipping at the edge of microstructures. Furthermore, strategies to reduce the microstructure dimensions and increase the flank angle of the microstructures are shown. ECDD is used for the dressing of the grinding wheels prior to the grinding experiments.

GRINDING WITH MULTIPLE MICROPROFILED METAL BONDED GRINDING WHEELS

The micro ECDD process is used to generate multiple microprofiled grinding wheels. Afterwards, the grinding of microstructures is investigated with these tools. Thereby, the dressing and grinding operations were carried out on the same grinding machine. The contact conditions in grinding are influenced by the tool properties like grain size and concentration as well as the process parameters. Among others the contact conditions are described by the chip thickness h_{cu} and the geometrical contact length l_g. Aluminum oxide samples are chosen for the investigations, due to the favorable machinability by microgrinding and the use of this material for example for the manufacturing of micro air guides. Crossed microstructures were machined by two orthogonal paths (FIGURE 1). Several microstructures were generated parallel in grinding with multiple micro profiled grinding wheels in contrast to micro grinding with single dicing blades. Thus, process economy is enhanced in grinding with multiple microprofiled grinding wheels.

Both structures in FIGURE 1 are machined with the same material removal rate. One structure is machined with a low infeed and a high feed rate and the other with a high infeed and a low feed rate.

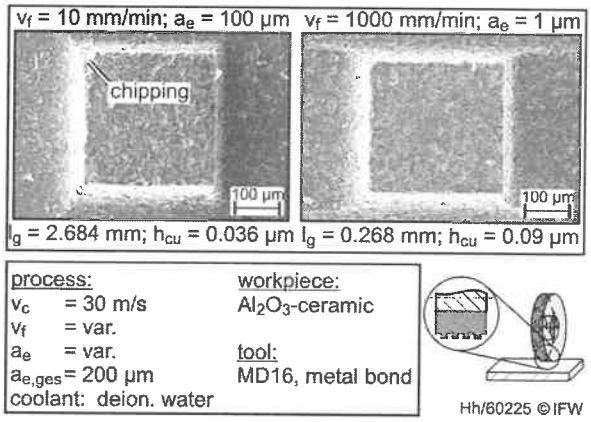

FIGURE 1. The effect of the process parameters on the chipping at the edges of microstructures

The SEM-micrographs show that grinding with a high infeed and a low feed rate produces larger chipping at the edge than grinding with a low infeed and a high feed rate. This is contrary to the results known for surface grinding. The geometrical contact length is in the range of the structure length for an infeed of 1 µm and a feed rate of 1000 mm/min. However, the geometrical contact length is about ten times longer than the structure length for an infeed of 100 µm and a feed rate of 10 mm/min. The gaps between the microstructures machined in the first grinding path results in an interrupted cut in the second

profile grinding process. Thus, the maximum contact length is shorter than the geometrical contact length if the geometrical contact length exceeds the microstructure dimensions. Considering this, the normal and tangential single grain forces, calculated from force measurements, are significantly higher in grinding with an infeed of 100 µm and a feed rate of 10 mm/min. This is the main reason for the increased edge break-out.

The minimum workpiece microstructure dimensions are limited by the flute width of the grinding wheel profile if the microstructures are machined with only one tool path. The structure size can be reduced if a shift strategy with two parallel tool paths with the offset Δz is used (FIGURE 2). There, two cases are distinguished. The bar width of the grinding wheel profile is larger than the flute width in the first case. Then, the microstructure dimensions are reduced proportionally to the offset between the two tool paths. In the second case, the bar width of the grinding wheel profile is smaller than the flute width, like shown in FIGURE 2. Then, the microstructure dimensions are reduced until the offset between the tool paths according the bar width of the grinding wheel profile. The microstructures machined in the first tool path are segmented in the second tool path if the offset exceeds the bar width of the grinding wheel profile.

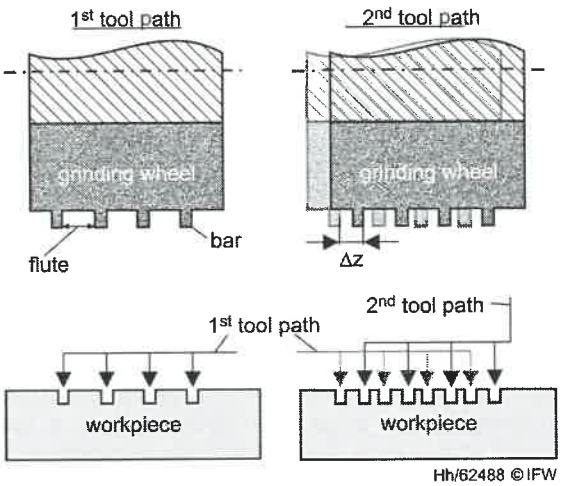

FIGURE 2. Reduction of microstructure dimensions by grinding with shift strategy

The detailed SEM-micrograph in FIGURE 3 shows a small microstructure, which was machined by the segmentation of a larger microstructure, produced in the first tool path. However, the flat top of the 200 µm high microstructure with an edge length of about 40 µm shows brittle material breakout. The chipped area is close to the size of several ceramic material grains ($d_K \approx 15$ µm). This means, that the workpiece material properties, e.g. the grain size and the fracture toughness, have a significant influence on the chipping at the edge of the microstructures.

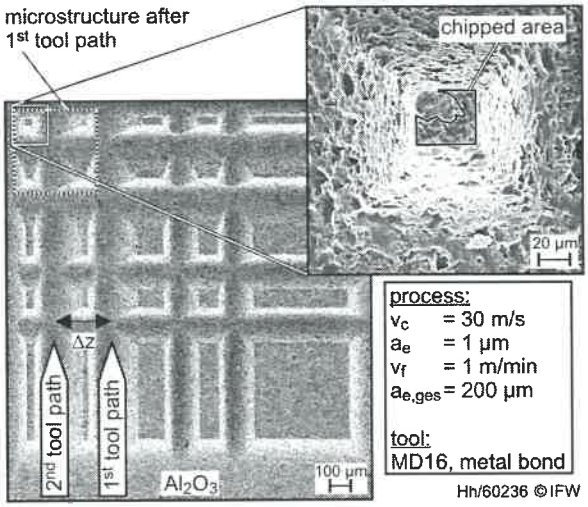

FIGURE 3. The limitation of minimum microstructure dimensions by the material properties

Thus, in the following the edge quality of microstructures machined in aluminum oxide ($d_K < 1$ µm), zirconium oxide and cemented carbide ($d_K < 1$ µm) is analyzed.

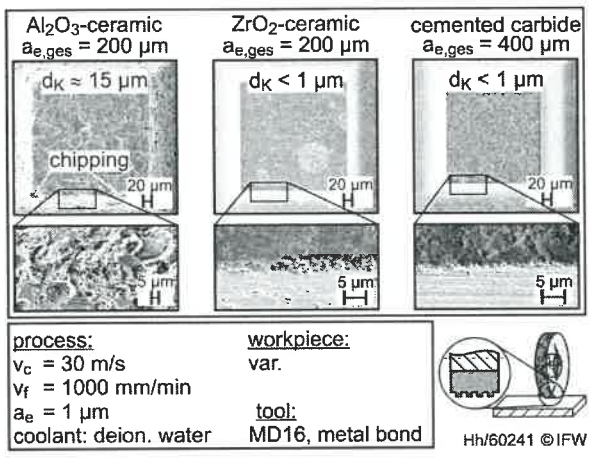

FIGURE 4. The influence of the workpiece material on the dimensions of the edge chipping

All samples are machined with the same process parameters except the total infeed

$a_{e,ges}$. The samples differ in the initial state of the material prior and after sintering beside the material itself. The zirconium oxide and cemented carbide are fine grained and have a low porosity. The aluminum oxide has coarse grains in the range of about 15 µm and a higher porosity. The fracture toughness of zirconium oxide is twice as high and the fracture toughness of cemented carbide is up to five times higher than for aluminum oxide. The SEM-micrographs show that the edge quality is higher for zirconium oxide and cemented carbide (FIGURE 4). The chipping for aluminum oxide reaches more than 10 µm. The chipping is about 3 µm for zirconium oxide and less than 2 µm for cemented carbide. The edge quality increases with increasing fracture toughness and decreasing material grain size. Thus, the further reduction of the microstructure dimensions by using different offset Δz or higher infeed and the increase of the height to width ratio is investigated at cemented carbide.

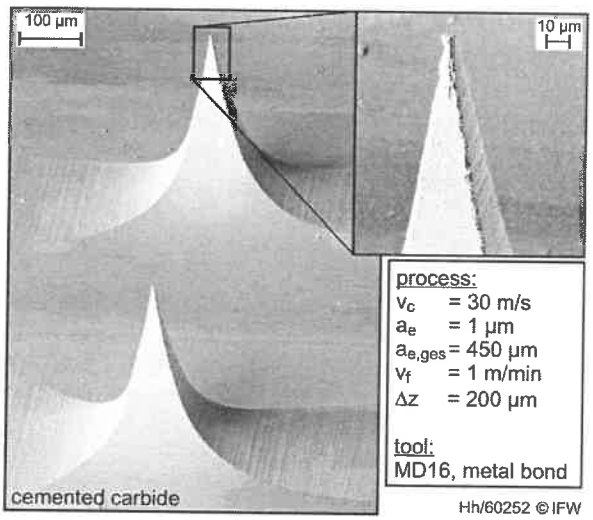

FIGURE 5. Minimum microstructure dimensions in cemented carbide

FIGURE 5 shows the minimum microstructure dimensions machined in cemented carbide. Both structures were machined parallel. The microstructure top is reduced to a sharp tip with a radius of about 3 µm at a structure height of about 400 µm. However, the flanks of the structures are not perpendicular due the grinding wheel micro profile. The dressing process is not able to generate perpendicular profile flanks. The flank angle of the microprofiles, dressed on the grinding wheel, is about 78°. Thus, further investigations were carried out to gain perpendicular profile flanks with advanced dressing and grinding strategies.

GRINDING WITH UNDERCUT PROFILES

A grinding wheel with an undercut profile is used for grinding microstructures with perpendicular flanks. Only one side of the grinding wheel microprofile is dressed with an undercut to clarify the influence of the undercut profile on the machined microprofile shape. The undercut profile is dressed in two steps. The feed direction of the micro electrode is perpendicular to the grinding wheel surface in the first step. The electrode is fed under the tilt angle γ in the second step to generate the undercut (FIGURE 6). The tilt angle γ is set in the range of 15° to 30°. The dimensions of the microstructures machined with two crossed tool paths are not the imprint of the grinding wheel microprofile. They are generated by the projected grinding wheel microprofile resulting from the grinding wheel rotation. Thus, two flanks of the machined microstructures are expected to be perpendicular when grinding with the undercut microprofiled grinding wheel described above.

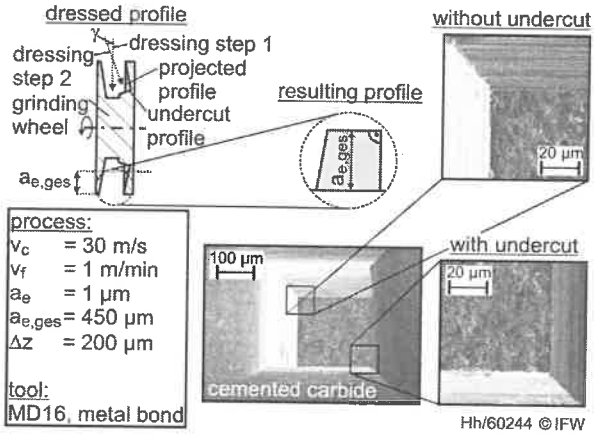

FIGURE 6. Influence of the undercut profile on the microstructure flanks

FIGURE 6 shows a machined microstructure. The flanks machined with an undercut profile are perpendicular except the lower third of the microstructure. The flanks machined with a standard grinding wheel profile have a flank angle below 90°. The detailed SEM micrographs of the corners machined without and with undercut profile underline the significant difference in the shape of the edges. The corner machined without undercut profile shows a smooth crossover from the top area to the

flanks. The corner machined with undercut profile shows a sharp crossover from the top area to the perpendicular flanks. Thus, grinding with an undercut profile enables the machining of perpendicular microstructure flanks and sharp edges.

Further experiments have been carried out to machine square shaped microstructures with higher aspect ratios. Therefore, a shift strategy in grinding was used. The best results, shown in FIGURE 7 were gained by an offset of 200 µm between the two grinding paths. The total height of the machined structure is about 450 µm. The square shaped part of the microstructure is about 350 µm high and has an edge length of about 60 µm. This results in an aspect ratio of about 6.

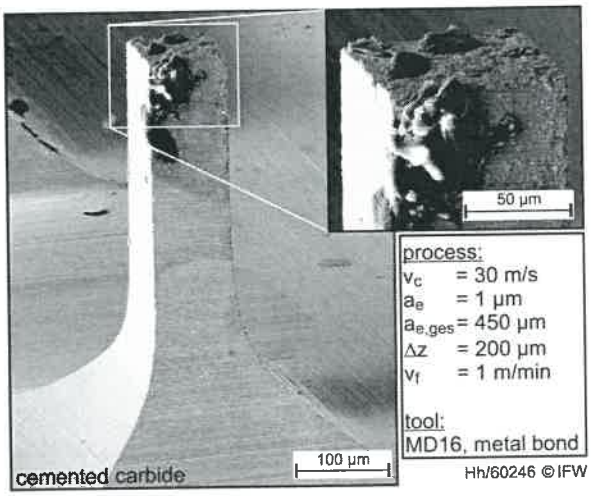

FIGURE 7. Microstructure with perpendicular flanks and high aspect ratio

RESULTS AND CONCLUSIONS

The investigations show that several microstructures can be machined parallel by the use of multiple microprofiled grinding wheels. The process parameters have a significant influence on the edge of the machined microstructures. The best edge quality is gained at a high feed rate and a low infeed. Furthermore, the material properties influence the edge quality. It is increased by smaller material grain size and higher fracture toughness. The minimum size of the protruded microstructures being machined in one tool path is limited by the flute width of the grinding wheel microprofile. The microstructure dimensions can be further reduced by shift grinding with two parallel grinding paths with the offset Δz. With shift grinding strategy micro tips with a height of about 400 µm and a tip radius of about 3 µm are ground. These micro tips point out a further limitation of the microstructure geometry by the grinding wheel microprofile. Perpendicular flanks cannot be ground at the microstructures due to the flank angle below 90° at the dressed microprofiles. Thus, grinding with an undercut profile was investigated to grind perpendicular microstructure flanks. In this case, the shape of the machined microstructure depends on the projected grinding wheel microprofile resulting from the grinding wheel rotation. Square shaped protruded microstructures with a minimum edge length of about 60 µm and an aspect ratio of about 6 were ground with the combination of undercut profile and shift grinding strategy.

ACKNOWLEDGEMENTS

These research works have been conducted in the scope of the collaborative research centre (SFB) 516 "Design and Manufacturing of Active Microsystems" in the particular project B3 "Micromachining".

REFERENCES

[1] Hesselbach, J.; Hoffmeister, H.-W.; Hlavac, M.: Micro-Ginding - Efficient Technique for Microstructuring Hardened Steels. In: Production Engineering - Research and Development (WGP), Volume 12, Number 1, pp. 1-4, 2005.

[2] Klocke, F., Klink, A., Schneider, U:: Electrochemical oxidation analysis for dressing bronze-bonded diamond grinding wheels. In: Production Engineering - Research and Development (WGP), Volume 1, Number 2, pp. 141-148, 2007.

[3] Xie, J.; Tamaki, J.; Kubo, A.; Iyama, T.: Application of electro-contact discharge dressing to a fine-grained diamond grinding wheel. In: Journal of the Japan Society for Precision Engineering, 67(11), 2001, pp. 1844-1849.

[4] Denkena, B.; de Leon, L.; Wang, B.; Hahmann, D.: Development in the Dressing of Super Abrasive Grinding Wheels. In: Key Engineering Materials, Vol. 404 (2009), pp. 1-10.

[5] Denkena, B.; de Leon, L.; Hahmann, D.: Dressing of micro profiles by wire electro discharge dressing. In: Proceedings of the 9th International conference of the euspen, 2009, pp. 146-149.

WEAKLY COPPER-FULLERENOL LAYER ON CHEMICAL MECHANICAL POLISHING USING WATER SOLUBLE FULLERENOL

Hirotaka Kishida[1], Yasuhiro Takaya[1], Terutake Hayashi[1], Masaki Michihata[1], Ken Kokubo[2]
[1]Division of Mechanical Engineering, Osaka University
2-1 Yamadaoka Suita, 565-0871, Japan
[2]Division of Applied Chemistry, Osaka University
2-1 Yamadaoka Suita, 565-0871, Japan

INTRODUCTION

The copper damascene process is commonly used to fabricate multilayer interconnection of copper for high-performance semiconductor devices. Chemical mechanical polishing (CMP), a polishing technology in which a chemical reaction by an additional chemical agent and mechanical removal by abrasive grains of slurry are both used, has become a key technology on fabricating high-density integrated circuits on semiconductor devices with multilayer interconnections. When stacking circuit layers by the copper dual damascene process based on CMP, each layer needs to have high flatness. The continuing reduction in the design rule has necessitated circuit layers having higher flatness than conventional ones, in which colloidal silica, whose diameter is more than 20 nm, is currently used as abrasive grains of slurry.

A polishing process using smaller abrasive grains than conventional one is one of the basic solutions for achieving high flatness. Water soluble fullerenol molecules, which has suitable features such as uniform particle size, solubility in water, small particle size (<1 nm), and the fact that it is metal free, has been proposed as abrasives for use in the slurry for Cu-CMP[1].

It has been found that the surface roughness of a copper wafer polished using a slurry containing fullerenol abrasives varies depending on the type of fullerenol used. It is confirmed that $C_{60}(OH)_{36}$ and $C_{60}(OH)_{44}$ based slurry exhibit high planarization efficiency comparing to $C_{60}(OH)_{26}$. The differences is caused by chemical reactivity of fullerenol for copper since both $C_{60}(OH)_{36}$ and $C_{60}(OH)_{44}$ solutions exhibit high chemical reactivity[1]. The fullerenol is considered to have different role in addition to abrasives. However, the removal mechanism of matter using fullerenol abrasives in the Cu-CMP process has not yet been clarified.

In this study, the use of water-soluble fullerenol for copper removal is investigated to estimate the removal mechanism. The material removal rate of the slurry at various kind of fullerenol, whose chemical reactivity is different, is investigated. X-ray photoelectron spectroscopy (XPS) analysis is also conducted to identify the surface compounds formed on the copper in the presence of fullerenol.

EXPERIMENT

Development of Fullerenol Slurry

The composition of the slurry is shown in Table 1. Hydrogen peroxide is added to distilled water as an oxidizer, triammonium citrate and triammonium phosphate trihydrate as chelating agents, 1,2,3-benzo-triazole as a preservative. Fullerenol is added as abrasive grains. 3 type of fullerenol slurry using $C_{60}(OH)_{26}$, $C_{60}(OH)_{36}$, $C_{60}(OH)_{44}$ are prepared. The solution is stirred using an ultrasonic washing machine for 30 min.

Polishing Experiment

A polishing experiment is carried out using $C_{60}(OH)_{26}$, $C_{60}(OH)_{36}$ and $C_{60}(OH)_{44}$ to determine the polishing rate. The experimental apparatus is shown in Figure 1. It consists of a polishing head unit for rotation of the test piece and the rotary table unit for rotating polishing pad. The test piece has dimension of 10 mm^2, and it consists of a silicon base with a 1.6-μm-thick

TABLE 1. Composition of fullerenol slurry.

Compornent	Concentration (wt %)
Hydrogen peroxide	1.6
1, 2, 3, benzotriazole	0.12
Ammonium phosphate	0.5
Ammonium citrate	0.5
Fullerenol	0.1

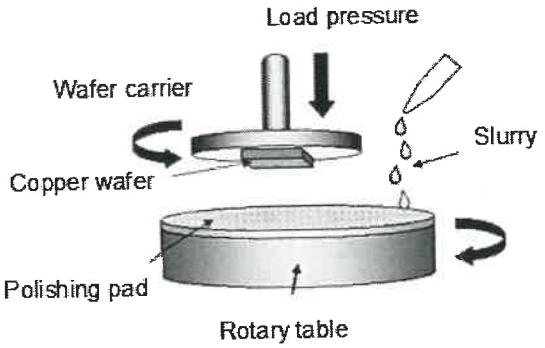

FIGURE 1. Experimental apparatus.

copper film. The test peace is attached to the polishing head; the head rotated counterclockwise at 60 rpm under an applied pressure of 25 kPa controlled by an air cylinder. IC 1000 (Nitta Haas) is used as a polishing pad, which is attached to the rotary table; the table is rotated counterclockwise at 60 rpm. These counterclockwise rotations are calibrated using an RM2000 handy tachometer. Polishing is carried out for 5 min. The removal rate is evaluated by measuring the thickness of the copper film, which is determined from the cross section of the wafer in an SEM image, through the polishing procedure.

Analysis of Surface Condition

The changes in the surface condition of the copper sample because of the effect of fullerenol is studied using an XPS system AXIS 165x (SHIMADZU). Copper wafer samples are dipped for 1 h in different fullerenol solutions. 3 type of fullerenol solution containing 0.1 wt% of $C_{60}(OH)_{26}$, $C_{60}(OH)_{36}$, $C_{60}(OH)_{44}$ are prepared and 0.8 wt% of hydrogen peroxide is added to these solutions. The ambient temperature is 25°C. After this procedure, XPS analysis is conducted. X-radiation from an Mg source (1253.6 eV) is used. In order to clarify state of fullerenol and copper, narrow scan spectra of the 2p orbital of Cu (928~970 eV) and 1s orbital of C (277 ~300 eV) are recorded at an electron pass energy of 40 eV.

The condition of the dipped copper wafer is observed by SEM. Thickness of the surface layer is determined from the cross section of the wafer in an SEM image. The polishing experiment is carried out on the dipped wafer to evaluate the mechanical removability of the surface layer. Polishing is carried out for 30 s using distilled water as a slurry to exclude

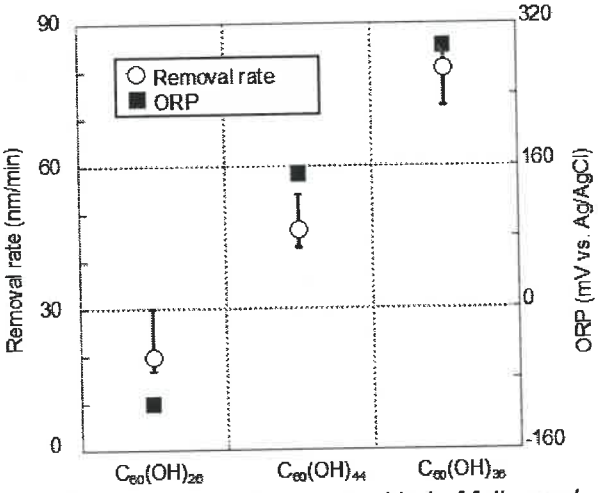

FIGURE 2. Relationship among kind of fullerenol, ORP value, and removal rate of slurry.

chemical removal of the surface. SEM observation is carried out after polishing to evaluate the change in the surface condition.

RESULT AND DISCUSSION

Reactivity of Fullerenol and Removal Rate

Figure 2 shows the CMP removal rates, type of fullerenol, and ORP value of fullerenol solution. Positive and negative ORPs imply that the material has oxidative and reduction power, respectively. It is important factor for Cu-CMP because of chemical reaction with copper is oxidation-reduction reaction. ORP value of fullerenol solutions are determined by Takaya et al[1]. The copper removal rate increases with the ORP value of fullerenol. $C_{60}(OH)_{36}$ based slurry has highest removal rate around 80 nm/min. The correlation between the ORP value and the removal rate indicates that the chemical reactivity of fullerenol as an oxidizer is related to the mechanism of copper removal using fullerenol in the CMP process.

Surface Composition

Figure 3 shows the XPS spectra of the 2p orbital of Cu for a copper surface dipped in chemical solution containing fullerenol and hydrogen peroxide. Each spectrum shows absorptions at 933.7, 942.5, 953.5 and 961.7 eV, indicating that the copper surface is oxidized to cupric II compound[2]. Spectra of the surface dipped in $C_{60}(OH)_{36}$ and $C_{60}(OH)_{44}$ are much weaker than that of $C_{60}(OH)_{26}$. It indicates that there are other type of atoms on the surface of former.

Figure 4 shows the XPS spectra of the 1s orbital of C. Spectra of the surface dipped in $C_{60}(OH)_{36}$ and $C_{60}(OH)_{44}$ shows absorptions at both 284.6 and 286.4 eV. The former peak indicates nonoxygenated carbons, C-C and C=C bonds in the fullerenol. Absorption with a binding energy higher than that of nonoxygenated carbon corresponds to oxygenated carbon. The latter peak indicates single bond monooxygenated carbons, C-O bond[2], which exists in fullerenol. Spectra of the surface dipped in $C_{60}(OH)_{26}$ shows a weak absorption comparing to other spectra at 284.6 eV and no peak at 286.4 eV, indicating carbon contamination.

These spectra indicate that $C_{60}(OH)_{36}$ and $C_{60}(OH)_{44}$, which have high chemical reactivity, react with copper to form cupric II - fullerenol complex. $C_{60}(OH)_{26}$ cause no reaction with copper and CuO is formed by the oxidation of hydrogen peroxide.

Appearance of the Surface Layer

Table 2 shows surface composition, SEM images of the surface and cross section after dipping in each solution containing fullerenol and hydrogen peroxide. The figure indicates that the sample dipped in $C_{60}(OH)_{36}$ and $C_{60}(OH)_{44}$ solution has cracks around its surface. It indicates that the layer on the surface is brittle layer. Particularly, there are many cracks on the surface dipped in $C_{60}(OH)_{36}$. The layer on the surface is determined to be a cupric II-fullerenol complex layer from the result of XPS analysis.

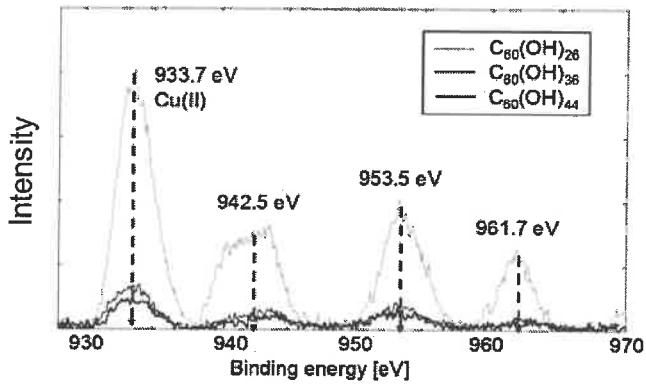

FIGURE 3. XPS spectrum of 2p orbital of Cu for a copper surface dipped in fullerenol ($C_{60}(OH)_{26}$, $C_{60}(OH)_{36}$, $C_{60}(OH)_{44}$) and hydrogen peroxide.

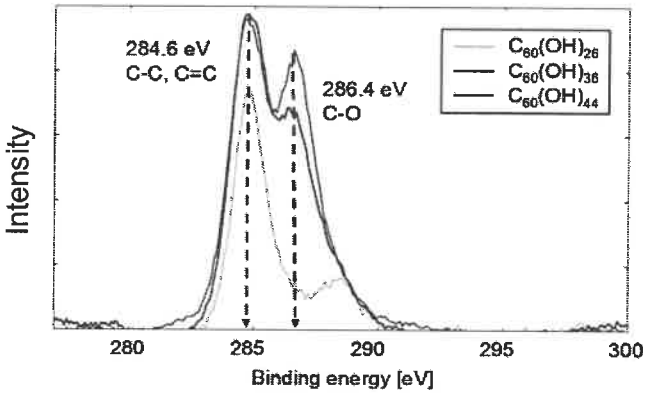

FIGURE 4. XPS spectrum of 1s orbital of C for a copper surface dipped in fullerenol ($C_{60}(OH)_{26}$, $C_{60}(OH)_{36}$, $C_{60}(OH)_{44}$) and hydrogen peroxide.

TABLE 2. Surface composition, SEM images of the surface and cross section after dipping in each solution containing fullerenol and hydrogen peroxide.

Chemical solution	$C_{60}(OH)_{26}$ and hydrogen peroxide	$C_{60}(OH)_{36}$ and hydrogen peroxide	$C_{60}(OH)_{44}$ and hydrogen peroxide
Surface composition	CuO	Cu(II)-fullerenol complex	Cu(II)-fullerenol complex
SEM micrograph of the surface	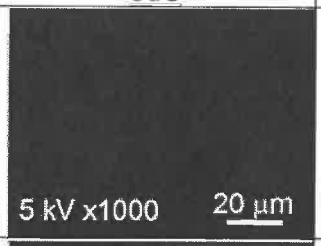	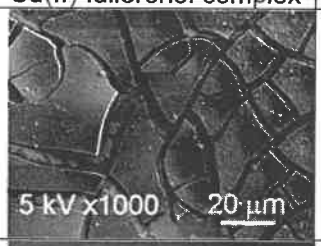	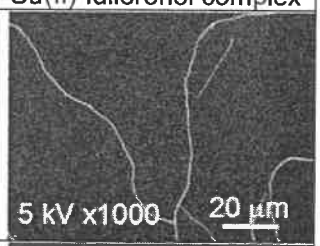
SEM micrograph of the cross section	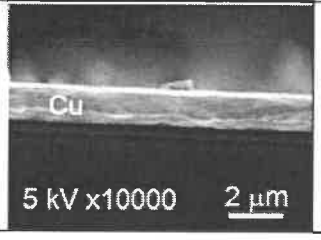	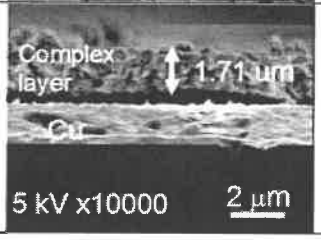	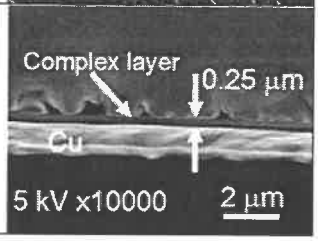

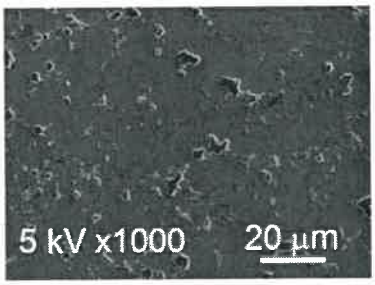

FIGURE 5. SEM image of the surface after polishing.

Thickness of the complex layer on the surface is determined by SEM image of the cross section as 1.71 μm in the solution containing $C_{60}(OH)_{36}$ and 0.25 μm in the solution containing $C_{60}(OH)_{44}$ .The complex layer is undetectable on the surface dipped in the solution containing $C_{60}(OH)_{26}$. Thickness of the surface layer increases with the copper removal rate and ORPs of fullerenol.

Mechanical Removability

Figure 5 shows an SEM image of the surface after polishing of a wafer dipped in a solution of 0.1 wt% $C_{60}(OH)_{36}$ and 0.8 wt% hydrogen peroxide. The figure shows that many parts of the cracked film on the surface are removed. This implies that the cupric II - fullerenol complex layer on the copper surface, which has many cracks, is easily removed by the frictional force between the polishing pad and the copper surface.

Role of Fullerenol

$C_{60}(OH)_{36}$ and $C_{60}(OH)_{44}$, which have high chemical reactivity, react with copper to form cupric II - fullerenol complex layer. It is brittle layer having many cracks on the surface. It can be easily removed by the frictional force between the polishing pad and the copper surface.

The removal mechanism of matter using water soluble fullerenol for copper removal is as follows. Fullerenol and hydrogen peroxide react with copper to form cupric II - fullerenol complex. The complex layer on the surface is a brittle layer. This layer is removed by the frictional force between the polishing pad and the copper surface. The copper surface is exposed to the slurry. The cupric II - fullerenol complex brittle layer is formed by the chemical reaction again. Copper is removed by repeating this procedure. This is consistent with the result that the copper removal rate increases with the ORP value of fullerenol solution, indicating the chemical reactivity of fullerenol. Chemical reactivity of fullerenol to form cupric II - fullerenol complex brittle layer is the key factor of CMP using fullerenol.

In the experiment of this paper, copper is dipped for 1 hour to grow surface complex layer detectable. However, during the polishing process, surface layer formation and its removal are occurred in significantly short time. It shows that the thickness of surface complex layer formed during the polishing process should be significantly thin. This is one of the reason that fullerenol based slurry shows high planarization efficiency.

CONCLUSION

In order to clarify the use of water-soluble fullerenol for copper removal, surface state is investigated by XPS analysis and SEM observation to the copper dipped with chemical solution containing fullerenol. XPS analysis shows that $C_{60}(OH)_{36}$ and $C_{60}(OH)_{44}$, which have high chemical reactivity, react with copper to form cupric II - fullerenol complex. $C_{60}(OH)_{26}$ cause no reaction with copper. The polishing experiment to the dipped surface shows that the cupric II - fullerenol complex layer is brittle and exhibits good removability. This brittle nature of the surface layer enables material removal to proceed rapidly. This is consistent with the result that the copper removal rate increases with an increase in the chemical reactivity of fullerenol. Chemical reactivity of fullerenol to form cupric II - fullerenol complex brittle layer is the key factor of CMP using fullerenol.

ACKNOWLEDGEMENT

This research was supported by the Ministry of Education, Science, Sports and Culture, Grant-in-Aid for Scientific Research (B), 21360064, 2010.

REFERENCES

[1] Takaya Y, Tachika H, Hayashi T, Kokubo K. and Suzuki K. Performance of water-soluble fullerenol as novel functional molecular abrasive grain for polishing nanosurfaces. CIRP Annals - Manufacturing Technology. 2009; 58: 495-498.

[2] Moulder J.F, Stickle W.F, Sobol P.E and Bomben K.D. Handbook of X Ray Photoelectron Spectroscopy, Physical Electronics. 1995.

VIBRATION ATTENUATION IN OPTICAL PITCH

Mohammad Mainuddin[1], and Brigid A. Mullany[1]
[1]Department of Mechanical Engineering and Engineering Science
University of North Carolina at Charlotte
Charlotte, NC, USA

INTRODUCTION

Optical polishing pitch has been used to obtain high quality optical surface finishes with little subsurface damage. A pitch tool consists of a metal platen coated with a layer of polishing pitch whereby pitch is a viscoelastic material naturally derived from tree resin [1]. Synthetic versions are also produced [2]. Polishing with pitch was first introduced by Sir Isaac Newton in the 1700's and has since been used to produce high quality optical surfaces [3]. Pitch polishing can generate surfaces with roughness and flatness values less than 1 Å RMS and $\lambda/20$ respectively [4]. As pitch is viscoelastic it has the ability to flow (creep) with time [5], enabling the pitch to deform and make good contact with the work piece. The influence of temperature and preparation methods on its long term response has been described in several published papers [1, 6, and 7]. Until recently, the short term (millisecond domain) dynamic response of pitch has not received much attention. Previous work by this research group utilized an impact frequency response test to evaluate the effect of pitch type and age on the transient responses [8, 9]. These tests demonstrate that each grade (hardness) and type of pitch (natural or synthetic) has unique dynamic properties. Age also affects the response of natural pitches.

During polishing the system is more likely to be subjected to steady state than transient vibrations, i.e. consistent machine/process vibrations. Are all vibrations transferred through the pitch to the workpiece surface? Do vibrations have an impact on polishing outcomes such as roughness and material removal rates (MMRs)? Recent work done by the group utilized a shaker table (described later) to impart steady state vibrations into the pitch sample across a wide frequency bandwidth (50 Hz - 16 kHz) [9]. Initial results revealed that all vibrations input into the pitch sample were transmitted through the pitch. The transmitted process vibrations do not undergo any attenuation, but are somewhat amplified as shown in Figure 1 [10]. Vibration transmission through the pitch should be controllable if their affect on MRRs and surface finishes are to be determined.

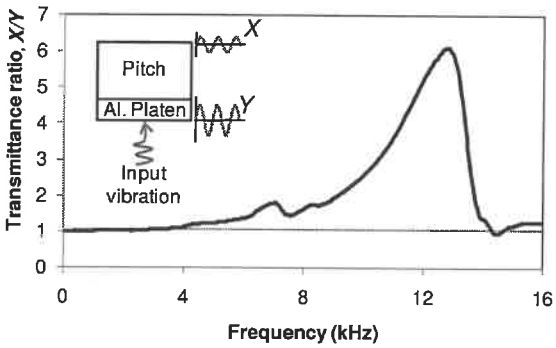

*FIGURE 1. Transmission of vibrations through pitch (*Acculap™VeryFirm*) [10].*

As early testing indicated all pitches failed to attenuate vibrations a passive damping material is required. Nine different materials (vinyl, gum, neoprene, viton, polyurethane, nitraile (Buna N), rubber, cork, and lead) were evaluated on the shaker table to assess their ability to provide attenuation between 50 Hz and 16 kHz. Completed experiments show that at lower frequencies (50 Hz to 450 Hz) the input vibrations are somewhat amplified as they pass through the passive damping sheets, but at higher frequencies (above 550 Hz) the input vibrations are significantly attenuated. The following sections provide more details on the materials tested, the experimental set up, and the results.

SAMPLE PREPARATION

In this experimental investigation, two different sample configurations are tested. The first configuration, Type-A, identifies the damping quality of different passive damping materials. It consists of the passive damping material adhered to an aluminum platen (6 mm thick and 50 mm in diameter), see Figure 2(a). An alternative version of Type-A samples has an additional thin sheet of lead attached to the damping material to increase the mass of the sample. The second configuration, Type-B,

consists of a Type-A samples with 50g of pitch attached the damping material, see Figure 2 (b). A parameter termed as Inverse Quality Factor, Q^{-1} [11] is used to identify the damping quality of different materials. Higher Q^{-1} value means higher damping ability.

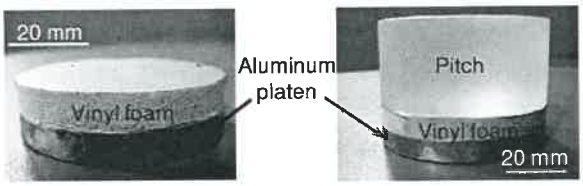

a b

FIGURE 2. (a) Type-A, and (b) Type –B Sample.

To generate Type-A samples, different damping sheets are cut to size and glued (3M Super 77 Aerosol Spray Adhesive) on to the aluminum platen. Acculap™VeryFirm pitch is used in Type-B samples. A defined mass (50g) of melted pitch is poured into a cylindrical shaped silicon molds which contains the platen and passive damping material as its base. Type-B samples are cooled overnight before removing from the molds. The evaluated Type-A and Type-B samples are listed in Table 1 and Table 2. While more materials than listed in Table 1 were tested, preliminary testing eliminated them from full testing.

TABLE 1. Evaluated Type-A foam samples.

Type-A	
Name	**Damping material**
A1	3.18 mm Vinyl Extra Soft
A2	3.18 mm Vinyl Soft
A3	3.18 mm Gum Extra Soft
A4	3.18 mm Gum Soft
A5	3.18 mm Polyurethane Extra Soft
A6	3.18 mm Viton Extra Soft
A7	3.18 mm Neoprene Extra Soft
A8	6.35 mm Gum Extra Soft
A9	1.1 mm lead sheet (≈ 24g) between 3.18 mm Vinyl Extra Soft layers
A10	1.6 mm lead sheet (≈ 35g) between 3.18 mm Vinyl Extra Soft layers
A11	9.53 mm Vinyl Soft
A12	6.35 mm Vinyl Soft
A13	12.7 mm Gum Soft
A14	6.35 mm Gum Soft
A15	3.18 mm lead sheet (64g) on A12

TABLE 2. Evaluated Type-B samples.

Type-B	
Name	**Damping material**
B1	Acculap™VeryFirm on A12
B2	Acculap™VeryFirm on A15

Samples A1 – A7 have same thickness and used to identify the damping quality of different materials. Test results will show (Figure 5) that Vinyl Soft and Vinyl Extra Soft foams have the best damping quality among the tested materials. Samples A8 – A15 evaluated different thicknesses of the Vinyl and Gum foams to determine if the Q^{-1} could be further improved. Samples with added lead sheeting are also evaluated.

EXPERIMENTAL SETUP AND TEST PROCEDURE

The test setup consists of a shaker table (BK Vibration Exciter Type 4809) driven by a HP35639A dynamic signal analyzer (DSA). The shaker table can vibrate up to 20 kHz with a maximum displacement of 8 mm. The sample under investigation is screwed onto the shaker table. The vibrations entering and exiting the sample are monitored by two accelerometers (PCB 352B10) that operate up to 17 kHz. See figure 3 for a schematic of the set-up, figure 4 illustrates photos of the shaker table and mounted sample.

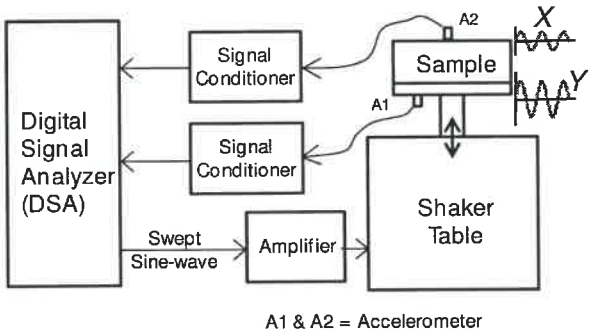

FIGURE 3. Block diagram of the test setup.

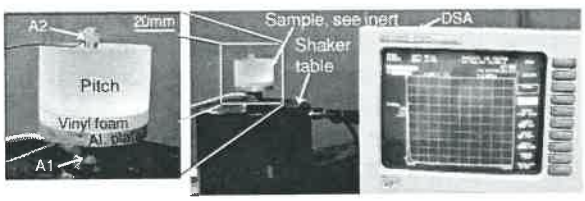

FIGURE 4. Close up of sample mounted on shaker table.

In this investigation the samples were subjected to a swept sine wave input (50 Hz to 5 kHz, preliminary tests shown that above 5 kHz all input vibrations are damped out). Step increments were 12.375 Hz. Typical vibration amplitudes range from 30 μm to 2.5 nm. The resulting accelerometer readings are monitored by the DSA, and the ratio of the top accelerometer (A2) output (*X*) to the bottom accelerometer (A1) output (*Y*), i.e. the vibration transmittance (*X/Y*) is plotted versus the input frequency. The results from testing all samples listed in Table 1 and Table 2 are given in the following section.

RESULTS AND ANALYSIS

In most cases multiple samples of each material were evaluated. Each curve in the graphs represents a samples' typical response. Note for the sake of clarity the full frequency response (up to 5 kHz) is not illustrated in the graphs. In all cases with increased frequency (above 1450 Hz) the transmittance continued to decay to less than 0.02. Samples were evaluated with respect to the Q^{-1} factor, maximum vibration amplification, and the frequency at which $X/Y <$ 0.5 (50% attenuation).

Results for Type-A samples

Figure 5 depicts the response curves for samples A1 to A7.

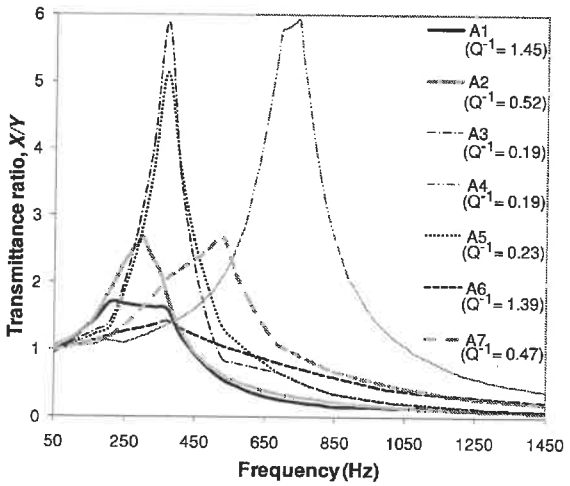

FIGURE 5. Vibration transmission for different damping materials.

Calculation of the Q^{-1} factor from the experimental data revealed that sample A1 (Vinyl Extra Soft) has the highest Q^{-1} value (1.45), and 50% attenuation was attained at the lowest input frequency (540 Hz). While the Q^{-1} value for A2 (Vinyl Soft) was not as high (0.52), it did provided 50% attenuation at a similar frequency to A1 and thus is considered for further evaluation. From an application point of view A2 is preferred over A1 as it is considered more mechanically robust and not as compressive as A1 suggesting it would be better suited for use on an actual polishing tool. Sample A6 has a high Q^{-1} factor but is not considered further at this point for two reasons, firstly, 50% attenuation doesn't occur until 925 Hz and secondly, like Vinyl Extra Soft it is also considered too soft to withstand the cyclic loading and unloading of an actual polishing process.

The frequency response curves for different thickness soft foams and samples with added lead sheeting are given in Figure 6. Samples A11, A12, A15 are of most interest. The shapes of the frequency responses for both Vinyl Soft samples (A11 and A12) are very similar, as are their Q^{-1} values (0.81 and 0.82 respectively). The only difference between the samples is their thickness. From a practical standpoint the thinner A12 (6.35 mm) is preferred over the thicker A11 (9.53 mm) sample. The thinner sample is expected to be easier implement on actual tooling. The thinner sample is also cheaper.

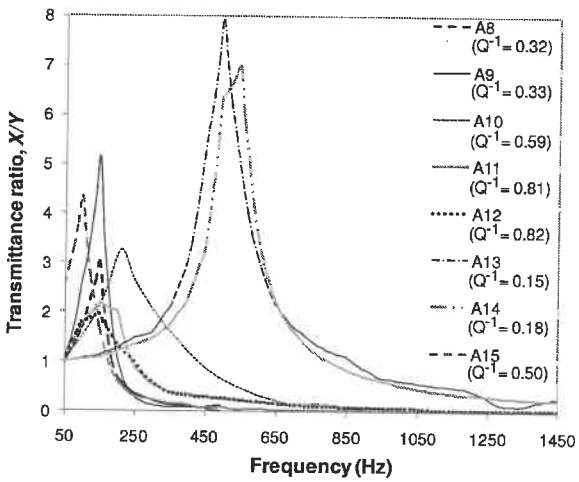

FIGURE 6. Vibration transmission curves for different thicknesses and variations of samples.

Sample A12 has a natural frequency at 149 Hz with a peak amplification value of 1.97 and 50% attenuation observed at 315 Hz. Sample A15 is the same as A12 but will an additional lead disk (3.18 mm thick, 64g) adhered to the top surface. As expected the additional mass reduced the

samples' natural frequency from 315 Hz to 99.5 Hz, with a maximum amplification value of 4.35. While this value is significantly higher than that obtained with A12, the sample is remains of interest as 50% attenuation is observed at the lower frequency of 212 Hz. Both A12 and A15 were chosen for testing with pitch.

Results for sample Type-B

Figure 7 compares the dynamic responses of samples A12 to B1, and A15 to B2. Addition of the pitch onto the sample does alter the responses some-what, however the overall trends remain the same. Pitch samples without an intermediate damping sheet showed no vibration attenuation below 10 kHz [10], refer back to figure 1. In addition to providing attenuation the damping materials reduce the maximum vibration amplification, the maximum *X/Y* for sample B1 and the sample in figure 1 are approximately 3 and 6 respectively. This shows the ability of this approach to control vibration transmission through the pitch to the work piece.

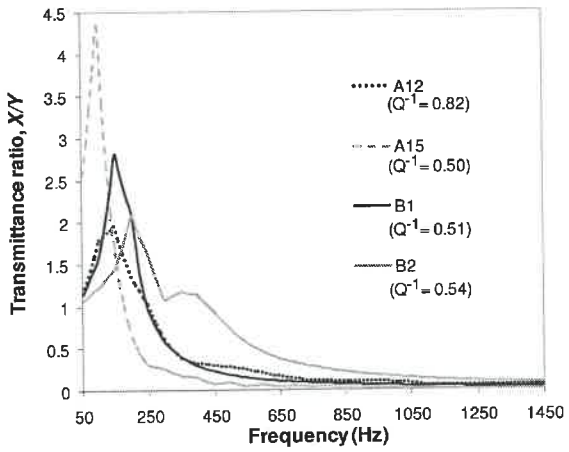

FIGURE 7. Comparison between Type-A and Type-B samples.

SUMMARY AND FUTURE WORK

Passive damping materials can be used between the pitch and the metal platen to reduce vibration transmission. Vinyl foam is the best damping material among those tested. Increasing the overall sample mass through the addition of lead sheeting, further reduced vibration amplification (sample B2 versus B1). Experimental work is underway to test the damping materials on actual pitch tools and to determine if the process vibrations have a significant influence on the polishing outcomes (roughness and MMRs).

ACKNOWLEDGEMENTS

This material is based upon the work supported by the National Science Foundation under Grant No. 0747637. Any opinions, findings, and conclusions or recommendations expressed in this material are those of the authors and do not necessarily reflect the views of the National Science Foundation.

REFERENCES

[1] Gillman B, Tinker F. Fun facts about pitch and the pitfalls of ignorance. Proceedings of SPIE. 1999; 3782: 72-79.

[2] Sutton S. Development of new synthetic optical polishing pitches. In: *Optical Society of America.* 2004.

[3] Newton I. Opticks. Reprint of the 4th edition. 1931; 104.

[4] Leistner A. J. Fabrication and testing of precision spheres. Metrologia. 1992; 28: 503-506.

[5] Findley W. N, Lai J. S, K Onaran. Creep and relaxation of nonlinear viscoelastic materials. Introduction to linear viscoelasticity. North-Holland Publishing Company. New York: 1976.

[6] Brown N.J. Optical polishing pitch. Preprint of a paper prepared for submission to the Optical Society of America workshop on Optical Fabrication and Testing. Nov. 10-12, 1977; San Mateo, CA.

[7] DeGroote J.E, Jacobs S.D, Gregg L, Marino A, Hayes J. Quantitative characterization of optical polishing pitch. Proceedings of SPIE. 2001; 4451: 209–221.

[8] Mullany B, Corcoran E. An innovative look at precision polishing tools. Proceedings of 3rd CIRP International Conference on High Performance Cutting, Dublin, Ireland: June 12-13, 2008; 589-598.

[9] Mullany B, Turner S. Optical polishing pitches: Impact frequency responses and indentation depths. Applied Optics. 2010; 49-3: 442–449.

[10] Mullany B, Beaman J. The Response of Pitch to Higher Frequency Vibrations. Topical Meeting of the Optical Fabrication & Testing (OF&T). Jackson Hole, WY, OThB5, June 2010.

[11] Graesser E. J, Wong C. R. The Relation of Traditional Damping Measure for Materials with High Damping Capacity: A Review. ASTM Special Technical Publication. 1992; 1169: 316-343.

INCREASES IN CORROSION RESISTANCE AND WATER REPELLENCY OF METAL MOLD SURFACE BY EB POLISHING

Akira OKADA [1], Yoshiyuki UNO [1], and Kensuke UEMURA [2]
[1]Graduate School of Natural Science and Technology
Okayama University
Okayama City, Okayama, Japan
[2]R&D Center
Nagata Seiki
Tsubame, Niigata, Japan

INSTRUCTIONS

The surface finishing of metal molds is generally done by hand lapping in order to attain small surface roughness without micro cracks. However, this process requires high technical skills and takes a long time, which leads to high cost. Therefore, high efficient finishing process is strongly required.

In our previous papers, a new surface finishing method for metal molds by large-area electron beam irradiation, namely EB polishing was proposed [1-3]. In the EB polishing method, an EB with a high energy density can be irradiated without focusing the beam, and EB with a maximum diameter of 60 mm can be used for instant melting of metal surface.

The experimental results in the previous papers clarified that the surface roughness on wide area uniformly decreases to less than 1μmRz in a few minutes under appropriate conditions. Even if the surface tilts against EB irradiating direction, the surface roughness could be well improved, which means that in the case of small mold with tilting surfaces, the smoothing of the whole surface is possible without moving or tilting the mold.

Furthermore, a very thin resolidified layer is formed on the surface by EB polishing. However, the structure of the resolidified layer has not yet been made clear sufficiently. Neither has the surface characteristics affecting the life of metal molds, such as corrosion resistance, repellency, wear resistance and so on.

In this study, the surface structure of EB polished metal mold steel SKD11 was observed by TEM, and also component analysis was carried out by EDX. As one of the important surface characteristics for long life of metal mold, resistance to corrosion is quantitatively evaluated by measuring the anode polarization current density. The effects of EB polishing condition on the corrosion resistance are also discussed. Furthermore, water repellency of EB polished surface was tested by measuring the contact angle of water.

LARGE-AREA EB IRRADIATION METHOD

Figure 1 schematically illustrates the large-area EB irradiation equipment and the generation mechanism for the Large-area EB [4] [5]. Unlike conventional EB irradiation performed in vacuum, argon gas of about 10^{-2} Pa is mixed beforehand in the chamber. Firstly, a magnetic field is generated by the solenoid coil set at the outer side of chamber. When the magnetic field achieves a maximum intensity, a pulse voltage is applied to the ring anode. The electrons generated by the Penning effect move towards the anode. A Lorentz force is simultaneously added to the electrons, and so they move spirally. Next, argon gas atoms are ionized by repeated collision with electrons, and plasma generates near the anode. When the plasma intensity reaches a maximum, a pulse voltage is applied to the cathode, and the electrons are accelerated by high electric field due to the electric double layer formed near cathode. Then, EB with high

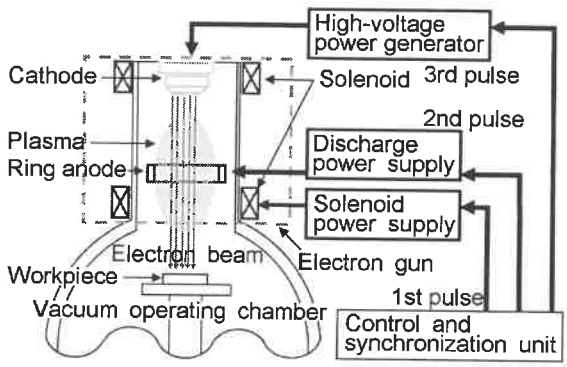

FIGURE 1. Large area EB irradiation equipment

energy density is irradiated onto the workpiece surface.

The plasma is effective in sustaining the EB for sufficient time. That is, by passing through the plasma region, the Coulomb's force between electrons is decreased and the linearity of the EB can be improved. In this system, the EB irradiation is carried out in a series of pulses. By this mechanism, high energy density EB can then be generated without concentrating the beam. Thus EB with a maximum effective diameter of about 60mm has an energy density high enough to melt or evaporate metal surface instantly.

EB polishing conditions are shown in Table 1. The EB irradiation time of one pulse is only 2μs, and the pulse frequency is set to 0.2Hz. Metal mold steel, SKD11 in JIS specifications is prepared as the workpiece material. The surface is beforehand ground, and the surface roughness is arranged to about 3μmRz.

SURFACE STRUCTURE

EB irradiating pulse duration is only a few micro seconds. Therefore, the effect of heat conduction on the surface is small, and so little heat energy penetrates into the material. Then the material removal by melting and evaporation occurs adjacent to the surface. Consequently, very thin resolidified layer is formed on the EB polished surface.

The resolidified layer formed by EB polishing is considered to have a different structure from that of the matrix. Figure 2 shows the energy distribution type X-ray spectroscopy (EDX) of the surface before and after EB polishing. As can be seen from the figure, Cr and O peaks become higher than those before EB polishing. It means that contents of Cr and O increase on EB polished surface. SKD11 generally includes large size chromium carbide and/or chromium oxide in the matrix, It is guessed that the chromium might have been uniformly rearranged and resolidified on the surface by EB polishing.

In order to investigate the surface structure, observation by a transmission electron microscope (TEM) was carried out. Figure 3 shows the micrographs of cross sections and the diffraction patterns for the area just below the surface. At the surface before EB polishing, large crystal grains can be clearly observed. For EB polished surfaces, the crystal grains become small and less distinct. That is, a marked change in surface structure occurs. On the other hand, the diffraction patterns indicate that the crystal structure is retained even after EB polishing.

TABLE 1. EB polishing conditions

Acceleration *voltage*	*V*	30 kV
Pulse duration	*Dp*	2 μs
Pulse frequency	*Fp*	0.2 Hz
Energy density	*Ed*	3, 7 J/cm^2
Number of pulses	*N*	1 - 50 shot

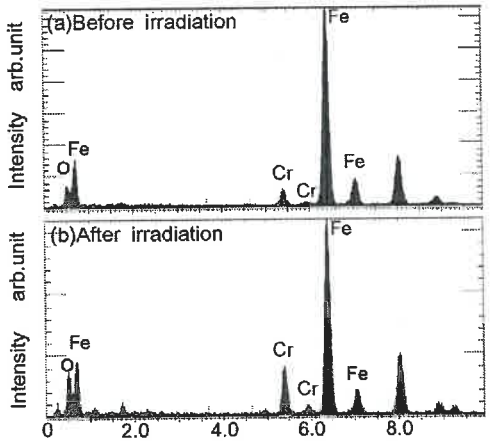

FIGURE 2.EDX spectra of surface before and after EB polishing

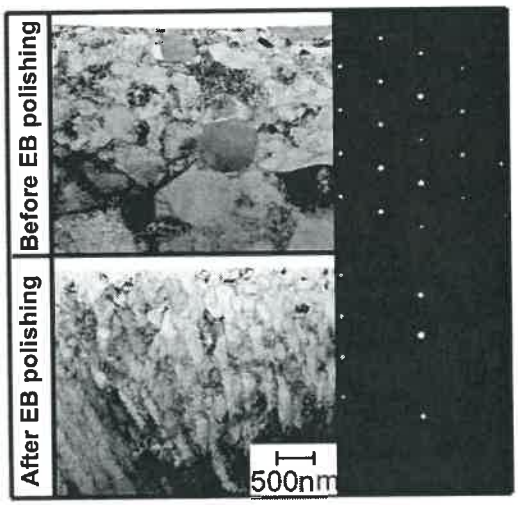

FIGURE 3. TEM images and diffraction patterns

CORROSION RESISTANCE

Figure 4 shows the EB polished and non-EB polished samples left for 1 year in the atmosphere. The center circular part of the workpiece is the EDMed surface and the surrounding part is the ground one. In the case of non-EB polished workpiece, the ground surface has extensively been rusty. Moreover,

the EDMed surface has been somewhat rusty, although the EDMed surface generally has high corrosion resistance. On the other hand, in the case for EB polished sample, there is no rust at all, where very glossy surface could be kept.

In order to accurately evaluate the corrosion resistance of EB irradiated surface, the anodic polarization curves are measured by an electrochemical analysis system. The electrolyte is 3% NaCl solution.

Figure 5 shows the anodic polarization current density curves of EB polished surfaces with the energy density 3J/cm^2 and the surface before EB polishing. As shown in the figure, the anodic polarization current density increases with the potential in any surfaces. The equilibrium potentials for EB polished surface are larger than that for non-EB polished surface. The current densities for EB polished surface are smaller than those for the non-EB polished surface at all potentials. Furthermore, the current density becomes smaller with an increase of number of pulses in EB polished surfaces. That is, corrosion resistance can be improved by EB polishing, and it varies with the number of EB irradiation.

Figure 6 shows the anodic polarization current density curves in case of Ed=7J/cm^2. Also under this condition, the corrosion resistance becomes higher by EB polishing. Moreover, it is found that the current density for 7J/cm^2 becomes much higher than that for 3J/cm^2. The remarkable improvement of corrosion resistance is caused by the formation of the uniform chromium layer on the EB polished surface as discussed above.

WATER REPELLENCY

The contact angle of water droplets over EB polished surface was tested in order to evaluate the water repellency. A water-drop of 2mm in diameter is put on the workpiece surface using a syringe, and the height and radius of the drop were measured through a microscope. The contact angle θ is given in the following.

$$\theta=2\tan^{-1}(h/r) \qquad (1)$$

Figure 7 shows the variations of contact angle with energy density of EB. The contact angle for EB polished surface is larger than that for ground SKD11 surface 75°, and hand polished one 77° for all EB conditions. In EB polished surfaces, the contact angle becomes larger with increasing the number of EB pulses. However, it does not change so much by the energy density. From these results, the water repellency of metal mold surface can be improved by EB

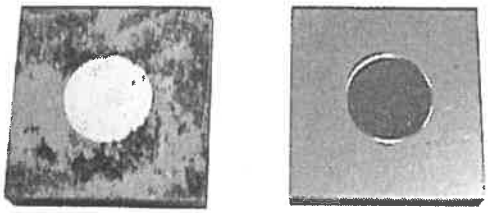

(a)Non-EB polished (b)EB polished

FIGURE 4. Workpieces left for 1 year in atmosphere

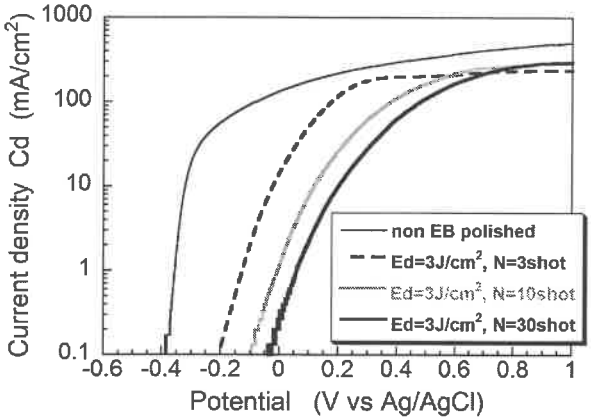

FIGURE 5. Anodic polarization current curves (Ed=3J/cm^2)

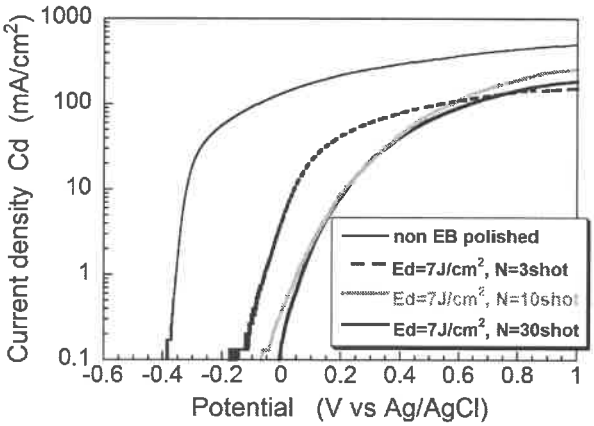

FIGURE 6. Anodic polarization current curves (Ed=7J/cm^2)

polishing, and it can be controlled by the number of EB irradiation.

The improvement of water repellency by EB polishing might be caused by the increasing of the Cr component on the surface as shown in Figure 2. According to Cassie's law, the contact angle θ^* for a liquid on a composite surface

consisting of two components is expressed as follows,

$$\theta^*=\varphi_1\cos\theta_1+\varphi_2\cos\theta_2 \quad (2)$$

where, θ_1 is the contact angle for the surface of component 1, φ_1 is the area ratio of component 1 on the composite surface. θ_2 is the contact angle for component 2, and φ_2 is the area ratio of component 2.

Figure 8 shows the contact angles of water droplets on pure Fe, pure Cr and SKD11 surfaces. The contact angle on Cr surface is the highest, and that on Fe surface is the lowest. The contact angle for SKD11 is between those for Fe and Cr, which corresponds well with Cassie's law. The contact angle for SKD11 becomes larger by EB polishing, because Cr content becomes higher on the surface by EB polishing. Also, it exceeds that for Cr. The increase in water repellency by EB polishing is caused not only by the increase of Cr content on the surface but also by the surface structure changes shown in Figure 3.

CONCLUSIONS

In this study, the structure of the resolidified layer formed on the EB-polished metal mold steel surface was analyzed, and the surface characteristics such as corrosion resistance and water repellency were also evaluated. Main conclusions obtained are as follows.

(1) In thin resolidified layer formed on metal mold steel by EB polishing, the crystal grain size becomes small and chromium is uniformly rearranged in the layer.
(2) The corrosion resistance and the water repellency of metal mold surface can be greatly improved by EB polishing, since the surface structure changes and Cr content increased on the surface.
(3) The corrosion resistance and the water repellency of EB polished surface vary with EB polishing conditions.

ACKNOWLEDGEMENT

This work was financially supported by Grant-in-Aid for Scientific Research B (No. 20360069), Japan Society for the Promotion of Science.

REFERENCES

[1] Uno Y, Okada A, Uemura K, Raharjo P, Furukawa T, Karato K. High Efficiency Finishing Process for Metal Mold by Large-area Electron Beam Irradiation. Precision Engineering. 2005; 29:449-455.

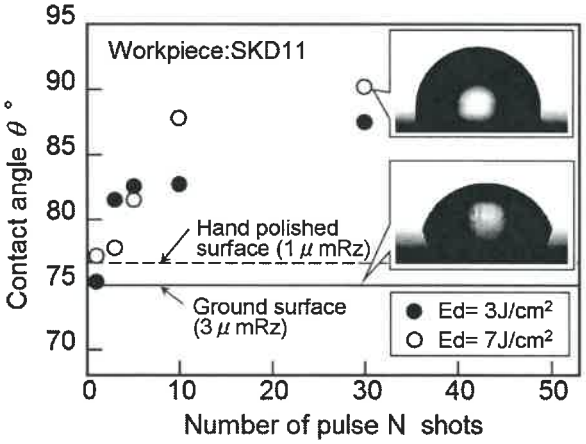

FIGURE 7. Contact angle of water droplet

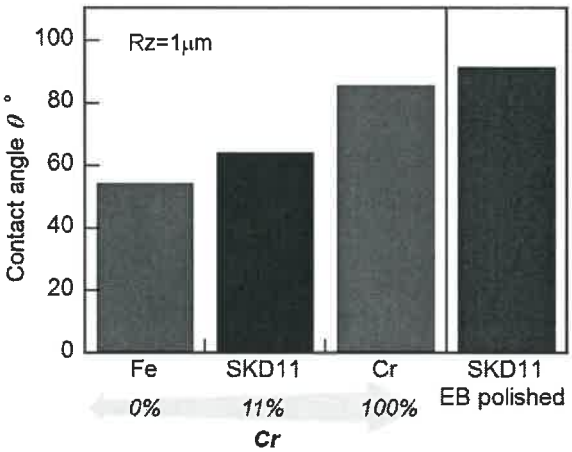

FIGURE 8. Contact angles of water droplets on surface for various materials

[2] Uno Y, Okada A, Uemura K, Raharjo P. Method of Surface Treatment of a Die by Electron Beam Irradiation and the Treated Die. 2003: Patent US2003/0183743.
[3] Okada A, Uno Y, Daichi Y, Sano S. High Efficiency EB Polishing of Metal Mold. Proc. of the 15th ISEM. 2007: 409-414.
[4] Proskurovsky D I, Rotshtein V P, Ozur G E. Use of Low-energy, High-current Electron Beams for Surface Treatment of Materials. Surface and Coating Technology. 1997; 96:117-122.
[5] Proskurovsky D I, Rotshtein V P, Ozur G E, Ivanov Y F, Markov A B. Physical Foundations for Surface Treatment of Materials with Low Energy. High Current Electron Beams, Surface and Coating Technology. 2000;125:49-56.

NEW METHOD FOR DETERMINATION OF VOLUMETRIC POSSITIONING ERROR

Ba Chinh Bui[1,2], Jooho Hwang[1], Chan-Hong Lee[1], Chun-Hong Park[1]

[1]Ultra-Precision Machine Systems Research Team, Nano Convergence & Manufacturing Systems Research Division, Korea Institute of Machinery and Materials, 104, Sinseongno, Yuseong-Gu, Daejeon 305-343, South Korea
[2]Department of Nano-Mechatronics, Korea University of Science and Technology,113,Gwahangno, Yuseong-Gu,Daejeon 305-333, South Korea

INTRODUCTION

The volumetric error of a CNC machine tool or a CMM is determined by 21 errors, including 3 linear errors, 6 straightness errors, 3 perpendicular errors, 9 angular errors and non-rigid body errors of the machine tool. Measuring all of these errors with direct use of laser interferometer and other equipments is very complicated and time consuming. Hence, as many as 21 separate setups and measurements are needed for the linear, straightness, angular and perpendicular errors. In recent years, many researchers have reported on the evaluation of volumetric errors such as a conventional method namely diagonal measurement has been recommended for quick check on the volumetric errors of the machine [1, 2]. However, it is impossible to distinguish among the linear, straightness and perpendicular errors of each axis from the results of diagonal tests; thus, there is not enough information to determine which error is the main source of volumetric errors.

Recently, a vector method developed by Wang can overcome the disadvantage of conventional diagonal method and provide linear accuracy, straightness and perpendicular of X, Y, Z from only 4 step-diagonals data [3]. However, this method still has many limitations as identified by Chapman that errors in the alignment of flat mirror and laser beam will introduce additional errors which cannot be separated from linear displacement errors in the axes of machine [4].

Therefore, in this paper, a new method namely Multi Diagonal Method (MDM) is introduced. In this method, the laser interferometer and circular mirror with 4 body conventional diagonals and 2 modified diagonal measurements are used, thanks to which the linear, straightness errors of each axis and perpendicular errors can be distinguished without the limitations of vector method.

NEW DIAGONAL METHOD

The Multi Diagonal Method is one of the four body diagonals as Fig.1, which is used as reference and then compared with other diagonal measurements in which x and y are modified Δx and Δy as Fig.2 and Fig.3. The equipments are used in this method are the same as the equipments are used in conventional body diagonal measurement which is recommended by the B5.57 and ISO 230 standards [1, 2].

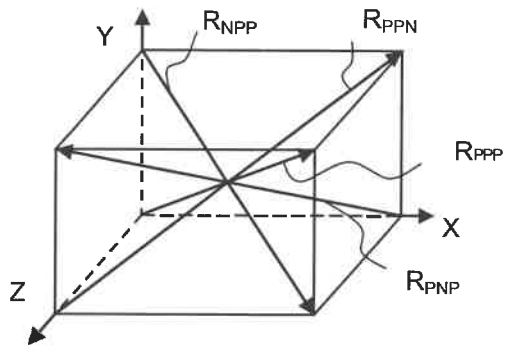

FIGURE.1. Four body diagonal directions

The purpose of this method is to determine the real angle between x, y, z axis and reference diagonal and then use decomposition to get real volumetric including R_{xreal}, R_{yreal} ,R_{zreal}.

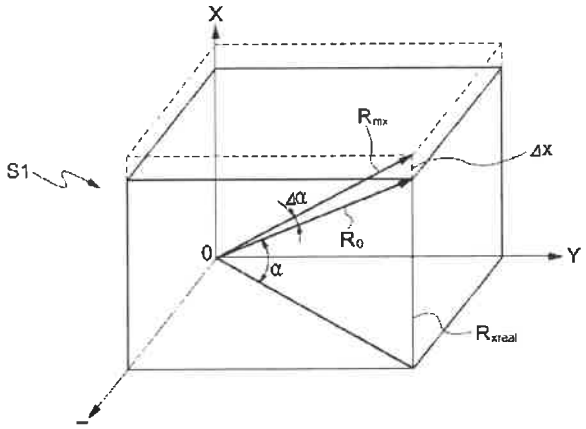

FIGURE.2. Modified Diagonal with changing Δx

From Fig.2 the angle α can be calculated as:

$$R_{xreal} + \Delta x = R_{mx} \sin(\alpha + \Delta\alpha) \quad (1)$$

From Eq. (1), it becomes

$$R_{mx} \sin\Delta\alpha \cos\alpha - (R_0 - R_{mx} \cos\Delta\alpha)\sin\alpha = \Delta x \quad (2)$$

Where the Δα is identified by using cosine law

$$\Delta\alpha = \cos^{-1}\left(\frac{R_0^2 + R_{mx}^2 - \Delta x^2}{2R_0 R_{mx}}\right) \quad (3)$$

By solving Eq. (2), the angle α is determined as:

$$\alpha = \frac{\pi}{2} - \sin^{-1}\left(\frac{R_{mx} \sin\Delta\alpha}{\Delta x}\right) \quad (4)$$

Where:

R_0: Length of the original diagonal (as reference)

R_{mx}: Length of diagonal after changing x axis

Δx: Length of movement x axis

Δα: Angle between original and modified diagonal after moving x axis

α: Real angle between x axis and diagonal direction

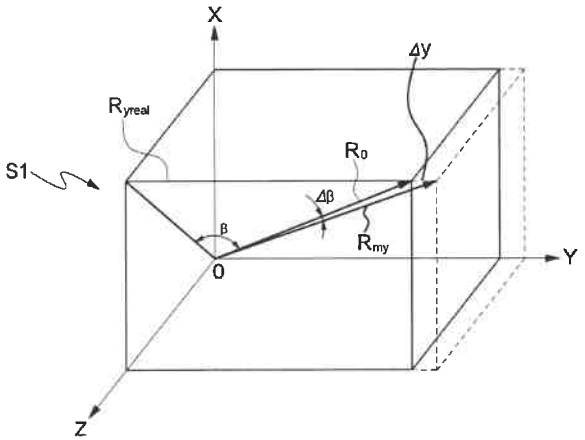

FIGURE.3. Modified Diagonal with changing Δy

The same processing with the model in Fig.3, the angle β can be calculated as:

$$\Delta\beta = \cos^{-1}\left(\frac{R_0^2 + R_{my}^2 - \Delta y^2}{2R_0 R_{my}}\right) \quad (5)$$

$$\beta = \frac{\pi}{2} - \sin^{-1}\left(\frac{R_{my}^2 \sin\Delta\beta}{\Delta y}\right) \quad (6)$$

Where:

R_0: Length of the original diagonal (as reference)

R_{mx}: Length of diagonal after changing x axis

Δy: Length of movement x axis

Δβ: Angle between original and modified diagonal after moving y axis

β: Real angle between y axis and diagonal direction

As above equations, each block of step movements can be calculated. To measure volumetric error of machine working zone including S block as Fig.4 these equations (3), (4), (5), (6) become:

$$\Delta\alpha(i) = \cos^{-1}\left(\frac{R_0^2(i) + R_{mx}^2(i) - \Delta x^2(i)}{2R_0(i)R_{mx}(i)}\right) \quad (7)$$

$$\alpha(i) = \frac{\pi}{2} - \sin^{-1}(i)\left(\frac{R_{mx}(i)\sin\Delta\alpha(i)}{\Delta x(i)}\right) \quad (8)$$

METHODS, PRACTICES, AND STANDARDS FOR EVALUATING ON-MACHINE TOUCH TRIGGER PROBING OF WORKPIECES

Ronnie R. Fesperman, Shawn P. Moylan, and M. Alkan Donmez
Manufacturing Metrology Division
National Institute of Standards and Technology (NIST)*
Gaithersburg, MD, USA

ABSTRACT

This paper presents work being performed by NIST to evaluate test methods prescribed by the new draft standard for determination of on-machine measuring performance of numerically controlled machine tools [1]. The measuring performance of a machining center, equipped with a strain gage style touch trigger probing module, is evaluated according to this standard in order to validate the proposed test methods and to generate a baseline set of data to be used in the development of on-machine measurement uncertainty budgets. Probing repeatability, two-dimensional (2D) and three-dimensional (3D) probing errors and errors in identifying the workpiece coordinate system (WCS) in the machine coordinate system (MCS) are evaluated and the results presented.

INTRODUCTION

Using computer numerically controlled (CNC) machine tools as inspection platforms by employing on-machine touch trigger probing systems has become increasingly more attractive to many machine tool users. The most common uses of touch trigger probing systems on CNC machine tools include establishment of the WCS in the MCS in preparation for the subsequent machining operations as well as on-machine inspection of the machined workpiece. In some cases, probing is used to quickly validate machine geometric and/or thermal deformations by measuring a standard artifact located in the machine work volume [2-4]. Key benefits of implementing this technology include fast and accurate setups and the detection of machining errors, thus reducing scrap and rework. However, concerns exist over the fact that the machine structure and position feedback systems used to manufacture workpieces are the same systems used for measuring workpieces, and thus the errors that occur during machining may also occur during measuring, preventing the detection of errors on the workpieces. Therefore, this "error coupling" must be considered and assessed carefully for any on-machine measurement application.

A draft international standard, ISO/DIS 230-10, has recently been developed to help users of on-machine touch trigger probing systems evaluate the measuring performance of their machine tools [1]. The standard describes test methods designed to evaluate the combined effects of the probe, the probing hardware and software, signal transmission system, signal conditioning hardware, the environment, and the machine tool, on measuring performance. We evaluated several test methods described in this draft standard by measuring the performance of a CNC machining center (Fig. 1) equipped with a strain gage style touch trigger probing module. Descriptions of the tests performed, the measurement results, and a description of how this data will be used in the development of on-machine touch trigger probing uncertainty budgets are provided in the following sections.

PROBING SYSTEM

The probing system used with this machine is a commercially available strain gage style touch trigger probe. The probe, with a 100 mm long carbon fiber stylus and 6 mm diameter ruby sphere tip, is mounted in the machine spindle. It can be driven along the $\pm X$-, $\pm Y$-, and $-Z$-axes. Communication between the probe and machine controller is via a wireless optical transmission system and a wired machine interface module. The effective radius and effective length of the probing system, as calibrated for these tests,

* Official contribution of the National Institute of Standards and Technology (NIST); not subject to copyright in the United States. The full descriptions of the procedures used in the paper require the identification of certain commercial products and their suppliers. The inclusion of such information should in no way be construed as indicating that such products or suppliers are endorsed by NIST or are recommended by NIST or that they are necessarily the best materials, instruments, software or suppliers for the purposes described

was 5.879 mm and 268.886 mm, respectively. A nominal probing feedrate of 300 mm/min was used for each test.

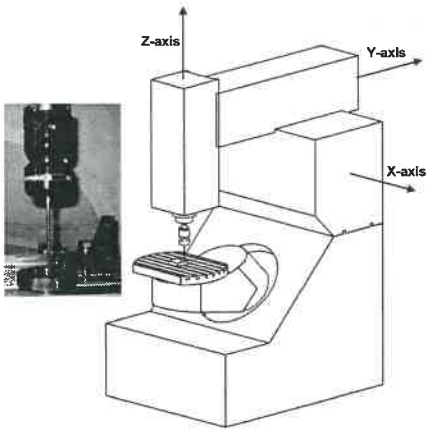

FIGURE 1. Schematic of the machining center used in this evaluation of ISO/DIS 230-10

REFERENCE ARTIFACTS

Three reference artifacts, a 50.8 mm grade B gage block, a 45.7 mm diameter ring gage, and a 25.4 mm diameter calibration sphere were used in this evaluation. Each artifact was allowed to thermally equilibrate in the machine shop environment before any tests were performed.

TEST METHODS

We conducted tests designed to evaluate probing repeatabilities, probing errors, feature size measurement errors, and the errors in determining workpiece location and orientation. These tests assess the capability of the machine to make measurements with varying degrees of complexity. Such complexity ranges from detecting a contact point along a single axis of motion, to detecting a feature involving motion along vectors in space and processing the collection of contact point data. The tests evaluated were performed with the prescribed artifacts located at different positions in the MCS from the position where probe calibration occurred. Descriptions for each test are provided below.

Probing Repeatability

Three tests were conducted to evaluate probing repeatability: 1) single-point surface location repeatability, 2) circle center location repeatability, and 3) sphere center location repeatability.

Single-Point Surface Location

In this test three surfaces of a reference block are aligned to the MCS. Surfaces normal to the *X*-, *Y*-, and *Z*-axes are individually and uni-axially probed ten times. The single-point surface location repeatability along each axis, $R_{SPT,X}$, $R_{SPT,Y}$, and $R_{SPT,Z}$, is calculated as the range of the individual coordinate values.

Circle Center Location

A reference ring is aligned paraxially to the machine *Z*-axis. A WCS is established at the ring center by probing the ring with four points equally spaced around the ring inner circumference. The ring center coordinates in the *XY* plane are calculated using a best fit circle algorithm and recorded. The measurement process is repeated ten times. Probing repeatability parameters, $R_{CIR,X}$ and $R_{CIR,Y}$, are calculated as the range of the recorded *X*- and *Y*- center values.

Sphere Center Location

A reference sphere is probed with one point at the pole and four points equally spaced around the equator. The measurement process is repeated ten times and the *X*-, *Y*-, and *Z*-axis sphere center coordinates for each measurement are determined using a least squares best fit sphere algorithm. Probing repeatability parameters, $R_{SPH,X}$, $R_{SPH,Y}$, and $R_{SPH,Z}$, are calculated as the range of the center coordinates along *X*-, *Y*-, and *Z*-axes, respectively.

2D Probing Error

A reference ring is probed with 25 points equally spaced around the ring circumference. The ring center is determined using a least squares best fit circle algorithm and the radial distances from the center to the measured points are determined. 2D probing error, $P_{FTU,2D}$, is calculated as the range of the measured radial distances.

3D Probing Error

A reference sphere is probed in the radial direction with 25 points spaced around the upper half of the sphere circumference. One probing point is located at the sphere pole, four points are equally spaced 22.5° below the pole, eight points are located 45° below the pole, four points are 67.5° below the pole, and eight points are 90° below the pole. The sphere center is determined using a least squares best fit sphere algorithm and the radial distances from the center to the measured points are calculated.

3D probing error, $P_{FTU,3D}$ is calculated as the range of the radial distances.

Workpiece Location and Orientation

This test assesses the capability of a machine to determine the location and orientation of a workpiece before it initiates machining operation. A reference block is mounted on the work table, skewed by approximately 1° about the *X*-, *Y*-, and *Z*-axes in the MCS. The WCS orientation and origin are determined by probing the reference block and recorded in the active work offset. Four points on the top surface of the block are then probed in the *Z*-direction of the WCS. $E_{PLA,Z}$, WCS reference plane identification error, is calculated as the range of the recorded *Z*-coordinates in the WCS. Next, two points are probed parallel to the *Y*-axis of the WCS on the surface aligned parallel to the WCS *XZ*-plane. $E_{LIN,Y}$, WCS orientation identification error, is calculated as the difference between the two *Y*-coordinates in the WCS. The reference block corner or WCS origin location coordinates, X_{COR}, Y_{COR}, and Z_{COR}, are then measured by probing one point on each of the three reference block surfaces used to define the WCS origin. Last, the reference block size is measured. $E_{EST,Y}$, the effective stylus tip diameter error, is calculated as the difference between the measured size and the calibrated size of the reference block.

Feature Size Measurement Performance

The following three tests were conducted to evaluate feature size measurement performance.

Web Size

A reference block is aligned along the *X*-axis of the machine and its length is measured ten times. Then the block is aligned along the *Y*-axis and its length is again measured ten times. The measurement performance parameters, $E_{WEB,X}$ and $E_{WEB,Y}$, are calculated as the average of the differences between the reference block calibrated length and the measured values along the *X*- and *Y*-directions, respectively. $R_{WEB,X}$ and $R_{WEB,Y}$, are calculated as the range of the measured values for each axis.

Circle Diameter

A reference ring is aligned paraxially to the machine *Z*-axis and its inner diameter is measured by probing four points equally spaced around its circumference. The ring diameter is calculated using a least squares best fit circle algorithm. The measurement is repeated ten times and the performance parameter, $E_{CIR,D}$, is calculated as the average differences between the ring calibrated diameter and the measured diameter values. $R_{CIR,D}$, is calculated as the range of the recorded diameter values.

Sphere Diameter

A reference sphere is probed with five points in radial directions parallel to the machine axes. One probing point is located at the sphere pole and four are equally spaced around the sphere hemisphere. The sphere diameter is calculated using a least squares best fit sphere algorithm. The performance parameter, $E_{SPH,D}$, is calculated as the average of the differences between the reference sphere calibrated diameter and the measured diameter values. $R_{SPH,D}$ is calculated as the range of the measured diameter values.

MEASUREMENT CYCLES

Several CNC measuring cycles are provided with the machine control software, e.g., probing of a surface, a web, or a hole. Whenever applicable, these standard measuring cycles were used to perform a prescribed test method. The cycles used included:

- a cycle for measuring a surface normal to the axis of travel
- a cycle for measuring a hole with four points parallel to the machine axes
- a cycle for measuring a sphere with five points parallel to the machine axes
- a cycle for fitting a least squares best fit circle to four points.

For tests where the standard measuring cycles were not applicable, custom CNC programs were generated and analyses of the probing points were performed post-process on a personal computer. Custom CNC programs were generated for tests requiring the probing of a reference ring with more than four points and the probing of a reference sphere with more than five points. The circle fitting algorithm provided by the controller is limited to fitting a circle to a maximum of four points. Because of this limitation, analyses requiring a circular fit to more than four points and analysis requiring a spherical fit were performed via post-processing on a personal computer using least squares best fit methods.

MEASUREMENT RESULTS

The results from the above mentioned tests are given in Tables 1 – 3.

TABLE 1. Probing Repeatability & Error Results

Single Point			
$R_{SPT,X}$:	1.10 µm	$R_{SPT,Y}$:	0.70 µm
$R_{SPT,Z}$:	0.50 µm		
Circle Center			
$R_{CIR,X}$:	0.70 µm	$R_{CIR,Y}$:	0.80 µm
Sphere Center			
$R_{SPH,X}$:	0.40 µm	$R_{SPH,Y}$:	0.71 µm
$R_{SPH,Z}$:	0.43 µm		
Probing Error			
$P_{FTU,2D}$:	3.30 µm	$P_{FTU,3D}$:	3.82 µm

TABLE 2. Workpiece Location and Orientation Results

WCS Errors			
$E_{PLA,Z}$:	4.14 µm	$E_{LIN,Y}$:	1.0 µm
$E_{EST,Y}$:	21.7 µm		
WCS Location			
X_{COR}:	81 µm	Y_{COR}:	314 µm
Z_{COR}:	68 µm		

TABLE 3. Feature Size Measurement Performance Results

Web Size			
$E_{WEB,X}$:	16.8 µm	$R_{WEB,X}$:	1.10 µm
$E_{WEB,Y}$:	20.8 µm	$R_{WEB,Y}$:	0.70 µm
Circle Diameter			
$E_{CIR,D}$:	-17.8 µm	$R_{CIR,D}$:	1.70 µm
Sphere Diameter			
$E_{SPH,D}$:	17.0 µm	$R_{SPH,D}$:	0.44 µm

DISCUSSION OF RESULTS

The measurement results suggest that probing repeatabilities for on-machine measurements are small, approximately 1 µm and below. However, the test results also suggest that significant errors exist in the probing systems ability to accurately determine the location of the workpiece in the MCS and to accurately measure feature size. The X-, Y-, and Z-axis linear positioning repeatabilities, as defined by standards [5], for this machine tool are 3.6 µm, 3.5 µm, and 5.1 µm, respectively. A comparison of the positioning repeatabilities and probing repeatabilities suggest that linear axis positioning repeatability may not be a good indication of the machine tool's probing performance, i.e., the probing performance may be better than the linear positioning performance. In addition, simulation of the 2D and 3D probing error tests with our virtual machine tool model based on the quasi-static positioning errors of the machine resulted in simulated probing errors of 1.4 µm and 1.7 µm, respectively. A comparison of the simulated and measured probing errors suggests that the machine's positioning errors may contribute as much as 44 % to the probing error.

CONCLUSIONS

The test methods prescribed by ISO/DIS 230-10 have been used to evaluate the measuring performance of a CNC machine tool equipped with a strain gage style touch trigger probing module. Each test method was efficiently performed and did not require the use of any expensive equipment. The measurement performance parameters obtained for various probing scenarios prescribed in the standard provided all necessary information to estimate the overall uncertainties of on-machine part probing with this system.

FUTURE WORK

The measurement results produced by this evaluation will be used in the development of measurement uncertainty budgets for measuring part specific features on machine tools using touch trigger probing. Simulations of the test methods using our virtual machine tool model will help us prioritize the contributors to the on-machine measurement uncertainty and, in the long term, will aid in the prediction of acceptable part features and tolerances to be manufactured with this system.

REFERENCES

[1] ISO/DIS 230-10, Test code for machine tools – Part 10: Determination of measuring performance of probing systems of numerically controlled machine tools

[2] Omari M., Ajao D., Kampmann G. Schmadel I., Machine Tool Accuracy Quick Check in Automotive Tool and Die Manufacturing, Proceedings of the International Conference on Smart Machining Systems, 2007

[3] ISO 230-3:2001, Test code for machine tools – Part 3: Determination of thermal effects

[4] McGlauflin, M.L., Moylan, S.P., Error motions of a non-orthogonal rotary axis, Proceedings of the 23rd ASPE annual Meeting, 2008

[5] ISO 230-2:2006(E), Test code for machine tools – Part 2: Determination of accuracy and repeatability of positioning numerically controlled axes

AN ESTIMATION METHOD FOR FIVE DEGREE FREEDOM ERROR MOTIONS OF THE PRECISION SPINDLE

Jooho Hwang[1], Jongyoup Shim[1], and Chun-Hong Park[1]
[1]Department of Ultra Precision Machine and Systems
Korea Institute of Machinery and Materials (KIMM)
Daejeon, Republic of Korea

INTRODUCTIONS

The error motion of a machine tool spindle directly affects the surface errors of machined parts. The error motions of the spindle are not desired errors in the three linear direction motions and two rotating motions. Those are usually due to the imperfect of bearings, stiffness of spindle, assembly errors, external force or unbalance of rotors. The error motions of the spindle have been needed to be decreased to desired goal of spindle's performance. The level of error motion is needed to be estimated during the design and assembly process of the spindle.

In this paper, the estimation method for the five degree of freedom (5 D.O.F) error motions of the spindle is suggested. To estimate the error motions of the spindle, waviness of shaft and bearings, external force model was used as input data. And, the estimation models are considering geometric relationship and force equilibrium of the five degree of the freedom. To calculate error motions of the spindle, not only imperfection of the shaft, bearings, such as rolling element bearing, hydrostatic bearing, and aerostatic bearing, but also driving elements such as worm, pulley, and direct driving motor systems, were considered.

FIVE D.O.F ERROR MOTION MODEL OF SPINDLE

To make the general motion model of spindle, not only location but also numbers of the bearings are considered to be defined as shown in Figure 2. The geometrical relationship is explained as equations (1) and (2). Equation (1) explain the displacement of shaft on the each bearing parts and equation (2) indicates the shaft in the point that users want to know. Where the subscript *i* means the orders of the bearing from the left and 1 means No. 1 bearing on the left side of the spindle. In here, θ_x and θ_y are tilt error motion rotating x or y axis, respectively.

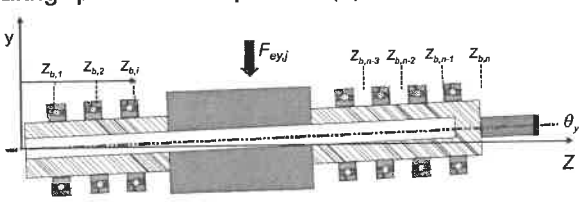

FIGURE 1. Geometrical models of spindle

$$\begin{aligned}
\delta_{bxi} &= \delta_{bx1} + (z_{bi} - z_{b1}) \cdot \theta_y \\
\delta_{byi} &= \delta_{by1} + (z_{b,i} - z_{b1}) \cdot \theta_x \\
\delta_{bzi} &= \delta_z
\end{aligned} \tag{1}$$

$$\begin{aligned}
\delta_x &= \delta_{bx1} + (z - z_{b1}) \cdot \theta_y \\
\delta_y &= \delta_{by1} + (z - z_{b1}) \cdot \theta_x \\
\delta_z &= \delta_{bzi}
\end{aligned} \tag{2}$$

When we assume the shaft is motioned like rigid body. Following equilibrium equation can be derived. From the three direction equilibrium of the spindle, equation (3) is derived.

$$\begin{aligned}
\sum_i^n f_{bx,i} &= \delta_{bx1} \sum_{i=1}^n K_{bx,i} + \theta_y \sum_{i=1}^n K_{bx,i}(z_{bi} - z_{b1}) - \sum_j^m f_{ex,j} \\
\sum_i^n f_{by,i} &= \delta_{by1} \sum_{i=1}^n K_{by,i} + \theta_x \sum_{i=1}^n K_{by,i}(z_{bi} - z_{b1}) - \sum_j^m f_{ey,j} \\
\sum_i^n f_{bz,i} &= \delta_z \sum_{i=1}^n K_{bz,i} - \sum_j^m f_{ez,j}
\end{aligned} \tag{3}$$

Where, the $f_{bx,i}$, $f_{by,i}$, and $f_{bz,i}$ are reaction force of each bearings due to geometrical imperfection of the shaft to x, y, and z direction, respectively. And Z_b is location of the bearings to be fixed.

From the moment equilibrium of the spindle, equation (4) can be derived.

$$\begin{aligned}
\sum_i^n f_{by,i}(z_{bi} - z_{b1}) &= \delta_{by1} \sum_{i=1}^n K_{by,i}(z_{bi} - z_{b1}) + \theta_x \sum_{i=1}^n K_{by,i}(z_{bi} - z_{b1})^2 \\
&\quad - \sum_i^n (f_{bz,i} - K_{bz,i}\delta_z) y_{bi} - \sum_j^m f_{ey,j} z_{r,j} - \sum_j^m f_{ez,j} y_{r,j} \\
\sum_i^n f_{bx,i}(z_{bi} - z_{b1}) &= \delta_{bx1} \sum_{i=1}^n K_{bx,i}(z_{bi} - z_{b1}) + \theta_y \sum_{i=1}^n K_{bx,i}(z_{bi} - z_{b1})^2 \\
&\quad - \sum_i^n (f_{bx,i} - K_{bz,i}\delta_z) x_{bi} - \sum_j^m f_{ex,j} z_{r,j} - \sum_j^m f_{ez,j} x_{r,j}
\end{aligned} \tag{4}$$

From, the equations (1)~(4), equation (5) can be derived. The first 5X5 matrix of left term means stiffness matrix of the spindle and two summed matrix of right side mean reaction force of the bearing and external force from torque transmitter, respectively.

$$\begin{bmatrix} -\sum K_{bx,i} & 0 & 0 & 0 & -\sum K_{bx,i}(z_{bi}-z_{ti}) \\ 0 & -\sum K_{by,i} & 0 & \sum K_{by,i}(z_{bi}-z_{ti}) & 0 \\ 0 & 0 & -\sum K_{bz,i} & 0 & 0 \\ 0 & \sum K_{by,i}(z_{bi}-z_{ti}) & \sum K_{bz,i}\cdot y_{bi} & -\sum K_{by,i}(z_{bi}-z_{ti})^2 & 0 \\ -\sum K_{bx,i}(z_{bi}-z_{ti}) & 0 & \sum K_{bz,i}\cdot x_{bi} & 0 & -\sum K_{bx,i}(z_{bi}-z_{ti})^2 \end{bmatrix} \begin{bmatrix} \delta_{bx1} \\ \delta_{by1} \\ \delta_z \\ \theta_x \\ \theta_y \end{bmatrix}$$

$$= \begin{bmatrix} \sum_i^n f_{bx,i} \\ \sum_i^n f_{by,i} \\ \sum_i^n f_{bz,i} \\ -\sum_i^n f_{by,i}(z_{bi}-z_{ti}) + \sum_i^n f_{bx,i}\cdot y_{bi} \\ \sum_i^n f_{bx,i}(z_{bi}-z_{ti}) - \sum_i^n f_{bz,i}\cdot x_{bi} \end{bmatrix} + \begin{bmatrix} \sum_j^m f_{ex,j} \\ \sum_j^m f_{ey,j} \\ \sum_j^m f_{ez,j} \\ -\sum_j^m f_{ey,j}z_{r,j} + \sum_j^m f_{ez,j}y_{r,j} \\ \sum_j^m f_{ex,j}z_{r,j} - \sum_j^m f_{ez,j}x_{r,j} \end{bmatrix} \quad (5)$$

The reaction force of the bearing can be defined as equation (6).

$$f_e(\theta) = \sum_{k=1}^{\infty} TF(2\pi\cdot k)(a_k \cos 2\pi\cdot k + b_k \sin 2\pi\cdot k) \quad (6)$$

The meaning of equation (6) is Fourier series of the profile on bearings surface and TF is influence coefficient of bearings due to bearing type such as angular contact ball, hydrostatic, or aerostatic bearings [1]. Once we get the displacement of the shaft at bearing 1, we can calculate any error motion of the spindle from the equation (2).

The NSK 6204Z angular contact bearing model is calculated and shown in figure 2. The spatial frequency indicates k of equation 6. Most of frequency shows cancelling out except dominant frequencies [2]. Owing to moving effect of the ball element the input profile of the errors come out less than dominant frequencies. The phase of figure2 gives the information about it.

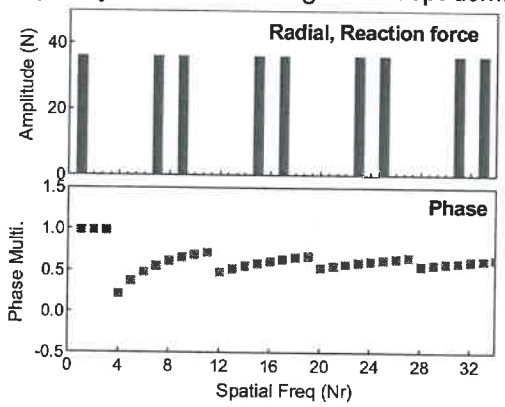

FIGURE 2. Influence coefficient of NSK 6204Z bearing

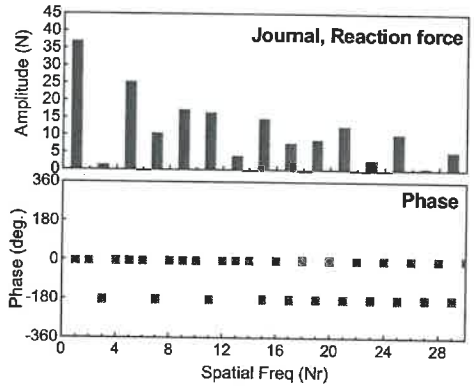

FIGURE 3. Influence coefficient of 4-pad hydrostatic bearing

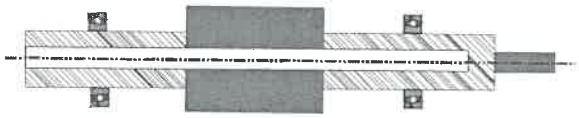

FIGURE 4. Application example for the spindle

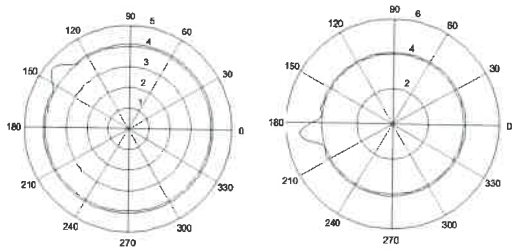

(a) bearing 1 *(b) bearing 2*

FIGURE 5. Profile errors of the shaft

Figure 3 shows the influent coefficient of a 4-pad hydrostatic bearing and it also shows the dominant frequencies. Every amplitude was not same as shown in the figure because of averaging effect of the hydrostatic bearings.

ERROR ANALYSIS OF AN SPINDLE

Effects of bearings

The suggested method was applied to simple supported bearing systems as shown in figure 4. The profile error(roundness) of bearing parts are defined as figure 5 and those are also assumed to be applied to axial motion.

Figure 6 shows the results of rotational errors of spindle from equation (5), when the influence coefficient of the figure 2 is used as bearing.

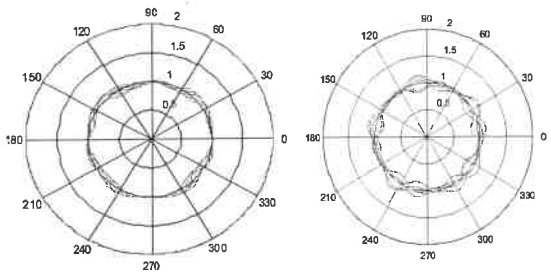

(a) Radial error (b) Axial error

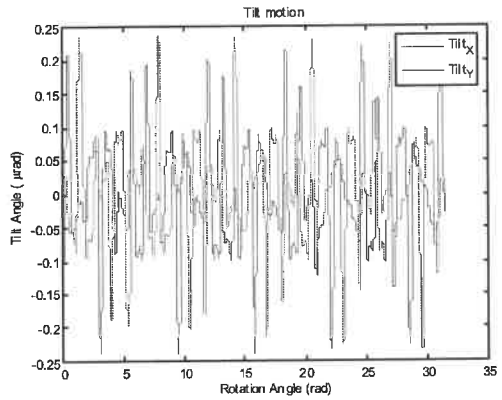

(c) Tilt error

FIGURE 6. Rotational errors of a ball bearing spindle

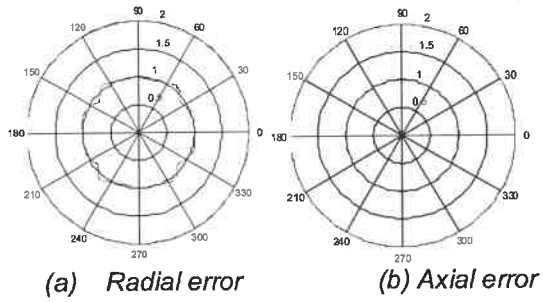

(a) Radial error (b) Axial error

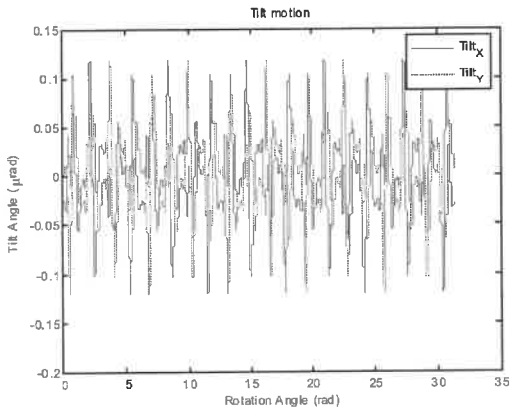

(c) Tilt error

FIGURE 7. Rotational errors of a hydrostatic bearings spindle

The effect of the asynchronous errors due to rolling element is shown in each motion.
Figure 7 shows the results of a rotational errors of the hydrostatic oil bearing spindle. As shown in the figure, it shows the zero asynchronous errors and smoothed motion errors. The advantage of the suggested methods is that the easy extension of the model. Usually, the error model of spindle supported by typical bearing is not easy to change according to change of bearing. But, the suggested influence coefficient method is easy to check the effect of changed bearings. Because the form of the bearing information is provided as data shown in figure 2 and 3.

Effects of Driving Components

The effect of driving component also easy to applied, when the suggested method is applied. Direct drive (D.D.) motor and pulled system was regarding in this application. When a permanent magnet type D.D. motor or belt and pulley systems are defined as equation (7) or (8), respectively, it's possible to be applied to equation (5).

$$F_e = 2\cos(39\phi) + 0.2random \quad (7)$$

$$F_{ey} = 24\cos(\phi) + 2.4\cos(50\phi) \quad (8)$$

where, random is modeled by random function and stands for electrical noise effect of the motor.

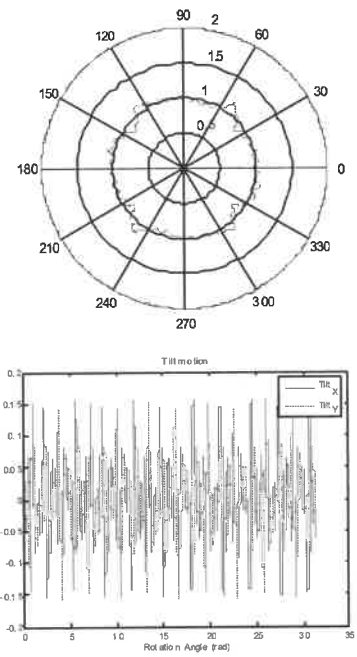

FIGURE 8. Rotational errors of a hydrostatic bearings spindle driven by D.D. motor

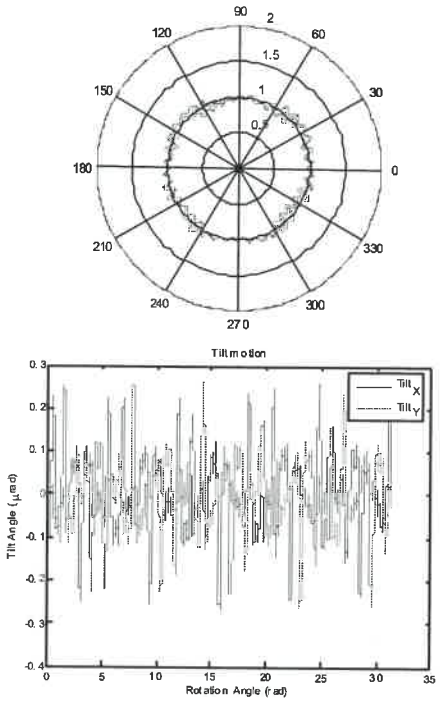

FIGURE 9. Rotational errors of a ball bearing spindle driven by D.D. motor

The effect of rotational errors due to DD motor are shown in figure 8 and 9. And the effect of belt and pulley systems are shown in figure 10 and 11. The suggested method has also good

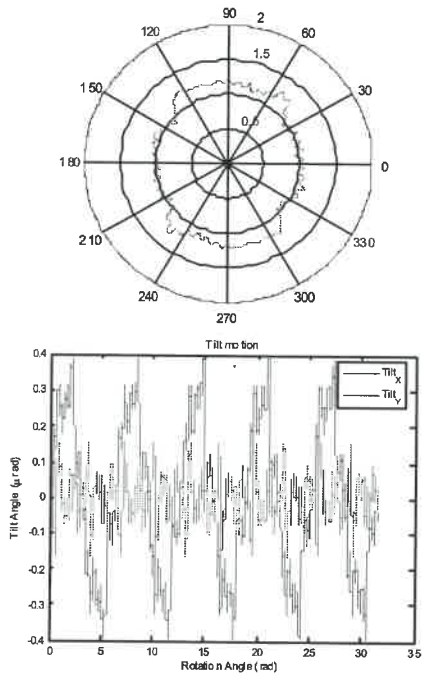

FIGURE 10. Rotational errors of a hydrostatic bearings spindle driven by belt and pulley system

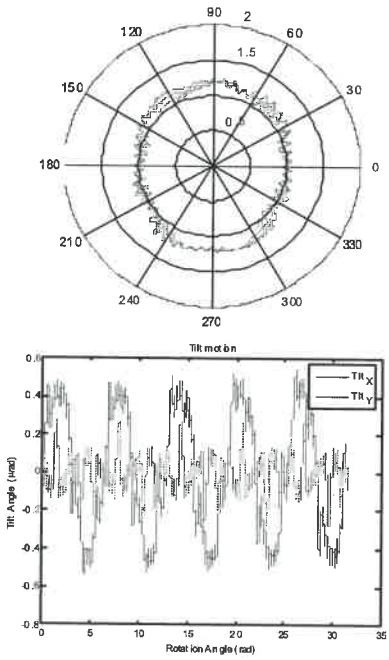

FIGURE 11. Rotational errors of a ball bearing spindle driven by belt and pulley system

advantage, once the driving force is modeled according to rotational position of the spindle.

CONCLUSIONS AND FURTHER STUDY

In this paper, an estimation method for the five degree of freedom (5 D.O.F) error motions of the spindle is suggested. To estimate the error motions of the spindle, waviness of shaft and bearings, external force model was used as input data. And, the estimation models are considering geometric relationship and force equilibrium of the five degree of the freedom. From the simulation results, we confirmed that this method has advantage of exact and fast calculation for the rotational errors of spindle.

The effect of vibration in high speed motion regarding vibration response of driving force and unbalance model will be added. And, experimental comparison will be performed to confirm the estimation method.

REFERENCES

[1] Shamoto E, Park C-H. Analysis and Improvement of Motion Accuracy of Hydrostatic Feed Table. CIRP Annals. 2001; 50: 285-290.

[2] Jang G, Jeong S-W. Vibration Analysis of a Rotating System Due to the Effect of Ball Bearing Waviness. Journal of Sound and Vibration. 2004; 269: 709-726.

POSITIONING REPEATABILITY EVALUATION OF HYDROSTATIC BEARING GUIDED PRECISION MACHINE

Jongyoup Shim[1*], Chinh B. Bui[2], Jooho Hwang[1], Chang-Kyu Song[1] and Chun-Hong Park[1]

[1]Korea Institute of Machinery & Materials, 171 Jang-dong, Yuseong-gu, Daejeon, Korea

[2]Department of Nano Mechatronics, University of Science and Technology Daejon, Korea

INTRODUCTION

An ultraprecision multi-axis machine tool was designed and developed in our laboratory [1]. The machine tool has four moving axes which are comprised of three linear axes and one rotational axis (C-axis). It has gantry type structure and the Z-axis is on the X-axis and the C-axis, on which workpiece is located, is inside the Y-axis. This machine is designed for manufacturing micro-patterns on large surface area and it can manufacture micro-patterned mold for LCD (Liquid Crystal Display) diffusion film and light guide plate and fuel cell membrane and anti-reflection film for solar cell panel. Each X and Y axis has 500 mm travel and Z axis has 110 mm travel. All the three linear axes and C-axis adopt hydrostatic bearing and the feeding oil temperature is controlled by a cooler and the whole machine components are in the environmentally controlled room.

In order to assess the accuracy of the machine the repeatability needs to be evaluated. The laser interferometer is adopted for the measurement because of the long travel range and pressure and temperature sensors are used for refractive index compensation. For temperature measurement a few thermocouples are located around the beam path and the Edlen's formula is used to compensate refractive index induced error. From the previous experiments performed, machine deformation due to temperature condition and moving stage location contributes to positioning repeatability (and also accuracy). The temperature condition includes ambient air, machine tool (temperature gradient exists) and feeding oil temperature. Ten thermocouple sensors are located on machine tool body, such as guiding rail and moving table. The positioning repeatability experiment has been performed simultaneously measuring those environmental data. And repeatability performance is influenced by the oil cooler temperature set value. In this paper, assessment of positioning precision of our machine tool by repeatability experiment and discussions about performance affecting parameters are presented.

MACHINE DESCRIPTION

Figure 1 shows the 4-axis machine which was designed and developed in our laboratory. The machine has X, Y, Z and C axes and it has gantry structure for X and Z axes. The Y-axis is on the base body and the C-axis is inside Y-axis table structure for compactness. In order to achieve high precision and high stiffness structure, all the bearing components are using hydrostatic bearing. And for the actuator coreless BLDC linear motors are adopted and linear encoders are used for positioning feedback sensor. The size of machine is 1,300 x 1,800 mm^2 and movement stroke of X- and Y-axis is 550 mm and Z-axis has 110 mm stroke.

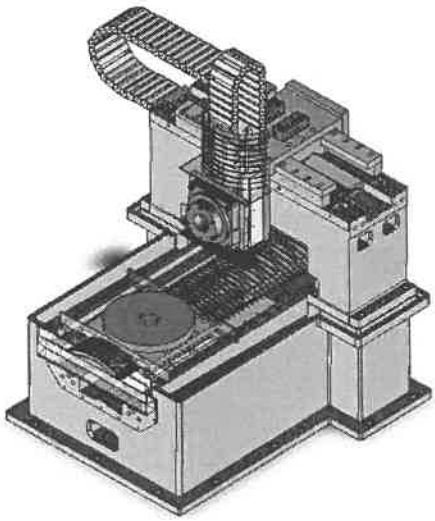

FIGURE 1. The 4-axis machine tool which is adopting hydrostatic bearings.

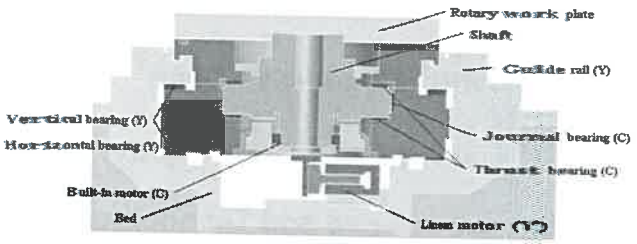

FIGURE 2. Cross-sectioned view of the Y- and C-axis table structure.

The Z-axis is on X-axis table and has counter-balancing mechanism which is using air cylinder. The whole machine is supported by four semi-active type vibration isolators.

The hydrostatic bearing stiffness is the one of important machine characteristics in order to achieve high precision machining. The Y-axis vertical bearing stiffness is 1,348 N/μm and horizontal stiffness is 1,010 N/μm. The C-axis table is inside Y-axis table and therefore the stiffness from the work to base frame is lowered by the series connection of the Y- and C-axis bearing structure. Therefore, the Y-axis bearing stiffness is designed to have higher stiffness than X-axis bearing. The X-axis bearing stiffness is 1,030 N/μm and 867 N/μm in the vertical and horizontal direction respectively.

TABLE 1. 4-axis machine tool specifications

		specifications
Size		1,300 × 1,800 × 1,200 mm
C-axis	Feed table	Oil hydrostatic
	Motor	Brushless DC motor
	Feedback	Encoder, accuracy 2"
Y-axis	Feed table	Oil hydrostatic
	Motor	Coreless linear motor
	Feedback	Laser scale, resolution 0.34 nm
X-axis	Feed table	Oil hydrostatic
	Motor	Coreless linear motor
	Feedback	Laser scale, resolution 0.34 nm
Z-axis	Feed table	Oil hydrostatic
	Motor	Coreless linear motor
	Feedback	Laser scale, resolution 0.34 nm

REPEATABILITY EXPERIMENT

Repeatability performance has been investigated using laser interferometer displacement sensor. The experiment stroke is 400 mm and the laser interferometer is generally satisfactory for measuring submicron accuracy. However, the laser interferometer has disadvantage of being affected by environmental physical values such as air temperature, air pressure and air humidity. In principle the displacement is calculated by homodyne or heterodyne detection method and those two methods are related with the wavelength in the beam path of laser light. The wavelength variation in the beam path contributes to the displacement error in the laser interferometer measurement. For example, 1 °C of temperature variation causes 1 ppm measurement error and therefore the environment effects need to be compensated for submicron measurement accuracy.

Figure 3 shows the general Michelson interferometer schematic. The displacement can be calculated by phase difference between two beams reflected from reference mirror and target mirror respectively. As for dead path effect wavelength variation is considered and eq. (1) shows the displacement formula by the above parameters. The lower-case index indicates initial and final position of the target mirror and eq. (2) shows the relation between wavelength and refractive index [2][3].

$$\Delta L = \Delta\phi\left(\frac{\lambda_f}{4\pi}\right) + \left(L_i - L_r\right)\frac{\Delta\lambda}{\lambda_i} \tag{1}$$

$$\lambda_{air} = \frac{\lambda_{vac}}{n} \tag{2}$$

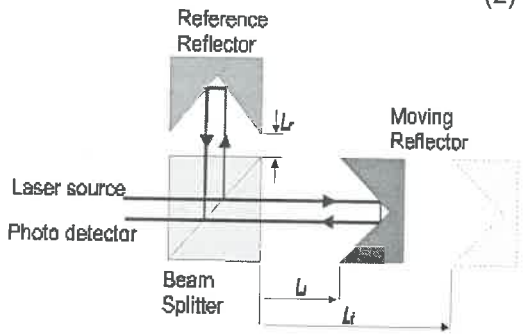

FIGURE 3. Michelson interferometer schematic showing dead path and movement definition for compensation formula.

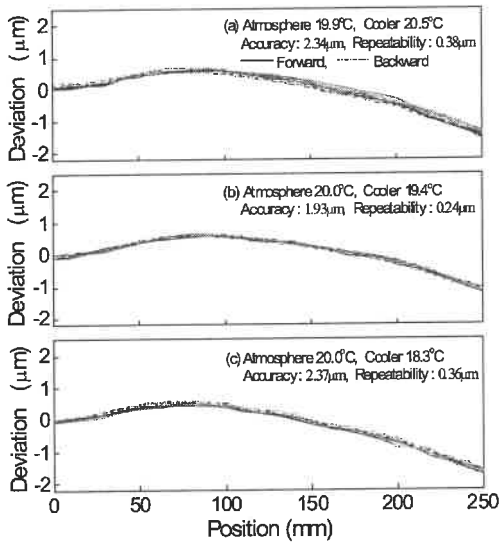

FIGURE 4. Repeatability experiment with varying supply oil temperature. This result is pre-tested with other 1-axis hydrostatic bearing table.

Hydrostatic bearing has many advantages such as no friction motion, high damping capacity and high precision positioning. However, supply oil temperature and related temperature variation of rail and table are those sources of deteriorating precision positioning capability of the hydrostatic bearing machine. Our pre-study has revealed that oil cooler temperature set-up value contributes to machine positioning repeatability and this result can be explained by speculation (this has been also experimentally investigated). The temperature difference between rail (base frame also) and table causes local thermal heating (or cooling) and therefore makes thermal deformation at the table position. When the table is positioned at a position, thermal deformation affects the positioning error and therefore deteriorates the repeatability capability of hydrostatic bearing machine. The pre-study revealed that about 0.5 ℃ difference case (see figure 4) shows best repeatability performance among those cases which are all have small temperature difference between table and rail (and also base frame).

In order to check control stability of the table (Y-axis), at the center position after steady state of temperature gradient being reached the positioning stability is measured by capacitive sensor and the control feedback sensor is linear encoder.

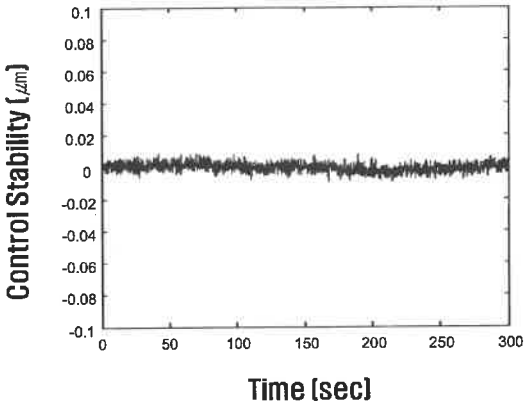

FIGURE 5. Feedback control stability experiment of Y-axis. Long term stability is within 10 nm.

Therefore, figure 5 shows that there is little effect of the control system on repeatability.

With those above information and pre-studied results, oil cooler condition has been set up and repeatability experiment has been performed. The movement range is 400 mm and the elapsed time for full measurement is about 30 minutes. The laser interferometer data was compensated with the Edlen's formula for correcting error from environment variation. And the whole machine is in the environmentally controlled room and the average air temperature was about 21 ℃, air pressure about 1,000 mbar, humidity about 50 %. And there are ten thermocouple sensors to measure base frame, guide rail, air, table, oil and column temperature. Those thermocouple sensors are calibrated to have the same temperature values within 0.2 ℃. As shown in the figure 6, the repeatability of 0.18 μm / 400 mm has been achieved. The positioning repeatability is worse in the 150 ~ 300 mm region and this is due to the thermal expansion effect by the temperature difference between table and rail. After first positioning error data being achieved, the linearity error of the linear scale is compensated with that data and the resulting positioning accuracy is about 0.36 μm. Figure 7 shows the temperature sensor data during the repeatability experiment of figure 6. The table temperature is lower than the base body by about 0.5 ℃ and the returning oil temperature is almost same as that of table.

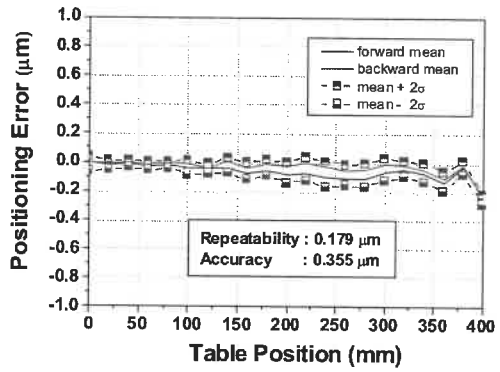

FIGURE 6. Repeatability experiment result. 0.18 μm / 400 mm repeatability and 0.36 μm accuracy are achieved.

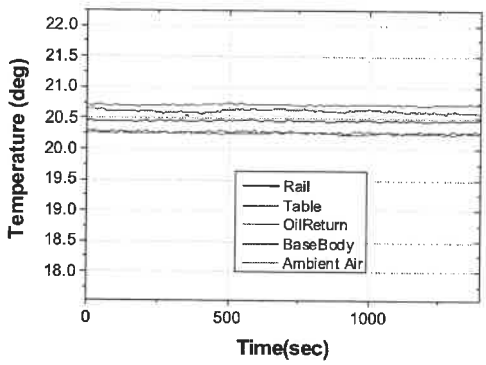

FIGURE 7. Thermocouple temperature sensor data during repeatability experiment.

CONCLUSION

Positioning repeatability has been evaluated for 4-axis machine tool which adopts hydrostatic bearing. By compensating laser interferometer displacement data more stable and reliable position data has been achieved. Effects of hydrostatic bearing operating condition on positioning error have been investigated and control stability has been also checked. 0.18 μm / 400 mm repeatability performance has been achieved by our hydrostatic bearing machine tool.

DISCUSSION

In order to investigate those sources of positioning error in the aspect of repeatability, experiments regarding hydrostatic bearing related parameters are to be done.

REFERENCES

[1] Chun Hong Park, Chang Kyu Song, Jooho Hwang, Byung-Sub Kim Development of an Ultra Precision Machine Tool for Micromachining on Large Surfaces. International Journal of Precision Engineering and Manufacturing. 2009; 10: 85-91.

[2] Norman Bobroff Recent advances in displacement measuring interferometry. Measurement Science and Technology. 1993; 4: 907-926.

[3] Jack Stone, Steven D. Phillips, Gary A. Mandolfo Corrections for wavelength variations in Precision Interferometric Displacement Measurements. Journal of Research of the National Institute of Standards and Technology. 1989.; 101: 671-674

MANUFACTURING PROCESS ERROR SIGNATURE AND CMM UNCERTAINTY COSTS

Darek Ceglarek[1], Giovanni Moroni[2], and Stefano Petrò[2]
[1] Digital Laboratory, WMG
University of Warwick
Coventry, CV4 7AL, United Kingdom
[2]Department of Mechanical Engineering
Politecnico di Milano
Via La Masa 1, 20156, Milan, Italy

INTRODUCTION

Conformance testing is based on measurements performed on pre-selected Key Product Characteristics (KPC), and is a key to ensure product functionality. However, conformance tests are expensive: the overall "uncertainty cost" comes from cost for performing measurement (measurement cost), and cost due to inspection errors (error cost). Unfortunately, measurement cost increase as uncertainty decreases, while inspection errors reduce as uncertainty reduces.

A commonly adopted measurement system for geometric error evaluation is a "Coordinate Measuring Machine" (CMM). Wilhelm *et al.* have identified [1] several sources of CMMs measurement uncertainty. In particular the sampling strategy can significantly affect measurement uncertainty. In fact, in geometric tolerance verification only those zones of the surface which deviate the most from the design nominal geometry affect the geometric error. It has also been observed that anomalous zones of the part profile/surface tend to be the same throughout a stable production. It may therefore be stated that the part presents a "manufacturing process error signature" (MPES), that is geometric error behavior is similar in every part.

Ceglarek and his team [2] developed methods to model part variation patterns of pre-assembled components to compensate dimensional variability caused by upstream manufacturing processes. In recent years several studies have suggested that the interaction between sampling strategy and manufacturing process error signature can be analyzed in order to generate very effective sampling strategies (e.g. Summerhayes *et al.* [3], or Colosimo *et al.* [4]). However, these approaches are currently limited to form error verification. Moreover, the criteria proposed lack a correct economic point of view.

This work proposes a methodology optimizing the sampling strategy when estimating geometric error by using CMM gages. The method is based on a cost function depending on the sampling strategy, so the sampling strategy will be the best trade-off between measurement cost and error cost. An uncertainty evaluation similar to the one in ISO/TS 15530-3 standard is implicit in the methodology. A discussion will be proposed on the impact of lack of tracing ability of CMM gages [5]. An industrial case study will be proposed involving parallelism between planes.

PROPOSED METHODOLOGY

The proposed methodology is based on repeated measurements of few calibrated workpieces. The sampling strategy for these measurements should be as dense as possible, and uniformly spaced, regardless of the considered geometric tolerance. From these dense samplings a pre-selected subset of points is selected, and then a suitable costs function is used to evaluate this strategy. By varying the subset of measurement points, the subset which minimizes the cost function is determined. By applying the methodology to more than one calibrated workpiece, the sampling strategy will tend to concentrate sampling points exactly in those areas which are anomalous (deviate the most from design nominal geometry) throughout the whole production.

The basic structure of the function to evaluate uncertainty costs C_I for a single workpiece can be written as

$$C_I = C_M + C_E \tag{1}$$

where C_M is "measurement cost", namely, the cost of performing a single measurement task, and C_E is the "errors cost", that is the cost generated by inspection error. The proposed methods

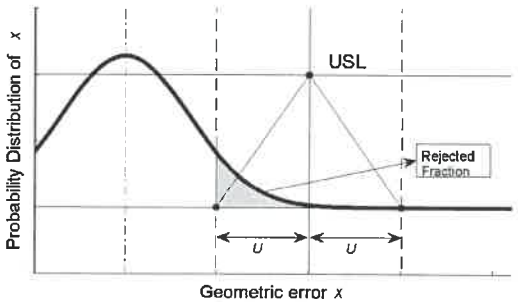

FIGURE 1. Rejected fraction of conforming produced parts in presence of an USL.

is applicable in cases where C_E is large enough to significantly affect the probability of type I and type II measurement errors.

Evaluation of C_M

For a CMM, the cost related to the sampling strategy depends essentially on time involved in taking measurements. Neglecting fixed times for system set-up, measurement time depends on the sample size, so it is possible to express C_M as

$$C_M = c_M t \simeq c_M t_p n = c_p n \qquad (2)$$

where c_M is the CMM hourly cost, t is the time required to perform the measurement task, t_p is the time for sampling a single point, n is the sample size, and then c_p can be interpreted as "cost for sampling a single point".

Evaluation of C_E

The evaluation of C_E, depending on the approach chosen by the manufacturer to deal with measurement errors, is quite subjective. In this work, a simple approach is proposed based on the fraction of parts rejected even if conforming.

Suppose a single sided specification limit SL has been defined for some KPC of a workpiece, as depicted in Figure 1. Suppose only an Upper Specification Limit (USL) exist, as usual in geometric tolerances. This means that a part is non conforming if the real value of the KPC $x > USL$. Suppose now that conformance to a tolerance has to be proved, and the ISO 14253-1 standard approach for stating conformance is followed: this standard suggests that a part should be stated non conforming if $y > USL - U$, where y is the measurement result, and U is the expanded uncertainty. Moreover, suppose that x, behaves according to some statistical distribution (e.g. a Gaussian distribution). Therefore, if uncertainty increases, a higher number of parts will be rejected, even if they should be accepted (Figure 1). C_E may then be evaluated as

$$C_E = c_w P\left(USL - U < x \leqslant USL\right) \qquad (3)$$

where c_W is the cost of type I error, $P\left(USL - U < x \leqslant USL\right)$ can be regarded as the probability that the real geometric error falls between $USL - U$ and USL, so we cannot state conformance for the part, but the part is conforming. Therefore, this probability represents the average fraction of conforming parts declared non conforming. Usually, only an upper bound exists for a geometric tolerance, so Eq. (3)considers only an upper bound. However if both upper and lower bound exist, Eq. (3) can be easily modified.

This expression of error cost neglects parts which are considered conforming even if they do non conform, which come with a cost, of course. In fact, the probability that this happens if ISO 14253-1 rule is followed is very low.

Uncertainty evaluation

The ISO/TS 15530-3 technical specification proposes a procedure to evaluate measurement uncertainty which is based on raw data obtained from repeated measurements of a calibrated artifact. From raw data, some terms are estimated, such as: u_{cal} (uncertainty contribution due to calibration uncertainty), u_{p} (uncertainty contribution due to measurement procedure), u_{W} (uncertainty contribution due to variability of the manufacturing process), and b (measurement bias). The term U (expanded uncertainty, see GUM and VIM) is evaluated as

$$U = k\sqrt{u_{\text{cal}}^2 + u_{\text{p}}^2 + u_{\text{W}}^2} + |b| \qquad (4)$$

where k is the expansion factor. To evaluate the influence of the manufacturing signature on the uncertainty, more than a calibrated part as to be adopted. However formulas in ISO/TS 15530-3 are not suitable for this. Therefore, a modification of the standard is proposed, so that more than one calibrated artifact may be used. In particular, the b term (the average bias) should be evaluated as

$$b = \frac{\sum_{j=1}^{m}\sum_{i=1}^{r_m}\left(y_{i,j} - x_{\text{cal},j}\right)}{m r_m} \qquad (5)$$

In Eq. (5) m is the number of calibrated artifacts adopted, r_m is the measurement repetitions num-

ber for each artifact, $y_{i,j}$ is the measurement result (estimated geometric error) of the i^{th} measurement repetition of the j^{th} artifact, and $x_{\text{cal},j}$ is the reference value for the j^{th} artifact (calibrated geometric error). It is supposed that each calibrated workpiece is measured the same number of times; to be as similar to ISO 15330-3 standard as possible, it is suggested $r_m \geq 10$. Then, to estimate u_{p}, a pooled standard deviation could be used:

$$u_{\text{p}} = \sqrt{\frac{\sum_{j=1}^{m}\sum_{i=1}^{r_m}(y_{i,j}-\bar{y}_j)^2}{m(r_m-1)}} \qquad \bar{y}_j = \sum_{i=1}^{r_m}\frac{y_{i,j}}{r_m} \tag{6}$$

Substituting Eq. (5) and (6) in Eq. (4) an evaluation of U which takes into account more than one calibrated artifact, and then the interaction between the sampling strategy and the MPES, is obtained.

Strategy optimization

Having identified a methodology to evaluate uncertainty based on raw data, the next step is choosing a sampling strategy that minimizes the uncertainty cost. The solution of the problem is not straightforward. Suppose that r_m dense measurements of m calibrated parts have been obtained, and that the sampling strategy is the same for every measurement. To solve the minimization problem, the sampling points corresponding to any sampling strategy may be extracted from these clouds of points. The extracted subsets of points can be introduced in the measurement uncertainty estimation procedure. If the sampling pattern is effective, i.e., it is able to detect regions of the feature that deviate the most, then uncertainty will be low. The identification of an optimal pattern can be seen as an optimization problem where at most any different alternative pattern is compared. However, due to the combinatorial nature of the problem, it is not possible to consider any strategy. Therefore, genetic algorithms or simulated annealing algorithms should be adopted for optimal strategy definition, given the discrete nature of the problem.

Finally, even if the optimization of the strategy is based on the presence of a MPES, explicit knowledge of the signature is not required for the optimization itself.

CASE STUDY

As a case study, the parallelism defined in point (e) of Table 3 in the ISO 10791-7 standard is considered. Ten parts were milled and a 0.045 mm

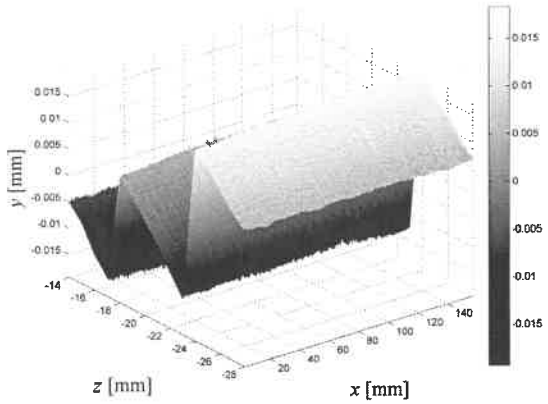

FIGURE 2. Case study MPES (average on ten toleranced planes).

parallelism tolerance was defined. The manufacturing cost was evaluated in 40 , that is taken as c_W. Then tolerances and datum features were sampled by means of a CMM, on a uniformly spaced sampling strategy, with a point density of 1 point/mm^2; a total of 3720 points were sampled on each part (1395 on the datum feature, and 2325 on the toleranced feature). Measurement was repeated ten times for each part. Finally, every part was calibrated with a standard calibration uncertainty $u_{\text{cal}} = 0.001$ mm. From calibrated parallelism errors, it was ascertained that parallelism for these part was distributed according to a $N(0.0402, 0.019)$ Gaussian statistical distribution (mean and standard uncertainty expressed in [mm]). The average surface of the ten toleranced surfaces is plotted in Figure 2: it is apparent that the surface presents a sawtooth profile and a trend along the y axis.

Finally, a simulated annealing algorithm was applied in order to select an optimal sampling strategy. Please note a parallelism is being considered, so sample size sums both the points sampled on the toleranced feature and the corresponding datum, and, throughout the optimization process, sampling points are left free to "migrate" from datum to toleranced feature and vice versa. Optimal strategy was compared to a standard Hammersley strategy. Figure 3 shows the behavior of expanded uncertainty ($k = 2$, $u_{\text{w}} = 0$) as the sample size varies. As expected, as the sample size increases uncertainty reduces; it is apparent that the proposed strategy greatly outperforms Hammersley strategy. Therefore, the proposed strategy should be useful even if the systematic error b term is compensated. Finally,

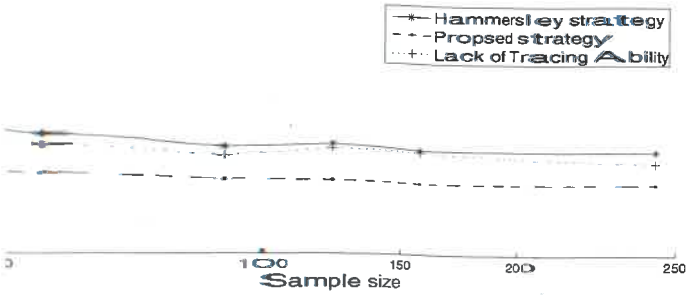

easurement expanded uncertainty size increases.

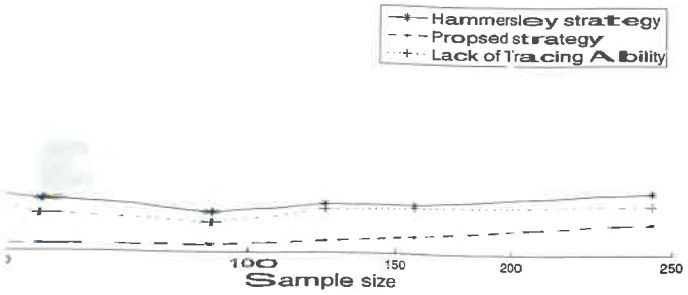

ncertainty cost as the sample size

s the relationship between uncer-
sample size. Non monotonic be-
that initially uncertainty is large,
then uncertainty quickly drops,
educe. However, as the sample
ncertainty improvement does not
more for sample size increase,
increase. Anyway, because of
ty the proposed strategy always

ck of tracing ability

ing ability' means that instead of
iven sampling points on the fea-
may actually measure the area
The lack of tracing ability may
al factors including alignment er-
pe of the measured surface, and
iability of parts. This limitation
s of coordinate measuring sys-
an additional source of uncer-
nds to inflate the measurement
tainty.

al problem for signature based
t, the ability of this kind of strate-
optimal results relies on its abil-

ity to measure exactly a particular point on a surface. In fact, Figures 3-4 show that a shift in the same direction of all sampling points equal to 1 mm is sufficient to greatly reduce performance of the proposed strategy. Therefore, if adopting a signature optimized sampling strategy, great care should be taken to ensure that parts are correctly traced.

CONCLUSIONS

In this paper a methodology has been proposed to be able to plan sampling strategies for inspecting geometric tolerances. The generated strategy optimizes uncertainty cost. Uncertainty cost is mainly linked to the number of sampling points taken, and the probability of errors. The optimization of the sampling points locations is based on the presence of a "manufacturing signature", that is a systematic behavior of the real geometric feature. The proposed methodology suggests the measurement of uncertainty evaluation which takes into account the interaction between the sampling strategy as well as manufacturing signature. Therefore, though the comparison of several possible sampling strategies, the one characterized by the optimal interaction may be selected.

REFERENCES

[1] Wilhelm RG, Hocken R, Schwenke H. Task Specific Uncertainty in Coordinate Measurement. CIRP Annals-Manufacturing Technology. 2001;50(2):553–563.

[2] Huang W, Ceglarek D. Mode-based decomposition of part form error by discrete-cosine-transform with implementation to assembly and stamping system with compliant parts. CIRP Annals-Manufacturing Technology. 2002;51(1):21–26.

[3] Summerhays KD, Henke RP, Baldwin JM, Cassou RM, Brown CW. Optimizing discrete point sample patterns and measurement data analysis on internal cylindrical surfaces with systematic form deviations. Precision Engineering. 2002;26(1):105 – 121.

[4] Colosimo BM, Moroni G, Petrò S. A tolerance interval based criterion for optimizing discrete point sampling strategies. Precision Engineering. 2010;34(4):745 – 754.

[5] Huang W, Kong Z, Ceglarek D, Brahmst E. The analysis of feature-based measurement error in coordinate metrology. IIE Transactions. 2004;36(3):237–251.

INVESTIGATIONS OF METROLOGICAL MODELS FOR THE NANOMEASURING AND NANOPOSITIONING MACHINE WITH RESPECT TO THE MEASUREMENT UNCERTAINTY BY MEANS OF A MONTE CARLO SIMULATION

Philipp Kreutzer[1], Roland Füßl[1], Eberhard Manske[1], Nataliya Dorozhovets[1]
[1]University of Technology Ilmenau
Institute of Process Measurement and Sensor Technology
P.O: Box 100 565, D-98684 Ilmenau, Germany

INTRODUCTION

Owing to the increased demands for specific measurement tasks of meso scale objects with nanometer uncertainty, required mainly in microelectronics, optics or precision engineering industries, the nanomeasuring and -positioning machine (NPMM) was developed by the Institute of Process Measurement and Sensor Technology (IPMS) in cooperation with the SIOS Messtechnik GmbH[1] and the ZBS Ilmenau[2]. It has a measuring range of 25mm x 25mm x 5mm. The positioning resolution is less than 0.1nm. The positioning repeatability is less than 0.3nm and the combined positioning uncertainty for a 3D measurement task is about 7nm. In contrast to most of the commercial available coordinate measuring machines (CMM's), where the probe system is moved, the NPMM has a fixed changeable probe system and the sample is moved by a corner mirror. This movement is detected by three fiber-coupled He-Ne-laser interferometers (x-, y- and z-direction) and two angular sensors. The interferometer measuring beams intersect in one virtual point to avoid Abbe errors [1], [2]. Regardless which probe system is used to fulfill the measurement task, each measured result is directly connected with the associated measurement uncertainty which is calculated based on the uncertainty budget. This document deals with a new approach of a vectorial modular model to express the uncertainty budget and to evaluate the measurement result and the associated measurement uncertainty. The modular modeling allows easy to insert or to remove new sub-models and to analyze their effects on the total measurement uncertainty. The various models can be differentiated among others into the cosine-error model, the Abbe-error model (finite accuracy to adjust the Abbe-offset to zero) and the interferometer model. The effects of these errors with respect to the resulting uncertainties are calculated by means of a Monte Carlo Method (MCM). Comparisons with the linear approach of the "Guide to the Expression of Uncertainty in Measurement" (GUM) [3] have shown that the proposed procedure is a good alternative to achieve measurement results with reasonable uncertainty estimation especially for the non-linear parts of the system.

METROLOGICAL MODELLING

Figure 1 illustrates schematically the NPMM [4].

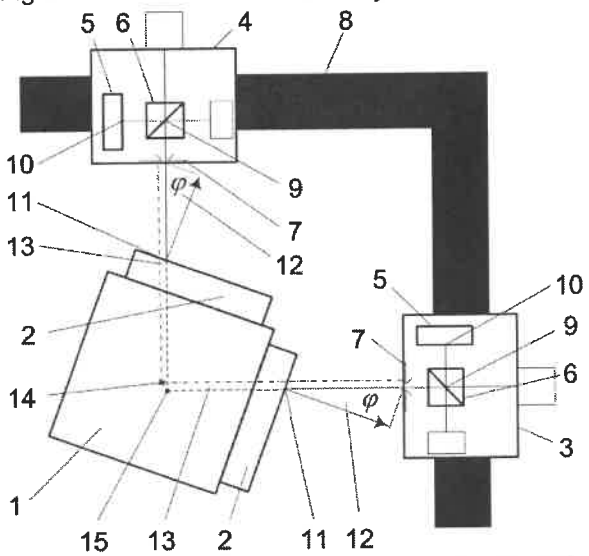

FIGURE 1. Schematic Illustration of the NPMM (1: corner mirror, 2: mirror plates, 3,4: x-,y-interferometer, 5: reference mirror, 6: polarizing beam splitter, 7: diaphragm, 8: NPMM frame, 9: Interferometer Center Point (ICP), 10: Interferometer Reference Point (IRP), 11: Mirror Reference Point (MRP), 12: Tilt angle, 13: Abbe-offset, 14: ideal point of intersection, 15: sample point).

Each measurement task represents the evaluation of the measurement result and the associated measurement uncertainty. The basis is

[1] www.sios.de
[2] www.zbs-ilmenau.de

the availability of the uncertainty budget. It includes all quantities which contribute to the measurement uncertainty and is expressed by the modular concept. An example which utilizes this concept is a measuring task between the touch point A (subscript *a*) and the touch point B (subscript *b*) (Eq. 1).

$$\vec{r}_M = \vec{r}_{Bb} - \vec{r}_{Aa} - \vec{r}_{ab} = \begin{pmatrix} x_M \\ y_M \\ z_M \end{pmatrix} \quad (1)$$

The measurement result is the norm (Eq. 2).

$$|\vec{r}_M| = \sqrt{{x_M}^2 + {y_M}^2 + {z_M}^2} \quad (2)$$

$\vec{r}_{Bb}$ and $\vec{r}_{Aa}$ are the distance vectors relating to a joint origin. $\vec{r}_{ab}$ considers the potential drift during the measurement. Eq. 1 and 2 are essential to calculate the measurement result. A qualified statement to the associated measurement uncertainty is not possible yet. It is indispensable to substitute the distance vectors by sub vectors to describe the different influences on the measurement. Therefore the metrological chains have to be defined (Figure 2). Table 1 explains the different sub vectors.

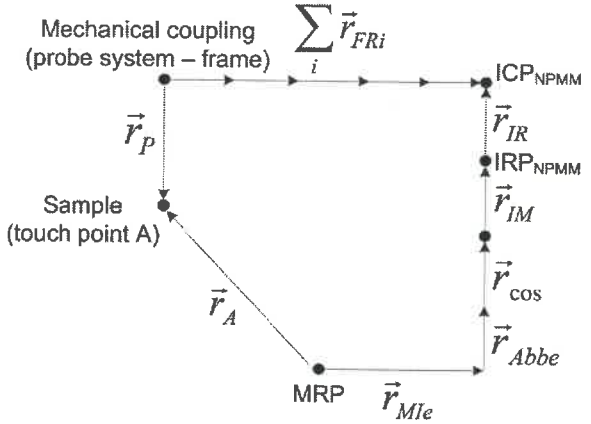

FIGURE 2. Metrological chain (touch point A).

TABLE 1. Sub vectors of the model.

$\vec{r}_p$	Probe system vector
$\vec{r}_{FRi}$	NPMM frame vector
$\vec{r}_{IR}$	Interferometer reference beam vector
$\vec{r}_{IM}$	Interferometer measuring beam vector
$\vec{r}_{cos}$	Cosine-error vector
$\vec{r}_{Abbe}$	Abbe-error vector
$\vec{r}_{MIe}$	Corner mirror error vector

Mathematically the distance vector $\vec{r}_M$ is (Eq. 3).

$$\vec{r}_M = \vec{r}_{Pb} - \vec{r}_{Pa} + \sum_i \vec{r}_{FRai} - \sum_i \vec{r}_{FRbi} - \vec{r}_{IRa} + \vec{r}_{IRb} - \vec{r}_{IMa} + \vec{r}_{IMb} - \vec{r}_{cosa} + \vec{r}_{cosb} - \vec{r}_{Abbea} + \vec{r}_{Abbeb} - \vec{r}_{MIea} + \vec{r}_{MIeb} + \vec{r}_{ab} \quad (3)$$

Interferometer Model

It is described through the vectorial components $\vec{r}_{IR}$ (reference beam vector) and $\vec{r}_{IM}$ (measuring beam vector). $\vec{r}_{IM}$ is evaluated as follows (Eq. 4, 5).

$$\vec{r}_{IMa} = \frac{\vec{\delta}_{IMa} \cdot \lambda_{0a}}{2n_a} \quad (4)$$

$$\vec{r}_{IMb} = \frac{\vec{\delta}_{IMb} \cdot \lambda_{0b}}{2n_b} \quad (5)$$

$\vec{\delta}_{IM}$ is the order of interference and depends on the uncertain phase shifting angle φ. This angle is determined by two 16bit A/D converters and an arctan lookup table with 256 * 256 elements. n is the refractive index of air. It is calculated by environmental data obtained by sensors and the modified Edlén formulae [5]. After a few simplifications the difference between the two touch points referring to the measuring beam vector is (Eq. 6).

$$\Delta\vec{r}_{IM} = \vec{r}_{IMb} - \vec{r}_{IMa} = \frac{(\vec{\delta}_{Imb} - \vec{\delta}_{Ima}) \cdot \lambda_{0a}}{2n_a} + \frac{\vec{\delta}_{Imb} \cdot \lambda_{0a}}{2n_a} \cdot \frac{\Delta\lambda_0}{\lambda_{0a}} - \frac{\vec{\delta}_{Imb} \cdot \lambda_{0a}}{2n_a} \cdot \frac{\Delta n}{n_a} \quad (6)$$

The difference of the reference beam vector $\vec{r}_{IR}$ is expressed by a linear thermal expansion model (Eq. 7).

$$\Delta\vec{r}_{IR} = \vec{r}_{IRb} - \vec{r}_{IRa} = \vec{r}_{IRa} \cdot \alpha_{th}(\vartheta_b - \vartheta_a) \quad (7)$$

It consists of the varying thermal expansion coefficient α_{th} and the material temperatures of the mechanical setup of the interferometer reference unit ϑ_a and ϑ_b.

Cosine-Error

Although the movements of the corner mirror in x- and y-direction are controlled by angular sensors it has to be assumed that there are still imperfections in the straightness of these movements. An error occurs if the value of this stage tilting changes within the measurement. Besides this (cosine-) error evoked by stage tilting are adjustment errors of the interferometer measuring beams. They are not perpendicular to the surfaces of the corner mirror due to misalignment. Additionally the flatness deviation of the corner mirror as an error source has to be included, although there is a correction polynomial for compensation. To summarize, misalignment (φ_{AD}), imperfect flatness (φ_{FL}) and stage tilting (φ_{TI}) cause an "optical" cosine-error ($\Delta\vec{r}_{cos-D}$) at the diaphragm of the interferometer because the emitted and the reflected measuring beams are not parallel (cf. Figure 1). The tilt

of the corner mirror (stage tilting φ_{TI}) causes as well a "geometrical" cosine-error ($\Delta\vec{r}_{cos-M}$).
The error angle of the "optical" cosine-error is (Eq. 8)

$$\varphi = \varphi_{TI} + \varphi_{AD} + \varphi_{FL} \tag{8}$$

and further (Eq. 9).

$$\Delta\vec{r}_{cos-D} = -\begin{bmatrix}(x_{IMi} + x_{IR} - x_{ICD})(\varphi_y^2 + \varphi_z^2)\\(y_{IMi} + y_{IR} - y_{ICD})(\varphi_z^2 + \varphi_x^2)\\(z_{IMi} + z_{IR} - z_{ICD})(\varphi_x^2 + \varphi_y^2)\end{bmatrix} \tag{9}$$

The "geometrical" cosine-error is Eq. (10, 11).

$$\varphi = \varphi_{TI} \tag{10}$$

$$\Delta\vec{r}_{cos-M} = \begin{bmatrix}(x_{MP})\left(\frac{\varphi_{TIy}^2 + \varphi_{TIz}^2}{2}\right)\\(y_{MP})\left(\frac{\varphi_{TIz}^2 + \varphi_{TIx}^2}{2}\right)\\(z_{MP})\left(\frac{\varphi_{TIx}^2 + \varphi_{TIy}^2}{2}\right)\end{bmatrix} \tag{11}$$

TABLE 2. Explanation of the subscripts.

$\overline{IMi}$	Distance Mirror-IRP (ideal)
$\overline{IR}$	Distance IRP-ICP
$\overline{ICD}$	Distance ICP-Diaphragm
$\overline{FR}$	Distance Probe-ICP
$\overline{MP} = \overline{FR} - \overline{IR} - \overline{IM}$	Distance Mirror-Probe

Abbe-Error

As mentioned above, one particular benefit of the NPMM is the possibility to measure Abbe-offset free in all three axes. The fact that there is only a finite accuracy in the adjustment of the interferometer measuring beams to the conjoint point of intersection make it although inevitable to build up a vectorial Abbe-error sub-model. This error occurs whenever there is a misalignment $\vec{r}_{mis}$ between the interferometer measuring beams and the object to be measured in connection with a tilt angle $\vec{\varphi}_t$. Mathematically the three-dimensional Abbe-error is the cross product (Eq. 12).

$$\vec{r}_{Abbe} = \vec{\varphi}_t \times \vec{r}_{mis} \tag{12}$$

SIMULATION

A common and accepted method to analyze the quality of a measurement is the usage of the GUM uncertainty framework. It is based on the law of propagation of uncertainties and the assumption that the output quantity follows a Gaussian- or a scaled and shifted t-distribution to calculate the best estimate of the measurement and the associated (expanded) uncertainty. Additionally the model is linearized by a first-order Taylor series approximation. Whenever these assumptions do not fulfill the postulated requirements other methods like numerical or analytical evaluation have to be considered. This document shows a numerical solution by a Monte Carlo Method (MCM). The main advantages of the MCM are the exact analysis of linear, partly nonlinear and nonlinear models as well as the exact treatment of asymmetric probability density functions (pdf's) of the measurand. In contrast to the propagation of uncertainties (GUM), MCM propagates probability distributions to derive an empirical distribution for the measurand which is essential to get the desired statistical values like the mean value as the best estimate or the standard deviation as the measurement uncertainty. The 95% coverage interval represents the expanded uncertainty in terms of the GUM. Further information about evaluating the measurement result and the associated uncertainty by means of the MCM are provided for instance in [6] or [7].

Uncertainty Budget

Due to the establishment of the metrological model which includes all uncertain quantities in a mathematical meaning, the uncertainty budget has to be created. Selected metrological sub-models (interferometer model, cosine-error model, Abbe-error model) to express this budget are described. As an example Table 3 shows the uncertain quantities of the Abbe-error component and the statistical description on the basis of prior knowledge. The uncertain influences are the Abbe-offset $\vec{r}_{mis}$ and the tilt angle $\vec{\varphi}_t$. They are characterized by an empirical rectangular distribution with the parameters given in Table 3.

TABLE 3. Evaluation of the input quantities.

Input	Estimate	Parameter	Distribution
Offset	0	Half-width 0.1mm	Rectangular
Tilt angle	0	Half-width $\varphi_{tx} = 1''$ $\varphi_{ty} = 1''$ $\varphi_{tz} = 2''$	Rectangular

Result

The measurement result and the associated measurement uncertainty are calculated with MATLAB. Based on equation 3, the model is

evaluated M-times whereas M is the number of Monte Carlo trials. The result is an empirical pdf of the measurand Y in order to calculate the desired statistical values. In this document, the metrological model (cf. Eq. 3) is simplified in this way that only the previous described sub-models have uncertain quantities. An associated empirical pdf of the measurand is shown in Figure 3. Figure 4 displays the corresponding empirical cumulative density function and the 95% coverage interval.

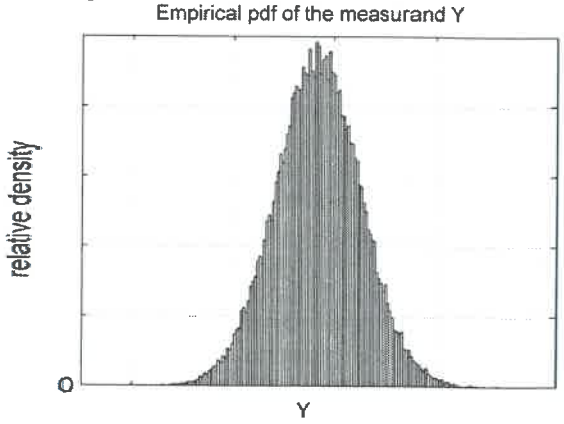

FIGURE 3. Empirical probability density function of the measurand.

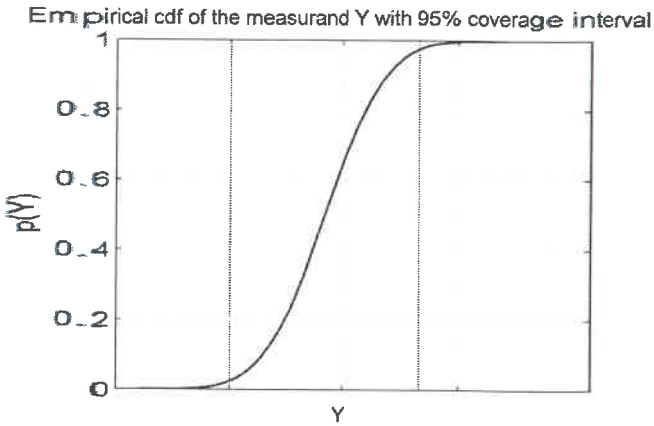

FIGURE 4. Empirical cumulative density function of the measurand with a 95% coverage interval.

CONCLUSION

This document presents the evaluation of the measurement result and the associated measurement uncertainty. In detail the measurement of a distance is simulated. Contrary to the GUM, the measurement result and the measurement uncertainty are evaluated numerically by means of a Monte Carlo Method. Instead of the propagation of uncertainties, the MCM is a tool to evaluate the complete measurement result by the propagation of the probability distributions of the input values. The output is the empirical pdf of the measurand, whereas the best estimate is the measurement result. The standard deviation is the measurement uncertainty whose basis of calculation is the uncertainty budget with all influences on the measurement. For this reason, a new approach of a vectorial model to establish the metrological chain of a measurement was created. The following research about the model has to be precised step by step. Moreover it is important to have a closer look at possible correlations of the input quantities and hence the generation of correlated pseudo random numbers.

ACKNOWLEDGEMENTS

The collaborative research center SFB 622 "Nanopositionier- und Nanomessmaschinen" is supported by the German Research Foundation and the Ministry of Science, Research and Arts. The authors wish to thank all those who have contributed to these developments.

REFERENCES

[1] G. Jäger et al., "Nanomeasuring and Nanopostioning Engineering", 3rd International Symposium on Precision Mechanical Measurements, Proc. SPIE, Vol. 6280, 2006

[2] I. Schmidt, "Beiträge zur Verringerung der Messunsicherheit der Nanopositionier- und Nanomessmaschine", PhD thesis, Technische Universität Ilmenau, 2008

[3] Deutsche Fassung, "Leitfaden zur Angabe der Unsicherheit beim Messen", Ref. Nr. ENV 13005:1999D, 1999

[4] Ph. Kreutzer et al., "Monte Carlo Simulation to Determine the Measurement Uncertainty of a Metrological Scanning Probe Microscope Measurement", Scanning Microscopy, Proc. SPIE, Vol. 7378; Monterey, CA, 2009

[5] G. Bönsch, E. Potulski, "Measurement of the refractive index of air and comparison with modified Edlén's formulae", Metrologia 35, pp. 133-139, 1998

[6] "Evaluation of measurement data – Supplement 1 to the "Guide to the expression in measurement" – Propagation of distributions using a Monte Carlo method", JCGM 101:2008, First edition 2008

[7] M.G. Cox et al., "Uncertainty and Statistical Modelling", Software Support for Metrology – Best Practice Guide No. 6, 2001

SHORT RANGE DISPLACEMENT SENSOR USING OPTICAL PICK-UP TRACKING SIGNAL

Chang-Woo Lee[1], Jun-Yeob Song[1], Tae-Ho Ha[1], Jae-Hak Lee[1]
[1]Department of Ultra Precision Machines and Systems,
Korea Institute of Machinery and Materials,
171, Jang-dong, Yuseong-gu, Daejeon, 305-343, S. Korea

INSTRUCTIONS

Recently there are a lot of micro high added value products. Micro stage is used frequently to produce or study these products. This micro stage is required full closed-loop control to satisfy demanded accuracy. For full closed-loop control in micro stage, short range displacement sensor is required with micrometer resolution. Measurement range of this sensor is from a few millimeters to several tens millimeters and the resolution must become micrometer or sub-micrometer. Conventional displacement sensor is used linear scale or gap sensor etc. Liner scale is displacement sensor with a resolution of sub-micrometer in several hundred millimeters measurement range. But generally a head size of linear scale is big and expensive for the micro stage. The resolution of gap sensor is very high but the measurement range is too short to use in micro stage. So short range displacement for the micro stage is developed with a resolution of one micrometer in this study.

The principle of this sensor is optical pick-up tracking signal method called three-beam method. When the tracks are helically formed on the optical disk, since the sectors of a single track are not equidistant from the center of the rotation of the disk, tracking control is necessary in the read mode. This tracking control has been conventionally performed by a push-pull method or a three beam method wherein the single laser beam is separated into three beams. The three beam method is more often used because it is more stable for the tilting of optical disk or the defect of optical disk than the push-pull method. As high track density is increased, the improvement of the precision in the optical pick-up is needed. The track pitch of CD is 1.6 ㎛, the track pitch of DVD is 0.74 ㎛ and the track pitch of blue-ray disk is 0.32 ㎛. Sensor resolution which is using optical disk track signal is sufficient to apply the micro-stage. The resolution of this sensor by dividing electrically may have a higher resolution. The sensor using optical pick-up is cost-effective for micro stage.

MEASURING PRINCIPLE

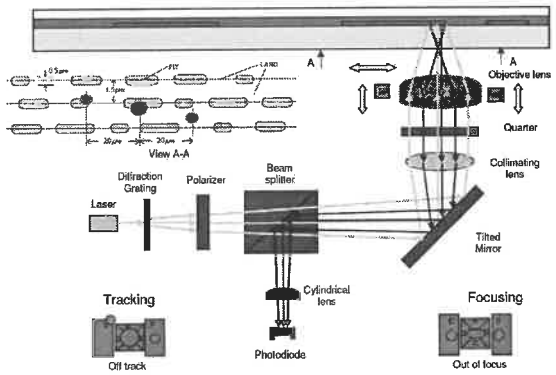

FIGURE 1. Basic principles of CD-ROM drive [1]

Optical pick-up consists of laser diode, diffraction grating, polarizer, polarizer beam splitter, collimating lens, quarter wave plate, objective lens and photodiode. The laser beam is divided into three beams by the diffraction grating. The three beams go through a polarized beam splitter and are polarized parallel to the page of polarizer beam splitter. Polarizer beam splitter is only transmits polarizations parallel to the page. The three beams are collimated and pass through a quarter-wave plate. The three beams are converted into the circular polarized beams. The circular polarized three beams are focused on the optical disk by an object lens. The intensity of three beams is modulated according to the pit on the disc. The reflected three beams pass through the quarter wave plate again and converted into polarized perpendicular to the original beam. Polarizer beam splitter is transmits polarizations parallel to the page but is reflected polarizations vertical to the page. The three beams go through the cylindrical lens and the intensity of three beams is detected by a photodiode. The cylindrical lens generates the focusing signal.

EXPERIMENT SETUP

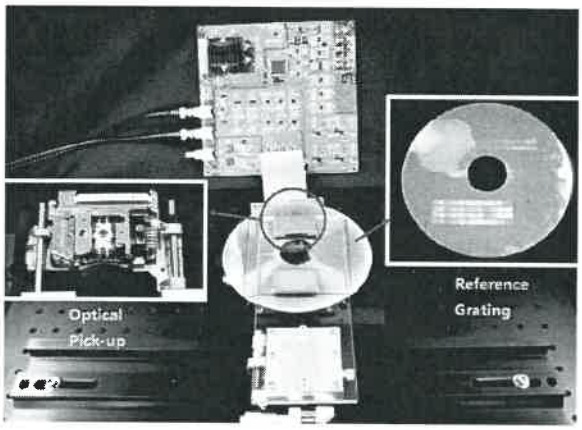

FIGURE 2. Experimental setup

Experimental consists of an optical pick-up, a reference grating, a control board, an oscilloscope and three micro stages. The optical pick-up is used currently so parts can be supplied cheaply. The operating temperature is from 0 ℃ to 65 ℃. The pick-up is available for both the DVD and CD. In this paper, CD mode is used.

Three micro stages consist of X, Y, Z 3-axis with micrometer position resolution. These stages are manual type. Z-axis stage is separated from X-axis, Y-axis stage. X-axis and Y-axis stage moves the grating. X-axis stage is used to select the grating and Y-axis stage is used to move the grating so track signal is generated. Z-axis stage is used to move the pick-up to focus onto the grating. In this experimental setup, focusing servo is not operated to evaluate the performance of track signal in accordance with the focus error. When the relative motion of pick-up and grating is generated to make a track signal, grating is moved to prevent the oscillation of object lens.

The control board can select CD or DVD mode and control laser diode power. This board also can generate the focus and track signal from the photodiode signal.

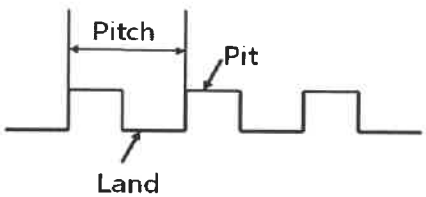

FIGURE 3. Reference grating feature

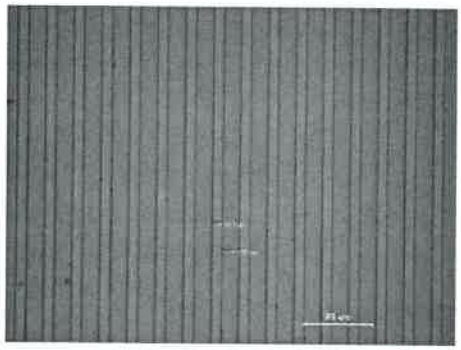

FIGURE 4. Group 1 reference grating (land : pit = 2 ㎛ : 6 ㎛)

TABLE 1. Reference grating configuration

Group 1 (pitch:8 ㎛) Land : pit	Group 2 (pitch:10 ㎛) Land : pit	Group 3 (pitch:20 ㎛) Land : pit	Group 4 (pitch:20 ㎛) Land : pit
2 : 6	2 : 8	2 : 18	10 : 10
3 : 5	4 : 6	4 : 16	12 : 8
5 : 3	6 : 4	6 : 14	14 : 6
6 : 2	8 : 2	8 : 12	16 : 4

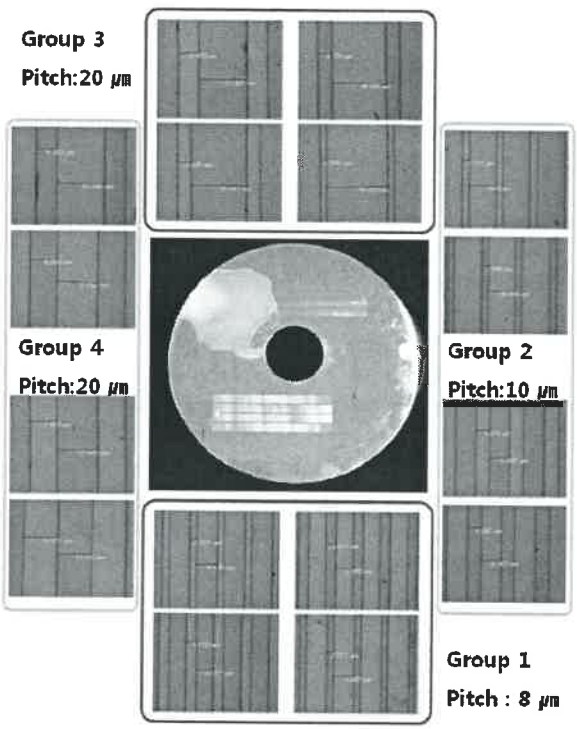

FIGURE 5. Reference grating configuration

The reference grating has 4 groups which have 4 different patterns, so there are 16 different patterns. Pit in this pattern is connected unlike the CD disk as shown in figure 4. The height of pit is $\lambda/4$ so that track signal is maximum. Figure 5 and table 1 show the different pattern configurations. Pattern group is divided by the length of the pitch. The length of pitch is 8 ㎛, 10 ㎛ and 20 ㎛. The reason why the pitch of the pattern is not equal to the pitch of CD is easy to display. The pitch of the pattern must be an integer times. The reason why the pitch of pattern is longer is beneficial to create the precision pattern. The resolution of sensor is acquired by electrical dividing the signal. Through experiments, the pattern is founded with the maximum signal to noise ratio. In this study, focusing beam is used unlike conventional linear scale, so the relation between the length of focus and signal to noise ratio is studied. If mechanical moving error is out of focus range, pick-up sensor is not available.

EXPERIMENTAL RESULT

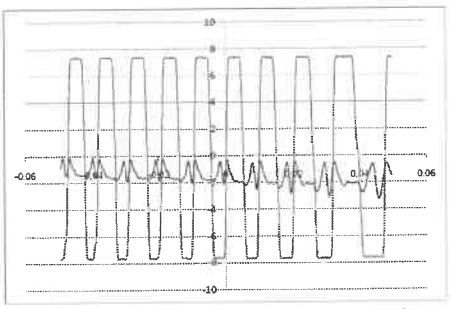

FIGURE 6. Group 1 land 2 ㎛, pit 6 ㎛

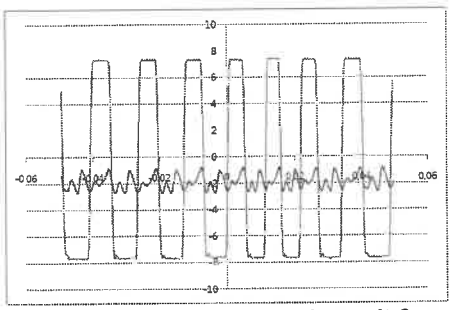

FIGURE 7. Group 1 land 6 ㎛, pit 2 ㎛

Figure 6 and figure 7 shows the track signal and focus signal. The blue line stands for track signal and the red line stands for focus signal. These patterns in figure 6 and figure 7 are outstanding in signal to noise ratio. If there is 10 ㎛ focus error, the track signal distortion is less than 5%. Sensor using optical pick-up can be applied to the micro stage that vertical moving error is less than 10 ㎛.

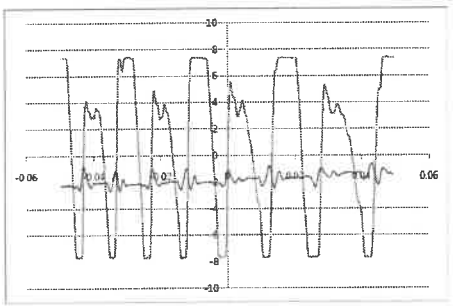

FIGURE 8. Group 2 land 4 ㎛, pit 6 ㎛

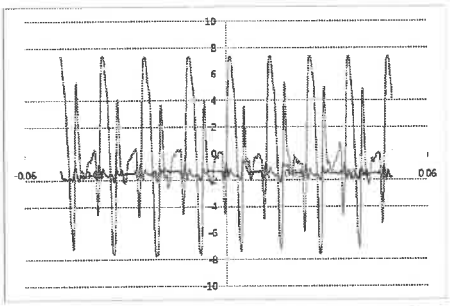

FIGURE 9. Group 3 land 6 ㎛, pit 14 ㎛

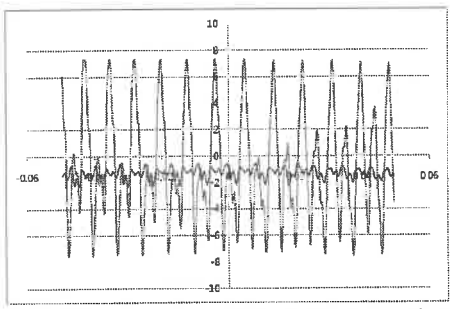

FIGURE 10. Group 4 land 14 ㎛, pit 6 ㎛

Figure 8, figure 9 and figure 10 also show the track signal and focus signal. As shown figure the track signal is difficult to use the position sensor signal. Because the difference between the pitch of the pattern and the pitch of CD is too much, the signal distortion is large not to be used. The other patterns are similar to these patterns.

GRATING PRODUCTION

In this study, the grating can be made by CD manufacturing method. This method provides a cheap grating. Figure 11 shows a grating produced in CD manufacturing. But this grating is amiss for a displacement sensor grating,

because this grating is shrunk in process of production. Different shrinkage depending on the location of the disk is very difficult to correct. It does not make to secure accuracy of displacement sensor. To solve this problem, a wafer produced by lithography is used for displacement sensor grating in this paper. But the disadvantage is that prices of grating are rising. Figure 12 shows the grating produced by lithography process.

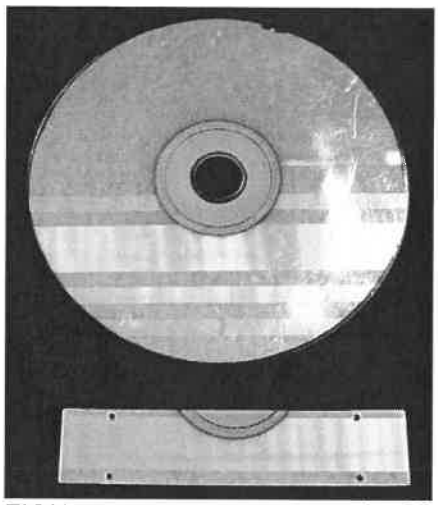

FIGURE 11. Grating produced by CD manufacturing method

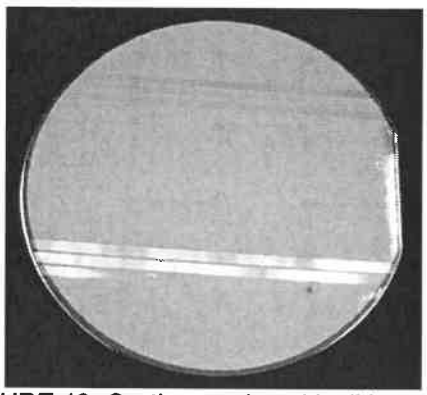

FIGURE 12. Grating produced by lithography process

FUTURE WORK

In this study, basic experiments is performed to evaluate that pick-up is available as a displacement sensor. Optical system will be design to fit into displacement sensor for micro stage. A compact optical system and control board must be designed for micro stage. Figure 13 shows the first design sensor head to be simplified. The controller must be designed to operate this head. The accuracy and reliability of this sensor also must be evaluated.

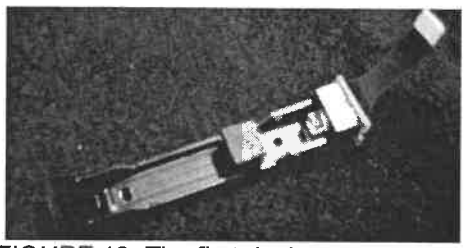

FIGURE 13. The first design sensor head

REFERENCES

[1] Yonas T. Tadesse, P. S. Gandhi, Development of Mechatronic system for demonstration of the focusing system of CD-ROM drive. The 10th Mechatronics Forum Biennial International Conference, Penn State Great Valley, PA June 19-21, 2006

[2] Yoon Young Kim, Jin Hong Kim and Jun Young Han, A new optical pickup suspension design, International Journal of Solids and Structures, Volume 36, Issue 17, 1 June 1999, Pages 2541-2556

[3] Sang Heon Lee, Kwang Suk Jung, Precision Displacement Measurement Using Astigmatism, Journal of the Korean Society for Precision Engineering, Vol. 25, No 7, July 2008, Pages 87-94

NON-LITHOGRAPHIC FABRICATION OF CARBON NANOTUBE-BASED SENSORS FOR SMALL-SCALE FORCE AND DISPLACEMENT SENSING

Michael Cullinan, Robert Panas, Cody Daniel and Martin L. Culpepper
Department of Mechanical Engineering
Massachusetts Institute of Technology
Cambridge, Massachusetts

SYNOPSIS

In this paper, we present a method for placing carbon nanotube (CNT) based piezoresistive sensors onto metallic flexural elements that were created via micromachining. Electron beam evaporation is used to deposit (1) an insulating ceramic thin film layer and (2) metal traces upon the flexure. A shadow mask is used to define the wire patterns. Either a tungsten wire or a focused ion beam (FIB) is then used to define a 1-5 μm gap in the wire traces. Dielectrophoresis is then used to orient/position the CNT sensors across the gap. Finally, the structure is coated with a thin ceramic layer to protect the sensor and mitigate noise. When the flexure element is deflected, the CNTs strain which results in a measurable change in resistance. Several meso-scale test devices were produced using this fabrication method. The results of these test devices show that functional CNT-based piezoresistive sensors may be fabricated without conventional integrated circuit (IC) microfabrication technologies. In this paper, we will present the design of the devices, discuss their performance, and present general design rules for manufacturability and performance optimization.

INTRODUCTION

Current MEMS manufacturing techniques are based on IC chip fabrication techniques such as photolithography and deep reactive ion etching (DRIE) which have been developed over the last half century. These techniques offer very high dimensional resolution but are generally limited to silicon processing which results in brittle MEMS devices. IC fab equipment also is extremely expensive, on the scale of $100's millions to billions for a fab line. This makes MEMS manufacturing prohibitively expensive since MEMS devices are typically produced in much smaller quantities than IC chips. Prototyping alone can cost 10's of thousands of dollars in an IC MEMS facility and require months to a year to complete [1]. Therefore, new fabrication techniques need to be developed to meet the needs of MEMS prototyping and manufacturing.

In this paper, we present the initial work towards a method that enables the design and fabrication of flexure-based, meso- and micro-scale force/displacement sensors fabricated using non-photolithographic micro-machining processes. In these sensors, CNTs are used as piezoresistive sensing elements. Piezoresistive sensors transduce strain in a flexing element into a resistance change. This resistance change may be used to measure the force on and displacement of a flexible element, e.g. flexure beam. Silicon-based piezoresistive sensors are commonly found in small-scale pressure sensors, accelerometers, AFM probes and nanopositioners. These sensors are typically fabricated via conventional IC processing techniques within dedicated microfabrication facilities/labs.

Our approach eliminates the need to use cost- and time-intensive photolithographic fabrication processes to create small-scale force/displacement sensors and thereby reduces cost and lead times for prototypes. Non-photolithographic micromachining processes are also attractive as they offer designers more flexibility in materials and geometry. These processes are not limited to IC microfabrication-compatible materials and 2½D geometries. We integrate CNTs with the flexure elements, thereby taking advantage of the CNTs relatively high gauge factor which equates to greater sensitivity. CNT-based piezoresistors have been measured to have gauge factors that are an order of magnitude larger than silicon-based piezoresistors [2]. CNTs are also attractive for use as they may be assembled onto existing flexure structures and therefore do not require

photolithography-based microfabrication processes. These characteristics make CNTs promising transduction elements for use with micromachining to produce fine resolution, small-scale force and displacement sensors.

TEST STRUCTURE DESIGN

The design and fabrication of a cantilever test structure showcases the potential capabilities of non-photolithographic MEMs manufacturing techniques. These small cantilever test structures are designed for use in testing CNT-based strain sensors. In these test structures, a 0.6" long cantilever beam is attached to a 0.082" thick base. Two 0.128" diameter mounting holes are drilled in the base to attach the test structure to the testing jig. A secondary 0.062" diameter hole for hanging weight on the beam is made at the end of the cantilever.

A conductive wire trace is deposited on to the top surface of the beam in order to allow CNT-based strain sensors to be placed onto the beam. These wire traces start at a contact pad on the stationary base and run out a short length of the beam before returning to a another contact pad next as seen in Figure 1. A small gap is made across the trace so that carbon nanotube resistors can be deposited onto the beam. These CNTs stretch between over the gap in the trace and complete the electrical circuit between the two electrodes. When the beam deflects, the carbon nanotubes are strained and their resistance changes. By measuring the change in resistance, it is possible to determine the force or displacement applied to the end of the beam.

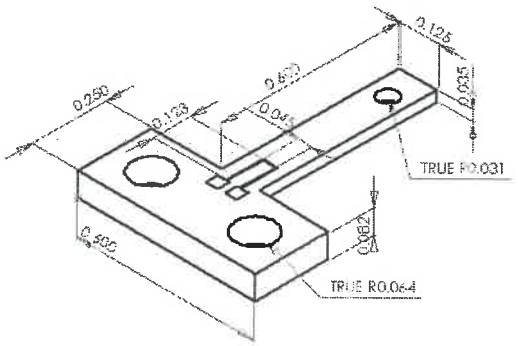

FIGURE 1: Test Structure Schematic

The base material for the test structure is variable since non-photolithographic manufacturing methods are suitable for many different types of materials. For the first set of tests, 6061-T6 aluminum was used for the beam, alumina was used as an insulating material between the beam and trace, titanium was used for the trace, and steel shim stock was used for the mask. Subsequent beams were made of acrylic. This allows the alumina deposition step to be eliminated and proof-of-concept polymer MEMS device to be created.

FABRICATION

The test cantilever beams were cut from 0.060" 6061-T6 aluminum stock using an Intellitek Benchman MX Desktop Mill. The toolpath was designed for a 1/16" endmill running at 10,000 rpm. This allowed all features to be machined without a tool change. Total manufacturing time for each beam was 5 minutes. A jig was also made for mounting the cantilever to an optical table.

The placement of the CNT-based strain gauge onto the beam requires an electrical trace to be deposited onto the base of the beam. A physical ~5 μm gap must be created in the trace measuring so that CNT-based piezoresistors can be integrated into the sensor. To this end, a shadowmask was manufactured using a Microlution 363-S micromill. The mask was cut from 0.005" thick steel shim, using a .003" endmill running at 50,000 rpm. A feed rate of 30 mm/min was used to cut the 100 μm wide trace path. A 1/16" tool was then used to cut the mask from the stock material and to cut mounting holes in the mask so that the mask could be affixed to the cantilever beam.

In order to make the ~5 μm gap in the wire traces, a tungsten wire tip was placed over the wire trace on the shadow mask. The tungsten wire tip was made by etching a 150 μm diameter tungsten wire. The tungsten wire was placed into a hole in a stainless steel fixture and etched using a 2M NaOH solution. A 2 VDC voltage was applied between the tungsten wire anode and the stainless steel cathode. The etching process takes several minutes and produces a long conical point on the wire coming to a final tip radius of ~100nm. The wire is then placed across the trace using a microscope to get alignment correct. Finally, the wire is fixed in place using tape on both sides of the mask as shown in Figure 2.

Trace deposition begins by smoothing the surface of the cantilever beam with a 3M microfine sanding paper. The beams are then cleaned using Terg-A-Zyme detergent in an

ultrasonic cleaner. Finally they are washed with methanol and blown dry with Nitrogen.

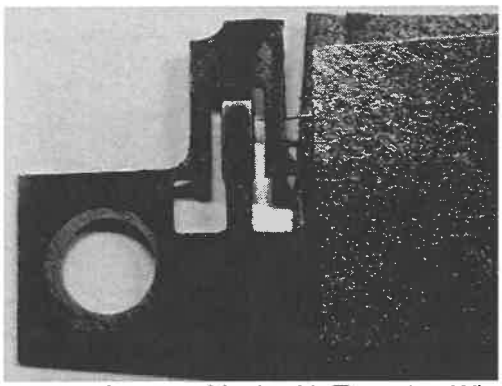

FIGURE 2: Shadow Mask with Tungsten Wire

For metal deposition, the cantilevers are placed into an electron beam evaporator and pumped down to 10^{-5} Torr. The cantilevers are first coated with 500 nm of aluminum oxide at a rate of 0.5 nm/s. This provides an insulting layer between the metal trace and the aluminum substrate. Next, the shadow mask is affixed to the cantilever beam using standard nuts and bolts. 100 nm of titanium is then deposited through the shadow mask at a rate of 0.3 nm/s. The parts are then cooled under vacuum for 10 minutes and are removed from the chamber. Finally, the mask is unbolted and removed, and the traces inspected for defects. This method produces titanium traces on top of the insulating alumina layer on the cantilever beam as shown in Figure 3. Prior tests in which the alumina was deposited through the shadow mask resulted in poor insulation between the conducting traces and the underlying aluminum due to unsatisfactory coating of the beam surface.

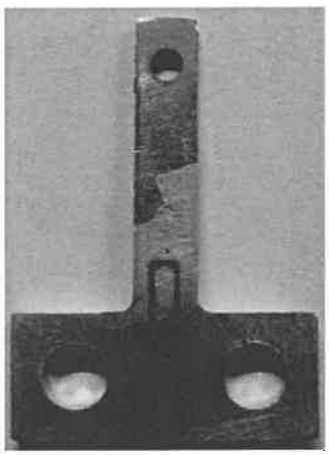

FIGURE 3: Test Structure with Metal Trace

After the test structure fabrication is completed, CNTs are deposited across the gap in the wire traces. CNTs are deposited onto these test flexures via dielectrophoresis. A droplet of a 3 µg/mL solution of SWCNTs in deionized water is placed on the electrodes of the test structure and a 5 MHz, 5V peak-to-peak AC voltage was used to direct the deposition of the SWCNTs. After 5 minutes, the test structure is rinsed with DI water and dried. Finally, the structure is coated with a thin ceramic layer to protect the sensor and mitigate noise [3].

RESULTS

Metal Trace Deposition

Several different types of metals including gold, palladium, and titanium were tested for use in the metal traces. These metals were chosen because of their Ohmic contact with CNTs [4]. Unfortunately, the gold and palladium contacts showed the tendency to flake off after deposition as shown in Figure 4. However, the titanium contacts did not suffer from this flaking tendency. Therefore, titanium ultimately was chosen as the wire trace material due to its superior bonding to aluminum and its low Schottky Barrier with carbon nanotubes.

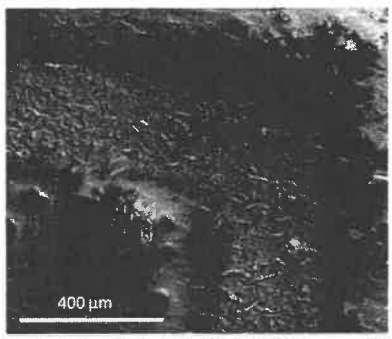

FIGURE 4: Flaking of Pd wire on Aluminum Beam

Gap Fabrication with Tungsten Wire

The quality of the gap in the metal trace on the test structures is completely determined the tungsten wire placement and geometry. When the tungsten wire is placed on top of the mask, and further away from the beam surface, it creates a blurred edge to the gap in the trace as some atoms diffuse in after passing the wire. In fact, when the deposition thickness is great enough the gap can disappear entirely as shown in Figure 5.

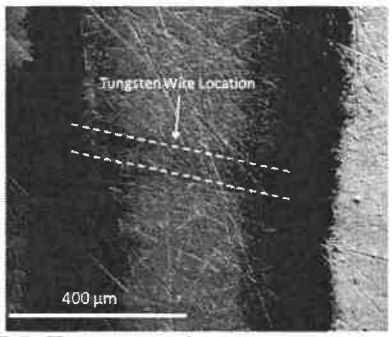

FIGURE 5: Tungsten wire on top

When the tungsten wire is placed between the mask and the beam, a sharply defined gap is produced. The dimensions of the gap match that of the wire very closely. This can be seen in Figure 6 where the gap in the metal trace matches the shape of the tungsten tip. Thus, with a long, narrow etching of the tungsten wire a well controlled gap can reliably be produced in the trace, allowing robust placement of carbon nanotube strain gauges onto a MEMS device of any material.

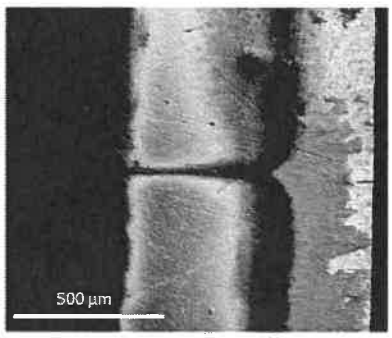

FIGURE 6: Tungsten Wire on Bottom

Gap Fabrication with FIB & CNT Deposition

Gaps in the metal traces can also be fabricated using a focused ion beam. The FIB is capable of producing very precise and uniform gaps in the metal traces as shown in Figure 7.

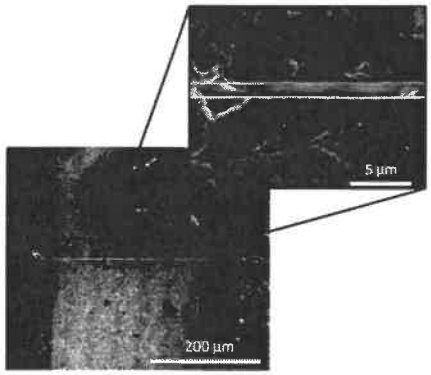

FIGURE 7: Test Structure with Gap Cut with FIB

However, the use of the FIB to fabricate the gaps doubles both the fabrication cost and time. Using the gaps fabricated with the FIB, it was possible to deposit CNT-based sensors onto the test structures as shown in Figure 8.

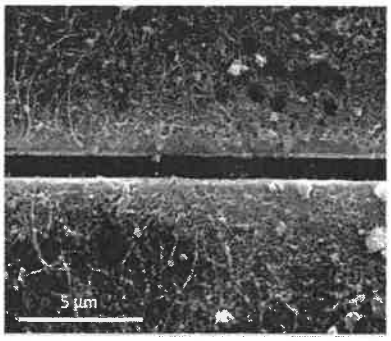

FIGURE 8: CNTs Deposited on Test Structure

CONCLUSIONS AND FUTURE WORK

This work shows that carbon nanotube based sensors can be fabricated on mesoscale devices without the use of expensive IC fabrication equipment. This reduces the prototyping cost of such sensors from around $10-30k to less than $100 and reduces the fabrication time from about 3-6 months to less than 3 days. However, more work still needs to be done to improve the sensor fabrication using tungsten wire shadow masks. These improvements in device fabrication will help to increase device quality while reducing the fabrication cost and time.

REFERENCES

[1] Tadigadapa, S.A.; Najafi, N., "Developments in microelectromechanical systems (MEMS): A manufacturing perspective," Journal of Manufacturing Science and Engineering, Transactions of the ASME, 2003, v 125, p 816-23.

[2] C Stampfer, A Jurgenson, R Linderman, D Obergfell, S Roth and C Hierold. Nano-electromechanical Displacement Sensing Based on Single-Walled Carbon Nanotubes. Nano Letters. 2006; 6: 1449-1453.

[3] T Helbling, C Hierold, C Roman, L Durrer, M Mattmann and V Bright. Long Term Investigations of Carbon Nanotube Transistors Encapsulated by Atomic-Layer-Deposited Al_2O_3 for Sensor Applications. Nanotechnology. 2009; 20: 1-9.

[4] D Hongjie. Carbon Nanotubes: Opportunities and Challenges. Surface Science. 2002; 500: 218-241.

DESIGN AND CHARACTERIZATION OF A 6 DEGREE-OF-FREEDOM MESO-SCALE NANOPOSITIONER WITH INTEGRATED STRAIN SENSING

Christopher M. DiBiasio[1] and **Martin L. Culpepper[2]**
[1]The Charles Stark Draper Laboratories
Cambridge, Massachusetts
[2]Department of Mechanical Engineering
Massachusetts Institute of Technology
Cambridge, Massachusetts

ABSTRACT
The success of many application areas (e.g. probe-based nanomanufacturing) hinges on the ability to design and realize low-cost, high-performance multi-degree of freedom (MDOF) nanopositioners. In meso-scale MDOF nanopositioners, the sensing system must be integrated into the structure of the nanopositioner. The only viable candidates for many small-scale, low-cost sensing systems are piezoresistive sensors.

A meso-scale 6-DOF nanopositioner was designed and tested. Polysilicon piezoresistors were surface micromachined onto a microfabricated silicon nanopositioner. The nanopositioner was actuated with moving magnet Lorentz force actuators. The final prototype costs less than $300 US and was found to have 10's of μm range, nm-level resolution, and a 100 Hz 1st natural frequency. System calibration was difficult as commercially available six-axis metrology systems for small-scale devices in a nascent technology. As a result of the preceding, the measured accuracy of the sensing system can only be claimed to be better than 17% in-plane and 30% out-of-plane. Models indicate that the system should exhibit worst case errors of a few percent; therefore this paper also serves as an indicator that new, improved metrology systems are needed for small-scale devices.

INTRODUCTION
Meso-scale, 6-axis nanopositioners possess unique characteristics due to their small size. They (a) are lower-cost ($100s vs. $10,000s US), (b) exhibit smaller thermally-induced errors, and (c) possess higher natural frequencies than their macro-scale counterparts. To be practical, they require a missing element, i.e. a cost- and size-appropriate sensing system. In general, macro-scale sensors are too large and expensive to integrate within these devices. Integrated sensors are therefore required to enable 6 axis closed loop nanopositioning within a meso-scale package. Given this capability, small-scale, 6-axis nanopositioners would then enable massively parallel probe-based nanomanufacturing processes such as dip-pen nanolithography (DPN) and nano-electrical discharge machining (nEDM).

NANOPOSITIONER DESIGN
The nanopositioner design is based upon the 6 degree-of-freedom (DOF), monolithic HexFlex flexure system [1-3]. Figure 1 shows our meso-scale HexFlex, less actuators and electronics. This design is attractive as (i) its 2½D geometry may be microfabricated and (ii) its in-plane symmetry and thin profile yield low thermal sensitivity [1].

FIGURE 1: *Meso-scale HexFlex nanopositioner*

Figure 2 shows how in-plane stage motion is achieved by applying combinations of in-plane forces; and how out-of-plane motions are achieved by out-of-plane forces.

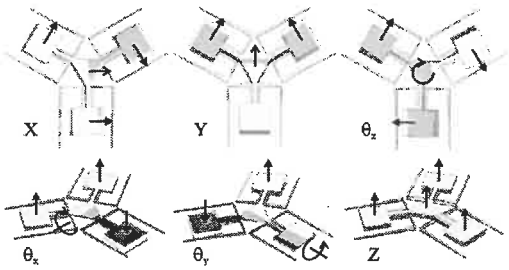

FIGURE 2: HexFlex actuation-motion examples

Each actuator tab is driven by a moving magnet Lorentz force motor [3-4]. As shown in Fig. 3, a periodic magnet array is attached to each actuator tab. Each array interacts with a set of nested coils that are contained within a flexible circuit that is attached to the bottom of a hexagonal aluminum heat spreader plate.

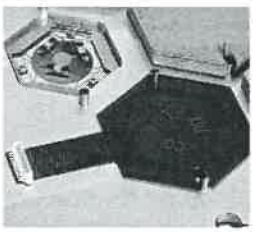

FIGURE 3: Flex circuit and heat spreader plate

A periodic magnet array and nested coils allows each actuator to impart two independent actuation forces [4-6] to the HexFlex. The 1st coil in each set imparts in-plane forces and the 2nd imparts out-of-plane force. Coil-magnet spacing was set at 150 µm, which enables each actuator to provide ~10 mN of force. These actuators are able to drive the device through a work volume 50x50x50 µm^3. The linearity of the device's Z axis response, shown in Fig. 4, is similar to the behavior in other axes.

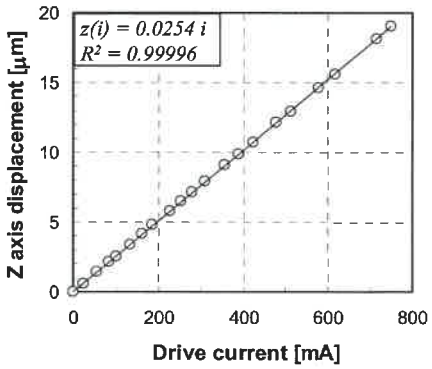

FIGURE 4: Z motion vs. actuator drive current

Six piezoresistive strain sensors [7-14] were microfabricated atop the flexure elements as shown in Fig. 5. The combination of flexures and piezoresistors were used due to (1) ease of integration, (2) microfabrication compatibility, (3) insensitivity to electromagnetic noise/fields, and (4) ability to sense sub-nm displacements when thermal compensation techniques are used.

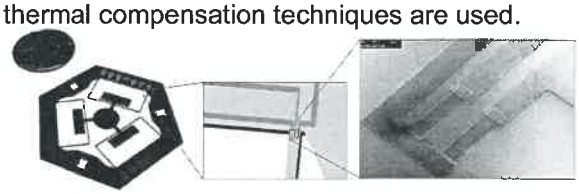

FIGURE 5: Location and shape of sensor

As shown in Fig. 5, the sensors work in pairs. A 1st sensor is placed along the neutral axis of the beam and the 2nd is placed at the beam's edge. The sensor on the beam's neutral axis is subjected to strain from out-of-plane bending while the sensor on the edge of the beam is subjected to strain from in- and out-of-plane bending. Their combined readings may be used to extract the in- and out-of-plane bending of six flexures. A minimum of three pairs, e.g. 6 sensors, enable 6 axis displacement sensing.

As the stage moves, the supporting flexures strain and cause a resistance change, ΔR_{sensor}, in the sensor(s) atop the flexure. The change in resistance is:

$$\Delta R_{sensor} = \pi_l E \varepsilon_l R_{sensor} \quad (1)$$

In Eq. 1 R_{sensor} is the nominal resistance of the sensor, E is the elastic modulus, and ε_l is the strain applied along the longitudinal axis of the sensor. The longitudinal piezoresistive coefficient, π_l, for polysilicon is typically 20x10^{-11} Pa^{-1} [13-14]. Given each sensors' strain, Eq. 2 may be used to determine stage displacements.

$$\boldsymbol{\delta} = \left[\Delta x \quad \Delta y \quad \Delta z \quad \Delta\theta_x \quad \Delta\theta_y \quad \Delta\theta_z \right]^T = \mathbf{J}\,\boldsymbol{\varepsilon} \quad (2)$$

In Eq. 2, $\boldsymbol{\delta}$, is stage displacements and $\boldsymbol{\varepsilon}$ is the longitudinal strains for each sensor. The Jacobian, $\boldsymbol{J}$, is a function of flexure geometry.

MICROFABRICATION

A 304 nm layer of thermal oxide was grown upon a 150mm diameter, 400µm thick silicon wafer. This provides electrical insulation for the piezoresistor and metal contact layers. A 530nm layer of N-type polysilicon (resistivity = 0.01749 Ω-cm) was deposited and patterned on the oxide to form piezoresistors. A 500nm layer of aluminum was deposited and patterned to form electrical contacts. Deep reactive ion etching was used to create the stage and flexures. Wafer and die level images of the HexFlex nanopositioners are shown in Figs. 6 and 7.

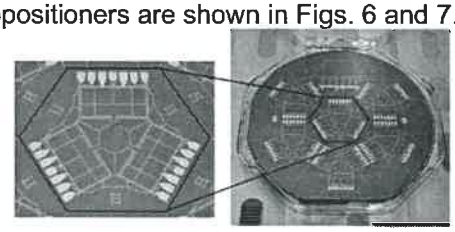

FIGURE 6: Wafer prior to separation of dies

FIGURE 7: mesoHexFlex separated from wafer

EXPERIMENTAL RESULTS

The motions of the HexFlex prototype were measured with a μMech Technologies G2 MEMS Motion Analyzer (MMA) [15]. The system consists of a CCD array that views a portion of the sample through a 20x microscope objective. The MMA measures the motion of a rigid object by performing dynamic image analysis on regions of interest (ROIs) contained within the initial image.

The HexFlex was commanded to move during six tests wherein the stage was commanded to move in only one axis. Ideally this does not induce parasitic motion errors; therefore the off-axis motions that are seen are used to set calibration coefficients. A six channel precision bridge circuit was used to measure sensor output during the quasi-static motion experiments. In the tests, temperature was controlled and test duration was short, therefore thermal compensation was not used.

RESULTS AND DISCUSSION

Figure 8 shows a plot of the stage's motion during a test wherein the stage was commanded to move only along the *x* axis.

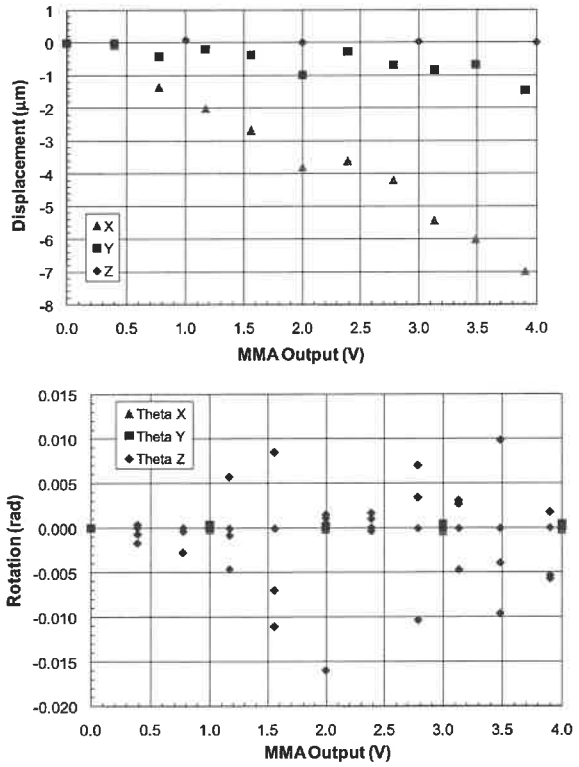

FIGURE 8: Motion of the HexFlex stage in response to a commanded motion in the x axis.

The error bars in Fig. 8 are smaller than the data markers. In-plane translational and rotational errors are ±10 nm and ±150 μrad respectively while out-of-plane translational and rotational errors are ±0.5 nm and ±55 μrad respectively. Note that the 7 μm *x* axis displacement is accompanied by roughly 1 μm *y* axis parasitic motion. Note the difficulty the MMA had in measuring rotation and out-of-plane motion. This was a consequence of the image processing software and does not reflect the performance of the nanopositioner.

A repeatability test was run to verify that the image processing algorithm was causing the error. Note that even though the actuators received identical inputs, the *x* axis motion of the stage as measured by the MMA system varied by as much as ±0.75 μm. As the HexFlex architecture [1-3] has been shown to be linear and repeatable, it is reasonable to assume that the majority of the error in measuring the stage motion is due to the repeatability and performance of the image processing algorithm used by the MMA. The image processing algorithm is not as repeatable as needed to fully understand the device's performance limits. Subsequently, we were unable to find a commercial instrument, or easily assembled commercial components that could measure the stage.

During each measurement, the output from particular sensors was monitored by a separate DAQ system. Figure 9 shows an example plot (plots for other axes are similar) of the output from each sensor during a commanded motion in the *x* axis. The error bars corresponding to voltage fluctuations are smaller than the data markers. The worst case voltage error is less than 4.5%. The linearity of the plotted behavior is represented by the worst R^2 value of 0.939.

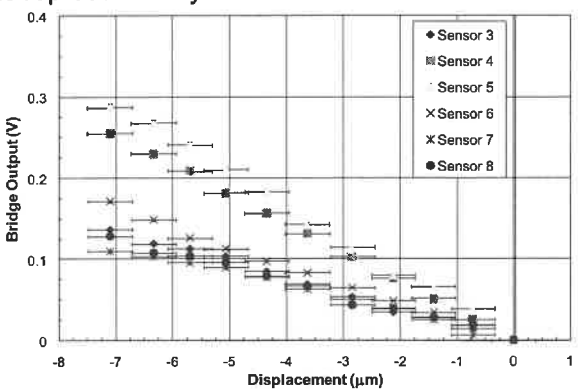

FIGURE 9: Bridge output from each sensor during a commanded motion in the x axis.

A multi-variable regression was performed in order to determine the resolution and accuracy of the piezoresistive sensors as defined by the available metrology equipment. The results of the multi-variable regression are presented in Table 1. The measured stage range is a function of the calibration fixture and is not the inherent nanopositioner range. The as-fabricate coil-magnet gap was larger than originally designed, and this reduced range. It should be noted that the range on each axis could be increased ~50% if the current in the coils is increased from 1.0 A to the maximum limit of 1.5 A. The results in Table 1 indicate that while the strain sensors are operating close to their theoretical performance, the calibration equipment limits the measured accuracy. Better metrology and calibration equipment is therefore required to characterize these types of systems.

TABLE 1: Device performance

Range	x	± 18.2	µm
	y	± 15.7	µm
	z	± 2.6	µm
	θ_x	± 3.7	mrad
	θ_y	± 5.8	mrad
	θ_z	± 35.5	mrad
Resolution	x	22	nm
	y	37	nm
	z	3	nm
	θ_x	320	µrad
	θ_y	2	µrad
	θ_z	39	µrad
1^{st} Mode		113	Hz
Cost (w/o DAQ)		~500	$ US

REFERENCES

[1] Culpepper, M.L., Anderson G., 2004, Design of a low–cost nano–manipulator which utilizes a monolithic, spatial compliant mechanism, Precision Engineering, 28; 469–482.

[2] Culpepper, M.L., Chen, S., 2006, Design of a Compliant, Micro–scale, Six–axis Nanopositioner–The Micro–HexFlex, Precision Engineering, 30 314–24.

[3] C.M. DiBiasio and M.L. Culpepper. "Design of a Six Degree of Freedom Nanopositioner for Use in Massively Parallel Probe-based Nanomanufacturing." Proc. ASPE, Monterey, CA (2009).

[4] Golda, D.S., 2008, Design of a high-speed, meso-scale nanopositioners driven by electromagnetic actuators," MIT Ph.D. Dissertation.

[5] Golda, D., Culpepper, M.L., 2008, Modeling 3D Magnetic Fields for Precision Magnetic Actuators that Use Non–Periodic Magnet Arrays, Precision Engineering, 32, 134-42.

[6] Golda, D., Culpepper, M.L., 2006, A Scalable Six–axis Electromagnetically–driven Nanopositioner for Nanomanufacturing, Proc. of the Annual Meeting of the American Society for Precision Engineering, 313–316.

[7] Smith, C.S., 1954, Piezoresistance Effect in Germanium and Silicon, Physical Review, 94, 42-49.

[8] Tufte, O.N., Stelzer, E.L., 1962, Piezoresistive Properties of Silicon Diffused Layers. Journal of Applied Physics, 34, 313.

[9] French, P.J., Evans, A.G.R., 1985, Polycrystalline Silicon Strain Sensors, Sensors and Actuators, 8, 219.

[10] French, P.J., Evans, A.G.R., 1986, Polycrystalline Silicon as a Strain Gauge Material, Journal of Physics E: Scientific Instruments, 19, 1055.

[11] Duc, T.C., Creemer, J.F., Sarro, P.M., 2007, Piezoresistive Cantilever Beam for Force Sensing in Two Dimensions, IEEE Sensors Journal, 7, 96.

[12] Senturia, S.D., 2001, Microsystem Design Kluwer.

[13] Bhat, K.N., Bhattacharya, E., DasGupta, A., and DasGupta N. Polysilicon Piezoresistive Pressure Sensors using Silicon-on-Insulator Approach. Proceedings of SPIE Vol. 5062, 2003.

[14] Bahreyni, B., Shafai, C., 2005, Fabrication of Piezoresistive Sensors in Standard MEMS Foundry Processes, Proceedings of the 4th IEEE Conference on Sensors, 215.

[15] Umech Technologies. MEMS Motion Analyzer Handbook. (2003).

ELECTROMAGNETIC-FORCE-DRIVING TYPE MEMS SWITCH USING HIGH PERFORMANCE NdFeB/Ta THIN FILM PERMANENT MAGNET

Masato Ishibashi[1], Ryo Tanabe[1], Tadahiko Shinshi[1] and Minoru Uehara[2]
[1]Precision and Intelligence Laboratory
Tokyo Institute of Technology
Yokohama, Kanagawa, Japan
[2]Magnetic Materials Research Laboratory
Hitachi Metals, Ltd.
Osaka, Japan

INTRODUCTION

Because they have higher isolation and lower insertion loss compared to semiconductor switches, the last decade has seen the development of several types of MEMS (Micro Electro Mechanical Systems) switch. Many of these are electrostatically actuated and so need high drive voltages, limiting the initial gap between the contact points to a few micrometers [1-3]. Such small gaps between the contact points limit the isolation properties of the switch.

Other MEMS switches are electromagnetically actuated at low voltages [4]. However, these usually require electrical power to maintain the switch in both the on and off positions. Y. Zhang et al. proposed an electromagnetically actuated MEMS switch using permanent magnets in order to save on the power consumption required to maintain the switch in the on and off positions [5]; however, the performance of permanent magnets used in MEMS switches is inferior to that of conventional sintered NdFeB magnets.

A high performance NdFeB/Ta thin film permanent magnet (TFPM), which not only has a high remnant flux density and a high coercive force similar to those of conventional sintered NdFeB magnets, but also has high heat tolerance, was developed [6]. A 4mm long cantilever type micro actuator using the TFPM and an air-core coil to generate bi-directional out-of-plane displacement up to 700μm was developed [7].

The purpose of this research is to apply a cantilever type micro actuator using the TFPM to a MEMS switch, which is expected to have good electrical isolation due to the gap of several hundreds of microns between the contact points, and thus significantly reduce the electrical power needed to maintain the switch in the on and off positions. This switch was fabricated and experimentally evaluated.

PROPOSED MEMS SWITCH

MEMS Switch Configuration

Fig. 1 show the configuration of the proposed electromagnetically actuated MEMS switch. The switch consists of a paddle-shaped cantilever with a TFPM at the tip, an air-core coil, a ferromagnetic film and electrodes as contact points. The on/off switching motion is realized using the deformation induced in the cantilever by the resultant force from the Lorenz force between the coil and the TFPM, the reluctance force between the ferromagnetic film and the TFPM, and the restoring force of the cantilever.

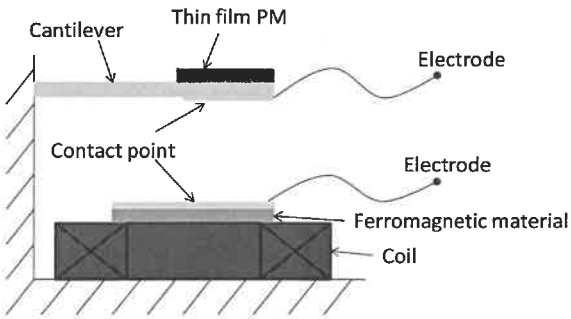

FIGURE 1. Configuration of MEMS switch using thin film PM

Driving Principle

The principle of the on/off switching is shown in Fig. 2. Fig. 2(1) shows the initial position in which the switch is off without any current through the coil. On supplying a current to the coil, an attractive force acts on the TFPM and the cantilever bends downward as the current increases.

For any displacement, as shown in Fig 2(2), where the sum of the attractive forces between the coil and the TFPM and between the TFPM and the ferromagnetic film is greater than the restoring force of the cantilever, the TFPM is pulled in the direction of the ferromagnetic film.

The switch is maintained in the on position without any coil current since the attractive force between the TFPM and the ferromagnetic film is larger than the restoring force of the cantilever due to the nonlinear characteristics of the magnetic force, as shown in Fig. 2(3).

Fig. 2(4) shows the transition from the on to the off position. The contact points release when a reverse current is supplied to the coil. In this case the sum of the Lorentz force and the restoring force of the cantilever is greater than the attractive force between the TFPM and the ferromagnetic film. The cantilever returns to its initial position where the restoring force of the cantilever is greater than the attractive force acting on the TFPM and no further current is required to maintain the cantilever in this position.

DESIGN

MEMS Switch Structure

Fig. 3 shows the structure of the MEMS switch. A paddle-shaped cantilever type micro actuator is used to move the contact point of the MEMS switch. This actuator, which has a driving range of more than several hundreds of micrometers, is suitable for the MEMS switch because the large gap ensures high electrical isolation.

The main structural component of the actuator is a SiN paddle-shaped cantilever consisting of a 2mm×0.4mm×0.003mm cantilever combined with a 2mm×2mm×0.003mm plate. A 3μm thick TFPM is deposited on the plate. The ferromagnetic layer is a 2mm×2mm×0.005mm Ni thin film set beneath the TFPM plate of the actuator. A U-shaped coil made of 0.25mm diameter copper wire is placed under the Ni film. The distance between the coil and the Ni film is 380μm.

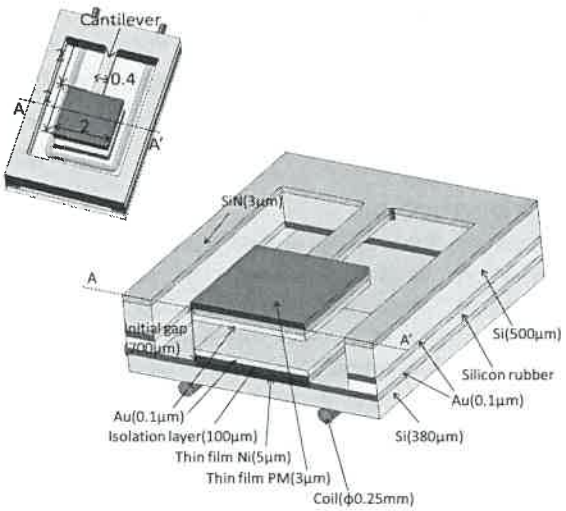

FIGURE 3. Structure of the proposed MEMS switch

Setup of the Initial Gap between the TFPM and the Ferromagnetic Film

In order to realize the proposed switching method, the initial gap between the TFPM and the ferromagnetic film needs to be determined. The attractive force F_F induced by the Ni film, the Lorentz force F_C generated by the current in the coil and the restoring force of the cantilever F_S act on the TFPM. F_F and F_C are simulated using three dimensional magnetic field analysis software (Ansoft, Maxwell 3D Ver.12.2), and F_S is calculated using the differential equation of the deflection curve of the cantilever.

In order to maintain the switch in the on position, Eq. (1) should be satisfied for zero gap, where the TFPM touches the ferromagnetic film.

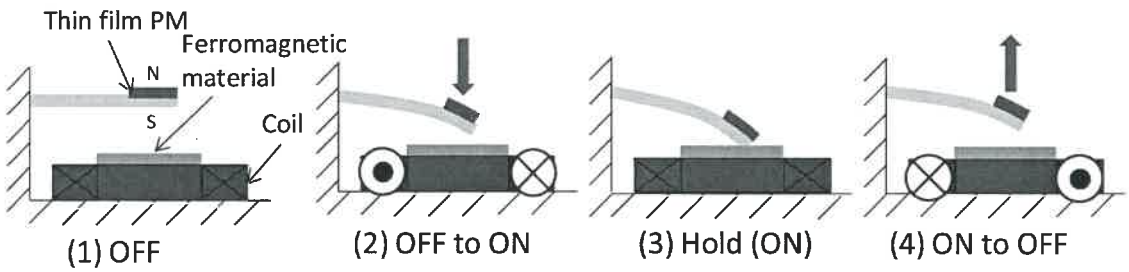

FIGURE 2. Principle of the proposed MEMS switch

$$F_S < F_F \quad (1)$$

On the other hand, in order to maintain the switch in the off position, Eq. (2) should be satisfied at some point between zero gap and the initial gap.

$$F_S > F_F \quad (2)$$

F_S and F_F were simulated for various gaps between the TFPM and the Ni film, as shown in Fig. 4. The results of this analysis indicate that the above condition is satisfied for an initial gap of more than 600μm. In the prototype MEMS switch, the initial gap was set to 700μm.

At zero gap, the attractive force between the TFPM and the Ni film was much greater than the largest Lorentz force produced by the coil. Therefore, a 100μm thick isolation layer was placed on top of the Ni thin film. The simulated pull-in and pull-out currents for an initial gap of 700μm are about -0.5A and 0.35A, respectively.

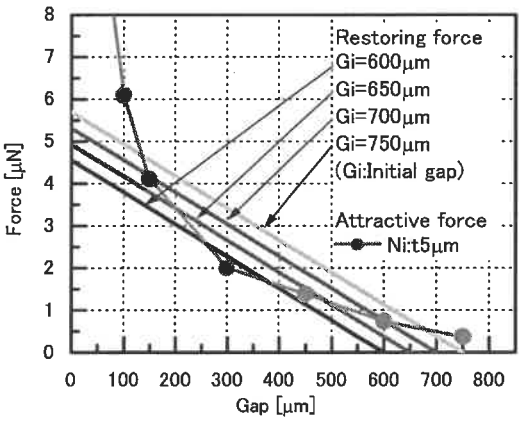

FIGURE 4. Comparison of simulated restoring and attractive forces

FABRICATION PROCESS

Fabrication of the Cantilever With a TFPM

The cantilever was fabricated on a 500μm-thick Si substrate. A 3μm thick SiN film was deposited on both surfaces using low pressure chemical vapor deposition (LPCVD). Next, Cu was sputtered and patterned on both surfaces of the substrate. The exposed SiN was removed from both sides using reactive ion etching (RIE), and the exposed Si was removed in TMAH. Then, the 3μm thick TFPM was deposited on the plate at the end of the cantilever using a magnetron sputtering process at a temperature of 475 degree Celsius using a Ti hard mask to control the shape. After deposition of the TFPM, a 1μm thick Cr was deposited on the TFPM at room temperature using a sputtering process. The cantilever with the TFPM and the Cr thin film was annealed at 450 degree Celsius for one hour. The tensile stress generated in the Cr by annealing cancels the compressive stress in the TFPM. Finally, a current pulse was used to magnetize the TFPM vertically with respect to the plate. The Si substrate was sandwiched between glass substrates to restrict the deformation of the cantilever due to the magnetic force induced by eddy currents during pulse magnetization.

Assembly

The cantilever was deformed due to its weight and the residual stress in the TFPM. In order to set the initial gap between the Ni film and the tip of the cantilever to 700μm, 400μm thick Si rubber films were inserted between the upper Si substrate and the lower one, on which the coil and the multilayer film consisting of a polyimide film and a Ni film were attached, with Au coatings. Fig. 5 shows a photograph of the fabricated MEMS switch.

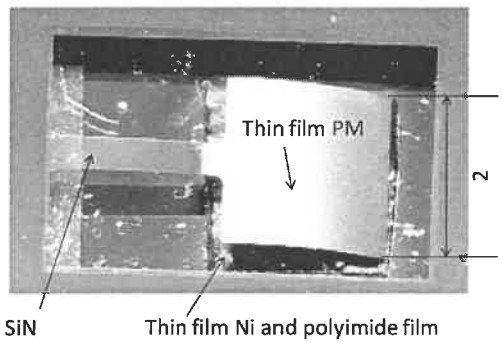

FIGURE 5. Fabricated MEMS switch

EXPERIMENTS

Measurements of the Cantilever Displacement

The displacement of the cantilever was measured with an optical fiber displacement sensor in order to ensure the MEMS switch makes contact.

The sinusoidal current was supplied to the coil, the cantilever displacement was measured. The pull-in/-out currents are -0.43A and 0.25A, respectively. These values are 14% and 29% smaller than the designed values.

Fig. 6 shows the measured cantilever displacement with a rectangular current supplied to the coil. Step 1 shows the switching on motion. Step 2 shows the switch in the on position without current. Step3 shows the switching off motion. Finally, Step 4 shows the MEMS switch returned to the off position without any current.

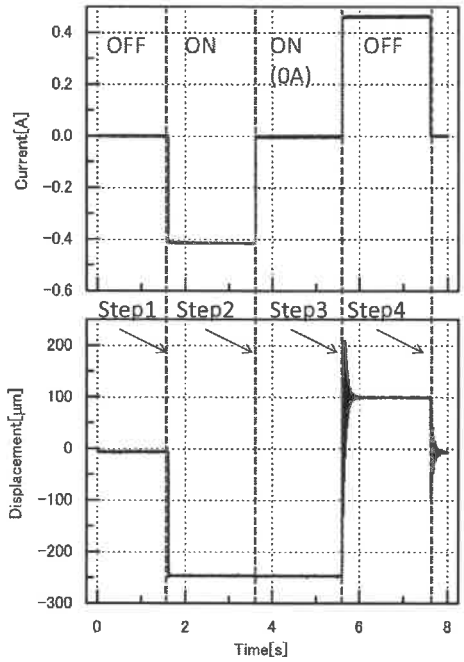

FIGURE 6. Input current and cantilever displacement

Switching Tests

In this experiment, 0.1μm thick Au electrodes were deposited for the contact points. The continuity of the MEMS switch was measured with the contact points touching without any current supplied to the coil. Continuity was not realized because the area of contact was small due to the residual deformation of the TFPM, and also because of the lack of contact pressure.

In order to increase the contact area, the cantilever was reversed to take advantage of the residual deformation of the cantilever. Furthermore, in order to increase the contact pressure, a -1.6A current was supplied to the coil to drive the switch. Under these conditions continuity between the contact points was realized.

CONCLUSION

In this paper, a MEMS switch consisting of a TFPM, a paddle-shaped cantilever on to which the TFPM was deposited, an air-core coil and a ferromagnetic film, was proposed and fabricated. The switch had a gap of several hundreds of microns between the contact points, and no electrical power was needed to maintain it in either the on or off positions. Based on simple driving experiments, the proposed switching action was demonstrated. In these experiments, the pull-in current was -0.43A and the pull-out current was 0.25A. Although continuity between the switch contacts wasn't realized in the original MEMS switch, optimizing the shape of the contact and increasing the contact area and the contact pressure enabled continuity.

In future work, the continuity is to be improved, the electrical isolation properties evaluated and life time tests carried out.

ACKNOWLEDGEMENT

This work was partly supported by the Adaptable and Seamless Technology Transfer Program (A-STEP) of the Japan Science and Technology Agency.

REFERENCES

[1] KC. L. Goldsmith, Z. Yao, S. Eshelman, D. Denniston. Performance of Low-Loss RF MEMS Capacitive Switches. IEEE Microwave and guided wave letters. 1998; 8(8)

[2] Y. L. Lai, L. Chang. Design of electrostatically actuated MEMS switches. Colloids and Surfaces A: Physicochem. Eng. Aspects. 2008; 313-314: 469-473

[3] C. H. Chu, W. P. Shih, S. Y. Chung, H. C. Tsai, T. K. Shing, P. Z. Chang. A low actuation voltage electrostatic actuator for RF MEMS switch applications. Journal of micromechanics and microengineering. 2007; 17: 1649-1656

[4] N. Dimitrakopoulos, R. E. Miles and A. C. Hartley. Large Throw Magnetic MEMS Actuated RF Switch. MEMS Sensors and Actuators 2006. The Institution of Engineering and Technology Seminar on. 2006: 223-230

[5] Y. H. Zhang, G. Ding, Z. Shun, D. Gu, B. Cai, Z. Lai. Preparing of a high speed bistable electromagnetic RF MEMS switch. *Sensor and Actuators A*,2007; 134: 532-537

[6] M. Uehara. Microstructure and permanent magnet properties of a perpendicular anisotropic NdFeB/Ta multilayered thin film prepared by magnetron sputtering. Journal of Magnetism and Magnetic. 2004; 284: 281-286

[7] S. Goto, R. Tanabe, S. Yao, J. Sakurai, T. Shinsihi, M. Uehara, H. Yamamoto. Displacement Measurement and Positioning Control of a Cantilever Type Micro Actuator Using High-performance NdFeB/Ta Thin-film Permanent Magnet. in Proc. 2009 precision engineering spring Conf. 2009: 793-794

DIRECT, HIGH-SPEED MILLING OF POLYMER MICROCHAMBER ARRAYS

Christopher R. Phaneuf, Craig R. Forest
G.W. Woodruff School of Mechanical Engineering
Georgia Institute of Technology
Atlanta, GA, USA

ABSTRACT
The limitations of semiconductor microfabrication techniques and the growing need for low-cost, disposable lab-on-a-chip platforms demands a method for rapid production of polymer microdevices. Current techniques for polymer device fabrication are impractical for low-volume production and suffer from dimensional constraints. We have developed a method for the fabrication of microchamber arrays using high-speed CNC milling to yield channel widths as low as 125 µm and average surface roughness of 350 nm. This approach has proven to be an invaluable tool for fast and flexible fabrication of polymer microdevices.

INTRODUCTION
Miniaturization of chemical and biological techniques has heralded a multitude of microfluidic applications. Traditionally, glass and silicon have been the preferred substrates for these platforms. Micro-scale features are fabricated using methods borrowed from the semiconductor industry such as wet etching, LIGA, and DRIE, and require expensive, hazardous, and slow processes that severely limit practicality, especially in the early design phases [1]. As a lower cost alternative, polydimethylsiloxane (PDMS) has become a ubiquitous polymer for devices made by soft lithography. Still, this approach requires tedious mold fabrication and yields devices insufficiently robust for applications outside of a laboratory. As the field of microfluidics matures, shifting towards affordable, disposable, and commercially viable platforms, conventional materials and the accompanying techniques are being replaced [2]. Instead, rigid polymers such as PMMA, polycarbonate, and cyclic olefin copolymers (COC) are preferred and techniques such as micromolding, laser etching, and direct milling have emerged as effective solutions.

Micromolding by injection molding and hot embossing are ideal for high-volume production of devices but can suffer from de-molding challenges. Also, these methods require a master, which can be slow to fabricate and therefore not amenable to fast prototyping. Laser etching is fast and affordable but incompatible with many materials and presents difficulties achieving accurate depths and smooth surface finish. Direct milling is a less common approach based on directly machining a polymer substrate and has been demonstrated for microfluidic applications [3]. Tool paths are programmed for CNC milling using CAD-CAM software and design changes are implemented by altering simple code. After experimenting with the above techniques, we found direct milling to be the most promising for fast turnaround (e.g. 5 min per device), wide-ranging dimensions, consistency, and minimal cost. Here we discuss the direct milling process applied to developing microchip-based diagnostic devices.

MATERIALS AND METHODS
We used a 3-axis vertical milling center (Haas, OM-1A) capable of accurate positioning within 10 µm and repeatability of 6 µm. The spindle operates at speeds up to 30,000 rpm, enabling the use of miniature end mills (Harvey Tool) and drill bits (Drill Bit City) with sub-millimeter diameters. Our substrate material of choice was Zeonor 1420R (Zeon Chemicals), a biocompatible cyclic olefin copolymer with a relatively high glass transition temperature of 136°C. Other materials tested include PMMA and polycarbonate.

A custom aluminum fixture (Figure 1) was milled and used to align and rigidly hold the workpiece, since small part deflections can easily damage the fragile tooling. A corner relief was pocketed into the fixture to allow repeatable positioning. Strap clamps were laser cut from 0.125" acrylic, which was chosen to avoid marring the surface of the workpiece. These are configured in a third-class lever arrangement and the screws can be hand-tightened to provide ample clamping force.

Prior to milling, each tool is zeroed to the top surface of the workpiece. This was accomplished us-

ing a multimeter to detect electrical conductivity between the tip of the tool and the base of the fixture by moving in 0.0001" increments. The tools were then offset by the thickness of the workpiece, which was precisely measured using a dial probe indicator.

Microchamber designs were creating in Solidworks and transferred to MasterCAM for generating toolpaths and outputting g-code. Climb milling was used to minimize burr formation and bursts of compressed air were used to clear chips. Finished devices were cleaned with ethanol and dried with compressed air or nitrogen.

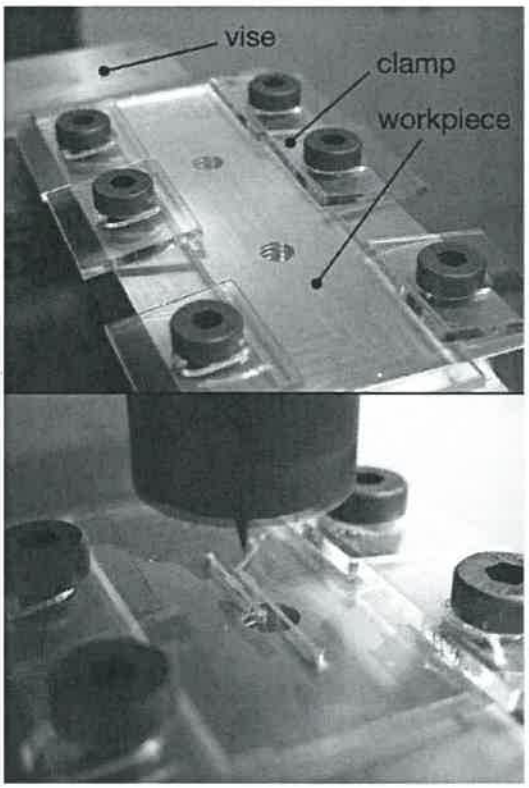

FIGURE 1. An aluminum fixture allows repeatable positioning and acrylic clamps tightly grip workpiece (above). A 125 µm diameter endmill pockets a PCR device in less than 5 min (below).

Back-end processing for the milled devices include enclosing the channels and sealing the ports once loaded with a sample. Our channels were encapsulated in a 2 min process by thermal bonding of a 100 µm Zeonor film using a hot press operating at 100 psi and heated to 140°C. Sealing the device is best accomplished with curing PDMS in the ports to prevent evaporation and suppress bubble formation.

EXPERIMENTAL RESULTS

A four-chamber device (Figure 2) was fabricated for an application we are pursuing involving infrared heating of multiple aqueous samples in an array of 1 µL microchambers. It features 250 µm wide, 125 µm deep lead-in channels and 500 µm wide, 1 mm deep reaction chambers milled at 30,000 and 20,000 rpm, respectively. Other geometries creating by direct milling include microchannel electrophoresis devices requiring tooling as small as 125 µm in diameter. Maximum channel depths are typically three times the diameter of the tool but have been demonstrated up to ten times the diameter with specialized long reach tooling. Minimum channel depths are determined by the z-axis resolution of the milling machine and the precision of the tool zero. Total machining time ranged from 5 to 10 min depending on the feature complexity and tool size.

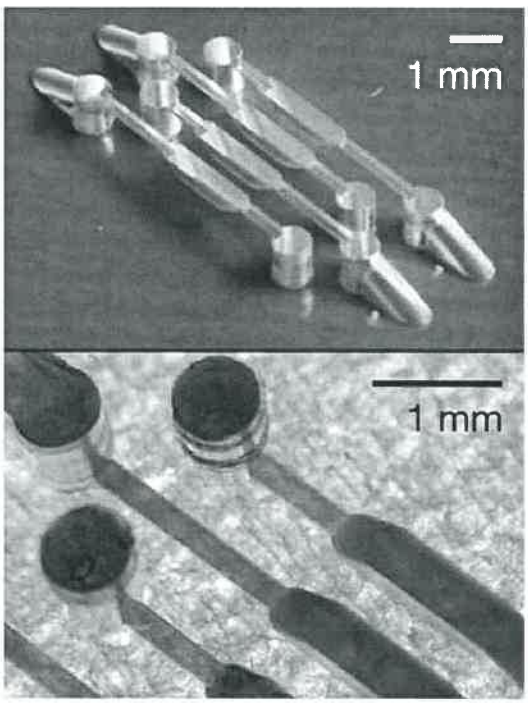

FIGURE 2. The four-chamber device was milled from a 2 mm-thick COC substrate at spindle speeds up to 30,000 rpm and feed rates around 20 inches per min. The milled part (above) is sealed by thermal bonding of a 100 µm film and shown filled with a dye solution (below).

Bonded devices have been used repeatedly without suffering delamination or mechanical damage. Surface roughness was measured using

a Taylor Hobson Talysurf Surface Profilometer. A sample of Zeonor 1420R was machined at various depths using a 250 µm diameter 4-flute square end mill operating at 30,000 rpm and tilt-corrected profile data was collected along the bottom of the channels. Average surface roughness was found to be roughly 350 nm, which is an order of magnitude lower than typical reported values for machined devices [2]. Still, surface roughness and other imperfections can lead to trapped air bubbles upon filling with a liquid. Sealing the ports with PDMS helps prevent the expansion of any entrained gas if the device is heated. Long tool life was observed after repeated operations given appropriate machining parameters.

CONCLUSION

By applying machining techniques to the fabrication of microfluidic devices, we have demonstrated an effective way to produce geometries with dimensions and aspect ratios impossible with other methods. With careful fixturing and tool zeroing, highly precise parts can be attained in a short period. Tweaks to the design and machine settings, such as feedrate and spindle speed, can be made on-the-fly through software to allow optimization of part quality and efficacy for its intended application.

Drawbacks to direct milling include burr formation and compromised optical clarity. We found that burrs can be minimized by climb milling all edges. Remaining burrs are removed with bursts of compressed air. Precision is limited by the user's ability to set accurate zeroes and the machine's positioning resolution. Additionally, this approach is not economical for higher volume production. Direct milling requires higher than average spindle speeds and therefore is not possible with most standard machine shop equipment. A spindle speeder, or high speed spindle attachment, is an option for achieving higher spindle speeds in order to use the required small-scale tooling.

Given the right equipment, direct milling is a straightforward and effective method for fast turnaround microfabrication. We have successfully created several different devices from multiple materials and will continue to push the limits of this technique.

ACKNOWLEDGMENTS

We would like to acknowledge the Georgia Institute of Technology for funding and access to equipment, Mark McJunkin for helping advise machine tool operation, and the Department of Homeland Security for its generous support.

REFERENCES

[1] Ziaie B, Baldi A, Lei M, Gu Y, Siegel RA. Hard and soft micromachining for BioMEMS: review of techniques and examples of applications in microfluidics and drug delivery. Advanced drug delivery reviews. 2004; 56: 145-172.

[2] Becker H, Gartner C. Polymer microfabrication technologies for microfluidic systems. Analytical and Bioanalytical Chemistry. 2007; 390: 89-111.

[3] Rainelli A, Stratz R, Schweizer K, Hauser P. Miniature ow-injection analysis manifold created by micromilling. Talanta. 2003; 61: 659-665.

HEAT-CONTROLLED INJECTION MOLDING OF NANOSTRUCTURED OPTICAL ELEMENTS

Takehiro Mitsuda[1], Keisuke Nagato[1], Shuntaro Hattori[1], Tetsuya Hamaguchi[1], and Masayuki Nakao[1]
[1]Department of Mechanical Engineering, Graduate School of Engineering The University of Tokyo, 7-3-1 Hongo,Bunkyo-ku, Tokyo, Japan

INTRODUCTION

Optical elements with nanostructures such as diffraction gratings, photonic crystals, and antireflection structures are important for new optical devices. Especially the antireflection structure is expected to be various applications [1]. The lithography process for VLSI is generally expensive [2]. Recently, nanoimprint has been developed as a low cost fabrication method [3]. In thermal nanoimprint, a nanostructured mold is pressed on a polymer surface, imprinted by heating, and after cooling down the mold is released. Because of the heat capacities of the heater and cooler, there is a limit in cycle time. On the other hand, injection molding is a high-throughput reproductive technique; the melted polymer is injected into the cold nanostructured mold. Injection molding also has an advantage in terms of the flexibility of component shape. From these advantages, we propose that the antireflection structures are produced by injection molding. However, replicating the nanostructures is assumed to be difficult because of the skin layer. The surface of the polymer is cooled quickly with the mold because the thermal conductivity of the mold is larger than the polymer. Therefore, the temperature of the polymer surface momentarily drops to below the glass transition point (Tg), forming the skin layer. Because the skin layer is hard and can not be filled in the nanostructures, the replication of the nanostructures is difficult.

In this study, to delay the formation of skin layer we heated the mold with the heater [4]. Figure 1 shows the behavior of the polymer in a general injection molding and that in the heat-controlled injection molding. We examined the relationship between the temperature of the mold and the replication of the antireflection structures. The temperature of the mold was controlled by the heater. The replication when the temperature of the mold was set to less than Tg because the polymer can not harden at Tg or more and to be demolded at once.

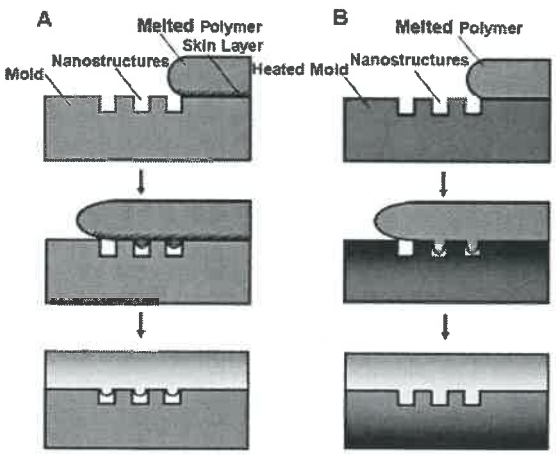

FIGURE 1. The behavior of the polymer (A) in general injection molding and (B) in the heat controlled injection molding.

EXPERIMENTAL

Main Setup

The schematic of the mold used in the experiment is shown in Figure 2. The stamper is set up on the mold base (A7075, JIS, thermal conductivity: 130 W/m·K). A thermocouple is made by a 50-μm-diameter chromel wire and an alumel wire and is sandwiched between the heater and the stamper to measure the temperature of stamper. The heater and the insulator are set between the mold base and the base. The mold is heated by the heater to keep preset temperature. The polymer we used is polystyrene (PS, Tg: 100°C, thermal conductivity: 0.108 W/m·K, molecular weight: 100,000), and it is injected with an injection molding machine Roboshot S-2000i5A (Fanuc,

Ltd). PS is heated to 240°C and injected from the nozzle.
Figure 3 shows an image of the stamper using a scanning electron microscope (SEM, S-4000: Hitachi), which has conic-holes with 300 ~ 400 nm depth and 200 nm pitch in average (the aspect ratio is 1.5 ~ 2).

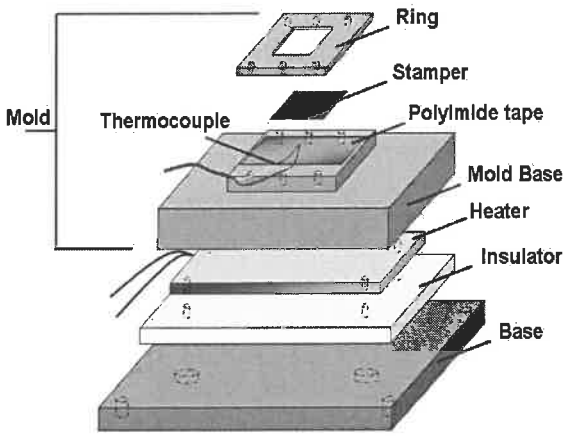

FIGURE 2. The schematic of the mold.

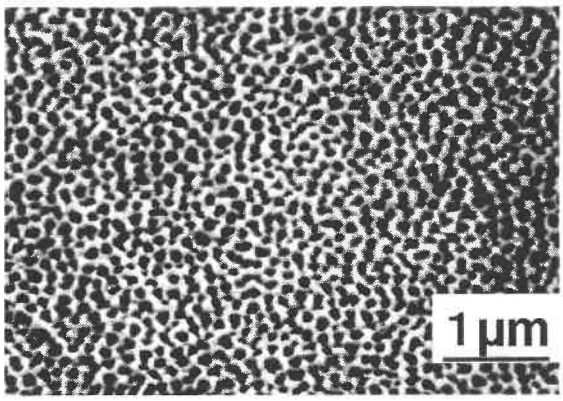

FIGURE 3. SEM image of the stamper (Tilt angle: 30°).

Replication of Plate

First, we prepared a ring (Figure 2) to replicate the plate. In this study, we call the replicas replicated with this ring the plate. We replicate the plate by full shot and short shot. We call the full-shot replica full shot and the short-shot replica short shot. Short shot is the replicating form which a mold cavity is not filled with the material. So the melted polymer flows naturally in short shot.

Replication of Box

Second, we prepared the ring to replicate the box. The ring (A7075) has the taper of 5°. In this study, we call the replicas replicated with this ring the box. Full shot is replicated with this ring. In the injection molding, when the time until the polymer reaches the surface of the stamper is long, the replication does not go well. However, it is expected that the replication can be improved because the mold used in this study can be raised the temperature as a whole. Figure 4 shows the schematic of the mold of the box. The mold has antireflection structures on the top side.

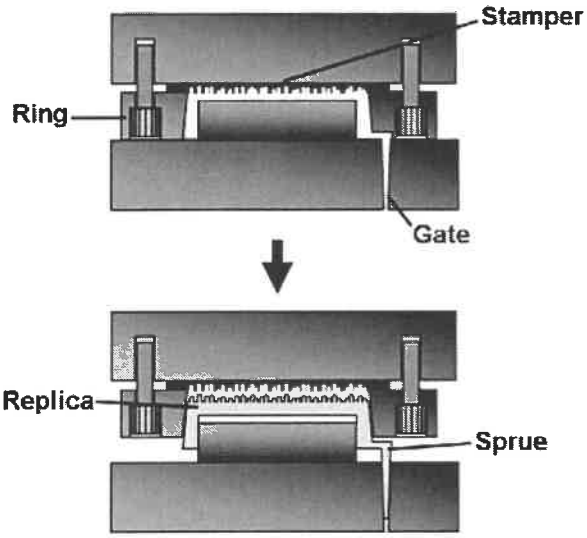

FIGURE 4. The schematic of the mold of the box.

RESULTS AND DISCUSSION

The temperature of the mold was changed from 30 to 100°C at intervals of 10°C. The polymer temperature when shot was 240°C. The dwelling was 10 sec with 300 MPa replicated below 90°C. On the other hand, the heater was stopped and the replica was cooled 120 sec when replicating at 100 °C. However, replicating with short shot was assumed that the dwelling pressure application was 0 Pa. Figure 5 shows overview of the plate. The plate was 33 × 34 × 2 mm^3.

Figures 6(A-C) show SEM images of replicas; (A) at 20 °C, (B) 80 °C, and (C) 120°C. The conic-array was low-height in (A). On the other hand, conic-array is higher in (B) and (C). However, (B) and (C) were almost the same as

externals. As a result, the replication was improved when the temperature of the mold is increased.

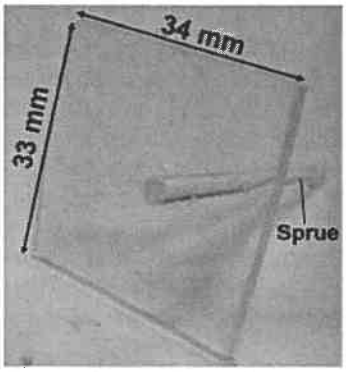

FIGURE 5. Overview of full shot of the plate.

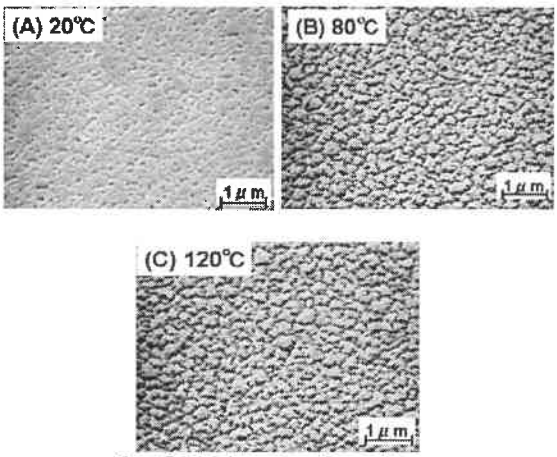

FIGURE 6. SEM image of replica (full shot of the plate) at (A) 20°C, (B) 80°C, (C) 120°C (Tilt angle: 30°).

Figure 7 shows an overview of short shot. The replica was discoid of about 25 mm in diameter. Figure 8 shows the result of the reflectivity of the plate. Square plots show full shot of the plate and diamond plots show short shot of the plate. The plotted datum is the reflectivity at the wavelength of 550 nm, and the error bar shows the reflectivity at the wavelength of 450 nm and 650 nm. The replica was put on a black PMMA plate whose surface is coated with glycerin. This setup can prevent the reflect light from the back because reflective index of glycerin is same as PS (1.6). The reflectivity of the replica was measured with a spectrophotometer (CM-2600d, KONICA MINOLTA). The reflectivity was taken at 6 points randomly selected from two or more replicas of the same condition, and the average was assumed to be the reflectivity. The reflectivity of PS without antireflection structures is about 6 %. At 30 °C, the reflectivity of both full shot and short shot were about 5%. However, the reflectivity has decreased with heating the mold. At 40, 50, and 60 °C, the reflectivity of full shot was lower than the reflectivity of short shot. At 70, 80, 90, and 100 °C, the reflectivity of full shot and the reflectivity of short shot reached almost the same. In addition, the reflectivity at 90 °C and the reflectivity at 100 °C were the same (about 1%).

These results indicate that melted polymer flows into antireflection structures without pressure before it is solidified if the mold is heated to around Tg.

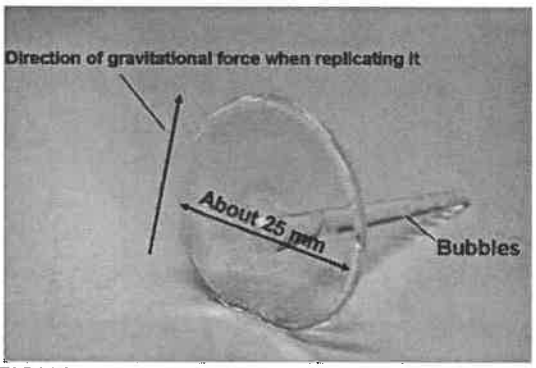

FIGURE 7. Overview of short shot of the plate.

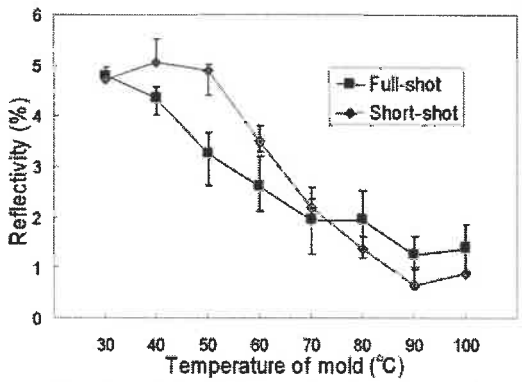

FIGURE 8. The reflectivity of visible light (the plate: full shot and short shot).

Figure 9 shows overview and side view of the box. The replica was 35 × 35 × 5 mm and thickness 1.3 mm at all sides. The used polymer is also PS. The antireflection structures were on the top side of replica. The condition in the injection temperature and the dwelling time are the same in both the plate and the box. Figure 10 shows the result of the reflectivity of visible light. Triangle plots show the reflectivity of the box. The measurement method is the same as the plate. At 30 °C, the reflectivity of the box was

about 5%. However the reflectivity of the box was decreased with heating the mold. Furthermore, at 80, 90 and 100 °C, the reflectivity of the box was the same as that of full shot of the plate. This indicates that even if the time until the polymer reaches the surface of the stamper is long, the replication of nanostructures becomes possible by heating the mold to around Tg.

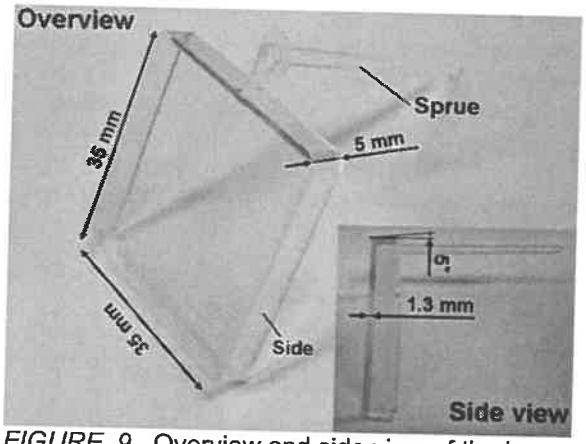

FIGURE 9. Overview and side view of the box.

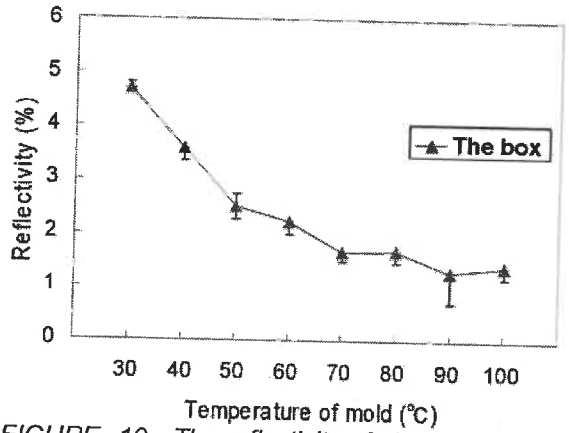

FIGURE 10. The reflectivity of visible light (the box).

Photograph of reflected images of fluorescent light is shown in Figure 11. These replicas are the box. The sides of replica were cut to put on a black PMMA plate coated with glycerin. The reflectivity of replica is (a) PS plate without antireflection structures (the reflectivity: 6%), (b) replica at 50°C (the reflectivity: 3%), (c) replica at 90°C (the reflectivity: 1%). The fluorescent light is reflected clearly in (a). However, the reflected light has grown dim in (b) and (c). Compare (b) and (c), the brightness of the reflected light is decreased in (c) with which the reflectivity is lower.

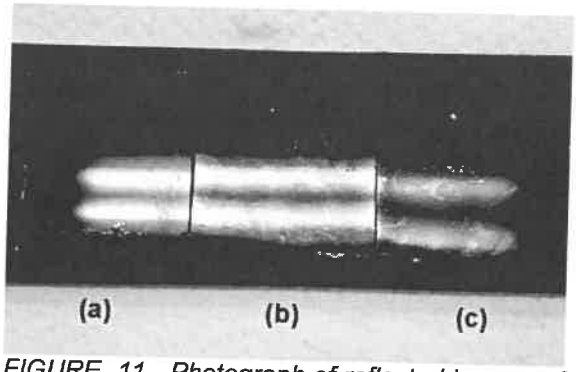

FIGURE 11. Photograph of reflected images of fluorescent light in (a) PS plate without antireflection structures (the reflectivity: 6%), (b) replica at 50°C (the reflectivity: 3%), (c) replica at 90°C (the reflectivity: 1%).

CONCLUSIONS

In this study, we proposed and demonstrated replicate antireflection structures on the surface of PS with heat-controlled injection molding. It was designed and fabricated that the plate 33 × 34 × 2 mm^3 and the box 35 × 35 × 5 mm whose thickness was 1.3 mm at all sides. Full shot of the plate, short shot of the plate, and full shot of the box were replicated at the temperature of mold from 30 to 100°C at intervals of 10°C. All of these replicas had antireflection structures on one of their sides. We measured the reflectivity of each replica. And, the experimental results show that if PS is used, the reflectivity of replica is decreased with heating the mold.

REFERENCES

[1] L Jay Guo. Recent progress in nanoimprint technology and its applications. Journal of Physics D: Applied Physics. 2004; 37: 123-141.

[2] Endoh S, and Hayashibe K. Nanomold Fabrication and Nanoimprint Devices Using Advanced Blu-ray Disc Technology. Japanese Journal of Applied Physics. 2009; 48: 06FD04.

[3] Q Chen, G Hubbard, P A Shields, C Liu, D W E Allsopp, W N Wang, and S Abbott. Broadband moth-eye antireflection coatings fabricated by low-cost nanoimprinting. Applied Physics Letters. 2009; 94: 263118.

[4] Hattori S, Nagato K, Hamaguchi T, and Nakao M. Rapid injection molding of high-aspect-ratio nanostructures. Microelectronic Engineering. 2010; 87: 1546-1549.

PENETRATION OF RESIDUAL LAYER IN NANOIMPRINT LITHOGRAPHY BY DIRECT OXIDATION OF PHOTOCATALYTIC FILM

Makoto Shimoda[1], Keisuke Nagato[1], Tetsuya Hamaguchi[1], and Masayuki Nakao[1]
[1]Department of Mechanical Engineering,
The University of Tokyo
Bunkyo-ku, Tokyo, Japan

INTRODUCTION

The demand for the practical use of the nanoimprint lithography (NIL) has risen for the miniaturization in two-dimensional micro/nano fabrication technology.

Photolithography is now used widely, however, has a few of difficulties such as the high equipment cost and the diffraction limit.

NIL, in which a resist on a substrate is patterned by mechanical pressing a nanostructured mold, is expected to be a post-technology of photolithography [1].

However, in order to use NIL practically, there is a problem of residual layer.

Residual layer is the part of resist which is remained in the convex part of mold by the viscosity in arranging resist by the nanoimprint.

Then the process of O_2-plasma etching is needed to remove residual layer in processing the substrate and this process causes a side etching.

Figure 1 shows the schematic that the side etching prevents the miniaturization, which means pattern destruction because etching can not be completely anisotropy i.e., the resist is etched not only vertically but also horizontally.

Here we propose the method of penetration of residual layer in NIL, which uses the oxidation of the titanium dioxide (TiO_2) under UV irradiation for the penetration of the residual layer.

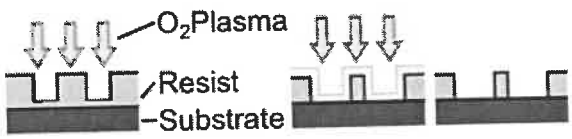

FIGURE 1. Schematic of the side etching.

MECHANISM OF OXIDATION OF PHOTOCATALYST

Figure 2 shows the remote oxidation mechanism of photocatalyst [2];

Free electrons and holes are generated by TiO_2 under UV irradiation (FIG 2b). A H_2O_2 is produced from H_2O by a pair of free electron and hole (FIG 2c, 2d). A H_2O_2 travels to the substrate by diffusion (FIG 2e). A hydroxyl radical is produced from a H_2O_2 under UV irradiation (FIG 2f, 2g). Resist is oxidized and decomposed by oxidation of Hydroxyl radicals (FIG 2h) [3]. Photocatalyic lithography in 100 μm order has been demonstrated using remote oxidation [4][5].

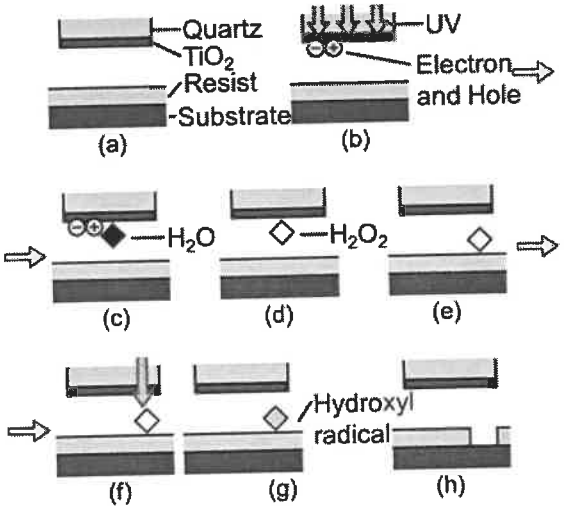

FIGURE 2. Remote oxidation mechanism of photocatalyst.

PROPOSAL OF METHOD OF PENETRATION OF PHOTOCATOLYST

In this paper we propose a method to penetrate the residual layer by direct oxidation of photocatalytic film. The remote oxidation is an isotropic etching and the diffusion of H_2O_2 reaches about 100 μm. Because of the isotropy, the groove broadens as wide as the resist thickness. On the other hand, the direct oxidation of residual layer after nanoimprint minimized the broadening of groove width (FIG 3). Pattern will be destructed around TiO_2 film as maximum residual layer thickness. So, TiO_2 should be arranged only in the convex parts of mold to make TiO_2 film thickness thin.

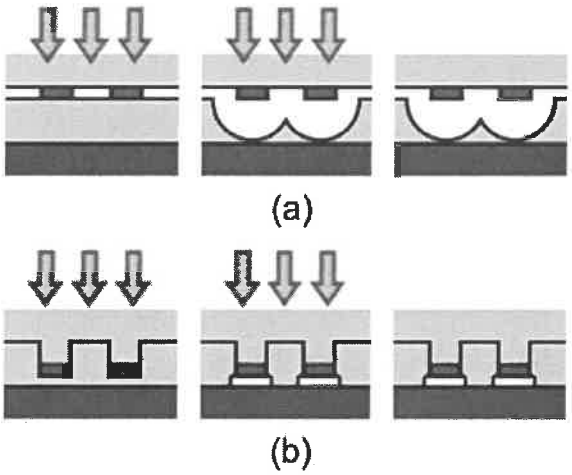

FIGURE 3. Conceptual diagram of Pattern destruction;
(a) photocatalytic lithography,
(b) NIL with the penetration of residual layer.

Figure 4 shows the conceptual diagram of penetration of residual layer. Nanoimprint is done using the quartz mold with micro/nano patterns of which TiO_2 is arranged in the convex parts (FIG 4b). The resist nearly TiO_2 film is decomposed under UV irradiation from the mold (FIG 4c, 4d). Mold is released (FIG 4e).

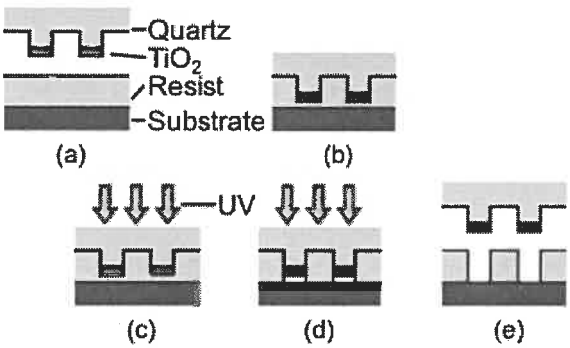

FIGURE 4. Conceptual diagram of the method to penetrate the residual layer.

FABRICATION OF MOLD

The molds were fabricated as follows (FIG 5);
Quartz plates were cleaned by ultrasonic bath with acetone, with ethanol and then with deionized water for 5 min. respectively.

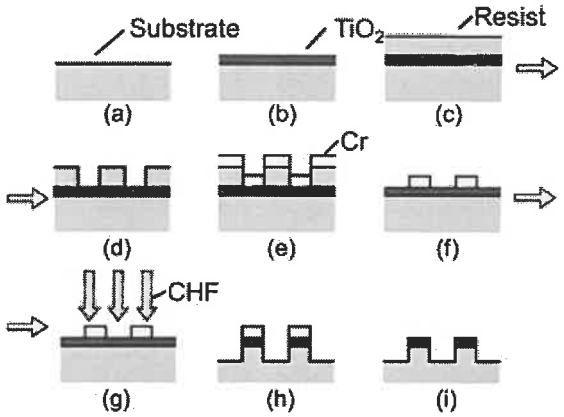

FIGURE 5. Process of fabrication of mold.

Ti was sputtered 100nm by magnetron sputtering (FIG 5b). The sputtering condition was decided according to other reports [6][7][8]. Resist was arranged in 1- and 2-μm-pitch line-and-space patterns by electron beam(EB) lithography (FIG 5c, 5d). Cr was sputtered 800nm and Cr on the resist was removed by lift-of (FIG 5e, 5f). The quartz plates and TiO_2 film were etched using arranged Cr as mask by Inductive-coupled-plasma reactive ion etching (ICP-RIE) (FIG 5g, 5h). The etching conditions are listed in Table 2. Cr was removed using etchants (FIG 5i). Figure 6 shows the schematic of the mold and figures 7(a1-b2) show the scanning electron microscopy (SEM, Hitachi S-4000) images.

TABLE 1. Etching conditions.

Etching gas	CHF_3
Antenna power (W)	400
Bias power (W)	150
Pressure (Pa)	1
Etching rate of Ti (nm/min)	60
Etching rate of SiO_2 (nm/min)	240

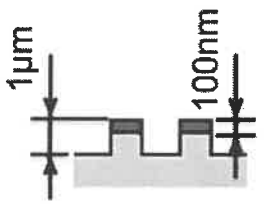

FIGURE 6. Schematic of the mold.

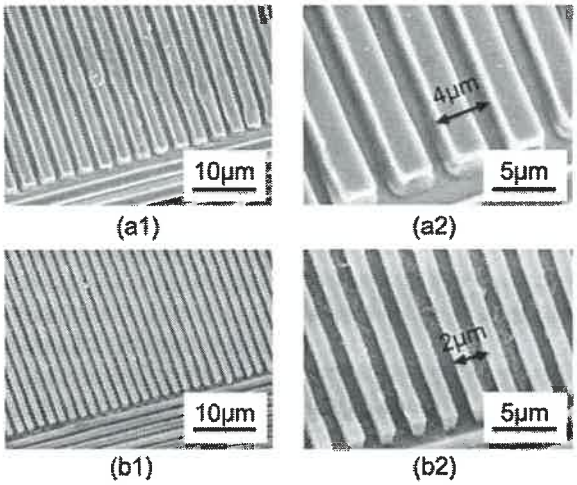

FIGURE 7. SEM image of the mold with 1-μm-depth and 1- and 2-μm-pitch line-and-space patterns which 200-nm-thick TiO_2 is arranged in the convex parts of. tilt: 30 degree.
(a1) (a2) 2-μm-pitch, (b1) (b2) 1-μm-pitch.

The result of X-ray diffraction (XRD) analysis of TiO_2 film is shown in Figure 8. The sputtering conditions are listed in Table2. In the XRD pattern, the diffraction peak of anatase was observed; anatase is one of the several crystal structures of TiO2 and known as photocatalyst.

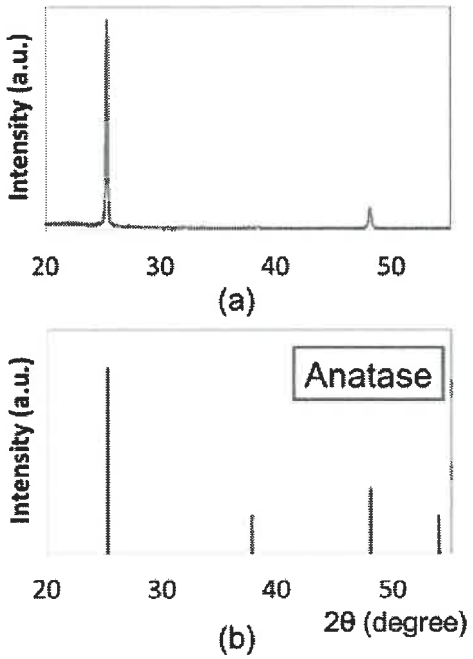

FIGURE 8. XRD pattern of TiO_2;
(a) Obtained spectrum,
(b) Reference spectrum.

TABLE 2. Sputtering conditions of TiO_2

Target	Ti
O_2 (sccm)	2.8
Ar (sccm)	6.8
Sputtering power (W)	40
Substrate temperature (degree)	300
Deposition rate (nm/min)	1
Sputterring pressure (Pa)	1

EXPERIMENTAL METHODS

Substrates were fabricated as follows; 1) Si substrates cleaned by ultrasonic bath with acetone, with ethanol and then with deionized water for 5 min. respectively. 2) Polymethylmethacrylate (PMMA) was dissolved in toluene, which concentration is 5mg/l, and spin coated at 2000rpm for 35 sec on the Si prates. The thickness of the PMMA film was 5 nm.
The substrates with TiO_2 were exposed to UV ramp for 1-3 hours (FIG 9). The spectrum pattern of the UV ramp is shown in figure 10.

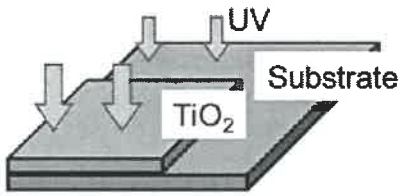

FIGURE9. Schematic of the exposure experiment.

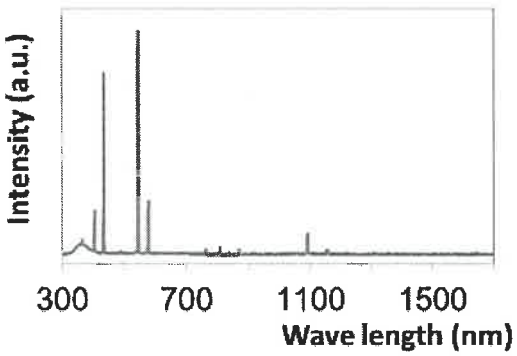

FIGURE 10. Spectrum pattern of the UV light.

EXPERIMENTAL RESULTS AND DISCUSSIONS

PMMA on Si substrate was resolved using oxidation of TiO_2. Figure 11 shows the SEM images of the surface of PMMA film and the

schematic. The change of surface structure was observed in the area with TiO_2.

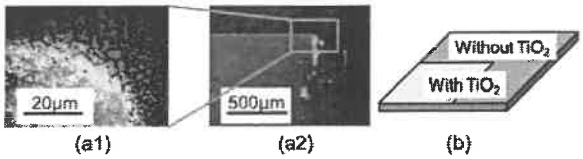

FIGURE 11. (a1)(a2) SEM images of the surface of PMMA film, (b) schematic.

Figure 12 shows the energy dispersive X-ray spectrometry (EDX) results of C/Si atomic ratio as a function of UV exposure time. The decrease of C/Si atomic ratio is observed with longer exposure time at only the area with TiO_2. This means that the change of surface structure was caused by the decomposition of PMMA.

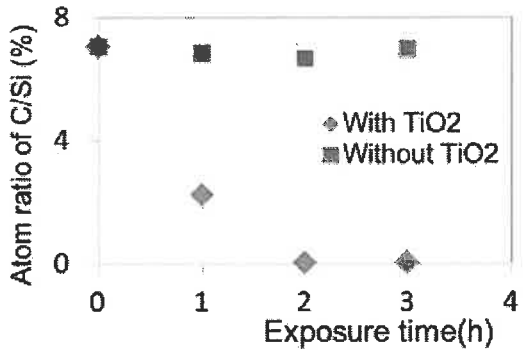

FIGURE 12. C/Si atomic ratio as a function of UV exposure time.

CONCLUSIONS

In this paper we have proposed "the penetration of the residual layer" method for nanoimprint lithography. We successfully fabricated the mold with 1-μm-depth and 1- and 2-μm-pitch line-and-space patterns of which 100-nm-thick TiO_2 is arranged in the convex parts. We confirmed the oxidation of PMMA resist by TiO_2 film.

ACKNOWLEDGEMENT

The mold were made using EB writer (F5112+VD01) donated by ADVANTEST Corporation and ICP-RIE (ULVAC CE300I) in the University of Tokyo VLSI Design and Education Center (VDEC).

REFERENCES

[1] Guo, L. J., Nanoimprint lithography: methods and material requirements. Advanced materials. Weinheim. 2007; 19: 495.

[2] Kubo, W., Tatsuma T., Fujishima, A. and Kobayashi, H. Mechanisms and Resolution of Photocatalytic Lithography. J. Phys. Chem. 2004; B, 108:3005.

[3] Sugiue, Y., Morii, H., Nagato, K., Tsuchiya, K., Hamaguchi, T. and Nakao, M.. Photocatalytic Nano-imprinting Using Direct Near-field Oxidation. ASPE Annual meeting 2007. 2007; 42: 299-302.

[4] Notsu, H., Kubo, W., Shitanda, I. and Tatsuma, T. Super-hydrophobic/superhydrophilic patterning of gold surfaces by photocatalytic lithography, Journal of Materials Chemistry. 2005; 15: 1523.

[5] Lee, J.P., and Sung, M. M., A new patterning method using photocatalytic lithography and selective atomic layer deposition. Journal of American chemical Society. 2003; 126: 28.

[6] Takeda, S., Suzuki, S., Okada, H. and Hosono, H. Photocatalytic TiO_2 thin film deposited onto glass by DC magnetron sputtering. Thin Solid Films. 2001; 392: 338-344.

[7] Mardare, D., Tasca, M., Delibas, M. and Rusu, G. I., On the structural properties and optical transmittance of TiO_2 r.f. sputtered thin films. Applied Surface Science. 2000; 156: 200-206.

[8] Zeman, P., and Takabayashi, S., Effect of total oxygen partial pressures on structure of photocatalytic TiO_2 films sputtered on unheated substrate. Surface and Coatings Technology. 2002; 153: 93-99.

MEASUREMENT OF CURRENT IN ELECTRO-CHEMICAL DISCHARGE MACHINING BY FORCED DISCHARGE DISPERSION

Katushi Furutani, Hiroyuki Shintani, Yasuo Murase, and Shuichi Arakawa
Department of Advanced Science and Technology
Toyota Technological Institute
Nagoya, Japan

INTRODUCTION

Precision or micro machining methods for insulated materials are demanded to build microsystems. Electro-chemical discharge machining (ECDM) is used to machine grooves and holes on insulated materials such as glass [1][2].

In ECDM, an insulated workpiece is immersed in an electrolyte. A tool electrode is gently pressed on the workpiece. When the electrode is completely covered with bubbles generated by the electrolysis, a discharge occurs through a gas film. The discharge heat accelerates the chemical reaction. Consequently, the workpiece surface is removed [1]. However, many cracks are observed around a machined hole because of the accumulation of discharge heat.

The forced discharge dispersion with multiple electrodes is useful to reduce cracks in electrical discharge machining (EDM) [3] and has been applied also to ECDM [4].

In this paper, the current pulses during ECDM were observed and classified according to their durations and peaks for the comparisons of machining performance by ECDM with those using multiple electrodes connected electrically in parallel and a single electrode.

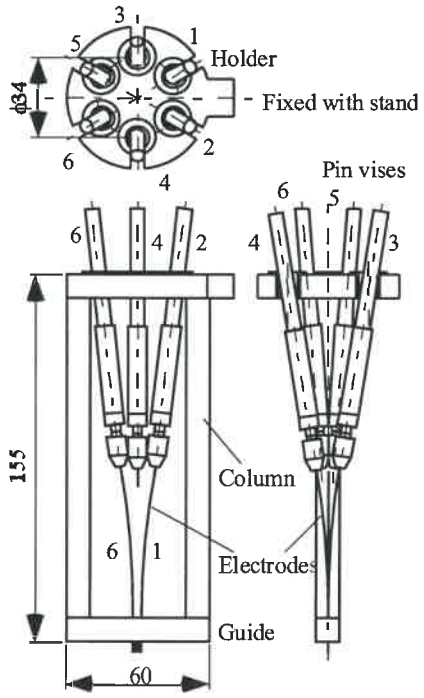

FIGURE 1. Machining unit.

EXPERIMENTAL SETUP

Fig. 1 shows a machining unit for ECDM [4]. A gravity-feed type unit for ECDM was made in which six electrodes were aligned radially at the upper holder and in line at the lower electrode guide with a pitch of 0.8 mm. The electrodes are insulated with fluorine resin tubes each other and exposed 4 mm in electrolyte.

Fig. 2 shows discharge circuits. The applied voltage was synchronously switched with MOS-FETs in the divided power circuit. A diode and resister were inserted in each branch to the electrode to prevent the reverse flow and to measure the current as voltage. Table 1 shows

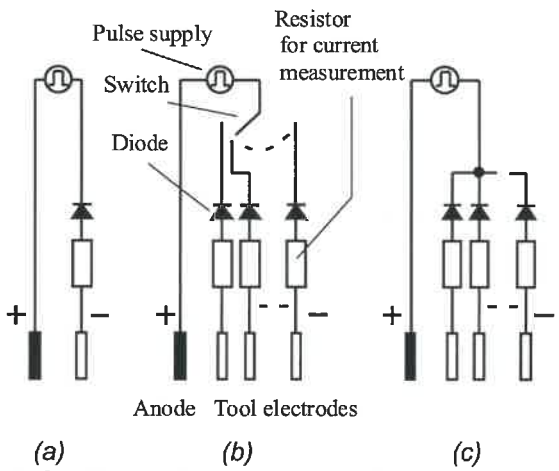

FIGURE 2. Discharge circuits. (a) single electrode, (b) divided power, (c) equi-potential power.

TABLE 1. Machining conditions.

Gap voltage	70 V
Pulse duration and interval	80 ms, 20 ms
Tool electrode	ϕ0.3 mm tungsten (-)
Anode	Graphite
Resistor for current measurement	1 Ω
Electrolyte	NaCl 10wt%
Mass of pin vise	19 g
Workpiece	t1.3 mm Soda lime glass
Machining time	0.5 - 40 min

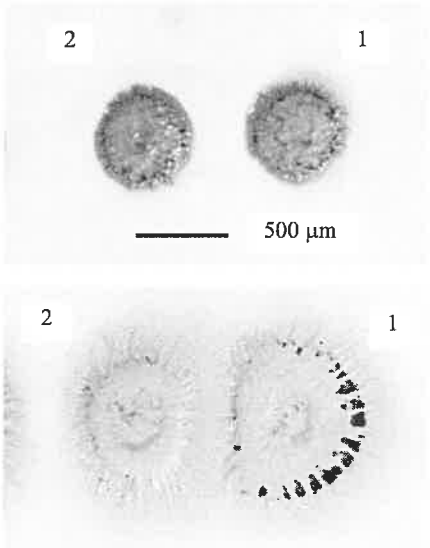

(a)

(b)

FIGURE 3. Examples of machining.
(a) Divided power, (b) Equi-potential power.

machining conditions. The polarity of the electrodes was set to negative. The working fluid was changed within 60 min.

EXPERIMENTS

The machining performance was compared among the single electrode, equi-potential power and divided power.

Fig. 3 shows examples of machined holes with multiple electrodes. All holes were round and their entrance edges were sharp by the divided power. Less cracks by the divided power ware observed than by the others because the workpiece was cooled during a pulse interval of 520 ms by the forced dispersion. The bubble amount covering the electrodes in the divided power was smaller than the others because of the pulse intervals. A hole was round by the single electrode though its entrance edge was

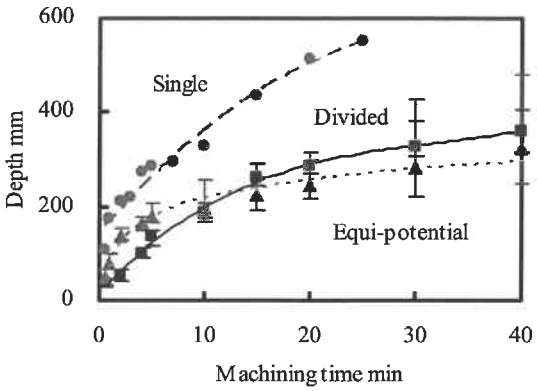

FIGURE 4. Depth of machining.

dull. Holes were oval, which major axis was orthogonal to the electrode arrangement in the equi-potential power. The abundant bubbles always remained around the electrodes. In addition, the spread area of the bubbles affected the ellipticity of the holes. Fig. 4 shows the relationship between hole depth and machining time. The machining depth by the single electrode was smaller than each sum by the others. Because the middle of the aligned electrodes was isolated with the bubbles, the holes at both end were deep by equi-potential power.

Fig. 5 shows machining current at an elapse .time of 40 min. In single electrode method shown in Fig. 5 (a), after current with a duration of several milliseconds flew, a series of spikelike current with a duration less than 100 μs flew for each applied voltage pulse. This process was observed with a high-speed camera. Bubbles were generated and grew when the voltage was applied. Then discharge occurred. The bubbles disappeared during intervals of the applied voltage. Therefore, the initial current generates bubbles and the following short pulses were mainly discharge. An offset current of 0.3 A flew even if there was no discharge. This shows that the discharge does not contribute the bubble generation. Fig. 5 (b) shows current waveforms in the divided power. Voltage was repetitively applied in sequence of the electrode number from 1 to 6. The same trends about the currents as those shown in Fig. 5 (a) were observed. Fig. 5 (c) shows current waveforms in the equi-potential power. Current pulses with a long duration and small peak were often observed. Gas amount at each electrode was always less than that in the divided power

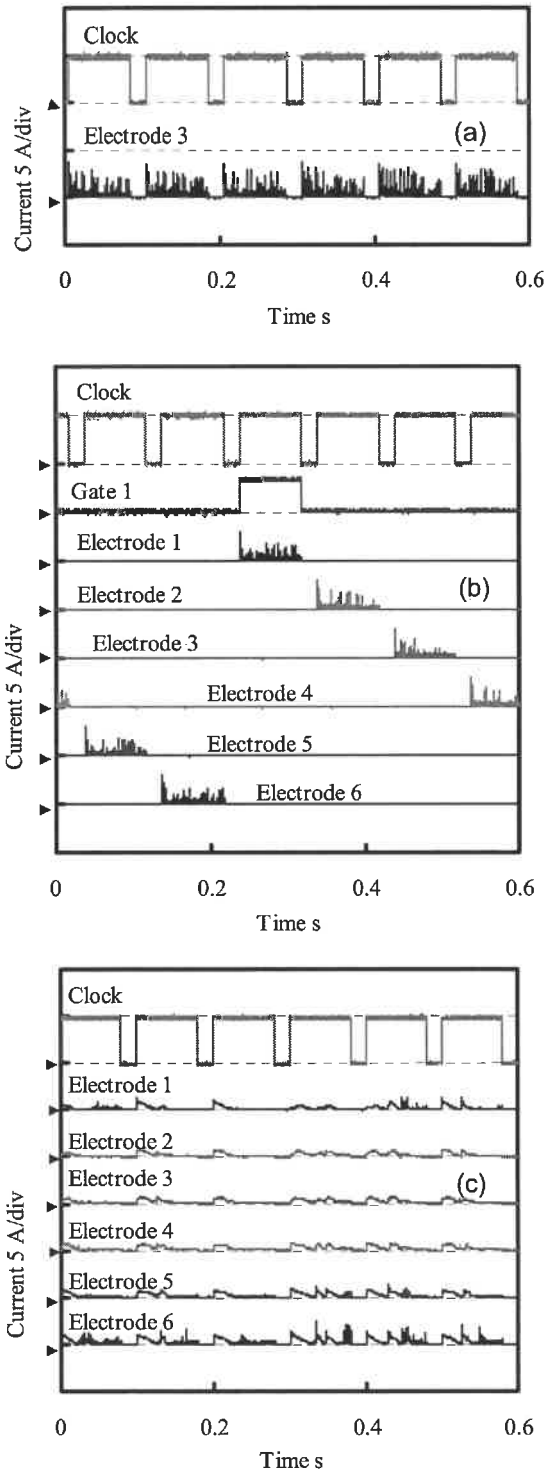

FIGURE 5. Machining current. (a) single electrode, (b) divided power, (c) equi-potential power.

because the current was distributed to all

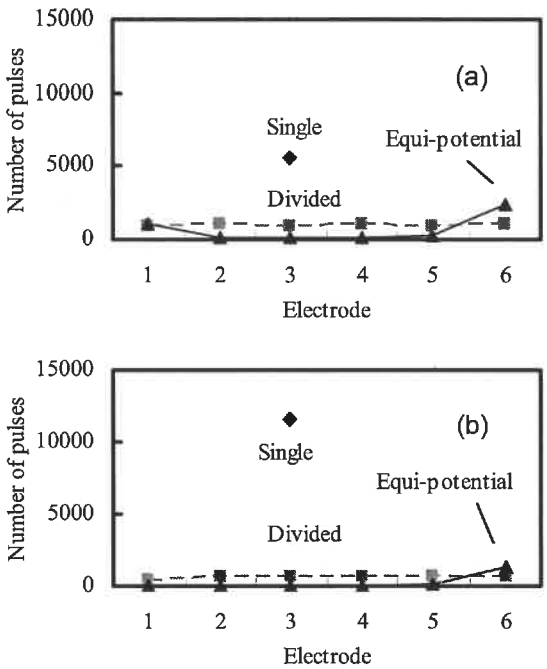

FIGURE 6. Distribution of pulses. (a) Initial, (b) After 40 min.

electrodes. The number of discharge was small and the peak of the current was small.

Fig. 6 shows number of discharge for 5 s at each electrode. The number of pulse in the divided power was a flat of 1000. Because Electrodes 1 and 6 are exterior, discharge easily occurred to electrolyte from them so that the number of pulse there was greater than the others in the equi-potential power.

Fig. 7 shows the number of discharge at other electrodes. Zero means that a series of discharge occurred at one electrode [5]. Frequency of 0 at Electrodes 1 and 6 was large and discharge concentrated there in the equi-potential power as shown in Fig. 7 (a). Because the voltage is applied to an electrode, no pulse was observed at the others in the divided power as shown in Fig. 7 (b).

Fig. 8 shows the number of pulse for 5 s at an elapse time of 30 min., classified every 20 μs as duration and 0.25 A as peak. In the divided power shown in Fig. 8 (b), pulse below a peak of 0.5 A and a duration of 20 μs were often observed at Electrode 2. Pulses with a duration of 100-200 μs was observed over 1 A. This trend was observed at the others. Although total

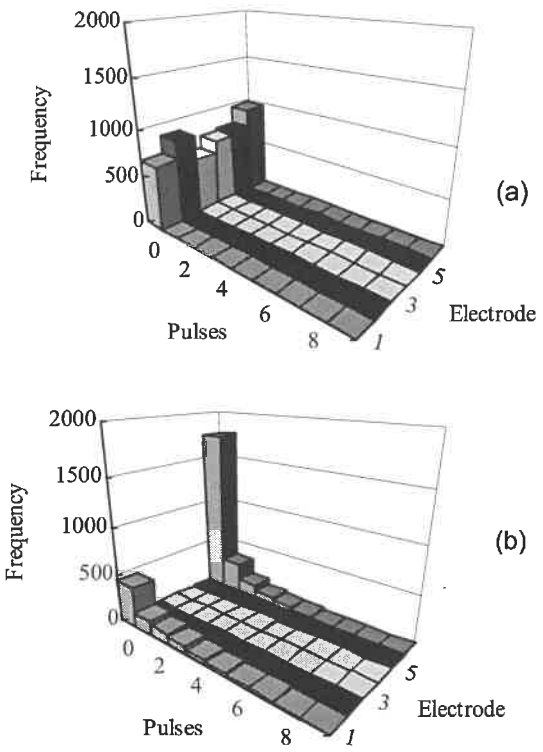

FIGURE 7. Number of discharge at other electrodes. (a) divided power, (b) equi-potential power.

number of pulse in the equi-potential power was smaller than the others, most were small peaks and short durations.

CONCLUSIONS

(1) The distribution trend of current peak and duration in the divided power was the same as that in the single electrode.
(2) The number of discharge at exterior electrode was larger than that at the others in the equi-potential power.

A part of this study was financially supported by Grant-in-Aid for Scientific Research (C) (21560134) by Ministry of Education, Culture, Sports, Science and Technology (MEXT), Japan.

REFERENCES

[1] Kurafuji H, Suda K. Electrical Discharge Drilling of Glass I, Ann. CIRP, 1968; 16: 415-419.
[2] Furutani K, Maeda H. Machining glass rod with lathe type electro-chemical discharge machine, J. Micromech. Microeng., 2008; 18, 6: 065006, 1-8.

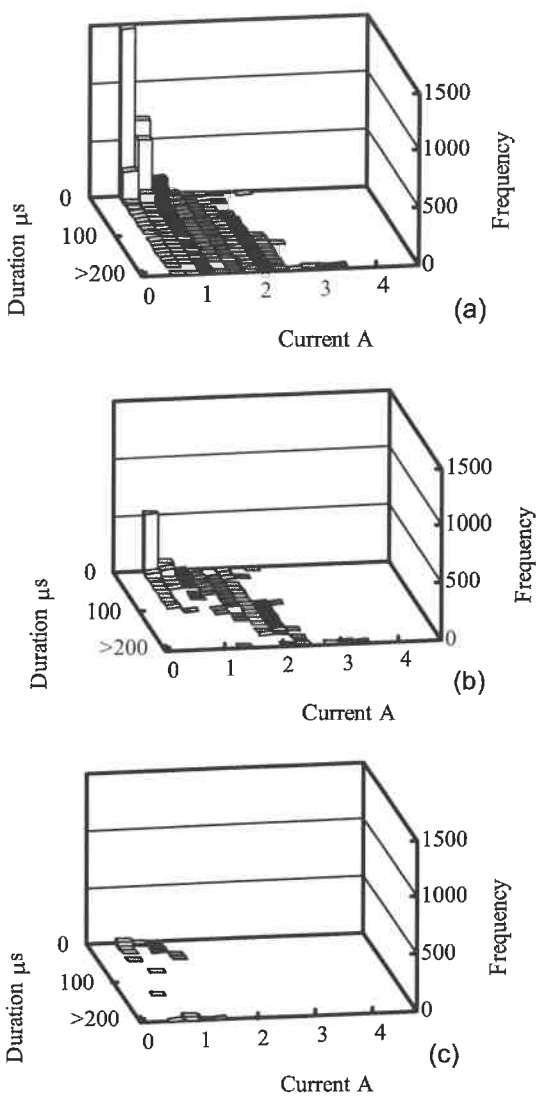

FIGURE 8. Distribution of peak current and duration. (a) single discharge, (b) divided power, (c) equi-potential power.

[3] Furutani K, Enami T, Mohri N. Three-dimensional Shaping by Dot-matrix Electrical Discharge Machining, Precis. Eng., 1997; 21, 2/3: 65-71.
[4] Furutani K, Murase Y, Shintani H, Arakawa S. Machining performance of electro-chemical discharge machining by forced discharge dispersion, Proc. Int. Conf. European Soc. Prec. Eng. Nanotechnol., San Sebastian, Spain, 2009; 138-141.
[5] Mohri N, Furutani K, Shirai K, Enami T. Forced Discharge Dispersion by Dot-Matrix Method, Ann. CIRP, 1997; 46, 1: 139-142.

OPTICAL DEFLECTION INDENTIFICATION BASED ON DARK-FIELD LASER SCATTERING FOR THE INSPECTION OF CRYSTALLINE SILICON WAFER IN SOLAR CELL

Gyung-Bum Kim*, Jeong-Seung Yeon **

***Applied Opto-Mechatronics Lab., Dept. of Aeronautical & Mechanical Design Engineering**
Chungju National University, Chungju, Chungbuk, 380-702, KOREA
****Graduate School of Chungju National Universuty**

ABSTRACT

In this paper, optical deflection of laser scattering has been investigated based on Rayleigh criterion for silicon wafer in solar cell. Geometric shapes and light scattering properties against a silicon wafer surface are parameterized and then a new laser scattering mechanism is designed based on the information. The optical deflection of laser scattering is experimentally identified with the pitch stage in the laser scattering mechanism, which makes the slope of silicon wafer surface adjusted. It is shown that the optical deflection of laser scattering agree with the presented model, exclusive of grazing angles which is satisfied with Rayleigh criterion.

KEYWORDS: Laser scattering, Optical deflection, Rayleigh criterion, Silicon wafer, Solar cell

1. INTRODUCTION

Recently, concerns on green energy become rising due to exhaustion of fossil energy and environmental contamination problems. Solar cell is considered as powerful renewable green energy. Mono-crystalline silicon based solar cell has a good conversion efficiency up to 27~37%. Mass production system of solar cell is almost similar to one of semiconductor and flat panel display and so could be easily implemented in our industry.[1]

The manufacturing process of solar cell is composed of chemical etching, texturisation, emitter diffusion, phosphor-silicate glass removal, anti-reflection coating, printing and co-firing, etc, as shown in Fig. 1. The total inspection for wafer topology, surface defects, micro crack and coating thickness is performed in every process. Specially, the inspection of surface defect and topology for silicon wafer is of importance according to the slimming of wafer. The micro crack inspection plays influential roles on the improvement of quality and productivity in solar cell. It has been reported that it is very difficult to detect micro cracks. A lot of infrared thermography and ultrasonic thermography has been proposed and applied to detect micro cracks so far.[1,2]

The device development of solar cell inspection is focused mostly on the inspection of macro defects, which include surface and topology defects. These macro defects are relatively visible and so it is enough to inspect them using image processing. However, micro defects such as scratch, pinhole, dent and inclusion, are not easy to detect because they are in a very shallow and wide region. Device researches for these micro defects have not been studied well.

In this paper, dark-filed laser scattering mechanism is newly designed for solar cell wafer. Based on the designed mechanism, optical defection of laser scattering is experimentally identified to extract comparatively simple and reliable micro defect detection information.

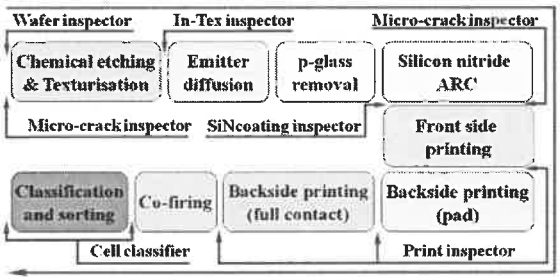

FIGURE 1. Production process of solar cell

2. OPTICAL DEFLECTION IDENTIFICATION BASED ON LASER SCATTERING

2.1 Design of laser scattering mechanism

Manufacturing processes such as polishing and wire sawing make silicon wafer surface damaged. To remove these surface damages, etching process is performed. Fig. 2 shows 3D images of mono crystalline silicon wafer which is measured by AFM(atomic force microscope) after Acid etching process. In case of machining process such as grinding and lapping, machined lay is made and its particular scattering pattern is formed. On the other hand, perfectly random surface topology is shown in silicon wafer surface after etching process. So, it is judged that it is not easy to analyze the random scattering pattern of silicon wafer surface.[3,4]

Geometric reflective characteristics of a surface are defined as the ratio of incident light irradiance to reflective light radiance. This is called as bidirectional reflectance distribution function.[5] Here, scattered light depends on micro surface topology, in case physical properties such as reflectance, color, and texture, etc, are constant. When it comes to electromagnetic properties, laser scattering pattern rely on light wavelength, material conductivity, surface roughness and the correlation between incident light direction and viewing detector. Here, laser scattering pattern is affected by geometric micro topology of reflective surface, and laser scattering intensity is changed by both incident angle and viewing one of laser.

Based on scattering property of silicon wafer and previous research results, laser scattering mechanism in Fig. 3 is newly designed to investigate the laser scattering pattern on crystalline silicon wafer. Detailed specifications are shown in Table 1. Vision system is applied in the detection part to catch hold of the inclination of scattering light. Spot-shaped laser with wavelength 636.6nm is used as light source. Mechanism parameters(θ_i , θ_o) are applied to investigate a specific tendency to laser scattering pattern according to the change of incident laser angle and viewing camera one. Also, the azimuth angle(ϕ_a) of camera is considered to identify the optical deflection of laser scattering in various directions. The pitch stage makes an inspection table slope slant and the inspection table is equipped to rotate by 360°. This laser scattering mechanism is designed to cope with the inline inspection using a linear motor in the future.

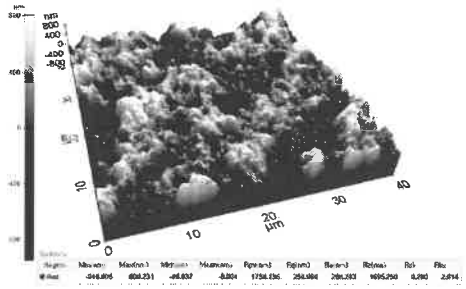

FIGURE 2. 3D AFM image of crystalline silicon wafer

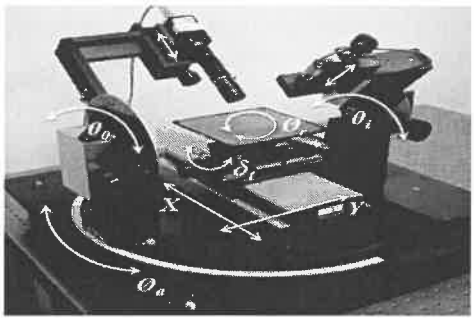

FIGURE 3. Laser scattering mechanism

TABLE 1. *Detailed specifications of laser scattering mechanism*

List	Specification
CCD Camera	Basler A631f Resolution: 1392×1040 Pixel size: 4.65 μm×4.65 μm Frame rate: 17fps Pixel resolution: 8bit Video output type: IEEE 1394
Lens	50mm CCTV Close-up ring
Laser	Stockeryale SNF Laser Wavelength: 636.6nm Shape: spot
Filter	Polarization filter ND filter
Motor	DCT linear pulse motor Repeatability Open loop: ± 5 μm Close loop: ± 2 μm
Motion controller	Ajinextek SMC2V030
Frame grabber	Matrox Solios

2.2 Analysis of laser scattering pattern

Surface roughness of crystalline silicon wafer is measured by AFM and its mean Rq is 0.267μm. Based on Rayleigh criterion[6], the incident angle

of laser has to be larger than 67.8°. It means that this condition makes inspected surface smooth or specular.

Four angles(45°, 60°, 70°, 80°) larger or smaller than Rayleigh criterion angle are selected and applied to investigate these phenomena through laser scattering patterns. The viewing angle of camera is equally specified by 10° from 0° to 80°. Fig. 4 shows laser scattering patterns depending on the change of viewing angle of camera at specific incident laser angle. Laser scattering components appear intensive at the incident angle 30°, while they get weak at the larger incident angle. Also, Scheimpflug effect is generated according as viewing angle of camera is large and so laser scattering components in vertical image direction get decreased. This means that a specific part of laser scattering components have to be used for scattering pattern analyses.

Laser scattering intensity is described in Fig. 5. The distributions of laser scattering intensity are almost similar to previous research results.[7] There is a strong intensity of laser scattering at the viewing angle 30° of camera corresponding to specular components at the incident angle 30° of laser in Fig. 5(a). Also, gaussian-shaped scattering intensity distributions are formed at the center of the specular components. Similarly, an intensive scattering intensity is shown at viewing angle 60° but the shape of gaussian distributions is a little deformed at the center of specular component in Fig. 5(b). In the case of incident angle 70° which is satisfied with Rayleigh criterion, laser scattering intensity is asymmetrically distributed in the shape of deformed gaussian, as shown in Fig. 5(c). The viewing angle with powerful scattering intensity is 60°. This is shifted by 10° from 70°. It means that non-intuitive phenomena of laser scattering are well represented. The distribution of scattered intensity in Fig. 5(d) has a asymmetric like that of Chi-square. This is regarded as the phenomenon that sepecular component get increased but diffuse one is decreased.

As a result, the distribution of scattered intensity is gaussian shape in the incident angle less than Rayleigh criterion. On the contrary, it is not gaussian shape. This means that inspected surface is smooth and specular.

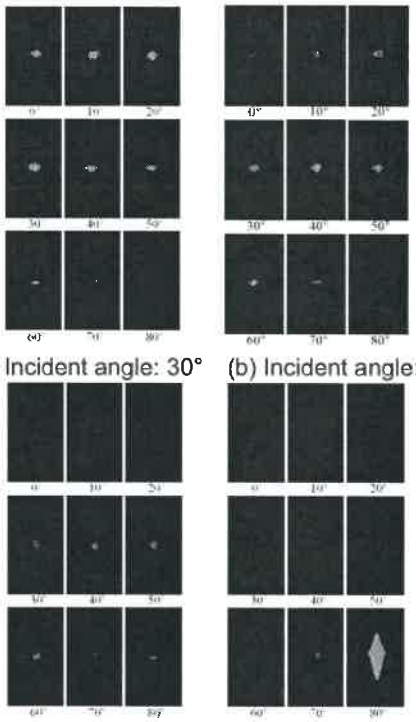

(a) Incident angle: 30° (b) Incident angle: 60°

(c) Incident angle: 30° (d) Incident angle: 60°

FIGURE 4. Laser scattering patterns on viewing angle of camera

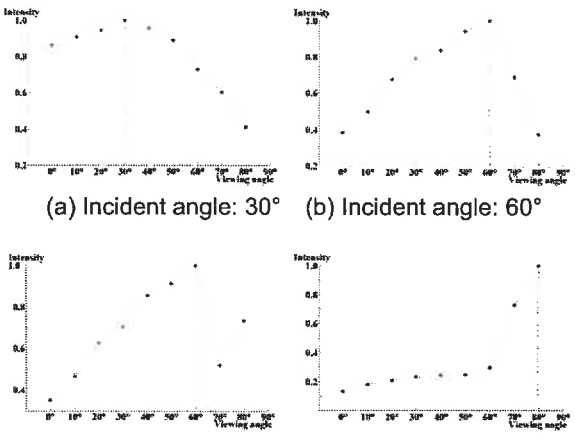

(a) Incident angle: 30° (b) Incident angle: 60°

(c) Incident angle: 30° (d) Incident angle: 60°

FIGURE 5. Distributions of laser scattering intensity on viewing angle of camera

2.3 Optical deflection identification

The reflective light direction of a surface is determined by the incident angle and the irregular micro topology on the surface make the optical scattering ray deflected. Specially, micro defects such as inclusion and dent are in locally very small slope and it is very difficult to detect them. The appropriate assumption is needed to visualize

the micro defects. It means that the specular components of micro defects are shifted by the deflection angle from local surface slope. This deflection angle can be geometrically derived and is twice maximum slope of local surface. Here, minimum viewing angle of camera becomes incident angle of laser minus the deflection angle. The 4 incident angles of laser based on Rayleigh criterion is experimented to identify these optical deflection in the vicinity of micro defects. The pitch stage is moved by 5° from 0° to 15° in order to reflect the local slope of micro defects. This means that the local slope of micro defects can be just simulated because of problems of the acquisition and machining of actual micro defects.

Fig. 6 shows optical deflections at the fixed incident angle depending on pitch stage angles, which is for the simulation of local micro defect slope. In case of incident angles less than Rayleigh criterion, the gaussian distribution of laser scattering intensity is represented at the center of the specular component, in spite of the change of wafer surface slope. Meanwhile, asymmetrically other distributions are formed in the center of specular area at the incident angle larger than Rayleigh criterion. It is shown that the strongest intensity component of laser scattering is deflected to a spatial region deviated from twice local surface slope at the incident angle of laser. However, the intensive scattering intensity is shown at the viewing angle 60° of camera which is shifted 10° from the specular component, in case of the incident angle 70°of laser and surface slope 0°. As a result, there are asymmetric scattered intensity distributions and also optical deflection direction is different from deflection modeling angle at the grazing angle larger than Rayleigh criterion.

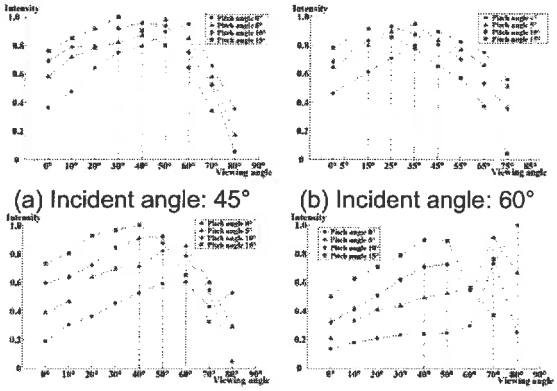

(a) Incident angle: 45° (b) Incident angle: 60°

(a) Incident angle: 70° (b) Incident angle: 80°

FIGURE 6. Optical deflection for 4 pitch stage angles

3. CONCLUSION

In this paper, dark-field laser scattering mechanism is newly designed based on optical scattering property of silicon wafer and research results related with scattering. Using the designed laser scattering mechanism, optical deflection of laser scattering is experimentally investigated for the extraction of comparatively simple and reliable micro defect detection information in silicon wafer of solar cell.

ACKONWLEDGEMENT

The work was supported by Korea Research Foundation Grant(2009-0064599) and 2009 Small & Medium Business Administration funded by Korea Government

REFERENCES

[1] Byelyayev, A., 2005, "Stress diagnostics and crack detection in full-size silicon wafers using resonance ultrasonic vibrations," Department of Electrical Engineering, Ph. D, University of South Florida

[2] Tsai, D. M., Chang, C. C. and Chao S. M., 2010, "Micro-crack inspection in heterogeneously textured solar wafers using anisotropic diffusion," Image and Vision Computing, pp. 491 – 501.

[3] Hong, Y. K., Kim, G. B., 2010, "A Study on the experimental identification of surface roughness using laser scattering image," KSME, Vol. 1, pp. 35-41.

[4] Hong, Y. K., Kim, G. B. and Jin, Y. J., 2010, "Laser scattering based identification of micro-surface conditions for the inspection of solar cell wafer," SPIE, Vol. 7584, pp. 1-7.

[5] John, C. Stover, 1995, "Optical Scattering Measurement and Analysis," SPIE Press

[6] Bakolias, C., 1996, "Oblique imaging of scattered light for surface inspection," Department of Mechanical Engineering, Ph. D, London University

[7] James, E. Harvey, Andrey Krywonos, etc, 2006, "Modified Beckmann-Kirchhoff scattering theory for rough surfaces with large scattering and incident angles," Applied Optics, pp.1-12.

FAST DETECTION OF MICRO DEFECTS USING MAGNETIC NONDESTRUCTIVE TESTING METHODS

Ryo Nakajima[1], Keisuke Nagato[1], Yasuhiro Kawamoto[1], Hirotoshi Kaito[1], Masayuki Nakao[1], and Tetsuya Hamaguchi[1]
[1]Department of Mechanical Engineering
The University of Tokyo
Tokyo, Japan

INTRODUCTION

Fast detection technologies for microcracks, i.e., small defects due to fatigue, on sliding surfaces of gears, bearings and rails are helpful in their quick defect-inspections or accelerated tests. In this paper, we propose two fast detection methods of microcracks using magnetic nondestructive testing.

We develop two methods; eddy current testing method and leakage magnetic flux testing method. These nondestructive testing methods realize low-cost in-situ inspections of defects of machine parts or real-time detection of microcracks in accelerated tests. In this study, we aim the real-time detection of microcracks in a twin disc test. Using the eddy current test, we actually detect the cracks in a twin disc test. In the leakage magnetic flux test, we simulated the leakage magnetic flux and indicated the possibility of detecting the microcracks using a giant magnetic resistance (GMR) device.

EDDY CURRENT TESTING METHOD

Figure 1 shows a schematic of eddy current test. When a coil gets close to the surface, eddy current occurs near the surface of the test specimen. If there is a crack on the specimen, the eddy current causes different magnetic flux. Therefore, the magnetic flux changes the electromotive force generated by the electromagnetic induction coil.

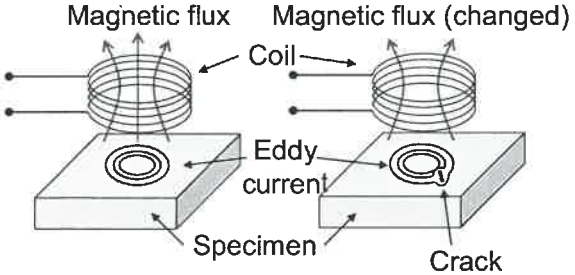

FIGURE 1. Schematic of eddy current test

Experimental

We measure the thermally refined carbon steel specimen containing an artificial crack, confirme the dimensions of the crack can be detected. The length in the running direction, the width, depth of the artificial crack was 100, 300, 50 μm, respectively. This crack is made by electric discharge machining (EDM). The detection speed of the sensor is 2.7 m/s.

We also detect cracks on the twin disc test specimen in situ. Twin disc test is an acceleration test of pitting that is a surface defect of gears. A diagram of the twin disc test is shown in Figure 2. We measure the rotating specimen surface around per a certain rotation number. We also record the testing data when the testing output signal exceeds the threshold. Signals are associated with the position by the pulse signal using a hall sensor. The specimen with 26 mm diameter rotates at 2000 rpm and this surface speed is 2.7 m/s.

We use self-induced self-comparison type detection coil that is 5mm diameter. The test frequency is 1MHz.

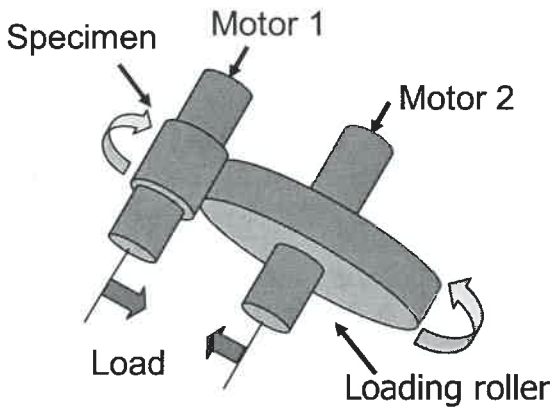

FIGURE 2. Diagram of twin disc test

Results

Figure 3 shows an output signal of the artificial crack measured by the eddy current testing method. The marked peak represents the crack.

Proposal of Measurement of Crack Depth

In preceding section, we think the magnetic sensor's height from the surface of the specimen is constant. But in some situations, the sensor's height changes randomly by effects of the surface's roughness, defects, debris or lubricant. Figure 10 shows the relationship between magnetic field strength and vertical distance from a crack. Magnetic field strength decreases in inversely proportional to distance. Therefore it is difficult to estimate the depth of the crack from sensor output signals.

Our proposal is that two GMR sensors place in different height and measure magnetic field strength using the couple of sensors. We can decide how long it is from the surface to the sensors if we make a comparison between the difference of two sensor's signals and the relationship data between magnetic field strength, crack depth and vertical distance.

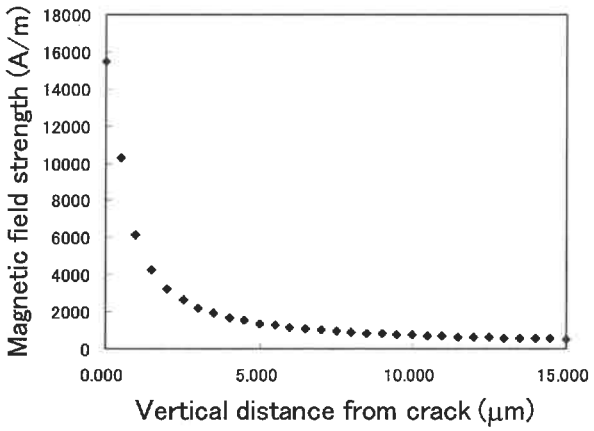

FIGURE 10. Relationship between magnetic field strength and vertical distance from crack

CONCLUSION

We proposed two fast crack detection methods. In the eddy current testing method, we could detect an artificial crack with the sized of the 300×50×100 μm. Furthermore, we detected a natural crack with the width of about 250 μm during a twin disk test. We could also detect the growing of the crack after 250 μm long in situ.

In leakage magnetic flux method, we calculated leakage flux from a crack. And we showed a possibility to detect 1×50 μm cracks when a GMR sensor is approached to the specimen surface within 9 μm. We proposed a method to measure crack depths even if sensor height changes randomly.

REFERENCES

[1] Yang Lijian, Liu Gang, Zhang Guoguang, Gao Songwei. Sensor development and application on the oil-gas pipeline magnetic flux leakage detection. Proceedings of the 2009 9th International Conference on Electronic Measurement & Instruments (ICEMI 2009). 2009; p 2-876-8

[2] M.N.Baibich, J.M.Broto, A.Fert, F.Nguyen Van Dau, F.Petroff, P.Eitenne, G.Creuzet, A.Friederich, and J.Chazelas. Giant Magnetoresistance of (001)Fe /(001)Cr Magnetic Superlattices. Physical Review Letters. 1988; v61, n21, pp.2472–2475.

[3] Qin,G.W, Ren,Y.P, Xiao,N, Yang,B, Zuo,L, Oikawa,K. Development of high density magnetic recording media for hard disk drives: Materials science issues and challenges. International Materials Reviews. 2009; v 54, n 3, p 157-179

[4] FJ Franklin, GJ Weeda, A Kapoor, EJM Hiensch. Rolling contact fatigue and wear behavior. Wear. 2005; v 258, n 7-8, p 1048-54.

THE EFFECT OF LASER HEATING ON THE DUCTILE TO BRITTLE TRANSITION OF SILICON CARBIDE

Deepak Ravindra[1], H. Bogac Poyraz[2], and John Patten[3]
[1,2,3]Manufacturing Research Center
Western Michigan University
Kalamazoo, Michigan, USA

INTRODUCTION

Semiconductors and ceramics, such as silicon carbide, share common characteristics of being nominally hard and brittle, which stems from their covalent chemical bonding and crystal structure. These materials are important in many engineering applications, and are particularly difficult to machine in traditional manufacturing processes due to their extreme hardness and brittleness [1]. Silicon carbide (SiC) has many desirable properties, such as excellent wear resistance, chemical stability, and high strength even at elevated temperatures. All of these properties make it an ideal candidate for tribological, semiconductor, MEMS and optoelectronic applications. In spite of all these characteristics, the difficulty during machining and material removal has been a major obstacle that limits the wider application of this material [1]. The plastic deformation of SiC materials at room temperature is much less than in metals, which means they are more susceptible to fracture during material removal processes. Surface cracks generated during machining are generally subsequently removed in lapping and polishing processes, which significantly increases the machining time and cost. Machining mirror-like surface finishes contribute significantly to the total cost of a part. In some cases, grinding alone can account for 60-90% of the final product cost [2]. In this context, developing a cost effective method to achieve a flawless surface in ultra fine surface machining of an optical lens or mirror has become a challenge. In many engineering applications, products require a high quality surface finish and close tolerances to function properly. This is often the case for products made from semiconductor or ceramic materials. The real challenge is to produce an ultra precision surface finish in these nominally brittle materials at low machining cost.

Current limitations for brittle material machining include the high cost of processing and low product reliability. The cost is mainly due to the high tool cost, rapid tool wear, long machining time, low production rate and the manufacturing of satisfactory surface figure and form. The low product reliability is primarily due to the occurrence of surface/subsurface damage, i.e., cracks and brittle fracture. Ductile regime machining of nominally brittle semiconductors and ceramics has been continuously studied and developed in the last two decades [3-11, 20]. Laser assisted micro/nano machining is another important development in ductile regime machining of brittle materials [12, 13].

In past research, it has been demonstrated that ductile regime machining of these materials is possible due to the high pressure phase transformation (HPPT) occurring in the material caused by the high compressive and shear stresses induced by the single point diamond tool tip [14, 15]. To further augment the ductile response of these materials, traditional scratch/single point diamond turning tests are coupled with a micro-laser assisted machining (μ-LAM) technique [16]. A schematic of the basic underlining concept of the μ-LAM process is shown in Figure 1. This hybrid method can potentially increase the critical depth of cut (DoC), i.e., a larger ductile-to-brittle transition, (DBT), depth, in ductile regime machining, resulting in a higher material removal rate. μ-LAM was previously successfully carried out on single crystal Si yielding a significantly greater DBT (for the scratch performed with laser heating) [18].

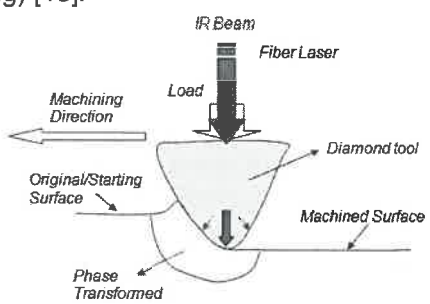

Figure 1. A schematic cross-section of the μ-LAM process.

The objective of the current study is to determine the effect of laser heating (using the μ-LAM process) on the DBT of single crystal 4H-Silicon Carbide (SiC) using scratch testing. The scratch tests were carried out to examine the effect of laser heating and thermal softening of the high pressure phases formed under the diamond tip. The effects of laser heating were studied by verifying the depths of cuts and the nature of the scratches (i.e. ductile, DBT or brittle) for diamond stylus scratch tests carried out on single crystal SiC with increasing loads (thrust force). The load range was selected such that the scratches show both ductile and brittle response (with a DBT region within the scratch). Cutting forces and three-dimensional cutting profiles were investigated.

EXPERIMENTAL PROCESS

The scratch tests were performed on a Universal Micro-Tribometer (UMT) which is produced by the Center for Tribology Research Inc. (CETR). This equipment was developed to perform comprehensive micro-mechanical tests of coatings and materials at the micro scale. This system facilitates the cutting speeds as low as 1μm/sec at nanometric cutting depths. The tribometer is a load controlled device where the required thrust force (Fz) is programmed by the user to obtain the desired DoC (based on the tool geometry and work piece material properties). The equipment includes a dual-axis load cell that is capable of continuously monitoring and recording the thrust and cutting forces, Fx, (obtained as an output parameter from the cutting experiment). A typical scratch test setup along with the μ-LAM system is shown in Figure 2. All scratch tests were performed on a single crystal 4H-SiC wafer. All cuts were performed on the {1010} plane along the <1010> direction.

A 90° conical single crystal diamond stylus (with a spherical end tip radius of 5μm) was used as the scratch tool. The details of the diamond tip attachment are depicted in Figure 3. An infrared (IR) diode fiber laser (λ=1480nm and P_{max}=400mW) with a Gaussian profile with a beam diameter of ~10μm was used in this study. The laser beam is guided through a 10μm fiber optic cable to the ferrule, which is attached to the diamond stylus. The μ-LAM system is configured in such a way that the laser beam passes through the diamond tip and impinges on the work piece material at the tool work piece interface . [19]

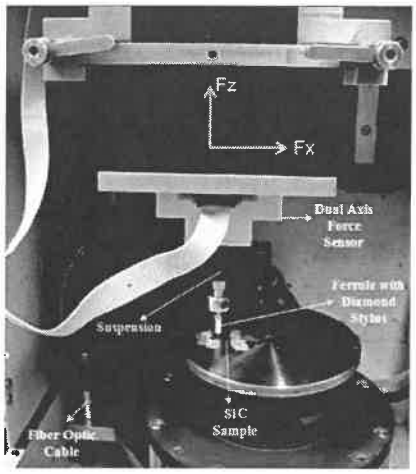

Figure 2. μ-LAM setup.

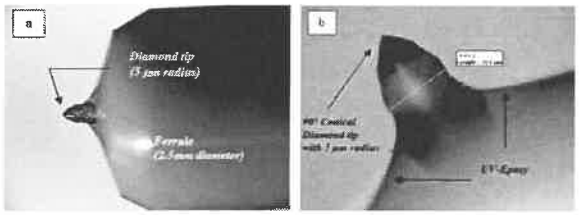

Figure 3. Diamond tip attachment: (a) 5μm radius diamond tip attached on the end of the ferrule using epoxy, (b) Close up on diamond tip embedded in the solidified epoxy [19].

Scratch tests were chosen to be the principle method of investigation in this study as it is a better candidate for evaluating machining conditions than indenting because the mechanics during scratching are more applicable to the machining process such as single point diamond turning (SPDT). In this study, two conditions of scratches were performed: with and without laser heating. The scratches were carried out at low cutting speeds (1 μm/sec) in order to maximize the thermal softening of the material during the laser heating. Scratch lengths of 500 μm were produced on the SiC wafer specimen. The loads were increased linearly with time from 2 mN to 70 mN along the scratch. The scratch test parameters are summarized in Table 1.

Table 1. Scratch testing parameters.

Scratch No.	Loads (mN)	Machining Condition	Cutting Speed (μm/sec)	Laser Power (mW)
1	*2-70*	*no laser*	*1*	*0*
2	*2-70*	*with laser*	*1*	*350**

**350mW is the laser power, approximately 150mW is actually delivered to the work piece material, the balance of the laser power is lost due to scattering and reflections.*

RESULTS

Figure 4 shows two scratches that represent the two conditions: without (scratch 1) and with laser heating (scratch 2). The load range (2-70 mN) performed on these scratches were ideal for this study as it had both the ductile and brittle regime along the same scratch. The DBT is identified somewhere between the ductile and brittle regime of the scratch using optical microscopy, white light interferometry and force analysis (from variations in cutting forces). It is seen in Figure 4 that the scratch performed without laser heating exhibits brittle fracture along the cut much before the scratch performed with laser heating.

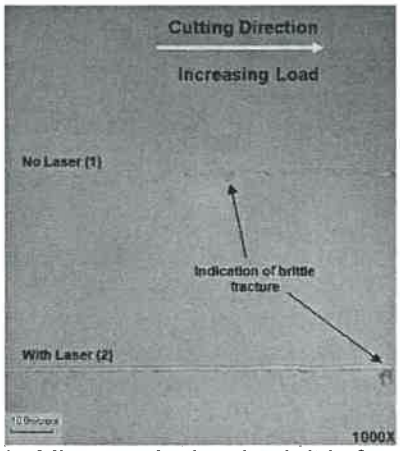

Figure 4. Micrograph showing brittle fracture along the scratch.

To study the effects of laser heating on the DBT of the material, two-dimensional scratch/groove profiles obtained using a white light interferometric profilometer were analyzed. Figure 5 shows the cross-section of the two scratches taken at an equal thrust force of approximately 35mN. It can be seen that the scratch performed with laser heating (left) exhibits a perfectly ductile behavior whereas the scratch done without laser heating (right) indicates slight fracture (brittle behavior) of the material. The DBT depth identified for the scratch performed without laser heating just before the point of fracture is approximately 105nm. The brittle behavior is identified by the imperfect pattern of the groove edge which is a representation of the stylus imprint on the material. It is important to note that from Figure 5, the scratch performed without laser heating is (apparently) deeper (210nm vs. 113nm) as it is difficult to control the DoC when the material removal mechanism is brittle (i.e. difficult to predict the DoC due to fracture of the material). The clear and defined edges that depict the stylus imprint is a good indication of ductile response of the material (as seen in the scratch performed with laser heating).

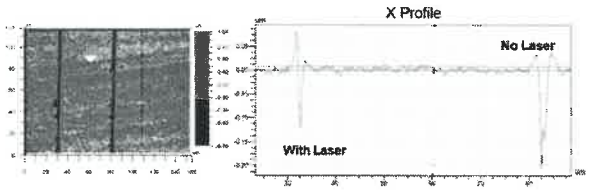

Figure 5. Cross-section of the scratches obtained from a white light interferometer profilometer.

Figure 6 shows the cross-section of the same two scratches (at a different point) taken at an equal thrust force of approximately 40mN. The DBT depth identified for the scratch performed with laser heating just before the point of fracture is approximately 240nm. At this load, the scratch performed with no laser heating shows signs of severe fracture. In comparison, the DBT depth of the scratch performed with laser heating was approximately 135nm greater than the DBT depth of the scratch performed without laser heating.

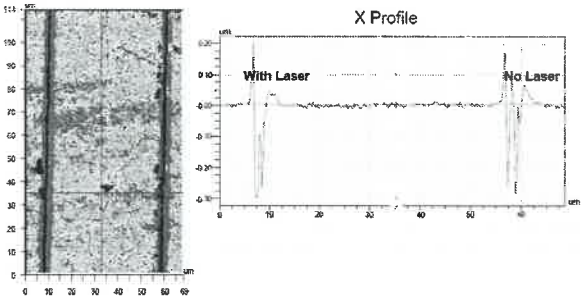

Figure 6.Cross-section of the scratches obtained from a white light interferometer profilometer.

From Table 2, it is seen that the cut performed with laser heating yields in a slightly higher cutting force. This is due to the higher thrust force (40mN vs. 35mN) and larger depth of cut (240nm vs. 105nm).

Table 2. Scratch test results.

Machining Condition	Fz (mN)	Fx (mN)	DoC (nm)	Scratch Nature
no laser	35	12*	105	DBT
with laser	40	14*	240	DBT

**Just before the first point of fracture.*

CONCLUSION

Micro-Laser assisted scratch tests were successful in demonstrating the enhanced

A NOVEL EXPOSURE METHOD BASED ON DISSOLVED OXYGEN CONTROL FOR NANO-STEREOLITHOGRAPHY USING EVANESCENT LIGHT

Satoru Takahashi[1], Toshimune Nagano[1], Yusuke Kajihara[2], and Kiyoshi Takamasu[1]
[1]Department of Precision Engineering,
[2]Department of Basic Science,
The University of Tokyo
Bunkyo-ku, Tokyo, Japan

INTRODUCTION

In recent years, micro-fabrication technologies have developed dramatically and fabrication methods have become required by which small devices on the order of micrometer can be fabricated precisely. In particular, methods of fabricating MEMS and microscopic optical devices as typified by a photonic crystal are in huge demand. Micro-stereolithography is one of the advanced micro-manufacturing methods that can fabricate complex 3D microstructures by curing the liquid photosensitive resin [1-4]. In micro-stereolithography, a layer-by-layer process can fabricate 3D micro structures with better productivity due to the one-shot area exposure compared to a two-photon-absorption process, but cannot realize submicrometer spatial resolution due to the diffraction limit of exposure light.

In order to overcome this critical problem, we're proposing a novel micro-stereolithography method [5-6] using evanescent light instead of propagating light. We consider the application of the near-field optics and use evanescent light as the exposure energy for curing photosensitive resin. Since evanescent light energy does not propagate but localizes within the near-field region, surplus growth is not generated. Furthermore, the resolution is independent of the diffraction, so that fabrication of 3D microstructures with 100-nanometer scales is expected.

In the research of nano-stereolithography using evanescent light, however, it is true that the cured size control in the vertical direction is not very difficult to be less than 100 nm [6], but the cured size control in the lateral direction is difficult. Actually, there remains a big problem that we cannot experimentally fabricate even about 20 μm sized structures for a long enough exposure time.

In this paper, in order to overcome this critical problem, we analyze the curing characteristics of an evanescent light exposure, focusing on a single layer and discuss about a novel exposure method based on dissolved oxygen.

CONCEPT OF NANO-STEREOLITHOGRAPHY USING EVANESCENT LIGHT

In this section, we describe the characteristics of evanescent light that is a key factor of this method and explain the nano-stereolithography.

Evanescent Light Characteristics

When a light propagates in materials with different refractive indices, the light beam will be partially refracted at a boundary surface, and partially reflected. Assuming that an angle of incidence is shallower than the critical angle, the light beam will stop crossing the boundary altogether and instead internally reflect back. Under this total internal reflection condition, there faintly emerges light energy with a localizing size of about 100 nm at the boundary (Figure 1). This energy is evanescent light.

Concept of Nano-stereolithography

Figure 2 shows a schematic diagram of the nano-stereolithography process using evanescent light. First, the incident beam at a shallower angle than the critical angle generates evanescent light at the boundary, which cures liquid photosensitive resin (Figure 2(a)). Next the

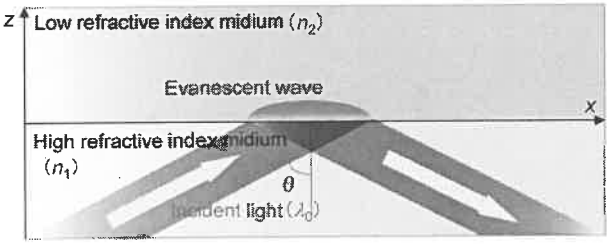

FIGURE 1. Evanescent light emerging under TIR condition.

cured resin adhering on the base rod is lifted and liquid resin is refilled at the boundary surface (Figure 2(b)). Then the evanescent light, which is modulated by a variable mask such as an LCD, exposes and cures a next layer (Figure 2(C)). Doing this loop repeatedly, desired object is fabricated (Figure 2(d)).

Since the evanescent light energy is localized within the range of the wavelength, the thickness of the cured resin layer is expected to be about 100-nanometer scales. In addition, there occurs no optical transmission, which makes it possible to fabricate overhang structure. Consequently, it is expected that we can realize a flexible fabrication with a resolution of sub-micrometer.

EVAENSCENT LIGHT ENERGY EXPOSURE EXPERIMENT FOR ANALYSIS OF CURING CHARACTERISTICS

Experimental Apparatus with Lateral Evanescent Light Distribution Dynamic Control Unit

In order to analyze the cured characteristics of evanescent light exposure especially in the lateral direction, we developed a nano-stereolithography system (Figure 3), with which we can dynamically control an evanescent light exposure area. This system mainly consists of a solid-state diode pumped laser providing visible output at 488 nm as a light source, a high-power objective with a numerical aperture of 1.65, a resin tank located on the objective, and a digital mirror devices (mirror size:13.7 μm, 769 x 1024 mirrors) allowing us to precisely control the lateral evanescent exposure area with a lateral resolution of 250 nm.

Fundamental Evanescent Light Exposure Experiments

Figure 4 shows a typical comparison of a cured single layer by evanescent light with conventional propagating light, lateral shape of which is geometric shape. The lateral shape of the cured resin of evanescent light is not very sharp by comparing one of propagating light. Especially, almost a hexagonal shape is obtained in a star-shaped exposure. Table 1 shows results of evanescent light exposure experiments in changing the size of a lateral exposure area with constant exposure energy

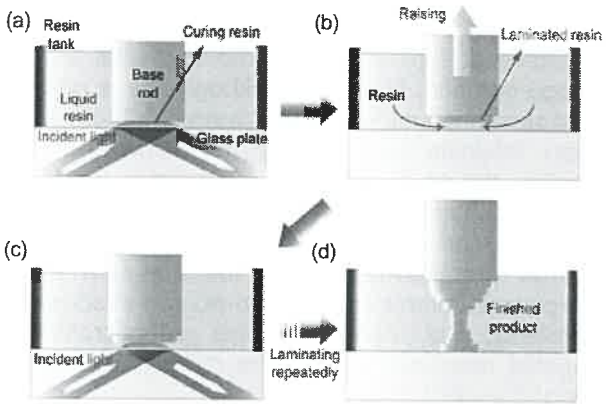

FIGURE 2. Schematic diagram of the nano-stereolithography process using evanescent light.

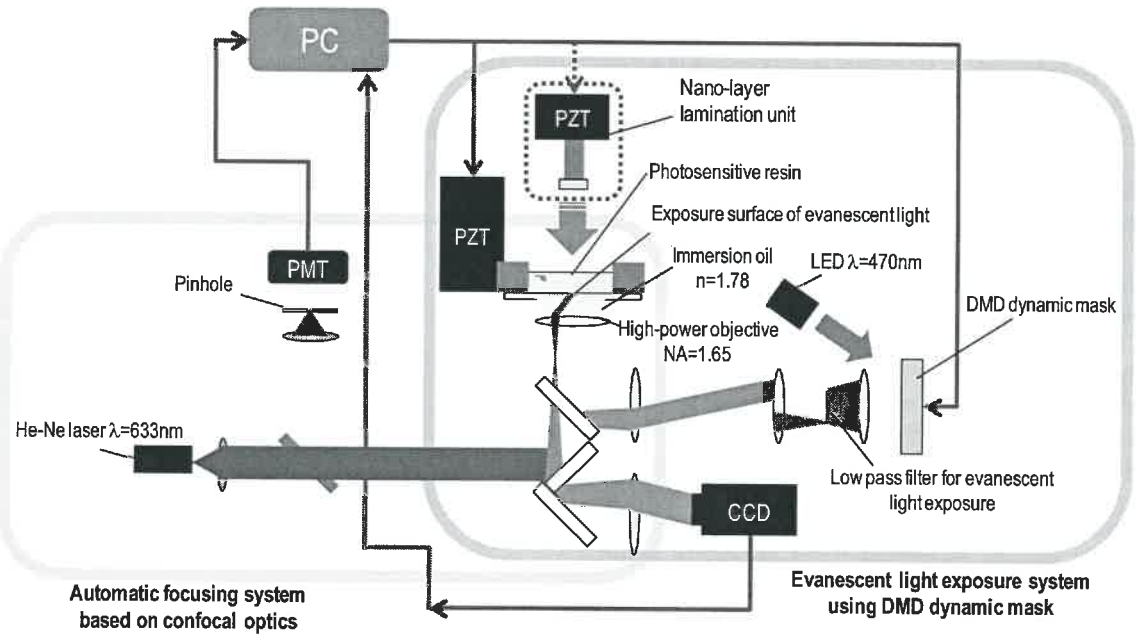

FIGURE 3. A nano-stereolithography system using DVD dynamic mask.

POSITION MEASUREMENT FOR MINIATURE ROBOT USING MOVING LINE LASERS

Akihiro Torii[1], Tomohiro Yamada[1], Akiteru Ueda[1] and Kae Doki[1]
[1]Faculty of Engineering
Aichi Institute of Technology
Toyota, Aichi, Japan

INTRODUCTION

The concept which is based on the use of many miniature robots with appropriate functions of precision work was suggested [1]. A precision manufacturing system was organized by many miniature robots. When the miniature mobile robot contributes to collaborative work in manufacturing with other robots or machines, the robots must know its position. The position of the miniature robot should be monitored individually and measured over the global area by using non-contact measuring instruments.

In the conventional robot positioning, there are many robot localization and navigation systems. For example, on-board navigation system using gyroscopes for mobile robotics applications was proposed [2]. The system, however, required additional sensors on the miniature robot.

In this paper, the concept of the position measurement system is proposed. The proposed system uses moving landmarks which are the reference of the position measurement. On-board photodetectors and the operation time are used to obtain the position of the robot. The system is suitable for the miniature robot which can carry a limited number of sensors. The proposed measurement system can measure the positions of multiple mobile robots.

POSITION MEASUREMENT SYSTEM

The proposed measurement method consists of position sensitive detectors (PSDs) and line laser projectors. Three PSDs are carried by the mobile robot, which is the target of the position measurement. The line laser projectors which move on linear stages and surround the mobile robot are used as the moving landmarks.

Position Sensitive Detector

Figure 1 shows the photograph of the PSD. The PSD is an optoelectronic position sensor using photodiode surface resistance. Unlike discrete element detectors such as CCD, the PSD provides continuous position data along with the belt-shape longitudinal direction, and it features high position resolution and high-speed response.

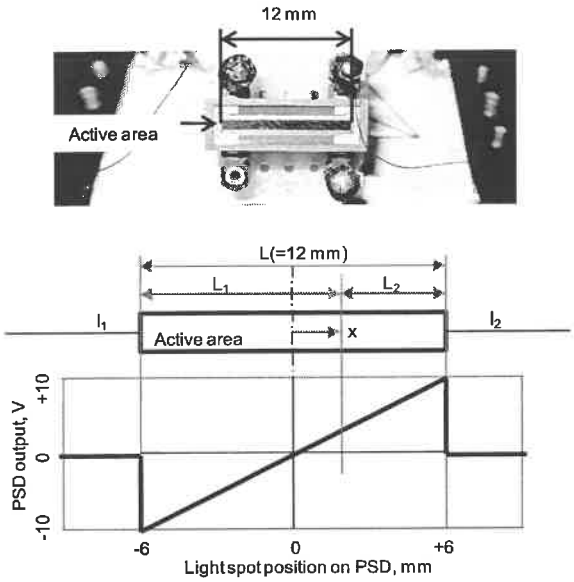

FIGURE 1. PSD and its output.

The schematic PSD output is also shown in Figure 1. When light is applied to the photoactive surface, the light generates photocurrent I_1 and I_2 on the photoactive surface and the current flows to both sides of the active area. The current flows across the surface, and the difference of two currents indicates the position of the light spot. The current is proportional reversely to the resistance of the PSD surface. Since the photoactive surface has a belt-shaped constant width, the resistance is proportional to the length of the photoactive area.

When photocurrent I_1 and I_2 are obtained from both electrodes, the light spot position x on the PSD surface can be found by the sum and difference of these current by

$$x = (L/2) \cdot (I_2 - I_1)/(I_2 + I_1) \quad (1)$$

where L denotes the length of the PSD active surface.

In the experiment, the PSD (S3932, Hamamatsu Photonics) is used. The length of the photoactive surface is 12 mm. We developed an electrical circuit which outputs from -10 V to +10 V according to the light spot position from -6 mm to +6 mm.

PSDs on Robot

The triangle-shape PSDs are carried by a miniature robot as shown in Figure 2. The proposed position measurement system uses three PSDs arranged in an equilateral triangle. The side of the imaginary triangle is determined by the length of the PSD. There are dead zones near the corner of the triangle, since the photoactive area is at the centre of the PSD. In Figure 2, the distance between the centre and the side is h=14.4 mm.

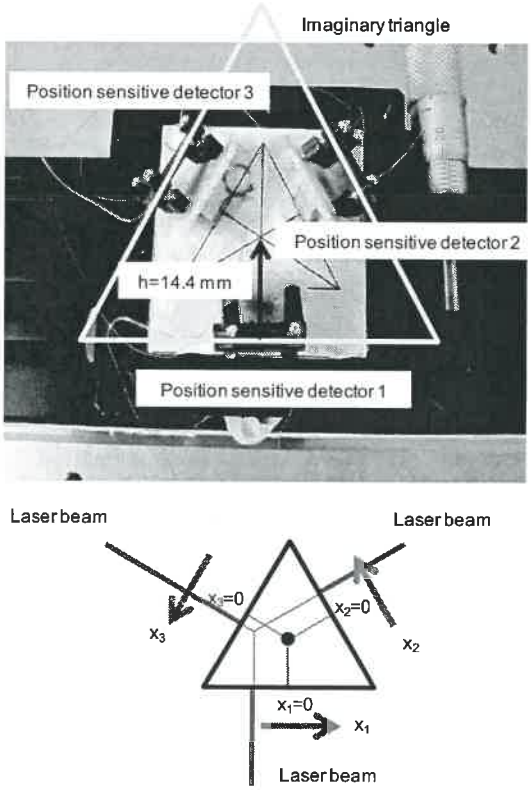

FIGURE 2. Triangle PSDs and laser beams.

Figure 2 also shows the schematic diagram of the PSD triangle on a miniature robot and incident laser beams. Each laser beam falls on the photoactive area of each PSD. The axis along with the longitudinal direction of the PSD surface is expressed as x_1, x_2 and x_3, respectively. When the beam is applied to the centre of the PSD, the PSD output equals to zero (0).

Moving Line Lasers

Moving line lasers are references of the position measurement as shown in Figure 3. The moving laser consists of a line laser projector and a linear stage. The linear stages are arranged in an equilateral triangle around the measurement target. The moving line laser realizes a reciprocating motion. The lasers are placed above the target. This structure prevents an obstacle which is between the light source and the PSD blocking the laser beam.

In the experiment, the height of line laser projectors is about 100 mm. The wavelength, power, and projection angle of the line laser projector is 670 nm, 5 mW and 45 degrees, respectively. The positions of the moving lasers are synchronized with each other. The speed of the moving line lasers is 200 mm/s in both the directions.

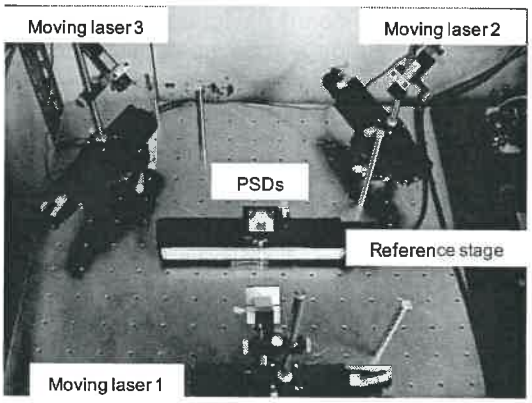

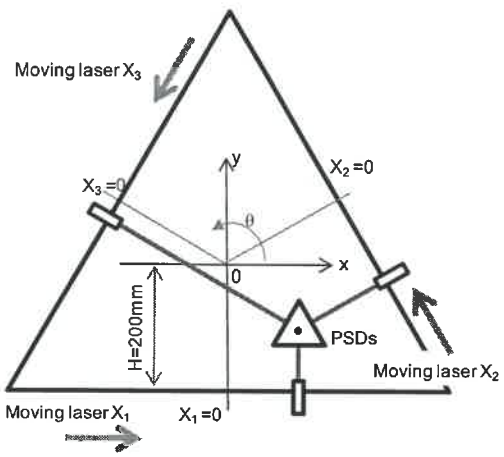

FIGURE 3. Moving lasers and laser beams.

Figure 3 also indicates the coordinate of the position measurement. The position of the linear stage is expressed by capital letters X_1, X_2, and X_3. The laser beams intersect at one point when the moving lasers are positioned at their center of the stage. The length between the triangle center and the side is H=200 mm.

MEASUREMENT PRINCIPLE

The position and orientation of a miniature robot is expressed from the geometrical consideration by

$$\theta = \arcsin\frac{((X_1+X_2+X_3)/(3H))}{\sqrt{1+((x_1+x_2+x_3)/(3h))}} - \arctan\frac{x_1+x_2+x_3}{3h} \quad (2)$$

$$x = \frac{2X_1-X_2-X_3}{3} - \frac{2x_1-x_2-x_3}{3}\cos\theta \quad (3)$$

$$y = \frac{X_2-X_3}{\sqrt{3}} - \frac{x_2-x_3}{\sqrt{3}}\cos\theta \quad (4)$$

All variables and constants are indicated in Figures 2 and 3 [3]. When the laser beams fall on the centre of the PSDs, x_1, x_2 and x_3 equal zero, and the equations are simplified. While the laser beams keep falling on the PSD surface, the position and orientation of the miniature robot is obtained by equations (2-4).

The proposed measurement system, however, uses the back-and-forth motion of the moving landmark. While the laser beams miss the PSDs, the position and orientation of the miniature robot should be estimated. We can detect the position of the moving landmark where the laser beam falls on the centre of the PSD surface. The differential of the laser position (dX_i/dt, i=1, 2, 3) and the PSD output (dx_i/dt, i=1, 2, 3) are used. The PSD output is the relative velocity of the mobile robot and the moving laser. The velocity of the miniature robot is obtained by adding or subtracting these values. The central position of the PSD is estimated by these results and time elapsed.

The position of the moving laser, which is determined by the measurement system, is indicated in Figure 4(a). Since the moving lasers realize synchronized back-and-forth motion, their position shows the triangle waveform. The laser position is simply expressed as X. The PSD output is illustrated in Figure 4(b). Since the PSD output is obtained only when the laser light falls on the PSD surface, the PSD output is estimated by the extrapolation of the PSD signal.

Once the PSD centre is estimated, the position and orientation of the mobile robot is obtained by equations (2-4), where the PSD outputs x_1, x_2, and x_3 are zero (0). The moving laser position X_1, X_2, and X_3 are replaced by the estimated values.

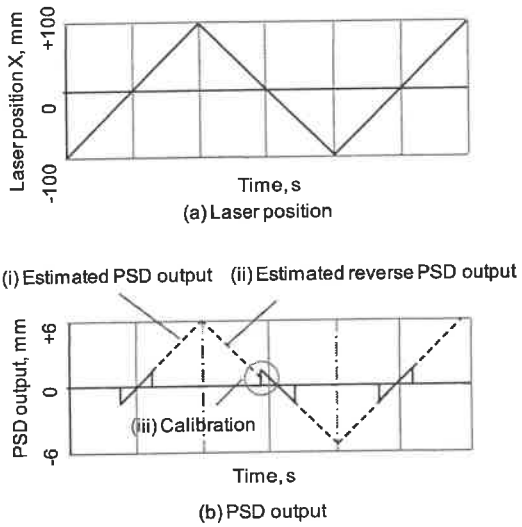

FIGURE 4. Estimation of the PSD centre.

EXPERIMENTAL

Figure 3 also shows the experimental setup. In the experiment, a one-dimensional linear stage simulates a miniature robot, indicated as reference stage in Figure 3. The linear stage instead of the miniature robot is used as a measurement target. The position of the linear stage is used as the reference position. Since we do not use a rotary stage, the orientation of the target is determined as zero (0). Three moving lasers move in synchronization with each other from -50 mm to +50 mm, and the speed is 20 mm/s.

In the experiment, the reference stage carrying three PSDs moves along with the horizontal (x-) axis at a constant speed (6.25 mm/s). The position of the center of the PSD is obtained by the PSD outputs and the moving lasers' positions. The position of the PSDs is calculated.

EXPERIMENTAL RESULTS

The PSD outputs the light spot position on the PSD surface while the light falls on the PSD surface, and outputs zero when the light spot is out of the PSD surface. At the beginning of the measurement, the laser cannot fall on the PSD surface. The robot position cannot be measured.

Figure 5 shows the measurement results of the moving PSDs, which simulate a mobile robot in a linear motion. At the beginning of the measurement, the system cannot measure nor estimate the PSD position since the landmark lights do not fall on the PSD surface. At the time t is 0.5 s, one laser falls on a PSD surface and x_1 is obtained. The robot's position, however, cannot be measured because x_2 and x_3 are not obtained.

The position of the PSDs is calculated after all the PSDs detect the position of the light spot position, i.e. t is larger than 3.2 s. When the PSDs detect the light spot and they can obtain the time when the light spot cross the centre of the PSD, the position of the robot can be measured by equations (2-4).

After the time t is larger than 3.6 s, all the PSD estimated the zero crossing time, and the robot's position can be obtained. The proposed system estimates that the measurement target moves linearly in the x direction with 6.25 mm/s, which corresponds to the reference speed. The position in y-direction is almost zero (0). After the moving lasers reverse the moving direction at t is 5 s, the estimated PSD output x_1 changes the gradient of the output signal.

SUMMARY

This paper described a position measurement system for a small mobile robot. The robot carried photodetectors and electronic circuits. The system used three linear stages which carried three line laser projectors above the robot. The line projectors and linear stages were used as landmarks. The position of the projectors are synchronized with one another, and their positions are identified by the measurement time elapsed.

Three PSDs were installed on a mobile robot, although we used a reference stage in the experiment. The laser projectors can fall the laser beams on the PSD surfaces, and the PSDs output laser positions on their surfaces. The position of the robot is obtained by the PSD outputs and the positions of the laser projectors.

In the experiment, we monitored the PSD outputs which indicated the laser beam position on the PSDs. The position of the moving landmark was monitored. The position of the robot was calculated by the estimated central positions of the PSDs. The position of the mobile robot was measured and estimated.

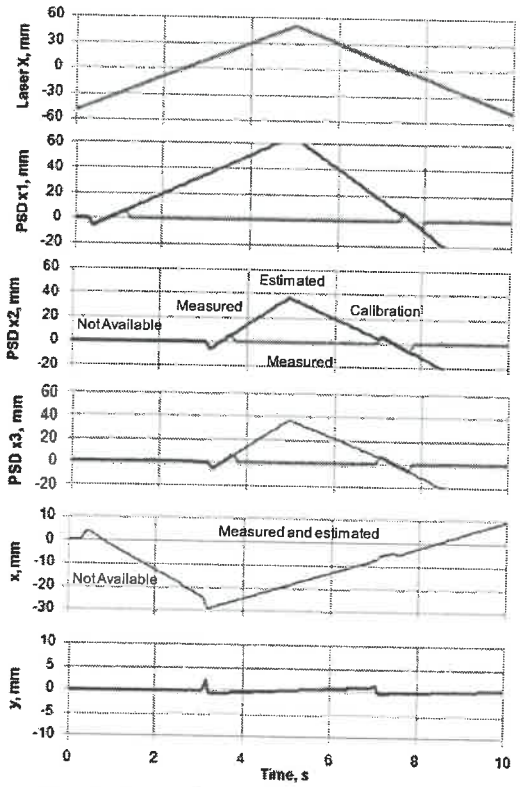

FIGURE 5. Experimental result obtained by a moving target. The robot moves in x-direction at 5 mm/s

ACKNOWLEDGEMENTS

Part of this work was supported by Grant-in-Aid for Scientific Research (C) (20560245).

REFERENCES

[1] Aoyama H, Nakano H, Hayakawa N, Sasaki A, Shimokohbe A. Miniature Robots for Ultra Precision Measurement and Machining. Proceedings of the 7th Int. Precision Engineering Seminar, Kobe, Japan. 1993; 275-289

[2] Barshan B, Durrant-Whyte H F. Inertial Navigation Systems for Mobile Robots. IEEE Transactions on Robotics and Automation. 1995; 11(3); 328-342

[3] Torii A, Inoue T, Doki K, Ueda A. A Macro/Micro Position Measurement System for a Miniature Robot, IEEJ Trans. EIS, 2005; 125(12); 1830-1836 (in Japanese)

STUDY ON MULTI-LAYERING OF METAL MICRO-REACTOR USING DIFFUSION BONDING

Kensuke Tsuchiya[1], Toru Nunokawa[1], Atsunori Kikuchi[2] and Masayuki Nakao[2]
[1]Institute of Industrial science
The University of Tokyo
Meguro-ku, Tokyo, Japan
[2] Department of Mechanical Engineering
The University of Tokyo
Bunkyo-ku, Tokyo, Japan

1. INTRODUCTION

A micro-reactor (MR) is reaction container arranged with micro flow channels in the reaction area of size several tens to hundreds in micro-meters. This type of reactor, compared to conventional batch-type reactors, allows high-speed mixing reaction, easy temperature control with high heat exchange performance, and easy to manage reaction time[1-2], however, a single micro flow channel has small yield, so the reactor requires arranging multiple micro flow channels in parallel with high pressure resistance when the flow volume increases with high velocity. MRs in the past have been produced with glass or plastic but these material have low heat conductivity and problems with chemical resistance in case of plastic, and shock resistance for glass made ones. A number of reactions are thus, beyond what these simple material reactors can handle.

To counter the dilemma, we developed a multi-layered metal MR using laser welding [3], however, the laser spot welding caused waving in the thin plate that hindered stacking a large number of layers, and completely sealing the flow path was not easy with spot welding. In addition, we foresaw that the reaction heat with high density multi-layering would cause unwanted heat exchange among adjacent flow channels.

This study in this paper reports our new prototype of multi-layered metal MR produced by diffusion bonding. Part of our goal was to produce cooling channels with improved heat dissipation and we report our evaluation of its temperature controllability.

2. MULTI-LAYERING TECHNOLOGY WITH DIFFUSION BONDING

Diffusion bonding is a type of face bonding. It allows high precision bonding of hollow parts and simultaneous bonding of multiple bonding faces perpendicular to the direction of pressure. These properties prove effective in producing multi-layered MRs. For the reactor, we used type 316 stainless steel (SUS316) with high corrosion resistance and mechanical strength.

We first carried out a series of bonding tests to find the optimum conditions for diffusion bonding by varying the parameters of bonding temperature and pressure. The tests proceeded by; pumping down the reactor to vacuum of about 5×10-3 Pa, heating the reactor up to 900 degrees Celsius and holding the temperature there for 45 minutes to attain uniform temperature distribution in the material, heating it up again to the bonding temperature, pressurizing the reactor at 10Mpa for 4 hours while holding the bonding temperature constant, and then cooling it down in air to ambient temperature. Table 1 shows the temperature and pressure conditions we tested. The surface roughness of the bonding faces was 0.2 micro-meters. Fig. 1 shows the cross sections of the bonded test pieces at each temperature.

TABLE 1. Bonding condition.

Bonding Time	4hours
Bonding Temperature	1000°C, 1050°C 1100°C, 1150°C
Bonding Pressure	5MPa, 10MPa
Surface Roughness	Ra:0.2μm

We then put the test pieces through tensile and Charpy impact tests to evaluate the bonding strength. We also cut the test pieces and observed the cross sections to measure the contact area ratio to the boundary area. We correlated the results of tensile strength, Charpy impact values, and contact area ratio with the

bonding conditions. We also measured the deformation in the direction of pressure.

Fig. 2 shows the results of tensile and impact tests. They show that both tensile strength and Charpy impact values increase with bonding temperature up to 1,100 degrees Celsius but remain unchanged even when it goes higher. With a bonding temperature of 1,100 degrees Celsius, the tensile strength at the bonded area is about the same with the original material and the Charpy impact value about 50% of that. Fig. 3 shows the relation between calculated contact area ratio and bonding strength. The figure indicates a monotonic increase of strength with the contact area.

Fig. 4 shows deformation against bonding temperature and pressure. The graph shows larger strain in the pressure direction with higher bonding temperature and pressure.

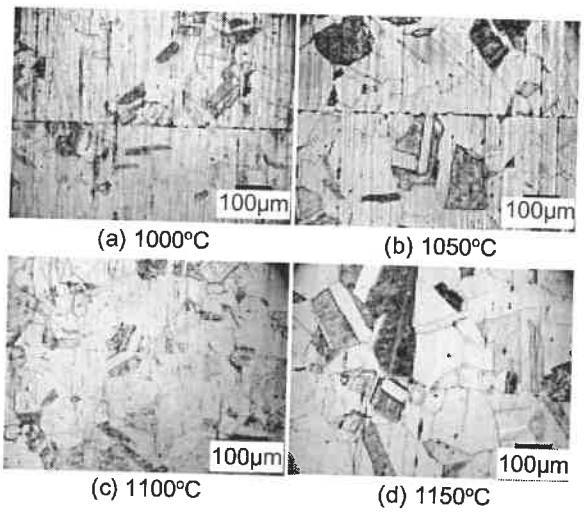

FIGURE 1. Cross section of the diffusion bonded test pieces at various temperature.

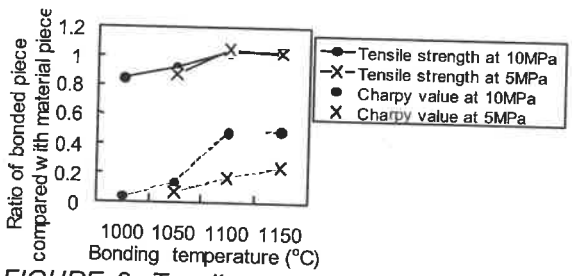

FIGURE 2. Tensile strength and Charpy value ratio of bonded piece compared with material piece.

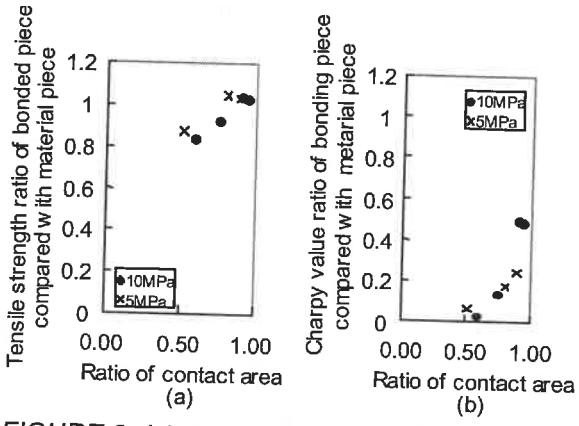

FIGURE 3. (a) Tensile strength ratio toward ratio of contact area (b) Charpy value ratio toward ratio contact area.

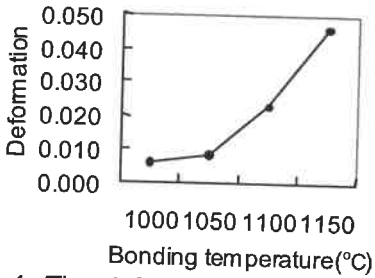

FIGURE 4. The deformation of test piece after diffusion bonding.

Given these results, we set our optimum bonding conditions for higher bonding strength with small deformation to a bonding temperature of 1,100 degrees Celsius and bonding pressure of 10MPa.

3. EVALUATING THERMAL PERFORMANCE OF DIFFUSION BONDED MR

3.1 Comparison with MR of different material

The MR we fabricated is made of metal with high thermal conductivity (SUS316, thermal conductivity 16.7W/m.K) compared to plastic or glass. This subsection reports our tests to compare the heat exchange performance of metal MR and MRs of other material.

For comparison, we made MRs with the same flow channel configuration, one with SUS316 and the other with polymethyl methacrylate (PMMA, thermal conductivity 0.19W/m.K). The configuration had three layers with flow channels of width 1mm by height 500 micro-meters and length 90mm. We bonded the SUS316 MR with the optimum conditions from the previous section. We produced the PMMA MR by

machining flow channels on PMMA plates and melting their surfaces with acetone to bond them together.

We ran heated water through the SUS316 and PMMA MRs and measured the temperature drop at the exit from that at the entrance. Fig. 5-(a) shows the resulting temperature differences with passing times of 0.5sec and 1.0sec. The results clearly show larger heat extraction with the diffusion bonded SUS316 MR.

3.2 Comparing different bonding methods

We next compared SUS316 MRs made with different bonding methods. One of the MRs was the diffusion bonded one from the previous subsection and the second one we made with the exact same configuration but by bonding the plates with laser welding [3].

We compared the heat extraction performance of the two MRs with the same test of finding the temperature differences between the entrance and exit. Fig. 5-(b) shows the difference of temperature differences by subtracting the difference with the laser welded MR from the difference with the diffusion bonded MR with passing times of 0.5, 1.0, and 2.0 seconds. The results vary with the passing time, however, consistently show larger heat extraction with the diffusion bonded MR. The reason is bigger thermal resistance among the laser welded layers with discrete adhesion, compared to that with diffusion bonded layers with complete adhesion.

Furthermore, the laser welded thin plates showed distortion from local heating. That will hamper larger multi-layering for the MR. Diffusion bonding, on the other hand, uniformly heats and pressurizes the plates and thus is ideal for stacking up more layers.
All the above observations and results give the win to diffusion bonded MR.

4. LARGER MULTI-LAYERED MR WITH DIFFUSION BONDING AND ITS PERFORMANCE

4.1. Multi-layered MR

Targeting improved yield, we built a 20 layered MR with 10 reaction flow channel layers, and 10 cooling flow channel layers. The cooling flow channel layers placed in an alternating fashion with the reaction flow channel layers reduce heat buildup in the multi-layered MR and improved the heat exchange efficiency. Fig. 6 shows the flow channels we produced. Both the reaction and cooling flow channels were 1mm wide and 500 micro-meters high. Channels in the flow layers and the cooling layers were 300 micro-meters apart. We applied the diffusion bonding conditions we found in Section 2. Fig. 7 shows the cross section of our MR. The figure shows the strong adhesion with hardly any voids at the boundaries. The flow channel cross sectional shapes also show little deformation.

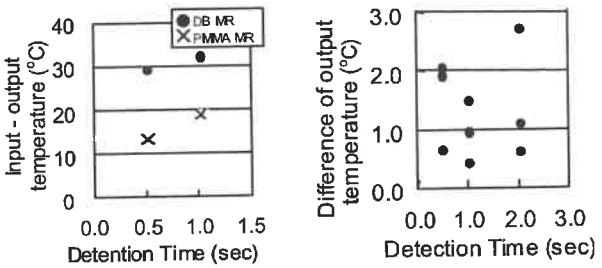

FIGURE 5. (a) Input-output temperature of diffusion bonded MR and PMMA MR, (b) Difference of output temperature between diffusion bonded MR and laser welded MR

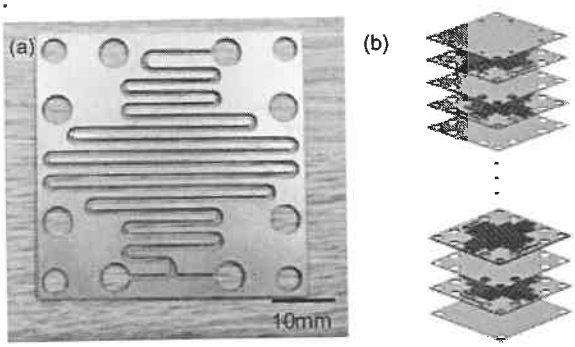

FIGURE 6. (a) A Channel layer for the multi-layered MR, (b) configuration of the structure of the multi-layered MR.

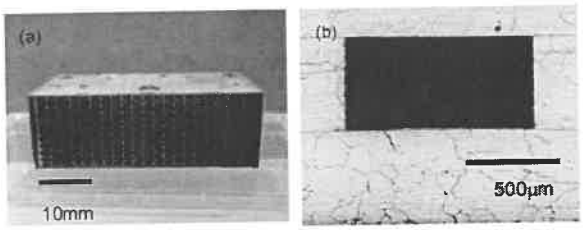

FIGURE 7. Cross section of the whole the multi-layered MR, (b) enlarged section of a channel.

4.2. Evaluating improved heat exchange performance with cooling layers

To evaluate heat exchange performance with cooling flow layers, we carried out nitration of benzene in our MR. Benzene nitration is a heat generating reaction of mixed acid and benzene that produces nitrobenzene, the main product, at a reaction temperature around 50 degrees Celsius, but the process generates more by-products if the reaction temperature reaches about 90 degrees Celsius. For this study, we evaluated the effect of heat exchange by measuring the yield of the main product with and without cooling water to the cooling layer. Solution injected to the reaction layers was 19.4ml mixed acid and 5.5ml benzene. The reaction solution flow rate was 13.8mm/sec and that of cooling water 138mm/sec. We checked and confirmed there were no leakage from the boundary during the reaction processes.

Fig. 8 shows the MR temperature measured at the point near mixed acid joins to benzene. Fig. 9 shows the results of the processes. Selection rate is the ratio of the main product in the overall production. The results show that the rate of main product went up when cooling water was injected. The cooling water cooled the reaction heat inside the MR. We thus confirmed that cooling layers in multi-layered MRs can improve the heat exchange efficiency.

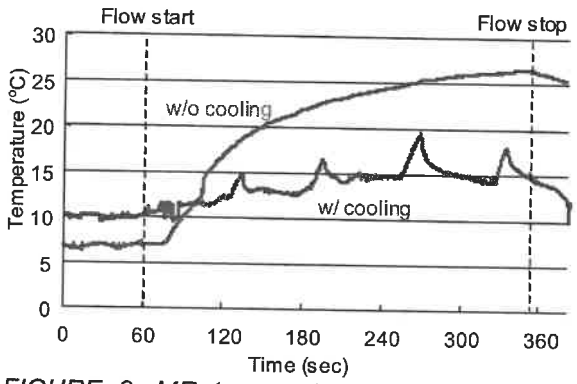

FIGURE 8. MR temperature measured at the point near mixed acid joins to benzene.

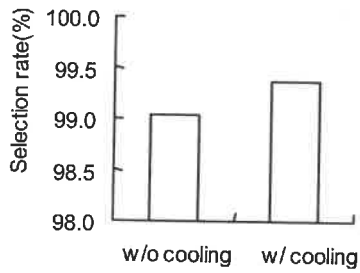

FIGURE 9. Selection rate of nitrobenzene.

5. CONCLUSION

Our study led to the following conclusions

- We found the optimum bonding conditions for SUS316 in building micro-reactors with diffusion bonding.
- We compared the thermal performance of micro-reactors made of plastic and metal and showed that the thermal conductivity of the material affects the heat exchange efficiency. We also demonstrated better performance of a diffusion bonded micro-reactor compared to one with a different bonding method.
- We produced a 20 layer micro-reactor with cooling layers. Arranging cooling flow channels in multi-layered micro-reactors can improve heat exchange efficiency.

REFERENCES

[1] T. Kim and S. Kwon, Proc. IEEE MEMS2008, Tucson, pp. 980-983,

[2] Cathy Ke, et. al., Sensors and Actuators, B, 120(2007), pp. 538-544,

[3] K. Tsuchiya, et. al., Proc. ASPE Annual meeting 2004, Vol. 34(2004), pp. 678-681.

BIOMOLECULAR-IMAGING DEVICE USING LIGHT-ADDRESSED EXCITATION ON A PHOTOCATALYST SUBSTRATE

Atsushi Yamamoto[1], Jun Suzurikawa[2], Keisuke Nagato[1], Tadashi Tsukada[1], Aya Tanaka[1], Tetsuya Hamaguchi[1] and Masayuki Nakao[1]
[1]Department of Mechanical Engineering, Graduate school of Engineering
The University of Tokyo
7-3-1 Hongo, Bunkyo-ku, Tokyo, Japan
[2]Department of Assistive Technology,
Research Institute of National Rehabilitation Center for Persons with Disabilities
4-1 Namiki, Tokorozawa, Saitama, Japan

INTRODUCTION

In order to electrochemically and/or electrophysiologically monitor in-situ activities of cultured cells adhering on a substrate, micro-electrode arrays (MEAs) patterned on the substrate have been utilized. MEAs allow non-invasive and multisite monitoring with the fine temporal resolution. However, the spatial resolution of MEAs is limited by their electrode numbers and densities. MEAs, therefore, can access cells only in the vicinity of the electrode pads.

One possible solution to the limited spatial resolution is a light addressing technique, which enables to optically generate a virtual electrode at a desired site on a photoconductive substrate, not depending on predefined electrode positions. There have been many applications of this technique reported, including light addressable potentiometric sensors (LAPS) [1], pH or chemical imaging and cell manipulation. Although these applications have the potential to replace previous cell monitoring methods with the MEAs, they mainly utilize the electrolyte-insulator-semiconductor interface and there have been few reports on light addressed measurement with redox reactions and the induced faradic current at the electrode-electrolyte interface. Such an amperometric measurement with charge transfer is a prerequisite for biosensing of uncharged biological molecules.

In this study we describe a light addressable amperometric sensing (LAAS) [2] for in-situ monitoring of glucose in a biological solution. In order to achieve the sensing with charge transfer at the photo-electorode/electrolyte interface, we utilized titanium dioxide (TiO_2) as a photoconductor. Because TiO_2 has the strong oxidation power under UV illumination, the addressed photo-anode on the TiO_2 electrode will generate a redox current that is proportional to the local concentration of organic compounds as illustrated in Figure 1.

Our final goal is to obtain a distribution image of glucose and can measure the activity level of each cell. For that goal, we made TiO_2 electrodes and examine the characteristics of them. First, we examine the correlation between photocurrent and concentration of glucose, and then attempted to improve the sensitivity of TiO_2 electrodes with Titanium (IV) chloride ($TiCl_4$) post-treatment. We also examined the light addressing ability. Experiments and results of them are reported.

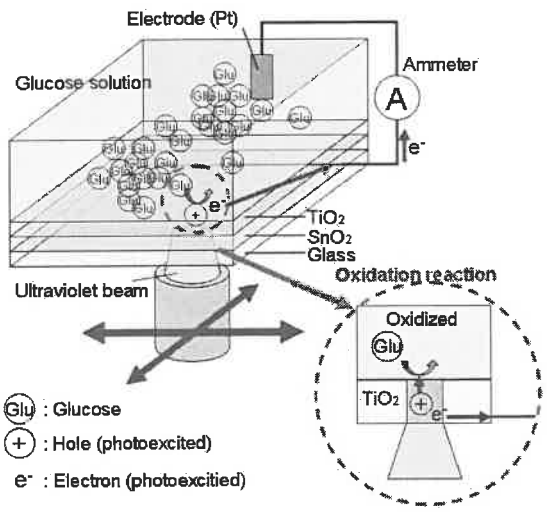

FIGURE 1. Schematic diagram of light addressable amperometric sensing.

EXPERIMENTAL

Materials

Conductive glass sheets (AGC Fabritech Co.,LTD.) were used as substrates for TiO_2 film coating. TiO_2 particulate slurry, STS-21

(ISHIHARA SANGYO KAISHA., LTD.) was prepared. Particles in STS-21 consist of anatase phase. D(+)-glucose and titanium (IV) chloride (Wako Pure Chemical Industries, Ltd) were used without further purification. Phosphate buffer saline (PBS, GIBCO 20012-027) was used as an electrolyte solution and solvent of glucose. All other reagents used were of analytical grade unless otherwise stated.

Preparation of TiO_2 Electrodes

TiO_2 particulate slurry STS-21 was stirred one night on VORTEX GENIE2 (M&S Instruments Inc) so that particulates were dispersed. Conductive glass sheets were cleaned first with acetone for 10 min, second with ethanol for 5 min and third with deionized water for 5 min in an ultrasonic bath (W-210R, HONDA ELECTRONICS) and then dried in airflow and washed with corona discharge (CFG-500, Shinko Electric & Instrumentation Co., Ltd.) before the TiO_2 slurry was coated. After these pretreatments the TiO_2 slurry was spin-coated on the glass substrates and then calcinated in an oven at 500 °C. A wire to external devices was bonded on the SnO_2 electrode with conductive epoxy (CW2400, ITW Chemtronics). A plastic dish was attached as a solution chamber. The morphology of the TiO_2 film was characterized by a scanning electron microscope (SEM) (S-4000, HITACHI). The thickness of the film was ca. 1.7 µm. A Pt film and an Ag/AgCl electrode were used as a counter and a reference electrode, respectively (Figure 2).

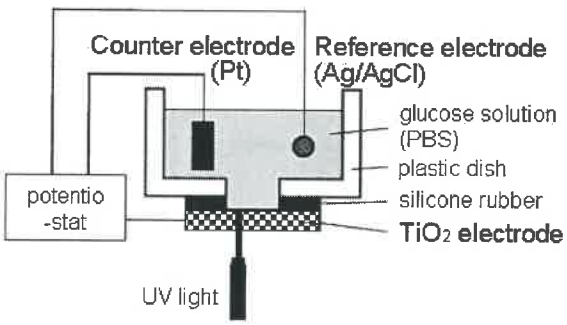

FIGURE 2. Experimental setup.

Titanium (IV) Chloride Post-Treatment

The TiO_2 electrode calcined was immersed in a 0.05 mM aqueous solution of $TiCl_4$ at 70 °C for 30 minutes, then rinsed with deionized water, and caicined again in an oven at 450 °C for 30 min [3].

Photoelectrochemical Measurements

The TiO_2 electrode was set on a microscope (IX71, OLYMPUS) equipped with mercury lamp (USH-1030L, USHIO INC.). UV light was extracted through a band-pass filter (U-MWU2, OLYMPUS). TiO_2, Pt and Ag/AgCl electrodes were connected to the potentiostat (HAL-3001, Hokuto Denko Corporation). Photocurrents were recorded by LabVIEW (National Instruments). The intensity of the illumination was measured at the wavelength of 343 nm with a photodiode power meter (PD300-UV, OPHIR).

Experiment 1: Evaluation of the Concentration Sensitivity

In order to evaluate the concentration sensitivity of the electrode, photocurrents were measured in test solutions with 7 different glucose concentrations from 0 to 10 mM. The light intensity was 2.9 mW/cm^2 and the diameter of UV light spot was 100 µm.

Next, to evaluate the concentration sensitivity of the electrode at lower concentration, photocurrents were measured in test solutions, whose concentration was changed more minutely; 7 concentrations from 0 to 1.8 mM. The light intensity and the diameter of UV light spot were same as those described above.

Experiment 2: Attempt to Improve the Concentration Sensitivity with $TiCl_4$ Post-Treatment

In order to improve the electrode sensitivity, we introduced and evaluated the $TiCl_4$ post-treatment, which is routinely utilized for fabrication of dye-sensitized solar cells [3]. By hydrolysis from a $TiCl_4$ solution, pure TiO_2 is deposited on a rather impure film from STS-21. The $TiCl_4$ treatment is, therefore, expected to increase a charge transfer rate at the electrolyte-semiconductor interface and thus the sensitivity of the electrode.

Photocurrents were measured with 11 different concentrations of glucose from 0 to 10 mM. The light intensity and the diameter of UV light spot were same as **Experiment 1**.

Experiment 3: Measurement of Photocurrent at Different Spots

In order to examine whether the glucose oxidation occurs at the point of the TiO_2 electrode where UV light is irradiated or not, two glucose solutions with different concentrations were prepared on a TiO_2 electrode and photocurrents were measured at each spot. The solutions of 2 mM and 10 mM glucose were

fixed with agarose. Figure 3 shows the schematic of the experiment. The diameter of UV light spot was changed into 3 sizes.

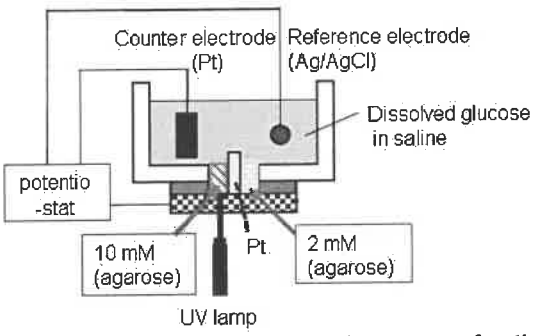

FIGURE 3. Schematic diagram of the experiment.

RESULTS AND DISCUSSION

Preparation of TiO2 Electrodes

Figure 4 is a cross-sectional surface of TiO_2 particulate film. A homogeneous TiO_2 particulate film was made.

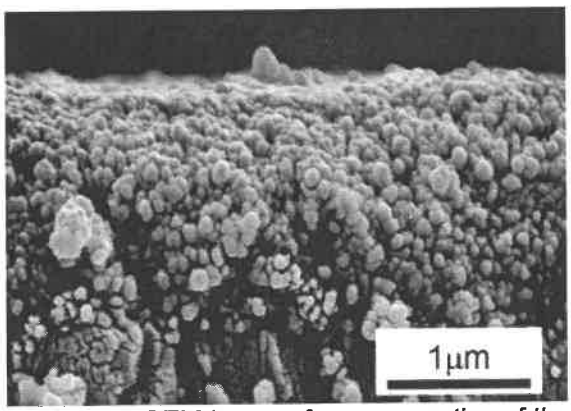

FIGURE 4. SEM image of a cross section of the TiO_2 film.

Experiment 1

Figure 5 shows the photocurrent profiles induced in solutions with different concentration of glucose. The photocurrent values after the initial capacitive currents seem to correlate with the glucose concentration. Then, we calculated the averaged values of photocurrents between 4.5 and 5 s, and plotted them as the function of glucose concentration in Figure 6. This result demonstrates that the photocatalytic oxidation current can be used as an index of glucose concentration. However, the relationship between the current and concentration was not linear throughout the tested range.

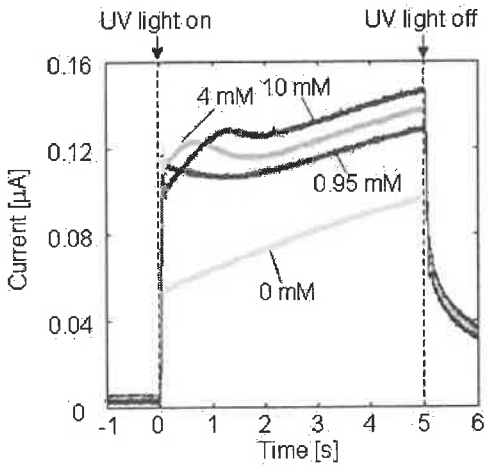

FIGURE 5. Photocurrent waveforms for blank PBS and PBS containing glucose at different concentrations. From bottom to top: 0, 0.95, 4, 10 mM glucose.

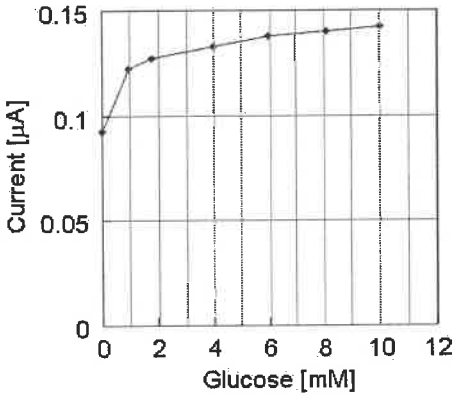

FIGURE 6. Photocurrent as a function of concentration of glucose.

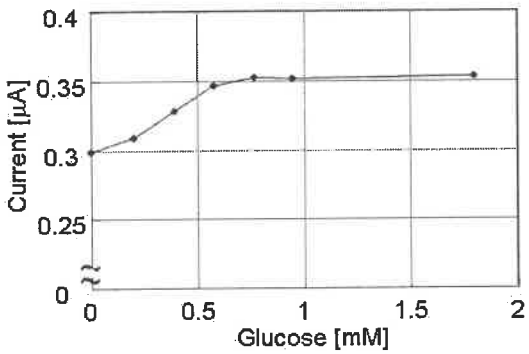

FIGURE 7. Photocurrent as a function of concentration of glucose lower than 1.8 mM.

Photocurrents for glucose concentration below 1 mM were plotted in Figure 7. A linear correlation was observed in this concentration range. It seems that oxidative ability of this TiO_2

electrode may saturate higher than 0.77 mM. According to Yang et al [4], the general equation for complete mineralization of an organic compound, $C_yH_mO_jN_kX_q$, on a TiO_2 electrode is

$$C_yH_mO_jN_kX_q + (2y\text{-}j)H_2O \rightarrow yCO_2 + qX^- + kNH_3 + (4y\text{-}2j+m\text{-}3k)H^+ + (4y\text{-}2j+m\text{-}3k\text{-}q)e^-$$

So, the equation of glucose is

$$C_6H_{12}O_6 + 6H_2O \rightarrow 6CO_2 + 24H^+ + 24e^-$$

Following reactions also occurred at each electrode.

TiO_2) $2Cl^- \rightarrow Cl_2 + 2e^-$

Pt) $2H^+ + 2e^- \rightarrow H_2$

Ag/AgCl) $AgCl + e^- \rightarrow Ag + Cl^-$

The total reaction consists of electrolysis of water and oxidation of glucose. The reaction rate constant depends on concentration, so the reaction rate of the former reaction is constant and the change of photocurrent was caused by the change of the reaction rate of the latter reaction. The solution contains 0.154 mM of Cl^-, which is enough to keep ion conductivity of the electrolyte, and the Ag/AgCl electrode has enough reaction area, so it is thought that the change of the slope of the correlation line means the photocatalytic ability of the TiO_2 electrode saturated.

Experiment 2

Figure 8 shows the photocurrents for different concentrations of glucose measured with $TiCl_4$-treated electrode. The photocurrent values increased compared with those by the untreated. This means that $TiCl_4$ post treatment enhanced reaction rate, and so photocurrent. The slope of the correlation line was also larger than that by the untreated (compared with Figure 6); almost twice. This means that both the reaction rate of electrolysis of water and that of oxidation of glucose were increased

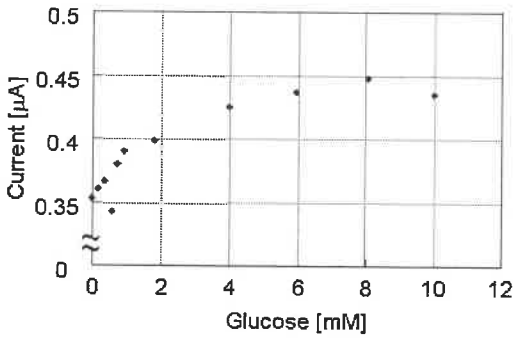

FIGURE 8. Photocurrent as a function of concentration of glucose with $TiCl_4$ post treatment.

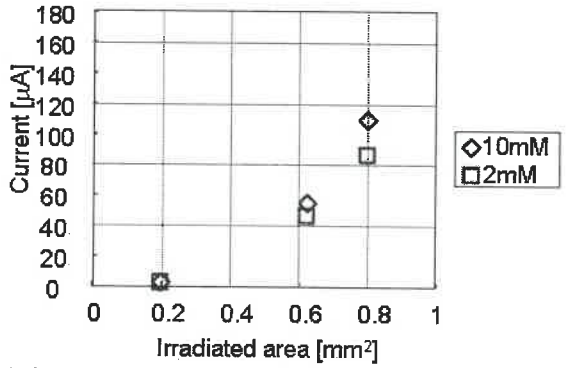

FIGURE 9. Measured photocurrent values. The Photocurrent was larger at higher concentration spot.

Experiment 3

Figure 9 shows the result. Photocurrent was larger at higher concentration spot. This shows that the point to conduct glucose oxidation can be designed with UV light spot on our TiO_2 electrode, and so the researched sensor has light-addressing ability.

CONCLUSION

The TiO_2 electrode we researched has sensitivity to glucose at the range of 0~10mM, and it was higher below 1mM. $TiCl_4$ post-treatment increased the photocurrent and improved the sensitivity. It was also proved that our sensor has an ability of light-addressing through an experiment.

REFERENCE

[1] Hafeman D G, Parce J W, McConnell H M. Light-sddressable potentiometric sensor for biochemical systems. Science. 1988; 240: 1182-1185

[2] P M Sommeling, B C O'Regan, R R Haswell, H J P Smit, N J Bakker, J J T Smits, J M Kroon, J A M van Roosemalen. Influence of a TiCl4 Post- Treatment on Nanocrystalline TiO2 Films in Dye-Sensitized Solar Cells. J. Phys. Chem. B, 2006; 110: 19191-19197

[3] M Yang, L Li, S Zhang, G Li, H Zhao. Preparation, characterisation and sensing application of inkjet-printed nanostructured TiO2 photoanode. Sensors and Actuators B, 2010; 147: 622-628

[4] Suzurikawa J, Takahashi H, Nakao M, Takayama Y, Jimbo Y. Light-addressable electrode with hydrogenated amorphous silicon and low-conductive passivation layer for stimulation of cultured neurons. Appl. Ohys Lett. 2007; 90: 093901

EVALUATING THE SENSITIVITY OF PERIODIC ERRORS IN HETERODYNE INTERFEROMETRY

Vasishta Ganguly, Nam Ho Kim, Hyo Soo Kim, and Tony Schmitz
Department of Mechanical and Aerospace Engineering
University of Florida
Gainesville, FL, USA

1. INTRODUCTION

Heterodyne displacement measuring interferometry offers high resolution, high accuracy displacement measurement for non-contact applications. However, the accuracy is limited by non-linearities, or periodic errors, which depend on misalignments in the optical setup. These errors are non-cumulative in nature and repeat with each unit wavelength change in the optical path. The purpose of this study is to complete a sensitivity analysis using the analytical periodic error model from Cosijns et al. [1]. Sensitivity analysis is used to study how the uncertainty in model output is related to the uncertainty in the input parameters [2-5]. Local sensitivity analysis involves computing the derivative of the model output with respect to the input. However, this definition is local in nature because the derivative must be evaluated at a fixed point in the input space.

While a gradient-based local sensitivity approach does provide an estimate for the periodic error dependence on setup misalignments, it does not account for the associated uncertainties. In order to provide a better estimate of model sensitivity, global sensitivity techniques are used here. Variance-based global sensitivity analysis methods explore the space of input parameters by selecting a judicious number of randomly selected data points from the input parameter space and provide a more informative and robust estimate of the behavior of the model output with respect to variation in the model input [2]. In this study, a variance-based Monte Carlo approach is used to estimate both the individual and total effect Sobol' sensitivity indices for each of the model inputs [2, 6-7]. The study reveals that rotational misalignment of the polarizing beam splitter, α, the rotational misalignment of the mixing polarizer, θ, and non-orthogonality, β_{err}, between the two ideally linearly polarizations laser frequencies are most influential on the output uncertainty.

2. PERIODIC ERROR FORMULATION

For an ideal single pass interferometer, the two coherent, collinear, orthogonally polarized laser frequencies, f_1 and f_2, are perfectly separated at the polarizing beam splitter and are directed into the reference and measurement arms of the interferometer. However, due to imperfect optical performance there is leakage of each frequency into both the measurement and reference arms. This frequency leakage may occur due to: non-orthogonality of the two frequencies emitted from the laser source; rotational misalignment of the laser beam with respect to the polarizing beam splitter (PBS); ellipticity of the polarization states; different transmission coefficients for the individual laser beams at the PBS; and rotational misalignment of the polarization axes with respect to the mixing polarizer. Ghost reflections, non-linearities in the phase measuring electronics, and beam shear have also been found to induce periodic errors.

Cosijns et al. [1] developed an analytical model for periodic error taking into consideration the rotational misalignment of the input laser beam with respect to the PBS, non-orthogonality of the linearly polarized frequencies, ellipticity in the polarizations of the two frequencies, rotational misalignment of the mixing linear polarizer (LP), and the different transmission coefficients for the PBS. All other parameters are assumed to be ideal. This study uses the Cosijns et al. [1] model to compute sensitivity of the periodic error with respect to the contributing optical imperfections. The first and second order periodic errors are identified analytically and are summed to obtain the worse case periodic error. Sensitivity analysis is performed with respect to this sum.

3. SENSITIVITY ANALYSIS

Saltelli et al. [5] define sensitivity as: "The study of how the uncertainty in the output of a model can be apportioned to different sources of uncertainty in model input." This study focuses

on identifying which parameters in the heterodyne interferometry setup are most influential on periodic error by performing a sensitivity analysis. Given this information, efforts in aligning the interferometer may be optimized.

3.1 Global Sensitivity Analysis

Although local, or gradient-based, sensitivity analysis does provide a measure of the local response of the outputs obtained by varying each input parameter individually, it is ineffective for exploring the entire input parameters space in the case of uncertain inputs. The volume of the space explored is zero because the sensitivity is calculated only at one point with respect to one parameter, while all other parameters are kept constant. In order to obtain better estimates of variation of the outputs over the entire input parameter space, global sensitivity analysis is applied. Variance-based methods enable the computation of output sensitivities given uncertain inputs. These methods compute the output values at a number of points in the input parameter space and use information ascertained from a large number of model evaluations to calculate the sensitivity of the output with respect to each input. Global sensitivity measures provide an estimate of how much output variance would be reduced if a particular input parameter was fixed at a certain value.

3.2 The Sobol' Method

Sobol' suggested a Monte Carlo method for computing global sensitivity indices of arbitrary groups of factors [8]. The individual effect of an input is defined as the reduction in output variance when the input is fixed at a certain value. The sensitivity index, S_i, is defined in terms of the unconditional variance of the output, V(Y), and the variance in the output Y when the input parameter, X_i, is fixed, $V[E(Y|X_i)]$; see Eq.1.

$$S_i = \frac{V[E(Y|X_i)]}{V(Y)} \tag{1}$$

This index represents the primary (first order) effect of X_i on Y without taking into consideration interaction effects. These individual effect sensitivity indices identify which parameters most influence output variation and can be used in a factor prioritization setting.

The total effect sensitivity index takes into consideration the interactive effects of the various input parameters on output variance. The total effect sensitivity index, S_{Ti}, is expressed in terms of V(Y) and the output variance $V[E(Y|X_{\sim i})]$, which is the variance computed when all parameters except X_i are fixed. See Eq. 2.

$$S_{Ti} = 1 - \frac{V[E(Y|X_{\sim i})]}{V(Y)} \tag{2}$$

The total effect sensitivity indices can be used in a factor fixing setting. If $S_{Ti} \approx 0$, then X_i can be fixed at any value within its input range without affecting the output variance.

3.2.1 Calculation of Sobol' sensitivity indices

A Monte Carlo approach is used to compute the Sobol' sensitivity indices, where larger sample sizes yield increased accuracy of the results. The step-by-step procedure adopted to calculate the sensitivity indices follows.

1. Define two N x k matrices, A and B, using a Latin hypercube sampling technique where N is the number of samples and k is the number of input parameters. The column of each matrix corresponds to an input parameter with values within its input uncertainty range. Note that A and B are generated independently and are separate matrices.

$$A,B = \begin{bmatrix} x_1 & x_2 & \cdots & x_{k-1} & x_k \\ x_1^2 & x_2^2 & \cdots & x_{k-1}^2 & x_k^2 \\ \vdots & \vdots & \ddots & \vdots & \vdots \\ x_1^{N-1} & x_2^{N-1} & \cdots & x_{k-1}^{N-1} & x_k^{N-1} \\ x_1^N & x_2^N & \cdots & x_{k-1}^N & x_k^N \end{bmatrix} \tag{3}$$

2. Define a C_i matrix for each input parameter by replacing the i^{th} column (i = 1 to k) of the B matrix with the i^{th} column of the A matrix.

$$C_i = \begin{bmatrix} x_{1B} & x_{2B} & \cdots & x_{iA} & \cdots & x_{k-1B} & x_{kB} \\ x_{1B}^2 & x_{2B}^2 & \cdots & x_{iA}^2 & \cdots & x_{k-1B}^2 & x_{kB}^2 \\ \vdots & \vdots & \ddots & \vdots & \ddots & \vdots & \vdots \\ x_{1B}^{N-1} & x_{2B}^{N-1} & \cdots & x_{iA}^{N-1} & \cdots & x_{k-1B}^{N-1} & x_{kB}^{N-1} \\ x_{1B}^N & x_{2B}^N & \cdots & x_{iA}^N & \cdots & x_{k-1B}^N & x_{kB}^N \end{bmatrix} \tag{4}$$

3. Compute the model output using input samples from the A, B, and C_i matrices; this

generates the output vectors. Each row of the A, B, and C_i matrices forms a single input data point.

$$y_A = \begin{bmatrix} f(A) \\ f(A^2) \\ \vdots \\ f(A^{N-1}) \\ f(A^N) \end{bmatrix} y_B = \begin{bmatrix} f(B) \\ f(B^2) \\ \vdots \\ f(B^{N-1}) \\ f(B^N) \end{bmatrix} y_{C_i} = \begin{bmatrix} f(C_i) \\ f(C_i^2) \\ \vdots \\ f(C_i^{N-1}) \\ f(C_i^N) \end{bmatrix} \quad (5)$$

4. The individual effect sensitivity indices are:

$$S_i = \frac{\frac{1}{N}\sum_{j=1}^{N} y_A{}^j y_{C_i}{}^j - f_o{}^2}{\frac{1}{N}\sum_{j=1}^{N} \left(y_A{}^j\right)^2 - f_o{}^2}, \text{ where } f_o{}^2 = \left(\frac{1}{N}\sum_{j=1}^{N} y_A{}^j\right)^2. \quad (6)$$

5. The total effect sensitivity indices are:

$$S_{Ti} = \frac{\frac{1}{N}\sum_{j=1}^{N} y_B{}^j y_{C_i}{}^j - f_o{}^2}{\frac{1}{N}\sum_{j=1}^{N} \left(y_A{}^j\right)^2 - f_o{}^2}. \quad (7)$$

4. PREDICTING PERIODIC ERROR FROM INPUT UNCERTAINTY

Given the most important parameters in Cosijns et al. model (α, θ, and β_{err} identified using the sensitivity analysis), the expected value of periodic error for a given combination of setup uncertainties can be determined. A Monte Carlo simulation (MCS) is used to evaluate the expected periodic error for uncertain inputs. The expected value of the periodic error is considered to be the value below which 95% (2σ) of the periodic error values computed during the MCS lie. A sample size of 2000 is used to perform the MCS.

Expected periodic error is computed for a complete array of uncertainties in the non-orthogonality of the two frequencies, rotational misalignment of the PBS, and rotational misalignment of the mixing LP. The uncertainties in the ellipticities and transmission coefficients are kept constant due to their low sensitivity. Contour plots are plotted here for different values for uncertainty in the mixing polarizer orientation.

From the simulation data, a regression fit with higher-order terms was completed in order to obtain an expression for the expected value of periodic error, pe (the sum of first and second order contributions). A satisfactory fit was obtained with the inclusion of cubic terms. The expression is of the form:

$$pe = b_0 + \sum_{p=1}^{k} b_p x_p + \sum_{p=1}^{k}\sum_{q=p}^{k} b_{pq} x_p x_q + \sum_{p=1}^{k}\sum_{q=p}^{k}\sum_{r=q}^{k} b_{pqr} x_p x_q x_r, \quad (8)$$

where the b terms are the regression coefficients, k is the number of variables (α, θ, and β_{err}), and x gives the uncertainties in α, θ, and β_{err}. This expression provides an estimate of the expected value of periodic error given uncertainties in the setup misalignments. The expression does not incorporate uncertainty in the beam ellipticities, $d\varepsilon_1$ and $d\varepsilon_2$, or transmission coefficients, ξ and χ; their uncertainties are assumed to be constant.

5. RESULTS

5.1 Sobol' Sensitivity Indices

The Sobol' individual effect and total effect sensitivity indices are computed using the Monte Carlo approach described previously with a sample size of 1×10^6. The input parameter uncertainty ranges used in the analysis are listed in Table 1 (normal distributions were assumed).

TABLE 1. Uncertainty ranges for input parameters.

Parameter	Uncertainty range (3σ)
α	5 deg
θ	5 deg
$d\varepsilon_1$	1 deg
$d\varepsilon_2$	1 deg
ξ	0.05
χ	0.05
β_{err}	1 deg

Table 2 shows the individual effect, total effect, and interactive effect sensitivity indices computed for first and second order periodic errors. As can be seen from the results, for the given input range, periodic order error is mainly dominated by β_{err}. However, the total sensitivity index for α and θ are also significant, indicating that their interactive effects with other parameters are important. The angular orientations α, θ, and β_{err} are the main interacting parameters. The beam ellipticities, $d\varepsilon_1$ and $d\varepsilon_2$, and the transmission coefficients, ξ

and χ, have little influence. Other simulations conducted with different input uncertainty values produced similar results.

TABLE 2. Sobol' sensitivity indices.

	Individual effect S_i	Total effect S_{Ti}	Interactive effect $S_{Ti} - S_i$
α	**0.125**	**0.411**	**0.286**
θ	0.034	**0.304**	**0.270**
$d\varepsilon_1$	0.036	0.135	0.099
$d\varepsilon_2$	0.038	0.135	0.097
ξ	0.002	0.013	0.011
χ	0.002	0.014	0.012
β_{err}	**0.387**	**0.641**	**0.254**

5.2 Periodic Error Prediction

Expected values of periodic error are computed for an array of input uncertainties (α = 0 to 5 deg, θ = 0 to 5 deg, and β_{err} = 0 to 1 deg). Contour plots are then plotted in the α-β_{err} plane for different values of θ uncertainty. From these plots, the expected value of periodic error can be identified for a given combination of input parameter uncertainties. The uncertainty in the ellipticities is fixed at 1 deg; the transmission coefficient uncertainties are 0.05. The periodic error is evaluated in nm. Figure 1 shows a contour plot for uncertainty in θ of 2 deg.

Using these results, a regression fit (with higher order terms) to the expected periodic error, pe, yields Eq. 9, where insignificant terms have been eliminated. Note that the α, θ, and β_{err} terms are the 3σ normally-distributed uncertainties. Equation 9 can be used to estimate the expected periodic error given uncertainties in α, θ, and β_{err} for any single pass heterodyne interferometer setup.

$$pe = 0.4115 + 0.2807\beta_{err}^2 + 0.0011\alpha^2\theta + 0.0009\alpha\theta^2 - 0.0048\alpha\theta - 0.0788\beta_{err} + 0.0182\alpha\beta_{err} + 0.0005\alpha^3 - 0.0092\alpha\beta_{err}^2 \quad (9)$$

6. CONCLUSIONS

The Sobol' global sensitivity indices method was used to evaluate individual and total effect sensitivity indices. The sensitivity indices obtained from this analysis suggested periodic error depends mainly on the rotational misalignments α, θ, and β_{err}. Only β_{err} showed a significant individual effect; however, α and θ interact with each other as well as with β_{err} and significantly affect periodic error. This suggests that, in order to restrict periodic error to a low value, the rotational alignment of the laser beams with the PBS and the rotational alignment of the mixing polarizer must be accurate. Also, a laser source with orthogonal (linearly polarized) frequencies must be selected. The contour plots as well as the expression for expected value of periodic error can be a useful tool in predicting periodic error when the uncertainties in the optical setup misalignments are known.

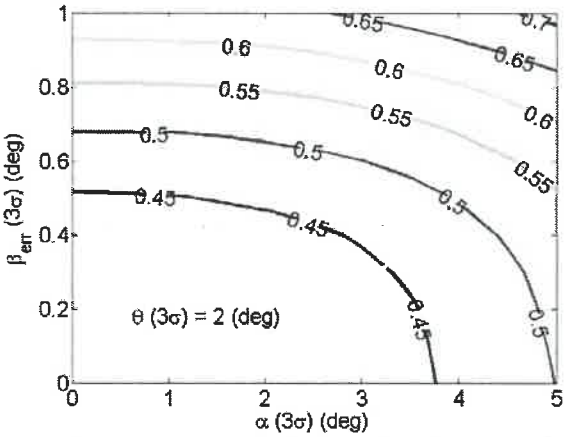

FIGURE 1. Contour plot for expected periodic error (θ = 2 deg).

7. REFERENCES

[1] Cosijns S, Haitjema H, Schellekens P. Modeling and verifying non-linearities in heterodyne displacement interferometry. Precision Eng 2002;26:445-455.

[2] Saltelli A, Andres T, Campolongo F. Global Sensitivity Analysis. A Primer. Wiley, 2008.

[3] Saltelli A. Sensitivity analysis for importance assessment. Risk Analysis 2002;22:579-590.

[4] Homma T, Saltelli A. Importance measures in global sensitivity analysis of nonlinear models. Rel Eng Sys Safety 1996;52:1-17.

[5] Saltelli S, Tarantola S, Chan K. Quantitative model independent method for global sensitivity analysis of model output. Technometrics 1999;41:39-56.

[6] Cukier R, Levine H, Schuler K. Nonlinear sensitivity analysis of multiparameter model systems. J Comp Phys 1978;26:1-42.

[7] Sobol' IM. Sensitivity analysis for non-linear mathematical models. Math Modeling Comp Exp 1993;1:407-414.

[8] Sobol' IM. Global sensitivity indices for nonlinear mathematical models and their Monte Carlo estimates. Math Comp Simul 2001;55:271-80.

COMPRESSION MOLDING OF REFRACTIVE AND DIFFRACTIVE HYBRID GLASS LENSES

Peng He[1], Fei Wang[2], Likai Li[1], Kyriakos Georgiadis[2], Fritz Klocke[2] and Allen Y. Yi[1]
[1]Department of Integrated System Engineering
The Ohio State University, Columbus, OH, USA
[2]Fraunhofer Institute for Production (IPT), Aachen, Germany

INTRODUCTION

Refractive and diffractive hybrid lenses have been designed and implemented for some industrial applications. These optical elements however are limited to low volume production or specific materials such as polymers. Although plastic lenses can be fabricated using injection molding into different geometries at high volume, these optics do not perform well under rigorous conditions of high temperature, pressure and humidity that are required for many precision applications (e.g., military applications). On the other hand, optical glasses have been and will continue to be the materials of choice for high precision imaging optics. Unfortunately, glass materials are extremely difficult to process using conventional methods. As an alternative to traditional glass lens manufacturing processes, compression molding of glass lenses can be a very attractive approach [1-3].

The aim of this research is to demonstrate a feasible glass diffractive optics molding process by integrating established precision mold making, heat transfer and rheological modeling of glass materials. The primary goal of this research is to verify proper glass and mold materials, and process parameters that will satisfy pre-defined design criteria for compression molding of diffractive glass aspherical optical elements thus resulting in lower cost and high quality products. In addition, numerical modeling software for optical efficiency simulation will also be evaluated. The proposed process is a net shape, high volume manufacturing method therefore it allows optical manufactures to design compact optical systems using optical glasses that were not available before. The results from this research can be integrated in optical design, fabrication and assembly therefore providing industry with the possibility of low cost, compact and high performance optical systems utilizing hybrid precision glass optics.

OPTICAL DESIGN

Optical Mold Preparation

In this research, a refractive-diffractive hybrid singlet lens aimed to compensate for chromatic aberrations in visible light range was designed using software Zemax (www.zemax.com). The features of the hybrid lenses are listed in Table 1.

Table 1: Hybrid lens design features

F/#	4
Lens diameter	18 mm
Center thickness	3 mm
Glass type	P-SK57 (n_d=1.5870, υ_d=59.6001)
Wavelength	F, D, C (486.1327, 587.5618, 656.2725) nm

The DOEs (diffractive optical elements) could be designed either on the planer surface (first surface in Figure 1) or aspherical surface (second surface). However, DOEs on the second surface are good for sine condition [3], which reduces the design error. This is also a preferred design for mold fabrication, which can minimize the tool alignment issue during diamond turning because the DOEs and aspherical profile are on the same surface. Figure 1 is the layout of the refractive and diffractive hybrid lens.

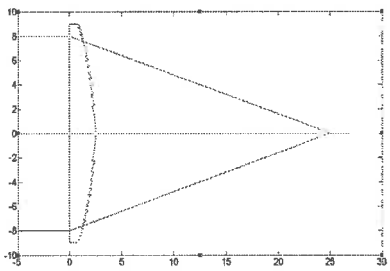

Figure 1: diffractive and refractive hybrid lens design

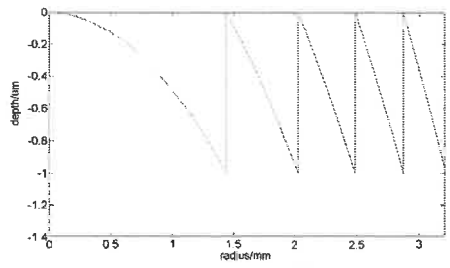

Figure 2: diffractive element close up view

Figure 2 illustrates the details of the diffractive element shape. In this design, aspherical surface is described by Equation 1,

$$z = \frac{cr^2}{1+\sqrt{1+(1+k)c^2r^2}} + a_2r^2 + a_4r^4 \qquad (1)$$

where the curvature of the optical surface c = -1/69.312 and the conical constant k = -18.3594, a_2 = -3.936369x10^{-3} a_4 = -3.179234x10^{-6}. The diffractive profile is decribed by the following equation:

$$\Phi = -417.418\rho^2 + 2.0909\rho^4 + 3.0827\rho^6 \qquad (2)$$

where, ρ ($0<\rho<1$) is the normalized radial aperture coordinate and the height d is given by

$$d = \frac{\lambda_d \Phi}{2\pi(n_d - 1)} \qquad (3)$$

where $0<\Phi<2\pi$.

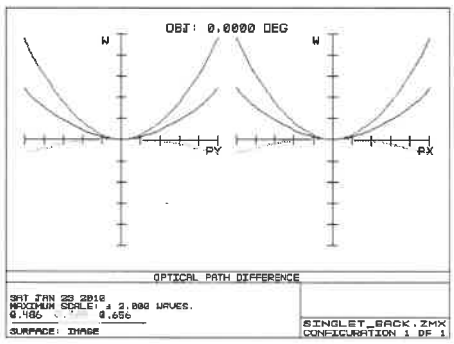

Figure 3: OPD of the diffractive and refractive hybrid lens

EXPERIMENTS

Optical Mold Preparation

To create the diffractive pattern on the mold surface, diamond turnable 715 copper nickel alloy was selected for this experiment. The aspherical substrate was first diamond turned on the Moore 350 FG ultraprecision machine. A special single point diamond cutter with 2 μm half radius (Edge Technology, Indianapolis, Indiana) was used to machine the diffractive features. Prior to experiments, mold surfaces were coated with a 5 nm Titanium and 100 nm Platinum.

Molding Process

The mold assembly was heated to 715 °C (thermocouple reading) in vacuum on a laboratory scale molding system (Figure 4). The description of the system can be found elsewhere [1]. Connecting rods, electrical cables were removed for clarity. In this system, a Transducer Techniques THC-500V load cell was used to measure applied load and control molding process. Based on the sensitivity of the loadcell and the signal conditioning software, a resolution of 0.09 N can be achieved [1].

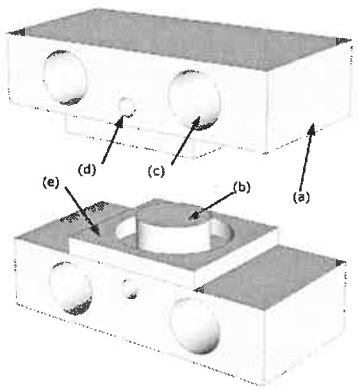

Figure 4: Schematic of the close up view of the compression forming stage: (a) mold heating pedestals (b) Nickel mold (c) heating cartridges (d) thermocouple position (e) substrate holder

A typical molding process consists of heating, molding and releasing stages. Figure 5 shows the temperature and load conditions for this process. To start, glass gob is first heated to 715 °C and kept for 2 hours and 45 mins to make sure the glass has a uniformed temperature distribution above T_g (glass transmission temperature). Then during the molding (forming) stage, the bottom mold gradually moved up to apply load on the glass gob. The softened glass gob is deformed into the desired shape between the two molds. The maximum molding load was about 510 N before it started decreasing due to the viscoelastic nature of glass. The molded glass was kept between two molds for 45 s then cooled down in 160 s to allow the optic to reach the desired geometry. The last step was to

remove the molded glass by lowering the bottom mold. To avoid oxidization, N_2 was introduced to purge the chamber and then pumped out to create the vacuum in the chamber. The pressure was kept at about 30 millitorr during the entire experiment.

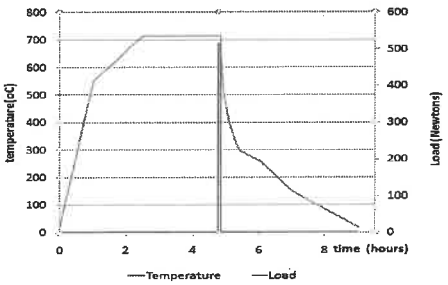

Figure 5: Molding conditions for P SK57 Glass refractive and diffractive lenses

RESULTS AND DISCUSSION

Replication Accuracy

The molded DOEs were measured for geometric accuracy and surface finish. Wyko (Veeco NT9100 optical profiler) scans of the coated mold and molded glass were performed on the same surface. A close up view of the diffractive features is plotted in Figure 6. It can be seen that the DOE features were successfully transferred to the glass substrate. The difference between the molded glass optics and the mold may have resulted from the glass thermal shrinkage and is currently under investigation.

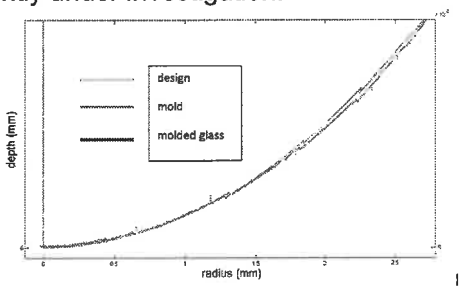

Figure 6: close up view of DOEs

Surface Evaluation

The surfaces of the molded lens were also measured by using Wyko optical profilometer (as shown in Figure 7). The diffractive profile and molded surface finish are illustrated in the 2D color scan. As compared to a previous study [2], it appears that current mold glass combination does not produce the surfaces for imaging optics. Efforts to improve surface roughness and de-molding are currently underway.

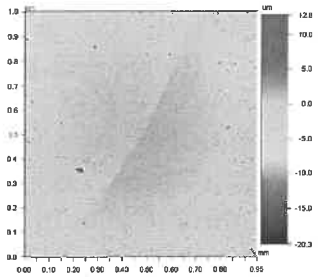

Figure 7: Wyko scan of a molded hybrid lens

CONCLUSION

To compensate the chromatic aberrations, an all glass refractive-diffractive lens provides an alternative to a lens assembly with the same function, which is usually bigger and heavier than the hybrid lens. By use of single point diamond turning, aspherical and DOE features were created on the same mold surface and the need for alignment was eliminated.

The molding experiments demonstrated that the non-planer profile with micro features could be fabricated on glass surfaces by compression molding, leading to a promising way to produce high-quality, low-cost hybrid lenses.

ACKNOWLEGEMENTS

This work was supported in part by the German Research Foundation (DFG) within the SFB/TR4 "Process Chains for the Replication of Complex Optical Elements." AY acknowledges SFB/DFG for providing financial support for travel to Aachen. The research was also supported by the National Science Foundation (USA) under Grant No. 0547311. Any opinions, findings, and conclusions or recommendations expressed in this material are those of the authors and do not necessarily reflect the views of the National Science Foundation.

REFERENCES

[1] K. Fischbach, et al., "Investigation of the Effects of Process Parameters on the Glass-to-Mold Sticking Force during Precision Glass Molding," in press, *J. Vac. Sci Technol. B*, June (2010).

[2] A. Y. Yi, et al., "An Innovative Precision Compression Molding Process of Glass Diffractive Optics by Use of Fused Silica Wafer Mold and Low T_g Optical Glass," *J. Micromech. Microeng.*, 16 (10), 2000-5 (2006).

[3] Y. Tanaka, et al., "Diffractive-Refractive Achromatic Lens for Optical Disk System by Molding", *Opt. Rev.* 5 334-9 (1998).

DEVELOPMENT OF A LASER-GUIDED DEEP-HOLE MEASUREMENT SYSTEM WITH LOWER PRODUCTION COST

Akio Katsuki[1], Hiromichi Onikura[1], Takao Sajima[1], Hiroshi Murakami[2], Tsuyoshi Satou[3], Hironori Nishi[3], Valentine Pietri[4], and Hazrad MD. Ali[5]
[1]Department of Mechanical Engineering, Faculty of Engineering, Kyushu University 36, 744 Motooka, Nishi-ku, Fukuoka 812-8581, Japan
[2]Kagoshima University, Kagoshima, Japan,
[3]Graduate School of Engineering, Kyushu University
[4]IFMA, Clermont-Ferrand, France, [5]IIUM, Kuala Lumpur, Malaysia

INTRODUCTION

The accuracy of very deep holes, such as diameter, roundness, cylindricity, and straightness has to be precisely measured for many applications, e.g., the rotation shafts of jet engines and high-speed trains, cylinder used for plastic injection molding, and cylinder liner of ship engines. Existing home measurement systems have limitations for holes with a large length to diameter ratio, in which case different measurement devices are used separately. A laser-guided deep-hole evaluating probe is proposed to evaluate the accuracy of deep holes using a single device.

In our first study [1], a laser-guided probe with a diameter of 110 mm was fabricated. An electric micrometer was used to measure hole accuracy. The measured data was transferred wirelessly from an antenna fixed at the top of the probe to a radio detector set in front of the probe.

In the study, the radio was absorbed by the hole wall and the measurement became easily over scale, particularly in high sensitivity. Therefore, in our successive study [2] [3], a laser interferometer was used to detect the hole accuracy.

In the present study, a probe is fabricated using skids instead of piezoelectric actuators and its performance is examined. The use of skids reduces the production cost because they are less expensive as compared to piezoelectric actuators.

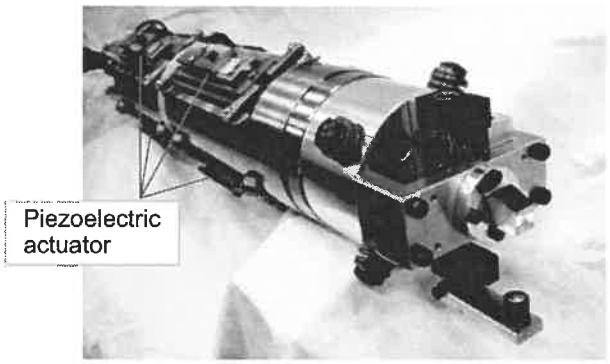

FIGURE 1. Measurement probe.

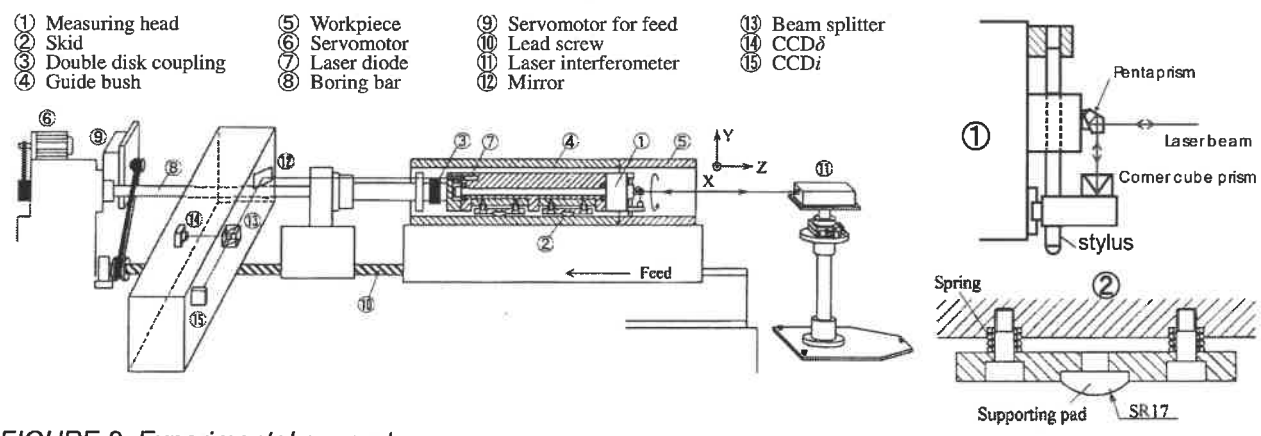

FIGURE 2. Experimental apparatus.

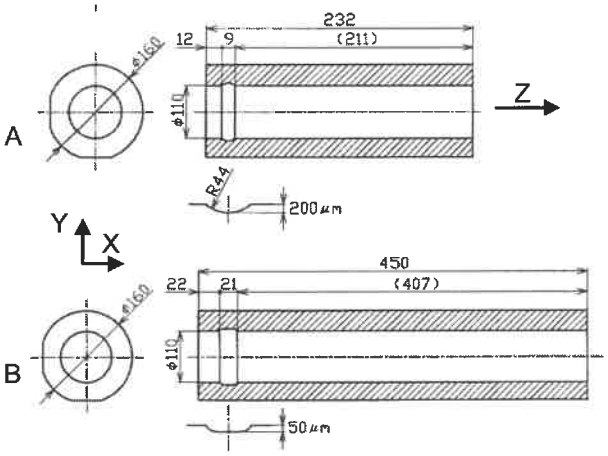

FIGURE 3. Shape of workpieces.

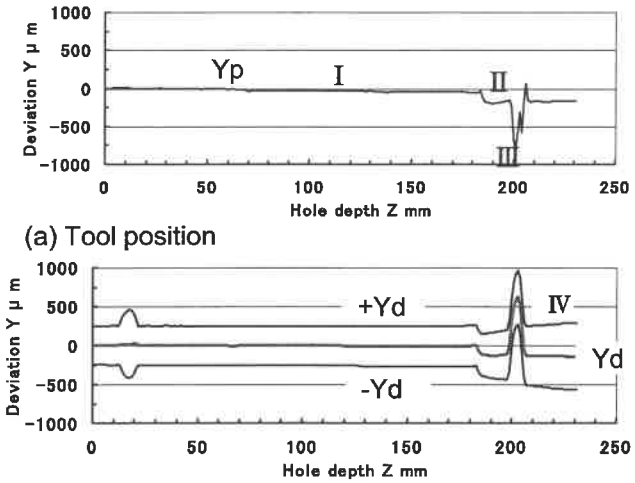

(a) Tool position

(b) Hole deviation measured by the probe.

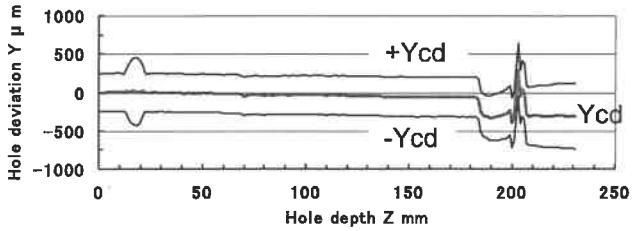

(c) Corrected hole deviation

FIGURE 4. Tool position and hole deviation measured by using probe (workpiece A).

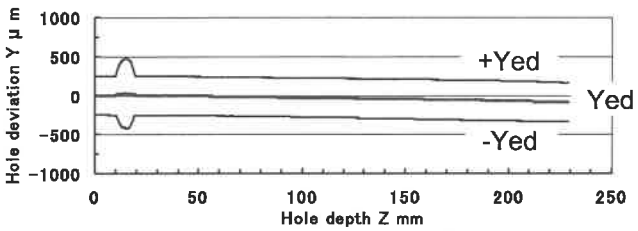

FIGURE 5. Hole deviation measured by using an electric micrometer (workpiece A).

MEASUREMENT PRINCIPLE

The experimental apparatus used in this study is shown in Fig. 2. The measurement unit consists of a pentaprism and a corner cube prism fixed on a stylus. A laser interferometer is set in front of the probe. The laser beam (He-Ne laser; power: 1 mW, wavelength: 632.8 nm) is incident on the pentaprism, which deflects the beam toward the corner-cube prism. The reflected beam returns via the pentaprism to the interferometer. The measuring length, response speed, and resolution of the laser interferometer are 0 to 10m, 0 to ±2.0 m/s, and 0.01 μm, respectively. A diameter of the laser beam is 5 mm.

EXPERIMENTAL METHOD

Workpieces

The shapes of workpiece are shown in Fig. 3. The workpieces are fabricated from duralumin (JIS A2017-T4). Workpiece A has a 200-μm-deep groove with a curvature radius of 44 mm between depths of 12 mm and 21 mm. Workpiece B has a 50-μm-deep groove with a flat bottom surface in a circumference direction between depths of 22 mm and 43 mm.

Experimental Method

The hole accuracy is measured by using a deep-hole boring machine (Fig. 2). The hole accuracy is measured by rotating the measurement-unit and moving the workpiece along the longitudinal direction.

First Experiment (Workpiece A)

The workpiece (**5**) is fed by 1 mm after each complete rotation of measurement unit for scanning the hole wall. The rotational speed of the unit is 12 rpm. In the first experiment, workpiece A is used. Supporting pads of the two front skids can enter a 200-μm-deep groove during the experiment.

Second Experiment (Workpiece B)

The second experiment is carried out after resolving the problems encountered during the first experiment. The experimental conditions are the same as those in the first experiment. Workpiece B is used so that the supporting pads of both the rear and front skids can enter the groove. The depth of the groove is one-fourth of

the depth of workpiece A. Measurement condition is much lenient than that of first experiment, as the probe inclines slightly and more slowly than the first experiment.

Third Experiment (Workpiece B)

Four sides (+Y, +X, -Y, -X) of the hole wall in workpiece B are individually scanned along the longitudinal direction (Z direction) by using the probe and an electric micrometer. The scanning speed of the probe is 240 mm/min.

RESULTS

First Experiment (Workpiece A)

The distance between the stylus and the supporting pads of the two front skids is 189 mm, and the distance between the supporting pads of the front skids and those of the rear skids is 160 mm.

Figure 4 shows the tool position, hole deviation and hole deviation corrected adjusting the tool position. Figure 4(b) shows the variation in hole deviation with hole depth. +Yd, –Yd, and Yd indicate the deviation of the +Y and –Y sides of the hole wall and the center of the machined hole, respectively. Yd is the average value of +Yd and –Yd. Figure 5 shows hole deviation measured by using an electric micrometer. The variation in the deviation of the hole wall on each side is measured by scanning the hole wall using an electric micrometer, which is fixed using a dial gage holder at the position of the double disk coupling of the rotation-proof apparatus [1]. In Fig.4 (b), the hole deviation over depth region I corresponds well with that measured by using the electric micrometer (Fig. 5). In region I, the two front skids enter the hole. In region II, the probe is found to be displaced, although the supporting pads of the skids do not enter the groove. This displacement is due to the rolling of the skid holder. In region III, the supporting pads of front skids enter the groove. In region IV, the measurement bar slips in the longitudinal direction, thereby increasing the deviation. However, no deviations are observed in Fig. 5.

The relationship the tool position and the hole deviation for the +Y side of the hole wall is theoretically given by Eq. (1).

$$Yp+(+Yd) = (+Ycd) = (+Yed) \qquad (1)$$

However, this relationship is not observed in Figs. 4 and 5 after the supporting pads of the front skids enter the groove.

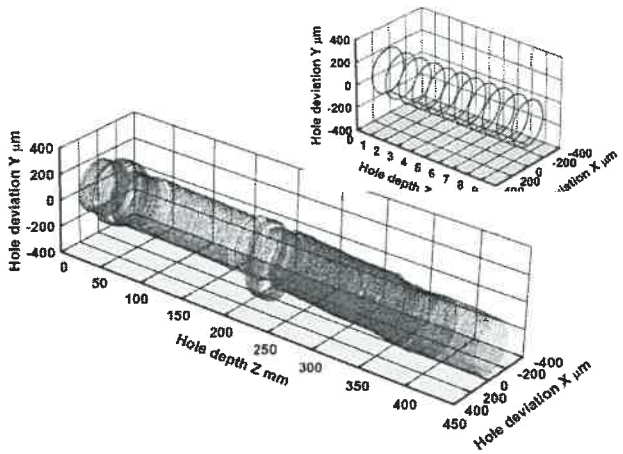

FIGURE 6. Shape of hole measured by using probe.

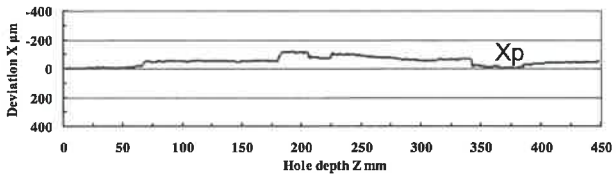

(a) Tool position measured by CCD cameras

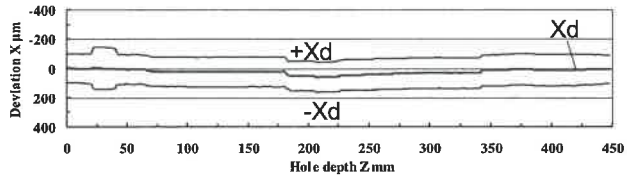

(b) Hole deviation measured by the probe

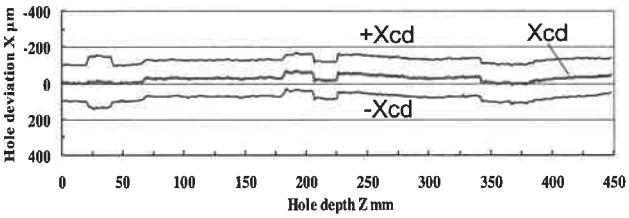

(c) Corrected hole deviation

FIGURE 7. Tool position and hole deviation measured by using the probe (workpiece B).

The coordinates of CCD image sensor is distorted when the laser spot comes near its edge. This distortion affects the detection accuracy of the probe position and inclination when the laser beam shift is large. This large shift occurs when the supporting pads of the front skids enter the groove.

The roundness of the hole is measured at a depth of 70 mm, and compared with that obtained using a roundness tester (Type 100, Taylor Hobson Ltd.). The measured roundness corresponded well in terms of shape and value with that obtained using the roundness tester.

Second Experiment (Workpiece B)

The second experiment is carried out after resolving the problems of rolling of the skid holder, slipping of the measurement bar, and distortion of coordinates of CCD cameras. Figure 6 shows the shape of the hole. Figure 7 shows the probe position, hole deviation, and hole deviation corrected adjusting the probe position. The corrected hole deviation shown in Fig. 6(c) does not correspond well with that measured by using the electric micrometer, as shown in Fig. 9.

Third Experiment (Workpiece B)

In the first and second experiments, the acquired data are corrected using the tool position. However, the tool position is not acquired while circumferentially scanning the hole wall, but just after a feed of 1 mm. There is a time lag between the tool position measurements, and, therefore, hole deviation is determined. During scanning using the probe, the probe positions corresponding to the scanned points of the hole wall cannot be obtained because the acquisition speed from the CCD cameras is seven frames in one rotation.

In the third experiment, the time lag is removed by scanning along the longitudinal direction (Z-direction). The corrected hole deviation obtained by using the probe, corresponds well with that obtained by using the electric micrometer both in terms of shape and value (Figs.8 and 9).
The relationship between the probe position and the hole deviation for the +Y side of the hole wall is theoretically given by Eq. (2).

$$(+Yp) + (+Yd) = (+Ycd) = (+Yed) \qquad (2)$$

CONCLUSIONS

A deep hole measurement probe is fabricated using skids instead of piezoelectric actuators and its performance is examined. The experimental results show that the straightness and roundness of holes can be evaluated using the probe under flexible measurement conditions.

ACKNOWLEDGMENTS

The support of the Fukuoka Industry, Science and Technology Foundation (Industry-Government-Academia Joint R&D Project for the Fukuoka Industry, Science and Technology Foundation), (Japan), is gratefully acknowledged. The cooperation of Mr. Thomas Caetano, an intern student at IFMA, and Yasushi Adachi, a graduate student of Kyushu University, is greatly appreciated.

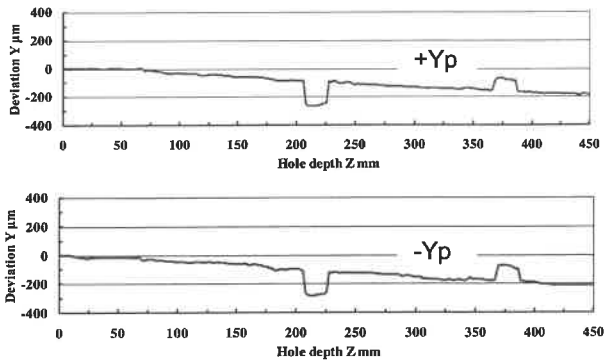

(a) Tool position measured using CCD cameras

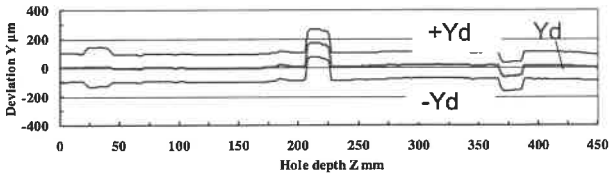

(b) Hole deviation measured by using probe

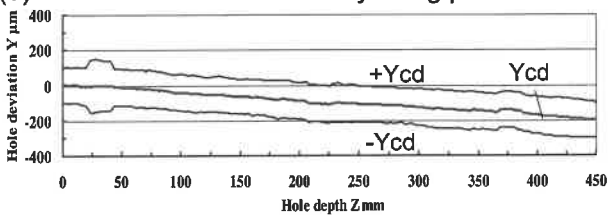

(c) Corrected hole deviation

FIGURE 8. Correction of hole deviation in each Y direction (workpiece B).

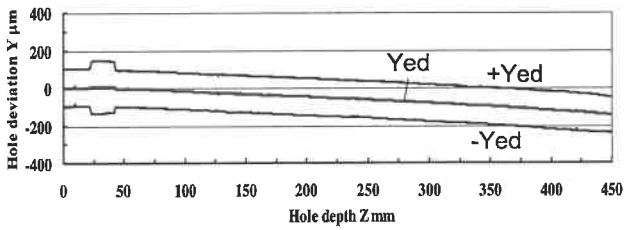

F IGURE 9. Hole deviation measured by an electric Micrometer (workpiece B).

REFERENCES

[1] Katsuki A, Onikura H, Sajima T, Mohri A, Murakami H. International Conference on Control, Automation & Systems. 2001; 743-746.

[2] Katsuki A, Onikura H, Sajima T, Zhen JG, Park HK, Murakami H. 6th **euspen** International Conference, 2006; 524-527.

[3] Katsuki A, Onikura H, Sajima T, Park HK, Nakanishi T, Murakami H. Proc. of LEM21. 2007; 893-896, Fukuoka.

NON-CONTACT ADAPTIVE OPTIC ACTUATOR SYSTEM FOR WAVEFRONT DISTORTION CORRECTION

Rudolf Saathof, Jo Spronck, Robert Munnig Schmidt
PME:Mechatronic System Design
Delft University of Technology, Delft, The Netherlands

INTRODUCTION

Adaptive optic systems are used in ground-based telescope systems for correcting atmospheric wavefront distortions. Current adaptive optic systems are also used in microscopes, high power lasers and tomography to correct for tissue density and heat effects. Requirements for optical systems are more demanding in terms of resolution and manufacturing. While conventional adaptive optic systems correct for wavefront aberration in the atmosphere, imaging systems suffer from quasi-static like creep and hysteresis and dynamic vibrations that are transferred from a machine frame to the optical components.

Traditional adaptive optic systems make use of a deformable mirror consisting of many individual actuators attached to a reference frame to correct its shape. However, the approach of using actuators attached between a frame and the deformable mirror is unsatisfactory because integrated actuators typically change the mirror surface shape during assembly. Additionally, the added stiffness between the vibrating frame and the optical component reduces performance. Furthermore, the large number of actuators and digital-to-analog output channels increases the system complexity, which drives up the cost and reduces system robustness since each individual actuator must be characterized and verified.

In this research we aim to replace conventional actuation systems with a contactless actuation principle. The basic idea is to use a radiant heat source and a controllable mask (or map) on the back of the mirror. In the ideal case, the mirror will have an absorptive coating behind its mirror surface which will absorb the radiative heat, causing an increase in temperature and a deformation of the mirror surface. The shape and speed of deformation can be controlled by adjusting a controllable mask, which selectively blocks portions of the radiative heat source.

This paper discusses the basic proof of concept and preliminary experiments which show a wavefront change by deforming a mirror using the radiant power absorbed from an applied light source. We use a simple homodyne Michelson interferometer which has a reference mirror and a deformable mirror. The deformable mirror has black paint on the back of the mirrored surface, which absorbs the optical power from a white light source. Using this concept and a circular absorptive spot, we demonstrate a deformation of about 120 nm which is directly correlated to the shape of the applied mask.

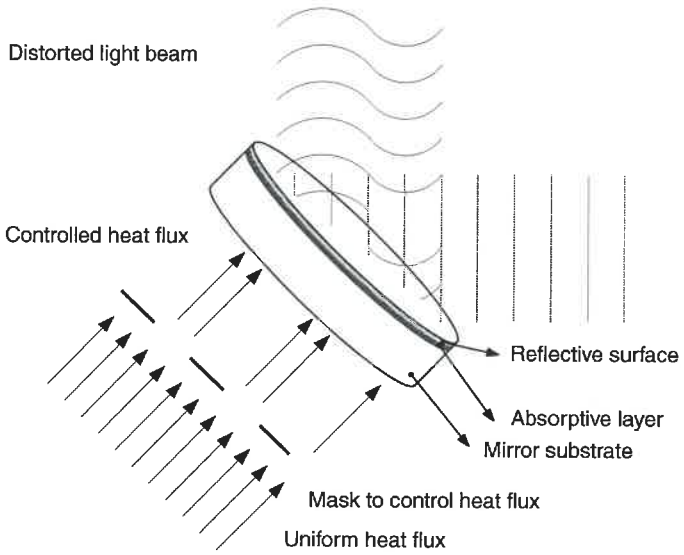

FIGURE 1. An example of the actuation principle. A distorted light beam is corrected after reflecting off a deformable mirror. The correction is done by heating a layer underneat the reflective coating of a mirror.

ACTUATION PRINCIPLE

Ideally, mirrors in precision optical systems contain a homogeneous substrate which is stiff and correctable over the whole surface [1]. Further requirements to correct for quasi-static aberrations is a time constant in the order of magnitude of the frequency of the aberrations and an accuracy in the order of magnitude of the aberrations. The deformable mirror has to correct over the whole surface to correct for the whole aperture.

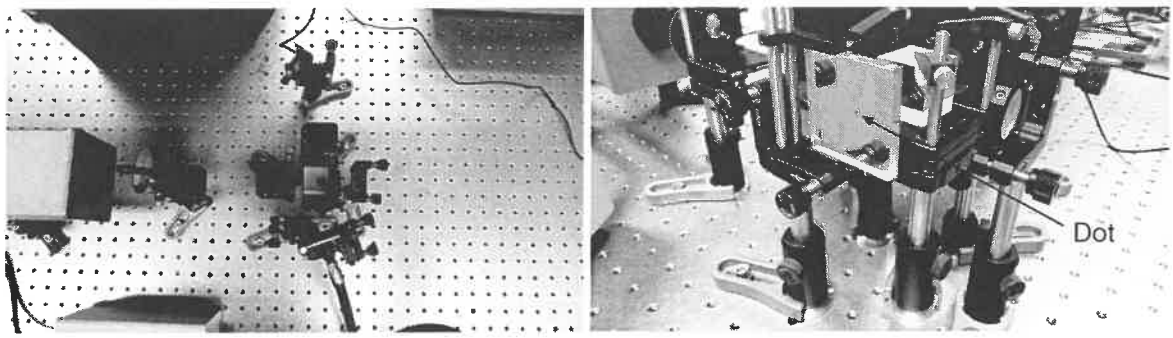

FIGURE 2. The experimental setup, with the Michelson interferometer and the deformable mirror (a), and the deformable mirror with the small painted dot on the center of the mirror (b).

The actuation principle is shown in Figure 1. The principle consist of a mirror and a radiant heat source. The substrate of the mirror is continuous, has a high thickness compared to conventional deformable mirrors and is transparent for the radiant heat source. The transparency is needed since the thermal radiation has to be transmitted through substrate to the reflective surface.

The mirror has a bi-layered coating. The coating layer at the substrate side is absorptive for the wavelength of the radiant heat source and the top layer is reflective for the wavelength used in the optical system. The absorptive layer absorbs the radiation, causing an increase in temperature. The thermal expansion of the mirror surface will cause a deformation at the mirror surface since the absorptive layer is directly positioned under the reflective layer.

The deformation is controlled by placing an adaptable mask in between the mirror substrate and radiative heat source. The adaptable mask should be able to change from totally transmissive to totally opaque for the wavelength of the radiative heat source.

This deformable mirror can be used in a closed loop configuration, using a beamsplitter, which splits of a part of the light to a wavefront sensor, and a control algorithm to calculate the compensation signal, in order to control the mask between the radiant heat source and the deformable mirror.

EXPERIMENTAL SETUP

To demonstrate the feasibility of this concept, a measurement mirror was prepared with a fixed mask and a homodyne interferometer was used to measure the deformation. For a preliminary proof of concept, full surface control is not needed and therefore the mirror is deformed locally.

The prepared mirror is based on a standard optical mirror with an aluminum reflective coating where part of the coating is replaced by an ab-

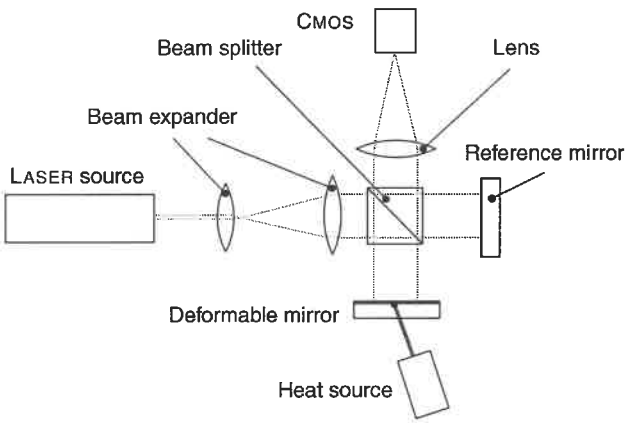

FIGURE 3. A schematic view of the experimental setup. The figure shows an homodyne Michelson interferometer, using a commercial Ne-He laser source, which bundle is expanded to 25 mm. One of the interferometer arms has the deformable mirror and the other is the reference mirror. At the point where the beam has its interference pattern, the beam is converged using a lens, in order to fit the spot on the CMOS camera.

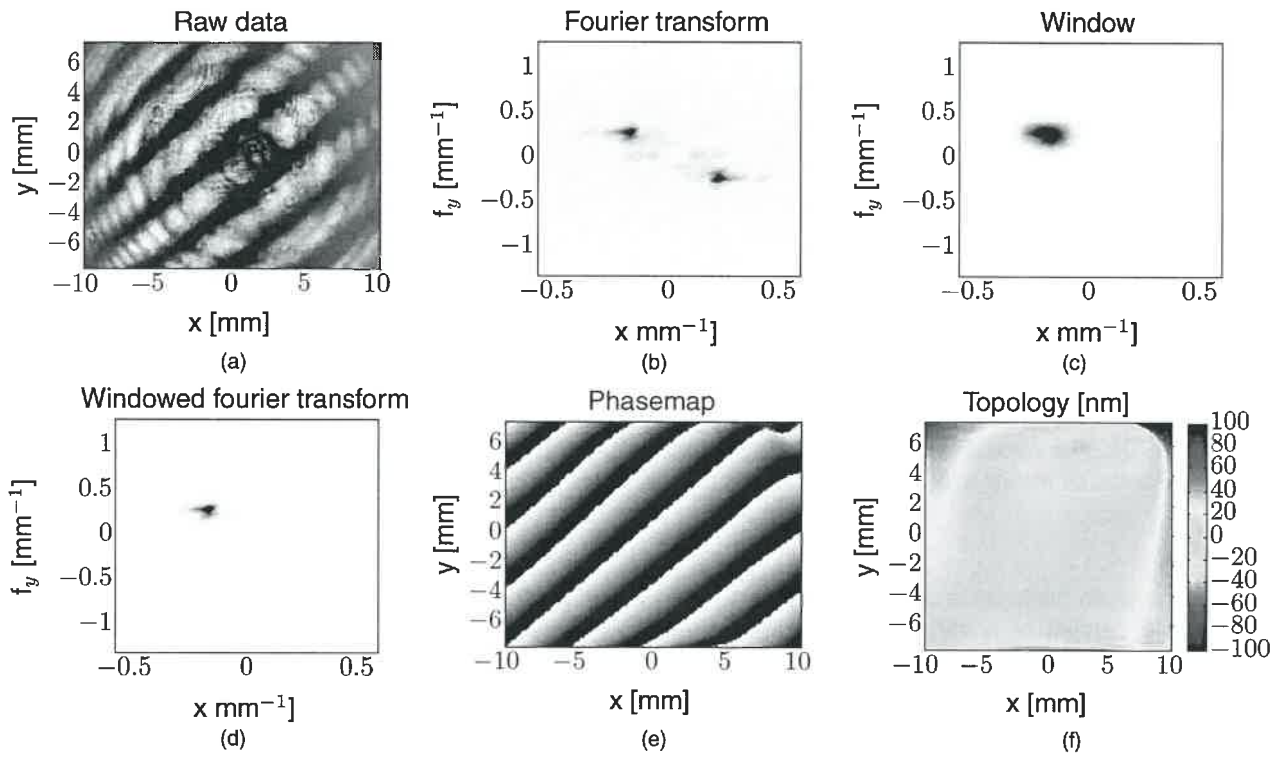

FIGURE 4. The carrier fringe method: The fringes on a 120× 160 pixel CMOS detector (a) are first 2d fourier transformed (b), one of the two dominant peaks in the Fourier transform is windowed (d) with a Hanning window (c) and this data is inverse Fourier transformed. The angle is taken from this inverse Fourier transform, and a phasemap is created (e). This procedure band pass filters the intensity pattern on the CMOS chip and obtains a phasemap that represent the deformation of the deformable mirror. Finally, this phasemap is unwrapped, the tilt and offset are removed and gives the topology of the deformable mirror [2].

sorbing black dot, as shown in Figure 2. The black dot absorbs the radiation from the radiative heat source.

The radiative source is a white light source, which is transmitted from the source with a glass fiber cable, and bundled to expose the black dot on the mirror. The measured output intensity of the white light source is about 200 mW. The absorption of the light in the black dot will cause a local temperature raise leading to a deformation on the mirror surface, due to the thermal expansion of the material. The deformation caused by this local thermal expansion is measured using an interferometer.

The measurement setup consists of an homodyne Michelson interferometer, which is schematically shown in Figure 3 and a picture of the setup is shown in Figure 2(a). The interferometer consists of two mirrors, of which one is the prepared deformable mirror, and a second reference mirror. The interference pattern is shown on a CMOS camera, which has an USB connector to capture the data and process it on a computer, using MATLAB.

A carrier fringe method was used to process the interference pattern measured by the CMOS camera, which principle is shown in Figure 4. One of the mirrors is tilted to get the carrier fringe which moves over the mirror while deforming. The interference pattern is captured ten times per second, and analyzed afterwards.

Because the initial topology of the deformable mirror is not of interest but rather the change from its initial state, the initial topology is removed from each subsequent topology to obtain the change from its initial state. This analysis results in a change of the mirror surface over time.

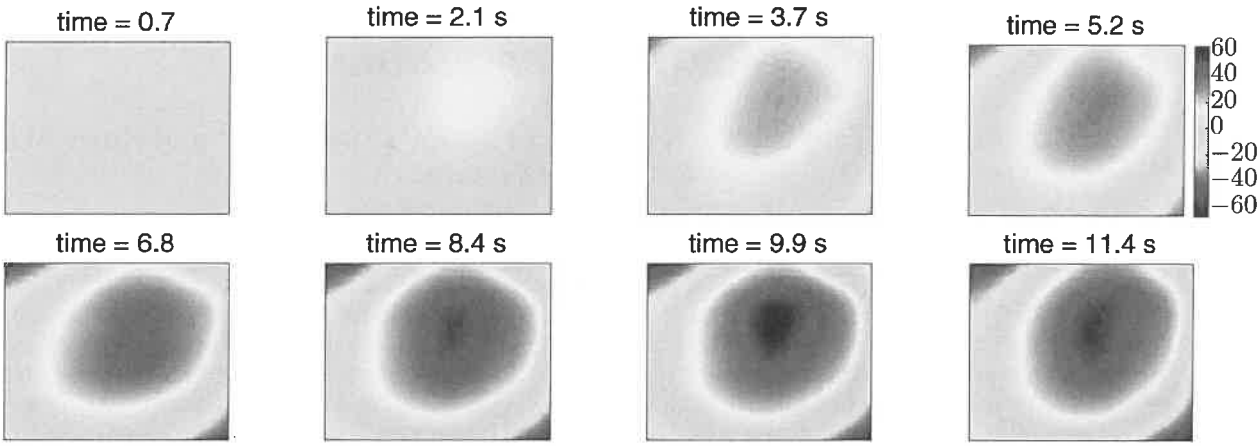

FIGURE 5. The change of shape due to the appliance of the heat for an area of 18× 11 [mm] in eight time steps

RESULTS

Figure 5 shows the change in the surface shape of the mirror over time. A bump with a magnitude of 120 nm is shown on the place of the black dot. Additionally, the deformation is circular, which is the result of the inserted heat on one point. However, the shape of the deformation is not very smooth. First, this is due to an inhomogeneous exposure of the CMOS chip and ghost fringes on the CMOS detector. This causes irregularities in the fringe pattern, which show up in the results. Second, the irregularities may be caused by thermal aberrations in the interferometer.

The time constant of this principle is about 10 seconds. This time constant is low enough to correct for quasi-static aberrations in optical systems [3].

CONCLUSIONS

This paper showed a proof of concept of a contactless deformable mirror actuation concept. This experiment shows a local deformation of 120 nm with a time constant of 10 seconds. A homodyne Michelson interferometer is used to show the deformation. The optical setup suffered from thermal aberrations that took place because of a thermal unstable environment, and convection caused by the heating of the deformable mirror. Improvements of the measurement can be made by testing this principle in a vacuum environment and by using other interferometric techniques like phase stepping or shifting, or by using a wavefront sensor and a closed loop configuration.

The next step in this research is to see what resolutions both in lateral and normal direction on the mirror would be possible, and to apply a bi-layered coating instead of the black dot.

ACKNOWLEDGMENTS

I would like to thank Jonathan D. Ellis for the help with the optical setup and writing this paper and the "Pieken in de Delta" project for funding and support.

REFERENCES

[1] Bach H, Krause D. Low thermal expansion glass ceramics. Springer Verlag; 2005.

[2] Jansen MJ. Development of a wafer geometry measuring system: A double sided stitching interferometer [PhD Dissertation]. Technische Universiteit Eindhoven; 2006.

[3] Hello P, Vinet JY. Numerical model of transient thermal effects in high power optical resonators. J Phys I France. 1993;3:717–732.

"NEXCERA", ZERO THERMAL EXPANSION CERAMICS FOR OPTICAL APPLICATIONS

Jun Sugawara[1], Hiroto Unno[1], Nobumasa Kosugi[1], Yuji Kuma[1] and Kozo Abe[1]
[1]Ceramics Division,
Krosaki Harima Corporation,
Kitakyushu City 806-8586, Japan

INTRODUCTION

NEXCERA, a cordierite ($2MgO\text{-}2Al_2O_3\text{-}5SiO_2$) based polycrystalline ceramic has been developed as a cutting-edge material with both an extremely low thermal expansion coefficient of < 0.03 ppm/K and superior mechanical properties. NEXCERA differs fundamentally from a conventional low thermal expansion glass (LTEG) in consisting of a kind of the crystal and slight amorphous phases along grain boundaries. Accordingly, NEXCERA has high dimensional stability for long-term passage and temperature changes as compared to LTEG [1,2]. Taking advantage of these properties, NEXCERA is used as calibration tools and primary standards in the precision metrology field requiring high accuracy and reliability, in addition to structural components of steppers for LSI lithography [3].

In the previous paper, the advantage of NEXCERA as an optical reflecting mirror was discussed through the manufacture of ultra light-weight boxed structures [4]. The present work has been conducted to evaluate the results of surface finishes for actual mirrors. Special emphasis has been placed on the effect of improving ceramic material on the smooth surface achieved by the polishing.

CERAMICS PROCESSING FOR MIRRORS AND EXPERIMENTAL PROCEDURE

Two kinds of mixed powders of cordierite and sintering additives according to ceramic compositions were ball-milled together with organic binder and water. The slurries thus obtained were dried to granulated powders, and then isostatically pressed into chalk-like blocks. The compressed blocks were machined into desired shapes such as disk-shaped top-plates and ribbed bodies of 401 mm in diameter and 83 mm in height, by making use of a machining center equipped with cutting tools. The machined bodies were once dewaxed at 350 °C in air, and then sintered at 1360 °C in an Ar-gas flow atmosphere. The sintered bodies were ground using diamond wheels, and then some bodies were bounded to form boxed structures of 340 mm in diameter by the diffusion method, as shown in Fig. 1 and the previous paper [4]. After that, the hollow bodies and some specimens were ground, lapped and finally polished to obtain fine finishes for mirror surfaces.

The finished roughness was measured by Zygo New View 7300. The flatness when the mirror was setting vertically was measured by Zygo GPI-XPD 12 inch. The flatness when the mirror was supported horizontally on three points around the perimeter was also measured by Japanese ultimate flatness interferometer developed by national institute of advanced industrial science and technology (AIST), as given in Fig. 2 [5]. To confirm structural properties, finite element method (FEM) calculation was carried out under aforementioned condition.

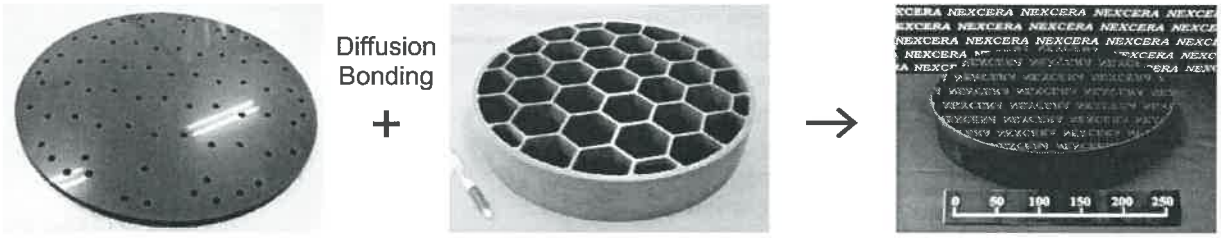

(a) Top-plate (b) Hexagonal rib arranged body (c) Boxed mirror

FIGURE 1. Bonding process of the mirrors. (a) top-plate, (b) hexagonal rib arranged body and (c) boxed mirror.

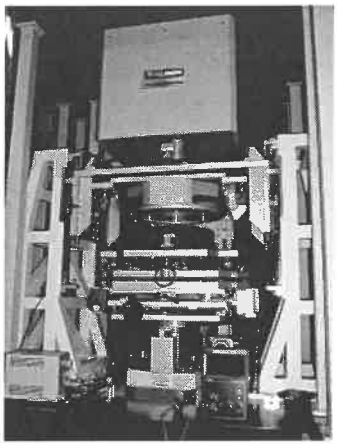

FIGURE 2. Japanese ultimate flatness interferometer developed by AIST [5].

RESULTS AND DISCUSSIONS

The productivity for smooth surfaces of NEXCERA and improved material

Table 1 compares two kinds of low thermal expansion materials such as original NEXCERA and improved material for polishing in terms of various characteristics. There is practically no difference between two materials in mechanical and thermal properties.

TABLE 1. The comparison of characteristics of NEXCERA and improved material

		NEXCERA	Improved Material
Bulk Density	g/cm^3	2.50	2.55
Young's Modulus	GPa	130	140
Poisson's Ratio	-	0.30	0.31
Flexural Strength	MPa	210	230
Fracture Toughness	MPa$^{1/2}$	1.2	1.2
Hardness HV	GPa	8.0	8.1
Thermal Expansion Coefficient	10^{-6}/K (23°C)	< 0.03	< 0.03
Thermal Conductivity	W/m K (23°C)	3.7	4.2
Specific Heat	J/g K	0.83	0.78

The disk specimens of 150 mm in diameter and 30 mm in thickness were polished with diamond slurry and/or ceria slurry to get insights into the productivity for smooth surfaces of two materials. Figure 3 illustrates the surface roughness of two materials, which were polished with diamond slurry and ceria slurry.

For NEXCERA, some dimples of around 100 nm in depth are recognized on the surface therefore, an averaged-roughness (*Ra*) is adversely affected, as given in Fig. 3 (a). For improved

(a) NEXCERA / *Ra* 0.67 nm, PV 132 nm

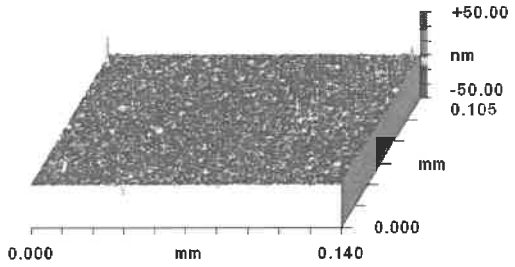

(b) Improved material / *Ra* 0.36 nm, PV 32 nm

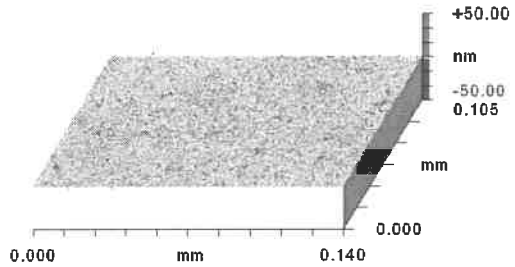

FIGURE 3. The Bird's eye view of surface roughness of (a) NEXCERA and (b) improved material, which were polished with diamond slurry and ceria slurry.

(a) NEXCERA / *Ra* 2.40 nm, PV 261 nm

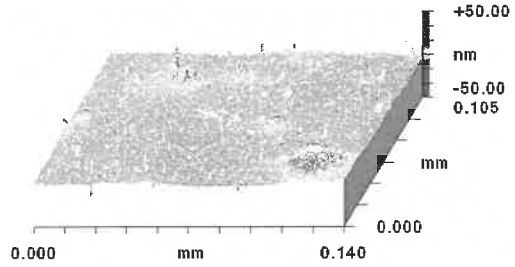

(b) Improved material / *Ra* 0.65 nm, PV 34 nm

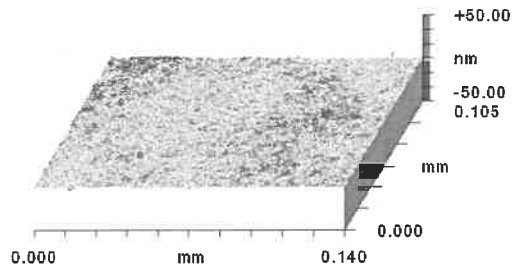

FIGURE 4. The Bird's eye view of surface roughness of (a) NEXCERA and (b) improved material, which were polished with ceria slurry.

material, the mirror surface achieved by the polishing turns to be extremely smooth with *R*a of 0.36 nm, as shown in Fig. 3 (b).
Figure 4 shows the surface roughness of two materials, which were polished with only ceria slurry, being a severe condition which exhibits a high chemical action. The difference of two materials in *R*a is noticeable compared to the polishing with diamond slurry and ceria slurry. It indicates that improved material has a more homogeneous mechanochemical polishing rate from a microstructural point of view, as compared with original NEXCERA. Thus, improved material is thought to be more applicable for a reflecting mirror requiring high accuracy.

Ultra light-weight boxed mirrors

The ultra light-weight mirrors were manufactured using MEXCERA and improved material. Light weight can be attained by making top-plates and ribbed bodies bond together to form boxed structure by means of the diffusion method shown in Fig. 1 and the previous paper [4]. The specifications of the boxed mirrors are shown in table 2. To confirm structural properties, the mirrors with two types of ribbed body such as concentric and hexagonal rib arrangement were fabricated as shown in table 3.

TABLE 2. Specifications of light-weight mirrors.

Diameter	mm	340
Height	mm	70
Rib Thickness	mm	3
Rib Depth	mm	55
Accuracy Diameter Region	mm	300
Thickness on Mirror Side	mm	10 or 7
Weight	kg	5.4, or 4.8
Apparent Density	g/cm^3	0.85, or 0.76

TABLE 3. The details of manufactured mirrors and measurement results of flatness when the mirrors are setting vertically. The letters attached in the table represent as follows; Con.: concentric, Hex.: hexagonal, Nex.: NEXCERA, and Imp.: improved material.

Mirror Number		A	B	C	D
Material		Nex.	Nex.	Nex.	Imp.
Cell Arrangement		Con.	Hex.	Hex.	Hex.
Thickness on Mirror Side	mm	10	10	7	10
Flatness	nm	55	48	94	57

The mirrors with both rib arrangements using NEXCERA and improved material are accurately finished to less than $\lambda/10$, as shown in table 3 and Fig. 5. However, mirror number C is finished to only around 100 nm in flatness yet, due to the thin thickness on mirror side. For all mirrors, no surface irregularity along the rib arrangement is recognized. Thus, the rib arrangements have no effect on flatness of mirrors for the conditions. However, the surface shape is not a uniform convex or concave over the entire surface, and local convex and concave are still found. Therefore, there is still room for improvement in the polishing technique.

(a) A / Flatness 55 nm

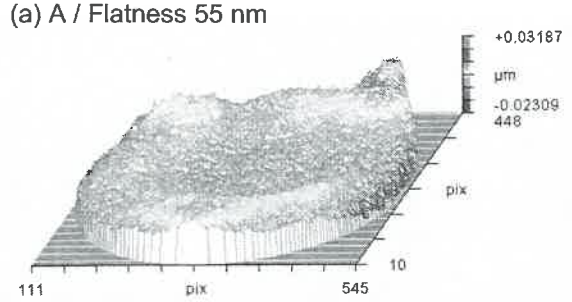

(b) B / Flatness 48 nm

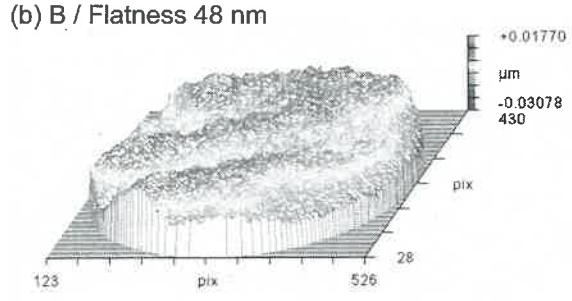

(c) D / Flatness 57 nm

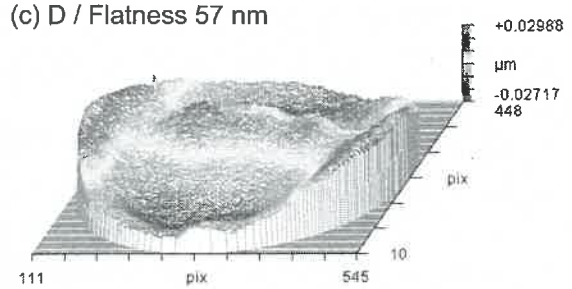

FIGURE 5. The bird's-eye vies of flatness measured by GPI of (a) mirror number A, (b) B and (c) D.

The flatness when the mirrors are supported horizontally on three points of 166 mm in radius is given in Fig. 6. The flatness change shows that the mirror changes its shape with the dead weight. Dead weight deformations of the mirrors

are thought to be from 30 to 40 nm, and independent of rib arrangements, almost corresponding to FEM results shown in previous paper [4].

(a) A / Flatness 36 nm

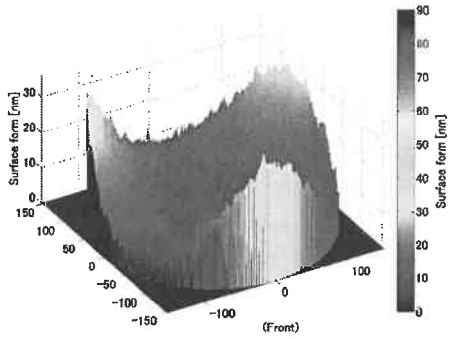

(b) B / Flatness 45 nm

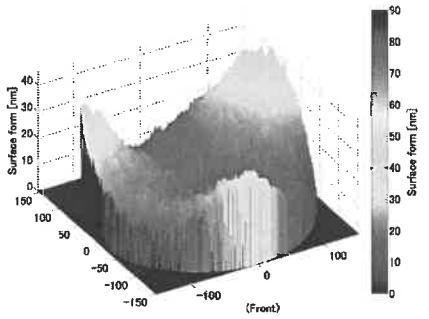

(c) D / Flatness 80 nm

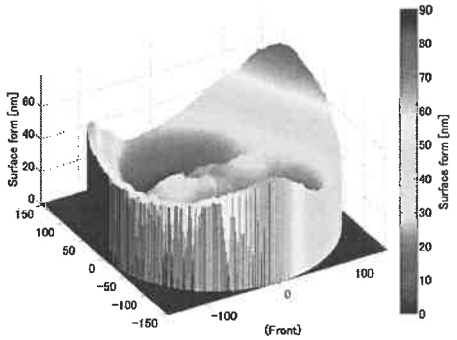

FIGURE 6. The bird's-eye vies of flatness measured by Japanese ultimate flatness interferometer of (a) mirror number A, (b) B and (c) D.

CONCLUSIONS

The fine polishing finishes improved material to an extremely smooth surface with *Ra* of 0.36 nm. The improved material has high productivity for smooth surfaces as compared with original NEXCERA. The light-weight boxed mirrors of 340 mm in diameter can be polished to a precise flatness of less than $\lambda/10$, without adverse effect of rib arrangements and ceramic materials. Dead weight deformations when the mirrors are supported on three points around the perimeter are found to be quite small and approximately corresponding to the results of FEM calculations. As a consequence of this work, it is expected that NEXCERA will be applied to the mirror using in the field of ultra precision metrology and outer space.

REFERENCES

[1] F.Bayer-Helms, H. Darnedde and G. Exner Metrologia. 1985; 21: 49-57.

[2] R. Schodel and Bonsch, Interferometric measurements of thermal expansion, length stability and compressibility of glass ceramics. Proc. of the 3rd euspen International Conference. 2002; 691-694.

[3] J. Sugawara, H. Unno and N. Kosugi, Applications of Low Thermal Expansion Ceramics to Ultra Precision Machine Tool and Precision Metrology Field. HEAT technical committee Open symposium No6 JSAT 2008.

[4] H. Unno, J. Sugawara, N. Kosugi, Y. Kuma, K. Abe and T. Aoki, "NEXCERA", Zero Thermal Expansion Ceramics for Ultra Precision Applications. Proc. of the 10th euspen International Conference. 2010; 1: 160-163.

[5] T. Takatsuji, N. Ueki, K. Hibino, S. Osawa and T. Kurosawa, Japanese Ultimate Flatness Interferometer (FUJI) and its preliminary experiment. Proc. SPIE. 2003; 4401: 83.

MATHEMATICAL MODEL FOR SHEET GLASS IN AIR BEARING

Abdul Mohsen Al Husseini, Mark Schattenburg, and Mireille Akillian

MIT Space Nanotechnology Lab
Massachusetts Institute of Technology
Cambridge, MA, USA

INTRODUCTION

Flat glass sheets with high surface quality are in demand for technologies such as flat panel displays and x-ray telescope optics. Commercially available glass sheets of <1 mm thickness typically have a surface waviness on the order of hundreds of microns, rendering it a challenge to utilize progressively thinner sheets. A method of thermally shaping individual sheets of glass using porous mandrels as air bearings (Figure 1) was demonstrated by Akilian and Schattenburg to reduce surface waviness to a few microns [1]. The air bearing is designed to constrain the glass during the cooling cycle of the furnace, thus "freezing in" the desired shape.

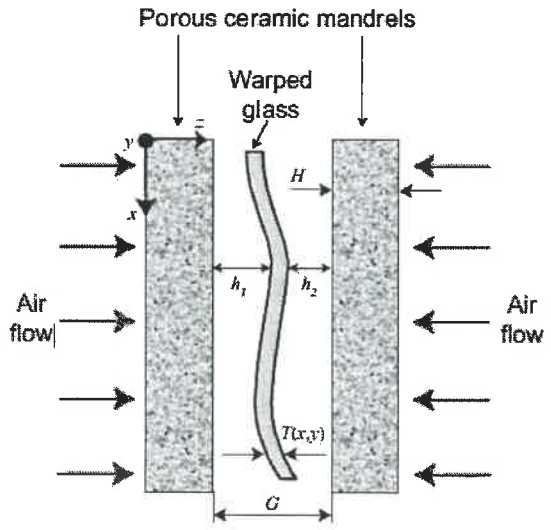

FIGURE 1. Thin glass sheet placed between two ceramic bearings, with air flowing through mandrels and against the sheet to change its surface topography. Assembly apparatus not shown.

A detailed mathematical model of the process has been developed, allowing prediction of final surface quality based on process parameters including air pressure, imperfections on the mandrel surface, glass thickness variations and orientation of the gravity vector during the process.

Improvements over earlier surface quality results are reported through achieving feedback control of process pressure and minimizing the pressure difference between opposing mandrels. Closed-loop control also allowed verification of the developed mathematical model, and experimental testing was conducted to optimize process parameters for future iterations of the slumping process.

MATHEMATICAL MODEL

An earlier mathematical model [2] identified the equations governing the flow in porous mandrel and into the gap between the mandrel and the glass sheet. The model successfully predicted mandrel surface pressure distribution based on supply pressure, with the assumption of a constant gap.

The equations were generalized to allow for spatially variable gaps *h(x,y)*, yielding:

$$\nabla^2 p' = 0$$

$$\nabla \cdot (h^3 \nabla p) = 12 k_z \left. \frac{\partial p}{\partial z} \right|_{z=H'}$$

Where *p(x,y)* is the pressure in the gap of size *h(x,y)* between the glass and porous mandrel, and *p'(x,y,z)* is the pressure in the porous mandrel of thickness *H*. These equations are derived from Darcy's equation of creeping flow in porous media with Reynold's number *Re<1*, the continuity equation, and a modified Reynold's equation. Identical equations can be applied to the other side of the mandrel with different pressure and gap variables.

A MATLAB script was then written to predict the final glass shape, according to the flowchart depicted in Figure 2. The inputs are: glass thickness profile *t(x,y)*, initial shape *s(x,y)*, sheet

density and angle of tilt (θ) with respect to the gravity vector.
At each iteration step, gap information is used to calculate the surface force (pressure) profiles on either side of the glass sheet using a finite difference scheme. The total force on the glass sheet is then used to compute the new positions of individual sheet elements. Convergence occurs when the script yields zero net force on all elements.

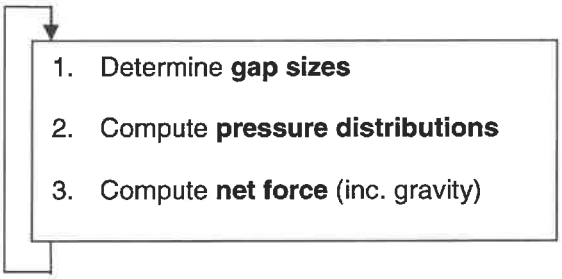

FIGURE 2. Flowchart of MATLAB script. At each iteration, pressure distributions and net forces and calculated based on gap sizes. A new position profile is computed, and the process is repeated until convergence.

The simulation was performed on square sheets of Schott D-263 borosilicate glass, which has a density of 2.51 g/cm^3. The sheets were 400 microns thick and with an area of 100 cm^2.

The effect of apparatus tilt on the shape profile was investigated. Figure 3 depicts the peak-to-valley results for different angles, at a supply pressure of 0.3 *psi.*

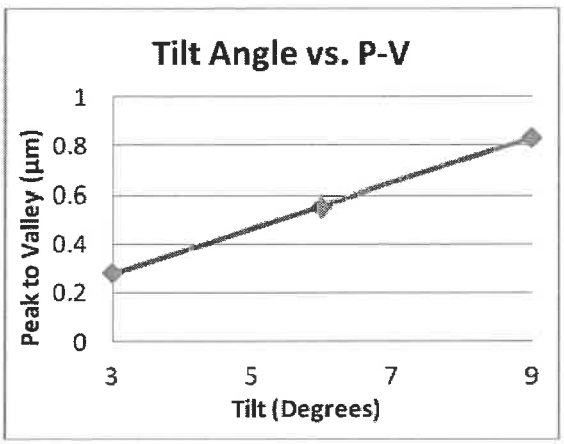

FIGURE 3. Plot showing the effect of apparatus tilt on the surface topology of flat glass over an area of 80x80 mm.

These results from a 80x80 mm subset of the100x100 mm domain to eliminate the artifacts caused by the boundary conditions. Zernike polynomial coefficients were obtained for the domain to characterize the topology. As can be seen for Figure 4, the dominant mode was the defocus term from the Z^0_2 Zernike function. Other coefficients were several orders of magnitude lower, suggesting that gravity affects the glass sheet in an axially-symmetric manner.

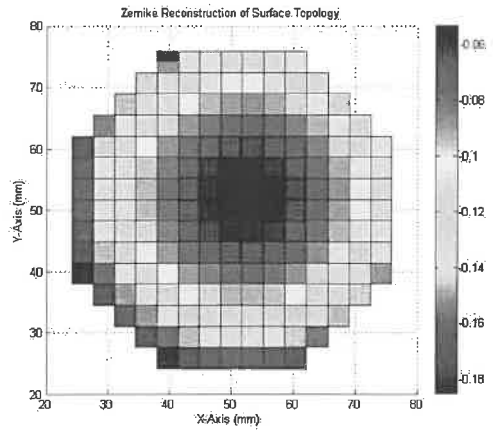

FIGURE 4. Plot of the surface topology Zernike reconstruction. Z-axis is in microns.

Due to the 1 atm pressure boundary conditions at the mandrel's perimeter, gravity is the only force acting near the edges. To avoid erroneous iterations, a mapping from pressure nodes to sheet elements (back and forth) was conducted before calculating total force and new sheet element positions.

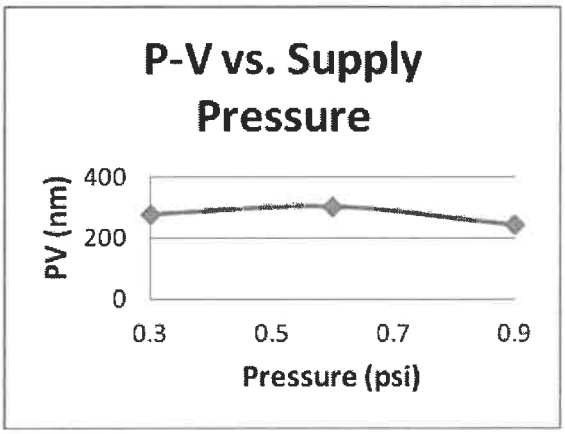

FIGURE 5. Plot showing the effect of changing the supply pressure at a constant angle (3 degrees)

According to the simulation results in Figure 5, varying the supply pressure had little effect on the bow sheets experienced due to gravity. In fact, the variations were within 60 nm; equal to the computational precision of this model and hence can be considered equal.
Additional simulations revealed that different supply pressures on either side would simply displace the sheet to a new plane and not induce bow.
Therefore, we conclude that the most sensitive parameter to control in future slumping apparatus design is the mandrel tilt.

MODEL VERIFICATION

Figure 6 shows the assembled ceramic plates inside the furnace. Two independent pressure lines are introduced into the furnace in the form of 4 m-long bent tubes connected to each housing. A stagnant line is taken from each plenum to the outside, and connected to high precision pressure transducers to monitor the pressure inside each plenum during the slumping process.

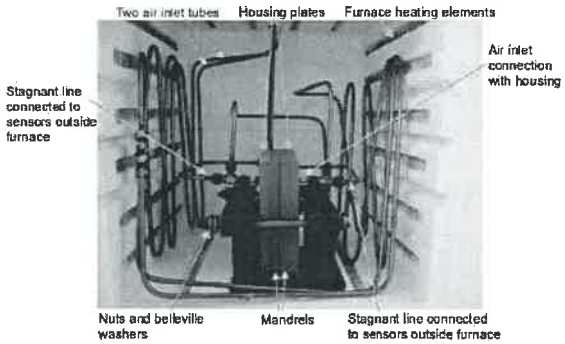

FIGURE 6. Photograph of sheet glass (not shown) held between two flat mandrels inside a furnace of dimensions 11"x15"x13"

Although both tubes were bent identically and placed close to each other inside to ensure heating at the same rate and minimize of pressure fluctuations in the lines, different pressures are observed for each plenum at varying temperatures. Having equal pressures is essential to ensure repeatability of slumping results.

The process was previously controlled with manual flow control valves at the beginning of the experiment, and periodically adjusted as necessary during the slumping process. This however was a major source of repeatability error since the tool's flow control valves have a course resolution, making it difficult for the user to open them the exact same amount every time an experiment was conducted.

Closed-loop control of the pressure-loop was established using LabVIEW, with the setup depicted in Figure 7.

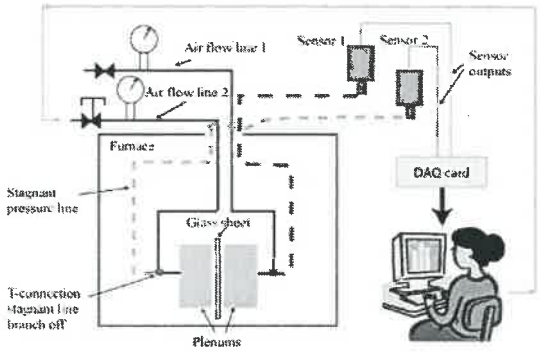

FIGURE 7. Data Acquisition Setup

Previously, the overall surface difference between runs varied by 1.6 μm p-v and 0.35 μm rms. During the writing of this document, the first closed loop experiments were being conducted to verify the mathematical model.

REFERENCES

[1] M. Akilian and M.L. Schattenburg. "Reducing the warp of sheet glass," J. Soc. Information Display 18, #3, 240-248 (2010).
[2] M. Akilian. Methods of Improving the Surface Flatness of Thin Glass Sheets and Silicon Wafers, Ph.D. thesis, Massachusetts Institute of Technology, Department of Mechanical Engineering, 2008

DESIGN PRINCIPLES AND PRACTICES FOR RAPID PROTOTYPING OF MESO- AND MICRO-SCALE FLEXURES VIA MICROMILLING

Joshua B. Gafford, Robert M. Panas, Michael A. Cullinan and Martin L. Culpepper
Department of Mechanical Engineering
Massachusetts Institute of Technology
Cambridge, MA, United States

ABSTRACT
The purpose of this research is to generate the knowledge required to prototype high-quality mesoscale flexural devices via micromilling. Several HexFlex microflexural devices were successfully micromilled from various aluminum alloys. Total machining time, including setup and tool changes, was around 1.5 hours per part. The integrity of each part was verified using optical microscopy and white-light interferometry to validate the process. Ultimately, it was shown that micromilling is a feasible process for rapid, low-volume manufacturing of mesoscale nano-positioners (±3 μm within specified dimensions) with surface roughnesses of less than 300 nm.

INTRODUCTION
Micromilling is the ideal manufacturing technique for quick, inexpensive prototyping (~hour/part, $10-$100/part) of meso- and micro-scale flexural devices because it offers the process and material flexibility that is absent from conventional microfabrication techniques. Micromilling will make it possible to expand the material catalog for MEMS devices in a low-volume environment and enable designers to manufacture larger and more robust structures.

BACKGROUND
Mesoscale nanopositioners offer the potential for high bandwidth (kHz-scale) operation due to their small scale while remaining large enough for feasibly locating a payload on the stage. The cost of these cm scale devices is often driven by the cost of sensing. External sensors such as capacitive probes and laser interferometers [1] are commonly used in nanopositioners. These sensors, however, generally cost on the order of $10k/axis [2]. Integrated capacitive or piezoresistive sensing offer the possibility of significantly reducing sensing costs to roughly $50/axis. Integrated sensing requires μm/nm-scale features on a mesoscale nanopositioner.
A fabrication method is needed that is capable of producing: i) cm-scale mechanical parts, with ii) um/nm-scale electrical features, and iii) with the structure made from materials that are robust. No established process chain is able to meet these requirements at a low cost. Macroscale machining can produce cm-scale parts from robust materials at low cost, but cannot produce μm/nm-scale features. Integrated circuit (IC) photolithographic fabrication has been used to produce mesoscale nanopositioners, but it results in high prototyping costs and brittle structures. Prototyping alone can cost $10's of thousands [3] and require months to a year to complete. Non-photolithographic (NPL) microfabrication methods offer the potential to meet all of the conditions at low cost.

Several types of operations are required to fabricate a mesoscale electromechanical system including bulk and surface micromachining. Micromilling is studied here as a method for the desired NPL bulk micromachining. Micromilling is a commonly used NPL method for fabricating micron scale features into structures with cm-scale dimensions [4]. The main focus of micromilling research has been the fabrication of micromolds and other microtools [4]. This paper explores the potential use of micromilling in making mesoscale mechanically active structures such as flexures.

MICROMILLING FLEXURES
A case study is presented in which several HexFlex mesoscale nanopositioning devices, developed by MIT's Precision Compliant Systems Laboratory (PCSL), are micromilled. HexFlex is ~4 cm in diameter with flexure elements that are as small as 200 μm in thickness, 200 μm in width and several mm in length.

Setup & Machining
The HexFlex devices were cut using Microlution 363-S 3-axis horizontal micro-milling machine. Two aluminum alloys were used: Al 6061-T6 sheet stock and Al 1100 shim stock. Pictures of the machined HexFlexes are shown in Figure 1.

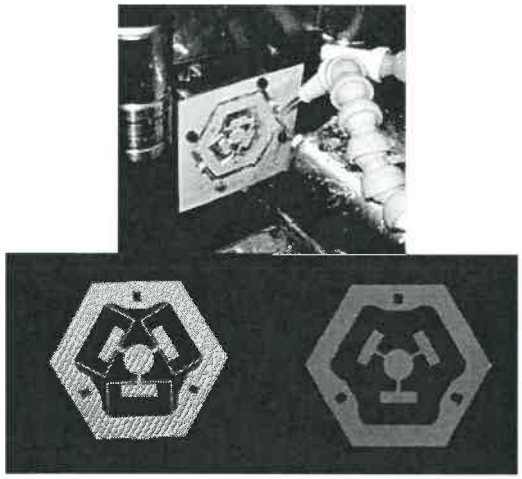

FIGURE 1. (clockwise from top) Al 1100 HexFlex being machined in the micromill, Al 1100 HexFlex, Al 6061-T6 HexFlex

Unlike conventional end-mills, there is no vice to quickly secure parts and no edge-finding/zeroing process to specify a zero with respect to a desired datum surface on the workpiece. For this research, a sacrificial fixture was developed specifically for HexFlex fabrication that screws onto the micromill pallet via four 10-32 socket-head cap screws. The fixture is machined out of 6061-T6 Aluminum and has four 4-40 threaded holes lining the periphery that secure the piece of raw stock to the fixture. Double-sided adhesive is placed in between the stock and the sacrificial fixture to provide viscous damping. FEA simulations determined that the HexFlex's first 3 modes of vibration are around 400 Hz. As micromilling necessitates spindle speeds between 10,000 RPM and 50,000 RPM (166 Hz – 833 Hz), unrestrained vibration is a potential concern. The adhesive also serves to minimize large-scale deflection of the thin (200 μm) flexural blades against normal cutting forces. The separate components and the entire pallet-fixture-stock assembly are shown in Figure 2.

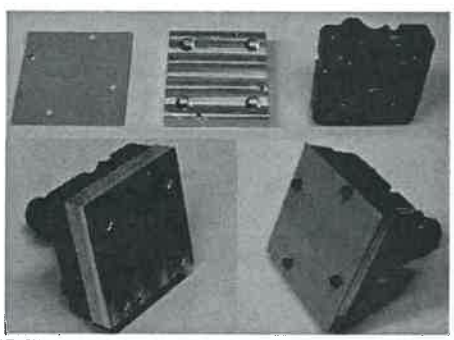

FIGURE 2. Hardware setup for micromilling HexFlex nanopositioners

Toolpaths were generated and post-processed using HSMWorks, a CAM package developed by Dassault systems. The process consists of five steps: (1) cutting to depth (thickness of stock minus desired part thickness) and roughing out the hexagonal shape, (2) roughing out the interior pockets, (3&4) finishing the interior contours, and (5) finishing the hexagonal contour and separating the finished part from the uncut stock. The post-processed G-code was uploaded into the Microlution control panel using the process parameters summarized in Table 1.

TABLE 1. Process parameters for HexFlex machining

Step	1	2	3&4	5
Toolpiece Diameter [mm]	3.175	1.016	0.381	3.175
Spindle Speed [RPM]	17,000	36,000	50,000	17,000
Cutting Feed [mm/min]	254	229	127	254
Axial DOC [mm]	0.30	0.15	0.06	0.30
Final Depth [mm]	-0.553	-0.953	-0.953	-0.953
Machining Time [min:sec]	13:55	16:58	28:12	3:16

Theory

For the purpose of this research, the cutting force F_C was approximated to be a function of chip load f_t, axial depth of cut b_{axial} and a "material coefficient" K_m that is an empirically-determined value. Dimensional analysis shows the relationship to be as follows:

$$F_c = f\left(K_m\left[\frac{N}{\text{mm}^2}\right], b_{axial}, [\text{mm}], f_t[\text{mm}]\right) \quad (1)$$

$$\Pi_1 = \text{Constant} = \frac{F_c}{K_m \cdot b_{axial} \cdot f_t} \quad (2)$$

$$\therefore F_c = \text{Constant} \cdot K_m \cdot f_t \cdot b_{axial} \quad (3)$$

The material coeffiecient K_m is both material and process dependent. The constant is a by-product of dimensional analysis and may be used to roughly scale the cutting forces to other materials. Ziegert et al. performed several tests to estimate K_m for Aluminum 6061 using Bao and Tansel's analytical cutting force model [6,7]. By power-fitting data obtained from Ziegert's results to solve for K_m as a function of f_t*b_{axial}, the cutting forces that a tool experiences during nominal operating conditions may be quickly approximated by inputting f_t and b_{axial} specific to the process. A review of literature found that the cutting force estimation in Equation 3 may be scaled to other aluminum alloys roughly by the ratio of the shear strength of the workpiece to

that of Aluminum 6061. This is somewhat intuitive, as the primary mode of resistance against the cutting tool during operation is the shear resistance of the workpiece over the primary shear plane where chip formation is generated. Equation 3 may be modified:

$$F_c \approx \left(\frac{\tau_y^{workpiece}}{\tau_y^{6061}} \right) 50.47 \cdot (f_t \cdot b_{axial})^{.445} \quad (4)$$

Equation 4 is simplified in nature when compared to more complex micromilling cutting models [6,8,9], but the intent was to create a quick way of estimating relevant cutting forces in order to provide a rational foundation for the selection of machining parameters. Equation 4 was used to approximate the stress tensor $\bar{\sigma}$ (consisting of shear stresses from the normal and feed forces, torsional shear due to feed forces on the tool cutting edge and normal stress from the feed force) within the toolpiece during nominal cutting conditions:

$$\bar{\sigma} = \begin{bmatrix} 0 & \tau_{torsion} & \tau_{nshear} \\ \tau_{torsion} & 0 & \tau_{fshear} \\ \tau_{nshear} & \tau_{fshear} & \sigma_{bend} \end{bmatrix} \quad (5)$$

Stress invariants were used to back out the principle stresses in the toolpiece, and Mohr's brittle failure criterion was applied to calculate process factors-of-safety (instantaneous and fatigue-driven). Cutting parameters (depth of cut, spindle speed, and feed rate) from Table 1 were then selected based on acceptable factors-of-safety that ensured optimum tool life.

Results and Observations

The machined HexFlexes were inspected using optical microscopy and white-light interferometry to quantify dimensional precision and the extent of burr formation for facing operations.

Dimensional Precision

In order to quantify the precision with which the micromill machined the thin flexural blades, microscopic images of the HexFlex devices were taken and analyzed in LabView. Blade thickness was measured at ten unique locations, and uncertainty was calculated with 95% confidence using statistical methods. The specified thickness of the thin blades is 200 µm, and the measured mean thickness of the blades on the machined HexFlex is 197±4.62 µm. The Microlution mill spec sheet claims a positional accuracy of ±2 µm, which is less than the deviation observed empirically. The undershot blade thickness is an encouraging result, as it means that the end mill wasn't disengaging during finishing contour passes as a result of blade deflection or vibration. Figure 3 shows a graphical representation of measured vs. ideal blade thickness (within 95% confidence).

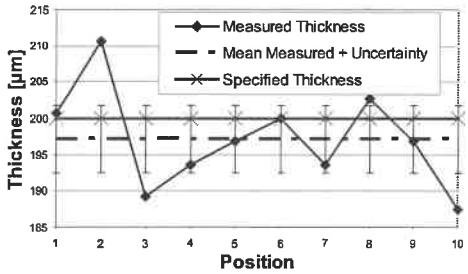

FIGURE 3. Run chart of measured blade thickness. Sample size = 10, Mean = 197 µm, St. Dev. = 6.46 µm, Uncertainty = ± 4.62 µm.

Surface Roughness

The surface roughness was averaged at ten unique locations on four Al 6061-T6 HexFlex devices milled with different machining parameters to obtain an overall average surface roughness for each HexFlex. Uncertainties were calculated using statistical methods. Empirical measurements were correlated with the polynomial surface roughness dependence devised by Lee and Dornfield [10].

$$R_a = 43.6 + 439 f_t + 46.3 f_t^2 + 1256 v_c - 990 f_t v_c \quad (6)$$

Figure 4 shows a comparison of the interferometer measurements with the theoretical polynomial surface roughness fit given in Equation 6 based on chip load. The data points represented are for the 3.175 mm end-mill (Spindle speed = 17,000 RPM) with varying feed rates (254 mm/min, 203 mm/min, and 152 mm/min). A relatively sufficient agreement exists between theoretical values and measured values (from an order of magnitude standpoint).

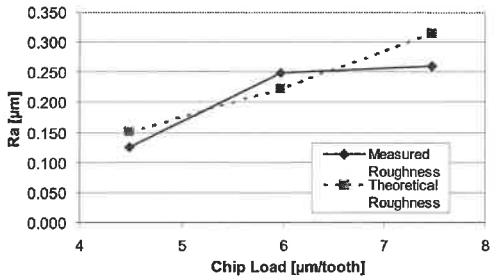

FIGURE 4. Measured surface roughness vs. theoretical surface roughness for Al 6061-T6 HexFlex devices

The best surface finish was 0.125 ± 0.041 µm, achieved with the 3.175 mm endmill at a cutting feed rate of 152 mm/min. It is worth noting that this surface finish is superior to that of uncut stock (which was found to be 0.212 ± 0.019 µm). An observable trend is that as chip load decreases, surface finish becomes more uniform across the entire part (most likely a result of reduced chatter/vibrations induced by decreased cutting forces).

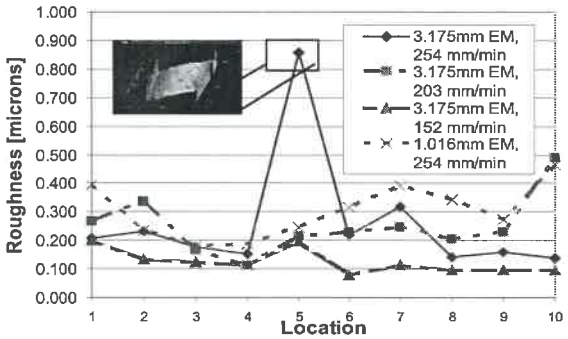

FIGURE 5. Measured surface roughness data for four Al 6061-T6 Hexflex devices

Surprisingly, the worst surface finish was achieved with the 1.016 mm end mill (spindle speed = 38,000) at a feed rate of 254 mm/min. This process had the lightest chip load and slowest surface speed of all the tests, so the expectation was that it would achieve the best finish. According to Equation 6, the theoretical surface finish is 0.110 µm, but actual measurements yielded an average surface finish of 0.303 ± 0.068 µm (approximately 175% error). The significant discrepancy may be a result of unfavorable stochastic process alterations (such as adhesive delamination, tool runout, or workpiece vibration).

CONCLUSION AND FUTURE WORK

It has been demonstrated herein, both through theory and practice, that micromilling is a feasible alternative to traditional microfabrication methods for designers seeking to rapidly prototype high-quality and to-spec mesoscale nanopositioners in a low-volume environment. Post-machining observations and analyses showed micromilled HexFlex devices to be within ±3 µm of specified dimensions, giving an indication of what a designer should expect to achieve as far as assigning tolerances. Additionally, the surface roughness was found to be less than 300 nm in the general case, and as low as 125 nm in the optimum case (superior to that of uncut stock).

In the future, more parametric tests could be performed to determine the absolute optimum machining parameters for micromilling flexures that will minimize machining time and maximize the quality of the product.

REFERENCES

[1] Kim, W., Verma, S. Shakir, H., "Design and precision construction of novel magnetic-levitation-based multi-axis nanoscale positioning systems, *Precision Engineering*, 2007, Vol. 31, pp. 337-350.

[2] Slocum, A.H., "Precision Machine Design," Eaglewood Cliffs, NJ: Prentice-Hall, Inc., 1992.

[3] Tadigadapa, S.A.; Najafi, N., "Developments in microelectromechanical systems (MEMS): A manufacturing perspective," Journal of Manufacturing Science and Engineering, Transactions of the ASME, 2003, v 125, p 816-23.

[4] Huo, D., Cheng, K., Wardle, F., "Design of a five-axis ultra-precision micro-milling machine—UltraMill. Part 1: holistic design approach, design considerations and specifications," The International Journal of Advanced Manufacturing Technology, v 47, n 9-12, p 867-77, Apr 2010.

[5] Ko, J.H., Heisel, U., "Mechanistic Cutting Force Model for Micro Ball-end milling." Proceedings of the 2nd International Conference on Micromanufacturing 2007 September 10-13, 2007 Greenville, SC.

[6] Bao, W.Y., Tansel, I.N., "Modeling Micro-End-Milling Operations, Part I: Analytical Cutting Force Model." International Journal of Machine Tools & Manufacture, 2000, Vol. 40. pp 2155-2173

[7] Ziegert, J. and Pathak, J., "An Ultra-High Speed Spindle for Micro-Milling."

[8] Perez, H., Vizan, A., Hernandez, J.C., Guzman, M., "Estimation of Cutting Forces in Micromilling through the Determination of Specific Cutting Pressures." Journal of Materials Processing Technology, Vol. 190. pp. 18-22

[9] Bissacco, G., Hansen, H.N. and Slunsky, J. "Modeling the cutting edge radius size effect for force prediction in micro milling" CIRP Annals - Manufacturing Technology Volume 57, Issue 1, 2008, Pages 113-116

[10] Lee, K. and Dornfeld, D.A. "Micro-burr formation and minimization through process control." *Precision Engineering*, 2005, Vol. 29. pp. 246-252

INTEGRATED PRESCAN OPTICS FOR LASER PRINTERS

Kenneth P. Garrard and Alex Sohn
Precision Engineering Center
North Carolina State University
Raleigh, North Carolina, USA

INTRODUCTION

In the manufacture of laser print engines, one of the costliest and most challenging subsystems are the prescan optics. This group of components illustrated in Figure 1 conditions the laser beam from the exit aperture of a small diode laser and allows it to be directed to the surface of the paper and focused to a spot size as small as 10 µm. Typically, the prescan optics consists of the laser diode, a collimating lens to bring the laser beam as close as possible to collimated and a cylindrical lens to remove the astigmatism from the nearly collimated beam. The optics and their alignment add a significant cost to the final product, so the goal is to simplify the design and use materials that are less expensive to procure and manufacture.

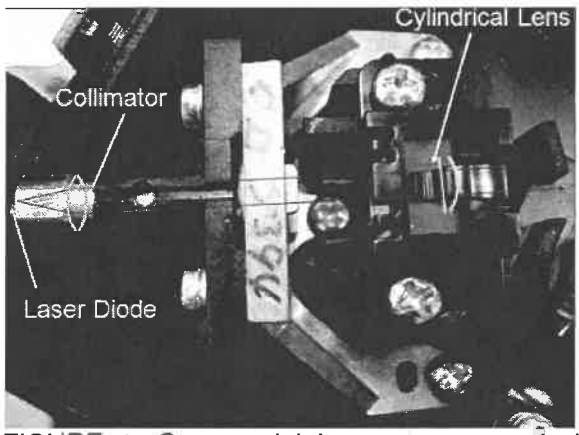

FIGURE 1. Commercial laser prescan optical system.

A reflective optical system for a laser prescan unit has been proposed and designed. This optical system can be machined from a single piece eliminating the need to assemble and align the two mirrors. However the optical surfaces in their final orientation are not rotationally symmetric about any axis. Matlab™ software for generating the tool path data needed to machine a prototype of this optical system using a fast tool servo has been developed. The optical system was machined on an ASG 2500 Diamond Turning Machine augmented with a fast, long-range tool servo (FLORA II) driven by a PMDi controller [1].

OPTICAL SYSTEM DESIGN

Figure 2 shows the conventional system of Figure 1 in a schematic form. The collimating lens and the cylindrical lens are commonly made of optical glass and must be ground and polished. Cheaper polymer lenses cannot be used due to the change in refractive index in the material with temperature. The printer must operate in an environment with a wide temperature range.

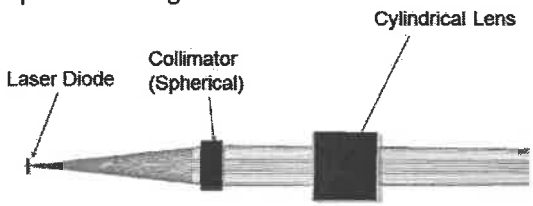

FIGURE 2. Commercial laser prescan optical system.

If the lenses shown in Figure 2 are replaced with reflective optics, the refractive index of the material becomes irrelevant. Thus, molding polymer reflectors becomes a distinct possibility. One possible layout for such a design using reflective optics is shown in Figure 3.

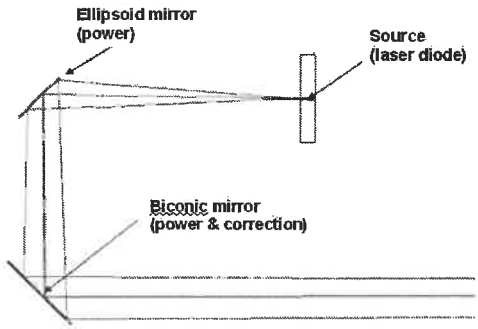

FIGURE 3. Two mirror reflective design.

The primary mirror is an ellipsoid and it removes most of the divergence from the beam while the secondary mirror removes whatever divergence remains as well as the aberrations due to laser diode astigmatism and the off-axis placement of

the primary mirror. Thus, the secondary mirror is biconic.

As a prototype, both mirrors were machined into the end of a small cylinder using the FLORA II fast too servo. As shown in Figure 4, the mirrors have a substantially larger radius than the radius of rotation and appear as two flat regions in a conical parent surface. The cross section in Figure 4 shows the spacing of the mirrors and the laser source.

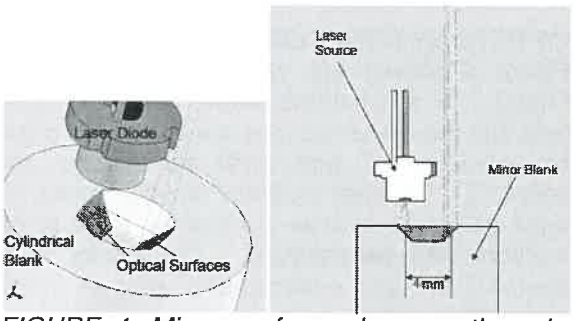

FIGURE 4. Mirror surfaces, beam path and a cross section of the system.

FABRICATION

Both optical surfaces can be machined in a single setup on a metal substrate, guaranteeing the alignment of the two mirrors. The volume of material to be removed is quite small and the prototype can be fabricated without rough machining a spherical pocket or slot prior to performing the final machining operation. Machining time will be on the order of a few minutes. The diamond tool must be selected to reach into the pocket and machine the non-rotationally surface without touching the clearance face of the tool.

Geometric Analysis

Each mirror can be defined as a general biconic in Cartesian coordinates as,

$$Z(x,y)=\frac{c_{XZ}\cdot(y-y_0)^2+c_{YZ}\cdot(y-y_0)^2}{1+\sqrt{1-(1+k_{XZ})\cdot(x-x_0)^2\cdot c_{XZ}^2-(1+k_{YZ})\cdot(y-y_0)^2\cdot c_{YZ}^2}}$$

where the origin is (x0,y0,0), c_{XZ} is the curvature in the XZ plane, c_{YZ} is the curvature in the YZ plane and k_{XZ} and k_{YZ} are the conic constants in the two orthogonal planes. The prototype design parameters are given in Table 1 and the apertures and their orientation with respect to each other are defined in Table 2.

TABLE 1. Prescan mirror surface parameters.

	Plane	Curvature	*k*
M1	XZ	1/30	1
	YZ	1/30	1
M2	XZ	1/13.905686	-2.396222
	YZ	1/34.682089	-60.00092

TABLE 2. Prescan mirror aperture definitions.

	Aperture radius	Aperture center	Translation x, y, z	Tilt x, y, z
M1	0.573	0,0	0,+2,0	+π/4,0,0
M2	0.917	0,0	0,-2,0	-π/4,0,0

Both mirrors are on-axis (i.e., no decenter) and M1 is an oblate ellipsoid of revolution while M2 is a non-rotationally symmetric surface of two very different hyperboloids. These two sufaces are shown in Figure 5. They have been translated to the correct separation but not tilted. Figure 6 shows M1 and M2 after tilting the mirrors. The chief ray is at the center of each aperture is shown as a dotted line. The mirrors appear as flat disks since their curvature is large compared to the radius of their separation. The two circles define the aperture of the mirror system.

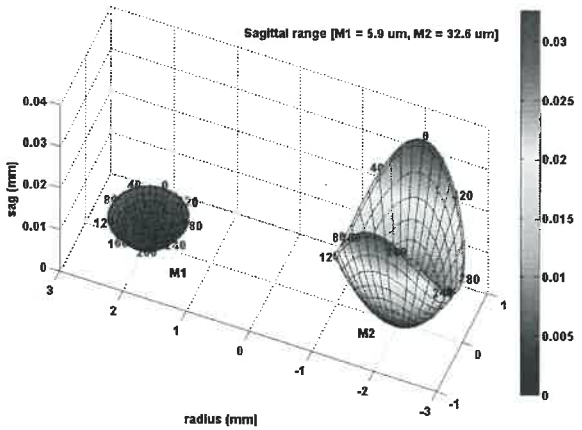

FIGURE 5. M1 and M2 surfaces.

Tool Path Generation

The ASG 2500 diamond turning machine can be programmed to produce an asphere while the FTS moves the tool in the sagittal direction as a function of the spindle rotation angle and the cross-feed axis position. The FTS motion plus the underlying asphere form the desired mirror surfaces. The mirror curvatures are much smaller than that of the best-fit asphere (i.e., they are "flatter" than the asphere), thus the

shape of the FTS motion within the mirror apertures will be convex.

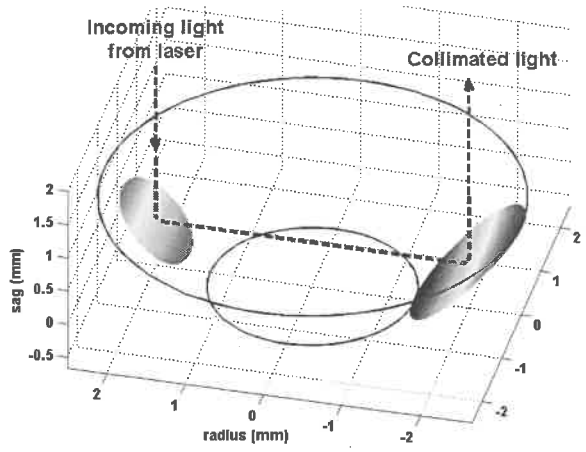

FIGURE 6. Laser prescan optical system.

Surface finish and form fidelity are likely to be improved if the range of FTS excursion is minimized. Compensation must also be made for the radius of the tool. This compensation is done along meridians from the axis of rotation to the edge of the workpiece. An asphere is then subtracted from the result to form a 2D lookup table of FTS positions as a function of radial angular position. A part program for the DTM is created to machine the aspheric shape. A Matlab script has been written to perform these calculations and generate a lookup table for the FLORA II controller as well as the aspheric motion program. The design file needed by the *Polaris 3D* spherical profilometer [2] to measure the resulting part is also output. The steps in this algorithm are as follows.

1. Generate a circular aperture grid for each mirror, M1 and M2.
2. Calculate z positions for each (x,y) point within the apertures.
3. Translate and rotate the mirror surface data sets to their positions in the optical system.
4. Create a cylindrical coordinate grid for the optical system whose center is on the axis of rotation of the DTM spindle.
5. Find all data points on the cylindrical grid in the tilted elliptical apertures of M1 and M2.
6. Interpolate mirror surface data to the cylindrical coordinate aperture grid.
7. Extend the aperture masks to equal radii and uniform angles.
8. Perform tool radius compensation along each meridian in each aperture.
9. Interpolate compensated points onto a common radial grid.
10. Find the mid-range sagittal value at each radius.
11. Fit a radial polynomial to the mid-range data. This is the asphere machined by the DTM.
12. Form a table of residuals. This is the FTS excursion.
13. Output a design file for the Polaris3D spherical measuring machine.

The tilted apertures for M1 and M2 in the cylindrical coordinates of the optical system are ellipses. But the FTS control system requires a matrix of data to describe the motion of the tool. Each row contains height data at a radius and each column is at an angle. The rows and columns need not be equally spaced, but the matrix must be plaid; that is, all rows (radii) have a data point for each column (angle). Thus Step (7) extends the elliptical apertures to angular segments.

The origin of the cylindrical coordinate system is (θ=0, r=0); however this is not necessarily the optimal location for the axis of rotation. The (x, y) center of a least squares asphere fit to the system data for the prescan optics has an origin 17 µm from (0,0). In this case, the FTS excursion is reduced by only a few micrometers by including this additional translation of the mirrors. To reduce the complexity of the system analysis and machining setup, the origin was fixed at (0,0). In Step (11), the best fit asphere was found to be very close to conical for this optical system.

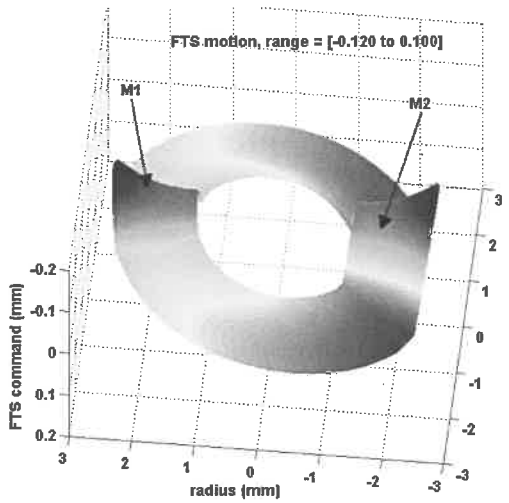

FIGURE 7. FTS component of tool path.

Subtracting the best fit asphere from the radius compensated tool positions gives a table of FTS positions for machining the optical system. These positions are on a fine cylindrical grid with a maximum spacing of 16 µm between grid points. Figure 7 shows the complete FTS tool path within the radial aperture of the mirrors. The tool positions are extended 10° to either side of each aperture so that the FTS doesn't abruptly change direction at the edge of the desired clear aperture. The space between the mirrors in the azimuthal direction is a linearly interpolated surface that is added to the asphere swept out by the DTM axes.

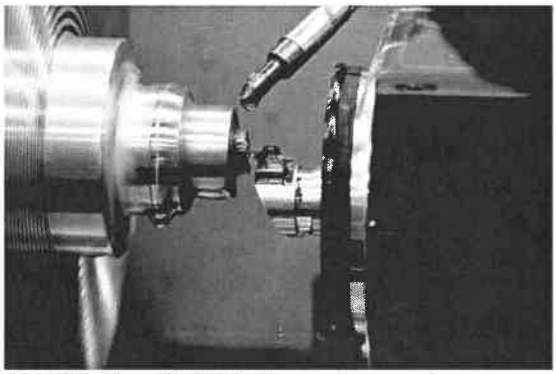

FIGURE 8. FLORA II machining the prescan mirrors.

RESULTS

The prescan optical system was machined using the FLORA II actuator mounting on the ASG 2500 DTM (see Figure 8). The FLORA II control system was programmed to perform bilinear interpolation over the cylindrical grid of sag values for the excursion shown in Figure 7. The controller positions the tool servo and two counter-balance masses using feedback and feedforward control and thus needs commanded position, velocity and acceleration. The interpolation grid was evenly spaced in radius from 1.27 mm to 2.6 mm in increments of 16 µm. The angular spacing was uniform within the mirror apertures at 0.13°, which gives a maximum arc length of 6 µm between points. For this optical system, the best fit polynomial order was set to 1, so the aspheric surface swept out by the DTM was a cone. The cone angle is very close to 45°. An 82.7 µm radius tool was used to cut the finish pass at 80 rpm with a cross feed rate of 0.16 mm/min, yielding a feed/rev of 2 µm. Interestingly, the surface finish measurement in Figure 10 of the M2 mirror shows a repeating pattern at 35 µm, much wider than the expected tool feed marks. While the surface finish is not stunning, 24 nm RMS is quite good considering the high accelerations of the servo at the aperture transitions.

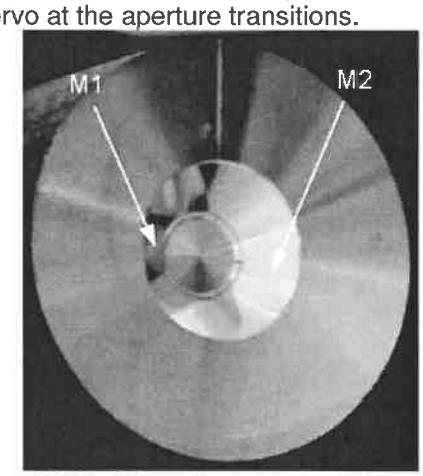

FIGURE 9. The finished part.

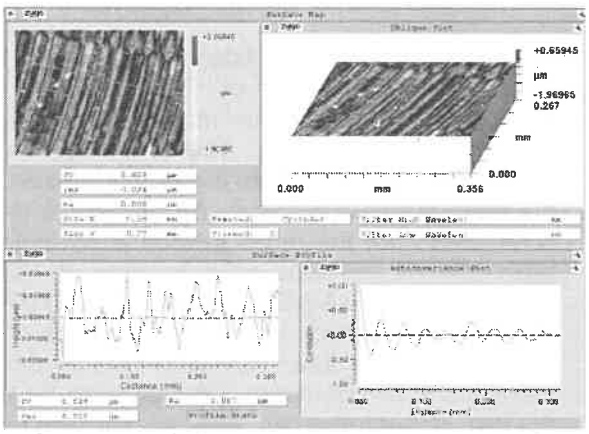

FIGURE 10. Surface finish measurement of M2.

CONCLUSIONS

A design for a reflective prescan laser optical system has been completed. Tool path generation for an arbitrary biconic two mirror system has been coded in Matlab. The data tables needed to machine the mirrors with the FLORA II FTS control system are generated by this Matlab script. In addition a motion program is output describing the best-fit rotationally symmetric asphere that is machined simultaneously by a Diamond Turning machine.

REFERENCES

[1] Zdanowicz, E., Design of a Fast Long Range Actuator -- FLORA II. Master's Thesis, North Carolina State University, 2009.

[2] Sohn, A., Garrard, K., Dow T. The Spherical Profilometer Polaris 3D. Proceedings of the 24th Annual Meeting of the ASPE; 47: 43-46.

EVALUATION OF HYDROXIDE CATALYSIS BONDING STRENGTH

Hyo Soo Kim and Tony L. Schmitz
Department of Mechanical and Aerospace Engineering
University of Florida
Gainesville, FL, USA

INTRODUCTION

The ability to bond solid materials is critical in high precision applications. Existing bonding methods include, e.g., optical contacting, epoxy bonding, and frit bonding [1]. Optical contacting, a room temperature process, is highly sensitive to surface contamination and can lead to unreliable bond strength. The interface thickness for epoxy bonds is relatively large, which is undesirable in optical applications due to refractive index mismatching between the interface and the substrate. In addition, the mechanical strength of epoxy bonds varies with temperature and chemical environment. Frit bonding is a high-temperature process which produces mechanically strong and chemically-resistant bonds in most cases. Furthermore, the frit bond is opaque which is unusable in transmission optics.

Hydroxide catalysis bonding (HCB), a room-temperature chemical bonding technique, was developed to overcome the limitations imposed by the existing methods. The purpose of this paper is to study the bonding conditions which affect the mechanical strength using HCB. The mechanical strength of the HCB depends on various factors including, but not limited to, the amount of the bonding solution per unit area, concentration of the hydroxide ions dissolved in de-ionized (DI) water, and curing time. In this paper, shear strength test results for glass-to-glass bonding for these variables are presented. In many applications, metal-to-glass bonding is also required, e.g., optical assemblies mounted to a metal substrate. Therefore, aluminum-to-glass bonding was also investigated. The shear strength for the aluminum-to-glass bonding is also reported.

HCB BACKGOUND

HCB was first described by Gwo [2-4] to join the fused silica components which formed the star-tracking space telescope used in the Gravity Probe B space experiment [4]. Follow-on efforts have further explored the process. Preston et al. [5] studied the mechanical strength of various materials including BK7-to-BK7 and silicon carbide (SiC)-to-BK7 bonding while Veggel et al. [6, 7] tested SiC-to-SiC and silicon (Si)-to-Si bonding. Elliffe et al. [8] reported mechanical strength variations based on different types of bonding solution and concentrations of hydroxide ions (OH^-) for various materials.

HCB is a process of hydration and dehydration of the bonding interface through hydroxide catalysis. Aqueous solutions of hydroxides such as sodium hydroxide (NaOH) and potassium hydroxide (KOH) with or without silicate are employed for this technique. The HCB technique consists of three steps [6]: 1) hydration and etching, where hydroxide ions (OH^-) in the solution act as a catalyst and etch the silica surface in contact; 2) polymerization, where siloxane chains (silicate-like network) and water are formed; and 3) dehydration, where the water migrates and evaporates. The HCB technique enables bonding between a variety of materials if a silicate-like network can be formed at the surfaces; this is the case for most oxide-containing materials, including silica, Zerodur, fused silica, ULE glass, and granite. Like most bonding techniques, surface roughness and global flatness of the bonding area for the HCB technique are required to achieve precision bonding with high mechanical strength.

EXPERIMENTAL SETUP

The materials used in the experiments were microscope glass slides (water-white glass) and aluminum samples. The 25 mm × 75 mm glass slides were cut into 15 mm × 25 mm sections using a dicing machine. The roughness at five different areas (5.88 mm^2) on the surface to be bonded was measured using a scanning white light interferometer (SWLI). The mean arithmetic average deviation (R_a) was 6.5 nm. The global peak to valley (PV) flatness covering the whole bonding area (307.5 mm^2) was 3.2 μm. A commercially-available aluminum (Al 5052) polished on one side was also used for bonding. The 300 mm × 300 mm aluminum sheet was also cut into 15 mm × 25 mm sections. The

mean surface roughness (R_a) and the global PV flatness for the aluminum pieces were 66.6 nm and 10.3 μm, respectively. The thickness of both materials was 1 mm.

The pieces were cleaned in an ethyl alcohol ultrasonic bath for 10 minutes and then removed. The remaining alcohol on the surface was removed using an optical wipe and the surface was observed using a magnifier with a high intensity light source. Any remaining particles were removed using a wet ethyl alcohol wipe. Bonding was performed in a class 100 laminate flow clean cube at room temperature to avoid any airborne particles which could degrade the bonding strength. Figure 1 depicts the bonding process using a jig where the pieces are aligned to have a bonding area of 307.5 mm^2 (15 mm × 20.5 mm). The bonding solution used in this experiment was sodium silicate solution, containing ~14% of sodium hydroxide (NaOH) and ~27% of silicon dioxide (SiO_2), dissolved in DI water. The bonding solution was dispensed on the top surface of the bottom piece using a micropipette as shown in Fig. 1(A). The second piece was then gently placed on the first piece. See Fig. 1(B). Light pressure was applied to the top piece to uniformly spread the solution. The bonded pieces were left to settle in the jig for about 5 minutes [9] and then carefully moved to another location in the clean cube for curing.

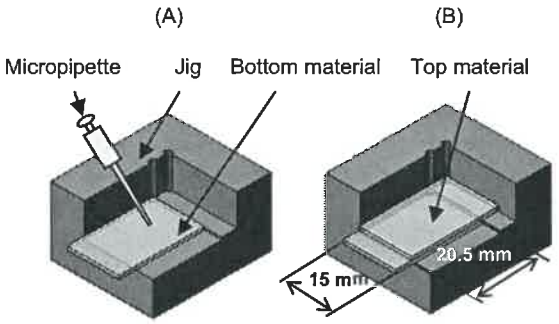

FIGURE 1. The pieces are bonded using a jig for alignment. (A) The bonding solution is dispensed on the bottom piece. (B) The top piece is placed on the bottom substrate.

Figure 2 shows the test setup used to measure the shear strength of the bonding interface using an axial load frame. A small vise was used to vertically support the bonded sample so that the force axis was parallel to the bonding interface. Note that the vise did not restrict vertical motion of the sample, but was simply used as an alignment tool. After a sample was loaded on the lower crosshead, a downward force was applied by the upper crosshead with a speed of 10 mm/min until the sample bond was broken.

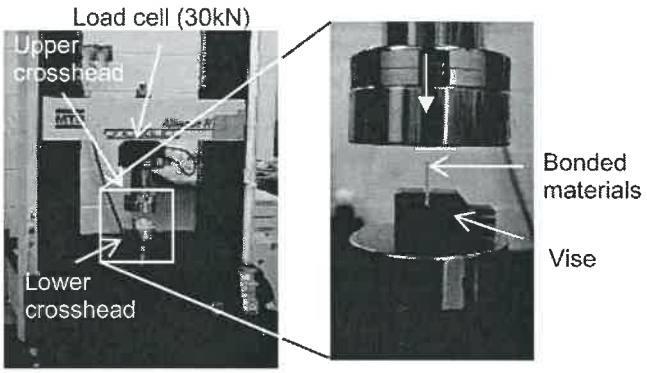

FIGURE 2. Shear strength test setup using an axial load frame with 30 kN load cell.

EXPERIMENTAL RESULTS

This section presents experimental shear strength results for glass-to-glass and aluminum-to-glass bonding for variations in the amount and concentration of the bonding solution and curing time. Each glass-to-glass test included ten bonded samples to determine the mean strength and standard deviation; the aluminum-to-glass tests used five samples.

In Fig. 3, the 10 shear strength profiles for glass-to-glass bonding with 2.0 μl of the bonding solution and a volume ratio of 1:4 (sodium silicate solution:DI water) are shown. The mean breaking shear strength (3.5 MPa) and standard deviation (0.5 MPa) are agree with previously reported BK7-to-BK7 bonding tests [5].

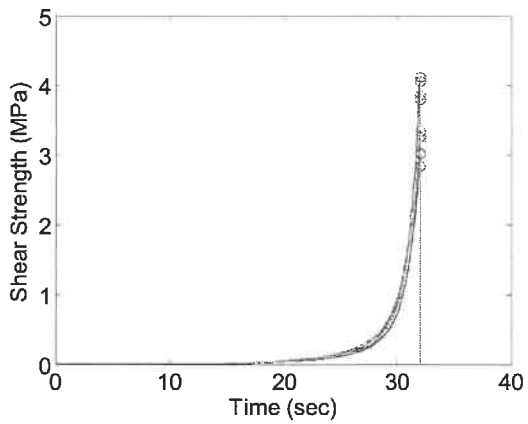

FIGURE 3. Shear strength profiles for glass-to-glass bonding.

To understand the effect of the amount of solution applied to the bonding area, the glass pieces were bonded with five different amounts of solution {0.5, 1, 2, 3, and 5} μl over the bonding area of 307.5 mm^2. The volume ratio and curing time for this test were 1:4 and 48 hours, respectively. Figure 4 shows the mean breaking shear strengths (circles) and standard deviations for each amount of solution. The test result indicates that the bond shear strength is not strongly dependent on the amount of solution for sodium silicate solution.

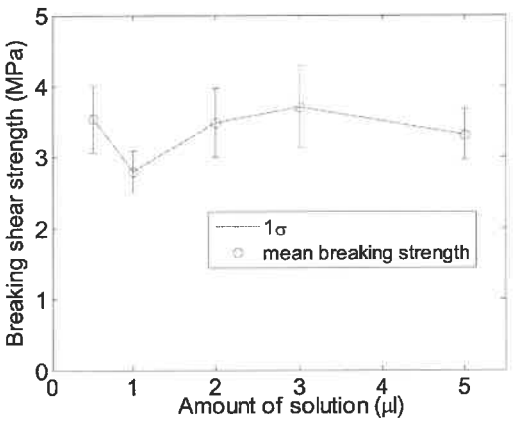

FIGURE 4. Breaking shear strengths for various amounts of bonding solution.

In Fig. 5, the mean breaking strengths for a wide range of concentrations (volume ratio between sodium silicate solution and DI water in this experiment) are shown. There is no significant strength difference for volume ratio between 1:2 and 1:50.

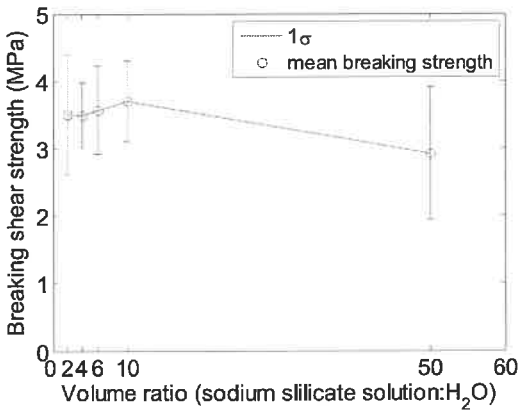

FIGURE 5. Breaking shear strengths at various concentrations of bonding solution (volume ratio of sodium silicate solution to DI water).

In the curing time variation test, 2.0 μl and a 1:4 volume ratio were used. These numbers were arbitrarily selected since the shear strength was shown to be insensitive to the amount and concentration of the bonding solution. Figure 6 shows the breaking shear strengths for the various curing time from 1 hr to 168 hr (1 week). The bond strength increased with curing time; the mean strength at 1 week was nearly twice that of the 48 hr cure. This contradicts the results presented in [5] that showed constant shear strength for curing times from 18 hr to 11 days. However, it supports [1] which reported that full strength was achieved only after four weeks of curing time. Follow-on testing will include longer curing times (up to four weeks) to determine a minimum time for desired strength when using sodium silicate solution.

The deviation of strength for the 24 hr samples was larger than the higher curing times as shown in Fig. 6. This is investigated in Fig. 7. The mean shear strength (3.5 MPa) for six (A in Fig. 7) out of ten samples were much higher (about three times) than the strength (1.1 MPa) for the remaining four samples (B in Fig. 7). The six samples with higher strength were broken during the shear test, while the rest (lower strength) were separated without breaking. It was concluded that the 24 hr curing time is the transition time between a permanent and "separable" bond for 2.0 μl of sodium silicate solution with a 1:4 volume ratio.

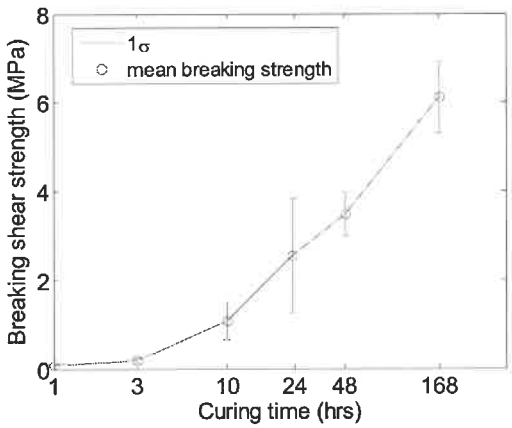

FIGURE 6. Breaking shear strength at various curing time.

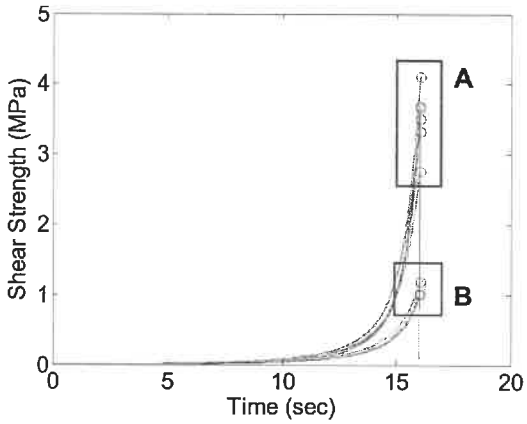

FIGURE 7. Shear strength profiles for the samples with a 24 hr curing time.

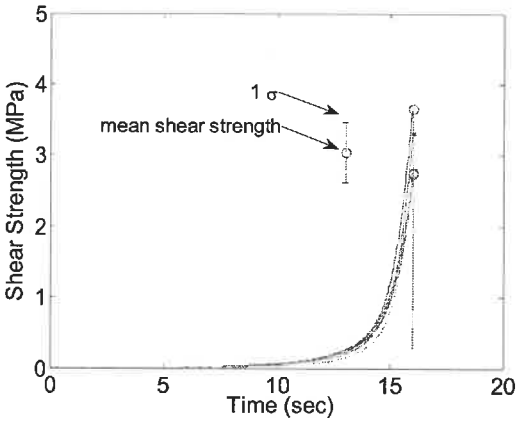

FIGURE 8. Shear strength profiles for aluminum-to-glass bonding.

Finally, the shear strength for aluminum-to-glass bonding is presented in Fig. 8. Five samples were bonded using 2.0 μl of bonding solution and a 1:4 volume ratio. The curing time was 48 hr. The mean breaking shear strength of 3.1 MPa was slightly less, but still comparable, to the glass-to-glass results under the same conditions. This result is surprising because: 1) a large figure mismatch for the aluminum-to-glass interface was present; and 2) only the native oxide for the aluminum surface was used.

CONCLUSIONS

In this work, the shear strength for glass-to-glass and aluminum-to-glass bonding using the hydroxide catalysis bonding technique was evaluated. It was determined that the solution amount and concentration did not have a significant effect on the strength for the sodium silicate solution tested here. However, it was found that the bond strength increased significantly with room-temperature curing times up to one week.

REFERENCES

[1] Prabhu, K, Schmitz T, Ifju, P, Daly, J. A Survey of Technical Literature on Adhesive Applications for Optics, Proceedings of the SPIE. 2007; 6665.

[2] Gwo DH. Hydroxide-Catalyzed Bonding. United States Patent No. 6548176B1. 2003.

[3] Gwo DH. Ultraprecision and Reliable Bonding Method. United States Patent No. 6548176 B1. 2001.

[4] Gwo DH. Ultraprecision Bonding for Cryogenic Fused-silica Optics. Proceedings of the SPIE. 1997; 3435.

[5] Preston A, Balaban B, Mueller G. Hydroxide-bonding Strength Measurements for Space-based Optical Missions. International Journal of Applied Ceramic Technology. 2008; 5(4): 365-372.

[6] Veggel A, Ende D, Bogenstahl J, Rowan S, Cunningham W, Gubbels G, Nijmeijer H. Hydroxide Catalysis Bonding of Silicon Carbide, Journal of the European Ceramic Society 2008; 28: 303-310.

[7] Van Veggel A, Scott J, Skinner D, Bezensek B, Cunningham W, Hough J, Martin I, Murray P, Reid S, Rowan S. Strength Testing and SEM Imaging of Hydroxide-catalysis Bonds between Silicon. Classical and Quantum Gravity. 2009; 26: 175007-175020.

[8] Elliffe E, Bogenstahl J, Deshpande A, Hough J, Killow C, Reid S, Robertson D, Rowan S, Ward H, Cagnoli G. Hydroxide-catalysis Bonding for Stable Optical Systems for Space. Classical and Quantum Gravity 2005; 22: S257-S267.

[9] Reid S, Cagnoli G, Elliffe E, Faller J, Hough J, Martin I, Rowan S. Influence of Temperature and Hydroxide Concentration on the Settling Time of Hydroxide-catalysis Bonds. Physics Letters A. 2006; 363: 341-345.

ECO-FRIENDLY MICRO ELECTROCHEMICAL MACHINING

Shi Hyoung Ryu[1], and Jong Sun Yu[1]
[1]Department of Mechanical Engineering
Chonbuk National University
Jeonju, Korea

INTRODUCTION

Micro/nano-technology has been developed rapidly in recent years in almost all the science and engineering fields. To overcome the limitations of MEMS processes based on photolithography, other micro/nano-manufacturing techniques have been advanced or newly developed. Micro electrochemical machining (MECM) is one of the most promising manufacturing technologies applicable to conductive hard metals and semiconductors. After a novel MECM technique was suggested by Schuster et al. [1], several research papers have reported on pulsed ECM applications for micro-drilling, -grooving, and -milling. But in most cases regardless of workpiece materials, toxic and harmful electrolytes such as HCl, H_2SO_4, HF, $HClO_4$ solutions have been used. To develop a safe and environmentally friendly MECM process, Ryu et al. [2] introduced citric acid electrolyte for micromachining stainless steel. In this paper, MECM characteristics in a citric acid electrolyte are investigated when a micro-shaft tool electrode is adopted. Also, a micro-grooving technique with thin foil electrode and an electrochemical reverse drilling method are newly suggested.

ELECTROCHEMICAL CHARACTERISTICS OF STAINLESS STEEL IN CITRIC ACID

As an organic acid, citric acid has been widely used for flavoring and as a preservative in food and beverages for its well-known nature of safety and healthfulness. In industry, citric acid is used for metal cleaning, such as stain removal and is employed as a sequestering agent to control deposition rates in metal deposition processes. Citric acid does not form insoluble precipitates on the electrode surface or in the electrolyte solution. In this research, for developing eco-friendly electrochemical process, anhydrous citric acid ($C_6H_8O_7$) is used as an electrolyte after dissolving it into distilled water. Stainless steel is broadly used for mechanical parts in automotive and aerospace industries due to its high corrosion resistance and good mechanical properties. In this research, austenitic stainless steel 304 (SS 304) which has good formability and corrosion resistance is used as a work material. For electrochemical machining of SS 304, main alloy components such as iron, chromium, and nickel should be dissolved electrochemically. Chromium in stainless steel forms a dense and thin stable chromium oxide (Cr_2O_3) film when exposed to air and this passive layer increases corrosion resistance. In citric acid solution, chromium has two oxidation states as +3 or +6 valance and they compose stable citrate complexes [3]. Nickel is dissolved in acid solution less than pH 6 and Ni^{2+} makes stable complex with citric acid [4]. Citrate ions chelate with Fe^{2+} and Fe^{3+} to form Fe(II) citrate and Fe(III) citrate complex ions which accelerate the iron dissolution [5].

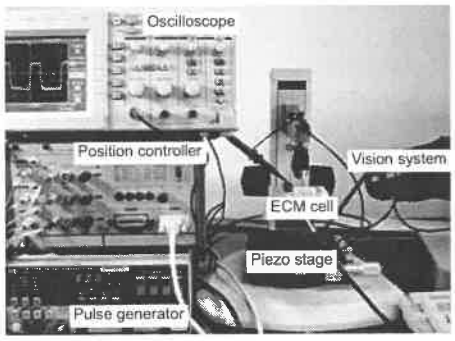

FIGURE 1. Micro electrochemical machining system.

EXPERIMENTAL SET-UP

The electrochemical cell is mounted on a PI piezo nano-stage and the tool electrode is located above the electrochemical cell as shown in figure 1. After the tool electrode approaches the work piece, that is immersed in the citric acid electrolyte, ultra short voltage pulses are applied between the tool electrode and work material. By moving the nano-stage following a programmed path, the workpiece is dissolved into the electrolyte and the final microstructure is achieved. By using a 1GHz oscilloscope and a CCD vision system, the interelectrodes gap voltage is measured for monitoring machining

state. Machined features are observed by a JEOL 6400 scanning electron microscopy and surface texture including roughness is measured by a Zygo NewView 5000 surface profiler.

MICRO-DRILLING AND -MILLING WITH A MICRO-SHAFT ELECTRODE

Tungsten wire of 10 μm in diameter is used for the tool electrode. Commercial micro-wire is cut and fixed in a micro-drill chuck. Micro-drilling and –milling experiments are conducted on variations of electrolyte concentrations, pulse parameters such as amplitude, duration, frequency, and tool electrode base potential. As electrolyte concentration increases up to 0.3 M, the machining speed increases. The conditions of pulse amplitude is in the range of 11.0 ~ 11.5 V and a tool electrode base potential of –3.5 ~ –3.0 V are the most appropriate for machining precise micro-hole with good surface quality. Tool electrode feeding speed of 0.1 ~ 0.15 μm/sec for micro-hole drilling and 1.0 ~ 2.0 μm/sec for micro-milling are recommended for producing fine micro-features without short-circuit occurrence between electrodes. In the pulse duration of 350 ~ 380 nsec with a 1 MHz pulse frequency shows good experimental performance with respect to less machining gap, higher straightness, precise feature shape and better surface quality. Tool over hang length also plays an important role in MECM. When the tool electrode is shorter than 1 mm, an electrolyte covers the entire tool electrode through capillary effects causing the electric field to disperse. Therefore, the current density is insufficient for smooth machining. When tool over hang is longer than 2 mm, evolved bubbles of hydrogen and oxygen shake tool electrode resulting in poor hole shape.

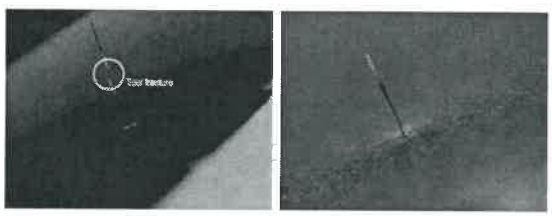

FIGURE 2. (a) fractured tool electrode at high voltage, and (b) welded part on the work material.

Long tool electrodes applied on high pulse potential over than 12 V are frequently fractured at the tool center due to Joule heating effect caused by a short-circuit between the electrodes as shown in figure 2a. In this case, the lower part of the broken electrode welds on the work material as shown figure 2b. Figure 3 shows a drilling result on 100 μm thick SS 304 stainless steel foil at 0.1 μm/sec feeding speed with 1.4 mm tool electrode over hang. Hole entrance diameter is 37 μm and exit diameter is 34 μm. Machining gap is about 13 μm at the entrance and the tool diameter is 10 μm. Fig. 3 shows a drilled micro-hole on 50 μm thick SS 304 foil. The entrance diameter is 26 μm and exit diameter is 23 μm. Hence, the machining gap is 8 μm and the hole aspect ratio is about 2. However, under more strict conditions such as shorter pulse duration and lower peak voltage, holes are not perforated in most cases. When machining gap is too small, the dissolved metal ions are not flushed well from the interelectrodes gap and new electrolyte is not supplied sufficiently to the dissolution site by convection or diffusion.

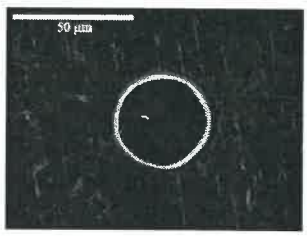

FIGURE 3. Micro-hole of 37 μm drilled on 100 μm thick SS 304 plate. 380 nsec pulse duration, 1 MHz pulse frequency, 11.4 V pulse voltage, -3.2 V tool base potential, and 0.1 μm/s feed speed.

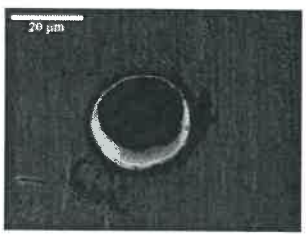

FIGURE 4. Micro-hole of 26 μm drilled on 50 μm thick SS 304 plate. 380 nsec pulse duration, 1 MHz pulse frequency, 11.2 V pulse voltage, -3.2 V tool base potential, and 0.15 μm/s feed speed.

When the dissolution condition is quite tight, some peculiar nanostructures are observed on the inner wall surface. In figure 5, about 200 nm size craters are formed and distributed on the

other several micrometer size craters. Some possible causes of this phenomenon can be explained as follows. Firstly, the structures may be formed by the simultaneous intergranular corrosion together with pitting corrosion of austenitic stainless steel. Similar honey comb type granular and pitting corrosions were observed on SS 304 material immersed in low concentration HCl [6]. Because chromium concentration at granular boundary is lower than that of granular center, granular boundary is comparatively weak when exposed to corrosion circumstance. Small interelectrodes gap makes it hard to supply sufficient fresh electrolyte on the dissolution area hence less corrosion resistant region dissolves firstly and this mechanism may produce such microstructures. Secondly, these craters might be EDM marks in the vicinity of tool electrode and workpiece interface. Electrolyte connection between tool electrode and workpiece is temporarily broken by the generated blanket of bubbles. Then partial EDM happens and the discharge marks remain on the surface. Thirdly, Micro-bubbles dispersion and the related electric field distortion may induce the observed structures. The generated microstructures also seem like the microstructures formed by anodic aluminum oxidation or other metals oxidation. Therefore, the microstructures could be formed through similar anodic oxidation procedure.

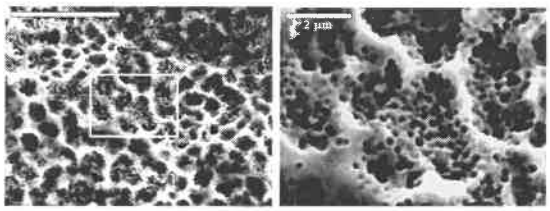

FIGURE 5. Surface texture formed on the inner wall under strict electrochemical condition.

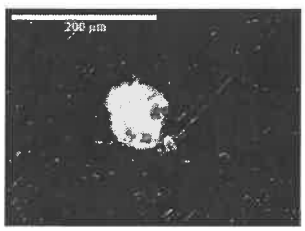

FIGURE 6. Micro-hand pattern inscribed by electrochemical milling. 380nsec pulse duration, 1MHz pulse frequency, 11.2V pulse voltage, -3.2V tool base potential, and 1 μm/s feed speed.

Figure 6 shows a micro-hand pattern machined by electrochemical milling. Length and width of the hand pattern are 80 μm and 65 μm, respectively. Tool feeding speed is 1 μm/sec and tool is fed into z direction twice with 3 μm step length. Machined depth is 8.0 μm and average surface roughness, Ra, is 0.32 μm. Machined feature is inscribed well following the programmed tool path but edge sharpness and surface quality should be improved.

MICRO-GROOVING WITH A THIN FOIL ELECTRODE

Demands for the micro-channels are increasing for bio-applications, micro fuel cell, micro heat exchanger, and actuator. Electrochemical machining is a suitable process to make high quality micro-channel on the metals surface. However, electrochemical milling by feeding of a micro-shaft tool has a drawback of machining speed. So, in this paper, electrochemical micro-grooving technique using thin foil electrode is suggested.

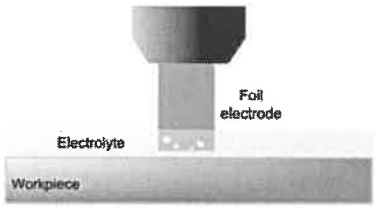

FIGURE 7. Schematics of micro-grooving with a thin foil electrode by MECM.

Figure 8 shows the grooving results on the SS 304 plate with a 20 μm thick SS 304 foil electrode. Tool feeding speed is 0.03 μm/s and pulse amplitude is 8.6 V at tool base potential of -1.6 V with 1 MHz pulse frequency. A 42 μm wide, 18 μm deep single groove (figure 8a) and a 34 μm wide, 17 μm deep double groove (figure 8b) are machined which have good straightness and surface roughness of 11 nm Ra.

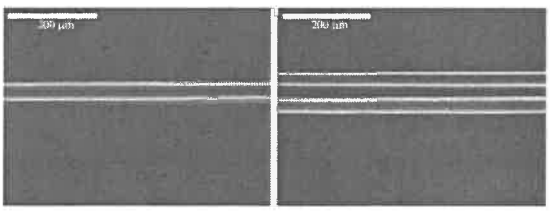

FIGURE 8. (a) single and (b) double micro-grooves machined by MECM with thin foil electrode.

MICRO-ELECTROCHEMICAL REVERSE DRILLING

In MECM, as machining depth increases, machining time increases exponentially because the dissolved metal ions are hardly flushed. To improve machining speed in MECM, electrochemical reverse drilling method is suggested. In reverse drilling shown in figure 9, the tool electrode is located under the workpiece and fed into the upper direction as machining progresses. An electrolyte is attached to the bottom of the work material by surface tension. We intended that the heavy metal ions are removed well by the gravity effect.

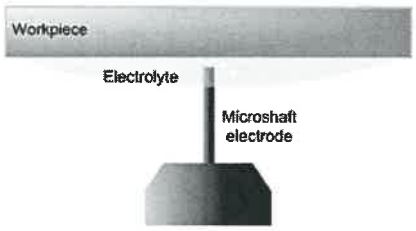

FIGURE 9. Schematics of electrochemical reverse drilling.

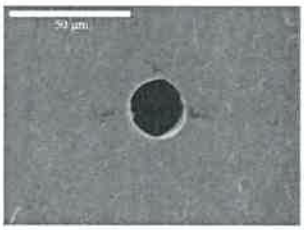

FIGURE 10. Drilled hole with 29 μm entrance and 23 μm exit by electrochemical reverse drilling.

Figure 10 shows a drilling result at the condition of 11 V pulse amplitude and -3.6 V tool base potential with 400 ns pulse duration at 1 MHz pulse frequency. Entrance and exit diameters are measured as 29 μm and 23 μm, respectively. Machining speed is 0.2 μm/s and it corresponds to 50 % speed improvement compared to the conventional electrochemical drilling. Different to expectation, an apparent increase of machining depth is not achieved through reverse drilling. Trapped bubbles at the upper inside hole possibly hinder deeper drilling. Additionally, sticky condition formed at interelectrodes gap with a low Reynolds number can make it hard to remove metal ions by the gravity effect.

CONCLUSIONS

Eco-friendly micro electrochemical machining process is investigated with citric acid electrolyte. Using tungsten micro-wire with 10 μm in diameter as a tool electrode, micro-hole, -groove, and complex structures are fabricated on SS 304 by the pulsed ECM. Precise microstructures are obtained by controlling the pulse amplitude, duration, frequency, tool feeding speed, and electrolyte concentration. We show that micro-grooving with thin foil electrode can be an effective method for various potential applications. Also, to improve machining speed, electrochemical reverse drilling technique is newly suggested and shows good performance especially in micro-drilling. Presented ECM methods are cost effective, flexible, and eco-friendly technique applicable to the micro-fabrication with hard metals.

ACKNOWLEDGEMENTS

This research was supported by Basic Science Research Program through the National Research Foundation of Korea(NRF) funded by the Ministry of Education, Science and Technology (KRF-2008-331-D00041).

REFERENCES

[1] Schuster R, Kirchiner V, Allongue P, Etrl G. Electrochemical Micromachining. Science. 2000; 289: 98-101.

[2] Ryu S. Micro Fabrication by Electrochemical Process in Citric Acid Electrolyte. Journal of Materials Processing Technology. 2009; 209: 2831-2837.

[3] Lambrou P, Christou S, Fotopoulos A, Foti F, Angelidis T, Efstathiou A. The Effects of the Use of Weak Organic Acids on the Improvement of Oxygen Storage and Release Properties of Aged Commercial Three-way Catalysts. Applied Catalysis B: Environmental. 2005; 59: 1-11.

[4] Zelenin O. Interaction of the Ni^{2+} Ion with Citric Acid in an Aqueous Solution. Russian Journal of Coordination Chemistry. 2007; 33: 346-350.

[5] Chu C, Wan C. Effect of Citric Acid as a Chelating Agent on Anodic Behaviour of Pure Iron with Potentiostatic and Cyclic Voltammetry Methods. Materials Chemistry and Physics. 1993; 33: 189-196.

[6] Li L, Caenen P, Celis J. Effect of Hydrochloric Acid on Pickling of Hot-rolled 304 Stainless Steel in Iron Chloride Based Electrolytes. Corrosion Science. 2008; 50: 804-810.

SELF CALIBRATION OF THE LINEARITY ERROR OF ANGLE SENSORS FOR DIFFERENTIAL LASER AUTO-COLLIMATION

Yutaka Uda[1], Shoichi Shimada[1], and Yasuyuki Go[2]
[1]Department of Mechanical Engineering
Osaka Electro-communication University
Neyagawa, Osaka, Japan
[2]Machine Design Division
Nagase Integrex Co., Ltd.
Seki, Gifu, Japan

BACKGROUD

Demands for long mechanical and optical parts which have high straightness or flatness are increasing. Examples are seen in a flat panel for display, a throttle die for thin film production and machine elements of semiconductor equipments. Although the length of the parts exceeds 1 m, the requirement for their figure accuracy becomes higher than 0.1μm. However, there is no useful method to evaluate precisely the figure accuracy of the long parts. The reasons are inevitable difficulties in manufacturing long tangible datum and to avoid the effect of gravity and environment. Developing the ultra-precision measuring machine for long parts is an urgent need.

In the previous papers, a new concept of straightness measuring machine based on in-situ differential laser auto-collimation (DLAC) is proposed. The principle of figure measuring with DLAC is the accumulation of difference angle in inclination between two probing points along a straight line on the surface to be measured successively measured step by step using laser auto-collimation. The alignment error of two laser beams and two angle detectors causes a large quadratic component on measured profile through all the measuring distance as same as the influence of zero adjustment error of the probes in 3-point method.

To develop a straightness measuring machine based on DLAC, the angle sensor is one of the most important parts. To measure the straightness of the large parts exceeds 1m with the accuracy less than 0.1μm, the resolution of the sensor is required to be higher than 10 μrad. The dynamic range larger than 1 mrad is desirable for assembling the alignment of laser beams. Moreover the size and weight of the sensor mast be small and light.

To meet the requirements, an angle sensor was proposed based on the principle of critical angle between refraction and reflection of a glass prism. When a laser beam passes from glass into air, the ratio of beam intensities of refraction and reflection remarkably changes around the critical angle of the prism. The directional deviation of a laser beam the incident angle of which is near the critical angle of the prism can be detected with high sensitivity. Therefore, by leading the reflected laser beam from a surface to be measured into the prism, the inclination angle of the surface can be precisely measured.

However, the prism surface is not absolutely flat and refractive index is not uniform in the whole region of the prism surface. These cause a linearity error in the output signal of the angle sensor.

In this paper, the self calibration apparatus of the linearity error of angle sensors is proposed using a kind of cantilever and the validity of the apparatus was confirmed by a preliminary experiment.

SELF CALIBRATION OF DISPLACEMENT SENSORS

The first self calibration system of the linearity error of displacement sensors was proposed by Prof. Kiyono [6]. Figure 1 illustrates the outline of the system. The system is constructed from two sensors and a lever system. One of the sensors is fixed at the reference side and the other is fixed at the calibration side. Owing to the magnification of the lever system, the displacement of the target at the reference side is *n* times as large as that at calibration side. The calibration is done as following procedures.

Step(1) Calibration over a whole measuring range of the sensor at reference side
The displacement of the target at the reference side is increased from the lower limit to the upper limit of the range of the sensor, while readings of both sensors are sent to the computer.

Step(2) Sifting of the linear stage
When the reading attains to the upper limit of the range in the reference side, the sensor is sifted by means of the linear stage so that its reading

resumes approximately the original value at the lower limits.

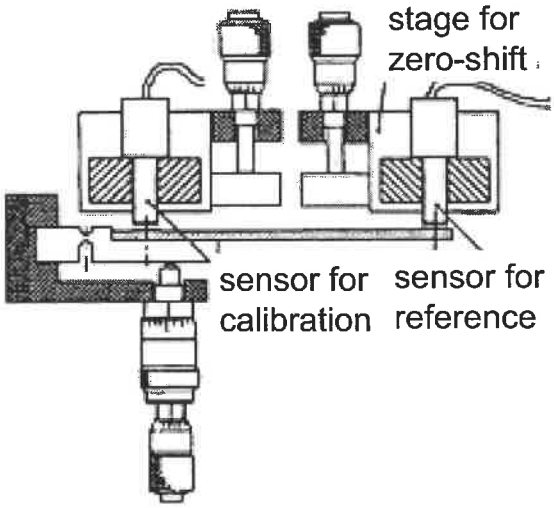

FIGURE 1. Mechanical structure of the calibration system of displacement sensors

Step(3) Data acquisition over full range of the sensor to be calibrated

The cycles of Step(1) and (2) are repeated n times until the displacement of the target at the calibration side reaches to the upper limit of the range of the sensor.

The calibration process is started by putting the sensor A whose sensitivity is known beforehand on the reference side. The sensor has unknown linearity error $E_{A0}(x)$ as shown in Fig.2.

Using the mean sensitivity *Sa* of the sensor A, the displacement of the target at the calibration side can be estimated. Therefore a calibration curve of the sensor C can be plotted as in Fig.3 with the data obtained in the above process.

The amount of original uncertainty in the ordinate in Fig.2 is reduced to 1/n in the abscissa in Fig.3. The relation is expressed in the following equation:

$$E_{B1}(x) = \frac{E_{A0}(x) \cdot S_B}{n \cdot S_A} \qquad (1)$$

where the term S_B is the mean sensitivity of the sensor B. In most cases we can assume $S_B/S_A=1$. In general, the calibration data are expressed approximately by a polynomial obtained by the least squares method. Then the error of the calibration curve is given as follows:

$$F_{B1}(x) = \frac{E_{A0}(x) \cdot S_B}{n \cdot S_A} + f_{B1}(x) \qquad (2)$$

Where the second term is the fitting error of the least squares approximation.

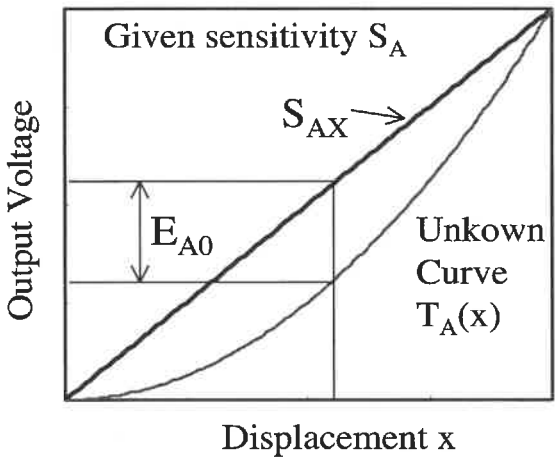

FIGURE 2. Input-output relation of a displacement sensor

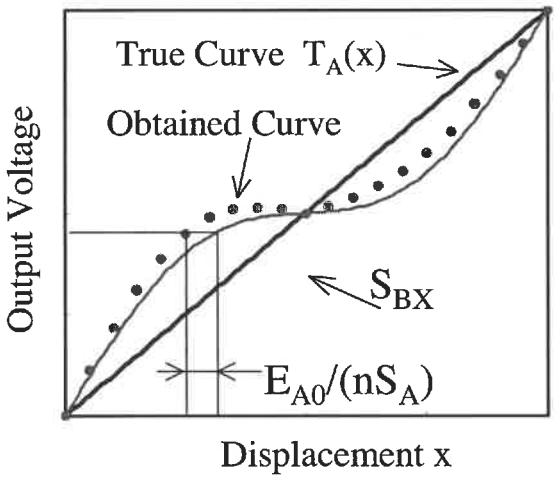

FIGURE 3. Reduction of the uncertainty after the step(3)

Step(4) Exchange of roles of two sensors.

The positions and roles of both sensors are exchanged and the same processes (1) to (3) are followed once more. In this case the calibration curve of the sensor B (reference side) has been obtained in the above process. The uncertainly in the resulted calibration curve of the sensor A is presented as,

$$F_{A1}(x) = \frac{E_{A0}(x)}{n^2} + \frac{f_{B1}(x) \cdot S_A}{n \cdot S_B} + f_{A1}(x) \qquad (3)$$

Thus the uncertainty is reduced to about $(1/n)^2$ of the original one.

Step(5) Correction of estimated magnification of the lever.

In the most cases the magnification of the lever system initially estimated is not accurate enough. If the estimated value and its true value are n' and n respectively, the sensitivity obtained in the step (4) becomes as follows:

$$S_A' = S_A(n/n')_2 \quad (4)$$

Since the sensitivity of the sensor A is given and should be fixed, the true magnification n can be re-estimated as:

$$n = n'\sqrt{S_A'/S_A} \quad (5)$$

Step(6) Converging calculation.

The procedure (1) to (4) is repeated until the calibration curves of both sensors approach to the final converging ones. Really, only one set of data of calibration for each sensor should be acquired. The converging calculation can be forwarded by only correcting the reference values of the abscissa repeatedly. The correction is progressed by applying the last calibration curve of the reference sensor in the present stage.

DESIGN OF SELF CALIBRATION APPARATUS FOR ANGLE SENSORS

The validity of calibration system of displacement sensors described above is indebted to the constant ratio of displacement between reference side and calibration side of the lever within the whole dynamic range of the sensors. In that sense, if the ratio of slope between reference side and calibration side of the lever is constant, angle sensors can be calibrated in the same manner as that for displacement sensors.

Figure 4 shows deflection of a cantilever under a concentrated load at the free end of the lever. The slope dy/dx and deflection y at the position x are obtained by Eqs.(6) and (7).

$$\frac{dy}{dx} = \frac{W}{EI}\left(lx - \frac{x^2}{2}\right) \quad (6)$$

$$y = \frac{W}{EI}\left(\frac{lx^2}{2} - \frac{x^3}{6}\right) \quad (7)$$

Both of the magnitude of slope and deflection at a certain location along the cantilever are proportional to the concentrated load. They can be also controlled with the displacement given by a micrometer at the free end of the cantilever instead of load.

Figure 5 is a self calibration apparatus for angle sensors proposed. The apparatus is constructed from two mirrors, A and B, mounted on the cantilever of copper. The mirrors are targets of a couple of angle sensors. The length, width and thickness of the cantilever are 200mm, 40mm and 2mm, respectively. The distances from the fixed end of the cantilever to the center of mirrors are 30mm and 180mm, respectively. The cantilever is so set as to deflect in horizontal direction to avoid the influence of gravity. The slope continuously changes along the cantilever as expressed in Eq. (6). Therefore, longitudinal positioning error of angle sensor inevitably involves a measuring error of slope. To avoid the influence of positioning error, two rigid and flat blocks of aluminum are attached on both side of the cantilever for a base plate of the target mirrors. As the blocks have high rigidity, the change in slope within the length of the blocks is suppressed less than 0.1μrad.

Figure 6 shows the result of slope at the mirrors A and B calculated by Eq.(6) under the deflection of 3μm and 6μm at the free end of the cantilever.

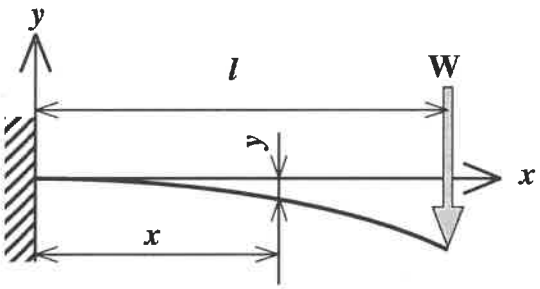

FIGURE 4 Concentrated load deflection of cantilever

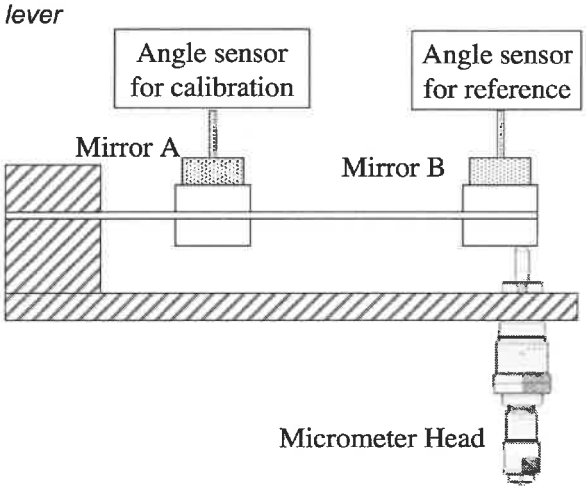

FIGURE 5 Mechanical structure of the calibration system of angle sensors

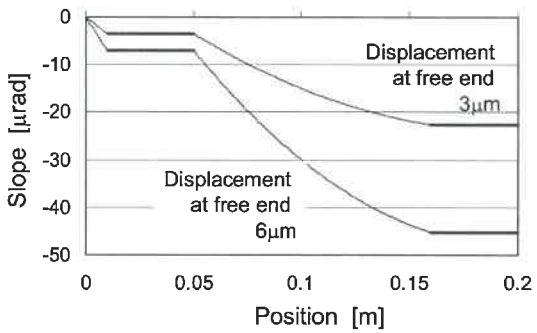

FIGURE 6 Calculated result of slope

PRELIMINARY EXPERIMENT FOR VALIDITY OF THE APARATUS

The angle sensors which have the resolution less than 0.1μrad. and the dynamic range larger than 100μrad. are now under developing. Therefore, the calibration apparatus developed for angle sensors is evaluated using an auto-collimator (NIKON 6B).

The cantilever is bended by giving displacement with micrometer head at the free end of the cantilever. The slopes of the mirrors at the reference and calibration sides are measured separately. The results of the experiments are summarized in Fig. 7. The blue and red lines show change in inclination angle obtained by least squares method at the reference and calibration sides, respectively. The ratio of inclination angle between the mirrors at reference and calibration side is constant. The result suggests that the linearity error of the angle sensors can be successfully calibrated using the apparatus proposed.

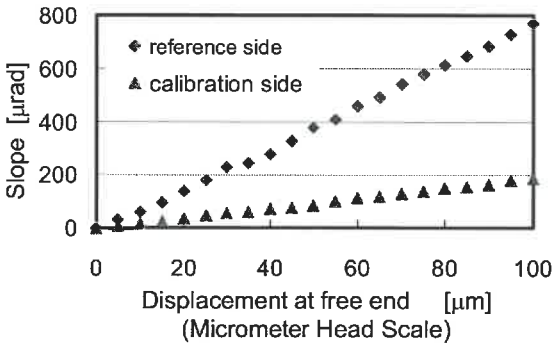

FIGURE 7 Slopes at mirrors vs. Displacement at free end (micrometer head scale)

SUMMERY

A self calibration apparatus of angle sensors is proposed using a kind of cantilever. The validity of the apparatus is confirmed by the preliminary experiment. Then the linearity error of angle sensors can be calibrated using the apparatus proposed.

ACKNOWLEDGMENT

The authors express their thanks to Professor S. Kiyono for his useful suggestions and advices.

REFERENCES

[1] Kiyono S, Fukaya N, Kume T. "Differential Laser Autocollimation Method (1st Report)". J.S.P.E. 1989; Vol.55 No.2; 412-417

[2] Kiyono S, Kume T, Asakawa Y, Kamada O. "Differential Laser Autocollimation Method (2nd Report)". J.S.P.E. 1991; Vol.57 No.4; 652-657

[3] Uda Y, Shimada S, Go Y. "Development of Straightness Measuring Machine for Long Parts using In-Situ Self Calibration Laser Differntial Auto-Collimation –Influence of Probe Assemble Error-". 2007; Proc. 22-ASPE Annual Meeting; 359-362

[4] Uda Y, Shimada S, Go Y. "Study of an interpolation of flatness data measured by successive differential laser auto-collimation ". 2008; Proc. 23-ASPE Annual Meeting; 603-606

[5] Uda Y, Shimada S, Go Y. "Influence of alignment error between two laser beams on straightness measurement using in-situ differential laser auto-collimation". 2009; Proc. 24-ASPE Annual Meeting; 442-445

[6] Kiyono S, Morishima K, Sugibuchi T. "Self Calibration of displacement sensors" . 1992; Proc. 7-ASPE Annual Meeting; 305-308

TOOL WEAR IN DIAMOND TURNING OF STEELS

Naomichi Furushiro[1], Masahiro Higuchi[1], Tomomi Yamaguchi[1], Shuntaro Terauchi[2], Shigetaka Matsuda[2], and Shoichi Shimada[3]
[1]Kansai University
Suita, Osaka, Japan
[2]Osaka Yakin Kogyo Co., Ltd.
Higashi-Yodogawa, Osaka, Japan
[3]Osaka Electro-Communication University
Neyagawa, Osaka, Japan

INTRODUCTION

Excessive tool wear occurs when commercial steel alloys are single-point diamond turned. Therefore, development of diamond-turnable steels are awaited in the manufacture of molds for high-precision, complex optical components.
In this paper, wear suppression factors of diamond tool in turning of steels are discussed based on the results of thermodynamic analysis, cutting tests, and metallographic analyses.

WEAR MECHANISM OF DIAMOND TOOL

Fig. 1 shows a scanning electron micrograph of tool wear at the nose point in turning of steel.
Tanaka et al. stated that some thermo-chemical reactions between a diamond tool and a workmaterial cause tool wear [1]. The mechanisms of tool wear are classified into four types, i.e., oxidization-deoxidization reaction, carbonization, carbon diffusion into work material, and graphitization.
It is necessary to know the cutting temperature to judge whether the chemical reactions happen. Sato et al. [2] investigated the temperatures on the rake faces in cutting of 0.45%carbon steel and SUS304 with diamond tools by the depth of 10 microns. The temperatures on the rake faces were about 623 K in case of 0.45%carbon steel and 873 K in case of SUS304, respectively.
We used thermodynamics analysis to investigate the interactions. The energy change can be calculated using the following equation and thermo-chemical data:

$$\Delta G_T^\circ = \Delta H_T^\circ - T\Delta S_T^\circ$$

$$= \Delta H_{298K}^\circ + \int_{298K}^{T} \Delta C_P dT - T\Delta S_{298K}^\circ - T\int_{298K}^{T} \frac{\Delta C_P}{T} dT \quad (1)$$

where ΔH° is the standard enthalpy change, ΔS° is the standard entropy change, ΔC_P is the difference between the heat capacities of the reactants and products at constant pressure, and T is the temperature.

Then, the mechanism of the diamond tool is presumed referring to above-mentioned temperatures and the change in Gibbs free energy.
First, diamond can deoxidize Fe_3O_4 at the temperature higher than 773K [3]. Therefore, the deoxidization does not happen in cutting of carbon steel.
Second, there is little possibility of iron carbide formation by diamond at the temperature lower than 873K because the energy change $\Delta G^\circ_T = 33.43 - 18.89 \times 10^{-3}\, T \ln T + 61.45 \times 10^{-3}\, T > 0$ [kJ/mol] (298K < T < 873K) for $3Fe + C_D = Fe_3C$.
Third, the diamond graphitizes at temperature above 1100 K in the presence of iron [4]. Therefore, diamond is presumed not to be worn by graphitization because these cutting temperatures are lower than this temperature.
Consequently, the mechanism of tool wear in diamond turning of steel is the diffusion of the carbon atoms in diamond into iron.

Based on the thermodynamics analysis, vacuum contact heating tests simulating wear process of diamond tool in cutting were carried out.

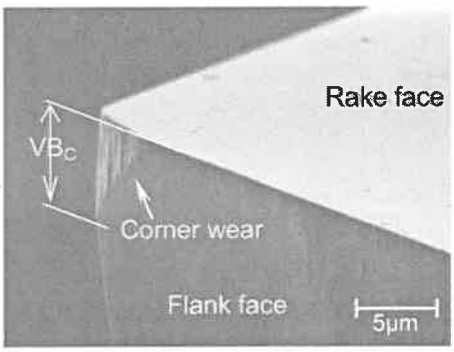

Fig. 1. SEM micrograph of flank of diamond tool after turning SK3 steel.

VACUUM CONTACT HEATING TEST SIMULATING WEAR PROCESS

For a simplified experiment simulating the essential wear process, a vacuum contact heating test is proposed. Figure 2 shows the schematic illustration of the test. A diamond specimen in contact with Fe wire was heated at different temperatures from 673 K to 973 K, in a vacuum of 4.2×10^{-3} Pa for 3 hours. In the tests, erosion pits were generated on the specimen surface due to thermo-chemical reaction with the wire. The cross section of the pit is shown in Figure 3 (a). After the tests, the distribution of carbon concentration on a cross section of each wire was examined by energy dispersive X-ray spectroscopy (EDX).

Figure 3 (b) shows the concentration profile of carbon diffused into Fe wire at 973 K in 4.2×10^{-3} Pa for 3 hours. The carbon concentration shows the maximum value on the wire surface and decreases as the depth increases. The depth where the carbon concentration decreases to the background level is defined as the diffusion depth. These results imply that the carbon atoms of diamond surface directly diffused into Fe, or dissociated carbon atoms from the diamond surface diffused into Fe.

In general, the chemical reaction rate tends to increase with a temperature rise, and this temperature dependence is described by an Arrhenius equation of the following form:

$$\kappa = A\exp\left(-\frac{E}{RT}\right) \qquad (2)$$

where κ is the reaction rate, A is the frequency factor, E is the activation energy, T is the absolute temperature, and R is the gas constant. If the carbon diffusion into the wire is thermal activation process as chemical reaction, the diffusion coefficient will obey the equation.

Figure 4 shows the Arrhenius plots of the carbon diffusion coefficient into Fe wire. The diffusion coefficient D is calculated from the Einstein equation as follows:

$$D=\frac{x^2}{2t} \qquad (3)$$

where x is the average diffusion depth and t is heating time. The diffusion coefficient increases as the temperature rises. The activation energy was 44 kJ/mol, at the same order of the literature [5]. The carbon diffusion coefficient and the activation energy were small; that is, the diffusion rate was not high, whereas the energy barrier of the diffusion was not high.

This result suggests that the difference of the diffusibility influences the wear in turning of steel.

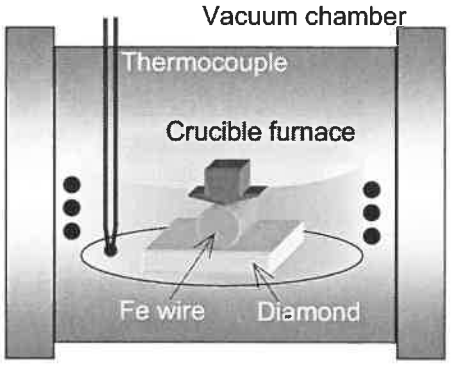

Fig. 2. Schematic diagram of vacuum contact heating test

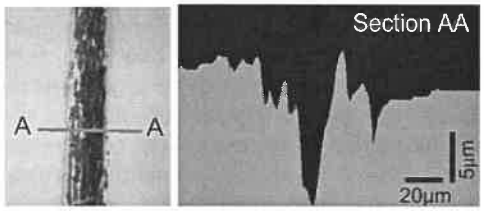

(a) Diamond surface

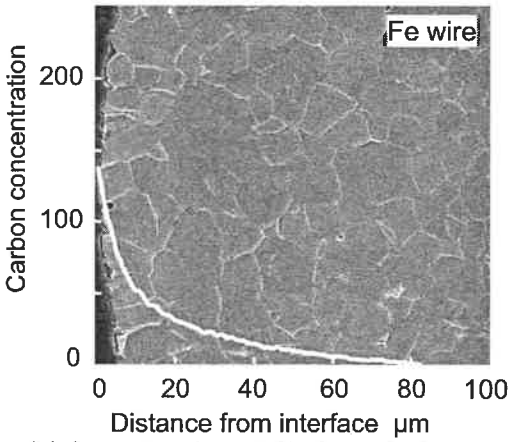

(b) Concentration profile for carbon diffusion in iron

Fig. 3 Erosion pattern on diamond surface and carbon diffusion into pure Fe wire: T=973 K, t=3 h.

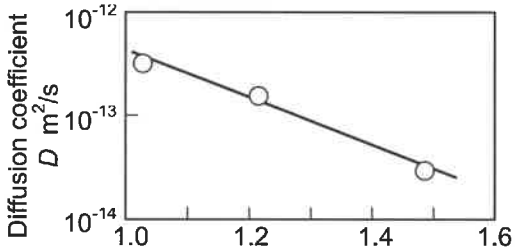

Fig. 4. Arrhenius plot of diffusion coefficient versus reciprocal temperature for diffusion of carbon in Fe wire.

MACHINABILITY OF STEEL

EXPERIMENTAL METHOD

As a preliminary investigation, various quenched and tempered steels were turned using single-crystal diamond tools, and tool wears were measured using a scanning electron microscope. Table 1 shows the detailed tool geometries and cutting conditions.

RESULTS AND DISCUSSIONS

Maximum wear was observed at the tool nose, and its extent varied for different steels.

Fig. 5 shows the relationship between hardness of steel and the corner wear.

The wear is not influenced by the hardness because the correlation coefficient is very low.

To clarify the reasons, metallographic analysis of the steels used in the turning experiments was performed by X-ray diffraction.

This analysis revealed that the steels had considerably different microstructures that could be classified into four broad groups: α-ferrite, α-ferrite + γ-austenite, γ-austenite, and α-ferrite + carbide compounds (e.g., Fe_3C, $Cr_{23}C_6$, and WC).

On the basis of this result, we analyzed whether a causal relationship exist between the microstructure of the steel and the nose wear of the diamond tool.

To ensure unbiased analysis, an inductive inference technique known as C4.5 was applied to the tool wear measurement and phase analysis results.

C4.5 generated valuable classification rules in the form of a decision tree that had branches associated with the matrix phases of the steels and leaves associated with the extent of nose wear.

Fig. 6 shows the decision tree. The tree described the following two rules: steels whose microstructures consist of α-ferrite and carbide phases (e.g., JIS SK5, JIS SKS3, and JIS SUS420J2) wore the tool nose slightly, whereas steels whose microstructures consist of α-ferrite, α-ferrite + γ-austenite, or γ-austenite wore the tool nose severely.

Hence, the presence of carbon compounds in the α-ferrite matrix appears to be very effective in reducing the nose wear of diamond tools.

To confirm this hypothesis, diamond turnabilities of steels in which carbon atoms remain as a solid solution in the martensite phase instead of forming carbon compounds were investigated.

Table 1. Machining parameters used to assess the flank wear on diamond tools.

Cutting tool	
Material	Monocrystalline diamond la
Crystallograhic orientation	(100) rake plane / (110) front plane
Included angle	130°
Rake angle	0°
Clearance angle	7°
Cutting conditions	
Cutting speed	3.35 m/s
Feed rate	3 μm/rev
Depth of cut	3.5 μm
Cutting length	20 m
Coolant	Air

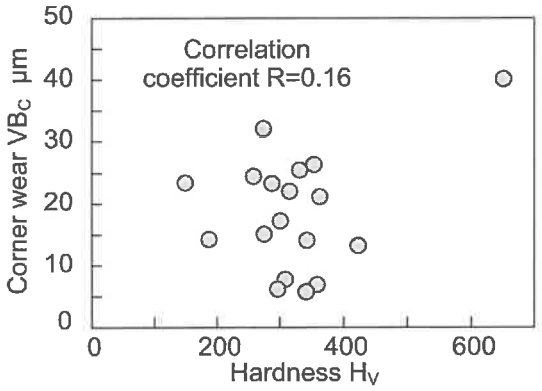

Fig. 5. Corner wear of diamond tool versus hardness of steel.

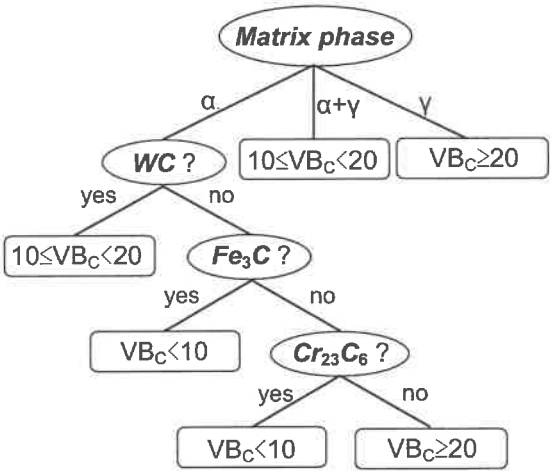

Fig. 6. Decision tree classifying the tool wear into three categories by the matrix phase and carbide.

Fig. 7 shows the X-ray diffraction patterns of tempered steel and a quenched one. Fig. 8 shows the scanning electron micrographs of tempered steel and quenched one. Fig. 9 shows the corner wear of diamond tools in turning of tempered steels and quenched ones.

Turning experiments revealed that steels supersaturated with carbon atoms (i.e., quenched JIS SK5 and JIS SUS420J2) severely wore the tool nose.

Therefore, it can be concluded that the formation of small carbon compound particles that are uniformly dispersed within a continuous α-ferrite matrix suppresses nose wear of diamond tools.

CONCLUSIONS

In this paper, wear mechanism and wear suppression factors of diamond tool were discussed based on thermodynamics analysis and erosion test, and the wear of diamond tools in turning of several steels.

The thermodynamics analysis and the erosion test suggest that carbon atoms in diamond diffuse into iron.

The wear of diamond tools in turning of several steels suggests that metallographic structures of steels influence the diffusibilities of carbon atoms, and thus influence the wear rate.

The machinability test shows the wear suppression factors of diamond tool in turning of steels are as follows:

(1) Carbides precipitation, e.g., Fe_3C, $Cr_{23}C_6$, and WC, in αFe prevents diamond tools from severe wears.

(2) Oversaturated carbon solution in steel matrix does not prevent diamond tools from severe wears.

REFERENCES

[1] Tanaka H, Shimada S, Ikawa N, Higuchi M, Obata K. Difference in Wear Patterns of Diamond Cutting Tool Depending on Work Materials. Proc. of 10th ICPE; 2001: 179-183.

[2] Sato M, Yamazoe K, Tanaka H, and Shimada S. Measurement of Rake Face Temperature of Diamond Cutting Tool by Radiation Thermometer. Proc. of Autumn Conf. of JSPE. 2009: 633-634.

[3] Kubaschewski O, Alcock CB. Metallurgical ThermoChemistry, Pergamon Press: 1979.

[4] Thornton AG, Wilks J. Clean Surface Reactions between Diamond and Steel. Nature. 1978; 274: 792-793.

[5] Callister Jr WD. Materials Science and Engineering. John Wiley & sons. Inc.: 2007.

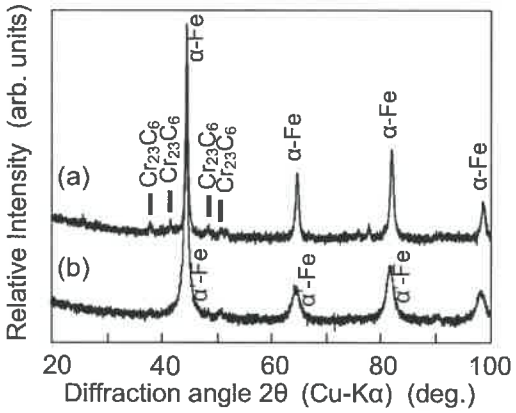

Fig. 7. X-ray diffraction patterns for (a) quenched and tempered SUS420J2 steel and (b) quenched steel.

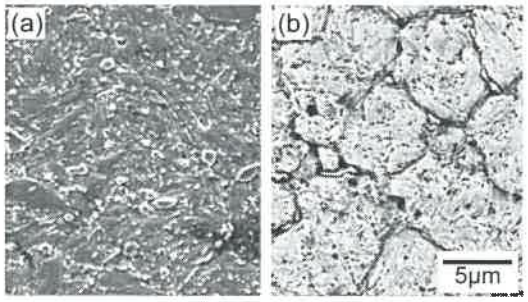

Fig. 8. SEM micrographs showing microstructures of (a) quenched and tempered SUS420J2 steel (b) quenched steel.

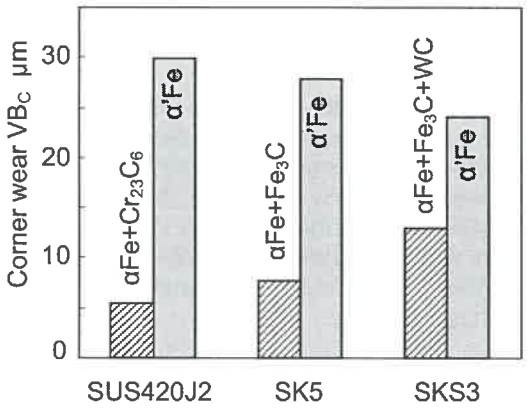

Fig. 9. Corner wear of diamond tool when turning quenched and tempered steels (checked bars) and quenched steels (grey bars).

A STUDY ON ULTRA-FINE MACHINING OF MICRO SQUARE TYPE PYRAMID PATTERN ON LARGE-AREA ROLL MOLD

Tea-Jin Je[1], Sang-Cheon Park[2], Doo-Sun Choi[1], Yeong-Eun Yoo[1], Eun-chae Jeon[1], Jae-Sung Yoon[1], Sung-Hwan Jang[1], and Kyung-Hyun Whang[1]
[1]Nano-Mechancial Systems Research Division
Korea Institute of Machinery and Materials (KIMM)
Daejeon, Korea
[2]Ubiquitous MEMS and Micro Engineering Research Center (UMEMSME)
National Institute of Advanced Industrial Science and Technology (AIST)
Tsukuba, Japan

INTRODUCTION

LCD(Liquid Crystal Display) BLU(Back Light Unit) consists of light guide plate and a few kinds of patterning films such as reflective film, diffuser film and luminance enhancement film. Many studies are recently performed to manufacture optical films with low cost by continuous forming technology with roll mold and to use composite multi-functional optical films instead of a few kinds of films in LCD BLU with roll mold, too [1][2]. The representative composite patterns are micro lens array pattern and micro square type pyramid pattern whose sizes are several tens of micro meter [3][4]. The micro lens array pattern can be manufactured by roll-to-roll forming technology using a roll mold which is exposed by laser and developed. However, the micro square type pyramid pattern cannot be manufactured by the etched roll mold. The roll mold for the pyramid pattern should be machined by micro cutting technology using ultra-precise lathe M/C.

The purpose of this study is to machine micro square type pyramid patterns on a large roll mold by micro cutting technology for manufacturing high performance composite optical films. Several things were necessary for this study such as ultra-precise machining system, diamond tool, optimal machining conditions and controlled environment [5]. Especially, the tool position should be controlled very precisely because micro square type pyramid pattern can be machined by firstly moving the diamond tool to circular direction for making micro prism patterns and then secondly moving the tool vertically (longitudinal direction). If the tool is located wrongly at the second moving, the top apex of the pyramid pattern would be not sharp. Ultra-precise rotating system for the machining tool was designed and installed with accurate position measuring system of the tool into roll mold machining system for solving the problems, and ultra-fine micro square type pyramid pattern on the roll mold was machined in this study.

MACHINING METHOD OF MICRO SQUARE TYPE PYRAMID PATTERN

A flat mold and a roll mold can be used for manufacturing light guide plate or optical film having micro square type pyramid pattern. Generally, the flat mold is used for small optical components while the roll mold for larger ones. The method of machining the pyramid pattern on the flat mold is presented in Figure 1 [6]. When horizontal and vertical prism patterns are overlapped, the pyramid pattern can be made as shown in Figure 1(a). If the diamond tool rotates 45°, rhombic pyramid pattern is obtained.

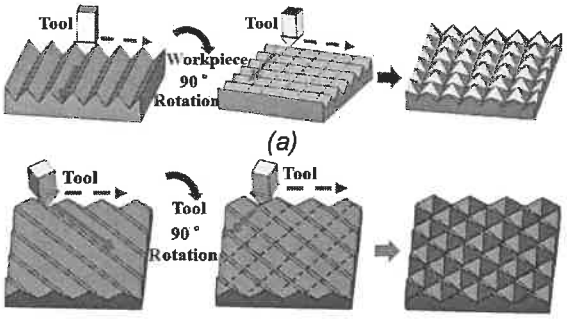

FIGURE 1. Machining method of micro square type pyramid pattern on flat mold.

Figure 2(a) contains schematic diagrams how to machine the pyramid patterns on the large roll mold. First, spiral prism pattern is machined along circumference of the roll mold, and then the second prism pattern is machined along axial direction. The roll mold rotates continuously at the first step, however, the roll

mold stops during machining and rotate just pattern pitch after machining one line at the second step.
Figure 2(b) shows how to machine diamond type pyramid pattern. First, spiral prism patterns are machined along oblique line on the roll mold using a 90° V shape tool. Next, other spiral prism patterns are machined along opposite oblique line. Since the tool should move fast rapidly during roll mold's rotating, a few technologies are very important such as to control rotation of the roll mold discretely, to move of the tool long and to install the tool at exact positon with very high resolution.

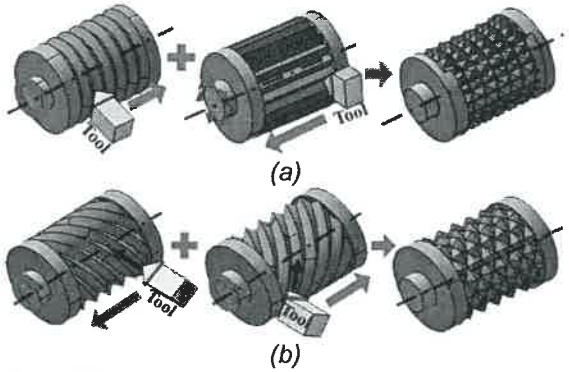

FIGURE 2. Machining method of (a) square type pyramid pattern and (b) diamond type pyramid pattern on roll mold.

TECHNICAL CHALLENGES OF MACHINING PYRAMID PATTERN

The major technical difficulty of machining micro square type pyramid pattern is mismatch of the apex of the pyramid. The mismatch is induced by positioning error of the tool at the second machining. When the flat mold rotates 90° after the first machining, the relative height of the tool from the flat mold can be different from the height at the first machining due to insufficient accuracy of rotating stage. A similar problem is occurred in the case of the roll mold. When the tool rotates 90° after the first machining, the relative height of the tool also varies. When the tool is located higher than expected, machining depth of the second prism pattern is smaller than expected and the apex would be a line (Figure 3(a)). When the tool is located lower, the apex collapses and the height of the pyramid would be lower than designed (Figure 3(b)). There are also cross lines having different height on base plane at the two cases. When the tool is not located facing vertical direction perfectly from the first prism pattern, machining error is also occurred.

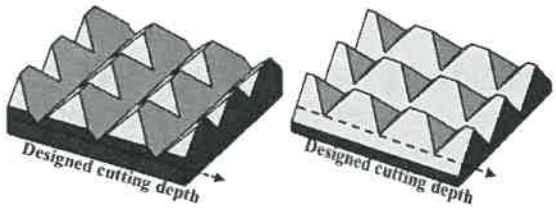

FIGURE 3. Examples of machining errors of machining pyramid patterns.

A precise tool rotating was designed and installed with a tool position calibration system solving the problems, and ultra-fine micro square type pyramid pattern on roll mold was machined in this study.

MACHIINING SYSTEM

Figure 4 presents a photo and a schematic diagram of ultra-precise machining system used in this study. The system consisted of rotating axis (C axis), cutting axis (X axis) and feeding axis (Z axis). Hydraulic static bearing spindle controlling the C axis can rotate up to 500rpm, divide until 0.0001°, therefore, can machine micro prism pattern under 50μm pitch. Linear motors control X axis and Z axis with 10nm repeatability. The maximum size of the roll mold which this system can machine is 350mm diameter, 1,600mm length and 350kg weight.

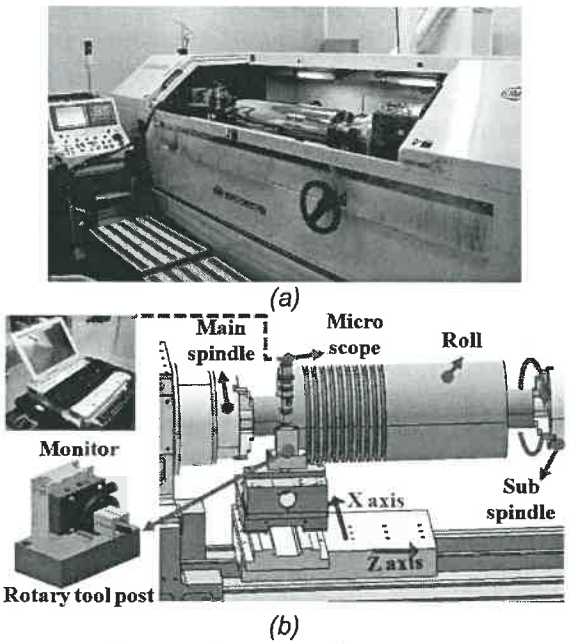

FIGURE 4. (a) A photo and (b) a schematic diagram of ultra-precise machining system.

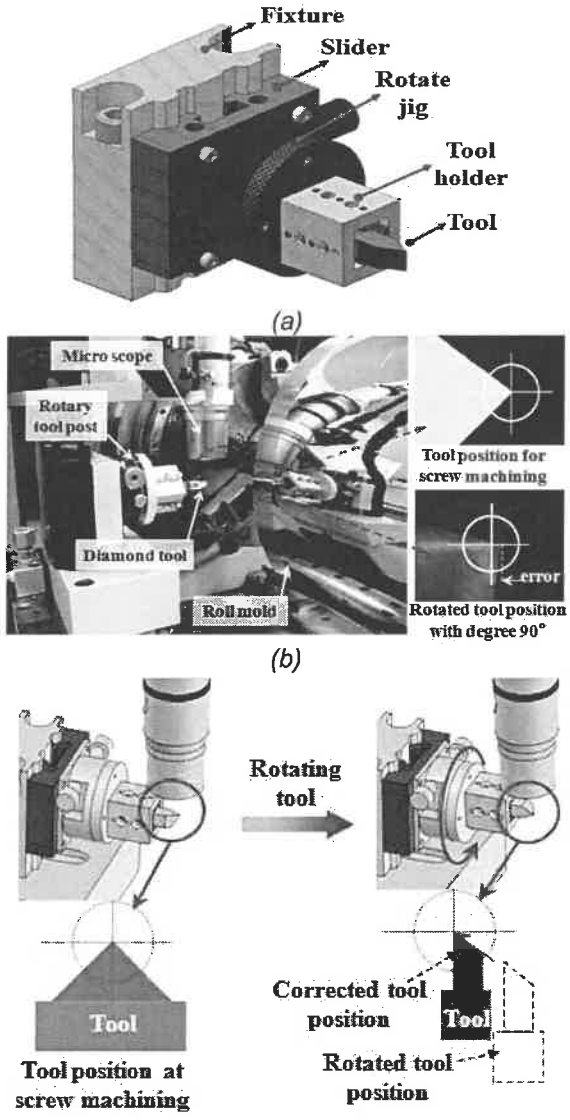

FIGURE 5. (a) A schematic diagram of precise rotation system, (b) how to measure and (c) how to calibrate the relative height of the tool.

Figure 5 shows the precise tool rotating system and how to measure and calibrate the position of the tool with the tool position calibration system. The rotating system consisted of a micro drive module whose rotating accuracy was 360°±0.01° and position accuracy was 1μm. The tool position calibration system had an optical microscope whose magnification was 20~100 times. It was possible to control the relative height of the tool constantly after the first machining in virtue of the system.

Experiments of machining micro square type pyramid pattern and discussion

The roll mold was machined by 90° diamond tool for verifying the rotating system. The machined roll mold plated by copper has 1,200mm length and 300mm diameter. The target shape of the pyramid pattern was 50μm pitch and 25μm height. The details are explained in Figure 6.

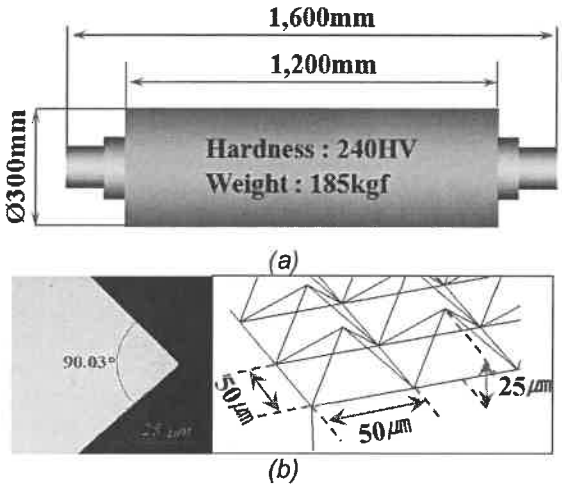

FIGURE 6. (a) Specifications of machined roll mold and (b) a tool and shape of pyramid pattern.

The first machining (spiral prism pattern) was performed by moving the tool at 50μm/rev along the circular direction on the roll mold rotating at 300rpm. Then, the tool was rotated 90° and moved longitudinally at each 50μm circular direction step by step. The relative height of the tool was observed and calibrated by the measuring system after 90° rotation and before the second machining. Each machining of the first and the second step consisted of the same four overlapping machining passes which were 10μm, 10μm, 10μm and 5μm in order, and the total machining depth was 35μm. The details of machining conditions are presented in Table 1.

TABLE 1. Machining conditions of pyramid pattern

Machining order	1st step	2nd step
Machining method	Screw machining	Shaping
Tool setting degree	0°	90°
Spindle RPM	300	-
Division degree	-	0.0191°
Feed rate of Z axis	50 μm/rev	8000 mm/min
Length of machining	1000 mm	

Pitch of pattern	50 ㎛			
Depth of machining (/pass)	1st	2nd	3rd	4th
	10 ㎛	10 ㎛	10 ㎛	5 ㎛

Results of each overlapping machining pass are presented in Figure 7. The photos are replicas of the machined patterns on the roll mold. Since the final surface of the roll mold was lower than as started (total machining depth: 35μm, the height of the pattern: 25μm), the roll mold was machined very slightly at the first overlapping pass of the second step as shown in Figure 7(a). Some prism pattern were formed at the second pass (Figure 7(b)), and pyramid patterns were observed at the third pass, however, the apex of the pyramid pattern was still a line (Figure (7c)). Finally, the pyramid patterns were formed completely and the apex was machined as a point at the fourth pass as shown in Figure 7(d). The machining result was much improved after installing the precise tool rotating system and the tool position calibration system developed in this study. The improvement can be verified clearly by comparing Figure 7(d) and Figure 3(b).

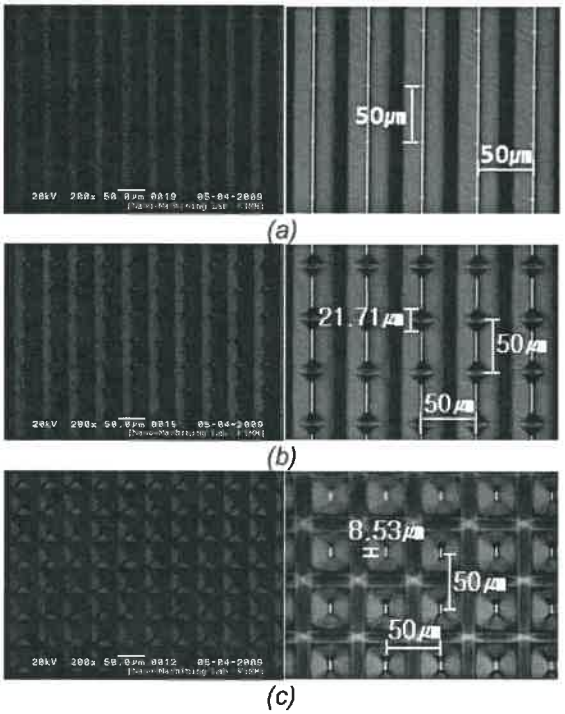

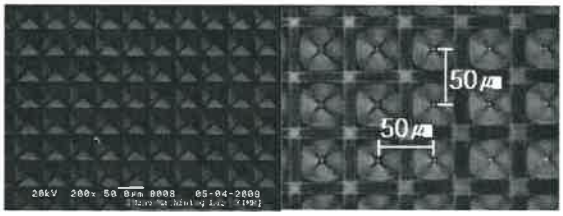

FIGURE 7. Replicas of machining patterns of (a) 1st pass, (b) 2nd pass, (c) 3rd pass and (d) 4th pass.

CONCLUSIONS

1. A precise tool rotating system and a tool position calibration system were developed and installed at ultra-precise machining system for machining micro square type pyramid.
2. The two systems played very important role to machine sharp pyramid pattern (pitch 50μm and height 25μm) accurately and to decrease machining errors significantly.
3. The new systems can be applied to machine more complex patterns such as triangle type pyramid pattern.

REFERENCES

[1] Kim S, et al. Micropatterns of W-Cu Composites Fabricated by Metal Powder Injection Molding. Metals and materials international. 2007; 13(5): 391-395.

[2] Park S, Je T. A Study on Micro Prism Pattern Roll Mold Processing using Cutting Method of Multiple Screw Thread. Proceeding of the KSPE 2008 Spring Conference. 2008: 629-630.

[3] Kim S, Yoo Y, Seo Y, Je T, Whang K, Choi D. Fabrication of Ni Stamper based on Micro-Pyramid Structures for High Uniformity Light Guide Pane(LGP). J. of KSPE. 2006; 23: 174-178.

[4] Shin Y, Choi S, Park S, Lee E. 4-Prism sheet of back light unit for LCD. United States Patent. No. 0097708A1, 2007.

[5] Je T, Park S, Choi D, et al. Influence upon Machining Accuracy of Micro-Pattern Roll Mold Processed by Temperature Variation. Korean Society For Technology of Plasticity. 2008; 18(2): 107-111.

[6] Je T, Choi D. A study of the manufacturing technology for micro pattern mold of large area using planing method. Proceeding of the KSPE 2007 Spring Conference. 2007: 777-778.

DIAMOND TOOL WEAR REDUCTION MECHANISMS IN ELLIPTICAL VIBRATION ASSISTED MACHINING

Brandon M. Lane, Thomas A. Dow, Ronald O. Scattergood
Precision Engineering Center
North Carolina State University
Raleigh, North Carolina, USA

INTRODUCTION

Studies [1] have shown the benefits of applying micrometer-scale elliptical vibration (EVAM) motion to a tool during diamond turning (DT). In this process, the tool comes out of contact with the workpiece over part of each cycle. Reported benefits include a decrease in machining forces, tool temperatures and wear of the diamond tool. The particular causes for decrease in force and wear using EVAM depend, to some extent, on the general lack of understanding of tool wear mechanics of a normal DT operation. The research discussed here will provide insight into EVAM cutting mechanics and create the necessary foundation for future industrial implementation.

A baseline understanding of tool wear for standard (non-vibration) DT is necessary before proceeding with EVAM wear studies. Correlation of diamond tool wear with standard models allows different workpiece materials or chemical processes to be evaluated. Paul and Evans [2] studied the chemical aspects of diamond tool wear. They theorized that the volumetric wear rate would follow the Arrhenius equation:

$$\frac{dV}{dt} = A \exp\left(\frac{E_a}{RT}\right) \qquad (1)$$

where V is the worn volume, R is the gas constant (8.3144 J/mol), and T is process temperature (K). A and E_a, the pre-exponential constant and activation energy, are empirical constants specific to the interacting materials. The wear rate dependence on temperature is the same function for catalytic reactions or diffusive reactions [2], though individual process contributions are not considered here.

To determine the empirical constants, tool wear and tool temperatures must be determined. To measure the tool wear, a process called Electron Beam Induced Deposition (EBID) has been developed and a tool cutting model is used to estimate the tool temperature.

EBID [3] is performed in a scanning electron microscope (SEM) by creating a hydrocarbon line on the diamond tool perpendicular to the cutting edge. This line provides the contrast needed to measure the edge and create a 2D worn profile. If orthogonal cutting is conducted with a straight-edged tool, the worn volume can be estimated as the 2D worn area multiplied by the workpiece width. Because EBID process requires costly time on the SEM, a technique using a scanning white light interferometer (SWLI) was developed that allows rapid wear land measurements in addition to the more precise EBID measurements [4].

The second input needed is the local tool temperature. Since this is nearly impossible to measure, a finite element (FE) cutting model was used to estimate the tool/workpiece temperatures. AdvantEdge, developed by ThirdWave Systems, provides the forces and temperatures necessary to complete the Arrhenius model for tool wear.

An elliptical tool vibration routine was recently added to AdvantEdge. An EVAM simulation provides tool temperatures which are then supplied to the Arrhenius wear model developed from conventional machining experiments. A conventional cutting simulation with the same parameters depth of cut and surface speed allows direct comparison of forces, temperatures and other factors that may contribute to tool wear.

CONVENTIONAL MACHINING ON ST1215

Experimental Setup

To crate the orthogonal cutting conditions, fins were machined into a 4" diameter round of St1215. The fins were 1.2 mm wide and the straight-edged diamond tool (supplied by Chardon Tool) was 2.1 mm wide. This creates a localized section of wear on the tool, shown in Figure 1.

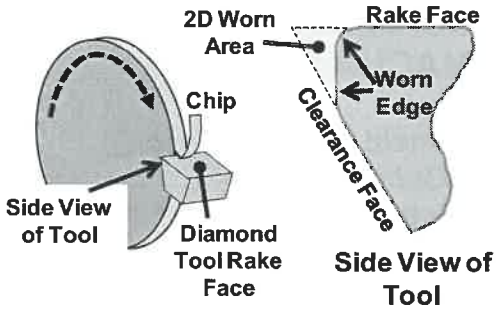

FIGURE 1. Schematic of orthogonal machining St1215 experiments and measured 2D worn area.

One steel fin was machined at 1 µm depth of cut at 1.06 m/s on an ASG 2500 DT machine with a continuous stream of Mobilmet Omicron cutting fluid and compressed air to remove the chips. After machining a certain distance (typically 20 m), the tool was removed and cleaned. A 5% nitric acid solution was used to remove any pickup incurred while machining. The worn edge of the tool was examined via SWLI or a combination of SWLI and EBID [3,4]. This process was repeated for successive machining distances, and volumetric wear loss as a function of time was acquired. This process was then repeated for machining speeds of 2.12 m/s and 4.24 m/s for a total of three volumetric wear rates.

Conventional Machining FE Simulations

Three two-dimensional machining simulations were created in AdvantEdge that mimicked the conventional machining experiments [4]. AdvantEdge supplies a library of tool and workpiece materials. St1215 was not available, so AISI-1118 steel was used in the simulation. Density, hardness, and thermal conductivities of 1215 and 1118 steel differ less than 10% [5]. Contour temperature plots from simulation results showed the maximum tool temperature occurred at the tool tip, and steady state values were extracted from the simulation results.

Arrhenius Wear Model Results

Wear rates determined from conventional machining experiments were combined with maximum tool temperatures from FE simulations to create an Arrhenius plot shown in Figure 2. Three points are shown; one for each machining speed. Though the three points did not show a linear trend, a range of Arrhenius empirical constants are suggested and given in Table 1.

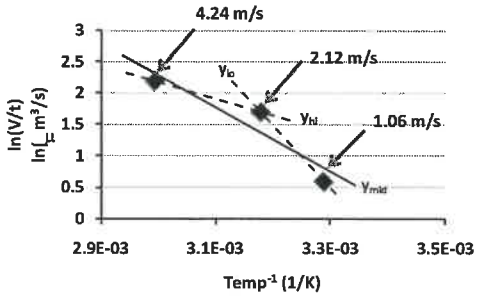

FIGURE 2. Arrhenius plot of measured diamond tool wear rate and peak tool temperatures from FE simulations.

TABLE 1. Arrhenius constants from Figure 3.

Line in Figure	Activation Energy, E_a	Pre-exponential Constant, A
y_{hi}	83.5 kJ/mol	4.08×10^{14} µm³/s
y_{mid}	42.5 kJ/mol	4.5×10^{7} µm³/s
y_{lo}	22.1 kJ/mol	2.52×10^{4} µm³/s

Review of several papers [2] indicated activation energy estimates from 80-300 kJ/mol for catalytic metal-on-metal reactions or graphitic carbon diffusion into various metals. The lower E_a determined in Figure 2 and Table 1 is likely a result of constant tool contact with new, untouched workpiece material during the cutting process.

EVAM SIMULATIONS

An EVAM simulation was created in AdvantEdge utilizing the elliptical toolpath routine. Figure 3 shows the simulated workpiece and tool size, and the FE simulation mesh. For comparion, a conventional machining simulation was also created with the vibration turned off.

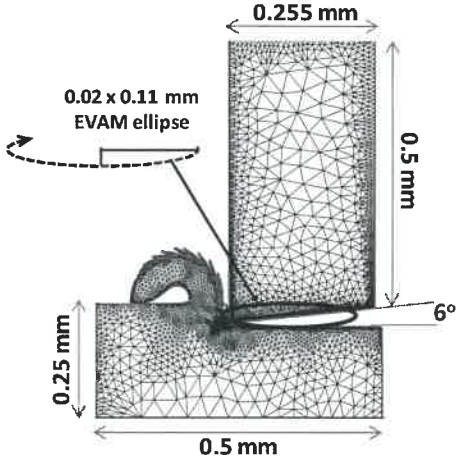

FIGURE 3. Simulated tool size, mesh, and boundary conditions.

Table 2 gives the cutting conditions assumed in the AdvantEdge EVAM simulation. Depth of cut in the EVAM simulation is defined as distance from workpiece surface to the lowest point of the toolpath.

TABLE 2. Cutting parameters for EVAM FE simulations

Depth of Cut	40 µm
Ellipse Minor Axis	20 µm
Ellipse Major Axis	110 µm
EVAM Frequency	10 kHz
Workpiece Velocity	0.2 m/s

Forces, Temperature, and Chip Formation

Maximum tool temperatures and forces were extracted from the EVAM and conventional machining simulations, shown in Figure 4.

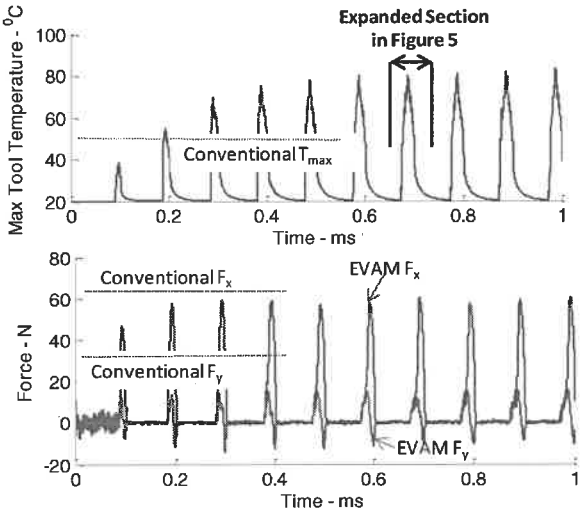

FIGURE 4. Maximum tool temperature and tool forces extracted from the St1118 EVAM simulation.

Peak tool temperatures from the EVAM simulation were higher than steady state temperatures from the conventional machining simulation. This is due to the higher peak tool tip velocity during EVAM. The horizontal speed ratio (HSR) is an important EVAM parameter [1] created by dividing the forward velocity of the ellipse center by the peak ellipse velocity. Larger values of HSR produces higher EVAM velocities that lead to higher tool temperature. Another observation is the negative F_y force seen at timepoint C in Figure 6. This is due to higher speed of the tool vs. the chip that 'lifts' the chip from the workpiece. This change in direction of the tool force has been proposed as a key factor for the reduced tool forces in EVAM [6].

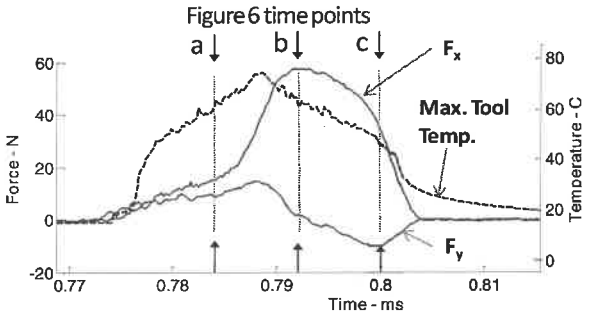

FIGURE 5. Expanded view of data composing 7th peak in Figure 4.

The heat generated in the primary shear zone is shown in Figure 7. Initially, the EVAM tool creates a smaller chip with localized heating. As the tool contacts the main chip, the shear zone extends behind the main chip. Friction is then reversed as the tool pushes and lifts the chip.

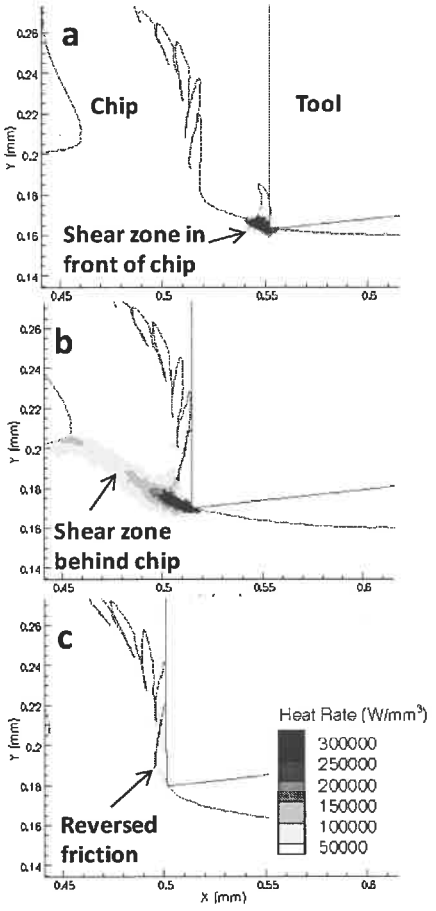

FIGURE 6. Heat generation rate contour plot of tool and chip from the EVAM simulation. Screenshots correlate to time points in Figure 5.

To fully understand the benefits of EVAM, multiple simulations varying ellipse shape, HSR, material and heat transfer parameters must be compared. Increasing peak tool temperature shown in Figure 4 (top) is a result of the workpiece heating up toward a steady state value each time the tool comes in contact. This shows that the relative heat transfer rates of the diamond and workpiece are important factors when considering EVAM tool temperatures.

Arrhenius Wear Model Applied to EVAM

Applying Eq. 1 to the temperature during an EVAM cycle gives the wear rate (dV/dt) as a function of time in Figure 7. During the EVAM cycle, however, the tool is only in contact a fraction of the total EVAM period (about 25%). The average wear rate is determined by finding the total wear volume during contact, then averaging over the total EVAM cycle period.

$$\left(\frac{dV}{dt}\right)_{Avg.} = \frac{1}{T_{Total}}\left(\int_{T_{Contact}} \frac{dV}{dt}\,dt\right) \qquad (2)$$

During conventional machining, the tool is always in contact and T_{Total} is equivalent to $T_{Contact}$ in Eq. 2.

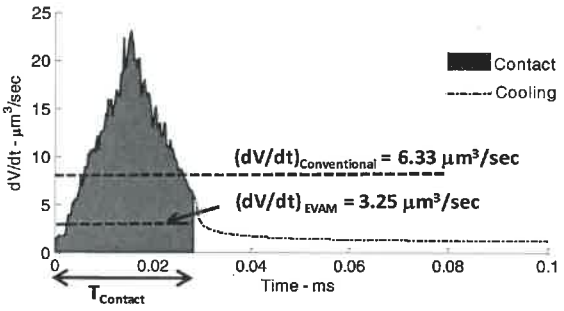

FIGURE 7. Maximum tool temperature for one EVAM cycle (Figure 5) is applied to the Arrhenius wear model (Equation 1) to give the dV/dt curve. Average wear rate for the EVAM tool is determined by integrating the dV/dt curve according to Equation 2.

Figure 7 shows that although the peak temperature during the EVAM cycle is higher than the steady state temperature in conventional machining, the average wear rate is nearly 50% less. This is because the calculated wear rate only applies while the tool is in contact but the average wear rate depends on the total time. However, as HSR decreases, EVAM temperatures increase due to higher velocities. This suggests that an HSR exists where the EVAM wear rate equals that of conventional machining and demonstrates that HSR is an important parameter in determining tool wear in addition to its relationship with surface finish.

CONCLUSIONS

1.) A chemical wear model was developed based on the Arrhenius equation. Wear measurements made during conventional DT of St1215 were coupled with tool temperatures obtained from FE simulations to construct an Arrhenius plot. The proposed activation energy is in the range of 22-83 kJ/mol.

2.) An EVAM cutting simulation was compared with a conventional cutting simulation with the same machining parameters minus tool vibration. Peak EVAM tool temperatures were higher than steady state conventional machining temperatures due higher peak velocities. But despite higher temperatures, application of the Arrhenius wear model gives an average wear rate of the EVAM tool 50% less than conventional machining. Reduced contact time is the major contributor to the lower EVAM wear rate.

ACKNOWLEDGEMENTS

ThirdWave Systems provided AdvantEdge machining simulation software and the elliptical tool motion module. Special thanks Chardon Tool for supplying diamond toolsThis paper was written as part of work supported by NSF grant SMMI-0800560 monitored by G. Hazelrigg.

REFERENCES

[1] Brehl DE, Dow TA. Review of Vibration-Assisted Machining, Precision Engineering. 2008; 32: 153-172.

[2] Paul E, Evans CJ, Mangamelli A, McGlauflin ML, Polvani RS, Chemical Aspects of Tool Wear in Single Point Diamond Turning, Precision Engineering. 18; 4-19

[3] Shi M, Lane B, Mooney CB, Dow TA, Scattergood R, Diamond Tool Wear Measurement by Electron-beam-induced Deposition, Precision Engineering. 2010; Article in press.

[4] Lane B, Development of Predictive models for Abrasive and Chemical Wear of Diamond Tools, MS Thesis, North Carolina State Univesity, 2010

[5] Matweb.com

[6] Shamoto E, Moriwaki T, Study on Elliptical Vibration Assisted Machining, Annals of the CIRP: 1994; 43: 35-38

HIGH SPEED MILLING OF AN ALVAREZ OPTIC

Jennifer L. Lineberger[1], Brian S. Dutterer[1], Matthew A. Davies[1]
Paul Smilie[2] and Thomas J. Suleski[2]
[1]Mechanical Engineering Department
[2]Department of Physics and Optical Science
University of North Carolina at Charlotte
Charlotte, NC, USA

INTRODUCTION

Single crystal diamond turning of "soft semiconductors", such as germanium in the ductile mode, has been established [2] and has many uses for infrared devices. The goal of this work is to enable multi—axis contour machining of zinc selenide and germanium to generate freeform surfaces. The practical goal which has driven the research is the manufacture and testing of an Alvarez lens for the infrared regime. We believe this will be the first Alvarez lens, an optical device with many potential uses. The project has: (1) involves the design of small scale milling tools with negative rake angles that had not previously been available and tested in these materials; (2) testing to determine if ductile mode milling is possible and under what conditions; (3) determination of milling parameters necessary for producing surface finish and quality of freeform optics suitable for use in the infrared. While we have focused on germanium and zinc selenide for this project, the general results and approach are expected to be broadly applicable to other materials as well.

Alvarez Lens

The Alvarez lens was invented in 1967 by Luis Alvarez [1]. It is a two-element lens, composed of two cubic phase plates, with the capability of variable focal length through lateral shifts. Each cubic phase plate is composed of a flat surface on one side and a surface defined by a cubic equation on the other side (Eq. (1)).

$$z(x, y) = 0.0012\,(\tfrac{1}{3}x^3 + xy^2) + 2.5 \qquad (1)$$

When assembled, the two cubic surfaces are inverted with respect to each other and aligned along the z-axis so that at each point the total thickness of the material along z is constant. Thus, if aligned in the x-y plane, and the assembly acts as a plate of constant thickness with infinite focal length in z. When the plates are laterally shifted in the x-y plane, by an equal amount in opposite directions, a composite spherical surface is created from the combination of the shifted cubic surfaces. The composite spherical surface changes by varying the amount of lateral shift in the x-y plane, changing the focal length of the system. The Alvarez lens system is shown below in Figure 1.

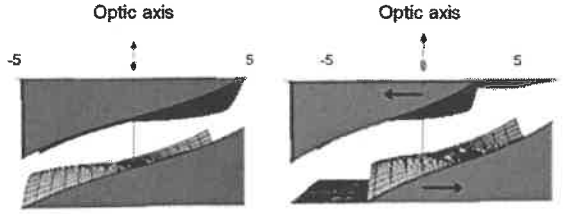

FIGURE 1. Orientation of the Alvarez lens cubic phase plates when aligned (left) and shifted (right).

Stated again, the goal of this work is to manufacture and test such a device in germanium, and later in zinc selenide, by diamond milling the freeform aspheric optical surfaces.

MACHINING TESTS

In order to manufacture the Alvarez lens design, it is necessary to understand the contour milling behavior of each material. To that end, a set of cutting experiments were designed and carried out using both turning (rotating part, stationary tool, no cut interruption, two axis motion) and milling configurations (rotating tool, interrupted cutting, three-five axes of motion). All cutting tests reported were completed using a spray mist of mineral oil for coolant. The materials for all cases were 27.5 mm diameter, single crystal germanium wafers and 30 mm diameter zinc selenide wafers. Prior to all experiments, these wafers were mounted to the C-axis with a vacuum chuck and turned on one side at the least aggressive of the parameter sets listed below to produce a planar optical surface perpendicular to the C-axis of the machine. The purpose of the turning experiments, which have been reported elsewhere in the literature for germanium [2-6], was to help in the tool design

and choice of parameters for the contour milling operations.

Turning Experiments

Turning Setup

Based upon previous work in literature [2-6], a set of turning parameters intended to span the ductile and brittle modes of machining were developed and used for both materials. Surface speed was held constant at 1 m/s, while depths of cut varied between 1 μm and 10μm for both materials and the feed rate was varied between 0.3 micrometers per spindle revolution (μm/rev) and 10 μm/rev. Twelve bands were cut into each type of material using multiple combinations of the aforementioned parameters. Single crystal diamond tools, having nose radii of approximately 1mm and a -25 ° rake angle were used.

Turning Results

Turning experiments in germanium and zinc selenide show that, consistent with existing literature, both materials can be machined in the ductile regime using a negative rake, single crystal diamond tool. Curiously, zinc selenide seemed to behave more favorably in the ductile regime and produced superior surface finishes below 0.5 nm R_a, that correspond quite well with theoretical prediction based on geometry alone.

Milling Experiments

Milling Setup

For the milling experiments, 11 square patches were raster milled using linear cutting movements directed toward the center of the wafer, with a constant step-over of 4 µm perpendicular to the radius of the wafer. The first set of patches (patches 2-7) maintained a constant feed rate (15 mm/min) with varying depths of cut (0.001-0.015 mm) at a constant spindle speed of 50000 rpm and thus a constant cutting (surface) speed. The second set of patches (8-11) maintained a constant depth of cut (0.002 mm) with varying feed rates (50-500 mm/min). Cuts were completed using single flute, single crystal diamond milling tools, with 1 mm nose radii and 0 ° rake angle and -45 ° rake angle. Figure 2 shows the machining setup.

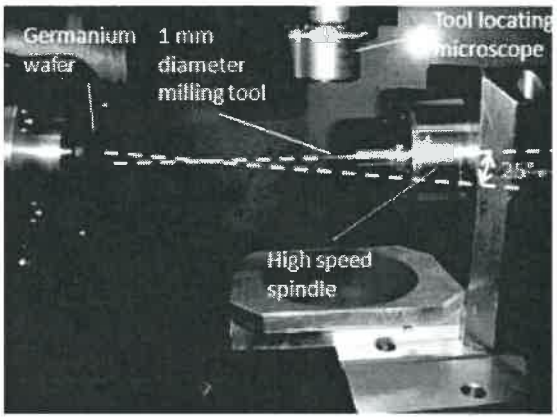

FIGURE 2. Moore 350FG machining setup, showing the rotation axis of the high speed spindle and milling tool, tilted by 25° relative to the C-axis, on which the sample is mounted.

Milling Results

Milling tests showed that both germanium and zinc selenide can be milled with a zero rake angle tool, as has been reported by Davis et al.[7]. After milling with a zero rake tool, the surface finish was limited to approximately 20 nm R_a. But milling with a negative rake tool, better surface finishes were produced than those produced using a zero rake tool by approximately 25%. The disadvantage of using a negative rake angle micro-endmill is that the surface errors (since the tool projection is elliptical) are not as easily understood and compensated for as those produced from using a zero rake angle tool. For this reason, a zero rake angle micro-endmill was used for the fabrication of the prototype germanium optic.

ALVAREZ LENS

Alvarez Lens Tests Setup

Through preliminary turning and milling tests, parameters to create this complex contoured surface were determined. A single crystal, zero rake angle micro-endmill from Contour was used to raster mill all the optical components of the Alvarez lens. A feed of 300 nm/rev, surface speed of 50,000 rpm, and a step-over of 4 µm was used for each cubic phase plate. Each plate was machined in one process to reduce thermal errors, tool location errors, and any possible control loop errors.

Alvarez Lens Results

For the first cubic phase plate (Figure 3), manufactured in germanium, surface roughness analysis and surface measurements were taken

to help determine the achieved surface finish and the actual machined surface.

FIGURE 3. Germanium Alvarez lens cubic phase plate.

Surface Finish Analysis and Results

Quantitative surface roughness measurements were taken across the surface of the first cubic phase plate. Nine different locations across the optic surface were measured in order to obtain an accurate average measurement of the surface roughness. To aid in eliminating error due to the surface curvature and stage tilt, fourth and lower order terms were removed in the measurement analysis. After examination in the scanning white light interferometer (SWLI), an average surface finish of 14 nm R_a or 17 nm RMS was achieved; where R_a values of approximately 2 nm were achieved along the tool feed paths. Average peak-to-valley was measured to be 122 nm, due primarily to the tool step-over.

From the SWLI data (Figure4), it can be seen that the center of the optic contained the best surface finish (9 nm R_a) and that the surface roughness increases gradually at the outer edges of the optic (16 nm R_a).

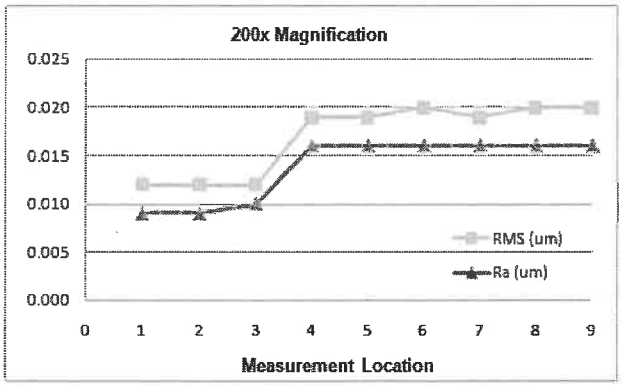

FIGURE 4. Germanium Alvarez lens surface roughness data: 200x magnification with 4th order removed.

Surface Measurement Analysis and Results

Once the Alvarez optic surface was machined and measured in the SWLI, the surface was then measured using a Leitz CMM to verify the contour of the surface. Four hundred data points were measured across the optic surface, in a 10 mm x 10 mm grid pattern, evenly spaced by 0.5 mm. Measurements were taken using a 3 mm ruby sphere probe. The collected data was imported into MATLAB for comparison with the theoretical surface equation (Eq. 1).

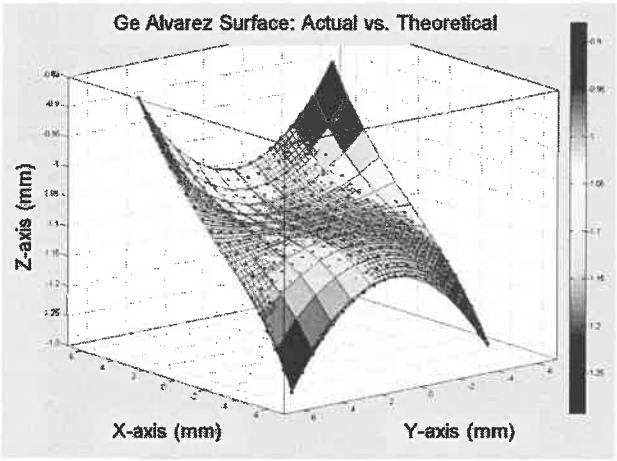

FIGURE 5. Germanium Alvarez cubic phase plate: Theoretical vs. Actual Surface.

Seen above in Figure 5, the "dotted" surface is the MATLAB generated surface fit to the CMM data. The solid surface was generated using the theoretical surface equation. Visually the two surfaces contain the same contour, having only variations on the order of 10 microns at the outer extremities of the part mostly due to a slight rotation between the measured data and the mathematical curve. MATLAB generated the following fit (Eq. 2) to the experimentally measured data.

$$z(x,y) = 0.0004056x^3 + 0.00119xy^2 + 2.4 \qquad (2)$$

Comparing Eq. 1 and Eq. 2, the coefficient for x^3 should theoretically be 0.0004, and it was measured to be 0.0004056, an error of 5.6×10^{-6}. The xy^2 coefficient was measured to be 0.00119 when it theoretically should have been 0.0012 an error of 1.0×10^{-5}. Finally, the standard error (root mean squared error) fr this surface fit is 0.9999. These errors are small enough to not affect the overall focusing capability of the Alvarez optic, but may affect the comparison of measured and theoretical change

in focal length as a function of shift; the behavior of the optic and will be reported in a later publication.

The second cubic phase plate has also been manufactured and the Alvarez optic is being assembled for testing.

CONCLUSIONS

A basic understanding of the machinability of germanium and zinc selenide has been gained through fundamental research and many trials of experimental machining and given us the knowledge needed for producing contoured surfaces, such as an Alvarez lens. A complete Alvarez lens has been machined in germanium, with an overall surface finish of approximately 14 nm R_a, where the machined surface contained minimal errors, on the order of 10^{-3}, when compared to the theoretical surface. Actual surface errors at particular locations on the optic surface are being examined. It may be that the machined surface is better than the capability of the CMM. Eventually the goal is to measure the surface on the machine with an LVDT and develop and algorithm for a surface correction program that generates a corrected toolpath wile the optic remains on the machine.

The final stages of the project consist of the testing the Alvarez lens setup to verify that it has the ability to produce variable focal lengths as a function of lateral shifts in the x-y plane. Once it is verified that the Alvarez lens operates as expected, another set of cubic phase plates will be manufactured in the second material, zinc selenide. While we have focused on germanium and zinc selenide for this project, the general results and approach that were discovered are expected to be applicable to many other materials as well.

ACKNOWLEDGEMENTS

We gratefully acknowledge II-VI Foundation's support of this research.

REFERENCES

[1] Alvarez, L.W. Two-element variable-power spherical lens, U.S Patent 3,305,294. February 21, 1967.

[2] Blackley, W. S. and R. O. Scattergood, Chip topography for ductile-regime machining of germanium, *Journal of Engineering for Industry, Transactions of* the ASME, 116(2), 263-266 (1994).

[3] Blake, P. N. and R. O. Scattergood, Ductile-Regime Machining of Germanium and Silicon, Journal of the American Ceramic Society, 73(4), 949-957 (1990).

[4] Yan, J., K. Maekawa, J. Tamaki, and A. Kubo, Experimental Study on the Ultraprecision Ductile Machinability of Single-Crystal Germanium, JSME International Journal, Series C, 47(1), 29-36 (2004).

[5] Yan, J., K. Maekawa, J. i. Tamaki, and T. Kuriyagawa, Micro grooving on single-crystal germanium for infrared Fresnel lenses, Journal of Micromechanics and Microengineering, 15, 1925-1931 (2005).

[6] Yan, J., Y. Takahashi, J. i. Tamaki, A. Kubo, T. Kuriyagawa, and Y. Sato, Ultraprecision machining characteristics of poly-crystalline germanium, JSME International Journal, Series C, 49(1), 63-69 (2006).

[7] G. E. Davis, J. W. Robleeb, A. R. Hedges, Comparison of Freeform Manufacturing Techniques in the Production of Monolithic Lens Arrays, Preprint (2009).

CREATION OF MICROGROOVE WITH TWO FLAT-ENDS FOR HARD MATERIAL

Yuto Misawa[1],Keiichi Nakamoto[1],Tohru Ishida[1],Yoshimi Takeuchi[1]
[1]Dept.of Mechanical Engineering, Graduate School of Engineering
Osaka University
Yamada 2-1, Suita, Osaka 565-0871, JAPAN

INTRODUCTION

In recent years, miniaturization and high performance are demanded for optical instruments, where microgrooves play an important role. Accordingly, it is required to create high accurate microgrooves on ultraprecision parts. To meet these demands, the development of a new machining technology is required to produce highly accurate and minute devices. Now, rotationally-symmetrical optical parts are manufactured by use of ultraprecision lathe. However, an ultraprecision lathe can not create asymmetrical shape. Machining technology by use of a high degree of freedom is required to create asymmetrical shape. Then, microgroove cutting technology using an ultraprecision machining center has been studied in our laboratory.

As microgroove cutting, two methods have mainly been used. One is the method with a rotational cutting tool, the other with a non-rotational cutting tool[1)]. In case of using a rotational cutting tool, it results in generation of microgrooves with long slopes at the cutting start and end points. On the other hand, a standard cutting with a non-rotational cutting tool can supress the length of slopes although slopes are not completely removed, as illustrated in Figure 1. The existence of slopes causes the unnecessary diffraction and the loss of light. In order to solve these problems, the creation of two flat-ends microgroove is expected in ultraprecision optical parts. Figure 2 shows a two flat-ends microgroove.

In the previous research, two cutting methods with a non-rotational cutting tool were devised so that the microgrooves with two flat-ends could be created[2)]. These methods were successfully applied for soft materials. However, the use of these methods for hard materials causes the breakage of a cutting tool. Thus, new cutting method for hard materials is required to apply for hard materials.

This research proposes a new cutting method with a non-rotational cutting tool for hard materials so that the microgrooves with two flat-ends can be created.

ULTRAPRECISION MACHINING CENTER

The 5-axis control ultraprecision machining centor used in the research is ROBOnano made by FANUC Ltd., which is equipped with three translational axes (X, Y, Z) and two rotational axes (B, C) as illustrated in Figure 3. The resolution of the translational axes and the rotational axes are 1nm and 0.00001 degree, respectively. Aerostatic bearings are employed for the sliding surfaces of all axes as well as their servo motors.

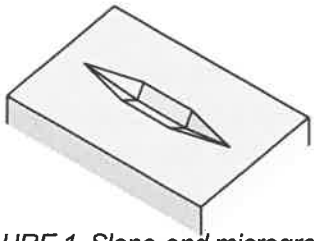

FIGURE 1. Slope-end microgroove

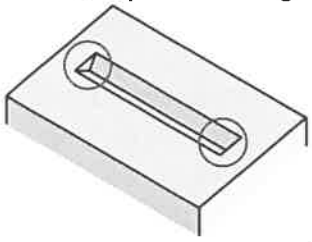

FIGURE 2. Microgroove with two flat-ends

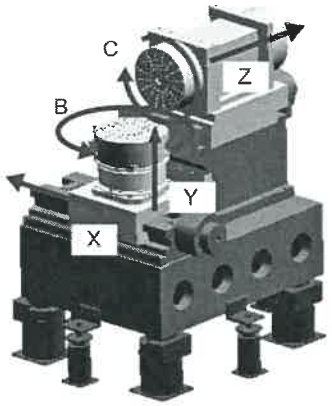

FIGURE 3. Structure of FANUC ROBOnano Ui

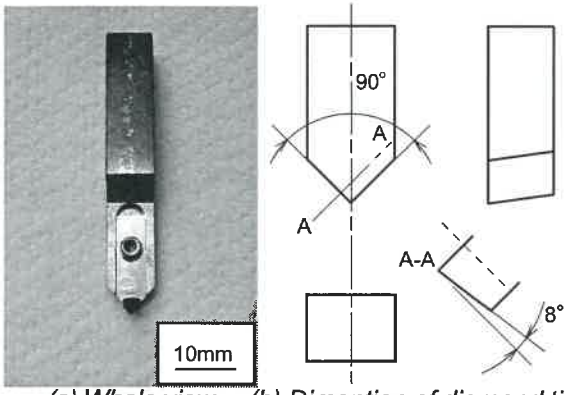

(a) Whole view (b) Dimention of diamond tip

FIGURE 4. Non-rotational single crystal diamond cutting tool

CREATION OF MICROGROOVES WITH SINGLE FLAT-END

Cutting tool

At first, a new cutting method for hard materials is proposed to create microgrooves with single flat-end. A cutting tool needs hardness and wear resistance to cut hard materials. In the research, the non-rotational cutting tool made of a single crystal diamond with the angle of 90 degree is used, as shown in Figure 4. The rake angle of this cutting tool is 0 degree, and the relief angle is 8 degree.

Machining method of single flat-end microgroove

Figure 5 shows the arrrangement of a non-rotational cutting tool and a workpiece. The workpiece is fixed on the B table. At first, the machining method of single flat-end microgroove is to indent the non-rotational cutting tool perpendicularly to the workpiece

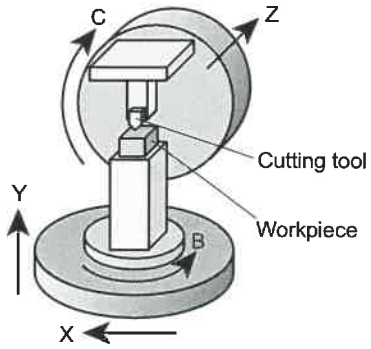

FIGURE 5. Arrangement of a cutting tool and a workpiece

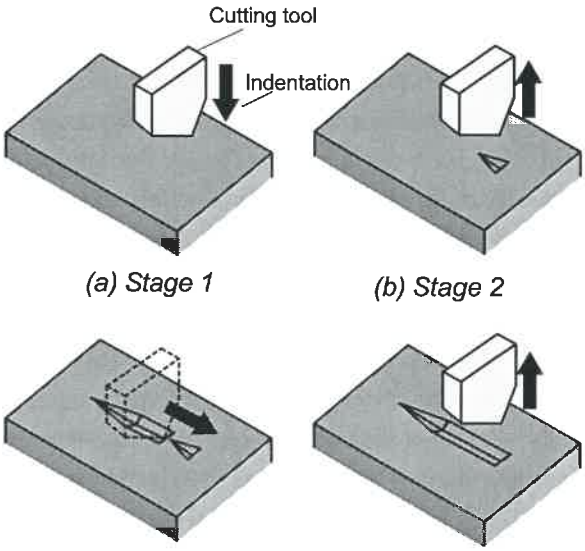

(a) Stage 1 (b) Stage 2

(c) Stage 3 (d) Stage 4

FIGURE 6. Machining method of single flat-end microgroove

surface, as illustrated in Figure 6(a). Next, the cutting tool is pulled up to cut from backward to the indentation point, as illustrated in Figure 6(b) and (c). Then, the cutting tool is moved upward, as illustrated in Figure 6(d). One cutting path consists of these four processes. By repeating this cutting path, single flat-end microgroovs with arbitrary depth can be created.

This method has two advantages, compared to the previous methods[2]. The first advantage is to be able to decide the depth of cut. The second one is that the negative tool rake angle does not become large. Thus, the cutting tool is not easily broken because the cutting force is supressed.

TABLE 1. Machining conditions

Depth of one indentation	1 μm
Depth of cut	1 μm
Indentaton rate	10 μm/min
Feed rate	50 μm/min
Cutting fluid	Kerosene

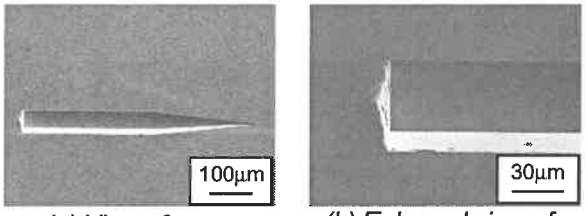

(a) View of groove (b) Enlarged view of groove end

FIGURE 7. Machined result

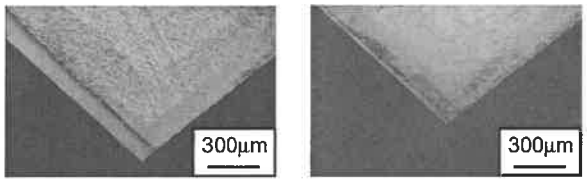

(a) Before machining (b) After machining

FIGURE 8. Rake surface of cutting tool

Machining conditions

Machining conditions are listed in Table 1. In the research, Ni-P plating is used as hard materials, whose vickers hardness is 500. Therefore, the feed rate and the indentation rate are set to be slow.

Results and Discussion

Figure 7 is SEM micrographs of machined result of Ni-P plating. These figures were taken above the workpiece surface at 30 degree. Machining time is 2 hours. Total machining distance is 2.8 mm. From these fiures, it found that single flat-end microgroove with sharp edge was machined. Figure 8 is the rake surface of cutting tool. From these fiures, the cutting tool was not broken after machining. Therefore, it is comfirmed that new cutting method can create microgrooves with single flat-end under the appointed machining conditions.

CREATION OF MICROGROOVE WITH TWO FLAT-ENDS

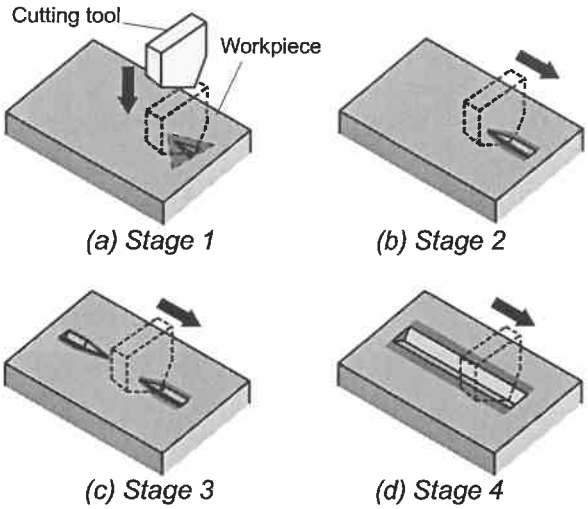

(a) Stage 1 (b) Stage 2

(c) Stage 3 (d) Stage 4

FIGURE 9. Machining method of microgroove with two flat-ends

Cutting method of microgroove with two flat-ends

The new cutting method is applied to create microgrooves with two flat-ends. The cutting method utilizes two microgrooves with single flat-end, as shown in Figure 9. At first, a microgroove with single flat-end is machined by the same method and the same non-rotational cutting tool, as illustrated in Figure 9(a) and (b). Next, B table is rotated by 180 degree. Then, another microgroove with single flat-end is machined, as illustrated in Figure 9(c). Finally, two microgrooves with single flat-end are connected, as illustrated in Figure 9(d). By using this cutting method, two flat-ends microgroovs with arbitrary depth can be created.

Position error correction (B axis)

The new cutting method of microgroove with two flat-end uses the rotation of B axis. Therefore, it is required to detect the rotational center of B axis, which can be detected by machining a soft material. In this research, oxigen-free copper is used as the soft material. At first, a microgroove is machined, as illustrated in Figure 10(a). Next, B table is rotated by 180 degree, and a microgroove is machined in the same way as illustrated in Figure 10(b). Then, the central coordinate O between the point A and B is measured, as illustrated in Figure 10(c). The co-

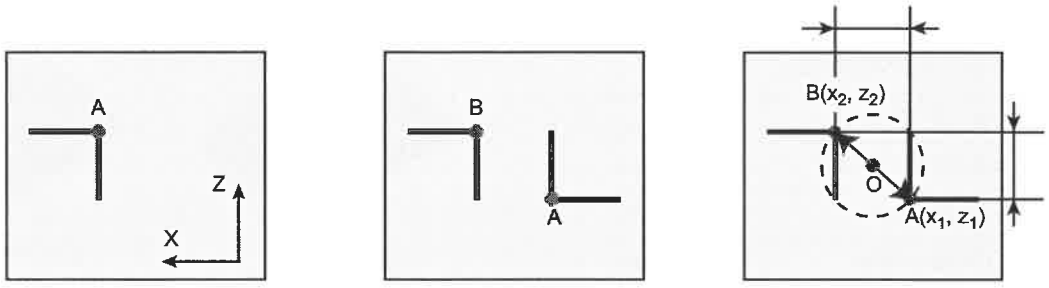

(a) Stage 1 (b) Stage 2 (c) Stage 3

FIGURE 10. Position error correction (B axis)

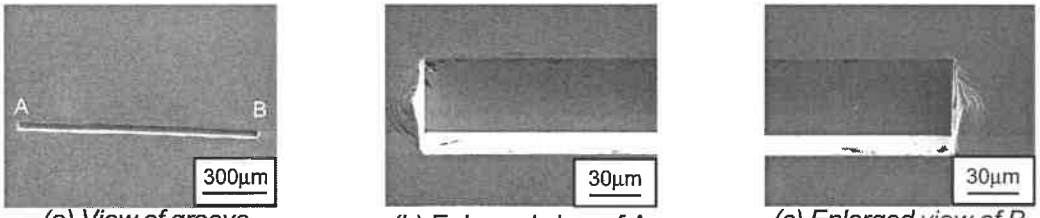

(a) View of groove (b) Enlarged view of A (c) Enlarged view of B

FIGURE 11. Machined result

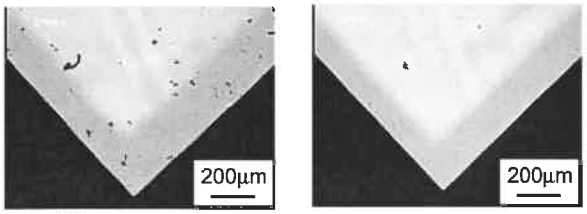

(a) Before machining (b) After machining

FIGURE 12. Rake surface of cutting tool

ordinate (x, z) of O is obtained by the following equation (1). From these processes, the rotational center of B axis is determined.

$$O(x,z)=\left(\frac{x_1+x_2}{2},\frac{z_1+z_2}{2}\right) \quad (1)$$

Results and Discussion

Figure 11 are SEM micrographs of machined result of Ni-P plating. These figures were taken above the workpiece surface at 30 degree. Machining time is 4 hours under the machining conditions shown Table 1.. Total machining distance is 11.1 mm. From these figures, it found that two flat-end microgrooves with sharp edge were created. Figure 12 are the rake surface of cutting tool, where the cutting tool was not broken after machining. Therefore, it is comfirmed that the new cutting method can create microgrooves with two flat-ends under the appointed machining conditions.

CONCLUSION

A new microgrooving method with two flat-ends on hard materials is proposed by repeating an indentation method to make a single flat-end. As the result of machining, it is confirmed that the new cutting method can be applicable to create two flat-end microgrooves on hard materials.

ACKNOWLEDGEMENT

The authors would like to expres their sincere gratitude to NIKON CORPORATION for providing Ni-P platting.

REFERENCES

[1] Tetsuya KUMON, Tohru ISHIDA, Yoshimi TAKEUCHI, Tomohiko KAWAI and Kiyoshi SAWADA Creation of Ultraprecision V-shaped Microgrooves Using Non-Rotational cutting Tools. Journal of the Japan Society for Precision Engineering. 2004; Vol. 70, No. 10: 1301-1305.

[2] Masahiro MUROTA, Takaaki SUZUMURA, Tohru ISHIDA, Yoshimi Takeuchi, Tomohiko Kawai and Kiyoshi Sawada Creation of Flat-end V-shaped Microgrooves by Non-Rotational cutting Tools. Journal of the Japan Society for Precision Engineering. 2004; Vol. 70, No. 5: 677-682.

THERMO-CHEMICAL WEAR STUDY ON ORTHOGONAL DIAMOND TURNING OF STEEL AND STAINLESS STEEL

Meirong Shi, Brandon Lane, Thomas A. Dow and Ronald O. Scattergood
Precision Engineering Center
North Carolina State University
Raleigh 27695, North Carolina, USA

INTRODUCTION

It is well known that ferrous materials are difficult to fabricate efficiently using the conventional diamond machining. The diamond tool wears at an extremely high rate when turning the ferrous materials, especially those with low carbon content. The wear rate of diamond turning mild steel has been estimated 10^4 times greater than that of turning brass with comparable hardness [1]. The very high rate of wear was generally believed to be caused by the thermo-chemical mechanism rather than a mechanical wear process [2].

Elliptical vibration assisted machining (EVAM) is proven to be one promising method to suppress the tool wear and improve the surface finish. However, the inherent mechanisms for the thermo-chemical diamond tool wear are still not clear, because many factors, such as temperature, pressure and the state of the tool-workpiece interface, are difficult to quantify during the wear process. To quantitatively explain the wear behavior of diamond tool during machining, accurate measurement of diamond tool wear as a function of the cutting distance for given machining conditions and materials is necessary. A quantitative study of thermo-chemical wear of diamond tools while machining ferrous material is described in this work.

WORKPIECE MATERIAL SELECTION

1215 steel is a low carbon steel with good machinability. The composition is mainly pure iron (98.42-98.95%) and the carbon content is less than 0.09 % (by wt %). The Vickers hardness of 1215 steel is 1850 MPa. 416 stainless steel is martensitic when the sulfur content is >=0.15%. In this study, the 416 stainless steel was selected as another workpiece material. The Vickers hardness of 416 stainless steel is 1223 MPa. To separate the abrasive wear effect, 6061 Al, with a hardness of 1185 MPa, was selected as the baseline.

Hard inclusions in the workpiece material can cause abrasive grooves on the cutting tool. Microstructures of the 6061 Al, 1215 steel and 416 stainless steel were studied to further compare the abrasive wear. From the inclusion distribution in the three workpiece materials, it was found that 6061 Al has more and larger particles than 1215 steel and 416 stainless steel. For 6061 Al, the area fraction of the inclusions is 3% and the average size (area of the particle) is about 44 μm^2. They are 1.2%, 21 μm^2 for 1215 steel and 2.1%, 5 μm^2 for 416 stainless steel. From the comparison of microstructures and hardness of the three materials, it can be expected that 6061 Al will have comparable abrasive wear as 1215 steel and 416 stainless steel.

ORTHOGONAL CUTTING SETUP

Orthogonal machining of 6061 Al, 1215 steel and 416 stainless steel was performed on the ASG2500 diamond turning machine. Conditions for the three cutting experiments were similar. The average cutting speed was 2.8 m/s for 6061 Al and 2.13 m/s for 1215 steel. Two cutting speeds of 1.06 m/s and 2.13 m/s were used for 416 stainless steel. The depths of cut were 2 µm for 6061 Al and 1 µm for both 1215 steel and 416 stainless steel, respectively. Four 6061 Al disks with the total of 10 km cutting distance were machined to study the gradual abrasive wear. For 1215 steel, a total cutting distance was only 20 m in 5 m increments. In the case of two cutting experiments on 416 stainless steel, total cutting distances of 90 m and 85 m were used. The width of the disks for 6061 Al, 1215

steel and 416 stainless steel were 0.81 mm, 1.2 mm and 1 mm, respectively. The same single crystal diamond tools were used in the cutting experiments (relapped between experiments), which have a flat nose with 6° clearance angle. The edge radius of the new sharpened diamond tool was 16 to 25 nm, respectively. All cutting experiments were done with the cutting fluid and air flow.

Diamond tool wear was measured using electron-beam-induced deposition (EBID) in a field emission scanning electron microscope (FESEM) and also with a white light interferometer. Worn volume and wear rate were calculated based on the tool wear measurements. Cutting forces were collected and cutting chips were observed under the SEM and the optical microscope.

EXPERIMENTAL RESULTS

Tool Wear Results from the EBID Measurement

Wear results for cutting 6061 Al, 1215 steel and 416 stainless steel measured by EBID are shown in Figures 1-3. The analysis detail of EBID images can be found in [3]. From the EBID images of tool wear, it can be seen that wear patterns are different for 6061 Al, 1215 steel and 416 stainless steel. Figure 1 shows the worn profile of diamond tool cutting 6061 Al. The cutting edge was getting rounder and the wear land was gradually increased with the cutting distance. The angle between wear land and flank face is about 2°. The worn profile for 1215 steel is much different, as shown in Figure 2. A wear land, 25° away from the flank face, is formed after 5 m cutting. Gradual retracted wear lands are parallel to each other. The worn pattern for 416 stainless steel (Figure 3) is similar to that for 6061 Al except a much longer wear land which forms at a 2° angle with the flank face. Compared with diamond tool cutting 6061 Al, the diamond tool for cutting 1215 steel and 416 stainless steel are worn significantly after only several meters cutting.

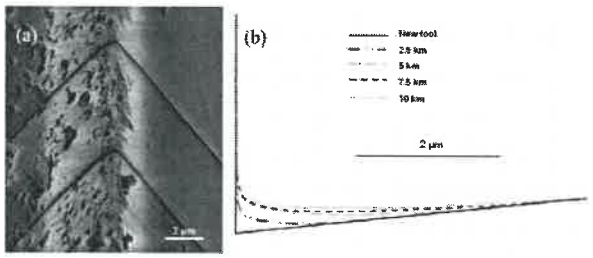

FIGURE 1. Wear result for cutting 6061 Al. (a) EBID lines on a worn diamond tool after cutting 7.5 km 6061 Al; (b) wear profiles of diamond cutting edge for cutting 6061 Al.

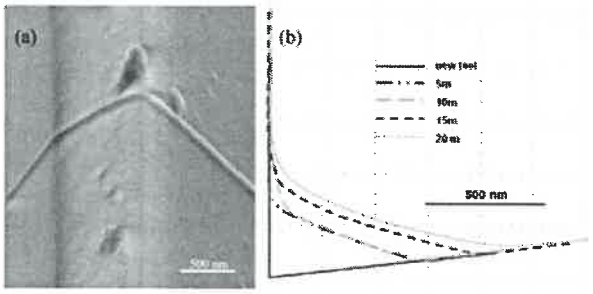

FIGURE 2. Wear result for cutting 1215 steel. (a) EBID lines on a worn diamond tool after cutting 15 m 1215 steel; (b) wear profiles of diamond cutting 1215 steel.

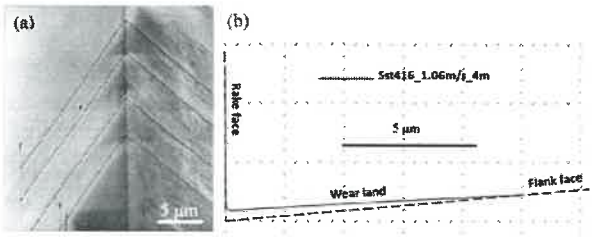

FIGURE 3. Wear result for cutting 416 stainless steel. (a) EBID lines on a worn diamond tool after cutting 4 m 416 stainless steel; (b) wear profiles of diamond cutting 416 stainless steel.

Tool Wear Results from the White Light Interferometer Measurement

To measure the tool wear more efficiently, a white light interferometer was used to supplement the EBID measurements. For the interferometer measurement, wear area can be tracked easily through the change of interference fringes. Figure 4 is an example of wear land length measurement using white light interferometer.

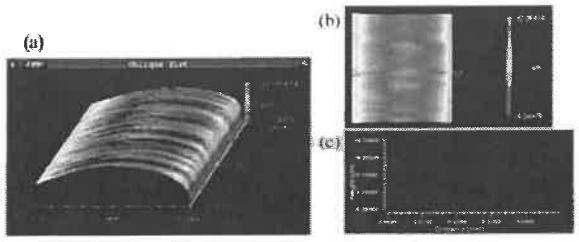

FIGURE 4. Wear land of the diamond tool after cutting 45 m 416 stainlesss steel at 2.13 m/s measured using white light interferometer. (a) Oblique plot; (b) surface profile; (c) wear land length measurement.

Wear Rate Comparison

After the worn area and worn volume is determined, wear rate was calculated as volume lost divided by contact time. For both 1.06 m/s and 2.13 /s cutting on 416 stainless steel, only the first five data points are used to calculate the wear rate. Figure 5 is the wear rate comparison for three different workpieces. The wear rate for 416 stainless steel is 18 times higher than that of 1215 steel and 2558 times higher than that of 6061 Al. The wear rate for 2.13 m/s and 1.06 m/s for cutting 416 stainless steel are of the same order. Compared with 6061 Al, the cutting distance for 1215 steel and 416 stainless steel are very short, so the worn volume caused by the abrasive wear can be ignored. The high wear rate is thought to be due to the thermal-chemical diamond wear effect.

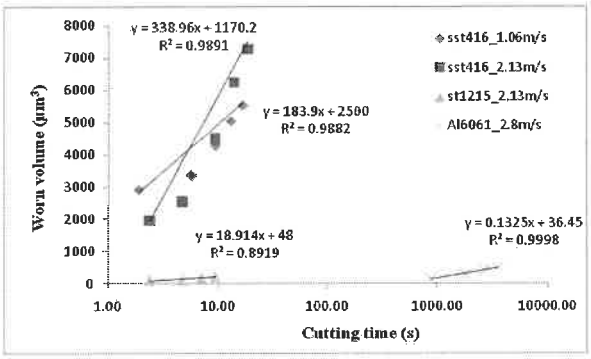

FIGURE 5. Wear rate comparison for cutting different workpiece materials.

Tool Forces for Cutting 416 Stainless Steel

For the 416 stainless steel cutting, tool forces changed dramatically. The thrust force and cutting force were stable only for a relatively short cutting distance. Figure 6 shows the tool force plots for 2.13 m/s cutting. For the first 0-5 m cutting, there is a gradual increase in both thrust force and cutting force (Figure 6a). This is due to the increased cutting width which is a result of the misalignment of the workpiece and the diamond tool. The thrust force and cutting force reached the steady state during the following cutting until to 35 m (Figure 6b and c). After 35 m, the cutting process became unstable. Figure 6d shows that the thrust force and cutting force changed periodically. The thrust force decreased while at the same time the cutting force increased. It appears that the tool does not cut but only rubs the workpiece intermittently. From SEM observations, adhering material layers were found on the rake face. This is thought to be due to built-up layers formed, although the cutting time is short. The built up edge plows on the workpiece surface, while the tool is kept feeding-in and pushed by the workpiece. The thrust force is getting larger and larger until the tool does cutting again, and very thick chips are generated.

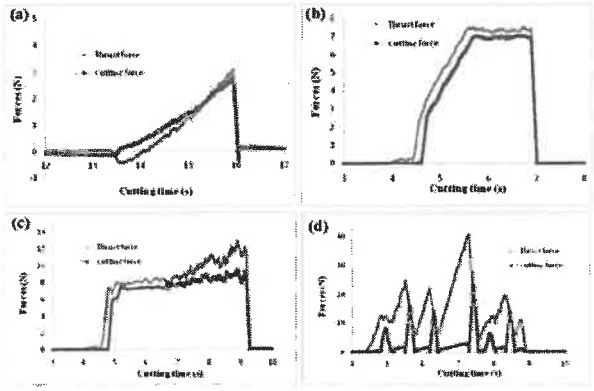

FIGURE 6. Tool forces at 2.13 m/s cutting 416 stainless steel for 0-5 m (a), 10-15 m (b), 15-25 m (c), 35-45 m (d) cutting distance.

Chips for Cutting 416 Stainless Steel

Thickness and surface features of the cutting chips changed remarkably during the cutting process for 416 stainless steel. Figure 7 shows some optical images of cutting chips from 15-25 m cutting at 2.13 m/s, while Figure 8 shows the images of 35-45 m cutting at the same cutting speed. Long and continuous chips are generated during 15-25 m cutting. The thickness of the chip is about 3 μm. Small grooves are observed on the shiny side which contacts the rake face of the cutting tool. For 35-45 m cutting, the chips are getting thicker.

Figure 8a shows chips with different thickness. The thickness of the thickest chip is about 13 μm. It also can be seen that the grooves on the surface are getting deeper and wider. More flaws are found, indicating the increased roughness of machined surface. The depth of cut was 1 μm in all cases.

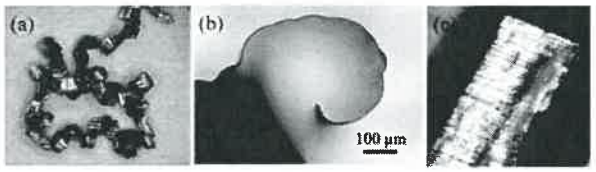

FIGURE 7. Cutting chips from 15-25 m cutting 416 stainless steel at 2.13 m/s. (a) Lower magnification image showing long continuous chips; (b) higher magnification image (80×) showing chip thickness; (c) image at 250× showing features on the chip surface of shiny side.

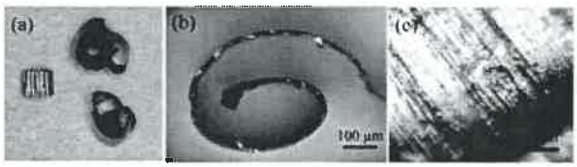

FIGURE 8. Cutting chips from 35-45 m cutting 416 stainless steel at 2.13 m/s. (a) Lower magnification image showing three kinds of chips with different thickness; (b) higher magnification image (80×) showing the thickness of the thickest chip; (c) image at 250× showing features on the chip surface of shiny side.

Liu et al. studied the diamond tool wear during 1D vibration assisted cutting on stainless steel 420. It was concluded that adhesion of workpiece material on the cutting edge plays a very important role in the cutting process [4]. This is consistent with the observation in the current work.

CONCLUSION

Conventional orthogonal diamond cutting on ferrous material is described in this work. 1215 steel and 416 stainless steel were selected as the target material. To separate the abrasive wear effect, 6061 Al with comparable hardness is selected as the baseline material. Microstructures of the workpiece materials show that 6061 Al has more and larger hard particles than 1215 steel and 416 stainless steel. From the quantitative measurement obtained using EBID, gradual wear profiles can be drawn from the EBID images directly. The tool wear pattern for cutting 416 stainless steel is similar to that for 6061 Al, while 1215 steel has a different worn profile. The wear rate of a diamond tool cutting 416 stainless steel is about three orders higher than that for cutting 6061 Al and 18 times higher than that for 1215 steel under similar cutting conditions. For cutting experiments on 416 stainless steel, tool forces and cutting chip images indicate that steady state cutting can only last for very short cutting distances. After a few tens of meters, the cutting process becomes unstable and the diamond tool plows and rubs on the workpiece surface. This is attributed to an adhesive layer formed on the rake face.

ACKNOWLEDGEMENTS

This project is funded by a grant from the National Science Foundation (CMMI-0800560).

REFERENCES

[1] Thornton AG, Wilks J. Clean surface reactions between diamond and steel. Nature. 1978; 274: 792-793.

[2] Paul E, Evans CJ, Mangamelli A, McGlauflin ML, Polvani RS. Chemical aspects of tool wear in single point diamond turning. Prec. Eng.. 1996; 18: 4-19.

[3] Shi M, Lane B, Mooney CB, Dow TA, Scattergood RO. Diamond tool wear measurement by electron beam induced-deposition. Prec. Eng.. 2010;34:718-721.

[4] Liu XD, Ding X. Diamond turning of stavax/glass assisted by ultrasonic vibration. SIMTech Technical Report, 2002.

ULTRA PRECISION SHAPING OF COMPLEX PROTOTYPES WITH MULTI FREEFORM SURFACES

Ralf Steinkopf[1], Andreas Kolbmueller[1], Andreas Gebhardt[1], Stefan Risse[1], Ramona Eberhardt[1], Andreas Tuennermann[1]
Karsten Lindig[2], Hans-Juergen Dobschal[2], Guenter Rudolph[2]

[1]Fraunhofer Institute for Applied Optics and Precision Engineering IOF, Germany
[2]Carl Zeiss AG, Corporate Research and Technology, Germany

INTRODUCTION

Optical designs for head-mounted devices benefit to a large extent from the use of freeform surfaces and often result in complex designs with two or three freeform surfaces in one single optical element. Prototypes are a convenient way to verify the optical design. But a number of things have to be taken into account.

Conventional designs with many optical elements offer the possibility of aligning the optical parts at the expense of greater installation space. But alignment processes are not feasible for highly complex prototypes – all the optical surfaces have to be realized in one single device. This means that the geometrical tolerances of the optical surfaces need to be specified tighter than usual and references must be used to ensure the positions of each optical surface with respect to their positions relative to each other.

This paper shows that by shaping with diamond tools and applying references at the part itself or the fixture, surface deviations far below 1 µm p.-v. and micro roughness's better than 10 nm rms can be achieved.

DATA TRANSFORMATION, COORDINATE SYSTEMS AND REFERENCES

The process chain for the manufacturing of prototypes with freeform elements contains several steps in which different coordinate systems are used and the data sometimes even must be transformed into different data types. The important data transfer stations are optical design, mechanical design (CAD), tool-path programming (CAM) and metrology. For rotationally symmetric optics, this chain is easy to handle. A line is used to describe them, so the mathematical formulae are straightforward, or in case of point clouds, the number of points is moderate. Just five degrees of freedom must be constrained. For freeforms, the situation is different. The complete surface must be described and all six degrees of freedom must be constrained. There is no commercial system available which for all types of freeforms offers a sustainable solution to transfer the data in one data format through the complete process chain. Thinking of a closed storage box with accumulating information at each station would be a good metaphor. Looking now to CAD related data types like .step or .iges, we find the container. This is true at least for freeforms with continuous surfaces and reasonable slopes. For other types of freeforms, more suitable solutions should be chosen. Working with one consistent file format over the whole process chain would be the ideal way.

But at least at the end of the process chain, the surface must be transformed to points, because the machine want to be fed with points and after manufacturing, the measuring machine works out points in the first instance.

However, the less the data is transformed to other file types, the more often random errors and systematic errors are avoided.

The shaping of the prototype is done with a Precitech FF700 ultra precision freeform machine. This machine opens up the possibility of using the same setup for turning and shaping processes and is paving the way to achieve very tight tolerances between reference surfaces and optical surfaces.

Different types of references are chosen for different tasks. A good method for complex prototypes is the use of fixed references on the part itself. These references remain during manufacturing and measurement but often have to be removed before assembly. But as long as one part has these references, it is very convenient to handle the part from different sides or in different coordinate systems, as often happens during machining and measurement. To make sure that mechanical deformations don't interfere with the results, FEM simulations are used to verify beforehand if the expected

deformations of the quality area are well beyond the limits of the tolerance budget [Figure1].
Thin parts, however, like eyeglasses, are easily deformable, so a fixed reference will not work. An alternative is to implement leading edges. These edges are used to adjust the part in the clamping fixture. Once adjusted, part and fixture remain as one unit during manufacturing and measurement. References for both processes can be machined easily on the fixture itself. It is clear that tight tolerances between leading edges and optical surfaces are the pre-condition for good systems.

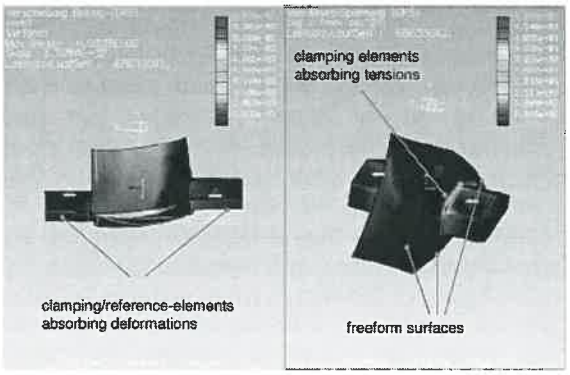

FIGURE1: FEM Simulation of an optical element with three freeform surfaces. The simulation shows how an irregularity of 10 µm at one of the reference and clamping elements is absorbed from both elements during clamping in a "perfect" fixture.

Looking at this topic in more detail, see-through head mounted displays are a good freeform demonstrator. They are used to display information, such as maps or graphics, while viewing the real scene. One possible optical design of such eyeglasses consists of two freeforms at the edge of a spherical body and one diffractive element in the center [Figure2].

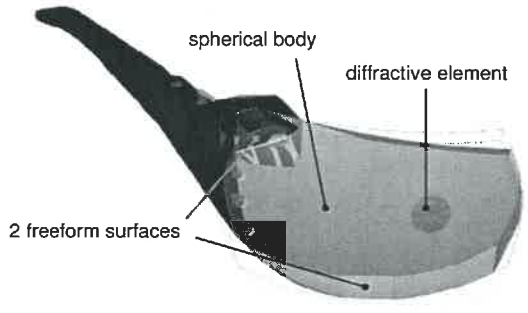

FIGURE2: CAD model of the eyeglass with several optical elements

The optical design software produces a CAD file by generating supporting points at the surface and interpolating with spline functions between these points. The resulting file represents all the optical surfaces with respect to their positions relative to each other and is a very convenient starting point for creating a volume model [Figure3].
However, it is important to make sure that the interpolation between the points, resulting from generating the surface, does not modify the optical design above the tolerance limit given for this step. The difference between the original points and the resulting surface heights at these points must be calculated and verified.
In some cases, it is necessary to extend the surface beyond the range given from the optical model. Such operations must be done very carefully. Extrapolation is far more susceptible to faults than interpolation.

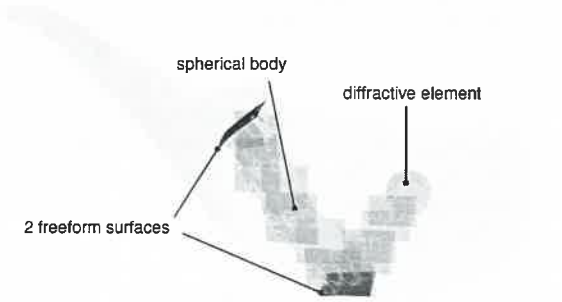

FIGURE3: Exported surfaces from optical design software are the input for the mechanical design.

Because of the easily deformable nature of the eyeglasses, the references for shaping and measuring were placed on the fixture in this case. The references consist of two flats and one hole. Flat number one is located on the backside of the fixture. This flat gives the Z-position and prevents tilt in the Y and Z axes. The other reference flat is used to gain information about the tilt in the X axis direction. The centre of the reference hole then represents the zero position of the machine coordinate system and the datum point of all optical surfaces.
After modeling the eyeglasses and the fixture, all parts were virtually assembled in the CAD system. At this point, the distance between the center of each optical surface and the coordinate origin at the ultra precision machine can be calculated. However, it must be rectified by the real positions of the references. To

recalculate the positions, the clamping fixture is measured after manufacturing with a coordinate measuring machine. Identified in this way, the error values must be added to the origin calculation. After these steps, the freeform surfaces are located at the known positions and the data is forwarded to the CAM software.
Depending on the CAM software, CAD files or point clouds can be forwarded. The CAM software is responsible for generating the tool path for the ultra precision machining. The software adds the radius of the tool to the surface and then transforms the surface data to points. Looking at these points in chronological order, they form mostly rectangular or spiral shapes – the tool-path of the machine.

ULTRA PRECISION MACHINING OF FREEFORM SURFACES AND REFERENCES

Single point diamond turning machines are the common manufacturing technique for various optical elements. Typically, applications range from infrared to near infrared wavelengths. But modern machines and finishing techniques today enable application in VIS and even UV light [1]. The materials span from crystals (e.g. germanium) to non-ferrous metals (e.g. aluminium) to polymer (e.g. PMMA). First experiments show that with the assistance of special tools and ultrasonic equipment, even steel and extreme hard ceramics like wolfram carbide can be machined [2].
Unlike conventional optics manufacturing techniques, where it is easy to make flats and spheres and – with difficulty – aspheres, there are almost no limits for ultra precision machining. State of the art machines with three to five axes work as efficient freeform generators. The definitions for freeform surfaces are not yet standardized, but all types have one thing in common – no center of rotation exists. This means that turning processes are not always the best choice as a manufacturing method. The advantage of turning is the fast and reproducible process. Even tiny tools achieve very good processing times because of the high cutting speed. Rastering processes on the other hand, as known from milling or shaping, have very low throughput times. The tool has to go over the surface line by line, and no linear axis can compare to the turning speed and simultaneous smooth run of a rotational axis. For this reason, turning is the preferred manufacturing technique, but some shapes need special procedures. One of these is shaping. Like milling, this process uses three linear axes to go over the surface, but the tool does not spin around an axis. On the contrary, no rotation is involved. This makes it interesting for step slopes, tiny parts, or undercuts, where rotating tools need too much space to operate [3]. Another benefit from shaping is the easy and fast setup process for the diamond tool. And even typical problems like vibrations from the fast rotating tool or, in the case of turning, from the rotation of asymmetric parts, are non-existent. The three linear axes move along the raster path in a simultaneous motion. Often the part is mounted on an air bearing spindle, so it is possible to use this setup for shaping and turning.

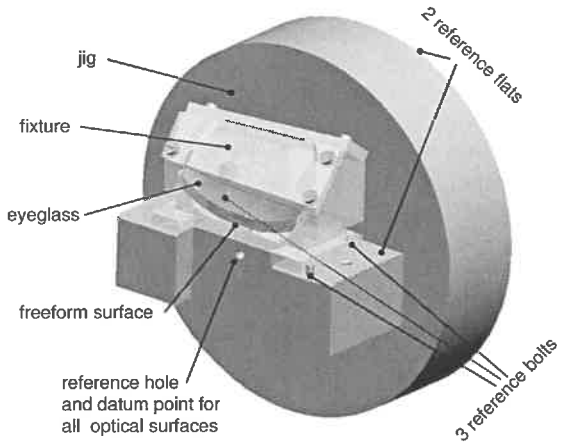

FIGURE4: Jig, fixture, and eyeglass built as one unit during all processes

However, raster processes mean long cutting times. In the case of the eyeglasses, two small areas with each just 50 mm² size had a total throughput time of 20 hours. This makes it important to monitor the environmental conditions. Typically, temperature shifts in periods of 30 to 120 minutes are not seen on parts with throughput times of ten minutes, as is typical during turning. But looking to cutting times measured in hours, such as for shaping processes, they will be observed on the measuring plot. A tight climate regime, in the range of ±0.25K, is necessary here.
Due to the two freeform surfaces on different edges of the eyeglasses, two different clamping fixtures must be used. This is far from the perfect way. To minimize the clamping failures, a special jig was designed and mounted on the standard vacuum chuck. The clamping device was positioned with leading bolts on this jig and mounted there. The jig holds the references

which are used to indicate the zero position at the coordinate system for ultra precision machining and measurement. Jig, clamping fixture, and eyeglass are then one unit during all processes (machining and measuring) on the respective surface performed [Figure4]. After finishing the first freeform surface, the next clamping fixture was positioned and mounted on the jig.

MEASUREMENT OF FREEFORM SURFACES

The measurement of the freeform surfaces is realized with the $2^{1/2}$d tactile measurement system UA3P from Panasonic, which works with almost interferometric accuracy and gives a fast and reliable overview of the shape deviation of optical surfaces.

However, transferring the prototype to the measurement machine means losing the position of the freeform surfaces. To identify the new positions, two ways are proven and tested.

The first way is to manufacture reference marks together with the measurement object. If the optical surface and reference marks are manufactured in one machine setup, a tight tolerance between them can be expected. A good example for such references is the use of three spheres located around the quality surface. By knowing the positions of these spheres, it is easy to calculate the position of the freeform surface [4].

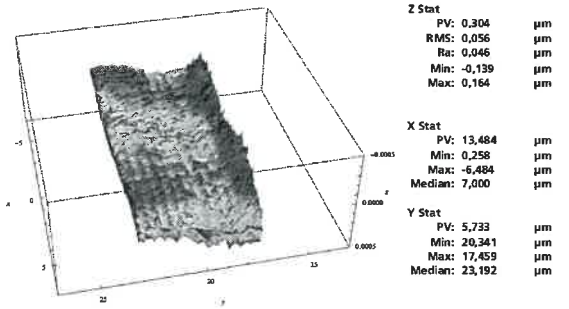

FIGURE5: Tactile measurement of one freeform surface. After eliminating runaway values and applying a moving average filter, the freeform surface is measured with 0.3µm p.-v. shape deviation.

The second way of measurement analysis was chosen for the eyeglass application. In this case, the references are carried out more like leading edges and are not manufactured in the same setup with the optical surface. This means that the error values are much larger. They typically range from 10 to 100 µm, depending on manufacturing tolerances and the length of the tolerance chain. To calculate the residuals, there must be a fit routine involved which allows a shifting and tilting of the surface in the range of the estimated error values. But it is important to check in advance that the expected values are well beyond the limits for the position error of the surfaces.

The eyeglasses, still mounted in the jig and clamping fixture, were positioned in the measurement machine. The leading edges of the jig were used to adjust the angle with respect to the measuring coordinate system. The reference hole was used to find the zero position. Therefore a reference ball with a bigger diameter than the hole was put on the edge and could be measured with the $2^{1/2}$d tactile measurement system.

The measurements of the eyeglasses at both freeform surfaces have shown that the shape deviation is well beyond 1 µm p.-v. [Figure5] and 10 nm rms surface roughness. The estimated position errors lies beyond 20 µm.

CONCLUSION

Highly complex prototypes with more than one freeform surface can be realized precisely with ultra precision shaping. To optimize the results, a process chain was chosen in which all the information, starting with the optical design, is stored and accumulated in a CAD related data format. The use of references ensures that the different quality areas of the prototype are manufactured in the correct position with respect to each other. Measurements with a tactile measuring system have shown that freeform surfaces with shape errors in the sub µm range p.-v. could be achieved.

REFERENCES

[1] Risse, S. et al, NiP Plated Mirrors for Astronomy and Space. Proc. of the 7th EUSPEN Bremen 2007; pp. 348-351

[2] Suzuki, H. et al, Precision Cutting of Aspherical Ceramic Molds with Micro PCD Milling Tools. CIRP Annals - Manufacturing Technology, Volume 56, Issue 1, 2007, pp. 131-134

[3] Steinkopf, R. et al, Metal Mirrors with Excellent Figure and Roughness. Optical Fabrication, Testing, and Metrology III. Proceedings of the SPIE, Volume 7102, pp. 71020C-71020C-12 (2008).

[4] Gebhardt. A. et al, Manufacturing of Freeforms with Well Defined Reference Structures. Category Ultra precision Machining, ASPE 2009, Annual Meeting

Authors Index

Abe, Kohzo 404
Achterberg, Jaron 196
Aguilar-Martin, Juan Jose 269
Ahn, Da Hoon 223, 242
Akillian, Mireille 408
Al Husseini, Abdul Mohsen 408
Ali, Md.A. Hazrat 396
Alzaydi, Ammar Ayad 117
Amin-Shahidi, Darya 121, 254
Aoyama, Hisayuki 85, 200
Arakawa, Shuichi 356
Arneson, David A. 129
Assaid, Thomas S. 25
Baas, Michiel 144
Babelay, Edwin F. 25
Baek, Sungtaek 223
Barber, Zeb 46
Barkman, William E. 25
Bauza, Marcin B. 73
Beaucamp, Anthony 57
Behrens, Leif 285
Berg, Trenton 46
Borchardt, Bruce R. 42, 125
Bos, Edwin 65
Boyden, Edward S. 246
Brouns, Derk S. G. 81
Brouwer, Dannis M. 226
Bucci, Brian A. 109
Bui, Chinh Ba 305, 317
Bulla, Benjamin 49
Burge, James H. 29, 261
Caskey, Gregory W. 269
Ceglarek, Darek 321
Chang, Wenlong 13
Chase, Steven 180
Cheung, Chi-Fai 281
Choi, Doo-Sun 435
Choi, Woohyuck 223
Chou, Y. Kevin 277
Chun, Byong-Sun 242
Chung, Sung-Chong 152, 156, 160
Cole, Daniel G. 109
Cuerden, Brian 261
Cullinan, Michael A. 333, 411
Culpepper, Martin L. 192, 333, 337, 411
Dambon, Olaf 49
Daniel, Cody R. 333
Davies, Angela D. 148
Davies, Matthew A. 443
Davis, Peter J. 273
de la Maza, Borja 77
Denkena, Berend 285, 289
Dergance, Michael J. 133, 246
DiBiasio, Christopher M. 337
Dixon, Robert Brent 188
Dobschal, Hans Juergen 455
Doki, Kae 377
Donker, Rilpho L. 81
Donmez, M. Alkan 37, 309
Dorozhovets, Nataliya 325
Dow, Thomas A. 188. 439, 451
Dubas, Brandon 265
Dutterer, Brian S. 443
Eberhardt, Ramona 53, 455
Edwards, Jack R. 188
Elfizy, Amr 117
Ellis, Jonathan D. 144
Emerick, Matthew 133
Engin, Serafettin 117
Enomoto, Toshiyuki 219
Erkorkmaz, Kaan 117
Ess, Markus 250
Estler, W. Tyler 42, 125
Farahi, Faramarz 148
Fesperman Jr., Ronnie R. 37, 309
Forest, Craig R. 133, 180, 246, 258, 345
Frank, Thomas 230
Funaki, Tatsuya 208
Furushiro, Naomichi 431
Furutani, Katsushi 356
Füßl, Roland 325
Gafford, Joshua B. 411
Gagnon, Eric 133
Ganguly, Vasishta 389
Garrard, Kenneth P. 415
Gebhardt, Andreas 455
Georgiadis, Kyriakos 393
Gleason, Benn 265

Go, Yasuyuki 427
Graham, Jaymes 93
Graziano, Arthur 164
Greenfield, Nathan 46
Gweon, Dae-Gab 223, 242
Ha, Tae-Ho 329
Hackel, Tobias 230
Hahmann, Dennis 289
Hamaguchi, Tetsuya 348, 352, 364, 385
Hamilton, James H. 273
Hastings, D. J. 93
Hata, Naoya 200
Hattori, Shuntaro 348
Hayashi, Terutake 293
He, Dongjue 204
He, Peng 393
Her, Ting-Hua 148
Higuchi, Masahiro 431
Hirata, Shinnosuke 200
Ho, L. T. 281
Hocken, Robert J. 121, 254
Hwang, Jooho 305, 313, 317
Ikram, Javaid 148
Ishibashi, Masato 341
Ishida, Tohru 447
Ito, So 85
Iwata, Futoshi 85
Jang, Sung-Hwan 435
Jansen, Maarten J. 140
Jared, Bradley H. 234
Je, Tae-Jin 435
Jeon, Eun-Cheae 435
Jonker, Jan Ben 226
Joslin, Andrew 164
Joswig, Andreas 53
Kagawa, Toshiharu 208
Kaito, Hirotoshi 364
Kajihara, Yusuke 373
Kang, Junmo 168
Karandikar, Jaydeep M. 172
Kasper, Ann 136
Kästner, Jan 289
Kato, Tomonori 208
Katsuki, Akio 69, 396
Kawagoishi, Norio 69
Kawamoto, Yasuhiro 364
Kawasaki, Kiyotaka 176
Kawashima, Kenji 208
Kaylor, Brant 46
Khim, Gyungho 238
Kikuchi, Atsunori 381
Kim, Gyung-Bum 360
Kim, Hyo Soo 389, 419
Kim, Hyo-Young 242
Kim, Hyunchang 223
Kim, Nam-Ho 389
Kim, Sug-Whan 261
Kishida, Hirotaka 293
Klocke, Fritz 49, 393
Knapp, Byron R. 129
Kobayashi, Yoshikazu 176
Kodandaramaiah, Suhasa B. 246, 258
Köhler, Jens 285, 289
Kokubo, Ken 293
Kolbmueller, Andreas 455
Kondo, Eiji 69
Kondo, Tsukasa 176
Kong, L. B. 281
Kosugi, Nobumasa 404
Kou, Hideyuki 85
Krawczyk, Thomas 285
Kreutzer, Philipp 325
Kuma, Yuji 404
Kumar, Uttara Vijay 17
Lane, Brandon M. 439, 451
Lee, Chan-Hong 305
Lee, Chang-Woo 329
Lee, Jae-Hak 329
Lee, Sanghoon 223
Lee, Sun Ho 223
Lee, Vincent 42, 125
Lee, Wah-Keat 372*
Li, Likai 393
Li, Melissa 180
Lin, Feilong 89
Lindig, Karsten 455
Lineberger, Jennifer Lynn 443
Ljubicic, Dean Marko 121
Lotz, Markus 230
Lu, Xiaodong 113
Ludwick, Stephen J. 109
Luo, Xichun 13

** Extended abstract unavailable at press time*

Mainuddin, Mohammad 297
Malik, Saifullah 246
Manske, Eberhard 325
Maruyama, Ryuji 21
Matsuda, Shigetaka 431
Matsumoto, A. 57
Mayr, Josef 250
McFarland, Justin T. 25
McKinnon, Michael 180
Mears, Laine 105
Medicus, Kate M. 140
Meijaard, Jaap Philippus 226
Michihata, Masaki 293
Miller, Jimmie A. 269
Misawa, Yuto 447
Mitsuda, Takehiro 348
Mizuguchi, Yuya 85
Montes-Solano, Carlos Alberto 105
Morel, Michael 81
Moroni, Giovanni 321
Mosaddegh, Peiman 184, 265
Moyer, Patrick J. 89
Moylan, Shawn P. 37, 309
Muddiman, David C. 188
Mullany, Brigid A. 297
Munnig Schmidt, Robert-Han 144, 400
Munteanu, Florin 33
Murakami, Hiroshi 69, 396
Murase, Yasuo 356
Murata, Tetsuya 176
Musgraves, David 265
Nagano, Mikinori 21
Nagano, Toshimune 373
Nagato, Keisuke 348, 352, 364, 385
Nakajima, Ryo 364
Nakamoto, Keiichi 447
Nakao, Masayuki 348, 352, 364, 381, 385
Namba, Yoshiharu 57
Ness, Dale C. 212
Nishi, Hironori 396
Novak, Erik L. 33, 277
Nowakowski, Bartosz K. 93, 97
Nunokawa, Toru 381
Ogilvie, Andrew 277
Oh, Chang Jin 29
Okada, Akira 301
Onikura, Hiromichi 69, 396
Oss, Daniel D. 129
Overcash, Jerald L. 121, 254
Painter, Howard 265
Pak, Nikita 133, 258
Panas, Robert M. 333, 411
Park, Chun-Hong 160, 238, 305, 313, 317
Park, Junkyu 223
Park, Sang-Cheon 435
Park, Won Hyun 261
Parker, Wesley C. 89
Parks, Robert E. 29
Patten, John A. 368
Peterson, Shawn C. 273
Petrò, Stefano 321
Phaneuf, Christopher R. 258, 345
Phillips, Steven D. 42, 125
Pietri, Valentine 396
Potturi, Amarnatha S. 188
Poyraz, H. Bogac 368
Ramasamy, Suresh Kumar 136
Ravindra, Deepak 368
Reese, Isaac M. 234
Reibel, Randy 46
Richardson, Kathleen A. 265
Riggs, Andrew W. 17
Risse, Stefan 53, 455
Ritchie, James M. 13
Robichaud, Guillaume 188
Roos, Peter 46
Rudolph, Guenther 455
Ryu, Shi Hyoung 423
Saad, Mohamed El-Sayed 269
Saathof, Rudolf 400
Sajima, Takao 69, 396
Sato, Tatsusi 204
Satou, Tsuyoshi 396
Sawyer, Daniel S. 42, 125
Scattergood, Ronald O. 439, 451
Schattenburg, Mark Lee 254, 408
Schmit, Joanna 33
Schmitz, Tony L. 17, 164, 172, 389, 419
Seugling, Richard M. 73, 273
Sheridan, Tim 129
Shi, Meirong 451
Shim, Jongoup 238, 313, 317

Shimada, Shoichi 427, 431
Shimoda, Makoto 352
Shinohara, Yuichiro 208
Shinshi, Tadahiko 204, 341
Shintani, Hiroyuki 356
Shirai, Kenji 176
Shu, Deming 372*
Shu, Will 13
Smeds, Kristofer 113
Smilie, P 443
Smith, Douglas T. 97
Smith, K. Scott 25
Smith, Stuart T. 73, 77, 89, 93, 97
Sohn, Alex 188, 415
Song, Chang Kyu 317
Song, Jun-Yeob 329
Soyama, Kazuhiko 21
Spaan, Henny A. M. 81
Spronck, Jo W. 144, 400
Steinkopf, Ralf 455
Steinlin, Markus 101
Stussi, David R. 216
Su, Peng 29
Sugawara, Jun 404
Sugihara, Tatsuya 219
Suleski, T. J. 443
Sun, Jining 13
Suzurikawa, Jun 385
Takahashi, Satoru 373
Takamasu, Kiyoshi 373
Takaya, Yasuhiro 293
Takeuchi, Yoshimi 447
Takiguchi, Tatsuya 61
Tanabe, Ryo 341
Tanaka, Aya 385
Telleria, Maria Jose 192
Terasaki, Kiyoshi 200
Terauchi, Shuntaro 431
Tohme, Yazid E. 184
Tomblin Jr., Johnny Edward 93
Torii, Akihiro 377
Trumper, David L. 121, 254
Tsuchiya, Kensuke 381
Tsukada, Tadashi 385
Tucker, Tommy 105
Tünnermann, Andreas 53, 455
Tursky, David A. 25
Uda, Yutaka 427
Ueda, Akiteru 377
Ueda, Masaki 61
Uehara, Minoru 341
Uemura, Kensuke 301
Unno, Hiroto 404
Uno, Yoshiyuki 301
Ushiki, Tatsuo 85
van den Bosch, P. P. J. 196
van Lierop, C. M. M. 196
Vipperman, Jeffrey S. 109
Wachtel, Peter 265
Wang, Fei 393
Wegener, Konrad 101, 250
Weikert, Sascha 101, 250
Weitz, D. 192
Whang, Kyung Hyun 435
White, William R. 277
Widdershoven, Ivo 81
Wilson, Michael John 273
Wong, Chan 105
Wood, Chris S. 212
Woody, Shane C. 73
Yamada, Tomohiro 377
Yamaga, Fumiya 21
Yamaguchi, Hitomi 168
Yamaguchi, Tomomi 431
Yamamoto, Atsushi 385
Yamamura, Kazuya 21, 61
Yamazaki, Dai 21
Yang, Raymond Hua 77
Yazzie, Dennis 234
Yeon, Jeong-Seung 360
Yi, Allen Y. 393
Yoo, Yeong-Eun 435
Yoon, Jae-Sung 435
Yu, Jong Sun 423
Yuzawa, Takashi 204
Zapata Ramos, Raúl Enrique 172
Zettsu, Nobuyuki 21, 61
Zhang, Xiaoyou 204
Ziegert, John C. 42, 105, 125, 184

** Extended abstract unavailable at press time*

ISBN 978-1-887706-56-8